Faculty of Engineering
University of Kragujevac

Ministry of Science, Technological Development and Innovation

11th International Congress
Motor Vehicles & Motors 2026
ECOLOGY - VEHICLE AND ROAD SAFETY - EFFICIENCY
Proceedings

University of Kragujevac

Department for Motor Vehicles and Motors

International Journal for Vehicle Mechanics, Engines and Transportation Systems

October 8th - 9th, 2026
Kragujevac, Serbia

11th International Congress
Motor Vehicles & Motors 2026

ECOLOGY - VEHICLE AND ROAD SAFETY - EFFICIENCY

BOOK OF PROCEEDINGS

October 8th - 9th, 2026
Kragujevac, Serbia

Publisher: The Faculty of Engineering of the University of Kragujevac
Serbia, 34000 Kragujevac, Sestre Janjić 6

For Publisher: Prof. Slobodan Savić, Ph.D.
Dean of the Faculty of Engineering

Editors: Prof. Danijela Miloradović, Ph.D.
Assist. prof. Nadica Stojanović, Ph.D.
The Faculty of Engineering of the University of Kragujevac

Technical preparation: Asisst. Prof. Nadica Stojanović, Ph.D.

Cover: Nemanja Lazarević

USB edition: Faculty of Engineering, University of Kragujevac, Kragujevac

ISBN: 978-86-6335-132-5

Year of publication: 2026.

Published on USB by: InterPrint
Aleksinačka St. nn, 34000 Kragujevac, Serbia

Number of copies: 100

CIP - Каталогизација у публикацији Народна библиотека Србије, Београд

629.3(082)(0.034.2)
621.43(082)(0.034.2)

INTERNATIONAL Congress Motor Vehicles & Motors (11 ; 2026 ; Kragujevac)
Ecology - Vehicle and Road Safety - Efficiency [Elektronski izvor] : proceedings / 11th international congress Motor vehicles & motors 2026, October 8th - 9th, 2026 Kragujevac, Serbia ; [editors Danijela Miloradović, Nadica Stojanović]. - Kragujevac : University, Faculty of Engineering, 2026 (Kragujevac : InterPrint). - 1 USB fleš memorija ; 1 x 2 x 6 cm

Sistemski zahtevi: Nisu navedeni. - Nasl. sa nasl. strane dokumenta. - Tiraž 100. - Bibliografija uz svaki rad.

ISBN 978-86-6335-132-5

a) Моторна возила -- Зборници b) Моторни са унутрашњим сагоревањем - - Зборници

COBISS.SR-ID 201905929

Publishing of this USB Book of proceedings was supported by
Ministry of Science, Technological Development and Innovation of the Republic of Serbia

Copyright © 2026 Faculty of Engineering, University of Kragujevac

This book is published online with Open Access and distributed under the terms of the Creative Commons Attribution License 4.0 (CC BY 4.0).

SCIENTIFIC BOARD

President

Prof. Danijela Miloradović, Ph.D., UniKg, FE, Serbia

Secretaries

Assist. Prof., Slavica Mačužić Saveljić, Ph.D., UniKg, FE, Serbia
Assist. Prof., Saša Milojević, Ph.D., UniKg, FE, Serbia

Members

Prof. Oday Ibraheem Abdulah, ANUni, CoE, Baghdad, Iraq
Assist. Prof. Ali Belhocine, UniMSM, FST, Mascara, Algeria
Emeritus Prof. Giovanni Belingardi, Ph.D., PoliTo, Turin, Italy
Prof. Murat Ciniviz, Ph.D., SelUni, FT, Konya, Turkey
Prof. Adrian Clenci Ph.D., UniPolBU, Bucharest, Romania
Prof. Bruno Dalla Chiara, Ph.D., PoliTo, Turin, Italy
Assoc. Prof. Aleksandar Davinić, Ph.D., UniKG, FE, Kragujevac, Serbia
Prof. Miroslav Demić, Ph.D., UniKG, FE, Kragujevac, Serbia
Prof. Jovan Dorić Ph.D., UniNS, FTS, Novi Sad, Serbia
Prof. Mohamed Ali Emam, Ph.D., HUni, FE, Cairo, Egypt
Prof. Jasna Glišović, Ph.D., UniKG, FE, Kragujevac, Serbia
Prof. Valentina Golubović Bugarski, Ph.D., UniBL, FME, Banja Luka, RS, Bosnia and Herzegovina
Assoc. Prof. Ivan Grujć, Ph.D., UniKG, FE, Kragujevac, Serbia
Prof. Rosen Hristov, Ph.D., TU Varna, Varna, Bulgaria
Prof. Aleksandra Janković, Ph.D., UniKG, FE, Kragujevac, Serbia
Assoc. Prof. Aleksandar Jovanović, Ph.D., UniKG, FE, Kragujevac, Serbia
Prof. Emrullah Hakan Kaleli, Ph.D., YTU, Istanbul, Turkey
Prof. Janez Kopač, Ph.D., UniLJ, FME, Ljubljana, Slovenia
Prof. Jovanka Lukić, Ph.D., UniKG, FE, Kragujevac, Serbia
Assist. Prof. Slavica Mačužić Saveljić, Ph.D., UniKG, FE, Kragujevac, Serbia
Assist. Prof. Saša Milojević, Ph.D., UniKG, FE, Kragujevac, Serbia
Assist. Prof. Slobodan Mišanović, Ph.D., CPTC Belgrade, Belgrade, Serbia
Prof. Alexander Novikov, Ph.D., OSUni, Orel, Russian Federation
Prof. Sreten Perić, Ph.D., UniD, MA, Belgrade, Serbia
Prof. Radivoje Pešić, Ph.D., UniKG, FE, Kragujevac Serbia
Prof. Snezana Petković, Ph.D., UniBL, FME, Banja Luka, RS, Bosnia and Herzegovina
Prof. Ralph Puetz, Ph.D., LUniAS, Landshut, Germany
Prof. Dragan Ružić, Ph.D., UniNS, FTS, Novi Sad, Serbia
Prof. Mikhail Shatrov, Ph.D., MADI, Moscow, Russian Federation
Assoc. Prof. Aleksandar Stevanović, Ph.D., UniPitt, Pittsburgh, USA
Assist. Prof. Nadica Stojanović, Ph.D., UniKG, FE, Kragujevac, Serbia
Assoc. Prof. Boris Stojić, Ph.D., UniNS, FTS, Novi Sad, Serbia
Prof. Radoje Vujadinović, Ph.D., UniMN, FME, Podgorica, Montenegro
Assoc. Prof. Predrag Živanović, Ph.D., UniBG, FTTE, Belgrade, Serbia

ORGANIZATIONAL BOARD

President

Asst. Prof., Nadica Stojanović, Ph.D., UniKg, FE, Serbia

Secretaries

Assist. Prof., Slavica Mačužić Saveljić, Ph.D., UniKg, FE, Serbia
Assist. Prof., Saša Milojević, Ph.D., UniKg, FE, Serbia

Members:

Prof. dr Jovanka Lukić, UniKg, FE, Kragujevac, Serbia
Prof. dr Jasna Glišović, UniKg, FE, Kragujevac, Serbia
Assoc. Prof. dr Aleksandar Davinić, UniKg, FE, Kragujevac, Serbia
Assoc. prof. dr Aleksandar Jovanović, UniKg, FE, Kragujevac, Serbia
Assoc. prof. dr Ivan Grujić, UniKg, FE, Kragujevac, Serbia

MVM2026 CONGRESS ORGANIZERS

Faculty of Engineering of the University of Kragujevac
Department for Motor Vehicles and Motors, FE Kragujevac
International Journal “Mobility & Vehicle Mechanics”

MVM2026 CONGRESS PATRONS

Ministry of Science, Technological Development and Innovation of the Republic of Serbia
Faculty of Engineering of the University of Kragujevac

MVM2026 CONGRESS REVIEWERS

Prof. dr Oday Ibraheem Abdulah, UniBAG, CoE, Baghdad, Iraq
Assist. Prof. dr Ali Belhocine, UniMSM, FST, Mascara, Algeria
Emeritus Prof. dr Giovanni Belingardi, PoliTo, Turin, Italy
Assoc. Prof. dr Aleksandar Davinić, UniKG, FE, Kragujevac, Serbia
Prof. dr Miroslav Demić, UniKG, FE, Kragujevac, Serbia
Prof. dr Jovan Dorić, UniNS, FTS, Novi Sad, Serbia
Prof. dr Jasna Glišović, UniKG, FE, Kragujevac, Serbia
Prof. dr Valentina Golubović Bugarski, UniBL, FME, Banja Luka, RS, Bosnia & Herzegovina
Assoc. Prof. dr Ivan Grujić, UniKG, FE, Kragujevac, Serbia
Prof. dr Rosen Hristov, TU Varna, Varna, Bulgaria
Assoc. Prof. dr Aleksandar Jovanović, UniKG, FE, Kragujevac, Serbia
Prof. dr Janez Kopač, UniLJ, FME, Ljubljana, Slovenia
Prof. dr Jovanka Lukić, UniKG, FE, Kragujevac, Serbia
Assist. Prof. dr Slavica Mačužić Saveljić, UniKG, FE, Kragujevac, Serbia
Assist. Prof. dr Saša Milojević, UniKG, FE, Kragujevac, Serbia
Prof. dr Danijela Miloradović, UniKG, FE, Kragujevac, Serbia
Assist. Prof. dr Slobodan Mišanović, CPTC Belgrade, Belgrade, Serbia
Prof. dr Radivoje Pešić, UniKG, FE, Kragujevac Serbia
Prof. dr Snezana Petković, UniBL, FME, Banja Luka, RS, Bosnia & Herzegovina
Prof. dr Dragan Ružić, UniNS, FTS, Novi Sad, Serbia
Assoc. Prof. dr Aleksandar Stevanović, UniPitt, Pittsburgh, USA
Assist. Prof. dr Nadica Stojanović, UniKG, FE, Kragujevac, Serbia
Assoc. Prof. dr Boris Stojić, UniNS, FTS, Novi Sad, Serbia

FOREWORD

For 47 years, a traditional international gathering - originally known as a Symposium and, since 2006, as the "Motor Vehicles and Motors" Congress - has been held biennially at the Faculty of Engineering (formerly the Faculty of Mechanical Engineering) of the University of Kragujevac. This year, the 11th International Congress "Motor Vehicles and Motors" took place in Kragujevac on October 8th–9th, 2026, under the traditional motto: "Ecology – Vehicle and Road Safety – Efficiency".

A large number of authors from both the country and abroad responded to the organizers' invitation, resulting in numerous high-quality submissions across the event's core areas: "Power Train Technology," "Vehicle Design and Manufacturing," "Vehicle Dynamics and Intelligent Control Systems," "Driver/Vehicle Interface, Information Systems, and Assistance Systems," and "Transport Challenges in Emerging Economies." Additionally, two topics were officially introduced for the first time: "Artificial Intelligence in Automotive Technology" and "Autonomous Vehicles".

A total of 63 papers were accepted for presentation following a rigorous peer-review process. The presentations were organized into sessions, including a newly introduced poster session dedicated to students and young researchers.

The Congress organizers extend their special gratitude to the distinguished scientists in the fields of motor vehicles and transportation who agreed to deliver three inspiring introductory lectures addressing the heart of contemporary issues in the sector: prof. dr Ralph Putz (Landshut University of Applied Sciences, Germany), prof. dr Aleksandar Stevanović (University of Pittsburgh, USA), and prof. dr. Isak Karabegović (Academy of Sciences and Arts of Bosnia and Herzegovina, Bosnia and Herzegovina).

We extend our sincere gratitude to the esteemed members of the Congress Scientific Committee—who also served as reviewers for the papers submitted for presentation—for their significant contribution to the overall quality of the accepted papers.

The organization of the Congress was once again supported by the Ministry of Science, Technological Development and Innovation of the Republic of Serbia, the Faculty of Engineering of the University of Kragujevac, and the International journal “Mobility & Vehicle Mechanics” and we sincerely thank them for their support.

Scientific Board and Organizational Board of MVM2026 Congress

PREDGOVOR

Već 47 godina, svake druge godine, na Fakultetu inženjerskih nauka (nekada Mašinskom fakultetu) Univerziteta u Kragujevcu održava se tradicionalan međunarodni skup, nekada nazivan Simpozijum, a od 2006. godine - Kongres „Motorna vozila i motori“. Ovogodišnji, 11. Međunarodni kongres „Motorna vozila i motori“ održan je u Kragujevcu od 8. do 9. oktobra 2026. godine, uz tradicionalni moto „Ekologija – Vozilo i bezbednost na putu – Efikasnost“.

Na poziv organizatora odazvao se veliki broj autora iz zemlje i inostranstva, što je donelo veliki broj prijavljenih kvalitetnih radova iz glavnih oblasti skupa: „Tehnologija pogonskog sistema“, „Dizajn i proizvodnja vozila“, „Dinamika vozila i inteligentni upravljački sistemi“, „Interfejs vozač/vozilo, informacioni sistemi i sistemi za pomoć“, „Transportni izazovi ekonomija u usponu“, uz prvi put zvanično promovisane teme – „Veštačka inteligencija u automobilskoj tehnologiji“ i „Autonomna vozila“.

Ukupan broj od 63 radova je prihvaćen za prezentaciju posle rigoroznog procesa recenziranja. Rad je organizovan po sekcijama, uz prvi put promovisanu poster sekciju namenjenu za studente i mlade istraživače.

Organizatori Kongresa su posebno zahvalni istaknutim naučnicima iz oblasti motornih vozila i saobraćaja koji su pristali da održe tri inspirativna uvodna predavanja koja zadiru u srž savremenih pitanja vezana za vozila i saobraćaj, a to su: prof. dr Ralph Putz (Landshut University of Applied Sciences, Nemačka), prof. dr Aleksandar Stevanović (University of Pittsburgh, SAD) i prof. dr Isak Karabegović (Akademija nauka i umjetnosti Bosne i Hercegovine, Bosna i Hercegovina).

Veliku zahvalnost dugujemo našim dragim članovima Naučnog odbora Kongresa, ujedno i recenzentima radova prijavljenih za prezentaciju na Kongresu, koji su mnogo doprineli ukupnom kvalitetu konačno prihvaćenih radova.

Organizaciju Kongresa i ovog puta su podržali: Ministarstvo nauke, tehnološkog razvoja i inovacija Republike Srbije, Fakultet inženjerskih nauka Univeziteta u Kragujevcu i Međunarodni časopis „Mobility & Vehicle Mechanics“, na čemu im se iskreno zahvaljujemo.

Naučni odbor i Organizacioni odbor Kongresa MVM2026

CONTENT

INTRODUCTORY LECTURES

MVM2026-IL1	Ralph Pütz	OPERATING COSTS OF PUBLIC TRANSPORT BUSES WITH DIFFERENT PROPULSION SYSTEMS AND VARIOUS TYPES OF RENEWABLE ENERGY OVER TIME – WHERE IS THE JOURNEY HEADING?	3
MVM2026-IL3	Isak Karabegović	COLLABORATIVE ROBOTICS AND ARTIFICIAL INTELLIGENCE IN THE AUTOMOTIVE INDUSTRY: SMART ASSEMBLY AND AUTOMATED QUALITY CONTROL	13

SECTION A
Power Train Technology

MVM2026-003	Ivan Grujic Aleksandar Davinic Zeljko Djuric Jovan Doric Milan Eremija Attila Kiss Sunny Narayan	THE INVESTIGATION OF THE COMBUSTION PROCESS OF THE BLEND OF THE CONVENTIONAL DIESEL FUEL AND BIODIESEL MADE FROM THE WASTE GRAPE SEEDS	35
MVM2026-008	Željko Đurić Ivan Grujić Nadica Stojanović Snežana Petković Jelena Adžić Milan Eremija	EXPERIMENTAL INVESTIGATION OF THE COMBUSTION PROCESS AND EFFICIENCY OF A DIESEL ENGINE IN THE CASE OF BIODIESEL FUEL APPLICATION	41
MVM2026-011	Milan Eremija Ivan Grujić Danijela Miloradović Željko Đurić Svetko Milutinović Nadica Stojanović	EXPERIMENTAL ANALYSIS OF EXHAUST GAS TEMPERATURE DURING THE USE OF BIODIESEL FUEL	53
MVM2026-013	Krasimir Markov Hristo Stanchev	INVESTIGATION OF THE FUEL CONSUMPTION AND EMISSIONS OF A DIESEL ENGINE RUNNING ON DIESEL WITH AN ADDITIVE	61
MVM2026-015	Milan Eremija Zoran Ristikić Svetko Milutinović Mesud Ajanović	EXPERIMENTAL INVESTIGATION OF THE INFLUENCE OF TIRE PRESSURE ON THE ROLLING RESISTANCE COEFFICIENT OF COMMERCIAL VEHICLES	67
MVM2026-025	Marko Lučić Mirjana Grdinić-Rakonjac Radoje Vujadinović Vladimir Pajković Ivan Grujić	ENERGY USE IN MONTENEGRO'S ROAD TRANSPORT SECTOR: TRENDS, FUEL STRUCTURE AND DEPENDENCE ON PETROLEUM-BASED FUELS	77

MVM2026-030	Vladimir Kočović Živana Jovanović Pešić Miloš Pešić Jelena Đusić Dragan Džunić	TRIBOLOGICAL PERFORMANCE OF BRASS SURFACES LUBRICATED WITH NEW AND USED ENGINE OILS	85
MVM2026-034	Mihailo Đuković Saša Milojević Slobodan Savić Blaža Stojanović Horia Abaitancei	APPLICATION OF A RADIAL HYDRAULIC MOTOR IN ALTERNATIVE VEHICLE DRIVE SYSTEMS	91
MVM2026-036	Marko Kitanović Slobodan Popović Nenad Miljić Predrag Mrđa	EFFECTIVE MIXTURE COMPOSITION IN THE ANGULAR DOMAIN IN SUPERCHARGED DISI ENGINE WITH MULTIPLE INJECTIONS	111
MVM2026-037	Petar Markov Radivoje Pušara Dragan Peruničić	A SINGLE-RANGE POLYNOMIAL MODEL FOR TEMPERATURE-DEPENDENT MIXTURE PROPERTIES IN COMBUSTION ENGINES WITH VARIABLE EGR RATES	125
MVM2026-038	Dragan Peruničić Petar Markov Radivoje Pušara	MODELING OF SPECIFIC HEAT RATIO FOR DISI ENGINES WITH COMPLEX MIXTURE FORMATION AND HIGH EGR RATES	139
MVM2026-041	Predrag Mrđa Slobodan Popović Nenad Miljić Marko Kitanović	EXPERIMENTAL AND CFD-BASED INVESTIGATION OF VAPOUR POCKET FORMATION IN AN INTERNAL COMBUSTION ENGINE COOLING SYSTEM	155
MVM2026-042	Nenad Miljić Predrag Mrđa Slobodan J. Popović	QUANTIFYING IMEP EVALUATION ERROR INDUCED BY PIEZOELECTRIC PRESSURE SENSOR AGEING IN INTERNAL COMBUSTION ENGINE INDICATION	165
MVM2026-051	Saša Milojević Marija Rafailović Michal Loman Branislav Šarkan Ján Vrábel Slobodan Savić	SAFETY AND OPERATIONAL CONSIDERATIONS FOR COMPOSITE HYDROGEN AND CNG STORAGE CYLINDERS IN VEHICLES	175
MVM2026-068	Mitar Mišić Stjepan Galamboš Boris Stojić Jovan Dorić Luka Sekicki	DEVELOPMENT OF AN ELECTRONIC MEASUREMENT SYSTEM FOR TURBOCHARGER WASTEGATE ACTUATOR RESPONSE-TIME TESTING	185
MVM2026-071	Mitar Mišić Stjepan Galamboš Jovan Dorić Boris Stojić Luka Sekicki	DESIGN AND IMPLEMENTATION OF A TEST BENCH FOR EVALUATING THE DYNAMICS OF PNEUMATIC WASTEGATE ACTUATORS	193

SECTION B
Vehicle Design and Manufacturing

MVM2026-006	Gordana Bogdanović Aleksandar Radaković Dragan Čukanović Petar Knežević Aleksandar Nešović	VARIATIONAL SHEAR CONTROL IN ESL–HSDT LAMINATES FOR AUTOMOTIVE STRUCTURES	203

MVM2026-007	Gordana Bogdanović Aleksandar Radaković Petar Knežević Dragan Čukanović Marko Milošević	FATIGUE ANALYSIS OF MATERIALS AND METHODS FOR CYCLE COUNTING UNDER ARBITRARY LOAD HISTORIES	211
MVM2026-009	Julija Boskovic Ivan Grujic Stefan Djuric Nadica Stojanovic Bogdan Zivkovic Milan Ivkovic Suzana Petrovic Savic	DEVELOPMENT OF AN EXPERIMENTAL FIVE-AXIS CNC SYSTEM USING STEPPER MOTORS	219
MVM2026-012	Saša Vasiljević Jasna Glišović Slobodan Vasiljević	ANALYSIS OF EXPERIMENTAL METHODOLOGIES FOR TESTING INNOVATIVE BRAKE SOLUTIONS	235
MVM2026-016	Ljubica Spasojević Zorica Djordjević Sonja Kostić Saša Jovanović	MODAL ANALYSIS OF A COMPOSITE CRANKSHAFT FOR AN INTERNAL COMBUSTION ENGINE (ICE)	245
MVM2026-017	Zvonko Petrović Suzana Petrović Savić Milica Tufegdžić Nikola Kostić Milena Petrović	MATHEMATICAL MODELING OF HYDRAULIC DRIVE FOR THE MITSUBISHI RV-2FRL INDUSTRIAL ROBOT: INFLUENCE OF MOMENT OF INERTIA ON SERVO VALVE RESPONSE TIME	253
MVM2026-022	Marko Delić Vesna Mandić Nada Ratković Nikola Komatina Dušan Arsić Nikola Kastratović	ANALYSIS OF THE INFLUENCE OF IMPORTANT FORMING PARAMETERS IN SHEET METAL STAMPING IN AUTOMOTIVE INDUSTRY USING FEA	267
MVM2026-024	Milan Simonović Dragan Adamović Đorđe Ivković Marko Simonović	ANALYSIS OF THE POSSIBILITY OF PREDICTING THE TENSILE STRENGTH OF ADVANCED STRUCTURAL STEELS USED IN THE AUTOMOTIVE INDUSTRY USING ARTIFICIAL NEURAL NETWORKS WITH DIFFERENT NUMBERS OF NEURONS IN THE HIDDEN LAYER	275
MVM2026-026	Nenad Petrović Živana Jovanović Pešić Dragan Džunić Vladimir Kočović Strahinja Milenković	CREATING CURVED MESHES BY HEAT-FORMING 3D-PRINTED PARTS	287
MVM2026-050	Danijela Tadić Jasna Glišović Nikola Komatina	COMPARATIVE ANALYSIS OF OBJECTIVE CRITERIA WEIGHTING METHODS FOR ELECTRIC VEHICLE EVALUATION	293
MVM2026-052	Dragan Čukanović Gordana Bogdanović Aleksandar Radaković Petar Knežević	APPLICATION, MODELLING AND BENDING ANALYSIS OF COMPOSITE LAMINATES IN MODERN VEHICLES	303
MVM2026-053	Mihajlo Jevtić Aleksandra Obradović Bogdan Todorović Nebojša Hristov Damir Jerković	FINITE ELEMENT ANALYSIS OF STRUCTURAL SUPPORT REACTIONS IN WHEELED MOBILE PLATFORM UNDER HIGH-INTENSITY IMPULSIVE LOADING	311

MVM2026-059	Dušan Milojević Nikola Kotorčević Đorđe Damljanović Nikola Živčević Dušan Arsić Fatima Živić	EFFECTS OF UNIT CELL GEOMETRY AND STRUT THICKNESS ON THE COMPRESSIVE BEHAVIOR OF 3D-PRINTED MECHANICAL METAMATERIALS	321
MVM2026-060	Nebojša Arsić Nenad Kostić Nenad Petrović Nenad Marjanović	APPLICATION OF 3D SCANNING AND CAD DEVIATION ANALYSIS AS A BASIS FOR PRESS TOOL OPTIMISATION IN THE AUTOMOTIVE INDUSTRY	325
MVM2026-061	Sandra Gajević Slavica Miladinović Nikola Mitrović Zorica Djordjević Saša Milojević Blaža Stojanović	APPLICATION OF LAMINATED COMPOSITES IN THE AUTOMOTIVE, AVIATION AND MARINE INDUSTRY	333
MVM2026-067	Luka Milić Ilija Vidović Matija Simanić Momir Drakulić Aleksandar Đurić	ADDITIVE MANUFACTURING AS A FABRICATION METHOD FOR A LIGHTWEIGHT TRACKED ROBOT PLATFORM	345
MVM2026-070	Dobrivoje Ćatić Vladimir Ćatić	A COMBINED FTA-FMEA PROCEDURE FOR PRODUCT DEVELOPMENT	355
MVM2026-073	Milan Blagojević Milan Bojović Živče Šarkoćević	REVERSE ENGINEERING OF A COMPLETE VEHICLE FOR THE DEVELOPMENT OF A MODULAR VEHICLE PLATFORM	363
MVM2026-076	Nenad Miloradović Rodoljub Vujanac Mirjana Piskulić	WAREHOUSE SYSTEMS IN THE AUTOMOTIVE INDUSTRY: A COMPARATIVE STUDY OF STORAGE SYSTEMS, HANDLING EQUIPMENT AND SAFETY CLEARANCE	369

SECTION C
Vehicle Dynamics and Intelligent Control Systems

MVM2026-001	Miroslav Demić Mikhail P. Malinovsky Andrija Vujičić	THEORETICAL-EXPERIMENTAL APPROACH TO THE DEVELOPMENT OF A METHOD FOR IDENTIFYING THE HEAT DISSIPATION RATE OF MOTOR VEHICLE SHOCK ABSORBERS	379
MVM2026-002	Aleksandar Jovanović Katarina Kukić Ana Uzelac Dušan Teodorović	DEEP Q-LEARNING ALGORITHM FOR TRAFFIC CONTROL AT A DISPLACED LEFT-TURN INTERSECTION	393
MVM2026-014	Boris Stojić Nebojša Nikolić Luka Sekicki	A FLEXIBLE COMPUTATIONAL MODEL FOR FUEL CONSUMPTION ESTIMATION IN ARBITRARY VEHICLE DRIVING CYCLES	403
MVM2026-018	Dušan Opsenica Ivan Blagojević Saša Mitić	THE INFLUENCE OF ELECTRIC VEHICLE CONFIGURATION ON VEHICLE DYNAMIC CHARACTERISTICS	413
MVM2026-023	Snežana Petković Valentina Golubović Bugarski Jelena Adžić Milan Eremija	ANALYSIS OF PARAMETERS INFLUENCING ROAD TANKER ROLLOVER	425

MVM2026-028	Momir Drakulić Aleksandar Đurić Sreten Perić	SENSITIVITY ANALYSIS OF A TERRAMECHANICS MODEL OF TRACK-TERRAIN INTERACTION WITH RESPECT TO VEHICLE DESIGN PARAMETERS	435
MVM2026-031	Marko Simonović Dragan Adamović Đorđe Ivković Milan Simonović	SELECTION OF MATERIALS FOR FRICTION COMPONENTS OF THE BRAKE MECHANISM	447
MVM2026-032	Zoran Papić Nenad Saulić Milja Simeunović	PREDICTION OF EES VALUES IN VEHICLE IMPACTS USING AI	461
MVM2026-035	Marijana Jeremić Lazar Krstić Miloš Ivanović Mihailo Lazarević Milan Matijević	DIGITAL TWIN DESIGN FOR TORSIONAL STIFFNESS ESTIMATION IN MOTOR-LOAD OSCILLATORY SYSTEMS USING PHYSICS-INFORMED NEURAL NETWORKS	471
MVM2026-040	Nebojša Jovičić Angelina Cvetanović Goran Bošković	EVALUATING THE EFFICIENCY OF OPTIMIZED WASTE COLLECTION ROUTES USING DATA ENVELOPMENT ANALYSIS	485
MVM2026-046	Aikaterini Zafeiri Clio Vossou Dimitrios Koulocheris	FLUID-STRUCTURE INTERACTION IN A TANK VEHICLE TRANSPORTING LIQUID FUEL	497
MVM2026-048	Ognjen Jovanović Milan Matijević	APPLICATION OF THE TIA PORTAL ENVIRONMENT FOR SOFTWARE-IN-THE-LOOP SIMULATION OF PLC CONTROL OF A FIRST-ORDER DYNAMIC SYSTEM	507
MVM2026-058	Nikola Gunić Hana Stefanović Milan Matijević	A NEW GENERATION OF WHEEL POSITION AND SPEED INTELLIGENT SENSORS FOR MOTOR VEHICLES	523
MVM2026-065	Danijela Miloradović Jasna Glišović Jovanka Lukić Nadica Stojanović	CONDITIONAL SPECTRAL ANALYSIS OF VEHICLE VIBRATION DATA	529
MVM2026-066	Matija Simanić Ilija Vidović Luka Milić Momir Drakulić Aleksandar Đurić	SIMULATION-BASED MOTION ANALYSIS OF A LIGHTWEIGHT TRACKED ROBOT USING WEBOTS	541
MVM2026-075	Branko Miličić Nikola Frlić Sekulić Miloš Mitrović Ivan Blagojević	IDENTIFICATION OF EFFECTIVE THERMO-PNEUMATIC TIRE PARAMETERS FROM REAL-WORLD ROAD TEST DATA	553

SECTION D
Driver/Vehicle Interface, Information and Assistance Systems

MVM2026-005	Slobodan Mišanović	THE INFLUENCE OF ENERGY DEMAND FOR PASSENGER COMPARTMENT CLIMATE CONTROL OF THE ENERGY EFFICIENCY OF ELECTRIC BUS	567
MVM2026-019	Dragan Ružić Miloš Vujković	DETERMINING THE FUEL CONSUMPTION REQUIRED FOR AIR-CONDITIONING OF A PASSENGER CAR UNDER REAL-WORLD CONDITIONS	579

MVM2026-020	Dragan Stojadinović Aleksandar Đurić Snežana Jovanović Miroslav Jovanović	THE INFLUENCE OF SEAT DESIGN AND SURFACE TYPE ON THE LEVEL OF VIBRATIONS EXPERIENCED BY A TRUCK DRIVER	589
MVM2026-063	Slavica Mačužić Saveljić Ognjen Matić Igor Saveljić	MACHINE LEARNING-BASED PREDICTION AND EXPLAINABILITY OF DRIVER DISCOMFORT AND FATIGUE: A DATA-DRIVEN EXTENSION OF A RAMSIS-BASED DIGITAL HUMAN MODEL STUDY	599
MVM2026-072	Jovanka Lukić Jasna Glišović Danijela Miloradović	COMPONENT COHERENCE-BASED ASSESSMENT OF MASKING EFFECTS IN TWO-DIRECTIONAL WHOLE-BODY VIBRATION	609
MVM2026-074	Milan Blagojević Saša Milojević Živče Šarkoćević Ivica Čamagić Dragan Lazarević	FIAT 500L REAR IMPACT PERFORMANCE IN EURO NCAP AND IIHS ASSESSMENTS	623

SECTION E
Transport Challenges in Emerging Economies

MVM2026-033	Janez Kopač Franci Pušavec	HIGHWAY ROAD TRAPS AS HIDDEN SOURCES OF CRASH RISK	633
MVM2026-044	Nadica Stojanović Ali Belhocine Ivan Grujić Željko Đurić Suzana Petrović Savić Oday I. Abdullah	THE IMPACT OF “DRUNK BUSTERS” ON THE ADEQUATE PERFORMANCE OF TASKS	645
MVM2026-055	Vladimir Vukašinović Dušan Gordić Vanja Šušteršič Mladen Josijević	SUSTAINABLE BIOFUELS FOR THE DECARBONISATION OF THE TRANSPORT SECTOR IN CITIES	659
MVM2026-062	Goran Bošković Nebojša Jovičić Angelina Cvetanović Saša Milojević	ASSESSMENT OF THE NUMBER OF END-OF-LIFE VEHICLES IN THE REPUBLIC OF SERBIA	669
MVM2026-064	Bojana Bošković Nadica Stojanović Saša Babić Milena Petrović Anđela Egerić	PREDICTION AND TIME-SERIES ANALYSIS OF ROAD DEATHS PER MILLION INHABITANTS IN THE REPUBLIC OF SERBIA AND THE EUROPEAN UNION FOR THE PERIOD 2012 TO 2030	677
MVM2026-069	Saša Jovanović Zorica Đorđević Danijela Nikolić Lozica Ivanović Saša Milojević	A SAW–BASED DECISION SUPPORT MODEL FOR THE SELECTION OF NEW AND USED PASSENGER CARS	691

Introductory Lectures

The 11th International Congress
Motor Vehicles & Motors 2026
Kragujevac, Serbia
October 8th - 9th, 2026

Motor Vehicles & Motors

MVM2026-IL1
https://doi.org/10.24874/CMVM2026.IL1
Review paper

Ralph Pütz[1]

OPERATING COSTS OF PUBLIC TRANSPORT BUSES WITH DIFFERENT PROPULSION SYSTEMS AND VARIOUS TYPES OF RENEWABLE ENERGY OVER TIME – WHERE IS THE JOURNEY HEADING?

ABSTRACT: It is essential to use scenarios to anticipate realistic developments in order to identify and rule out potential pitfalls. This study - for German boundary conditions but applicable to other European countries - therefore compares, across various time horizons from 2025 to 2040, the use of renewable energies in different propulsion technologies for electric mobility and internal combustion engines. It shows that excluding internal combustion engines is completely obsolete from an environmental perspective and, from an economic perspective, entails significant additional costs for transport operators and thus for the national economy. A return to technology neutrality is unavoidable and will help to limit the damage.

KEYWORDS: holistic ecological assessment, total vehicle costs, renewable energies, bus propulsion concepts, technology-neutrality, EU Clean Vehicles Directive

OPERATIVNI TROŠKOVI AUTOBUSA JAVNOG PREVOZA SA RAZLIČITIM POGONSKIM SISTEMIMA I VRSTAMA OBNOVLJIVIH IZVORA ENERGIJE KROZ VREME – KAKAV JE DALJI PRAVAC RAZVOJA?

SAŽETAK: Važno je koristiti scenarije za predviđanje realističnih budućih kretanja, kako bi se identifikovali i otklonili potencijalni nedostaci. Ova studija – zasnovana na uslovima karakterističnim za Nemačku, ali primenljiva i na druge evropske zemlje – upoređuje, kroz različite vremenske horizonte od 2025. do 2040. godine, primenu obnovljivih izvora energije u različitim pogonskim tehnologijama električne mobilnosti i motora sa unutrašnjim sagorevanjem. Pokazuje da isključivanje motora sa unutrašnjim sagorevanjem sa stanovišta zaštite životne sredine potpuno prevaziđeno i da, sa ekonomskog stanovišta, dovodi do značajnih dodatnih troškova za operatere javnog prevoza, a time i za nacionalnu ekonomiju. Povratak tehnološkoj neutralnosti je stoga neizbežan i pomoći će u ograničavanju štetnih posledica.

KLJUČNE REČI: holistička ekološka procena, ukupni troškovi vozila, obnovljivi izvori energije, koncepti pogona autobusa, tehnološka neutralnost, Direktiva EU o čistim vozilima.

[1] *Prof. Dr. Ralph Pütz, Landshut University of Applied Sciences, Am Lurzenhof 1, D-84036 Landshut, ralph.puetz@haw-landshut.de, https://orcid.org/0009-0000-5312-8778 (https://www.belicon-forschung.de)*

INTRODUCTION

It is, of course, legitimate and sensible to shape the future through (political) regulations; however, these regulations must always be based on the principle of technological neutrality and categorically exclude any form of ideology. For example, in the recent European elections, the European People's Party (EPP) campaigned on a pledge to reverse the decision to phase out internal combustion engines. From a technical perspective, a 'propulsion transition' involving the planned phase-out of locally ultra-clean combustion engines whilst simultaneously utilising renewable primary energy sources must, in any case, be scrutinised on the basis of a holistic assessment, whereas an 'energy transition' is indispensable. In contrast, the so-called 'EU Clean Vehicles Directive' (implemented in Germany since 2 August 2021) stipulates fixed quotas for the procurement of new public service buses with 'clean' and 'emission-free' powertrains, whilst mistakenly focusing solely on the driving subsystem (Tank-to-Wheel, TtW) in the definitions of 'clean' and 'emission-free'. The emissions and energy inputs associated with vehicle production, including powertrain and storage systems (cradle-to-gate, CtG), the generation and distribution of energy within the fuel supply chain (well-to-tank, WtT), and the subsequent recycling and disposal (end-of-life, EoL), are completely ignored, which is unacceptable, even though all these subsystems are highly relevant for a robust, holistic environmental (and also economic) assessment. Whilst the targeted removal of local pollutants such as particulate matter (particle mass PM and particle numbers PN) and nitrogen oxides (NO, NO_2) etc. from the exhaust is highly sensible, the removal of CO_2 from the exhaust is, by contrast, completely irrelevant, as greenhouse gas emissions have a 'global' impact and it is irrelevant whether CO_2 emissions arise in the upstream chain (WtT), during the driving cycle (TtW), in vehicle production (CtG) or during recycling/disposal (EoL). Consequently, considering only the actual driving operation (TtW) in isolation can lead to completely incorrect conclusions.

STARTING POINT: HOLISTIC ENVIRONMENTAL ASSESSMENT

Figure 1 below shows the results of a holistic life-cycle analysis based on key local and global criteria for the time horizon 'today' (the year 2025), using the example of a German public transport bus fleet that is operated by its first operator for the standard 15-year period. The result of this overall environmental assessment shows that, a priori, all of the drive variants examined using renewable energies, such as:

- Diesel bus Euro VI with HVO100 (Re-Fuel)
- Diesel bus Euro VI with E-Fuel (Power-to-Liquids, PtL)
- CNG bus Euro VI using biogas from waste (Re-Fuel)
- Fuel cell (FC) hybrid bus using green hydrogen produced from offshore wind power
- Overnight-Charger battery bus (ONC-BEV) with offshore wind power

are on a par with comprehensive sustainability standards and, compared to the current 'Euro 6 diesel engine with fossil EN590 DK' standard, deliver highly significant environmental improvements of around 70%. However, the claim that, under the EU Clean Vehicles Directive, all electric vehicles such as ONC-BEVs or FC hybrids are incorrectly declared as 'emission-free' compared to options with internal combustion engines is therefore completely unfounded and misleading. Ranges are shown as dotted lines in Figure 1.

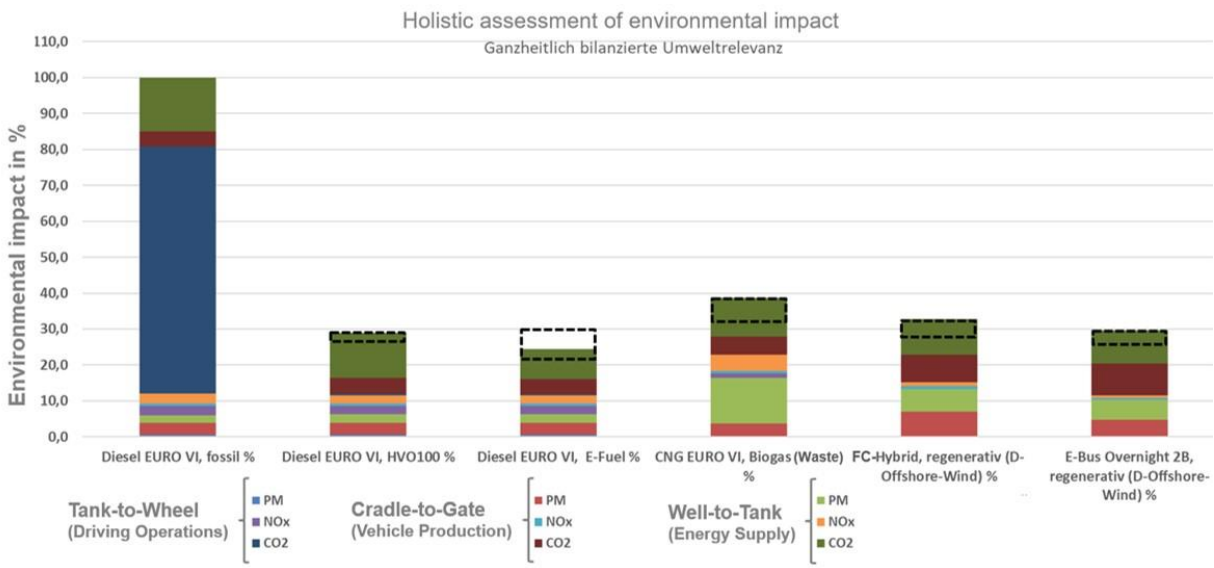

Figure 1 Holistic assessment of environmental impact of different propulsion systems with renewable energies

It should be noted that, in the case of the ONC-BEV (E-Bus Overrnight 2B), two battery packs were assumed for the 15-year operational period with the first operator, as most manufacturers now offer a warranty of up to seven years

on the battery. Given the reported findings that some operators apparently have two or even three battery packs in use after just a few years – which is, of course, covered by the warranty – it is highly questionable whether two battery packs will actually suffice over the long term during the bus's 15-year lifespan with the first operator. Furthermore, it is worth noting that when defective parts of a battery are replaced today, they are artificially aged for balancing purposes, whilst the bus is not available for PT operation.

The fuel cell hybrid bus discussed here should not be confused with a fuel cell range extender, as the latter is a battery-powered bus with a 'small' fuel cell range extender, whereas the fuel cell hybrid bus described here uses a fuel cell as its main power unit, working in conjunction with a 'small' battery for regenerative braking.

VEHICLE COSTS PLAY A DECISIVE ROLE, GIVEN THAT ENVIRONMENTAL IMPACT OF THE DIFFERENT PROPULSION SYSTEMS IS VIRTUALLY IDENTICAL

As the transport sector, unlike any other sector, remains dependent on the fossil fuel oil for over 90% of its energy needs, there is an inevitable call for alternative, more sustainable and cleaner fuels. Given the virtually equivalent environmental integrity of the options examined using renewable energy, as shown in Figure 1, and in view of the fierce competition in public transport and the fact that public funding is declining, the most economical option will ultimately be the most effective – provided that policymakers return to a policy of technological openness!

The World Energy Council (WEC) estimates that demand for PtX – i.e. power-to-liquids (PtL, E-fuels) and power-to-gases (PtG, E-gases) in 2050 at between 10,000 TWh (low demand) and 41,000 TWh (high demand), depending on the scenario, suggesting that the aforementioned high demand could be met by the potentially available global generation volumes. Another solution with a decidedly longer-term perspective would be the use of HVO100 in accordance with DIN EN 15940, which is produced synthetically from vegetable oils and residues that do not compete with the food and feed chain (e.g. from the meat and fish industries, catering, residues etc.), which are converted into hydrocarbons through a catalytic reaction with hydrogen (hydrogenation). In contrast to transesterification to produce so-called 'biodiesel' (PME; vegetable oil methyl ester), the reaction with hydrogen places lower demands on the origin and quality of the feedstocks. In recent years, mineral oil companies in particular, such as Neste Oy from Finland, Marbanaft from Sweden, Eni from Italy, Total from France and Aramco, have ramped up production of hydrogenated vegetable oil. Neste claims a 'well-to-wheel' CO_2 reduction of up to 90% for its own HVO100. However, the availability of HVO100 still depends significantly on the quantity and quality of the raw materials used in its production. Despite rising demand, these raw materials are likely to remain limited in the long term. Nevertheless, according to a recent study by the Karlsruhe Institute of Technology (KIT), the European Union has sufficient residual and waste materials to supply the entire road transport sector with climate-neutral liquid fuels.

E-fuels and HVO100 differ from fossil EN590 diesel fuel primarily in three respects: their density and calorific value are slightly lower than those of fossil diesel fuel, whereas the cetane number – a measure of the fuel's ignition quality – is significantly higher, at over 70 (up to 99). These fuels are oxygen-free and therefore exhibit high storage stability and slow engine oil ageing. The absence of aromatics contributes to a reduction in soot emissions during operation; however, due to the widespread use of diesel particulate filters (DPF) in German and European public transport, this does not result in any measurable improvements. A disadvantage is that the conversion of the feedstocks into HVO requires a large amount of hydrogen, which is currently (still) largely obtained from fossil fuels (e.g. natural gas reforming). Further potential for optimization would be offered by the use of hydrogen produced via electrolysis using renewable electricity. However, from an environmental and social policy perspective, it is essential to ensure that the fats and oils used for HVO production do not compete with food and feed production and, above all, are free from rainforest-destroying palm oil. Both E-fuels and HVO100 can be blended with any proportion of fossil diesel and require no changes to the refuelling infrastructure, which makes them suitable as drop-in fuels for existing diesel bus fleets and enables an immediate reduction in CO_2 emissions.

In contrast, domestic green hydrogen (produced by electrolysis using only renewable energy) requires, at the very least, a new and costly energy distribution and refuelling infrastructure; for battery-powered vehicles running on renewable electricity, it requires a new charging infrastructure at depots and a significant expansion of distribution networks and electrical energy storage facilities. The integration of renewable electricity into Germany's (and may be other country´s) existing power grids poses a further key challenge due to fluctuating generation and the need to ensure grid stability. Owing to high production costs and infrastructure requirements, the market ramp-up for hydrogen and fuel cell vehicles remains in the development phase despite government subsidies, whilst battery-powered electric mobility is being driven forward and implemented through government support.

Scenarios for the future development of energy costs

Data on the future development of prices for renewable energy and fuels are heavily dependent on future political factors and are therefore of limited reliability. Below, all scenarios are assumed, from today's perspective, to represent final prices for German public transport operators. Standard petrol station prices are significantly higher.

As regards liquid fuels, at the 'present' time horizon, HVO100 is approximately €0.15 per litre more expensive than fossil EN590 diesel at the purchase volumes typical for transport companies, whilst E-fuels – whose production facilities are still at the pilot or early stage and which are scarcely available in large quantities – are far from being economically viable; see Figure 2. Whilst prices for fossil diesel will continue to rise, prices for E-fuels – assuming some political support within the framework of technology neutrality – will fall significantly and could reach the price level of fossil diesel fuel by 2040. In contrast, a further decline in the price of HVO100 is to be expected. The E-fuels considered here originate from Patagonia or North Africa, as the well-to-tank efficiency of around 45 per cent means that regions where generation efficiency is of lesser importance due to the high and constant availability of renewable electricity (from wind and solar energy) are the preferred candidates for production.

In the case of gaseous fuels, the analysis considered biogas from waste and green hydrogen produced using German offshore wind power. Despite public subsidies, the price of hydrogen is still far from being economically viable today, but is expected to fall steadily as production costs continue to decrease due to economies of scale and cheaper renewable energy. In contrast, the price of biogas is expected to continue rising, as the production of biomethane depends on limited biomass inputs (e.g. agricultural residues such as straw and manure) and their rising costs, and economies of scale will not compensate for this; see Figure 3.

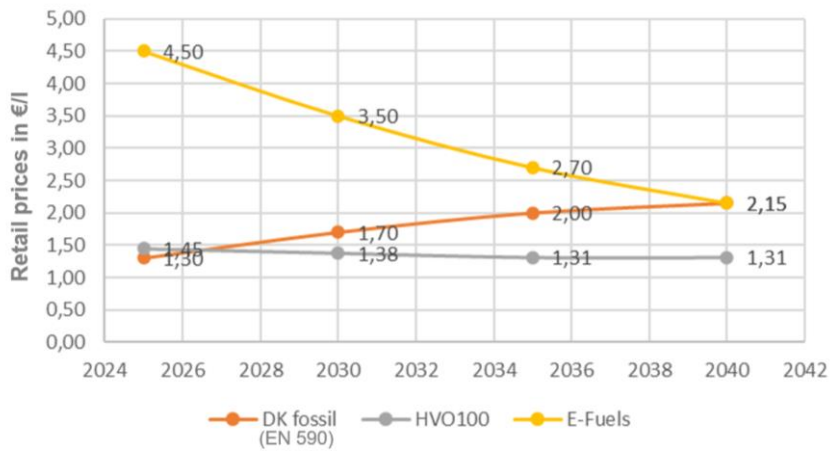

Figure 2 Forecast of price trends for liquid fuels

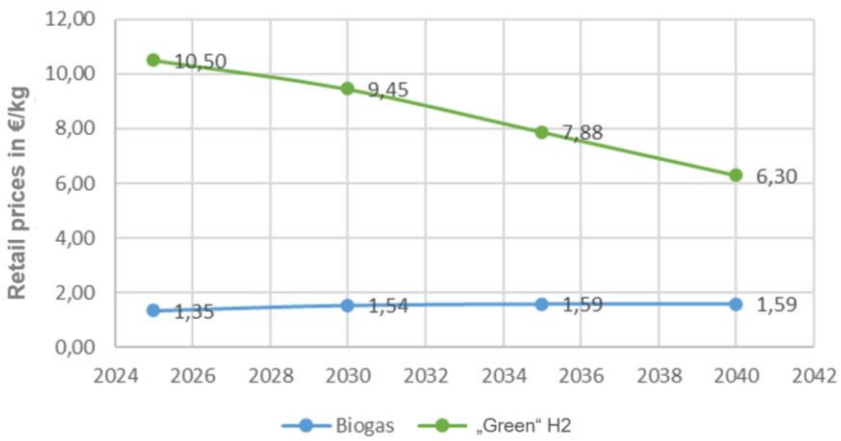

Figure 3 Forecast of price trends for gaseous fuels

It is assumed that the price of renewable electricity, here for Germany, will fall over the long term – based on the current price of €0.24/kWh for large-scale customers – as economies of scale and technological progress lead to a continuous decline in electricity generation costs – despite the costs of grid expansion and the construction of storage facilities – and are accompanied by reduced CO_2 pricing. German offshore wind power is used here as the source of renewable electricity; see Figure 4.

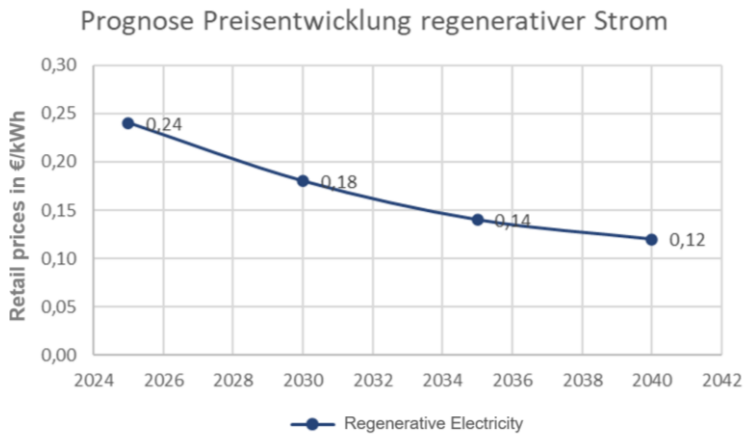

Figure 4 Forecast of price trends for renewable electricity

Scenarios for the future development of capital and maintenance costs

The capital service costs arising from depreciation and interest are based on a 15-year operational period for the respective fleets with the first operator. Consequently, a depreciation period of 15 years was also applied. Figure 5 shows the relative capital service costs of CNG buses, fuel cell hybrids and overnight charger battery buses (ONC-BEV) without subsidies, compared to a Euro VI diesel bus, whose capital service costs are set at 100 per cent and form the basis for comparison. For the diesel and CNG buses, a complete engine overhaul was included during the 15-year operational period, whilst for the fuel cell hybrid and the ONC-BEV, as already mentioned, a second battery was assumed. The capital service costs shown here are initially without subsidies. Whilst the capital service costs for the diesel and CNG buses were, for the sake of simplicity, assumed to be constant, highly significant cost reductions were applied for both the ONC-BEV and the FC-hybrid. Nevertheless, it is assumed that after ten years ('in the medium term') – taking the second battery into account – an ONC-BEV is still twice as expensive as a diesel bus.

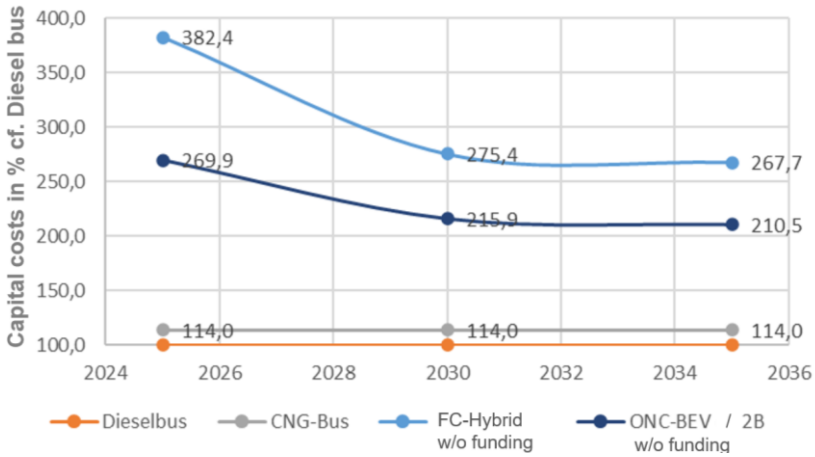

Figure 5 Expected trends in capital service costs for different propulsion concepts compared to EU VI Diesel bus

Figure 6 shows the expected trend in maintenance costs – comprising material and labour costs. Whilst, based on the author's experience, there are currently apparently highly significant additional costs for ONC-BEVs in the region of 55 to 60 per cent and even higher for fuel cell hybrids, these are expected to decrease gradually and significantly over time due to technological advancements; for diesel and CNG buses, however, maintenance costs were assumed to remain constant for the sake of simplicity. Nevertheless, it is not to be expected that maintenance costs for ONC-BEVs will reach the level of a diesel bus in the next decade, though they may well fall below the level of a CNG bus.

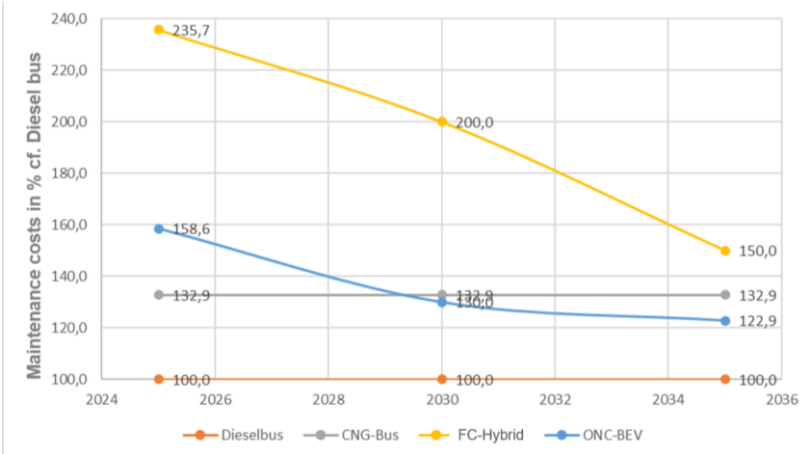

Figure 6 Expected trends in maintenance costs for different propulsion concepts

FORECAST OF THE VEHICLE COSTS OVER THE TIME HORIZONS OF THE PRESENT, THE SHORT TERM, THE MEDIUM TERM AND THE LONG TERM

Based on the development assumptions outlined before, the annual vehicle costs are now to be analysed over time, comprising:

- Capital costs (depreciation and interest)
- Energy costs when using renewable energy
- Maintenance costs (spare parts and labour)
- Additional infrastructure costs (compared to an established fleet of 100 diesel buses)

over time, whereby for the electric mobility options – FC-Hybrid and ONC-BEV – public funding for the vehicles was only considered as an additional option for the time horizon 'today'.

Time horizon 'today' (2025)

As Figure 7 shows, on the 'today' (2025) time horizon, of the environmentally equivalent options mentioned at the outset, electric mobility and the use of E-fuels are not economically viable without public funding; the FC-hybrid option is also not viable, even with public funding. Only the following options are economically viable 'today', shown in comparison to the diesel bus with HVO100 in the following order:

1. Diesel + HVO100 – without public funding: 100%
2. CNG + biogas – without public funding: 110%
3. ONC-BEV (2 batteries over the bus's lifetime) – with public funding: 117%

The use of an ONC-BEV is therefore only brought within the realm of economic viability today through massive public subsidies. It would, however, be completely wrong to adopt the approach frequently practised by transport companies of deploying a subsidised ONC-BEV without a second battery pack over the bus's lifetime, as this would paint a rosier picture of the economic situation, with annual vehicle costs at 112%.

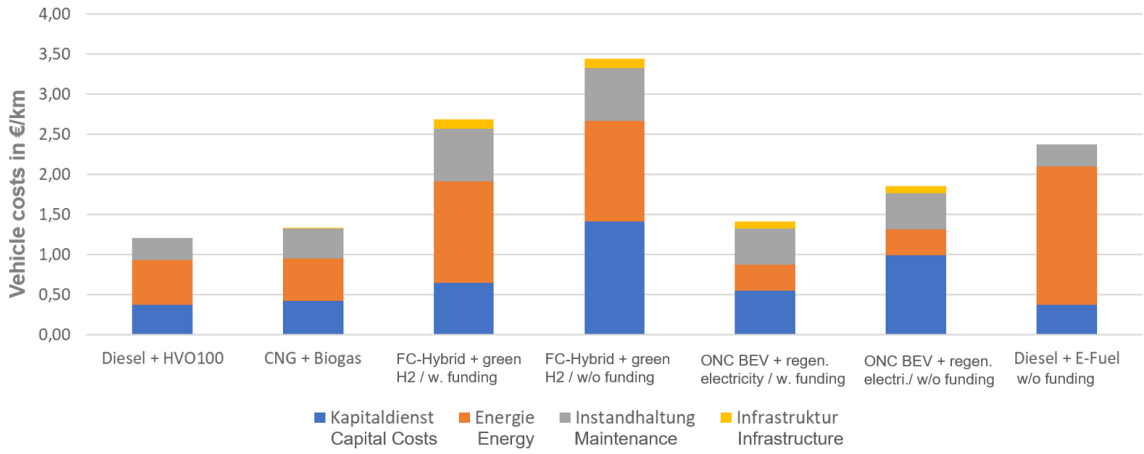

Figure 7 Vehicle costs for different propulsion concepts using regenerative energy as of 'today' (2025); including infrastructure

Time horizon: 'short term' (2030)

Over the 'short-term' time horizon (2030), by which point no further public start-up funding is taken into account, it becomes apparent that the ONC-BEV option is already approaching the threshold of economic viability without subsidies – albeit with significant additional costs, see Figure 8. Despite further cost reductions for the FC-Hybrid and E-Fuel options, these remain beyond the scope of economic viability.

The following options therefore remain economically viable in the 'short term', shown in comparison to the diesel bus with HVO100 in the following order:

1. Diesel + HVO100 – without public funding: 100%
2. CNG + biogas – without public funding: 119%
3. ONC-BEV (2 batteries over the bus's lifetime) – without public funding: 127%

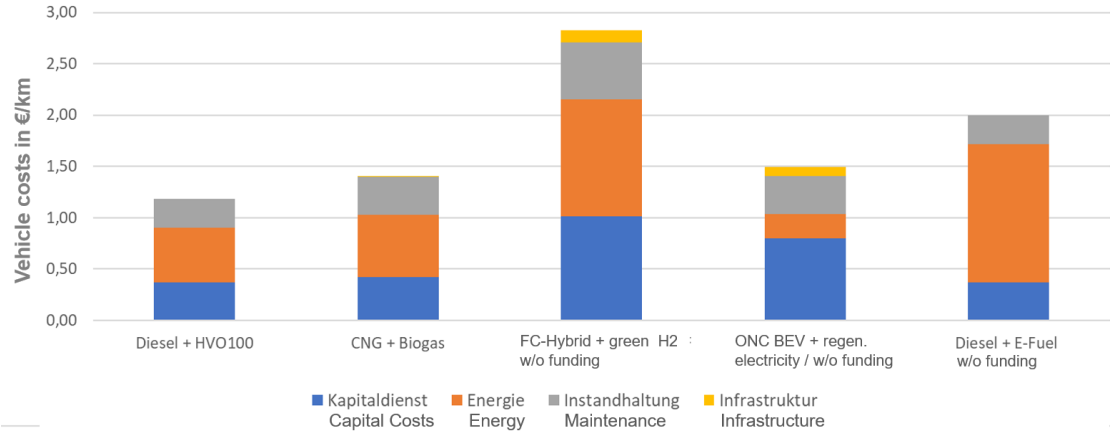

Figure 8 Expected vehicle costs for different powertrain concepts using regenerative energy over the 'short-term' timeframe (2030); including infrastructure

Time horizon: 'medium term' (2035)

The analysis for the 'medium-term' time horizon (2035) shows that the ONC-BEV option is already cheaper than the 'CNG + biogas' option even without subsidies; see Figure 9. Whilst the FC-Hybrid option remains virtually unviable economically despite further cost reductions, the E-Fuel option is already approaching economic viability.

The following options therefore remain economically viable in the 'medium term', albeit with a changed ranking, shown in comparison to the diesel bus with HVO100 in the following order:

1. Diesel + HVO100 – without public funding: 100%
2. ONC-BEV (2 batteries over the bus's lifetime) – without public funding: 122%
3. CNG + biogas – without public funding: 124%

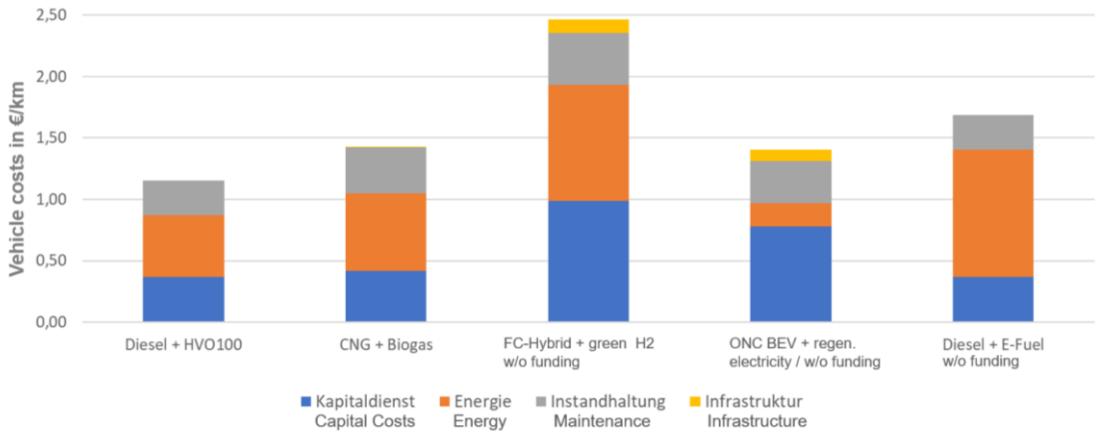

Figure 9 Expected vehicle costs for different powertrain concepts using regenerative energy over the 'medium-term' timeframe (2035); including infrastructure

However, given the current experience of some transport operators with battery lifespan, it is certainly legitimate to ask: What if, after a decade, it turns out that two battery packs are not sufficient for a 15-year service life in the ONC-BEV? In that case, the ratios shown in Figure 10 would apply:

1. Diesel + HVO100 – without public funding: 100%

2. CNG + biogas – without public funding: 124%
3. ONC-BEV (3 batteries over the bus's lifetime) – without public funding: 138%

The use of E-fuels, with relative vehicle costs of 146 per cent compared to the 'Diesel + HVO 100' option, would still be outside the scope of economic viability, but so too would the use of an ONC-BEV with three battery packs over the bus's lifetime.

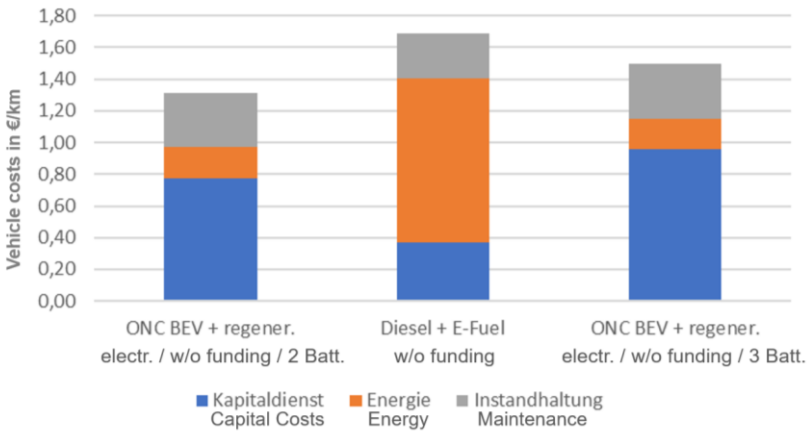

Figure 10 Expected vehicle costs for the ONC-BEV with two and three batteries over the vehicle's lifetime, compared with the 'diesel + E-fuels' option over the 'medium term' (2035); excluding infrastructure

Time horizon: 'long term' (2040)

A forecast for the 'long-term' time horizon (2040) is certainly a bold undertaking, as even a forecast covering a single decade – in this case up to 2035 ('medium term') – is fraught with numerous uncertainties, particularly of a political nature, as outlined at the outset. Nevertheless, the future development is to be forecast here on the basis of debt service and maintenance costs frozen over the 'medium-term' time horizon. Figure 11 then shows that the ONC-BEV option is continuing to converge with the 'Diesel + HVO100' option, but the 'Diesel + E-Fuel' option has already almost reached cost parity with the 'CNG + Biogas' option. The FC-Hybrid option was no longer considered here.

The following options are therefore apparently economically viable in the 'long term', shown in comparison to the diesel bus with HVO100 in the following order:

1. Diesel + HVO100 – without public funding, without infrastructure: 100%
2. ONC-BEV (2 batteries over the bus's lifetime) – without public funding, without infrastructure: 109%
3. CNG + biogas – without public funding, without infrastructure: 123%
4. Diesel + E-fuel – without public funding, without infrastructure: 128%

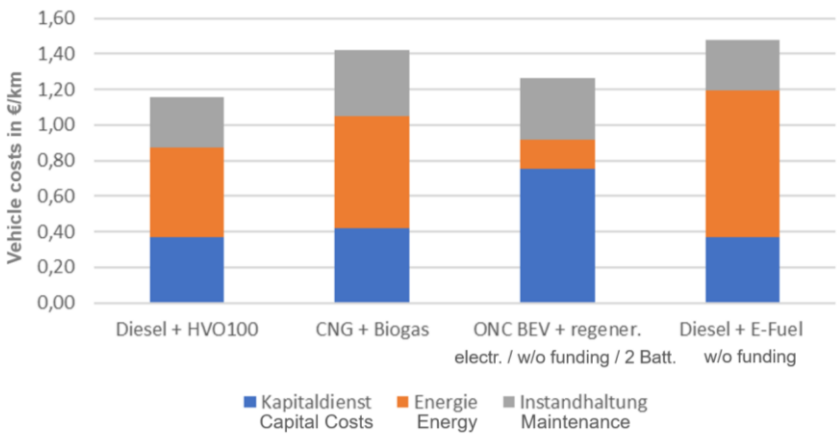

Figure 11 Expected vehicle costs for different powertrain concepts using regenerative energy over the 'long-term' time horizon (2040); excluding infrastructure

But what would the figures look like if it actually turned out that two battery packs were not sufficient for a 15-year service life in the ONC-BEV? In that case, the figures shown in Figure 12 would apply:

1. Diesel + HVO100 – without public funding: 100%
2. CNG + biogas – without public funding, without infrastructure: 123%
3. ONC-BEV (3 batteries over the bus's lifetime) – without public funding, without infrastructure: 127%
4. Diesel + E-fuel – without public funding: 128%

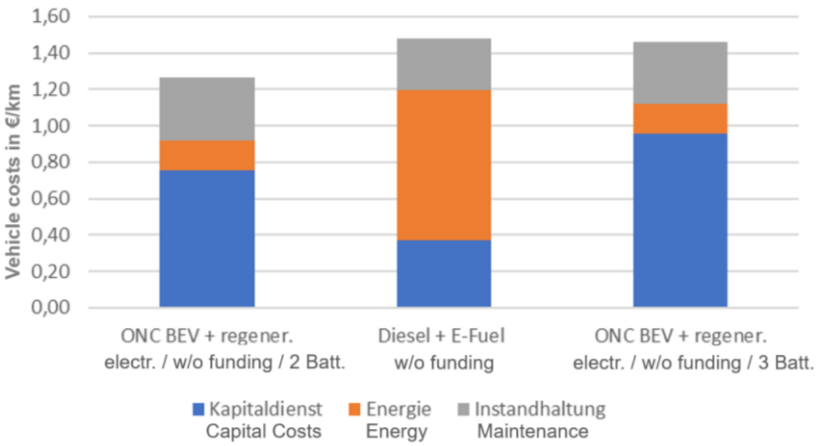

Figure 12 Expected vehicle costs for the ONC-BEV with two and three batteries over the vehicle's lifetime, compared with the 'diesel + e-fuels' option over the 'long-term' time horizon (2040); excluding infrastructure

CONCLUSIONS

Based on a holistic assessment, five public bus propulsion options using renewable energy were identified as being virtually equivalent in environmental terms, based on key local and global criteria, whilst offering a highly significant improvement in environmental performance compared to the current dominant use of diesel buses running on fossil EN590 diesel fuel in German public transport fleets. Three of the options examined involved the continued use of internal combustion engines, albeit with renewable fuels. The other two options involved electric mobility, which is declared 'emission-free' under the current EU Clean Vehicles Directive because, incorrectly, only one subsystem – driving operations (TtW) – is taken into account there.

In summary, Figure 13 shows the projected trend in vehicle costs for the options examined – excluding public subsidies. The reference here is the vehicle costs of the 'Diesel + HVO100' option over the time horizon 'today' (2025), whereby for the electric mobility options, the proportionate infrastructure costs were included only once in the base year 2025. It is evident that, even 'in the long term' (2040), the pure vehicle costs of the 'Diesel + HVO100' option will be around 9 per cent lower than those of the 'ONC-BEV + renewable electricity' option, provided that expenditure on the BEV refuelling infrastructure has been incurred beforehand.

The concluding analysis is therefore revealing: it uses an interpolation approach to estimate the expected average additional costs of all the options examined relative to the 'Diesel + HVO100' baseline over the time period 'from today to the long term' (2025 to 2040), as shown in Figure 14.

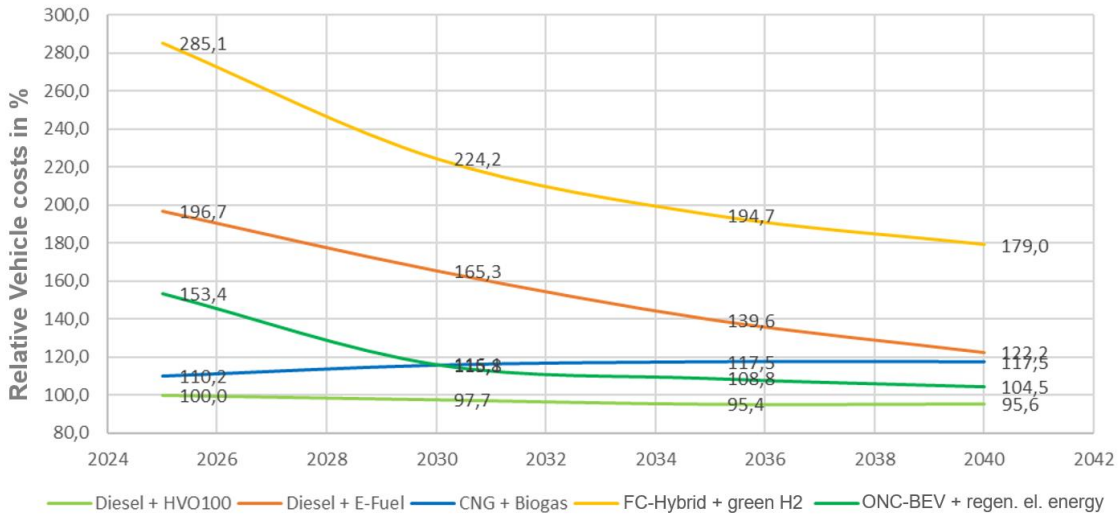

Figure 13 Expected trend in vehicle costs over time relative to the 'Diesel + HVO100' variant, based on the current time horizon; infrastructure costs are only taken into account once in 2025 ('today')

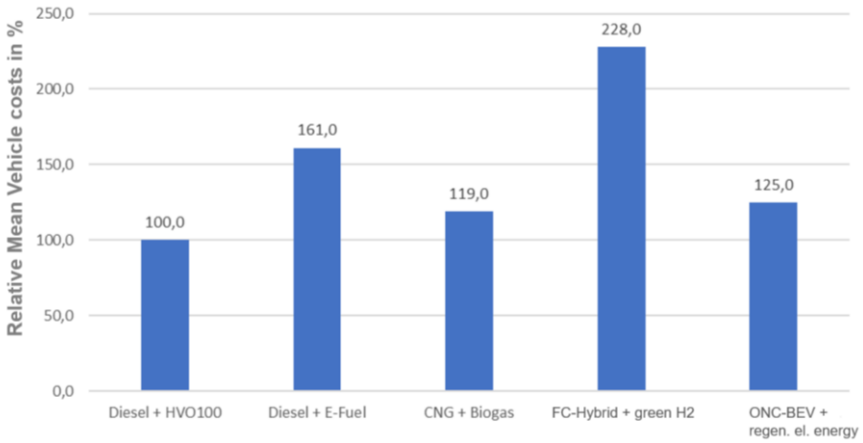

Figure 14 Relative average of total vehicle costs from 2025 to 2040 compared with the 'Diesel + HVO100' scenario; infrastructure costs included only once in 2025 ('today')

Accordingly, the 'restrictions' imposed by the EU Clean Vehicles Directive will, by 2040, result in vehicle-related additional costs for the German economy of around 25 per cent compared with the – environmentally equivalent – 'Diesel + HVO100' option if the ONC-BEV option is adopted, and for the FC-Hybrid option, by as much as around 128 per cent. Policy-makers must justify this to the public. An immediate switch to E-fuels would ultimately entail additional costs of around 61 per cent over the period from 2025 to 2040 without funding. By contrast, the 'CNG + Biogas' option would incur additional costs of just 19 per cent in total. The author considers it a farce that the three German transport companies that were once the 'cleanest' – Augsburg, Gießen and Oldenburg – are now forced to take a different path under the EU Clean Vehicles Directive.

This study for German boundary conditions but applicable to other European countries shows that ruling out internal combustion engines running on renewable fuels is completely obsolete from an environmental perspective and hardly justifiable from an economic one. An exclusive focus on electric mobility entails significant additional costs for transport operators. The paths dictated by the Clean Vehicles Directive are anything but technology-neutral and could prove economically disastrous – particularly if key industries are sacrificed and public finances are stretched beyond their limits due to one-sided requirements. A return to technology-neutrality is essential and will help limit the damage, as it is well known that 'all roads lead to Rome'.

REFERENCES

Heinz, A. (2026). Koch, Th. et al: Vom Rohstoff zur fossilfreien Mobilität: Europas Potenzial für einen erneuerbaren Kraftstoffmarkt; KIT.

Pütz, R. (2010) Strategic optimisation of public bus fleets (in German); Alba Fachverlag.

Pütz, R. (2021) With technology neutrality towards emission reduction – E-fuels as an alternative to E-mobility? (in German); DER NAHVERKEHR.

Pütz, R. (2022) A comprehensive ecological and economic assessment of different propulsion options, using the example of a public service bus (in German). In: S. Arlt, (Ed.), *Propulsion systems: Comparative life cycle assessments of various propulsion concepts for vehicles and stationary applications* (in German); Vulkan Verlag.

Pütz, R. (2025) The EU's energy and propulsion transition in the mobility sector, with a focus on Germany – is it feasible or not? (in German); DER NAHVERKEHR.

Pütz, R. (2026) Analysis of the operating costs of public service buses with different propulsion systems and fuels over time (in German); DER NAHVERKEHR.

The 11th International Congress
Motor Vehicles & Motors 2026
Kragujevac, Serbia
October 8th - 9th, 2026

Motor Vehicles & Motors

MVM2026-IL3
https://doi.org/10.24874/CMVM2026.IL3
Original scientific paper

Isak Karabegović[1]

COLLABORATIVE ROBOTICS AND ARTIFICIAL INTELLIGENCE IN THE AUTOMOTIVE INDUSTRY: SMART ASSEMBLY AND AUTOMATED QUALITY CONTROL

ABSTRACT: The modern automotive industry is undergoing an intensive technological transformation based on the principles of Industry 4.0 and Industry 5.0, where collaborative robots and artificial intelligence systems play a key role in improving manufacturing processes. This paper analyses the application of collaborative robots worldwide, with a particular focus on the automotive industry. An overview is given of the integration of collaborative robotics and artificial intelligence in assembly processes and automated quality control in the automotive industry. Special focus is placed on human–robot collaboration in flexible and intelligent manufacturing environments based on the principles of Industry 5.0, with the aim of optimizing assembly operations, increasing productivity, and reducing production errors. Modern methods based on machine learning, computer vision, and sensor data analysis for defect detection and real-time product quality monitoring are also discussed. The paper presents the possibilities of applying collaborative robotic systems in automotive component assembly, visual inspection, material handling, and adaptive process control. Technical, safety, and economic aspects of collaborative robot implementation are analysed, including increased manufacturing flexibility, reduced operational costs, and improved ergonomic working conditions. The research results indicate that the integration of collaborative robotics and artificial intelligence enables the development of intelligent manufacturing systems capable of autonomous decision-making, adaptive process management, and efficient quality control. Collaborative robotics and artificial intelligence, as fundamental technologies of Industry 4.0, represent a significant factor in the future development of smart factories and sustainable automotive manufacturing.

KEYWORDS: Collaborative Robots, Artificial Intelligence, Automotive Industry, Smart Assembly, Quality Control, Industry 5.0.

KOLABORATIVNA ROBOTIKA I UMJETNA INTELIGENCIJA U AUTOMOBILSKOJ INDUSTRIJI: PAMETNA MONTAŽA I AUTOMATIZIRANA KONTROLA KVALITETA

REZIME: Savremena automobilska industrija prolazi kroz intenzivnu tehnološku transformaciju zasnovanu na principima Industrije 4.0 i Industrije 5.0, pri čemu kolaborativni roboti i sistemi umjetne inteligencije imaju ključnu ulogu u unapređenju proizvodnih procesa. U radu se analizira primjena kolaborativnih robota u svijetu, s posebnim fokusom na automobilsku industriju. Dat je pregled integracije kolaborativne robotike i umjetne inteligencije u procesima montaže i automatizirane kontrole kvaliteta u automobilskoj industriji. Poseban naglasak stavljen je na

[1] *Isak Karabegović, Ph.D. Academy of Sciences and Arts of Bosnia and Herzegovina, Bistrik 7, 71000 Sarajevo, Bosnia and Herzegovina, isak1910@hotmail.com, https://orcid.org/0000-0001-9440-4441*

saradnju čovjeka i robota u fleksibilnim i inteligentnim proizvodnim okruženjima zasnovanim na principima Industrije 5.0, s ciljem optimizacije montažnih operacija, povećanja produktivnosti i smanjenja proizvodnih grešaka. Također su razmatrane savremene metode zasnovane na mašinskom učenju, računarskom vidu i analizi senzorskih podataka za detekciju nedostataka i praćenje kvaliteta proizvoda u realnom vremenu. U radu su predstavljene mogućnosti primjene kolaborativnih robotskih sistema u montaži automobilskih komponenti, vizuelnoj inspekciji, rukovanju materijalom i adaptivnom upravljanju procesima. Analizirani su tehnički, sigurnosni i ekonomski aspekti implementacije kolaborativnih robota, uključujući povećanje fleksibilnosti proizvodnje, smanjenje operativnih troškova i poboljšanje ergonomskih uslova rada. Rezultati istraživanja pokazuju da integracija kolaborativne robotike i umjetne inteligencije omogućava razvoj inteligentnih proizvodnih sistema sposobnih za autonomno donošenje odluka, adaptivno upravljanje procesima i efikasnu kontrolu kvaliteta. Kolaborativna robotika i umjetna inteligencija, kao temeljne tehnologije Industrije 4.0, predstavljaju značajan faktor budućeg razvoja pametnih fabrika i održive automobilske proizvodnje.

KLJUČNE REČI: kolaborativni roboti, umjetna inteligencija, automobilska industrija, pametna montaža, kontrola kvaliteta, Industrija 5.0.

INTRODUCTION

We are witnessing the fact that the automotive industry is undergoing an intensive digital transformation on a daily basis, fundamentally changing the way vehicles are designed, manufacturing processes are carried out, and the quality control of vehicles as products is performed. The continuous development of the core technologies of Industry 4.0, such as Cyber-Physical Systems (CPS), the Internet of Things (IoT), the Industrial Internet of Things (IIoT), Autonomous Robots (Industrial Robotics), Collaborative Robotics (Cobots), smart sensors, Artificial Intelligence (AI) and Machine Learning (ML), Big Data, simulation and digital twins, cloud computing, horizontal and vertical system integration, Additive Manufacturing (3D Printing), Augmented Reality (AR) and Virtual Reality (VR), Autonomous Mobile Robots (AMRs), Automated Guided Vehicles (AGVs), cybersecurity, and advanced automation systems, has enabled the creation of smart manufacturing environments in which information is collected and analysed in real time (Javaid, M. et al. 2022; Karabegović, I. et al. 2020). Automotive manufacturing companies are implementing the core technologies of Industry 4.0, thereby achieving a high level of connectivity among machines, sensors, robotic systems, and information platforms, which enables them to optimize manufacturing processes, reduce production costs, and improve product quality. Automotive companies, being exposed to the global market and increasingly demanding customer requirements, are compelled to implement flexible manufacturing systems capable of rapidly adapting to different vehicle models and individual customer requirements. The implementation of Industry 4.0 technologies not only involves the automation of manufacturing processes, but also the development of intelligent systems capable of making decisions based on data analysis and the prediction of future production states (Xu, X. et al. 2021). New-generation robotic systems play a particularly important role by enabling higher productivity, safety, and precision in manufacturing lines. Industry 4.0 represents the fourth industrial revolution based on the digitalization of manufacturing processes, the integration of cyber-physical systems, and machine-to-machine communication via the Internet. The primary objective of this concept is to create smart factories in which production processes operate autonomously, while continuously monitoring and optimizing system performance. The implementation of the core technologies of Industry 4.0 has made it possible to collect large volumes of data, analyse them, and support real-time decision-making. However, the evolution of industrial systems has demonstrated that complete automation cannot replace human creativity, experience, and the ability to make complex decisions. Consequently, the concept of Industry 5.0 has emerged in recent years, emphasizing a human-centric approach to manufacturing in which humans and intelligent technological systems jointly participate in value creation (Nahavandi, S. 2019). Industry 5.0 focuses on human–machine collaboration, sustainable manufacturing, and increasing the resilience of industrial systems to market and technological changes (Adel, A. 2022). Unlike Industry 4.0, which is primarily oriented toward automation and digitalization, Industry 5.0 integrates human capabilities with artificial intelligence, collaborative robotics, and advanced analytical systems. Such an approach enables the development of more flexible and intelligent manufacturing environments tailored to the needs of the modern automotive industry (Tóth, A. et al. 2023). Collaborative robots (cobots) represent one of the most important technologies of contemporary manufacturing systems. Unlike traditional industrial robots, which operate within physically separated work cells, cobots are designed to work safely in close proximity to human operators (Matheson, E. et al. 2019). Their design incorporates force sensors, vision systems, obstacle detection algorithms, and safety functions that enable direct collaboration with operators. In the automotive industry, collaborative robots are employed for component assembly, material handling, welding, adhesive application, product inspection, and final vehicle assembly operations. Their implementation contributes to increased productivity, reduced physical workload for workers, and improved ergonomic working conditions (Keshvarparast, A. et al. 2024). At the same time, collaborative systems provide greater manufacturing flexibility, which is particularly important in environments characterized by frequent vehicle model changes and increasing demands for product personalization. Modern concepts of human–robot collaboration are based on combining the precision, speed, and repeatability of robots with human judgment, creativity, and problem-solving capabilities. This form of interaction is becoming a key component of smart manufacturing systems and one of the fundamental pillars of Industry 5.0 development (Othman, U., & Yang, E. 2023). Artificial Intelligence

(AI) and Machine Learning (ML) are currently at the centre of the transformation of manufacturing processes and are most commonly used for manufacturing process optimization, predictive maintenance of equipment, automated production planning, quality control, and decision support. Machine Learning (ML) algorithms enable systems to analyse large volumes of data and identify anomalies that are not easily detectable using conventional analytical methods (Lee, J. et al. 2018). AI is particularly important in automated quality control. Through the application of computer vision, deep neural networks, and pattern recognition algorithms, it is possible to detect surface defects, assembly irregularities, and dimensional deviations with significantly greater accuracy and speed than traditional inspection methods (Zonta, T. et al. 2020). The aforementioned systems enable continuous monitoring of product quality throughout the entire production system, thereby reducing the probability of defective products. Artificial intelligence plays a key role in the development of intelligent collaborative robots (conots), because through the integration of deep learning methods, image processing, and sensor fusion, collaborative robots (conots) can recognize human movements, predict operator intentions, and adapt their behaviour in real time (Cherubini, A., & Navarro-Alarcon, D. 2021). This level of adaptability provides the foundation for the development of advanced human–robot collaboration systems in future manufacturing environments. The objective of this paper is to analyse the application potential of collaborative robotics and artificial intelligence in the automotive industry, with particular emphasis on smart assembly and automated quality control. The study provides an overview of contemporary technologies that enable the integration of humans, robots, and intelligent information systems within the frameworks of Industry 4.0 and Industry 5.0. The scientific contribution of this paper lies in the systematization of existing knowledge on collaborative robotic systems and AI methods applied in automotive manufacturing, as well as in the analysis of their integration to enhance productivity, product quality, and workplace safety. Particular attention is devoted to the development of human-centric manufacturing systems in which humans and intelligent robotic systems operate as equal participants in the production process. The research findings may serve as a foundation for the further development of advanced automation models and the digital transformation of the automotive industry.

METHODOLOGY AND DATA SOURCES

Comparative Approach and Selection of Indicators

For the analysis of the robotization of manufacturing processes in the automotive industry, a comparative approach was used, enabling the comparison of different countries and regions based on key indicators, as this approach allows the identification of trends, patterns, and variations in the automation of vehicle manufacturing processes. The indicators selected in this study include annual vehicle production, the number of patents, the number of installed industrial robots, robot density (the number of robots per 10,000 employees), as well as the integration of core Industry 4.0 technologies and the implementation policy of Industry 4.0. These indicators provide a comprehensive insight into the level of automation and digitalization in the automotive industry.

Data Sources

The data used in this study were collected from internationally recognized databases, statistical reports, and scientific literature to ensure the reliability, comparability, and representativeness of the results. The data sources include:

- *International Organization of Motor Vehicle Manufacturers (OICA)* – the primary source of annual motor vehicle production data by country and region, enabling the analysis of the relationship between the development of the automotive industry and the level of manufacturing process robotization (OICA, 2025).
- *World Intellectual Property Organization (WIPO)* – the source of data on global patent application trends and innovation activities in the fields of robotics, automation, and advanced manufacturing technologies (World Intellectual Property Organization, 2024).
- *Organisation for Economic Co-operation and Development (OECD)* – the source of patent statistics and internationally comparable indicators of technological innovation, used to analyse the development of robotics and collaborative robotics at the global level (Organisation for Economic Co-operation and Development, 2025).
- *European Patent Office (EPO – PATSTAT)* – the source of detailed data on patent applications and technological trends in robotics, automation, and the digital transformation of industry (European Patent Office, 2024).
- *International Federation of Robotics (IFR)* – the principal source of data on global robotization trends, including the number of installed industrial robots, robot density, sectoral distribution of robots, and market trends in industrial and collaborative robotics (International Federation of Robotics (IFR), 2024).
- *National statistical and industrial databases* – used as supplementary sources to verify data on industrial production, employment, and the development of the automotive industry in individual countries.
- *Scientific and professional literature indexed in the Web of Science and Scopus databases* – used to establish the theoretical framework of the research, review existing knowledge, and interpret the results obtained through statistical analysis.

The combination of these data sources enabled a comprehensive analysis of the relationship between the development of the automotive industry, the implementation of industrial and collaborative robots, and the intensity of innovation activities measured through patent applications.

Evaluation Criteria

Annual Vehicle Production

Vehicle production data are collected from OICA and national statistical offices (OICA, 2025). This indicator measures the total vehicle production in a given year, providing insight into the size and capacity of the automotive industry in different countries. In the context of the highest vehicle production, the analysis includes the top five countries—China, the United States of America, and India, which produced the largest number of vehicles in 2025—and the number of vehicles produced is presented in Table 1. Table 1 presents the annual vehicle production in the five selected countries in 2025, as well as the total global vehicle production.

Table 1 *Top Five Countries in the World by Motor Vehicle Production in 2025*

Rank	Country	Number of Vehicles Produced
1	China	34,530,738
2	United States	10,243,844
3	Japan	8,410,232
4	India	6,490,810
5	Germany	4,148,836
Worldwide Total		96,400,000

Source: OICA – *International Organization of Motor Vehicle Manufacturers*, Production Statistics 2025**.**

The data presented in Table 1 are particularly useful for analysing the digital transformation of the automotive industry, as they demonstrate that the countries with the highest investments in robotics, artificial intelligence, and Industry 4.0 technologies (China, the United States, Japan, and Germany) dominate global vehicle production.

Trends in Patent Activity in Robotics and Collaborative Robotics

In the field of robotics, the most important indicators of development and innovation potential are the number of filed and granted patents. It has been established that the number of patent applications in the field of robotic technology has been continuously increasing, owing to intensive research and development of new robotic systems, sensor technologies, control algorithms, as well as solutions based on artificial intelligence. In the field of collaborative robotics, there has been a significant increase in patent applications, as it enables efficient and safe collaboration between humans and robots within the same workspace. By analysing the number of filed patents, it can be observed that collaborative robotics occupies an important position within the total number of innovations in robotic technology. The increase in the number of patent applications reflects the growing industrial application of collaborative robots in manufacturing, logistics, medicine, and other sectors. Table 2 presents the trend in the total number of robotics patents and patents related to collaborative robotics during the period 2015–2025 (World Intellectual Property Organization, 2024; Organisation for Economic Co-operation and Development, 2025; European Patent Office, 2024).

Table 2 Comparative Analysis of Patent Applications in Robotics and Collaborative Robotics Worldwide During the Period 2015–2025

Year	Total Number of Robotics Patent Applications	Collaborative Robotics Patent Applications	Share of Collaborative Robotics
2015	18,500	1,200	6.5%
2016	21,300	1,650	7.7%
2017	24,900	2,300	9.2%
2018	28,700	3,100	10.8%
2019	31,500	4,200	13.3%
2020	34,800	5,600	16.1%
2021	39,200	7,400	18.9%
2022	43,500	9,300	21.4%
2023	47,800	11,500	24.1%
2024	52,600	13,900	26.4%
2025*	56,000	15,500	27.7%

Source: *Adapted and estimated based on data from the WIPO Patent Landscape Reports, OECD Patent Database, European Patent Office (EPO) PATSTAT Database, and reports published by the International Federation of Robotics (IFR).*
Note: *The data represent the number of patent applications filed with leading international patent organizations and do not refer to the number of granted or commercialized patents. The values for 2025 are estimates due to the time lag between patent filing and publication, which averages approximately 18 months.*

Based on the analysis of the data presented in Table 2, it can be concluded that over the past ten years there has been a continuous and intensive increase in patent applications in the field of robotic technology. In 2015, the number of patent applications amounted to 18,500, while in 2025 it increased to approximately 56,000 patent applications, representing a growth of about 203%. It can also be concluded that the growth in patent applications related to collaborative robotics has been even more pronounced, increasing from 1,200 patent applications to approximately 15,500, which represents an increase of about 12.9 times over the past ten years. Particularly significant is the continuous increase in the share of collaborative robotics within the total patent activity, rising from 6.5% in 2015 to 27.7% in 2025. This trend confirms that collaborative robots represent one of the fastest-growing areas of contemporary robotics research and development. The key drivers of the growth in the implementation of collaborative robots are presented in Table 3.

Table 3 Key Drivers of the Growth in Collaborative Robotics Patent Applications

FACTOR	IMPACT
Industry 4.0	Significant growth in manufacturing automation
Labour shortages	Accelerated adoption of collaborative robots (cobots)
Workplace safety	Safe operation without protective safety fences
AI integration	Development of intelligent collaborative systems
CNC machine tending	Fastest-growing application area

There is an increasing demand for flexible, safe, and intelligent robotic systems that enable efficient human–robot collaboration within a shared workspace, thereby increasing interest in patent protection in this field. Robotic technology is a core technology of Industry 4.0, particularly collaborative robotics, and the presented results indicate that the future development of robotic technology is being directed toward human-centric and collaborative working concepts, as well as intelligent manufacturing systems. The growing trend in patent applications suggests that collaborative robotics will continue to play an important role in the transformation of industrial processes, logistics, healthcare, and other sectors over the next decade.

Number of Installed Industrial and Collaborative Robots Worldwide

The third indicator evaluates the number of newly installed industrial robots in manufacturing processes and the estimated number of newly installed collaborative robots (cobots). The data presented in Table 4 are based on IFR reports, which provide detailed statistics on robot installations by industry (International Federation of Robotics (IFR), 2024 & 2025).

Table 4 Annual Global Number of Newly Installed Industrial Robots and Collaborative Robots Worldwide (2015–2025)

Year	Total Number of Newly Installed Industrial Robots	Newly Installed Collaborative Robots	Share of Collaborative Robots
2015	254,000	8,500	3.3%
2016	294,000	11,000	3.7%
2017	381,000	16,500	4.3%
2018	423,000	23,000	5.4%
2019	387,000	28,500	7.4%
2020	390,000	34,000	8.7%
2021	526,000	49,500	9.4%
2022	553,000	58,000	10.5%
2023	541,000	60,000	11.1%
2024	542,000	67,000	12.4%
2025*	555,000	75,000	13.5%

Note: *The data for 2025 represent estimates based on International Federation of Robotics (IFR) growth trends and the projected development of the collaborative robotics market.*

Analysis of the data in Table 4 leads to the conclusion that the total number of implemented industrial robots continuously increased from 2015 to 2025, rising from 254,000 robot units in 2015 to approximately 555,000 robot units, representing a 2.18-fold increase. Likewise, the trend in the implementation of collaborative robots over the same period increased from 8,500 robot units to approximately 75,000 robot units, which is 8.82 times higher. This growing trend in robot implementation indicates that an intensive global transformation of manufacturing processes toward a higher level of automation is taking place. By analysing the last column of Table 4, we conclude that the share of collaborative robots in total installations increased from 3.3% to 13.5% in only ten years. We conclude that the implementation of collaborative robots has a significantly higher growth rate compared to first-generation traditional industrial robots, primarily due to the increasing demand for flexibility and human-centric manufacturing solutions. This growing trend in the adoption of industrial robots, and particularly collaborative robots, confirms the implementation of the core technologies of Industry 4.0 and Industry 5.0, where robotics is one of the fundamental

technologies of these industrial paradigms because it enables more efficient human–robot collaboration in modern manufacturing environments. Compared with other industrial sectors, the automotive industry is the largest user of robotic technologies at the global level. The high degree of automation in manufacturing processes, the need for precision and quality, and the requirements for increased productivity have led to the intensive application of industrial and collaborative robots in the production of vehicles and their components. An analysis of the estimated newly installed industrial and collaborative robots in the world's leading automobile-producing countries is presented in Table 5, with particular emphasis on their application in the automotive industry industry (International Federation of Robotics (IFR), 2024 & 2025).

Table 5 Trend in the application of industrial and collaborative robots in the five leading countries in the world and in the automotive industry in 2025.

Country	Industrial Robots (Newly Installed Units)	Collaborative Robots	Industrial Robots in the Automotive Industry	Collaborative Robots in the Automotive Industry
China	310,000	37,200	108,500	16,740
United States	36,000	4,320	14,400	2,160
Japan	46,000	5,290	18,400	2,650
Germany	28,000	3,360	12,600	1,680
India	11,500	1,380	3,450	620
Total	431,500	51,550	157,350	23,850

Note: *The values represent estimated figures for 2025 based on trends reported by the International Federation of Robotics (IFR). The number of industrial robots deployed in the automotive industry was estimated according to the share of the automotive sector in total annual robot installations (30–45%, depending on the country). The number of collaborative robots in the automotive industry was estimated based on their increasing adoption in assembly operations, material handling, quality inspection, welding, and final assembly processes*

The trend in the implementation of industrial and collaborative robots in the world's five leading countries—China, the United States, Japan, Germany, and India—in 2025, as presented in Table 5, shows that the automotive industry continues to be the leading sector compared with other industries. China is the world's leading country in robot implementation, having deployed approximately 108,000 robot units in the automotive industry alone in 2025. The implementation trend in Japan and Germany is also at a remarkably high level, both across all industries and within the automotive industry, while the United States continues to increase the adoption of collaborative robots in final assembly and logistics processes. At the same time, India is recording the fastest relative growth due to the expansion of manufacturing capacities by both domestic and international vehicle manufacturers. This trend in robot adoption in the automotive industry confirms that the automotive sector remains the key driver of the research, development, and implementation of advanced robotic technologies in the global market.

Robot Density per 10,000 Employees in Industry

One of the main indicators showing the level of automation of manufacturing processes in a particular industrial sector is the robot density per 10,000 employees in that industrial sector or in the entire industry of a country. The robot density indicator enables an objective comparison of the level of implementation of robotic technologies among different countries and industrial sectors, regardless of their size or number of employees. By analysing this indicator, we can observe a significant difference between the overall manufacturing industry and the automotive industry, which is considered the most highly automated manufacturing sector in the world. For the analysis of this indicator, the data presented in Table 6 are based on the data on industrial robot density in the manufacturing and automotive industries presented in Table 6 are based on IFR reports, which provide detailed statistics on robot installations in the manufacturing and automotive industries for the world's top five countries: China, Germany, Japan, the United States, and India, as well as the corresponding world average industry (International Federation of Robotics (IFR), 2025; Karabegović, I. 2025; Karabegović, I. et al. 2020).

Table 6 Industrial Robot Density Indicator per 10,000 Employees in the Manufacturing and Automotive Industries in the World's Top Five Countries in 2024

Country	Industrial Robot Density in the Manufacturing Industry	Industrial Robot Density in the Automotive Industry
China	470	1,250
Germany	429	1,500
Japan	419	1,470
United States	295	1,320
India	30	280
Global Average	162	1,020

Note: *Robot density represents the number of operational industrial robots per 10,000 employees. The values for the manufacturing industry are based on data published by the International Federation of Robotics (IFR), whereas the values for the automotive industry are estimated on the basis of sector-specific IFR analyses, which indicate that the automotive sector achieves a substantially higher robot density than the average manufacturing industry.*

Based on the data presented in Table 6, we conclude that the automotive industry in the five selected leading countries is the most highly automated sector compared to other industrial sectors. Among these five leading countries, the robot density indicator in the manufacturing industry ranges from 30 robots per 10,000 employees in India to 470 robots in China. However, in the automotive industry, the robot density indicator in almost all of the observed countries exceeds 1,000 robots per 10,000 employees. The highest robot density indicator is recorded in Germany, amounting to approximately 1,500 robots, which allows us to conclude that Germany maintains a very high level of automation in vehicle and automotive component manufacturing. China has been investing intensively in robotization and the modernization of its manufacturing capacities year after year, which has enabled it to become the world's leading economy. Despite its significantly lower level of automation, India demonstrates continuous growth as a result of the expansion of its domestic automotive industry. These indicators confirm that the automotive sector remains the key driver of research, development, and implementation of advanced robotic technologies at the global level.

Integration of Smart Technologies and Digitalization Policies

The indicator of smart technology integration and digitalization policies assesses the extent to which the core Industry 4.0 technologies, such as the Internet of Things (IoT), Industrial Internet of Things (IIoT), Autonomous Robots (Industrial Robotics), Collaborative Robotics (Cobots), smart sensors, Artificial Intelligence (AI) and Machine Learning (ML), Big Data, simulation and digital twins, cloud computing, horizontal and vertical system integration, Additive Manufacturing (3D Printing), Augmented Reality (AR) and Virtual Reality (VR), Autonomous Mobile Robots (AMR), Automated Guided Vehicles (AGV), cybersecurity, and advanced systems, are integrated into industrial manufacturing systems. Their integration into manufacturing systems is one of the key indicators of the digital transformation of advanced industry. By implementing these technologies, manufacturing processes are optimized, operating costs are reduced, productivity is increased, predictive maintenance is introduced, product quality is improved, and greater flexibility and adaptability of manufacturing systems to market requirements are achieved. In addition to the technological component, the level of industrial digitalization also depends on national policies, investments in research and development (R&D), the development of digital infrastructure, the education of a skilled workforce, and cooperation between industry, academia, and government institutions. Therefore, the assessment of smart technology integration is based on a combination of quantitative and qualitative indicators that enable a comprehensive evaluation of the digital maturity of industrial systems. Table 7 presents the key indicators for assessing the integration of smart technologies in the world's five leading economies during the 2024–2025 period (PwC, 2025; McKinsey & Company, 2025; World Economic Forum, 2025; Statista, 2025; Organisation for Economic Co-operation and Development, 2025; Deloitte, 2025; United Nations Industrial Development Organization; 2025).

Table 7 Indicators for Assessing the Level of Integration of Core Industry 4.0 Technologies into the Manufacturing Processes of the World's Top Five Countries: China, the United States, Japan, Germany, and India (2024/2025)

INDICATOR	China	United States	Japan	Germany	India	Source / Remarks
Share of smart factories in total manufacturing (%)	42	38	36	40	17	PwC; OECD
Adoption of IoT systems in manufacturing lines (%)	71	68	65	69	29	McKinsey; IFR
Adoption of AI and predictive analytics in manufacturing (%)	61	54	57	59	21	WEF; Statista
Adoption of Digital Twin technology in manufacturing (%)	39	34	36	41	12	Deloitte; WEF
Investment in digital infrastructure (USD billion)	210	125	58	47	27	OECD; IMF
Number of smart industrial zones / clusters	62	48	31	36	22	UNIDO
R&D expenditure (% of GDP)	2.6	3.5	3.4	3.1	0.9	OECD
Number of industrial IoT devices (million)	1,460	1,150	620	510	310	Statista
Industrial digital maturity level (scale 1–5)	4.4	4.6	4.5	4.7	3.1	Deloitte Industry 4.0 Index

Note: *The data represent the latest available values for the 2024–2025 period and were collected from internationally recognized reports and databases. For certain indicators, estimated values based on current industrial digital transformation trends were used to facilitate international comparisons among the world's leading industrial economies.*
Source: *Authors' compilation based on data from OECD (2025), World Economic Forum (2025), International Federation of Robotics (2025), UNIDO (2025), Statista (2025), Deloitte (2025), PwC (2025), McKinsey & Company (2025), and the IMF Digital Economy Report (2025).*

Based on the data on the magnitude of the indicators assessing the degree of integration of the core Industry 4.0 technologies into the manufacturing processes of the world's top five countries, we conclude that China is the country with the leading position in the implementation of IoT systems, artificial intelligence, the number of smart industrial zones, and investments in digital infrastructure, confirming its strategy of accelerated development of smart

manufacturing processes. China achieves a high level of digitalization in manufacturing processes because it maintains a leading position in research and development of Industry 4.0 technologies. Germany and Japan are characterized by a high degree of implementation of digital twins, automation, and advanced manufacturing technologies, which is the result of their long-standing industrial tradition and strong technological base. India records lower values for most of the analysed indicators but demonstrates significant growth potential owing to accelerated investments in digital infrastructure, industrial automation, and digital manufacturing transformation programs. All five countries—China, the United States, Japan, Germany, and India—are developing artificial intelligence technologies, the Industrial Internet of Things, and digital twins, which are becoming key elements of the smart factories of the future. The successful integration of smart technologies represents one of the fundamental prerequisites for increasing industrial competitiveness and the effective implementation of the Industry 4.0 concept. At the same time, the growing application of these technologies creates the technological foundation for the further development of collaborative robotics, autonomous manufacturing systems, and digitally connected value chains, which will play a key role in the future transformation of the automotive and other high-technology industries. To obtain a more comprehensive picture of the dynamics of industrial digital transformation, Figure 1 presents the estimated trend of IoT and AI technology integration into the manufacturing processes of the world's leading economies during the period 2018–2025 (PwC, 2025; McKinsey & Company, 2025; World Economic Forum, 2025; Statista, 2025; Organisation for Economic Co-operation and Development, 2025; Deloitte, 2025; United Nations Industrial Development Organization; 2025).

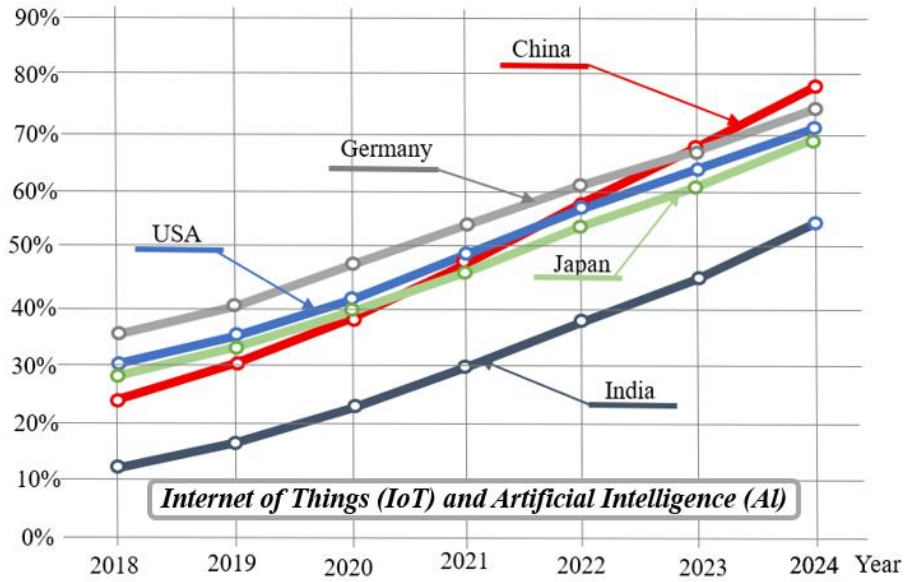

Note: *This represents an estimated trend of IoT and AI technology integration.*

Figure 1 Trend of IoT and AI technology integration in industrial manufacturing in the world's top five countries: China, the United States, Japan, Germany, and India during the period 2018–2025 (prepared by the authors based on (PwC, 2025; McKinsey & Company, 2025; World Economic Forum, 2025; Statista, 2025; Organisation for Economic Co-operation and Development, 2025; Deloitte, 2025; United Nations Industrial Development Organization; 2025)).

Based on Figure 1, we conclude that the five top countries analysed—China, the United States, Japan, Germany, and India—have recorded continuous growth in the implementation of IoT and AI technologies in manufacturing processes, with China standing out as the country achieving the most pronounced growth trend. We conclude that the United States, Germany, and Japan maintain a high level of digital integration owing to strong investments in innovation, research and development, and advanced manufacturing technologies. These trends confirm that digitalization is becoming one of the key factors of competitiveness in modern industry. Although all the observed countries pursue the same goal—increasing the efficiency, flexibility, and resilience of industrial manufacturing—their approaches to digital transformation differ significantly. The United States relies on market-driven innovation, a strong private sector, and advanced technology companies that lead the development of artificial intelligence, cloud infrastructure, and industrial digital platforms. China applies a coordinated government approach through national digitalization strategies and industrial modernization programs, together with the intensive implementation of 5G networks, the Internet of Things, and artificial intelligence-based technologies. Germany and Japan represent examples of highly developed industrial economies that successfully combine traditional manufacturing excellence with modern digital technologies. Germany bases its digital transformation on the Industry 4.0 concept, while Japan is intensively developing the Society 5.0 concept, which emphasizes the integration of digital technologies into industry and society. Both countries achieve a high level of digital maturity, particularly in the areas of automation, digital twins, robotics, and smart manufacturing systems. India is in a phase of accelerated digital transformation and records significant progress owing to national initiatives aimed at developing digital infrastructure, smart manufacturing, and the digitalization of small and medium-sized enterprises. Although it lags behind the leading

industrial economies according to most of the analysed indicators, its high growth rate and strong development of the IT sector indicate considerable potential for further improving digital competitiveness. The cumulative results presented in Table 7 and Figure 1 indicate the transition of industry from the phase of basic digitalization to the phase of intelligent industrial optimization, in which artificial intelligence, the Internet of Things, digital twins, and advanced data analytics become integral parts of manufacturing processes and business decision-making. These technologies no longer represent only support for manufacturing but are key drivers of productivity, innovation, and sustainable competitive advantage. Based on the conducted analyses, it can be concluded that digital policies, investments in research and development, the development of digital infrastructure, and the application of smart technologies play a decisive role in strengthening industrial competitiveness and the technological resilience of national economies. At the same time, the results confirm that China and the United States are currently leading the global digital transformation of industry, while Germany and Japan maintain a leading position in advanced industrial automation. These trends create a solid foundation for the further development of collaborative robotics, autonomous manufacturing systems, and artificial intelligence-based industrial solutions, which will mark the next phase of the evolution of global manufacturing.

APPLICATION OF COLLABORATIVE ROBOTICS AND ARTIFICIAL INTELLIGENCE IN ASSEMBLY AND QUALITY CONTROL PROCESSES IN THE AUTOMOTIVE INDUSTRY

The modern automotive industry represents one of the most technologically advanced application areas of collaborative robotics and artificial intelligence. Intense global competition, increasing product quality requirements, shorter vehicle life cycles, and the growing demand for flexible manufacturing have encouraged automotive manufacturers to develop intelligent manufacturing systems based on human–robot collaboration. Within such systems, collaborative robots perform repetitive, physically demanding, and highly precise operations, while human operators carry out tasks requiring experience, judgment, and decision-making capabilities (Villani, V. et al. 2018). One of the most significant application areas of collaborative robots is the assembly of automotive components. Unlike conventional industrial robots that operate within isolated work cells, collaborative robots enable direct interaction with operators in a shared workspace. This approach is particularly suitable for the assembly of electronic components, vehicle interior modules, air-conditioning systems, and electric vehicle components, where a combination of human flexibility and robotic precision is required. Research has shown that the implementation of collaborative robots can increase assembly process productivity by more than 20%, while simultaneously reducing workers' physical workload and improving ergonomic working conditions (Leng, J. et al. 2022). The development of artificial intelligence has further enhanced the capabilities of collaborative robotic systems. Through the integration of machine learning algorithms and deep neural networks, robots become capable of object recognition, motion planning, and adaptation to changes in the manufacturing environment. Such systems can analyse sensor data in real time and make decisions without requiring continuous operator intervention. Deep learning algorithms play a particularly important role by enabling adaptive control of robotic systems operating in complex manufacturing processes (Piccarozzi, M. et al. 2024). In the automotive industry, quality control represents one of the most critical stages of the manufacturing process. Traditional inspection methods often depend on human factors, which may result in subjective assessments and variations in product quality. The application of artificial intelligence and computer vision enables the automation of quality inspection processes while significantly improving defect detection accuracy. High-resolution cameras combined with deep learning algorithms enable the identification of surface defects, assembly irregularities, missing components, and dimensional deviations with a level of accuracy and speed substantially exceeding that of conventional inspection methods (Zafar, M. H. et al. 2024). Convolutional Neural Networks (CNNs) play a particularly important role by enabling the automatic detection and classification of product defects. These methods achieve considerably higher accuracy than conventional machine vision systems and provide continuous quality monitoring throughout the entire manufacturing process. Research has demonstrated that deep learning-based systems can achieve defect detection accuracies exceeding 95%, significantly reducing the number of defective products reaching end users (Ghahramani, M. et al. 2020). In addition to quality control, artificial intelligence plays an important role in predictive maintenance of manufacturing equipment. Modern manufacturing systems generate vast amounts of operational data related to machines, robots, tools, and production lines. By analysing these data, it is possible to identify patterns that precede equipment failures and schedule maintenance interventions in a timely manner. This approach reduces unplanned downtime, increases equipment availability, and lowers maintenance costs. According to recent studies, AI-based predictive maintenance systems can reduce maintenance costs by 20–30% while increasing equipment availability by more than 15% (Carvalho, T. P. et al. 2019). Digital Twins are also becoming increasingly important, representing virtual models of manufacturing systems synchronized with real production processes. By integrating collaborative robots, sensors, and AI algorithms, different production scenarios can be simulated before implementation in the actual manufacturing environment. Digital Twins enable the optimization of robot trajectories, the identification of production bottlenecks, and the improvement of quality control processes. Such systems are becoming an essential tool for the development of smart factories and next-generation industrial systems (Feng, X., & Wan, J. 2024). The application of collaborative robotics is particularly prominent in electric vehicle manufacturing. The complex assembly processes of battery systems, electronic components, and control systems require a high level of precision and flexibility. Collaborative robots enable safe cooperation with operators during battery module assembly and the handling of sensitive components. At the same

time, AI systems optimize manufacturing parameters and continuously monitor process quality, thereby improving the reliability and safety of the final product (Valette, E. et al. 20203). Despite their numerous advantages, the implementation of collaborative robotics and artificial intelligence faces several challenges. Among the most important are ensuring the safety of human–robot collaboration, data security, interoperability among heterogeneous systems, and the need for continuous workforce education and training. In addition to technical aspects, successful implementation also requires organizational changes involving the development of new employee competencies and the adaptation of business processes to the digital manufacturing environment (Dhanda, M. et al. 2025). Based on the available research, it can be concluded that the integration of collaborative robotics and artificial intelligence represents one of the principal directions for the future development of the automotive industry. The combination of human capabilities and intelligent robotic systems enables improvements in productivity, product quality, and manufacturing flexibility, while simultaneously enhancing workplace safety and ergonomics. It is expected that further advances in artificial intelligence, advanced sensing technologies, and Digital Twin systems will further accelerate the transformation of the automotive industry toward the concepts of Industry 5.0 and fully interconnected smart factories.

IMPLEMENTATION COLLABORATIVE ROBOTS IN THE AUTOMOTIVE INDUSTRY AND CASE STUDIES

Implementation of Collaborative Robots on Assembly Lines

In addition to the two primary applications of collaborative robots in the processes of automobile body welding and painting, the assembly of automotive components also represents one of the most significant application areas. In recent years, advanced manufacturing systems in the automotive industry have required a high degree of flexibility, reduced production time, as well as the ability to adapt to different vehicle models. Unlike first-generation industrial robots that operate in enclosed spaces, collaborative robots enable direct collaboration with workers in a shared workspace, and this approach makes it possible to combine human decision-making capabilities with robotic precision, resulting in increased productivity and reduced errors in assembly processes. A very common and significant application of collaborative robots in the assembly process includes: the assembly of electronic components, vehicle interior trim, doors, instrument panels, and battery modules of electric vehicles. In these assembly processes, collaborative robots perform repetitive tasks that require high precision, while the operator carries out final inspections and more complex manipulations, as shown in Figure 2 (Villani, V. et al. 2018; Bdiwi, M. et al. 2018).

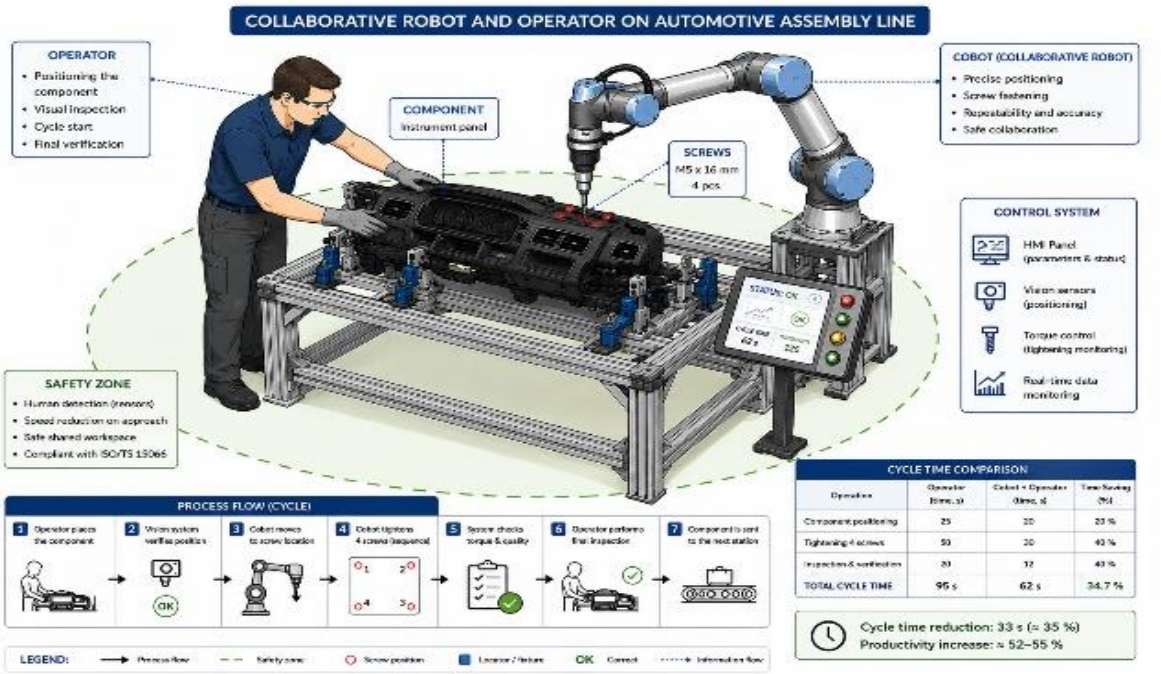

Source: Authors' own illustration based on the literature synthesis; visualization assisted by generative AI (2026).

Figure 2 Assembly process of an automotive instrument panel in an intelligent manufacturing cell, illustrating collaboration between a worker and a collaborative robot during assembly (prepared by the authors).

Figure 2 illustrates a modern assembly cell in the automotive industry based on the concept of collaboration between a human and a collaborative robot. The worker performs the positioning and inspection of the vehicle instrument panel component, while the collaborative robot simultaneously carries out the precise fastening operation using an

electric screwdriver. The assembly cell is equipped with a component positioning system, a digital control panel, and a display for monitoring production parameters in real time. The presented configuration illustrates the Industry 5.0 concept, in which human flexibility, experience, and decision-making capabilities are combined with the precision, repeatability, and reliability of a collaborative robot. This form of collaboration enables increased productivity, reduced assembly time, and improved quality of assembly operations (Kakade, S. et al. 2023).

Table 8 Comparison of Assembly Time Between a Worker and a Collaborative Robot

Parameter	Worker	Collaborative Robot (Cobot)
Assembly time per component (s)	95	62
Components assembled per hour	38	58
Average error rate (%)	2.8	0.7
Rework rate (%)	3.2	0.9
Productivity (%)	100	153

The data presented in Table 8 show that the collaborative robot achieves a reduction in assembly time of approximately 35% in this example, while productivity increases by more than 50%. At the same time, the number of errors and the need for additional product corrections are significantly reduced.

Table 9 Estimated Daily Production of the Assembly Cell

Parameter	Worker	Collaborative Robot (Cobot)
Components per shift	304	464
Components per day (3 shifts)	912	1,392
Annual production	228,000	348,000

The values presented in Tables 8 and 9 indicate the significant potential of collaborative robotics for optimizing assembly processes in the automotive industry. The observed reduction in cycle time of approximately 35% and the increase in productivity of more than 50% confirm that the integration of cobots contributes to more efficient utilization of production resources and increased production capacity. At the same time, the reduction in the error rate from 2.8% to 0.7% and the need for rework from 3.2% to 0.9% indicate a significant improvement in the quality of assembly operations. From an annual perspective, the increase in production capacity by approximately 120,000 components confirms the economic justification for implementing collaborative robotic systems in modern manufacturing environments based on the principles of Industry 5.0.

Implementation of Artificial Intelligence Systems in the Quality Control of Automotive Parts

In the manufacturing process of the automotive industry, quality control represents a critical stage of the production process. Traditional visual quality control has so far been based on human work and is often limited by subjective assessments, fatigue, and variations in inspection quality. The development of advanced Industry 4.0 technologies such as artificial intelligence, computer vision, and deep neural networks has enabled the automation of inspection processes in manufacturing, resulting in a significant increase in the reliability of defect detection. Advanced artificial intelligence systems use high-resolution cameras, laser sensors, and deep learning algorithms to identify surface defects, cracks, irregular gaps, missing components, and dimensional deviations, as shown in Figure 3 (Zhou, C. et al. 2022; Sun, Y. et al. 2023).
Figure 3 illustrates an intelligent automated quality control system for automotive components based on the integration of a collaborative robot, a 3D machine vision system, and artificial intelligence (AI) algorithms. The collaborative robot manipulates a 3D camera that performs detailed surface scanning of an automotive body component to identify manufacturing deviations and potential defects. The AI system employs deep learning and computer vision techniques to automatically detect surface scratches, cracks, dents, deformations, missing holes, and dimensional deviations from the product's CAD model.

The illustrated workstation incorporates a safety zone equipped with laser scanners and safety barriers in accordance with the ISO/TS 15066 standard, thereby enabling safe human–robot collaboration within a shared workspace. The inspection workflow includes component positioning, automated 3D scanning, AI-based analysis of the acquired data, classification of inspection results as acceptable (OK) or defective (NOK), followed by the automatic generation of inspection reports and transmission of data to the manufacturing information system.

The comparative analysis presented in the figure demonstrates that the implementation of the AI system and the collaborative robot reduces inspection time by approximately 79%, increases the number of inspected components per hour by more than fourfold, and improves defect detection accuracy from 92% to 99%. Such systems represent an essential element of the digital transformation of the automotive industry and the development of smart factories based on the principles of Industry 4.0 and Industry 5.0 (Yan, J. et al. 2024).

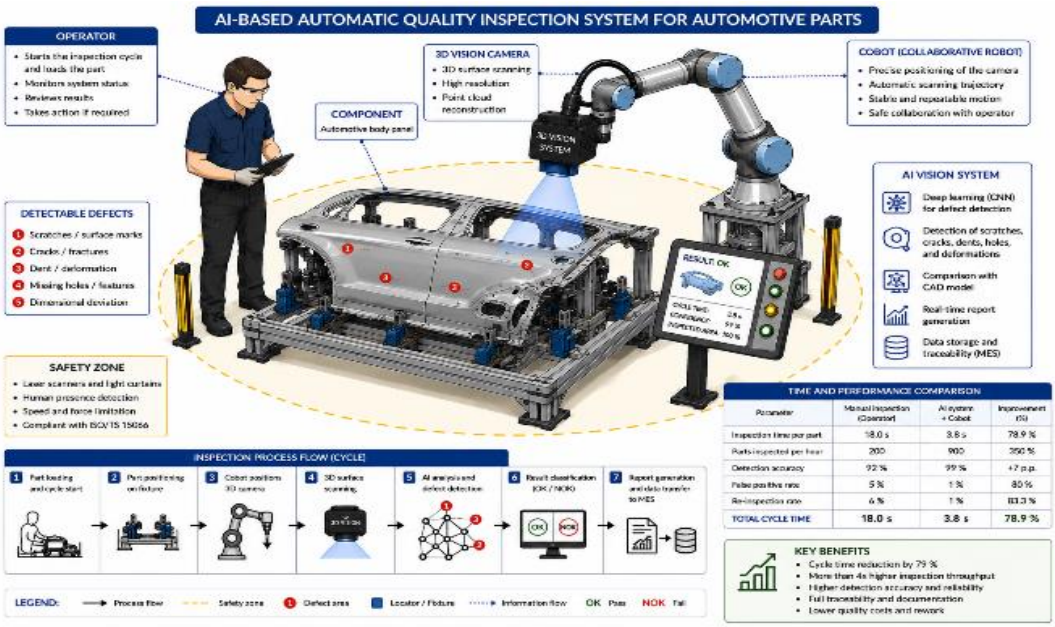

Source: Authors' own illustration based on the literature synthesis; visualization assisted by generative AI (2026).

Figure 3 Implementation of an Advanced Quality Control System for Automotive Parts Based on a Collaborative Robot and Artificial Intelligence (prepared by the authors).

Table 10 Comparison of the Performance of Quality Control Systems

Parameter	Worker	AI + Collaborative Robot (Cobot)
Inspection time (s)	18	4
Components inspected per hour	200	900
Detection accuracy (%)	92	99
False-positive rate (%)	5	1
Repeated inspections (%)	6	1

The data presented in Table 10 show that the AI system enables a reduction in inspection time of approximately 78%**,** while increasing the detection accuracy from 92% to 99%.

Table 11 Detection Efficiency for Different Types of Defects

Defect Type	Worker (%)	AI System (%)
Scratches	89	98
Cracks	87	99
Missing components	94	100
Dimensional deviations	85	98

The results presented in Tables 10 and 11 clearly demonstrate the effectiveness of integrating collaborative robots, 3D machine vision systems, and artificial intelligence algorithms into automotive quality control processes. The reduction in inspection time by approximately 79% and the more than fourfold increase in inspection throughput represent a significant contribution to improving the productivity of manufacturing systems. Furthermore, the achieved 99% detection accuracy confirms the high reliability of AI-based systems in identifying various types of manufacturing defects, including scratches, cracks, missing components, and dimensional deviations. The reduction in the number of false-positive detections and the need for repeat inspections further contributes to lowering quality-related costs, improving manufacturing traceability, and enhancing the overall efficiency of quality management systems in the automotive industry.

Intelligent Material Handling and Logistics

It is well known that material handling in the automotive manufacturing process was carried out using forklifts and manual transport systems, which represents an important part of the overall process where time is consumed and production delays occur. The development of advanced technologies has led to the development of autonomous mobile robots (AMRs) and collaborative robots, enabling the creation of intelligent logistics systems that autonomously deliver components from the warehouse to the production process and transport finished products back to the warehouse (Boysen, N. et al. 2021). By integrating AI algorithms, it is possible to optimize movement trajectories, reduce delays, and increase the efficiency of material transportation (Fragapane, G. et al. 2022).

The figure illustrates an intelligent logistics system in the automotive industry based on the integration of an autonomous mobile robot (AMR), a collaborative robot (cobot), and a digital production management system. The autonomous mobile robot (AMR) autonomously transports automotive components between the warehouse, intermediate zones, and assembly stations using Simultaneous Localization and Mapping (SLAM) technology, obstacle avoidance sensors, and route optimization algorithms. The collaborative robot performs the automatic loading and unloading of components from the AMR platform and precisely positions the parts at the assembly stations. The system enables safe human–robot collaboration within a shared workspace through the implementation of laser scanners, operator presence detection systems, and safety functions in accordance with the requirements of the ISO/TS 15066 standard. The presented process flow includes the creation of a logistics task in the MES system, autonomous route planning, component pickup, transportation to the assembly line, automatic unloading using the collaborative robot, and the return of the AMR system to the next logistics task. The integration of AMR and cobot technologies enables continuous material flow, reduced transportation time, and increased flexibility of manufacturing systems.

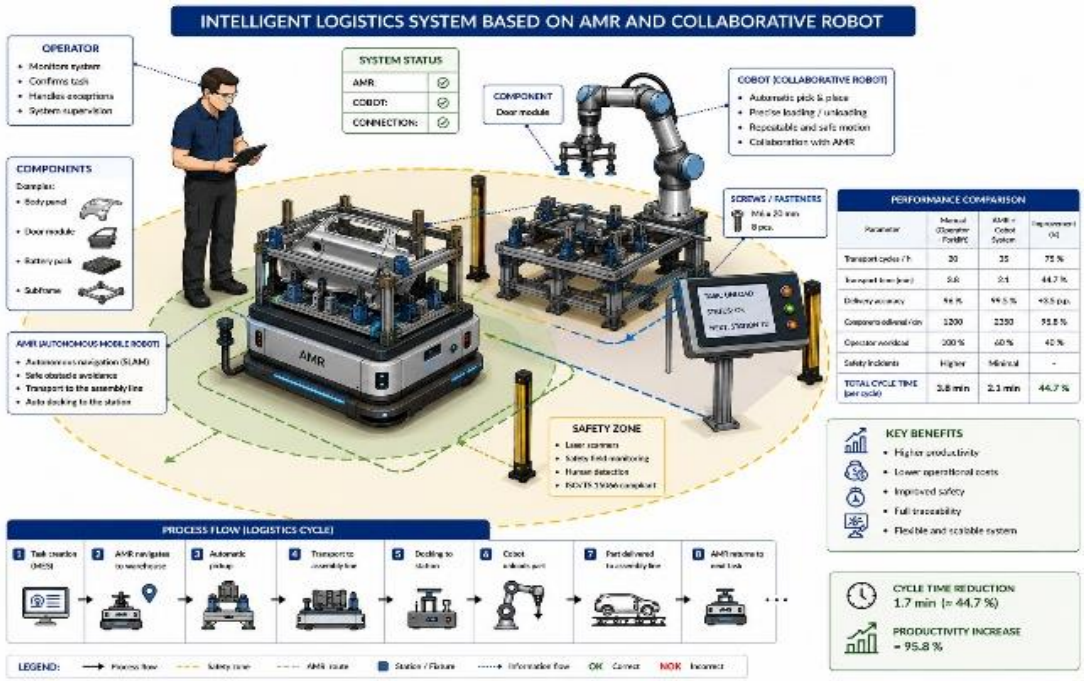

Source: Authors' own illustration based on the literature synthesis; visualization assisted by generative AI (2026).

Figure 4 Intelligent Logistics System for Material Handling and Transportation of Automotive Components in the Automotive Industry Based on an Autonomous Mobile Robot (AMR) and a Collaborative Robot

The comparative analysis presented in the Figure 4 shows that the implementation of the intelligent logistics system increases the number of transport cycles from 20 to 35 cycles per hour (as shown in Table 12), reduces transportation time by approximately 45%, and increases the daily component delivery capacity by nearly 96% compared to traditional transportation based on operators and forklifts. At the same time, operator workload is significantly reduced, workplace safety is improved, and the traceability of logistics processes is enhanced. Such systems represent an important element of Industry 4.0 and Industry 5.0 smart factories, where autonomous logistics, artificial intelligence, and collaborative robotics enable the development of flexible, digitally connected, and highly productive manufacturing environments (Matt, O. et al. 2026).

Table 12 *Comparison of Logistics Performance*

Parameter	Worker + Forklift	AMR + Collaborative Robot (Cobot)
Transportation cycles per hour	20	35
Transportation time (min)	3.8	2.1
Delivery error rate (%)	3.5	0.5
Safety incidents	Higher risk	Minimal

Table 13 Material Handling Performance

Performance Indicator	Worker	Intelligent System
Components transported per day	1,200	2,350
Productivity (%)	100	196
Operating costs (%)	100	72
System availability (%)	90	98

The data presented in Tables 12 and 13 clearly show that the integration of AMR systems and collaborative robots represents a significant step toward the development of autonomous intralogistics within smart factories. The

increase in the number of transported components from 1,200 to 2,350 per day, together with the increase in productivity from 100% to 196%, confirms the high potential of these technologies for optimizing logistics processes. At the same time, the reduction in operating costs from 100% to 72% and the increase in system availability from 90% to 98% indicate significant economic and organizational benefits of implementing intelligent logistics solutions. Particularly significant is the reduction in delivery errors and safety risks, confirming that AMRs and collaborative robots enable more reliable, flexible, and safer material handling in modern automotive manufacturing systems based on the principles of Industry 4.0 and Industry 5.0.

Case Studies of Leading Global Automotive Companies

Over the past decade, the world's leading automotive manufacturers have invested extensively in the development and implementation of collaborative robotics, artificial intelligence (AI), and the digital technologies of Industry 4.0 and Industry 5.0. These investments are driven by the need to increase productivity, improve product quality, reduce manufacturing costs, and enhance the flexibility of production systems. Collaborative robots enable safe cooperation with human operators within a shared workspace, while artificial intelligence systems facilitate the analysis of large volumes of data, process optimization, and real-time decision-making. As a result, leading automotive manufacturers are developing smart factories based on the integration of humans, robots, and intelligent information systems (Peruzzini, M., & Pellicciari, M. 2017).

Table 14 Application of Collaborative Robotics and Artificial Intelligence in Leading Automotive Companies

Company	Application of Collaborative Robots	Application of Artificial Intelligence
Toyota	Door and electronic component assembly	Predictive maintenance
BMW	Final vehicle assembly	Visual inspection
Mercedes-Benz	Human–robot collaborative assembly stations	Digital Twins
Volkswagen	Electric vehicle battery assembly	AI-based production optimization
Tesla	Battery module assembly	AI-based quality control

Toyota is regarded as one of the pioneers of manufacturing automation and robotization in the automotive industry. In its production facilities, the company employs collaborative robots for the assembly of vehicle doors, electronic components, and interior finishing elements. At the same time, artificial intelligence systems analyse production-line data to predict equipment failures and optimize maintenance activities. This approach reduces unplanned downtime, while increasing the availability of manufacturing systems. BMW utilizes collaborative robots during the final stages of vehicle assembly, particularly in the installation of interior components, control modules, and instrument panel assemblies. Through the integration of machine vision and artificial intelligence, BMW has developed advanced automated visual inspection systems capable of detecting defects and manufacturing deviations in real time. Consequently, the quality of the final product is improved, while costs associated with customer claims and product rework are reduced. Mercedes-Benz develops manufacturing systems based on the Industry 5.0 concept, in which humans and robots operate as equal partners throughout the production process. Collaborative robots are employed for the assembly of complex components, while Digital Twin technology enables the simulation and optimization of manufacturing processes before their implementation in the real production environment. This approach contributes to greater manufacturing flexibility and faster adaptation to new vehicle models (Guo, Y. et al. 2024).

Volkswagen extensively utilizes collaborative robots in the production of electric vehicles and battery assembly systems. The application of artificial intelligence enables production planning optimization, material flow management, and performance analysis of manufacturing lines. Particular emphasis is placed on the development of smart factories that integrate all manufacturing resources into a unified digital ecosystem. Tesla represents one of the most advanced examples of artificial intelligence implementation in the automotive industry. The company employs AI systems for manufacturing process optimization, automated quality control, and battery module production management. Through the integration of machine vision, deep learning, and robotic systems, Tesla achieves a high level of automation, precision, and productivity in electric vehicle manufacturing (Mourtzis, D. et al. 2023).

The analysis of these industrial examples confirms that leading automotive manufacturers are increasingly transitioning from conventional automated systems toward intelligent manufacturing systems based on the collaboration of humans, collaborative robots, and artificial intelligence. This approach enables the development of more flexible, productive, and sustainable manufacturing environments that form the foundation of future smart factories.

Analysis of System Productivity and Performance

Based on the previously analysed case studies, an overall assessment of the impact of collaborative robotics and artificial intelligence on manufacturing system performance in the automotive industry can be conducted. The integration of collaborative robots into assembly operations, AI-based systems into quality control, and autonomous

logistics systems into material handling results in significant improvements in productivity, product quality, and workplace safety. It is particularly important that these improvements affect not only individual operations but also the overall manufacturing system (Ribeiro, J. et al. 2021). The results presented in Table 15 demonstrate that the combination of collaborative robots and artificial intelligence increases productivity by approximately 60%, while reducing the overall production cycle time by approximately 35%. At the same time, the number of quality defects is reduced by more than 70%, directly contributing to improved product reliability and lower costs associated with warranty claims and product rework.

Table 15 Overall Comparison of Manufacturing System Performance

Performance Indicator	Worker	Collaborative Robot + AI
Productivity	100%	160%
Cycle time	100%	65%
Quality defects	100%	25%
Quality-related costs	100%	60%
Workplace safety	Moderate	High
System availability	90%	98%

The reduction of quality-related costs to approximately 60% of their initial value confirms the economic viability of investing in intelligent manufacturing systems. A particularly significant benefit is the improvement of workplace safety, as collaborative robots perform physically demanding, repetitive, and potentially hazardous tasks, thereby reducing operator workload and minimizing the risk of occupational injuries. Furthermore, the increase in system availability from 90% to 98% indicates greater manufacturing reliability achieved through the implementation of predictive maintenance, continuous process monitoring, and intelligent management of manufacturing resources.

From the perspective of Industry 5.0, the obtained results confirm that the greatest benefits arise from the synergy between human capabilities and intelligent technological systems. While humans retain the primary role in decision-making, solving complex problems, and supervising manufacturing processes, collaborative robots and AI systems ensure high precision, speed, and repeatability of operations. This collaborative model enables the development of human-centric manufacturing systems that simultaneously improve productivity, product quality, and manufacturing sustainability. Based on the overall analysis, it can be concluded that collaborative robotics and artificial intelligence represent the key technological pillars of future smart factories in the automotive industry. Their integration enables the development of flexible, digitally connected, and autonomous manufacturing systems capable of meeting the demands of modern markets, mass product customization, and sustainable industrial development (Renard, D. et al. 2024; Kusiak, A. 2018).

CHALLENGES AND FUTURE TRENDS

Despite the significant advantages offered by collaborative robotics and artificial intelligence, their widespread implementation in the automotive industry faces numerous technical, organizational, economic, and safety-related challenges. Although modern collaborative robots enable direct cooperation with human operators, ensuring human–robot safety remains one of the key factors for successful implementation. The development of reliable systems for operator presence detection, motion tracking, and automatic robot speed adaptation continues to represent an important research challenge. Particular attention is being devoted to the advancement of safety standards such as ISO 10218 and ISO/TS 15066, which define the requirements for safe collaboration between humans and collaborative robotic systems. Another major challenge concerns the integration of diverse digital technologies within a unified manufacturing environment. Modern factories employ a wide variety of heterogeneous systems, including robots, sensors, AI algorithms, Manufacturing Execution Systems (MES), Enterprise Resource Planning (ERP) platforms, Digital Twins, and industrial Internet of Things (IIoT) networks. Interoperability among these systems represents a fundamental prerequisite for the development of fully connected smart factories. At the same time, the growing volume of data generated during manufacturing processes requires the development of efficient methods for data processing, analysis, and protection against cyber threats. Data security, manufacturing system resilience, and effective management of digital resources are becoming increasingly important elements in the successful transformation of modern industry toward the Industry 5.0 paradigm (Ivanov, D. 2023). The implementation of collaborative robots and artificial intelligence also requires substantial financial investment. The costs associated with equipment acquisition, system integration, workforce training, and the adaptation of manufacturing processes may represent limiting factors, particularly for small and medium-sized enterprises (SMEs). Nevertheless, the long-term benefits achieved through increased productivity, reduced errors, improved product quality, and lower operating costs generally justify the initial investment. In addition to technical and economic challenges, the development of new workforce competencies represents another critical factor. The industry of the future requires professionals capable of working in environments where humans, robots, and artificial intelligence operate as an integrated system. Consequently, educational institutions and industry must develop new training programs encompassing robotics, artificial intelligence, data analytics, Digital Twin technologies, and the management of smart manufacturing systems. Future trends in the automotive industry are directed toward increasing levels of manufacturing autonomy. More extensive adoption of generative artificial intelligence, Digital Twins, Autonomous Mobile Robots (AMRs), advanced

machine vision systems, and intelligent collaborative robots capable of autonomous real-time decision-making is expected. Furthermore, the development of 5G and future 6G communication networks will further enhance manufacturing system connectivity and enable more efficient data exchange among machines, robots, and digital information platforms. A particularly significant trend is the evolution of Industry 5.0, which places humans at the centre of the manufacturing process. Unlike approaches based solely on automation, Industry 5.0 promotes collaboration between humans and intelligent technologies with the objective of creating more flexible, sustainable, and resilient manufacturing systems. Within such an environment, collaborative robots will not replace human workers but will function as intelligent partners that complement human capabilities and enable higher levels of productivity, product quality, and manufacturing innovation (Ivanov, D. 2023).

At the same time, future developments in collaborative robotics are expected to focus on improving the quality of human–robot interaction, where safety, ergonomics, intuitive operation, and technology acceptance by operators will play essential roles. Advanced AI-based systems will enable robots to better understand human intentions, exhibit adaptive behaviour, and collaborate more effectively in dynamic manufacturing environments. Such an approach represents one of the fundamental prerequisites for the development of next-generation human-centric manufacturing systems, which are expected to characterize Industry 5.0 and the smart factories of the future (Coronado, E. et al. 2022).

CONCLUSIONS

The modern automotive industry is undergoing an intensive transformation driven by the technologies of Industry 4.0 and Industry 5.0, in which collaborative robotics and artificial intelligence represent the principal drivers of smart manufacturing systems. The analysis of global trends has demonstrated a continuous increase in the deployment of industrial and collaborative robots, growing patent activity in the field of robotics, and the extensive integration of digital technologies such as artificial intelligence, the Internet of Things, Digital Twins, and advanced automation systems. The research findings confirm that collaborative robots provide significant advantages in automotive component assembly processes. The analysis presented in the industrial application section demonstrated a cycle time reduction of approximately 35%, a productivity increase exceeding 50%, and a substantial reduction in both assembly errors and rework requirements. At the same time, the integration of artificial intelligence into quality control systems increases defect detection accuracy from 92% to 99%, while significantly expanding inspection capacity and reducing quality-related costs. Particularly important results have been achieved in the field of intelligent material handling and logistics, where the integration of Autonomous Mobile Robots (AMRs) and collaborative robotic systems enables productivity improvements approaching 100%, reduces transportation time, and increases the availability of logistics systems. These findings confirm that the combination of collaborative robotics and artificial intelligence contributes to the development of flexible, efficient, and highly automated manufacturing environments. The analysis of leading global automotive manufacturers, including Toyota, BMW, Mercedes-Benz, Volkswagen, and Tesla, demonstrated that the future of manufacturing is based on the integration of humans, robots, and intelligent information systems. These companies already employ collaborative robots, machine vision systems, Digital Twins, and artificial intelligence algorithms to optimize manufacturing processes, improve quality control, and manage logistics operations.

Based on the conducted analyses, it can be concluded that collaborative robotics and artificial intelligence constitute the fundamental technologies of future smart factories. Their integration enables increased productivity, improved product quality, reduced operating costs, enhanced workplace safety, and the development of human-centric manufacturing systems based on the principles of Industry 5.0. It is expected that further advances in artificial intelligence, Autonomous Mobile Robots (AMRs), Digital Twin technologies, and next-generation communication networks will further accelerate the transformation of the automotive industry toward fully connected, intelligent, and sustainable manufacturing systems of the future.

REFERENCES

Adel, A. (2022). Future of industry 5.0 in society: Human-centric solutions, challenges and prospective research areas. *Journal of Cloud Computing*, 11(1), 40. https://doi.org/10.1186/s13677-022-00314-5

Bdiwi, M., Pfeifer, A., & Sterzing, A. (2018). A new strategy for ensuring human safety in human–robot collaboration environments. *Procedia CIRP*, 72, 77–82. https://doi.org/10.1016/j.procir.2018.03.019

Boysen, N., Emde, S., Hoeck, M., & Kauderer, M. (2021). Part logistics in the automotive industry using autonomous mobile robots. *European Journal of Operational Research*, 292(1), 82–99. https://doi.org/10.1016/j.ejor.2020.10.053

Carvalho, T. P., Soares, F. A. A. M. N., Vita, R., Francisco, R. P., Basto, J. P., & Alcalá, S. G. (2019). A systematic literature review of machine learning methods applied to predictive maintenance. *Computers & Industrial Engineering*, 137, 106024. https://doi.org/10.1016/j.cie.2019.106024

Cherubini, A., & Navarro-Alarcon, D. (2021). Sensor-Based Control for Collaborative Robots: Fundamentals, Challenges, and Opportunities. *Frontiers in Neurorobotics*, 14, 576846. https://doi.org/10.3389/fnbot.2020.576846

Coronado, E., Kiyokawa, T., Ricardez, G. A. G., Ramirez-Alpizar, I. G., Venture, G., & Yamanobe, N. (2022). Evaluating quality in human–robot interaction: A systematic search and classification of performance and human-centered factors, measures and metrics towards an Industry 5.0. *Journal of Manufacturing Systems*, 63, 392–410. https://doi.org/10.1016/j.jmsy.2022.04.007

Deloitte. (2025). Smart manufacturing and Industry 4.0 survey. Deloitte Insights. https://www.deloitte.com

Dhanda, M., Rogers, B. A., Hall, S., Dekoninck, E., & Dhokia, V. (2025). Reviewing human–robot collaboration in manufacturing: Opportunities and challenges in the context of Industry 5.0. *Robotics and Computer-Integrated Manufacturing*, 93, 102937. https://doi.org/10.1016/j.rcim.2024.102937

European Patent Office. (2024). PATSTAT: EPO worldwide patent statistical database. European Patent Office. https://www.epo.org/en/searching-for-patents/business/patstat

Feng, X., & Wan, J. (2024). Digital twins for discrete manufacturing lines: A review. *Big Data and Cognitive Computing*, 8(5), 45. https://doi.org/10.3390/bdcc8050045

Fragapane, G., Ivanov, D., Peron, M. et al. (2022). Increasing flexibility and productivity in Industry 4.0 production networks with autonomous mobile robots and smart intralogistics. *Annals of Operations Research*, 308, 125–143 https://doi.org/10.1007/s10479-020-03526-7

Ghahramani, M., Qiao, Y., Zhou, M. C., O'Hagan, A., & Sweeney, J. (2020). AI-based modeling and data-driven evaluation for smart manufacturing processes. *IEEE/CAA Journal of Automatica Sinica*, 7(4), 1026–1037. https://doi.org/10.1109/JAS.2020.1003114

Guo, Y., Liu, Y., Sun, S., & Wang, L. (2024). Human-centered artificial intelligence for smart manufacturing: A review. *Machines*, 12(2), 96. https://doi.org/10.3390/machines12020096

International Federation of Robotics (IFR). (2024, August 11), Global robot density in factories doubled in seven years (press release / World Robotics Executive Summary) https://ifr.org/ifr-press-releases/news/global-robot-density-in-factories-doubled-in-sevenyears?utm_source=chatgpt.com

International Federation of Robotics (IFR). (2025). World Robotics 2025: Industrial robots. International Federation of Robotics. https://ifr.org/worldrobotics

Ivanov, D. (2023). The Industry 5.0 framework: Viability-based integration of the resilience, sustainability, and human-centricity perspectives. *International Journal of Production Research*, 61(5), 1683–1695. https://doi.org/10.1080/00207543.2022.2118892

Javaid, M., Haleem, A., Singh, R. P., Khan, I. H., & Suman, R. (2022). Understanding the adoption of Industry 4.0 technologies in improving environmental sustainability. *Sustainable Operations and Computers*, 3, 203–217. https://doi.org/10.1016/j.susoc.2022.01.008

Kakade, S., Narde, V., & Vikhe Patil, K. (2023). Applications of collaborative robots in agile manufacturing. *Journal of Vibroengineering*, 25(4), 682–695. https://doi.org/10.21595/jve.2023.23238

Karabegović, I. (2025). A Comparative Analysis of the Role of Industrial and Humanoid Robots as Drivers of Efficiency and Flexibility in the Automotive Industry. *Journal Mobility & Vehicle Mechanics* 51(1), 31- 45. https://doi.org/10.24874/mvm.2025.51.01.03

Karabegović, I, Karabegović, E, Mahmić, M, & Husak, E. (2020), The implementation of Industry 4.0 using industrial and service robots in production processes. In I.Karabegović, L. Banjanović-Mehmedović, & P. Dašić, (Eds.), *Handbook of Research on Integrating Industry 4.0 in Business and Manufacturing* (pp. 1-30). IGI Global Scientific Publishing. https://doi.org/10.4018/978-1-7998-2725-2.ch001

Karabegović, I., Karabegović, E., Mahmić, M., & Husak, E. (2020). Implementation of Industry 4.0 and Industrial Robots in the Manufacturing Processes. In Karabegović, I. (Eds) *New Technologies, Development and Application II*. NT 2019. Lecture Notes in Networks and Systems, vol 76. Springer, Cham. https://doi.org/10.1007/978-3-030-18072-0_1

Keshvarparast, A., Azarkish, M., & Ahmadi, A. (2024). Collaborative robots in manufacturing and assembly systems: A systematic literature review. *Journal of Intelligent Manufacturing*, 35, 2065–2118. https://doi.org/10.1007/s10845-023-02137-w

Kusiak, A. (2018). Smart manufacturing. *International Journal of Production Research*, 56(1–2), 508–517. https://doi.org/10.1080/00207543.2017.1351644

Lee, J., Davari, H., Singh, J., & Pandhare, V. (2018). Industrial artificial intelligence for industry 4.0-based manufacturing systems. *Manufacturing Letters*, 18, 20–23. https://doi.org/10.1016/j.mfglet.2018.09.002

Leng, J., Sha, W., Wang, B., Zheng, P., Zhuang, C., Liu, Q., Wuest, T., Mourtzis, D., & Wang, L. (2022). Industry 5.0: Prospect and retrospect. *Journal of Manufacturing Systems*, 65, 279–295. https://doi.org/10.1016/j.jmsy.2022.09.017

Mata, O., Ponce, P., Perez, C., Ramirez, M., Anthony, B., Russel, B., Apte, P., MacCleery, B., & Molina, A. (2026). Digital twin designs with generative AI: Crafting a comprehensive framework for manufacturing systems. *Journal of Intelligent Manufacturing*, 37(3), 1049–1072. https://doi.org/10.1007/s10845-025-02583-8

Matheson, E., Minto, R., Zampieri, E. G. G., Faccio, M., & Rosati, G. (2019). Human–robot collaboration in manufacturing applications: A review. *Robotics*, 8(4), 100. https://doi.org/10.3390/robotics8040100

McKinsey & Company. (2025). The state of AI and digital manufacturing 2025. McKinsey Global Institute. https://www.mckinsey.com

Mourtzis, D., Angelopoulos, J., & Panopoulos, N. (2023). Autonomous Mobile Robots in Smart Manufacturing: Current Status, Challenges and Future Perspectives. *Machines*, 11(5), 564. https://doi.org/10.3390/machines11050564

Nahavandi, S. (2019). Industry 5.0—A human-centric solution. *Sustainability*, 11(16), 4371. https://doi.org/10.3390/su11164371

OICA (n.d.). *International Organization of Motor Vehicle Manufacturers*. Retrieved September 27, 2025, from https://www.oica.net/category/production-statistics/2023-statistics/

Organisation for Economic Co-operation and Development. (2025). *OECD patent database*. OECD Publishing. https://www.oecd.org/en/topics/science-technology-and-innovation.html

Organisation for Economic Co-operation and Development. (2025). OECD digital economy outlook 2025. OECD Publishing. https://www.oecd.org/digital

Othman, U., & Yang, E. (2023). Human–robot collaborations in smart manufacturing environments: Review and outlook. *Sensors*, 23(12), 5663. https://doi.org/10.3390/s23125663

Peruzzini, M., & Pellicciari, M. (2017). A framework to design a human-centred adaptive manufacturing system. *Advanced Engineering Informatics*, 33, 330–349. https://doi.org/10.1016/j.aei.2017.05.003

Piccarozzi, M., Silvestri, L., Silvestri, C., & Ruggieri, A. (2024). Roadmap to Industry 5.0: Enabling technologies, challenges, and opportunities towards a holistic definition in management studies. *Technological Forecasting and Social Change*. 205, 123467. https://doi.org/10.1016/j.techfore.2024.123467

PwC. (2025). Digital factories and smart manufacturing survey 2025. PricewaterhouseCoopers. https://www.pwc.com

Renard, D., Saddem, R., Annebicque, D., & Riera, B. (2024). From sensors to digital twins toward an iterative approach for existing manufacturing systems. *Sensors*, 24(5), 1434. https://doi.org/10.3390/s24051434

Ribeiro, J., Lima, R., Eckhardt, T., & Paiva, S. (2021). Robotic process automation and artificial intelligence in Industry 4.0. *Procedia Computer Science*, 181, 51–58. https://doi.org/10.1016/j.procs.2021.01.104

Statista. (2025). Industrial Internet of Things (IIoT) statistics and market data. Statista. https://www.statista.com

Sun, Y., Song, K., & Yan, Y. (2023). Deep-learning-based defect detection in industrial inspection systems. *Sensors*, 23(4), 2158. https://doi.org/10.3390/s23042158

Tóth, A., Nagy, L., Kennedy, R., Bohuš, B., Abonyi, J., & Ruppert, T. (2023). The human-centric Industry 5.0 collaboration architecture. *MethodsX*, 11, 102260. https://doi.org/10.1016/j.mex.2023.102260

United Nations Industrial Development Organization. (2025). Industrial development report 2025. UNIDO. https://www.unido.org

World Intellectual Property Organization. (n.d.). *Patent Landscape Report*. Retrieved 2024, from https://www.wipo.int/publications/en/details.jsp?id=4757

Xu, X., Lu, Y., Vogel-Heuser, B., & Wang, L. (2021). Industry 4.0 and Industry 5.0—Inception, conception and perception. *Journal of Manufacturing Systems*, 61, 530–535. https://doi.org/10.1016/j.jmsy.2021.10.006

Zonta, T., da Costa, C. A., da Rosa Righi, R., de Lima, M. J., da Trindade, E. S., & Li, G. P. (2020). Predictive maintenance in Industry 4.0: A systematic literature review. *Computers & Industrial Engineering*, 150, 106889. https://doi.org/10.1016/j.cie.2020.106889

Valette, E., El-Haouzi, H., & Demesure, G. (2023). Industry 5.0 and its technologies: A systematic literature review upon the human place into IoT- and CPS-based industrial systems. *Computers & Industrial Engineering*, 184, 109426. https://doi.org/10.1016/j.cie.2023.109426

Villani, V., Pini, F., Leali, F., & Secchi, C. (2018). Human–robot collaboration in industrial settings: Safety, intuitive interfaces and applications. *Mechatronics*, 55, 248–266. https://doi.org/10.1016/j.mechatronics.2018.02.009

World Economic Forum. (2025). Global lighthouse network: Advancing smart manufacturing. World Economic Forum. https://www.weforum.org

Yan, J., Lei, Y., Li, N., & Wang, X. (2024). Artificial intelligence-enabled predictive maintenance in smart manufacturing: A review. *Machines*, 12(3), 182. https://doi.org/10.3390/machines12030182

Zafar, M. H., Langås, E. F., & Sanfilippo, F. (2024). Exploring the synergies between collaborative robotics, digital twins, augmentation, and Industry 5.0 for smart manufacturing: A state-of-the-art review. *Robotics and Computer-Integrated Manufacturing*, 89, 102769. https://doi.org/10.1016/j.rcim.2024.102769

Zhou, C., Zhang, P., & Xu, X. (2022). Machine vision and deep learning for intelligent quality inspection in manufacturing. Machines, 10(9), 791. https://doi.org/10.3390/machines10090791

SECTION

A

Power Train Technology

- SI Engines
- CI Engines
- Alternative Fuel Engines
- Hybrid & Electrical Power Systems
- Fuel Cell Systems
- Aftertreatment Systems
- Transmission Systems

The 11th International Congress
Motor Vehicles & Motors 2026
Kragujevac, Serbia
October 8th - 9th, 2026

Motor Vehicles & Motors

MVM2026-003
https://doi.org/10.24874/CMVM2026.003
Original scientific paper

Ivan Grujic[1]
Aleksandar Davinic[2]
Zeljko Djuric[3]
Jovan Doric[4]
Milan Eremija[5]
Attila Kiss[6]
Sunny Narayan[7]

THE INVESTIGATION OF THE COMBUSTION PROCESS OF THE BLEND OF THE CONVENTIONAL DIESEL FUEL AND BIODIESEL MADE FROM THE WASTE GRAPE SEEDS

ABSTRACT: The fact that the oil crisis happens around the world, the alternatives for the conventional diesel fuel can be considered as the future solution. the best option for the biodiesel production, is to produce it from the waste. In this way, the production doesn't affect on the food production, even more, the potential waste can be used for something useful. In the paper is conducted the experimental analysis of the combustion process of the blend made from conventional diesel fuel and biodiesel fuel made from waste grape seeds. The proportion of the investigated blend is the 86 %vol of the diesel fuel and 14 %vol of the biodiesel fuel. All results were compared to the combustion process when diesel fuel is used as only fuel. On the basis of the results, have come the conclusions and propositions what is necessary to conduct in the future researches.

KEYWORDS: combustion, diesel, biodiesel, waste, grape seeds

[1] *Ivan Grujic, Faculty of Engineering University of Kragujevac, Sestre Janjic 6 34000 Kragujevac, ivan.grujic@kg.ac.rs, https://orcid.org/0000-0003-0572-1205*
[2] *Aleksandar Davinic, Faculty of Engineering University of Kragujevac, Sestre Janjic 6 34000 Kragujevac, davinic@kg.ac.rs, https://orcid.org/0009-0002-0260-3430*
[3] *Zeljko Djuric, University of Banja Luka, Faculty of Mechanical Engineering, Bulevar vojvode Stepe Stepanovica 71, 78000 Banja Luka, Republic of Srpska, zeljko.djuric@mf.unibl.org, https://orcid.org/0009-0001-8573-6038*
[4] *Jovan Doric, University of Novi Sad, Faculty of Technical Sciences, Dositeja Obradovića square 6, Novi Sad, jovan_d@uns.ac.rs, https://orcid.org/0000-0002-4532-4880*
[5] *Milan Eremija, Senior Assistant, University of East Sarajevo, Faculty of Transport and Traffic Engineering, milan.eremija@sf.ues.rs.ba, https://orcid.org/0009-0000-1551-1231*
[6] *Attila Kiss, John von Neumann University, 6000 Kecskemét Izsáki Street 10, kiss.attila@nje.hu*
[7] *Sunny Narayan, School of Engineering and Sciences, Tecnológico de Monterrey, 64000 Monterrey Av. Eugenio Garza Sada 2501 Sur, rarekv@gmail.com*

ISTRAŽIVANJE PROCESA SAGREVANJA MEŠAVINE KONVENCIONALNOG DIZEL GORIVA I BIODIZELA GORIVA NAPRAVLJENOG OD OTPADNIH SEMENKI GROŽĐA

REZIME: Činjenica da se naftna kriza dešava širom sveta, alternative za konvencionalno dizel gorivo mogu se smatrati budućim rešenjem. Najbolja opcija za proizvodnju biodizela jeste njegova proizvodnja iz otpada. Na ovaj način, proizvodnja ne utiče na proizvodnju hrane, štaviše, potencijalni otpad se može iskoristiti za nešto korisno. U radu je sprovedena eksperimentalna analiza procesa sagorevanja mešavine napravljene od konvencionalnog dizel goriva i biodizel goriva napravljenog od otpadnih semenki grožđa. Proporcija ispitivane mešavine je 86 %vol dizel goriva i 14 %vol biodizel goriva. Svi rezultati su upoređeni sa procesom sagorevanja kada je dizel gorivo korišćeno kao jedino gorivo. Na osnovu rezultata, doneti su zaključci i predlozi šta je potrebno sprovesti u budućim istraživanjima.

KLJUČNE REČI: sagorevanje, dizel gorivo, biodizel gorivo, otpad, semenke grožđa

INTRODUCTION

Biodiesel represents one of the most established renewable alternatives to conventional diesel fuel (D100) in road transportation. Its application is motivated by the need to reduce dependence on fossil fuels and to improve the sustainability of the transport sector. Nevertheless, biodiesel differs from conventional diesel in several important physicochemical properties, including density, viscosity, oxygen content, volatility, and heating value. These differences directly influence fuel injection, ignition, combustion development, heat release, and, consequently, the energy and environmental performance of diesel engines (Ekbom, T. 2023; Nguyen, V. G. et al. 2023; Knežević, D. M. et al. 2020).

Most commercially available biodiesel is produced through alcohol-based transesterification and consists predominantly of fatty acid esters. The properties of the resulting fuel depend not only on the production process but also on the origin and chemical composition of the feedstock. Consequently, biodiesel obtained from different vegetable oils, animal fats, or waste materials may exhibit considerably different combustion characteristics and engine performance. For this reason, the selection of an appropriate feedstock is an important aspect of biodiesel development, particularly when the objective is to combine acceptable engine performance with improved resource utilization (Ekbom, T. 2023; Nguyen, V. G. et al. 2023; Hunich, J. et al. 2021).

In practical applications, biodiesel is generally used as a component of blends with conventional diesel rather than as a neat fuel. The use of biodiesel–diesel blends can facilitate the integration of renewable fuels into existing diesel-engine technology without requiring substantial engine modifications. However, increasing the biodiesel fraction may alter combustion characteristics and may result in changes in brake thermal efficiency (BTE), brake-specific fuel consumption (BSFC), cylinder pressure, and heat release behavior. Previous investigations have demonstrated that these effects depend strongly on the type of biodiesel and its concentration in the blend (Asokan, M. A. et al. 2021; Gautam, R., & Kumar, S. 2020; Behçet, R. et al. 2014).

Research has increasingly focused on biodiesel obtained from waste materials because such feedstocks can reduce production costs while simultaneously providing a useful route for valorizing residues generated by agricultural and food-processing activities. Waste animal fats, used cooking oils, fish-processing residues, and other biomass-derived materials have been investigated as potential biodiesel feedstocks, with their effects on combustion and engine performance differing according to their physicochemical characteristics (Gautam, R., & Kumar, S. 2020; Behçet, R. et al. 2014; Emma, A. F. et al. 2022). Biodiesel derived from waste materials is therefore of particular interest because its use may provide both energy-related and environmental benefits.

Among the potential waste-derived feedstocks, grape-processing residues represent an interesting resource for biodiesel production. The wine industry generates substantial quantities of solid residues, including grape seeds, which contain oil suitable for conversion into biodiesel. The utilization of grape seed oil can contribute to the valorization of an otherwise underutilized by-product while reducing the reliance on oils obtained from purpose-grown energy crops. Previous studies have investigated grape seed-derived biodiesel and its blends with conventional diesel, demonstrating that the resulting fuels can be used in compression-ignition engines and that their combustion and performance characteristics are generally comparable to those of conventional diesel, although differences in efficiency and fuel consumption may occur (Chelladorai, P. et al. 2018; Azad, A. K. & Rasul, M. G. 2019).

Despite the growing body of research on biodiesel from various renewable and waste feedstocks, further investigation is required to establish the influence of the biodiesel fraction on the combustion process and engine efficiency under different operating conditions. This is particularly relevant for biodiesel produced from waste grape seed oil, for which the relationship between blend composition, heat release characteristics, and brake thermal efficiency remains worthy of further examination.

Objective and Scope of the Research

The objective of this study is to evaluate the influence of the proportion of biodiesel produced from waste grape seed oil in blends with conventional diesel fuel on the combustion process and energy efficiency of a diesel engine. Particular attention is given to the heat release rate and brake thermal efficiency obtained under different engine operating conditions. The experimental investigation compares conventional diesel fuel (D100) with B7 and B14 blends, thereby enabling the effect of increasing the waste grape seed biodiesel content to be assessed within a practically relevant concentration range.

The results are intended to contribute to a better understanding of the combustion behavior of waste-derived biodiesel blends and to provide additional evidence regarding their suitability as alternative fuels for conventional compression-ignition engines.

EXPERIMENTAL PROCEDURE

The combustion process was investigated by measuring the instantaneous in-cylinder pressure over the engine cycle. The experimental setup consisted of a pressure measurement and crank-angle recording system, comprising a piezoelectric pressure transducer, signal-conditioning units, an optical crank-angle encoder with TDC detection, and a digital data-acquisition system. The measuring chain included an AVL QC32D pressure sensor (1), Kistler 5007 amplifier (2), angle encoder (3), optical transmitter (4), AVL 365CC signal multiplier (5), AVL Indimeter 619 acquisition system (6), and AVL IndiCom 1.2 (7) software, Figure 1.

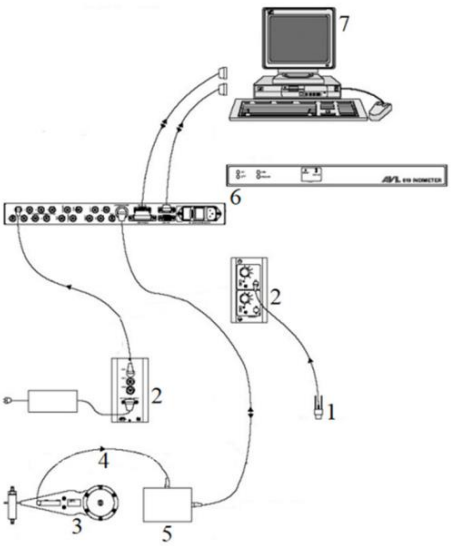

Figure 1 The measuring chain

Prior to the measurements, the pressure transducer was calibrated using a dead-weight calibration procedure. The resulting calibration coefficient was 9.97 bar/V. The engine operating points were selected based on its performance characteristics. To ensure that the selected speeds were defined according to a standardized procedure and could subsequently be compared with results from other studies, the reference speeds were determined in accordance with the European Stationary Cycle (ESC) methodology.

Since the tested engine is intended for applications in small agricultural machinery, particular attention was given to medium-high and full-load operation, which represent characteristic working conditions for this type of engine. Accordingly, the combustion analysis was performed at BMEP values of 1.4 bar, corresponding to low-load operation, respectively.

Three fuels were investigated: conventional diesel fuel (D100), and blend containing biodiesel produced from waste grape seed oil, namely B14. For each operating condition, pressure data were recorded over 50 consecutive engine cycles. Each measurement was repeated three times, and the obtained results were subsequently averaged.

During testing, the required engine speed and load were first established and maintained at the selected operating point. Measurement stability was assessed primarily from the variation in engine speed during data acquisition. The minimum, mean, and maximum engine speeds, together with their standard deviations, were determined for each operating condition to characterize the stability of the experimental regimes.

RESULTS AND DISCUSSION

The results obtained for the in-cylinder pressure and heat release rate are presented in Figures 2–4. These parameters were selected to provide an assessment of the combustion process for the investigated fuels under the considered engine operating conditions. The in-cylinder pressure traces provide an overall indication of the development of combustion and the associated pressure rise, while the heat release rate enables a more detailed assessment of the intensity and temporal distribution of the combustion process.

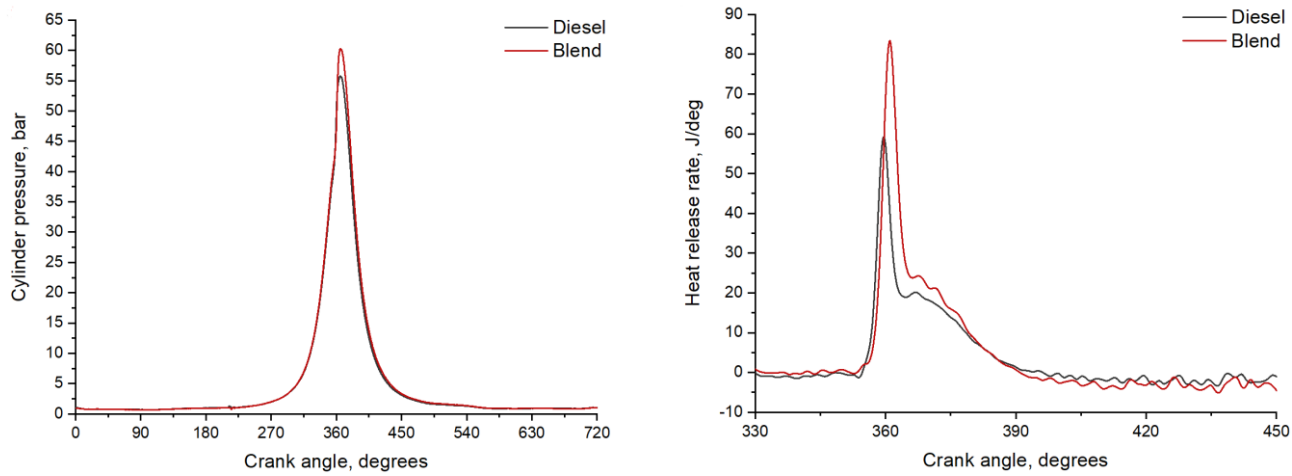

a) b)

Figure 2 Cylinder pressure (a) and heat reease rate (b) for engine speed 1635

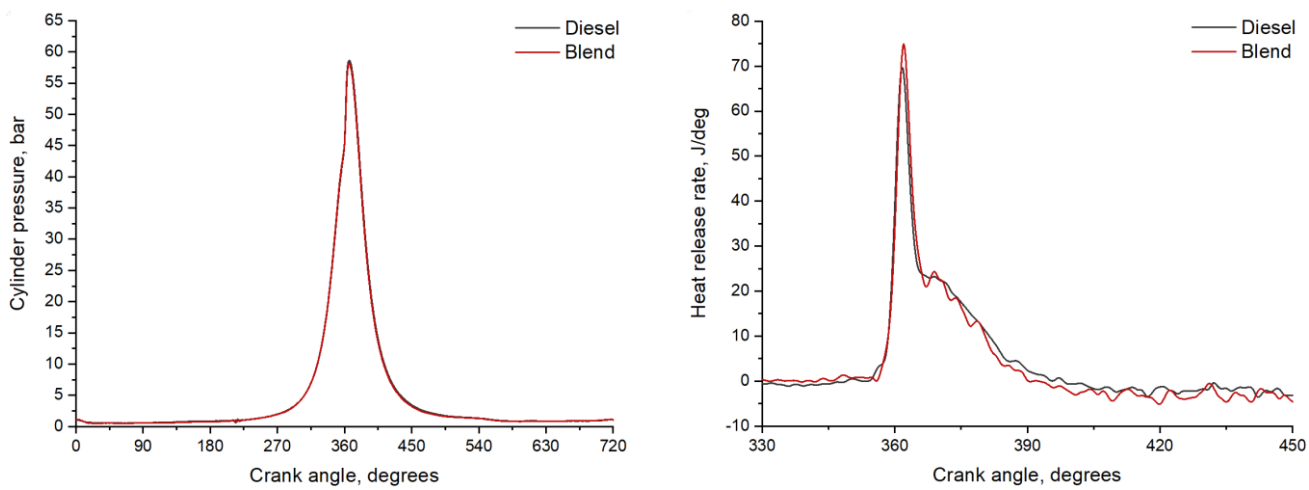

a) b)

Figure 3 Cylinder pressure (a) and heat reease rate (b) for engine speed 1937

A general tendency toward more intense combustion can be observed for the biodiesel–diesel blends compared with conventional diesel fuel. This behavior is reflected in both the in-cylinder pressure development and the heat release rate, with the differences being particularly evident during the period of uncontrolled combustion. The biodiesel blends generally exhibit a more pronounced heat release during this stage, indicating a faster energy release once the accumulated fuel becomes involved in the combustion process. Consequently, the pressure rise associated with this phase is also more pronounced than that observed for D100 under comparable operating conditions.

The observed behavior can primarily be associated with changes in the ignition delay period resulting from the physicochemical characteristics of the biodiesel-containing fuels. The use of biodiesel blends appears to extend the period between the start of fuel injection and the onset of significant combustion. Such an extension of the induction period allows a larger fraction of the injected fuel to accumulate in the combustion chamber before the onset of the uncontrolled combustion phase. Once ignition occurs, the accumulated fuel is rapidly consumed, resulting in a more

intense premixed combustion phase and, consequently, a higher rate of heat release. This mechanism provides a plausible explanation for the more pronounced combustion intensity observed for B7 and B14 compared with D100.

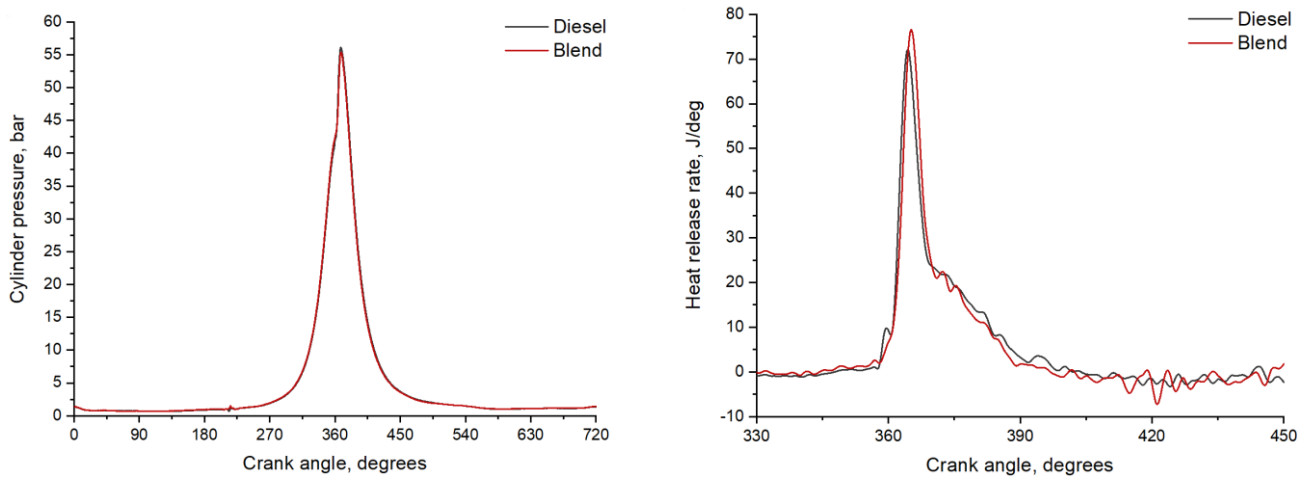

a) b)

Figure 4 Cylinder pressure (a) and heat reease rate (b) for engine speed 2239

The increase in ignition delay observed for the biodiesel-containing blends may be related to their less favorable volatility characteristics compared with conventional diesel fuel. Reduced fuel volatility can affect the evaporation and preparation of the injected fuel for combustion, thereby influencing the time required to form an adequately combustible mixture. As a consequence, a greater amount of fuel may be present in a combustible state at the moment of ignition, promoting a more rapid release of the accumulated chemical energy during the subsequent uncontrolled combustion phase. The observed differences should therefore be interpreted primarily as a consequence of the altered fuel preparation and ignition characteristics associated with the use of biodiesel.

The effect is most pronounced at the lowest investigated engine speed. This behavior is consistent with the shorter available time for the individual combustion phases as engine speed increases. With increasing rotational speed, the duration of the combustion process expressed in crank-angle-related temporal terms changes, reducing the opportunity for differences in fuel preparation and ignition delay to develop to the same extent. Accordingly, the differences between the combustion characteristics of D100 and the biodiesel–diesel blends gradually become less pronounced as engine speed increases.

At higher engine speeds, the pressure development and heat release characteristics of the biodiesel blends consequently tend to approach those obtained with conventional diesel fuel. This indicates that the influence of the biodiesel component on the combustion process is strongly dependent on engine speed, with the effect of the altered fuel properties being most evident under low-speed operation. Overall, the results indicate that the addition of biodiesel produced from waste grape seed oil modifies the combustion process primarily through its influence on the ignition and premixed combustion phases, while the magnitude of this influence decreases with increasing engine speed.

CONCLUSIONS

This study investigated the influence of biodiesel produced from waste grape seed oil on the combustion process of a compression-ignition engine when used in blends with conventional diesel fuel. The analysis was based on in-cylinder pressure and heat release rate measurements obtained for D100, B7, and B14 fuels under medium-high and full-load operating conditions and at different engine speeds.

The results indicate that the addition of waste grape seed biodiesel modifies the combustion process compared with conventional diesel fuel. In general, both biodiesel–diesel blends exhibited a tendency toward more intense combustion, particularly during the uncontrolled combustion phase. This behavior was reflected in the more pronounced heat release and corresponding changes in the in-cylinder pressure development. The observed differences are primarily associated with changes in the ignition delay and fuel preparation characteristics of the biodiesel-containing blends.

The increased intensity of the uncontrolled combustion phase can be attributed to the accumulation of a larger quantity of fuel during the extended induction period preceding the onset of combustion. Once ignition occurs, this accumulated fuel undergoes relatively rapid combustion, resulting in a higher heat release rate compared with D100. The observed extension of the induction period is most likely related to the less favorable volatility characteristics of the biodiesel used in the investigated blends, which can influence fuel evaporation and mixture preparation.

The influence of biodiesel addition was found to be most pronounced at the lowest investigated engine speed. With increasing engine speed, the differences between the combustion characteristics of the biodiesel blends and D100 gradually decreased. At higher speeds, the pressure and heat release characteristics of B7 and B14 approached those of conventional diesel fuel, indicating a reduction in the relative influence of biodiesel on the combustion process.

Overall, the results demonstrate that waste grape seed oil biodiesel can be incorporated into conventional diesel fuel without fundamentally altering the combustion behavior of the engine. However, its presence affects the intensity and temporal development of combustion, with the magnitude of these effects depending on the biodiesel concentration and engine operating conditions. The findings support the potential use of waste grape seed biodiesel as a renewable fuel component while highlighting the importance of considering engine speed and blend composition when evaluating its combustion characteristics.

ACKNOWLEDGMENTS

This work presents the results of research conducted within projects financially supported by the Ministry of Science, Technological Development and Innovation of the Republic of Serbia, under Contract No. 451-03-34/2026-03/200107, dated 5 February 2026.

REFERENCES

Asokan, M. A., Senthur Prabu, S., Prathiba, S., Sai Akhil, V., Daniel Abishai, L., & Surejlal, M. E.(2021). Emission and performance behaviour of flax seed oil biodiesel/diesel blends in DI diesel engine. *Materials Today: Proceedings*, 46(17), 8148-8152. https://doi.org/10.1016/j.matpr.2021.03.108

Azad, A. K., & Rasul, M. G. (2019). Performance and combustion analysis of diesel engine fueled with grape seed and waste cooking biodiesel. *Energy Procedia*, 160, 340-347. https://doi.org/10.1016/j.egypro.2019.02.166

Behçet, R., Yumrutas, R., & Oktay, H. (2014). Effects of fuels produced from fish and cooking oils on performance and emissions of a diesel engine. *Energy*, 71, 645-655. https://doi.org/10.1016/j.energy.2014.05.003

Chelladorai, P., Varuvel, E. G., Martin, L. J., & Bedhannan, N. (2018). Synergistic effect of hydrogen induction with biofuel obtained from winery waste (grapeseed oil) for CI engine application. *International Journal of Hydrogen Energy*, 43(27), 12473-12490. https://doi.org/10.1016/j.ijhydene.2018.04.155

Emma, A. F., Alangar, S., & Yadav, A. K. (2022). Extraction and characterization of coffee husk biodiesel and investigation of its effect on performance, combustion, and emission characteristics in a diesel engine. *Energy Conversion and Management: X*, 14, 100214. https://doi.org/10.1016/j.ecmx.2022.100214

Ekbom, T. (2023). IEA bioenergy T39. *Biofuel news*. https://task39.ieabioenergy.com/wp-content/uploads/sites/37/2023/07/IEA-BioenergyT39-Biofuel-News-62-final.pdf

Gautam, R., & Kumar, S. (2020). Performance and combustion analysis of diesel and tallow biodiesel in CI engine. *Energy Reports*, 6, 2785-2793. https://doi.org/10.1016/j.egyr.2020.09.039

Hunich, J., Hrzaczek, P., Geca, M., Rybak, A., & Mikulski, M. (2021). Comparative study of combustion and emissions of diesel engine fuelled with FAME and HVO. *Combustion Engines*, 184(1), 72-78. https://doi.org/10.19206/CE-135066

Knežević, D. M., Petrović, V. S., Vorotović, G. S., & Pajković, V. R. (2020). Combustion characteristics of several types of biofuel in diesel engine. *FME Transactions*. 48(2), 319-328.

Nguyen, V. G., Pham, M. T., Linh Le, N. V., Cuong Le, H., Truong, T. H., & Cao, D. N. (2023). A comprehensive review on the use of biodiesel for diesel engines. *International Journal of Renewable Energy Development*, 12(4), 720-740. https://doi.org/10.14710/ijred.2023.54612

The 11th International Congress
Motor Vehicles & Motors 2026
Kragujevac, Serbia
October 8th - 9th, 2026

Motor Vehicles & Motors

MVM2026-008
https://doi.org/10.24874/CMVM2026.008
Original scientific paper

Željko Đurić[1]
Ivan Grujić[2]
Nadica Stojanović[3]
Snežana Petković[4]
Jelena Adžić[5]
Milan Eremija[6]

EXPERIMENTAL INVESTIGATION OF THE COMBUSTION PROCESS AND EFFICIENCY OF A DIESEL ENGINE IN THE CASE OF BIODIESEL FUEL APPLICATION

ABSTRACT: In wine-producing regions, oil extracted from waste grape seeds can be used as a feedstock for biodiesel production. This paper presents the results of experimental research on combustion process parameters and engine efficiency when using conventional diesel fuel (D100) and blends of conventional diesel fuel with biodiesel produced from waste grape seed oil. Four biodiesel–diesel blends with biodiesel contents of 7%, 14%, 21%, and 28% by volume (B7, B14, B21, and B28) were used. The tests were conducted on a single-cylinder direct injection diesel engine at full load at engine speeds of 1635 rpm, 1937 rpm, and 2239 rpm. It was found that all blends exhibited a higher peak (maximum) heat release rate (HRR) and higher peak (maximum) cylinder pressure than D100. Blends with higher biodiesel contents (B21 and B28) had the heat release centroid located closer to top dead center (TDC), which is favorable for indicated thermal efficiency (ITE). The engine achieved a higher brake thermal efficiency (BTE) with the B14 blend (0.296 at 1635 rpm, 0.324 at 1937 rpm, and 0.277 at 2239 rpm) than with the B7, B21, and B28 blends. In terms of engine efficiency, the B14 blend exhibited performance comparable to that of D100.

KEYWORDS: biofuels, biodiesel, differential heat release law, cumulative heat release law

[1] *Željko Đurić, University of Banja Luka, Faculty of Mechanical Engineering, Bulevar vojvode Stepe Stepanovica 71, 78000 Banja Luka, Republic of Srpska, zeljko.djuric@mf.unibl.org, https://orcid.org/0009-0001-8573-6038*
[2] *Ivan Grujić, Faculty of Engineering, University of Kragujevac, 6 SestreJanjic STR., 34000 Kragujevac, Serbia, ivan.grujic@kg.ac.rs, https://orcid.org/0000-0003-0572-1205*
[3] *Nadica Stojanovič, Faculty of Engineering, University of Kragujevac, 6 SestreJanjic STR., 34000 Kragujevac, Serbia, nadica.stojanovic@kg.ac.rs, https://orcid.org/0000-0002-4199-0587*
[4] *Snežana Petković, University of Banja Luka, Faculty of mechanical engineering,* Banja Luka, *snezana.petkovic@mf.unibl.org, https://orcid.org/0009-0009-2878-0436*
[5] *Jelana Adžić, University of Banja Luka, Faculty of mechanical engineering, Banja Luka,* jelena.adzic@mf.unibl.org, *https://orcid.org/0009-0008-7892-7208*
[6] *Milan Eremija, University of East Sarajevo, Faculty of Transport and Traffic Engineering Doboj, Doboj, milan.eremija@sf.ues.rs.ba, https://orcid.org/0009-0000-1551-1231*

EKSPERIMENTALNO ISTRAŽIVANJE PROCESA SAGOREVANJA I EFIKASNOSTI DIZEL MOTORA ZA SLUČAJ PRIMENE BIODIZEL GORIVA

REZIME: U područjima gde se proizvode veće količine vina, kao jedna od sirovina za proizvodnju biodizel goriva može se koristiti i ulje od otpadnih semenki grožđa. U radu su prikazani rezultati eksperimentalnih istraživanja parametara procesa sagorevanja i efikasnosti motora za slučaj primene konvencionalnog dizel goriva (D100) i mešavina konvencionalnog dizel goriva i biodizel goriva dobijenog od ulja otpadnih semenki grožđa. Korišćene su četiri mešavine sa zapreminskim udelima biodizel goriva od 7%, 14%, 21% i 28% (B7, B14, B21 i B28). Ispitivanje je rađeno na jednocilindričnom dizel motoru sa direktnim ubrizgavanjem na punom opterećenju, pri brojevima obrtaja 1635 min^{-1}, 1937 min^{-1}, 2239 min^{-1}. Ustanovljeno je da sve mešavine imaju veću maksimalnu brzinu oslobađanja toplote i veći maksimalan pritisak u cilindru nego D100. Mešavine sa većim udelima biodizel goriva (B21 i B28) imaju težište procesa oslobađanja toplote bliže spoljnoj mrtvoj tački (SMT), što je povoljno sa aspekta indikatorskog stepena korisnosti. Primenom mešavine B14 motor ima veći efektivni stepen korisnosti (0,296 na 1635 min^{-1}, 0,324 na 1937 min^{-1} i 0,277 na 2239 min^{-1}) nego primenom mešavina B7, B21 i B28. Mešavina B14 se, sa aspekta efikasnosti motora, može smatrati ravnopravnom sa D100.

KLJUČNE REČI: biogoriva, biodizel, diferencijalni zakon oslobađanja toplote, integralni zakon oslobađanja toplote

INTRODUCTION

Biodiesel has been commercially used for several decades and has traditionally been produced from edible vegetable oils through transesterification process. Over the last decade, biodiesel has increasingly been produced from waste-derived feedstocks, including waste oils and residues generated by the food and beverage industry. Nikolić, B. D. et al. (2025) reported that, in 2022, approximately 27% of global biodiesel production originated from waste-derived feedstocks.

In terms of physicochemical properties, biodiesel differs significantly from conventional diesel, while considerable variations can also be observed among different biodiesel types depending on the feedstock and production process employed. In addition, diesel engines are primarily designed to operate on conventional diesel, therefore, investigating the combustion characteristics of biodiesel is essential for its efficient utilization while maintaining engine performance and efficiency. Although alternative biodiesel production methods have been investigated and developed, transesterification remains the most widely used production process. All biodiesel fuels considered in this study were produced through transesterification and were used either as neat biodiesel or, more commonly, as blends with conventional diesel.

The effects of biodiesel on combustion characteristics, ITE, BTE, and engine performance parameters have been extensively investigated in numerous studies. Numerous studies have focused on first-generation biodiesel fuels, while recent research has increasingly focused on second-,third-,and fourth-generation biodiesel fuels.

Objective and Scope of This Research

This paper presents an investigation of the combustion process, with particular emphasis on heat release rate parameters and engine efficiency. The aim of the study is to evaluate the influence of different fuels (D100, B7, B14, B21, and B28) on combustion parameters and engine efficiency. The experimental investigation was carried out at full load at engine speeds of 1635 rpm, 1937 rpm, and 2239 rpm.

Review of Previous Research

First-generation biodiesel fuels are produced through the transesterification of edible vegetable oils derived from dedicated oil crops, such as rapeseed, soybean, palm, sunflower, and corn. The cylinder pressure evolution differs between conventional diesel fuel and biodiesel fuels derived from rapeseed, soybean, and palm oils. According to Knežević, D. (2014), variations in the pressure rise rate and maximum pressure are also observed among individual biodiesel fuels, depending on the feedstock used for biodiesel production. These differences are evident both for neat biodiesel fuels and for B50 biodiesel–diesel blends.

Ayhana, V. et al. (2020) reported that, despite the less favorable physicochemical properties of biodiesel fuels, including higher density, increased viscosity, and lower volatility compared with conventional diesel fuel, the use of an optimized biodiesel blending ratio can improve engine performance under specific operating conditions. Blends containing corn oil biodiesel demonstrated higher effective power output and lower specific fuel consumption compared with diesel fuel.

According to Mehra, K. S. & Goel (2025), the cost of feedstocks used for biodiesel production represents approximately 75–90% of the total production cost. The high cost of edible feedstocks has encouraged the increased utilization of alternative feedstocks, including waste cooking oils, by-products from the food and beverage industry, and non-edible oil crops cultivated on marginal or low-quality land. Biodiesel produced from these feedstocks is generally classified as second-generation biofuel. The combustion characteristics and heat release behavior of second-generation biodiesel fuels vary significantly depending on the feedstock type and biodiesel blending ratio, which consequently affects engine efficiency and fuel consumption.

Can, Ö. (2014) reported that B5 and B10 biodiesel blends produced from waste cooking oil and conventional diesel fuel exhibit lower heating values (LHV) compared with conventional diesel fuel. As a result, the application of these blends leads to an increase in brake-specific fuel consumption (BSFC) of up to 4% and a reduction in BTE of up to 2.8% compared with conventional diesel operation.

Erdogan, S. et al. (2019) investigated the combustion characteristics of biodiesel blends produced from beef bone marrow and conventional diesel fuel. Their results showed that, at low engine loads, the B20 blend exhibited a higher peak heat release rate compared with diesel fuel.

Biodiesel suitable for application in compression ignition (CI) engines can also be produced from various types of agricultural and industrial waste. Emma, A. F. et al. (2022) reported that low-percentage blends containing biodiesel derived from coffee husk oil can be used in diesel engines without significant modifications. Furthermore, these blends demonstrated improved combustion characteristics compared with conventional diesel fuel.

Waste grape seeds, generated as a by-product of wine production, represent a potential feedstock for biodiesel production. Chelladorai, P. et al. (2018) investigated the application of neat biodiesel produced from waste grape seed oil in a single-cylinder direct-injection diesel engine. Their results showed that, at full engine load and an engine speed of 1500 rpm, the BTE was 6.4% lower compared with conventional diesel fuel.

Contributions

The biodiesel fuel used to produce the blends differs significantly from D100 in terms of calorific value and kinematic viscosity (Table 3). The research determined:

- Whether the engine can operate stably with blends B7, B14, B21, and B28 at full load;
- Which blend exhibits the most favorable heat release profile from the perspective of ITE, and whether there is a clear trend in the heat release profile with increasing biodiesel content in the blend;
- With which blend the engine achieves the highest BTE;
- Whether there is a clear trend in ITE and BTE depending on the proportion of biodiesel in the blend.

EXPERIMENTAL SETUP

For the experimental investigation, a single-cylinder direct-injection (DI) diesel engine – DMB 3DA450 (Figure 1, Table 1) – was used. The engine is equipped with a mechanical fuel injection system. The fuel injection timing was fixed at 21 °CA before top dead center (BTDC) for all tested fuels, including the conventional fuel and its blends. The combustion process was analyzed based on the indicated cylinder pressure.

Table 1 Test engine characteristics

Name	Description
Model	DMB SDA 450
Power/engine speed, kW/rpm	7.3/2500
Torque/engine speed, Nm/rpm	28/1700
Engine combustion sys./cooling	Direct injection/Air cooled engine
Engine displacement, cm^3	454
Number of cylinders	1
Piston diameter/piston stroke, mm	85/80
Compression ratio, -	17.5:1
Injection timing	21 °CA BTDC fixed (factory setup)

Table 1 (continuation)

Parameters of engine valve mechanism	Intake valve opens 16 °CA BTDC
	Intake valve closes 40 °CA ABDC
	Exhaust valve opens 40 °CA BBDC
	Exhaust valve closes 16 °CA ATDC
	Valve overlap 32 °CA

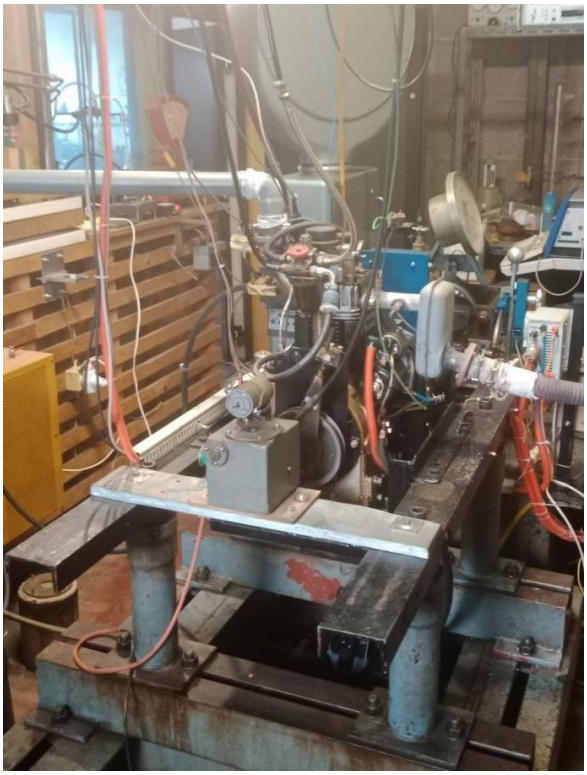

Figure 1 Test engine

The pressure inside the cylinder was measured using the measurement system shown in Figure 2. The measurement system consists of analog and digital components. The analog part includes a piezoelectric pressure sensor and an amplifier for signal conditioning. The digital part consists of a crankshaft angle optical marker and SMT position, an optical transmitter, as well as a signal multiplier.

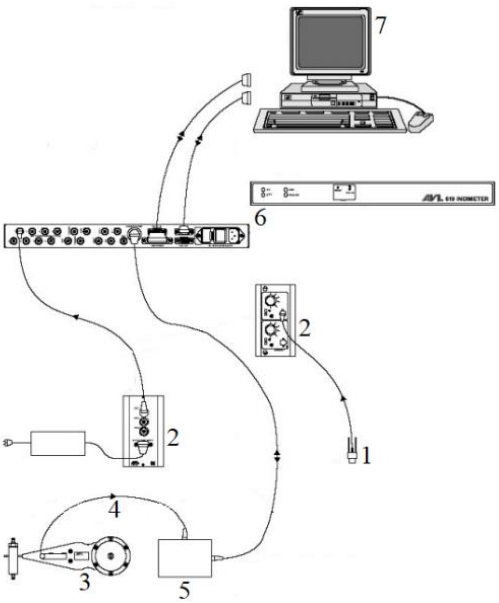

Figure 2 The measuring chain for the cylinder pressure: 1 – pressure sensor AVL QC32D, 2 – signal amplifier KISTLER 5007, 3 – angle encoder, 4 – optical transmitter, 5 – signal multiplier AVL 365CC, 6 – acquisition system AVL Indimeter 619, 7 – computer with acquisition software AVL IndiCom 1.2

EXPERIMENTAL INVESTIGATION

The engine operating speeds used in the experimental investigation were determined in accordance with the European Stationary Cycle (ESC) procedure (EUR-Lex.europa.eu. 1999). The standardized test procedure was applied to ensure better comparability of the obtained results with other authors in the future.

The engine tests were conducted using conventional diesel fuel (D100) and four biodiesel–diesel fuel blends. Biodiesel was produced through a batch transesterification process. Methanol was used as the alcohol reactant, with an oil-to-methanol molar ratio of 6:1. Potassium hydroxide (KOH) was used as the catalyst in an amount of 1 wt.% relative to the oil mass. The transesterification reaction was carried out at a temperature of 63 °C and atmospheric pressure for 60 min. The main properties of the produced biodiesel are presented in Table 2. The conventional diesel fuel (D100) complies with the requirements specified in the SRPS EN 590:2022 standard. The fuel blends were prepared to ensure that all four mixtures had approximately the same LHV as the reference diesel fuel. The biodiesel energy fractions of 5%, 10%, 15%, and 20% corresponded to volumetric fractions of 7%, 14%, 21%, and 28%, respectively; therefore, the blends were designated as B7, B14, B21, and B28. This approach enables a more accurate evaluation of the influence of biodiesel addition on engine thermal efficiency by minimizing the effect of differences in fuel energy content.

Table 2 Characteristics of the biodiesel fuel

Property	Unit	EN-14214 Limit	Measured Value	Meth. of testing
Density (at 15 °C)	kg/m^3	860–900	885	SRPS EN ISO 3675. (2007)
Kinematic viscosity (at 40 °C)	Mm^2/s	3.5–5	5.15	SRPS EN ISO 3104. (2024)
Flash point	°C	>101	>185	SRPS EN ISO 2719. (2021) SRPS EN ISO 3679. (2022)
Lower heating value	MJ/kg		33.965	ASTM 240 (Internet Archive. 2009)
Ester content	%(m/m)	>96,5	97.3	SRPS EN ISO 14103. (2020)

RESEARCH RESULTS AND DISCUSSION

The rate of heat release during the different phases of combustion is a key parameter governing the efficiency of converting the fuel's chemical energy into thermal energy. The HRR also influences the cylinder pressure variation, which in turn affects the mechanical loads on the engine and the level of noise emitted by the engine. The combustion process parameters can be most effectively analyzed using the cylinder pressure variation diagram (Figure 3) and the differential and cumulative heat release rate diagrams (Figure 4).

Table 3 presents the main combustion parameters, including the maximum cylinder pressure, its corresponding crank angle relative to top dead center (TDC), the maximum heat release rate, its corresponding crank angle relative to TDC, and the crank angles corresponding to 5%, 10%, 50%, and 90% of the total heat released during the cycle.

In all three operating regimes, the fuel blends exhibited higher peak heat release rates than D100. The highest peak heat release rate was observed at the lowest engine speed (1635 rpm) for the B21 blend, reaching 163.1 kJ·m^{-3}·°CA^{-1}. At engine speeds of 1937 rpm and 2239 rpm, the B28 blend exhibited the highest peak heat release rates, amounting to 133 kJ·m^{-3}·°CA^{-1} and 156.16 kJ·m^{-3}·°CA^{-1}, respectively.

The blends reached their peak heat release rates at later crank angles, except for B7 at 1937 rpm, where B7 and D100 reached their peak heat release rates simultaneously at 2 °CA. This trend in the peak heat release rate and the crank angle corresponding to its maximum relative to TDC can be attributed to injection timing, ignition delay, and the oxygen content of the biodiesel fuel in the blends.

Blends with a higher biodiesel content generally exhibit a higher peak heat release rate; however, this trend is not consistent under all operating conditions, as the mixture formation and combustion processes are influenced by numerous parameters whose effects may vary across different operating regimes.

Due to their higher peak heat release rates, the blends also exhibit higher peak cylinder pressures (Figure 3), which ultimately result in greater mechanical loads and higher levels of engine noise.

In modern diesel engines, however, this issue is mitigated through the use of multiple injection strategies, which enable better control of the combustion process. The peak heat release rates of the blends occur at later crank angles

relative to TDC than that of D100, which partially mitigates the effects associated with their higher peak heat release rates, such as increased mechanical loads and engine noise.

Table 3 Combustion process parameters at 100% load (1635 rpm, 1937 rpm, and 2239 rpm)

Parameter	**Value/Description**				
	D100	B7	B14	B21	B28
Load			100%		
Engine speed, rpm			1635		
Maximum cylinder pressure, bar	70.45	74.05	74.84	76.13	75.06
Position of the maximum cylinder pressure relative to TDC, °CA	9	9	9	8	8
Maximum heat release rate, kJ·m^{-3}·°CA^{-1},	106.8	133.26	151.54	163.1	155.43
Position of the maximum heat release rate relative to TDC, °CA	0	1	1	1	1
Crank angle for 5% fuel burned, °CA	-1.38	-1.62	-1.19	-1.03	-1.32
Crank angle for 10% fuel burned, °CA	-0.59	-0.66	-0.34	-0.19	-0.39
Crank angle for 50% fuel burned, °CA	8.33	6.91	6.75	6.45	6.30
Crank angle for 90% fuel burned, °CA	25.52	22.97	23.29	22.95	22.06
Engine speed, rpm			1937		
Maximum cylinder pressure, bar	67.59	71.84	72.52	72.53	72.78
Position of the maximum cylinder pressure relative to TDC, °CA	9	10	10	10	10
Maximum heat release rate, kJ·m^{-3}·°CA^{-1},	98.32	127.32	131.6	132.7	133
Position of the maximum heat release rate relative to TDC, °CA	2	2	3	3	3
Crank angle for 5% fuel burned, °CA	0.08	-0.29	0.20	0.11	0.04
Crank angle for 10% fuel burned, °CA	0.92	0.73	1.17	1.08	1.07
Crank angle for 50% fuel burned, °CA	9.46	8.62	8.46	8.24	8.30
Crank angle for 90% fuel burned, °CA	26.51	25.08	24.93	24.79	23.90
Engine speed, rpm			2239		
Maximum cylinder pressure, bar	65.22	69.02	68.66	68.82	69.45
Position of the maximum cylinder pressure relative to TDC, °CA	10	9	9	9	9
Maximum heat release rate, kJ·m^{-3}·°CA^{-1},	115.65	148.01	152.99	145.9	156.16
Position of the maximum heat release rate relative to TDC, °CA	4	5	5	5	5
Crank angle for 5% fuel burned, °CA	2.02	2.07	2.39	2.35	2.16
Crank angle for 10% fuel burned, °CA	2.94	3.16	3.47	3.43	3.27
Crank angle for 50% fuel burned, °CA	10.34	9.75	9.75	9.62	9.61
Crank angle for 90% fuel burned, °CA	28.26	27.99	27.93	28.11	27.36

Based on the cumulative heat release curve, it is possible to determine how the fraction of fuel burned changes during the combustion process. From the perspective of ITE, the position of the combustion centroid, defined as the crank angle at which 50% of the total heat is released, is particularly important. The rate of heat release during the second half of the combustion process is largely determined by the flow within the combustion chamber, as the flow characteristics affect the supply of oxygen to the flame zone.

For all three operating regimes, 50% of the total heat is released earlier when the blends are used compared with D100. When blends are used, the combustion rate increases with increasing biodiesel content in the blend, except at 1937 rpm, where the earliest occurrence of 50% heat release is observed for B21.

For all three operating regimes, 90% of the total heat is released earlier with the blends than with D100, with the earliest occurrence observed for B28. This trend in the heat release process is likely influenced by the oxygen content of the biodiesel fuel.

Therefore, considering the combustion process parameters and their impact on ITE, the use of biodiesel–diesel blends is more favorable than D100.

The values of the engine efficiency parameters are presented in Table 4. It can be observed that all blends exhibit favorable combustion characteristics. In almost all operating regimes, with only a few exceptions, the blends exhibit more complete combustion and higher ITE values than D100. This can be attributed to the oxygen content of the blends and the appropriate injection timing of 21 °CA BTDC.

a)

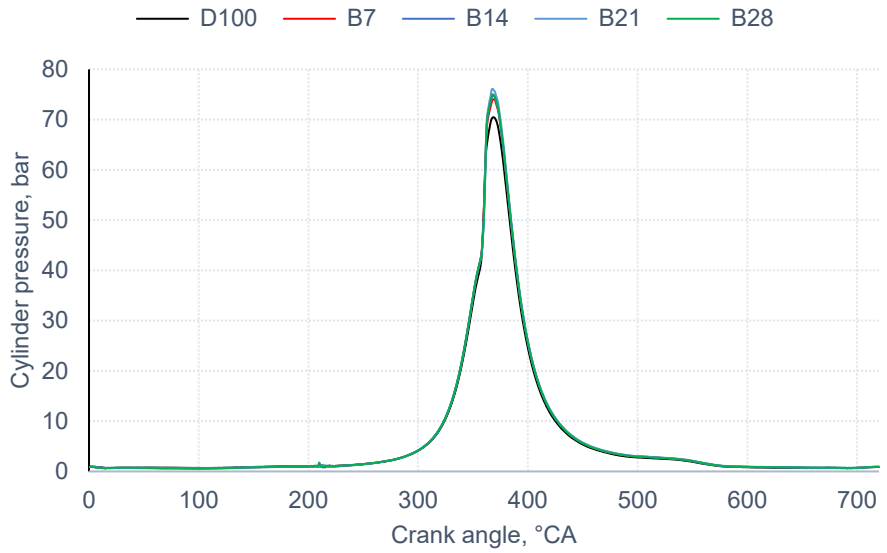

b)

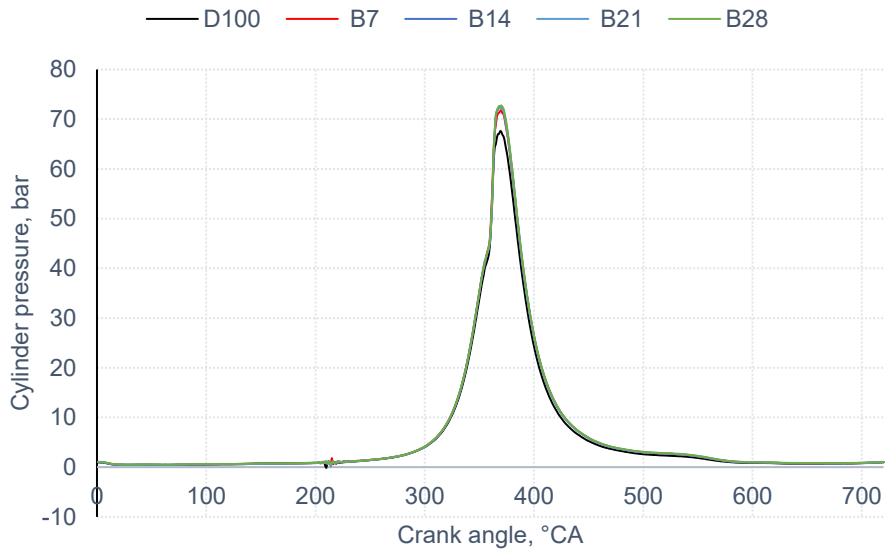

c)

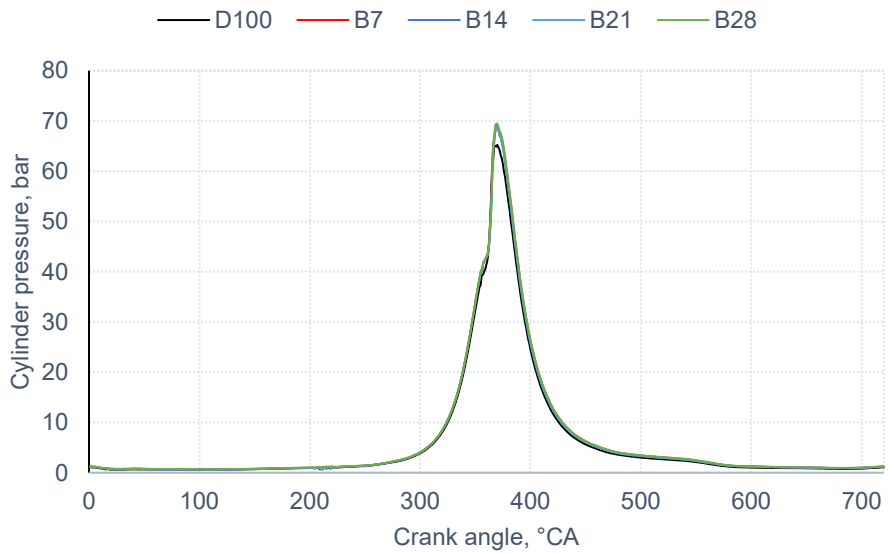

Figure 3 Cylinder pressure vs. crank angle at full load:
a) 1635 rpm
b) 1937 rpm
c) 2239 rpm

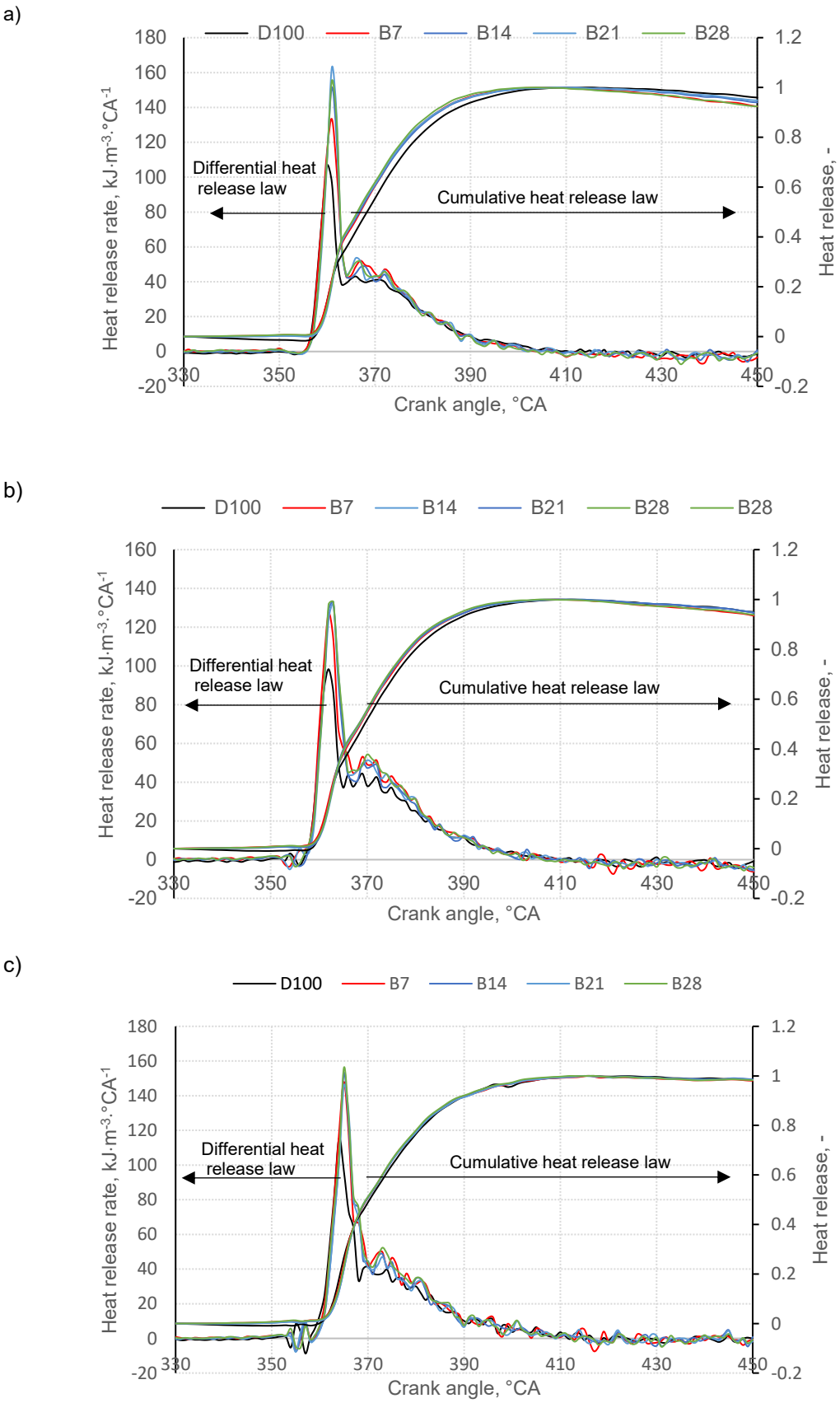

Figure 4 Differential and cumulative heat release laws at full load: a) 1635 rpm, b)1937 rpm, and c) 2239 rpm

In terms of BTE, the blends exhibit values comparable to those of D100 and, under certain operating regimes, even higher values. Among all the blends, B14 stands out, exhibiting relatively high BTE values of 0.296 at 1635 rpm, 0.324 at 1937 rpm, and 0.277 at 2239 rpm.

It can also be observed that there is no clear trend in ITE and BTE with increasing biodiesel content in the blends that is consistent across all engine operating regimes at full load.

Djurić, Ž. et al. (2026) presented almost identical results from tests conducted on a single-cylinder, direct-injection engine fueled with D100 and blends of biodiesel produced from waste grape seed oil and conventional diesel fuel (B7 and B14) at 75% and 100% engine load.

A.K. Azad & M.G. Rasul (2019) tested a four-cylinder diesel engine fueled with D100 and blends of biodiesel derived from waste grape seed oil and conventional diesel fuel (B5 and B10). B10 and D100 exhibited identical peak heat release rate values, whereas B5 exhibited slightly lower values than B10 and D100. When using the blends, the engine exhibited lower BTE, leading the authors to conclude that increasing the biodiesel content in the blend reduces engine efficiency.

Table 4 Indicated, mechanical, and brake thermal efficiency of the engine at full load

Parameter	**Value/Description**				
	D100	B7	B14	B21	B28
Load			100%		
Engine speed, rpm			1635		
Indicated thermal efficiency, -	0,403	0,394	0,411	0,395	0,386
Mechanical efficiency, -	0.747	0.723	0.721	0.719	0.715
Brake thermal efficiency, -	0.301	0.285	0.296	0.284	0.276
Engine speed, rpm			1937		
Indicated thermal efficiency, -	0.364	0.381	0.452	0.400	0.383
Mechanical efficiency, -	0.755	0.724	0.717	0.690	0.711
Brake thermal efficiency, -	0.275	0.276	0.324	0.276	0.272
Engine speed, rpm			2239		
Indicated thermal efficiency, -	0.378	0.393	0.389	0.375	0.383
Mechanical efficiency, -	0.744	0.696	0.712	0.695	0.701
Brake thermal efficiency, -	0.281	0.273	0.277	0.261	0.268

CONCLUSIONS

The effects of biodiesel fuel application on combustion process parameters and engine efficiency depend on the feedstock used for fuel production, the production method, and the conditions under which the fuel is utilized. Based on the investigation of the combustion process parameters of biodiesel blends produced from waste grape seed oil and conventional diesel fuel at full engine load, the following conclusions can be drawn:

- Although biodiesel fuel has a lower heating value and higher kinematic viscosity, the use of B7, B14, B21, and B28 blends ensures stable engine operation at full load.
- The blends exhibit higher peak heat release rates than D100, resulting in a higher pressure rise rate and higher peak cylinder pressure, which are associated with greater mechanical loads and increased engine noise.
- At 1937 rpm, the peak heat release rate increases with increasing biodiesel content in the blend, whereas at the other engine speeds, no clear trend in the peak heat release rate with increasing biodiesel content is observed.
- The peak heat release rates of the blends occur at later crank angles than that of D100, which partially mitigates the effects associated with higher pressure rise rates, such as increased mechanical loads and engine noise.
- The peak heat release rates occur at the same crank angle for all blends, except for B7 at 1937 rpm.
- The heat release centroid is located closer to TDC for the blends than for D100, which has a positive effect on ITE when the blends are used.
- The heat release centroid is closest to TDC for B28, at 6.30 °CA ATDC at 1635 rpm and 9.61 °CA ATDC at 2239 rpm, and for B21, at 8.24 °CA ATDC at 1937 rpm.
- In all cases, the position of the peak cylinder pressure is shifted closer to TDC due to the relatively advanced injection timing, which was set for operation with the earlier diesel fuel formulation (CN ≥ 45). Optimization of the injection timing could result in more favorable combustion characteristics.
- In terms of BTE, the blends exhibit values comparable to those of D100, with B14 showing the most favorable values: 0.296 at 1635 rpm, 0.324 at 1937 rpm, and 0.277 at 2239 rpm.
- No clear trend in ITE and BTE with increasing biodiesel content in the blends is observed that is consistent across all engine operating regimes at full load.

Abbreviations

The following Abbreviations are used in this manuscript:

D100	Conventional diesel fuel
B7	Fuel blend with 7% of biodiesel made from grape seeds
B14	Fuel blend with 14% of biodiesel made from grape seeds
B21	Fuel blend with 21% of biodiesel made from grape seeds
B28	Fuel blend with 28% of biodiesel made from grape seeds
HRR	Heat release rate
TDC	Top dead center
ITE	Indicated thermal efficiency
BTE	Brake thermal efficiency
BSFC	Brake-specific fuel consumption
LHV	Lower heating values
CI	Compression ignition
CA	Crankshaft angle
BTDC	Before top dead center
ATDC	After top dead center
BDC	Bottom Dead Center
ABDC	After Bottom Dead Center
BBDC	Before Bottom Dead Center
KOH	Potassium hydroxide

ACKNOWLEDGMENTS

This work presents the results of research conducted within projects financially supported by the Ministry of Science, Technological Development and Innovation of the Republic of Serbia, under Contract No. 451-03-34/2026-03/200107, dated 5 February 2026.

REFERENCES

Ayhana, V., Çangalb, Ç., Cesura, İ., Çobana, A., Ergena, G., Çaya, Y., Kolipa, A., & Özsert, İ. (2020). Optimization of the factors affecting performance and emissions in a diesel engine using biodiesel and EGR with Taguchi method. *Fuel*, 261, 116371. https://doi.org/10.1016/j.fuel.2019.116371

Azad, A.K. & Rasul. M.G. (2019). Performance and combustion analysis of diesel engine fueled with grape seed and waste cooking biodiesel. *Energy Procedia*, 160, 340-347. https://doi.org/10.1016/j.egypro.2019.02.166

Can, Ö. (2014). Combustion characteristics, performance and exhaust emissions of a diesel engine fueled with a waste cooking oil biodiesel mixture. *Renewable Energy*, 87, 676-686, https://doi.org/10.1016/j.enconman.2014.07.066

Chelladorai, P., Varuvel, E. G., Martin, L. J., Bedhannan, N. (2018), Synergistic effect of hydrogen induction with biofuel obtained from winery waste (grapeseed oil) for CI engine application. *International Journal of Hydrogen Energy,* 43(27), 12473-12490, https://doi.org/10.1016/j.ijhydene.2018.04.155

Djuric, Z., Grujic, I., Glisovic, J., Gordic, D., Milasinovic, A., & Stojanovic, N. (2026). Experimental determination of combustion process parameters of biodiesel fuel made from waste grape seeds, *Processes,* 14(9), 1368, https://doi.org/10.3390/pr14091368

Emma, A. F., Alangar, S., & Yadav, A. K. (2022). Extraction and characterization of coffee husk biodiesel and investigation of its effect on performance, combustion, and emission characteristics in a diesel engine. *Energy Conversion and Management: X,* 14, 100214, https://doi.org/10.1016/j.ecmx.2022.100214

Erdogan, S., Balki, M. K., & Sayin, C. (2019). Combustion analysis of biodiesel derived from bone marrow in a diesel generator at low loads. *International Journal of Automotive Engineering and Technologies*, 8 (2), 76-82. https://doi.org/10.18245/ijaet.535081

EUR-Lex.europa.eu. (1999, December 13). DIRECTIVE 1999/96/EC OF THE EUROPEAN PARLLAMENT AND OF THE COUNCIL. https://eur-lex.europa.eu/legal-content/EN/TXT/PDF/?uri=CELEX:31999L0096

Internet Archive. (2009). ASTM D240 − 09: Standard Test Method for Heat of Combustion of Liquid Hydrocarbon Fuels by Bomb Calorimete. https://archive.org/details/gov.law.astm.D0240.09

Mehra, K. S., & Goel, V. (2025). Unveiling next-generation biodiesel Technologies: Techno-Economic and energy breakthroughs for sustainable production. *Biomass and Bioenergy*, 199, 107910, https://doi.org/10.1016/j.biombioe.2025.107910

Nikolić, B. D., Marković, S. D., Petrović, N. S., Marinković, D. Z. & Jovanović, V. D. (2025) Biodiesel and feedstockspossibilities and characteristics a Review. *Thermal Science*, 29(5A), 3477-3490. https://doi.org/10.2298/TSCI250205058N

SRPS EN ISO 3675. (2007). Crude Petroleum and Liquid Petroleum Products—Laboratory Determination of Density—Hydrometer Method. Institute for Standardization of Serbia: Belgrade, Serbia.

SRPS EN ISO 3104. (2024). Petroleum Products—Transparent and Opaque Liquids—Determination of Kinematic Viscosity and Calcu-lation of Dynamic Viscosity. Institute for Standardization of Serbia: Belgrade, Serbia.

SRPS EN ISO 2719/A1. (2021). Determination of Flash Point—Pensky-Martens Closed Cup Method—Amendment 1: Thermometers Correction. Institute for Standardization of Serbia: Belgrade; Serbia.

SRPS EN ISO 3679. (2022). Determination of Flash No-Flash and Flash Point—Rapid Equilibrium Closed Cup Method. Institute for Standardization of Serbia: Belgrade; Serbia.

SRPS EN 14103. (2020) Fat and Oil Derivatives—Fatty Acid Methyl Esters (FAME)—Determination of Ester and Linolenic acid Methyl Ester Contents. Institute for Standardization of Serbia: Belgrade; Serbia.

Кнежевић, Д. (2014). *Истраживање процеса сагоревања и издувне емисије дизел мотора при погону биогоривима*. Докторска дисертација. Београд.

The 11th International Congress
Motor Vehicles & Motors 2026
Kragujevac, Serbia
October 8th - 9th, 2026

Motor Vehicles & Motors

MVM2026-011
https://doi.org/10.24874/CMVM2026.011
Original scientific paper

Milan Eremija[1]
Ivan Grujić[2]
Danijela Miloradović[3]
Željko Đurić[4]
Svetko Milutinović[5]
Nadica Stojanović[6]

EXPERIMENTAL ANALYSIS OF EXHAUST GAS TEMPERATURE DURING THE USE OF BIODIESEL FUEL

ABSTRACT: The application of biofuels in internal combustion engines is gaining increasing importance from the aspects of improving energy efficiency, reducing the consumption of fossil fuels, and decreasing greenhouse gas emissions. In the field of diesel engines, particular attention has been directed toward the use of biodiesel and its blends with conventional diesel fuel, with the aim of improving the environmental characteristics of the propulsion system while maintaining satisfactory engine performance characteristics. The aim of this paper is to determine the influence of different blending ratios of biodiesel and conventional diesel fuel on exhaust gas temperature. The laboratory testing conducted for the purposes of this study was carried out in an engine testing laboratory equipped with modern measuring and testing equipment intended for the analysis of propulsion and environmental characteristics of internal combustion engines. The applied laboratory equipment enabled precise monitoring and evaluation of relevant operating parameters during the experimental investigation. During the experimental research, exhaust gas temperature parameters were monitored using four different types of fuel, namely biodiesel–diesel fuel blends (BD7, BD15, BD20, and BD30). The obtained results indicate that increasing the concentration of biodiesel in fossil diesel fuel leads to a reduction in exhaust gas temperature. The significance of this study is reflected in the consideration of the possibilities for wider application of biodiesel fuels in modern propulsion systems, as well as in the analysis of their influence on the environmental characteristics of internal combustion engines.

KEYWORDS: diesel fuel, biodiesel, exhaust gas temperature, diesel engines

[1] *Milan Eremija, Senior Assistant,* University of East Sarajevo, *Faculty of Transport and Traffic Engineering,* milan.eremija@sf.ues.rs.ba, https://orcid.org/0009-0000-1551-1231
[2] *Ivan Grujić Assistent professor, University of Kragujevac, Faculty of Engineering,* ivan.grujic@kg.ac.rs, https://orcid.org/0000-0003-0572-1205
[3] *Danijela Miloradović, Ph.D., professor, Faculty of engineering, University of Kragujevac, Sestre Janjić 6, 34000 Kragujevac, Serbia,* neja@kg.ac.rs, https://orcid.org/0000-0003-1427-9789
[4] *Željko Đurić, teaching assistant, University of Banja Luka, Faculty of Mechanical Engineering,* zeljko.djuric@mf.unibl.org, https://orcid.org/0009-0001-8573-6038
[5] *Svetko Milutinovic, Assistant, University of East Sarajevo, Faculty of Transport and Traffic Engineering,* svetko.milutinovic@sf.ues.rs.ba
[6] *Nadica Stojanović, Assistent professor, University of Kragujevac, Faculty of Engineering,* nadica.stojanovic@kg.ac.rs, https://orcid.org/0000-0002-4199-0587

EKSPERIMENTALNA ANALIZA TEMPERATURE IZDUVNIH GASOVA PRI UPOTREBI BIODIZEL GORIVA

REZIME: Primjena biogoriva u motorima sa unutrašnjim sagorijevanjem sve više dobija na značaju sa aspekta povećanja energetske efikasnosti, smanjenja potrošnje fosilnih energenata i redukcije emisije gasova sa efektom staklene bašte. U oblasti dizel motora posebna pažnja usmjerena je na upotrebu biodizela i njegovih mješavina sa konvencionalnim dizel gorivom, sa ciljem unapređenja ekoloških karakteristika pogonskog sistema uz zadržavanje zadovoljavajućih eksploatacionih performansi motora. Cilj rada jeste utvrđivanje uticaja različitih mješavinskih odnosa biodizela i konvencionalnog dizel goriva na temperaturu izduvnih gasova. Laboratorijsko ispitivanje za potrebe ovog rada sprovedeno je u laboratoriji za ispitivanje motora, opremljenoj savremenom mjerno-ispitnom opremom namijenjenom za analizu pogonskih ni ekoloških karakteristika motora sa unutrašnjim sagorijevanjem. Primijenjena laboratorijska oprema omogućila je precizno praćenje i evaluaciju relevantnih radnih parametara tokom eksperimentalnog istraživanja. Tokom eksperimentalnog istraživanja praćeni su parametri temperature izduvnih gasova pri upotrebi četiri različite vrste goriva, odnosno mješavina biodizela i dizel goriva (BD7, BD15, BD20 i BD30). Dobijeni rezultati ukazuju da povećanjem koncentracije biodizela u fosilnom dizel gorivu dolazi do smanjenja temperature izduvnih gasova. Značaj rada ogleda se u sagledavanju mogućnosti šire primjene biodizel goriva u savremenim pogonskim sistemima, kao i u analizi njegovog uticaja na ekološke karakteristike motora sa unutrašnjim sagorijevanjem

KLJUČNE REČI: dizel gorivo, biodizel, temperatura izduvnih gasova, dizel motori

INTRODUCTION

Biodiesel represents one of the alternative fuels for use in diesel engines and has been the subject of extensive research due to the increasing need to promote renewable energy sources and reduce dependence on fossil fuels. Its physicochemical properties differ from those of conventional diesel fuel, which may affect the combustion process, engine operating characteristics, and exhaust emissions (Wenbo & Haeng Muk Cho, 2024; Azad et al. 2023).

Exhaust gas temperature (EGT) is one of the parameters that can be used to assess the thermal behaviour of an engine. Previous studies indicate that variations in the biodiesel content of a fuel blend may have different effects on EGT, with the resulting temperature values depending on fuel properties, biodiesel blend ratio, and engine operating conditions (Azad et al. 2023; Guirong et al. 2020). The objective of this study is to experimentally investigate the effect of different biodiesel mass fractions in diesel fuel on the exhaust gas temperature of a Volkswagen 1.9 TDI PD BKC engine. The experiments were conducted at engine load levels of 50% and 100%, using BD7, BD15, and BD20 fuel blends, in order to determine variations in exhaust gas temperature as a function of fuel composition and engine load.

POSSIBILITIES FOR THE APPLICATION OF BIODIESEL IN INTERNAL COMBUSTION ENGINES

Biodiesel is a renewable alternative fuel for diesel engines, primarily produced from vegetable oils and animal fats. Its use may contribute to reductions in CO_2 emissions, particulate matter, carbon monoxide, aromatic compounds, and sulfur oxides. In addition to its environmental benefits, biodiesel is characterized by biodegradability and low toxicity, while its production from locally available renewable feedstocks may contribute to reducing dependence on fossil fuels and supporting local economic development. Biodiesel can be used in diesel engines as a neat fuel or, more commonly, in blends with fossil diesel fuel. According to standard nomenclature, B100 denotes a fuel containing 100% biodiesel, whereas B5 and B20 denote blends containing 5% and 20% biodiesel, respectively. At relatively low biodiesel blend ratios, such blends can generally be used without significant engine modifications; however, the applicability of neat biodiesel depends on engine design, manufacturer specifications, and fuel quality. Biodiesel intended for use in diesel engines should comply with the requirements of the EN 14214 standard. Biodiesel can be blended with mineral diesel fuel at different ratios, provided that an appropriate blending procedure is applied to ensure a homogeneous mixture. According to (Babić, 2013), biodiesel blending can be performed by spraying, directly in the fuel tank, or in the fuel line upstream of the tank.

In addition to the aforementioned advantages, the use of biodiesel is associated with certain limitations. A particular concern is its less favourable low-temperature performance, namely higher cloud point and pour point compared with conventional diesel fuel. As the temperature decreases, crystal formation and an increase in viscosity may occur,

impairing fuel flow and delivery and potentially causing clogging of fuel system components. Therefore, suitable additives may be used under low-temperature operating conditions to improve the low-temperature properties of the fuel. Another limitation is the higher distillation temperature of biodiesel, which may affect mixture formation and increase the potential for fuel dilution of the lubricating oil. Under such conditions, more frequent monitoring and replacement of the engine lubricating oil may be required.

REVIEW OF RELEVANT LITERATURE

Karrar & Hyder (2026.) investigated the effects of biodiesel and biodiesel–diesel blends on the operating characteristics of an internal combustion engine under different engine load conditions, with particular emphasis on variations in exhaust gas temperature (EGT). Tests conducted using neat diesel fuel (D100) and biodiesel blends with different biodiesel contents (D10, D20, D30, D40, D50) demonstrated a pronounced increase in exhaust gas temperature with increasing engine load, regardless of the fuel type used. According to the author, this trend can be attributed to the increased amount of fuel required at higher engine loads, resulting in a more intensive combustion process and, consequently, higher in-cylinder temperatures. Compared with neat diesel fuel, the use of biodiesel resulted in an increase in exhaust gas temperature of approximately 6.8%, particularly at full engine load. The author attributed this behaviour to the specific physicochemical properties of biodiesel, particularly its oxygen content, which may affect combustion characteristics and exhaust gas temperature. Similar trends were also observed for biodiesel produced from waste cooking oil (WCO), with the higher oxygen content of the fuel influencing combustion characteristics and EGT as engine load increased (Genet, et al. 2026.).

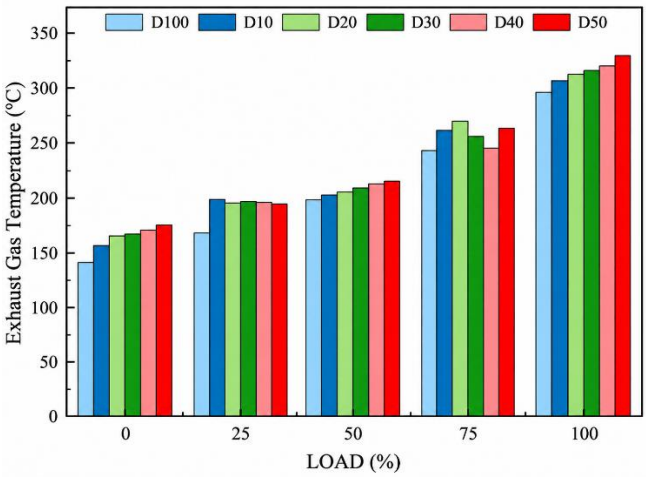

Figure 1 Variation in exhaust gas temperature as a function of engine load for diesel fuel and different biodiesel blends (Karrar & Hyder, 2026)

Karabulut et al. (2024.) investigated the effect of biodiesel content on exhaust gas temperature (EGT) and found that increasing the biodiesel fraction resulted in a decrease in EGT. At 1500 min^{-1} and full engine load, EGT values for B10, B20, B50, and B100 were 10.00%, 19.31%, 25.14%, and 32.35% lower, respectively, than that of conventional diesel fuel (B0). The reduction in EGT was primarily attributed to the lower heating value of biodiesel and its combustion characteristics, with a greater proportion of the fuel being burned before the onset of the expansion stroke. At the same time, increasing engine load and rotational speed resulted in higher EGT due to the increased amount of heat released during combustion.

Sabah et al. (2025) investigated the effects of engine load and biodiesel–diesel blend composition on exhaust gas temperature (EGT). The results showed that EGT increased with increasing engine load, which was attributed to higher fuel consumption and more intensive heat release during combustion. Most of the investigated biodiesel blends exhibited higher EGT values than conventional diesel fuel, which was associated with the oxygen content of biodiesel and more complete combustion. As an exception, the NC(CaO)B10 blend exhibited a lower exhaust gas temperature than diesel fuel and the other blends at full engine load, which was attributed to its more favourable fuel atomization and evaporation characteristics.

Mensih et al. (2025.) investigated the effect of biodiesel–ethanol blends on exhaust gas temperature (EGT). The results showed that EGT increased with increasing engine load, while all investigated blends exhibited lower EGT values compared with neat diesel fuel (D100). At full engine load and without exhaust gas recirculation, the reductions in EGT for the D80CB20, D80CB10E10, D60CB40, and D60CB20E20 blends were 4%, 11%, 8%, and 19%, respectively, compared with D100. The reduction in exhaust gas temperature was attributed to the lower heating value, higher latent heat of vaporization, and oxygen content of biodiesel and ethanol, which contributed to lower combustion temperatures.

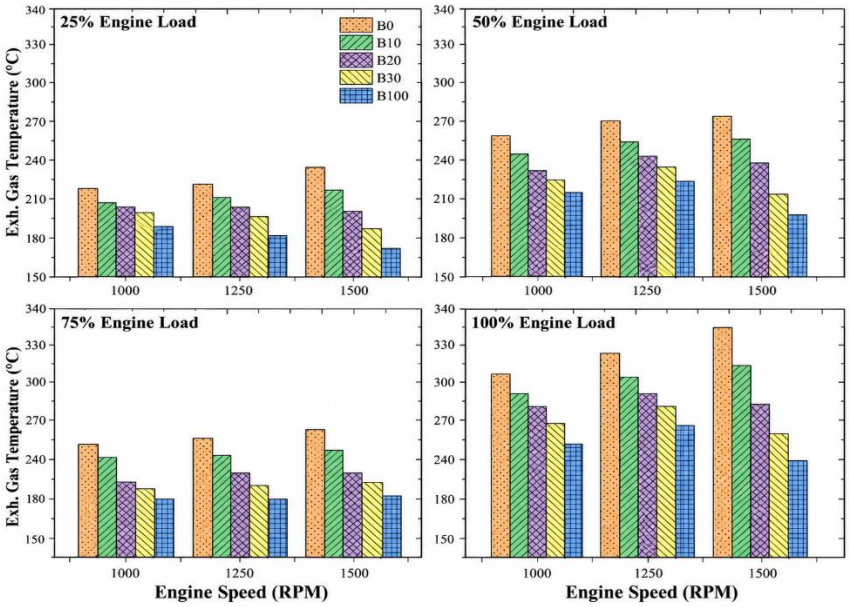

Figure 2 Variation in exhaust gas temperature (Karabulut et al. 2024)

Sudarsanam et al. (2025.) investigated the effects of fuel composition and nano-additives on exhaust gas temperature (EGT). The results showed that increasing the biodiesel content in biodiesel–alcohol blends tended to reduce EGT compared with neat diesel fuel. Ternary blends containing pentanol exhibited lower EGT values than the corresponding blends containing butanol. In contrast, the addition of 25 and 50 ppm Al_2O_3 nanoparticles increased EGT by approximately 1.5% and 5–6%, respectively, which was associated with more intensive combustion and higher in-cylinder temperatures. Furthermore, increasing engine load resulted in higher EGT values for all tested fuels due to the increased amount of injected fuel and greater heat release during the combustion process.

Figure 3 presents the effect of the investigated fuels on exhaust gas temperature (EGT) at different engine load conditions. El-Shafay et al. (2022.) reported that EGT increased with increasing engine load due to the greater amount of fuel required to meet the increased load demand. Under all investigated operating conditions, conventional diesel fuel exhibited the lowest EGT values, whereas biodiesel–diesel blends showed an increase in EGT with increasing biodiesel content. Compared with diesel fuel, the maximum EGT increases were 2% for B5, 3% for B10, 5% for B15, and 8% for B20. These variations were associated with the characteristics of the biodiesel blends and their influence on the combustion process. Similar findings have been reported by other researchers investigating the effects of biodiesel blends on exhaust gas temperature (Chen, Y. et al. 2007).

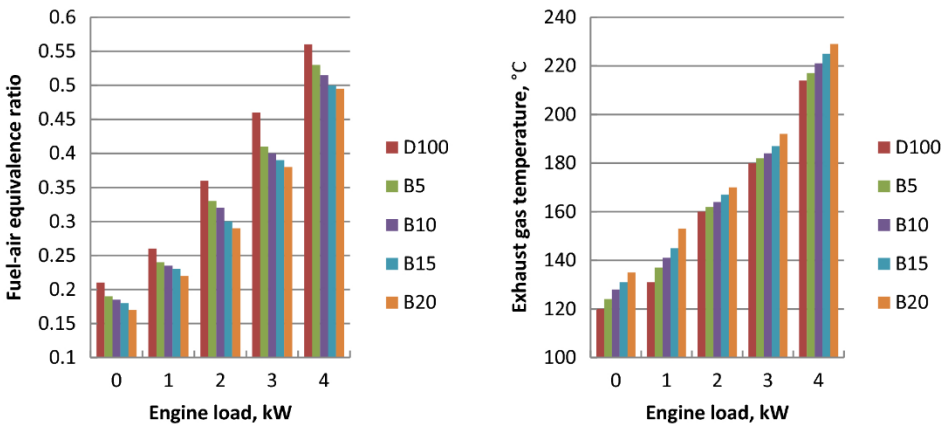

Figure 3 Variation of the fuel–air equivalence ratio and exhaust gas temperature (Text) as a function of engine load (El-Shafay et al. 2022)

The results of available studies indicate that the effect of biodiesel on exhaust gas temperature is not consistent. Some authors have reported an increase in EGT when using biodiesel, attributing this behaviour to its higher oxygen content and more intensive combustion, whereas other studies have reported a decrease in exhaust gas temperature, primarily due to the lower heating value of biodiesel and differences in combustion characteristics. The observed variations in results may also be attributed to the type of biodiesel, its proportion in the fuel blend, engine operating conditions, and engine design characteristics.

METHODOLOGY

Test Fuels and Engine Load Conditions

The experimental investigation was conducted in an engine testing laboratory equipped with advanced measurement and test instrumentation manufactured by AVL, designed for experimental studies of engine performance and combustion processes. Three fuel blends with different biodiesel mass fractions in fossil diesel fuel were investigated:

- BD7 – a blend containing 7% biodiesel and 93% fossil diesel fuel;
- BD15 – a blend containing 15% biodiesel and 85% fossil diesel fuel;
- BD20 – a blend containing 20% biodiesel and 80% fossil diesel fuel.

The specified proportions represent the mass fraction of biodiesel in the total mass of the fuel blend (m/m). This approach enabled the comparative assessment of the effect of different biodiesel contents on the investigated engine parameter. The tests were conducted at two engine load conditions. The first corresponded to a partial load of 50%, while the second represented full engine load of 100%. Exhaust gas temperature (EGT) was measured under both operating conditions. The primary parameter investigated was exhaust gas temperature, with the aim of assessing the influence of biodiesel mass fraction and engine load on EGT. The obtained experimental results were used to compare engine behaviour when operating with BD7, BD15, and BD20 fuel blends under partial and full load conditions.

Equipment for Measuring Exhaust Gas Temperature

Thermocouples are commonly employed for exhaust gas temperature measurements under experimental conditions. Their main advantages include a simple construction, compact dimensions, relatively rapid response, and a wide operating temperature range. Their operating principle is based on the Seebeck effect. When two electrical conductors made of dissimilar materials are joined and their junctions are maintained at different temperatures, a thermoelectric voltage is generated in the electrical circuit. The magnitude of this voltage depends on the temperature difference between the measuring, or hot, junction and the reference, or cold, junction. A Type K thermocouple is particularly suitable for measuring exhaust gas temperature. This thermocouple type has a wide operating temperature range and is widely used in industrial and laboratory measurement applications. Thermocouples with similar designs and characteristics have also been employed in experimental investigations of exhaust gas temperature, including the study conducted by Papaioannou et al., in which thermocouples of different diameters were used to investigate their influence on the measured exhaust gas temperature (Papaioannou et al., 2018; Son S & Kolasa A, 2006). The AVL F-FEM-AIS measurement system supports Type B, E, J, K, N, R, S, and T thermocouples. According to the technical documentation, the measuring range of a Type K thermocouple extends from −50 °C to 1372 °C, making it suitable for temperature measurements within the exhaust system of an internal combustion engine (AVL List, 2014). The following figure shows the Type K thermocouple used for exhaust gas temperature measurement in the Engine Testing Laboratory of the Faculty of Transport and Traffic Engineering in Doboj.

Figure 4 Thermocouple for exhaust gas temperature measurement

Within the scope of the present experimental investigation, the thermocouple signal was acquired using the AVL F-FEM-AIS module. The F-FEM-AIS is a Fast Front End Module designed for the acquisition of analog signals. The module enables the measurement of electrical voltage, current, electrical resistance, temperature, pressure, and other physical quantities. It is equipped with 16 analog input channels, each of which can be configured according to the connected sensor and the requirements of the specific measurement (AVL List, 2014.). During thermocouple measurements, the F-FEM-AIS performs acquisition and conditioning of the thermoelectric signal, analog-to-digital conversion, and sensor characteristic linearization. For a Type K thermocouple, the manufacturer specifies 64 linearization points for converting the hot-junction voltage into temperature. Available sampling frequencies are 1, 2, 5, 10, and 20 Hz (AVL List, 2014.). The following figure illustrates the connection of the thermocouples to the F-FEM-AIS module.

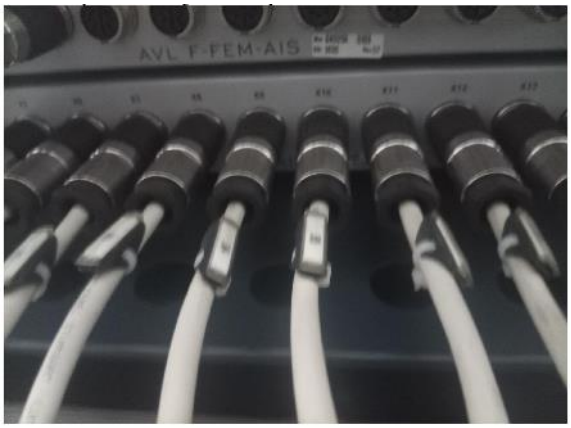

Figure 5 Connection of thermocouples to the F-FEM-AIS module

RESULTS AND DISCUSSION

The experimental results obtained for the three biodiesel–diesel blends (BD7, BD15, and BD20) indicate that, at a partial engine load of 50%, exhaust gas temperature (EGT) decreases with increasing biodiesel content in the fuel (Figure 6). The highest EGT was recorded for the BD7 blend, whereas a progressive decrease in temperature was observed with increasing biodiesel content in BD15 and BD20. This trend may primarily be associated with the lower heating value of biodiesel compared with fossil diesel, resulting in a greater quantity of the biodiesel blend being required to maintain the same engine operating condition. Increasing the biodiesel fraction also alters the physicochemical properties of the fuel, particularly its viscosity, density, and evaporation characteristics, thereby affecting mixture formation and combustion. Consequently, at 50% engine load, an increase in biodiesel content was associated with a reduction in exhaust gas temperature. The obtained result suggests that, under this operating condition, a higher biodiesel fraction may be associated with lower heat losses through the exhaust system.

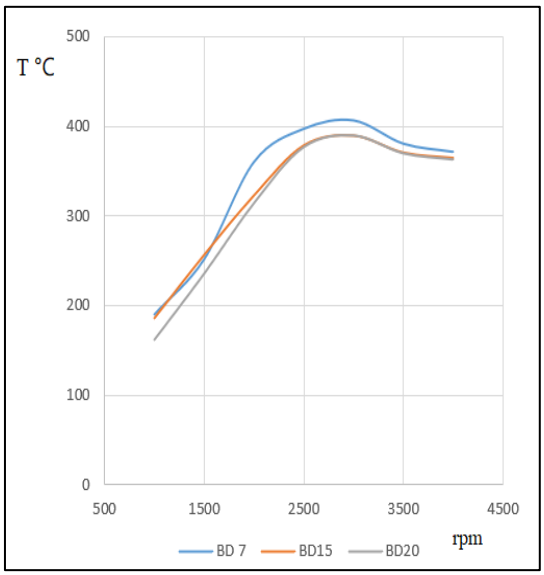

Figure 6 Exhaust gas temperature at a partial engine load of 50%

A similar trend was observed at full engine load of 100% (Figure 7). With increasing biodiesel content in the fossil diesel fuel, i.e., from BD7 to BD15 and BD20, a progressive decrease in exhaust gas temperature (EGT) was observed. The results indicate that, under the analysed operating conditions, increasing the biodiesel fraction in the

investigated blends was associated with a reduction in EGT. This behaviour may primarily be attributed to the lower heating value of biodiesel compared with fossil diesel, as well as to changes in the combustion process resulting from differences in the physicochemical properties of the fuels.

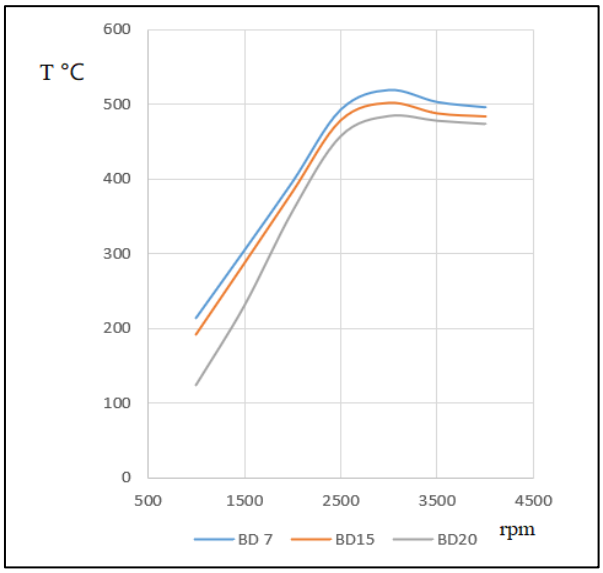

Figure 7 Exhaust gas temperature at full engine load (100% load)

Furthermore, as shown in Figures 6 and 7, exhaust gas temperature (EGT) increases with increasing engine load. Higher engine load requires greater torque output, resulting in a larger quantity of fuel being injected and combusted within the cylinder. Consequently, the amount of heat released during combustion increases, leading to higher combustion product temperatures and, consequently, higher exhaust gas temperatures. In addition, higher engine loads are associated with increased mean in-cylinder temperature, which further contributes to the rise in the temperature of the gases leaving the cylinder. The observed increase in EGT with increasing engine load is consistent with the expected behaviour of diesel engines and indicates a direct relationship between engine load, injected fuel quantity, and engine thermal loading.

CONCLUSION

Based on the experimental investigation of the BD7, BD15, and BD20 biodiesel–diesel blends, it can be concluded that increasing the biodiesel content resulted in a decrease in exhaust gas temperature (EGT) at engine loads of 50% and 100%. The observed trend may be associated with the lower heating value of biodiesel compared with conventional diesel fuel, as well as with its different physicochemical properties affecting the combustion process. Conversely, increasing engine load resulted in higher exhaust gas temperatures for all investigated blends, which can be attributed to the greater amount of injected fuel and increased heat release during combustion.

The obtained results indicate that EGT is influenced by both fuel composition and engine operating conditions. An increase in biodiesel content was associated with a progressive decrease in exhaust gas temperature, whereas increasing engine load had the opposite effect. These findings suggest that biodiesel may affect the thermal behaviour of the engine and potentially contribute to reduced thermal loading; however, its overall effect should be assessed in conjunction with other engine operating parameters.

Future research should include a larger number of biodiesel–diesel blends and a wider range of engine operating conditions to provide a more comprehensive assessment of the influence of biodiesel content on combustion and temperature characteristics. Particular attention should be given to the simultaneous analysis of exhaust gas temperature, brake-specific fuel consumption, effective power, and thermal efficiency in order to provide a more complete evaluation of the effects of biodiesel on engine performance. Further studies should also address emissions of NOx, CO, HC, and particulate matter, as well as engine behaviour at different rotational speeds and under variable load conditions. Long-term testing would additionally be valuable for assessing the effects of biodiesel on thermal stability, engine wear, and operational reliability. Integrating these parameters could contribute to a more reliable determination of the optimal biodiesel content as a balance between engine performance, fuel consumption, thermal loading, and exhaust emissions.

ACKNOWLEDGMENTS

Research presented in this paper was supported by Ministry of science, technological development and innovation of the Republic of Serbia, contract registration number 451-03-34/2026-03/200107.

REFERENCES

AVL List GmbH, F-FEM-AIS, -AIN, -AIS HV, -CAIS, -CAIN, -AIT Operating Manual, User's Guide, AT1197E, Rev. 13, Graz, Austria, 2014.

Azad A.K., Doppalapudi, A. T., Khan, M. M. K., Hassan, N. M. S., & Gudimetla, P. (2023). A landscape review on biodiesel combustion strategies to reduce emission. *Energy Reports*, 9, 4413-4436. https://doi.org/10.1016/j.egyr.2023.03.104

Babić, I. (2013). Biodiesel blending with mineral diesel fuel and its storage possibilities. In *Proceedings of the Festival of Quality*, A356–A361.

Chen, Y. C., He, Y. L. & Cheng, J. (2007). Study on extraction and deacidfication of oils and fats of natural plants by supercritical carbon dioxide. *Journal of Yangtze University*, 4, 45–47.

El-Shafay A. S., Alqsair, U. F., Abdel Razek, S. M., & Gad, M. S. (2022). Artificial neural network prediction of performance and emissions of a diesel engine fueled with palm biodiesel. *Scientific Reports*, 12, 9286. https://doi.org/10.1038/s41598-022-13413-9

Genet, N., Menelik, M., Mekonen, W., Gzate, Y., Leul, A., & Demisie, F. (2024). Experimental investigation on diesel engine performance and emission characteristics using waste cooking oil blended with diesel as biodiesel fuel. *Discover Energy*, 4, 26. https://doi.org/10.1007/s43937-024-00051-7

Gerhard, K. (2006). Analyzing biodiesel: Standards and other methods. *Journal of the American Oil Chemists' Society*, 83, 823–833. https://doi.org/10.1007/s11746-006-5033-y

Wu, G., Ge, J. C., & Choi, N. J. (2020). A comprehensive review of the application characteristics of biodiesel blends in diesel engines. *Applied Sciences*, 10(22), 8015. https://doi.org/10.3390/app10228015

Karabulut M., Cenk Sayın, Sinan Erdoğan, (202). Effects of an exhaust system equipped with a thermoelectric generator on combustion, performance, emissions, and energy recovery in a diesel engine using biodiesel. *Energies*, 17(5), 1083. https://doi.org/10.3390/en17051083

Hasan K. S., & Hyder, H. (2026). Experimental investigation of thermodynamic irreversibility and exergy destruction in a diesel engine fueled with waste cooking oil biodiesel blends. *International Journal of Heat and Technology*, 44(3), 1215-1226. https://doi.org/10.18280/ijht.440327

Kumar, M., Ansari, N. A., & Gautam, R. (2025). Sustainable waste to energy approach using waste derived biodiesel diesel and ethanol blends in a CRDI diesel engine. *Scientific Reports*, 15, 33559. https://doi.org/10.1038/s41598-025-18502-z

Papaioannou, N., Leach, F., & Davy, M. (2018, 17 September). Effect of thermocouple size on the measurement of exhaust gas temperature in internal combustion engines. In *International Powertrains, Fuels & Lubricants Meeting*, Heidelberg, Germany https://doi.org/10.4271/2018-01-1765

Farouk, S. M., Tayeb, A. M., Abdel-Hamid, S. M. S., Osman, R. M., & Mustafa, H. M. M. (2025). Enhanced performance and reduced emissions in compression-ignition engine fueled with biodiesel blends synthesized via CaO and MgO nano catalysts. BMC Chemistry, 17, 241. https://doi.org/10.1186/s13065-025-01604-0

Son, S., & Kolasa, A. (2007, 16 April). Estimating actual exhaust gas temperature from raw thermocouple measurements acquired during transient and steady state engine dynamometer tests. In *SAE World Congress & Exhibition*, Detroit, Michigan, United States https://doi.org/10.4271/2007-01-0335

Sudarsanam, M., Jayaprabakar, J., Rao, Y. K. S. S., Venu, H., Thirugnanasambandam, A., Yadav, A. S., Alam, T., Sharma, A., & Ansu, A. K. (2025). Experimental investigation on a diesel engine using waste cooking oil biodiesel-alcohol-diesel ternary blends with Al2O3 nanoparticles. *Scientific Reports*, 15, 42979. https://doi.org/10.1038/s41598-025-26974-2

Ai, W., Cho, H. M. (2024). Predictive Models for Biodiesel Performance and Emission Characteristics in Diesel Engines: A Review. *Energies*, 17(19), 4805. https://doi.org/10.3390/en17194805

The 11th International Congress
Motor Vehicles & Motors 2026
Kragujevac, Serbia
October 8th - 9th, 2026

Motor Vehicles & Motors

MVM2026-013
https://doi.org/10.24874/CMVM2026.013
Technical paper

Krasimir Markov[1]

Hristo Stanchev[2]

INVESTIGATION OF THE FUEL CONSUMPTION AND EMISSIONS OF A DIESEL ENGINE RUNNING ON DIESEL WITH AN ADDITIVE

ABSTRACT: The increase in the environmental requirements to vehicles necessitates the study of new fuels and additives to standard fuels. Additives can be purchased separately from the fuel or be included directly in the standard fuel before its sale. In the second case, they are designated as premium diesel. According to manufacturers, they improve engine performance. The aim of the article is to study the fuel consumption and emissions of a diesel engine with a common rail injection system operating with premium diesel. Standard diesel and premium diesel were purchased from one seller from the retail network in Bulgaria. The experimental methodology included conducting a load characteristic of the engine at two engine speeds, during which exhaust gases were measured with a gas analyzer. The results show a variable nature of fuel consumption, PM emissions and NOx emissions when using the premium diesel compared to standard diesel.

KEYWORDS: diesel engine, premium diesel, fuel consumption, emissions

ISTRAŽIVANJE POTROŠNJE GORIVA I EMISIJE DIZEL MOTORA KOJI RADI NA DIZEL GORIVO SA ADITIVOM

REZIME: Povećanje ekoloških zahteva za vozila nameće proučavanje novih goriva i aditiva za standardna goriva. Aditivi se mogu kupiti odvojeno od goriva ili se mogu direktno uključiti u standardno gorivo pre njegove prodaje. U drugom slučaju, gorivo se označava kao premium dizel. Prema proizvođačima, aditivi poboljšavaju performanse motora. Cilj rada je proučavanje potrošnje goriva i emisije dizel motora sa „common rail“ sistemom ubrizgavanja koji radi sa premium dizelom. Standardni dizel i premium dizel su kupljeni od jednog prodavca iz maloprodajne mreže u Bugarskoj. Eksperimentalna metodologija je uključivala snimanje karakteristike opterećenja motora pri dve brzine motora, tokom kojih je sadržaj izduvnih gasova meren pomoću gasnog analizatora. Rezultati pokazuju promenljivu prirodu potrošnje goriva i emisija čestica (PM) i azotnih oksida (NOx) pri korišćenju premium dizela u poređenju sa standardnim dizelom.

KLJUČNE REČI: dizel motor, premium dizel, potrošnja goriva, emisija izduvnih gasova

[1] *Krasimir Markov, Department of Engine and Vehicles, University of Ruse, Bulgaria, krmarkov@uni-ruse.bg*
[2] *Hristo Stanchev, Department of Engine and Vehicles, University of Ruse, Bulgaria, hstanchev@uni-ruse.bg*

INTRODUCTION

The increase in the environmental requirements to vehicles necessitates the study of new fuels and additives to standard fuels. Additives can be purchased separately from the fuel or be included directly in the standard fuel before its sale. In the second case, they are designated as premium diesel. According to manufacturers, they improve engine performance.

The literature review shows the premium diesel is investigated as a fuel for diesel engines in vehicles and power generators. The literature analysis of the premium diesel in this article is focused only to the diesel engines in vehicles. Chen, K.-S. et al. (2010) investigate fuel consumption and emissions of diesel engine working with premium diesel-biodiesel blends and bio-solution additive. The source of biodiesel is palm oil. The premium diesel is used for the base fuel. The results showed up to 12.4% reduction of the fuel consumption, up to 90.1% reduction of PM emissions and up to 69.3% reduction of PAHs when using the 64% diesel – 20% biodiesel – 16% additive blend compared to pure premium diesel. Gavaskar, T. et al. (2023) study the performance and emissions of a single-cylinder engine working with mixture of acetylene gas, biodiesel, premium diesel and additive. The source of biodiesel is jackfruit seed oil. The premium diesel is used for base fuel. At full load, the results showed higher BSFC with 8.24%, higher NOx emissions with 13.29%, lower BTE with 5.14%, lower in-cylinder pressure with 3.73%, lower HC emissions with 23.36%, lower CO emissions with 23.92% and lower PM emissions with 14.72% when using the mixture of 80% premium diesel – 20% biodiesel – 50 ppm additive and 6 l/min acetylene gas in comparison to the premium diesel. Lin, Y.-C. et al. (2008) research the particle size distribution from diesel engine fueled with palm-biodiesel blends and paraffinic fuel blends. The premium diesel is used as a fuel in the blends and as a base fuel. Yuan, C.-S. et al. (2009) study the reduction of carbonyl emissions from a heavy-duty diesel engine at US transient cycle test by use of paraffinic/biodiesel blends. The premium diesel is used as a fuel in the blends and as a base fuel. Wang, H.-K. et al. (2012) investigate the emission reduction of air pollutants from a heavy-duty diesel engine running on premium diesel mixed with various amounts of H_2/O_2. The premium diesel is used as a fuel in the blends and as a base fuel. The results showed reduced BSFC with 12.6%, reduced PAHs emissions with 32.3%, reduced HC emissions with 9.5%, reduced CO emissions with 7.2%, reduced PM emissions with 19.3% and increased NOx emissions with 9.9% when using the mixture of premium diesel and 60 l/min H_2/O_2 compared to premium diesel. Chiavola, O. et al. (2021) study the operation cycle of diesel common-rail injection pump via pressure measurement in piston working chamber. The premium diesel is used as reference fuel. Cueva, M. et al. (2025) analyze the emissions and fuel consumption of a truck using a mixture of diesel and additive on high-altitude roads. The additive was cerium oxide. The premium diesel is used as fuel in the mixture with additive and as a base fuel. The results showed reduction of fuel consumption with 1%, reduction of PM emissions with 27.1%, increase of HC emissions with 24.2% and increase of NO_x emissions with 24.9% when using the mixture compared to the premium diesel. Costagliola, M.A. et al. (2025) investigate the effect of additives on fuel consumption optimization in heavy-duty diesel vehicles. The results showed decrease of fuel consumption with 1.1% when using premium diesel compared to standard diesel.

The literature analysis shows important research gap – there is no investigation of emissions when using premium diesel compared to standard diesel. The aim of the article is to study the fuel consumption and emissions of a diesel engine with a common rail injection system operating with premium diesel.

MATERIALS AND METHODS

An engine Fiat 1.9 JTD has been tested in laboratory condition on DC dynamometer. The fuel consumption is determined by mas flow method. For precise NOx concentration measurement special analyser ECM NO_x 5210 (g) is used. The exhaust smoke is measured by OPA-101 Nextech diesel smoke opacity meter. The technical specifications of equipment are given in next tables.

Table 1 Engine Specification

Engine	FIAT 1.9 JTD
Maximum power	60 kW at 4000 min^{-1}
Maximum torque	196 Nm at 1500 min^{-1}
Displacement	1910 cm^3
Fuel system	Common-Rail
Intake system	Turbocharger
Compression ratio	18.5
Bore	82 mm
Stroke	90.4 mm
Number of valves	2

Table 2 ECM NOx 5210(g) gas analyser

Component	Range
NOx	0 – 8000 ppm
λ	0.4 - 25
AFR	6 – 364
Φ	0.04 – 2.5
O_2	0 – 25 vol. %
FAR x 10 000	27 - 1667

Table 3 OPA-101 Nextech smoke opacity meter

Parameter	Range (accuracy)
Opacity	0 – 100% (0,01%)
Absorbtion coefficient K	0 – 21.42 m^{-1} (0,01 m^{-1})
Engine oil temperature	0 – 120 °C
Engine speed	0 – 5000 min^{-1}

The research studies the brake specific fuel consumption (BSFC), NO_x emissions and PM emissions when engine operates with premium diesel and the standard diesel is used as reference fuel. Standard diesel and premium diesel were purchased from one seller from the retail network in Bulgaria. According to the seller, the premium diesel contains an additive that reduces the fuel consumption and emissions (not stated exactly which emissions). The additive contains cetane number improver, lubricity improvers, corrosion inhibitors, polymer detergents/solvent oil and demulsified/antifoam agents. The experimental methodology included conducting a load characteristic of the engine at two engine speeds, during which exhaust gases were measured with gas analyzers. The fuel consumption was measured by stopwatch and scale through mass flow method.

RESULTS AND ANALYSIS

The results for the BSFC, NO_x emissions and PM emissions will be presented continuously. The analysis will follow each result.

The results for the BSFC are shown in Figure 1. For engine speed 1800 min^{-1}, it is visible the BSFC is lower for premium diesel compared to standard diesel. The highest decrease is 9,3% at 9 kW engine load. For engine speed 2400 min^{-1} at low engine loads the BSFC is lower for premium diesel but at medium engine loads is higher for premium diesel in comparison to standard diesel. The highest decrease is 7.55% at 13 kW engine load while the highest increase is 6.34% at 25 kW engine load.

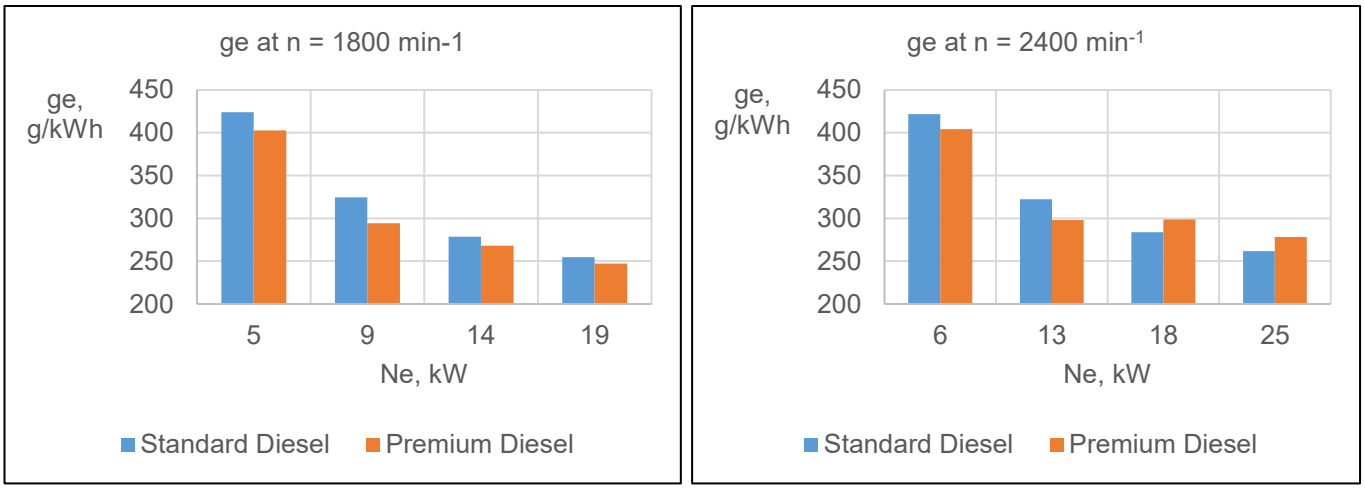

Figure 1 Results for BSFC

The results for the NO_x emissions are shown in Figure 2. For both engine speeds, it is visible that at low loads, the NO_x emissions are similar for premium and standard diesel and there is no clear trend. The difference become clear at medium loads. For engine speed 1800 min^{-1} at 14 kW and above, the NOx emissions for premium diesel are lower than the standard diesel. The highest reduction of NO_x emissions is 25,83% at 19 kW engine load. For engine speed 2400 min^{-1} at 18 kW and above there is opposite effect and the NOx emissions for premium diesel are higher than the standard diesel. The highest increase is 15% at 25 kW engine speed. The decrease of NOx emissions could be explained with the cetane improver additive. It shorter the ignition delay following to burn of lower amount of accumulated fuel and as a result lower in-cylinder temperature. In the same time for 25 kW engine load (2400 min^{-1})

the higher injected fuel in combination with the earlier start of combustion is reason for higher temperature in the cylinder chamber and as a result a higher NO_x emissions.

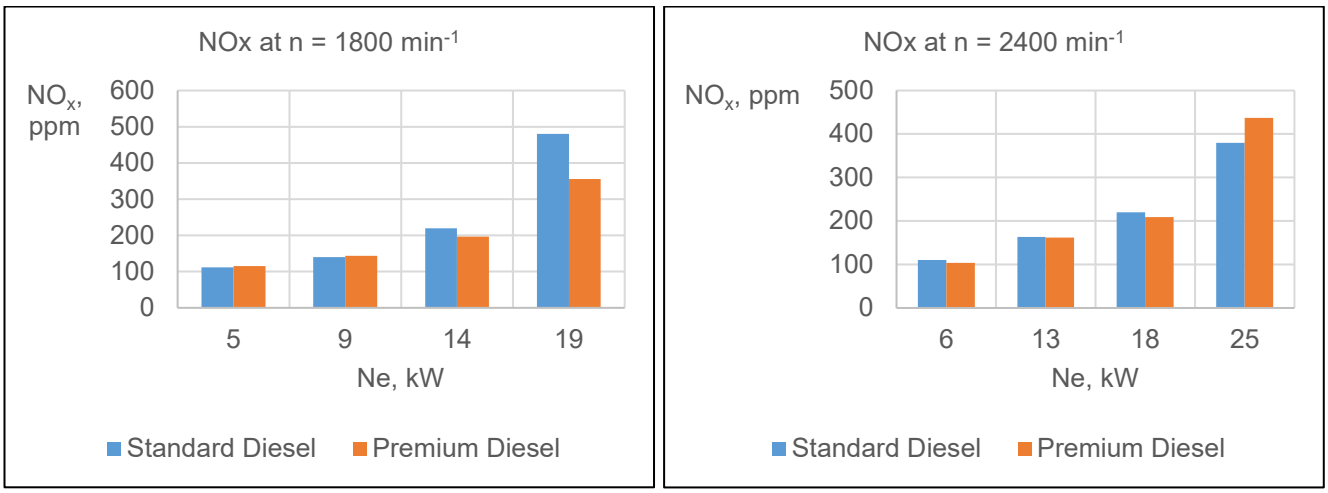

Figure 2 Results for NO_x emissions

The results for PM emissions are shown in Figure 3. For both engine speeds, the PM emissions are lower for premium diesel compared to standard diesel. For engine speed 1800 min^{-1}, the highest decrease is 35.71% at 5 kW engine load. For engine speed 2400 min^{-1}, the highest decrease is 37.5% at 25 kW engine load. The results could be explained with the cetane improver and polymer detergents of the additive that is used in the premium diesel. The cetane improver could enhance the start of combustion following to easier, faster and smooth combustion process. The polymer detergents and solvent oils remove the carbon dispositions.

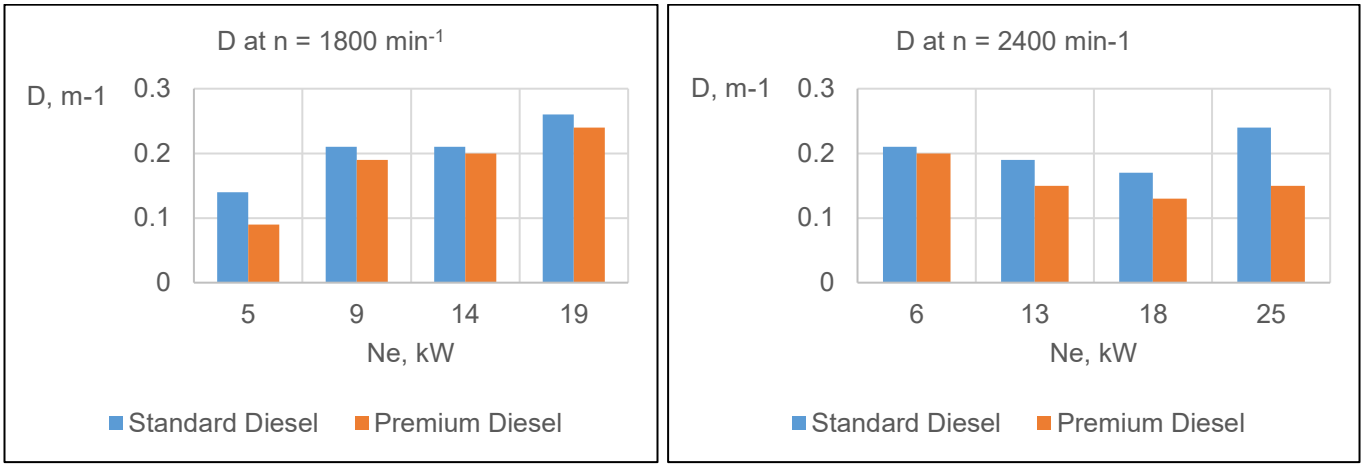

Figure 3 Results for PM emissions

CONCLUSIONS

The article studied the brake specific fuel consumption, NO_x emissions and PM emissions of a common rail direct injection diesel engine fueled with premium diesel. The test methodology included proceeding of engine load characteristic. The standard diesel was used as a reference fuel. The result showed there is no clear trend for the brake specific fuel consumption and NO_x emissions. The results highly depend from the engine load and additive ingredients in the premium diesel. The results for PM emissions showed reduction for all engine loads at both engine speeds.

ACKNOWLEDGMENTS

The study was conducted with the support of University of Ruse “Angel Kanchev”, project FNI 2026-FT-02 “Research on the efficiency of vehicles”.

REFERENCES

Chen, K.-S., Lin, Y.-C., Hsieh, L.-T., Lin, L.-F., Wu, C.-C. (2010). Saving energy and reducing pollution by use of emulsified palm-biodiesel blends with bio-solution additive. *Energy*, 35, 2043-2048. https://doi.org/10.1016/j.energy.2010.01.021

Gavaskar, T., Venkata Ramanan, M., Arun, K., Arivazhagan, S. (2023). The combined effect of green synthesized nitrogen-doped carbon quantum dots blended jackfruit seed biodiesel and acetylene gas tested on the dual fuel engine. *Energy,* 275, 127296. https://doi.org/10.1016/j.energy.2023.127296

Lin, Y.-C., Lee, C.-F., Fang, T. (2008). Characterization of particle size distribution from diesel engines fueled with palm-biodiesel blends and paraffinic fuel blends. *Atmospheric Environment*, 42, 1133-1143. https://doi.org/10.1016/j.atmosenv.2007.10.046

Yuan, C.-S., Lin, Y.-C., Tsai, C.-H., Wu, C.-C., Lin, Y.-S. (2009). Reducing carbonyl emissions from a heavy-duty diesel engine at US transient cycle test by use of paraffinic/biodiesel blends. *Atmospheric Environment*, 43, 6175-6181. https://doi.org/10.1016/j.atmosenv.2009.09.007

Wang, H.-K., Cheng, C.-Y., Lin, Y.-C., Chen, K.-S. (2012). Emission reductions of air pollutants from a heavy-duty diesel engine mixed with various amounts of H_2/O_2. *Aerosol and Air Quality Research,* 12, 133-140. https://doi.org/10.4209/aaqr.2011.08.0122

Chiavola, O., Flattini, E., Lancione, S., Palmieri, F. (2021). Operation cycle of Diesel CR Injection Pump via Pressure Measurement in Piston Working Chamber. *Energies,* 14, 5385. https://doi.org/10.3390/en14175385

Cueva, M., Valle, S., Cevallos, A., Ormaza, J., Calvopina, H., Montero, F. (2025). Analysis of emissions and fuel consumption of a truck using a mixture of diesel and cerium oxide on high-altitude roads. *Vehicles,* 7, 85. https://doi.org/10.3390/vehicles7030085

Costagliola, M.A., Marchitto, L., Piras, M., Berra, A. (2025). Effect of Performance Packages on Fuel Consumption Optimization in Heavy-Duty Diesel Vehicles: A Real-World Fleet Monitoring Study. *Energies,* 18, 5542. https://doi.org/10.3390/en18205542

The 11th International Congress
Motor Vehicles & Motors 2026
Kragujevac, Serbia
October 8th-9th, 2026

Motor Vehicles & Motors

MVM2026-015
https://doi.org/10.24874/CMVM2026.015
Original scientific paper

Milan Eremija[1]
Zoran Ristikić[2]
Svetko Milutinović[3]
Mesud Ajanović[4]

EXPERIMENTAL INVESTIGATION OF THE INFLUENCE OF TIRE PRESSURE ON THE ROLLING RESISTANCE COEFFICIENT OF COMMERCIAL VEHICLES

ABSTRACT: This paper presents experimental investigations of the influence of tire pressure on the rolling resistance coefficient in commercial vehicles, with the aim of analysing vehicle operating characteristics under different operating conditions. The experimental investigations were conducted in a vehicle testing laboratory equipped with a chassis dynamometer. Measurements on the chassis dynamometer were performed using the "coastdown" testing method. The testing procedure included accelerating the vehicle to a speed of 40 m/s (144 km/h), after which, with the gearshift lever in the neutral position, the free deceleration method was applied. During the deceleration process, the vehicle speed variation was measured within the range from 104.6 km/h to 8.1 km/h, in order to determine parameters relevant for the analysis of motion resistance and the rolling resistance coefficient. Analysis of the results obtained from the conducted experimental investigations indicated that maintaining a constant rolling resistance coefficient under varying vehicle load conditions requires appropriate adjustment of tire pressures on both the front and rear axles. The obtained results confirm the significant influence of proper tire pressure regulation on the stability of vehicle operating characteristics, energy efficiency, and reduction of motion resistance.

KEYWORDS: commercial vehicle, tires, tire pressure, vehicle load, rolling resistance coefficient.

[1]*Milan Eremija, Senior Assistant, University of East Sarajevo, Faculty of Transport and Traffic Engineering, milan.eremija@sf.ues.rs.ba, https://orcid.org/0009-0000-1551-1231*
[2]*Zoran Ristikić, Assistent professor, University of East Sarajevo, Faculty of Transport and Traffic Engineering, zoran.ristikic@sf.ues.rs.ba,*
[3]*Svetko Milutinovic, Assistant, University of East Sarajevo, Faculty of Transport and Traffic Engineering, svetko.milutinovic@sf.ues.rs.ba,*
[4]*Mesud Ajanović, Full professor, University of East Sarajevo, Faculty of Transport and Traffic Engineering, mesud.ajanovic@sf.ues.rs.ba*

EKSPERIMENTALNA ISTRAŽIVANJA UTICAJA PRITISKA U PNEUMATICIMA NA KOEFICIJENT OTPORA KOTRLJANJA KOD PRIVREDNIH VOZILA

REZIME: U radu su predstavljena eksperimentalna istraživanja uticaja pritiska u pneumaticima na koeficijent otpora kotrljanja kod privrednih vozila, sa ciljem analize eksploatacionih karakteristika vozila u različitim uslovima rada. Eksperimentalna istraživanja su sprovedena u laboratoriji namjenjenoj za ispitivanje vozila opremljenom šasijskim dinamometrom. Mjerenja na šasijskom dinamometru realizovana su primjenom „coastdown“ metode ispitivanja. Postupak ispitivanja obuhvatao je ubrzavanje vozila do brzine od 40 m/s (144 km/h), nakon čega je, pri neutralnom položaju ručice mjenjača, primijenjena metoda slobodnog usporavanja vozila. Tokom procesa usporavanja vršeno je mjerenje promjene brzine vozila u opsegu od 104,6 km/h do 8,1 km/h, sa ciljem određivanja parametara relevantnih za analizu otpora kretanja i koeficijenta otpora kotrljanja. Analizom rezultata dobijenih nakon sprovedenih eksperimentalnih istraživanja utvrđeno je da održavanje konstantne vrijednosti koeficijenta otpora kotrljanja pri promjeni opterećenja vozila zahtijeva odgovarajuću promjenu pritiska u pneumaticima prednje i zadnje osovine. Dobijeni rezultati ukazuju na značajan uticaj pravilne regulacije pritiska u pneumaticima na stabilnost eksploatacionih karakteristika vozila, energetsku efikasnost i smanjenje otpora kretanja.

KLJUČNE REČI: privredno vozilo, pneumatici, pritisak u pneumaticima, opterećenje, koeficijent otpora kotrljanja.

INTRODUCTION

Under real-world operating conditions, a motor vehicle predominantly travels under non-uniform motion. The motion of the vehicle is opposed by various resistive forces that must be overcome by the vehicle’s powertrain. The resistances to motion include rolling resistance, aerodynamic drag, grade resistance, acceleration (inertial) resistance, and the resistance associated with a towed vehicle. Vehicle performance is determined not only by the maximum engine torque or maximum engine power, but also by the vehicle’s behaviour under partial and full load conditions and at different engine operating regimes.

Rolling resistance arises as a consequence of the continuous deformation of the tyres during rolling contact with the road surface. Its magnitude is affected by tyre characteristics, tyre inflation pressure, vehicle mass, road surface condition, vehicle speed, and tyre geometry and temperature. Incorrect tyre inflation pressure may adversely affect driving safety, ride comfort, and tyre service life, while also increasing fuel consumption and contributing to adverse environmental impacts (Clark & Schuring, 1988; Pillai & Fielding-Russell, 1992; Pillai, 2004; Świeczko-Żurek et al. 2017).

Commercial vehicles are, by virtue of their intended use, subjected to frequent variations in load. Consequently, the tyre inflation pressure appropriate for an unloaded vehicle may not be suitable when the vehicle is loaded. The primary objective of this study was to experimentally determine the functional relationship between vehicle load, tyre inflation pressure, and the rolling resistance coefficient, with particular emphasis on assessing the possibility of maintaining a constant rolling resistance coefficient by adjusting the tyre inflation pressures on the front and rear axles. The topic remains relevant in current regulatory and testing practice. UN Regulation No. 117 continues to regulate tyre rolling resistance and specifies test conditions related to tyre load and inflation pressure, while SAE J2263:2020 and SAE J2264:2023 provide current coastdown-based procedures for road-load determination and chassis-dynamometer road-load simulation, respectively.

ROLLING RESISTANCE AND THE EFFECT OF TYRE INFLATION PRESSURE

Tyres represent the only vehicle components that are in direct contact with the road surface. In addition to safety and ride comfort requirements, tyres have a significant impact on the energy efficiency of a vehicle. Reducing the rolling resistance coefficient decreases tyre deformation and heat generation, while simultaneously reducing fuel consumption and harmful emissions.

The rolling resistance of tyres decreases with increasing inflation pressure on a level road surface, while all other parameters remain constant. As the inflation pressure increases, the vertical deflection and deformation of the tyre decrease, thereby reducing hysteresis losses. On the other hand, variations in vehicle load increase the radial deformation of the tyre sidewall and may increase rolling resistance. In the present investigation, a constant static

tyre radius was used as a practical indicator of approximately constant vertical tyre deflection; however, this assumption does not imply that the contact-patch area, its shape, or the contact-pressure distribution remain strictly constant as load and inflation pressure change (Pillai, 2004; Kühlwein, 2016; Wang et al., 2020).

TEST VEHICLE AND EXPERIMENTAL EQUIPMENT

The experimental investigations were conducted using a Volkswagen light commercial vehicle of category N1, model 7J0 Transporter. The vehicle has a gross vehicle mass of 3000 kg, a curb mass of 1898 kg, and a payload capacity of 1102 kg. It is equipped with six seats and a diesel engine. New Viking WinTech Van 215/65 R16 C 109/107 R tyres were fitted to both the front and rear axles.

The laboratory investigations were conducted at the Technical Laboratory Centre of the Faculty of Transport and Traffic Engineering in Doboj using an AVL Roadsim Chassis Dyno 48″ 4WD MiM chassis dynamometer. This dynamometer belongs to the class of active dynamometers and enables testing of vehicles equipped with front-wheel drive, rear-wheel drive, and all-wheel drive systems. The dynamometer is designed to simulate road load under different vehicle speeds and enables the measurement of vehicle speed, acceleration, tractive force, power, and parameters relevant to the determination of rolling resistance.

Figure 1 Test vehicle positioned on the chassis dynamometer rollers

Prior to the commencement of testing, the dynamometer was warmed up by operating at no load for one hour. The wheelbase of the test vehicle was 3400 mm; therefore, the roller spacing of the dynamometer was adjusted accordingly. The vehicle was subsequently centred and securely restrained. At the rear, the vehicle was secured using the original tow hitch, while at the front it was secured at the designated attachment point for forced towing. The lateral restraints equipped with sensors were used to automatically stop the rollers in the event of lateral displacement of the vehicle.

Tyre inflation pressure was checked using a calibrated pressure gauge, while the ambient temperature in the laboratory during the initial testing was 16.5 °C. The static radius of the unloaded tyre was measured using a height gauge and was found to be 329.2 mm. Eight identical coastdown measurements were performed for each defined test condition. The resulting datasets were processed using the dynamometer software and the mean values were used for further analysis. The repeated measurements were used to assess and reduce the influence of random variation between individual coastdown runs. A complete metrological uncertainty budget was not established in the original experimental programme; therefore, the reported results should be interpreted as repeatability-controlled comparative measurements rather than as a certification measurement of tyre rolling resistance. The principal controlled quantities were tyre pressure, vehicle load, initial tyre condition, test procedure, dynamometer warm-up and laboratory temperature.

METHODOLOGY OF THE EXPERIMENTAL INVESTIGATION

The testing was conducted in two main measurement groups. In the first group, the tyre inflation pressures were kept constant at 3.3 bar on the front axle and 2.9 bar on the rear axle. The vehicle was tested in the unloaded condition and subsequently with additional loads of 200, 400, 600, 800, and 1000 kg. In the second test group, at the same load levels, the tyre inflation pressures were progressively increased with the aim of maintaining a constant static tyre radius of 329.2 mm. In this work, the constant static radius was treated as an experimental constraint intended to keep the vertical tyre deflection approximately unchanged; it was not assumed to guarantee an exactly constant contact-patch area. For the unloaded vehicle, the tyre inflation pressures of 3.3 bar on the front axle and 2.9 bar on

the rear axle were verified. The measured static tyre radius was 329.2 mm. The vehicle was then accelerated to a speed of 40 m/s (144 km/h), after which the transmission selector was shifted into neutral and the vehicle was allowed to decelerate under the action of motion resistances. To improve repeatability, eight identical coastdown tests were performed for each test condition. During free deceleration, the vehicle speed was recorded over the range from 104.6 km/h to 8.1 km/h.

The coastdown measurement records were used to obtain the parameters F_0, F_1, and F_2 employed by the AVL system to describe the effective resistance force as a function of speed under the defined chassis-dynamometer test condition. These parameters are road-load model coefficients and must not be interpreted as tyre rolling-resistance coefficients by themselves. Their use in the present study, including the separation and interpretation of the resistance component attributed to rolling-related losses, is clarified in Section 4.1.

Methodology for Calculating the Rolling Resistance Coefficient

Based on the coastdown test, the AVL chassis-dynamometer software determines the parameters F_0, F_1, and F_2 that approximate the measured resistance force as a function of vehicle speed. In a conventional on-road coastdown test, the resulting road-load polynomial represents the combined road-load force and generally contains rolling, aerodynamic, and other mechanical resistance components (SAE J2263:2020). In the present chassis-dynamometer experiment, the vehicle body is stationary relative to the laboratory air; therefore, the aerodynamic drag associated with the vehicle moving through ambient air at road speed is not physically present in the same manner as in an on-road coastdown test. The AVL adaptation procedure also accounts for dynamometer-related losses. Consequently, the remaining resistance component used in this study predominantly reflects tyre–roller rolling losses together with residual mechanical losses of the drivetrain and rotating components. For this reason, R_k and f_k reported in this paper are interpreted as effective rolling-resistance-related quantities of the complete vehicle under the specified chassis-dynamometer conditions, and not as a standardized tyre-only rolling resistance coefficient obtained according to UN Regulation No. 117 or an ISO/SAE tyre drum test. SAE J2264:2023 provides the current recommended practice for chassis-dynamometer road-load simulation using coastdown techniques.

$$f_k = \frac{R_k}{G}$$

where G denotes the vehicle weight for the respective test condition and R_k denotes the effective rolling-resistance-related force determined from the chassis-dynamometer coastdown model for the selected speed interval. As an example, for the vehicle loaded with an additional mass of 1000 kg, with tyre inflation pressures of 3.3 bar on the front axle and 2.9 bar on the rear axle, the AVL vehicle-related coefficients used in the calculation were F_0 = 276.251, F_1 = 1.4257, and F_2 = 0.005357. The calculated values for the characteristic speed intervals are presented in the following table.

Table 1 Example of the Calculation of Rolling Resistance and the Rolling Resistance Coefficient for an Additional Load of 1000 kg

Speed v [m/s]	Rolling resistance force R_k [N]	Rolling resistance coefficient f_k
5	283,513	0,015131
10	291,044	0,015533
15	298,842	0,015949
20	306,908	0,016380
25	315,242	0,016824
30	323,843	0,017284
35	332,713	0,017757
40	341,850	0,018245
Mean value	311,744	0,016638

Repeatability, Measurement Uncertainty and Static-Radius Assumption

For each test condition, eight coastdown runs were performed using the same test procedure. The mean values were used in subsequent calculations in order to limit the influence of random run-to-run deviations. Because the original experimental programme was not designed as a metrological certification study, expanded measurement uncertainty was not calculated from a complete uncertainty budget. Accordingly, the numerical results are primarily used for comparative analysis between load and inflation-pressure conditions. The constant static radius of 329.2 mm was adopted as a repeatable geometric control parameter representing approximately constant vertical tyre deflection. It should not be interpreted as proof of an exactly constant contact-patch area or contact-pressure distribution, which may change with load and inflation pressure.

Table 2 Tyre Inflation Pressures Used to Maintain a Constant Static Tyre Radius of 329.2 mm

Additional load [kg]	Front axle [bar]	Rear axle [bar]
0	3,3	2,9
200	3,4	3,4
400	3,6	3,9
600	3,8	4,3
800	4,1	4,6
1000	4,5	4,8

ANALYSIS OF THE RESEARCH RESULTS

Variation in Vehicle Load at Constant Tyre Inflation Pressure

The measurement results obtained at constant tyre inflation pressure showed that the rolling resistance coefficient increases with increasing vehicle speed, as well as with increasing vehicle load. For all investigated load levels, the dependence of the rolling resistance coefficient on vehicle speed within the tested range can be approximated with a high degree of accuracy by a linear function.

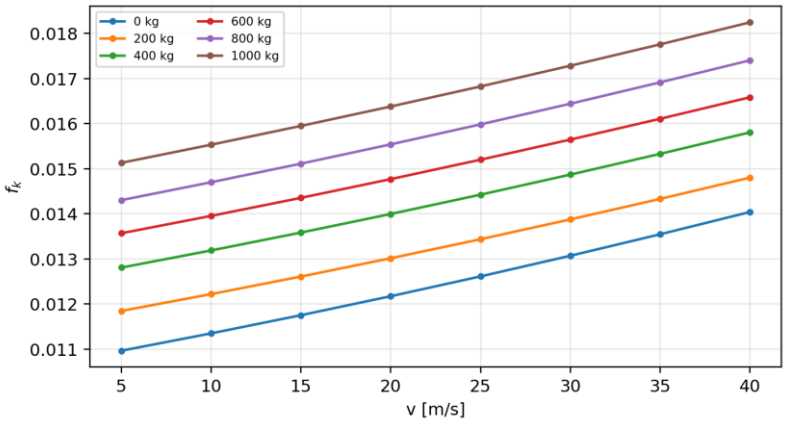

Figure 2 Approximated dependence of the rolling resistance coefficient on vehicle load variation at constant tyre inflation pressure (front axle: 3.3 bar; rear axle: 2.9 bar)

The aforementioned relationship demonstrates that the laboratory investigation confirmed the assumption of a linear functional dependence of the rolling resistance coefficient on changes in vehicle load under constant tyre inflation pressure.

Variation in Vehicle Load with Tyre Inflation Pressure Adjustment

In the second group of measurements, the tyre inflation pressure was increased with increasing vehicle load in order to maintain a constant static tyre radius of 329.2 mm. At an additional load of 200 kg, the tyre inflation pressure was 3.4 bar on both axles, whereas at an additional load of 1000 kg, it was 4.5 bar on the front axle and 4.8 bar on the rear axle.

The measurements showed that, despite maintaining a constant static tyre radius, the effective rolling-resistance-related coefficient increased with increasing total vehicle weight. This behaviour is consistent with increasing radial sidewall deformation and internal hysteresis losses as load increases. Nevertheless, tyre inflation pressure adjustment reduced the increase compared with the test condition in which the inflation pressure remained constant. Because the static radius was used only as a geometric control parameter, the results do not imply that the tyre contact patch remained exactly unchanged.

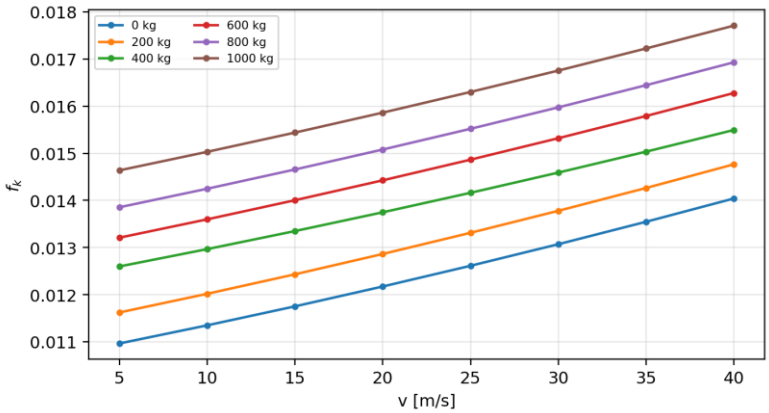

Figure 3 Variation of the rolling resistance coefficient as a function of vehicle speed and load variation in order to maintain a constant static tyre radius (r_s = 329.2 mm)

Table 3 Mean Values of the Rolling Resistance Coefficient at Varying Tyre Inflation Pressure and Constant Static Tyre Radius

Additional load [kg]	Mean value of f_k
0	0.012474
200	0.013133
400	0.013993
600	0.014686
800	0.015338
1000	0.016119

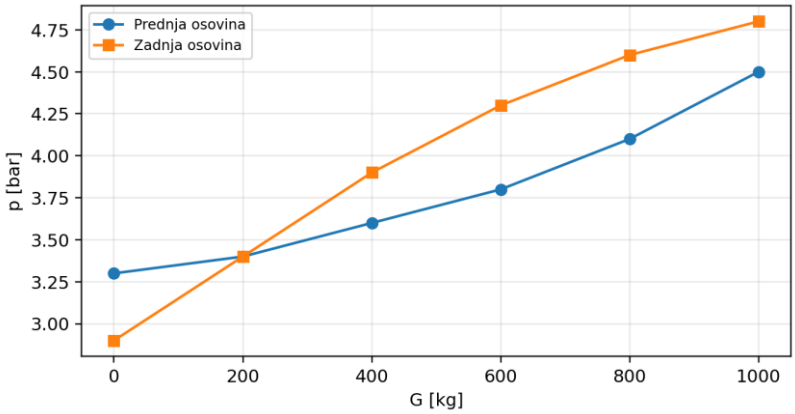

Figure 4 Approximated relationship between tyre inflation pressure on the front and rear axles and vehicle load variation in order to maintain a constant static tyre radius

A direct comparison of the two measurement groups shows that adjusting the tyre inflation pressure to maintain a constant static tyre radius mitigates the increase in the rolling resistance coefficient. The effect of pressure adjustment becomes more pronounced as the vehicle load increases; however, the rolling resistance coefficient does not return to the value corresponding to the unloaded vehicle.

Table 4 Comparative Mean Values of the Rolling Resistance Coefficient for the Two Test Conditions

Additional load [kg]	Constant tyre inflation pressure f_k	Tyre inflation pressure adjustmentf_k	Reduction [%]
0	0,012474	0,012474	0,00
200	0,013269	0,013133	1,02
400	0,014252	0,013993	1,82
600	0,015024	0,014686	2,25
800	0,015800	0,015338	2,92
1000	0,016638	0,016119	3,12

Tyre Inflation Pressure Required to Maintain a Constant Rolling Resistance Coefficient

Since maintaining a constant static tyre radius was not sufficient to keep the rolling resistance coefficient constant, the obtained functions were approximated. Based on the resulting mathematical relationships, the tyre inflation pressures for the front and rear axles were calculated for different vehicle load levels, with the aim of maintaining an approximately constant value of the rolling resistance coefficient.

Table 5 Calculated Tyre Inflation Pressure Values Required to Maintain a Constant Rolling Resistance Coefficient

Additional load [kg]	Front axle [bar]	Rear axle [bar]
0	3.300	2.900
200	3.368	3.491
400	3.435	4.082
600	3.502	4.673
800	3.570	5.264
1000	3.638	5.855

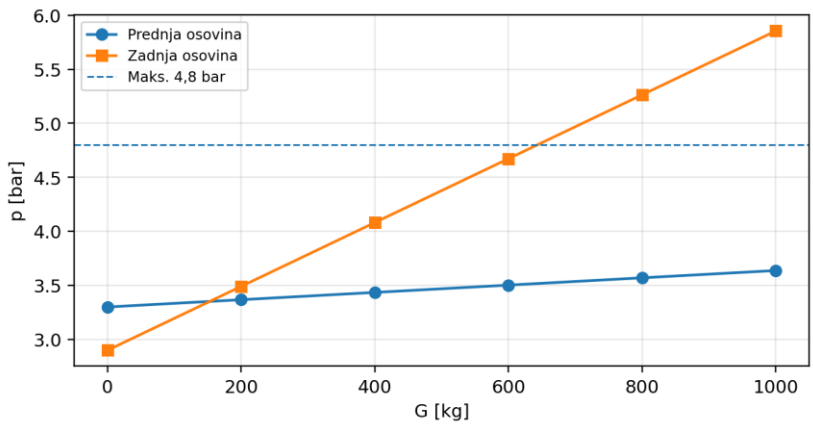

Figure 5 Approximated relationship between tyre inflation pressure on the front and rear axles and vehicle load variation in order to maintain a constant rolling resistance coefficient

The obtained values indicate a practical limitation to the application of such a pressure regulation strategy. The tyres fitted to the test vehicle have a maximum permissible inflation pressure of 70 psi, corresponding to approximately 4.8 bar. For additional loads exceeding 600 kg, the calculated tyre inflation pressure for the rear axle exceeds this limit, whereas the inflation pressures for the front axle remain below the permissible value. Therefore, at higher load levels, particular attention must be paid to the selection of tyres with appropriate structural characteristics and a suitable permissible inflation pressure. It is particularly important to note that the mathematically determined inflation pressure required to maintain a constant rolling resistance coefficient does not automatically constitute a technically permissible value. For the rear axle, the calculated inflation pressure was 5.264 bar at an additional load of 800 kg and 5.855 bar at an additional load of 1000 kg, both of which exceed the maximum permissible pressure of approximately 4.8 bar for the tyres used in the test. Consequently, the established functional relationship must be interpreted in conjunction with the load-carrying capacity, structural characteristics, and permissible inflation pressure of the specific tyre.

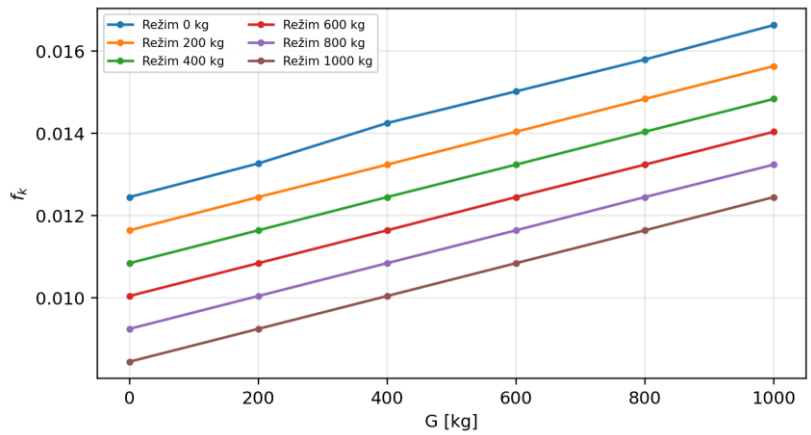

Figure 6 Approximated relationship between the rolling resistance coefficient, tyre inflation pressure, and vehicle load, with the aim of maintaining a constant rolling resistance coefficient under laboratory test conditions

DISCUSSION OF THE RESEARCH RESULTS

The results of the laboratory investigation demonstrate that vehicle load and tyre inflation pressure are interrelated parameters that cannot be considered independently when analysing the rolling resistance of a commercial vehicle. At constant tyre inflation pressure, an increase in the additional load from 0 to 1000 kg resulted in an increase in the mean rolling resistance coefficient from 0.01247 to 0.01664. When the tyre inflation pressure was adjusted with the aim of maintaining a constant static tyre radius, the mean rolling resistance coefficient at an additional load of 1000 kg was 0.01612. Thus, the increase in rolling resistance was mitigated, but not completely eliminated. A comparison of the mean values shows that, at an additional load of 1000 kg, pressure adjustment while maintaining a constant static tyre radius reduced the rolling resistance coefficient from 0.016638 to 0.016119, corresponding to a reduction of approximately 3.1% compared with the constant-pressure condition. This result demonstrates that tyre inflation pressure adjustment has a measurable effect, while simultaneously confirming that maintaining a constant static tyre radius from a geometrical perspective is insufficient to completely eliminate the effect of the increased vehicle mass.

The observed trends are consistent with the findings reported by Clark and Schuring (1988) and Pillai (2004), according to which vehicle load and tyre inflation pressure are major factors affecting rolling losses. More recent studies support the continued relevance of these parameters. Wang et al. (2020) showed that tyre load and inflation pressure alter both contact stresses and rolling resistance in truck/bus tyres, while Zhu and Yan (2023) experimentally investigated the combined effects of speed, inflation pressure, load and temperature on heavy-duty tyre rolling resistance. Ejsmont et al. (2024) further emphasized that rolling-resistance results depend strongly on the measurement method and test surface. The present results complement these studies by describing the response of a complete light commercial vehicle under controlled load variations on a chassis dynamometer. The findings also support the interpretation that static tyre radius alone cannot fully characterize rolling losses because internal deformation, hysteresis, load distribution and tyre–roller interaction remain relevant.

From a practical perspective, the results confirm the need to adjust tyre inflation pressure in commercial vehicles according to the actual vehicle load, but strictly within the limits specified by the tyre and vehicle manufacturers. Increasing the inflation pressure beyond the permissible value solely to reduce rolling resistance is unacceptable. When a particular load condition requires an inflation pressure exceeding the permissible limit, the appropriate solution should be sought through the selection of tyres with a higher load-carrying capacity or with different structural characteristics.

CONCLUSION

Based on the laboratory investigations conducted on the AVL Roadsim Chassis Dyno 48″ 4WD MiM chassis dynamometer, it can be concluded that tyre inflation pressure has a significant effect on the effective rolling-resistance-related coefficient of the tested light commercial vehicle under the specified laboratory conditions. The coastdown testing method enabled the determination of speed-dependent resistance parameters and comparative analysis at different vehicle speeds, load levels and tyre inflation pressures. At constant tyre inflation pressures of 3.3 bar on the front axle and 2.9 bar on the rear axle, a nearly linear relationship was obtained between the calculated effective coefficient and additional vehicle load. The results should be interpreted as complete-vehicle chassis-dynamometer measurements rather than as standardized tyre-only rolling resistance values.

Adjustment of tyre inflation pressure with the aim of maintaining a constant static tyre radius reduced the increase in the rolling resistance coefficient; however, a constant value of the coefficient could not be achieved. This was primarily attributed to the additional radial deformation of the tyre sidewalls resulting from the increase in vehicle load. Approximation of the obtained functions established the functional relationship between the tyre inflation pressures on the front and rear axles and vehicle load required to maintain a constant rolling resistance coefficient. The obtained results indicate that appropriate tyre selection and adjustment of tyre inflation pressure in accordance with vehicle load and the permissible pressure limits can reduce motion resistance, tyre deformation, and heat generation. Consequently, this may contribute to reduced fuel consumption, transportation costs, and harmful emissions, while maintaining the required safety and vehicle handling characteristics.

REFERENCES

Clark, J. D., & Schuring, D. J. (1988). Load, speed and inflation pressure effects on rolling loss distribution in automobile tires. *Tire Science and Technology*, 16(2), 78–95. https://doi.org/10.2346/1.2148800

Ejsmont, J., Ronowski, G., Ydrefors, L., Owczarzak, W., Sommer, S., & Świeczko-Żurek, B. (2024). Comparison of tire rolling resistance measuring methods for different surfaces. *International Journal of Automotive Technology*, 25, 965-976. https://doi.org/10.1007/s12239-024-00092-w

Kühlwein, J. (2016). Driving resistances of light duty vehicles in Europe: Present situation, Trends, and scenarios for 2025. ICCT White Paper. https://theicct.org/wp-content/uploads/2021/06/ICCT_LDV-Driving-Resistances-EU_121516.pdf

Pillai, P. S. (2004). Effect of tyre overload and inflation pressure on rolling loss (resistance) and fuel consumption of automobile and truck/bus tyres. *Indian Journal of Engineering & Materials Sciences*, 11, 406–412.

Pillai, P. S., & Fielding-Russell, G. S. (1992). Tire rolling resistance from whole-tire hysteresis ratio. *Rubber Chemistry and Technology*, 65(2), 444–452.

SAE International: Road Load Measurement Using Onboard Anemometry and Coastdown Techniques. SAE Recommended Practice J2263_202005, revised May 2020. https://doi.org/10.4271/J2263_202005

SAE International: Chassis Dynamometer Simulation of Road Load Using Coastdown Techniques. SAE Recommended Practice J2264_202301, revised January 2023. https://doi.org/10.4271/J2264_202301

Świeczko-Żurek, B., Ronowski, G., & Ejsmon, J. (2017). Tyre rolling resistance and its influence on fuel consumption. *Combustion Engines*, 168(1), 62–67. https://doi.org/10.19206/CE-2017-110

United Nations Economic Commission for Europe (UNECE): UN Regulation No. 117 - Tyres, Rolling Resistance, Rolling Noise and Wet Grip, Revision 6, Amendment 2, 2025.

Wang, H., Al-Qadi, I. L., & Stanciulescu, I. (2020). Analysis of contact stresses and rolling resistance of truck-bus tyres under different working conditions. *Sustainability*, 12(24), 10603. https://doi.org/10.3390/su122410603

Zhu, C., & Yan, J. (2023). Experimental investigation on rolling resistance and temperature of the heavy-duty vehicle tires. *SAE Technical Paper*, 2023-01-0754. https://doi.org/10.4271/2023-01-0754

The 11th International Congress
Motor Vehicles & Motors 2026
Kragujevac, Serbia
October 8th - 9th, 2026

Motor Vehicles & Motors

MVM2026-025
https://doi.org/10.24874/CMVM2026.025
Original scientific paper

Marko Lučić[1]
Mirjana Grdinić-Rakonjac[2]
Radoje Vujadinović[3]
Vladimir Pajković[4]
Ivan Grujić[5]

ENERGY USE IN MONTENEGRO'S ROAD TRANSPORT SECTOR: TRENDS, FUEL STRUCTURE AND DEPENDENCE ON PETROLEUM-BASED FUELS

ABSTRACT: Road transport represents one of the most important sectors of energy use in Montenegro, with a strong dependence on petroleum-based fuels. This paper provides a descriptive analysis of energy use in Montenegro's road transport sector, with special attention to fuel structure and consumption trends. The analysis uses official statistical data for the period 2014–2024 and examines the consumption of diesel fuel, gasoline, liquefied petroleum gas and electricity in road transport. It focuses on the dominant fuel types, shifts in consumption patterns and the extent to which road transport continues to rely on conventional petroleum-based fuels. The results indicate that diesel fuel has the leading role in road transport energy consumption, while gasoline has a lower but still relevant share and liquefied petroleum gas remains marginal. The observed trends confirm that Montenegro's road transport sector is still characterized by a high dependence on petroleum-based fuels, with limited diversification of final energy use away from petroleum-based fuels.

KEYWORDS: road transport, energy use, fuel consumption, petroleum-based fuels, Montenegro

[1] *Marko Lučić, University of Montenegro, Faculty of Mechanical Engineering, Džordža Vašingtona bb, 81000 Podgorica, markol@ucg.ac.me, https://orcid.org/0009-0004-9978-5967*
[2] *Mirjana Grdinić-Rakonjac, University of Montenegro, Faculty of Mechanical Engineering, Džordža Vašingtona bb, 81000 Podgorica, grdinicm@ucg.ac.me, https://orcid.org/0000-0003-3497-7744*
[3] *Radoje Vujadinović, University of Montenegro, Faculty of Mechanical Engineering, Džordža Vašingtona bb, 81000 Podgorica, radojev@ucg.ac.me, https://orcid.org/0000-0002-4356-0556*
[4] *Vladimir Pajković, University of Montenegro, Faculty of Mechanical Engineering, Džordža Vašingtona bb, 81000 Podgorica, pajkovic@ucg.ac.me, https://orcid.org/0000-0003-2252-5070*
[5] *Ivan Grujić, University of Kragujevac, Faculty of Engineering, Sestre Janjić 6, 34000 Kragujevac, Serbia, ivan.grujic@kg.ac.rs, https://orcid.org/0000-0003-0572-1205*

POTROŠNJA ENERGIJE U SEKTORU DRUMSKOG SAOBRAĆAJA CRNE GORE: TRENDOVI, STRUKTURA GORIVA I ZAVISNOST OD NAFTNIH GORIVA

REZIME: Drumski saobraćaj predstavlja jedan od najznačajnijih sektora potrošnje energije u Crnoj Gori, uz izraženu zavisnost od naftnih goriva. U ovom radu data je deskriptivna analiza potrošnje energije u sektoru drumskog saobraćaja Crne Gore, sa posebnim osvrtom na strukturu goriva i trendove potrošnje. Analiza je zasnovana na zvaničnim statističkim podacima za period 2014–2024. godine i obuhvata potrošnju dizel goriva, benzina, tečnog naftnog gasa i električne energije u drumskom saobraćaju. Osnovni cilj rada je identifikovanje dominantnih vrsta goriva, promjena u obrascima potrošnje i stepena zavisnosti drumskog saobraćaja od konvencionalnih naftnih goriva. Rezultati ukazuju da dizel gorivo ima vodeću ulogu u ukupnoj potrošnji energije u drumskom saobraćaju, dok benzin ima manji, ali i dalje značajan udio, a tečni naftni gas marginalnu ulogu. Uočeni trendovi potvrđuju da sektor drumskog saobraćaja Crne Gore i dalje karakteriše visok stepen zavisnosti od naftnih goriva, uz ograničene strukturne promjene u finalnoj potrošnji energije.

KLJUČNE REČI: drumski saobraćaj, potrošnja energije, potrošnja goriva, naftna goriva, Crna Gora

INTRODUCTION

Transport represents one of the key sectors of final energy consumption and plays an essential role in economic activity, mobility, tourism and the movement of goods. At the same time, it remains highly dependent on petroleum-based fuels, particularly in road transport. Road transport accounts for the dominant part of domestic transport energy demand, making it one of the most important sectors for analysing energy consumption, fuel structure and opportunities for improving energy efficiency (European Environment Agency, 2025). This dependence also makes transport one of the more challenging sectors in the broader energy transition, as mobility systems continue to rely heavily on fossil fuels and conventional vehicle technologies (Intergovernmental Panel on Climate Change, 2023).

This pattern is also evident at the European level. Road transport is the largest consumer of final energy within the transport sector, while diesel fuel and gasoline remain the dominant energy sources (Eurostat, 2026). Although the use of electricity, biofuels and other alternative energy sources has increased in recent years, conventional petroleum-based fuels still have a leading role in aggregate road transport energy consumption. The structure and evolution of road transport fuel consumption are therefore particularly relevant in countries where the transition towards alternative energy sources in transport is still at an early stage.

The transition towards sustainable mobility has become a central element of transport and climate policy, particularly in Europe. The European Commission's Sustainable and Smart Mobility Strategy defines the transformation of the transport system as one of the key elements of the broader transition towards a more sustainable, smart and resilient mobility system (European Commission, 2020). However, achieving sustainable mobility requires more than the introduction of new, cleaner vehicle technologies. It also involves changes in transport planning, travel behaviour, land use and policy frameworks (Banister, 2008). The transition is further complicated by increasing mobility demand, long vehicle lifetimes and the continued dominance of fossil fuels, making transport one of the more challenging sectors to decarbonise (Creutzig et al. 2015). In this context, examining the consumption of diesel fuel, gasoline, liquefied petroleum gas and electricity can provide insight into current fuel-use patterns and the extent to which conventional energy sources continue to dominate.

A significant part of previous research has focused on the determinants of transport energy demand. Liddle and Huntington (2020) analysed gasoline and diesel demand using a large international panel of countries and demonstrated the importance of economic activity, fuel prices and structural characteristics of the transport sector. Achour and Belloumi (2016) applied decomposition analysis to the transport sector and identified economic output, transport intensity, population and energy intensity as important drivers of energy use. Tsemekidi Tzeiranaki et al. (2023) analysed historical energy consumption trends in the European road transport sector and highlighted the influence of vehicle fleet characteristics, transport activity, fuel prices and energy efficiency policies.

These studies indicate that road transport energy demand reflects a combination of technological, economic and structural factors. However, a clear picture of how energy use itself has evolved over time remains an important starting point, particularly before applying more complex modelling, forecasting or decomposition methods. This is especially relevant for smaller national transport systems, where aggregate consumption data can provide a direct insight into the level of dependence on conventional fuels and the extent of structural change over time.

This perspective is particularly relevant to Montenegro, where road mobility and freight transport continue to rely mainly on conventional petroleum-based fuels. Although sustainable mobility, electric vehicles and alternative fuels have become increasingly prominent in policy discussions, the evolution and composition of final energy consumption in Montenegrin road transport have received limited attention from a simple statistical perspective. For this reason, a descriptive analysis of energy use trends can provide a useful basis for understanding the main consumption patterns and the current position of petroleum-based fuels in the road transport sector.

The aim of this paper is to examine the evolution of energy use in Montenegro's road transport sector over the 2014–2024 period, focusing on fuel structure, changes in consumption and the sector's continued dependence on petroleum-based fuels. The analysis covers diesel fuel, gasoline, liquefied petroleum gas and electricity, which represent the energy sources included in the available road transport energy statistics. Rather than applying modelling, forecasting or emission calculation methods, the study provides a descriptive statistical overview of observed energy consumption patterns and their changes over time, thereby establishing a factual basis for understanding the current energy structure of road transport in Montenegro.

DATA AND METHODOLOGICAL APPROACH

Data sources

The analysis is based on official statistical data published by the Statistical Office of Montenegro. Data on diesel fuel, gasoline and liquefied petroleum gas consumption were taken from the official balance of oil products, while data on electricity use in road transport were taken from the electricity balance (Statistical Office of Montenegro, 2026a, 2026b). The analysis covers the period from 2014 to 2024, comprising eleven annual observations and representing the most recent period for which comparable official data on road transport energy use by energy source were available at the time of the study. The analysis considers four energy sources: diesel fuel, gasoline, liquefied petroleum gas and electricity.

Diesel fuel, gasoline and liquefied petroleum gas are classified as conventional petroleum-based fuels, while electricity is included in order to provide a more comprehensive overview of final energy use in road transport. Given the continued dominance of petroleum-based fuels in Montenegro's road transport sector, the analysis places particular emphasis on their consumption and their contribution to overall energy use.

Data preparation and units

The Statistical Office of Montenegro provides data on petroleum product consumption both in physical units and in energy units. In this paper, values expressed in terajoules [TJ] were used in order to ensure direct comparability between different energy sources. The use of TJ is especially important because petroleum-based fuels and electricity are originally expressed in different units, while a common energy unit is necessary for analysing the total structure of final energy use.

For diesel fuel, gasoline and liquefied petroleum gas, the values expressed in TJ were taken directly from the official balance of petroleum products. For electricity, values expressed in TJ were taken from the electricity balance where available. Electricity use in road transport appears only in the final years of the observed period, while earlier years are presented as 0.0 TJ in the comparative tables.

Total road transport energy use was calculated as the sum of all analysed energy sources:

$$E_{total} = E_{diesel} + E_{gasoline} + E_{LPG} + E_{elctricity} \quad (1)$$

$\boldsymbol{E_{total}}$ – total energy use in road transport [TJ];
$\boldsymbol{E_{diesel}}$ – energy use from diesel fuel [TJ];
$\boldsymbol{E_{gasoline}}$ – energy use from gasoline [TJ];
$\boldsymbol{E_{LPG}}$ – energy use from liquefied petroleum gas [TJ];
$\boldsymbol{E_{elctricity}}$ – electricity use in road transport [TJ].

Methodological approach

The paper applies a descriptive statistical approach to examine patterns and changes in road transport energy use over the observed period. The purpose of this approach is to present and interpret the main trends in road transport energy use, without applying modelling, forecasting or emission calculation methods. The analysis relies on actual observed statistical data to describe the evolution of energy use and identify its main structural characteristics.

The methodological procedure included several steps. First, annual data were collected for each of the four energy sources considered in the study. Second, total annual energy use in road transport was calculated for each year. Third, changes in the consumption of each energy source were examined separately over time. Fourth, the share of each energy source in total annual energy use was calculated. Finally, the values recorded in the initial year and the final year of the observed period were compared in order to identify the main changes that occurred over the study period and assess shifts in the relative importance of the different energy sources.

The share of each energy source in total road transport energy use was calculated as follows:

$$S_i = \frac{E_i}{E_{total}} \cdot 100 \tag{2}$$

where:
S_i – share of energy source *i* in total road transport energy use [%];
E_i – annual energy use of the selected energy source *i* [TJ];
E_{total} – total annual energy use in road transport [TJ].

The absolute change between 2014 and 2024 was calculated as:

$$\Delta E_i = E_{i,2024} - E_{i,2014} \tag{3}$$

where:
ΔE_i – absolute change in energy use of energy source *i* [TJ];
$E_{i,2024}$ – energy use of energy source *i* in 2024 [TJ];
$E_{i,2014}$ – energy use of energy source *i* in 2014 [TJ].

The relative change between 2014 and 2024 was calculated as:

$$R_i = \frac{E_{i,2024} - E_{i,2014}}{E_{i,2014}} \cdot 100 \tag{4}$$

where:
R_i – relative change in energy use of energy source *i* [%];
$E_{i,2024}$ – energy use of energy source *i* in 2024 [TJ];
$E_{i,2014}$ – energy use of energy source *i* in 2014 [TJ].

The analysis uses the following indicators: annual energy use by energy source [TJ], total annual energy use in road transport [TJ], share of each energy source in total road transport energy use [%], absolute change between 2014 and 2024 [TJ] and relative change between 2014 and 2024 [%].

This methodological approach enables a clear overview of the development of road transport energy use in Montenegro and provides the basis for assessing the extent to which the sector remains dependent on petroleum-based fuels.

RESULTS AND DISCUSSION

The analysis of road transport energy use in Montenegro covers the period 2014–2024. The results are presented in three stages: total energy use, changes in consumption by energy source and the contribution of each source to overall energy use.

Table 1 Road transport energy use by energy source, 2014–2024

Year	Diesel [TJ]	Gasoline [TJ]	LPG [TJ]	Electricity [TJ]	Total [TJ]
2014	5321.7	1489.3	318.9	0	7129.9
2015	5744.5	1516.1	375.1	0	7635.7
2016	7047.1	1574	389.2	0	9010.3
2017	7820.2	1578.5	389.2	0	9787.9
2018	8601.8	1587.4	393.9	0	10583.1
2019	9054.5	1600.8	393.9	0	11049.2
2020	7892.8	1199.5	323.6	0	9415.9
2021	10173.5	1698.9	403.3	0	12275.7
2022	10378.5	1712.3	398.6	0	12489.4

Table 1 (continuation)

Year	Diesel [TJ]	Gasoline [TJ]	LPG [TJ]	Electricity [TJ]	Total [TJ]
2023	10459.7	1850.5	342.3	0.7	12653.2
2024	11014.9	1970.9	304.8	1.1	13291.7

The analysis includes diesel fuel, gasoline, liquefied petroleum gas and electricity, with all values expressed in terajoules [TJ] to enable direct comparison between different energy sources. The underlying data were obtained from the official energy balances published by the Statistical Office of Montenegro: diesel fuel, gasoline, and liquefied petroleum gas from the petroleum products balance (Statistical Office of Montenegro, 2026a) and electricity from the electricity balance (Statistical Office of Montenegro, 2026b). The annual values for each energy source are presented in Table 1.

Total energy use in road transport

The total energy use in Montenegro's road transport sector increased significantly during the observed period. In 2014, total energy use amounted to 7129.9 TJ, while in 2024 it reached 13291.7 TJ. This represents an increase of 6161.8 TJ, or approximately 86.4%. The lowest total energy use was recorded in 2014, while the highest value was recorded in 2024. Table 1 shows that this growth occurred within a highly concentrated energy structure, with diesel fuel remaining the dominant source throughout the period. Its share increased from approximately 74.6% of total energy use in 2014 to 82.9% in 2024. In contrast, the share of gasoline declined from 20.9% to 14.8%, while LPG decreased from 4.5% to 2.3%. Electricity was recorded only in 2023 and 2024 and accounted for a negligible share of total energy use. The trend of total road transport energy use during the analysed period is presented in Figure 1.

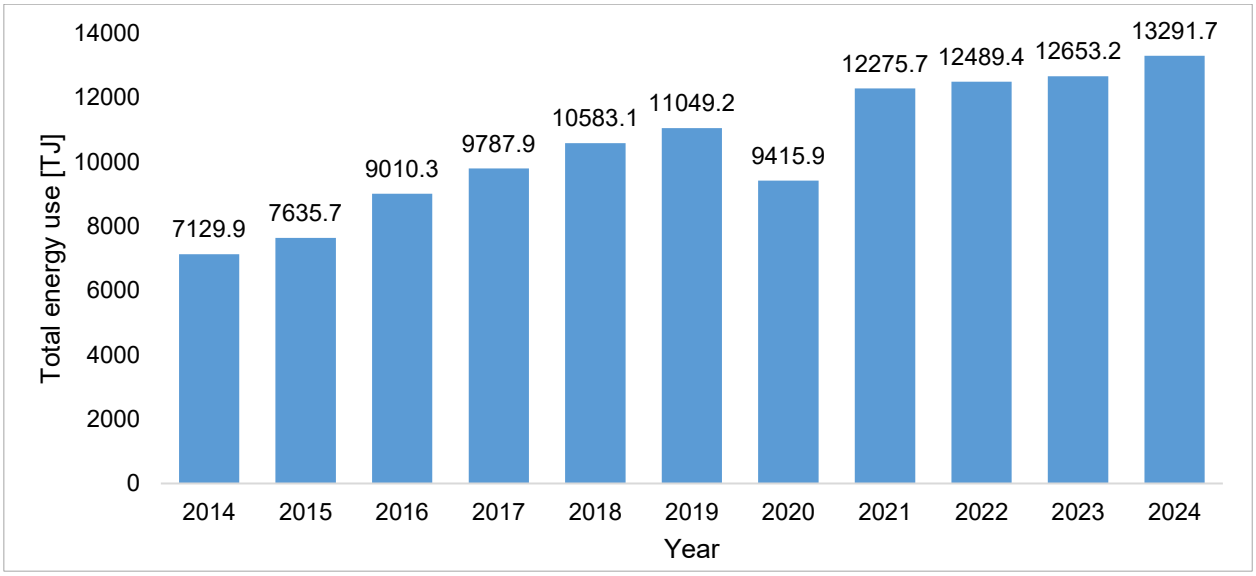

Figure 1 Total energy use in Montenegro's road transport sector, 2014–2024

The general trend therefore reflects both a substantial expansion in energy demand and a strengthening of diesel's predominance. The increase in total energy use was mainly driven by diesel fuel consumption, given its consistently large contribution to the sector. The only notable interruption occurred in 2020, when total consumption decreased from 11049.2 TJ in 2019 to 9415.9 TJ, a decrease of approximately 14.8%. This temporary decline was followed by a strong recovery in 2021, when total energy use increased to 12275.7 TJ, after which the upward trend resumed and culminated in the highest recorded value in 2024. This decline coincided with the COVID-19 pandemic and the associated restrictions on mobility, although the present descriptive analysis does not attempt to quantify the contribution of individual drivers (European Environment Agency, 2025).

These results indicate that, despite discussions on sustainable mobility and alternative energy sources in transport, the aggregate energy demand of road transport in Montenegro remains strongly connected with conventional petroleum-based fuels, with diesel becoming even more prominent over the study period.

Energy use by source

The structure of energy use by source shows that diesel fuel had the dominant role during the entire period. Diesel fuel consumption increased from 5321.7 TJ in 2014 to 11014.9 TJ in 2024. This represents an increase of 5693.2 TJ, or approximately 107.0%. This was the largest absolute increase among the analysed energy sources. Annual energy use by individual energy source is presented in Figure 2.

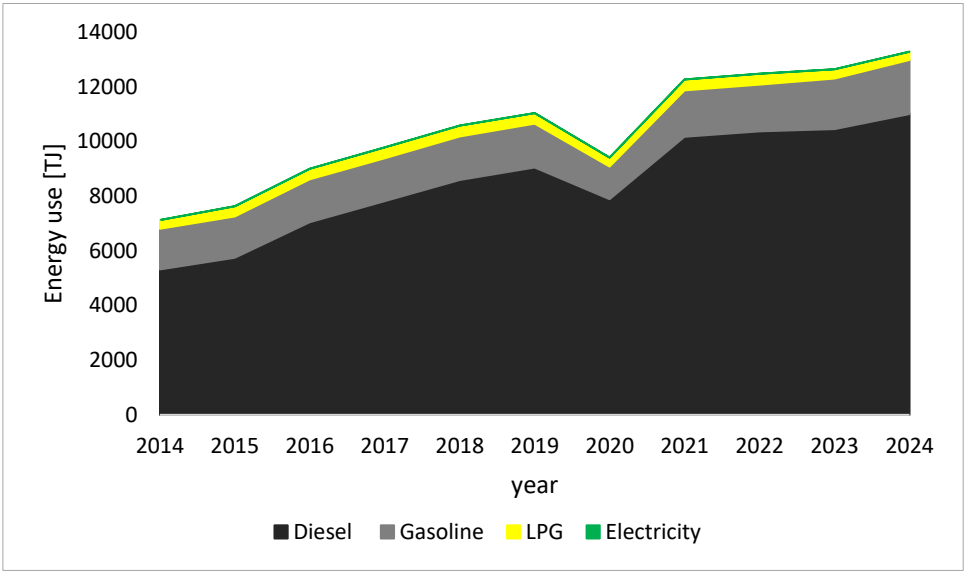

Figure 2 Energy use by source in road transport, 2014–2024

Gasoline was the second most important energy source in road transport. Its consumption increased from 1489.3 TJ in 2014 to 1970.9 TJ in 2024, which represents an increase of 481.6 TJ, or approximately 32.3%. Although gasoline consumption increased in absolute terms, its growth was much weaker than the growth of diesel fuel consumption.

Liquefied petroleum gas had a much smaller role in road transport energy use. LPG consumption decreased from 318.9 TJ in 2014 to 304.8 TJ in 2024, representing a decrease of 14.1 TJ, or approximately 4.4%. Although LPG can be considered an alternative petroleum fuel, its contribution to total road transport energy use remained limited throughout the analysed period.

Electricity appeared in the official data only in the final years of the observed period. Electricity consumption in road transport amounted to 0.7 TJ in 2023 and 1.1 TJ in 2024. Compared with diesel fuel, gasoline and LPG, these values are extremely low. Therefore, electricity is statistically visible, but its contribution to total final energy use in road transport remains negligible.

Fuel structure and dependence on petroleum-based fuels

The analysis of fuel shares provides a clearer insight into the structure of road transport energy use. In 2014, diesel fuel accounted for 74.6% of total energy use in road transport. By 2024, its share increased to 82.9%. This confirms that diesel fuel not only increased in absolute terms, but also became more dominant in the overall fuel structure.

Gasoline had a different trend. Although gasoline consumption increased in absolute terms, its share in total energy use decreased from 20.9% in 2014 to 14.8% in 2024. This shows that gasoline remained a relevant energy source, but its relative importance declined due to the stronger growth of diesel fuel consumption.

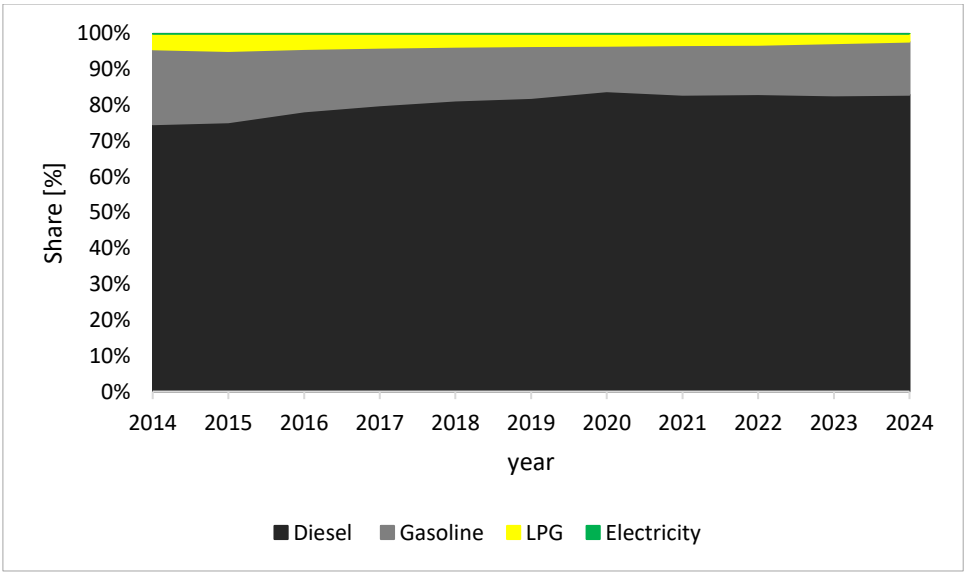

Figure 3 Fuel structure of road transport energy use, 2014–2024

The share of LPG decreased from 4.5% in 2014 to 2.3% in 2024. This confirms the marginal role of LPG and indicates that this fuel did not contribute significantly to the diversification of road transport energy use. The share of electricity in 2024 was approximately 0.01%, which further confirms that electricity has not yet become an important energy source in aggregate road transport energy indicators. Figure 3 presents the fuel structure of road transport energy use and shows the relative contribution of each analysed energy source to total annual consumption. For comparison, the EU-27 road transport energy mix in 2023 was less concentrated in diesel: gas/diesel oil accounted for 63.7%, motor gasoline for 26.2%, renewables and biofuels for 6.7%, liquefied petroleum gases for 2.1%, natural gas for 0.8%, and electricity for 0.5% of final road transport energy consumption (Eurostat, 2026). This comparison highlights the particularly strong diesel dominance and the still very limited role of electricity in Montenegro.

A comparison between the first and the last year of the observed period is presented in Table 2.

Table 2 Comparison of energy use and shares between 2014 and 2024

Energy source	2014 [TJ]	2024 [TJ]	Absolute change [TJ]	Relative change [%]	Share in 2014 [%]	Share in 2024 [%]
Diesel	5321.7	11014.9	+5693.2	+107	74.6	82.9
Gasoline	1489.3	1970.9	+481.6	+32.3	20.9	14.8
LPG	318.9	304.8	-14.1	-4.4	4.5	2.3
Electricity	0	1.1	1.1	-	0	0.01
Total	7129.9	13291.7	+6161.8	+86.4	100	100

The comparison confirms that the structure of road transport energy use changed primarily through the increasing dominance of diesel fuel. Diesel fuel increased both in absolute consumption and in percentage share. Gasoline increased in absolute terms, but its share decreased, while LPG decreased both in absolute and relative terms. Electricity appeared only at the end of the period, but its share remained negligible.

These findings confirm a high dependence of Montenegro's road transport sector on petroleum-based fuels. In 2024, diesel fuel, gasoline and LPG together accounted for almost the entire final energy use in road transport. The most important structural characteristic is the dominant and increasing role of diesel fuel, which strongly determines the total energy profile of the sector.

The results also show that fuel diversification in road transport remains limited. LPG did not increase its role, while electricity is still too small to change the aggregate structure of energy use. Therefore, the energy transition in road transport is not yet clearly visible through final energy consumption indicators.

From the perspective of transport energy policy, these results suggest that short-term improvements should focus on energy efficiency, rational fuel use and gradual reduction of dependence on diesel fuel. Measures related to vehicle fleet renewal, improved technical condition of vehicles, better fuel efficiency and more efficient organization of road transport could be particularly important. In the longer term, stronger fuel diversification and a gradual increase in the use of alternative energy sources will be necessary in order to change the current structure of final energy use.

Overall, the analysed period shows that Montenegro's road transport sector experienced a significant increase in final energy use, while remaining strongly dependent on conventional petroleum-based fuels. The dominant role of diesel fuel, the secondary role of gasoline, the marginal role of LPG and the negligible contribution of electricity represent the main characteristics of the sector's energy structure.

CONCLUSIONS

This paper analysed energy use in Montenegro's road transport sector for the period 2014–2024, with special focus on fuel structure, consumption trends and dependence on petroleum-based fuels. The analysis was based on official statistical data and all values were presented in terajoules in order to enable direct comparison between different energy sources.

The results show that total energy use in road transport increased significantly during the observed period, from 7129.9 TJ in 2014 to 13291.7 TJ in 2024. This represents an increase of approximately 86.4%. The increase was mainly driven by diesel fuel consumption, which more than doubled during the analysed period. Diesel fuel remained the dominant energy source in road transport, increasing its share from 74.6% in 2014 to 82.9% in 2024.

Gasoline remained the second most important energy source, although its relative importance decreased. Its share declined from 20.9% in 2014 to 14.8% in 2024, despite an increase in absolute consumption. Liquefied petroleum gas had a marginal role in the fuel structure and its share decreased from 4.5% to 2.3%. Electricity appeared in the

official data only in the final years of the observed period, but its contribution to total road transport energy use remained negligible.

The main conclusion of the paper is that Montenegro's road transport sector is still strongly dependent on conventional petroleum-based fuels, particularly diesel fuel. The analysed data do not indicate substantial diversification away from petroleum-based fuels. On the contrary, the fuel structure became increasingly concentrated in diesel, whose share of total road transport energy use increased from 74.6% in 2014 to 82.9% in 2024. Therefore, future transport energy policies should place stronger emphasis on energy efficiency, vehicle fleet renewal, rational fuel use and gradual diversification of energy sources in road transport.

The findings provide a concise statistical basis for further discussion on sustainable mobility and energy use in Montenegro's road transport sector. Future research could extend this analysis by including vehicle fleet characteristics, emission indicators, electricity use in road transport and scenario-based assessments of future transport energy demand.

REFERENCES

Achour, H., & Belloumi, M. (2016). Decomposing the influencing factors of energy consumption in Tunisian transportation sector using the LMDI method. *Transport Policy*, 52, 64–71. https://doi.org/10.1016/j.tranpol.2016.07.008

Banister, D. (2008). The sustainable mobility paradigm. *Transport Policy*, 15(2), 73–80. https://doi.org/10.1016/j.tranpol.2007.10.005

Creutzig, F., Jochem, P., Edelenbosch, O. Y., Mattauch, L., Vuuren, D. P. van, McCollum, D., & Minx, J. (2015). Transport: A roadblock to climate change mitigation? *Science*, 350(6263), 911–912. https://doi.org/10.1126/science.aac8033

European Commission. (2020). Sustainable and Smart Mobility Strategy – putting European transport on track for the future. European Commission.

European Environment Agency. (2025). Sustainability of Europe's mobility systems 2025 (EEA Web Report No. 02/2025). European Environment Agency. https://doi.org/10.2800/4890019

Eurostat. (2026). Final energy consumption in transport—Detailed statistics—Statistics Explained—Eurostat.

Intergovernmental Panel on Climate Change (Ed.). (2023). Transport. In Climate Change 2022: Mitigation of Climate Change. Cambridge University Press. https://doi.org/10.1017/9781009157926.012

Liddle, B., & Huntington, H. (2020). 'On the Road Again': A 118 country panel analysis of gasoline and diesel demand. Transportation Research Part A: Policy and Practice, 142, 151–167. https://doi.org/10.1016/j.tra.2020.10.015

Statistical Office of Montenegro. (2026a). Balance of petroleum products in Montenegro, 2014–2024.

Statistical Office of Montenegro. (2026b). Electricity balance in Montenegro, 2023–2024.

Tsemekidi Tzeiranaki, S., Economidou, M., Bertoldi, P., Thiel, C., Fontaras, G., Clementi, E. L., & Franco De Los Rios, C. (2023). The impact of energy efficiency and decarbonisation policies on the European road transport sector. *Transportation Research Part A: Policy and Practice*, 170, 103623. https://doi.org/10.1016/j.tra.2023.103623

The 11th International Congress
Motor Vehicles & Motors 2026
Kragujevac, Serbia
October 8th-9th, 2026

Motor Vehicles & Motors

MVM2026-030
https://doi.org/10.24874/CMVM2026.030
Original scientific paper

Vladimir Kočović[1]
Živana Jovanović Pešić[2]
Miloš Pešić[3]
Jelena Đusić[4]
Dragan Džunić[5]

TRIBOLOGICAL PERFORMANCE OF BRASS SURFACES LUBRICATED WITH NEW AND USED ENGINE OILS

ABSTRACT: This study investigates the tribological behaviour of brass specimens lubricated with new and used SAE 10W-40 and SAE 30 engine oils under controlled laboratory conditions. Experimental tests were performed using a TPD-95 tribometer in a block-on-disc configuration according to ASTM G77. All tests were conducted at a normal load of 20 daN, a sliding speed of 0.5 m/s, and a duration of 600 s with continuous lubrication. The coefficient of friction was continuously monitored, while wear was evaluated through wear scar measurements and calculated wear volume. The results showed that lubricant ageing affected the two oil types differently. Used SAE 10W-40 produced a lower steady-state coefficient of friction and approximately 30% lower wear volume compared with the new oil. In contrast, used SAE 30 resulted in higher friction and more than three times greater wear volume than new SAE 30. Among all tested conditions, new SAE 30 provided the best wear resistance. The findings demonstrate that the tribological performance of used engine oils depends strongly on lubricant type, service condition, and interaction with the brass–steel contact.

KEYWORDS: brass, engine oils, tribological behaviour, coefficient of friction, wear

[1] *Vladimir Kočović, University of Kragujevac, Faculty of Engineering, Sestre Janjić 6, 34000 Kragujevac, vladimir.kocovic@kg.ac.rs, https://orcid.org/0000-0003-1231-0041*
[2] *Živana Jovanović Pešić, University of Kragujevac, Faculty of Engineering, Sestre Janjić 6, 34000 Kragujevac, zixi90@gmail.com, https://orcid.org/0000-0002-1373-0040*
[3] *Miloš Pešić, University of Kragujevac, Institute for Information Technologies - National Institute of the Republic of Serbia, Liceja Kneževine Srbije 1A 34000 Kragujevac, milospesic@uni.kg.ac.rs, https://orcid.org/0000-0002-3405-5216*
[4] *Jelena Đusić, University of Kragujevac, Faculty of Engineering, Sestre Janjić 6, 34000 Kragujevac, jelenadjusic24.2009@gmail.com, https://orcid.org/0009-0004-8630-9304*
[5] *Dragan Džunić, University of Kragujevac, Faculty of Engineering, Sestre Janjić 6, 34000 Kragujevac, dzuna@kg.ac.rs, https://orcid.org/0000-0002-1914-1298*

UTICAJ NOVIH I KORIŠĆENIH MOTORNIH ULJA NA TRIBOLOŠKO PONAŠANJE MESINGANIH POVRŠINA

REZIME: U ovom radu ispitano je tribološko ponašanje uzoraka od mesinga podmazivanih novim i korišćenim motornim uljima SAE 10W-40 i SAE 30 u kontrolisanim laboratorijskim uslovima. Eksperimentalna ispitivanja izvedena su na tribometru TPD-95, u konfiguraciji blok-na-disku, u skladu sa standardom ASTM G77. Sva ispitivanja sprovedena su pri normalnom opterećenju od 20 daN, brzini klizanja od 0,5 m/s i trajanju od 600 s, uz kontinuirano podmazivanje. Koeficijent trenja praćen je tokom celog ispitivanja, dok je habanje procenjeno na osnovu merenja širine traga habanja i izračunate zapremine pohabanog materijala. Rezultati su pokazali da starenje maziva različito utiče na ispitivana ulja. Korišćeno ulje SAE 10W-40 dalo je niži koeficijent trenja u ustaljenom režimu i približno 30% manju zapreminu habanja u odnosu na novo ulje. Nasuprot tome, korišćeno SAE 30 ulje pokazalo je veće trenje i više od tri puta veću zapreminu habanja u odnosu na novo SAE 30 ulje. Najbolju otpornost na habanje pokazalo je novo SAE 30 ulje. Dobijeni rezultati potvrđuju da tribološke performanse korišćenih motornih ulja značajno zavise od vrste maziva, njegovog radnog stanja i interakcije sa kontaktom mesing–čelik.

KLJUČNE REČI: mesing, motorna ulja, tribološko ponašanje, koeficijent trenja, habanje

INTRODUCTION

Friction and wear are important factors affecting the efficiency, reliability, and service life of mechanical systems containing components in relative motion. Appropriate lubrication is one of the most effective approaches for reducing frictional losses and protecting contacting surfaces from excessive wear. The resulting tribological behaviour depends on operating conditions, the properties of the contacting materials, and the physical and chemical characteristics of the lubricant.

Brass alloys are widely used for bearings, bushings, guides, valves, and other machine components due to their favourable combination of mechanical properties, corrosion resistance, machinability, and tribological characteristics. Feyzullahoğlu, E. et al. (2008) investigated the tribological behaviour of brass and tin-based bearing materials under oil-lubricated conditions and demonstrated that friction and wear are strongly influenced by sliding distance, sliding speed, applied load, and material properties. Feser, T. et al. (2013) further showed that the lubricated sliding behaviour of brass against steel is closely related to interfacial and near-surface processes. Their results indicated that the formation of ZnO within the wear track and carbon-containing layers on the counterface may contribute to favourable running-in behaviour and friction reduction.

Engine oils are formulated to provide effective lubrication and surface protection over a wide range of operating conditions. During service, however, their properties change as a result of oxidation, thermal degradation, contamination, and additive depletion. Wei, L. et al. (2021) reported changes in total acid number, total base number, viscosity, and oxidation stability of engine oils with increasing operating mileage. Similarly, Al Sheikh Omar, A. et al. (2021) demonstrated that oil ageing, soot contamination, and additive depletion can significantly affect lubricant performance. These changes may consequently modify the ability of the lubricant to reduce friction and protect contacting surfaces from wear.

However, lubricant ageing does not necessarily lead to an immediate deterioration of tribological performance. Ezzat, F.M.H. (1993) observed a pronounced reduction in the coefficient of friction and a decrease in wear for some used engine oils under reciprocating sliding conditions. Moon, W.S. and Kimura, Y. (1990) also demonstrated that the friction and wear behaviour of used gasoline engine oils depends strongly on their degree of deterioration and associated changes in their chemical characteristics. More recently, Džunić, D. et al. (2025) compared new SAE 10W-40 oil with used oils collected from gasoline and diesel engines using an aluminium–steel tribological pair. Under the investigated conditions, the used oils exhibited lower coefficients of friction and smaller wear scars than the new lubricant, with the oil collected from a diesel engine showing the most favourable short-term tribological behaviour.

These findings indicate that the tribological performance of used engine oils is determined by a complex interaction between lubricant condition, material pair, and operating conditions. Therefore, the present study investigates the tribological behaviour of brass surfaces lubricated with new and used SAE 10W-40 and SAE 30 engine oils under identical laboratory conditions. The aim is to evaluate the influence of lubricant condition and viscosity grade on friction and wear and to provide further insight into the interaction between brass surfaces and new and service-aged engine oils.

MATERIALS AND METHOD

This study investigated the tribological behaviour of brass specimens lubricated with two commercial motor oils, SAE 10W-40 and SAE 30, in both new and used conditions. The main physicochemical properties of the investigated oils are presented in Table 1.

Table 1. Physicochemical properties of SAE 10W-40 and SAE 30 motor oils

Property	SAE 10W-40	SAE 30
Viscosity Index	155	95
Density (g/ml @ 15.6°C, ASTM D4052)	0.86	0.88
Flash Point (°C, ASTM D93)	212	210
Pour Point (°C, ASTM D97)	-45	-30

Experimental testing was performed using a TPD-95 tribometer in accordance with ASTM G77. The tribometer operates in a block-on-disc configuration, in which a stationary block specimen is pressed against a rotating disc under a defined normal load. This configuration enables the determination of friction and wear characteristics under controlled sliding conditions.

The counterbody disc was made of EN 25CrMo4 steel with a hardness of 60–64 HRC and a ground surface finish, while all test blocks were made of brass. The disc diameter was 35 mm, and the dimensions of the block specimens were 15×10×6.35 mm.

Prior to tribological testing, all brass blocks were subjected to an identical surface preparation procedure in order to obtain comparable initial surface conditions. The specimens were sequentially ground using silicon carbide abrasive papers with grit sizes P600, P1200, and P2000. Grinding was performed on a mechanical grinder at a rotational speed of 500 rpm, with each side of the specimen ground for 1 min at each preparation stage. This procedure provided a progressively finer surface finish and reduced differences in the initial surface condition between the tested specimens.

All tribological tests were conducted under identical operating conditions. The applied normal load was 20 daN, the sliding speed was maintained at 0.5 m/s, and the test duration was 600 s. Continuous lubrication was supplied to the contact zone throughout each test using a reservoir containing 30 ml of lubricant.

According to the lubricant type and condition, four experimental groups were defined:

1. Br-10W-40-N – brass specimens tested with new SAE 10W-40 multigrade engine oil.
2. Br-10W-40-U – brass specimens tested with used SAE 10W-40 multigrade engine oil.
3. Br-SAE30-N – brass specimens tested with new SAE 30 monograde engine oil.
4. Br-SAE30-U – brass specimens tested with used SAE 30 monograde engine oil.

The used lubricants were collected after one complete service interval. The SAE 10W-40 oil had been used for approximately 10,000 km in a diesel-powered passenger vehicle, whereas the SAE 30 oil had been used for approximately 100 operating hours in a tractor engine.

During each test, the coefficient of friction was continuously monitored. After testing, the wear scar width on the brass blocks was measured and used to calculate the volume of material removed during sliding.

The wear volume was calculated from the geometry of the wear scar using the following expression:

$$V = \left(\frac{306.25}{2} \cdot 2arcsin\left(\frac{b}{35}\right) - \frac{\sqrt{306.25 - \frac{b^2}{4}} \cdot b}{2} \right) \cdot 6.35 \quad (1)$$

where:
(V) – wear volume, mm³,
(b) – wear scar width, mm,
306.25 – square of the disc radius
6.35 – width of the block specimen, mm.

The expression accounts for the circular geometry of the rotating disc and determines the cross-sectional area of the wear scar produced on the stationary block. Multiplication of this area by the specimen width provides the corresponding volumetric material loss.

RESULTS AND DISCUSSION

Figure 1 presents the variation of the coefficient of friction as a function of sliding distance for brass specimens lubricated with new and used SAE 10W-40 engine oil. Each curve represents the mean behaviour obtained from three repeated measurements performed under identical testing conditions, while the surrounding band indicates the variability between the measurements.

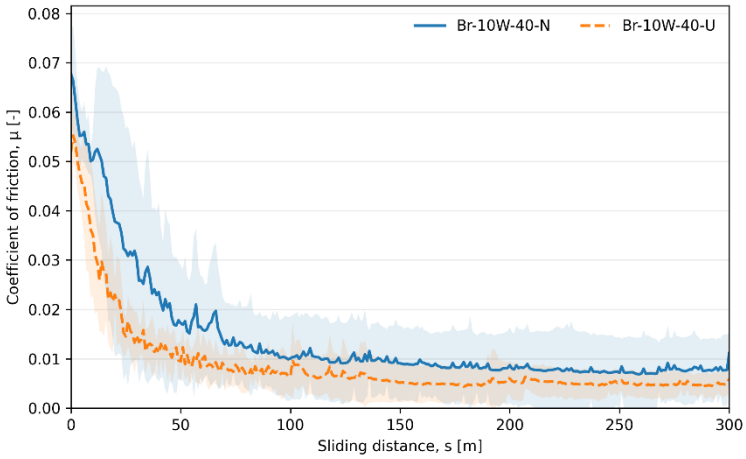

Figure 1 Coefficient of friction as a function of sliding distance for Br-10W-40-N and Br-10W-40-U samples

Both lubricants exhibited a pronounced running-in period during the initial part of the test, characterized by a rapid decrease in the coefficient of friction. After approximately 80–100 m of sliding distance, the friction curves became considerably more stable. The new SAE 10W-40 oil exhibited a higher coefficient of friction throughout most of the test compared with the used lubricant.

During the final part of the sliding test, the average coefficient of friction was approximately 0.0077 for the Br-10W-40-N group and 0.0051 for the Br-10W-40-U group. Thus, the used SAE 10W-40 oil produced an approximately 35% lower steady-state coefficient of friction than the new oil. This result indicates that, under the investigated conditions, service ageing of SAE 10W-40 oil did not lead to deterioration of its friction-reducing capability when applied to the brass–steel contact.

The lower coefficient of friction observed for the used SAE 10W-40 oil may be associated with changes in lubricant composition occurring during service, including the presence of degradation products and changes in the concentration or activity of surface-active compounds. These compounds may influence the formation of a boundary film at the brass surface. However, since the chemical composition of the used oils was not analysed in the present study, this explanation should be considered a possible mechanism rather than a confirmed cause.

Figure 2 shows the corresponding friction behaviour of brass specimens lubricated with new and used SAE 30 engine oil.

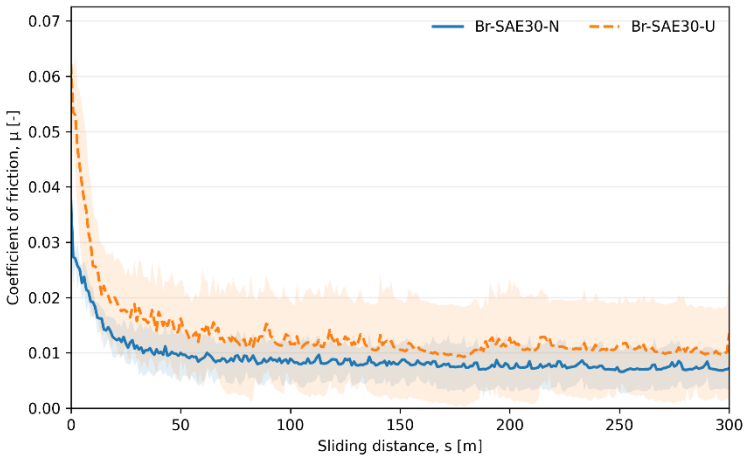

Figure 2 Coefficient of friction as a function of sliding distance for Br-SAE30-N and Br-SAE30-U samples

A different trend was observed for SAE 30 compared with SAE 10W-40. Both SAE 30 oils showed an initial decrease in friction followed by a relatively stable sliding regime. However, the used SAE 30 oil consistently exhibited a higher coefficient of friction than the new lubricant over most of the sliding distance.

In the final part of the test, the mean coefficient of friction was approximately 0.0074 for the Br-SAE30-N specimens and 0.0108 for the Br-SAE30-U specimens. Consequently, the used SAE 30 oil produced an approximately 46% higher steady-state coefficient of friction than the new SAE 30 oil. This result suggests that the changes occurring during the service of the SAE 30 lubricant adversely affected its ability to maintain low friction in the investigated brass–steel contact.

The opposite trends obtained for SAE 10W-40 and SAE 30 are particularly important. They demonstrate that the effect of lubricant ageing cannot be described simply as either beneficial or detrimental. Instead, the tribological response depends on the oil formulation, its service history, and its interaction with the contacting materials.

Wear behaviour was evaluated from three wear-scar-width measurements for each lubricant condition. The mean wear scar widths were 2.639 mm for Br-10W-40-N, 2.343 mm for Br-10W-40-U, 1.434 mm for Br-SAE30-N, and 2.128 mm for Br-SAE30-U. The corresponding wear volumes, calculated using the geometrical relationship described in the Materials and Methods section, are presented in Figure 3.

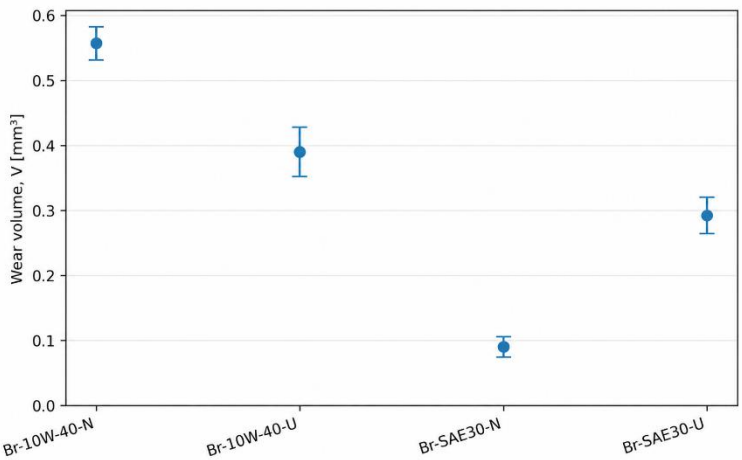

Figure 3 Comparison of wear volumes for Br-10W-40-N, Br-10W-40-U, Br-SAE30-N, and Br-SAE30-U samples. Error bars represent standard deviation based on three measurements

The largest wear volume was obtained for the specimens lubricated with new SAE 10W-40 oil, with an average value of approximately 0.557 mm³. In contrast, the specimens lubricated with used SAE 10W-40 oil exhibited a mean wear volume of approximately 0.390 mm³, corresponding to a reduction of about 30%. The wear results therefore follow the same general trend as the friction measurements for SAE 10W-40: the used oil produced both a lower coefficient of friction and lower material loss.

The most favourable wear behaviour was obtained with new SAE 30 oil. The Br-SAE30-N specimens exhibited an average wear volume of only approximately 0.090 mm³, substantially lower than all other investigated groups. After service, however, the tribological performance of SAE 30 deteriorated considerably. The average wear volume increased to approximately 0.292 mm³, more than three times the value obtained with new SAE 30 oil. The mean wear scar width similarly increased from approximately 1.434 to 2.128 mm.

These results reveal a clear difference between the effects of lubricant ageing for the two investigated viscosity grades. For SAE 10W-40, the used lubricant reduced both friction and wear compared with the new oil. In contrast, used SAE 30 produced both higher friction and substantially greater wear than its new counterpart. New SAE 30 provided the best overall wear protection among the investigated lubricants, whereas new SAE 10W-40 resulted in the highest volumetric wear.

The results also demonstrate that lubricant performance cannot be assessed solely on the basis of viscosity grade or whether the oil is new or used. The interaction between lubricant condition and the brass surface appears to play a decisive role. Further physicochemical characterization of the used oils, including viscosity, oxidation, acidity, contamination, and additive depletion, would be required to identify the mechanisms responsible for the observed differences.

CONCLUSIONS

The present study investigated the tribological behaviour of brass surfaces lubricated with new and used SAE 10W-40 and SAE 30 engine oils under identical block-on-disc testing conditions. The results showed that lubricant ageing had a markedly different effect depending on the oil type.

For SAE 10W-40, the used oil exhibited a lower coefficient of friction and a smaller wear volume compared with the new lubricant, indicating improved tribological behaviour under the applied test conditions. In contrast, the used SAE 30 oil produced both a higher coefficient of friction and significantly greater wear than the new SAE 30 oil. Among all tested conditions, new SAE 30 provided the best wear resistance, while new SAE 10W-40 resulted in the highest material loss.

These findings confirm that the influence of oil ageing on brass tribological performance cannot be evaluated independently of lubricant formulation and service history. The interaction between the lubricant and the brass–steel contact plays a decisive role in determining friction and wear behaviour. Further characterization of the used oils, particularly in terms of viscosity, oxidation, contamination, acidity, and additive depletion, would be valuable for explaining the mechanisms responsible for the observed differences.

ACKNOWLEDGMENTS

This paper is the result of research conducted under the author's contract No. 451-03-34/2026-03/200107, dated February 5, 2026, supported by the Ministry of Science, Technological Development and Innovation, Republic of Serbia.

REFERENCES

Al Sheikh Omar, A., Motamen Salehi, F., Farooq, U., Morina, A., & Neville, A. (2021). Chemical and physical assessment of engine oils degradation and additive depletion by soot. *Tribology International*, 160, 107054. https://doi.org/10.1016/j.triboint.2021.107054

Džunić, D., Kočović, V., Jovanović Pešić, Ž., Mitrović, S., & Erić, M. (2025). A comparative study on the tribological behavior of new and used 10W-40 engine oil applied in gasoline and diesel engines. *40th International Conference on Production Engineering – Serbia 2025.* https://doi.org/10.46793/ICPES25.178D

Ezzat, F. M. H. (1993). The friction and wear of fresh and used engine oils during reciprocating sliding. *Wear*, 169(2), 167–172. https://doi.org/10.1016/0043-1648(93)90294-V

Feser, T., Stoyanov, P., Mohr, F., & Dienwiebel, M. (2013). The running-in mechanisms of binary brass studied by in-situ topography measurements. *Wear*, 303(1–2), 465–472. https://doi.org/10.1016/j.wear.2013.03.047

Feyzullahoğlu, E., Zeren, A., & Zeren, M. (2008). Tribological behaviour of tin-based materials and brass in oil lubricated conditions. *Materials & Design*, 29(3), 714–720. https://doi.org/10.1016/j.matdes.2007.02.018

Moon, W.-S., & Kimura, Y. (1990). Wear-preventing property of used gasoline engine oils. *Wear*, 139(2), 351–365. https://doi.org/10.1016/0043-1648(90)90056-G

Wei, L., Duan, H., Jin, Y., Jia, D., Cheng, B., Liu, J., & Li, J. (2021). Motor oil degradation during urban cycle road tests. *Friction*, 9(5), 1002–1011. https://doi.org/10.1007/s40544-020-0386-z

The 11th International Congress
Motor Vehicles & Motors 2026
Kragujevac, Serbia
October 8th - 9th, 2026

Motor Vehicles & Motors

MVM2026-034
https://doi.org/10.24874/CMVM2026.034
Original scientific paper

Mihailo Đuković[1]
Saša Milojević[2]
Slobodan Savić[3]
Blaža Stojanović[4]
Horia Abaitancei[5]

APPLICATION OF A RADIAL HYDRAULIC MOTOR IN ALTERNATIVE VEHICLE DRIVE SYSTEMS

ABSTRACT: The transition toward alternative vehicle propulsion systems has created a need for innovative drive concepts capable of improving efficiency, reliability, and operational flexibility. This paper presents a concept of a vehicle drive system based on the application of a radial hydraulic motor. The proposed solution is analysed from the aspect of power transmission, torque generation, and potential integration into specialized vehicle platforms. Particular attention is given to the advantages of hydraulic drive systems in applications requiring high torque at low rotational speeds. The paper also discusses future research directions involving numerical simulations, performance verification, and possible implementation in lightweight transport vehicles and minibuses.

KEYWORDS: radial hydraulic motor, alternative propulsion systems, vehicle drive, hydraulic transmission, powertrain analysis

PRIMENA RADIJALNOG HIDROMOTORA U ALTERNATIVNIM POGONSKIM SISTEMIMA

REZIME: Prelazak na alternativne pogonske sisteme vozila stvorio je potrebu za inovativnim konceptima pogona koji mogu poboljšati efikasnost, pouzdanost i operativnu fleksibilnost. Ovaj rad predstavlja koncept sistema pogona vozila zasnovanog na primeni radijalnog hidrauličnog motora. Predloženo rešenje je analizirano sa aspekta prenosa

[1] *Mihailo Đuković, M.Sc. student, Faculty of Engineering University of Kragujevac, Kragujevac 34000, Sestre Janjić 6, Serbia, mihailo.djukovic.02@gmail.com*
[2] *Dr Saša Milojević, prof. assist. Faculty of Engineering University of Kragujevac, Kragujevac 34000, Sestre Janjić 6, Serbia, sasa.milojevic@kg.ac.rs, https://orcid.org/0000-0003-0569-047X*
[3] *Dr Slobodan Savić, full prof. Faculty of Engineering University of Kragujevac, Kragujevac 34000, Sestre Janjić 6, Serbia, ssavic@kg.ac.rs, https://orcid.org/0000-0001-6609-4845*
[4] *Dr Blaža Stojanović, full prof. Faculty of Engineering University of Kragujevac, Kragujevac 34000, Sestre Janjić 6, Serbia, blaza@kg.ac.rs, https://orcid.org/0000-0003-4790-2856*
[5] *Dr Horia Abaitancei, full prof. Institute of Automotive Engineering Transilvania University of Brasov, Brasov, Strada Insitutului 9, Romania, h.abaitancei@unitbv.ro, https://orcid.org/0009-0001-8569-2194*

snage, generisanja obrtnog momenta i potencijalne integracije u specijalizovane platforme vozila. Posebna pažnja je posvećena prednostima hidrauličnih pogonskih sistema u primenama koje zahtevaju visok obrtni moment pri malim brzinama rotacije. U radu se takođe razmatraju budući pravci istraživanja koji uključuju numeričke simulacije, verifikaciju performansi i moguću implementaciju u lakim transportnim vozilima i minibusevima.

KLJUČNE REČI: radijalni hidraulični motor, alternativni pogonski sistemi, pogon vozila, hidraulični prenos, analiza pogonskog sklopa

INTRODUCTION

Modern transport vehicles require high efficiency, reliability, and operational flexibility under increasingly demanding urban and interurban operating conditions. Frequent acceleration and deceleration, variable payloads, and the requirement for compact and efficient drivetrain configurations necessitate the development of alternative propulsion architectures. Consequently, the development of high-performance and flexible vehicle drive systems remains an important research direction in modern transportation engineering (Guzzella & Sciarretta, 2005).

Conventional mechanical transmissions offer high efficiency but suffer from structural complexity, substantial weight, and limited flexibility in torque distribution and drivetrain layout. These limitations drive the investigation of alternative vehicle propulsion concepts. In modern vehicle design, individual in-wheel electric drives have attracted significant attention due to their ability to provide independent torque control at individual wheels, improving traction control and vehicle manoeuvrability (Popovici et al. 2026). However, the application of electric hub drives may involve challenges related to power density, thermal management, and integration of electric components within the wheel assembly, particularly in vehicles with increased mass and demanding operating conditions. In this context, hydrostatic radial piston drives represent a promising alternative for transport vehicles and minibuses requiring high starting torque and compact drivetrain configurations (Tanaka et al. 2013).

Hydrostatic systems can transmit substantial power within compact dimensions, providing flexibility in drivetrain packaging and the arrangement of the prime mover and wheel-drive units. Comparative evaluations of electric, hydraulic, and pneumatic rotary actuation systems indicate that hydraulic solutions can provide high torque density and favourable low-speed operating characteristics, making them suitable for vehicle propulsion applications (Tanaka et al. 2013). Among hydraulic solutions, multi-stroke radial piston motors are particularly promising due to their High-Torque Low-Speed (HTLS) characteristics, making them well suited for direct or near-direct wheel-drive applications requiring high starting torque, compact installation, and flexible power transmission (Abaitancei et al. 2016; Li et al. 2024; Mannesmann, 1998; Dindorf, 2024; Bašta, 1986; Savić, 1986)

The objective of this paper is to investigate the application of radial piston hydraulic motors in transport vehicle and minibus drivetrains using a multi-domain simulation model developed in *Simcenter Amesim* (Siemens Digital Industries Software, 2020). The proposed drive concept is analysed from the aspects of power transmission, torque generation, volumetric leakage, and thermal behaviour under representative vehicle operating conditions. The scientific contribution of this work lies in the development and application of a mathematical and simulation framework for evaluating the suitability of radial hydraulic motors as an alternative propulsion solution for transport vehicles and minibuses, providing a basis for further optimization, performance verification, and experimental validation.

HYDRAULIC PROPULSION SYSTEMS

Hydrostatic drive systems represent an important alternative to conventional mechanical transmissions in modern motor vehicles, particularly in applications requiring continuous speed regulation and high torque at low rotational speeds. In a hydrostatic drive, mechanical energy supplied by the prime mover is converted into hydraulic energy by a hydraulic pump and subsequently converted back into mechanical energy by one or more hydraulic motors (Abaitancei et al. 2016; Krstić, 2003).

The application of hydrostatic drive systems (HST) in mobile machines and specialized vehicles is motivated by the need for flexible drivetrain configurations, compact component arrangement, and precise control of vehicle speed and wheel torque. Unlike conventional mechanical transmissions, hydrostatic drives enable stepless speed regulation and rapid changes in the direction of rotation without the need for conventional multi-stage gearboxes. These characteristics make hydrostatic systems particularly suitable for vehicles operating under variable load conditions and requiring high starting torque and precise low-speed control (Abaitancei et al. 2016; Krstić, 2003).

The hydrostatic drivetrain considered in this work is based on the use of a hydraulic pump connected to the prime mover and radial piston hydraulic motors integrated into the drive-wheel assemblies. This configuration eliminates several conventional mechanical transmission components, such as the mechanical gearbox, cardan shafts, and conventional differentials, allowing greater flexibility in drivetrain packaging and torque distribution (Abaitancei et al.

2016; Savić, 1986; Krstić, 2003). The proposed system architecture and the corresponding hydraulic fluid flow paths are presented in Figure 1.

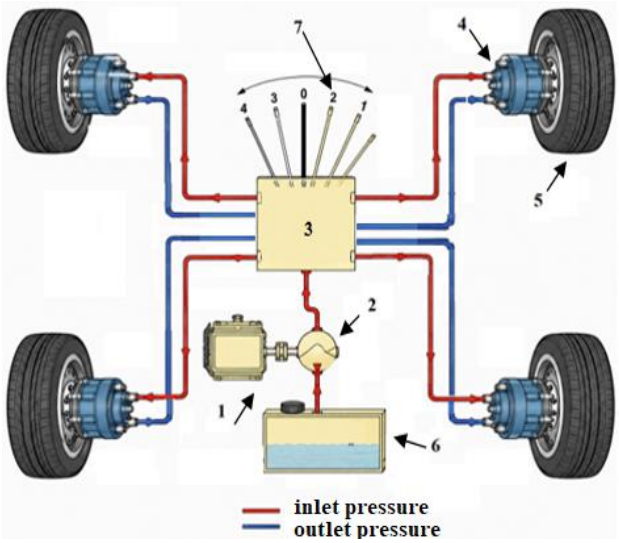

Figure 1 Schematic representation of the hydraulic drive system (Sonale, 2024)

In vehicles equipped with a hydrostatic drivetrain, the main components include the prime mover, hydraulic pump, hydraulic motors, directional and control valves, reservoir, and fluid lines. The system operates by circulating hydraulic fluid through a closed hydraulic circuit. The prime mover (1), which may be an internal combustion engine, electric motor, or another mechanical energy source, drives the hydraulic pump (2). The pump draws hydraulic fluid, typically oil, from the reservoir (6) and supplies it to the hydraulic circuit (Abaitancei et al. 2016; Savić, 1986; Krstić, 2003).

The load generated by the hydraulic motors and flow resistance establishes the required fluid pressure in the delivery line. Pressurized fluid (red lines) is directed through the control valve block (3), which regulates its flow toward the hydraulic motors integrated into the wheel hubs (4). This configuration enables the hydraulic energy to be independently supplied to individual drive wheels, providing increased flexibility in drivetrain layout and torque distribution (Abaitancei et al. 2016; Savić, 1986; Krstić, 2003).

The radial piston hydraulic motors convert the hydraulic energy into mechanical power. Fluid pressure acts on the motor pistons, producing reciprocating motion that is transformed into rotary motion of the rotor and drive wheel (5). The generated torque provides the driving force required for vehicle propulsion. After passing through the motor, the low-pressure fluid (blue lines) returns to the reservoir (6), where it can be cooled and filtered before re-entering the hydraulic circuit, depending on the system configuration (Savić, 1986; Krstić, 2003).

RADIAL HYDRAULIC MOTOR

The radial piston hydraulic motor is a low-speed, high-torque hydraulic motor widely used in applications requiring high torque at relatively low rotational speeds (Figure 2). Its operating principle is based on the conversion of hydraulic energy into mechanical energy through the radial reciprocating motion of pistons. Due to their high torque density, compact configuration, and ability to operate at low speeds, radial piston motors are suitable for applications requiring high starting torque and precise low-speed operation (Bašta, 1986; Savić, 1986).

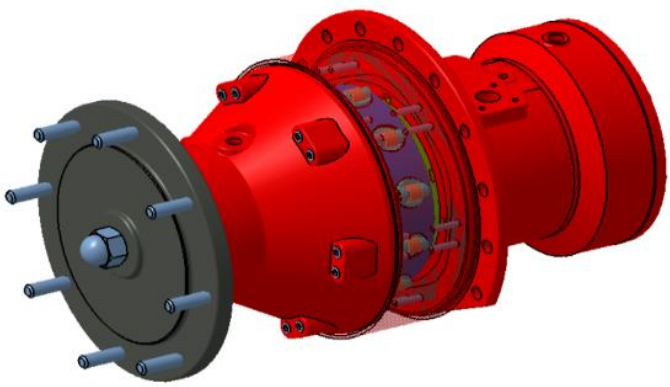

Figure 2 3D model of Radial piston hydraulic motor

The multi-stroke radial piston hydraulic motor features a robust construction designed to withstand high hydraulic pressures and demanding operating conditions. Its specific geometry and kinematic configuration enable multiple working strokes during a single rotor revolution, resulting in high displacement and torque generation at relatively low rotational speeds. These characteristics make radial piston motors particularly suitable for direct or near-direct wheel-drive applications in transport vehicles and minibuses (Bašta, 1986; Savić, 1986; Giavarini 2022).

Construction and principle

A multi-stroke radial piston hydraulic motor consists of several main components, as illustrated in Figure 3:

1. Cam-profile stator: the stationary component with a multi-lobe internal cam profile that determines the piston displacement and number of working strokes per rotor revolution.
2. Rotor (cylinder block): the rotating component containing the radially arranged cylinder chambers. It is connected to the output shaft and transfers the generated torque to the driven element.
3. Piston assemblies with rollers: radially arranged pistons that reciprocate within the cylinder chambers. Rollers at the outer ends of the pistons maintain contact with the stator profile and transmit the generated force to the rotor.
4. Flow distribution pair: the hydraulic distribution mechanism that controls the connection between the individual cylinder chambers and the high- and low-pressure ports, ensuring the appropriate sequence of fluid admission and discharge.
5. Output drive shaft: the rotating shaft through which the generated torque is transmitted to the driven wheel or other mechanical load.
6. Motor housing (casing): the stationary outer housing that supports the internal components and provides structural protection for the motor assembly.

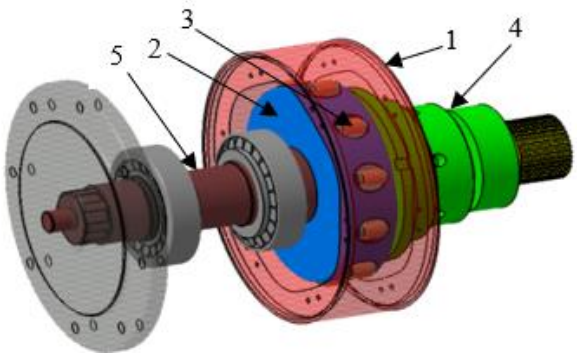

Figure 3 Key parts of radial hydraulic motor

The operating principle is based on the conversion of hydraulic energy into mechanical torque through cyclic radial piston motion. During the working stroke, pressurized hydraulic fluid is supplied to a cylinder chamber through the flow distribution pair (4). The resulting pressure force moves the piston (3) radially outward. The piston roller follows the cam profile of the stator (1), generating a tangential force that produces rotation of the rotor (2) and output shaft (5) (Giavarini 2022).

As the rotor continues to rotate, the piston reaches the end of its working stroke and the corresponding cylinder chamber is disconnected from the high-pressure supply. During the return stroke, the geometry of the stator profile causes the piston to move radially inward while the flow distribution pair connects the chamber to the low-pressure outlet. The hydraulic fluid is consequently discharged from the chamber (Giavarini 2022).

The continuous repetition of these cycles produces rotary motion of the output shaft and enables the motor to generate high torque at low rotational speeds. The resulting torque characteristics make radial piston motors suitable for applications in which high starting torque and controlled low-speed operation are required, such as transport vehicles operating under frequent acceleration and deceleration (Giavarini 2022).

The internal clearances between the piston-cylinder interfaces and within the flow distribution pair are important for the volumetric performance of the motor. Under elevated pressure differences, these clearances can result in internal volumetric leakage, reducing the effective flow available for torque generation and consequently affecting the overall efficiency of the motor. Therefore, the analysis and quantification of internal leakage represent an important aspect of evaluating radial piston motors for vehicle propulsion applications (Giavarini 2022).

Main characteristics and comparison with conventional drivetrains

Radial piston hydraulic motors are classified as high-torque, low-speed (HTLS) displacement machines. Their multi-stroke operating principle enables several working strokes during one rotor revolution, resulting in high displacement and torque generation at relatively low rotational speeds (Tanaka et al., 2013). This characteristic is particularly advantageous for wheel-drive applications, where high starting torque and controlled low-speed operation are required.

When integrated into a hydrostatic drivetrain, radial piston motors can be positioned directly at or near the driven wheels. Such an architecture can reduce the number of conventional mechanical transmission components, including mechanical gearboxes, drive shafts, and differentials, depending on the selected drivetrain configuration. This provides greater flexibility in component arrangement and may contribute to more compact drivetrain packaging and simplified torque distribution (Bašta, 1986; Savić, 1986; Giavarini 2022).

Compared with axial piston hydraulic motors, radial piston motors generally provide lower rotational speeds and higher torque characteristics, making them particularly suitable for direct-drive applications. Axial piston motors used for wheel propulsion may require additional mechanical reduction depending on the required wheel torque and operating speed. The use of a radial piston motor can therefore reduce or eliminate the need for additional mechanical reduction in applications where its speed and torque characteristics match the requirements of the driven wheel (Bašta, 1986; Savić, 1986; Giavarini 2022).

For transport vehicles and minibuses, these characteristics can be particularly relevant during vehicle launch, low-speed manoeuvring, and frequent stop-and-go operation. The combination of high starting torque, compact installation, and flexible hydraulic power distribution makes radial piston motors a potential alternative to conventional mechanical drivetrain configurations.

APPLICATION OF RADIAL HYDRAULIC MOTORS TO EASY TRANSPORT VEHICLES AND MINIBUSES

Radial piston hydraulic motors have a specific and practical application on easy transport vehicles like mini – trucks and minibuses. They are used in these vehicles primarily due to the need for compactness, high starting torque and the elimination of heavy mechanical components. Urban transport solutions and light-duty commercial vehicles operate under distinct spatial constraints and highly transient duty cycles (Figure 4). To optimize chassis packaging and maximize structural volume, a decentralized hydrostatic propulsion framework is introduced. This layout bypasses the rigid configurations imposed by conventional multi-speed gearboxes, split differentials, and linear drive shafts, offering an inherently modular fluid-power alternative (Abaitancei et al., 2016; Dindorf, 2024).

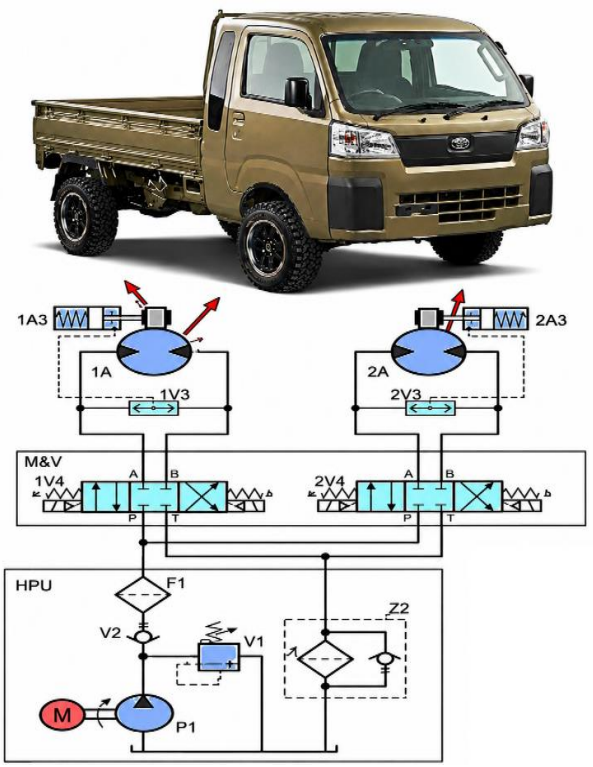

Figure 4 Schematic diagram of conventional hydraulic propulsion system of the mini – truck

The structural deployment of the system relies on an integrated fluid delivery network segregated into three operational segments: the Central Generating Group, the Symmetric Flow Distribution Nodes, and the Peripheral Hub Actuating Units. Mechanical power from the prime mover—which can be tailored as a highly efficient internal combustion engine or a zero-emission electric motor—is directly converted into hydraulic energy via a variable displacement axial piston pump (P1) equipped with electro-proportional displacement control (Dindorf, 2024).

To safeguard the closed-loop system against transient pressure spikes during abrupt decelerations, a dual-directional flushing and shock-absorber valve manifold is integrated directly at the pump boundary (Abaitancei et al. 2016; Mannesmann, 1998; Dindorf, 2024). System fluid undergoes continuous purification through a micro-glass media filter situated in the low-pressure charging line, while operating temperatures are strictly regulated by a modulated, smart-bypass air-oil cooling matrix to ensure stable fluid viscosity during intense stop-and-go driving profiles.

Power allocation to the traction points is governed by two decentralized Axial Manifold Blocks (AMB-L and AMB-R), which act as an intelligent fluid-power differential. The left-side manifold distributes high-pressure oil in a parallel loop to the front and rear radial-piston hub motors (M-1 and M-2), while the right-side manifold simultaneously supplies motors M-3 and M-4 (Mannesmann, 1998; Dindorf, 2024).

This fluid-power configuration introduces distinct operational paradigms specifically engineered for light utility platforms and passenger minibuses (Mannesmann, 1998; Dindorf, 2024):

- Volumetric Floor Optimization in Passenger Transports: Traditional mechanical drivetrains dictate the chassis height due to the physical envelope of the transmission tunnel and rear axle differential housings. By integrating multi-cam radial piston motors directly within the wheel rims, all mechanical driveline components are completely extracted from the under-chassis zone. This facilitates an absolute low-floor configuration, creating a continuous, flat passenger platform that optimizes cabin ergonomics, increases standing passenger capacity, and ensures rapid, step-free ingress and egress.
- Dynamic Work-Cycle Adaptability for Light Utility Vehicles: Light commercial mini-trucks require extreme torque variability when transitioning from empty highway transit to fully laden, low-speed work operations (e.g., municipal maintenance or waste collection). The multi-stroke radial motors utilized in this system feature selectable displacement configurations (multi-displacement switching). At low speeds, the motors operate at full volumetric displacement to maximize starting tractive effort and gradeability. For high-speed transport, individual motor sub-chambers can be hydraulically isolated or shifted into a low-drag freewheeling state, drastically minimizing parasitic fluid shear losses and boosting fuel economy.

Mathematical model

To evaluate the conceptual performance of a high-torque radial piston hydraulic motor for light-duty transit and utility operations, a comprehensive mathematical model is established. This model defines the relationship between hydraulic input energy, internal mechanical and volumetric losses, and the dynamic output performance required to propel mini-trucks and minibuses under demanding urban stop-and-go profiles and variable payload conditions.

The rotational speed of the radial hydraulic motor is directly governed by the volumetric flow rate of the hydraulic fluid supplied to its cylinders. The theoretical flow rate Q_{th} [m³ s⁻¹], which assumes zero leakage and ideal geometry, is defined as (Giavarini 2022):

$$Q_{th} = V_d \cdot n \tag{1}$$

where:

- V_d is the displacement of the radial motor [m³ rev⁻¹];
- n is the rotational speed of the motor shaft [rps].

In light commercial vehicles and minibuses, high operational pressures during acceleration from a standstill lead to internal fluid bypass across the piston-cylinder clearances and the distribution valves. Therefore, the actual flow rate Q_{act} required by the motor is expressed as (Giavarini 2022):

$$Q_{act} = Q_{th} + Q_{leak} \tag{2}$$

where Q_{leak} represents the internal volumetric leakage flow rate [m³ s⁻¹].

Radial piston motors are categorized as Low-Speed High-Torque (LSHT) drives, making them ideal for mini-trucks handling maximum payload launch efforts and transit platforms navigating steep urban inclines. The ideal or theoretical torque T_{th} [Nm] generated by the motor depends strictly on its geometric displacement and the differential pressure (Giavarini 2022):

$$T_{th} = \frac{V_d \, \Delta p}{2\pi} \tag{3}$$

where

$$\Delta p = p_{in} - p_{out} \tag{4}$$

is the pressure drop across the motor [Pa].

The actual torque T_{act} delivered to the vehicle's wheel hub is lower than the theoretical value due to mechanical friction between moving components (pistons, rollers, and multi-cam lobes). It is calculated as (Giavarini 2022):

$$T_{act} = T_{th} - T_{loss} = T_{th}\eta_{hm} \tag{5}$$

where:

- T_{loss} is the total friction torque loss [Nm];
- η_{hm} is the hydro-mechanical efficiency of the motor.

The conversion of hydraulic power into mechanical power determines the overall tractive and acceleration capability of the commercial vehicle. The hydraulic input power P_{hyd} [W] delivered by the system pump is given by (Giavarini 2022):

$$P_{hyd} = Q_{act} \, \Delta p \tag{6}$$

The effective mechanical power P_{mech} [W] available at the output wheel hub to drive the mini-truck or minibus is defined as (Giavarini 2022):

$$P_{mech} = T_{act}\omega = T_{act}\frac{2\pi n_{rpm}}{60} \tag{7}$$

where:

- ω is the angular velocity of the shaft [rad/s];
- n_{rpm} is the shaft speed in revolutions per minute [rpm].

Compact utility platforms and minibuses operate under highly variable thermal cycles due to intensive braking energy recovery and continuous urban idling, which drastically alters oil viscosity and loss characteristics. The internal leakage flow Q_{leak} can be mathematically modeled using the Wilson-based hydraulic loss approach (Giavarini 2022):

$$Q_{leak} = \frac{C_s V_d \Delta p}{\mu} \tag{8}$$

where:

- C_s is the dimensionless laminar leakage coefficient of the radial motor;
- μ is the dynamic viscosity of the hydraulic fluid [Pa·s].

The volumetric efficiency η_v is then formulated as (Giavarini 2022):

$$\eta_v = \frac{Q_{th}}{Q_{act}} = 1 - \frac{Q_{leak}}{Q_{act}} \tag{9}$$

The torque loss T_{loss} comprises both Coulomb (constant) friction and viscous fluid shear friction within the motor housing (Giavarini 2022):

$$T_{loss} = \left(C_f V_d \Delta p\right) + \left(C_v V_d \mu \omega\right) \tag{10}$$

where:

- C_f is the mechanical friction coefficient;
- C_v is the viscous drag coefficient.

Consequently, the total efficiency of the hydraulic drive η_t is expressed as (Giavarini 2022):

$$\eta_t = \eta_v \eta_{hm} = \frac{P_{mech}}{P_{hyd}} \tag{10}$$

After defining the geometric relationships and theoretical flow characteristics within the radial piston hydraulic motor itself, it is necessary to establish a connection between the internal operating parameters of the fluid and the external resistances acting on the vehicles. Since the analyzed hydraulic motor is intended for direct wheel drive, the operating pressure and required fluid power are directly dictated by the road requirements in terms of torque and power. For this reason, a dynamic analysis of the vehicles was carried out below by identifying individual types of friction and resistance to movement that occur in real operating conditions.

Rolling resistance primarily depends on the hysteresis of the tire material, friction due to microslip at the tire-road contact, and friction within the wheel bearing assembly itself. Since the rolling resistance coefficient is affected by a large number of factors (vehicle speed, tire pressure, load, soil characteristics), the following polynomial formulations for force F_{roll}, torque T_{roll}, and power P_{roll} are used to evaluate this resistance at a generic road gradient (Giavarini 2022; Wong, 2008):

$$F_{roll} = m \cdot g \cdot k \cdot \cos\alpha \tag{11}$$

$$T_{roll} = m \cdot g \cdot r_w \cdot k \cdot \cos\alpha \tag{12}$$

$$P_{roll} = m \cdot g \cdot k \cdot v \cdot \cos\alpha \tag{13}$$

where:

- m is total vehicle mass [kg],
- g is acceleration due to gravity [m s^{-2}],
- k is rolling resistance coefficient,
- r_w is wheel radius [m],
- v is truck speed [m/s] and
- α – road gradient [°].

Aerodynamic drag depends on the air density ρ, the vehicle frontal area A_f, the drag coefficient C_f, and the relative speed of the vehicle v_r. Its classical formulation for force, moment, and power is defined by the expressions (Giavarini 2022; Wong, 2008):

$$F_a = \frac{1}{2} \cdot \rho \cdot A_f \cdot C_f \cdot {v_r}^2 \tag{14}$$

$$T_a = \frac{1}{2} \cdot \rho \cdot A_f \cdot C_f \cdot {v_r}^2 \cdot r_w \tag{15}$$

$$P_a = \frac{1}{2} \cdot \rho \cdot A_f \cdot C_f \cdot {v_r}^3 \tag{16}$$

The vehicle frontal area A_f in equations (14—16) represents the projected front surface of the chassis and is determined based on the overall vehicle dimensions using the empirical formulation (Wong, 2008):

$$A_f = W \cdot H \cdot k \tag{20}$$

where:

- W is the overall vehicle width (excluding mirrors) [m],
- H is the overall vehicle height [m], and
- k is the empirical shape factor, which ranges between 0.80 and 0.85 for the considered vehicle classes (commercial vans and light trucks with rounded profiles) [16].

These values are completely independent of the road gradient. When driving on a flat road $\alpha = 0$, the characteristic speed v_c represents the point at which rolling resistance and aerodynamic drag are equal. Due to the speed-level dependence, for all values $v < v_c$ rolling resistance dominates, while at higher speeds aerodynamic drag becomes the dominant factor (Giavarini 2022).

The component of the drag force that directly depends on the angle of inclination of the surface α and the weight of the vehicle is determined through the following system of equations (Giavarini 2022; Wong, 2008):

$$F_s = m \cdot g \cdot \sin\alpha \tag{17}$$

$$T_s = m \cdot g \cdot r_w \cdot \sin\alpha \tag{18}$$

$$P_s = m \cdot g \cdot v \cdot \sin\alpha \tag{19}$$

When achieving acceleration a, the inertial load of the rotating parts must be properly taken into account via the apparent mass of the vehicle m_{app} (Giavarini 2022; Wong, 2008):

$$m_{app} = m + J_{mot} \cdot \frac{{\tau_I}^2}{{r_w}^2} + J_{trans} \cdot \frac{{\tau_{II}}^2}{{r_w}^2} + \frac{J_w}{{r_w}^2} \tag{20}$$

Where J_x represents the moments of inertia of individual rotating elements (engine, transmission and wheels), while τ_I and τ_{II} are the gear ratios between individual subassemblies (in the case of direct in-wheel drive where the hydraulic motor is inside the hub, these gear ratios are 1). The impact of acceleration on the dynamic demands of the vehicle is expressed as (Giavarini 2022; Wong, 2008):

$$F_{app} = m_{app} \cdot a \tag{21}$$

$$M_{app} = m_{app} \cdot a \cdot r_w \tag{22}$$

$$P_{app} = m_{app} \cdot a \cdot v \tag{23}$$

By knowing all the individual resistance components, it is possible to precisely quantify at any time the total required torque and power that the radial piston hydraulic motors must deliver to the vehicle wheels for any defined road driving conditions.

SIMULATION MODEL, RESULTS AND DISCUSSION

To evaluate the hydrostatic powertrain concept for light commercial configurations and tactical transport applications, a comprehensive multi-domain simulation model was established within the *Simcenter Amesim* environment (Siemens Digital Industries Software, 2020). The developed simulation frameworks directly couple the high-pressure hydraulic network with the longitudinal dynamics of two-axle vehicle platforms, with the powertrain topologies structurally differentiated according to the technical designs and specific operational requirements of each vehicle class. Figure 5 illustrates the multi-domain simulation scheme for the lightweight transport vehicle platform.

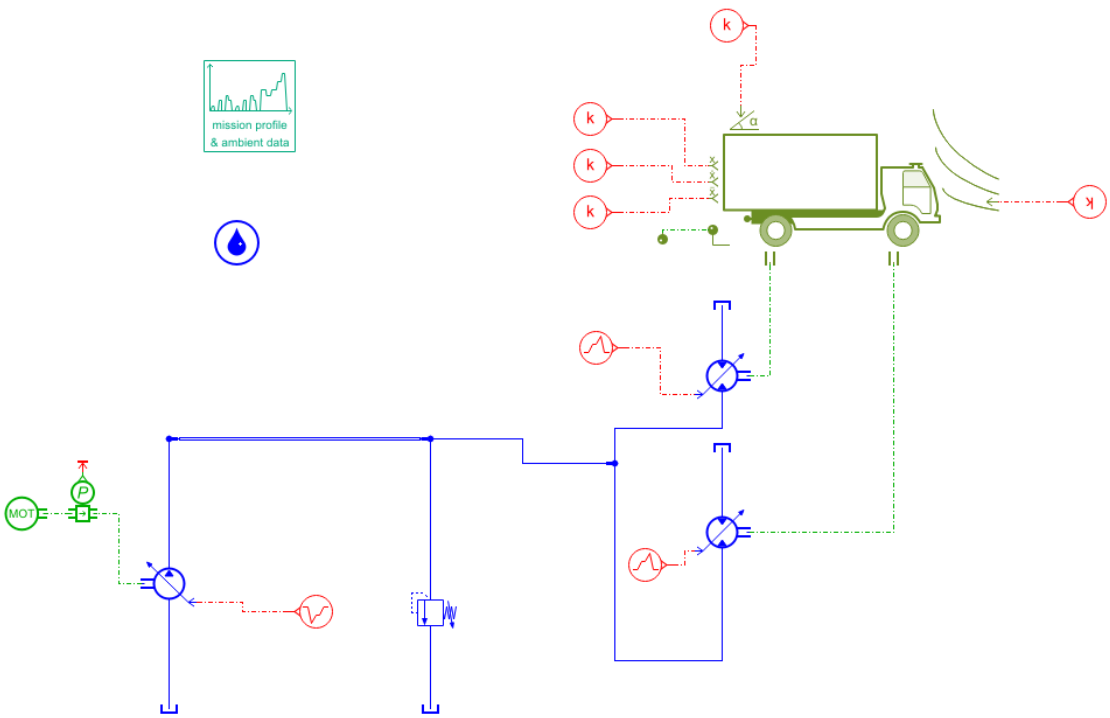

Figure 5 The lightweight transport vehicle drive diagram (Siemens Digital Industries Software, 2020)

The hydrostatic drive layer of both models consists of a primary pump unit that delivers the working fluid under pressure to the radial piston hydraulic motors located in the vehicle wheels. An advanced feature of this multi-domain concept is reflected in the integration of dynamic boundary conditions of the external environment (via a block diagram with k-coefficients), which actively introduces the effects of terrain slope, aerodynamic drag, and variable tire rolling resistance into the calculation. In order to provide a comprehensive analysis and verification under different

operating conditions, simulations were conducted independently. The basic geometric, aerodynamic, and hydraulic parameters implemented in these simulation frameworks are summarized in Table 1 (for the Suzuki Carry DA16T mini-truck) and Table 2 (for the Toyota HiAce V minibus).

Table 1 Operational parameters of the Suzuki Carry DA16T (Carfolio, n.d.; Wong, 2008; Totten & De Negri, 2012)

Quantity	Values	Reference
Total vehicle mass	1100 kg	Vehicle specification (Carfolio, n.d.)
Tire Specification	145/80 - R12 (r = 0.268 m)	Vehicle specification (Carfolio, n.d.)
Prime Mover Speed	2000 rpm	Simulation boundary condition (Siemens Digital Industries Software, 2020)
Engine power	37 [kW]	Standard engine parameter (Carfolio, n.d.)
Pump Displacement	200 [cm^3 rev^{-1}]	Simulation boundary condition (Siemens Digital Industries Software, 2020)
In-Wheel Motors Displacement	125 [cm^3 rev^{-1}]	Simulation boundary condition (Siemens Digital Industries Software, 2020)
Vehicle length	3395 [mm]	Standard vehicle dimensions (Carfolio, n.d.)
Vehicle width	1475 [mm]	Standard vehicle dimensions (Carfolio, n.d.)
Vehicle height	1765 [mm]	Standard vehicle dimensions (Carfolio, n.d.)
Rolling resistance coeficient	0.015	Road condition parameter (Wong, 2008)
Aerodynamic drag coeficient	0.45	Aerodynamic property for this vehicle type (Carfolio, n.d.)
Vehicle frontal area	2 [m^2]	Determined via vehicle geometry (Carfolio, n.d.)
Fluid density	850 [kg m^{-3}]	Hydraulic oil property (Totten & De Negri, 2012)
Dynamic viscosity	51 cP	Hydraulic oil property (Totten & De Negri, 2012)
Road slope	0 %	Flat terrain baseline
Wind velocity	10 [m s^{-1}]	Headwind condition

Table 2 Operational parameters of the Toyota HiAce V (Auto-Data, n.d.; Wong, 2008; Totten & De Negri, 2012)

Quantity	Values	Reference
Total vehicle mass	3100 kg	Vehicle specification (Auto-Data, n.d.)
Tire Specification	185/75 R15 (r = 0.329 m)	Vehicle specification (Auto-Data, n.d.)
Prime Mover Speed	2000 rpm	Simulation boundary condition (Siemens Digital Industries Software, 2020)
Engine power	100 kW	Standard engine parameter (Auto-Data, n.d.)
Pump Displacement	500 [cm^3 rev^{-1}]	Simulation boundary condition (Siemens Digital Industries Software, 2020)
In-Wheel Motors Displacement	250 [cm^3 rev^{-1}]	Simulation boundary condition (Siemens Digital Industries Software, 2020)
Vehicle length	4695 [mm]	Standard vehicle dimensions (Auto-Data, n.d.)
Vehicle width	1695 [mm]	Standard vehicle dimensions (Auto-Data, n.d.)
Vehicle height	1980 [mm]	Standard vehicle dimensions (Auto-Data, n.d.)
Rolling resistance	0.015	Road condition parameter (Wong, 2008)
Aerodynamic drag coeficient	0.38	Aerodynamic property for this vehicle type (Auto-Data, n.d.)
Vehicle frontal area	2.8 [m^2]	Determined via vehicle geometry (Auto-Data, n.d.)
Fluid density	850 [kg m^{-3}]	Hydraulic oil property (Totten & De Negri, 2012)
Dynamic viscosity	51 cP	Hydraulic oil property (Totten & De Negri, 2012)
Road slope	0 %	Flat terrain baseline
Wind velocity	10 [m s^{-1}]	Headwind condition

The headwind velocity of 10 m/s (World Meteorological Organization [WMO], 2021) was adopted as a representative boundary condition for moderate gale testing environment to evaluate the powertrain under demanding ambient

factors. The aerodynamic drag coefficients C_f of 0.45 for the mini-truck and 0.38 for the minibus are selected based on standard empirical vehicle data from the literature for open-bed utility platforms and standard single-volume van profiles, respectively. The dynamic speed response of a light commercial vehicle and a minibus operating under a headwind profile of 10 [m s-1] are shown in Figures 6 and 7.

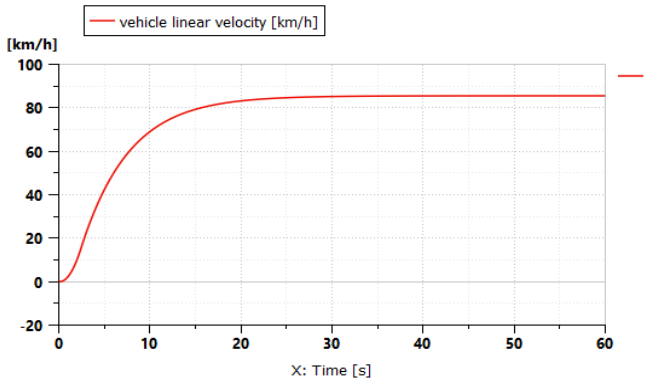

Figure 6 Diagram of simulated mini – truck velocity in 60 s operational cycle (Siemens Digital Industries Software, 2020)

The mini-truck's transient response comprises three distinct operating phases. During the initial activation (0–2 s), the vehicle remains stationary while the prime mover accelerates to 2000 rpm and pilot pressure disengages the spring-applied hydraulically released (SAHR) hub brakes. Once fully released, progressive acceleration begins. The high geometric displacement of the in-wheel radial piston motors generates substantial starting torque, enabling the 1100 kg chassis to overcome static inertia. Due to realistic power and torque limits now imposed on the prime mover, the acceleration curve exhibits a physical, non-linear trend as rolling and aerodynamic resistances scale with speed. Beyond the 25th second of the 60-second cycle, the vehicle reaches a quasi-steady state, asymptotically stabilizing at a maximum cruising velocity of approximately 85 km/h. This updated response validates the drivetrain's capability to deliver realistic transit performance under continuous aerodynamic loading.

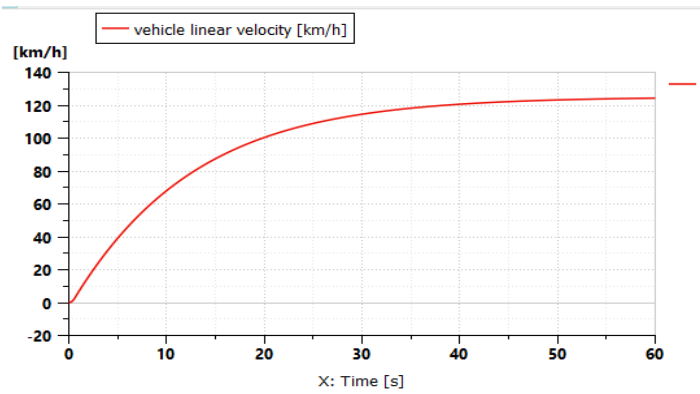

Figure 7 Diagram of simulated minibus velocity in 60s operational cycle (Siemens Digital Industries Software, 2020)

The larger minibus platform exhibits a distinct dynamic behavior due to its significantly higher mass of 3500 kg. While the initial pressure buildup and SAHR brake disengagement require roughly 1.5 seconds, the subsequent acceleration phase demands a greater energy throughput to counteract the increased structural inertia. To sustain velocity buildup under these conditions, the layout utilizes an optimized pump displacement of 500 cm^3/rev feeding the dual 250 cm^3/rev in-wheel motors. The resulting acceleration curve shows a more gradual gradient than the light truck, reflecting the physical impact of realistic prime mover torque limits. As velocity increases, aerodynamic drag—amplified by the larger 2.82 m^2 frontal area—becomes the dominant resistance factor, causing the acceleration to taper off asymptotically. The minibus eventually establishes a steady-state cruise beyond the 55th second, leveling off at 125 km/h. This response validates that the scaled hydrostatic configuration provides sufficient power reserves without violating physical boundaries.

The dynamic torque requirements at the wheel hubs of these vehicles are quantified in Figures 8 and 9.

The transient wheel torque response directly mirrors the vehicle's velocity profile phases. Since the total driving torque is equally distributed among the traction points, the diagram illustrates the localized torque input at a single axle (Port 2). During the initial launch phase (0–2.5 s), the axle torque rapidly escalates to a peak of approximately 580 Nm. This maximum effort is critical to overcome static chassis inertia and counteract the dynamic resistance during SAHR hub brake disengagement. Immediately following this peak, as the vehicle gains velocity, the torque

profile exhibits a smooth exponential decay, marking the transition to steady-state cruising. By the 25th second of the expanded 60-second cycle, the torque stabilizes at a quasi-steady value of approximately 105 Nm. This residual torque represents the continuous mechanical effort required by each in-wheel radial motor to actively balance the combined aerodynamic drag and rolling resistance at maximum cruising speed.

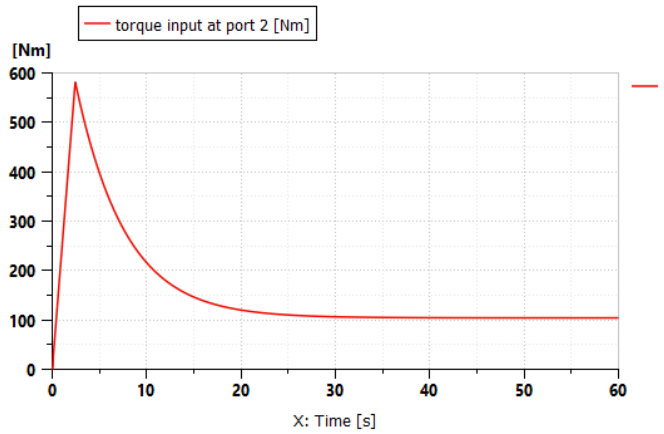

Figure 8 Simulated torque input profile at one axle of the mini – truck (Siemens Digital Industries Software, 2020)

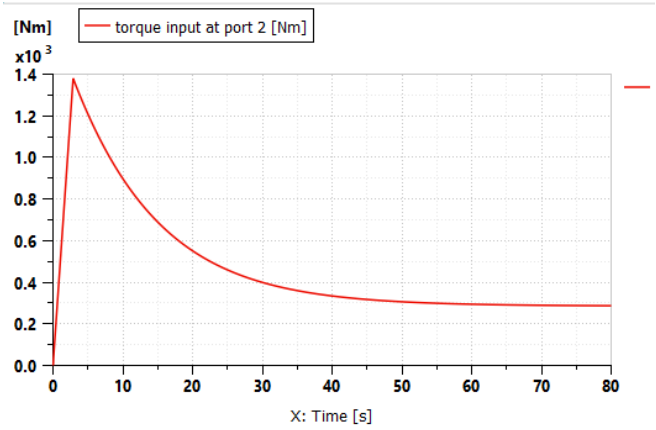

Figure 9 Simulated torque input profile at one axle of the minibus (Siemens Digital Industries Software, 2020)

A similar physical correlation is observed for the heavier minibus platform. At the initial launch point, the single axle torque sharpens dramatically to a peak of approximately 1480 Nm. This higher starting effort is directly dictated by the increased structural inertia of the vehicle operating under realistic prime mover limitations. Following the successful disengagement of the SAHR brakes, the torque profile exhibits a gradual exponential decay as the minibus accumulates momentum, maintaining a steady energy transfer throughout the extended transient regime. By the 55th second, the torque asymptotically levels off at a quasi-steady value of approximately 290 Nm.

Next, diagrams of resistive load of the vehicles are shown in Figures 10 and 11.

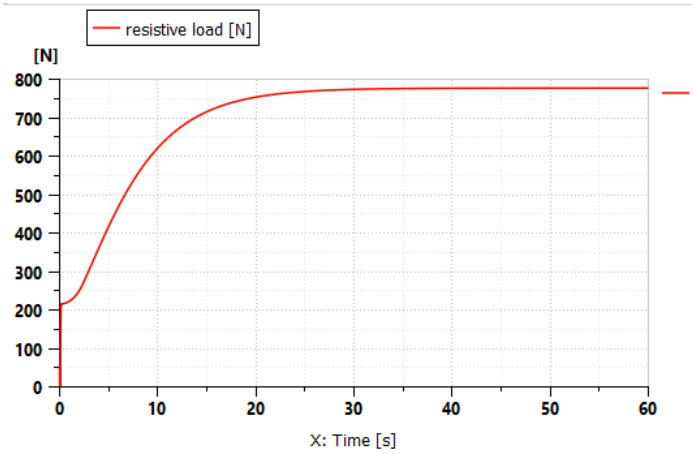

Figure 10 Simulated resistive load of the mini-truck (Siemens Digital Industries Software, 2020)

For the lightweight mini-truck, the resistive load initiates at approximately 214 N during the standstill phase—reflecting the combined baseline of rolling resistance and static headwind drag—before escalating quadratically to an

asymptotic cruising threshold of roughly 775 N. In contrast, the heavier minibus platform exhibits a significantly higher baseline resistance of approximately 500 N due to its 3500 kg chassis, progressively scaling up over an extended transient regime to stabilize at a quasi-steady value of 1732 N. For both vehicle configurations, the non-linear, parabolic progression of the curves accurately validates the quadratic influence of aerodynamic drag as velocity increases, confirming that a precise mechanical and fluid-power equilibrium is established once the maximum cruising limits are reached.

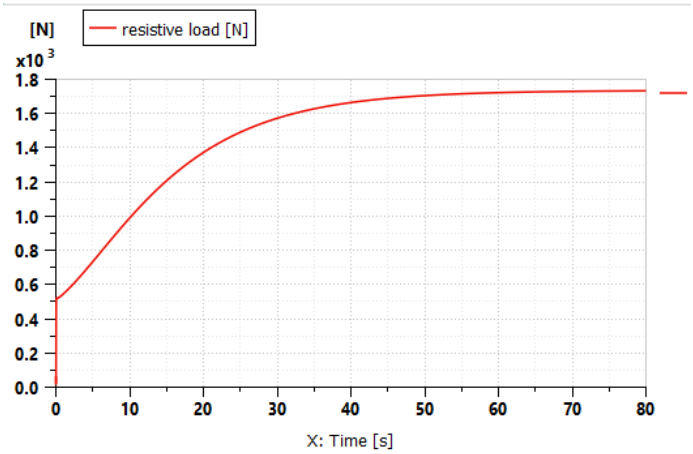

Figure 11 Simulated resistive load of the minibus (Siemens Digital Industries Software, 2020)

The total mechanical power demand delivered by the prime mover are shown in Figures 12 and 13.

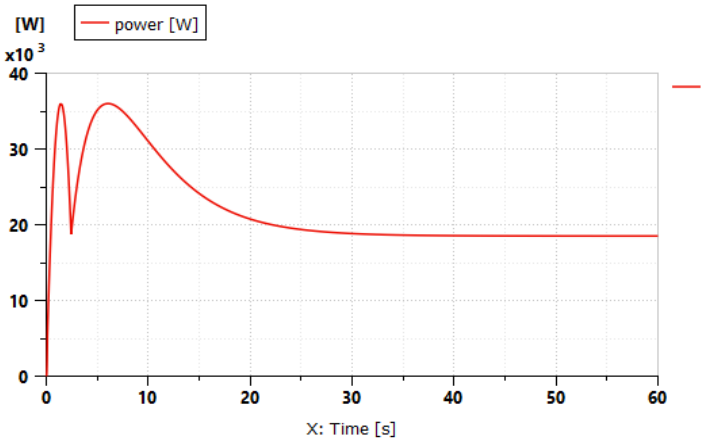

Figure 12 Simulated engine power of the mini-truck (Siemens Digital Industries Software, 2020)

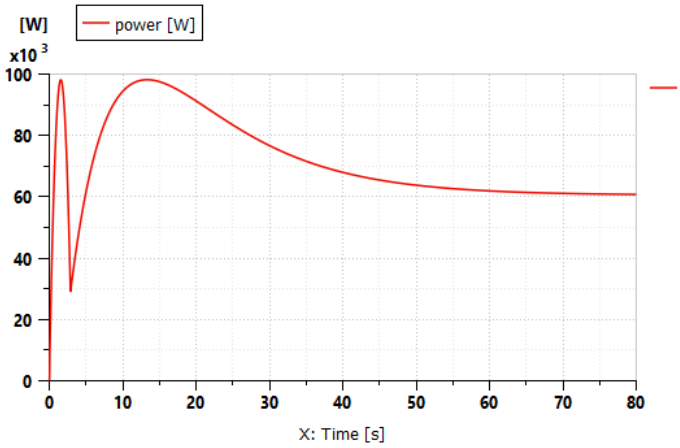

Figure 13 Simulated engine power of the minibus (Siemens Digital Industries Software, 2020)

Both profiles exhibit a highly realistic dual-peak transient behavior directly linked to the operational milestones. The initial sharp peak—reaching approximately 36 kW for the light utility truck and 95 kW for the heavier minibus—corresponds to the intensive energy throughput required to build pilot pressure within the closed hydraulic loops and successfully disengage the SAHR hub brakes. Immediately following this launch phase, a temporary drop occurs as static vehicle inertia is overcome, which is then followed by a secondary broad peak (36 kW and 98 kW, respectively) representing the maximum energy allocation during dynamic acceleration. Beyond the transient regimes, as both platforms establish aerodynamic and mechanical equilibrium, the mechanical power demand asymptotically

stabilizes at constant quasi-steady state values of approximately 18.5 kW for the mini-truck and 61 kW for the minibus.

The effective mechanical power delivered to the vehicle's driving axle is illustrated in Figures 14 and 15.

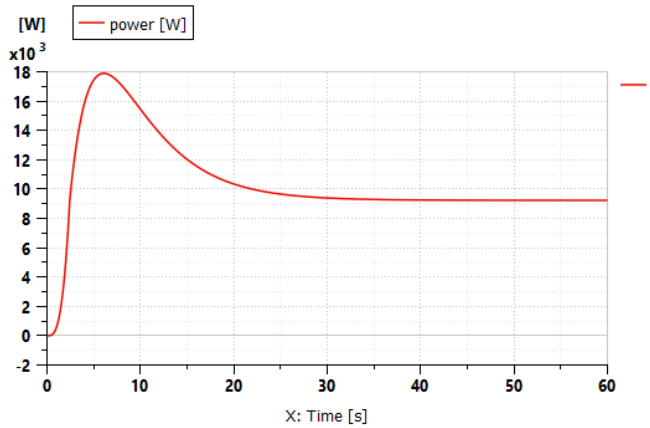

Figure 14 Simulated axle power of the mini-truck (Siemens Digital Industries Software, 2020)

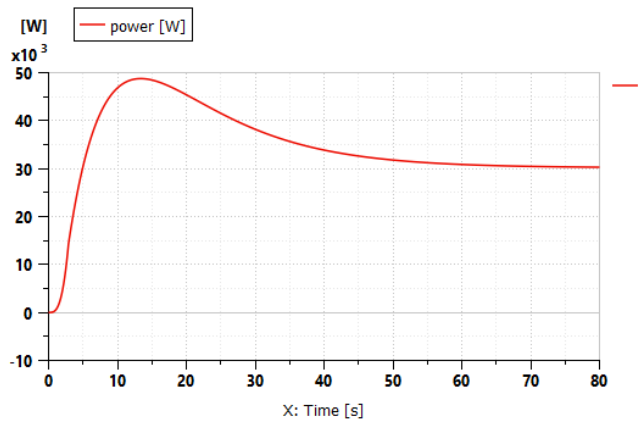

Figure 15 Simulated axle power of the minibus (Siemens Digital Industries Software, 2020)

During the initial standstill interval (0–2 s), the axle power remains at zero for both configurations until the SAHR brakes are fully disengaged. Throughout the intensive acceleration phase, the mini-truck axle power surges to a peak of approximately 18 kW, while the heavier minibus reaches a maximum axle power of 48 kW to overcome its structural inertia. In the steady-state cruising regime, the axle power asymptotically stabilizes at roughly 9.2 kW for the light truck and 30 kW for the minibus. Comparing these traction outputs to the total engine power profiles (Figures 13 and 14) clearly quantifies the dynamic volumetric and mechanical losses within the hydrostatic circuit, providing the required numerical verification for the overall drivetrain efficiency under continuous loading.

To assess operational limitations under severe conditions, a separate simulation evaluates vehicle traction on a steep 4,5° road gradient (8% gradient) (AASHTO, 2018). To ensure a rigorous comparison, all hardware and fluid parameters remain identical to those in Tables 1 and 2. This analysis focuses on how continuous gravity loading alters the drivetrain kinematics, pressure profiles, and volumetric leakage. The results are shown in Figures 16 – 25.

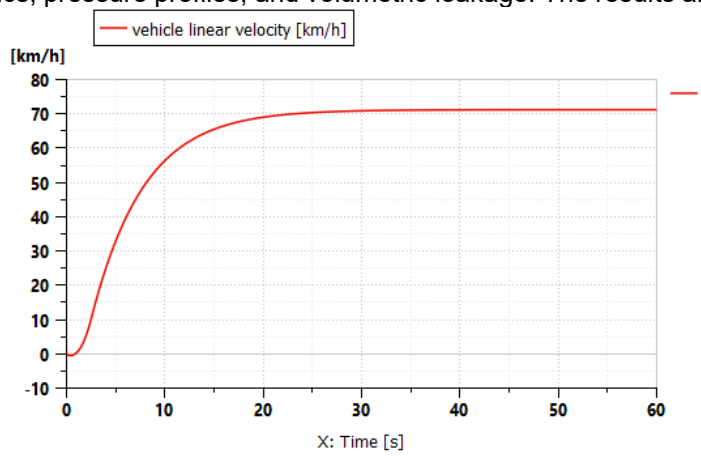

Figure 16 Diagram of simulated mini-truck velocity under the slope of 8% (Siemens Digital Industries Software, 2020)

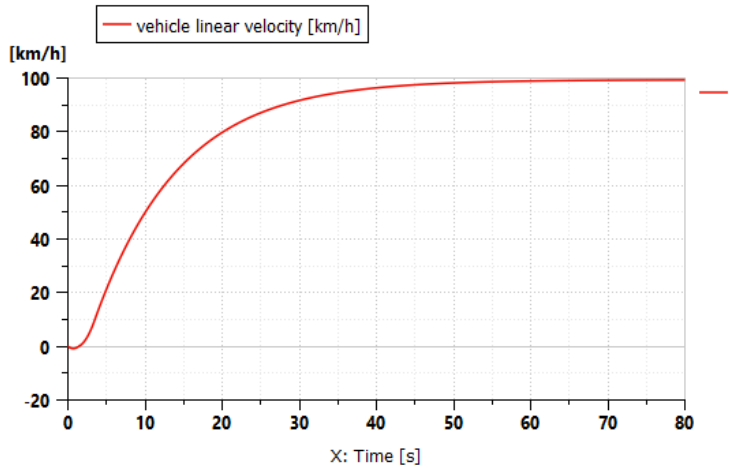

Figure 17 Diagram of simulated minibus velocity under the slope of 8% (Siemens Digital Industries Software, 2020)

Compared to the level road simulations, the introduction of a constant 8% road gradient causes a noticeable drop in the maximum cruising velocities for both platforms due to the continuous gravitational loading. Specifically, the maximum stabilized speed decreases from 85 km/h to approximately 71 km/h for the mini-truck, and from 125 km/h to roughly 97 km/h for the minibus, validating the realistic power limitations of the configured prime mover under steep incline profiles.

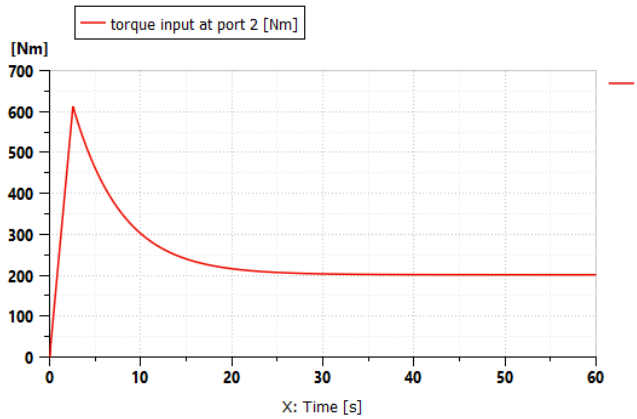

Figure 18 Diagram of simulated mini-truck axle torque under the slope of 8% (Siemens Digital Industries Software, 2020)

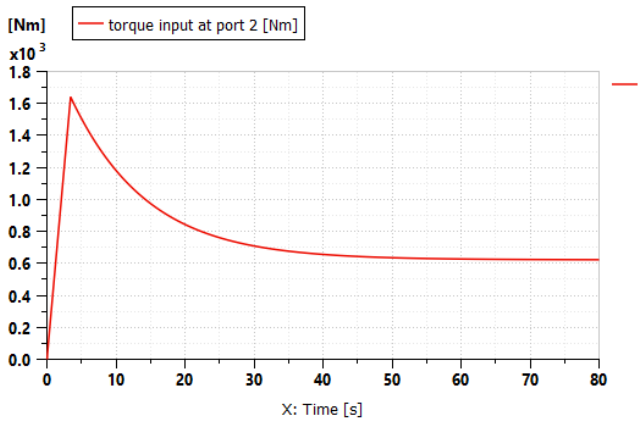

Figure 19 Diagram of simulated minibus axle torque under the slope of 8% (Siemens Digital Industries Software, 2020)

Overcoming the continuous gravity component on the 8% incline forces a substantial upward shift in torque baselines, with the mini-truck requiring a steady-state value of 200 Nm compared to its original 105 Nm level-road baseline. Similarly, the heavier passenger platform demands a much higher continuous cruising effort of approximately 620 Nm, while its launching peak sharpens to 1630 Nm, clearly capturing the severe load conditions now acting on the hydrostatic drive.

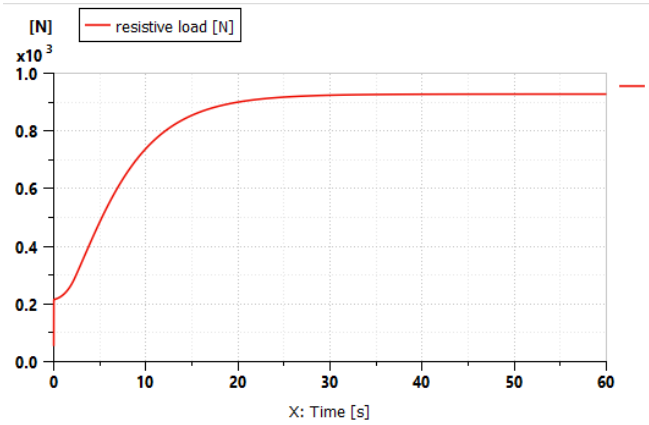

Figure 20 Simulated mini-truck resistive load under the slope of 8% (Siemens Digital Industries Software, 2020)

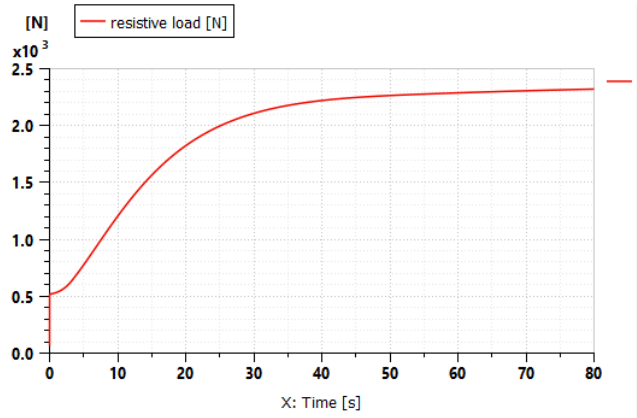

Figure 21 Simulated minibus resistive load under the slope of 8% (Siemens Digital Industries Software, 2020)

A significant amplification in the continuous load profiles is observed as the vehicles transition to the uphill simulation scenario. Cruising at maximum stabilized speeds requires a sustained tractive effort of approximately 930 N for the light utility truck, whereas the heavier passenger platform levels off at a demanding 2300 N. This smooth parabolic growth from the initial static thresholds accurately maps the combined impact of rolling friction, aerodynamic forces, and constant gravity, confirming that the hydrostatic system successfully maintains equilibrium under severe duty conditions.

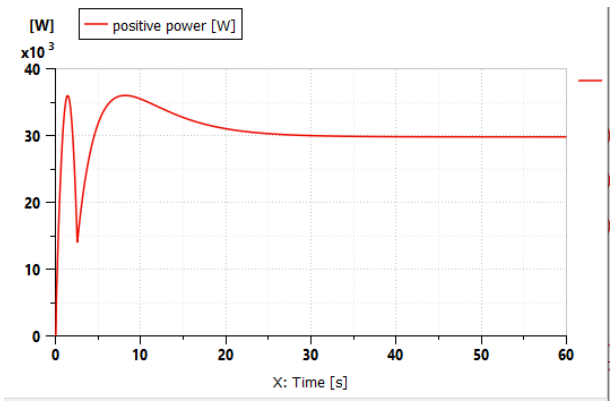

Figure 22 Simulated mini-truck engine power under the slope of 8% (Siemens Digital Industries Software, 2020)

The mechanical power demanded from the prime mover escalates significantly to overcome the combined gravitational and aerodynamic loads during the uphill transit. Both platforms retain the characteristic dual-peak transient distribution, where the initial torque surge for brake disengagement forces a sharp power draw of 36 kW for the light truck and 97 kW for the minibus. Following a brief drop as the static resistance is broken, dynamic acceleration drives a secondary energy peak before the power profiles asymptotically level off at their respective cruise baselines. Due to the constant incline gravity, the final steady-state power requirement locks at 30 kW for the utility vehicle and 94 kW for the passenger platform, successfully demonstrating a rigorous and closed energy balance within the limited boundaries of the HPU submodel.

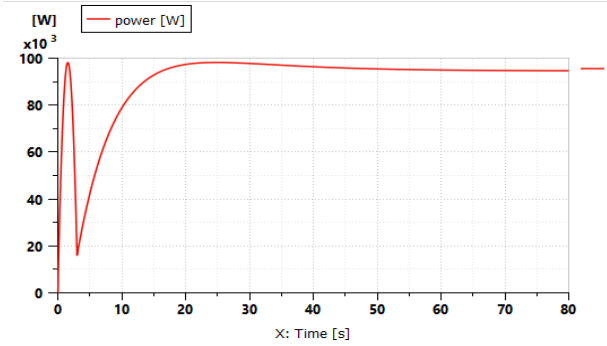

Figure 23 Simulated mini-truck engine power under the slope of 8% (Siemens Digital Industries Software, 2020)

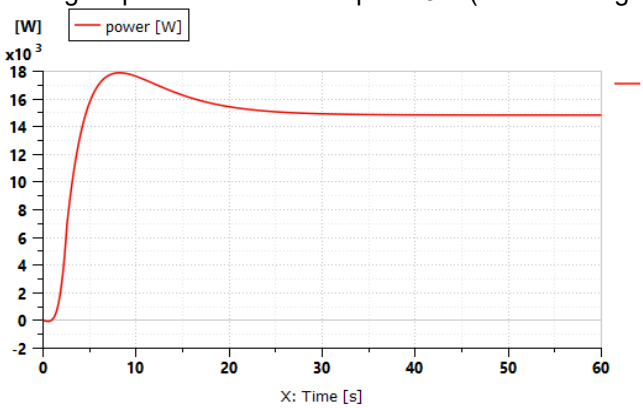

Figure 24 Simulated mini-truck axle power under the slope of 8% (Siemens Digital Industries Software, 2020)

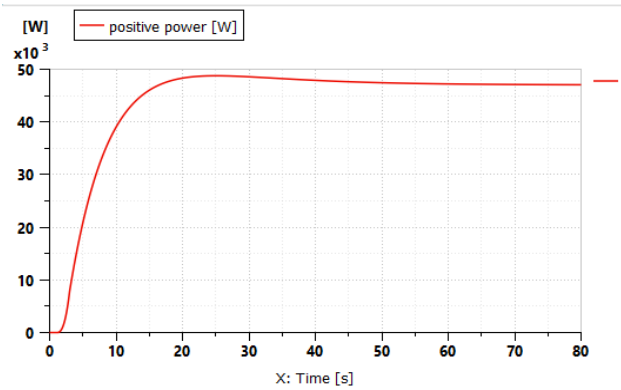

Figure 25 Simulated minibus axle power under the slope of 8% (Siemens Digital Industries Software, 2020)

The mini-truck axle power levels off at approximately 15 kW after overcoming a transient acceleration peak of 18 kW. Conversely, the more massive passenger platform requires a far higher continuous traction output of roughly 47 kW, stabilizing smoothly after a transient peak of 48.5 kW. These elevated thresholds represent a substantial increase from the respective level-road baselines of 9.2 kW and 30 kW, directly quantifying the additional tractive power required to counteract gravitational resistance.

Overall, the obtained simulation results demonstrate that the proposed hydrostatic drivetrain is capable of providing the required vehicle motion under both level-road and inclined-road operating conditions. The developed multi-domain models provide a suitable basis for evaluating the dynamic behaviour of the investigated configurations and for further optimization of the main hydrostatic drivetrain parameters.

CONCLUSIONS

In this work, a vehicle propulsion system concept based on the application of a multi-stroke radial piston hydraulic motor as an alternative solution for light utility vehicles and minibuses was successfully analysed and numerically evaluated. Through the development of a mathematical and multi-domain simulation model in the Simcenter Amesim environment, the power transmission characteristics, torque generation, and dynamic response of the vehicle under representative operating conditions were investigated, including the effects of headwind and road gradient.

The updated simulation results confirm the physical feasibility of the proposed hydrostatic propulsion system under realistic prime mover power limitations. For the light utility truck, the system achieved a maximum steady-state velocity of 85 km/h on a level road, with an individual wheel starting torque peak of approximately 580 Nm. For the heavier minibus platform, configured with an optimized pump displacement of 500 cm³/rev, the system achieved a steady-state velocity of 125 km/h on level terrain and developed a peak single-hub launch torque of approximately 1480 Nm, demonstrating the high-torque low-speed (HTLS) characteristics of the proposed drive. Furthermore, simulations under an 8% road gradient demonstrated the expected performance reduction caused by continuous gravitational loading, with steady-state velocities decreasing to approximately 71 km/h for the light utility truck and 97 km/h for the minibus, respectively. The calculated overall powertrain efficiency stabilized at approximately 49–50% during steady-state cruising for both vehicle configurations, representing the ratio between the mechanical power delivered to the driving axles and the hydraulic power supplied to the powertrain.

Compared with conventional mechanical drivetrains, which generally provide higher transmission efficiencies at high vehicle speeds but require stepped gearboxes, cardan shafts, differentials, and associated mechanical components, the proposed decentralized hydrostatic concept eliminates the need for these elements at the wheel ends. This architecture provides greater freedom for packaging, including potential low-floor integration in minibuses, while enabling continuously variable transmission characteristics without discrete gear shifts. Compared with battery electric vehicle (BEV) architectures, which generally provide higher drivetrain energy efficiency, the proposed hydrostatic system offers high torque density and favourable torque-to-weight characteristics, making it particularly attractive for heavy-duty and low-speed utility applications where compact and continuously controllable high-torque propulsion is required.

Future research will focus on further optimization of volumetric efficiency and leakage-related parameters, investigation of the thermal behaviour of the hydraulic fluid under prolonged loading, and experimental validation of the developed simulation model on a physical vehicle prototype.

REFERENCES

Abaitancei, H., Radu, S., Muntean, B., Irmia, C. (2016). Multi-domain and durability analysis of a hybrid hydraulic vehicle, *Applied Mechanics and Materials*, 823, 217-222. https://doi.org/10.4028/www.scientific.net/AMM.823.217

American Association of State Highway and Transportation Officials (AASHTO), 2018. *A Policy on Geometric Design of Highways and Streets* (7th ed.). AASHTO, Washington, DC.

Auto-Data. (n.d.). Vehicle technical specifications. Retrieved from auto-data.net

Bašta, T. M. (1986). *Mechanical hydraulics*, Faculty of mechanics, Belgrade.

Carfolio. (n.d.). *Automobile specifications and characteristics*. Retrieved from carfolio.com

Dindorf, R. (2024). Functional safety of the hydraulic drive control system of a tracked undercarriage. *The Archives of Automotive Engineering - Archiwum Motoryzacji*, 103(1), 21-37. https://doi.org/10.14669/AM/178310

Giavarini, F. (2022). *Analysis and Simulation of a Radial Piston Hydraulic Motor* [Master's thesis, Politecnico di Torino]

Guzzella, L. & Sciarretta, A. (2005). *Vehicle propulsion systems: Introduction to modeling and optimization* (2. ed.). ETH Zurich. https://doi.org/10.1007/3-540-28853-8

Krstić, B. (2003). *Hidrodinamički prenosnici snage u agregatima motornih vozila* [Hydrodynamic power transmitters in motor vehicle units] (Monograph). Faculty of mechanics, Kragujevac.

Li, C., Jiang, T., Liu, C., Xu, H., & Shi, G. (2024). Investigation of the leakage in the flow distribution pair of radial piston hydraulic motors through CFD analysis and experiments. Flow Measurement and Instrumentation, 96 102555. https://doi.org/10.1016/j.flowmeasinst.2024.102555

Mannesmann R. (1998). *Hydrostatic transmissions for wheeled and tracked vehicles*. Technical Handbook, Rexroth Hydraulics.

Popovici, V., Grigoras, I. R., Rakosi, E., Ulian, T. M., Manolache, G., Popa, A. G., & Petrovan, S. (2026). A new approach to in-wheel motor solutions for electric vehicles. *World Electric Vehicle Journal*, 17(2), 87. https://doi.org/10.3390/wevj17020087

Savić, V. (1986). *Oil hydraulics, hydraulic components and systems*, Zenica.

Simcenter Amesim, Siemens Digital Industries Software, 2020.

Sonale balu. (2024). *Understanding how a tracked vehicle works.*

Tanaka, K., Okazaki, T., & Urabe, T. (2013, 6-9 October). Comparative study on dynamic characteristics of hydraulic, pneumatic and electric motors. *Proceedings of the ASME/BATH 2013 Symposium on Fluid Power and Motion Control. ASME/BATH 2013 Symposium on Fluid Power and Motion Control.* Sarasota, Florida, USA. https://doi.org/10.1115/FPMC2013-4459

Totten, G. E., & De Negri, V. J. (Eds.). (2012). Handbook of Hydraulic Fluid Technology (2nd ed.). CRC Press.

Wong, J. Y. (2008). *Theory of ground vehicles* (4th ed.). John Wiley & Sons.

World Meteorological Organization. (2021). *Manual on Codes (The Beaufort Wind Scale)*. Geneva, Switzerland: WMO.

The 11th International Congress
Motor Vehicles & Motors 2026
Kragujevac, Serbia
October 8th-9th, 2026

Motor Vehicles & Motors

MVM2026-036
https://doi.org/10.24874/CMVM2026.036
Original scientific paper

Marko Kitanović[1]
Slobodan Popović[2]
Nenad Miljić[3]
Predrag Mrđa[4]

EFFECTIVE MIXTURE COMPOSITION IN THE ANGULAR DOMAIN IN SUPERCHARGED DISI ENGINE WITH MULTIPLE INJECTIONS

ABSTRACT: To analyse and optimize the mixture formation process in a direct-injection spark-ignition (DISI) engine, a numerical simulation was developed based on models for fuel injection, primary and secondary liquid fuel breakup and evaporation. The main objective is to assess the state of the air-fuel mixture and level of homogenisation prior to combustion – a factor influencing heat release rate and pollutant formation. High pressure injector was modelled using Bernoulli equation combined with discharge coefficient model by von Kuensberg-Sarre. The Wave-Breakup Model was applied to primary breakup, followed by for secondary breakup simulation based on Arcoumanis model. Breakup time parameters were derived from the breakup models. Sauter Mean Diameters (SMD) of the resulting atomized droplets were simulated using Chi-Squared distribution. As a reference, evaporation was simulated for single injection, followed by comparative study of double injection strategies. Analysis covered the effect of split injection ratios with fixed start of injection (SOI) and fixed end of injection (EOI) angles, respectively. A double injection strategy increases the mass of unevaporated fuel at start of combustion. The study demonstrates that fuel evaporation can be optimized through multiple injection strategies, depending on whether the start or end of injection is fixed.

KEYWORDS: direct injection spark ignition engine, fuel injection, fuel split ratio, spray breakup, fuel evaporation

[1] *Marko Kitanović, PhD, assistant professor, University of Belgrade, IC Engines Dept., Kraljice Marije 16, Belgrade, Serbia, mkitanovic@mas.bg.ac.rs, https://orcid.org/0000-0002-3931-802X*
[2] *Slobodan Popović, PhD, associate professor, University of Belgrade, IC Engines Dept., Kraljice Marije 16, Belgrade, Serbia, spopovic@mas.bg.ac.rs, https://orcid.org/0000-0002-6332-9589*
[3] *Nenad Miljić, PhD, associate professor, University of Belgrade, IC Engines Dept., Kraljice Marije 16, Belgrade, Serbia, mkitanovic@mas.bg.ac.rs, nmiljic@mas.bg.ac.rs, https://orcid.org/0000-0003-3564-0203*
[4] *Predrag Mrđa, PhD, associate professor, University of Belgrade, IC Engines Dept., Kraljice Marije 16, Belgrade, Serbia, mkitanovic@mas.bg.ac.rs, pmrdja@mas.bg.ac.rs, https://orcid.org/0000-0001-5534-6322*

SASTAV SMEŠE U UGAONOM DOMENU KOD NATPUNJENOG BENZINSKOG MOTORA SA VIŠESTRUKIM DIREKTNIM UBRIZGAVANJEM GORIVA

REZIME: Da bi se analizirao i optimizovao proces obrazovanja smeše u benzinskom motoru sa direktnim ubrizgavanjem, razvijena je numerička simulacija zasnovana na modelima za ubrizgavanje goriva, primarni i sekundarni raspad i isparavanje kapljice. Glavni cilj je procena stanja smeše vazduh-gorivo i nivoa homogenizacije pre početka sagorevanja – faktora koji utiču na brzinu oslobađanja toplote i emisiju toksičnih komponenata. Brizgač je modeliran korišćenjem Bernulijeve jednačine u kombinaciji sa modelom za koeficijent pražnjenja mlaznice fon Kuensberg-Sarea. Model Wave-Breakup je primenjen za primarni raspad mlaza, dok je sekundarni raspad proračunat Arkumanisovim modelom. Vremena raspada izvedena su iz modela primarnog i sekundarnog raspada. Sauterov srednji prečnik (SMD) kapljica simulirani su korišćenjem Hi-kvadrat raspodele. Kao referentni slučaj, isparavanje je simulirano za jednostruko ubrizgavanje. Uporednom analizom obuhvaćeno je dvostruko ubrizgavanje i efekat raspodele goriva za pojedinačna ubrizgavanja sa fiksnim uglovima početka ubrizgavanja (UPU) i fiksnim uglovima kraja ubrizgavanja (UKU). Dvostruko ubrizgavanje, očekivano, povećava masu goriva u tečnom stanju na početku sagorevanja. Studija pokazuje da se isparavanje goriva može optimizovati kroz strategiju višestrukog ubrizgavanja, u zavisnosti od toga da li je definisan početak ili kraj ubrizgavanja..

KLJUČNE REČI: benzinski motor sa direktnim ubrizgavanjem, ubrizgavanje goriva, odnos mase goriva za pojedinačna ubrizgavanja, raspad mlaza, isparavanje goriva

INTRODUCTION

Downsizing and downspeeding represent the mainstream technologies in gaining fuel efficiency and low pollutant emissions in internal combustion engines (ICE). Supercharging, particularly high-pressure turbocharging, followed by ever increasing compression ratios as the basic presumption of high efficiency ICE process prevail today in modern design concepts. In combustion of homogenous charge pre-ignition and knocking combustion seem to be more challenging to solve than ever before. Transition from homogenous charge, or more precisely – charge of higher level of homogenisation, to charge of lower degree of homogenisation, namely stratified charge, proved to be the answer for concept more resilient to irregular combustion in SI ICE. This, in case of direct injection (DI) involves the implementation of number of advanced strategies of multiple fuel injections per engine cycle, referred to as split injection (Han et al. 2020).

Advantages are few to refer. Injection in early intake stage provides, in the most general form, highly homogenised lean mixture resistant to pre-ignition, while the second one (and subsequent if exists) during compression phase provides more focused enrichment within the narrow area around the spark plug, stabilizing the ignition and the flame in the early stage of combustion. From the fuel mixture formation standpoint, proper injection strategy focusing on positive effect of gas density on fuel spray penetration enables fuel to be delivered during the late compression phase, minimizing wall wetting and piston surface evaporation (Stiesch, G. et al. 2001). Combustion duration can be shortened, the knock limit extended, while in lean and low-temperature combustion (L-LTC) concepts, charge stratification can be achieved with improved ignition stability. Short and generally insufficient time for complete evaporation of the fuel delivered in compression phase, leads to compromised or poor air-fuel mixture homogenisation leading further to increased THC and soot emission (Park et al. 2011).

This study focuses on this important aspect of complex injection strategy in DISI ICE through development of reasonably simple and computationally efficient simulation method for evaluating the mixture composition up to the onset of combustion. The mathematical models governing the injection process, including primary and secondary breakup, atomization, and evaporation phenomena are presented. Single and double injection strategies for several split ratios are analysed using the model simulation, and conclusions referring to split ratio and injection phasing were drawn based on the observed trends.

SIMULATION MODELS

The simulation model used in this study comprises the number of mathematical sub-models covering fuel injection process, primary and secondary breakup, and fuel evaporation. Governing equations were introduced and explained in detail followed by the approximation models for the temperature-pressure dependant gasoline properties and high-pressure gasoline direct injector (HP-GDI) used in simulation.

Fuel injection velocity and fuel spray model

Figure 1 illustrates a typical fuel injection event, presenting the electrical current signal and timing signal during the injection process. The injection process starts when the injector coil becomes energized, causing the needle to move off the seat after a brief delay. The fuel injection rate increases, gradually reaching its maximum value (dependent on the operating conditions) and remains fairly constant before the injector is switched off which is followed by gradual flow decrease during needle move back to the seat.

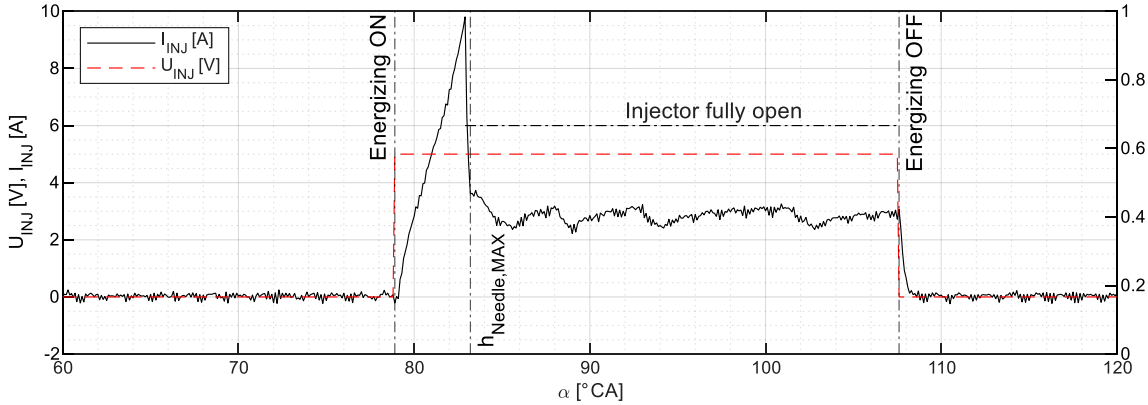

Figure 1 Typical injection event operating variables: electrical current and timing signal

The fuel injection velocity can be approximated using the expression, based on Bernoulli's equation valid only for quasi-stationary, incompressible and one-dimensional flow conditions. If pressure drop in high-pressure line and injector itself is neglected ($p_{F,rail}$), and pressure of fuel on nozzle outlet assumed equal to the charge pressure in combustion chamber (p_{gas}), further simplification can be achieved, and compensated in accuracy for real conditions by introduction of nozzle discharge coefficient (C_D):

$$u_{inj} = C_D \cdot \sqrt{\frac{2 \cdot \Delta p}{\rho_F}} = \sqrt{\frac{2 \cdot (p_{F,inj} - p_{F,cyl})}{\rho_F}} \approx \sqrt{\frac{2 \cdot (p_{F,rail} - p_{gas})}{\rho_F}} \tag{1}$$

Hence, the fuel mass flow through the injector nozzle can be modelled by the following equation:

$$\dot{m}_{inj} = A_N \cdot \rho_F \cdot u_{inj} = \pi \cdot {D_N}^2 \cdot C_D \cdot \sqrt{\frac{\rho_F \cdot (p_{F,rail} - p_{gas})}{8}} \tag{2}$$

Discharge coefficient can be modelled by a several empirical or semiempirical equations. Basic and well documented widely used approach for general application and injector nozzle flow as well is model of Lichtarowicz (Lichtarowicz et al., 1965), however for the low-cavitation nozzle design, phenomenological model developed by von Kuensberg-Sarre (Sarre et al., 1999) specifically for high-pressure diesel injector flows. This model, yet simple, accounts for injector nozzle geometry related losses (inlet nozzle radius and nozzle length) and friction losses related to injection pressure and combustion chamber conditions (injection velocity, Reynolds number):

$$C_D\left(Re, \frac{r_{0N}}{D_N}, \frac{L_N}{D_N}\right) = \frac{1}{\sqrt{\xi_r + f \cdot \frac{L_N}{D_N} + 1}} \tag{3}$$

Nozzle inlet loss coefficient is available in literature for general application (Desantes et al. 2016; Idelchik, 2008) as a function of inlet radius and given in tabular form. Instead, polynomial approximation of tabulated data is given in following form:

$$\xi_r = \sum_{i=0}^{4} a_i \cdot \left(\frac{r_{0N}}{D_N}\right)^i \tag{4}$$

Nozzle wall friction coefficient is calculated using the Blasius' criteria:

$$f = \max\left(\frac{0{,}316}{Re^{0.25}}, \frac{64}{Re}\right) \tag{5}$$

Simple iterative calculation is performed to determine the discharge coefficient throughout the entire injection event. The technical details of the fuel injector used in the simulation models are given in Table 1. Figure 2 depicts the discharge coefficient vs. Reynolds number for flow conditions in considered in experiment. Values were calculated using general model by Lichtarovicz and model by von Kuensberg-Sarre considering several nozzle inlet radius values. Differences are visible in low Reynold number range related to injector opening and closing phases and some increase related to improved flow conditions in nozzle channel for applied nozzle inlet R-chamfering. Model by von Kuensberg-Sarre expectedly introduces discontinuity as a consequence of applied Blasius criteria, and for smooth transition necessary for calculation, results were approximated by a logistic sigmoid function.

Table 1 Fuel injector parameters

Parameter	**Value**
Number of injector orifices	6
Nozzle diameter	$D_N = 180 \cdot 10^{-6}\ m$
Nozzle length	$L_N = 4 \cdot D_N$
Nozzle inlet radius	$r_{0N} = 15\ \cdot 10^{-6}\ m$
Needle rising time	$NRT = 0.45\ \cdot 10^{-3}\ s$

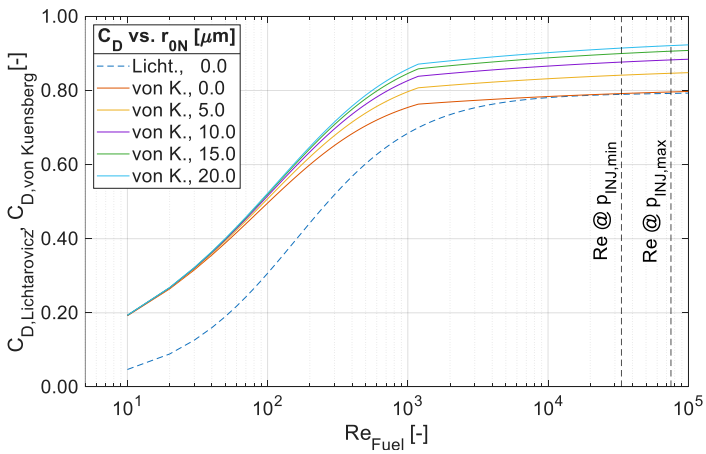

Figure 2 Influence of nozzle inlet radius on nozzle discharge coefficient calculated for expected Reynolds number range (models Lichtarovich and von Kuensberg-Sarre)

Models for fuel properties

Density variation against the temperature for pure gasoline and range of gasoline–butanol blends are well documented by Trost (Trost et al. 2021). For pure gasoline, expression is given in general exponential form against reference pressure and temperature:

$$\rho(p_0, T) = \rho(p_o, T_0) \cdot e^{b \cdot T} \tag{6}$$

The isothermal bulk modulus can be calculated using Klaus – O'Brien correlations (Klaus & O'Brien, 1964). First, bulk modulus at reference temperature is calculated for given pressure, considering known bulk modulus for reference pressure:

$$k_T(p, T_0) = k_T(p_0, T_0) + 5.30 \cdot p \tag{7}$$

Considering bulk modulus dependence against temperature, second correlation enables calculation of bulk modulus at given pressure and temperature:

$$\log\left[\frac{k_T(p, T_0)}{k_T(p, T)}\right] = B(p) \cdot (T - T_0) \quad \Rightarrow \quad k_T(p, T) = \frac{k_T(p, T_0)}{exp[B(p) \cdot (T - T_0)]} \tag{8}$$

Finally, the fuel density for given pressure and temperature is calculated combining equations of Trost and Klaus:

$$\rho(p,T) = \rho(p_0,T_0) \cdot \left[1 + \frac{p-p_0}{k_T(p,T)}\right] \tag{9}$$

The fuel viscosity against temperature is modelled using the Vogel–Fulcher–Tammann–Hesse (VFTH) exponential correlation equation, considering known viscosity at reference pressure and temperature:

$$\mu(p_0,T) = \mu(p_0,T_0) \cdot exp\left(\frac{b}{c+T}\right) \tag{10}$$

Correction for pressure is given in general exponential form by Barus:

$$\mu(p,T) = \mu(p_0,T_0) \cdot exp[\alpha(p,T) \cdot p] \tag{11}$$

Piezocoefficient is considered to change with both pressure and temperature, however for the temperature range in case of injection event, the influence of temperature can be neglected, yielding final form of expression:

$$\mu(p,T) = \mu(p_0,T) \cdot exp(\alpha \cdot p) \tag{12}$$

Coefficients used in equations (6), (8) and (11) could be found in literature (Arkoudeas, 2022; Klaus & O'Brien, 1964; Trost et al. 2021).

Primary and secondary breakup

The graphic macro interpretation of the fuel spray geometry is presented in Figure 3. Two distinct mechanisms of the liquid fuel breakup into ligaments and droplets are recognized (Stiesch, G., et al., 2001). The first one appears at very injection nozzle orifice or in its proximity and is referred as the primary breakup. During this process, usually initiated in the very nozzle channel by the cavitation onset, the intact liquid phase is disintegrated into ligaments and droplets. This process is presented in Figure 4. Initially formed droplets, whose size is considerably large and usually comparable to the nominal nozzle diameter, undergo additional deformation and fragmentation, resulting in the formation of smaller droplets being subsequently entrained by the surrounding air. This process, referred as the secondary breakup, will be discussed in the next section.

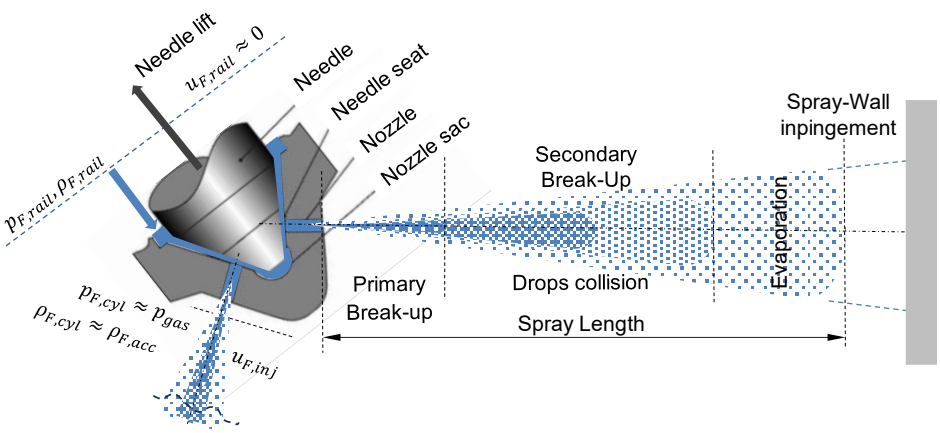

Figure 3 Macro interpretation of the fuel spray geometry

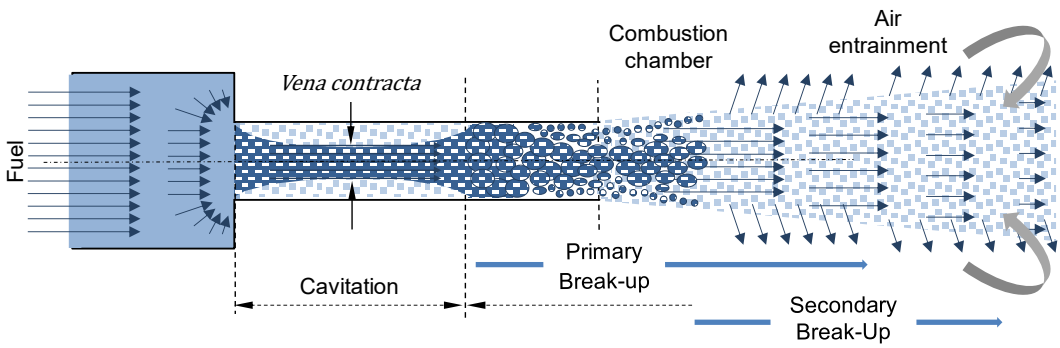

Figure 4 Graphic interpretation of primary and secondary breakup

Primary Breakup

The Wave-Breakup Model (WBM) presented by Reitz (Baumgarten, C., 2006; Reitz, R. D., 1987; Stiesch, 2003) is used to simulate the primary breakup. According to Reitz, primary breakup mechanism considers development and growth of small surface disturbances caused by the aerodynamic forces and viscous friction acting on the injected liquid jet. A simplified schematic of the primary jet breakup according to the WBM is presented in Figure 5.

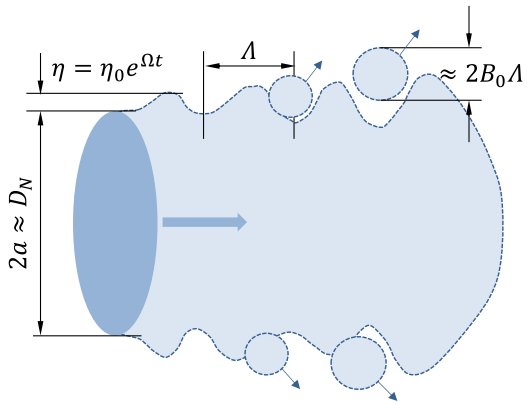

Figure 5 Representation of primary breakup in the WBM by way of surface perturbation growth

The liquid jet is approximated by cylindrical form whose size corresponds to nominal nozzle diameter, the flow is considered quasi-stationary and the gas in combustion chamber incompressible. The liquid surface is initially disturbed by small perturbations characterised by the amplitude η and by the range of wavelengths λ. The amplitudes of these disturbances, initiated by internal nozzle flow effects such as turbulence, friction and often by the cavitation, start to grow exponentially once the liquid comes into interaction with the surrounding gas (air), while the growth rate is described by the complex value ω. Based on the assumption that only the fastest growing perturbation ultimately leads to breakup, the fastest growth rate Ω, and its corresponding wavelength Λ are considered for calculation of the droplet diameter produced by the primary breakup:

$$\frac{\Lambda}{a} = 9{,}02 \cdot \frac{(1 + 0{,}45 \cdot Oh^{0{,}5}) \cdot \left(1 + 0{,}4 \cdot Ca^{*0{,}7}\right)}{\left(1 + 0{,}87 \cdot We_g^{1{,}67}\right)^{0{,}6}} \tag{13}$$

$$\Omega \left(\frac{\rho_F \cdot a^3}{\sigma_F}\right)^{0{,}5} = \frac{0{,}34 + 0{,}38 \cdot We_g^{1{,}5}}{(1 + Oh)\left(1 + 1{,}4 \cdot Ca^{*0{,}6}\right)} \tag{14}$$

Parameters, namely Ohnesorge number, gas Weber number, liquid Weber number, liquid Reynolds number and modified capillary number are presented in following equations:

$$Oh = \frac{We_l^{0.5}}{Re_l} \tag{15}$$

$$We_g = \rho_{cyl} \cdot {u_{inj}}^2 \cdot \frac{a}{\sigma_F} = \rho_{cyl} \cdot {u_{inj}}^2 \cdot \frac{0.5 \cdot D_N}{\sigma_F} \tag{16}$$

$$We_l = \rho_F \cdot {u_{inj}}^2 \cdot \frac{a}{\sigma_F} = \rho_F \cdot {u_{inj}}^2 \cdot \frac{0.5 \cdot D_N}{\sigma_F} \tag{17}$$

$$Re_l = \frac{u_{inj} \cdot a}{\nu_F} = \rho_F \cdot \frac{u_{inj} \cdot 0.5 \cdot D_N}{\mu_F} \tag{18}$$

$$Ca^* = Oh \cdot We_g^{0.5} = \sqrt{\frac{\rho_{cyl}}{\rho_F}} \cdot \frac{u_{inj} \cdot \mu_F}{\sigma_F} = \sqrt{\frac{\rho_{cyl}}{\rho_F}} \cdot Ca_F \tag{19}$$

Critical droplet diameter is evaluated according to Reitz as linear function of critical wavelength Λ:

$$D_{BU,1,crit} \approx 2 \cdot B_0 \cdot \Lambda \quad (B_0 = 0.61) \tag{20}$$

Depending on flow conditions, critical droplet diameter, being a complex function of flow conditions, is further compared to nominal nozzle diameter as to gain final assessment of the droplet diameter in the primary breakup:

$$D_{BU,1} = \begin{cases} D_{BU,1,crit}, & D_{BU,1,crit} < D_N \\ min \begin{cases} 2 \cdot \left(\frac{3 \cdot \pi \cdot a^2 \cdot u}{8 \cdot \Omega}\right)^{+0,33} \\ 2 \cdot \left(\frac{3 \cdot a^2 \cdot \Lambda}{16}\right)^{+0,33} \end{cases}, & D_{BU,1,crit} \geq D_N \end{cases} \tag{21}$$

Secondary Breakup

The secondary breakup is represented as disintegration of droplets into smaller ones caused by aerodynamic forces resulting from the relative velocity between the droplet and the surrounding gas. Surface tension opposes to this process, maintaining the droplet spherical shape and resisting deformation. This is characterized by the gas-phase Weber number, quantifying the ratio of aerodynamic to surface tension forces. Expectedly, from the nature of the process, smaller droplets, being compact, require greater relative velocities for breakup. Experimental studies have shown that different breakup modes and mechanisms emerge depending on the Weber number.

Arcoumanis (Arcoumanis, C. et al. 1997) compiled experimental findings from available experimental studies and integrated into phenomenological model which is here used to simulate the secondary breakup of fuel droplets.

Seven distinct droplet breakup modes are referenced in the study, each characterized Weber number range and empirical relationship that describes the resulting Sauter Mean Diameters (SMD) and breakup times. These breakup modes are listed in Table 2. For the vibrational, bag and bag and stamen breakup modes, the SMD was found dependent on the primary breakup fuel drop diameter and the gas-phase Weber number:

$$SMD = \frac{4 \cdot D_{BU,1}}{4 + 0.5 \cdot \left(1 + 0.19 \cdot \sqrt{We_g}\right)} \tag{22}$$

and for the remaining four modes, the SMD is given in following expression:

$$SMD = 6.2 \frac{\sigma_F}{\rho_g \cdot {U_{inj}}^2} \cdot \left(\frac{\rho_F}{\rho_g}\right)^{0.25} \cdot \sqrt{\frac{\mu_F}{\rho_F \cdot D_{BU,1} \cdot U_{inj}}} \cdot We_g \tag{23}$$

Table 2 Breakup times for different secondary breakup modes

Breakup mode	**Dimensionless breakup time τ [-]**	**Weber number We [-]**
Vibrational	$\frac{\pi}{4} \cdot \left[\frac{\sigma_F}{\rho_F \cdot d^3} - 6.25 \cdot \frac{\mu_F}{\rho_F \cdot d^2}\right]^{-0.5}$	$We_g \leq 12$
Bag	$6 \cdot \left(We_g - 12\right)^{-0.25}$	$12 < We_g \leq 18$
Bag and stamen	$2.45 \cdot \left(We_g - 12\right)^{0.25}$	$18 < We_g \leq 45$
Chaotic	$14.1 \cdot \left(We_g - 12\right)^{-0.25}$	$45 < We_g \leq 100$
Sheet stripping		$100 < We_g \leq 350$
Wave crest stripping	$0.766 \cdot \left(We_g - 12\right)^{0.25}$	$350 < We_g \leq 1000$
Catastrophic		$1000 < We_g < 2760$

The resulting secondary breakup time (in SI units) for different modes is calculated using the function of dimensionless breakup time:

$$t_{BU,2} = \tau \cdot \frac{D_{BU,1}}{U_{rel}} \cdot \sqrt{\frac{\rho_F}{\rho_g}} \tag{24}$$

The SMD of fuel droplets resulting from the secondary breakup are further used as a reference value for modelling the droplet size distribution. Chi-Square distribution with eight degrees of freedom is calculated using the method proposed by Hiroyasu (Hiroyasu & Kadota, 1974). The median fuel droplet diameter from this distribution is 22.4% larger than the reference SMD. This cumulative distribution is discretized into five intervals, ranging from 10% to 90% in 20% increments. The corresponding SMDs from these intervals are then incorporated into the simulation model.

Fuel evaporation

Droplet evaporation determines the quality of the mixture formation process, and consequently all other processes, namely ignition, combustion, and pollutants formation. On micro scale, evaporation influences the spatial and temporal variation of the excess-air ratio, and hence ignition timing and heat release rate. The energy required for evaporation is transferred from the combustion chamber gas to the droplets through conductive, convective, and radiative heat transfer mechanisms. From that process arises mass transfer from the droplet surface to the gas via diffusion and convection, and from that, complete disappearance of the droplet as a final and most preferable result. The fuel evaporation rate is calculated using the following differential equation (Borman & Johnson, 1962; Jung & Assanis, 2001):

$$\frac{dm_{F,v}}{dt} = \pi \cdot D_{drop} \cdot N \cdot D_m \cdot Sh \cdot \frac{p_t}{R_v \cdot T_m} \cdot \ln\left(\frac{p_t}{p_t - p_{v,sat}}\right) \tag{25}$$

where N represents the number of droplets that have undergone primary and secondary breakup processes; Dm denotes the fuel vapor mass diffusivity, pt stands for total pressure and $p_{v,sat}$ for saturation pressure of the fuel vapor. Sherwood and Schmit numbers are defined respectively:

$$Sh = 2 + 0.6 \cdot Re_l^{\frac{1}{2}} \cdot Sc^{\frac{1}{3}} \tag{26}$$

$$Sc = \frac{\mu_m}{\rho_m \cdot D}$$

Where the mean value of density and temperature at the fuel droplet boundary are given in following expressions:

$$\rho_m = \frac{p_t \cdot M_m}{R_u \cdot T_m} \tag{27}$$

$$T_m = 0.5 \cdot (T_a + T_v)$$

During the breakup phase, the injected fuel is assumed to atomize into fine droplets, with diameters corresponding to the discretized intervals of the Chi-Square distribution. During the evaporation process, the rate of the droplet diameter decrease is evaluated by the following equation:

$$\frac{dD_{drop}}{dt} = \left(\frac{2}{9 \cdot \pi \cdot \rho_F}\right)^{\frac{1}{3}} \cdot \frac{\left(\frac{dm_{F,l}}{dt} \cdot N - m_{F,l} \cdot \frac{dN}{dt}\right)}{N^2} \cdot \left(\frac{m_{F,l}}{N}\right)^{-\frac{2}{3}} \tag{28}$$

The masses of the atomized fuel in its liquid and vapourised state are related in following differential equation:

$$\frac{dm_{F,l}}{dt} = m_{drop} \cdot \frac{dN}{dt} - \frac{dm_{F,v}}{dt} \tag{29}$$

Similarly, the number of fuel droplets during the breakup period can be determined by solving the differential equation:

$$\frac{dN}{dt} = \frac{N_t}{t_{break}} \tag{30}$$

where N_t is the total number of fuel droplets in the atomized state, calculated upon the injected fuel mass and the diameters of fuel droplets following the breakup period. The system of differential equations presented in this subsection is solved over the duration of the injection events, with an angle step of 0.1 CAD. At each interval, the injection velocity, delivered mass of fuel, initial fuel droplet diameters of the size distribution intervals, total number of droplets, and breakup time are calculated and used to establish the initial conditions for the system of differential

equations. The system of differential equations is solved in the time domain with a variable time step, for each angle step, up to the onset of combustion. The results – the fuel vapor mass, droplet diameter, atomized liquid fuel mass, and the number of fuel droplets are obtained as functions of time.

Engine cycle data

Previously presented equations require the cylinder gas pressure and temperature values to assess the gas density used in the primary and secondary breakup models. Additionally, the difference between injection and cylinder gas pressure is necessary to evaluate the injection and breakup time parameters. The total pressure and gas temperature values are needed to determine the Sherwood number and calculate the evaporation rate, among other factors. Indicated pressure was acquired at the ICED Laboratory using a single-cylinder research engine and were utilized in this study to simulate and analyse the mixture formation process in several strategies. The basic cycle parameters are listed in Table 3.

Table 3 Engine cycle parameters

Indicated mean effective pressure	$IMEP = 15.984$ bar
Intake manifold pressure	$p_{INT} = 1.394$ bar
Exhaust manifold pressure	$p_{EXH} = 1.07$ bar
Intake manifold temperature	$T_{INT} = 295$ K
Start of combustion	$SOC = 356.1$ CAD

SIMULATION RESULTS

In this section a detailed analysis of the simulation results produced for various fuel injection strategies has been presented. A baseline case – single injection positioned in the intake stroke, provides a reference for subsequent comparisons and analysis covering several double injection strategies. The ratio of the fuel mass portion delivered during the first and the second injection cycles is systematically varied within the range from 30/70 to 70/30. Two scenarios were analysed: the first one in which the start of injection (SOI) timing for both events was held constant, leaving the end of injection (EOI) to be adjusted to the fuel mass split ratio, and the second one in which, opposed to the first, the EOI timing is fixed for both events, allowing the SOI to adjust accordingly. This approach enables better understanding how injection timing and fuel mass distribution affects fuel evaporation dynamics and mixture formation.

The first part of the numerical experiment focuses on three distinct finite fuel quantities, delivered during single injection event in the intake stroke at different crank angle positions close to each other. The evaporation process for these quantities was tracked from SOI to SOC. The earliest injected fuel is characterised by the smallest mass of vaporized fuel. This is closely connected to several factors, which can be better understood by analysing the other parameters governing the fuel evaporation presented in Figure 6.

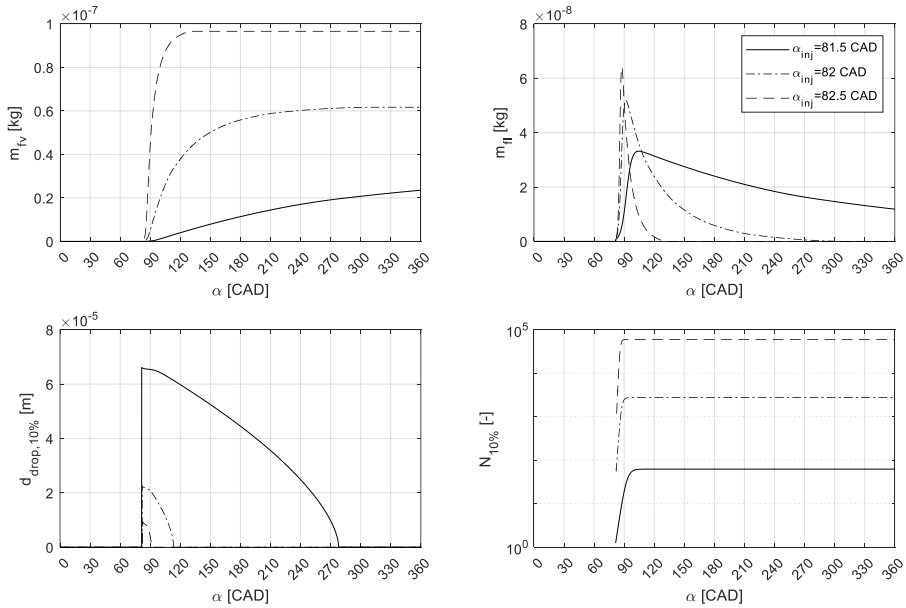

Figure 6 Fuel evaporation dynamics: vaporized fuel mass, atomized liquid fuel mass, 10th percentile droplet size variation and number of atomized droplets for three finite fuel quantities injected at different crank angle positions

The subplot depicting the number of atomized droplets (N10%) shows that both breakup processes take the longest time to complete in case of the earliest injected fuel mass. The initial droplet size (d10) presented in the separate sub-plot, for the earliest injected mass is up to 3 times larger than that of the fuel injected just 0.5 CAD later due to the low Weber numbers at low injection velocities which is expected to be the case in the early stage of injector needle lift. The difference, relative to the latest injected fuel mass is even larger.

The atomized liquid fuel mass curve (m_{fl}) corresponding to the earliest injection shows, following an initial rise during the breakup period a significantly lower negative gradient compared to two other consecutively delivered fuel masses, which is attributed to the very low evaporation rate closely connected to large diameter droplets delivered during the initial stage of needle lift. The 10th percentile droplet diameter reaches zero, indicating complete evaporation in that percentile group, however, a portion of the injected fuel remains unevaporated prior the SOC at the end of the compression stroke. Quite opposite, the fuel portions delivered 0.5 and 1.0 CAD later present high initial gradients of both vaporised (m_{fv}) and atomised liquid fuel mass (m_{fl}). The most indicative for understanding the process is the largest vaporized mass on case of the latest delivered fuel mass (82.5 CAD), which is related to higher injection velocities achieved in later stages of needle lift. With injection velocity increased, the total number of droplets in each percentile group rises, followed by a continual decrease in droplet diameters. This reflects in higher gradients in the atomized liquid fuel mass curves (mfl), shorter breakup time and increased evaporation rates. As illustrated in Figure 6 only the earliest delivered fuel mass (81.5 CAD) fails to reach complete evaporation prior to SOC.

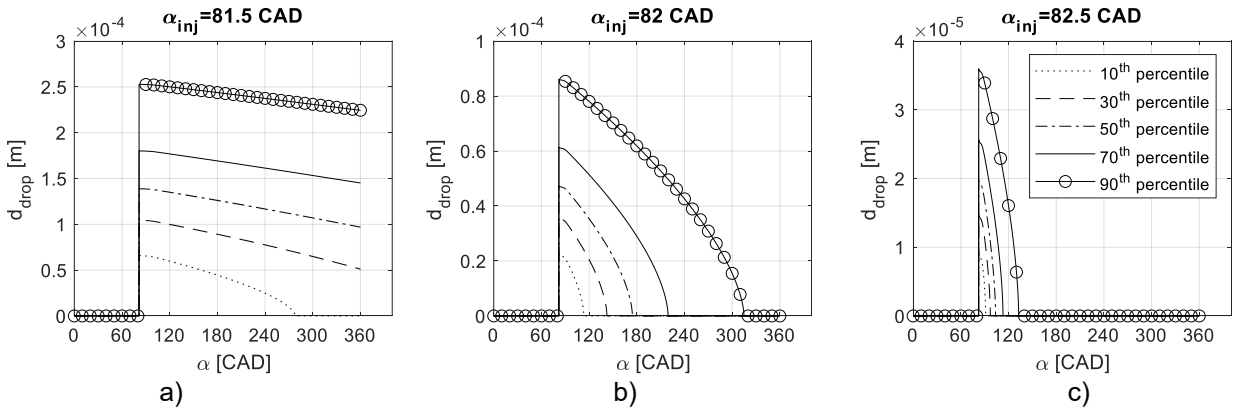

Figure 7 Droplet diameter histories during evaporation for all atomized fuel percentile groups for three injection quantities delivered during the injector opening period

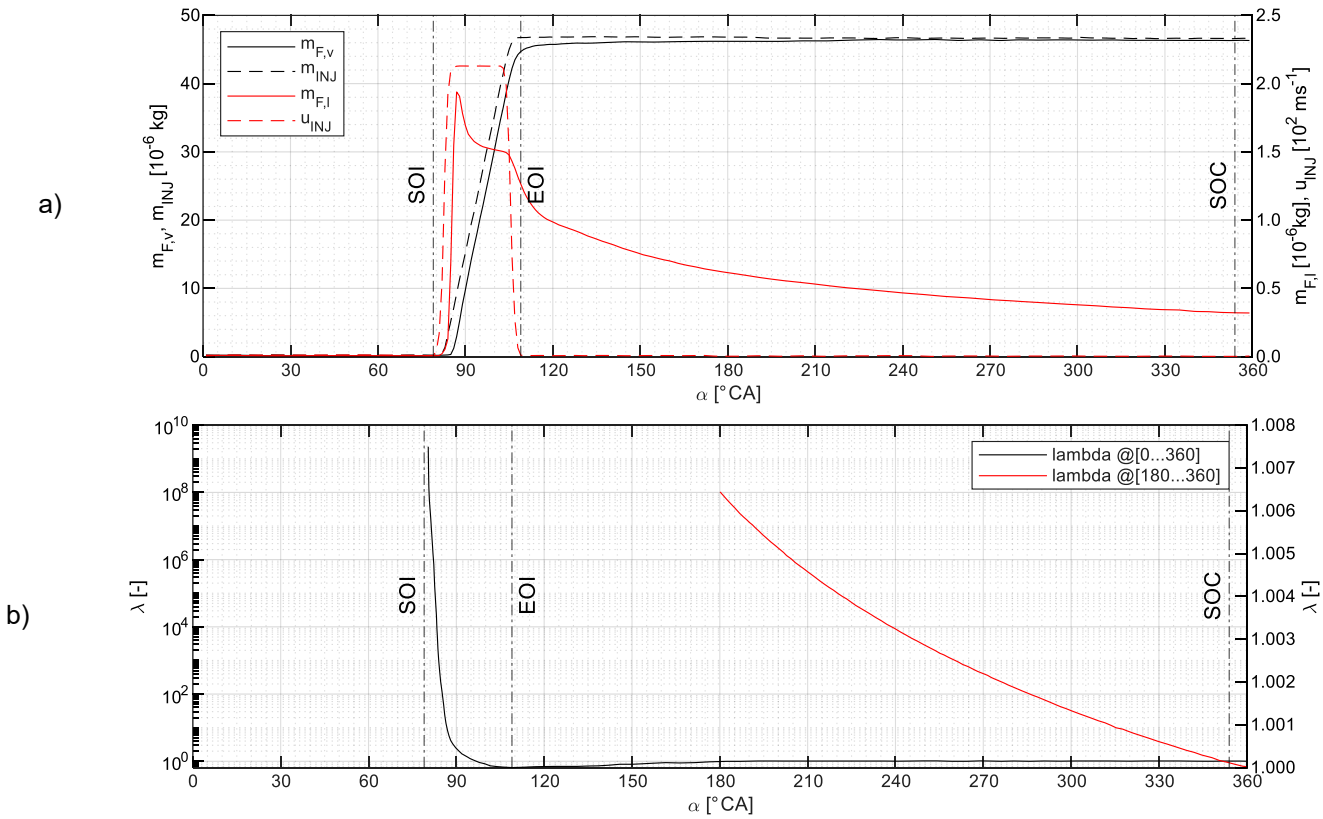

Figure 8 Cumulative fuel evaporation dynamics – vaporized fuel mass, injected fuel mass, atomized liquid fuel mass, fuel injection velocity (a) and excess-air ratio (b): single injection strategy

Droplet diameter histories during the evaporation process for three previously analysed injection quantities have been presented for five discrete atomized fuel percentile groups. Only the smallest fuel droplets formed during the earliest injection stage reach complete evaporation. The four other percentile groups fail to evaporate completely by the end of compression stroke showing small negative gradient in diameter and progressively decreasing gradients for higher percentiles. For the fuel masses delivered in later stages, all droplet percentile groups reach complete evaporation by the end of compression stroke. Significant increase in evaporation rate is observed in both cases as the injection progresses along the injector needle rising time.

By integrating the fuel evaporation parameters (m_{fv}, m_{fl}) at each discrete crankshaft position, the contributions of the discrete fuel quantities injected up to that position are accounted for and accumulated. In that way cumulative curves for the vaporized and atomized liquid fuel mass were generated covering complete process from SOI to SOC.

Cumulative curves for vaporized fuel and atomized liquid fuel and variation of the excess-air ratio during the intake and compression stroke is presented in Figure 8 for a single injection cycle. After an initial delay relative to SOI, the vaporized fuel mass (Figure 8a) increases and follows closely the trend of injected fuel mass. After the injection is aborted, the vaporized fuel mass continues to increase slowly reaching the level of cumulative mass of injected fuel by the end of compression stroke. The process is influenced by the breakup time of the fuel droplets, increasing with droplet diameter and decreasing with injection velocity, which is critical for fuel mass delivered during the needle opening and closing phase. Conversely, the atomised fuel increase with the highest rates right after the injector starts to open and reaches the peak value after the injector needle reaches full lift. During the nominal injection rate, the atomized fuel mass decreases moderately due to simultaneous evaporation, but speeds up once the injection ceases. However, a residual atomized liquid fuel mass remains present at the onset of combustion, which corresponds mostly to the presence of large droplets produced during the injector's opening and closing phases.

The excess-air ratio history is presented in Figure 8b, ranging from pure air at the start of injection cycle, down to expected level of 1 for stoichiometric combustion. It decreases sharply towards the sub-stoichiometric value during the intake stroke (incomplete air intake process) and recovering to approximately 1.0064 at the start of compression. When combustion begins, the excess-air ratio is stoichiometric, even though approximately 0.68% of the injected fuel remains unevaporated.

Cumulative curves for vaporized fuel and atomized liquid fuel and variation of the excess-air ratio during the intake and compression stroke is presented in Figure 9 for a double injection cycle, covering the case of equal mass distribution (split factor 50/50). Similar to single injection case, the start of the first injection (SOI1) is positioned at 80 CAD, while the second injection is shifted in the combustion stroke starting at 260 CAD (SOI2). Due to increased cylinder pressure (back pressure) during the compression process, the energizing time (ET) for the second injection is positively corrected to compensate decreased fuel flow rate (ET1=0.952 ms, ET2=0.954 ms for the first and second injections, respectively).

a)

b)

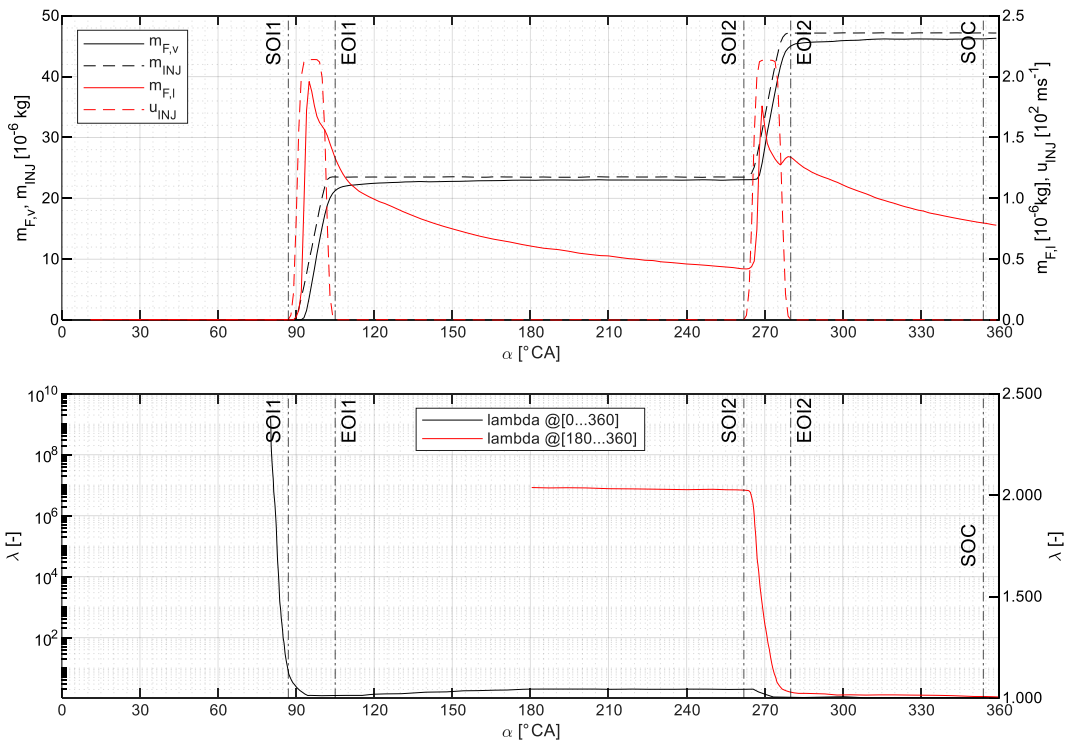

Figure 9 Cumulative fuel evaporation dynamics – vaporized fuel mass, injected fuel mass, atomized liquid fuel mass, fuel injection velocity (a) and excess-air ratio (b): double injection cycle strategy (first/second injected mass: 50%/50%)

The vaporized fuel mass follows an expected pattern seen in case of single injection cycle, where phases of higher gradients relate to the timing of the fuel injection. Conversely, compared to the first injection, the atomized liquid fuel mass shows a significantly smaller increase during the second injection, while the average droplet breakup time is reduced by approximately 20%. This can be related to the disproportionate increase in the evaporation rate of droplets produced during the second injection, caused by higher Weber numbers, increased cylinder gas densities, and the subsequent reduction in both the primary and secondary droplet diameters.

The mixture is lean at the start of the compression stroke as a result of the first injection. The final excess-air ratio, just before the SOC, is 1.0171, which is slightly higher than that observed in a single injection cycle. Two additional low injection velocity phases (injector energising/deenergising) result in decrease of overall mass of vaporised fuel, although the conditions in the chamber during the second injection are more favourable for the evaporation process (higher temperature, decreased spray penetration, decreased droplet size). According to estimation, more than 1.65% of fuel injected in cylinder remains in liquid state.

The fuel mass distribution between the first and second injection (split ratio) was varied from 30/70 (30% of fuel mass allocated to the first injection) to 70/30 (70% of fuel mass allocated to the first injection) in increments of 10%. The effects of evaporation process simulated for the case of fixed SOI for both injections are presented in Figure 10a. If SOI for both injection cycles remains fixed, increasing the split ratio toward the second injection forces the end of injection (EOI) angle closer to the start of combustion (SOC), reducing the available time for complete fuel evaporation. As the injection duration prolongs later in the cycle, important effects occur enhancing the process of evaporation: one obvious – increasing charge temperature, and the second one – charge pressure, enhancing evaporation through decreased spray penetration and droplet size.

Reduced time and favourable thermodynamic are opposed to each other, but according to simulation the latter prevail. As the split ratio shifts toward the second injection, the mass fraction of unevaporated fuel at the end of the compression stroke decreases to 1.64% at a split ratio of 30/70.

Tracking the injected fuel quantity and its state towards TDC, reveals that nearly all of the fuel in liquid state comes from the injector opening and closing sequences, as a result of low injection velocities and low Weber numbers. With the SOI for both injection cycles fixed, the excess-air at the end of the compression is reflected by the flow conditions at the injector closure. The Figure 10b presents the fraction of fuel injected during the injector closing phase that remains unevaporated at the TDC. The evaporation rate for the second injection increases as the split ratio shifts toward it, primarily due to the elevated gas density in the cylinder. The evaporation rate of fuel delivered during the first injection closing phase increases with a shift in mass distribution toward the second injection, mainly due to time available for complete evaporation of large size droplets originated during injector closing. The gas density has no particular influence on atomization and evaporation of the fuel delivered during the first injection since the variation of the charge pressure and temperature during injection remain small.

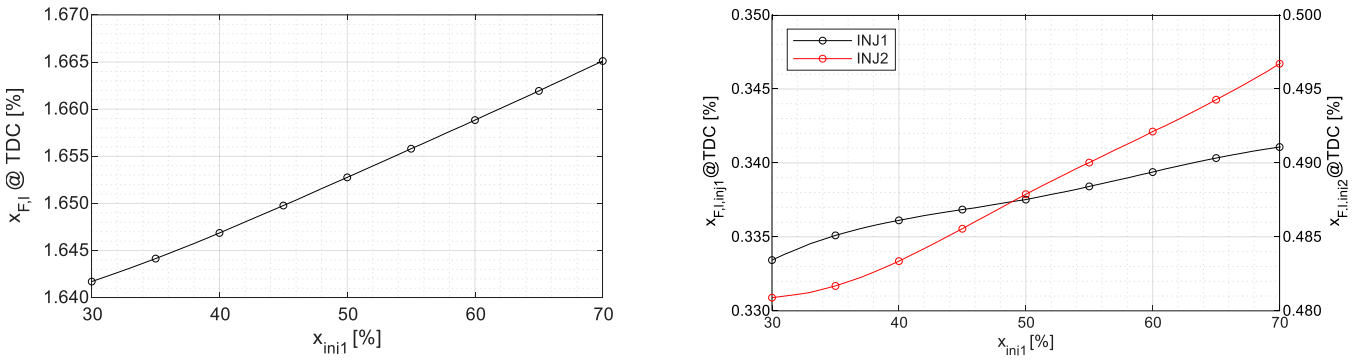

a) b)

Figure 10 Fuel mass split factor variation with fixed SOI: mass fraction of unevaporated fuel at SOC (a), mean evaporation rate of fuel quantities injected during injector closing period (b)

The effects of evaporation process simulated for the case with fixed end of injection for both injections are presented in Figure 11. End of injection (EOI) positions are fixed at 100 CAD and 280 CAD for the first and second injection, respectively. Increasing the fuel mass allocated to the first injection influenced reduction in the mass fraction of unevaporated fuel at the SOC, reaching a minimum of 1.649% at split ratio 70/30, which is opposite to the trend observed in fixed-SOI case. By increasing the fuel mass of the first injection, corresponding start of injection (SOI1) shifts towards start of the cycle allowing more time for evaporation of fuel droplets atomized under less favourable flow and thermodynamic conditions.

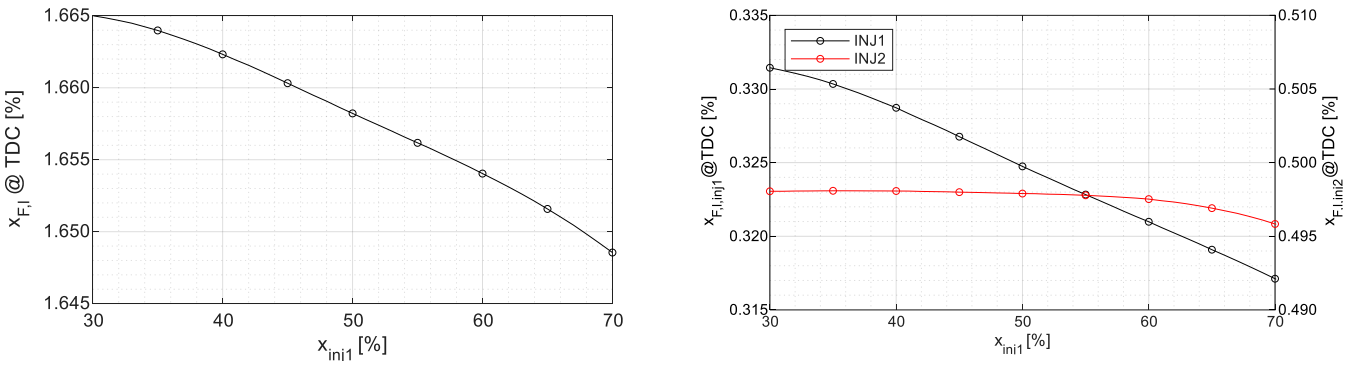

a) b)

Figure 11 Fuel mass split factor variation with fixed EOI: mass fraction of unevaporated fuel at SOC (a), mean evaporation rate of fuel quantities injected during injector opening period (b)

The charge pressure and temperature remain relatively constant during intake process so the the SMDs and breakup time exhibit minimal variation with changes in SOI1 timing. Analysis further shows that fuel split ratio directly influences the atomization conditions of the second injection by shifting the SOI2 later in the compression stroke as the second injection portion decreases, or earlier as it increases. By shifting SOI2 toward TDC, less time remains available for evaporation. However, this is compensated by more favourable thermodynamic conditions for evaporation. By advancing SOI2, more time for evaporation is available, however the result of atomisation is worsened due to decreased gas density. The influence of split ratio on fuel mass delivered at the injector closing phase remaining in liquid state is presented in Figure 11b. The fuel split ratio has a negligible effect on the evaporation rate of fuel delivered during the opening phase of the second injection, up to a split ratio of approximately 50/50. Further increase of split ratio results in a reduced fraction of unevaporated fuel, which comes as a consequence of increased charge density.

CONCLUSIONS

A generally simple and computationally efficient numerical simulation model has been developed to study the effects of complex injection strategies on mixture formation process in DISI ICE. The objective was to evaluate the level of fuel evaporation during mixture formation, particularly in the final stage of compression stroke, prior to combustion onset. Expectedly, compared to the single injection, double injection strategy demonstrated increase of the mass of unevaporated fuel at SOC.

This is mainly attributed to the additional injector actuation and doubled the number of injector opening and closing ramps during which atomization conditions are suboptimal. The fuel impingement and fuel penetration into piston-cylinder gap and their effects on evaporation have not been considered in the numerical experiment, which may show increased mass of unevaporated fuel at SOC.

The fuel split ratio has been varied within the range 30/70 … 70/30 and the results of the simulation show that fuel evaporation can be optimized through different strategies, depending on whether the SOI or EOI is fixed. In continuation of the study, more complex injection strategies are to be investigated and correlated to experimental data, focusing particularly on the soot and unburned hydrocarbons. This will make possible to determine what condition and what particular injection strategy contribute to the mass of unevaporated fuel present at SOC and so have the dominant influence on pollutant emission, by retaining fast combustion rates and pre-ignition/knock resilience as prerequisites for improved fuel economy.

ACKNOWLEDGEMENT

The results presented in this paper are the result of the research supported by the Ministry of Science, Technological Development and Innovation of the RS under Contract 451-03-34/2026-03/ 200105, February 5, 2026.

REFERENCES

Arcoumanis, C., Gavaises, M., & French, B. (1997). Effect of Fuel Injection Processes on the Structure of Diesel Sprays. SAE 970799. *SAE International Congress & Exposition*. https://www.sae.org/papers/effect-fuel-injection-processes-structure-diesel-sprays-970799

Arkoudeas, P. (2022). Gasoline Lubricity. In Crude Oil—New Technologies and Recent Approaches. IntechOpen. https://doi.org/10.5772/intechopen.101302

Baumgarten, C. (2006). Mixture Formation in Internal Combustion Engine. Springer Berlin Heidelberg. https://doi.org/10.1007/3-540-30836-9

Borman, G. L., & Johnson, J. H. (1962). Unsteady Vaporization Histories and Trajectories of Fuel Drops Injected into Swirling Air (SAE Technical Papers SAE 620271). SAE International. https://doi.org/10.4271/620271

Desantes, J. M., López, J. J., Carreres, M., & López-Pintor, D. (2016). Characterization and prediction of the discharge coefficient of non-cavitating diesel injection nozzles. *Fuel*, 184, 371–381. https://doi.org/10.1016/j.fuel.2016.07.026

Han, T., Singh, R., Lavoie, G., Wooldridge, M., & Boehman, A. (2020). Multiple injection for improving knock, gaseous and particulate matter emissions in direct injection SI engines. *Applied Energy*, 262, 114578. https://doi.org/10.1016/j.apenergy.2020.114578

Hiroyasu, H., & Kadota, T. (1974, February 1). Fuel Droplet Size Distribution in Diesel Combustion Chamber. SAE 740715. SAE International Off-Highway and Powerplant Congress and Exposition. https://doi.org/10.4271/740715

Idelchik, I. E. (2008). Handbook of Hydraulic Resistance, 4th Edition Revised and Augmented. Begell House. https://www.begellhouse.com/ebook_platform/monograph/book/5877598576b05c67.html

Jung, D., & Assanis, D. N. (2001, March 5). Multi-Zone DI diesel spray combustion model for cycle simulation studies of engine performance and emissions. SAE 2001-01-1246. *SAE 2001 World Congress*. https://doi.org/10.4271/2001-01-1246

Klaus, E. E., & O'Brien, J. A. (1964). Precise Measurement and prediction of bulk-modulus values for fluids and lubricants. *Journal of Basic Engineering*, 86(3), 469–473. https://doi.org/10.1115/1.3653145

Lichtarowicz, A., Duggins, R. K., & Markland, E. (1965). Discharge coefficients for incompressible non-cavitating flow through long orifices. *Journal of Mechanical Engineering Science*, 7(2), 210–219. https://doi.org/10.1243/JMES_JOUR_1965_007_029_02

Park, C., Kim, S., Kim, H., Lee, S., Kim, C., & Moriyoshi, Y. (2011). Effect of a split-injection strategy on the performance of stratified lean combustion for a gasoline direct-injection engine. *Proceedings of the Institution of Mechanical Engineers, Part D: Journal of Automobile Engineering*, 225(10), 1415–1426. https://doi.org/10.1177/0954407011406469

Reitz, R. D. (1987). Modeling Atomization Processes in High-Pressure Vaporizing Sprays. *Atomisation Spray Technology*, 3(4). https://www.scirp.org/reference/referencespapers?referenceid=88393

Sarre, C. von K., Kong, S.-C., & Reitz, R. D. (1999). Modeling the Effects of Injector Nozzle Geometry on Diesel Sprays (SAE 1999-01-0912). SAE International. *International Congress & Exposition*. https://doi.org/10.4271/1999-01-0912

Stiesch, G. (2003). *Modeling Engine Spray and Combustion Processes*. Springer. https://doi.org/10.1007/978-3-662-08790-9

Stiesch, G., Merker, G. P., Tan, Z., & Reitz, R. D. (2001, March 5). Modeling the Effect of Split Injections on DISI Engine Performance. SAE 2001-01-0965. *SAE 2001 World Congress*. https://doi.org/doi.org/10.4271/2001-01-0965

Trost, D., Polcar, A., Boldor, D., Nde, D. B., Wolak, A., & Kumbár, V. (2021). Temperature dependence of density and viscosity of biobutanol-gasoline blends. *Applied Sciences*, 11(7), 3172. https://doi.org/10.3390/app11073172

The 11th International Congress
Motor Vehicles & Motors 2026
Kragujevac, Serbia
October 8th - 9th, 2026

Motor Vehicles & Motors

MVM2026-037
https://doi.org/10.24874/CMVM2026.037
Original scientific paper

Petar Markov[1]
Radivoje Pušara[2]
Dragan Peruničić[3]

A SINGLE-RANGE POLYNOMIAL MODEL FOR TEMPERATURE-DEPENDENT MIXTURE PROPERTIES IN COMBUSTION ENGINES WITH VARIABLE EGR RATES

ABSTRACT: Calculation accuracy of temperature-dependent thermodynamic gas properties is of critical importance for simulation and analysis of internal combustion engines processes, particularly in cases of complex mixture formation strategies and high EGR rates. High-accuracy simulations rely on multiple temperature range polynomials for each gas component derived from NASA/JANAF/NIST databases, introducing discontinuities, increased processing and complexity. As an alternative, single-range logarithmic polynomials (VoLP) offer improved computational efficiency while retaining comparable accuracy. A critical review of existing reference and simplified models is provided, identifying key sources of inaccuracy, focusing on problems in representation of variable air-fuel ratio during compression and high EGR rates as a common answer to pre-ignition and knocking combustion. In this work, single-range, single-polynomial formulation for the isentropic coefficient is developed to account for effects of temperature, excess-air ratio, and residual gas fraction. The model was calibrated against reference datasets over a temperature range relevant to spark-ignition engine operation. Prediction capabilities were assessed in comparison with reference datasets and compared to widely used simplified approximations, showing a lower deviation from the reference data across the complete temperature range. The presented model offers a computationally efficient alternative for thermodynamic engine simulation and optimisation, and is a promising candidate for real-time analysis and control, although this remains to be confirmed against experimental data.

KEYWORDS: gas properties, isentropic coefficient, EGRR, direct injection, engine simulation

[1] *Petar Markov, MSc, student, University of Belgrade, IC Engines Dept., Kraljice Marije 16, Belgrade, Serbia, 1032-2024@studenti.mas.bg.ac.rs*
[2] *Radivoje Pušara, MSc, student, University of Belgrade, IC Engines Dept., Kraljice Marije 16, Belgrade, Serbia, 1010-2024@studenti.mas.bg.ac.rs*
[3] *Dragan Peruničić, MSc, student, University of Belgrade, IC Engines Dept., Kraljice Marije 16, Belgrade, Serbia, 1017-2024@studenti.mas.bg.ac.rs*

POLINOMSKA APROKSIMACIJA KARAKTERISTIKA RADNE MATERIJE KOD MOTORA SA VISOKIM UDELOM RECIRKULISANIH PRODUKATA SAGOREVANJA

REZIME: Tačnost proračuna termodinamičkih svojstava gasa zavisnih od temperature ključna je za simulaciju i analizu procesa u motorima sa unutrašnjim sagorevanjem, naročito u slučajevima složenih strategija formiranja smeše i većih udela zaostaih produkata sagorevanja. Simulacije visoke tačnosti se oslanjaju na polinome definisane za više temperaturnih opsega za svaku komponentu gasa, izvedene iz NASA/JANAF/NIST baza podataka, što dovodi do diskontinuiteta, povećanog računarskog opterećenja i složenosti modela. Logaritamski polinomi formirani na jedinstvenom temperaturnom opsegu (VoLP), kao alternativa, pružaju veću računarsku efikasnost uz zadržavanje slične ili čak manje tačnosti. Dat je kritički pregled postojećih referenci i pojednostavljenih modela, pri čemu su identifikovani ključni izvori greške, sa posebnim fokusom na probleme pri predstavljanju promenljivog odnosa goriva i vazduha tokom sabijanja i većih udela zaostaih produkata sagorevanja, koje predstavljaju uobičajen pristup rešavanja problema prevremenog paljenja smeše i detonantnog sagorevanja. U ovom radu razvijena je formulacija koeficijenta izentrope sa jednim temperaturnim opsegom i jednim polinomom, kojom se u obzir uzimaju uticaj temperature, koeficijenta viška vazduha i udela zaostalih gasova. Model je kalibrisan prema referentnim skupovima podataka u temperaturnom opsegu relevantnom za rad motora sa paljenjem svećicom. Sposobnost modela za predviđanje procenjena je poređenjem sa referentnim skupovima podataka, kao i sa široko korišćenim temperaturnim aproksimacijama, pri čemu je pokazano manje odstupanje od referentnih podataka u celokupnom temperaturnom opsegu. Predloženi model predstavlja računarski efikasnu alternativu za termodinamičke simulacije i optimizaciju motora, kao i obećavajuću osnovu za analizu i upravljanje u realnom vremenu, što tek treba potvrditi eksperimentalno.

KLJUČNE REČI: svojstva gasa, koeficijent izentrope, EGRR, direktno ubrizgavanje, simulacije rada motora

INTRODUCTION

Cylinder pressure modelling and heat release analysis have been established in the literature as important and standard tools for engineers and researchers when developing and testing new engines (Heywood, 1988), since ability to accurately model and extract information from cylinder pressure is important for the interpretation and validity of the results (Klein, 2007)

That is why accurate knowledge of the temperature-dependent thermodynamic properties of the in-cylinder working fluid specific heats at constant pressure and volume, and their ratio, the isentropic coefficient („γ“) — is required for reliable simulation and analysis of internal combustion engine processes. In single-zone heat release models, γ dictates the relationship between the measured cylinder pressure and the apparent heat release rate, so even small errors in γ propagate into significant errors in the estimated combustion parameters.

The working fluid composition changes continuously through the engine cycle, from a fresh air-fuel mixture during intake and compression to combustion products during and after heat release. High-fidelity representations of this behavior typically rely on multi-range polynomial curve fits for each individual gas species, most commonly derived from the NASA, JANAF or NIST thermochemical datasets. While accurate, this approach requires evaluating and blending a large number of species-specific polynomials at every time step, and the transition between temperature ranges (typically split around 1000 K) introduces discontinuities in the computed properties — a well-documented numerical issue that becomes more severe as the number of temperature bands increases.

As a computationally efficient alternative, single-range polynomial correlations for γ as a function of temperature alone have been widely used in engine simulation and real-time applications, calibrated at a fixed nominal operating point and expressed as a low-order rational function of temperature (Klein & Eriksson, 2004), which has since become a standard reference for fast γ evaluation in single-zone heat release analysis. However, these models are essentially one-dimensional because they are fitted only against temperature at a single, fixed mixture composition, they do not capture how γ shifts with excess-air ratio (λ) or with the fraction of recirculated exhaust gas (x_{RG}) — even though both are first-order effects on mixture specific heat.

This limitation is increasingly relevant in modern spark-ignition engines, where variable mixture formation strategies and high exhaust gas recirculation rates are widely used as a primary means of mitigating pre-ignition and knocking combustion. Under such conditions, the assumption of a fixed nominal composition underlying conventional single-range γ(T) correlations is no longer justified, and the resulting error grows systematically as λ and x_{RG} depart from the calibration point.

The aim of this work is therefore to develop a single-range polynomial for γ that retains the computational simplicity of conventional temperature-only correlations while explicitly accounting for the combined effects of temperature, excess-air ratio and residual gas fraction. The proposed model is calibrated against a reference dataset generated from multi-range NASA 9 property data over a temperature range relevant to spark - ignition engine operation, and its predictive accuracy is compared against both the reference dataset and widely used simplified γ(T) approximations across the complete range of operating conditions considered. Hereafter, the proposed model is referred to as the SRPM.

MODEL FORMULATION AND METHODOLOGY

Reference dataset

The reference thermodynamic properties were generated using a mixture property approach based on NASA nine-coefficient polynomials (Gordon & McBride, 1994; Burcat & Ruscic, 2005), with octane as reference fuel and a simplified frozen-composition combustion product model (Ferguson & Kirkpatrick, 2016) using the 12-component species nomenclature of (Olikara & Borman, 1975). The product composition is obtained from complete-combustion stoichiometry and contains no dissociated species, so it is frozen with respect to temperature and independent of pressure. Reference data were generated over a temperature range of 300 to 3000 K in steps of 30 K, an excess-air ratio range of 1.0 to 3.0 in steps of 0.1, and a residual gas mass fraction range of 0.0 to 0.4 in steps of 0.05.

$$\frac{c_p(T)}{R} = a_0T^{-2}+a_1T^{-1}+a_2T^0+a_3T+a_4T^2+a_5T^3+a_6T^4 \tag{1}$$

$$\frac{h(T)}{RT} = -a_0T^{-2}+a_1\frac{\ln T}{T}+a_2+\frac{a_3}{2}T+\frac{a_4}{3}T^2+\frac{a_5}{4}T^3+\frac{a_6}{5}T^4+\frac{a_7}{T} \tag{2}$$

Baseline - air

The specific heat at constant pressure of the oxidizer, $c_{p,A}(T)$, was obtained as the limiting case of the mixture model for $\lambda\rightarrow\infty$. Convergence to a pure air state was verified numerically by evaluating $c_{p,A}$ at successively larger λ (10^2-10^7) and selecting the smallest λ beyond which the relative change in $c_{p,A}$ fell below a 10^{-2}% tolerance. The resulting $c_{p,A}(T)$ baseline was fitted with 5th – order polynomial in normalized temperature:

$$T_{mean}=\frac{1}{n}\sum_{i=1}^{n}T_i \tag{3}$$

$$T_{std}=\sqrt{\frac{1}{n-1}\sum_{i=1}^{n}(T_i-T_{mean})^2} \tag{4}$$

$$T_n=\frac{T-T_{mean}}{T_{std}} \tag{5}$$

$$c_{p,A}(T)\approx\sum_{k=0}^{5}a_kT_n^k \tag{6}$$

T_{mean} and T_{std} are the mean value and standard deviation of temperature over the temperature range 300:30:3000K. Normalization was necessary to avoid bad conditioning while fitting, especially at higher temperature magnitudes (T^4 terms at T≈3000 K), which would otherwise produce coefficients on the order of 10^{13} and cause unstable extrapolation. The same normalisation is applied to the excess-air ratio. The reference curve and the SRPM fit are shown in Figure 1b.

Figure 1a presents the specific heat of three mixture components versus temperature. All three curves follow the same trend and differ mainly in their gradient with temperature. This motivates the introduction of two correction terms Δ_{AF} and Δ_{RG}, that isolate the composition-driven deviation from the air baseline, separately for the unburned and fully burned state of mixture, allowing each to be fitted with a comparatively low-order polynomial in temperature and excess-air ratio. A fresh mixture of air and representative fuel, in this case octane is labeled as AF and residual gas as representative of fully burned mixture at the end of combustion in ideal case with label RG.

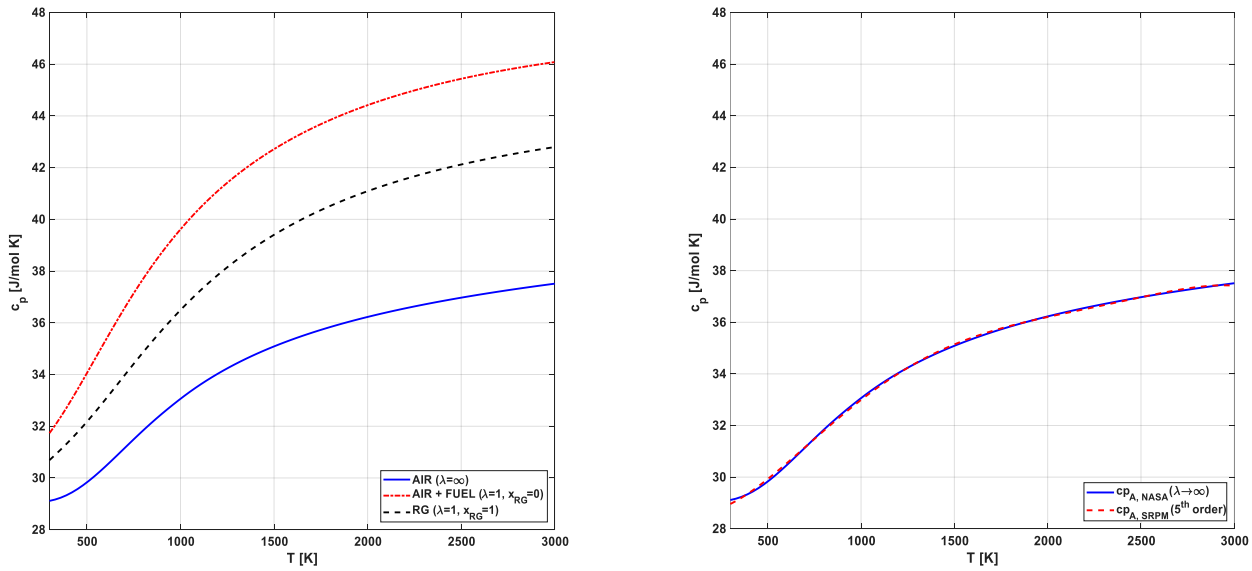

a) b)

Figure 1 c_p for pure air, air-fuel (octane) mixture and residual gas: created with NASA 9 polynomial (a), c_p for pure air: reference NASA 9 and fitted SRPM (b)

Composition – correction terms

The effect of mixture composition on specific heat was represented through two correction terms relative to the air baseline $\Delta_{AF}(T, \lambda)$ for the fresh air-fuel mixture when x_{RG} is 0 and for fully diluted combustion product state when x_{RG} is 1; this limiting state is used as the blending endpoint in Eq. (13) and is not itself a modelled operating condition. From Figure 1a, the correction terms can be written in the following form:

$$\Delta_{AF}(T_n, \lambda_n)=c_{p,\,AF}(T_n, \lambda_n)-c_{p,\,A}(T_n) \tag{7}$$

$$\Delta_{RG}(T_n, \lambda_n)=c_{p,\,RG}(T_n, \lambda_n)-c_{p,\,A}(T_n) \tag{8}$$

As with the temperature (5), the excess-air ratio (9) was also normalized:

$$\lambda_n=\frac{\lambda-\lambda_{mean}}{\lambda_{std}} \tag{9}$$

so that both independent variables enter the fit on the same scale.

The initial problem is that Δ_{AF} and Δ_{RG} are both dependent on two independent variables, temperature and excess-air ratio. The goal is to approximate those curves with a single polynomial basis on a discrete set of reference points, obtained from NASA thermodynamic calculations for different combinations of temperature and excess-air ratio. The idea for this method follows from the fact that any polynomial fit, regardless of the number of variables, is a linear model in its coefficients, even though it is nonlinear in the variables themselves. Instead of seeking a simple linear fit, a sum of basis functions is constructed and the best linear combination is determined. For two variables, the natural generalization is for the basis functions to be products of powers in each variable (10).

$$\phi_{\{i,j\}}(T_n, \lambda_n)=T_n^i\,\lambda_n^j \tag{10}$$

Tensor is formed as vector product of $\{T^0,\ldots, T^{n_T}\} \times \{\lambda^0, \ldots, \lambda^{n_\lambda}\}$.

$$\Delta(T_n,\lambda_n) \approx \sum_{i=0}^{n_T}\sum_{j=0}^{n_\lambda} c_{ij}\,T_n^i\,\lambda_n^j \tag{11}$$

For example, we have m reference points $(T_k, \lambda_k, \Delta_k)$, k=1, …, m from there we create matrix:

$$A_{k(i,j)}=T_k^i\lambda_k^j \tag{12}$$

where each column corresponds to one pair (i, j) and each row to one reference point. Eq. 11 applies to both Δ_{AF} and Δ_{RG} with their respective degrees (n_T and n_λ) and coefficient matrix.

The same procedure is applied to each fuel considered, so that the evaluation routine retrieves the coefficients of the relevant fuel from a stored structure. The coefficients are held as an $(n_T+1)\times(n_\lambda+1)$ matrix rather than as a single vector. Each row corresponds to one power of T_n ($i=0\ldots n_T$) and within that row, the entries are the λ coefficients ($j=0\ldots n_\lambda$) describing how that temperature contribution varies with the excess-air ratio. Eq. 11 returns $\Delta(T_n, \lambda_n)$ from this matrix as a weighted double sum.

Specific heat and gas constant of a mixture

The mixture c_p was obtained by linear blending between the air-fuel and residual gas states:

$$c_{p,\,AFR}(T_n, \lambda_n, x_{RG})=c_{p,\,A}(T_n)+(1-x_{RG})\cdot\Delta_{AF}(T_n, \lambda_n)+x_{RG}\cdot\Delta_{RG}(T_n, \lambda_n) \tag{13}$$

The specific gas constant R was found to be effectively independent of temperature (verified by evaluating R at temperatures of 400, 1200 and 2200 K for fixed $x_{RG}=0.2$, with negligible spread). $R_{AF}(\lambda_n)$ and $R_{RG}(\lambda_n)$ were therefore each fitted with a second order polynomial in normalized λ at a reference temperature (1000K) and calculated gas constant for mixture:

$$R_{AF}(\lambda_n)\approx a_0+a_1\lambda_n+a_2\lambda_n^2 \tag{14}$$

$$R_{RG}(\lambda_n)\approx b_0+b_1\lambda_n+b_2\lambda_n^2 \tag{15}$$

$$R_{AFR}(\lambda,x_{RG})=(1-x_{RG})\cdot R_{AF}(\lambda)+x_{RG}\cdot R_{RG}(\lambda) \tag{16}$$

The mixture specific heat at constant volume follows from Mayer's relation and the γ is then obtained directly:

$$c_{v,\,AFR}=c_{p,\,AFR}-R_{AFR} \tag{17}$$

$$\gamma(T_n, \lambda_n, x_{RG})=\frac{c_{p,\,AFR}}{c_{v,\,AFR}} \tag{18}$$

Comparison with temperature-only models

To evaluate the importance of retaining T and λ dependence, the SRPM was compared against three temperature-only γ polynomials commonly used in single-zone heat release analysis: linear (Gatowski et al., 1984), quadratic (Brunt et al., 1998), and exponential (Egnell, 1998), which are calibrated by least-squares regression against the reference model evaluated at the nominal operating point. All four models were then evaluated across the T and λ grid, allowing the error of temperature-only models to be quantified as λ and x_{RG} depart from their calibration point, in the direct contrast to the SRPM's error, which remains bounded across the full domain.

RESULTS AND DISCUSSION

Baseline and correction terms

The pure air specific heat baseline $c_{p,\,A}(T)$ was fitted with a maximum relative error of 0.53% over the complete 300:30:3000 K temperature range. Figure 2 shows that the SRPM closely matches the NASA 9 reference in the middle range from 500 to 2800 K, while a slight deviation occurs at the ends (below 350 K and above 2800 K), which is negligible when the temperature range of the engine cycle (intake air ~400 K and peak cycle temperature ~1800 K) is considered.

The model was evaluated toward the pure air with λ up to 10^6, far outside the fitted domain of 1.00 to 3.00, just for illustration, not as validity claim. The maximum relative error of γ was 1.37%, mean error was 0.28%, confirming that error growth outside the intended operating range remains gradual rather than divergent. SRPM was also tested for pure fuel with maximum relative error of 1.18%, for representative excess-air ratio.

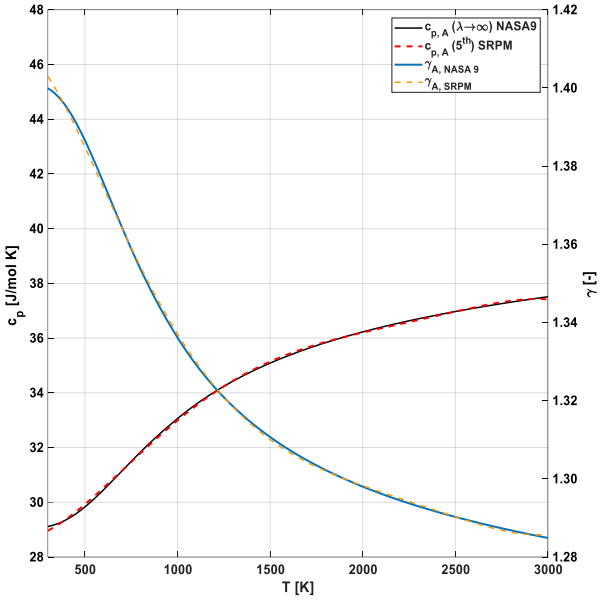

Figure 2 Pure air specific heat baseline and gamma: reference with NASA 9 polynomial vs. SRPM with 5th order polynomial

The composition correction terms $\Delta_{AF}(T, \lambda)$ and $\Delta_{RG}(T, \lambda)$ were reproduced with maximum relative errors of 0.43% and 2.21% respectively, small quantities superimposed on the air baseline, whose contribution to final γ error is correspondingly reduced. The gas constant was confirmed to be temperature independent to within numerical precision and the fitted air gas constant of 287.01 J/(kg·K), which agrees with the literature reference 287.05 J/(kg·K).

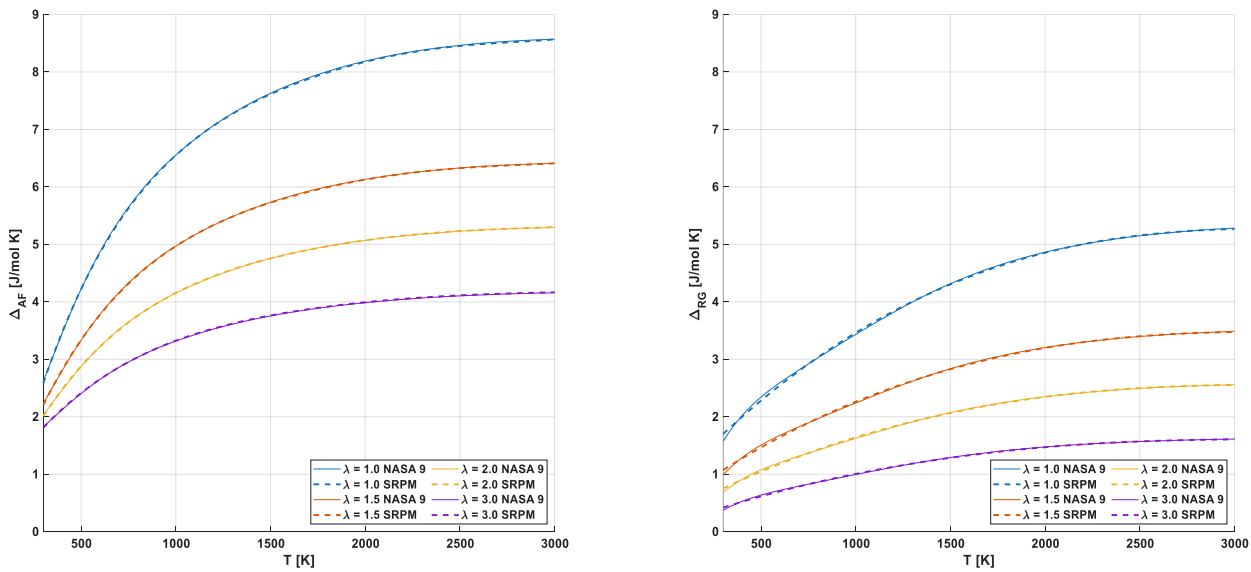

a) b)

Figure 3 Δ_{AF} NASA 9 vs. SRPM (a), Δ_{RG} NASA 9 vs. SRPM (b)

Model verification against the reference dataset

Evaluated across the complete grid (N = 17199 points; T = 300:30:3000 K, λ = 1.0:0.1:3.0, x_{RG} = 0.00:0.05: 0.40), the SRPM achieved an RMSE(γ) of 6.02×10^{-4}, a maximum relative error of 0.28% and a mean relative error of 0.034%.

The largest single deviation occurred at T = 300 K, λ = 1.0 and x_{RG} = 0.0, consistent with the steep curvature of γ(T) at low temperature.

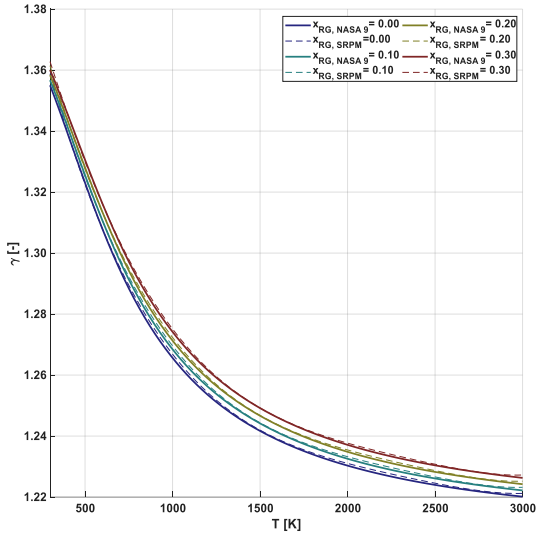

Figure 4 Isentropic coefficent of the residual gas vs. Temperature: comparison of NASA 9 and SRPM models for a range of residual gas concentrations (λ = 1)

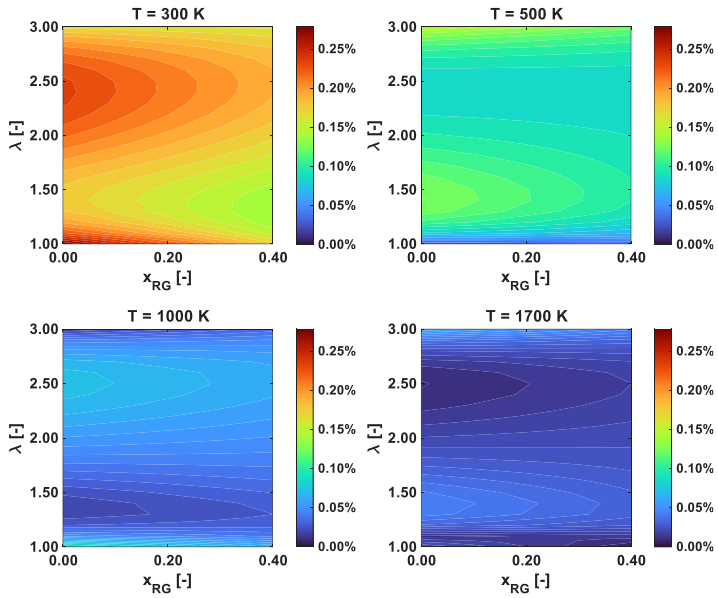

Figure 5 Mean relative error of γ across the λ and x_{RG} domain, at four selected temperatures (300, 500, 1000 and 1700 K)

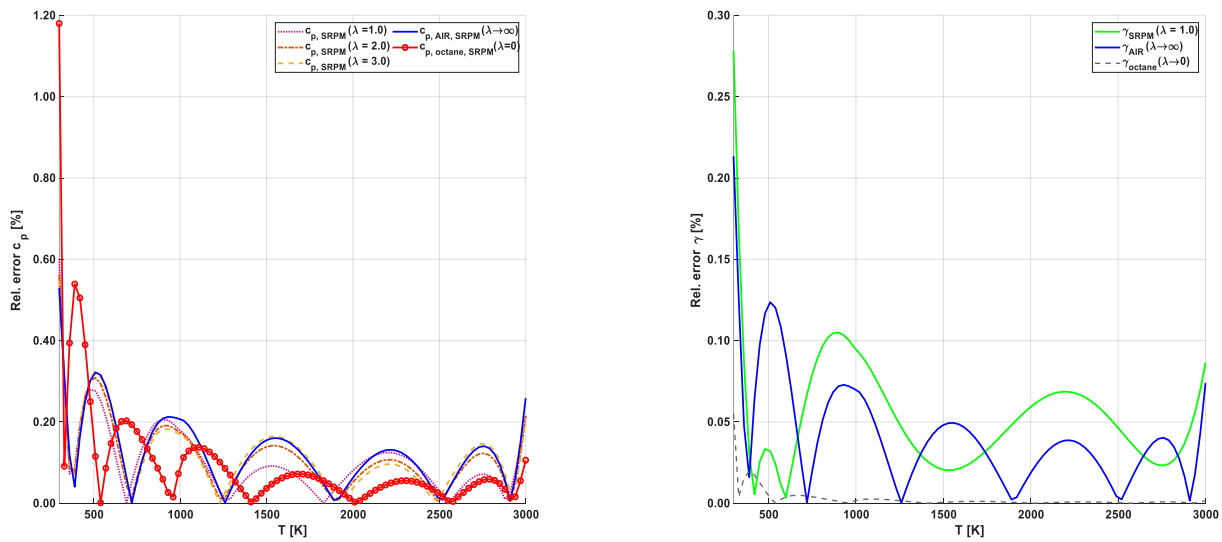

a) b)

Figure 6 Model error versus temperature for pure air, pure octane and the mixture: relative error of c_p (a) and of γ (b), both at x_{RG}= 0.

The model was additionally tested at operating points outside the fitted grid, where the SRPM gave a maximum relative error in γ of 0.24% and a mean relative error of 0.04%.

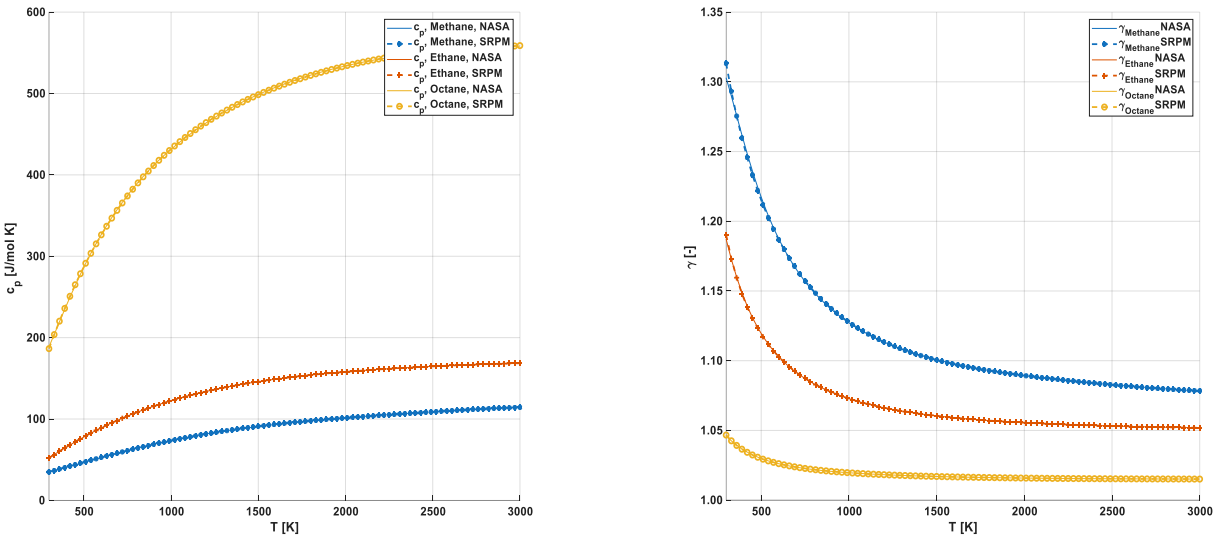

a) b)

Figure 7 Comparison of NASA 9 and SRPM models: specific heat at constant pressure (a) and isentropic coefficient (b) versus temperature for a range of pure alkanes

To assess whether the single-range polynomial approach works for different fuels, the same fitting method was applied independently to methane, ethane and octane representing the alkane series of fuels. Figure 7 shows that single 5th order polynomial reproduces the NASA reference specific heat and their ratio closely across full temperature range, with mean relative error of 0.2%, 0.07% and 0.09% respectively for specific heat at constant pressure and for γ gives 0.036%, 0.008% and 0.002% respectively. This indicates that the SRPM can be applied to fuels of substantially different molecular size, supporting its use as the basis for a broader fuel database.

Comparison with temperature-only models

Three widely used single-range temperature models linear (Gatowski et al. 1984), quadratic (Brunt et al. 1998) and exponential (Egnell, 1998) were calibrated by least-squares regression against the reference model at the nominal point (λ=1 and x_{RG}=0). Evaluated only at this point, the best approximation is achieved with the Egnell model, while the Brunt and Gatowski models produce errors of increasing magnitude, depending on model complexity, Figure 8.

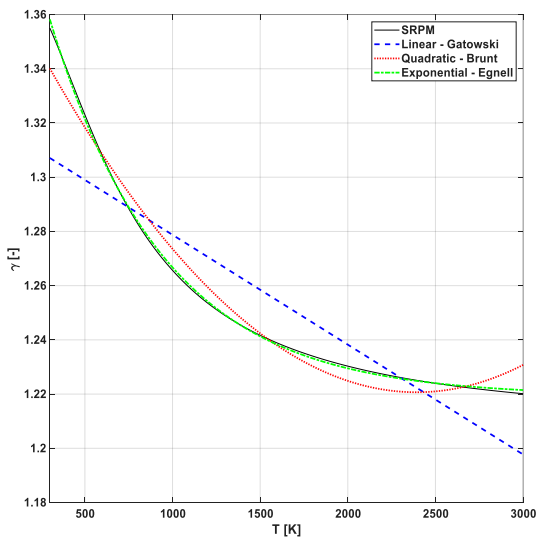

Figure 8 Comparison of simplified models against the SRPM at calibration point λ = 1 x_{RG} = 0

However, evaluated across the full grid, all three models degrade substantially, with mean relative errors of 2.54%, 2.25% and 2.25%, respectively (mean error based on all cases λ=1.0…3.00 and x_{RG}=0.00…0.35). Notably, the quadratic and exponential models achieve almost identical mean relative error over the full grid (2.25% each), despite the exponential model fitting the calibration curve itself considerably more accurately (mean error of 0.06% vs. 0.38% at λ = 1, x_{RG} = 0); since the calibration point accounts for well under 1% of the evaluation grid, the aggregate mean is dominated by the shared structural error from ignoring λ and x_{RG} rather than by differences in local fit quality. By

construction, each returns a single γ value for a given temperature regardless of λ or x_{RG}, so the prediction error grows as the operating point moves away from the calibration point, as shown in Figure 9. Egnell was chosen as representative since it showed the lowest error among the three.

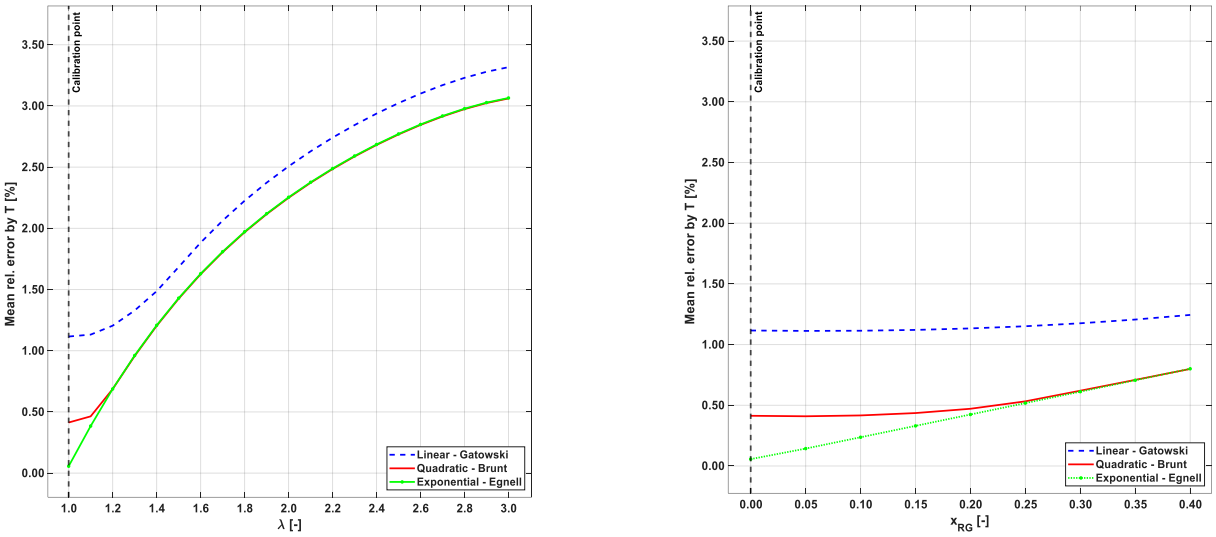

a) b)

Figure 9 Error growth moving from calibration point (λ = 1, x_{RG} = 0) λ varible, x_{RG} fixed (a), Error growth moving from calibration point (λ = 1, x_{RG} = 0) λ fixed, x_{RG} variable (b)

The model's generalization capability was further verified on an independent out of sample grid, where the maximum relative error remained almost unchanged at 0.24%. Even when extrapolated far beyond the fitted range toward the pure air limit, the error increased to 1.37%, confirming numerically stable behaviour outside the intended operating envelope. Presented in Figure 9a, excess-air ratio has a bigger impact on error of simpler models than EGRR. Results of relative error compared to SRPM will be shown later in sub-section Physical role of residual-gas fraction. The relative error for the full excess-air ratio and EGR rate range is presented in Table 1.

Table 1 Accuracy comparison NASA 9, SRPM and Egnell

Model	Max rel. Error [%]	Mean rel. error [%]
Exponential - Egnell	3.588	2.246
SRPM	0.28	0.034
NASA 9	/	/

Physical role of residual gas fraction

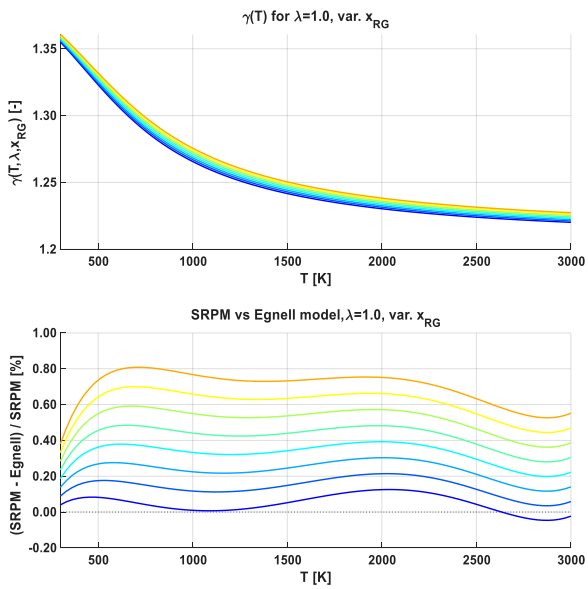

Figure 10 Effect of x_{RG} on *γ(T)* at λ=1.0 family of curves and rel. error of Egnell model with increasing x_{RG}

The new model's response to different values of EGR rate, with a fixed excess-air ratio, is presented in Figure 10. The reference point is assumed to be the stoichiometric ratio, since all simplified models are calibrated at an excess-

air ratio of 1 and EGR rate of 0. As expected, gamma decreases with increasing temperature and rises with higher EGR rates. Figure 10b shows the error introduced by the Egnell model, which does not account for EGR rate at all; in the temperature range of 500 K to 1700 K (the standard range for the engine cycle), this error is around 0.8%. This suggests that any further development of the model could be inspired by the form of the Egnell model. This result corresponds to an excess-air ratio of 1, i.e., the calibration point of the Egnell model; moving away from this operating point yields the results shown in Figure 11:

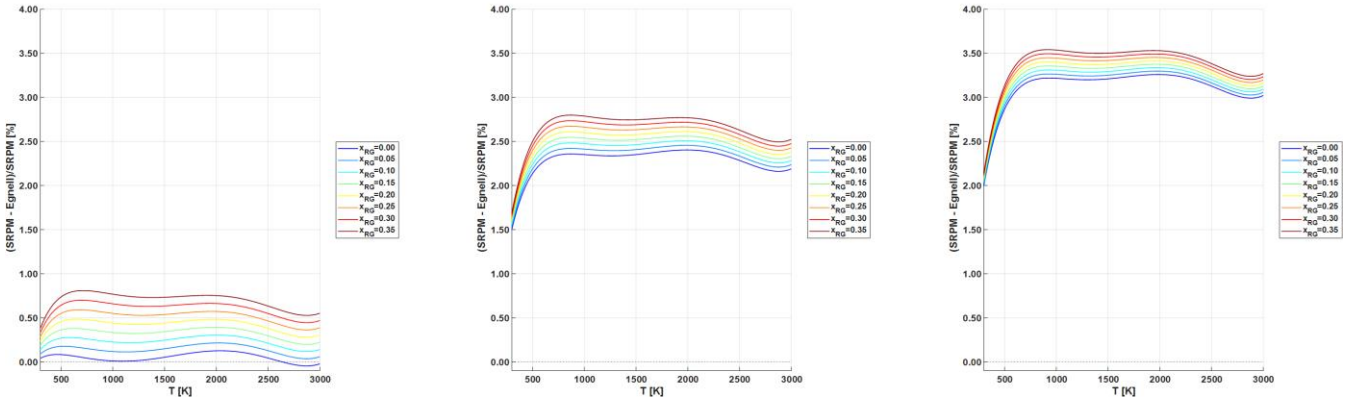

Figure 11 Effect of x_{RG} on γ(T) for different excess-air ratio (λ = 1.0, 2.0, 3.0) family of curves and rel. error of Egnell model with increasing x_{RG}

The effect of excess-air ratio on models such as Egnell's, previously shown in Figure 10, is now considered for the case in which the model's operating point moves away from the calibration point. The relative error grows to a maximum of around 0.80% at 700 K, 2.80% at 860 K, and 3.55% at 900 K, respectively. Such models are reasonable to use for stoichiometric mixtures; however, as the operating point moves away from stoichiometric conditions, the resulting error must be taken into account.

Computational time

All timings were measured in MATLAB R2025b under Windows 10 Pro 22H2, on an AMD Ryzen 5 5600X processor (6 cores, 3.7 GHz base clock) with 32 GB RAM, using default MATLAB settings with no explicit parallelisation. Each model was evaluated at 10^5 randomly sampled (T, λ, x_{RG}) combinations; the procedure was repeated 5 times and the reported value is the mean time per single function call, where one call denotes one evaluation of γ at one operating point.

The new model required 7.23×10^{-6} s per call on average, versus 0.041–0.057 × 10^{-6} s for the temperature-only models, i.e. the SRPM is roughly 125 to 176 times slower per call than these correlations. This reflects the additional polynomial evaluations for the composition dependent terms. The absolute cost remains small in engine simulation terms, at microsecond scale, evaluating γ once per computational step is not a bottleneck relative to the surrounding cycle simulation and is negligible compared to the discontinuity avoidance and species blending overhead of multi range NASA polynomial evaluation. The relevant comparison for real time feasibility is therefore not against simplified models, whose accuracy penalty (Table 1) limits their applicability when λ or x_{RG} vary appreciably, but against the multi range reference approach the SRPM is intended to replace.

Table 2 Average computational cost per function call

Model	Time [10^{-6} s per call]
NASA 9	271.8
Exponential - Egnell	0.057
SRPM	7.23

These values are reported for reference only, since a direct comparison between a detailed model (NASA 9, SRPM or VoLP) and these deliberately simple correlations is of limited meaning. The coefficient base for one fuel is generated in approximately 1.25 s, and this is required only once per fuel. The meaningful comparison is therefore between the multi-range NASA 9 model and the SRPM in the evaluation phase. Averaged over 10^5 random combinations, the mean time per call is 7.23 × 10^{-6} s for the SRPM and 271.8 × 10^{-6} s for the NASA 9 reference model.

Independent verification against an alternative single-range formulation (VoLP)

To enable a direct comparison using fuel-specific coefficients available in the VoLP database, a parallel model instance was calibrated for octane.

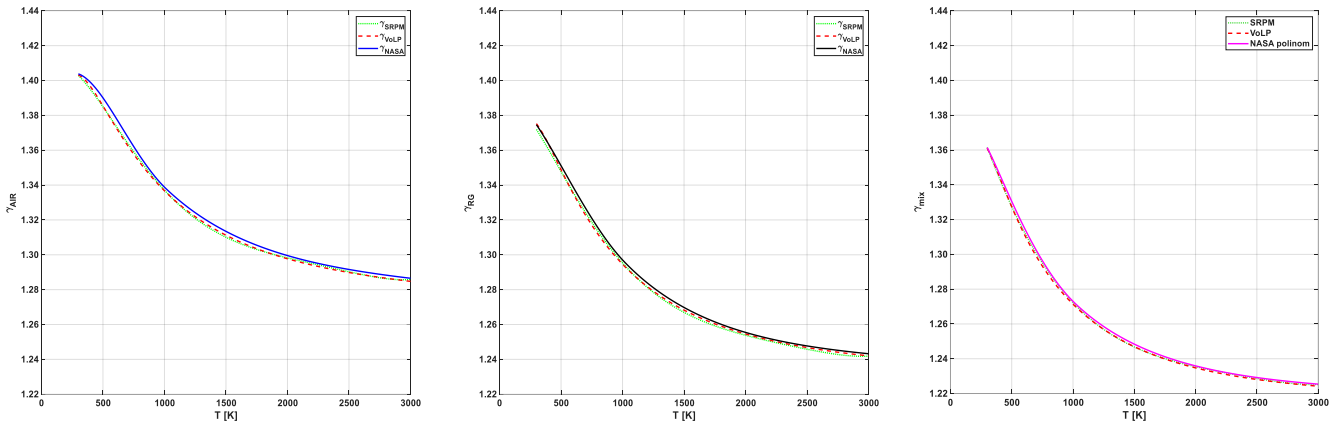

a) b) c)

Figure 12 Comparison of NASA 9, VoLP and SRPM models for three gas compositions: pure air (a), residual gas (*λ= 1*) (b), air-fuel-residual gas (*λ= 1*) (c)

To assess the SRPM against a fundamentally different single-range approach, the fitted octane model was compared with 5th order logarithmic polynomial (VoLP) formulation(Lanzafame & Messina, 2001, 2005, 2007),which represents *γ(T)* using 5th order polynomial in *ln(T+100)* rather than a power series expansion in T. Unlike the temperature-only correlations discussed above, VoLP is not restricted by construction to a single calibration composition; it is evaluated here for the same octane fuel, air and combustion products compositions used by the SRPM, isolating the comparison to the choice of functional form rather than compositional coverage.

Three cases were compared over 300 K to 3000 K temperature range: pure air (Figure 12a), pure combustion products (Figure 12b) by frozen-equilibrium composition and the mixture (Figure 12c). For air and residual gas products, the two formulations agree closely across full temperature range (Air: Maximum relative error = 0.396% and mean error of 0.18%, RG: Maximum relative error = 0.307% and mean error of 0.13%), confirming that the two independently derived property databases – one NASA polynomial based, the other VoLP based – are mutually consistent for single component gas states.

For the full mixture, agreement remains good at low to moderate temperature but the two models diverge smoothly above approximately 2000 K (Maximum relative error 0.285% and Mean error 0.126%). Comparison of relative errors for three models and three different gas mixtures are presented in Table 3:

Table 3 Mean error of models for different cases

Model	Mean error [%]		
	$\lambda = 1.00$, $x_{RG} = 0.2$		
	Pure air	RG	Mixture
NASA 9	Ref.	Ref.	Ref.
VoLP	0.178	0.127	0.126
SRPM	0.176	0.175	0.085
	$\lambda = 2.00$, $x_{RG} = 0.2$		
	Pure air	RG	Mixture
NASA 9	Ref.	Ref.	Ref.
VoLP	~0.178	~0.127	0.149
SRPM	~0.178	~0.175	0.143

The results rest entirely on a numerical comparison with NASA reference data. The reference dataset assumes complete combustion products with no dissociation, so above approximately 2000 K it represents a frozen rather than an equilibrium mixture, which is acceptable for single-zone spark ignition analysis, where mass-averaged temperatures stay below 1800 K.

CONCLUSIONS

In this paper, a new model for the γ as a function of temperature, excess-air ratio and residual gas fraction is presented. The objective was to formulate a simpler alternative to the NASA/NIST/JANAF polynomials and to have only one polynomial that covers the whole range of temperatures and other two variables. Model was built based on curve of specific heat ratio for pure air and two correction terms that represent differences between pure air and other states of working fluid during the cycle.

SRPM was checked with three much simpler models which are based just on temperature and which are calibrated only for one specific case, excess-air ratio 1 and EGR rate 0%, so the accuracy of SRPM against them was evaluated over reference NASA model. SRPM showed accuracy of mean relative error 0.034% and the best of those three simpler models (Egnell, 1998) showed mean error of 2.25% over whole domain of temperatures, EGR rate and excess-air ratio. Moving away from the calibration point, the temperature-only models degrade progressively: the Egnell model deteriorates faster with increasing excess-air ratio, while the residual gas fraction has a smaller effect, Figure 9. That shows that excess-air ratio is dominant source of error for such models, because with higher excess-air ratios we get less fuel and more air, which illustrates the influence of the increased oxygen and nitrogen content on the mixture properties. While a change of EGR rate with fixed excess-air ratio changes the fraction of the mixture with combustion products with similar heat capacity.

Independent test with another single-range alternative, VoLP from Lanzafame and Messina, showed good matching for different working fluid states (pure air, RG and mixture).

Calculation time was also a part of a test, because the idea was to use SRPM on test bench, SRPM works with database for fuel which the engine is working at that moment and it needs around 1.25 sec to make that base but only the first time of working with given fuel. While SRPM calculation time was evaluated with 100000 different combinations over 5 times, so we can calculate mean time and we got around 7×10^{-6} s per call which is slower than the simplified correlations but approximately 38 times faster than the reference model which makes it a practical alternative to the reference model and a suitable basis for further development.

Further work on this model will be concentrated on extended calibration for additional fuels over expanded excess-air ratio ranges to go to more lean mixtures and verification SRPM in calculation of heat release and in - cylinder pressure analysis.

ACKNOWLEDGEMENT

The results presented in this paper are the result of the research supported by the Ministry of Science, Technological Development and Innovation of the RS under Contract 451-03-34/2026-03/ 200105, February 5, 2026.

REFERENCES

Brunt, M. F. J., Rai, H., & Emtage, A. L. (1998). The calculation of heat release energy from engine cylinder pressure data. *SAE Technical Papers*, 724. https://doi.org/10.4271/981052

Burcat, A., & Ruscic, B. (2005). *Third millennium ideal gas and condensed phase thermochemical database for combustion*. Technion Aerospace Engineering (TAE) Report # 867, January 2001. https://doi.org/10.2172/925269

Egnell, R. (1998). Combustion diagnostics by means of multizone heat release analysis and NO calculation. *SAE Technical Papers*, 724. https://doi.org/10.4271/981424

Ferguson, C. R., & Kirkpatrick, A., T. (2016). *Internal combustion engines: Applied thermosciences*, Third edition. https://doi.org/10.1002/9781119454564

Gatowski, J.A., Balles, E.N., Chun, K.M., Nelson, F.E., Ekchian, J.A., & Heywood, J. B. (1984). *Heat Release Analysis of Engine Pressure Data*. https://doi.org/10.4271/841359

Gordon, S., & Mcbride, B. J. (1994). Computer Program for Calculation Complex Chemical Equilibrium Compositions and Applications. *Analysis*, 1–64.

Heywood, J. B. (1988). *Internal combustion engine fundamentals*. McGraw-Hill, New York.

Klein, M. (2007). Single-Zone Cylinder Pressure Modeling and Estimation for Heat Release Analysis of SI Engines. https://www.diva-portal.org/smash/get/diva2:24199/FULLTEXT01.pdf

Klein, M., & Eriksson, L. (2004). A specific heat ratio model for single-zone heat release models. *SAE Technical Papers*, 1–14. https://doi.org/10.4271/2004-01-1464

Lanzafame, R., & Messina, M. (2001). V order logarithmic polynomials for thermodynamic calculations in ICE. *SAE Technical Papers*, 724, 7–9. https://doi.org/10.4271/2001-01-1912

Lanzafame, R., & Messina, M. (2005). New gases thermodynamics properties models to Predict Combustion Phenomena. *SAE Technical Paper* 2005-01-2112, 1. https://doi.org/10.4271/2005-01-2112

Lanzafame, R., & Messina, M. (2007). A new approach to newton-raphson method to evaluate thermodynamics properties for a "in-equilibrium" combustion mixture. *SAE Technical Papers*, 724. https://doi.org/10.4271/2007-01-0024

Olikara, C., & Borman, G. L. (1975). A computer program for calculating properties of equilibrium combustion products with some applications to I.C. engines. *SAE Technical Papers*. https://doi.org/10.4271/750468

The 11th International Congress
Motor Vehicles & Motors 2026
Kragujevac, Serbia
October 8th - 9th, 2026

Motor Vehicles & Motors

MVM2026-038
https://doi.org/10.24874/CMVM2026.038
Original scientific paper

Dragan Peruničić[1]

Petar Markov[2]

Radivoje Pušara[3]

MODELING OF SPECIFIC HEAT RATIO FOR DISI ENGINES WITH COMPLEX MIXTURE FORMATION AND HIGH EGR RATES

ABSTRACT: The gas specific heat ratio (SHR) is essential for thermodynamic simulation and analysis of combustion in engines, particularly under complex multi-injection strategies and gasoline/hydrogen fuelling and increased EGR rates. Simplified models approximate the SHR using linear, quadratic or exponential correlations, while simplicity comes on cost of poor sensitivity to transient air, fuel and exhaust gas fractions during mixture formation and combustion. An improved yet simple methodology for cycle-resolved calculation of the SHR is presented. Fuel mass flow is predicted using a Bernoulli-based model of high-pressure gasoline injector corrected for nozzle geometry, pressure and temperature dependent gas and fuel properties during the injection in compression phase. Air and fuel mass fractions, equivalence ratio, and EGR dilution were evaluated continuously, enabling accurate determination of the instantaneous working-fluid composition and corresponding SHR in the crank-angle domain. Model accuracy is assessed against reference NASA polynomials for individual gas component presuming ideal gas mixture for single and multiple injections in stoichiometric and lean operation of DISI engine. Deterministic heat release rate evaluation based on the First law of thermodynamics is compared with three widely used simplified specific heat ratio coefficient models demonstrating improved combustion phasing accuracy (MFB5-MFB90).

KEYWORDS: specific heat ratio, direct injection, spark ignition engine, EGR, mixture formation

[1] *Dragan Peruničić, MSc, student, University of Belgrade, IC Engines Dept., Kraljice Marije 16, Belgrade, Serbia,* *1017-2024@studenti.mas.bg.ac.rs*
[2] Petar Markov*, MSc, student,* University of Belgrade, IC Engines Dept., Kraljice Marije 16, Belgrade, Serbia, 1032-2024@studenti.mas.bg.ac.rs
[3] *Radivoje Pušara, MSc, student,* University of Belgrade, IC Engines Dept., Kraljice Marije 16, Belgrade, Serbia, 1010-2024@studenti.mas.bg.ac.rs

MODELIRANJE ODNOSA SPECIFIČNIH TOPLOTA U MOTORIMA SA DIREKTNIM UBRIZGAVANJEM, KOMPLEKSNIM OBRAZOVANJEM SMEŠE I VISOKIM UDELIMA EGR-a

REZIME: Odnos specifičnih toplota gasa neophodan je za termodinamičke simulacije i analizu sagorevanja u motorima, pogotovo pri kompleksnim strategijama sa više ubrizgavanja, pri ubotrebi benzina/vodonika i povećanim udelima EGR-a. Pojednostavljeni modeli predviđaju koeficijent izentrope pomoću linearnih, kvadraturnih ili eksponencijalnih relacija, međutim, jednostavnost dolazi na uštrp male osetljivosti na promenljivost strujanja vazduha, udele goriva i recirkulisanih/zaostalih gasova tokom formiranja smeše i sagorevanja. Predstavljen je poboljšan, jednostavan model za ciklusno sračunavanje koeficijentra izentrope. Maseni protok goriva predviđan je modelima na bazi Bernulijeve jednačine za visokopritisne benzinske brizgače sa uvedenim korekcijama za geometriju mlaznice, promenljiva svojstva gasa i goriva na povišenim temperaturama i pritiscima koji se javljaju tokom procesa ubrizgavanja u taktu sabijanja. Maseni odnosi vazduha i goriva, koeficijent viška vazduha i procenat EGR razblaženja su kontinualno sračunavani, što je omogućilo precizno poznavanje trenutnog sastava radnog fluida i njegovog koeficijenta izentrope u ugaonom domenu. Preciznost modela proverena je u odnosu na proračun sa NASA polinomima za svaku komponentu gasa ponaosob, pretpostavljajući idealnu smešu gasa, i to pri pojedinačnom i višestrukom ubrizgavanju pri radu sa stehiometrijskom ili siromašnom smešom u motorima sa direktnim ubrizgavanjem benzina. Deterministički model oslobađanja toplote zasnovan na Prvom zakonu termodinamike poređen je sa tri najčešće korišćena, pojednostavljena modela koeficijenta izentrope, demonstrirajući preciznije predviđanje karakterističnih faza u procesu sagorevanja (MFB5-MFB90).

KLJUČNE REČI: odnos specifičnih toplota, direktno ubrizgavanje, motori sa upaljenjem pomoću varnice, EGR, obrazovanje smeše

INTRODUCTION

In the field of engine testing and combustion diagnostics, the specific heat ratio is one of the key thermodynamic parameters used in a wide range of simulations and calculations. Its accurate determination is particularly important in engine indication, heat-release analysis, and combustion-phasing evaluation, where errors associated with an inappropriate specific heat ratio formulation may become comparable to, or even exceed, those introduced by incorrect cylinder-pressure referencing. Despite this sensitivity, the specific heat ratio is still frequently represented by simplified empirical correlations that depend primarily on temperature and therefore have limited capability to account for transient changes in working-fluid composition. This limitation becomes increasingly important in modern direct-injection spark-ignition (DISI) engines, where multiple injection events, variable fuel-split strategies, exhaust gas recirculation (EGR), and late mixture formation continuously alter the in-cylinder composition throughout the high-pressure part of the engine cycle. Under such conditions, the instantaneous proportions of air, fuel, residual gases, recirculated combustion products, and newly formed combustion products directly affect the thermodynamic properties of the working fluid and, consequently, the specific heat ratio.

In this paper, a cycle-resolved model for the determination of the specific heat ratio is proposed. The approach combines a temperature- and composition-dependent polynomial thermodynamic model with a hydraulic model for predicting the instantaneous injected fuel mass. The mixture composition, in-cylinder temperature, and specific heat ratio are continuously updated in the crank-angle domain from intake valve closing to exhaust valve opening. The hydraulic submodel accounts for injector-flow characteristics, including pressure difference, nozzle geometry, viscous losses, and cavitation effects, while the thermodynamic formulation evaluates the properties of the individual mixture components using polynomial correlations. The resulting specific heat ratio histories are subsequently applied to deterministic heat-release analysis and compared with the commonly used Gatowski et.al. (1984), Egnell et al. (1998) and Brunt et al. (1998) empirical models under operating conditions characterized by EGR variation and different multi-injection strategies.

MODEL FORMULATION AND METHODOLOGY

Fuel injector hydraulic model

A set of data from three different working regimes that has been previously collected on the engine test bed was

used as a guideline for this model. Data like rail pressure, excitation current signal from the injectors, number of injections, duration and position of the injections, and the in-cylinder pressure curve has been taken from these operating points as a basis for injection cycle calculations.

The fuel jet velocity through the injector nozzle was predicted using the Bernoulli equation, which for the quasi-steady conditions, and completely neglected viscous effects, heat transfer and flow contraction gives following expression:

$$u_{th} = \sqrt{\frac{2(p_{rail} - p_{cyl})}{\rho_{fuel}}} \tag{1}$$

Hence, the mass flow was calculated as:

$$\dot{m} = C_d A_0 u_{th} \tag{2}$$

Change in flow section has been modelled based on the collected excitation current signal from the injector, in a manor where the length of the opening and closing ramps was devised from the peak analysis of the signal, and the change from fully open to fully closed flow section was modelled with a shape function.

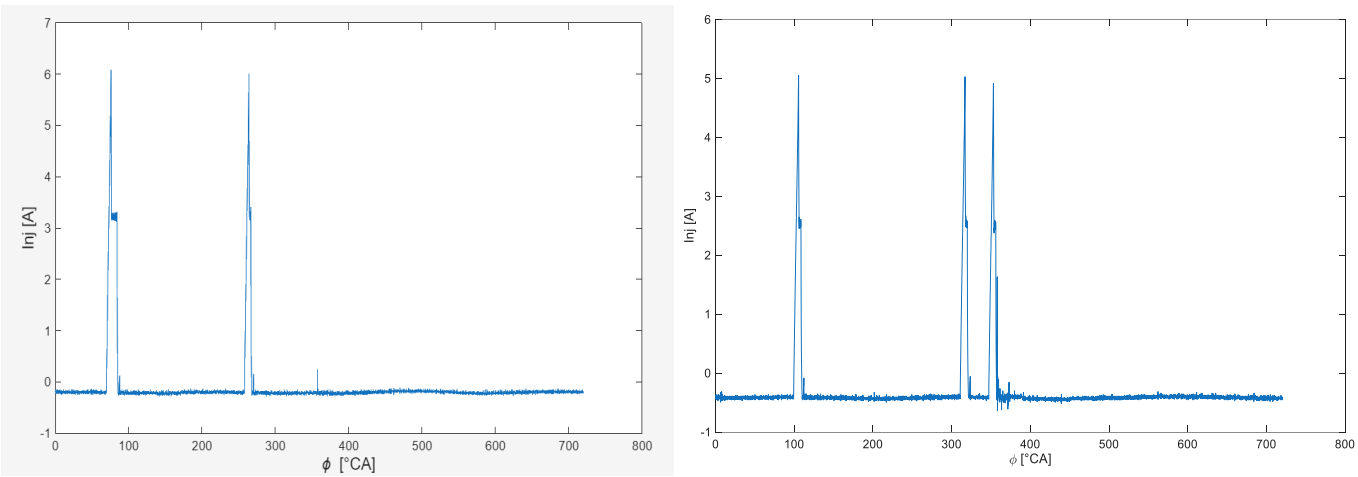

a) b)

Figure 1 General presentation of excitation current profile for double (a) and triple injections (b)

To evaluate injector nozzle discharge coefficient, model of von Kuenssberg-Sarre (von Kuensberg Sarre, Kong, & Reitz, 1999) was chosen being capable to include design features and cavitating flow conditions. For non-cavitating flow condition discharge coefficient is calculated as follows:

$$C_d = \frac{1}{\sqrt{\xi_r + f\frac{L_n}{D_n} + 1}} \tag{3}$$

The loss coefficient at the nozzle entrance ξ_r depends on nozzle inlet radius and can be retrieved from tabulated data as in the work of Idelchik (2008) and Desantes et al. (2016). The viscous friction coefficient f is calculated according to the Blasius correlation as a function of Reynolds number (von Kuensberg-Sarre et al. 1999). To represent more closely the actual fluid discharge process through the cavitating nozzle, the von Kuenssberg-Sarre model introduces following correlation based on cavitation number K (von Kuensberg-Sarre et al. 1999). and contraction coefficient C_c (Nurick, 1976).

$$C_d = C_c\sqrt{K} \tag{4}$$

To establish a selection mechanism between the two forms of this model, the onset of cavitation is defined based on the critical cavitation number, which, according to the Macian model, is given by:

$$K_{crit} = PR^{0,01968} RR^{-0,2156} ARR^{-0,0375} DR^{0,3088} \tag{5}$$

The dimensionless terms in Equation (11) are defined against design parameters for the reference injector used in experimental verification of the Macian model. Reference data could be found in literature (Macian et al. 2003). For $K < K_{crit}$, the flow is considered cavitating, whereas for $K > K_{crit}$, cavitation is assumed not to occur.

$$PR = \frac{pinj}{p_{inj\ ref}} \qquad RR = \frac{r0N}{r0N,ref} \qquad ARR = \frac{AR}{AR_{ref}} \qquad DR = \frac{D_{n,out}}{D_{n\ out\ ref}} \tag{6}$$

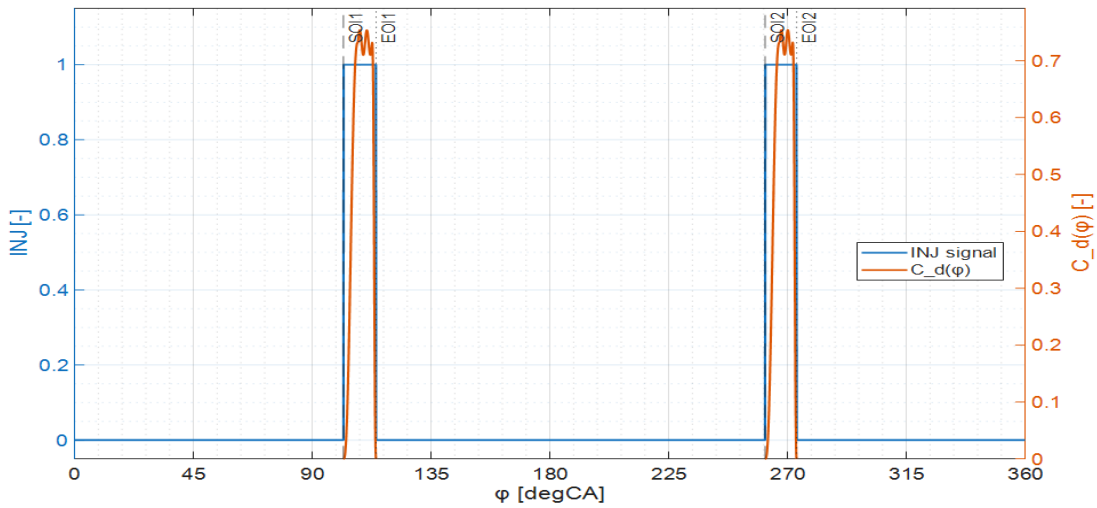

a)

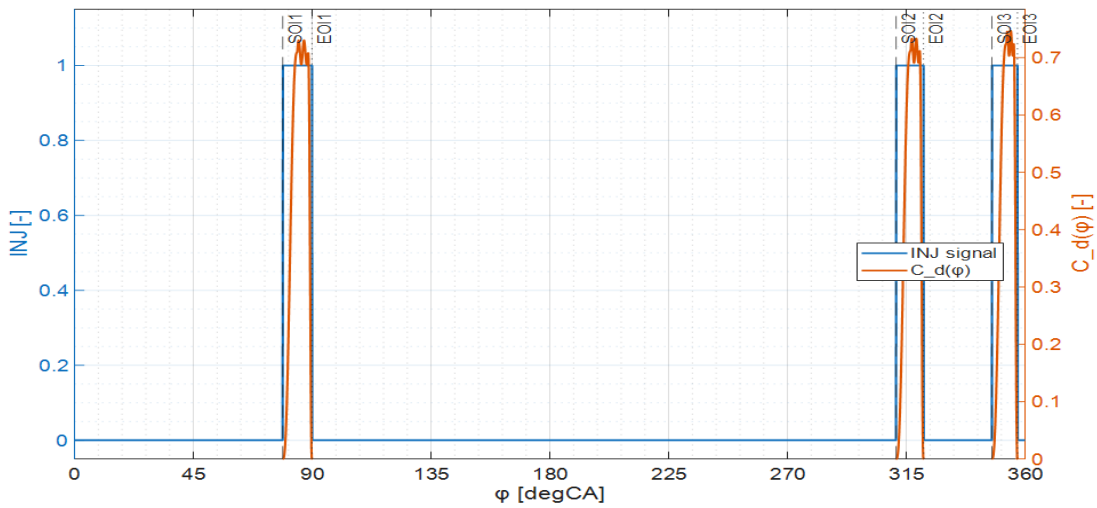

b)

Figure 2 Injection signal shape and C_d variation profile for operating conditions with two and three injection events

The hydraulic model was validated over multiple operating conditions by comparing the fuel mass obtained from the measured fuel consumption, converted to fuel mass per cycle, with the corresponding cycle fuel mass predicted by the model using test-bench data acquired at each operating condition.

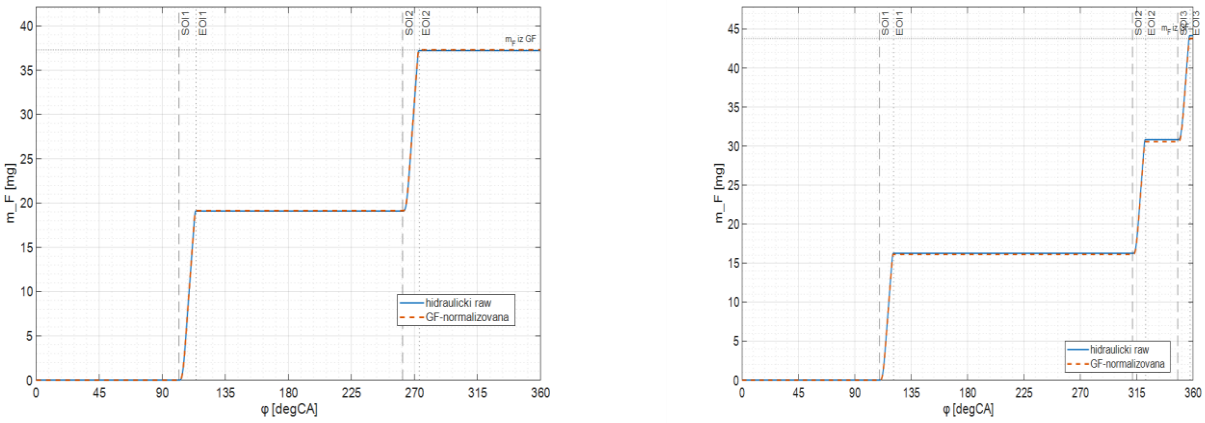

a) b)

Figure 3 Cumulative injected mass profiles for different injection strategies

Specific heat ratio model

The model was developed for application to direct-injection engines. The working fluid, consisting of air, fuel, and combustion products, is treated as an ideal gas. By applying Dalton's law, the following expression for the specific heat capacity of the working fluid at constant pressure is obtained:

$$c_{p,AFRG} = c_{p,A}y_A + c_{p,F}y_F + c_{p,RG}y_{RG} \tag{7}$$

where y represents the mole fraction of the component and c_p the specific heat capacity of the component. To determine the specific heat capacities in this manner, it is necessary to know the temperature dependence of the specific heat capacity of each component of the working fluid, as well as the mole fraction of the individual components of the working fluid throughout the engine cycle.

To address this problem, approximation functions developed by Gordon and McBride (Svehla & McBride, 1973) were employed to represent the thermodynamic properties of the working fluid as functions of temperature. Both seven- and nine-coefficient formulations are available; in the present work, the more recent and more accurate nine-coefficient formulation is adopted.

$$\frac{c_{p,i}(T)}{R} = a_{i1}T^{-2} + a_{i2}T^{-1} + a_{i3} + a_{i4}T + a_{i5}T^2 + a_{i6}T^3 + a_{i7}T^4 \tag{8}$$

To apply the formulation defined in Equation (8), the mole fractions of the individual components of the working fluid must also be determined. Since the model is formulated in the crank-angle domain, the injected fuel quantity obtained from the hydraulic model is first tracked. Once the modelled fuel quantity per cycle has been determined, the corresponding air quantity per cycle can be calculated using the following relation:

$$m_{A,c} = m_{F,c}\lambda AFR_{steh} \tag{9}$$

where AFR_{steh} is the stoichiometric air fuel ratio. The molar masses of air and fuel were determined based on their chemical composition. Finally, based on the known air mass and molar mass, the amount of air can be determined. The composition of the combustion products strongly depends on the mixture composition and the conditions prevailing during combustion. In the present work, formation of molecular hydrogen and carbon monoxide are neglected in the combustion products. The model assumes no dissociation and does not require the explicit evaluation of chemical-equilibrium constants; instead, a frozen-equilibrium assumption is adopted. The equations used to determine the molar concentrations of the individual combustion-product species are given in (Popović, 2013).

To determine the combustion products concentration in the intake manifold, a relation based on the ratio of the CO_2 mole fractions in the intake manifold and the exhaust gases is used. Equation (10) is applicable to direct injection (DI) ICE, since the presence of fuel in the intake mixture would otherwise affect the calculated composition.

$$EGRR = \frac{y_{CO2,int} - y_{CO2,Air}}{y_{CO2,exh} - y_{CO2,Air}} \tag{10}$$

The starting point of the model is taken as the crank-angle position corresponding to intake valve closing (IVC), since the phenomena occurring during the intake stroke are beyond the scope of this study. To estimate the temperature at this crank-angle position, the correlation proposed by Manz (Manz, P. W., 2001) was employed.

$$T_{IVC} = 0.833T_{INT} + C \tag{11}$$

where T_{int} represents the temperature in the intake manifold and C is a constant equal to 86 K. Knowing the temperature at the crank-angle position corresponding to intake valve closing, the specific heat ratio can be calculated using the Equation (12) and the following expressions:

$$\kappa(T,y) = \frac{c_p(T,y)}{c_v(T,y)} = \frac{c_p(T,y)}{c_p(T,y) - R_u} \tag{12}$$

At each crank angle position, the instantaneous composition of the working fluid is updated, accounting for the EGR rate and equivalence ratio. Together with the corresponding temperature, the updated composition is then used to recalculate the specific heat ratio, κ. To determine the in-cylinder temperature at every angle position during combustion, from the end of compression stroke to exhaust valve opening (EVO), the mass of the working fluid is assumed to remain constant over this crank angle interval. The trapped gas mass is first determined from the ideal-gas equation using the thermodynamic state at the intake valve closure which includes the mass of air, residual gases, recirculated combustion products and fuel delivered during the first injection cycle positioned in intake stroke. This mass is then used in the subsequent calculation of the instantaneous in-cylinder temperature throughout the combustion process:

$$m_{gas} = \frac{p_{IVC}V_{IVC}}{R_{gas}T_{IVC}} \tag{13}$$

$$T_i = \frac{p_i V_i}{R_{gas} m_{gas}} \tag{14}$$

To calculate the specific heat ratio (SHR), the mole fractions of the individual species in the working fluid mixture during combustion must also be known. The change of the mixture composition resulting from fuel combustion and the conversion of air and fuel into combustion products is described using the relation proposed by Lanzafame and Messina (2003), which relates the in-cylinder temperature ratio to the burned fuel fraction:

$$x_{bi} = \frac{T_i - T_{SOC}}{T_{EOC} - T_{SOC}} \tag{15}$$

where T_{SOC} is the temperature at ignition and T_{EOC} is the maximal in-cycle temperature corresponding to end of combustion (EOC). Subsequently, the fractions of burned and unburned air, together with the number of moles of newly formed combustion products, are determined at each crank angle step within the combustion interval defined by Equation (15). The change of mole fractions for air, fuel, and combustion products is presented in Figure 4.

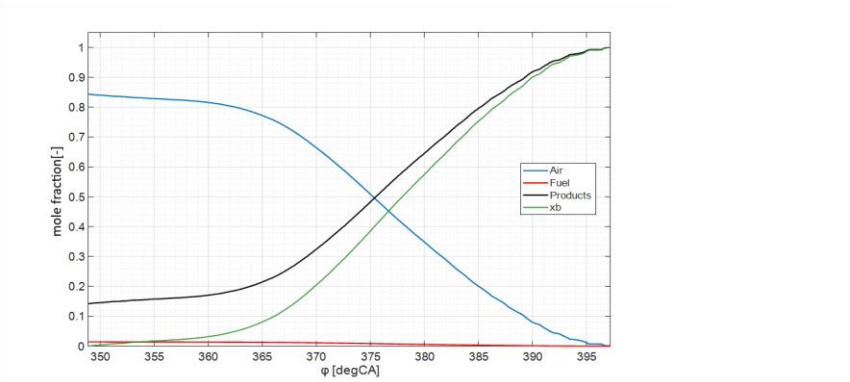

Figure 4 Mole fraction histories of air, fuel and combustion products during combustion

By combining all described sub-models, a continuous crank angle resolved calculation of the specific heat ratio is ultimately obtained over the high-pressure phase of the engine cycle. The comparison of results gained by proposed model and three approximations by Gatowsky Brunt and Egnell is presented in Figure 5.

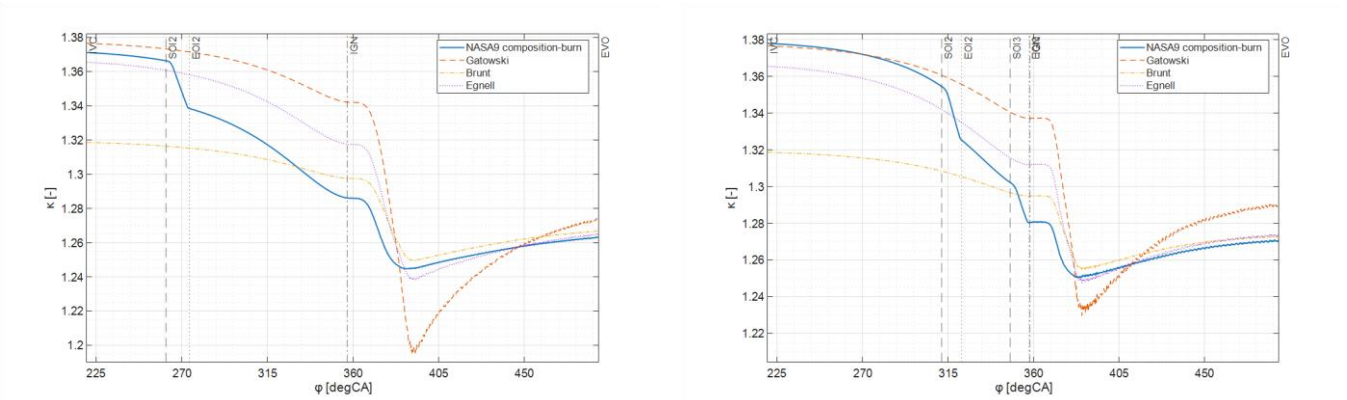

a) b)

Figure 5 Specific heat ratio histories for combustion cycles with different injection strategies: double injection (a), triple injection (b)

Heat release rate calculation

Accurate evaluation of the heat release rate (HRR) is essential for the analysis of combustion phasing and process efficiency. In deterministic heat release analysis based on the First Law of Thermodynamics, the SHR represents one of the key thermodynamic parameters influencing significantly the calculated heat release profile and the resulting mass fraction burned (MFB). The fundamental form of the First Law of Thermodynamics, assuming no heat transfer is occurring, is given by:

$$dQ = dU + dW = d(mu) + pdV = dmu + mdu + pdV \tag{16}$$

If mass leakage is neglected, by introducing well known expressions for specific heat and gas constant, final expression for net heat release is obtained in differential form in angular domain:

$$\frac{dQ_{net}}{d\varphi} = \frac{1}{\gamma - 1}\frac{dp}{d\varphi}V + \frac{\gamma}{\gamma - 1}p\frac{dV}{d\varphi} \tag{17}$$

Once the differential heat release rate dQ/dφ has been determined, the cumulative heat release Q_{cum} is obtained by integrating the heat release rate over the crank angle domain:

$$Q_{cum}(\varphi) = \int_{\varphi_{IVC}}^{\varphi EVO} \frac{dQ}{d\varphi}\, d\varphi \tag{18}$$

where φ_{IVC} represents the crank-angle position corresponding to the closing of the intake valve. The heat release during combustion phase could be analysed from the cumulative heat released from the onset of combustion up to a given crank angle position at which end of combustion (EOC) can be identified with the high level of certainty. The mass fraction burned (MFB) can be evaluated by normalizing the cumulative heat release with the total heat released over the combustion interval:

$$MFB(\varphi) = \frac{Q_{cum}(\varphi)}{Q_{cum}(\varphi_{EOC})} \tag{19}$$

where φ_{EOC} denotes the crank-angle position corresponding to the end of combustion. Characteristic combustion-phasing parameters, such as MFB5, MFB50, and MFB90, are then defined as the key crank angle positions at which 5%, 50%, and 90% of the total mass of fuel is burned, which is proportional to the heat release values if fuel leakage and unburned fuel are neglected.

RESULTS AND DISCUSSION

The results obtained using the proposed crank angle resolved SHR model are analysed in this section and compared with those obtained using three commonly applied empirical formulations. The comparison is performed for three representative engine operating conditions acquired on the test bench, providing a basis for evaluating the influence of the specific heat ratio formulation on the calculated heat release characteristics and combustion phasing.

For each operating condition, the resulting heat release rate, cumulative heat release and mass fraction burned are examined. Particular attention is given to characteristic combustion-phasing parameters, including MFB5, MFB50, and MFB90, in order to quantify the differences between the proposed model and the empirical approaches. The analysis is intended to assess whether the more detailed treatment of the working fluid composition and thermodynamic properties leads to a more consistent representation of the combustion process across different engine operating conditions.

Two injection EGR rate sweep

The first set of operating regimes is characterized by a double injection strategy with a 50/50 split factor (SF), while the EGR rate (EGRR) was varied from 0 to 25% as a part of an EGR rate sweep. The resulting figures are used to identify and quantify any differences between the proposed model and the empirical models in terms of the κ(φ) profiles and to assess how these differences affect the calculated heat release rate, cumulative heat release, and mass fraction burned (MFB).

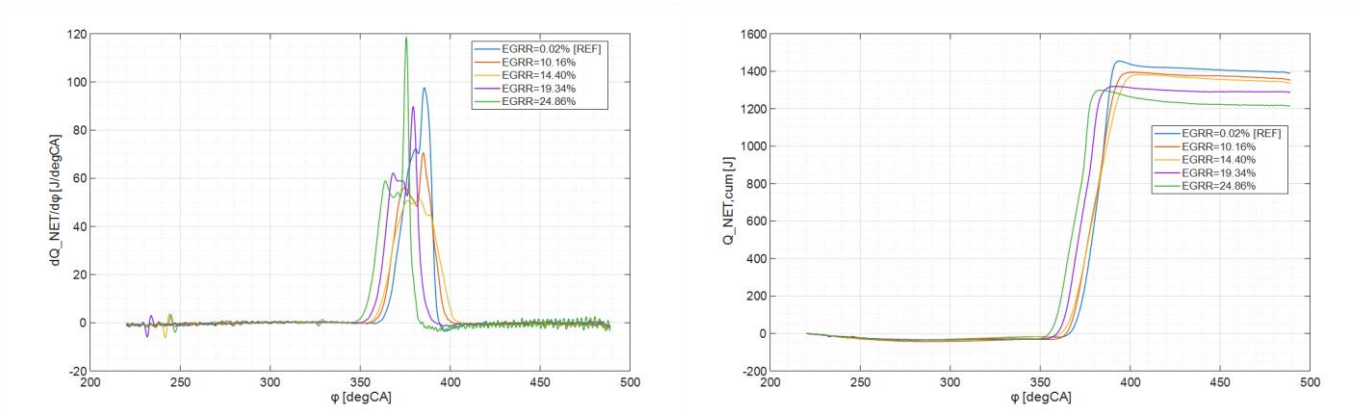

a) b)

Figure 6 Differential (a) and cumulative (b) heat release for EGR rate sweep (0…25%) with double injection (SF=50/50)

In Figure 6, the histories of the differential and cumulative heat release for EGRR sweep with double injection calculated by the proposed model are presented. A clear difference can be observed between the case without EGR and the case corresponding to the maximum EGRR.

Figure 7 presents direct comparison of SHR calculated using the proposed model and approximation models proposed by Gatowski, Brunt and Egnell. The histories of specific heat ratio were tracked from the intake valve closure (IVC) down to the exhaust valve open (EVO) covering complete compression, combustion and expansion phase. Moreover, the empirical models are unable to account for the changes in working fluid composition occurring during mixture formation and the early stages of combustion. As combustion progresses and the mixture composition approaches that of the fully formed combustion products, the difference between the proposed model and the empirical formulations gradually decreases. Expectedly, the simplest linear model proposed by Gatowski presented the worse results.

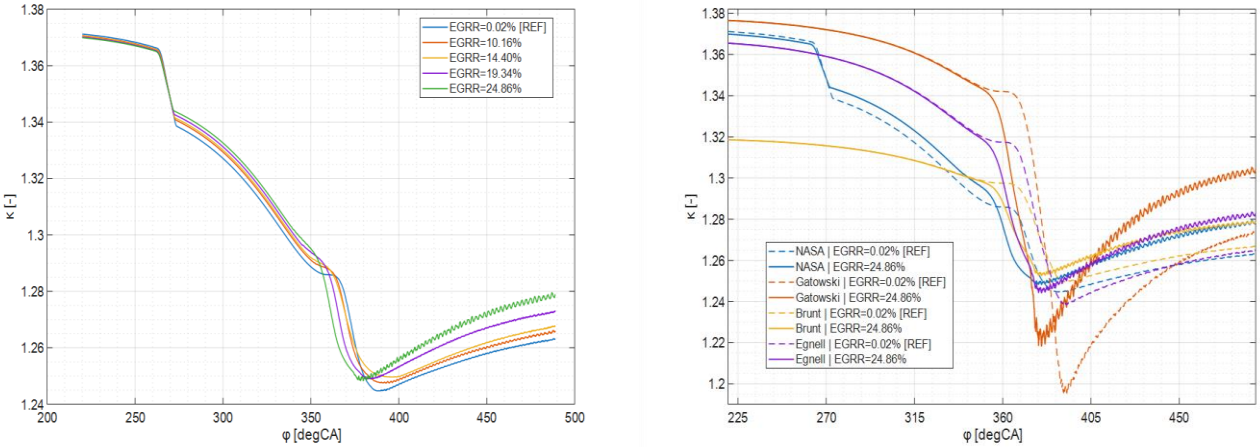

a) b)

Figure 7 Specific heat ratio histories calculated using proposed model and three approximation models: EGRR=0% (a), EGRR=25% (b)

Figure 8 illustrates the difference in the net cumulative heat release calculated using proposed model for SHR and three empirical models for two boundary EGR rates, 0% and 25%, respectively. The results indicate that the empirical models predict a considerably lower amount of net heat retained by the in-cylinder working fluid at the end of the combustion process. Numerical results on relative errors between empirical models (Gatowsky, Brunt, Egnell) and NASA reference model for the complete EGRR sweep are presented in Table 1.

The relative error ranges from approximately 2% to 9% depending on the empirical model. Gatowski and Egnell models exhibit more pronounced deviations, with relative errors of approximately 5% and 9%, respectively, whereas the Brunt formulation provides a surprisingly accurate prediction of the released heat, with a relative error of only 2–3%. Nevertheless, it should be emphasized that, in this type of thermodynamic analysis, where relatively small differences are of interest and a high level of precision and accuracy is required, relative errors of this magnitude cannot be regarded as negligible.

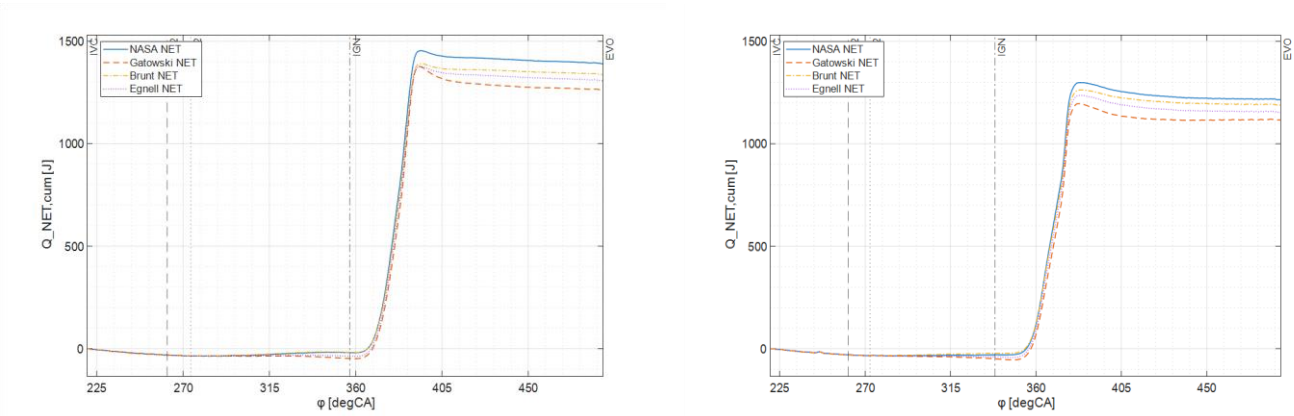

a) b)

Figure 8 Comparison of cumulative heat release calculated with different specific heat models for EGRR=0% (a) and EGRR=25% (b)

Table 1 Cumulative heat relative error for empirical SHR models (ref. model NASA)

Model	**Rel. error [%] (case EGRR=0%)**	**Rel. error [%] (case EGRR=25%)**
Gatowski	−9.20	−8.08
Brunt	−3.81	−2.13
Egnell	−5.97	−4.99

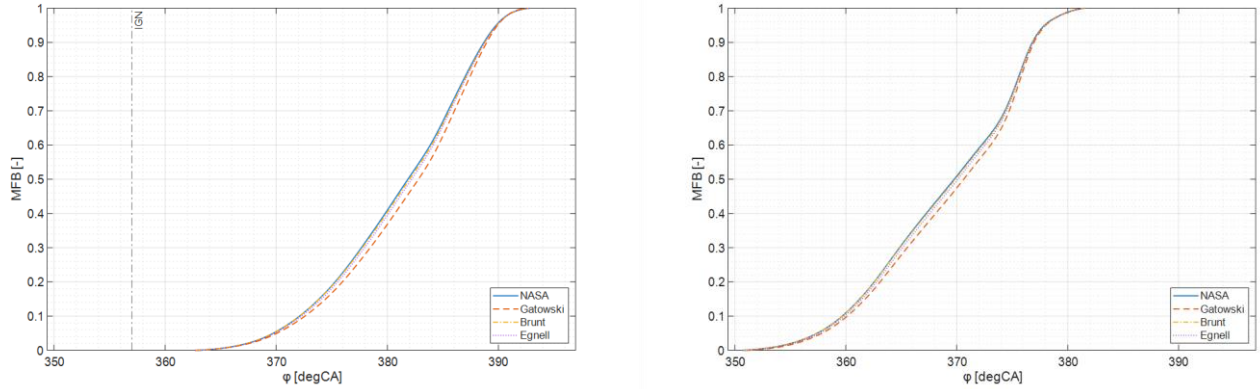

a) b)

Figure 9 Comparison of MFB profiles predicted by the proposed model and the empirical models: a) EGRR=0%, b) EGRR=25%

Figure 9 provides a comparison of the MFB curves predicted by the proposed model at two EGR rates, 0% and 25%, together with the corresponding MFB curves obtained using the three empirical formulations. The comparison is intended to highlight differences in the crank angle positions of the key combustion phasing points, namely MFB5, MFB50, and MFB90. The comparison is presented numerically in Table 2.

Table 2 Key MFB positions (NASA model) and deviations for empirical models for EGRR=0% and EGRR=25%

Model	**EGRR=0%**		
/	**MFB5**	**MFB50**	**MFB90**
NASA 9	369.73	381.85	388.69
Gatowski	-0.33	-0.95	-0.25
Brunt	0.02	-0.14	-0.06
Egnel	-0.12	-0.33	-0.09
/	**EGRR=25%**		
NASA 9	357.41	369.77	376.81
Gatowski	-0.44	-0.86	-0.15
Brunt	0.01	-0.10	-0.04
Egnel	-0.20	-0.32	-0.06

In applications where even a 0.5 CAD shift in the MFB50 position requires substantial effort and resources to achieve, the deviations produced by the Gatowski and Egnell formulations can be considered unacceptable. By contrast, the Brunt formulation, with an MFB50 error of approximately 0.1–0.2 CAD, provides a comparatively satisfactory prediction.

Double injection SF sweep

Split factor (SF) sweep in double injection strategy without EGR is further considered to investigate the sensitivity of the proposed model. Split factor sweep comprises 50/50, 60/40, 70/30, and 100/0 fuel mass ratios. The analysis is aimed at assessing the influence of the SF on the key parameters of the heat release model and on the resulting combustion characteristics.

Figure 10 illustrates the influence of the SF on the differential and cumulative heat release characteristics. From the cumulative heat release profiles, it can be observed that the post-combustion decay becomes progressively steeper as the amount of fuel injected during the later injection event is reduced and the mixture homogeneity is increased. Figure 11a presents the results of SHR produced by proposed model for a set of SF ratios covered by the experiment. The main difference is seen in the case of single injection (SF=100/00) during the early stage of compression, up to the position at which the second injection is engaged in split injection cycles. Again, the difference became significant during combustion as a result of delayed evaporation, changed ignition timing and combustion dynamics. Further, the difference again demonstrates the limited sensitivity of the empirical models to the changes in mixture composition. Figure 11b presents direct comparison of SHR for two boundary SF values (SF=50/50 and SF=100/00, respectively) provided by proposed model and three empirical models. Empirical models presented significant deviation relative to the reference model with different phasing and amplitudes during combustion, depending on model complexity.

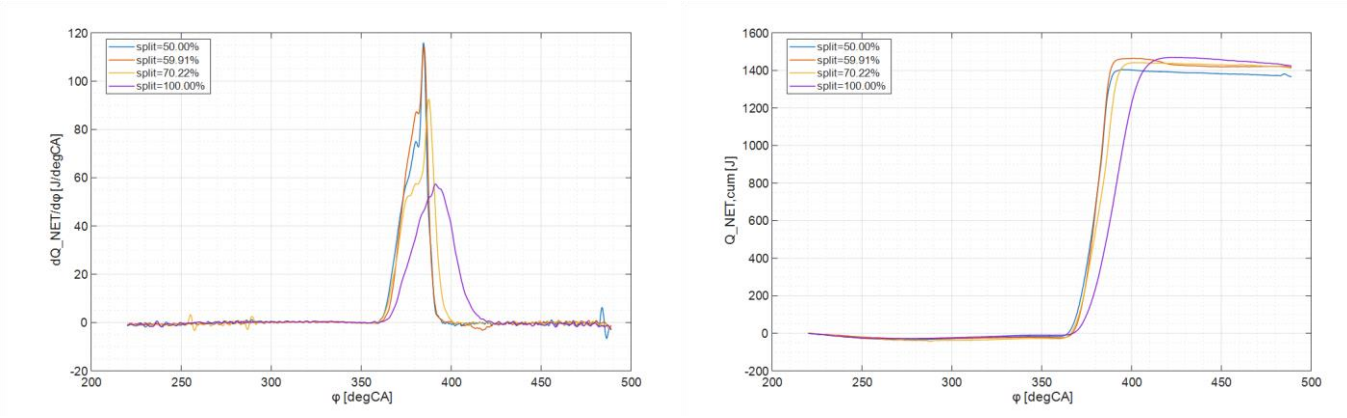

a) b)

Figure 10 Differential (a) and cumulative heat release (b): split factor in double injection strategy

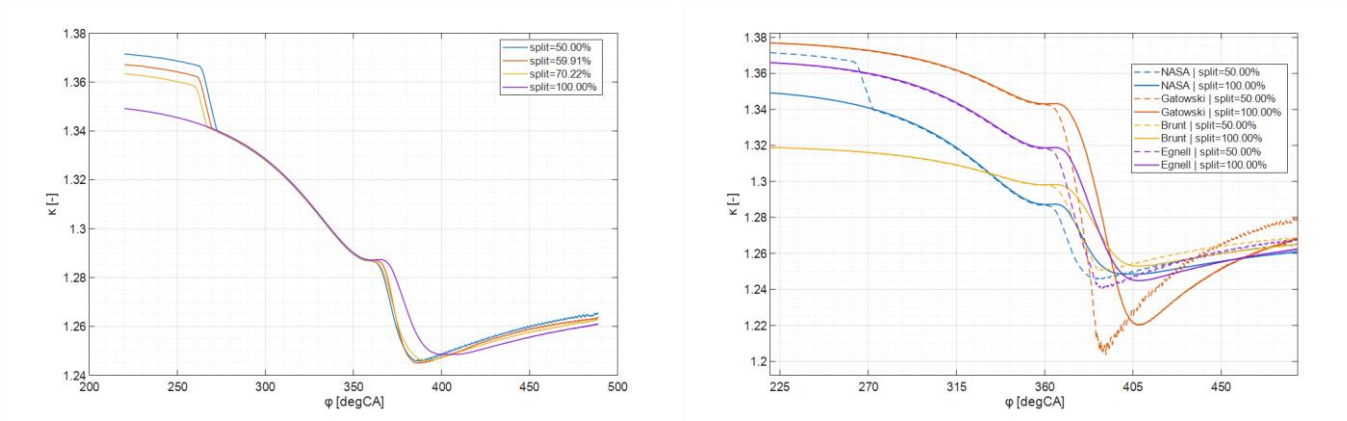

a) b)

Figure 11 Specific heat ratio histories calculated using proposed model for all SF values (a) and specific heat ratio histories calculated using proposed model and three approximation models: SF 50/50 and SF100/00 (b)

Figure 12 compares the cumulative heat release profiles for two SF cases (SF=50/50 and SF=100/00), with the corresponding predictions obtained using the three empirical models. The comparison is intended to assess how the choice of the SHR model influences the predicted cumulative heat release under different split injection conditions. The relative error ranges are slightly higher than those observed for the EGRR sweep; however, the differences remain relatively small. The relative error decreases as combustion begins with an increasingly homogeneous mixture.

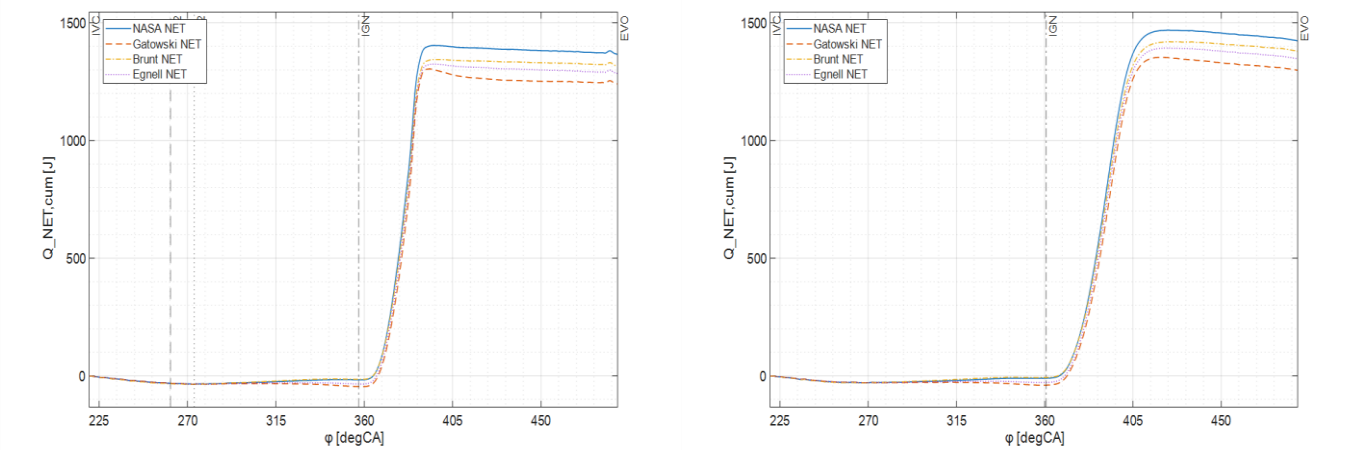

a) b)

Figure 12 Comparison of cumulative heat release calculated with different specific heat models for SF 50/50 (a) and SF 100/00 (b)

In Table 4 the MFB phasing positions MFB5, MFB50 and MFB90 of the proposed model are displayed, corresponding to the SF cases 50/50 and 100/00. The table also presents the angle differences between the corresponding combustion phasing positions predicted by the empirical models and those obtained using the proposed model. Differences in the MFB50 are again present and should not be neglected; however, they are considerably smaller

than those observed during the preceding EGRR sweep. This suggests that the empirical models provide better agreement under operating conditions without exhaust gas recirculation.

Table 3 Cumulative heat relative error for empirical SHR models (ref. model NASA)

Model	Rel. error [%] (SF=50/50)	Rel. error [%] (SF=100/00)
Egnell	-5.97	-5.38
Brunt	-3.64	-3.08
Gatowski	-9.23	-8.79

Table 4 Key MFB positions (NASA model) and deviations for empirical models for SF=50/50 and SF=100/00

Model	SF=50/50		
/	**MFB5**	**MFB50**	**MFB90**
NASA 9	367.95	380.13	386.46
Gatowski	-0.30	-0.77	-0.24
Brunt	0.01	-0.13	-0.08
Egnel	-0.11	-0.29	-0.10
/	**SF=100/00**		
NASA 9	373.36	390.39	402.65
Gatowski	-0.15	-0.79	-0.29
Brunt	0.06	-0.18	-0.23
Egnel	-0.06	-0.36	-0.25

Triple injection SOI1 sweep

Triple injection strategy without EGR, with a sweep in which the timing of the first injection is progressively shifted toward later crank angle positions is final data set used to test performance of the new SHR model. The sweep is organized around the start of the first injection (SOI1), while the end of the third injection (EOI3) remained fixed for all points and positioned to coincide with the ignition timing. The split factor is set for equal fuel mass distribution (SF=33/33/33).

The figure 13a presents the SHR histories for given SOI1 sweep, using proposed SHR model. Hardly visible difference can be seen during early and mid-compression phase where temperature influence is less pronounced. In the late compression phase, the difference increases which is attributed to the fuel delivered at the end of the first injection and accordingly adjusted ignition timing to maintain constant indicated mean effective pressure (IMEP). The similar trends are seen in results produced by empirical models, however, differences against the proposed model are additionally increased due to fuel mass delivered in the last injection cycle (INJ3).

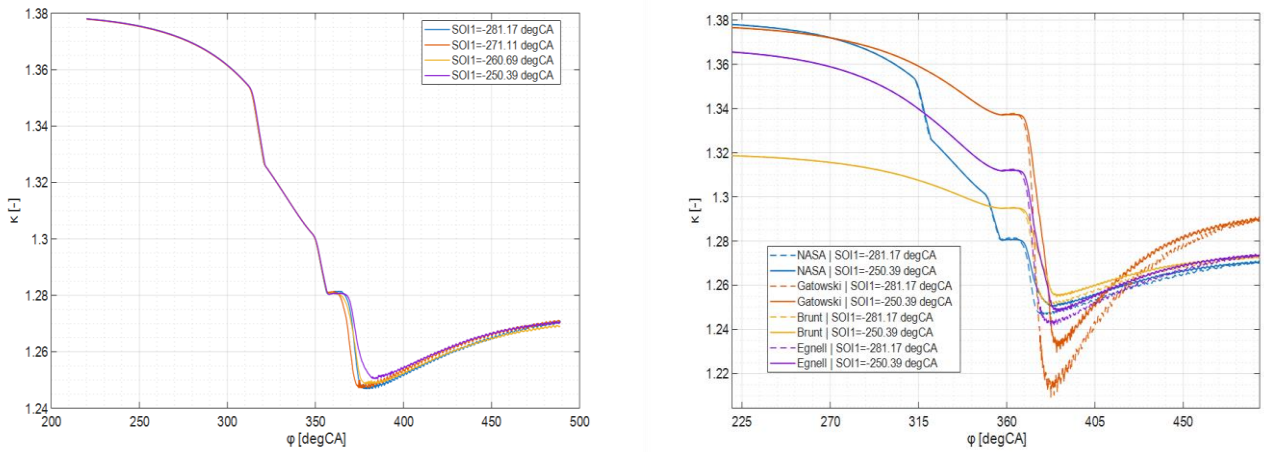

a) b)

Figure 13 Specific heat ratio histories calculated using proposed model and three empirical models: (a) model NASA, SOI1=-250…-280 CAD; (b) NASA vs empirical models SOI1=-250 CAD & SOI1=-280 CAD

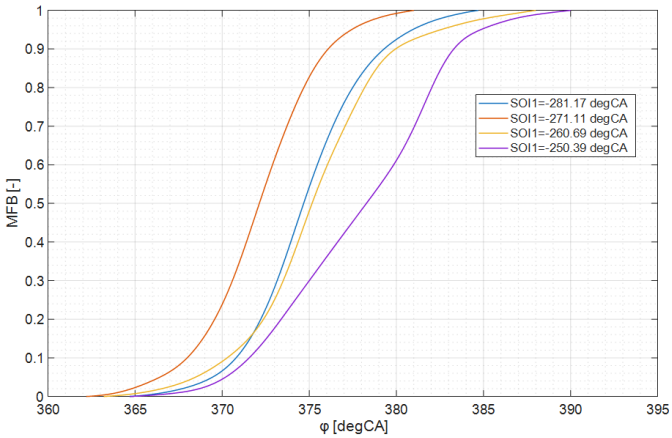

Figure 14 MFB profiles for all investigated sweep cases

Figure 14 illustrates the MFB profiles obtained for the different positions of the first injection (SOI1). Each operating point retains ignition position adjusted to required constant IMEP, however the difference between them is less than 1 CAD. Different ignition delay clearly visible in Figure 14 originates from the changed thermodynamic conditions at spark timing position and changed local mixture composition caused by first injection cycle position. The longest combustion period was spoted on the operating point with the injection position being the closest to spark timing.

Table 5 Cumulative heat relative error for empirical SHR models (ref. model NASA)

Model	Rel. error [%] (SOI1=-280°)	Rel. error [%] (SOI1=-250°)
Egnell	-4.79	-4.43
Brunt	-2.35	-1.81
Gatowski	-8.02	-7.88

Table 6 Key MFB positions (NASA model) and deviations for empirical models for two SOI1 positions

Model	**SOI1=-280°**		
/	**MFB5**	**MFB50**	**MFB90**
NASA 9	369.44	374.67	379.29
Gatowski	-0.16	-0.30	-0.26
Brunt	0.10	-0.07	-0.13
Egnel	-0.07	-0.12	-0.15
/	**SOI1=-250°**		
NASA 9	370.19	378.27	383.29
Gatowski	-0.05	-0.47	-0.12
Brunt	0.01	-0.13	-0.12
Egnel	-0.03	-0.24	-0.12

In Table 5 the MFB phasing positions MFB5, MFB50 and MFB90 of the proposed model are displayed, corresponding to the SOI1=-250 CAD and SOI1=-280 CAD cases. The table also presents the crank angle differences between the corresponding combustion phasing positions predicted by the empirical SHR models and those obtained using the proposed model. Differences in the MFB50 ranging from 0.1 to 0.3 CAD, are rather small, however, should not be neglected. Therefore, when high accuracy is required in the assessment of MFB50 shifts, the influence of the selected specific heat ratio formulation must be taken into account.

CONCLUSIONS

This study presented a crank angle resolved model for determining the specific heat ratio of the cylinder charge in DISI engines under operating conditions characterized by complex mixture formation. Unlike conventional empirical formulations, the proposed approach continuously accounts for variations in temperature and working fluid composition caused by fuel injection, EGR dilution, mixture formation strategy, and the progressive conversion of reactants into combustion products. The resulting $\kappa(\varphi)$ dynamics can therefore respond directly to changes in engine operating conditions and injection strategy rather than relying solely on a predefined empirical correlation.

The results demonstrate that differences in the specific heat ratio formulation propagate directly into the calculated heat release characteristics. For the investigated EGR rate sweep, the empirical formulations produced relative

deviations in cumulative released heat of approximately 2–9% compared to the proposed model. Among the evaluated correlations, the Brunt formulation showed the closest agreement, whereas Gatowski model exhibited the largest deviations, reaching approximately 8–9%. Egnell model generally provided intermediate results, with deviations of approximately 5–6%. The influence of the specific heat ratio formulation was also reflected in the calculated combustion phasing. Under the investigated EGR rate conditions, differences in MFB50 between the proposed model and the empirical correlations reached almost 1 CAD for the Gatowski formulation, while the Brunt model generally remained within approximately 0.1–0.2 CAD. Although such differences may appear small in absolute terms, they are not negligible in combustion analysis, where changes in MFB50 of only a fraction of a crank angle degree may be relevant for combustion optimization and calibration.

The double injection SF sweep further demonstrated that the influence of the selected κ formulation depends on the mixture formation process. As the injection strategy approached a more homogeneous, effectively single injection condition, the differences between the proposed approach and the empirical models generally decreased. Nevertheless, measurable differences in cumulative heat release and MFB50 remained, indicating that the influence of the thermodynamic model cannot be completely neglected even under comparatively homogeneous operating conditions. The most pronounced differences in the κ dynamics were observed for the triple injection operating condition, where the complex mixture formation process and the proximity of the final injection event to spark timing resulted in strong temporal variations of the working fluid composition. In this case, the empirical models were unable to reproduce the composition-driven transition captured by the proposed formulation over a substantial portion of the investigated crank angle domain. At the same time, shifting the first injection timing (SOI1) closer to the spark event influenced both the heat release phasing and combustion duration, further emphasizing the importance of accounting for mixture formation effects when evaluating combustion phasing.

Overall, the results indicate that simplified empirical specific heat ratio models can provide satisfactory estimates under certain operating conditions, with the Brunt formulation showing the best overall agreement among the three investigated correlations. However, their limited sensitivity to instantaneous mixture composition changes becomes increasingly important when high EGR rates, multiple injections, or strongly transient mixture formation strategies are employed. The proposed model provides a more physically based representation of the specific heat ratio under such conditions and enables the influence of mixture composition on heat release and combustion phasing to be explicitly captured.

ACKNOWLEDGMENTS

The results presented in this paper are the result of the research supported by the Ministry of Science, Technological Development and Innovation of the RS under Contract 451-03-34/2026-03/ 200105, February 5, 2026.

REFERENCES

Desantes, J. M., López, J. J., Carreres, M., & López-Pintor, D. (2016). Characterization and prediction of the discharge coefficient of non-cavitating diesel injection nozzles. *Fuel,* 184, 371–381. https://doi.org/10.1016/j.fuel.2016.07.026

Idelchik, I. E. (2008). *Handbook of Hydraulic Resistance* (4th ed., revised and augmented). Begell House. ISBN 978-1-56700-251-5. https://doi.org/10.1615/978-1-56700-251-5.0

Nurick, W. H. (1976). Orifice cavitation and its effect on spray mixing. *Journal of Fluids Engineering,* 98(4), 681–687. https://doi.org/10.1115/1.3448452

Macian, V., Payri, R., Margot, X., & Salvador, F. J. (2003). A CFD analysis of the influence of diesel nozzle geometry on the inception of cavitation. *Atomization and Sprays,* 13(5–6), 579–604. https://doi.org/10.1615/AtomizSpr.v13.i56.80

von Kuensberg Sarre, C., Kong, S.-C., & Reitz, R. D. (1999). *Modeling the effects of injector nozzle geometry on diesel sprays* (SAE Technical Paper No. 1999-01-0912). SAE International. https://doi.org/10.4271/1999-01-0912

Svehla, R. A., & McBride, B. J. (1973). *FORTRAN IV Computer Program for Calculation of Thermodynamic and Transport Properties of Complex Chemical Systems* (NASA Technical Note TN D-7056, Report E-6514). National Aeronautics and Space Administration, Lewis Research Center.

Manz, P. W. (2001). *Indiziertechnik an Verbrennungsmotoren* [Lecture notes]. Technische Universität Carolo-Wilhelmina zu Braunschweig.

Lanzafame, R., & Messina, M. (2003). ICE gross heat release strongly influenced by specific heat ratio values. *International Journal of Automotive Technology, 4*(3), 125–133.

Brunt, M. F. J., Rai, H., & Emtage, A. L. (1998). *The calculation of heat release energy from engine cylinder pressure data* (SAE Technical Paper No. 981052). SAE International. https://doi.org/10.4271/981052

Egnell, R. (1998). *Combustion diagnostics by means of multizone heat release analysis and NO calculation* (SAE Technical Paper No. 981424). SAE International. https://doi.org/10.4271/981424

Ferguson, C. R. (1986). *Internal Combustion Engines: Applied Thermosciences*. John Wiley & Sons. ISBN 978-0-471-88129-2.

Gatowski, J. A., Balles, E. N., Chun, K. M., Nelson, F. E., Ekchian, J. A., & Heywood, J. B. (1984). *Heat release analysis of engine pressure data* (SAE Technical Paper No. 841359). SAE International. https://doi.org/10.4271/841359

Heywood, J. B. (1988). *Internal Combustion Engine Fundamentals*. McGraw-Hill. ISBN 0-07-028637-X.

Popović, S. J. (2013). *Istraživanje i razvoj metode za analizu radnog procesa motora na osnovu merenja trenutne ugaone brzine kolenastog vratila* [Doctoral dissertation, University of Belgrade, Faculty of Mechanical Engineering

The 11th International Congress
Motor Vehicles & Motors 2026
Kragujevac, Serbia
October 8th - 9th, 2026

Motor Vehicles & Motors

MVM2026-041
https://doi.org/10.24874/CMVM2026.041
Original scientific paper

Predrag Mrđa[1]
Slobodan Popović[2]
Nenad Miljić[3]
Marko Kitanović[4]

EXPERIMENTAL AND CFD-BASED INVESTIGATION OF VAPOUR POCKET FORMATION IN AN INTERNAL COMBUSTION ENGINE COOLING SYSTEM

ABSTRACT: Effective thermal management of internal combustion engines is critical to maintain performance, particularly as modern engines continue to increase their specific power output. As part of ongoing research, the authors conducted experimental and simulation-based investigations on a series of test engines, focusing on the cylinder and cylinder head cooling system. During high-load testing, cooling-system anomalies prompted a detailed investigation. Analysis of the test bench data revealed transient vapour (steam) pocket formation within the cooling jacket at the cylinder liner. To better characterise the temperature field within the coolant passages, the engine was instrumented with an additional set of high-speed temperature sensors. The acquired experimental data served as input for developing a CFD simulation model in the AVL FIRE M environment. The simulation results confirmed the experimentally observed behaviour and provided insight into the local flow and heat transfer conditions contributing to vapour (steam) pocket formation. Based on these findings, the authors identified and proposed specific design modifications for the next-generation prototype engine's cooling system. This work demonstrates the value of combining high-speed experimental instrumentation with CFD simulation as an integrated approach for diagnosing and resolving thermal management issues during engine development.

KEYWORDS: IC Engine, Engine cooling, Vapour pocket formation, Engine testing, CFD simulation

[1] *Predrag Mrđa PhD, associate professor, University of Belgrade Faculty of Mechanical Engineering Department of Internal Combustion Engines, Kraljice Marije 16 11000 Belgrade Serbia, pmrdja@mas.bg.ac.rs,*
https://orcid.org/0000-0001-5534-6322
[2] *Slobodan Popović PhD, associate professor, University of Belgrade Faculty of Mechanical Engineering Department of Internal Combustion Engines, Kraljice Marije 16 11000 Belgrade Serbia, spopovic@mas.bg.ac.rs,*
https://orcid.org/0000-0002-6332-9589
[3] *Nenad Miljić PhD, associate professor, University of Belgrade Faculty of Mechanical Engineering Department of Internal Combustion Engines, Kraljice Marije 16 11000 Belgrade Serbia, nmiljic@mas.bg.ac.rs,*
https://orcid.org/0000-0003-3564-0203
[4] *Marko Kitanović PhD, assistant professor, University of Belgrade Faculty of Mechanical Engineering Department of Internal Combustion Engines, Kraljice Marije 16 11000 Belgrade Serbia, mkitanovic@mas.bg.ac.rs,*
https://orcid.org/0000-0002-3931-802X

EKSPERIMENTALNO I CFD ISTRAŽIVANJE POJAVE PARNOG ČEPA U SISTEMU HLAĐENJA MOTORA SA UNUTRAŠNJIM SAGOREVANJEM

REZIME: Održavanje termičkog nivoa motora sa unutrašnjim sagorevanjem (motora SUS) je od ključne važnosti za održavanje njegovih performansi. Imajući u vidu da moderni motori SUS imaju povišene specifične performanse, problem hlađenja cilindra i cilindarske glave je od velike važnosti. Sastavni deo procesa razvoja motora SUS je rad na istraživačkom motoru na kome se testiraju prototipska rešenja osnovnih i pratećih sistema motora, kao i različite strategije upravljanja radnim procesom. Autori ovog rada sprovode istraživanja na istraživačkim monocilindrima u okviru raznih projekata saradnje sa industrijom. U određenoj seriji ispitivanja, na višim opterećenjima motora, uočena je potreba za revidiranjem sistema hlađenja cilindra i cilindarske glave. Analizom snimljenih podatka na probnom stolu, uočen je prelazni fenomen stvaranja parnog čepa u sistemu hlađenja pri cilindarskoj košuljici. Potom, motor je opremljen dodatnim setom brzih senzora temperature kako bi se stvorila jasnija slika o temperaturnom polju unutar prostora rashladne tečnosti oko cilindra na željenim radnim režimima rada motora. Ti podaci su iskorišćeni kao osnova sa formiranje FIRE M modela u okviru simulacionog okruženja AVL AST. Nakon analize dobijenih rezultata, izvučeni su zaključci i smernice za unapređenje konstrukcije sledeće generacije istraživačkih motora.

KLJUČNE REČI: Motor SUS, Hlađenje motora, Parni čep, Ispitivanje motora, CFD simulacija

INTRODUCTION

In the Internal Combustion Engines Laboratory at the University of Belgrade, a series of long-term research projects in the combustion efficiency and mixture formation have been performed on the single cylinder research engine (SCRE) of the modular design covering several dozen different hardware configurations. The operating regimes investigated vary widely, ranging from the catalyst heat-up (cat-heat) regime, with an underheated engine and relatively low loads, through medium loads at an engine speed of n = 2000 min^{-1}, up to high specific loads at which the engine reaches up to 24 bar of Indicated Mean Effective Pressure (Heywood, 1988) (IMEP) at 5000 min^{-1}, burning either gasoline or gaseous hydrogen as a fuel.

During internal combustion engine testing, owing to the exceptional complexity of the test installation - where more than 300 quantities are measured and calculated for the single-cylinder research engine at a single stationary operating point - it is common practice to record so-called reference operating points. Reference operating points may be either motored (without combustion) or fired (with combustion), but their purpose is to provide insight into engine behaviour under identical control settings, with the engine fluids conditioned in the same manner (coolant temperature, oil temperature, fuel temperature, intake air temperature, etc.).

Following a series of tests at high loads and high engine speeds, a mismatch was observed in the results obtained at the reference operating points, which triggered an investigation into the actual cause of the engine damage and into the steps that should be undertaken to make the engine more durable in the next development and refinement iteration.

This paper presents the basic characteristics of the test installation, as well as the results of the engine failure analysis (teardown inspection), which indicated thermal overload. In addition, it shows how an additional set of sensors was incorporated into the cooling system to identify the engine cylinder's overheating zone. Based on the data acquired in this way, a CFD simulation was developed, and guidelines were provided to improve cylinder liner cooling.

EXPERIMENTAL SETUP

As already mentioned, the object under investigation is a single-cylinder research engine. The essential support systems for this engine are:

- Dynamic engine dynamometer (brake)
- Coolant temperature and pressure conditioning system
- Engine oil temperature and pressure conditioning system
- Low-pressure gasoline temperature and pressure conditioning system (when the engine is operated on gasoline)
- External supercharging system with intake air pressure and temperature conditioning (up to 4 bar absolute intake pressure at maximum flow rates)

- High-pressure gasoline injection system (up to 1200 bar)
- Combustion product composition analysis system, Microsoot and Smoke-meter
- Blow-by measurement system
- Open engine control unit, AVL RPEMS (Rapid Prototyping Engine Management System)
- External EGR system with a recirculation pump and cooling
- Data acquisition system for time-domain sampling
- Engine indicating system, AVL IndiCom
- Control and automation system based on the National Instruments LabVIEW software platform and the NI PXI and NI SCXI hardware platforms

Figure 1 shows the Single Cylinder Research Engine mounted on the test bench. Table 1 summarises the basic engine characteristics.

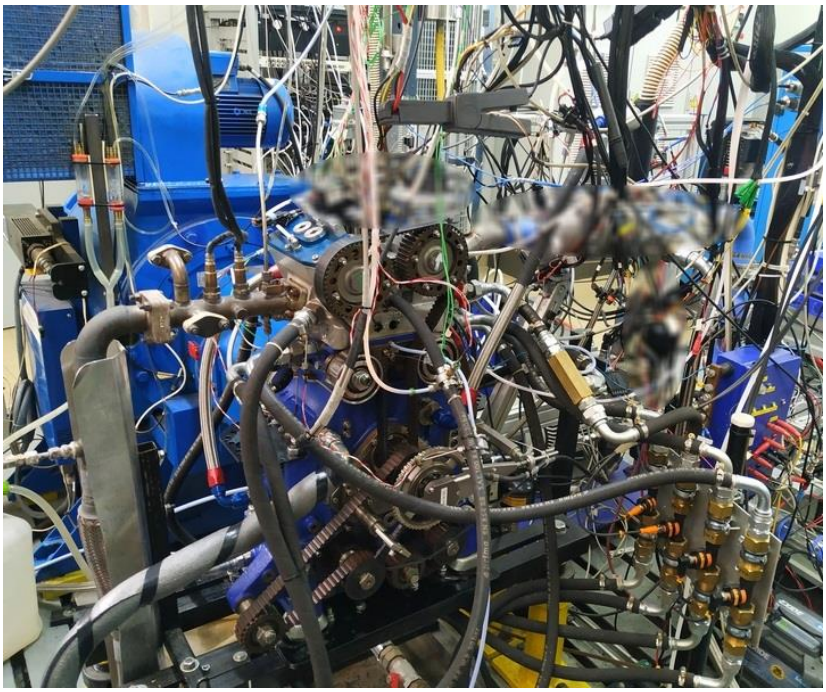

Figure 1 Single Cylinder Research Engine at the Internal Combustion Engines Department at University of Belgrade

Table 1 Basic Engine characteristics

Bore	81 mm
Stroke	90 mm
Ignition system	Central SP M12
PFP max	50 bar – 1200 bar
CR max	16
Charge motion	Tumble: 1.6-4.2

Valve opening duration	selection of IN/EX Cams.
Valve timing	EIVC-LIVC, DVVT, 0° – 60°
Injector position	Side DI, Central DI, and PFI
Combustion chamber	selection of pistons
Lean capability	stable at $\lambda > 2$
Piston cooling jet	switchable

The test plan defined operating points at elevated engine load, with an IMEP of approximately 24 bar and an engine speed of 4000 min^{-1}. A passive pre-chamber was investigated, together with different triple-injection strategies. After a certain number of tests, the operating point could no longer be reproduced with consistent results. It was the first sign that something was wrong with the experimental installation. In the next phase, the motored reference operating point was repeated (the engine was motored at 2000 min^{-1}, with the intake charge pressure forcibly raised to 1.1 bar absolute), as well as the reference operating point with the combustion (at 2000 min^{-1}, with combustion corresponding to an IMEP of 12 bar). The mixture composition, intake and exhaust cam phaser positions, ignition timing, and the thermal state of the engine fluids were all predefined and maintained.

After processing the data for the reference operating points, we observed a mismatch between IMEP and Brake Mean Effective Pressure (BMEP), i.e., the Friction Mean Effective Pressure (FMEP) had an offset. Under the given control settings, the engine exhibited degraded performance. The team double-checked the measurement chains for the in-cylinder pressure trace (engine indication) and the torque measurement. Once the team confirmed the measurement chains were functioning correctly, they initiated a teardown failure investigation of the engine. The recorded data showed a increase in the blow-by flow rate and an increase in total hydrocarbon (THC) emission.

ENGINE TEARDOWN INSPECTION AND CONSEQUENCES OF ENGINE THERMAL OVERLOAD

The mixture formation and ignition systems were inspected. No changes were found in the cooling or lubrication systems. Endoscopic inspection of the engine revealed that the valve seats were undamaged, but changes were observed on the intake valves. Deposits were observed in the fire zone (compression zone) of the cylinder due to combustion, but nothing significant. After removing the cylinder head, melting zones were observed on the intake valves, as shown in Figure 2 (on the bridge between the ports, since a four-valve head is used).

Figure 2 Intake valve damage resulting from insufficient cooling in the cylinder head

The cylinder and piston were found to be in good condition; slight changes attributable to normal operation were observed, but there was no significant scoring, scratches, melting zones, or fractures. After removing the piston rings from the piston, the free-state (open) ring gaps were measured and compared with a set of unused piston rings. Table 2 lists the free-state gap and thickness measurements for the piston rings used on the engine, together with those of a set of new, unused piston rings. The most significant difference was observed in the first compression ring. This indicates that the first compression ring has lost elasticity and that its sealing function has been compromised. Figure 3, on the far right, shows the appearance of the used and new first piston rings.

Table 2 Comparison of piston ring dimensions for the used and the new piston rings. All dimensions are approximate, with an accuracy of ±0.01 mm

		Used	New	Difference
First compression ring	Free state gap [mm]	8.10	12.34	4.24
	Thickness [mm]	2.86	2.86	-
	Height [mm]	1.18	1.18	-
Second compression ring	Free state gap [mm]	11.20	11.37	0.17
	Thickness [mm]	3.42	3.42	-
	Height [mm]	1.48	1.48	-
Top oil ring	No noticeable differences			
Bottom oil ring	No noticeable differences			

The reduction in the free-state ring gap is a consequence of the loss of piston-ring elasticity, which in turn results from excessive thermal loading, i.e., the inability to dissipate a sufficient amount of heat through the piston structure itself (by the engine oil that carries heat away from the underside of the piston) and through the cylinder liner.

The cylinder liner likewise showed signs of damage. The block design employs a wet cylinder liner, i.e., the cylinder is inserted into the engine block and is directly exposed to the coolant flow. Deposits and crystallisation zones of the ethylene glycol / distilled water solution (30%-70%) were observed on the cylinder liner outer surface, as shown in Figure 3, left. Figure 3 (middle) also shows a photograph of the piston with the piston rings mounted. No traces of melting or fracture are visible. In the fire zone of the piston, above the first piston ring, deposits are observed due to flame quenching in that zone, which is expected.

Figure 3 Deposits on the cylinder liner (left), deposits on the piston (middle), and appearance of the used and new piston rings (right)

Measurement of the Temperature Field within the Cylinder Block Coolant Chamber

After documenting the condition of the engine components, the engine was serviced. A series of coolant temperature sensors and flow meters were also added to the acquisition system to provide a clearer picture of the coolant temperature field within the cylinder block. Based on this information, CFD models will be developed within the Ansys Fluent (ANSYS, Inc., 2024) and AVL FIRE M (AVL List GmbH, 2024) simulation environments. Figure 4 shows the sensor layout within the cylinder block with the wet cylinder liner removed. The cylinder block has four coolant ports, i.e., two in the upper zone of the cylinder and two in the lower zone of the cylinder. In previous engine tests, the manufacturer-specified port configuration was used: an inlet port in the lower zone of the block on the intake side and an outlet port in the upper zone of the block on the exhaust side. The purpose of this investigation is to determine whether an alternative configuration might outperform the initial one, achieving a more favourable flow pattern within the coolant space and improved heat dissipation. In principle, a single selected inlet and a single selected outlet port could be used in the future; however, if the flow were balanced between two inlet ports and a single outlet port, the problem would become considerably more complex.

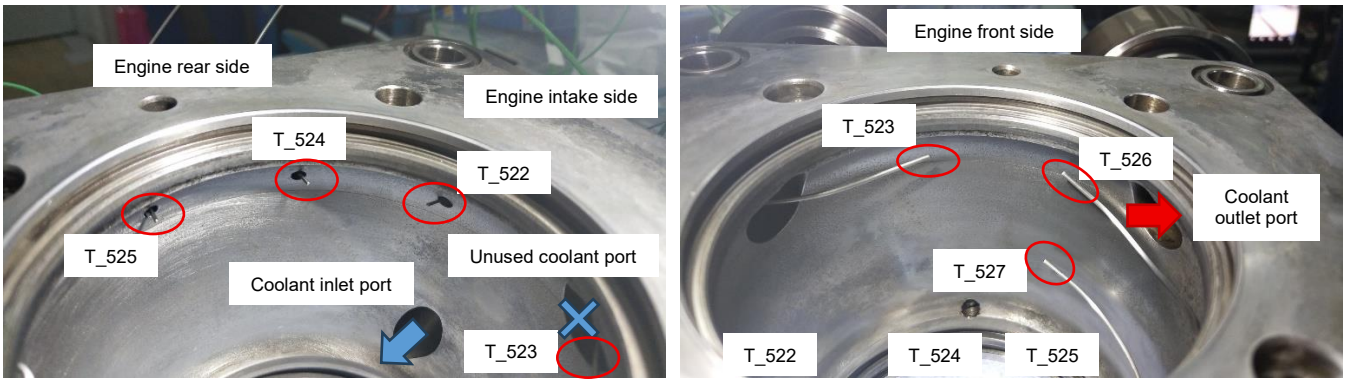

Figure 4 Position of the thermocouples within the cylinder block of the single-cylinder research engine

For temperature recording, Class A accuracy thermocouples with a 1 mm diameter were used, characterised by a very short response time, since vapour pocket formation was expected to occur in the cylinder cooling jacket during testing (Campbell et al., 1997; Finlay et al., 1987). Sensors with lower thermal capacity respond more quickly and are therefore better suited to detecting a local temperature rise should vapour pocket formation occur. The AVL coolant conditioning unit is equipped with a circulation pump and parallel lines for cooling or heating the coolant, depending on the operating regimes being realised on the test bench. The setpoint temperature for the closed-loop conditioning is the temperature at the engine coolant outlet port.

Regarding the experimental investigation, the tests were conducted in the following manner:

- First, a run-in test was carried out at an engine speed of n = 4000 min-1, from IMEP = 2 bar to IMEP = 10 bar. Figure 5 (left) shows the results of the test at IMEP = 10 bar, together with the temperature changes recorded by the previously added sensors and by the sensors at the coolant inlet and outlet ports of the cylinder block. Vapour pocket formation occurred in the measurement zones of two sensors, and temperatures rose significantly above the prescribed 90°C setpoint.
- Load sweep tests were then carried out. The engine speed was n = 2000 min^{-1}, and the engine load was gradually increased. Figure 5 (right) shows the results at a load of IMEP = 20 bar. The remaining main control parameters were a triple, late injection strategy and a fuel injection pressure of 1000 bar. The diagram shows that, at the lower engine speed, even though the load was increased, the vapour pocket

zone is smaller, with only one sensor indicating an elevated temperature. The following diagram, Figure 6 (left), shows the temperature during vapour pocket formation and the transient behaviour of its collapse and subsequent re-formation.

- Given that the system is unstable in these operating regimes, i.e., operating at the boundary of vapour pocket formation (Robinson et al., 1999, 2003), the following series of experiments was conducted at an identical load, with the coolant setpoint temperature at the cylinder block outlet port intentionally lowered to T_out = 88°C. The formation and collapse of the vapour pocket were observed, with a period of approximately 10 s.
- Since the goal is to enable testing at even higher loads (IMEP = 23 bar and above), a further reduction of the coolant temperature was necessary, down to as low as T_out = 80°C; however, these results are not shown here, since such a thermal level of the engine coolant is unacceptable for other reasons (primarily affecting the effectiveness of engine lubrication system).

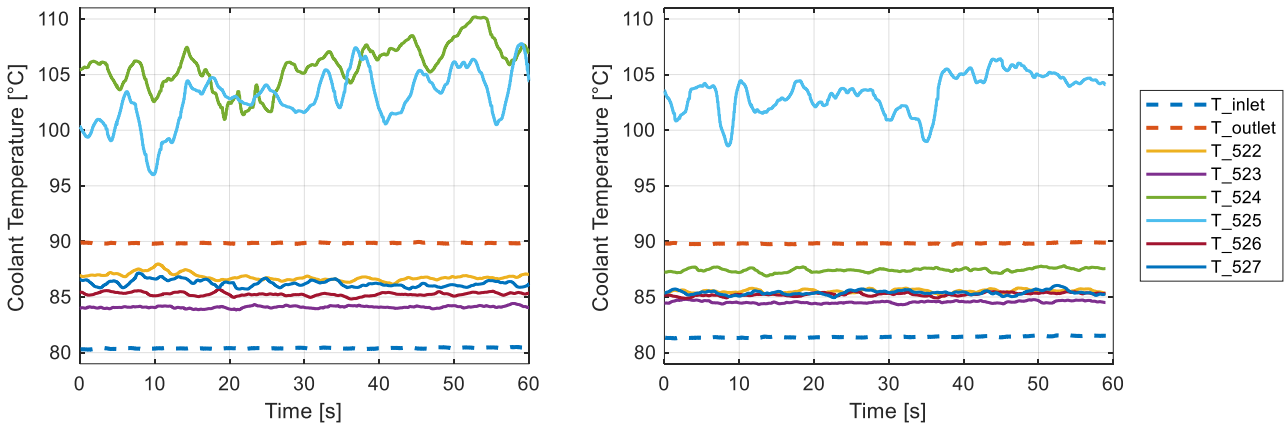

Figure 5 Coolant temperature change during the run-in regime at n = 4000 min⁻¹, IMEP = 2 bar (left), and coolant temperature change at n = 2000 min⁻¹, IMEP = 20 bar (right). The sensors detecting an elevated temperature are located within the vapour pocket

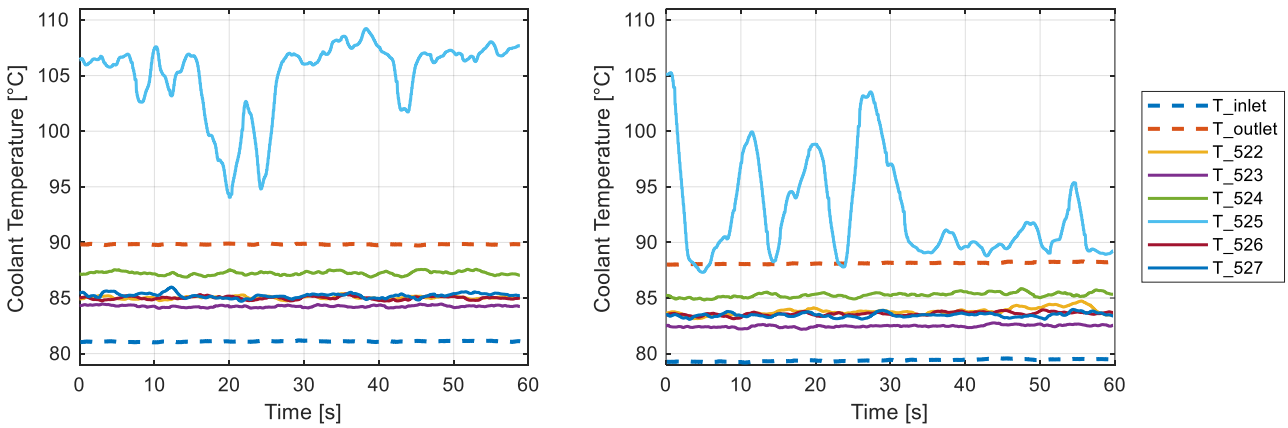

Figure 6 Observed collapse of the vapour pocket during engine testing at n = 2000 min⁻¹, IMEP = 21 bar, with late injection (left), and lowering of the engine's thermal level - coolant outlet temperature of 88°C- with repeated formation and collapse of the vapour pocket (right)

CFD MODEL

The simulation of coolant flow within the cylinder block will be carried out to determine the maximum amount of heat absorbed by the coolant, for given initial conditions of the coolant thermal state, the cooling jacket wall temperatures, and the varied flow rate, and this for different configurations of connecting the coolant conditioning system to the cylinder block itself. The ANSYS simulation environment was used for this purpose.

The cylinder head simulation model is considerably more complex and was carried out using the AVL FIRE M software tool, which is part of the AVL AST (Advanced Simulation Technologies) software suite. Below, we briefly present the design-point assumptions, limitations, and simulation results.

CFD Model of the Cylinder Cooling Jacket

The mesh was initially generated with 2 million triangular elements; however, it was later switched to a polyhedral mesh consisting of 1 million elements. Advantages of a polyhedral mesh include more accurate results in near-wall layers, fewer mesh elements (leading to faster simulation convergence), and improved graphical quality.

The first series of simulations was performed for the one input - one output case. The initial temperature conditions were T_1 = 84.8°C for the engine coolant at the inlet port and T_{cyl} = 120°C for the outer cylinder wall (the part of the cylinder in contact with the coolant space). At the inlet cross-section, the flow rate (i.e., the coolant inflow velocity) was specified, while at the outlet cross-section the absolute pressure was specified. This approach to defining the boundary conditions at the inlet and outlet cross-sections ensures numerical stability and improves the accuracy of the results.

Table 3 presents the simulation results for different coolant flow rates. As expected, as the flow rate increases, the amount of heat dissipated and the pressure drop both increase. The internal energy dissipation is calculated as:

$$U = C_v \cdot \dot{m} \cdot (T_2 - T_1) \tag{1}$$

where:

C_v Isobaric Specific Heat of the coolant at 85°C. For the simulation, data for pure water is used $C_v = 4200 \left[\frac{J}{kgK}\right]$

$\dot{m}_c$ Coolant flow rate.

T_2 Coolant outlet temperature,

T_1 Coolant inlet temperature.

Table 3 Simulation setup and results for the cylinder block coolant basic flow pattern

Simulation Input parameters			Simulation Results					
Name	v_1	T_1	T_2	ΔT	Δp	$\dot{m}_c$	$\dot{V}_c$	U
Unit	[m/s]	[°C]	[°C]	[°C]	[mbar]	[kg/s]	[l/min]	[W]
DP 0	0.73	84.8	86.03	1.23	11.25	0.207	12.4	-1073
DP 1	0.88	84.8	85.86	1.06	15.94	0.248	14.9	-1107
DP 2	1.03	84.8	85.73	0.93	21.39	0.289	17.4	-1134
DP 3	1.18	84.8	85.63	0.83	27.59	0.330	19.9	-1156
DP 4	1.32	84.8	85.55	0.75	34.57	0.371	22.3	-1176
DP 5	1.47	84.8	85.49	0.69	42.27	0.412	24.8	-1194

Figure 7 shows the flow field for design point 2 (DP2). Zones with lower flow intensity are evident, and, consequently, heat transfer is also reduced. These regions most closely correspond to the positions of sensors T_524 and T_525. The second series of simulations refers the two input - two output case. In this regard, several additional simulation configurations were set up, including the remaining coolant inlet and outlet ports. Table 4 presents the results of one such series of simulations, while Figure 8 (left) shows the results for DP0. Many combinations of inlet and outlet ports are possible, particularly when balancing the flow rate between the inlets and outlets is considered. A particular concept, involving the introduction of a spiral deflector, allows the use of a single coolant inlet and a single coolant outlet on the cylinder block, while achieving excellent performance in terms of heat dissipation and the thermal level of the engine cylinder. Figure 8 (right) shows the graphical flow field results.

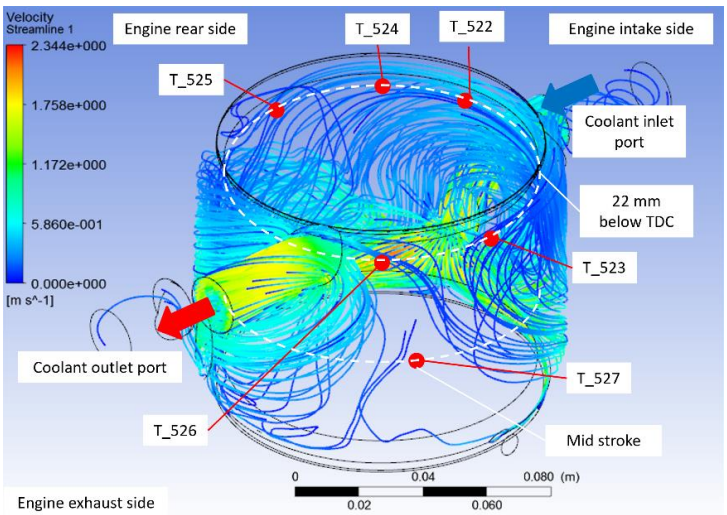

Figure 7 Simulation model results for the flow field within the cylinder cooling jacket, for a single coolant inlet and a single coolant outlet

Table 4 Simulation setup and results for the cylinder block coolant basic flow pattern.

Simulation Input parameters				Simulation Results					
Name	$v_{1(prim.)}$	$v_{1(sec.)}$	T_1	T_2	ΔT	Δp	$\dot{m}_c$	$\dot{V}_c$	U
Unit	[m/s]	[m/s]	[°C]	[°C]	[°C]	[mbar]	[kg/s]	[l/min]	[W]
DP 0	0.73	0.73	84.8	85.52	0.72	11.70	0.414	24.9	-1250
DP 1	0.88	0.88	84.8	85.40	0.60	16.53	0.496	29.8	-1247
DP 2	1.03	1.03	84.8	85.32	0.52	22.17	0.579	34.8	-1260
DP 3	1.18	1.18	84.8	85.26	0.46	28.51	0.661	39.7	-1271
DP 4	1.32	1.32	84.8	85.21	0.41	35.65	0.742	44.6	-1274

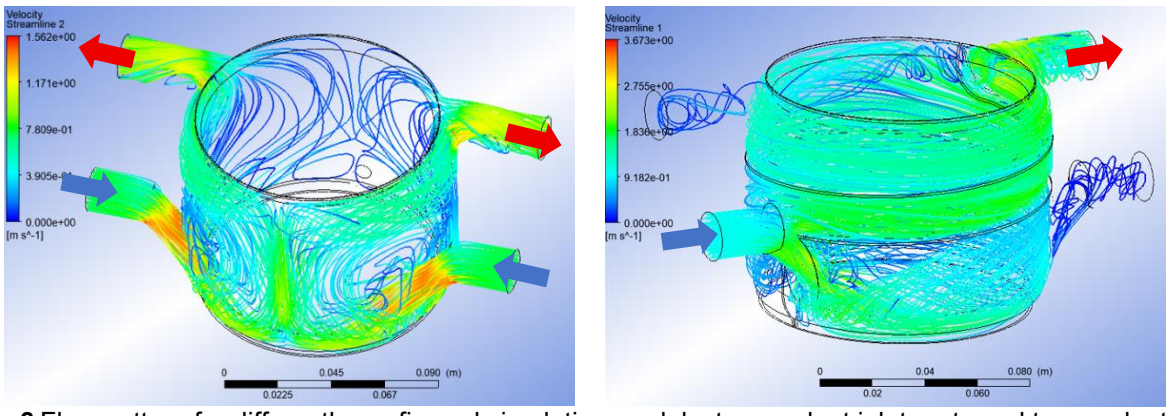

Figure 8 Flow pattern for differently configured simulation models: two coolant inlet ports and two coolant outlet ports (left), and simulation results for the spiral deflector concept (right)

CFD Model of the Cylinder Head

AVL FIRE M is a three-dimensional CFD simulation tool for analysing flow, heat transfer, and reactive processes in technically complex systems, widely used across the automotive, aerospace, and energy sectors. The software incorporates a broad set of validated physical and numerical models covering fluid flow, heat transfer, combustion, multiphase flow, and reactive processes, and is verified against experimental data to reduce uncertainty in industrial applications. Model setup, post-processing, and reporting are supported by a guided, GUI-based workflow, while user-defined coding interfaces remain available for developing custom models when required. As part of the AVL Simulation Desktop environment, together with AVL CRUISE M and AVL EXCITE M, the software further enables parameterisation, design-of-experiments studies, and numerical optimisation. Owing to its parallelised solvers and scalable simulation fidelity, FIRE M can be applied to problems ranging from simplified concept-level studies to high-resolution analyses, which was the primary reason it was selected for the cylinder head simulation presented in this paper.

The simulation is based on the cylinder head of the SCRE in use. In setting up the simulation, the cylinder head is considerably more complex than the engine cylinder because it comprises a larger number of sub-domains, such as:

- The material from which the cylinder head is made – solid aluminium block
- The cooling jacket within the cylinder head, ethylene glycol-water mixture (30-70%)
- The intake port – in correlation with the cylinder head, intake valves and intake valve seats
- The intake valves – in correlation with intake valve seats, guides, intake port and combustion chamber
- The intake valve seats – in correlation with intake valves, cylinder head, intake port and combustion chamber
- The intake valve guides – in correlation with the cylinder head and intake valves
- The exhaust port, valves, seats, and guides are the same as for the intake port, valves, seats, and guides, just for the exhaust
- The combustion chamber domain within the engine cylinder head – in correlation with intake and exhaust valves and seats.

Each domain has its own initial conditions for the simulation mesh setup, material composition, and initial phase state, as well as for the interactions between the model's individual domains. Equation control involves selecting the equations to include in the simulation model. In this case, the active equations govern momentum, continuity, energy, and turbulence. The turbulence model used is RANS, together with the generally accepted k-zeta-f sub-model (Hanjalić et al. 2004). No additional temperature measurements were taken before calibrating the cylinder head model.

Several categories of results are stored both in matrix form and as 2D and 3D graphical representations. For the cylinder head cooling jacket, the relevant information includes the boiling pressure, boiling temperature, boiling heat flux, bubble departure diameter, bubble lift-off diameter, and similar quantities (Gholinia et al., 2018; Kandlikar, 1990;

Mehdipour et al. 2016; Steiner et al. 2005). In addition to the solver-type parameters, tolerances, and the permissible number of iterations, there is an option to save all or part of the results as the simulation converges.

Given that the cylinder head has two coolant connections on the front side of the engine and two on the rear side (towards the flywheel), several configurations for connecting the cooling system are possible. For this occasion, we simulated the cases shown in Figure 9. It is also possible to simulate variants with a single coolant inlet and a single outlet, or with one inlet and two outlets, and vice versa, although these were not carried out on this occasion.

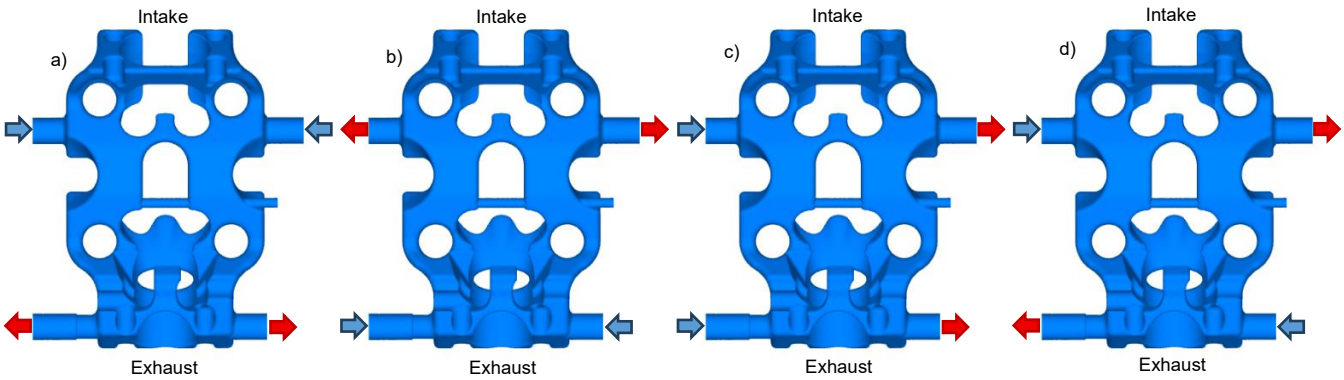

Figure 9 Flow pattern for cylinder heat-cooling jacket flow simulation setup

In general, very similar results are obtained regardless of which flow pattern is applied (a), (b), or (c). Pattern (d) is the least favourable, since the flow becomes localised in the central zone of the cylinder head, resulting in an increase in the temperature of the cylinder head material. Figure 10 (left) shows the temperature field of the boundary layer within the cylinder head coolant jacket. An elevated temperature can be observed in the dead zone (a structure through which the coolant cannot flow) located above the exhaust port in the cylinder head. Figure 10 (right) shows the velocity results for the given simulation and flow pattern (c) from Figure 9.

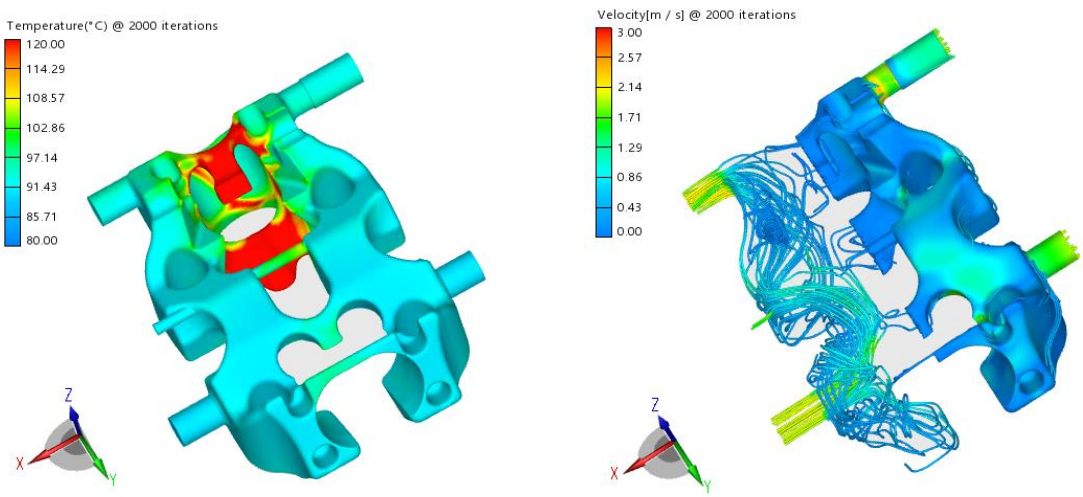

Figure 10 Temperature field (left) and flow velocity (right) within the cylinder head coolant jacket

CONCLUSIONS

Engine and cooling-system design are exceptionally complex, requiring knowledge across multiple areas of mechanical engineering, from measurement techniques and data processing to flow simulation and component design. Modern techniques and tools, such as the AVL FIRE M simulation environment, provide insight into numerous flow parameters; however, certain limitations remain. Specifically, the simulation is steady-state, and changes within the combustion chamber domain were excluded. In addition, fixed temperature values were prescribed for the individual domains and their respective parts (for example, the valve seat or the valve itself, i.e., the valve sections). Following this investigation, cylinder cooling was improved by increasing the contact surface area between the cylinder and the coolant, which does not pose a major technical challenge, since the wet cylinder liner is relatively simple in geometry. As for the cylinder head, it is exceptionally complex and very costly for this category of research engine.

ACKNOWLEDGMENTS

The results presented in this paper are the result of the research supported by the Ministry of Science, Technological Development and Innovation of the RS under Contract 451-03-34/2026-03/ 200105, February 5, 2026.

The authors thank their colleagues Vladimir Petrović and Nemanja Bukušić who performed engine experiments and Miloš Petrović, CFD Simulation Specialist, for valuable assistance in simulation and analysis.

REFERENCES

ANSYS, Inc. (2024). Ansys Fluent. ANSYS, Inc. https://ansys.synopsys.com/products/fluids/ansys-fluent

AVL List GmbH. (2024). AVL AST Fire M. AVL LIST GmbH Graz. https://www.avl.com/en/simulation-solutions/simulation-software/computational-fluid-dynamics-cfd-avl-fire-m

Campbell, N., Tilley, D., MacGregor, S., & Wong, L. (1997). Incorporating nucleate boiling in a precision cooling strategy for combustion engines. *SAE International*, 971791. https://doi.org/10.4271/971791

Finlay, I. C., Boyle, R. J., Pirault, J. P., & Biddulph, T. (1987). Nucleate and film boiling of engine coolants flowing in a uniformly heated duct of small cross section. *SAE International*, 870032. https://doi.org/10.4271/870032

Gholinia, M., Pourfallah, M., & Chamani, H. R. (2018). Numerical investigation of heat transfers in the water jacket of heavy duty diesel engine by considering boiling phenomenon. *Case Studies in Thermal Engineering*, 12, 497-509. https://doi.org/10.1016/j.csite.2018.07.003

Hanjalić, K., Popovac, M., & Hadžiabdić, M. (2004). A robust near-wall elliptic-relaxation eddy-viscosity turbulence model for CFD. *International Journal of Heat and Fluid Flow*, 25(6), 1047–1051. https://doi.org/10.1016/j.ijheatfluidflow.2004.07.005

Heywood, J. (1988). *Internal Combustion Engine Fundamentals*. McGraw-Hill Education.

Kandlikar, S. G. (1990). A general correlation for saturated two-phase flow boiling heat transfer inside horizontal and vertical tubes. *Journal of Heat Transfer*, 112(1), 219–228. https://doi.org/10.1115/1.2910348

Mehdipour, R., Baniamerian, Z., & Delauré, Y. (2016). Three-dimensional simulation of nucleate boiling heat and mass transfer in cooling passages of internal combustion engines. *Heat and Mass Transfer*, 52, 957–968. https://doi.org/10.1007/s00231-015-1611-6

Robinson, K., Campbell, N., Hawley, J., & Tilley, D. (1999, 1 March). A review of precision engine cooling. *International Congress & Exposition*, Detroit, Michigan, United States. https://doi.org/10.4271/1999-01-0578

Robinson, K., Hawley, J. G., & Campbell, N. A. F. (2003). Experimental and Modelling Aspects of Flow Boiling Heat Transfer for Application to Internal Combustion Engines. *Proceedings of the Institution of Mechanical Engineers, Part D: Journal of Automobile Engineering*, 217(10), 877–889. https://doi.org/10.1243/095440703769683289

Steiner, H., Kobor, A., & Gebhard, L. (2005). A wall heat transfer model for subcooled boiling flow. *International Journal of Heat and Mass Transfer*, 48(19–20), 4161–4173. https://doi.org/10.1016/j.ijheatmasstransfer.2005.03.032

The 11th International Congress
Motor Vehicles & Motors 2026
Kragujevac, Serbia
October 8th - 9th, 2026

Motor Vehicles & Motors

MVM2026-042
https://doi.org/10.24874/CMVM2026.042
Original scientific paper

Nenad Miljić[1]
Predrag Mrđa[2]
Slobodan J. Popović[3]

QUANTIFYING IMEP EVALUATION ERROR INDUCED BY PIEZOELECTRIC PRESSURE SENSOR AGEING IN INTERNAL COMBUSTION ENGINE INDICATION

ABSTRACT: In-cylinder pressure indication by a piezoelectric sensor constitutes the fundamental source of data in internal combustion engine research, whereby sensor sensitivity changes over the course of prolonged testing; that is, it gradually declines and thereby compromises the reliability of derived parameters. Prior work showed that this ageing can be tracked by changes in the calculated polytropic coefficient, particularly during the expansion process, providing an indicator that does not require frequent calibration. In the present work, these findings are extended by quantifying the consequence, that is, from the standpoint of working-process analysis, the most significant, namely, the error introduced into the evaluation of indicated mean effective pressure (IMEP). Based on a prolonged campaign on a single-cylinder research engine (approximately 1500 operating points, 200 hours), with mandatory cold and hot reference measurements, the drop in the polytropic coefficient is correlated with the corresponding deviation in IMEP. The results show that once the changes are relativised, the percentage values of both parameters are close. Thus, the polytropic coefficient may serve as an indirect indicator of IMEP accuracy. On the other hand, an adopted IMEP error tolerance (for example, 0.1 bar) can be translated into a polytropic-coefficient degradation threshold that signals the moment when sensor calibration becomes necessary.

KEYWORDS: internal combustion engine, piezoelectric pressure sensor ageing, in-cylinder pressure indication, IMEP evaluation

[1] *Nenad Miljić PhD, associate professor, University of Belgrade Faculty of Mechanical Engineering, Department of Internal Combustion Engines, Kraljice Marije 16 11000 Belgrade, Serbia, nmiljic@mas.bg.ac.rs,* https://orcid.org/0000-0003-3564-0203
[2] *Predrag Mrđa PhD, associate professor, University of Belgrade Faculty of Mechanical Engineering, Department of Internal Combustion Engines, Kraljice Marije 16 11000 Belgrade, Serbia, pmrdja@mas.bg.ac.rs,* https://orcid.org/0000-0001-5534-6322
[3] *Slobodan J. Popović PhD, associate professor, University of Belgrade Faculty of Mechanical Engineering, Department of Internal Combustion Engines, Kraljice Marije 16 11000 Belgrade Serbia, spopovic@mas.bg.ac.rs,* https://orcid.org/0000-0002-6332-9589

KVANTIFIKACIJA GREŠKE U IZRAČUNAVANJU SREDNJEG INDICIRANOG PRITISKA USLED STARENJA PIEZOELEKTRIČNOG SENZORA PRITISKA PRI INDICIRANJU MOTORA SA UNUTRAŠNJIM SAGOREVANJEM

REZIME: Indiciranje pritiska u cilindru piezoelektričnim senzorom predstavlja osnovni izvor podataka u istraživanju motora SUS, pri čemu se osetljivost senzora menja tokom dugotrajnih ispitivanja, odnosno postepeno opada i time narušava pouzdanost izvedenih parametara. U prethodnom istraživanju pokazano je da se ovo starenje može pratiti preko promene izračunatog koeficijenta politrope, naročito tokom procesa ekspanzije, čime se dobija indikator stanja koji ne zahteva često baždarenje senzora. U ovom radu se ta saznanja proširuju kvantifikovanjem posledice koja je sa aspekta analize radnog procesa najznačajnija, odnosno greške koja se unosi u proračun srednjeg indiciranog pritiska (SIP). Na osnovu dugotrajne kampanje ispitivanja na istraživačkom monocilindru (oko 1500 radnih režima, 200 časova), uz obavezna merenja hladne i tople reference, izvršena je korelacija promena koeficijenta politrope sa odgovarajućim odstupanjem SIP. Pokazuje se da su, kada se promene relativizuju, procentualne vrednosti oba parametra bliske, te koeficijent politrope može poslužiti kao posredni pokazatelj tačnosti SIP. Sa druge strane, usvojena tolerancija greške SIP-a (na primer 0.1 bar) može se prevesti u prag promene koeficijenta politrope koji ukazuje na trenutak kada baždarenje senzora postaje neophodno

KLJUČNE REČI: motor SUS, starenje piezoelektričnog senzora pritiska, indiciranje pritiska, evaluacija srednjeg indikatorskog pritiska

INTRODUCTION

In-cylinder pressure indication is an essential technique for collecting data on the phenomena occurring during the engine working cycle. Because of their precision, robustness and high-frequency response, measuring chains based on piezoelectric sensors became de facto standards in engine research laboratories more than fifty years ago. Their use, however, rests on a series of compromises: the sensor is exposed to extreme thermal loads, it must maintain a minimum non-linearity error over a very wide pressure range, and the piezoelectric measuring principle itself cannot deliver absolute pressure. Converting the charge-amplifier voltage signal into an absolute pressure trace and synchronising that trace with the crank-angle domain are therefore the two fundamental tasks of indication data processing, and errors in either domain propagate directly into the thermodynamic analysis. Randolph, A. L. (1990) showed that the relative magnitude of these errors can be significant, while Brunt, M. F. J. and Emtage, A. L. (1996) demonstrated their strong impact on evaluating the indicated mean effective pressure (IMEP).

Randolph, A. L. (1994) lists the numerous further influences that have to be minimised through carefully selected measures, from sensor installation to signal processing: electrical interference, mechanical vibration transferred into the electrical signal, errors in the charge amplifier gain, in the angular phase of the signal and in absolute pressure referencing, discretisation errors of the analogue-to-digital converter, uncertainty of the engine geometric parameters, and the short-term thermal shock analysed by Rosseel, E. et al. (1999) and Lee, S. et al. (2005). Most of these issues have been addressed with considerable success, and commercially available systems today integrate the complete measuring chain with dedicated acquisition hardware and real-time evaluation software.

The one issue that persists is the sensor itself, i.e. its sensitivity, which changes over time. The dominant root causes of this sensor ageing are the high span amplitude of the dynamic heat flux and the mechanical stresses imposed by the working process; a further contribution comes from combustion residue deposits building up on and around the sensing diaphragm, a mechanism which, as reported by Pischinger, R. (2002), can in extreme cases alone produce IMEP errors of 10% or more. For short-term tasks measured by a few testbed shifts, ageing is negligible, and a regular dead-weight calibration of the sensor/amplifier chain is sufficient. Long-term campaigns lasting weeks are a different matter: daily calibration would require repeated dismounting of the sensor, and the associated repeated disconnecting of the fragile coaxial cable and threading into a delicate mounting hole are themselves a risk of damage and of introducing additional error sources. The ageing gradient, moreover, depends not only on in-use time but also on the distribution of operating points–in particular, the amplitude and frequency of high-pressure gradients and the number of preignition and knock events–as well as on sensor design and mounting.

The Internal Combustion Engines Department (ICED) Laboratory at the University of Belgrade Faculty of Mechanical Engineering conducts extensive long-term research that relies heavily on in-cylinder indication, which motivated an

investigation into whether the sensor condition can be monitored during the testing process without removing the sensor from the engine. In the reference study, Mrđa, P. et al. (2025) showed that the polytropic coefficient evaluated from the reference operating-point pressure trace is a promising indicator: it drops systematically with accumulated engine work, although the in-cylinder conditions remain unchanged. The present paper summarises that finding and extends it in the direction that is, from the standpoint of working-process analysis, the most significant – the quantification of its consequence. The drop in the polytropic coefficient correlates with the deviation of the evaluated IMEP, so the polytropic coefficient can serve as an indirect measure of IMEP accuracy and, conversely, an adopted IMEP error tolerance can be translated into a polytropic coefficient threshold that signals when calibration becomes necessary.

EXPERIMENTAL SETUP, DATASET AND DATA EVALUATION

The investigation was conducted as a part of an intensive research campaign on the engine testbed at ICED, built around a versatile Single Cylinder Research Engine (SCRE) that allows many hardware changes to be implemented with reasonable effort. Table 1 lists the main features of the engine, dynamometer, and test cell.

Table 1 Engine, dynamometer and test cell main features

Engine	SCRE AVL 5404
Type	1 cylinder, 4-stroke, SI, 4 valves per cylinder, VVT
ECU	AVL RPEMS (Rapid Prototyping Engine Management System)
Fuel / injection	Gasoline; modular and configurable (PFI, side DI, central DI)
Ignition / charging	Modular (SI, PCI); external supercharging

Reference operating points

Daily testing follows a prepared test plan, and good practice at ICED introduced engine reference-state measurements as mandatory first and last steps of every daily testing batch, so important engine parameters can be tracked as indicators of the state of the testbed and the engine. The term reference implies that both the hardware configuration and the operating point settings are identical within a test batch. Because a batch often includes test plans with hardware changes, two reference types are defined as valid and representative. The Cold Reference (CR) is a strictly defined motored operating point without combustion, which minimises the effect of even minor hardware changes on the in-cylinder pressure build-up. The Hot Reference (HR) is a strictly defined operating point with combustion, providing realistic conditions but more susceptible to hardware changes. Both are run with identical setpoints for the engine ECU and all testbed systems that directly affect the process – intake air, fuel and exhaust after-treatment conditioning, and thermal management of the cylinder block and head.

The cold references were always adjusted to wide open throttle, no fuel injection, engine speed 2,000 min^{-1}, intake manifold absolute pressure 110 kPa (slightly boosted by an external air supply) and camshafts in the reference position, with coolant and lubricating oil conditioned at 90 °C and intake air at 25 °C. The hot reference was measured at 2,000 min^{-1} and a moderate load of 1,200 kPa IMEP, with a retarded ignition advance angle of 2 °CA ATDC to minimise the probability of preignition or knock and keep the indicating sensor as safe as possible; conditioning was identical. Throughout the batch, the camshafts, intake port tumble inserts, and compression ratio remained unchanged, whereas injector position, injection pressure, spark plug type, spark energy, and ignition coil type varied; changes were considered negligible for the reference operating process. The analysed sensor was a state-of-the-art M5-threaded, uncooled piezoelectric sensor with a nominal sensitivity of 20 pC/bar, coupled to an AVL MICROIFEM Gen 4 amplifier. A detailed specification is deliberately omitted, since the research does not aim to emphasise the behaviour of any particular sensor type or manufacturer; long-term experience at ICED shows that comparable sensors of the well-known vendors behave very similarly.

Test batch dataset

The test batch in focus gathered almost 1,500 quasi-stationary operating points with a total summed engine operating time of 200 hours, including about 70 cold and about 70 hot references.

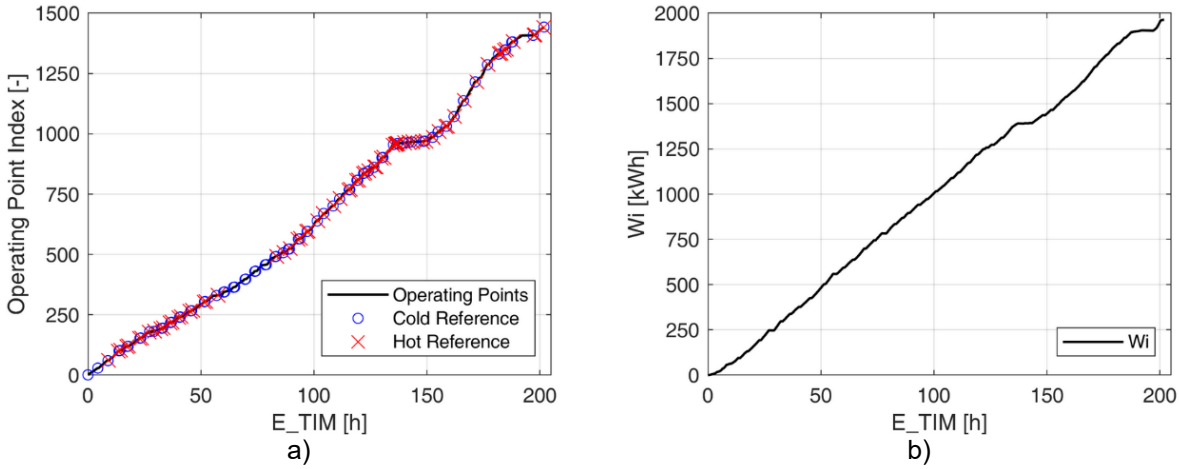

Figure 1 Test campaign overview: (a) number of recorded quasi-stationary operating modes with cold and hot reference indices; (b) cumulative indicated work

Figure 1a shows how the campaign intensity varied over time, along with the reference indices, and Figure 1b shows the build-up of the cumulative indicated work Wi. The near-linear correlation implies that the engine load was nearly constant, making Wi a convenient general indicator of the thermal load applied to the sensor and the natural abscissa for all subsequent trend diagrams. Besides IMEP, the maximum cycle pressure P_MX and the maximum pressure gradient PG_MX with their angular positions were monitored, as well as the Knocking Pressure Peaks indicator KP_PK, which delivers the absolute maximum of the rectified knock oscillations superimposed on the cylinder pressure (AVL List GmbH, 2024); its distribution confirms that engine operation was kept within an acceptable knock intensity margin. At 92% of the operating points, the engine speed was 2,000 min^{-1}; the remaining points were tested at 1,500, 3,000, and 4,000 min^{-1}, and every point was measured after thermal stabilisation, with an exhaust gas temperature deviation below 1 °C as the criterion.

Evaluation of the indicated parameters

Each operating-point measurement consists of 300 consecutive cycles recorded in the angular domain at a resolution of 0.1 °CA; parameters are calculated cycle by cycle and then averaged. A special focus is placed on the polytropic coefficients of the compression and expansion phases evaluated from the measured pressure trace. Both phases can be treated as polytropic processes and, because heat transfer is complex, the coefficient is variable but remains within commonly expected boundaries. As the sensor ages, heat transfer evaluation from the measured pressure curve changes, which is why changes in the evaluated coefficients are considered indicative. The averaged pressure curve was slightly filtered with a custom Savitzky-Golay filter (MathWorks, n.d.), and all combustion-related data were analysed using AVL Concerto software and the catool functions for the MathWorks MATLAB environment (Brown, B., 2023). Following Manz, P.-W. (2010), the evaluation starts from the relation of the polytropic process,

$$\frac{p_1}{P_2} = \left(\frac{V_1}{V_2}\right)^n \tag{1}$$

where p_1, p_2 and V_1, V_2 are the pressures and volumes at the boundaries of the treated angular window, from which the polytropic coefficient n follows as

$$n = \frac{\log(p_2) - \log(p_1)}{\log(V_1) - \log(V_2)} \tag{2}$$

The evaluation is conducted within a wide angular window of [−170 °CA, −5 °CA] for compression and [5 °CA, 170 °CA] for expansion, where 0 °CA denotes the combustion phase TDC, and a running average filter with a half-width of 15 °CA is applied, α being the current angle within the respective range:

$$n = \frac{\log\big(p(\alpha + hw)\big) - \log\big(p(\alpha - hw)\big)}{\log\big(V(\alpha - hw)\big) - \log\big(V(\alpha + hw)\big)} \tag{3}$$

$$compression: \quad \alpha = [-170°, -5°]CA$$

$$expansion: \quad \alpha = [5°, 170°]\ CA$$

ANALYSIS OF THE INDICATED PARAMETERS

Cold references

Figure 2a shows the log-log in-cylinder pressure trace for all recorded cold references. The first CR, measured with the newly installed sensor, is marked in blue and the last CR of the batch in red; the same marking is adopted in all subsequent figures. A slight change in the slope of the trace, i.e. of the polytropic coefficient, is evident and can be attributed to sensitivity and linearity drift. In the low-pressure part of the cycle, the traces match consistently and show no clear direction of deviation, implying that the reading deviation is negligible at low sensor load. As the load rises, the deviation becomes evident and acquires a clear direction, as shown in the detail of the high-pressure part in Figure 2b. The question is whether a numerical indicator can be found that is sufficiently indicative and whose monitoring over time allows conclusions about the extent of the sensitivity change.

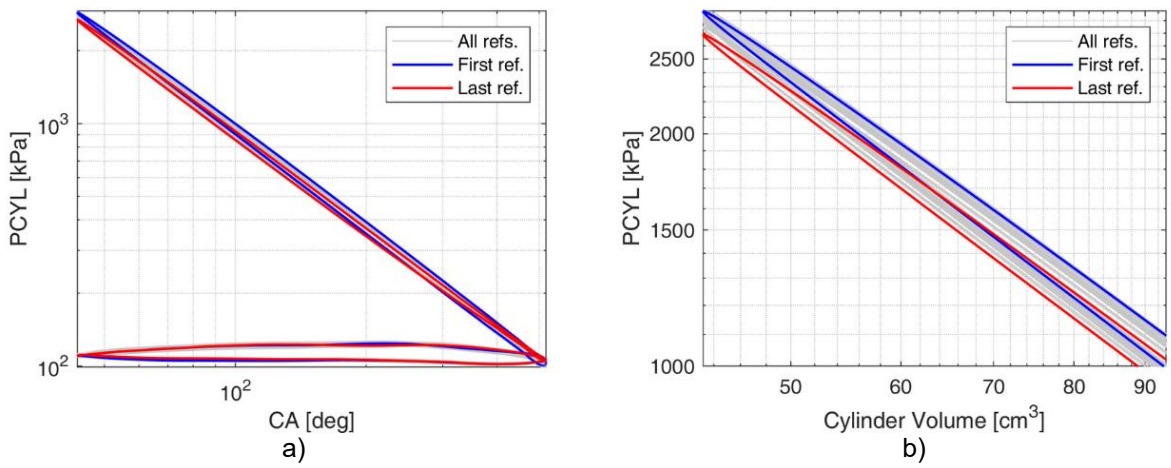

Figure 2 Cold references, first and last measurement emphasised: (a) in-cylinder pressure; (b) detail of the high-pressure part of the cycle

Figure 3a shows the average cycle maximum pressure of the cold references as a function of cumulative indicated work: a continuous, almost linear drop is observed. On all approximation diagrams, the R^2 score is given, along with the 95% confidence interval for the data (dotted lines). Figure 3b shows the maximum pressure rise gradient, which exhibits the same decreasing trend–the sensor progressively loses its ability to respond to rapid pressure changes in the same way. The angular positions of both maxima scatter within very narrow limits, which confirms a solid reproducibility of the reference operating point.

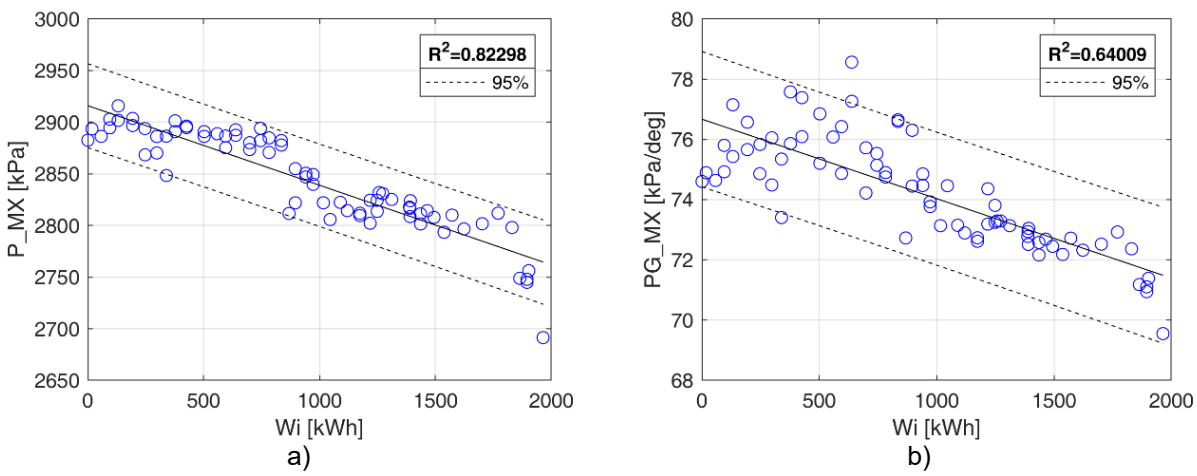

Figure 3 Cold references versus cumulative indicated work: (a) cycle maximum pressure; (b) maximum cycle pressure gradient

The polytropic coefficients of the cold references, evaluated according to equation (3), are shown in Figure 4. A significant drop over time is evident, although the in-cylinder conditions remained unchanged. This is particularly evident at the beginning of the compression phase, where heat transfer is less pronounced, and towards the end of the expansion phase, before the exhaust valve opens. The IMEP evaluated from the cold reference readings, shown later in Figure 5a, drifts in the same systematic manner; its values are negative because the cold reference is a

motored operating point. A separate analysis of the two parts of the cycle shows that the change of IMEPL (low-pressure part) is insignificant, since the pressure amplitudes during the low-pressure part are small, whereas IMEPH (high-pressure part) follows the trend of the total IMEP.

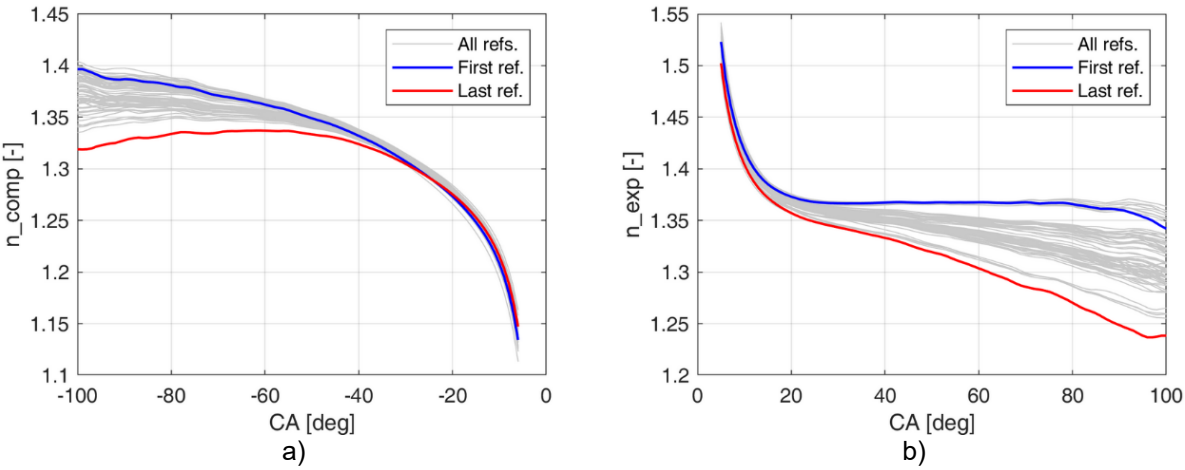

Figure 4 Polytropic coefficient for cold references: (a) compression; (b) expansion

Hot references

Although the cold references track sensitivity changes better, the hot references are much closer to the typical operating points defined by the test plans. Defining their control settings is delicate, since the point must be unique and reproducible across all hot reference measurements – which may differ in some aspects of the hardware configuration – without compromising engine safety. The conclusions drawn from the cold references are fully confirmed here: the maximum cycle pressure and the maximum pressure gradient both decrease as a consequence of the sensitivity change, so that for almost identical combustion cycles the sensor progressively loses the ability to follow the pressure change dynamics, while the angular positions of both maxima again scatter within small limits.

With repeated hot references, the IMEP gradually decreases, as shown in Figure 5b. Despite the scatter, a clear global decreasing trend is present. It appears to be opposite to the cold reference trend in Figure 5a, but it is in fact the same, since the cold reference points are motored and therefore deliver a negative output. Figure 5b illustrates the essence of the sensor ageing problem: although the in-cylinder conditions are unchanged, the repeated reference measurements indicate that the IMEP changes over time. The engine is permanently monitored for mechanical failures that could cause an IMEP change (blow-by gas flow measurement, friction loss plausibility check), and no mechanical issue was detected during this test batch, leading to the conclusion that the IMEP change is influenced solely by changes in sensor behaviour.

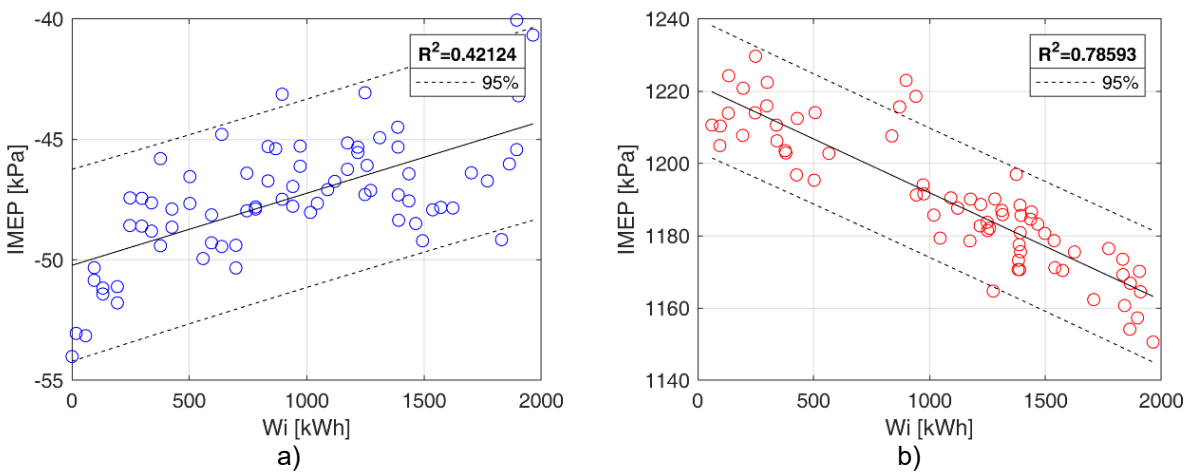

Figure 5 IMEP versus cumulative indicated work: (a) cold references; (b) hot references

For the combustion cycles, the angular ranges used to evaluate the polytropic coefficient are adjusted to limit the influence of heat release on the coefficient value. Figure 6 shows how the coefficient curves migrate over time. As already concluded for the cold references, the drop in sensor sensitivity produces a false indication of more intensive heat losses and thus lower polytropic coefficients in both phases of the process.

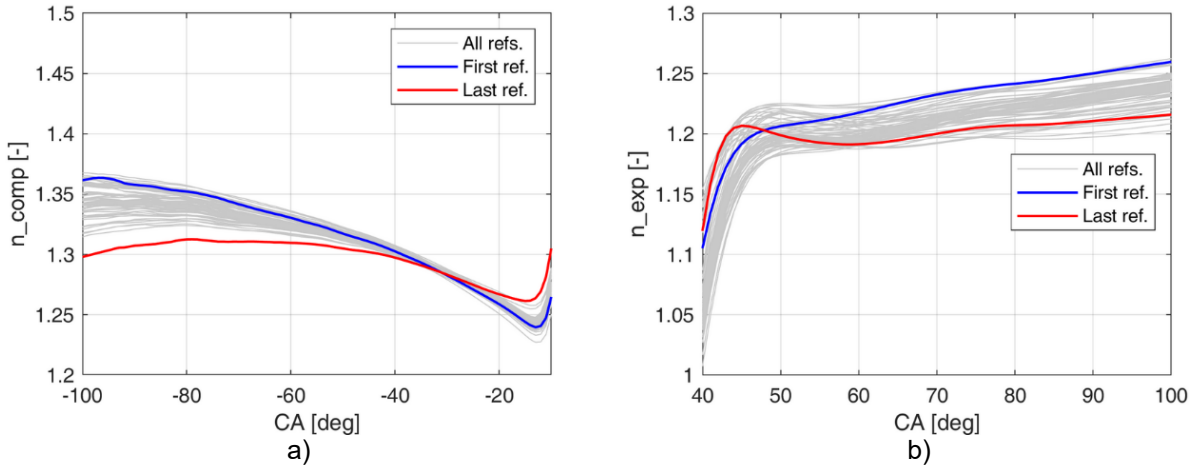

Figure 6 Polytropic coefficient for hot references: (a) compression; (b) expansion

Quantification of the IMEP evaluation error

The trends presented so far establish the polytropic coefficient as a qualitative indicator of sensor-sensitivity deterioration. For practical use during a campaign, however, the indicator must be tied to the accuracy of the parameter that matters most in working-process analysis, i.e., the IMEP. Figure 7 shows the polytropic coefficient of the cold reference cycles evaluated at 90 °CA ATDC – well inside the expansion phase, where the influence of the heat release is absent, and the indicated deviation is most pronounced – as a function of the cumulative indicated work. The trend closely resembles that of the hot-reference IMEP in Figure 5b, the first indication that the two quantities degrade proportionally.

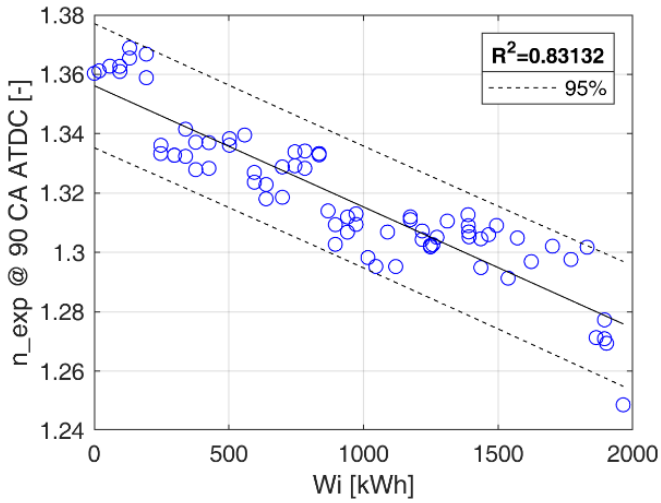

Figure 7 Polytropic coefficient for cold references at 90 °CA ATDC as a function of the cumulative indicated work

To make the comparison quantitative, both quantities are relativised with respect to their values at the beginning of the campaign, i.e. to the state of the freshly calibrated sensor (Wi = 0):

$$\partial n(W_i) = \frac{n_{exp}(W_i) - n_{exp,0}}{n_{exp,0}} \tag{4}$$

$$\partial IMEP(W_i) = \frac{IMEP(W_i) - IMEP_0}{IMEP_0} \tag{5}$$

where $n_{epx,0}$ and $IMEP_0$ are the values of the corresponding linear regressions at Wi = 0. Applying the regressions of Figure 5b and Figure 7 yields the relativised degradation rates summarised in Table 2. Both rates are negative and, more importantly, of the same order of magnitude, which confirms that the two quantities are not merely correlated in shape but comparable in relative amount.

Table 2 Relativised degradation rates of the polytropic coefficient and of the IMEP (95% probability bounds)

Quantity	Reference	Value at Wi = 0	Absolute rate	Relative rate [%/1000 kWh]
n_exp @ 90 °CA ATDC	CR	-1.353	$-3.538*10^{-5}$ 1/kWh	-2.6±0.34
IMEP	CR	-37.5 kPa	42 Pa/kWh	-14.3±1.3
Ratio k = δIMEP / δn	–	–	–	5.5±0.2

Figure 8 presents both relativised quantities on a common axis. The two trends run close together; the ratio of the relative rates is k ≈ 5.5. In other words, a 1% relative drop in the polytropic coefficient corresponds to an IMEP evaluation error of approximately 5.5% for such small IMEPs in a motored engine (actually cca. 0.02 bar IMEP!). Since k is a ratio of two relative slopes, it is dimensionless and independent of the units and of the absolute level of either quantity, which is what makes it transferable between reference definitions.

The practical consequence is a direct mapping between an adopted IMEP tolerance and a polytropic coefficient threshold. For a tolerance of ε = 2% the corresponding threshold is $\delta_{n,lim} = \varepsilon / k = 0.42\%$, i.e. an absolute drop of Δn_{exp} = 0.006 from the value recorded with the freshly calibrated sensor. This observation implies that the polytropic coefficient degradation tracking can be a sensitive tool for estimating the overall pressure sensor sensitivity loss – maybe even too strict. Since the observation is derived through the analysis of cold reference IMEP (high-pressure part) drop over time, having in mind that these IMEP values are small compared to the pressure sensor measuring range, a 2% estimate in absolute value is an extremely small value - something not applicable for tracking the IMEP changes of cycles with combustion. So, a fairer IMEP degradation could be defined via the absolute pressure value. If a target drop of 0.1 bar is defined as an acceptable margin for IMEP estimation of "hot" cycles, then the degradation target presented in % (from Cold reference IMEP evaluation) can be reformulated as a value change of up to 25% (0.1 bar IMEP equivalent for a motored engine).

At the degradation rate observed in this campaign, that threshold (0.1 bar drop in hot-cycle IMEP) is reached after approximately 1700 kWh of cumulative indicated work, i.e. after roughly 170 hours of engine operation at the load level typical of this test batch. Table 3 summarises the thresholds for several tolerance levels.

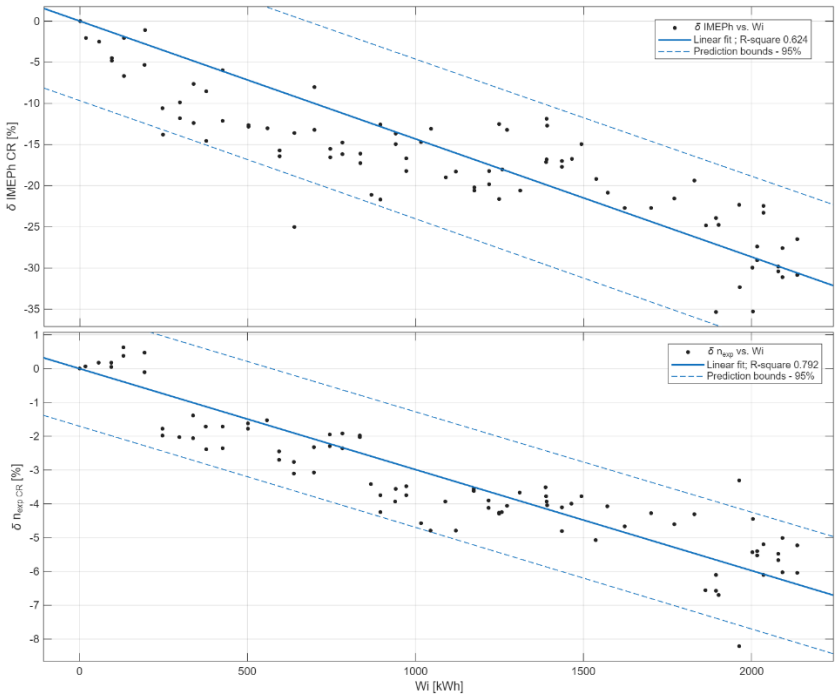

Figure 8 Relativised change of the IMEP (high-pressure part) and of the polytropic coefficient for ***cold references*** as a function of the cumulative indicated work

Table 3 Mapping of the adopted IMEP tolerance onto the polytropic coefficient threshold

IMEP tolerance ε [%] – hot cycle @ 12bar IMEP	Threshold δn_{lim} [%]	Absolute drop Δn_{exp} [–]	Wi_{lim} [kWh]	Operating time [h]
0.2 (0.025 bar)	1.1	0.015	425	42.5
0.4 (0.05 bar)	2.2	0.03	850	85
0.6 (0.075 bar)	3.3	0.045	1275	127.5
0.8 (0.1 bar)	4.4	0.06	1700	170

Three limitations should be stressed. First, the absolute degradation rate is campaign-specific – it depends on the load spectrum, on the knock exposure and on the sensor design and mounting – so the values of $W_{i,lim}$ in Table 3 must not be transferred to a different campaign without verification; the ratio k, on the other hand, describes the way in which a sensitivity drift propagates into the two evaluated quantities and is expected to be far less sensitive to these factors. Second, the mapping is valid only for gradual, sensitivity-type drift: a step change caused by a violent knock event, deposit shedding, or a mechanical issue does not follow the trend, which is why reference measurements must remain a mandatory part of every daily test batch. Third, the threshold check should be performed on the cold reference, which is free of combustion variability and therefore more reproducible with considerably less scatter, even though the tolerance itself is formulated for the IMEP of the fired operating points.

CONCLUSIONS

In-cylinder pressure sensor characteristics change over time during engine operation. Assuming reference operating-point measurements are a regular part of the test plan, the indicated parameters evaluated from those references provide valuable data for identifying sensitivity deterioration without frequent calibration checks. A prerequisite is an unambiguous hardware configuration of the elements that significantly influence the cylinder filling, so that the comparison of the reference pressure traces remains valid, and it is likewise essential to know to which operating regimes the sensor was exposed between two reference measurements, since points with high knock intensity can drastically change the sensor characteristics within a few working cycles. Among the evaluated parameters, the polytropic coefficient obtained from the cold reference pressure trace is the most promising indicator: cold references are straightforward to reproduce with high repeatability of the thermodynamic boundary conditions, and evaluating the coefficient itself is simple and undemanding.

The quantification presented here shows that, once relativised to the state of the freshly calibrated sensor, the drop in the polytropic coefficient evaluated at 90 °CA ATDC for the cold reference and the deviation of the IMEP evaluated at the hot reference are of comparable percentage magnitude, with a ratio of k ≈5.5. This allows the polytropic coefficient to serve as an indirect measure of IMEP evaluation accuracy and, conversely, to translate an adopted IMEP error tolerance into an explicit polytropic coefficient threshold. For a commonly acceptable tolerance of 0.1 bar of evaluated IMEP of the firing engine, the threshold amounts to a relative drop of roughly 4-5% of the polytropic coefficient, which under the conditions of the presented campaign was reached after approximately 170-180 hours of engine operation. Monitoring this single, easily evaluated number therefore provides an operationally meaningful criterion for deciding when to remove and recalibrate the pressure sensor.

ACKNOWLEDGMENTS

The results presented here are the result of research supported by the Ministry of Science, Technological Development and Innovation of the Republic of Serbia under the Contract 451-03-34/2026-03/ 200105 of 05.02.2026.

REFERENCES

AVL CONCERTO 6 | AVL. (n.d.). Retrieved 9 September 2026, from https://www.avl.com/en/testing-solutions/all-testing-products-and-software/connected-development-software-tools/avl-concerto

Brown, B. (n.d.). Catool Combustion Analysis TOOL - User Guide. Retrieved https://www.catool.org/files/catool_User_Guide_v8.pdf

Brunt, M. F. J., & Emtage, A. L. (1996). Evaluation of IMEP routines and analysis errors. SAE Transactions, 105, 749–763.

Lee, S., Bae, C., Prucka, R., Fernandes, G., Filipi, Z., & Assanis, D. N. (2005). Quantification of thermal shock in a piezoelectric pressure transducer. *SAE International*, 2005-01-2092. https://doi.org/10.4271/2005-01-2092

Manz, W. (2010). *Indiziertechnik an Verbrennungsmotoren* (Indicating Technology on Combustion Engines) [Vorlesung]. Technische Universitat Braunschweig, Institut für Verbrennungskraftmaschinen.

Design and Analyze Savitzky-Golay Filters—MATLAB & Simulink Example. (n.d.). Retrieved 9 September 2026, from https://uk.mathworks.com/help/signal/ug/design-and-analysis-of-savitzky-golay-filters.html

Mrdja, P., Popovic, S., Miljic, N., Kitanovic, M., & Bukusic, N. (2026). Analysis of the effect of piezoelectric sensor ageing on indicated parameters. *Thermal Science*, 30(1 Part B), 453–465. https://doi.org/10.2298/TSCI250407122M

Pischinger, R. (2002). *Engine Indicating—User Handbook*. AVL LIST GmbH.

Randolph, A. L. (1990). Methods of processing cylinder-pressure transducer signals to maximize data accuracy. *SAE Transactions*, 99, 191–200. https://doi.org/10.4271/900170

Randolph, A. L. (1994). Cylinder-Pressure-Based Combustion Analysis in Race Engines. *SAE International. Motorsports Engineering Conference & Expostion*. https://doi.org/10.4271/942487

Rosseel, E., Sierens, R., & Baert, R. S. G. (1999). Evaluating piezo-electric transducer response to thermal shock from in-cylinder pressure data. *SAE Transactions*, 108, 1431–1446.

The 11th International Congress
Motor Vehicles & Motors 2026
Kragujevac, Serbia
October 8th - 9th, 2026

Motor Vehicles & Motors

MVM2026-051
https://doi.org/10.24874/CMVM2026.051
Technical paper

Saša Milojević[1]
Marija Rafailović[2]
Michal Loman[3]
Branislav Šarkan[4]
Ján Vrábel[5]
Slobodan Savić[6]

SAFETY AND OPERATIONAL CONSIDERATIONS FOR COMPOSITE HYDROGEN AND CNG STORAGE CYLINDERS IN VEHICLES

ABSTRACT: The increasing adoption of compressed natural gas (CNG) and hydrogen as alternative automotive fuels has intensified the demand for reliable and safe high–pressure storage technologies. Composite pressure cylinders offer an efficient solution for onboard gaseous fuel storage owing to their high strength–to–weight ratio, corrosion resistance, and favorable fatigue performance. This paper presents a comprehensive analysis of operational conditions, installation requirements, inspection procedures, maintenance practices, and safety considerations associated with Type–3 composite cylinders used for onboard storage of CNG and hydrogen in road vehicles. The study examines the effects of pressure cycling, temperature variations, environmental exposure, mechanical damage, and operational handling on cylinder integrity and service life. Particular attention is given to mounting systems, thermal pressure relief devices, inspection methodologies, and damage assessment criteria. Additionally, the paper examines fueling and defueling procedures, risk mitigation measures, and end–of–life management practices. The analysis highlights the critical factors affecting cylinder reliability and identifies key safety measures necessary for safe long–term operation. The findings contribute to improved operational reliability, risk management, and safety performance of modern alternative–fuel vehicle systems.

[1] *Dr Saša Milojević, prof. assist. Faculty of Engineering University of Kragujevac, Kragujevac 34000, Sestre Janjić 6, Serbia, sasa.milojevic@kg.ac.rs, https://orcid.org/0000-0003-0569-047X*
[2] *Ms. Marija Rafailović, PhD student. Faculty of Engineering University of Kragujevac, Kragujevac 34000, Sestre Janjić 6, Serbia, marija.rafailovic@kg.ac.rs, https://orcid.org/0009-0001-2132-9249*
[3] *Dr Michal Loman, prof. assist. University of Žilina, Faculty of Operation and Economics of Transport and Communications, 010 26 Žilina, Univerzitná 8215/1, Slovakia, michal.loman@uniza.sk, https://orcid.org/0000-0003-4300-3802*
[4] *Dr Branislav Šarkan, prof. assist. University of Žilina, Faculty of Operation and Economics of Transport and Communications, 010 26 Žilina, Univerzitná 8215/1, Slovakia, branislav.sarkan@uniza.sk, https://orcid.org/0000-0002-5036-9223*
[5] *Dr Ján Vrábel, prof. assist. University of Žilina, Faculty of Operation and Economics of Transport and Communications, 010 26 Žilina, Univerzitná 8215/1, Slovakia, jan.vrabel@uniza.sk, https://orcid.org/0000-0002-1407-2924*
[6] *Dr Slobodan Savić, full prof. Faculty of Engineering University of Kragujevac, Kragujevac 34000, Sestre Janjić 6, Serbia, ssavic@kg.ac.rs, https://orcid.org/0000-0001-6609-4845*

KEYWORDS: Composite pressure cylinders; Hydrogen storage; compressed natural gas (CNG); vehicle safety; inspection and maintenance

BEZBEDNOSNI I EKSPLOATACIONI ASPEKTI PRIMENE KOMPOZITNIH REZERVOARA ZA SKLADIŠTENJE VODONIKA I KPG U VOZILIMA

REZIME: Sve veću primenu komprimovanog prirodnog gasa (KPG) i vodonika kao alternativnih goriva za vozila prati i potreba za pouzdanim i bezbednim tehnologijama za skladištenje ovih gasova pod visokim pritiskom. Kompozitni rezervoari predstavljaju efikasno rešenje za skladištenje gasovitih goriva u vozilima zbog povoljnog odnosa mase i zapremine, adekvatne čvrstoće, otpornosti na koroziju, kao i dobre otpornosti na zamor materijala.
U radu je data analiza uslova eksploatacije, zahteva za ugradnju, postupaka kontrole, održavanja i sistematizovani su osnovni uslovi sa aspekata bezbedne primene kompozitnih rezervoara tipa 3 za skladištenje KPG–a i vodonika u motornim vozilima. Razmatrani su uticaji cikličnih promena pritiska, temperaturnih promena i drugih uslova okoline, kao i mehaničkih oštećenja i načina rukovanja na konstrukciju i radni vek rezervoara. Posebna analiza je izvršena u delu uslova za pričvršćenje rezervoara, ugradnje uređaja i opreme za rasterećenje pritiska, metoda kontrole i kriterijuma za eventualnu procenu oštećenja rezervoara. Takođe su analizirani uslovi za bezbedno punjenje i pražnjenje rezervoara za potrebe servisiranja i održavanja, u cilju smanjenja rizika, i istraživano je postupanje sa rezervoarima na kraju radnog veka. Analizom su identifikovani ključni faktori koji utiču na pouzdanost rezervoara i definisane su osnovne mere i uslovi u cilju njihove bezbedne i dugoročne eksploatacije.

KLJUČNE REČI: Kompozitni rezervoari pod pritiskom, skladištenje vodonika, komprimovani prirodni gas (KPG), bezbednost vozila, kontrola i održavanje

INTRODUCTION

Composite high-pressure cylinders are increasingly used in automotive applications for the storage of compressed natural gas (CNG) and hydrogen. The safe operation of these systems is governed by defined pressure, temperature, and service conditions established by the applicable standards and certification requirements. Accordingly, the cylinders must be operated within their specified design and permissible operating limits throughout their service life. The Type–3 cylinders considered in this research feature a seamless 6061 aluminium alloy liner that is completely enclosed by a carbon–fiber/epoxy composite overwrap, providing the required structural reinforcement and pressure resistance, Figure 1 (Milojević, 2017; Luxfer Gas Cylinders, 2018).

Figure 1 Design of a Type 3 Composite Cylinder (AA6061 aluminium liner with carbon fibre/epoxy overwrap)

In general, the applicable design and safety requirements are specified by the relevant standards and regulations, including ISO 11439 and UN ECE 110R for natural gas applications, as well as Regulation (EU) 2019/2144 and UN Regulation No. 134 for hydrogen–fueled systems (UNECE, 2018; ISO, 2013; European Parliament & Council of the European Union, 2019; UNECE, 2019).

The cylinders are designed for a nominal service pressure of 20 MPa, referenced to an ambient temperature of 15 °C. During refueling, the filling pressure must be controlled so that, after thermal stabilization, the cylinder pressure does not exceed the specified service pressure under the reference temperature conditions. Therefore, the pressure applied during filling should be adjusted according to the actual gas temperature to ensure compliance with the maximum permissible filling pressure. The following approximate relationships can be used for estimating the corresponding pressure conditions (Luxfer Gas Cylinders, 2018):

$$P_{\mathrm{CNG}} = 176 + 1.6 \cdot T_{\mathrm{CNG}} \tag{1}$$

$$P_{H_2} = 189 + 0.73 \cdot T_{H_2} \quad (2)$$

Where are:

P [bar] – the corresponding pressures; and T [°C] – the temperatures of CNG and hydrogen, respectively.

For natural gas applications, the actual cylinder pressure is additionally influenced by the composition of the gas. Regardless of the operating temperature, the filling pressure must remain below the absolute maximum limit of 26 MPa. Furthermore, the cylinders should only be filled using compressors whose maximum discharge pressure does not exceed 1.5 times the specified nominal service pressure.

Hydrogen can also be stored in gaseous form within pressure vessels at substantially higher pressures than those typically used for natural gas. For example, a nominal service pressure of 35 MPa is specified at an ambient temperature of 15 °C. During filling, the pressure should be controlled so that, following thermal stabilization, the cylinder pressure does not exceed the specified service pressure of 35 MPa under the reference temperature conditions (Luxfer Gas Cylinders, 2018).

For hydrogen storage systems, the filling pressure is subject to an absolute upper limit of 43.75 MPa, which must not be exceeded irrespective of the gas temperature. Accordingly, the pressure applied during the refueling process should be determined by taking into account the actual hydrogen temperature, thereby ensuring that the pressure remains within the permissible filling limit. The following approximate calculations can be employed to estimate the appropriate filling pressure under different temperature conditions (Luxfer Gas Cylinders, 2018):

$$P_{H_2} = 331 + 1.26 \cdot T_{H_2} \quad (3)$$

During handling, transportation, and storage, Type–3 cylinders should be depressurized and carefully protected against mechanical damage, particularly to the carbon–fiber overwrap and aluminum liner. Appropriate personal protective equipment should be used, while contact with valves, fittings, and pressure–relief devices should be avoided. Cylinders must be secured against rolling, impacts, and accidental dropping. During storage, they should be protected from excessive heat, moisture, corrosive environments, UV radiation, and surface abrasion, with suitable protective plugs used to prevent contamination of open ports. Appropriate lifting equipment should be employed when necessary.

Type–3 cylinders can withstand normal contaminants encountered in automotive environments; however, exposure to highly corrosive acids, alkalis, or abrasive materials should be avoided. No additional protective coating is recommended, as it could hinder the visual detection of damage to the reinforcing fibers. The existing epoxy surface layer provides adequate protection of the composite overwrap. Particular care should also be taken to prevent the ingress of water into the cylinder, since moisture contamination may adversely affect its service life.

The operating temperature limits for CNG and hydrogen cylinders are defined by the applicable standards and regulations, including ISO 11439, UN ECE 110R, and Regulation (EU) 2019/2144 and UN Regulation No. 134. Under these conditions, the settled gas temperature may range from (−40) − 65 °C for CNG and up to 85 °C for hydrogen. The corresponding allowable temperature range for the cylinder materials extends from (−40) − 82 °C for CNG and up to 85 °C for hydrogen. For CNG cylinders, any local or transient temperature increase above 65 °C must be limited in duration and extent so that the gas temperature inside the cylinder remains below the specified maximum (UNECE, 2018; ISO, 2013; European Parliament & Council of the European Union, 2019; UNECE, 2019).

The cylinders are suitable for CNG, compressed hydrogen, and hydrogen–gas mixtures. The composition of CNG shall meet the requirements specified in ISO 11439 and UN ECE 110R, while Compressed hydrogen shall comply with the fuel quality requirements specified in ISO 14687:2025 (UNECE, 2018; ISO, 2013, 2025).

The service life of the cylinders is limited to approximately 15–20 years from the date of final inspection, depending on the applicable national requirements and specified annual filling cycles. The expiration date is indicated on the cylinder label. Once the specified service life or maximum number of filling cycles is reached, the cylinder must be permanently withdrawn from service. For CNG cylinders, the allowable number of fillings is limited to 1000 cycles per year of service life, while hydrogen cylinders are limited to 5000 filling cycles (Luxfer Gas Cylinders, 2018).

For hydrogen cylinders, the applicable regulations may permit a lower maximum number of filling cycles when an appropriate monitoring and control system is implemented. In such cases, the specified cycle limit is marked on the cylinder label, Figure 2, and the cylinder must be withdrawn from service once this limit has been reached.

Periodic external visual inspections of the composite overwrap are required after installation or reinstallation to identify possible defects. The inspection frequency and procedures shall comply with the applicable national standards and regulations; for CNG cylinders, UN ECE 110R specifies an interval of at least 48 months after the vehicle is placed into service. Shorter intervals may apply depending on the cylinder type and applicable type–

approval requirements. Inspections should be performed according to ISO 19078:2013 or national standards (UNECE, 2018; ISO, 2013).

Figure 2 Examples of CNG and Hydrogen Cylinder Labels

Routine hydraulic pressure testing is generally not required. Where such testing is mandated by national regulations, only appropriately treated water should be used, with chloride removal and suitable corrosion inhibitors, while exposure time should be minimized to protect the AA6061 aluminum liner from corrosion.

Cylinders that have been subjected to a vehicle collision shall undergo a re–inspection conducted by an agency authorized by the manufacturer and, where applicable, by the relevant regulatory authority. If the inspection confirms that the cylinder has not sustained any impact–related damage, it may be returned to service. However, if any damage resulting from the collision is identified, the cylinder shall be returned to the manufacturer for further assessment and evaluation.

Cylinders exposed to fire shall be immediately removed from service and shall not be returned to service unless their safety and structural integrity have been verified through an appropriate inspection and assessment. A cylinder may have been adversely affected by fire or excessive heat without exhibiting any visible signs of damage. Therefore, the prescribed inspection and assessment procedures shall be followed to ensure that the cylinder remains safe for further service.

CYLINDER AND EQUIPMENT INSTALLATION REQUIREMENTS

The cylinders shall be installed in accordance with the applicable installation requirements for the specific model. The installer is responsible for ensuring adequate protection of cylinder valves, pressure relief devices (PRD), and connections, in compliance with the applicable national standards and regulations.

All components must be suitable for a working pressure of at least the nominal service pressure of the cylinder, i.e., 20 or 35 MPa, depending on the cylinder type. Components used in accordance with UN ECE 110R and the relevant requirements for hydrogen vehicles must be approved for a working pressure corresponding to at least the maximum filling pressure of 26 or 43.75 MPa, respectively (Luxfer Gas Cylinders, 2018).

For fire safety, each cylinder must be equipped with an appropriate PRD compatible with the cylinder type and approved in accordance with the relevant standards.

Valves and End Plugs with O–Ring Seals

All valves and end plugs shall be provided with an O–ring sealing seat and shall have at least 7 engaged threads for 20 MPa cylinders and 11 engaged threads for 35 MPa cylinders. The components shall be tightened to the specified torque. Tapered threads shall not be used (Luxfer Gas Cylinders, 2018).

Before installation, the valve or end plug, mating threads, and sealing surfaces shall be inspected for damage and cleaned with a suitable detergent or solvent using a nylon brush. The surfaces shall then be dried with a clean cloth and kept free of dirt and debris. The specified O–ring shall be selected according to Table 1 and installed carefully without damage. Other O–rings shall not be used without prior qualification.

Table 1 Example: O–Ring Specifications and Tightening Torques for 1.125″ and 2.0″ Threads

Thread designation	O–ring dimensions [mm] (inside diameter x cross–section diameter)	Torque [Nm] 20 / 35 MPa cylinder series
1.125 – 12 UNF	28.17 x 3.53	217 (± 14) / 240 (± 10)
2.0 – 12 UN	50.39 x 3.53	305 (± 15) / 320 (± 10)

The valve or end plug shall be manually screwed into the cylinder port and tightened to the specified torque using appropriate tools. The required tightening torques shall comply with the values given in Table 1. After tightening, a

suitable torque–indicating compound shall be applied to the external joint between the end plug and cylinder neck to confirm completion of the installation (Luxfer Gas Cylinders, 2018).

For hydrogen service, the use of O–ring lubricant or anti–seize compound should be minimized to avoid potential gas contamination. If required, a thin film of suitable O–ring lubricant may be applied to the O–ring. A small amount of copper–free anti–seize compound may be applied to the first threads, as shown in Figure 3.a, while avoiding contact with the O–ring.

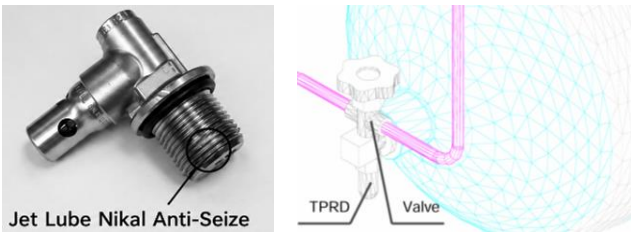

(a) (b)

Figure 3 (a) Application of Anti–Seize Compound to the Valve Thread; (b) Typical Valve and TPRD Assembly

Pressure Relief Devices

Thermally activated pressure relief devices (TPRDs) shall be incorporated into the cylinder piping system to provide controlled pressure relief in the event that the cylinder is subjected to fire or excessive heat, Fig.3.b. The required number and configuration of TPRDs shall be specified in the applicable installation drawing. The TPRD discharge outlets shall remain unobstructed and shall not be blocked, sealed, or covered by adjacent components or attachments.

For longer cylinders, a middle–plug TPRD may be installed at the center of the cylinder and connected to the valve or end plug by a dedicated TPRD pipe, Figure 4.

The TPRD pipe remains under cylinder pressure even when the valve is manually and/or electrically closed. Installation and servicing shall therefore be performed only by personnel trained in compression fitting installation.

The TPRD and pipe shall be positioned and installed in accordance with the applicable installation drawing and the manufacturer's instructions. The pipe shall be cleaned immediately before installation. The TPRD shall be secured using a saddle clamp with a rubber strip between the clamp and cylinder surface. The clamp shall be correctly positioned, tensioned, and locked in accordance with the manufacturer's instructions, Figure 4.

Figure 4 TPRD Pipe, Middle Plug and Saddle Bracket on Bus–Mounted Cylinders

A minimum clearance of 5 mm shall be maintained between the TPRD pipe and the cylinder surface. Where necessary, a soft elastomeric support may be installed between the pipe and cylinder, Figure 4 (Luxfer Gas Cylinders, 2018).

Cylinder Installation and Mounting

The cylinder, cylinder assembly, or cylinder rack, including the associated safety devices and complying with UN ECE 110R or Regulation (EU) 2019/2144 and UN Regulation No. 134, shall be securely installed and restrained to withstand the specified accelerations and decelerations given in Table 2, without failure or loosening of the mounting system. Compliance shall be demonstrated by appropriate testing or calculation, using a mass representative of the fully equipped and filled cylinder, cylinder assembly, or cylinder rack (UNECE, n.d.; UNECE, 2019; ISO, 2025).

As example, neck mount brackets are designed to securely fasten CNG or hydrogen storage cylinders to automotive vehicles in a horizontal position, Figure 5. Where neck mounting is specified, the cylinder model number includes the designation “N” at the end. The Figure 5 also shows the installation position of the cylinder on the factory–mounted roof rack of the bus (Milojević, 2017; Milojević et al., 2025).

Table 2 Required Accelerations and Decelerations for Gas Cylinders

Motor Vehicle Categories	M1 and N1	M2 and N2	M3 and N3
Vehicle Acceleration:			
– In the Direction of Travel	20·g	10·g	6.6·g
– Perpendicular to the Direction of Travel	8·g	5·g	5·g

Motor Vehicle Categories: M1 with ≤ 9 passengers or N1 (for goods) ≤ 3.5 t;
M2 with > 9 passengers and ≤ 5 t or N2 (for goods) > 3.5 t and ≤ 12 t;
M3 with > 9 passengers and > 5 t or N3 (for goods) > 12 t

The brackets shall only be used within the conditions specified in this Statement of Service. Installation shall comply with the applicable requirements of ISO 11439 and UN ECE 110R for CNG cylinders, or Regulation (EU) 2019/2144 and UN Regulation No. 134 for hydrogen cylinders (UNECE, n.d.; ISO, 2013; UNECE, 2019; ISO, 2025).

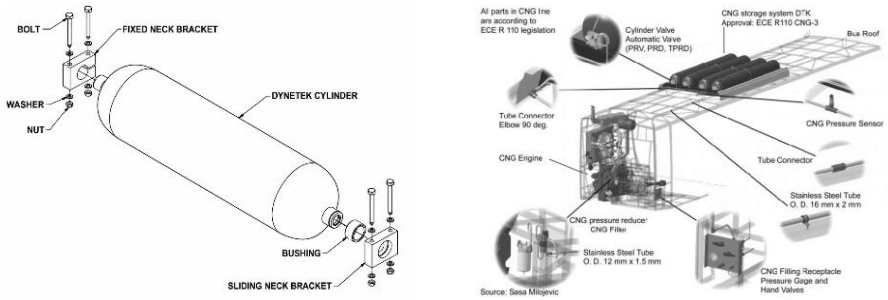

Figure 5 Cylinder Neck Mount Assembly and Installation of the Cylinder Rack on the Roof of a City Bus

Cylinders are installed using two neck–mounting brackets that secure the extended cylinder necks. One end of the cylinder is rigidly restrained, while the opposite end is allowed to slide within the bracket to accommodate dimensional changes caused by variations in temperature and internal pressure, Figure 5. When properly installed, the fixed neck–mounting bracket prevents longitudinal movement of the cylinder neck within the bracket up to a maximum longitudinal load of 17 kN. This load corresponds to the following weights for a fully filled cylinder, Table 3 (Luxfer Gas Cylinders, 2018):

Table 3 Permissible Total Cylinder Weight According to ECE R110, (EC) No. 79/2009, and (EC) No. 406/2010

Acceleration	20·g	10·g	6.6·g
Maximum Permissible Weight of a Filled Cylinder [kg]	86	173	262

Max. Permissible Weight of a Filled Cylinder = 17 kN / (9.81 m/s² x acceleration)

A neck mount bracket set consists of a fixed bracket, a sliding bracket, and a pre–installed high–molecular–weight polyethylene bushing. The fixed bracket is installed on the cylinder neck with the cylinder serial number and bracket marking facing outward and upward, while the sliding bracket is installed on the opposite neck in the same orientation. The cylinder is then placed on the vehicle rack and rotated to position the fixed (valve) end as required. The neck position in the sliding bracket shall be adjusted to provide sufficient clearance for cylinder expansion caused by pressure and temperature variations Figure 5.

The M12 sliding and fixed bracket bolts shall be selected according to the working loads, with minimum property classes of 70 for stainless steel and 8.8 for steel bolts. The bolts shall be tightened to the specified torque, but not less than 70 Nm, and secured against loosening using an appropriate locking method. After tightening the fixed bracket, the cylinder position shall be checked and readjusted if necessary (Luxfer Gas Cylinders, 2018).

Cylinder Protection and Shielding Requirements

The cylinder shall be installed with suitable protection and shielding to prevent damage under vehicle operating conditions. The shielding shall protect the cylinder from road debris, contact with cargo, excessive heat, harmful vehicle fluids, and prolonged UV exposure.

The shielding shall be installed without direct contact with the cylinder and without creating areas where debris or liquids can accumulate. It shall also prevent contact between the cylinder and vehicle components such as the frame, body panels, brake lines, and exhaust system, thereby reducing the risk of abrasion and surface damage. Open–mesh shielding is generally preferred because it minimizes the accumulation of water and other liquids while allowing visual inspection of the cylinder.

No additional coating shall be applied to the composite cylinder if it could adversely affect the composite material or interfere with visual inspection. The shielding and mounting arrangement shall also ensure that the cylinder identification markings remain clearly visible, including the cylinder label and barcode, the dome sticker and barcode, and the serial–number marking on the cylinder neck, Figure 6.

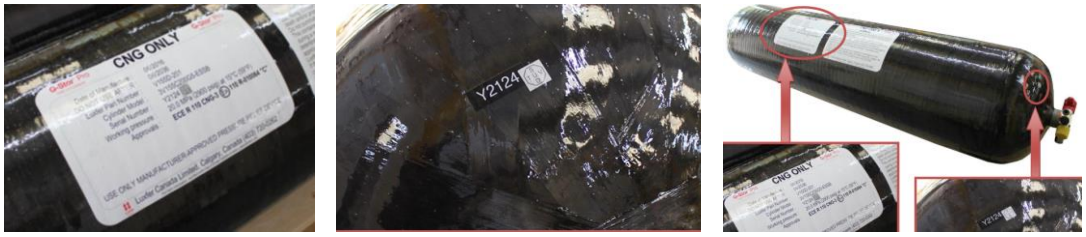

Figure 6 Cylinder Serial Number Locations

A permanent electrical connection between the cylinder, including its attached components, and the vehicle shall be provided to prevent the accumulation of static electrical charge and minimise the risk of sparking that could ignite escaping gas.

CYLINDER AND MOUNTING SYSTEM INSPECTION AND MAINTENANCE

When filling, defueling, inspecting, or servicing cylinders and associated components containing pressurized hydrogen or natural gas, appropriate safety precautions shall be followed. Only trained and authorised personnel shall fill, defuel, inspect, or service cylinders and components containing pressurized hydrogen or natural gas, following the manufacturer's procedures and using appropriate protective equipment.

All potential ignition sources, including open flames and heat sources, shall be eliminated. Electrical connections shall be disconnected where necessary, and the system shall be properly grounded to prevent sparking. The system and its components shall always be assumed to be pressurized. Fittings and ports shall therefore be opened slowly, and work shall be stopped immediately if gas leakage occurs or excessive torque is required.

Particular care shall be taken when a potentially flammable gas mixture may be present. Hydrogen is flammable in air at concentrations of approx. 4–74%, while natural gas is flammable at approx. 5–15%. Systems containing potentially flammable mixtures shall not be operated, stored, or transported and shall be properly purged before further work. Electrical connections shall not be made to systems containing a potentially flammable mixture (Luxfer Gas Cylinders, 2018; Loman et al. 2026).

Preparation of Cylinders and Components for Inspection and Maintenance

Depending on the maintenance activity, the cylinder and associated components may require defueling and/or purging before work begins. For visual inspection and leak testing, where no mechanical work is performed, the cylinder assembly shall be properly grounded. If maintenance is performed without breaking connection seals, such as re–torqueing fittings or end plugs, the assembly shall be grounded and defueled to prevent the ingress of air or debris. If connection seals must be broken, such as when replacing a valve or fitting, the cylinder or component shall be grounded, defueled, and purged before work begins.

The cylinder and associated components should be cleaned before visual inspection using clear or soapy water. Abrasive detergents and aggressive cleaning agents, such as acetone, solvents, or gasoline, shall not be used because they may damage the cylinder surface. A pressure washer may be used with a maximum spray pressure of 10 MPa and a minimum distance of 50 cm. The water jet shall not be directed at cylinder labels, solenoid valves, electrical connectors, or safety devices such as TPRDs (Luxfer Gas Cylinders, 2018).

Inspection of Cylinders and Components

Inspection is an essential safety measure for detecting damage to the cylinder or mounting system and identifying any adverse environmental effects during operation. Inspections shall be performed using appropriate tools, such as measuring instruments for determining defect dimensions, a flashlight, an adjustable mirror, and a cleaning cloth. Two types of inspections are specified: General Inspection and Certification Inspection, as summarized in Table 4.

The General Inspection is not mandatory but is recommended every 3 months to verify that the fuel storage system remains in good condition. It covers the mounting system and cylinder(s).

The mounting inspection shall verify that all brackets are undamaged and securely attached to the vehicle, with all bolts present and properly tightened. For belly–mounted systems, protection pads shall be present, in good condition, and each cylinder shall be securely restrained. Loose mounting components shall be re–secured in accordance with the applicable installation procedure. Damage to the mounting system may indicate vehicle accident involvement and requires a Certification Inspection. Missing or damaged components shall be replaced with approved parts.

Table 4 Inspection Categories Summary

Inspection Type	Description	Inspection Frequency
General Inspection	Performed by the driver, maintenance personnel, or other qualified service technician, this inspection is primarily visual and is intended to verify that the cylinder, mounting system, and piping are in good condition, properly secured, and free from visible damage.	Recommended every 3 months
Certification Inspection	Performed by trained personnel certified in accordance with applicable local regulations and requirements. This inspection provides a more detailed examination of the cylinder, mounting system, and piping.	Typically performed at commissioning and every 3–4 years, subject to local authority requirements.

The cylinders shall be inspected for signs of damage in accordance with the applicable inspection criteria, Table 5. Any indication of damage shall be assessed and appropriate corrective action determined. Minor cutting or abrasion limited to the outer pure epoxy resin layer is not considered critical and does not require further damage assessment.

Table 5 Cylinder Damage Types, Signs, and Potential Causes

Cylinder Damage Type	Signs of Damage	Potential Causes
Impact Damage	Dents, scratches, cracked or peeling laminate, or crazing (hairline cracks in the laminate)	Impact from a blunt object or dropping the cylinder
Cutting Damage	Cuts, scratches, gouges, or peeling laminate	Contact with a sharp or pointed object
Abrasion Damage	Scuffs, dull or whitish areas, or flat spots	Friction between the laminate and an object in contact with the cylinder
Fire or Excessive Heat Damage	Charred or discolored laminate, soft spots, blistering, or swelling	Exposure to direct flame, contact with an excessive heat source, or proximity to a high–temperature source
Weathering Damage	Cloudy appearance, discoloration, or soft spots	Exposure to UV radiation or water ingress through cracks in the laminate
Chemical Damage	Discoloration, soft spots, blistering, or swelling	Exposure to brake fluid or other corrosive fluids

The Certification Inspection is a detailed examination of the cylinder and mounting system performed by personnel certified in accordance with local regulations. The inspection frequency is determined by the relevant authorities and is typically every 4 years for CNG cylinders under UN ECE 110R and every 3 years for other cylinders. Following a vehicle accident, a Certification Inspection should be considered even if no visible damage is apparent (UNECE, n.d.; Milojević et al. 2025).

Before filling, the hazards associated with hydrogen and natural gas, including fire, explosion, and asphyxiation, shall be considered. Filling shall be performed in a well–ventilated area free of ignition sources, with appropriate leak testing, evacuation, and purging procedures to prevent the formation of flammable gas mixtures. Proper system design and operating procedures are essential for safe handling (Turek et al. 2024; Aldhafeeri et al. 2020).

Defueling shall be performed by controlled venting to approx. 0.2 MPa, preventing air ingress and safely discharging the gas through an appropriate venting or flare system. The procedure shall be performed outdoors in a controlled safety zone, with the system grounded, ignition sources eliminated, and appropriate protective equipment used (Luxfer Gas Cylinders, 2018).

CONCLUSIONS

The analysis confirms that the safe and reliable operation of Type–3 composite cylinders for CNG and hydrogen storage depends on proper control of operating conditions, installation, inspection, maintenance, and handling procedures. Particular attention should be given to pressure and temperature limits, secure mounting, protection against mechanical and environmental damage, and correct installation of pressure–relief devices.

Regular visual and certification inspections are essential for the early detection of damage and for maintaining cylinder integrity throughout its service life. Safe filling and defueling procedures, together with appropriate grounding, ventilation, purging, and control of ignition sources, are critical for reducing fire, explosion, and asphyxiation risks.

Overall, the implementation of appropriate technical and safety procedures, in accordance with applicable standards, regulations, and manufacturer requirements, provides the basis for extending operational reliability, minimizing risks, and ensuring the safe long–term use of composite CNG and hydrogen storage systems in vehicles.

ACKNOWLEDGMENTS

This research was performed by the APVV project SK–SRB–25–0028 Implementation of the process of measuring diesel particulate matter during emission inspection in the Slovak Republic and Serbia; number 001147721/007, Republic of Serbia, Ministry of Science, Technological Development and Innovation. This work has been also performed and funded as a part of activities within the projects 451–03–33/2026–03/200107 and 451–03–34/2026–03/200107, supported by the Republic of Serbia, Ministry of Science, Technological Development and Innovation.

REFERENCES

Aldhafeeri, T., Tran, M.-K., Vrolyk, R., Pope, M., & Fowler, M. (2020). A Review of Methane Gas Detection Sensors: Recent Developments and Future Perspectives. *Inventions*, *5*(3), 28. https://doi.org/10.3390/inventions5030028

European Parliament & Council of the European Union. (2019). *Regulation (EU) 2019/2144 of the European Parliament and of the Council of 27 November 2019 on type-approval requirements for motor vehicles and their trailers, and systems, components and separate technical units intended for such vehicles*. *Official Journal of the European Union, L 325*, 1–40.

International Organization for Standardization. (2013). *Gas cylinders-High pressure cylinders for the on-board storage of natural gas as a fuel for automotive vehicles* (ISO Standard No. 11439:2013). https://www.iso.org/obp/ui/en/#iso:std:iso:11439:ed-2:v1:en

International Organization for Standardization. (2013). *Gas cylinders-Inspection of the cylinder installation, and requalification of high pressure cylinders for the on-board storage of natural gas as a fuel for automotive vehicles* (ISO Standard No. 19078:2013).

International Organization for Standardization. (2025). *Hydrogen fuel quality-Product specification* (ISO Standard No. 14687:2025).

Loman, M., Harantová, V., & Milojević, S. (2026). Air Quality in Urban Mobility Hubs: An Analysis of Particulate Matter in Underground Transport Spaces. *Urban Science*, *10*(7), 412. https://doi.org/10.3390/urbansci10070412

Luxfer Gas Cylinders. (2018). *Carbon Composite Cylinder User Manual: Alternative Fuel Cylinders*.

Milojević, S. (2017). Sustainable application of natural gas as engine fuel in city buses: Benefit and restrictions. *Journal of Applied Engineering Science*, *15*(1), 81-88. https://doi.org/10.5937/jaes15-12268

Milojević, S., Stopka, O., Orynycz, O., Tucki, K., Šarkan, B., & Savić, S. (2025). Exploitation and Maintenance of Biomethane-Powered Truck and Bus Fleets to Assure Safety and Mitigation of Greenhouse Gas Emissions. *Energies*, *18*(9), 2218. https://doi.org/10.3390/en18092218

Turek, M., Kalupová, B., Cempírek, V., Tůmová, K. & Abramović, B. (2024). Electromobility and the Environment in the Czech Republic. *LOGI – Scientific Journal on Transport and Logistics*, *15*(1), https://doi.org/10.2478/logi-2024-0018

UN ECE Regulation No. 110 Rev.3-CNG and LNG Vehicles. http://www.unece.org/trans/main/wp29/wp29regs101-120.html

United Nations Economic Commission for Europe. (2019). *UN Regulation No. 134: Uniform provisions concerning the approval of motor vehicles and their components with regard to the safety-related performance of hydrogen-fuelled vehicles (HFCV)*.

The 11th International Congress
Motor Vehicles & Motors 2026
Kragujevac, Serbia
October 8th - 9th, 2026

Motor Vehicles & Motors

MVM2026-068
https://doi.org/10.24874/CMVM2026.068
Technical paper

Mitar Mišić[1]
Stjepan Galamboš[2]
Boris Stojić[3]
Jovan Dorić[4]
Luka Sekicki[5]

DEVELOPMENT OF AN ELECTRONIC MEASUREMENT SYSTEM FOR TURBOCHARGER WASTEGATE ACTUATOR RESPONSE-TIME TESTING

ABSTRACT: A low-cost electronic measurement system for experimental determination of the response delay of a pneumatic turbocharger wastegate actuator is presented. The test bench separates the excitation and measurement functions: a programmable logic controller generates a repeatable command for a 24 V solenoid valve, while an ESP32-based acquisition unit independently observes the valve-coil voltage and two position sensors. Galvanic isolation is provided by a PC817 optocoupler. A linear potentiometer detects actuator-rod motion and a rotary potentiometer detects wastegate-flap motion. The acquisition algorithm includes edge validation, adaptive motion thresholds, oversampling and automatic session statistics. The achieved time resolution is approximately 0.33 ms. Experimental testing over 501 actuation cycles, of which 429 were retained for analysis, demonstrated repeatable detection of actuator and flap dead times and enabled the influence of pneumatic-line length to be distinguished. The proposed architecture is suitable for laboratory investigation of electropneumatic automotive actuators where the timing relationship between an electrical command and mechanical response is of primary interest.

KEYWORDS: wastegate actuator; turbocharger; ESP32; data acquisition; automotive mechatronics

[1] *Mitar Mišić, Srednja škola Novi Bečej, Maršala Tita 5, 23272 Novi Bečej - Serbia, mmisic.ftn@gmail.com*
[2] *Stjepan Galamboš, University of Novi Sad, Faculty of Technical Sciences, Trg Dositeja Obradovića 6, 21000 Novi Sad, Serbia, bstojic@uns.ac.rs, https://orcid.org/0000-0003-3491-2860*
[3] *Boris Stojić, University of Novi Sad, Faculty of Technical Sciences, Trg Dositeja Obradovića 6, 21000 Novi Sad, Serbia, bstojic@uns.ac.rs, https://orcid.org/0000-0001-8344-1466*
[4] *Jovan Dorić, University of Novi Sad, Faculty of Technical Sciences, Trg Dositeja Obradovića 6, 21000 Novi Sad, Serbia, bstojic@uns.ac.rs, https://orcid.org/0000-0002-4532-4880*
[5] *Luka Sekicki, University of Novi Sad, Faculty of Technical Sciences, Trg Dositeja Obradovića 6, 21000 Novi Sad, Serbia, luka.sekicki@uns.ac.rs, https://orcid.org/0009-0007-9170-8352*

RAZVOJ ELEKTRONSKOG MERNOG SISTEMA ZA ISPITIVANJE VREMENA ODZIVA WASTEGATE AKTUATORA TURBOPUNJAČA

REZIME: Predstavljen je jeftin elektronski merni sistem za eksperimentalno određivanje kašnjenja odziva pneumatskog wastegate aktuatora turbopunjača. Na ispitnom stolu razdvojene su funkcije pobude i merenja: programabilni logički kontroler generiše ponovljivu upravljačku komandu za elektroventil napona 24 V, dok akviziciona jedinica zasnovana na ESP32 nezavisno prati napon na kalemu elektroventila i signale dva senzora položaja. Galvanska izolacija obezbeđena je pomoću optokaplera PC817. Linearni potenciometar registruje pomeranje klipnjače aktuatora, dok kružni potenciometar registruje pomeranje wastegate klapne. Algoritam za akviziciju obuhvata potvrdu ivice signala, adaptivne pragove detekcije pomeranja, oversampling i automatsko formiranje statistike merne sesije. Ostvarena vremenska rezolucija iznosi približno 0,33 ms. Eksperimentalna ispitivanja sprovedena tokom 501 ciklusa aktiviranja, od kojih je 429 zadržano za analizu, pokazala su ponovljivu detekciju mrtvog vremena aktuatora i klapne i omogućila izdvajanje uticaja dužine pneumatskog voda. Predložena arhitektura pogodna je za laboratorijska ispitivanja elektropneumatskih aktuatora u motornim vozilima kod kojih je od primarnog značaja vremenski odnos između električne upravljačke komande i mehaničkog odziva.

KLJUČNE REČI: wastegate aktuator; turbopunjač; ESP32; akvizicija podataka; mehatronika motornih vozila

INTRODUCTION

Precise boost-pressure control in turbocharged engines depends not only on the static characteristics of the wastegate actuator but also on the dynamics of the complete command chain (Thomasson et al. 2009). In a pneumatic wastegate system, the delay between the electrical command to the solenoid valve and the beginning of actuator motion includes electrical, pneumatic and mechanical contributions (Galindo et al. 2009; Szente & Vad, 2001). For experimental investigation of such short delays, the excitation source and the measurement system should be functionally separated, while the electrical command should be observed as close as possible to the boundary between the electrical and pneumatic domains.

The aim of this work is therefore to present the electronic and measurement architecture of a dedicated test bench developed for response-time measurements of a pressure-operated wastegate actuator. The mechanical and pneumatic arrangement is described only to the extent required to explain the measurement chain. Particular attention is given to galvanic isolation, acquisition of two displacement signals, robust detection of the excitation edge and the algorithm used to determine the beginning of motion.

TEST-BENCH CONCEPT AND MEASURED QUANTITY

The test bench consists of a pneumatic chain and an independent measurement chain. A Xinje XC3-32T-E programmable logic controller drives a 3/2 solenoid valve (3V210-06). The valve supplies a membrane-and-spring wastegate actuator through a polyurethane hose of 4 mm internal diameter. The actuator rod drives the wastegate flap through a lever mechanism. During the experiment the hose length was varied from 5 to 30 cm in 5 cm increments, while the remaining test conditions were kept unchanged.

The measured quantity is the dead time between the change of voltage at the solenoid-valve coil and the instant at which the corresponding position-sensor signal departs from its steady value by a prescribed threshold:

$$t_M = t_{det} - t_0 \tag{1}$$

Two dead times are obtained simultaneously: one for the actuator rod and one for the wastegate flap. Their difference provides an additional indication of the delay introduced by clearance in the mechanical linkage:

$$\Delta t = t_{M,\mathrm{flap}} - t_{M,\mathrm{rod}} \tag{2}$$

CONTROL AND ELECTRONIC MEASUREMENT SYSTEM

Functional architecture

The control and measurement functions are deliberately separated. The PLC generates the excitation, whereas the microcontroller only observes the excitation and sensor responses. The 24 V coil voltage is routed through an optocoupler to a digital input of the ESP32. At the same time, the ESP32 samples a linear potentiometer attached to the actuator rod and a rotary potentiometer attached to the flap shaft. Measured data are transferred to a computer through a serial USB connection. This architecture prevents the acquisition unit from participating in the control loop and reduces the possibility that its own command latency becomes part of the measured actuator delay.

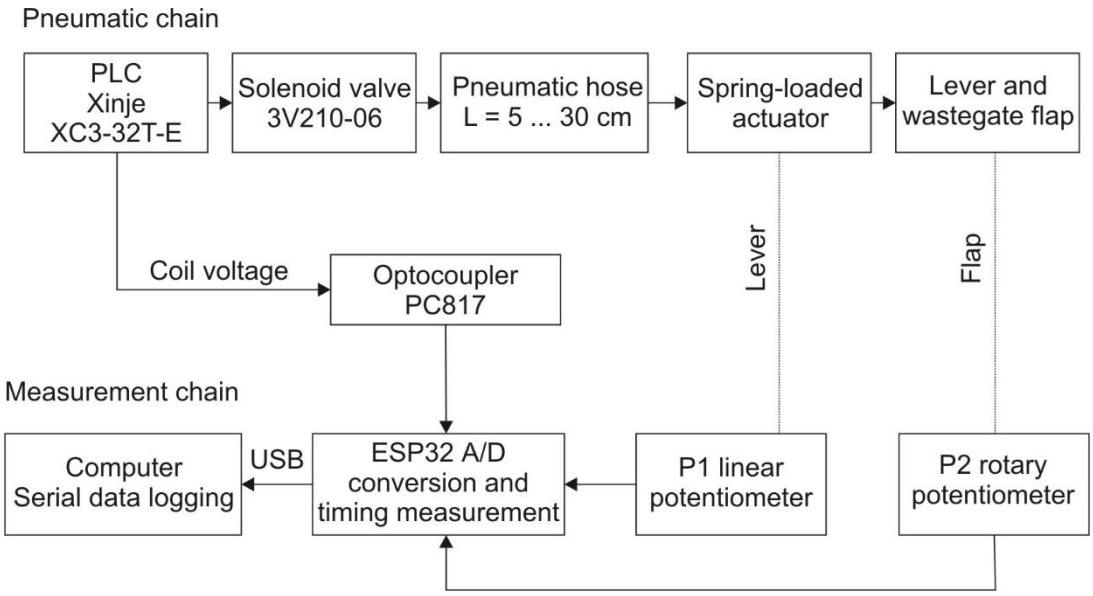

Figure 1 Block diagram of the measurement chain

Solenoid-valve excitation

The Xinje XC3-32T-E PLC generates a periodic excitation: output Y0 is ON for 1 s and OFF for 1 s. Two PLC timers alternately trigger each other, producing a 2 s period (0.5 Hz). The one-second interval between successive state changes is much longer than the measured dead time, allowing the actuator to reach a steady condition before the next transition. This provides repeatable initial conditions for opening and closing measurements.

Galvanic isolation and signal conditioning

The solenoid coil operates at 24 V, whereas the ESP32 uses 3.3 V logic. Direct connection is therefore unsuitable both because of the voltage-level mismatch and because switching an inductive coil can generate transient overvoltage and ground-coupled disturbances. A PC817 optocoupler is used between the control and measurement circuits. On the input side, a 5.6 kΩ series resistor limits the optocoupler LED current. On the output side, the phototransistor interfaces with ESP32 input IO18, with a 4.7 kΩ resistor defining the low state. The resulting logic is non-inverting: an energized solenoid corresponds to a high logic level at the microcontroller input.

During development, incorrect collector/emitter connection prevented reliable switching, and edge chatter was subsequently observed. The hardware connection was corrected and residual edge instability was handled in software by multi-sample validation and a lockout interval.

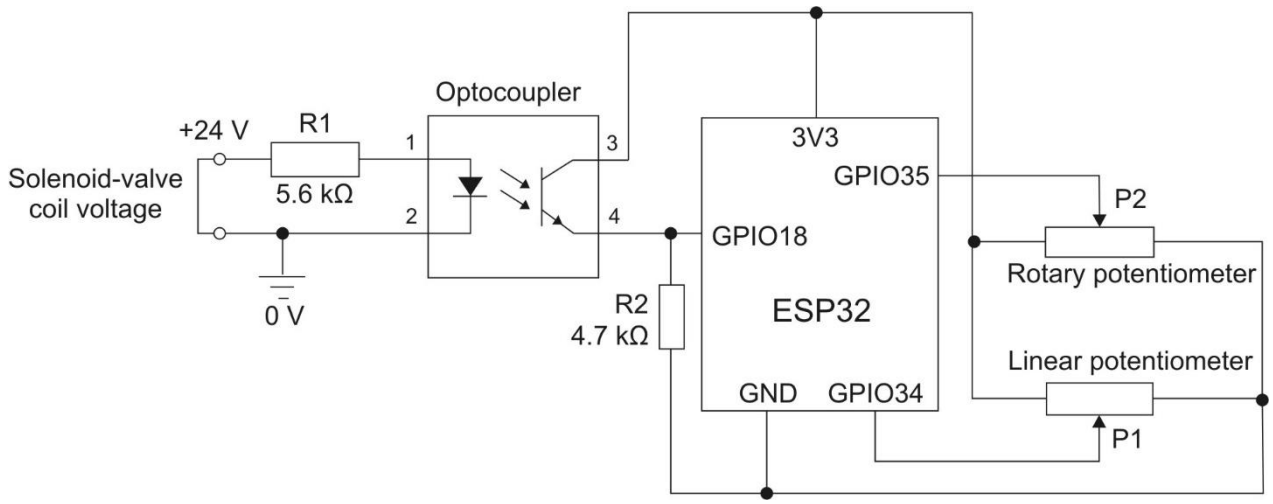

Figure 2 Electrical connection diagram

Position sensing and A/D acquisition

Two inexpensive resistive sensors are used because the measurement objective is the instant of motion onset rather than accurate absolute displacement. A 10 kΩ linear potentiometer with approximately 10 mm working stroke measures actuator-rod displacement, while a rotary potentiometer measures flap rotation over an effective angular range of approximately 15–20°. Both potentiometers are connected as voltage dividers between 3.3 V and ground, and their wipers are connected to ESP32 analog inputs IO34 and IO35. The ESP32 A/D converter is operated at 12-bit resolution. Each analog channel is read four times and averaged to reduce conversion noise.

DATA-ACQUISITION ALGORITHM

Detection of the electrical reference instant

The program continuously reads the optocoupler output and both analog channels. A new solenoid state is accepted only after the same new digital level has been detected in eight consecutive reads. Importantly, the time stamp assigned to the transition is the time of the first sample in that sequence, so validation does not intentionally add eight-sample delay to the measured value. After a valid edge, further transitions are ignored for 200 ms. This suppresses residual chatter while remaining well below the approximately one-second interval between genuine transitions.

Adaptive detection of motion onset

The steady-state value of each position channel is continuously estimated from the mean of the latest 48 readings. The motion threshold is set to 4% of the measured signal travel for the corresponding channel. This adaptive approach is required because the linear and rotary potentiometers use substantially different portions of the A/D range. Motion is accepted only when the deviation exceeds the threshold in three consecutive readings; the time of the first of these readings is stored as the onset time. The first cycle of each measurement session is used to establish the signal travel and is excluded from subsequent analysis.

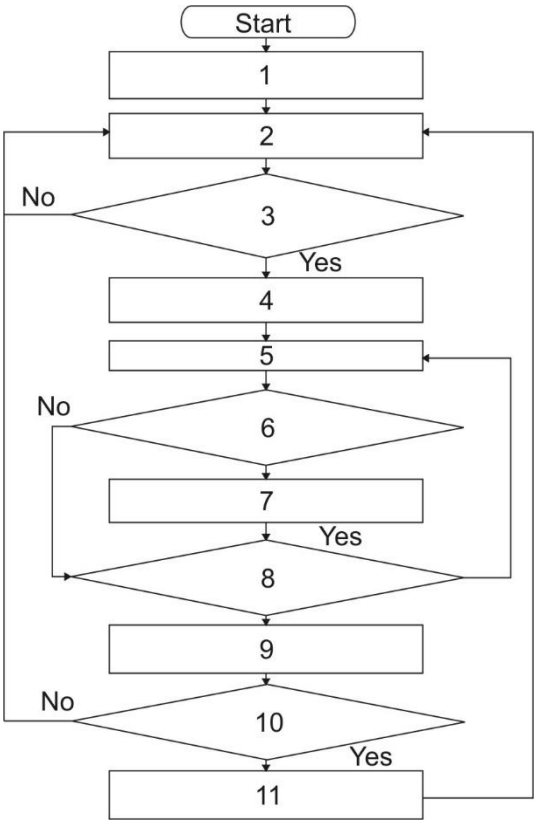

1. Configure A/D converter (12-bit) and serial communication with computer
2. Read signals from optocoupler and both potentiometers
3. Solenoid-valve state change confirmed over 8 readings?
4. Store transition time t_0, baseline values and threshold for each channel
5. Read both potentiometers
6. Channel deviation exceeds threshold in three consecutive readings?
7. Record dead time $t_M = t_{det} - t_0$
8. Both channels detected or 400 ms elapsed?
9. Output cycle data and update measurement-session statistics
10. 10 s elapsed without solenoid-valve state change?
11. Output measurement-session report and return to slow mode

Figure 3 Flow chart of the acquisition algorithm

Sampling rate and data output

Outside an active measurement, the program uses a 1 ms delay between loop iterations. After a valid excitation edge it enters a fast mode without the delay, achieving a time resolution of approximately 0.33 ms, corresponding to about 3 kHz. A measurement window is terminated after both channels have detected motion or after 400 ms. Each cycle is stored as a semicolon-separated record containing session number, cycle number, opening times, opening-time difference, closing times and closing-time difference. The software also calculates the mean, standard deviation, minimum and maximum values for the current session and automatically prints a session report after 10 s without further activity.

EXPERIMENTAL EVALUATION OF THE MEASUREMENT SYSTEM

Six pneumatic-line lengths (5, 10, 15, 20, 25 and 30 cm) were tested at a supply pressure of approximately 1.9–2.0 bar. A total of 501 actuation cycles were recorded and 429 were retained for analysis. The test programme was designed primarily to determine whether the measurement system could resolve physically meaningful changes in dead time and provide repeatable results.

Table 1 Opening dead time, mean value and standard deviation

Hose length [cm]	Rod opening [ms]	Flap opening [ms]	Accepted cycles
5	33.60 ± 1.01	41.15 ± 0.66	40
10	35.04 ± 1.01	42.12 ± 0.56	75
15	36.76 ± 1.20	44.40 ± 1.11	82
20	36.51 ± 1.19	43.25 ± 1.44	85
25	36.87 ± 1.19	43.80 ± 0.53	79
30	37.78 ± 1.20	45.84 ± 0.90	68

The measured opening delay increased with hose length. The fitted slope was 0.137 ms/cm for the actuator rod and 0.147 ms/cm for the flap, corresponding to approximately 1.4 ms additional delay per 10 cm of hose. Closing behaviour was different: the rod dead time remained near 26.9 ms and showed practically no dependence on hose length (reported fitted slope 0.003 ms/cm), while the flap showed only a weak dependence.

The distinction between the two position channels was also repeatable. During opening, the actuator rod preceded flap motion by an average of 7.29 ms and was detected first in all 429 accepted opening cycles. During closing, the average difference was 1.18 ms. The within-session scatter reported for the final data was approximately 0.7–3.3% of the measured value. These results demonstrate that the electronic system has sufficient temporal resolution and repeatability to separate the electrical-to-rod delay from the additional rod-to-flap delay.

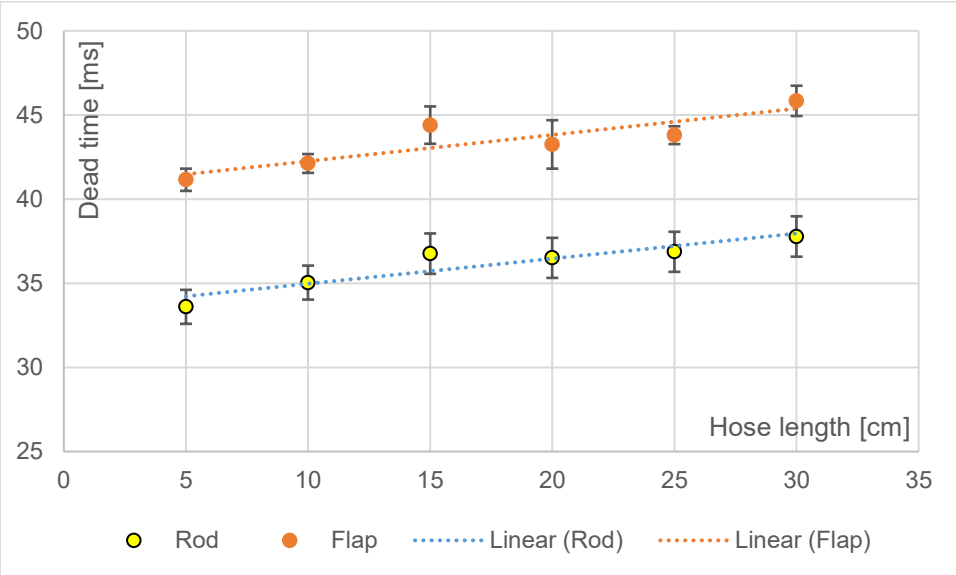

Figure 4 Opening dead time versus hose length

DISCUSSION

The main contribution of the presented test bench is not the use of individual low-cost components, but their organization into a measurement architecture in which excitation and observation are independent. Using the actual solenoid-coil voltage as the timing reference places t0 at the electrical/pneumatic interface and avoids including the controller's command-generation latency in the measured dead time. Galvanic isolation protects the 3.3 V acquisition electronics from the 24 V inductive circuit and prevents a common control-circuit ground from directly contaminating the analog sensor signals.

The software is an integral part of the measurement method. Multi-sample validation of the digital edge, oversampling of the analog inputs, adaptive thresholds and confirmation of motion over three consecutive samples were introduced specifically to suppress false detections. The achieved 0.33 ms loop resolution is small compared with the measured delays of roughly 27–46 ms. According to the thesis analysis, the maximum delay associated with three-sample confirmation is of the order of 1 ms, below approximately 3% of the measured quantity.

The principal limitations are that the wastegate flap was unloaded, tests were performed at room temperature, and pressure inside the actuator chamber was not measured. Consequently, the individual contributions of solenoid dynamics, pneumatic filling and mechanical friction cannot be separated. These limitations should be stated explicitly in a conference paper; they also define natural directions for further development, particularly the addition of a pressure transducer and testing under representative thermal and aerodynamic loading.

CONCLUSIONS

A dedicated electronic measurement system for wastegate-actuator response-time testing was developed and experimentally evaluated. The system combines PLC-based repeatable excitation, optically isolated observation of the 24 V solenoid-coil signal, two independent position sensors and ESP32-based data acquisition. Software filtering and adaptive event detection enabled reliable determination of the onset of rod and flap motion with approximately 0.33 ms time resolution. The system successfully distinguished changes in opening dead time caused by pneumatic-line length and consistently resolved the additional delay between actuator-rod and flap motion. The architecture therefore provides a practical low-cost platform for laboratory investigation of the dynamic response of electropneumatic automotive actuators.

ACKNOWLEDGMENTS

This research has been supported by the Ministry of Science, Technological Development and Innovation (Contract No. 451-03-34/2026-03/200156) and the Faculty of Technical Sciences, University of Novi Sad through project "Scientific and Artistic Research Work of Researchers in Teaching and Associate Positions at the Faculty of Technical Sciences, University of Novi Sad 2026" (No. 01-3609/1).

REFERENCES

Galindo, J., Climent, H., Guardiola, C., & Doménech, J. (2009). Modeling the vacuum circuit of a pneumatic valve system. *Journal of Dynamic Systems, Measurement, and Control*, 131(3), 031011. https://doi.org/10.1115/1.3089562

Szente, V., & Vad, J. (2001). Computational and experimental investigation on solenoid valve dynamics. In *Proceedings of the 2001 IEEE/ASME International Conference on Advanced Intelligent Mechatronics* (Vol. 1, pp. 618–623). IEEE. https://doi.org/10.1109/AIM.2001.936537

Thomasson, A., Eriksson, L., Leufvén, O., & Andersson, P. (2009). Wastegate actuator modeling and model-based boost pressure control. *IFAC Proceedings Volumes*, 42(26), 87–94. https://doi.org/10.3182/20091130-3-FR-4008.00012

The 11th International Congress
Motor Vehicles & Motors 2026
Kragujevac, Serbia
October 8th - 9th, 2026

Motor Vehicles & Motors

MVM2026-071
https://doi.org/10.24874/CMVM2026.071
Originat scientific paper

Mitar Mišić[1]
Stjepan Galamboš[2]
Jovan Dorić[3]
Boris Stojić [4]
Luka Sekicki[5]

DESIGN AND IMPLEMENTATION OF A TEST BENCH FOR EVALUATING THE DYNAMICS OF PNEUMATIC WASTEGATE ACTUATORS

ABSTRACT: This paper presents the design and implementation of a dedicated, custom-built test bench for evaluating the dynamics of pneumatic wastegate actuators, focusing on the precision manufacturing and structural integration of a novel measurement setup. Earlier engine-level models have used measured boost-pressure responses to characterize actuator dynamics, while gas-stand studies have focused on wastegate flow. The effect of pneumatic-line length on the delay from the valve command to the onset of rod and flap movement remains insufficiently documented. To overcome these limitations, a specialized test bench was designed using Autodesk Inventor and fabricated via fused deposition modeling from polylactic acid (PLA). The mechanical design incorporates a rigid flat baseplate, modular brackets with elongated mounting slots for fine-adjustment, and a precise kinematic linkage that replicates actual turbocharger geometry. The experimental setup enables the simultaneous monitoring of the linear displacement of the piston rod and the angular rotation of the flap via slide and rotary potentiometers, thereby distinguishing the rod response from the flap response and measuring their onset-time difference. In this context, dead time is precisely defined as the inherent actuation delay—specifically, the time interval from the electrical command change at the solenoid valve coil until the physical onset of movement at the component. The measured interval can include valve switching, pressure buildup or venting in the line and chamber, and the initial mechanical response; their separate contributions were not identified. Experiments were conducted by varying the length of the pneumatic hose (inner diameter of 4 mm) across six values ranging from 5 cm to 30 cm at a constant supply pressure. The results demonstrate the viability of the developed test bench and measurement method for comparing characteristics under controlled conditions, free from the influence of aerodynamic forces and variable temperatures.

KEYWORDS: wastegate actuator; automotive mechatronics, 3D printing, test bench

[1] *Mitar Mišić, Srednja škola Novi Bečej, Maršala Tita 5, 23272 Novi Bečej - Serbia, mmisic.ftn@gmail.com*
[2] *Stjepan Galamboš, University of Novi Sad, Faculty of Technical Sciences, Trg Dositeja Obradovića 6, 21000 Novi Sad, Serbia, bstojic@uns.ac.rs, https://orcid.org/0000-0003-3491-2860*
[3] *Jovan Dorić, University of Novi Sad, Faculty of Technical Sciences, Trg Dositeja Obradovića 6, 21000 Novi Sad, Serbia, bstojic@uns.ac.rs, https://orcid.org/0000-0001-8344-1466*
[4], *Boris Stojić University of Novi Sad, Faculty of Technical Sciences, Trg Dositeja Obradovića 6, 21000 Novi Sad, Serbia, bstojic@uns.ac.rs, https://orcid.org/0000-0002-4532-4880*
[5] *Luka Sekicki, University of Novi Sad, Faculty of Technical Sciences, Trg Dositeja Obradovića 6, 21000 Novi Sad, Serbia, luka.sekicki@uns.ac.rs, https://orcid.org/0009-0007-9170-8352*

PROJEKTOVANJE I IZRADA PROBNOG STOLA ZA ISPITIVANJE DINAMIKE PNEUMATSKIH WASTEGATE AKTUATORA

REZIME: U ovom radu je prikazano projektovanje i izrada namenskog probnog stola za ispitivanje dinamike pneumatskih *wastegate* aktuatora, sa posebnim akcentom na konstrukciju i preciznu izradu mernog sistema. U ranijim modelima na nivou motora odziv aktuatora je procenjivan na osnovu odziva pritiska natpunjenja, dok su se ispitivanja na gasnom probnom stolu bavila protokom kroz wastegate ventil. Uticaj dužine pneumatskog voda na kašnjenje od komande elektroventilu do početka pomeranja klipnjače i klapne još nije dovoljno dokumentovan. Radi prevazilaženja ovih ograničenja, u programu Autodesk Inventor konstruisan je namenski probni sto čiji su noseći elementi izrađeni 3D štampom od polilaktida (PLA). Mehanička konstrukcija obuhvata krutu osnovnu ploču, modularne nosače sa produženim otvorima (prorezima) za fino pozicioniranje i preciznu kinematičku vezu koja verno kopira geometriju kućišta turbopunjača. Postavka omogućava istovremeno praćenje pravolinijskog pomeraja klipnjače i zaokreta klapne preko kliznog i kružnog potenciometra, čime se izdvajaju odzivi klipnjače i klapne i određuje razlika vremena početka njihovog kretanja. U ovom kontekstu, mrtvo vreme je definisano kao inherentno kašnjenje sistema — vremenski interval od električne komande na kalemu elektroventila do početka fizičkog pomeranja posmatranog dela. Izmereni interval može da obuhvati prebacivanje elektroventila, porast ili pad pritiska u vodu i komori, kao i početnu reakciju mehanizma; njihovi pojedinačni doprinosi nisu određeni. Eksperimenti su sprovedeni promenom dužine pneumatskog creva (unutrašnjeg prečnika 4 mm) u šest vrednosti od 5 cm do 30 cm, pri konstantnom pritisku napajanja. Rezultati potvrđuju upotrebljivost razvijenog probnog stola i merne metode za poređenje karakteristika pod kontrolisanim uslovima, bez uticaja aerodinamičkih sila i promenljivih temperatura.

KLJUČNE REČI: wastegate aktuator; mehatronika motornih vozila, 3D štampa, probni sto

INTRODUCTION

Modern internal combustion engines almost universally employ turbocharging as a primary method for increasing specific power and reducing fuel consumption. Reducing engine displacement while maintaining or increasing output power—a process known as downsizing—is only feasible when air is supplied to the cylinders at pressures higher than atmospheric. This task is performed by the turbocharger, and the amount of energy extracted by the turbine from the exhaust gases must be continuously regulated to prevent boost pressure from exceeding allowable limits. This regulation is most commonly achieved via a *wastegate* valve, whose position is set by a pneumatic positive-pressure actuator. The response speed of this actuator directly determines how quickly and accurately the control system can regulate boost pressure.

Prior research has addressed different parts of the actuation chain: pneumatic valve circuits and solenoid dynamics (Galindo et al. 2009; Szente & Vad, 2001); a model of pneumatic wastegate pressure, position, and dynamics validated on an engine test bench (Thomasson et al. 2009); engine-cell estimation of wastegate position and flow including actuator and gas-load forces (Salehi et al. 2014); and gas-stand characterization of wastegate flow at prescribed openings (Serrano et al. 2017; Cordalonga et al. 2025). Transient turbocharger modelling also distinguishes fluid, mechanical, and thermal responses (Deng et al. 2021). These studies do not directly report the command-to-onset delays of both the rod and flap for controlled changes in pneumatic hose length. An in-service failure analysis linked rod deflection to localized diaphragm loading, further emphasizing the relevance of linkage geometry to tests closer to operating conditions (Li et al. 2025).

The primary contribution of this paper lies in the design and implementation of a dedicated test bench tailored specifically to isolate and evaluate the dynamic behaviour of the complete solenoid valve–line–actuator assembly. By constructing a specialized hardware environment, the setup enables precise measurement of the system's dead time—defined here as the inherent fluid-dynamic and mechanical delay spanning from the electrical command change at the valve coil to the physical onset of movement. Furthermore, the test bench incorporates a dual-sensor kinematic setup that successfully decouples the piston rod response from the flap response.

PROBLEM STATEMENT AND RESEARCH OBJECTIVE

Published actuator models and engine-level tests describe the coupled boost and wastegate response, while gas-stand studies mainly quantify turbine and bypass flow (Thomasson et al. 2009; Salehi et al. 2014; Serrano et al. 2017; Cordalonga et al. 2025). The present study asks a narrower question: how does a controlled change in pneumatic hose length affect the interval from the valve coil command to the onset of rod and flap movement? The

objective is to design and demonstrate a dedicated test bench for simultaneous measurement of the solenoid valve–line–actuator–linkage assembly at fixed supply pressure, with an unloaded flap and at room temperature.

The measured dead time spans the interval from a change in voltage at the solenoid valve coil to the first detected movement of the rod or flap. It may include valve switching, filling or venting of the pneumatic line and chamber, and the mechanical response needed to initiate movement. During opening, pressure must build sufficiently to overcome the return spring preload. Because pressure was not recorded, the individual contributions to the measured delay cannot be separated in this study.

To capture this phenomenon without engine-induced interferences, the testing was conducted using the newly designed test bench by varying the pneumatic hose length from 5 cm to 30 cm across six steps at a constant supply pressure and room temperature, utilizing an unloaded flap to eliminate external aerodynamic forces.

Limitation

The limitations of the investigation are as follows. The flap remained unloaded during all measurements, meaning that the results describe the behaviour of the mechanism without the aerodynamic force of the exhaust gases. The testing was conducted at room temperature, whereas under operating conditions the diaphragm works at a significantly higher temperature, which alters its elasticity. Absolute pressure within the pressure chamber was not measured; instead, only displacement was measured, meaning that the individual contributions of the various causes of dead time cannot be isolated. These limitations do not diminish the usefulness of the results, as the objective of the study is comparison under identical conditions rather than absolute characterization of the actuator in its installed state.

TEST BENCH DESIGN AND MEASUREMENT SETUP

To carry out the measurements described it was necessary to design a dedicated test bench. The requirement set for the design was that the actuator must be tested independently of the engine, in a setup that enables simultaneous monitoring of the piston rod displacement and the flap rotation, with a simple change of the pneumatic line length while keeping all other parameters constant between measurement series.

Test Bench Concept

The base of the test bench consists of a flat plate to which all elements are attached. The plate ensures a constant relative position between the actuator, the lever, and the measurement sensors, thereby eliminating the most common cause of result scatter in improvised setups, which is the shifting of elements between measurements. The actuator is mounted on a bracket that supports it by its spring-half housing, in the exact position it occupies when installed on the turbine housing.

The actuator piston rod acts on the lever via an eyelet, and the lever is fitted into a rotational pivot that represents the flap shaft. Linear rod displacement is thus converted into rotation around a fixed axis using the corresponding linkage geometry. The difference between the detected motion-onset times of rod and flap is reported as a timing indicator of their transmission. It cannot by itself quantify mechanical clearance, because the two sensors observe different motions and use threshold-based onset detection.

The flap on the test bench is unloaded, which was stated as a limitation in section 1. This choice avoids the influence of varying aerodynamic load; however, uncontrolled differences between measurement sessions may still affect the results. The general layout of the assembly is shown in Figure 1, the view from the opposite direction in Figure 2, and a detail in Figure 3.

Figure 1 Three-dimensional model of the test bench assembly

Figure 2 Test bench assembly, view from the opposite direction

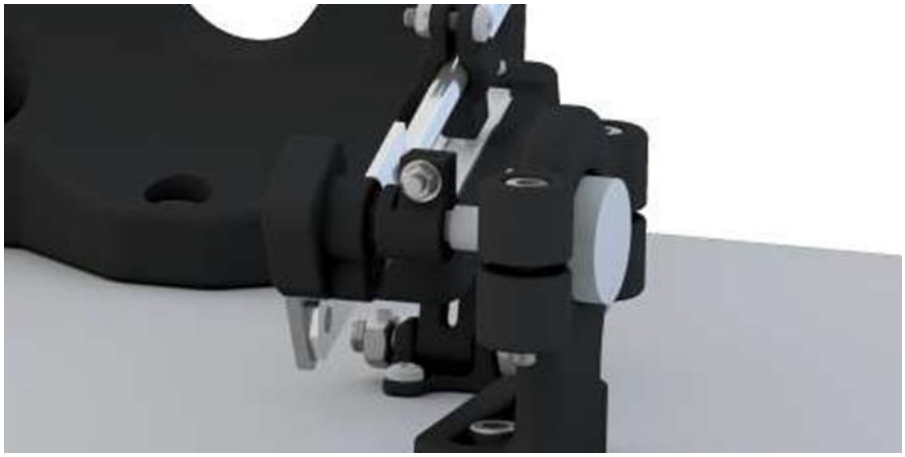

Figure 3 Detail of the joint connection of the piston rod and lever with the slide potentiometer bracket

The final appearance of the test bench is shown in Figure 4.

Figure 4 final appearance of the test bench

Three-Dimensional Modeling

All load-bearing elements of the test bench were ***modelled*** in the Autodesk Inventor software package, using a procedure that starts with a 2D sketch and extrusion of the basic shape, followed by adding holes, reinforcements, and fillets. The models were created as separate parts and then assembled into an assembly where constraints defined their relative positions and degrees of freedom. Such a procedure enabled verification of whether the piston rod remains free of collisions with the bracket throughout its entire stroke and whether the lever has sufficient clearance for rotation.

During modeling, special attention was paid to two aspects. First, all bolt holes were designed as elongated slots instead of circular holes, which enabled fine adjustment of the bracket position during assembly. Second, wall thicknesses were chosen so that the parts are sufficiently rigid for the arising loads, yet suitable for fabrication via material deposition without requiring a large amount of auxiliary (support) material.

From the adopted models, workshop documentation was derived, consisting of one drawing for each part, with necessary cross-sections, dimensions, material designations, and general tolerances according to the ISO 2768-m standard.

Parts Produced by 3D Printing

The load-bearing parts were produced via fused deposition modeling using polylactic acid (PLA). This material was chosen due to its satisfactory rigidity, low tendency to warp during cooling, and ease of fabrication. Since testing has a short duration and is conducted at room temperature, the limited thermal resistance of polylactic acid does not present an obstacle.

The largest part, the actuator bracket, absorbs the reaction force developed by the actuator and is therefore designed with reinforced ribs and a large contact surface resting on the plate. The smallest parts, the potentiometer coupling and the rod clamp, serve to connect the measurement sensors to the moving parts and were manufactured at an enlarged scale on the drawings for clarity.

Installation of Measurement Potentiometers

The slide potentiometer is positioned so that its slider directly tracks the displacement of the actuator piston rod. The connection is realized via a coupling clamped onto the rod, thereby eliminating slippage. The potentiometer body is attached to a bracket connected to the plate via a base, and slots on the base allow adjustment so that the slider occupies the middle portion of its stroke at rest. The working stroke of the slide potentiometer is 10 mm, covering the entire stroke of the piston rod.

The rotary potentiometer is positioned on the lever rotation axis so that its shaft tracks the rotation of the flap. Since the angular stroke of the flap is only about 15° to 20°, while the potentiometer has a significantly larger available angle, initial measurements showed that it is important to carefully adjust the initial position of the shaft. If the initial position is chosen close to the end of the available range, the output voltage reaches the limit of the analog-to-digital

converter's measuring range and clips, making the moment of motion onset indefinite. After adjusting the initial position, the scatter of measured times on this channel was significantly reduced. Both potentiometers are wired as voltage dividers between a 3.3 V supply and ground, with the wiper connected to an analog input of the microcontroller. Since, the moment of change is measured rather than the absolute value of displacement, calibration in units of length and angle was not necessary.

Pneumatic Installation

Air is supplied to the actuator via a 3/2-way valve (three ports, two positions), model 3V210-06, shown in Figure 5. The valve is spring-return, meaning that in the de-energized state it connects the actuator port to the exhaust, allowing the actuator spring to return the piston rod to its initial position. The operating pressure range of the valve is from 1.5 bar to 8 bar. The supply pressure was maintained within the range of 1.9 bar to 2.0 bar throughout all measurements and was not changed between series. Hose length was the only parameter intentionally varied; small supply-pressure fluctuations could still contribute to the observed scatter. A polyurethane hose with an inner diameter of 4 mm was placed between the valve and the actuator. Six lengths were tested: 5, 10, 15, 20, 25, and 30 cm. The hoses were cut to size and connected using quick-release fittings, so that changing the length took a short time and did not require moving any other element of the setup. Each hose change marked the beginning of a new measurement series.

Figure 5 Valve 3V210-06 with coil and ports

DISCUSSION AND ANALYSIS OF RESULTS

The supplied measurement log contains 501 recorded cycles for six hose lengths (5, 10, 15, 20, 25, and 30 cm). The 482 cycles marked “OK” were used for the plots; 19 cycles flagged as outliers were excluded. The first cycle of each session and one invalid 5 cm session had already been omitted from the log. Dead time is measured from the coil-voltage change to a displacement threshold of 4% of the measured stroke in each cycle. Figure 6 presents the arithmetic mean and sample standard deviation of accepted cycles at each length.

From 5 to 30 cm, mean opening dead time increased from 33.61 to 37.82 ms for the rod and from 41.14 to 45.91 ms for the flap. The six means show an overall upward trend, but not a strictly monotonic or proportional relationship: the 20 cm opening means are lower than those at 15 cm. The opening-rod standard deviation within a length was 1.09–1.42 ms. These observations are consistent with a contribution from the greater pneumatic volume, but without a pressure trace its share of the measured delay cannot be quantified.

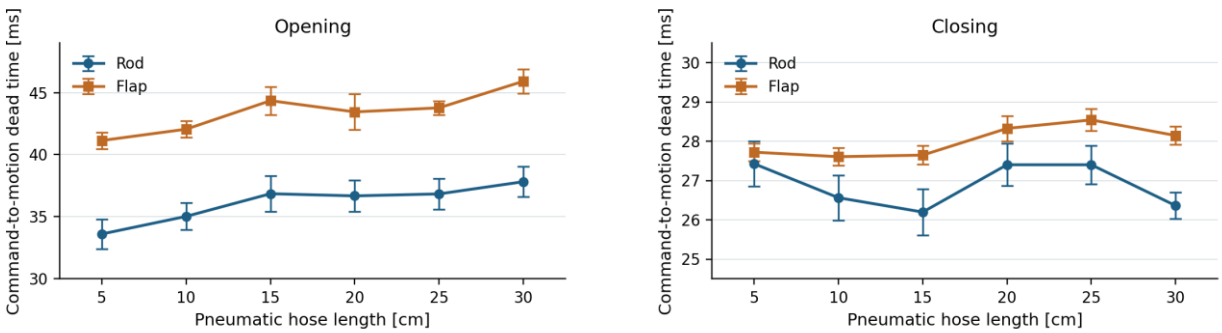

Figure 6 Mean dead time at opening and closing versus pneumatic hose length; error bars represent ±1 sample standard deviation. Accepted cycles per length: 42, 80, 89, 98, 103, and 70.

The closing phase shows a different pattern (Figure 6). The rod means range from 26.20 to 27.43 ms across the six lengths without a consistent monotonic change; the flap means range from 27.61 to 28.54 ms. The closing-rod

standard deviations (0.33–0.59 ms) are smaller than their opening counterparts. A spring-driven return after venting provides a plausible explanation for this asymmetry, although valve switching and pressure decay were not recorded separately.

The simultaneous measurements also yield the flap-minus-rod onset difference shown in Figure 7. In opening, the mean difference was 6.77–8.09 ms, and the rod was detected first in all 482 accepted cycles. In closing, the mean difference was 0.30–1.78 ms; the rod was detected first in 455 cycles, the times were equal in 16, and the flap was detected first in 11. With 0.33 ms recording resolution and separate displacement thresholds, this timing difference must not be interpreted as a direct measurement of joint clearance alone.

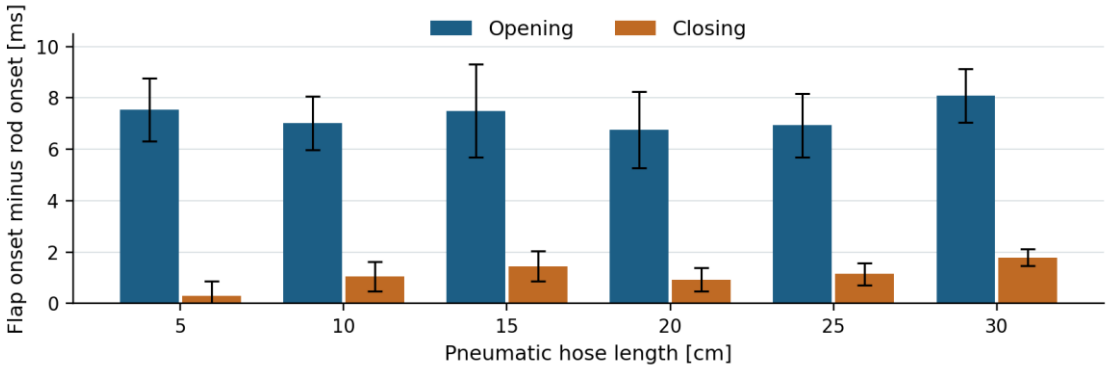

Figure 7 Mean difference between flap and rod motion-onset times for opening and closing; error bars represent ±1 sample standard deviation.

The figures therefore support a descriptive comparison within the tested, unloaded room-temperature setup. Error bars show scatter among accepted cycles rather than uncertainty in the mean across independent installations: most lengths were tested in one or two sessions. Additional pressure measurements, repeat sessions, controlled flap loading, and elevated-temperature tests are required before attributing the delays to individual physical causes or generalizing them to an installed turbocharger.

CONCLUSIONS

The successful realization of this research relied heavily on the dedicated design, 3D modeling, and physical fabrication of a specialized test bench. Modeled entirely within the Autodesk Inventor software package, the test bench was engineered to test the pneumatic wastegate actuator independently of an engine environment, featuring carefully designed components with elongated bolt holes for fine-tuning and optimized wall thicknesses for fused deposition modeling using polylactic acid (PLA). Complete workshop documentation with free-dimension tolerances according to ISO 2768-m ensured precise manufacturing, while the structural layout—utilizing a flat baseplate and a precise kinematic linkage—successfully eliminated component shifting and reproduced exact engine-like geometry, including joint clearances.

The dual-potentiometer arrangement resolved the onset of rod and flap movement separately. Among the accepted cycles, mean opening dead time increased by 4.21 ms for the rod and 4.77 ms for the flap between the 5 and 30 cm hoses, with departures from a monotonic trend at intermediate lengths. Closing rod dead time showed no comparable monotonic increase. The rod preceded the flap in all accepted opening cycles, whereas 27 closing cycles showed equal or reversed detected onset times. The measured onset-time difference is not a direct estimate of mechanical backlash. These results demonstrate the bench's value for controlled comparison, while the present measurements do not identify the separate pneumatic and mechanical contributions or establish in-service delays.

Future work should first add synchronized measurements of coil current and pressure at the valve outlet and actuator inlet or chamber. This would help separate electrical switching, line filling or venting, and the pressure threshold for motion, which the present displacement-only setup cannot resolve.

The rig should then be equipped with a calibrated, repeatable flap load and temperature control, using temperature-suitable parts where the current PLA brackets are unsuitable, to test how exhaust-gas loading and heating alter the observed delays. Finally, repeating the tests with other actuator and linkage specimens, hose diameters and supply pressures, and comparing selected conditions with an installed or gas-stand assembly would establish whether the room-temperature, unloaded trends transfer to service conditions. Pressure and position sensor calibration, together with an uncertainty analysis of motion-onset detection, should accompany these extensions.

ACKNOWLEDGMENTS

This research has been supported by the Ministry of Science, Technological Development and Innovation (Contract No. 451-03-34/2026-03/200156) and the Faculty of Technical Sciences, University of Novi Sad through project "Scientific and Artistic Research Work of Researchers in Teaching and Associate Positions at the Faculty of Technical Sciences, University of Novi Sad 2026" (No. 01-3609/1).

REFERENCES

Cordalonga, C., Marelli, S., & Usai, V. (2025). Performance analysis of a waste-gated turbine for automotive engines: An experimental and numerical study. *Machines*, 13(1), 54. https://doi.org/10.3390/machines13010054

Deng, Q., Pennycott, A., Zhang, Q., Avola, C., Pohorelsky, L., & Burke, R. (2021). Dimensionless quantification of small radial turbine transient performance. *Proceedings of the Institution of Mechanical Engineers, Part D: Journal of Automobile Engineering*, 235(1), 188–198. https://doi.org/10.1177/0954407020942035

Galindo, J., Climent, H., Guardiola, C., & Doménech, J. (2009). Modeling the vacuum circuit of a pneumatic valve system. *Journal of Dynamic Systems, Measurement, and Control*, 131(3), 031011. https://doi.org/10.1115/1.3089562

Li, R., Chen, J., Zhang, L., Tan, D., Hu, Y., Zhen, K., Dai, X., & Zhang, L. (2025). Contact-induced premature failure of a fabric-reinforced fluorosilicone diaphragm in an AE300 wastegate actuator. *AIP Advances*, 15(12), 125123. https://doi.org/10.1063/5.0306728

Salehi, R., Vossoughi, G. R., & Alasty, A. (2014). Modeling and estimation of unmeasured variables in a wastegate operated turbocharger. *Journal of Engineering for Gas Turbines and Power*, 136(5), 052601. https://doi.org/10.1115/1.4025498

Serrano, J. R., Arnau, F. J., Tiseira, A., & Samala, V. (2017). Experimental procedure for the characterization of turbocharger's waste-gate discharge coefficient. *Advances in Mechanical Engineering*, 9(10), 1687814017728242. https://doi.org/10.1177/1687814017728242

Szente, V., & Vad, J. (2001). Computational and experimental investigation on solenoid valve dynamics. In *Proceedings of the 2001 IEEE/ASME International Conference on Advanced Intelligent Mechatronics* (Vol. 1, pp. 618–623). IEEE. https://doi.org/10.1109/AIM.2001.936537

Thomasson, A., Eriksson, L., Leufvén, O., & Andersson, P. (2009). Wastegate actuator modeling and model-based boost pressure control. *IFAC Proceedings Volumes*, 42(26), 87–94. https://doi.org/10.3182/20091130-3-FR-4008.00012

SECTION

B

Vehicle Design and Manufacturing

- Body Structures
- Advanced Materials
- Recycling
- Manufacturing Systems
- Quality Systems in Automotive Industry

The 11th International Congress
Motor Vehicles & Motors 2026
Kragujevac, Serbia
October 8th - 9th, 2026

Motor Vehicles & Motors

MVM2026-006
https://doi.org/10.24874/CMVM2026.006
Technical paper

Gordana Bogdanović[1]
Aleksandar Radaković[2]
Dragan Čukanović[3]
Petar Knežević[4]
Aleksandar Nešović[5]

VARIATIONAL SHEAR CONTROL IN ESL–HSDT LAMINATES FOR AUTOMOTIVE STRUCTURES

ABSTRACT: An analytical formulation for the bending of laminated composite plates is developed based on the equivalent single-layer approach and higher-order shear deformation theory (ESL–HSDT). The key contribution lies in a variationally defined through-thickness shape function of exponential form, whose parameter is obtained by minimizing a functional governing the distribution of transverse shear deformation across the thickness. In this way, a direct link is established between the kinematic description and the distribution of shear energy, without increasing the kinematic order of the model. The solution is obtained in closed form using the Navier method for simply supported plates subjected to sinusoidal loading. The accuracy of the formulation is assessed through comparison with three-dimensional elasticity solutions and representative models from the literature. The results show that all considered formulations provide a comparable level of accuracy in predicting the global response, while the main differences arise in the transverse shear stresses. The proposed model yields the lowest overall deviation and provides a balanced and physically consistent distribution of shear energy through the thickness, confirming that the choice of the shape function represents a key mechanism for improving the accuracy of ESL–HSDT formulations.

KEYWORDS: Laminated plates, ESL–HSDT, Variational function, Shear energy, Navier solution

[1] *Gordana Bogdanović, University of Kragujevac, Faculty of Engineering, Sestre Janjić 6, 34000 Kragujevac, gocab@kg.ac.rs, https://orcid.org/0000-0001-7231-7400*
[2] *Aleksandar Radaković, Institute for Information Technologies Kragujevac, Jovana Cvijića bb, 34000 Kragujevac, aradakovic@uni.kg.ac.rs, https://orcid.org/0000-0002-7355-7403*
[3] *Dragan Čukanović, University of Priština, Faculty of Technical Sciences, Knjaza Miloša 7, 38220 Kosovska Mitrovica, dragan.cukanovic@pr.ac.rs, https://orcid.org/0000-0001-8370-748X*
[4] *Petar Knežević, University of Priština, Faculty of Technical Sciences, Knjaza Miloša 7, 38220 Kosovska Mitrovica, petar.knezevic@pr.ac.rs, https://orcid.org/0000-0003-4187-2879*
[5] *Aleksandar Nešović, Institute for Information Technologies Kragujevac, Jovana Cvijića bb, 34000 Kragujevac, aca.nesovic@uni.kg.ac.rs, https://orcid.org/0000-0002-1690-2389*

VARIJACIONA KONTROLA SMICANJA U ESL–HSDT LAMINATIMA ZA AUTOMOBILSKE KONSTRUKCIJE

REZIME: U radu je razvijena analitička formulacija savijanja laminatnih kompozitnih ploča zasnovana na ekvivalentnom jednoslojnom pristupu i teoriji višeg reda (ESL–HSDT). Ključni doprinos predstavlja varijaciono definisana funkcija oblika kroz debljinu u eksponencijalnoj formi, čiji se parametar određuje minimizacijom funkcionala koji upravlja raspodelom transverzalne smičuće deformacije kroz debljinu. Na taj način uspostavlja se direktna veza između kinematičkog opisa i raspodele smičuće energije, bez povećanja kinematičkog reda modela. Rešenje je dobijeno u zatvorenoj formi primenom Navierovog postupka za slobodno oslonjene ploče pod sinusoidalnim opterećenjem. Tačnost formulacije procenjena je poređenjem sa trodimenzionalnim rešenjima teorije elastičnosti i reprezentativnim modelima iz literature. Rezultati pokazuju da sve razmatrane formulacije obezbeđuju uporediv nivo tačnosti u predviđanju globalnog odziva, dok se razlike između modela prvenstveno manifestuju u transverzalnim smičućim naponima. Predloženi model ostvaruje najmanje ukupno odstupanje i obezbeđuje uravnoteženu i fizički konzistentnu raspodelu smičuće energije kroz debljinu, čime se potvrđuje da izbor funkcije oblika predstavlja ključni mehanizam za unapređenje tačnosti ESL–HSDT formulacija.

KLJUČNE REČI: Laminatne ploče, ESL–HSDT, varijaciona funkcija, energija smicanja, Navierovo rešenje

INTRODUCTION

An analytical formulation for the bending of laminated composite plates is developed based on the equivalent single-layer approach and higher-order shear deformation theory (ESL–HSDT) (Reddy, J. N. 2003 and Karama, M. et al. 2003). The key contribution lies in a variationally defined through-thickness shape function of exponential form, whose parameter is determined by minimizing a functional governing the distribution of transverse shear deformation across the thickness. In this manner, a direct link is established between the kinematic description and the distribution of shear energy, without increasing the kinematic order of the model. In addition to these approaches, layerwise models have also been developed in the literature, enabling a more detailed representation of through-thickness quantities, albeit at the cost of increased computational complexity (Cetkovic, M. 2015). Furthermore, considerable attention has been devoted to the development of through-thickness shape functions, both through analytical approaches (Joshan, Y. S. et al. 2017; Radaković, A. et al. 2020 and Atallah, K. E. et al. 2025) and numerical methods (Ye, W. et al. (2026)). The solution is obtained in closed form using the Navier method for simply supported plates subjected to sinusoidal loading. The accuracy of the formulation is assessed through comparison with three-dimensional elasticity solutions and representative models from the literature (Reddy, J. N. 2003; Karama, M. et al. 2003 and Radaković, A. et al. 2020). The results show that all considered formulations provide a comparable level of accuracy in predicting the global response, while the main differences arise in the transverse shear stresses. The proposed model yields the lowest overall deviation and provides a balanced and physically consistent distribution of shear energy through the thickness, confirming that the choice of the shape function represents a key mechanism for improving the accuracy of ESL–HSDT formulations. In this context, the present study introduces a variationally defined through-thickness shape function that enables a consistent control of shear deformation distribution without increasing the kinematic complexity of ESL–HSDT formulations.

2. THEORETICAL FORMULATION

An equivalent single-layer higher-order model with seven generalized unknown functions, u_0, v_0, w_b, w_s, θ_x, θ_y, and ϕ, is considered. The kinematic field is described in terms of the mid-plane displacements $u_0(x,y)$, $v_0(x,y)$, the bending and shear components of the transverse displacement $w_b(x,y)$, $w_s(x,y)$, the rotations $\theta_x(x,y)$, $\theta_y(x,y)$, and an additional scalar function $\phi(x,y)$accounting for transverse normal deformation.

The displacement field is defined as:

$$\begin{aligned} &u(x,y,z) = u_0 - z\left(w_{b,x} + w_{s,x}\right) + F(z)\left(w_{s,x} + \theta_x\right),\ v(x,y,z) = v_0 - z\left(w_{b,y} + w_{s,y}\right) + F(z)\left(w_{s,y} + \theta_y\right), \\ &w(x,y,z) = w_b + w_s + \phi F'(z) \end{aligned} \tag{1}$$

This representation enables an independent description of bending and shear contributions to the transverse displacement, while the additional term involving ϕintroduces transverse normal deformation without increasing the kinematic order.

The distribution of transverse deformation is governed by the through-thickness shape function $F(z)$, whose first and second derivatives directly enter the expressions for shear and transverse normal strains. In contrast to conventional approaches where this function is prescribed a priori, it is here defined in a variational form, allowing for a controlled distribution of shear deformation across the thickness.

Introducing the dimensionless coordinate $\zeta = z/h$, the following auxiliary function is adopted:

$$E = e^{-a\zeta^2} \tag{2}$$

and the shape function is expressed as:

$$F(z) = h\left[C\ erf(\sqrt{a}\zeta) + \frac{2}{a}\zeta E\right]. \tag{3}$$

Its derivatives are given by:

$$F'(z) = \left(1 - 4\zeta^2\right)E, \quad F''(z) = \frac{1}{h}E\left[-8\zeta - 2a\zeta\left(1 - 4\zeta^2\right)\right]. \tag{4}$$

The parameter α is determined variationally, linking the assumed kinematics to the through-thickness shear energy distribution and eliminating the need for predefined shear profiles while preserving the regularity of the displacement field. The strain field is derived from the assumed displacement field using the standard relations of linear elasticity. In accordance with the adopted kinematics, the resulting expressions naturally decompose into membrane, bending, and shear contributions, while the through-thickness distribution is governed by the shape function $F(z)$and its derivatives.

The in-plane normal strains are given by

$$\varepsilon_{xx} = u_{0,x} - z\left(w_{b,xx} + w_{s,xx}\right) + F(z)\left(w_{s,xx} + \theta_{x,x}\right),\ \varepsilon_{yy} = v_{0,y} - z\left(w_{b,yy} + w_{s,yy}\right) + F(z)\left(w_{s,yy} + \theta_{y,y}\right), \tag{5}$$

where the first term represents the membrane contribution, the linear term in $z$corresponds to bending, and the term involving $F(z)$accounts for the shear-related correction.
The in-plane shear strain is expressed as

$$\gamma_{xy} = u_{0,y} + v_{0,x} - 2z\left(w_{b,xy} + w_{s,xy}\right) + F(z)\left(2w_{s,xy} + \theta_{x,y} + \theta_{y,x}\right). \tag{6}$$

The transverse shear strains take the form

$$\gamma_{xz} = F'(z)\left(w_{s,x} + \theta_x\right), \quad \gamma_{yz} = F'(z)\left(w_{s,y} + \theta_y\right) \tag{7}$$

By introducing the additional scalar function $\phi(x, y)$, the transverse normal strain can be expressed as

$$\varepsilon_{zz} = \phi F''(z) \tag{8}$$

which extends the formulation to a quasi-three-dimensional level and enables a consistent evaluation of the stress state within the framework of linear elasticity.

In each lamina, the stress state is defined by an orthotropic constitutive relation in the local material coordinate system

$$\boldsymbol{\sigma}^{(k)} = \mathbf{Q}^{(k)}\boldsymbol{\varepsilon}^{(k)}, \tag{9}$$

where $\mathbf{Q}^{(k)}$denotes the stiffness matrix of the k-th layer.

The overall stress state is obtained by evaluating this relation at each point through the laminate thickness, where discontinuities in $\bar{\mathbf{Q}}^{(k)}$naturally arise between adjacent layers due to differences in fiber orientation and material properties.

Starting from the assumed displacement field and the corresponding strain components, the equilibrium equations in variational form are derived using the principle of virtual work. For a laminated plate, the following condition holds:

$$\delta\Pi = \delta U - \delta W = 0, \tag{10}$$

where δU denotes the virtual work of internal forces and δW the virtual work of external loading.
The virtual work of internal forces is expressed as the sum of contributions from all layers through the thickness:

$$\delta U = \sum_{k=1}^{N} \int_A \int_{z_k}^{z_{k+1}} \delta \boldsymbol{\varepsilon}^T \bar{\mathbf{Q}}^{(k)} \boldsymbol{\varepsilon} dz dA \tag{11}$$

where $\boldsymbol{\varepsilon}$ and $\delta\boldsymbol{\varepsilon}$ are the strain and virtual strain vectors, respectively, and $\bar{\mathbf{Q}}^{(k)}$ is the transformed stiffness matrix of the k-th layer in the global coordinate system.

For a sinusoidal transverse load $q(x, y)$, the virtual work of external forces is given by

$$\delta W = \int_A q(x,y) \delta w dA \tag{12}$$

Substituting the kinematic relations into δU and grouping terms with respect to the generalized unknowns {u_0, v_0, w_b, w_s, θ_x, θ_y, ϕ} yields a variationally consistent system with seven unknown functions. For simply supported plates, Navier's method is applied, expanding the unknowns in double Fourier series satisfying the boundary conditions. Substitution into the variational form and use of trigonometric orthogonality reduce the problem to a system of algebraic equations for each mode pair (m, n).

$$\mathbf{K}_{mn} \mathbf{d}_{mn} = \mathbf{f}_{mn}, \tag{13}$$

where $\mathbf{d}_{mn} = [U_{mn} \quad V_{mn} \quad W_{mn}^b \quad W_{mn}^s \quad \Theta_{mn}^x \quad \Theta_{mn}^y \quad \Phi_{mn}]^T$.

The matrix $\mathbf{K}_{mn}$ contains contributions from membrane, bending, shear, and transverse normal deformation, with its coefficients obtained through integration across the laminate thickness. The shape function $F(z)$, together with its derivatives $F'(z)$ and $F''(z)$, enters the system coefficients directly, thereby establishing a link between the adopted kinematics and the energetic response of the model.

3. NUMERICAL RESULTS AND DISCUSSION

To validate the proposed formulation, a simply supported laminated plate (SSSS) subjected to a sinusoidal transverse load is considered:

$$q(x,y) = q_0 \sin\left(\frac{\pi x}{a}\right) \sin\left(\frac{\pi y}{b}\right), \tag{14}$$

which enables the use of a Navier-type solution.

Consistent with the adopted formulation, the generalized unknowns are expanded in double Fourier series compatible with the boundary conditions and loading pattern:

$$\begin{aligned}
&u_0(x,y) = \sum_{m,n} U_{mn} \cos\left(\frac{m\pi x}{a}\right) \sin\left(\frac{n\pi y}{b}\right), \; v_0(x,y) = \sum_{m,n} V_{mn} \sin\left(\frac{m\pi x}{a}\right) \cos\left(\frac{n\pi y}{b}\right), \\
&w_b(x,y) = \sum_{m,n} W_{mn}^b \sin\left(\frac{m\pi x}{a}\right) \sin\left(\frac{n\pi y}{b}\right), \; w_s(x,y) = \sum_{m,n} W_{mn}^s \sin\left(\frac{m\pi x}{a}\right) \sin\left(\frac{n\pi y}{b}\right), \\
&\theta_x(x,y) = \sum_{m,n} \Theta_{mn}^x \cos\left(\frac{m\pi x}{a}\right) \sin\left(\frac{n\pi y}{b}\right), \; \theta_y(x,y) = \sum_{m,n} \Theta_{mn}^y \sin\left(\frac{m\pi x}{a}\right) \cos\left(\frac{n\pi y}{b}\right), \\
&\phi(x,y) = \sum_{m,n} \Phi_{mn} \sin\left(\frac{m\pi x}{a}\right) \sin\left(\frac{n\pi y}{b}\right).
\end{aligned} \tag{15}$$

A symmetric four-layer laminate with stacking sequence $[0/90/90/0]$ is considered. The following dimensionless material properties are adopted:

$$E_1 / E_2 = 25, \quad G_{12} / E_2 = 0.5, \quad G_{13} / E_2 = 0.5, \quad G_{23} / E_2 = 0.2, \nu_{12} = \nu_{13} = \nu_{23} = 0.25.$$

Material anisotropy is accounted for through the transformed stiffness matrices $\bar{\mathbf{Q}}^{(k)}$.

For comparison with reference solutions, the results are presented in dimensionless form:

$$\bar{w} = w\left(\frac{a}{2},\frac{b}{2},0\right)\frac{100E_2h^3}{q_0a^4},\ \bar{\sigma}_{xx} = \sigma_{xx}\left(\frac{a}{2},\frac{b}{2},\frac{h}{2}\right)\frac{h^2}{q_0a^2},\ \bar{\sigma}_{yy} = \sigma_{yy}\left(\frac{a}{2},\frac{b}{2},\frac{h}{4}\right)\frac{h^2}{q_0a^2}$$
$$\bar{\tau}_{xz} = \tau_{xz}\left(0,\frac{b}{2},0\right)\frac{h}{q_0a},\ \bar{\tau}_{yz} = \tau_{yz}\left(\frac{a}{2},0,0\right)\frac{h}{q_0a}. \tag{16}$$

This normalization allows for a direct comparison with three-dimensional elasticity solutions and representative results available in the literature.

Table 1. Comparison of normalized displacements and stress components with 3D elasticity solutions, with percentage deviations for different models

Model	w̄	Diff (%)	σ̄xx	Diff (%)	σ̄yy	Diff (%)	τ̄xz	Diff (%)	τ̄yz	Diff (%)	σ̄xy	Diff (%)	Avg Diff (%)
3D	1.954	–	0.720	–	0.663	–	0.219	–	0.291	–	0.047	–	–
Karama	1.920	-1.72	0.708	-1.65	0.639	-3.68	0.253	+15.57	0.227	-22.16	0.046	-2.13	7.8
Reddy	1.895	-3.04	0.673	-6.60	0.634	-4.34	0.239	+9.09	0.206	-29.07	0.044	-6.17	9.7
Present	1.925	-1.47	0.736	+2.22	0.639	-3.63	0.264	+20.46	0.244	-16.25	0.047	+0.64	7.4
Radaković	1.889	-3.31	0.667	-7.32	0.633	-4.48	0.237	+8.08	0.204	-30.07	0.044	-6.81	10.0

Table 1 presents a comparison between the obtained results and reference three-dimensional elasticity solutions. The relative deviations are expressed in percentage form as

$$\text{Diff}(\%) = \frac{X_{\text{model}} - X_{3D}}{X_{3D}} \times 100. \tag{17}$$

Results indicate that all considered formulations achieve close agreement with the reference solution in terms of global response, particularly for deflections and normal stresses σ_{xx} and σ_{yy}, with deviations remaining limited in magnitude. In contrast, more pronounced differences are observed in the transverse shear stresses, highlighting the dominant influence of the through-thickness shape function on the local stress state.

From an overall accuracy standpoint, the present model exhibits the most favourable balance across all response components, with a stable behaviour and no pronounced local deviations. The results suggest that the exponentially defined shape function enables a more flexible redistribution of shear energy, which translates into a more consistent agreement with the reference solution. The Karama model provides comparable predictions for normal stresses, but shows more pronounced deviations in the shear components, indicating a limited capability to accurately capture the through-thickness distribution. The Reddy and Radaković formulations exhibit a stable yet systematically conservative response in shear, with a tendency to underestimate peak values.

The largest discrepancies are observed in the τ_{yz} component, confirming that the representation of transverse shear deformation remains the primary challenge for equivalent single-layer models. This clearly demonstrates that the choice of shape function primarily governs the distribution of shear energy, while its influence on global response quantities is significantly less pronounced. The through-thickness distributions of normalized stress components for different shape functions are shown in Fig. 1. The normal stresses $\sigma_{xx}$and $\sigma_{yy}$are largely insensitive to the choice of shape function, indicating their dominant dependence on the global bending response. A similar trend is observed for σ_{xy}, confirming a consistent representation of membrane–bending coupling across all formulations. In contrast, the transverse shear stresses $\tau_{xz}$and τ_{yz}exhibit a pronounced dependence on the form of $F(z)$, with the largest differences occurring in the vicinity of the mid-plane. The present formulation produces a more pronounced yet smooth distribution of shear stresses in the central region of the laminate, without spurious oscillations or abrupt gradient changes. Compared to the other models, this behaviour indicates a more stable and physically consistent description of through-thickness response. By contrast, formulations based on more rigid shape functions (Reddy, Radaković) yield more diffuse distributions with reduced peak values, while the Karama model exhibits a faster decay through the thickness, limiting its ability to capture local gradients. These results highlight that the choice of shape function directly governs the quality of shear stress prediction, with the present model achieving a balanced representation that combines local adaptability with global stability.

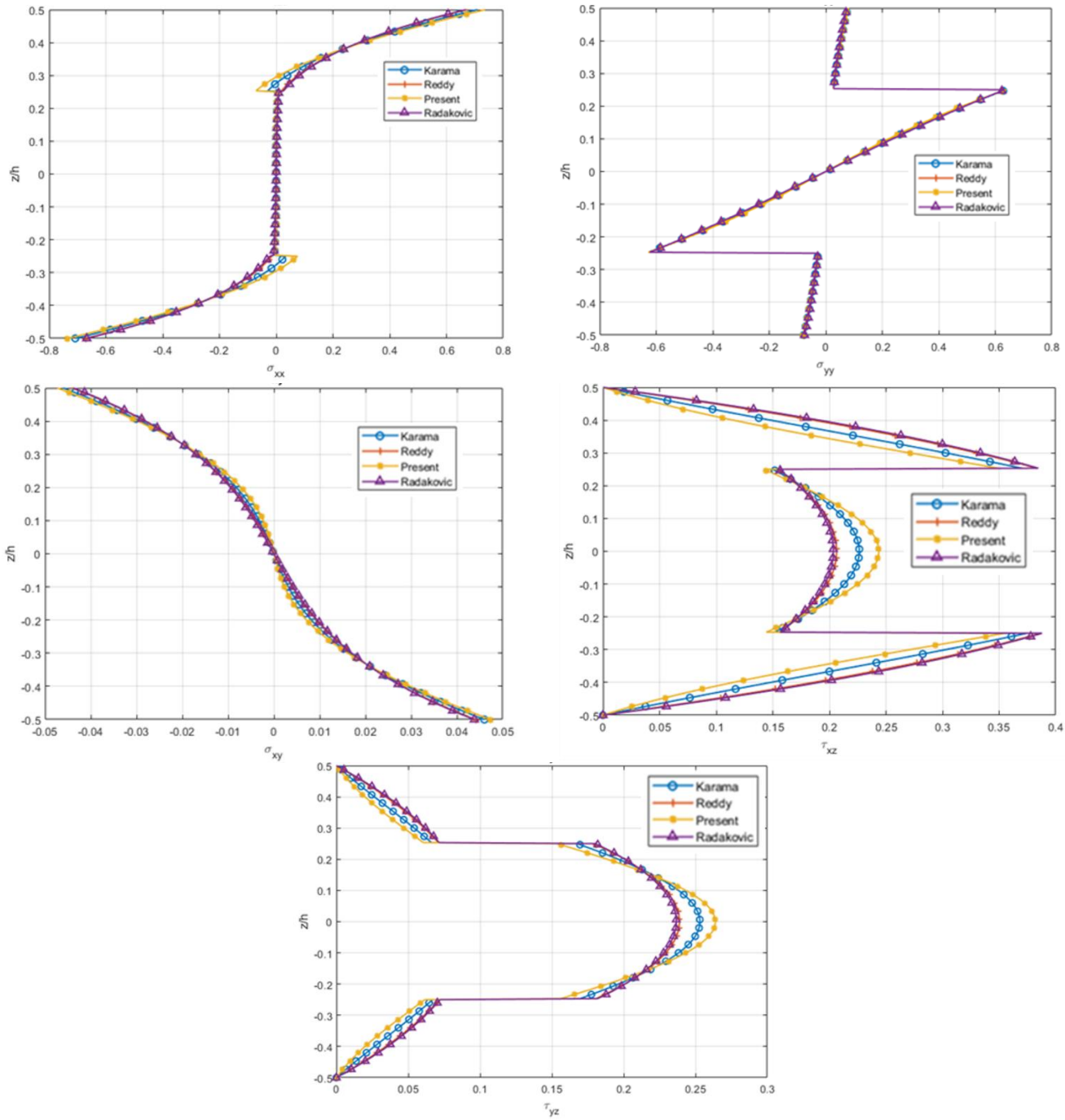

Figure 1 Through-thickness variation of normalized stress components (σ_{xx}, σ_{yy}, σ_{xy}, τ_{xz}, τ_{yz}) for different ESL–HSDT models

CONCLUSIONS

The proposed formulation enables a consistent description of through-thickness behaviour of laminated plates within the ESL–HSDT framework, without increasing kinematic complexity. The results show that differences between formulations do not stem from the global response, but from the manner in which transverse shear deformation is represented.

Numerical results confirm that all considered models provide comparable accuracy in predicting global quantities, while their differences are primarily reflected in the distribution of transverse shear stresses. The through-thickness analysis indicates that the choice of shape function directly governs the character of the local response, with different formulations effectively corresponding to different regimes of shear deformation distribution.

The present model exhibits a stable and consistent response across the entire thickness, without spurious oscillations and with a smooth stress field. This behaviour suggests that improving the description of shear effects does not require additional kinematic variables, but rather a more precise control of the through-thickness deformation field.

From a broader perspective, the findings indicate that further development of ESL–HSDT models should focus on the formulation of the shape function rather than on increasing the order of the theory. This provides a viable path toward more efficient modeling of laminated structures in applications where through-thickness effects are critical.

REFERENCES

Atallah, K. E., Ouinass, D., Zaoui, F. Z., Khoussa, H., Achour, B., Hassan, M. F., & Siregar, J. P. (2025). A refined quasi-3D higher-order shear deformation theory for static, free vibration, and buckling of laminated composite plates on Kerr-type foundation. *Next Materials*, 9, 101352. https://doi.org/10.1016/j.nxmate.2025.101352

Cetkovic, M. (2015). Thermo-mechanical bending of laminated composite and sandwich plates using layerwise displacement model. *Composite Structures*, 125, 388–399. https://doi.org/10.1016/j.compstruct.2015.01.051

Joshan, Y. S., Grover, N., & Singh, B. N. (2017). Analytical modelling for thermo-mechanical analysis of cross-ply and angle-ply laminated composite plates. *Aerospace Science and Technology*, 70, 137–151. https://doi.org/10.1016/j.ast.2017.07.041

Karama, M., Afaq, K. S., & Mistou, S. (2003). Mechanical behaviour of laminated composite beam by the new multi-layered laminated composite structures model with transverse shear stress continuity. *International Journal of Solids and Structures,* 40(6), 1525–1546. https://doi.org/10.1016/S0020-7683(02)00647-9

Radaković, A., Čukanović, D., Bogdanović, G., Blagojević, M., Stojanović, B., Dragović, D., & Manić, N. (2020). Thermal buckling and free vibration analysis of functionally graded plate resting on an elastic foundation according to high order shear deformation theory based on new shape function. *Applied Sciences*, 10(12), 4190. https://doi.org/10.3390/app10124190

Reddy, J. N. (2003). Mechanics of laminated composite plates and shells. *CRC Press*. https://doi.org/10.1201/b12409

Ye, W., Gan, L., Liu, J., Wang, P., Ji, C., Chen, L., Wang, H., & Song, X. (2026). Novel 3D semi-analytical formulation via SBFEM for thermal stress and buckling analyses of laminated plates with 2D discretization. *Composite Structures*, 382, 120055. https://doi.org/10.1016/j.compstruct.2026.120055

The 11th International Congress
Motor Vehicles & Motors 2026
Kragujevac, Serbia
October 8th - 9th, 2026

Motor Vehicles & Motors

MVM2026-007
https://doi.org/10.24874/CMVM2026.007
Technical paper

Gordana Bogdanović[1]
Aleksandar Radaković[2]
Petar Knežević[3]
Dragan Čukanović[4]
Marko Milošević[5]

FATIGUE ANALYSIS OF MATERIALS AND METHODS FOR CYCLE COUNTING UNDER ARBITRARY LOAD HISTORIES

ABSTRACT: This paper presents a comparative analysis of cycle counting methods used in fatigue analysis of materials subjected to variable amplitude loading. Several widely used methods, including peak counting, range counting, reservoir method, rainflow counting, and level crossing method, are applied to a representative load history. The obtained results are compared in terms of accuracy, physical relevance, and applicability in engineering practice. The rainflow counting method is identified as the most reliable approach due to its ability to accurately represent load cycles corresponding to material hysteresis behavior.

KEYWORDS: fatigue analysis, cycle counting, rainflow method, variable amplitude loading, structural engineering

ANALIZA ZAMORA MATERIJALA I METODE ODREĐIVANJA BROJA CIKLUSA PRI PROIZVOLJNOJ ISTORIJI OPTEREĆENJA

REZIME: U radu je prikazana komparativna analiza metoda za određivanje broja ciklusa koje se koriste u analizi zamora materijala izloženih opterećenju promenljive amplitude. Više široko primenjivanih metoda, uključujući peak

[1] *Gordana Bogdanović, University of Kragujevac, Faculty of Engineering, Sestre Janjić 6, 34000 Kragujevac, gocab@kg.ac.rs, https://orcid.org/0000-0001-7231-7400*
[2] *Aleksandar Radaković, Institute for Information Technologies Kragujevac, Jovana Cvijića bb, 34000 Kragujevac, aradakovic@uni.kg.ac.rs, https://orcid.org/0000-0002-7355-7403*
[3] *Petar Knežević, University of Priština, Faculty of Technical Sciences, Knjaza Miloša 7, 38220 Kosovska Mitrovica, petar.knezevic@pr.ac.rs, https://orcid.org/0000-0003-4187-2879*
[4] *Dragan Čukanović, University of Priština, Faculty of Technical Sciences, Knjaza Miloša 7, 38220 Kosovska Mitrovica, dragan.cukanovic@pr.ac.rs, https://orcid.org/0000-0001-8370-748X*
[5] *Marko Milošević, University of Priština, Faculty of Technical Sciences, Knjaza Miloša 7, 38220 Kosovska Mitrovica, marko.milosevic@pr.ac.rs, https://orcid.org/0009-0001-3534-8088*

counting metodu, range counting metodu, metodu rezervoara, metodu kišnog toka i metodu prelaska nivoa, primenjeno je na reprezentativnu istoriju opterećenja. Dobijeni rezultati su upoređeni sa aspekta tačnosti, fizičke opravdanosti i primenljivosti u inženjerskoj praksi. Metoda kišnog toka izdvojena je kao najpouzdaniji pristup zbog svoje sposobnosti da verno predstavi cikluse opterećenja koji odgovaraju histerezisnom ponašanju materijala.

KLJUČNE REČI: zamor materijala, brojanje ciklusa, metoda kišnog toka, opterećenje promenljive amplitude, građevinsko inženjerstvo

INTRODUCTION

Fatigue in materials can be defined as a microscopic phenomenon that manifests through the initiation and propagation of damage within a structural element or an entire structure. This degradation process occurs even under constant stress levels but is particularly pronounced under cyclic loading conditions.

Fatigue is one of the most common failure mechanisms in engineering structures subjected to repeated loading. Numerous civil engineering structures, including bridges, wind turbines, offshore structures and cranes, experience millions of loading cycles during their service life. Consequently, fatigue assessment has become an indispensable part of structural design and service-life prediction, as comprehensively discussed by Schütz, W (1996).

Besides civil engineering, fatigue plays an equally important role in the automotive industry, where structural components are continuously exposed to complex variable-amplitude loading caused by road irregularities, braking, acceleration, cornering, engine vibrations and thermal loading. The growing demand for lightweight structures, improved fuel efficiency and vehicle electrification has further increased the need for accurate fatigue-life prediction methods capable of analysing realistic service load histories. Modern durability assessment of automotive components therefore relies on measured load histories, cycle counting techniques and cumulative damage models. Recent investigations confirm that time-domain fatigue analysis combined with rainflow cycle counting remains one of the most reliable approaches for predicting the fatigue life of automotive components subjected to random loading (He, J. et al. 2026; Benasciutti, D., & Marques, J. M. E. 2022).

The materials most frequently investigated in automotive fatigue analysis include high-strength low-alloy steels (HSLA), advanced high-strength steels (AHSS), cast irons, aluminium alloys, magnesium alloys and, in high-performance applications, titanium alloys and fibre-reinforced composites. Typical fatigue-critical components include crankshafts, connecting rods, transmission shafts, suspension control arms, steering knuckles, wheel hubs, brake discs, exhaust manifolds, cylinder heads and welded chassis joints. Since these components operate under highly irregular loading histories, accurate fatigue-life prediction strongly depends on reliable cycle counting procedures capable of representing the actual loading process (He, J. et al. 2026; Benasciutti, D., & Marques, J. M. E. 2022; Bellec, E. et al. 2022).

A major contribution to practical fatigue analysis was made by Wöhler, who experimentally established S–N curves describing the relationship between the stress range S and the number of cycles to failure N (Wöhler, A. 1860). Subsequently, Palmgren introduced the cumulative damage concept (Palmgren, A.G. 1924), which was further developed by Miner into the well-known linear cumulative damage rule that remains one of the fundamental tools for fatigue-life assessment (Miner, M. A. 1945).

Initially, fatigue analysis was limited to constant-amplitude loading. However, real engineering structures are almost exclusively subjected to variable-amplitude loading histories. Consequently, modern fatigue assessment relies on cycle counting methods capable of transforming arbitrary loading histories into an equivalent set of constant-amplitude cycles. These methods are commonly combined with cumulative damage theories and have become indispensable in engineering practice for evaluating fatigue life under realistic operating conditions (Schijve, J. 1963; Dowling, N. E. 1971).

Among the available techniques, the rainflow counting method has become the reference approach because of its ability to identify physically meaningful closed loading cycles corresponding to hysteresis behaviour observed during cyclic deformation. Owing to its accuracy, robustness and compatibility with numerical fatigue analysis procedures, it has been incorporated into numerous engineering standards and commercial fatigue software packages and is widely used in the automotive, aerospace, mechanical and civil engineering industries (He, J. et al. 2026; Benasciutti, D., & Marques, J. M. E. 2022; Benasciutti, D., & Tovo, R. 2023).

The objective of this paper is to present a comparative analysis of the most widely used cycle counting methods for arbitrary load histories. Their theoretical background, computational characteristics, physical interpretation and engineering applicability are discussed and compared through a representative numerical example in order to identify the most suitable method for fatigue assessment under variable-amplitude loading.

METHODS FOR CYCLE COUNTING UNDER ARBITRARY LOAD HISTORIES

If the definition of Wöhler S–N curves represents the most significant milestone in fatigue analysis, the second most important contribution is attributed to Palmgren, A. G. (1924) and Miner, M. A. (1945), whose work led to the formulation of the linear cumulative damage rule, which remains widely used today. Together with cycle counting methods for arbitrary load histories, these approaches form the fundamental tools for practical fatigue analysis.

A wide number of cycle counting methods have been developed, each tailored to specific types of problems. The primary objective of any such method is to transform a variable-amplitude load history into an equivalent set of constant-amplitude cycles. Prior to applying any cycle counting technique, load histories are typically filtered to retain only local extrema, thereby reducing the dataset while preserving essential information.

In general, cycle counting methods can be classified into three main groups:

Peak counting methods focus on identifying peaks within load histories, detecting all local maxima and minima (Mercer, A., & Livesey, J. 1973). This approach decomposes the load history into full cycles; however, it tends to overestimate smaller stress ranges, leading to deviations from actual conditions. Additionally, major cycles may be interrupted when crossing the zero level, causing the largest stress ranges to be neglected. Due to these limitations, peak counting methods are applicable only to specific loading scenarios and have limited general use.

Range counting methods identify half-cycles between relative maxima and minima (Mercer, A., & Livesey, J. 1973). These half-cycles are then paired with corresponding half-cycles of equal magnitude and opposite sign to form full cycles. A key limitation of this approach is the inability to pair all half-cycles due to varying amplitudes. Furthermore, in certain load histories, large-amplitude cycles may be overlooked in favor of smaller ones. Despite these shortcomings, methods within this group—such as the reservoir method and the rainflow counting method—are the most widely used today. When combined with residue processing techniques, they provide highly effective tools for decomposing load histories into full cycles.

Level crossing methods involve defining several load levels (thresholds), and counting the number of times the load signal crosses these levels during loading increments. This method does not provide information on mean stress values or peak magnitudes. Additionally, cycles that do not exceed predefined thresholds are neglected. When the zero level is used as the reference threshold, the method is referred to as the *zero level crossing method*.

The **reservoir method** is typically applied to short time intervals and relatively simple load histories. Due to its simplicity, it is suitable for manual calculations (Knežević, P., & Milanović, M. 2015). This method represents a graphical interpretation of the rainflow method and yields equivalent results (Hoadley, P. W. et al. 2006).

In this approach, the load history is plotted with stress (or another relevant parameter) on the vertical axis and time on the horizontal axis. The considered segment begins and ends at the same maximum value, which also represents the global maximum. The resulting diagram is interpreted as a “reservoir” filled with fluid. The reservoir is then “punctured” at the point corresponding to the global minimum, defining the first cycle through its associated maximum (initial fluid level) and minimum (drain point). The remaining portions form smaller reservoirs, and the procedure is repeated by selecting the next lowest minimum.

Although the reservoir method is a useful engineering tool for fatigue analysis, its application is limited to relatively simple and short load histories. Its key advantages include algorithmic simplicity and the absence of residual (unclosed) cycles, unlike the rainflow method.

The **rainflow counting method (RFC)** is the most widely used technique for analyzing fatigue under variable-amplitude loading. Its acceptance is largely due to its physical interpretation, where each full cycle corresponds to a closed hysteresis loop in the stress–strain diagram.

The concept was first introduced by Matsuishi and Endo (Matsuishi M., & Endo, T. 1968), based on an analogy with raindrops flowing down a pagoda roof. The method identifies half-cycles and pairs them to form full cycles (range counting principle). A flow (half-cycle) is terminated when one of the following conditions is satisfied:

- a flow starting from a local maximum encounters a new flow originating from a higher maximum;
- a flow starting from a local minimum encounters a new flow originating from a lower minimum;
- the flow exits the load history;
- the flow intersects an already initiated flow.

A fundamental limitation of the original algorithm is the requirement for the complete load history, which prevents real-time data processing and demands significant memory storage.

To overcome these limitations, several computational algorithms have been developed, most notably:

- the **three-point criterion**,
- the **four-point criterion**.

These algorithms enable incremental analysis of load histories and extraction of closed hysteresis loops corresponding to full cycles.

The **three-point criterion** considers three successive local extrema P_i, P_{i+1}, i P_{i+2}, and defines stress ranges based on their differences. A cycle is identified and removed from the history when the following condition is satisfied:

$$Y = \left|P_{i+1} - P_i\right| \leq X = \left|P_{i+2} - P_{i+1}\right|, \tag{1}$$

Where $i=1, 2, 3,...,M-2$, and M is the length of the data series.

The **four-point criterion** extends this approach by introducing an additional point P_{i+3}, improving robustness in cycle identification. A cycle is extracted when:

$$Z = \left|P_{i+1} - P_i\right| \geq Y = \left|P_{i+2} - P_{i+1}\right| \leq X = \left|P_{i+3} - P_{i+2}\right|. \tag{2}$$

Where $i=1, 2, 3,...,M-3$, and M is the length of the data series.

The graphical representation of the three-point and four-point criteria of the rainflow counting method is shown in Figure 1.

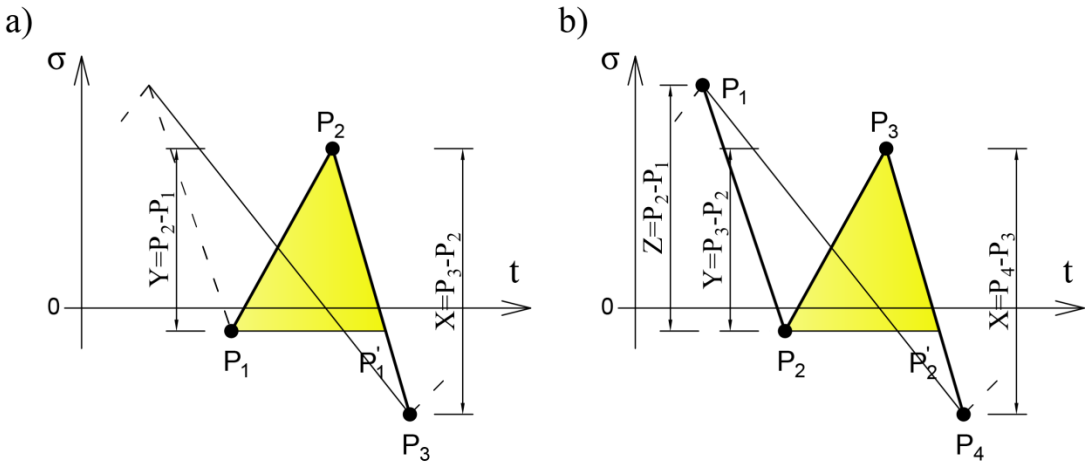

Figure 1 Rainflow Counting Method: a) three-point criterion; b) four-point criterion

These formulations provide a basis for efficient computational algorithms, as presented in (Knežević, P. et al. 2016). Further extensions, such as the **4+1** and **4+n point criteria**, improve computational speed at the expense of increased memory requirements.

Regardless of the applied criterion, residual (unclosed) cycles inevitably remain. Various residue processing techniques have been developed to address this issue (Marsh, G. et al. 2016). It should be noted that different rainflow implementations may yield slightly different results due to variations in algorithm initialization and cycle extraction procedures.

The rainflow method represents a nonlinear numerical algorithm rather than a closed-form mathematical function (Berglind, J. J. B. et al. 2015). Due to its reliance on complete datasets, it is primarily used as a post-processing tool rather than for real-time analysis. Alternative approaches, including stochastic and spectral methods, have been proposed for specific applications involving random loading processes.

NUMERICAL EXAMPLE AND COMPARISON

In order to illustrate the differences between various cycle counting methods and to evaluate their applicability in fatigue analysis, a representative numerical example is considered. The selected load history (Figure) corresponds to a sequence of stress extrema, previously filtered to retain only local maxima and minima, which is a standard preprocessing step in fatigue analysis.

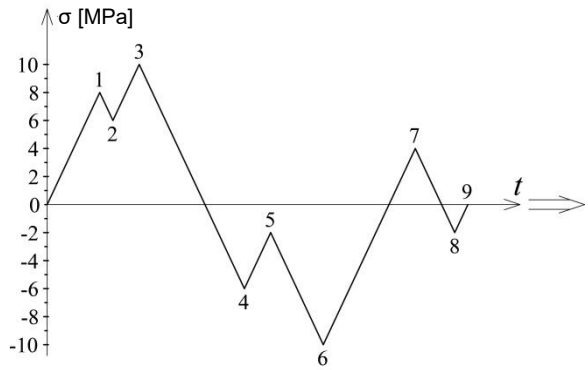

Figure 2 Load history

The primary objective of this example is to demonstrate how different cycle counting methods interpret the same variable-amplitude load history and how this affects the resulting cycle distribution. Since fatigue damage assessment is highly sensitive to the identified stress ranges and the number of cycles, even small differences between methods may lead to significant discrepancies in predicted fatigue life.

The considered load history is represented by stress values at its characteristic points in Table 1.

Table 1 Load history numerical data

Point	1	2	3	4	5	6	7	8	9
σ [MPa]	8	6	10	-6	-2	-10	4	-2	0

The analysis includes the application of the following groups of methods:

- peak counting methods,
- range counting methods (including the reservoir method and the rainflow counting method),
- level crossing methods.

For each method, the cycle counting procedure is presented step by step in order to clearly demonstrate how individual cycles are identified and extracted from the load history. Special attention is given to the treatment of large-amplitude cycles, the handling of residuals, and the pairing of half-cycles.

The results obtained using each method are presented in tabular form, including:

- stress range Δσ,
- mean stress (where applicable),
- number of cycles.

Finally, a comparative analysis is performed to highlight the key differences between the methods in terms of:

- accuracy and physical relevance,
- sensitivity to load sequence effects,
- computational efficiency and practical applicability.

This comparison provides a basis for selecting the most appropriate cycle counting method in engineering practice, particularly in the context of fatigue analysis of structures subjected to variable-amplitude loading.

Summary of Cycle Counting Results

The results of cycle counting for the given load history using different methods are summarized in the following tables.

Table 2 Results of cycle counting using different methods

Peak Counting Method

Stress Range Δσ	Number of Cycles
2	1
4	1
6	1
8	1
10	1
11	1

Table 2 (continuation)

Range Counting Method

Stress Range Δσ	Number of Cycles
2	1
4	1
6	1
8	1
14	1

Reservoir Method

Stress Range Δσ	Number of Cycles
20	1
16	1
10	1
6	1

Rainflow Counting Method (Reference)

Stress Range Δσ	Number of Cycles
20	1
14	1
10	1
6	1
4	1
2	1

Level Crossing Method

Stress Range Δσ	Number of Cycles
—	Not directly defined
Crossings (0-level)	6

Table 3 Comparative Overview of cycle counting methods

Method	Captures Large Cycles	Small Cycle Sensitivity	Residue	Practical Use
Peak counting	No	High (overestimation)	No	Limited
Range counting	Partial	Medium	Yes	Moderate
Reservoir	Yes	Medium	No	Manual analysis
Rainflow	Yes (accurate)	Balanced	Yes	Standard method
Level crossing	No	Low	—	Statistical use

CONCLUSIONS

The comparative analysis of cycle counting methods highlights significant differences in their ability to represent variable amplitude loading histories. Peak and level crossing methods show limited applicability due to their inability to accurately capture dominant stress cycles. Range-based methods provide improved results but still exhibit limitations in handling complex load sequences. The reservoir method offers a simple and intuitive approach suitable for manual calculations. However, the rainflow counting method proves to be the most accurate and widely applicable technique, as it provides a physically consistent representation of fatigue cycles and has become the most commonly adopted approach for fatigue life assessment in engineering practice.

Nevertheless, despite its advantages, the rainflow method also exhibits certain limitations, particularly related to the simplification of complex loading histories into equivalent closed cycles and the neglect of detailed material response during cyclic loading. Future research should therefore focus on the development of advanced cycle identification approaches based on models that consider the physical nature of complete fatigue cycles, such as various hysteresis-based models. Such approaches could provide a more accurate description of material behavior under arbitrary loading conditions by incorporating load sequence effects, cyclic plasticity, and the evolution of hysteretic energy dissipation. This could lead to improved fatigue life prediction methods beyond the capabilities of conventional cycle counting techniques.

REFERENCES

Bellec, E., Doudard, C., Facchinetti, M. L., Calloch, S., & Moyne, S. (2022). Loading classification proposal for fatigue design of automotive chassis parts: a relevant process for variable-amplitude and multi-input load cases. *International Journal of Fatigue*, 166, 107284. https://doi.org/10.1016/j.ijfatigue.2022.107284

Benasciutti, D., & Marques, J. M. E. (2022). Fatigue analysis of nonstationary random loadings measured in an industrial vehicle wheel: uncertainty of fatigue damage. *Metals*, 12(4), 616. https://doi.org/10.3390/met12040616

Benasciutti, D., & Tovo, R. (2023). Uncertainty of estimated rainflow damage in stationary random loadings and in those stationary per partes. *Applied Sciences*, 13(5), 2808. https://doi.org/10.3390/app13052808

Berglind, J. J. B., Wisniewski, R., & Soltani, M. (2015, 01-03 July). *Fatigue load modeling and control for wind turbines based on hysteresis operators*. 2015 American Control Conference (ACC), Chicago, IL, USA, pp. 3721-3727.

Dowling, N. E. (1971). Fatigue failure predictions for complicated stress-strain histories. https://www.ideals.illinois.edu/items/119944

He, J., Zhang, C., & Wan, R. (2026). Research on time-domain fatigue analysis method for automotive components considering performance degradation. *Applied Sciences*, 16(1) 40. https://doi.org/10.3390/app16010040

Hoadley, P. W., Frank, K. H., & Yura, J. A. (2006). Estimation of the fatigue life of a test bridge from traffic data. *Journal of Bridge Engineering*, 11(6), 141. https://doi.org/10.1061/(ASCE)1084-0702(2006)11:6(725)

Knežević, P., & Milanović, M. (2015). Određivanje broja ciklusa za zadatu istoriju opterećenja pri analizi zamora prema evrokodu. Zbornik radova Građevinskog fakulteta, Subotica, 31(28), 23–33. https://doi.org/10.14415/zbornikGFS28.02

Knežević, P., Šumarac, D., & Milanović, M. (2016). Primena metode kišnog toka pri određivanju broja ciklusa usled cikličnog opterećenja promenljive amplitude. 12th International Conference on Contemporary Theory and Practice in Construction. Banja Luka, Bosnia and Herzegovina, pp. 107–114.

Marsh, G., Wignall, C., Thies, P. R., Barltrop, N., Incecik, A., Venugopal, V., & Johanning, L. (2016). Review and application of Rainflow residue processing techniques for accurate fatigue damage estimation. *International Journal of Fatigue*, 82(3), 757-765. https://doi.org/10.1016/j.ijfatigue.2015.10.007

Matsuishi M., & Endo, T. (1968). Fatigue of metals subjected to varying stress. *Paper presented to Japan Society of Mechanical Engineers*, Fukuoka, Japan.

Mercer, A., & Livesey, J. (1973). Statistical counting methods as a means of analysing the load histories of light bridges. *Journal of Sound and Vibration*, 27(3), 399-410. https://doi.org/10.1016/S0022-460X(73)80354-2

Miner, M. A. (1945). Cumulative damage in fatigue. *Journal of Applied Mechanics*, 12(3), 159–164. https://doi.org/10.1115/1.4009458

Palmgren, A.G. (1924). Die Lebensdauer von kugellagern. *Zeitschrift des Vereines Deutscher Ingenieure*, 68(14), 339–341.

Schijve, J. (1963). The analysis of random load-time histories with relation to fatigue tests and life calculations. *Fatigue of Aircraft Structures*, 115-149.

Schütz, W. (1996). A history of fatigue. *Engineering Fracture Mechanics*, 54(2), 263–300. https://doi.org/10.1016/0013-7944(95)00178-6

Wöhler, A. (1860). Versuche über die festigkeit der eisenbahnwagenachsen. *Zeitschrift für Bauwesen*, 10(4), 160–161.

The 11th International Congress
Motor Vehicles & Motors 2026
Kragujevac, Serbia
October 8th - 9th, 2026

Motor Vehicles & Motors

MVM2026-009
https://doi.org/10.24874/CMVM2026.009
Original scientific paper

Julija Boskovic[1]
Ivan Grujic[2]
Stefan Djuric[3]
Nadica Stojanovic[4]
Bogdan Zivkovic[5]
Milan Ivkovic[6]
Suzana Petrovic Savic[7]

DEVELOPMENT OF AN EXPERIMENTAL FIVE-AXIS CNC SYSTEM USING STEPPER MOTORS

ABSTRACT: This paper presents an experimental five-axis CNC milling machine designed for the research, development, and testing of multi-axis CNC systems. NEMA 17 stepper motors were used as the drive system due to their simple implementation, low cost, and sufficient positioning accuracy for the development and testing of multi-axis CNC systems. The proposed system is not intended for demanding industrial operating conditions, but rather for creating a functional platform that enables the investigation of multi-axis motion control, axis synchronization, and the evaluation of different control strategies and toolpath generation methods. Special attention is given to the potential application of this concept in education, laboratory research, and the development of future CNC systems with larger dimensions and higher power capacities. The developed system also enables the analysis of fundamental kinematic and control parameters important for improving multi-axis machining and optimizing CNC system performance. The proposed model provides a better understanding of the operation of five-axis CNC machines, as

[1] *Julija Boskovic, Faculty of Engineering University of Kragujevac, Sestre Janjic 6, 34000 Kragujevac, Serbia, julijabkg@gmail.com, https://orcid.org/0009-0006-3031-2234*
[2] *Ivan Grujic, Faculty of Engineering University of Kragujevac, Sestre Janjic 6, 34000 Kragujevac, Serbia, ivan.grujic@kg.ac.rs, https://orcid.org/0000-0003-0572-1205*
[3] *Stefan Djuric, Faculty of Engineering University of Kragujevac, Sestre Janjic 6, 34000 Kragujevac, Serbia, Zastava TERVO d.o.o, Kosovska 4, 34000 Kragujevac, Serbia, stefan.djuric@zastavatervo.rs, https://orcid.org/0000-0003-0660-7551*
[4] *Nadica Stojanovic, Faculty of Engineering University of Kragujevac, Sestre Janjic 6, 34000 Kragujevac, Serbia, nadica.stojanovic@kg.ac.rs, https://orcid.org/0000-0002-4199-0587*
[5] *Bogdan Zivkovic, Faculty of Engineering University of Kragujevac, Sestre Janjic 6, 34000 Kragujevac, Serbia, Zastava TERVO d.o.o, Kosovska 4, 34000 Kragujevac, Serbia, bogdanzivkovic@mail.ru, https://orcid.org/0000-0003-4496-3231*
[6] *Milan Ivkovic, Faculty of Engineering University of Kragujevac, Sestre Janjic 6, 34000 Kragujevac, Serbia, milan.ivkovic@kg.ac.rs , https://orcid.org/0000-0001-5176-5837*
[7] *Suzana Petrovic Savic, Faculty of Engineering University of Kragujevac, Sestre Janjic 6, 34000 Kragujevac, Serbia, petrovic.savic@kg.ac.rs, https://orcid.org/0000-0002-5629-6221*

well as practical verification of design and control solutions before their implementation in more complex industrial systems.

KEYWORDS: multi-axis milling machine, stepper motors, CNC control, experimental system, industrial implementation

RAZVOJ EKSPERIMENTALNOG PETOOSNOG CNC SISTEMA KORIŠĆENJEM STEP MOTORA

REZIME: U radu je prikazana eksperimentalna petoosna CNC glodalica namenjena istraživanju, razvoju i testiranju višeosnih CNC sistema. Kao pogonski sistem korišćeni su NEMA 17 step motori koji su izabrani zbog jednostavne implementacije, pristupačne cene i dovoljne preciznosti za razvoj i testiranje višeosnih CNC sistema. Ovakav sistem nije namenjen za zahtevne industrijske uslove rada, već za formiranje funkcionalne platforme koja omogućava istraživanje upravljanja višeosnim kretanjem, sinhronizacije osa i ispitivanje različitih strategija upravljanja i putanja alata. Posebna pažnja posvećena je mogućnosti primene ovakvog koncepta u edukaciji, laboratorijskim istraživanjima i razvoju budućih CNC sistema većih dimenzija i snage. Razvijeni sistem omogućava i analizu osnovnih kinematskih i upravljačkih parametara koji su značajni za unapređenje višeosne obrade i optimizaciju rada CNC sistema. Razvijeni model omogućava bolje razumevanje rada petoosnih CNC mašina, kao i praktičnu proveru konstrukcionih i upravljačkih rešenja pre njihove implementacije na složenijim industrijskim sistemima.

KLJUČNE REČI: višeosna glodalica, step motori, CNC upravljanje, eksperimentalni sistem, industrijska implementacija

INTRODUCTION

The development of modern material processing technologies is closely associated with advances in the control and drive systems of computer numerical control (CNC) machine tools. Five-axis CNC machines are of particular importance in this field, as they enable the relative motion between the cutting tool and the workpiece to be controlled along five axes. The number, type, and arrangement of translational and rotational axes depend on the structural and kinematic configuration of the machine. Such configurations enable simultaneous positioning and orientation of the tool relative to the workpiece, thereby facilitating the efficient machining of components with complex geometries.

Depending on the machine design, the rotary axes may be located on the worktable, incorporated into the spindle head, or distributed between the table and the spindle in a combined configuration. The selected configuration directly affects the kinematic relationships within the system, the available workspace, and the strategy used for coordinating axis motion. Regardless of the specific structural arrangement, five-axis CNC systems offer significant advantages in the machining of geometrically complex surfaces, including a reduced number of workpiece setups and repositioning operations, shorter preparation and machining times, and improved surface quality. Consequently, these systems are widely applied in industries with demanding requirements regarding machining accuracy and component geometry, including the aerospace and automotive industries, tool and die manufacturing, and the production of medical implants and other precision components (Lu, Y. et al. 2023, Zhang, H. et al. 2024).

The increasing geometrical complexity of automotive components has created a growing demand for machining strategies capable of combining manufacturing flexibility with accurate control of complex tool - workpiece motion. A representative example is the machining of spiral bevel gears used in automotive transmission systems. Escudero, G. et al. (2022) experimentally investigated their manufacture using five axis double flank CNC machining with custom shaped tools. The proposed approach demonstrated the potential of five-axis machining for the efficient and accurate manufacture of complex gear geometries. The application of five-axis CNC machining in the automotive industry is not limited to transmission components, but also encompasses complex engine components, such as automobile cylinder blocks (Yan, J. 2022). Beyond these applications, the need for coordinated multi-axis motion is also evident in crankshaft manufacturing, where eccentric geometrical features impose additional requirements on tool and workpiece motion. In this context, Onodera, S. et al. (2025) developed a feature - based simultaneous four - axis machining approach for eccentric crankshaft features. These developments illustrate a broader transition in automotive manufacturing from conventional machining strategies towards increasingly flexible multi - axis solutions for complex components.

Future developments in multi - axis machining for automotive applications are also closely related to advances in intelligent process planning and digital manufacturing. In the field of crankshaft production, Amouzgar, K. et al. (2025) proposed a smart process planning framework based on CAD feature recognition, machining simulation and multi - objective optimization. Their study also considered the further use of artificial intelligence and adaptive process control in machining systems. These developments indicate that the future potential of multi - axis machining in the automotive industry will increasingly be associated with the integration of machining processes with intelligent and adaptive process - control strategies.

The realization of such advanced machining capabilities imposes significant requirements on machine tool drive and control systems. Industrial five axis CNC systems are therefore predominantly based on servo drives with position feedback provided by incremental or absolute encoders, together with digital current, velocity, and position controllers commonly arranged in a cascaded control structure. Such systems rely on computationally capable CNC controllers to perform tool path interpolation and real - time coordination of multiple machine axes (Rao, S.S. et al. 2026). Although these solutions provide high positioning accuracy and repeatability, as well as favourable dynamic performance, their implementation requires substantial investment in drive components, measurement systems, and control electronics. This may limit their suitability for educational applications, laboratory research, and the development of experimental machine concepts during the early stages of design.

In this context, increasing attention has been devoted to the development of low-cost functional platforms based on stepper motors for investigating and testing multi-axis motion-control concepts. Stepper motors are commonly operated in open-loop control systems, in which the rotor position is not measured directly but is inferred from the number of commanded input pulses. Although open-loop stepper drives cannot generally provide the same level of accuracy, reliability, and dynamic performance as closed-loop servo systems, their simple implementation, relatively low cost, uncomplicated control electronics, and satisfactory positioning resolution, particularly when microstepping is applied, make them suitable for experimental and educational CNC platforms (Vhu, C.-H. et al. 2022, Rao, S.S. et al. 2026).

A fundamental limitation of open - loop stepper - motor systems is the possibility of step loss when the torque required to execute the commanded motion exceeds the torque available from the motor at a given operating speed. Since no direct position feedback is available, the resulting positioning error cannot be detected or corrected during operation. Consequently, reliable application of stepper motors, particularly under variable loading conditions, requires an assessment of the dynamic feasibility of the prescribed motion. Such an assessment should determine whether the available motor torque is sufficient to satisfy the requirements imposed by the prescribed trajectory while accounting for motor speed, acceleration, inertia of the moving components, resistive effects, and external loads (Rao, S.S. et al. 2026).

Studies of multi-axis machining systems have largely focused on kinematic modelling and motion simulation in CAD/CAM environments in order to verify axis coordination, available ranges of motion, and tool-path continuity prior to physical implementation (Bošković, J. et al. 2026, Lu, Z. et al. 2023). Although such analyses are essential during the initial stages of machine development, kinematic verification alone does not provide information about the ability of the selected drive system to execute the prescribed motion under actual dynamic requirements. In the authors' previous research, a three-dimensional model of a five-axis CNC milling machine comprising three translational axes (*X*, *Y*, and *Z*) and two rotational axes (*A* and *C*) was developed. Kinematic simulation was performed in CATIA V5 R21, while the resulting position, velocity, and acceleration data for the individual axes were analysed in MATLAB enviroment. The results confirmed the functionality of the developed kinematic model and the feasibility of coordinated five-axis motion. However, the previous analysis did not address the dynamic feasibility of the prescribed trajectories with respect to the torque capability of the selected NEMA 17 stepper motors. Moreover, the influence of machining loads, particularly cutting forces, on the ability of the drive system to execute the required motion was not considered (Bošković, J. et al. 2026).

The dynamic requirements imposed on the drive system are also closely related to the characteristics of the prescribed tool path. In five-axis machining, the tool path is frequently approximated by a sequence of short linear segments, which may introduce discontinuities in tangent direction and curvature at segment junctions. Since five-axis motion requires simultaneous coordination of the Tool Centre Point (TCP) and Tool Orientation Vector (TOV), such discontinuities may produce abrupt changes in the velocity and acceleration demands of individual machine axes and consequently affect their dynamic behaviour. Zhang, H. et al. (2024) proposed a path-smoothing method based on sliding convolution windows, in which the TCP and TOV signals are processed while preserving their mutual synchronization. Their error-prediction model enables the deviation of the smoothed path to be controlled within prescribed tolerances through iterative adjustment of the convolution-window parameters (Zhang, H. et al. 2024).

Another important issue is the stability of kinematic mapping, particularly in the vicinity of singular configurations, where the inverse kinematic solution may become indeterminate or numerically unstable. This may result in abrupt changes in the commanded positions of the rotary axes and, consequently, increased dynamic demands on the drive system. Lu, Z. et al. (2023) developed a closed-loop inverse-kinematics approach based on a damped pseudoinverse of the Jacobian matrix and compensation of accumulated errors. The proposed method improves numerical stability

near singular configurations and reduces deviations between the commanded and realised trajectories (Lu, Z. et al. 2023).

In addition to tool-path continuity and kinematic stability, five-axis machining accuracy is influenced by geometric deviations between the nominal and machined surfaces. This issue is particularly relevant in flank milling of complex surfaces, where machining errors depend on both the tool trajectory and orientation and on the geometry of the cutting tool itself. Chu, C. et al. (2022) developed a computational method for the simultaneous optimisation of tool paths and tool geometry using continuous - function representations, with the aim of reducing overall geometric deviations and improving the contact conditions between the cutting tool and the machined surface. Although these approaches primarily address geometric and kinematic aspects of five - axis machining, they also demonstrate that the commanded motion may impose rapidly varying requirements on individual machine axes and therefore highlight the importance of considering the corresponding drive-system limitations (Chu, C. et al. 2022).

Related studies in multi - axis additive manufacturing further emphasise the importance of appropriate drive selection and coordinated axis motion. Sarwar, S. (2024) investigated motion planning and coordination for a mobile five-axis 3D-printing system, including the control of additional rotary axes, inverse - kinematics solutions, and collision avoidance (Sarwar, S. 2024). Liu, S. (2024) presented a 3D printer incorporating a rotary platform and stepper-motor drives, considering transmission ratios, operating speeds, and system torque requirements. Although these studies concern additive rather than subtractive manufacturing, they support the broader requirement that drive limitations must be considered when assessing the reliable execution of coordinated multi-axis motion (Liu, S. 2024).

Taken together, the available literature demonstrates substantial progress in tool - path accuracy, inverse - kinematics stability, and multi - axis motion coordination. However, comparatively less attention has been devoted to the dynamic feasibility of five - axis motion implemented using stepper - motor drives, particularly from the perspective of the torque available under varying operating loads. This issue becomes especially relevant in low - cost experimental CNC systems, where open - loop operation makes the available torque margin directly related to the risk of step loss and, consequently, to the reliability of trajectory execution.

The need for reliable kinematic and dynamic modelling is further reinforced by the long-term objective of developing a Digital Twin (DT) of the experimental five - axis CNC system. A DT can be regarded as a dynamic virtual representation of a physical system in which appropriate models are combined with data acquired from the physical counterpart to support state monitoring, analysis, and prediction of system behaviour. In CNC machine tools, the reliability of such a representation depends strongly on the fidelity of the underlying kinematic and dynamic models used to describe the position, velocity, acceleration, and loading of the individual machine axes (Rao, S.S. et al. 2026).

At the current stage of development, a virtual model of the experimental five - axis CNC milling machine has been established and kinematically verified. In parallel, NEMA 17 stepper motors intended to drive the translational and rotational axes have been selected and experimentally tested, while the mechanical integration of the complete machine is still in progress. At this stage, dynamic analysis provides an essential link between the existing kinematic model and the subsequent integration of the virtual and physical systems. In particular, it enables the capability of the selected motors to execute the prescribed trajectories to be evaluated with respect to their torque limitations before completion of the mechanical integration. The resulting analysis also provides a basis for further refinement of the dynamic model and its subsequent integration with data acquired from the physical system.

Accordingly, the aim of this study is to evaluate the dynamic feasibility of the previously defined five - axis CNC configuration, with particular emphasis on the ability of NEMA 17 stepper motors to execute the prescribed trajectories under different loading conditions. Two operating regimes are considered. The first represents motion without machining, in which the required drive torque is determined by the inertia of the moving components and the assumed resistive loads. The second additionally accounts for machining loads by incorporating cutting forces during milling, estimated using the Kienzle cutting - force model. In this way, the previously developed kinematic model is extended to include a dynamic feasibility assessment, providing a more realistic evaluation of the proposed five - axis CNC configuration and establishing a basis for the subsequent development of its DT.

MATERIALS & METHODS

The dynamic feasibility analysis of the five - axis motion was carried out through a sequence of interconnected steps. After defining the drive - system parameters and the mechanical characteristics of the individual axes, a synthetic test trajectory was established. The corresponding axis velocities and accelerations were determined analytically and subsequently converted to the motor side of the drive system. Based on the relationship between the required and available motor torque, a torque reserve indicator was defined as a criterion for the preliminary assessment of dynamic feasibility. The analysis was performed for motion without external process loading and, for the translational axes, for a reference loading scenario based on a simplified Kienzle cutting - force model (Figure 1).

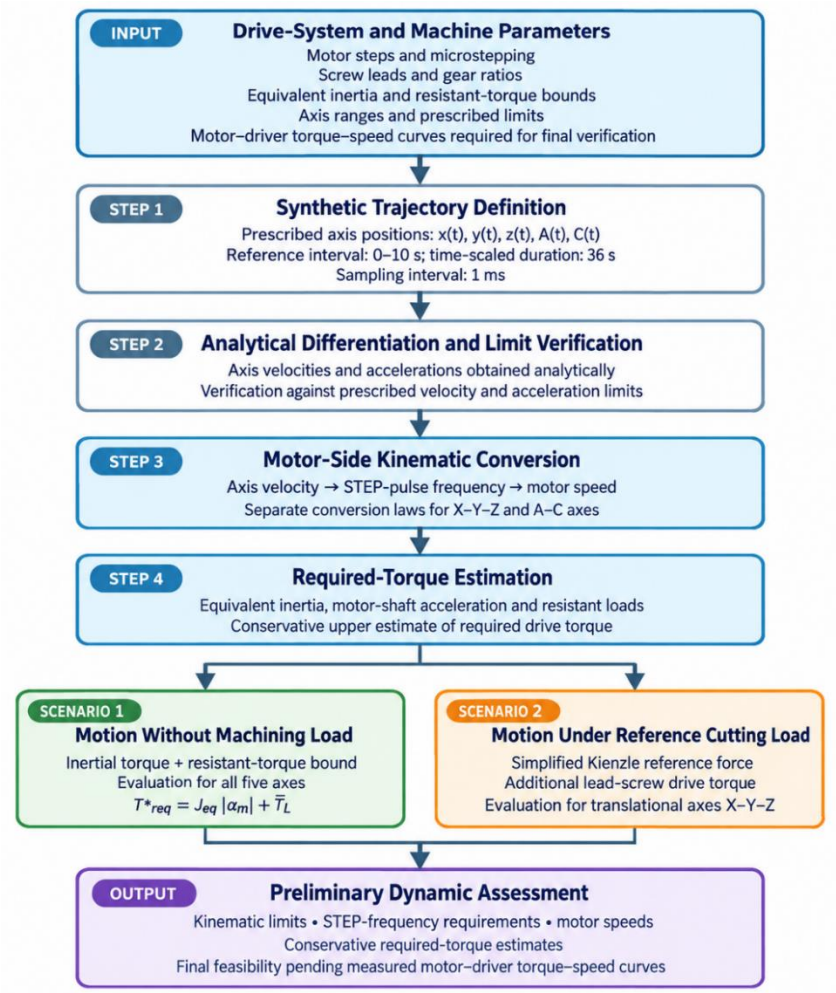

Figure 1 Algorithm flow for assessing the dynamic feasibility of five-axis CNC motion

For the preliminary dynamic assessment, harmonic and constant - velocity reference profiles were used to provide controlled and analytically differentiable excitation of the machine axes. Sinusoidal and shifted - cosine position profiles are suitable for this purpose because they provide smooth variations of position with explicitly defined velocity and acceleration characteristics (Hafez I. & Dhaouadi R. 2025). Accordingly, harmonic profiles were assigned to the *X*, *Z*, and *A* axes, while linear profiles were assigned to the *Y* and *C* axes to represent constant - velocity motion. The profile amplitudes were selected according to the available axis ranges, whereas the frequency parameters were selected according to the adopted kinematic limits of the experimental CNC system.

The original motion laws were defined over a reference time interval of 10s, after which a common time - scaling factor of $s_t=3.6$. was applied to all five axes. In the time - scaled analysis, each prescribed position profile was evaluated using the normalized time argument t/s_t, increasing the total motion duration from 10 s to 36 s. This transformation preserved the geometric shape of the prescribed trajectory and the relative synchronization of the axes, while reducing the corresponding velocities and accelerations by factors of s_t and s_t^2, respectively. All numerical results presented below therefore refer to the time - scaled position, velocity, and acceleration profiles. The numerical analysis was performed using a time step of $\Delta t=1$ *ms.*

The reference position profiles of the translational and rotational axes were defined by:

$$x(t) = \frac{H_x}{2}\sin(\Omega_x t), \tag{1}$$

$$y(t) = H_y - \mathrm{v}_{y0}t, \tag{2}$$

$$z(t) = \frac{H_z}{2}[1 - \cos(\Omega_z t)], \tag{3}$$

$$A(t) = A_{\max}\sin(\Omega_A t), \tag{4}$$

$$C(t) = \omega_{C0}t, \tag{5}$$

where the adopted trajectory parameters are $H_x = 90\ mm, H_y = 100\ mm, H_z = 70\ mm,\ A_{xmax} = 20\circ, \Omega_x = 0.4\ s^{-1},\ \Omega_z = \Omega_A = 0.3\ s^{-1}, v_{y0} = 8\frac{mm}{s}, \omega_{yC0} = 36°/s.$

For the *X* axis, the coordinate origin was placed at the midpoint of the available travel range, resulting in the admissible interval $-\frac{H_x}{2} \leq x(t) \leq \frac{H_x}{2}$. The prescribed motion therefore represents a synthetic test trajectory designed to simultaneously evaluate the kinematic and drive requirements of all five axes. It does not represent a specific machining tool path, nor is it intended to cover the entire available workspace of the machine. The common time scaling was introduced to reduce the required linear velocities to within the adopted limit of 5 mm/s, while preserving both the geometric shape of the trajectory and the relative temporal synchronization of the axes.

The velocity and acceleration of each axis were determined analytically as the first- and second - time derivatives of the corresponding generalized coordinate:

$$v_q(t) = \frac{\mathrm{d}q(t)}{\mathrm{d}t}, \tag{6}$$

$$a_q(t) = \frac{\mathrm{d}v_q(t)}{\mathrm{d}t} = \frac{\mathrm{d}^2q(t)}{\mathrm{d}t^2}, \tag{7}$$

here *q(t)* denotes the corresponding translational or rotational coordinate. Since the prescribed position profiles were available in analytical form, the corresponding velocity and acceleration profiles were obtained by direct analytical differentiation.

Based on Eqs. (1) - (3), the velocity and acceleration expressions for the translational axes are given by Eqs. (8) - (12), whereas differentiation of Eqs. (4) and (5) yields the corresponding expressions for the rotational axes, given by:

$$v_x(t) = \frac{H_x\Omega_x}{2}\cos(\Omega_x t), \tag{8}$$

$$a_x(t) = -\frac{H_x\Omega_x^2}{2}\sin(\Omega_x t), \tag{9}$$

$$v_y(t) = -v_{y0}, a_y(t) = 0, \tag{10}$$

$$v_z(t) = \frac{H_z\Omega_z}{2}\sin(\Omega_z t), \tag{11}$$

$$a_z(t) = \frac{H_z\Omega_z^2}{2}\cos(\Omega_z t). \tag{12}$$

$$\dot{A}(t) = \mathrm{A}_{max}\Omega_A\cos(\Omega_A t), \tag{13}$$

$$\ddot{A}(t) = -\mathrm{A}_{max}{\Omega_A}^2\sin(\Omega_A t), \tag{14}$$

$$\dot{C}(t) = \omega_{C0}, \ddot{C}(t) = 0. \tag{15}$$

For the adopted time-scaling factor s_t=*3.6*, he maximum absolute velocities of the translational axes are $\mathrm{vX}_{peak} = 5\frac{mm}{s}, \mathrm{vY}_{peak} = 2{,}22\frac{mm}{s}, \mathrm{vZ}_{peak} = 2{,}92\frac{mm}{s}$. The corresponding maximum absolute accelerations are $\mathrm{aX}_{peak} = 0.56\ \frac{mm}{s^2}, \mathrm{aY}_{peak} = 0, \mathrm{aZ}_{peak} = 0{,}24\frac{mm}{s^2}$. These values were obtained from the time - scaled profiles, for which velocities and accelerations are reduced by factors of s_t and s_t^2, respectively. All three translational axes therefore satisfy the velocity and acceleration limits of 5mm/s and 100 mm/s² adopted for the present preliminary numerical analysis. These limits represent numerical assessment criteria rather than experimentally determined performance limits of the physical prototype.

No separate velocity or acceleration limits were prescribed for the rotational axes *A* and *C*. Therefore, their calculated values were used only to determine the drive - related quantities and were not assessed against specific limiting criteria. Since some axes exhibit non - zero velocities at the boundaries of the analysed interval, the prescribed trajectory represents a segment of established motion rather than a complete motion cycle. Start up and stopping transients were not included, as their analysis would require separately defined acceleration and deceleration profiles and the corresponding transient drive - torque assessment.

For the translational axes *X, Y*, and *Z*, the stepper - motor shaft was assumed to be directly coupled to the lead screw. A screw lead of p_j= 1.25 mm/rev was adopted for all three axes.

For a stepper – motor - driven axis, the motor position is determined by the number of input pulses, whereas its rotational speed is determined by the STEP-pulse frequency. The total number of pulses required for one motor revolution depends on the number of full motor steps per revolution and the selected microstepping factor (Hughes, A. & Drury, B. 2019; Campbell, A.A. et al., 2014). Accordingly, the required STEP - pulse frequency for translational axis *j*, $j \in \{X, Y, Z\}$, is determined from the magnitude of the corresponding linear velocity as follows:

$$f_j(t) = \frac{N\, m_{\mathrm{mic}}}{p_j} \left| v_j(t) \right|, j \in \{X, Y, Z\}, \tag{16}$$

where *N* is the number of full motor steps per revolution, m_{mic} is the microstepping factor, and p_j is the screw lead.

For the rotational axes, the axis angular velocity is converted to the corresponding motor - shaft velocity using the transmission ratio. The required STEP - pulse frequency is therefore:

$$f_j(t) = \frac{N\, m_{\mathrm{mic}} i_j}{360} \left| \dot{\theta}_j(t) \right|, j \in \{A, C\}, \tag{17}$$

where $\theta_A = A, \theta_C = C$, and the transmission ratio is defined as $i_j = \frac{\omega_{m,j}}{\omega_{ose,j}}$. The STEP - pulse frequency is treated as a non - negative quantity, while the direction of motion is determined separately from the sign of the axis velocity and the adopted axis orientation. A limiting STEP - pulse frequency of $f_{lim} = 20000\mathrm{Hz}$ was adopted for each axis as a numerical control - system requirement rather than as an experimentally verified hardware limit. Accordingly, the required STEP - pulse frequency was assessed using the condition $f_j(t) \leq f_{j,max}$.

Starting from the lead - screw kinematic relationship between angular and linear displacement given by Iqbal. H. et al. (2022), the corresponding motor angular velocity and angular acceleration for each translational axis were obtained by differentiation with respect to time:

$$\omega_{m,j}(t) = \frac{2\pi}{p_j} v_j(t) \text{ i } \alpha_{m,j}(t) = \frac{2\pi}{p_j} a_j(t), j \in \{X, Y, Z\}. \tag{18}$$

For the rotational axes, the corresponding relationships are:

$$\omega_{m,j}(t) = \frac{\pi}{180} i_j \dot{\theta}_j(t) \text{ i } \alpha_{m,j}(t) = \frac{\pi}{180} i_j \ddot{\theta}_j(t), j \in \{A, C\}. \tag{19}$$

Since each STEP - pulse produces one commanded motor step or microstep and the pulse rate determines the motor rotational speed, as described by Campbell, A.A. et al. (2014), the magnitude of the motor angular velocity can alternatively be determined from the STEP - pulse frequency:

$$\left| \omega_{m,j}(t) \right| = \frac{2\pi f_j(t)}{N m_{mic}}. \tag{20}$$

The number of full motor steps per revolution and the microstepping factor determine the required STEP-pulse frequency but do not alter the mechanical relationship between axis displacement and motor-shaft rotation.

The available torque of a stepper - motor drive decreases with increasing operating speed and must therefore be evaluated using the torque - speed characteristic of the selected motor - driver combination. The holding torque specifies the motor capability at standstill and cannot, by itself, be treated as the torque available during motion (Campbell A. A. et al., 2014; Hughes A. and Drury B. 2019). Accordingly, the available motor torque is represented as:

$$T_{\mathrm{available},j}(t) = T_{\mathrm{lim},j}\left(\left| \omega_{m,j}(t) \right| \right), \tag{21}$$

where $T_{\mathrm{lim},j}$ pred denotes the limiting torque that the drive can deliver at the corresponding motor speed under steady - state operating conditions.

Following the motor - selection procedure for multi - axis CNC drives presented by Iqbal H. et al. (2022), the dynamic quantities and mechanical loads were referred to the motor shaft. The required motor torque was therefore expressed as the sum of the inertial and non-inertial load contributions:

$$T_{\mathrm{req},j}(t) = J_{\mathrm{eq},j} \alpha_{m,j}(t) + T_{\mathrm{L},j}(t), \tag{22}$$

where $J_{\mathrm{eq},j}$ is the total equivalent moment of inertia referred to the motor shaft and $T_{\mathrm{L},j}(t)$ pot is the signed torque required to overcome non-inertial loads. The signs of all contributions are defined relative to the adopted positive direction of motor rotation.

The equivalent inertia includes the motor - rotor inertia and the inertial contributions of the driven components referred to the motor shaft. For the translational axes, the translating masses are converted into an equivalent rotational inertia through the lead - screw kinematic relationship, whereas for the rotational axes the corresponding transmission ratio is taken into account.

When the instantaneous variation of the non - inertial load torque is not known, its magnitude may be represented by an adopted upper bound:

$$\left|T_{\mathrm{L},j}(t)\right| \leq \overline{T}_{\mathrm{L},j}, \tag{23}$$

Applying the triangle inequality to Eq. (22) then gives:

$$\left|T_{\mathrm{req},j}(t)\right| \leq J_{\mathrm{eq},j}\left|\alpha_{m,j}(t)\right| + \overline{T}_{\mathrm{L},j}. \tag{24}$$

Accordingly, the following conservative estimate of the required motor torque is adopted:

$$T^{*}_{\mathrm{req},j}(t) = J_{\mathrm{eq},j}\left|\alpha_{m,j}(t)\right| + \overline{T}_{\mathrm{L},j}. \tag{25}$$

Equation (25) does not represent the exact instantaneous drive torque. Instead, it provides a conservative upper estimate based on the adopted bound of the non - inertial loads. This formulation enables a preliminary assessment of the drive requirements even when the detailed time-dependent behaviour of the individual load components has not yet been identified.

To define a reference machining-load scenario, the tangential cutting-force component was estimated using the empirical Kienzle–Victor force model, which relates the cutting force to the undeformed chip width and thickness through the specific cutting-force coefficient and the corresponding material exponent (Klippel H. et al. 2024):

$$F_c = k_{c1.1}\, b\, h \left(\frac{h}{h_0}\right)^{-m_c}, \qquad h_0 = 1\ \mathrm{mm}, \tag{26}$$

where $k_{c1.1}$ is the specific cutting force at the reference undeformed chip thickness, $b = h = 1mm$ is the undeformed chip width, and h is the undeformed chip thickness, and m_c is the exponent of the model. For the reference numerical scenario, the following assumptions were adopted:

$$b_{\mathrm{ref}} = a_p, \qquad h_{\mathrm{ref}} = f_z. \tag{27}$$

The resulting reference cutting force is calculated as:

$$F_{\mathrm{ref}} = k_{c1.1}\, a_p\, f_z \left(\frac{f_z}{h_0}\right)^{-m_c}. \tag{28}$$

For the adopted parameter values $k_{c1.1} = 700\ \frac{\mathrm{N}}{\mathrm{mm}^2}, a_p = 1\ \mathrm{mm}, f_z = 0{,}03\ \mathrm{mm}, m_c = 0{,}25$ the resulting force is $F_{\mathrm{ref}} \approx 50{,}46\ \mathrm{N}$.

For a force F_j acting along a translational axis, the additional motor - shaft torque required to overcome this load through a directly coupled lead screw is (Iqbal, H. et al. 2022):

$$T_{\mathrm{cut},j} = \frac{|F_j| p_j}{2\pi \eta_{p,j}\, 1000}, \qquad j \in \{X, Y, Z\}, \tag{29}$$

where $\eta_{p,j}$ denotes the efficiency of the corresponding transmission.

In the reference loading scenario, each translational axis is assessed separately under a load of magnitude $\left|F_j\right| = F_{\mathrm{ref}}$. This approach enables a direct comparison of the responses of the three translational axes under the same prescribed reference load. The conservative upper estimate of the required motor torque for this scenario is therefore:

$$T^{*,\mathrm{ref}}_{\mathrm{req},j}(t) = J_{\mathrm{eq},j}\left|\alpha_{m,j}(t)\right| + \overline{T}_{\mathrm{L},j} + T_{\mathrm{cut},j}. \tag{30}$$

The transmission efficiency and the adopted resistive torques must be defined consistently to avoid accounting for the same losses more than once. The present machining - load assessment is restricted to the translational axes. Evaluation of the rotational axes under machining conditions would additionally require determination of the moments generated by the cutting forces about the *A* and *C* axes, based on the location of the force application point and the kinematic configuration of the machine.

A dimensionless torque feasibility ratio is defined as the ratio between the available motor torque and the adopted conservative estimate of the required motor torque:

$$\eta_{T,j}(t) = \frac{T_{\text{available},j}(t)}{T^*_{\text{req},j}(t)}. \tag{31}$$

The ratio is defined for a positive required torque; when the torque demand is zero, torque availability is assessed directly. The basic torque - feasibility criterion is:

$$T_{\text{available},j}(t) \geq T^*_{\text{req},j}(t), \text{ or equivalently } \eta_{T,j}(t) \geq 1. \tag{32}$$

For design purposes, an additional safety factor $S_j > 1$ may be introduced:

$$T_{\text{available},j}(t) \geq S_j T^*_{\text{req},j}(t), \text{ or equivalently } \eta_{T,j}(t) \geq S_j. \tag{33}$$

The appropriate safety factor should be selected according to the uncertainty of the input parameters, variability of the operating loads, and drive - system requirements.

In addition to the instantaneous torque feasibility ratio, the extent of torque - criterion violation over the analysed motion may be characterized by the percentage of the total time interval during which $\eta_{T,j}(t) < 1$:

$$P_j = \frac{100\%}{T} \int_0^T \mathbf{1}_{\{\eta_{T,j}(t)<1\}}\, dt. \tag{34}$$

Here, $\mathbf{1}_{\{\eta_{T,j}(t)<1\}}$ denotes an indicator function that takes the value *1* when the torque - feasibility criterion is not satisfied and 0 otherwise. For uniformly spaced time samples, P_j may be approximated by Eq. (35). For uniformly spaced time samples, the corresponding fraction of the analysed interval can be approximated as:

$$P_j \approx \frac{N_{\eta_{T,j}<1}}{N_t}\, 100\%. \tag{35}$$

RESULTS

The numerical analysis was performed for the prescribed synthetic five-axis trajectory over a total time interval of T = 36 s, using a time step of Δt = 1ms and a common time - scaling factor of st= 3.6. For the translational axes X, Y, and Z, a screw lead of 1.25 mm/rev was adopted.

The analysis provided the time histories of the positions, velocities, and accelerations of all five axes, together with the corresponding required STEP-pulse frequencies and motor angular velocities. Conservative upper estimates of the required drive torque were subsequently calculated. The torque requirements were first evaluated without an external machining load and then, for the translational axes, with the adopted reference machining load included.

The position profiles of the three translational axes and the two rotational axes over the analysed time interval are shown in Figure 2. The corresponding minimum and maximum axis positions are summarized in Table 1.

Table 1 Position ranges of the axes during the analysed trajectory

Axis	Minimum value	Maximum value
X, mm	−34.056	45
Y, mm	20	100
Z, mm	0	69.65
A, °	0	20
C, °	0	360

During the analysed motion, the X axis position varied between −34.056 mm and 45 mm, whereas the Y axis moved monotonically from 100 mm to 20 mm. The Z axis position increased from 0 to a maximum of 69.65 mm. For the rotational axes, the A axis position remained within the range from 0° to 20°, while the C axis completed the prescribed motion from 0° to 360°.

The simultaneous variation of the three translational coordinates defines the spatial trajectory shown in Figure 3. The resulting curve represents the path generated by the prescribed X, Y, and Z coordinates of the synthetic test trajectory over the 36 s interval.

The calculated velocity and acceleration values are summarized in Table 2. Among the translational axes, the highest maximum absolute velocity was obtained for the X axis (5 mm/s), followed by the Z axis (2.9167 mm/s) and the Y

axis (2.2222 mm/s). The corresponding maximum absolute accelerations were 0.5556 mm/s², 0.2431 mm/s², and 0mm/s², respectively. The zero acceleration of the Y axis is consistent with its prescribed constant - velocity motion.

For the rotational axes, the maximum angular velocity of the A axis was 1.6667 °/s, with a maximum angular acceleration of 0.1389 °/s². The C axis maintained a constant angular velocity of 10 °/s throughout the analysed interval and therefore exhibited zero angular acceleration. The maximum velocities of all three translational axes remained within the adopted limit of 5 mm/s, while their maximum accelerations were substantially below the adopted limit of 100 mm/s².
An additional characteristic of the prescribed trajectory is evident from the initial and final axis velocities listed in Table 3. Several axes exhibit non - zero velocities at one or both ends of the analysed interval. The results therefore correspond to a segment of established motion rather than to a complete motion cycle including acceleration from rest and final deceleration to rest. Start up and stopping transients are not included in the present analysis.

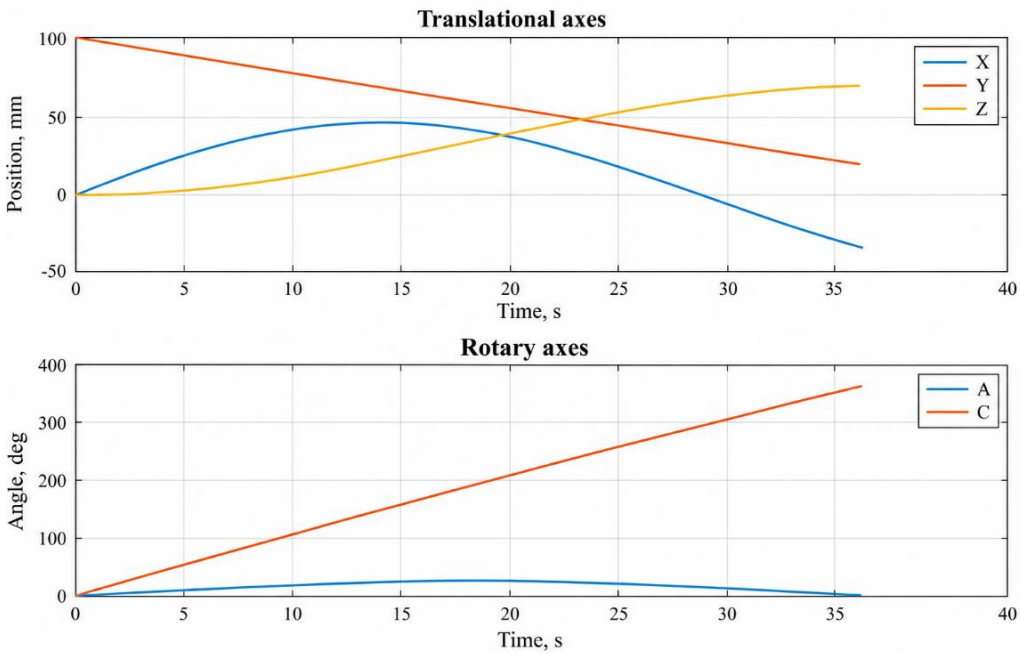

Figure 2 Position profiles of the translational and rotational axes during the analysed trajectory

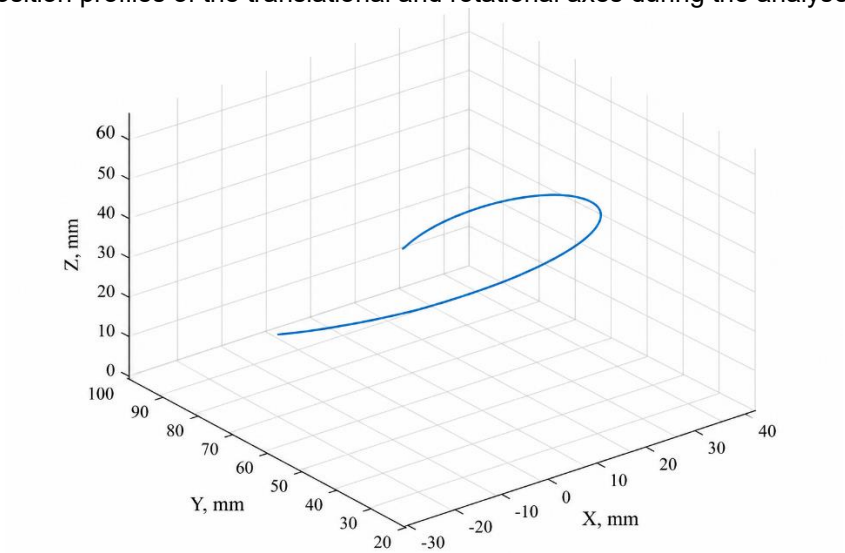

Figure 3 Spatial trajectory defined by the prescribed X – Y - Z coordinates

Table 2 Maximum absolute velocities and accelerations of the axes

Axis	Maximum absolute velocity	Maximum absolute acceleration
X	5 mm/s	0.5556 mm/s²
Y	2.2222 mm/s	0 mm/s²
Z	2.9167 mm/s	0.2431mm/s²
A	1.6667 °/s	0.1389 °/s²
C	10 °/s	0 °/s²

Table 3 Initial and final axis velocities

Axis	V_0	v_T
X	5 mm/s	−3.2682 mm/s
Y	−2.2222 mm/s	−2.2222 mm/s
Z	0.0000 mm/s	0.4116 mm/s
A	1.6667 °/s	−1.6500 °/s
C	10 °/s	10 °/s

Based on the calculated axis velocities and the adopted drive - system parameters, the required STEP - pulse frequencies and corresponding motor speeds were determined. Their time histories are presented in Figure 4, while the maximum values for each axis are summarized in Table 5.

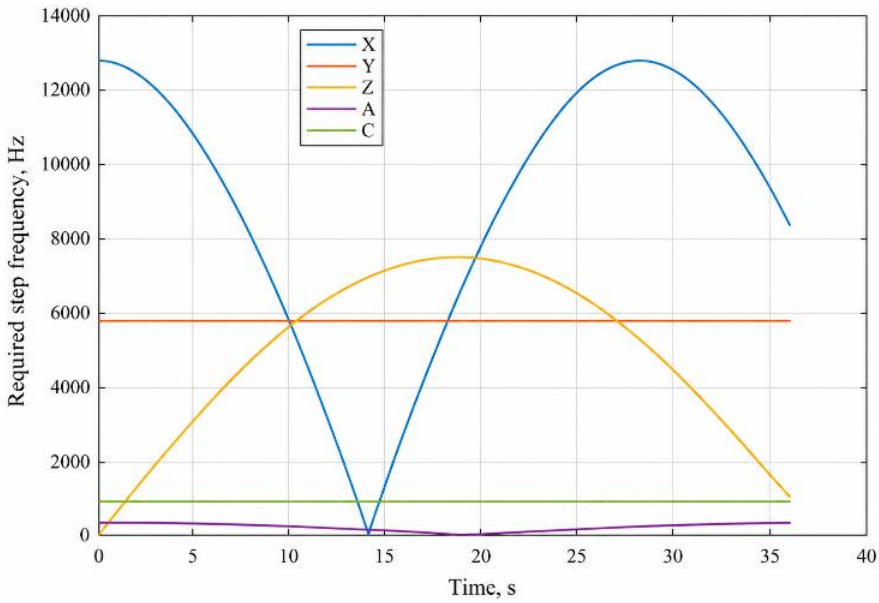

Figure 4 Required STEP frequencies during the analyzed trajectory

Table 5 Maximum STEP-pulse frequencies and motor speeds

Axis	Maximum STEP-pulse frequency	Maximum motor speed
X	12800 Hz	240 rpm
Y	5 688.89 Hz	106.67 rpm
Z	7 466.67 Hz	140 rpm
A	296.30 Hz	5.56 rpm
C	888.89 Hz	16.67 rpm

The required STEP - pulse frequencies follow the prescribed velocity profiles and therefore differ considerably among the individual axes. The *X* axis imposed the highest control - frequency demand, reaching a maximum of 12.8 kHz, followed by the *Z* and *Y* axes at 7.47 kHz and 5.69 kHz, respectively. The requirements of the rotational axes were substantially lower, with maximum frequencies of 0.296 kHz for the *A* axis and 0.889kHz for the *C* axis. The constant STEP - pulse frequency of the *Y* axis reflects its constant prescribed velocity. All calculated maximum STEP - pulse frequencies remained below the adopted limit of 20 kHz. The corresponding maximum motor speeds were 240 rpm for the *X* axis, 106.67rpm for the *Y* axis, and 140rpm for the *Z* axis. Considerably lower motor speeds were obtained for the rotational axes, with maximum values of 5.56 rpm for the *A* axis and 16.67 rpm for the *C* axis.

The dynamic requirements were subsequently evaluated using the equivalent moments of inertia, calculated motor angular accelerations, and adopted upper bounds of the non-inertial loads. Figure 5 compares the conservative upper estimates of the required motor torque for the translational axes under the two considered operating conditions: motion without the reference machining load and motion with the reference load included. The introduction of the reference load resulted in a clear increase in the required torque of all three translational axes. In contrast, the temporal variation of the required torque within each operating condition remained relatively small. This indicates that, under the adopted model assumptions, the difference between the two loading conditions has a considerably greater influence on the calculated torque demand than the inertial contribution associated with the prescribed trajectory.

Without the reference machining load, the maximum required torque was 0.020008 Nm for the *X* axis, 0.03 Nm for the *Y* axis, and 0.030005 Nm for the *Z* axis. For the rotational axes, the corresponding maximum values were

0.040001 Nm for the *A* axis and 0.015Nm for the *C* axis. The highest value among all five axes was therefore obtained for the *A* axis, as summarized in Table 6.

Application of the simplified Kienzle model yielded a reference cutting - force magnitude of *Fref* = 50.459 N. For the adopted screw lead of 1.25 mm/rev and a transmission efficiency of 0.85, this reference load corresponded to an additional torque of *Tcut* = 0.01181 Nm for each of the three translational axes.

DISCUSSION

The obtained results show that the adopted common time scaling enables the prescribed synthetic five-axis trajectory to be executed with relatively modest kinematic demands on the translational axes. The maximum linear velocity was 5mm/s for the *X* axis, while the corresponding values for the *Y* and *Z* axes were 2.2222 mm/s and 2.9167 mm/s, respectively. At the same time, the maximum translational accelerations remained well below the adopted limit of 100 mm/s². This behaviour is a direct consequence of the applied time scaling, which preserves the geometric form of the prescribed trajectory and the relative synchronization of the axes while reducing the associated velocity and acceleration demands.

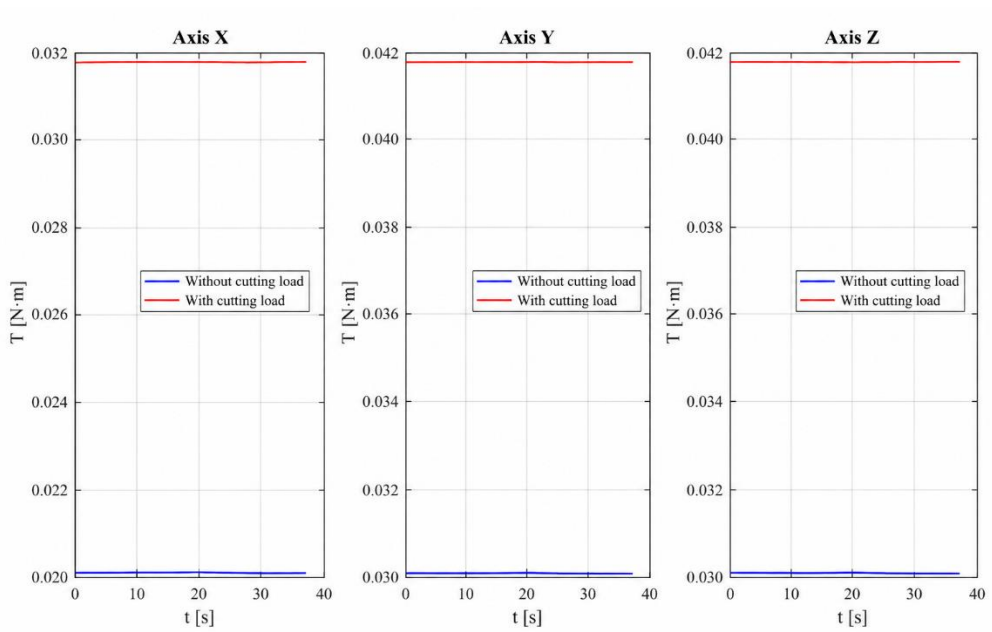

Figure 5 Conservative upper estimates of the required drive torque for the translational axes without and with the reference load

Table 6 Maximum required motor torques without the reference machining load

Axis	Maximum required torque, Nm
X	0.020008
Y	0.03
Z	0.030005
A	0.040001
C	0.015

The calculated results showed that the maximum absolute velocities and accelerations of all three translational axes remained within the limits adopted for the present preliminary analysis. However, these results apply only to the prescribed smooth trajectory segment and do not include acceleration from rest or final deceleration to rest. This distinction is important because the dynamic requirements of five-axis motion are strongly affected by trajectory continuity. Zhang, H. et al. (2024) showed that tangent and curvature discontinuities between consecutive linear tool-path segments may cause deceleration and fluctuations in axis velocities and accelerations. Consequently, the relatively low acceleration values obtained in the present study should not be interpreted as an inherent dynamic characteristic of the developed machine, but rather as a consequence of the particular trajectory and time-scaling factor adopted. Furthermore, the analysed interval does not include acceleration from rest or final deceleration to rest. Several axes exhibit non-zero velocities at the boundaries of the interval, indicating that the prescribed trajectory represents a segment of established motion. The inclusion of start-up and stopping transients could therefore result in higher acceleration levels and, consequently, greater inertial torque demands.

From the perspective of stepper-motor control, the highest required STEP-pulse frequency was obtained for the X-axis, reaching 12.8 kHz, which corresponds to 64% of the adopted numerical limit of 20 kHz. The corresponding maximum frequencies for the Y and Z axes were 5.69 and 7.47 kHz, espectively, while substantially lower values were obtained for the rotational axes. This distribution follows directly from the kinematic requirements and transmission characteristics of the individual axes, since the required STEP-pulse frequency depends on the motor speed and the number of commanded pulses per motor revolution. Within the adopted numerical framework, none of the five axes exceeded the 20 kHz criterion. However, this result should not be interpreted as experimental confirmation of the capability of a specific control system. The 20 kHz value was introduced solely as a criterion for the preliminary numerical assessment and does not represent an experimentally verified frequency limit of the actual controller–driver configuration.

Moreover, meeting the STEP - frequency requirement alone does not establish the dynamic feasibility of a stepper - motor drive. Dynamic feasibility also depends on whether the motor can provide the required torque at the corresponding operating speed. In an open - loop stepper drive, exceeding the available dynamic torque may result in loss of synchronism, skipped steps, or motor stalling. Therefore, stepper - motor operating capability should be evaluated using the pull - out torque - speed characteristic of the selected motor - driver combination, which represents the limiting load torque that can be sustained at a given steady operating speed without loss of synchronism (Hughes, A. and Drury, B. 2019; Campbell, A. A. R. et al., 2014). Since the available torque generally decreases with increasing motor speed, satisfaction of the STEP - frequency criterion cannot be treated as evidence that the required torque can also be delivered.

This distinction is essential for interpreting the present torque results. Although a nominal holding torque of 0.40Nm was adopted for the considered NEMA 17 motor, this value cannot be directly treated as the torque available during motion. Holding torque is a static characteristic specified at standstill, whereas the torque available during continuous operation depends on motor speed and on the electrical characteristics of the selected motor - driver combination. Campbell, A. A. R. et al. (2014) similarly emphasized that a stepper motor with a relatively high holding torque may nevertheless provide substantially lower torque at higher operating speeds and that the complete torque - speed characteristic should therefore be considered during motor selection. Hughes, A. and Drury, B. (2019) also identify the torque - speed relationship as a fundamental limitation of stepper - motor operation. This distinction is further reflected in the manufacturer guidance provided by Oriental Motor, which differentiates holding torque from pull - out torque and associate's operation beyond the pull - out torque - speed boundary with loss of synchronism.

This interpretation complements existing motor-selection procedures for customized multi-axis CNC systems. Iqbal, H. et al. (2022) considered motor selection for a low-cost five-axis CNC machine with an X-Y-Z-A-C configuration intended for educational and light manufacturing applications. Their procedure accounts for the mechanical configuration of the individual axes, the required drive torque, the inertia of the moving components, and the corresponding transmission arrangements. In this respect, their system is conceptually similar to the experimental platform investigated in the present study. The present analysis extends this perspective by emphasizing that, for a stepper-motor-driven system, torque feasibility cannot be established solely from the nominal or holding-torque specification. Instead, the required torque should ultimately be compared with the torque available from the selected motor–driver combination at the corresponding instantaneous operating speed.

The introduction of the reference machining load noticeably increased the torque requirements of the translational axes. The simplified Kienzle model yielded a reference cutting force of 50.45 N, corresponding to an additional motor - shaft torque of 0.01181 Nm. Consequently, the maximum required torque increased from 0.020008 Nm to 0.031818 Nm for the X axis and from approximately 0.03 Nm to 0.04181 Nm for the Y and Z axes. These increases show that the reference machining load represents a substantial part of the total torque demand. However, the Kienzle coefficients depend on the workpiece material, cutting speed, tool geometry, and other process conditions (Klippel, H. et al. 2024). Therefore, the calculated force should be interpreted as an idealized reference load rather than as a prediction of the resultant force generated during actual five - axis milling. Applying this force independently to the X, Y, and Z axes enables a controlled comparison of their drive requirements but does not represent the Cartesian decomposition of an actual cutting - force vector.

The obtained results provide a preliminary characterization of the drive - torque requirements and complement the motor - selection procedure for a comparable low - cost X-Y-Z-A-C CNC configuration presented by Iqbal, H. et al. (2022). However, they do not yet constitute final confirmation of the dynamic feasibility of the selected drives. Such confirmation requires the experimentally validated operating characteristics of the actual drive system.

Moreover, sufficient torque availability alone does not guarantee reliable stepper-motor operation. Excessive acceleration, inadequate drive conditions, and operation within resonance regions may also cause skipped steps or motor stalling (Campbell, A.A.R. et al. 2014). Experimental validation should therefore include realistic acceleration and deceleration profiles and a comparison between commanded and measured axis positions, as applied in the assessment of a stepper - driven tabletop CNC system by Rao S.S. et al. (2026). More generally, Halamka et al. (2021) demonstrated the importance of experimentally identified axis-dynamics models for the simulation and optimization of machine-drive control. Accordingly, a subsequent stage of the present research should include

experimental determination of the torque–speed characteristics of the selected NEMA 17 motor–driver combinations, implementation of realistic start-up and stopping profiles, and measurement of the resulting axis-position errors. Such validation would provide the experimental basis required for applying the proposed torque - feasibility ratio as a quantitative criterion for assessing dynamic feasibility.

These considerations are directly relevant to the planned development of a DT of the experimental machine. A representative CNC DT should extend beyond machine geometry and incorporate the kinematic, dynamic, drive, control, and process - related behaviour of the physical system. Scaglioni, B. and Ferretti, G. (2018), for example, developed a dynamic machine - tool model that integrates structural flexibility, the cutting process, transmission chains, and control systems, and validated its dynamic behaviour experimentally. Similarly, Shen, W. et al. (2020) proposed a Digital-Twin-based virtual commissioning approach that combines geometric, kinematic, and dynamic representations to support kinematic and dynamic commissioning, servo- system evaluation, and virtual machining. These studies confirm that the kinematic and torque models developed in the present analysis represent necessary components of the planned DT, while experimental identification and validation remain essential for achieving correspondence with the physical machine.

In this context, the analysis presented in this study should be regarded as an intermediate step between the previously developed and kinematically verified virtual model (Bošković, J. et al., 2026) and a future data - connected DT, rather than as a complete dynamic representation of the machine. Following the mechanical integration of the experimental system, the adopted equivalent inertias, resistive torques, transmission efficiencies, and drive characteristics should be identified or verified using measurements obtained from the physical machine. Scaglioni, B. and Ferretti, G. (2018) similarly demonstrated the importance of experimentally validated dynamic machine - tool models incorporating structural behaviour, transmission chains, control systems, and machining loads. Incorporating experimentally determined parameters and measured operating data into the present virtual model would enable its progressive refinement and improve its correspondence with the physical CNC system. Such an approach is consistent with Ward, R. et al. (2021), who integrated real - time CNC position and velocity data, model - based simulations, cutting - force estimation, and online feedback within a machining DT.

CONCLUSIONS

This study extended the previously developed kinematic model of an experimental five - axis CNC milling machine by introducing a preliminary assessment of the kinematic and dynamic requirements of the X, Y, Z, A, and C axis drives. For the analysed time - scaled synthetic trajectory, the translational axes remained within the velocity and acceleration limits adopted for the numerical analysis. The required STEP - pulse frequencies of all five axes also remained below the adopted criterion of 20 kHz, with the highest value of 12.8 kHz obtained for the X axis.

The calculated torque requirements were comparatively low for the considered motion without an external machining load. Introducing the Kienzle - based reference load increased the maximum torque requirements of the translational axes by approximately 59% for the X axis and 39.4% for the Y and Z axes. These results demonstrate that external process loading can contribute substantially to the overall drive demand and should therefore be considered together with the kinematic requirements when evaluating the suitability of the proposed stepper - motor drives. However, the adopted cutting force represents an idealized reference loading scenario and not a prediction of the resultant force generated during actual five - axis milling.

At the present stage, the results should be regarded as a preliminary assessment rather than as final confirmation of the dynamic feasibility of the selected NEMA 17 drives. Such confirmation requires experimentally determined torque - speed characteristics of the actual motor - driver combinations, identification of the relevant mechanical parameters, implementation of realistic start up and stopping profiles, and validation of the numerical model on the physical system. These steps will enable further refinement of the dynamic model and provide a basis for the subsequent development of a data - connected DT of the experimental five - axis CNC machine.

ACKNOWLEDGMENTS

The results presented in this paper were obtained through research conducted within projects financially supported by the Ministry of Science, Technological Development and Innovation of the Government of the Republic of Serbia, under Contract No. 451-03-34/2026-03/200107, dated 5 February 2026.

The authors also gratefully acknowledge Zastava TERVO d.o.o. for its support within activities related to the introduction of new technologies and the further development of existing ones

REFERENCES

Amouzgar, K., Wang, W., Eynian, M., & Ng. A.H.C. (2025). Smart process planning of crankshaft machining through multiple objectives optimization. *Procedia CIRP*, 134, 241-246. https://doi.org/10.1016/j.procir.2025.03.018

Bošković, J., Ivković, M., Pantić, M., Grujić, I., Živković, B., Petrović Savić, S., & Erić, M. (2026). Modeliranje i kinematska analiza petoosne glodalice. 45. JUPITER konferencija, Jun 2026, Inovacioni centar Mašinskog fakulteta u Beogradu, Univerzitet u Beogradu - Mašinski fakultet, 3.18. ISBN 978-86-6060-250-5

Campbell, A.A.R., Eifert, R. W., & Turner, G.C. (2014). Openstage: A Low-Cost Motorized Microscope Stage with Sub-Micron Positioning Accuracy. *PLOS One*, 24586468. https://doi.org/10.1371/journal.pone.0088977

Chu, C.-H., Zhou, Y., Liu, E.-M., & Tang, J. (2022). Optimal tool path generation and cutter geometry design for five-axis CNC flank milling of spiral bevel gears. *Journal of Computational Design and Engineering*, 9, 2024-2039. https://doi.org/10.1093/jcde/qwac103

Escudero, G.G., Bo, P., González-Barrio, H., Calleja-Ochoa, A., Bartoň, M., Norberto López de Lacalle, L. (2022). 5-axis double-flank CNC machining of spiral bevel gears via custom-shaped tools—Part II: physical validations and experiments. The International Journal of Advanced Manufacturing Technology, 119, 1647-1658 https://doi.org/10.1093/jcde/qwac103

Hafez, I., & Dhaouadi, R. (2025). Parameter Identification of a Flexible-Joint Robot Axis using Sinusoidal Position Tracking. *Journal of Intelligent & Robotic Systems*, 111(41). https://doi.org/10.1007/s10846-025-02244-1

Halamka, V., Moravec, J., Beneš, P., Neusser, Z., Koubek, T., Valášek, M., & Šika, Z. (2021). Drive axis controller optimization of production machines based on dynamic models. *The International Journal of Advanced Manufacturing Technology*, 116, 1277-1293. https://doi.org/10.1007/s00170-021-07160-w

Hughes, A., & Drury, B. (2019). *Stepping and switched reluctance motors*. In Electric Motors and Drives (Fifth Edition). (pp. 375-409). Newnes. https://doi.org/10.1016/B978-0-08-102615-1.00010-6

Iqbal, H., Khan, M. M. A., Ahmed, I., Yousuf, H., Khan, H., & Uddin, R. (2022). Design Procedure for Motor Selection in Custom-Made Multi-Axis CNC Machines. *Engineering Proceedings*, 20(1), 29. https://doi.org/10.3390/engproc2022020029

Klippel, H., Süssmaier, S., Zhang, N., Kuffa, M., & Wegener, K. (2024). Large-scale investigation of dry orthogonal cutting experiments Ti6Al4V and Ck45. *The International Journal of Advanced Manufacturing Technology*, 29, 2871-2908. https://doi.org/10.1007/s00170-024-14597-2

Liu, S. (2024). Structural design of a novel rotary platform 3D printer. *Journal of Physics Conference Series*, 2798(1), 012023. https://doi.org/10.1088/1742-6596/2798/1/012023

Lu, Z., Huo, G., & Jiang, X. (2023). Anovelmethod to minimize the five-axis CNC machining error around singular points based on closed-loop inverse kinematics. *The International Journal of Advanced Manufacturing Technology*, 128, 2237-2249. https://doi.org/10.1007/s00170-023-11991-0

Onodera, S., Tanaka, F., & Onosato, M. (2025). Eccentric machining using feature - based simultaneous four - axis machining using STEP - NC. *The International Journal of Advanced Manufacturing Technology*, https://doi.org/10.1007/s00170-025-16474-y

Rao, S.S., Padhi, S.N., & Bharadwaja, K. (2026). IoT-Driven Electronics Framework for Tabletop CNC Machines: Design, Implementation, and Performance Analysis. PREPRINT (Version 1) available at Research Square. https://doi.org/10.21203/rs.3.rs-10660733/v1

Sarwar, S. (2024). *Exploring the possibilities of collaboration in 5-axis mobile 3D printing*. MSc Thesis. Asian Institute of Technology School of Engineering and Technology Thailand. https://doi.org/10.13140/RG.2.2.23000.61446

Scaglioni, B. & Ferretti, G. (2018). Towards digital twins through object-oriented modelling: a machine tool case study. *IFAC-PapersOnLine*, 51, 613-618. https://doi.org/10.1016/j.ifacol.2018.03.104

Shen, S., Hu, T., Yin, Y., He, J., Tao, F., & Nee A.Y.C. (2020) Digital twin based virtual commissioning for computerized numerical control machine tools. In F. Tao, A. Liu, T. Hu, & A.Y.C. Nee (Eds) Digital Twin Driven Smart Design, Elsevier, 289-307. https://doi.org/10.1016/B978-0-12-818918-4.00011-7

Ward, R., Sun, C., Dominguez - Caballero, J., Ojo, S., Ayvar - Soberanis, S., Curtis, D., & Ozturk, E. (2021). Machining Digital Twin using real - time model - based simulations and lookahead function for closed loop machining control. *The International Journal of Advanced Manufacturing Technology*, 117, 3615–3629. https://doi.org/10.1007/s00170-021-07867-w

Yan, J. (2022). Noncontact Defect Detection Method of Automobile Cylinder Block Based on SVM Algorithm. *Mobile Information Systems*, 2022, 5849422. https://doi.org/10.1155/2022/5849422

Zhang, H., Wu, Y., Shen, Z., Zhang, P., Li, H., Lou, F. (2024). Five-axis path smoothing based on sliding convolution windows for CNC machining. *CIRP Journal of Manufacturing Science and Technology*, 49, 80-94. https://doi.org/10.1016/j.cirpj.2024.01.001

The 11th International Congress
Motor Vehicles & Motors 2026
Kragujevac, Serbia
October 8th - 9th, 2026

Motor Vehicles & Motors

MVM2026-012
https://doi.org/10.24874/CMVM2026.012
Review paper

Saša Vasiljević[1]
Jasna Glišović[2]
Slobodan Vasiljević[3]

ANALYSIS OF EXPERIMENTAL METHODOLOGIES FOR TESTING INNOVATIVE BRAKE SOLUTIONS

ABSTRACT: The development of the automotive industry, as well as the development of modern on-board systems, require detailed tests from the aspect of functionality and safety of the developed systems. The implementation of new materials, sensors and new braking systems requires advanced, reliable and highly accurate evaluation methods. This paper is dedicated to a comprehensive analysis of modern experimental methodologies used to test innovative brake solutions. The paper presents a detailed analysis of three types of experimental approaches to testing innovative brake solutions, i.e. the brake testing in laboratories, field tests and computer simulations. By analyzing the advantages and limitations of each of the mentioned approaches, the paper indicates the necessity of integrating hybrid testing methods (so-called Hardware-in-the-Loop - HiL systems), which successfully bridge the gap between isolated laboratory conditions and the complexity of real traffic.

KEYWORDS: experiment, methodology, brakes, system, innovations

ANALIZA EKSPERIMENTALNIH METODOLOGIJA PRI ISPITIVANJU INOVATIVNIH REŠENJA KOČNICA

REZIME: Razvoj automobilske industrije, kao i razvoj savremenih sistema na vozilu, zahtevaju detaljna ispitivanja sa aspekta funkcionalnosti i bezbednosti razvijenih sistema. Implementacija novih materijala, davača i novih načina rada sistema za kočenje zahteva napredne, pouzdane i visoko precizne metode evaluacije. Ovaj rad posvećen je sveobuhvatnoj analizi savremenih eksperimentalnih metodologija koje se koriste za ispitivanje inovativnih rešenja kočnica. U radu je prikazana detaljna analiza tri vrste eksperimentalnih pristupa ispitivanja inovativnih rešenja kočnica, odnosno ispitivanje kočnica u laboratorijama, terenska ispitivanja i računarske simulacije. Analizom prednosti i ograničenja svakog od navedenih pristupa, rad ukazuje na neophodnost integracije hibridnih metoda testiranja (tzv. Hardware-in-the-Loop - HiL sistemi), koje uspešno premošćuju jaz između izolovanih laboratorijskih uslova i kompleksnosti realnog saobraćaja.

KLJUČNE REČI: eksperiment, metodologija, kočioni sistem, inovacije

[1] *Saša Vasiljević, lecturer, Academy of Professional Studies Šumadija, Kragujevac, svasiljevic@asss.edu.rs, https://orcid.org/0000-0002-2235-1309*
[2] *Jasna Glišović, Full Professor, Faculty of Engineering University of Kragujevac, Kragujevac, Kragujevac, jaca@kg.ac.rs, https://orcid.org/0000-0002-8251-1722*
[3] *Slobodan Vasiljević, Despotovac, boba.vasiljevic2@gmail.com*

INTRODUCTION

The braking system is one of the most important systems when it comes to traffic and vehicle safety. Any failure of the braking system can have a significant impact on the occurrence of a traffic accident with consequences that can be fatal for humans (Haq, M. T. et al. 2023). According to data from LookupAPlate (2023), brake failures directly cause 0.44% of all traffic accidents, or about 264,000 accidents per year in the USA. Brake problems are the most common technical cause of accidents, accounting for 22% of all crashes caused by critical vehicle failures, while the risk of fatal accidents is significantly higher in older vehicles and heavy trucks. Similar data is presented in the report Arrive Alive (2026), which indicates that the braking system has an impact on a total of 25.05% of traffic accidents, considering only the vehicle factor, while in the total factors that influence the occurrence of a traffic accident, it has an impact of 2.29%.

In addition to all the consequences that can be caused by brake failure, an additional problem can arise when applying some of the modern innovative solutions to the braking system. The application of innovative solutions in the case of brakes represents a very big problem if the solutions are not sufficiently tested, so this can lead to greater unreliability in the application or some unforeseen failures. Today, the problem is perhaps even more complex than before, considering that modern vehicles generally combine mechanics and electronics. Therefore, tests must be conducted from the aspect of mechanical elements and the reliability of such parts of the braking system, and on the other hand, tests of the operation of electronics and algorithms according to which the operation of the system itself functions. Thus, today a large number of research on braking systems relates to the analysis of the validity of the algorithm according to which the electronic part of the braking system is activated and functions. According to Pfister et al. (2025), the development of braking technologies is particularly complex due to the interdisciplinary nature of the systems involved, which include multiple software and hardware subsystems interacting in different physics. These complexities are intensified when the systems must meet stringent performance, safety, and regulatory testing requirements on different platforms. The integration of these disparate components often leads to long product development timelines and an increased risk of costly late-stage failures.

Advanced experimental methods and techniques are used to test braking systems and innovations related to the braking system today. Tests are performed at different levels and by applying various combined test methods. The goal of such tests is to analyze the reliability of the system itself and of individual system components. In addition to testing the braking system itself, the analysis of the validity of the functioning is often also tested for the quality of integration of electronic and mechanical components of the system. Experimental methodologies described in the scientific literature rely on a structured testing hierarchy to validate braking innovations. These methods evaluate new brake-by-wire mechanics, sustainable friction materials, regenerative energy mixing and environmental impact profiles.

Considering the complexity of innovative solutions related to the braking system and, on the other hand, the importance of the braking system, the paper analyzes the experimental methods that have been and are used in researching innovations related to braking systems. In addition to the innovative solutions themselves, an analysis of the requirements placed on experimental technologies was performed. The aim of this paper is precisely to introduce modern experimental systems that are used in the analysis and verification of innovations related to the braking process and braking system.

REQUIREMENTS FOR MODERN EXPERIMENTAL BRAKE INSTALLATIONS

Brake innovation testing procedures combine advanced laboratory setups, inertial dynamometers, and real-world testing to evaluate mechatronic components, brake-by-wire systems, and friction materials. The procedure for testing innovative technical solutions in motor vehicle braking systems is a complex scientific and professional process aimed at verifying safety performance, functional stability, and reliability before their serial application. Depending on the nature of the innovation itself — whether it is new composite brake element materials, advanced stability control algorithms, or Brake-by-Wire systems — the tests are strictly codified (CITA, 2025). Scientific papers classify experimental testing for innovative vehicle brakes into four progressive levels, as shown in Figure 1, (Kumbhar, N. et al. 2016).

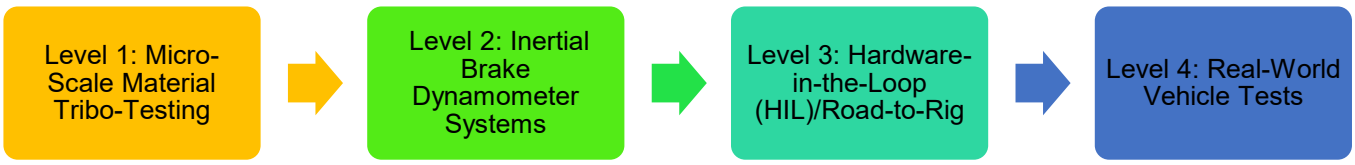

Figure 1 Levels of experimental testing of innovations in the case of braking systems

The primary regulatory framework in Europe and associated countries consists of the international regulations of the Economic Commission of the United Nations for Europe, more precisely UN ECE R13 for heavy commercial vehicles and UN ECE R13-H for passenger vehicles, while in the Republic of Serbia the processes of homologation and controlled attestation are carried out under the supervision of the Traffic Safety Agency (ABS) (DTC, 2026; United Nations Economic Commission for Europe, 2014; United Nations Economic Commission for Europe, 2021).

The experimental development of the innovation begins in laboratory conditions through the phases of numerical simulations (finite element method, modeling in environments like MATLAB/Simulink) and static tests of subsystems. A key step in this phase is Hardware-in-the-Loop (HIL) testing, where the actual Electronic Control Unit (ECU) is integrated with a computer model of vehicle dynamics to analyze the response time and transient characteristics of the system in milliseconds. After successful laboratory verification, the brake system prototype is installed in a dedicated test vehicle and subjected to rigorous testing on closed training grounds with dedicated tracks.

According to the requirements of the homologation protocols, the innovation must successfully pass three standardized groups of efficiency and thermal endurance tests, known as the Type 0, Type I and Type II cycles. Test Type 0 (testing of cold brakes) defines the measurement of the minimum stopping distance and the mean fully developed deceleration (MFDD) at defined initial speeds, with the initial temperature of the brake discs below 100 °C. Test Type I (test of loss of efficiency or Fade Test) implies a series of successive braking and acceleration in short time intervals with the aim of causing extreme thermal load of the brake pairs, whereby the innovative system must not show a drop in efficiency below the law prescribed percentage. The Type II test evaluates the long-term durability of the system when simulating long downhills under constant braking load.

Vehicle stability and distribution of braking force in critical situations represent an elimination criterion for any technical innovation. For this purpose, dynamic tests are carried out on so-called "split" surfaces, where one side of the vehicle brakes on a surface with a high coefficient of adhesion (dry asphalt), while the other side is on a surface with a low coefficient (ice or wet film). Innovative systems for managing the dynamics of braking must, in these asymmetric conditions, ensure that the direction of movement of the vehicle is maintained without the intervention of the driver on the steering wheel beyond the permitted limits, minimizing the risk of drifting or rotation of the vehicle.

When the innovation includes electronic components, microcontrollers or software algorithms (such as electro-mechanical brakes - EMB), the validation process extends to functional safety and cyber security standards. According to the international standard ISO 26262 (Road vehicles - Functional safety) (International Organization for Standardization, 2018), braking systems are categorized under the strictest level of safety integrity - ASIL D (PatSnap, 2026). This requires designers to implement hardware and software redundancy (e.g. backup subsystems of power supply and signal transmission) that guarantee that the system, in the event of a primary failure of the electronics, will go into a safe state and enable the vehicle to stop safely. Additionally, in accordance with the latest UN ECE R155 and R156 regulations, system resistance tests against unauthorized external intrusions and cyber threats are performed if the brake system supports wireless software updates (Over-the-Air).

DYNAMOMETER TESTS OF BRAKE INNOVATIONS

Dynamometer tests (dyno testing), which is shown in Figure 2, represent a key step in the development of brake innovations. They enable laboratory simulation of real driving conditions and extreme loads without the need for expensive and risky tests on the track. In the modern auto industry, tests are performed on sophisticated brake inertial dynamometers (Sporysz, B. 2024). They simulate the mass and inertia of the vehicle using heavy rotating flywheels or advanced electric motors with load simulation.

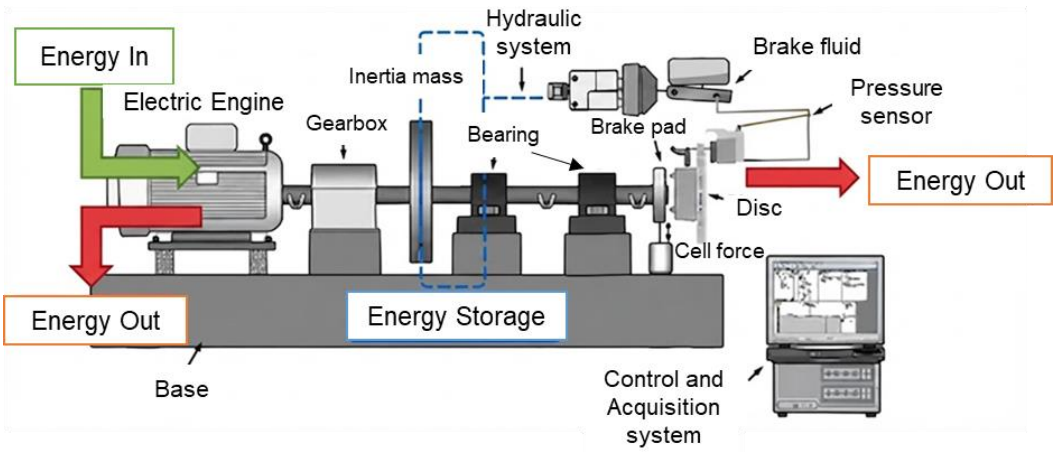

Figure 2 Inertial brake dynamometer for testing regenerative braking (Mendoza & Squadrani 2021)

Modern test benches, like advanced systems, consist of several subsystems:

- Drive electric motors are powerful AC motors (often over 400 kW) that accelerate the assembly to precisely defined speeds (and over 3500 rpm),
- Mechanical flywheels (Inertia), which is a combination of massive discs that store kinetic energy. Modern systems combine physical inertia with electrical simulation,
- Climatic chamber and environment simulation where there are closed systems that allow testing in the range from -40 °C to +50 °C, with sprinklers for water, salt water or snow.

Dynamometer tests of innovations follow strict global standards (eg SAE J2522 for brake material performance or SAE J3211 for vehicles with regenerative braking). During multi-day cycles, the following phases are executed:

- Burnishing/Bedding, which represents a series of 100 to 200 lighter braking operations so that the new pads fit perfectly on the disc and stabilize the friction.
- Maximum performance, which is performed by braking at speeds over 150 km/h with a pressure of up to 200 bar, which checks the maximum power and durability of the system.
- Thermal weakening (Fade & Recovery) which includes successive, aggressive braking that raises the disc temperature above 600 °C. The loss of braking power due to overheating is monitored, as well as the speed of recovery during cooling.
- Noise and vibration testing (NVH). Braking at different angles and pressures (mostly at lower speeds) inside the sound chamber to detect screeching or shaking.
- Particle emission measurement where it is necessary to close the assembly in a special chamber for the collection and measurement of microparticles (PM_{10} and $PM_{2.5}$) that are produced by material wear, which is key to the new Euro 7 environmental standards.

The use of an inertial brake dynamometer (Inertial Brake Dynamometer) is crucial for testing innovations for several reasons that cannot be replicated with classic laboratory tests:

- Realistic vehicle mass simulation: Instead of simply spinning a disc, this device uses massive, adjustable flywheels that physically store the exact kinetic energy of the vehicle in motion. When the brake is applied, it must stop the "real" weight of the car.
- Total safety during destructive tests: Innovations are often tested to the point of complete failure (eg bursting a disc or melting a wafer at 800 °C). On the dynamometer you do it without any risk to the life of the test driver or the destruction of the prototype vehicle.
- Perfect repeatability of the cycle (Reproducibility): On the track, the wind, air temperature and asphalt condition are constantly changing. A dynamometer in the laboratory allows the exact same test (e.g. 100 consecutive braking from 120 km/h to 0 km/h) to be repeated to millisecond and degree Celsius accuracy, which is necessary for a scientific comparison of old and new technology.
- Isolation and micron measurements: Because the assembly is fixed, engineers can place ultra-sensitive thermal imaging cameras, laser sensors to measure disc micro-wear, and highly sensitive noise (NVH) microphones, which is impossible to do in the wheel of a car speeding down a track.
- Simulation of extreme climatic conditions: Dynamometers enclosed in climate chambers can change conditions from Siberian -40 °C with salt spray (corrosion testing of innovative coatings) to desert +50 °C within minutes, speeding up the testing process by several months.

Although it brings enormous advantages, the use of an inertial brake dynamometer has two key drawbacks: the extremely high cost and the laboratory isolation of the hardware. The devices themselves, accompanying software and air-conditioned chambers cost hundreds of thousands of euros, and the complex assembly and calibration of each new prototype requires a lot of time and highly educated engineers. In addition, the consumption of electricity to drive massive flywheels and simulate high speeds drastically raises the operating costs of testing. Another big minus is the impossibility of perfect replication of the real world, primarily in terms of cooling and vehicle mechanics. On the dynamometer, the air cooling of the brake is simulated with artificial fans, which can never completely accurately convey the complex aerodynamics and the swirling of air around the wheel in motion. Also, the fixed laboratory assembly completely ignores the influence of the suspension, chassis vibrations and the real weight change of the vehicle during braking, which is why the final confirmation of the innovation must still be carried out on a real track.

EXPERIMENTAL TESTS OF BRAKES IN LABORATORY CONDITIONS

Experimental tests of brake system innovations in laboratory conditions (Figure 3) represent the first phase of physical validation of new solutions. Before the system is installed in an actual vehicle, the components are tested in a strictly controlled environment. The laboratory provides ideal conditions for the isolation of specific phenomena without the influence of external factors such as wind, weather or human error of the driver. In laboratory conditions, it is possible to test complete real vehicles, as well as individual parts of brake systems or specific brake innovations. Modern research centers are designed as modular systems, which allows engineers to adjust the level of testing depending on the stage of development in which the project is located. In this way, maximum flexibility is ensured, because the

technology can be checked from the level of raw material all the way to its full integration into the finished car (Markel, A. 2005).

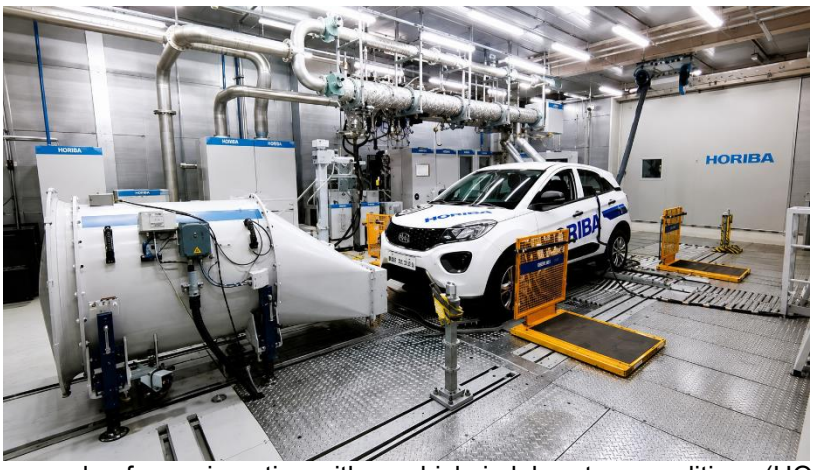

Figure 3 An example of experimenting with a vehicle in laboratory conditions (HORIBA, (n.d.))

For indoor testing of complete real vehicles, massive dynamometers with rollers (Chassis Dynamometers) are used, which are often located inside advanced climatic wind tunnels. The real vehicle is fixed with wheels on metal rollers that faithfully simulate road resistance, mass and inertia of the car in motion. A driver or robot-automator controls the vehicle inside the laboratory, while simulated winds of over 150 km/h and extreme temperatures from -40 °C to +50 °C enable safe monitoring of brake operation, ABS/ESP electronics and heat distribution throughout the chassis.

When developing a completely new concept or individual component, there is no need to spend resources on the entire vehicle, but only the targeted parts of the system are mounted on the laboratory benches. On inertial dynamometers for components, only one wheel assembly is isolated to analyze in detail innovative pad friction materials, anti-rust coatings or environmental particulate emissions. In addition, special robotic actuators perform material fatigue tests by pressing the brake calipers or master cylinder hundreds of thousands of times without stopping, checking the durability of the seals under extreme pressures.

This approach is particularly important for the development of modern Brake-by-Wire systems, where only electronics and mechatronics can be tested in the laboratory, completely separated from mechanical discs. Engineers place only an electronic brake pedal, sensors and a drag simulator on the test bench to calibrate software algorithms and check fail-safe modes in case of failure. Only when the individual part of the braking system proves its reliability and safety in these isolated laboratory cycles, it moves to the stage of its integration and testing at the level of the complete vehicle.

Testing of brake system innovations brings key benefits that directly affect the safety, ecology, performance and economic viability of new technologies before they reach the market. Here are the main benefits and reasons why conducting these rigorous tests is necessary:

- Brakes are the most important safety system on a vehicle. Detailed tests ensure that innovations (such as new alloys or software) function flawlessly in critical situations, reducing the risk of brake failure,
- New environmental standards for the first time limit the emission of particles that are caused by brake wear. Testing of innovative hard disc coatings (e.g. tungsten carbide) and new disc compounds directly proves a reduction of harmful PM_{10} and $PM_{2.5}$ particles by over 60%,
- In the case of electric and hybrid vehicles, the tests enable the perfect blending of electric motor braking and classic brakes. This maximizes the return of energy to the battery and extends the range of the vehicle, while maintaining a natural feel on the pedal,
- Electronic brake tests allow engineers to create faster response systems (under 100 milliseconds). This drastically shortens the stopping distance and enables better integration with ADAS systems for autonomous emergency braking,
- Through a combination of virtual simulations, HiL systems and laboratory tests, engineers can eliminate errors at an early stage. This prevents expensive recalls of production vehicles and accelerates the entry of new technology into the market,
- Tests enable the isolation and elimination of unpleasant sounds, screeching and vibrations. This ensures that the innovative brake system provides superior comfort for the driver and passengers, without irritating noises in the cabin.

EXPERIMENTAL TESTS IN REAL CONDITIONS

Real-World Vehicle Tests represent the final and most important stage in the development of brake innovations. While laboratories and dynamometers provide a theoretical basis, only on a real vehicle do engineers get an insight into how the brakes work in interaction with the entire mechanics, aerodynamics and electronics of the car. These tests are conducted through strictly defined protocols on closed proving grounds and public roads, and are focused on key aspects. Experimental tests of brake innovations in real conditions are the most important validation phase before serial production. Although simulations and dynamometers provide excellent initial data, it is only on the real track and in real traffic that the braking system faces the complex interplay of aerodynamics, suspension, vibrations and unpredictable environmental factors. Tests in field conditions (Off-road/Terrain testing) represent a special, extreme segment of experimental testing of brake innovations. Unlike flat asphalt on race tracks, off-road conditions (mud, sand, rock, deep water, sharp slopes) expose the brake system to unpredictable mechanical, thermal and environmental loads (The Brake Report, 2024). These tests are crucial for innovations intended for SUVs, pickup trucks, military, construction and agricultural machines, as well as for the calibration of modern electronic stability control systems.

Figure 4 Vehicle testing in real conditions (Robert Bosch GmbH, 2026)

The main mechanical challenge in off-road conditions is protection against accelerated wear and extreme thermal shocks. Sand and small gravel easily penetrate between the brake pad and disc, acting as an abrasive that can destroy the material, so innovative protective coatings and harder compounds of brake elements are tested in these conditions. In addition, when the vehicle descends a steep mountain pass, the brakes heat up to several hundred degrees, and a sudden entry into a deep puddle or river causes a dangerous thermal shock that can lead to cracking or warping of the discs.

In addition to mechanical durability, the field is the only place where innovative electronic systems and Brake-by-Wire algorithms can be precisely calibrated. On loose surfaces like gravel or sand, classic ABS would lengthen the stopping distance, so engineers here are testing specific "Off-road ABS" programs that deliberately allow short-term wheel locking so that the tire in front creates a wedge of gravel and stops faster. Also, systems for automatic hill descent control (Hill Descent Control) rely on millisecond reactions of the brakes, which on slippery and uneven ground must work in perfect synchronization so that the vehicle does not slide into the abyss.

In order to successfully carry out these tests, the prototype vehicle is equipped with robust, waterproof measuring equipment and high-resolution cameras that record the behavior of the jaws in the mud. After the tests are completed, the brake assembly is completely disassembled in the laboratory and analyzed under a microscope. Engineers measure micron damage on the surface of the disc and check whether the internal seals and rubbers have maintained 100% tightness, which is the final confirmation that the innovation is ready for serial production and the most difficult work tasks. Testing braking innovations under real road conditions brings key benefits that cannot be fully replicated in the lab or on simulators. Here are the main advantages of this method of testing:

- Actual aerodynamics and cooling. A vehicle in motion on the open road generates a natural vortex of air around the wheel. This enables a 100% accurate check of how the innovative discs are cooled under the influence of the actual aerodynamics of the car,
- Interaction with suspension and chassis. Braking on the right track involves realistic vehicle weight transfer, shock absorber operation and chassis vibrations. These factors directly affect the operation of the ABS/ESP electronics and cannot be faithfully simulated on a fixed laboratory bench,
- During fleet-tests (driving entire fleets of vehicles), the brakes cross tens of thousands of kilometers. It is the only way to check how the new materials react to a combination of moisture, dust, industrial road salt and small stones over time,

- Precise calibration for real drivers (Pedal Feel). Test drivers on public roads and training grounds provide subjective and objective insight into "pedal feel". That's key to fine-tuning the Brake-by-Wire system to make braking feel natural and predictable for the average driver,
- Validation with ADAS systems (Autonomous Braking). On the road, it is tested how the innovative brake actuators cooperate with the vehicle's radars and cameras. The exact reaction speed of the system is measured in moments when the car has to brake independently in emergency traffic situations.

HARDWARE-IN-THE-LOOP TEST BENCH

Hardware-in-the-loop (HIL) testing is an advanced cyber-physical testing methodology where real physical hardware components are connected in real time to a computer-simulated virtual environment, as shown in Figure 5. Instead of installing a new component in a physical test vehicle and driving it on a test track, the component is connected to a high-speed simulator that tricks the hardware into “thinking” that it is operating inside a real car moving under real-world road conditions. HIL testing involves simulating vehicle and environmental inputs to the electronic control unit (ECU) under test, leading it to believe that it is responding to real-world driving conditions on the open road. The HIL bench contains all relevant vehicle components. The simulator displays the inputs to real-world cameras and radar systems, which in turn send signals to the system under test to see if it is responding correctly to the inputs. For example, test scripts can create a scenario in which a vehicle traveling at 100 km/h around a curve in the rain encounters an unknown object on the road or an oncoming car swerving across the centerline. Cameras and radars connected to the HIL test bench send images to the ECU, and the system under test must process this data in real time and decide what to do (Aptiv,2026).

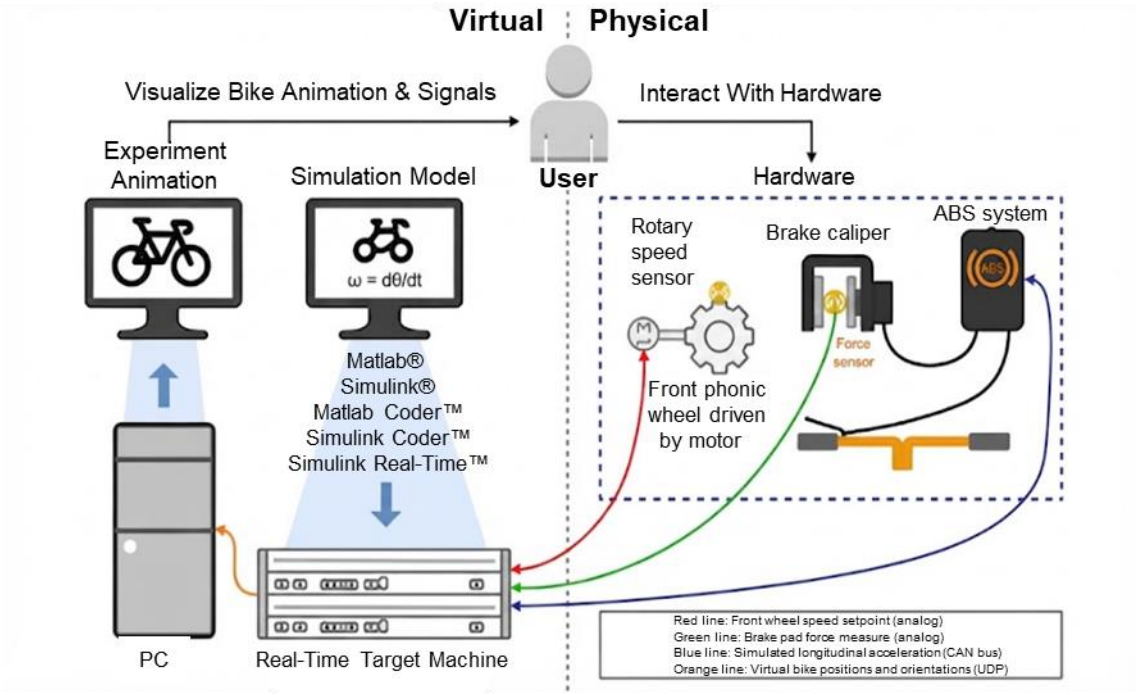

Figure 5 HIL testing scheme (Ramosaj, N. et al. 2023)

In a typical automotive brake speed control application, the setup balances physical hardware and virtual data. The physical objects are typically an electronic control unit (ECU) that runs control algorithms, actual hydraulic or pneumatic valves, and sometimes physical brake calipers, brake pipes, and pedals. A real-time computer simulator runs complex mathematical equations that model the mass of the vehicle, the dynamics of multiple tires, the coefficients of tire-road friction (μ), aerodynamics, and even the speeds of individual wheels (Pfister, F. et al. 2025). When the physical brake ECU commands the hydraulic valve to close, the virtual environment immediately registers the pressure change. The simulation model calculates the resulting vehicle deceleration and tire slip and sends simulated wheel speed sensor data back to the physical ECU in milliseconds (latency < 1 ms).

Hardware-in-the-Loop (HiL) test benches provide a bridge between pure computer software and physical on-track testing. When testing brake innovations, their application brings the following key advantages:

- Modern brakes are not just mechanics, but complex mechatronic systems driven by algorithms. HiL allows real brake electronics (ECU) and sensors to be connected to a virtual vehicle simulator. Engineers can test thousands of software scenarios in minutes, change parameters on the fly and calibrate system performance (such as brake force distribution) without waiting for a physical prototype of the entire car to be built.

- Testing braking innovations in extreme conditions on a straight track carries a huge risk of accidents. On the HiL table, you can simulate a burst brake hose, failure of a pressure sensor at a speed of 200 km/h, or a sudden transition from dry asphalt to ice (Split-Mu) in the middle of a bend. The system is tested to the absolute limits of safety, observing how the electronics react to critical failures (fail-safe modes) without any risk to the test driver.
- In electric vehicles, the coordination of the electrical (engine braking) and hydraulic (disc braking) systems is extremely complex. HiL stands allow simulation of electric drive, battery and torque operation in real time. Engineers can thus perfectly "iron" the transition between these two modes of braking on the pedals, ensuring maximum energy return (regeneration) with a natural feeling on the pedal for the driver,
- Unlike track tests that depend on weather conditions and availability, HiL systems operate 24/7. Tests are fully automated through scripts – the computer can independently, overnight, perform thousands of consecutive braking, simulating different vehicle weights, pad's wear levels and driving styles, generating complete fault reports ready for analysis.

CONCLUSIONS

Innovation is one of the key challenges in modern engineering. The application of certain innovations in mass production or the change of some systems, such as braking systems on motor vehicles, can lead to very negative effects if, before mass application or production, innovative solutions are not tested or their effectiveness and operation is not validated. That is why the process of testing the validity and functionality of the system must undergo rigorous experiments that give the exact answers as to whether the innovation is applicable, justified and above all safe for mass application. The importance of experimentation is especially important today when the mechanical and electronic parts of the system are integrated. The application of experiments in the testing of modern braking systems is very important for the reason of not only checking the integrated operation of the system, but also the operation of the activation algorithms and the operation of modern systems.

In order to successfully test modern braking systems and innovations that are being researched, there are certain procedures and regulations that the system must satisfy and function according to. Thus, today there are different levels of brake system testing, depending on the level at which the system is tested and how much of the system is tested, but on the other hand, what innovation in the brake system is tested. Nowadays, different levels and types of systems are mainly used, starting from the lowest level, where systems are tested on an inertial brake dynamometer, and on the other hand, real vehicles can also be tested. Experiments where real vehicles are used are experiments that can be applied in laboratory conditions as well as in a real environment, that is, on specialized tracks in a real traffic environment, that is, on roads. Each type of experiment that examines innovations related to the braking system has its advantages and disadvantages. When it comes to experimenting with brake systems, the importance of detailed testing is very important for reasons of importance to vehicle and traffic safety. Bearing in mind the mentioned importance, the braking system passes all levels of testing with the aim of detailed analysis and verification. If there are certain negative results of the innovation test, there may be a correction of the proposed engineering solution or its rejection. Today, hybrid experimental methods are increasingly being applied, combining real systems and simulations, that is, computer systems. In this way, more favorable tests are possible where different variants of the innovation can be tested. In the future, it will surely be improved even more and new experimental test methods will be developed that will eliminate existing shortcomings and speed up the very process of experimentation of braking system innovations.

REFERENCES

Aptiv. (2026, August 6). What is hardware-in-the-loop testing? Aptiv Insights. https://www.aptiv.com/en/insights/article/what-is-hardware-in-the-loop-testing

Arrive Alive. (2026, march). United Nations Decade of Action for Road Safety 2011-2020. https://www.arrivealive.co.za/united-nations-decade-of-action-for-road-safety-2011-2020

CITA (International Motor Vehicle Inspection Committee). (2025). White paper on brakes inspection: Reference value methods and dynamic testing methodologies. citainsp.org

DTC Dynamic Test Center AG. (2026). Braking effectiveness test. Retrieved from https://www.dtc-ag.ch/en/professional-services/active-safety/approval-examinations/braking-effectiveness-test

Haq, M. T., Ampadu, V.-M. K., & Ksaibati, K. (2023). An investigation of brake failure related crashes and injury severity on mountainous roadways in Wyoming. *Journal of Safety Research*, 84, 7–17. https://doi.org/10.1016/j.jsr.2022.10.003

HORIBA. (n.d.). Automotive Testing Centers. https://www.horiba.com/int/mobility/service/testing/

International Organization for Standardization. (2018). Road vehicles — Functional safety (ISO Standard No. 26262:2018). ISO.

Kumbhar, N., Patil, S. R., & Sawant, S. M. (2016). A comparative study on automotive brake testing standards. *Journal of The Institution of Engineers (India): Series M*,98, 527–531. https://doi.org/10.1007/s40032-016-0289-y

Lee, S., Shim, T., & Cho, B.-K. (2006). Development of a brake system for Lightweight Vehicle. *Design Engineering and Computers and Information in Engineering, Parts A and B*, 229–238. https://doi.org/10.1115/imece2006-15437

LookupAPlate. (2023, 17. november). Brake Failure Statistics: Causes, Prevention & Safety Tips. https://www.lookupaplate.com/blog/brake-failure-statistics/

Markel, A. (2005, April 1). Brake Dynamometer Testing: One Test is Worth a Thousand Expert Opinions. Import Car Magazine. https://www.import-car.com/brake-dynamometer-testing-one-test-is-worth-a-thousand-expert-opinions/

Mendoza, K., & Squadrani, F. (2021, April 9). Regenerative Braking Testing on Dynamometer (Part 1 of 4). The Brake Report. https://thebrakereport.com/regenerative-braking-testing-on-dynamometer-part-1-of-4/

PatSnap. (2026, April 22). ASIL-D braking redundancy in autonomous vehicles. PatSnap Resources. https://www.patsnap.com/resources/blog/articles/asil-d-braking-redundancy-in-autonomous-vehicles/

Pfister, F., Nygren, A., Klomp, M., Travagliati, A., Savi, L., Purtymun, B., & Agudelo, C. E. (2025). New testing methodologies for innovative brake systems. In P. E. Pfeffer (Ed.), *15th International Munich Chassis Symposium 2024: IMCS 2024. Proceedings* (pp. 91–105). Springer Vieweg. https://doi.org/10.1007/978-3-662-71062-3_8

Ramosaj, N., Fusco, C., & Viennet, E. (2023). Development of a hardware-in-the-loop test bench for validation of an ABS system on an e-bike. *The Evolving Scholar - BMD 2023, 5th Edition*. https://doi.org/10.59490/6504843acc05ff8f18f36576

Robert Bosch GmbH. (2026). Boxberg proving ground. Bosch Mobility. https://www.bosch-mobility.com/en/solutions/development-services/proving-grounds/proving-ground-boxberg/

SAE International. (2025, November 30). Inertia Dynamometer Brake Squeal Noise Test Procedure for Vehicles with Regenerative Systems (SAE Standard J3211). https://www.sae.org/standards/j3211-inertia-dynamometer-brake-squeal-noise-test-procedure-vehicles-regenerative-systems

Sporysz, B. (2024, May 9). Brake Dynamometer Development: Unveiling Precision and Performance; Electrification of Motorsports and Its Impact on the Automotive World [Bachelor's thesis, University of Virginia]. Libra ETD. https://libraetd.lib.virginia.edu/public_view/xk81jm732

The Brake Report. (2024, August 13). Brake Wear Testing: Correlation Between Vehicle and Dynamometer Testing (Part 1 of 3). The Brake Report. https://thebrakereport.com/brake-wear-testing-correlation-between-vehicle-and-dynamometer-testing-part-1-out-of-3/

United Nations Economic Commission for Europe. (2004). Braking tests and the required performance: Draft global technical regulation concerning passenger vehicle brakes (Report No. PVGTR-2004-18e). Retrieved from World Forum for Harmonization of Vehicle Regulations website: https://unece.org/DAM/trans/doc/2004/wp29grrf/PVGTR-2004-18e.pdf

United Nations Economic Commission for Europe. (2014). Regulation No. 13-H: Uniform provisions concerning the approval of passenger cars with regard to braking (Addendum 12H, Revision 3). Official Journal of the European Union. https://unece.org/sites/default/files/2021-05/GRVA-10-23e.pdf

United Nations Economic Commission for Europe. (2021). Regulation No. 13: Uniform provisions concerning the approval of vehicles of categories M, N and O with regard to braking (Addendum 12, Revision 9). UNECE.

Yadav, M., & Ranjan, R. (2022, August 16). Functional safety for braking system through ISO 26262. Retrieved from Mirabilis Design website: https://www.mirabilisdesign.com/functional-safety-for-braking-system-through-iso-26262/

The 11th International Congress
Motor Vehicles & Motors 2026
Kragujevac, Serbia
October 8th - 9th, 2026

Motor Vehicles & Motors

MVM2026-016
https://doi.org/10.24874/CMVM2026.016
Original scientific paper

Ljubica Spasojević[1]
Zorica Djordjević[2,*]
Sonja Kostić[3]
Saša Jovanović[4]

MODAL ANALYSIS OF A COMPOSITE CRANKSHAFT FOR AN INTERNAL COMBUSTION ENGINE (ICE)

ABSTRACT: Crankshafts are responsible for transforming the reciprocating motion of engine pistons into rotational motion. During their service life, due to the extremely high number of load cycles, crankshafts must exhibit high fatigue strength and durability. Furthermore, crankshafts, especially in diesel engines, operate at relatively low rotational speeds and high torque values, making them susceptible to resonant vibrations. The combination of these factors (high-cycle fatigue and resonant vibrations) can lead to a reduction in crankshaft service life. The subject of this paper is the investigation of potential improvements through the application of new materials with the lowest possible mass, while maintaining sufficient fatigue strength and dynamic stability. Using the software tools SolidWorks and Femap, both steel and composite crankshafts were modelled and numerically analysed. The research results indicate that the application of composite materials can significantly reduce the mass of the crankshaft without compromising its mechanical strength and dynamic stability.

KEYWORDS: crankshaft, composite materials, modal analysis, natural frequencies, deformations

MODALNA ANALIZA KOMPOZITNOG KOLENASTOG VRATILA MOTORA SA UNUTRAŠNJIM SAGOREVANJEM

REZIME: Kolenasta vratila imaju ulogu da naizmenično pravolinijsko kretanje klipova motora transformišu u rotaciono kretanje. Tokom radnog veka, zbog vrlo velikog broja ciklusa opterećenja, ova vratila moraju imati veliku otpornost na zamor i izdržljivost. Takođe, kolenasta vratila, pogotovo ako se radi o dizel motorima, rade pri malom broju obrtaja sa velikim vrednostima obrtnih momenata tako da su podložna rezonantnim vibracijama. Kombinacija ovih parametara (visokociklični zamor i rezonantne vibracije) dovodi do smanjenja radnog veka radilice. Predmet

[1] *Ljubica Spasojević, Faculty of Engineering, University of Kragujevac, Sestre Janjić 6, Kragujevac, ljubica18spasojevic@gmail.com, https://orcid.org/0000-0001-8605-3696*
[2] *Zorica Đorđević, Faculty of Engineering, University of Kragujevac, Sestre Janjić 6, Kragujevac, zoricadj@kg.ac.rs, https://orcid.org/0000-0003-0194-4698 (*Corresponding author)*
[3] *Sonja Kostić, Academy of Professional Studies Šumadija, Department in Kragujevac, Kosovska 8, Kragujevac, skostic@asss.edu.rs, https://orcid.org/0000- 0002-6120-6139*
[4] *Saša Jovanović, Faculty of Engineering, University of Kragujevac, Sestre Janjić 6, Kragujevac, dviks@kg.ac.rs, https://orcid.org/0000-0001-5916-2483*

ovog rada su poboljšanja u smislu potrage za novim materijalima sa što je moguće manjom masom, ali dovoljnom zamornom izdržljivošću i dinamičkom stabilnošću. Primenom softverskih alata SolidWorks i Femap izmodelirana su i numerički analizirana kako čelično tako i kompozitna vratila. Rezultati istraživanja pokazuju da se primenom kompozitnih materijala može znatno smanjiti masa kolenastog vratila, bez narušavanja njegove mehaničke otpornosti i gubitka stabilnosti..

KLJUČNE REČI: kolenasto vratilo, kompozitni materijali, modalna analiza, sopstvene frekvencije, deformacije

INTRODUCTION

The crankshaft is one of the most heavily loaded and geometrically most complex components of an internal combustion engine (ICE); it converts the reciprocating (back-and-forth) motion of the pistons into rotational motion, which is then transmitted to the drivetrain (Hoag & Dondlinger, 2016). Due to the combined effects of bending, torsion, and axial loading that act simultaneously in the fillet zones of the main and crank pin journals, crankshafts are susceptible to failure caused by high-cycle fatigue, which remains one of the most commonly reported causes of engine failure in service (Fonte, et al. 2013).

In addition to fatigue, crankshafts are subjected to periodically varying gas and inertial forces that excite torsional, axial, and bending oscillations. If the excitation frequency approaches one of the crankshaft's natural frequencies, resonance can occur, causing a sudden increase in dynamic stress and potentially leading to premature failure (Horváth & Égert, 2015). This risk is especially pronounced in low- and medium-speed, high-torque engines such as diesel engines, which is why the dynamic (modal) behaviour of the crankshaft must already be verified at the design stage.

At the same time, the automotive industry is under constant pressure to reduce vehicle mass in order to improve fuel consumption and lower harmful emissions. Fibre-reinforced polymer composites (FRP) offer a favourable combination of low density and high specific stiffness, and are therefore increasingly being considered as a replacement for conventional steel in structural and rotating vehicle components (Đorđević, 2018). Recent numerical studies on composite drive shafts, chassis, and crankshafts confirm that replacing steel with polymers reinforced with carbon, aramid, or glass fibres can simultaneously reduce mass and shift the natural frequencies outside the normal operating range (Samuel & Tayong, 2023; Wakshume, 2025; Sarnobat, et al. 2026).

The aim of this paper is to numerically investigate the modal behaviour of a passenger-vehicle crankshaft made of conventional steel (42CrMo4) and three composite alternatives - carbon-fibre-reinforced polymer (CFRP), aramid-fibre-reinforced polymer (AFRP), and glass-fibre-reinforced polymer (GFRP). The analysis focuses exclusively on fibre-reinforced polymers, as they represent the group of materials with the most realistic potential for structural application in crankshafts; using the finite element method (FEM), the first five natural frequencies were compared and the resulting mass reduction was determined.

LOADING AND CALCULATION OF THE CRANKSHAFT'S NATURAL FREQUENCIES

During engine operation, the crankshaft receives the force of the expanding combustion gases through the connecting rod at the crank pin (big-end) journal and converts it into torque, which is transmitted to the flywheel through the main journals. Since the load occurs intermittently and cyclically throughout the entire service life of the engine, the fillets of the main and crank pin journals, the lubrication holes, and the press-fitted joints represent critical, fatigue-sensitive locations of this component (Nikolić, 2004). These cyclic loads also cause angular, transverse, and axial oscillations of the crankshaft which, in the case of resonance, generate additional stresses that, combined with the base stresses, can lead to failure of the crankshaft.

The main cause of crankshaft vibration is its imbalance, which can lead to very large oscillation amplitudes and, as a result, damage to the crankshaft within a very short period of time. The intensity of the vibrations is influenced by many factors, such as the number and arrangement of the cylinders, the engine power, and others. For this reason, particular attention must be paid to calculating the natural frequency values and checking the possibility of resonance occurring in crankshafts.

Governing equations of modal analysis

The undamped free-vibration equation of motion of the discretised crankshaft is given by Equation (1), where K and M are the global stiffness and mass matrices assembled from the finite element model and q is the nodal displacement vector.

$$\left(\boldsymbol{K} - \omega^2 \boldsymbol{M}\right) \cdot \boldsymbol{q} = 0 \tag{1}$$

Non-trivial solutions require the determinant of the system to vanish, Equation (2); the n roots ω_i^2 of this characteristic equation are the squares of the natural circular frequencies of the crankshaft, and the associated eigenvectors are the corresponding mode shapes.

$$\left|\boldsymbol{K} - \omega^2 \boldsymbol{M}\right| = 0 \tag{2}$$

The natural frequency in Hz corresponding to each circular frequency is obtained from Equation (3).

$$f = \omega / (2\pi) \tag{3}$$

The critical rotational speed of the crankshaft can be calculated using the following expression:

$$n = 60 \cdot f / k \tag{4}$$

where:
n – critical rotational speed, min^{-1};
f – natural frequency, Hz;
k – harmonic order (for a four-cylinder engine, the fourth harmonic order is the most critical; therefore, k=4).

NUMERICAL MODEL AND METHODOLOGY

Geometry and finite element model

The crankshaft geometry (V-type engine; total length 583 mm, cylinder bore 80 mm, main and crank pin journal diameters of 60 mm and 55 mm, respectively) was created in SolidWorks according to standard recommendations for crankshaft dimensioning (Statków, 2024) and imported into Femap 2021.2. for finite element analysis. The crankshaft model was discretized using second-order tetrahedral finite elements. Figure 1 shows the model with the generated finite element mesh and the boundary conditions applied at the bearing locations, as well as on the part of the flange that connects to the flywheel. All analysed crankshaft variants had the same geometric dimensions, the same mesh, and the same boundary conditions. The only difference was the type of material used.

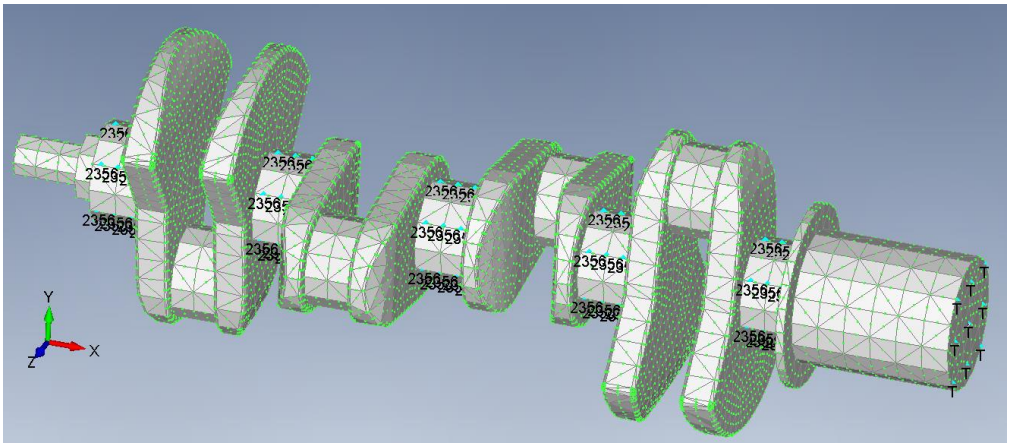

Figure 1 Crankshaft model

Material properties

A numerical modal analysis was carried out for the original steel crankshaft made of 42CrMo4 steel, as well as for composite crankshafts made of carbon-fibre-reinforced polymer (CFRP), aramid-fibre-reinforced polymer (AFRP), and glass-fibre-reinforced polymer (GFRP). Of the three composites considered, CFRP offers the highest specific stiffness and strength, along with excellent fatigue resistance, but also the highest material cost and pronounced

anisotropy (Đorđević, 2018). AFRP has lower stiffness than CFRP but very good impact and wear resistance. GFRP is the cheapest and easiest to process of the three materials, but has the lowest specific stiffness, which can result in lower natural frequencies compared to the steel variant for the same geometry. Comparative numerical studies of CFRP versus other fibre systems in vehicle structural components consistently show that CFRP provides the highest stiffness and natural frequencies, while glass- and aramid-fibre-reinforced variants sacrifice some dynamic stiffness in exchange for lower cost and easier manufacturing (Wakshume, 2025). The mechanical properties of the steel and the analysed composite materials are given in Table 1.

Table 1 Material properties used in the finite element model

Material	Young's Modulus E, GPa	Shear Modulus G, GPa	Poisson's Ratio ν	Density ρ, kg/m³
42CrMo4 steel	210	81	0,30	7850
CFRP	126	49	0,28	1810
AFRP	72	27	0,34	1310
GFRP	39	15.6	0,25	1910

RESULTS AND DISCUSSION

The results of the modal analysis of the steel crankshaft, for the first three oscillation modes, are shown in Figure 2.

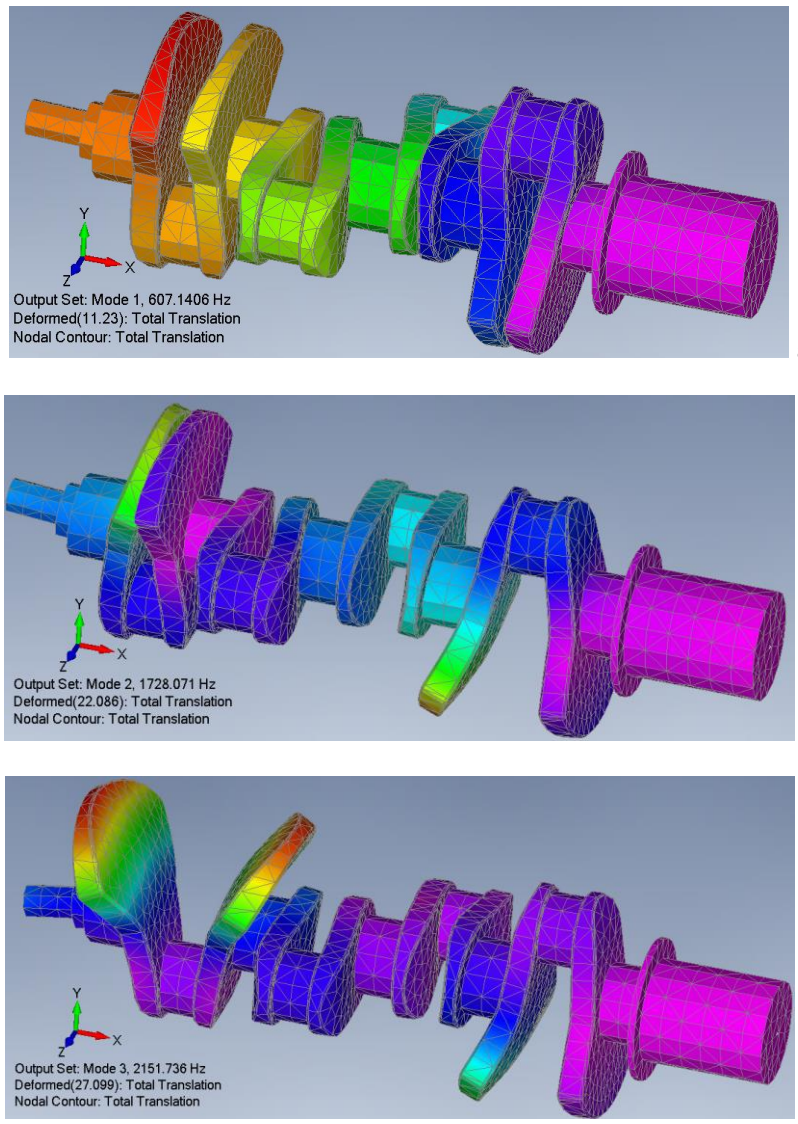

Figure 2 View of the crankshaft model for material 42CrMo4 at different modes: a) mode 1, b) mode 2, c) mode 3

The same analysis procedure was applied to the other crankshaft materials. The natural frequency values for the first five oscillation modes, for all four analysed crankshaft materials, are given in Table 2.

Table 2 First five natural frequencies of the crankshaft, Hz

Mode	42CrMo4	AFRP	CFRP	GFRP
1	607,1	868,7	980,3	532,3
2	1728,1	2476,2	2783,3	1512,1
3	2151,7	3085,6	3459,6	1880,2
4	2759,6	3949,4	4446,3	2415,8
5	2842,6	4089,3	4541,0	2471,2

As can be seen from Table 2, higher oscillation modes have significantly higher natural frequency values, but their oscillation amplitudes are smaller, so they represent a lower risk of failure during crankshaft operation. Based on the natural frequency values obtained for the first oscillation mode, the critical rotational speeds of the analysed crankshafts can be determined using equation (4). The resulting critical rotational speed values, for all analysed crankshaft materials, are shown graphically in Figure 3.

Looking at the obtained results, it can be concluded that the CFRP composite provides the crankshaft with the highest natural frequency values, i.e., the highest critical rotational speed, which almost completely eliminates the possibility of resonance occurring. AFRP follows immediately after it, also showing better characteristics compared to steel, while only the GFRP composite performs worse than steel. The main advantage of composites over steel is their high specific stiffness (the ratio of stiffness to mass), which directly affects the natural frequency values. This is precisely what leads to the observed behaviour of the different crankshaft materials.

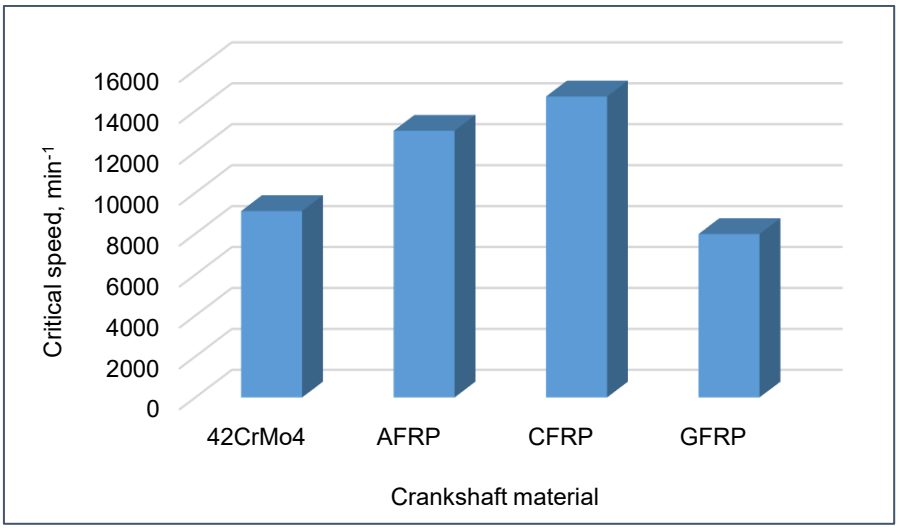

Figure 3 Graphical representation of the critical rotational speeds for the analysed crankshaft materials

The low mass of the composite crankshafts, and consequently their lower moment of inertia, also directly contributes to the increase in natural frequency values, i.e., critical rotational speeds. A graphical representation of the mass of the analysed crankshaft materials can be seen in Figure 4. It can be observed that the mass of the composite crankshafts is several times lower than that of the steel crankshaft.

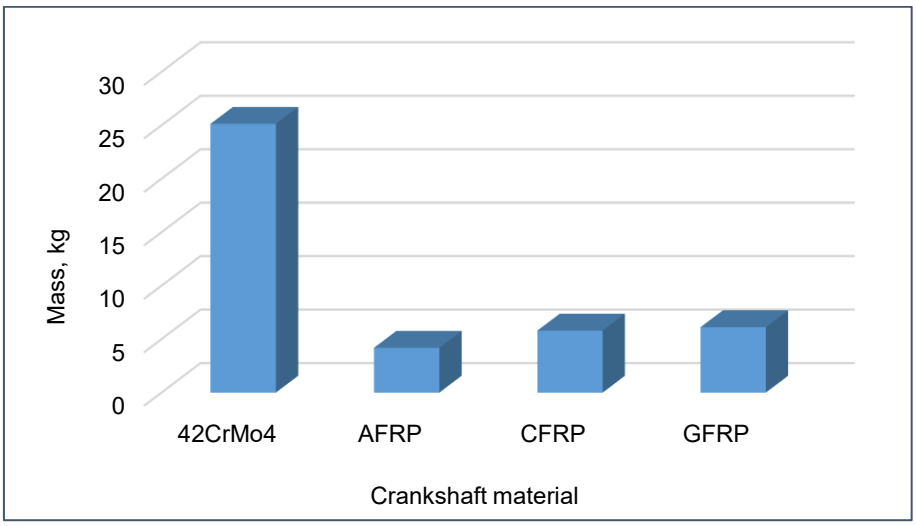

Figure 4 Graphical representation of the mass for the analysed crankshaft materials

The total modal displacements for the first oscillation mode, for the selected crankshaft materials, are shown graphically in Figure 5.

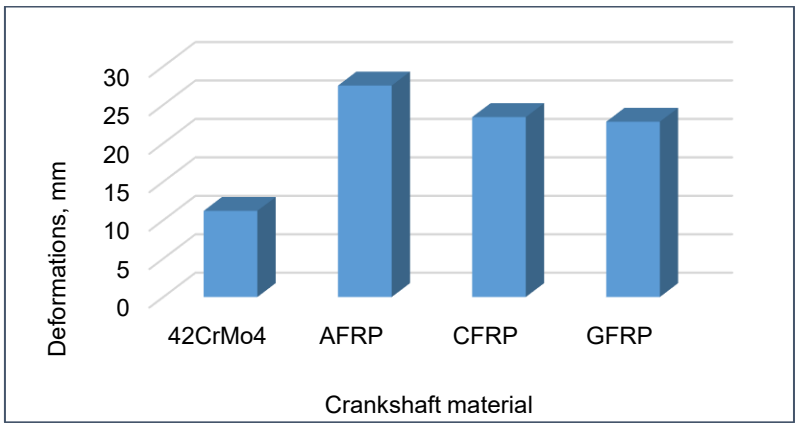

Figure 5 Graphical representation of the total displacements for the analysed crankshaft materials

The modal displacement values of the composite crankshafts are considerably higher than those of the steel crankshaft; however, the properties of the analysed composite materials are such that they can withstand the mentioned modal deformations.

MULTICRITERIA SELECTION OF CRANKSHAFT MATERIAL USING THE SAW METHOD

Methodology

The Simple Additive Weighting (SAW) method was applied to select the optimal crankshaft material. Four alternatives were evaluated using four criteria derived from the dynamic characteristics of the shaft: natural frequency (k1), critical rotational speed (k2), mass (k3), and total modal displacement (k4). The first two criteria are of the maximization type, whereas mass and modal displacement are minimized.

For max criteria:

$$r_{ij} = \left(x_{ij} - x_j^{\min}\right) / \left(x_j^{\max} - x_j^{\min}\right) \tag{5}$$

For min criteria:

$$r_{ij} = \left(x_j^{\max} - x_{ij}\right) / \left(x_j^{\max} - x_j^{\min}\right) \tag{6}$$

The values of the considered criteria for the selected materials (xij) are shown in Table 3.

Table 3 Values of the considered criteria for selected materials (xij)

Material	Natural frequency fs, Hz	Critical speed n_{cr}, min^{-1}	Mass m, kg	Total modal displacement, mm
42CrMo4 steel	607,1	9106,5	25,14	11,2
AFRP	868,7	13030,5	4,19	27,5
CFRP	980,3	14704,5	5,80	23,4
GFRP	532,3	7984,5	6,12	22,8
type of criteria	**max**	**max**	**min**	**min**

The values in Table 3 form the decision matrix. After normalization, the dimensionless values shown in Table 4 were obtained.

Table 4 Normalized values of the considered criteria (rij)

Material	k1	k2	k3	k4
42CrMo4 steel	0,167	0,167	0,000	1,000
AFRP	0,751	0,751	1,000	0,000
CFRP	1,000	1,000	0,923	0,252
GFRP	0,000	0,000	0,908	0,288

Weight coefficients are considered in two variants. In Variant I, greater importance was assigned to dynamic stability and low mass (w = 0.30; 0.30; 0.25; 0.15). In Variant II, all criteria were assigned equal importance (w = 0.25).

The values of the relative weighting coefficients are shown in the diagram in Figure 6.

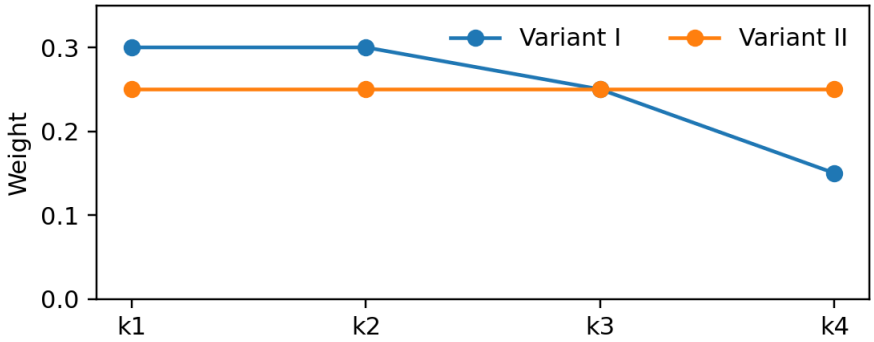

Figure 6 Relative weighting coefficients in the two variants

SAW results and discussion

The aggregate score for each alternative was calculated as Ai = Σ wj rij. The resulting scores and ranking are presented in Table 5.

Table 5 Aggregate SAW scores and ranking

Material	Variant I	Variant II	Rank
CFRP	**0,869**	**0,794**	**1**
AFRP	0,701	0,626	2
GFRP	0,270	0,299	3
42CrMo4 steel	0,250	0,334	4

The summary SAW results for the crankshaft materials considered are shown in Figure 7.

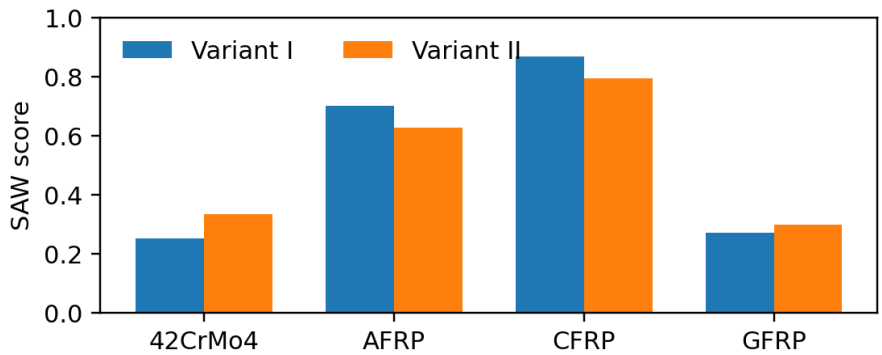

Figure 7 Aggregate SAW scores for the considered materials

Discussion

CFRP achieves the highest aggregate score in both variants. It combines the highest natural frequency and critical rotational speed with a relatively low mass, which makes it the most favourable alternative from the standpoint of the adopted criteria. AFRP ranks second, mainly because of its minimum mass and high dynamic performance. GFRP benefits from low mass but has the lowest natural frequency and critical speed. The 42CrMo4 steel exhibits the smallest modal displacement, but its substantially higher mass and lower dynamic indicators reduce its overall SAW score.

CONCLUSIONS

Based on the numerical modal and SAW analysis performed for both the conventional steel crankshaft and crankshafts made of composite materials (AFRP, CFRP, and GFRP), and on the results obtained, the following conclusions can be drawn:

1. By using composite materials, the natural frequencies of the crankshaft reach very high values, so that the critical rotational speeds are significantly higher than the maximum rotational speed the engine can reach, thereby eliminating the possibility of resonance;
2. Compared to steel, composite materials have a greater capacity to damp vibrations, meaning that the vibration amplitudes are considerably smaller, which reduces the risk of crankshaft failure;
3. By using composite materials, the mass of the crankshaft can be significantly reduced without compromising its mechanical strength.
4. The SAW analysis provides a clear ranking of the candidate crankshaft materials. CFRP is the optimal alternative in both weighting scenarios, followed by AFRP. The unchanged first and second positions indicate that the result is robust with respect to the two adopted weighting schemes.

Therefore, the use of composite crankshafts can contribute to reduced fuel consumption, improved vehicle dynamics, increased reliability and service life, as well as increased overall engine efficiency and a reduced negative impact on the environment.

ACKNOWLEDGMENTS

This work has been performed as a part of activities within the projects 451-03-34/2026-03/200107 supported by the Republic of Serbia, Ministry of Science, Technological Development and Innovation.

REFERENCES

Đorđević, Z. (2018). *Kompozitne konstrukcije* [Composite structures]. Faculty of Engineering, University of Kragujevac.

Fonte, M., Li, B., Reis, L., & Freitas, M. (2013). Crankshaft failure analysis of a motor vehicle. *Engineering Failure Analysis*, 35, 147–152. https://doi.org/10.1016/j.engfailanal.2012.11.014

Hoag, K., & Dondlinger, B. (2016). Cranktrain (Crankshafts, connecting rods, and flywheel). In Vehicular engine design (2nd ed., pp. 321–360). Springer.

Horváth, P., & Égert, J. (2015). Stress analysis and weight reduction of a one-cylinder engine crankshaft. *Acta Technica Jaurinensis*, 8(3), 201–217. https://doi.org/10.14513/actatechjaur.v8.n3.377

Raushan, R., Dhande, K. K., Jamadar, N. I., & Malwe, P. D. (2022). Material characterization, design and analysis of CF/PA66 drive shaft with high strength carbon steel. *Materials Today: Proceedings*, 64(1), 51-58. https://doi.org/10.1016/j.matpr.2022.03.512

Nikolić, V. (2004). *Mašinski elementi – teorija, proračun, primeri* [Machine elements – theory, calculation, examples]. Faculty of Mechanical Engineering, Kragujevac.

Samuel, M., & Tayong, R. B. (2023). 3D numerical analysis of the structural behaviour of a carbon fibre reinforced polymer drive shaft. *Results in Engineering*, 18, 101120. https://doi.org/10.1016/j.rineng.2023.101120

Sarnobat, S. S., Shiyekar, S. M., & Choudhary, K. (2026). Low-weight, high-durability crankshaft development using glass fiber composites: Numerical and experimental investigations. *Journal of Polymer & Composites*, 14(4). https://doi.org/10.37591/JOPC.vi.249342

Statków, P. R. (2024). *Calculations for I.C. engine crankshafts* (Publication 8/P). Lloyd's Register.

Wakshume, E. (2025). Lightweight composite optimization of URAL-4320 chassis using CFRP and BFRP: Structural and modal finite element analysis. *Results in Engineering*, 28, 108134. https://doi.org/10.1016/j.rineng.2025.108134

The 11th International Congress
Motor Vehicles & Motors 2026
Kragujevac, Serbia
October 8th - 9th, 2026

Motor Vehicles & Motors

MVM2026-017
https://doi.org/10.24874/CMVM2026.017
Technical paper

Zvonko Petrović[1]
Suzana Petrović Savić[2]
Milica Tufegdžić[3]
Nikola Kostić[4]
Milena Petrović[5]

MATHEMATICAL MODELING OF HYDRAULIC DRIVE FOR THE MITSUBISHI RV-2FRL INDUSTRIAL ROBOT: INFLUENCE OF MOMENT OF INERTIA ON SERVO VALVE RESPONSE TIME

ABSTRACT: This paper describes the application of alternative hydraulic drive systems to the Mitsubishi RV-2FRL industrial robot, a 6-axis manipulator with a payload of 2 kg and repeatability of ±0.02 mm. Although the robot originally utilizes AC servo motors, certain operating conditions (explosive environments, high force-to-weight ratio requirements) favour hydraulic actuation. The main contribution of this paper is a second-order mathematical model that explicitly links the robot's moment of inertia (J = 0.18 kg·m² for the J4 axis) with the servo valve time constant (tv). The model combines Newton's rotational dynamics, the hydraulic motor torque equation, first-order valve dynamics, and the oil continuity equation. The resulting transfer function yields the key relation: settling time ts. Simulation in MATLAB for varying tv (5 to 50 ms) and J (0.18 to 0.50 kg·m²) shows that to maintain the factory positioning accuracy of the RV-2FRL robot, the servo valve time constant must be below 10 ms. Valves with tv > 20 ms cause unacceptable phase lag and overshoot. It is demonstrated in this paper that hydraulic drive is theoretically feasible, but only high-performance servo valves (tv < 10 ms) satisfy the dynamic requirements of the robot, which explains why electric drives remain optimal for small precision robots.

KEYWORDS: alternative drive systems, hydraulic servo valve, moment of inertia, settling time

[1] *Zvonko Petrović, MSc, Academy of professional studies Šumadija-Department in Trstenik, Trstenik, zpetrovic@asss.edu.rs, https://orcid.org/0000-0002-4182-4095*
[2] *Suzana Petrović Savić, Assoc. Prof., Faculty of Engineering University of Kragujevac, Kragujevac, petrovic.savic@kg.ac.rs.com, https://orcid.org/0000-0002-5629-6221*
[3] *Milica Tufegdžić, PhD, Academy of professional studies Šumadija-Department in Trstenik, Trstenik, mtufegdzic@asss.edu.rs, https://orcid.org/0000-0003-3856-1498*
[4] *Nikola Kostić, PhD, Academy of professional studies Šumadija-Department in Trstenik, Trstenik, nkostic@asss.edu.rs, https://orcid.org/0009-0007-9494-5767*
[5] *Milena Petrović, MSc, Academy of professional studies Šumadija-Department in Trstenik, address, mpetrovic@asss.edu.rs, https://orcid.org/0009-0005-8443-7107*

MATEMATIČKO MODELIRANJE HIDRAULIČKOG POGONA INDUSTRIJSKOG ROBOTA MITSUBISHI RV-2FRL: UTICAJ MOMENTA INERCIJE NA VREMENSKI ODZIV SERVO-VENTILA

REZIME: U ovom radu opisana je primena alternativnih hidrauličkih pogonskih sistema na industrijskom robotu Mitsubishi RV-2FRL, manipulatoru sa 6 osa, nosivošću od 2 kg i ponovljivošću od ±0,02 mm. Iako robot originalno koristi AC servo motore, određeni radni uslovi (eksplozivne sredine, zahtevi za velikim odnosom sila-težina) favorizuju hidrauličko upravljanje. Glavni doprinos ovog rada je matematički model drugog reda koji eksplicitno povezuje moment inercije robota (J = 0,18 kg·m² za osu J4) sa vremenskom konstantom servoventila (t_v). Model kombinuje Njutnovu dinamiku rotacije, jednačinu momenta hidrauličkog motora, dinamiku ventila prvog reda i jednačinu kontinuiteta ulja. Dobijena prenosna funkcija daje ključnu relaciju: vreme smirivanja ts. Simulacijom u MATLAB-u za različite vrednosti t_v (od 5 do 50 ms) i J (od 0,18 do 0,50 kg·m²) pokazano je da za održavanje fabričke tačnosti pozicioniranja robota RV-2FRL, vremenska konstanta servoventila mora biti ispod 10 ms. Ventili sa t_v > 20 ms izazivaju neprihvatljivo kašnjenje faze i prelet. Pokazano je u radu da je hidraulički pogon teoretski izvodljiv, ali samo visokoperformasni servoventili (t_v <10 ms) zadovoljavaju dinamičke zahteve robota, što objašnjava zašto električni pogoni ostaju optimalni za male precizne robote.

KLJUČNE REČI: alternativni pogonski sistemi, hidraulički servo ventil, moment inercije, vreme smirivanja

INTRODUCTION

Industrial robots are complex mechatronic systems whose positioning accuracy and dynamic performance are strongly influenced by the characteristics of their actuation systems. Electric servo drives are predominantly used in small and medium-sized industrial robots because they provide high positioning accuracy, rapid response, and relatively straightforward control. However, hydraulic actuation may represent a suitable alternative under specific operating conditions, particularly when high force or torque capacity, a favourable power-to-weight ratio, or operation in specially configured hazardous environments is required (Merritt, 1967; Watton, 1989).

The Mitsubishi RV-2FRL, considered in this study, is a six-axis vertically articulated industrial robot originally actuated by AC servo motors. Owing to its compact structure, low payload, and high repeatability, it represents a demanding reference platform for assessing whether an alternative hydraulic drive can satisfy the dynamic requirements of a small precision robot. In this study, the J4 axis is selected for analysis, and its moment of inertia is incorporated into the mathematical model of the proposed hydrostatic servo drive.

A hydrostatic servo system typically comprises a servo valve that regulates the hydraulic fluid flow, a hydraulic actuator in the form of a motor or cylinder, and the associated mechanical load (Jelali & Kroll, 2003). The mathematical modelling of such systems is based on the coupled equations governing fluid-flow continuity, the force or torque equilibrium of the mechanical components, and servo-valve dynamics (Blackburn et al., 1960; Nichols & Reistad, 1999). The dynamic response of the system is primarily determined by the moment of inertia of the rotating components (J); the viscous damping coefficient (B); the hydraulic motor displacement (Dm); the effective bulk modulus of the hydraulic fluid (βe); the total fluid volume between the servo valve and the motor (vt); the servo-valve gain (Kv); and the servo-valve time constant (tv) (Merritt, 1967; Watton, 1989; Jelali & Kroll, 2003).

The theoretical foundations of hydraulic control and servo systems were established in the classical works of J.F. Blackburn et al. (1960) and Merritt (1967), which provided systematic descriptions of hydraulic components, flow–pressure relationships, actuator dynamics, and system response. J. Watton (1989) subsequently integrated these principles with mathematical modelling and computer-based simulation techniques. A more comprehensive treatment of the modelling, identification, and control of hydraulic servo systems was later presented by M. Jelali and A. Kroll (2003). These fundamental studies provide the theoretical basis for deriving models that couple servo-valve dynamics, hydraulic actuator behaviour, fluid compressibility, and mechanical-load dynamics.

Accordingly, the aim of this study is to develop a transfer-function-based mathematical model for evaluating the feasibility of hydrostatic actuation of the J4 axis of the Mitsubishi RV-2FRL robot. The model combines Newton's equation of rotational motion, the hydraulic motor torque equation, a first-order representation of the servo-valve dynamics, and the hydraulic fluid continuity equation. The resulting second-order transfer function explicitly relates the moment of inertia of the robot axis to the servo-valve time constant and enables their influence on the transient response of the system to be examined.

A comparative parametric analysis is performed in MATLAB for servo-valve time constants ranging from 5 to 50 ms and moments of inertia ranging from 0.18 to 0.50 kg·m². The dynamic behaviour of the system is evaluated using unit-step responses, with particular emphasis on settling time and overshoot. The analysis is intended to determine the range of servo-valve time constants for which the proposed hydraulic drive can satisfy the dynamic-response requirements associated with the J4 axis and to identify the limitations of hydraulic actuation when applied to small, high-precision industrial robots. MATLAB Control System Toolbox is used for model implementation and response analysis.

MATERIALS AND METHODS

Mitsubishi RV-2FRL Industrial Robot

The Mitsubishi RV-2FRL is a vertically articulated industrial robot manufactured by Mitsubishi Electric and belongs to the MELFA FR series. It is a stationary six-axis manipulator designed for high-speed and high-precision handling and assembly operations. The robot can be installed on the floor or ceiling, while wall-mounted installation is available as a customised configuration with a restricted operating range of the J1 axis (Mitsubishi Electric, 2020). The Mitsubishi RV-2FRL robotic system, including the manipulator and the associated CR800 controller (Figure 1).

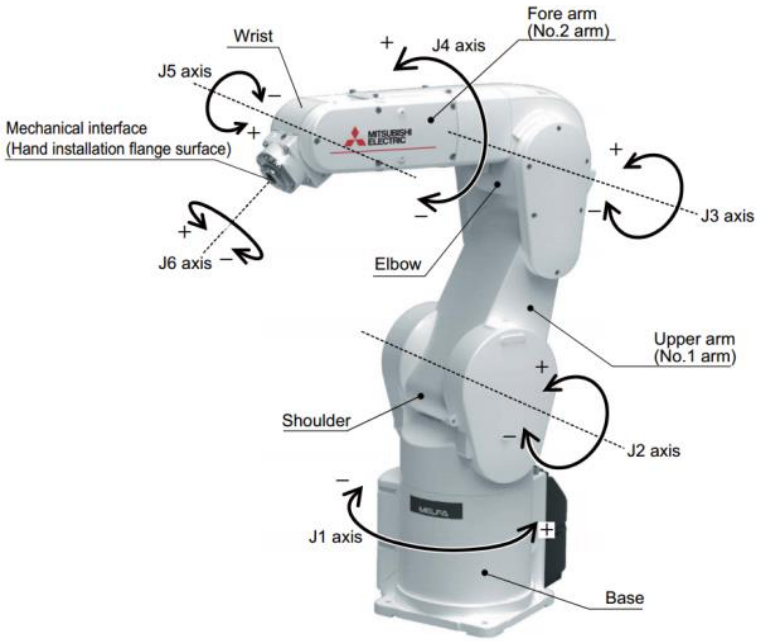

Figure 1 Mitsubishi RV-2FRL robotic system (Mitsubishi Electric, 2020)

The compact structure of the RV-2FRL, combined with its maximum reach of 649 mm and position repeatability of ±0.02 mm, makes it suitable for manipulation tasks requiring high precision within a relatively small workspace. The robot is originally actuated by AC servo motors, while the angular positions of its joints are measured using absolute encoders. Its principal technical characteristics are summarised in Table 1.

Table 1 Principal technical characteristics of the Mitsubishi RV-2FRL robot

Characteristic	**Specification**
Manufacturer	Mitsubishi Electric
Robot series	MELFA FR
Robot type	Vertically articulated industrial robot
Number of degrees of freedom	6
Joint configuration	Six revolute joints
Installation	Floor or ceiling; wall-mounted as a customised configuration
Rated payload	2 kg
Maximum payload	3 kg
Maximum reach radius	649 mm
Position repeatability	±0.02 mm
Drive system	AC servo motors
Position detection	Absolute encoders
Robot mass	21 kg
Compatible controller	CR800-02VD, standalone configuration

The robot has six revolute joints, denoted by J1–J6, which provide the rotational motions required for positioning and orienting the end effector. The permitted angular displacement of each joint is defined by its mechanical and control limitations. The operating ranges of the individual joints are presented in Table 2.

In addition to the individual joint limits presented in Table 2, the overall dimensions and operating envelope of the robot are shown in Figure 2.

Table 2 Operating ranges of the Mitsubishi RV-2FRL joints

Joint	Functional description	Minimum angle	Maximum angle	Total operating range
J1	Base rotation	−240°	+240°	480°
J2	Shoulder rotation	−117°	+120°	237°
J3	Elbow rotation	0°	+160°	160°
J4	Wrist rotation	−200°	+200°	400°
J5	Wrist bending	−120°	+120°	240°
J6	Tool-flange rotation	−360°	+360°	720°

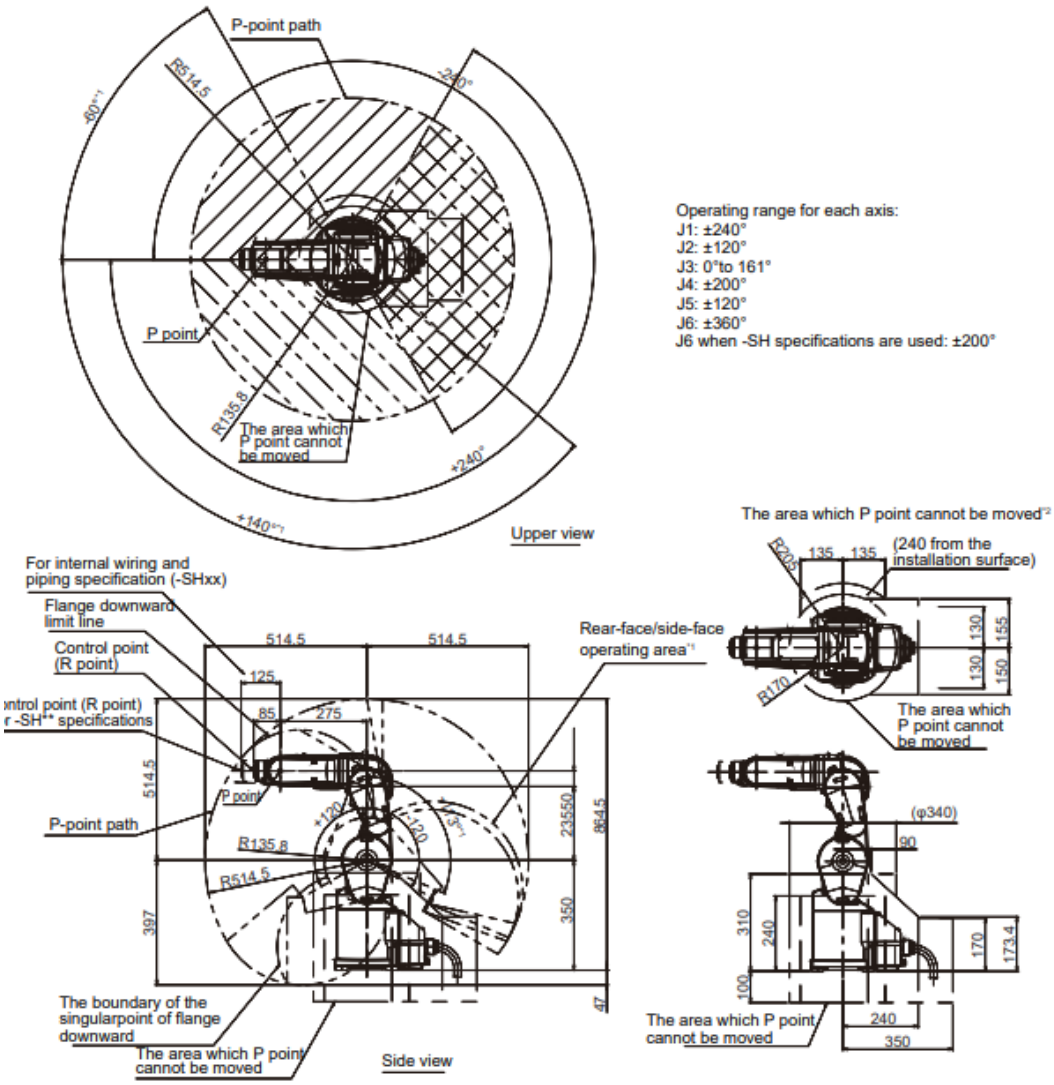

Figure 2 Overall dimensions and operating envelope of the Mitsubishi RV-2FRL robot [9]

Among the six joints, the J4 axis is selected for the analysis presented in this study. According to the manufacturer's specifications, the permissible torque of the J4 axis is 4.17 N·m, while the maximum permissible load inertia about this axis is 0.18 kg·m² (Mitsubishi Electric, 2020). In the proposed model, the latter value is adopted as the reference moment of inertia of the mechanical load. The J4 axis therefore provides the link between the technical characteristics of the original robotic system and the subsequent analysis of hydraulic actuation as an alternative drive solution.

Alternative Hydraulic Actuation of the J4 Axis

Although the Mitsubishi RV-2FRL is originally actuated by AC servo motors, the present study considers a hydrostatic servo drive as an alternative actuation concept for its J4 axis. Both electric and hydraulic servo drives

are governed by the mechanical equilibrium of the actuated joint, in which the drive torque must overcome the effects of inertia, friction, and external loading. However, the physical processes through which the driving torque is generated differ considerably. In an electric drive, torque is produced by an electric motor, whereas in a hydrostatic drive it results from the pressure difference across a hydraulic motor.

The analysis of hydraulic actuation is particularly relevant for robotic systems operating under demanding load conditions. Hydrostatic drives can generate high forces and torques while maintaining a favorable power-to-weight ratio, which makes them suitable for heavy-duty manipulators and other systems requiring high load capacity (Merritt, 1967). Nevertheless, their application to small precision robots is more challenging because fluid compressibility, leakage, and servo-valve dynamics may adversely affect the transient response and positioning performance.

Accordingly, the Mitsubishi RV-2FRL is used in this study as a reference platform for examining whether a hydrostatic servo drive can satisfy the dynamic requirements of a compact industrial robot. The J4 axis is selected because its technical parameters are available in the manufacturer's documentation and can be directly incorporated into the proposed mathematical model. The maximum permissible load inertia of 0.18 kg·m² specified for this axis is adopted as the reference value of the mechanical-load inertia. The influence of an increased load is subsequently examined by varying the moment of inertia up to 0.50 kg·m² (Mitsubishi Electric, 2020; Човић & Лазаревић, 2008).

Although hydrostatic drives are most commonly associated with heavy-duty industrial applications, they are also widely used in the automotive industry, particularly in vehicle steering systems, active suspension systems, braking systems, and robotic manipulators used in automotive assembly lines. The proposed approach is therefore directly applicable to automotive manufacturing environments where a high force-to-weight ratio and precise motion control are required.

Mathematical Model of the Hydrostatic Servo System

The proposed hydrostatic servo system is represented as a coupled system comprising four principal components: a servo valve, a hydraulic motor, a rotating mechanical load, and the hydraulic fluid volume contained in the connecting lines between the valve and the motor. The mathematical model is derived by combining the equations governing rotational motion, hydraulic motor behavior, servo-valve dynamics, and fluid-flow continuity.
To obtain a tractable transfer-function model, several simplifying assumptions are introduced. The system parameters are assumed to remain constant within the considered operating range, the hydraulic fluid properties are treated as uniform, and the servo valve is assumed to operate within its linear region. The effects of fluid compressibility and internal leakage are initially included in the complete model and subsequently neglected when deriving the reduced-order model. The model is linearized about a nominal operating point, and zero initial conditions are assumed when applying the Laplace transformation.

Mechanical and Hydraulic Actuator Dynamics

The mechanical subsystem comprises the hydraulic motor shaft and the attached rotating load. Its rotational dynamics are described using Newton's second law for rotational motion:

$$J \cdot \ddot{\theta}_m + B \cdot \dot{\theta}_m = T_m - T_L \,, \tag{1}$$

where J is the total moment of inertia of the motor and the mechanical load, B is the viscous damping coefficient, θ_m is the angular displacement of the motor shaft, T_m is the torque generated by the hydraulic motor, and T_L is the externally applied load torque.

Applying the Laplace transformation to Equation (1), under zero initial conditions, gives:

$$\left(J_S^2 + B_S\right) \cdot \theta_m\left(S\right) = T_m\left(S\right) - T_L\left(S\right) . \tag{2}$$

The relationship between the angular displacement of the motor shaft and the acting torques can then be expressed as:

$$\theta_m\left(S\right) = \frac{T_m\left(S\right) - T_L\left(S\right)}{J_S^2 + B_S} . \tag{3}$$

The hydraulic motor converts hydraulic energy, supplied in the form of pressurised fluid flow, into mechanical rotational energy. Under idealised operating conditions, the torque generated by the motor is proportional to the pressure difference across the motor:

$$T_m = D_m \cdot P_L \,, \tag{4}$$

where D_m is the hydraulic motor displacement, expressed in m³/rad, and (P_L=P_1-P_2) is the pressure difference between the motor inlet and outlet, expressed in Pa.
The theoretical flow required by the hydraulic motor is proportional to the angular velocity of its shaft:

$$Q_m = D_m \cdot \dot{\theta}_m \,. \tag{5}$$

Equations (4) and (5) establish the coupling between the hydraulic and mechanical domains of the proposed drive system.

Servo-Valve Dynamics and Flow Continuity

The servo valve regulates the direction and rate of hydraulic fluid flow supplied to the motor. Within the linear operating range, its dynamics can be approximated using a first-order transfer function (Jelali & Kroll, 2003):

$$\frac{X_v(S)}{U(S)} = \frac{K_v}{\tau_v \cdot s + 1} \,, \tag{6}$$

where xv is the valve-spool displacement, U is the control voltage, Kv is the servo-valve gain, and tv is the servo-valve time constant.

Assuming linearized operation around the selected working point, the valve flow is proportional to the spool displacement:

$$Q_V = K_q \cdot X_v \,, \tag{7}$$

where Kq is the valve flow gain. Combining Eq. (6) and (7) yields the transfer function relating the valve flow to the control signal:

$$\frac{Q_v(S)}{U(S)} = \frac{K_V \cdot K_q}{\tau_V \cdot s + 1} = \frac{K_Q}{\tau_V \cdot s + 1} \,, \tag{8}$$

where (K_Q=$K_v K_q$) represents the overall valve flow gain.

The flow-continuity equation describes the balance between the flow supplied by the servo valve, the flow consumed by the hydraulic motor, the flow associated with fluid compression, and internal leakage (Blackburn et al., 1960; Nichols & Reistad, 1999):

$$Q_v(S) = Q_m + Q_C + Q_l \,, \tag{9}$$

where Q_v is the flow supplied by the servo valve, Q_m is the flow required by the hydraulic motor, Q_c is the flow associated with hydraulic fluid compression, and Q_l is the internal leakage flow.

The flow component resulting from fluid compressibility is expressed as:

$$Q_C = \frac{V_t}{4 \cdot \beta_e} \cdot \frac{dP_L}{dt} \,, \tag{10}$$

where V_t is the total effective fluid volume between the servo valve and the hydraulic motor and β_e is the effective bulk modulus of the hydraulic fluid.

The internal leakage flow is represented by the following linearized relationship:

$$Q_l = K_l \cdot P_L \,, \tag{11}$$

where K_l is the internal leakage coefficient. Combining Equations (5), (9), (10), and (11) gives:

$$Q_v = D_m \cdot s \cdot \dot{\theta}_m + \frac{V_t}{4 \cdot \beta_e} \cdot \dot{P}_L + K_l \cdot P_L \,. \tag{12}$$

Applying the Laplace transformation to Equation (12), under zero initial conditions, yields:

$$Q_v(s) = D_m \cdot s \cdot \theta_m(s) + \left(\frac{V_t}{4 \cdot \beta_e} s + K_t \right) \cdot P_L(s) \cdot \tag{13}$$

Overall Transfer Function and Reduced-Order Model

The overall mathematical model is obtained by combining the mechanical-load dynamics, the hydraulic motor relationships, the servo-valve transfer function, and the fluid-flow continuity equation. The transformed equation of rotational motion is first rearranged as:

$$T_m(s) = \left(J \cdot s^2 + B \cdot s \right) \theta_m(s) + T_L(s) . \tag{14}$$

Substitution of the hydraulic motor torque relationship from Eq. (4) into Eq. (14) gives:

$$D_m P_L(s) = \left(J \cdot s^2 + B \cdot s \right) \theta_m(s) + T_L(s) . \tag{15}$$

The resulting expression for the load pressure is:

$$P_L(s) = \frac{\left(J \cdot s^2 + B \cdot s \right) \theta_m(s) + T_L(s)}{D_m} . \tag{16}$$

The valve flow is then obtained from Equation (13):

$$Q_v(s) = D_m \cdot s \cdot \theta_m(s) + \left(\frac{V_t}{4 \cdot \beta_e} s + K_l \right) P_L(s) \cdot \tag{17}$$

Substituting Equation (16) into Equation (17) and assuming $T_L=0$ gives:

$$Q_v(s) = \left[D_m s + \left(\frac{V_t}{4 \cdot \beta_e} s + K_l \right) \frac{J \cdot s^2 + B \cdot s}{D_m} \right] \cdot \theta_m(s) , \tag{18}$$

$$\frac{Q_m(s)}{Q_v(s)} = \frac{1}{D_m s + \left(\frac{V_t}{4 \cdot \beta_e} s + K_l \right) \frac{J \cdot s^2 + B \cdot s}{D_m}} , \tag{19}$$

$$\frac{Q_m(s)}{Q_v(s)} = \frac{D_m}{J \cdot \frac{V_t}{4 \cdot \beta_e} \cdot s^3 + \left(\frac{V_t \cdot B}{4 \cdot \beta_e} + J \cdot K_l \right) \cdot s^2 + \left(B \cdot K_l + D_m^2 \right) \cdot s} . \tag{20}$$

The condition $T_L=0$ indicates that no additional external disturbance torque is applied during the analysis. It does not imply the absence of mechanical loading, because the effects of the motor and load inertia remain included through the parameter *J*.

By incorporating the servo-valve relationship defined by Equation (8), the overall transfer function between the control signal *U(s)*, and the angular position of the motor shaft $\theta_m(s)$, is obtained:

$$G(s) = \frac{Q_m(s)}{U(s)} = \frac{K_Q \cdot D_m}{a_3 \cdot s^3 + a_2 \cdot s^2 + a_1 \cdot s + a_0} . \tag{21}$$

The denominator coefficients of the transfer function are defined as:

$$\frac{Q_m(s)}{Q_v(s)} = \frac{D_m}{J \cdot \frac{V_t}{4 \cdot \beta_e} \cdot s^3 + \left(\frac{V_t \cdot B}{4 \cdot \beta_e} + J \cdot K_l \right) \cdot s^2 + \left(B \cdot K_l + D_m^2 \right) \cdot s} . \tag{22}$$

$$a_3 = J \cdot \frac{V_t}{4 \cdot \beta_e} ; \; a_2 = \left(\frac{V_t \cdot B}{4 \cdot \beta_e} + J \cdot K_l \right) \cdot \tau_v ; \; a_1 = \left(B \cdot K_l + D_m^2 \right)$$

The complete transfer function includes the effects of servo-valve dynamics, mechanical inertia, viscous damping, fluid compressibility, and internal leakage. It therefore provides the basis for analysing the dynamic response of the proposed hydrostatic servo drive under different operating conditions.

For a preliminary assessment of the dominant system dynamics, a reduced-order model is also considered. By neglecting the effects of fluid compressibility and internal leakage, the complete transfer function is reduced to a second-order form:

$$\frac{Q_m(s)}{Q_v(s)} = \frac{D_m}{s(J \cdot s + B) + D_m^2 \cdot \tau_v \cdot s + D_m^2} = \frac{D_m}{J \cdot s^2 + \left(B + D_m^2 \cdot \tau_v\right) \cdot s + D_m^2}, \tag{23}$$

$$G_2(s) = \frac{Q_m(s)}{U(s)} = \frac{K_Q \cdot D_m}{J \cdot s^2 + \left(B + D_m^2 \cdot \tau_v\right) \cdot s + D_m^2}. \tag{24}$$

This simplification enables a direct assessment of the influence of the mechanical-load inertia and servo-valve time constant on the dominant transient behaviour of the system. The corresponding second-order characteristic equation is:

$$J \cdot s^2 + \left(B + D_m^2 \cdot \tau_v\right) \cdot s + D_m^2 = 0. \tag{25}$$

2.4. Evaluation of the Transient Response

The transient response of the proposed hydrostatic servo drive is evaluated using its response to a unit-step control input. For the second-order model defined by Equation (25), the settling time within a ±2% tolerance band can be approximated as:

$$t_s \approx \frac{4}{\zeta \cdot \omega_n}, \tag{26}$$

where $\omega_n = \sqrt{\frac{D_m^2}{J}}$ – is the undamped natural frequency and $\zeta = \frac{B + D_m^2 \cdot \tau_v}{2 \cdot \sqrt{J \cdot D_m^2}}$ – is the damping ratio of the equivalent second-order system.

The analytical expression for the settling time is applicable when the transient response is dominated by a pair of underdamped complex-conjugate poles. For the complete third-order model defined by Eq. (21), the settling time is determined numerically from the simulated unit-step response. The numerical analysis is performed in MATLAB using Control System Toolbox (MathWorks, 2024).

MATLAB Implementation and Simulation Procedure

Based on the derived mathematical model, including the complete transfer function given by Eq. (21) and the reduced-order model defined by Eq. (25), the dynamic response of the proposed hydrostatic servo system was simulated in MATLAB R2024a using Control System Toolbox (MathWorks, 2024). The simulations were performed to quantify the effects of the servo-valve time constant t_v and the total moment of inertia J on the transient response of the system.

The nominal parameter values adopted for the simulations are presented in Table 3. The reference moment of inertia, (J=0.18 kg·m^2), corresponds to the maximum permissible load inertia specified by the manufacturer for the J4 axis of the Mitsubishi RV-2FRL robot (Mitsubishi Electric, 2020). The remaining hydraulic parameters were selected from representative values reported in the literature and were kept constant throughout the parametric analysis (Merritt, 1967; Jelali & Kroll, 2003).

The mathematical model was implemented in MATLAB by defining the nominal system parameters and calculating the transfer-function coefficients according to Eq. (22). The transfer function was then created using the tf function, while the response to a unit-step input was obtained using the step function. The transient-response characteristics were determined using step info, with the settling-time threshold set to 2%.

Two sets of simulations were performed. In the first set, the total moment of inertia was maintained at its reference value of (J=0.18 kg·m^2), while the servo-valve time constant was varied from 5 to 50 ms. For each value of t_v, the transfer-function coefficients were recalculated and the corresponding unit-step response was obtained. This

analysis was conducted to determine how the dynamic response of the servo valve affects the settling time and overshoot of the complete drive system.

Table 3 Nominal parameters of the hydrostatic servo-system model

Parameter	Value
Reference moment of inertia (J), kg·m²	0.18
Viscous damping coefficient (B), N·m·s/rad	0.01
Hydraulic motor displacement (D_m), m³/rad	$5\cdot10^{-6}$
Effective bulk modulus (β_e), Pa	$1.2\cdot10^{9}$
Total fluid volume between the valve and motor (v_t), m³	$50\cdot10^{-6}$
Overall valve flow gain (K_Q), m³/(s·V)	$1\cdot10^{-6}$
Internal leakage coef m³/(s·Pa)ficient (K_l),	$1\cdot10^{-12}$

In the second set of simulations, the servo-valve time constant was fixed at t_v=10 ms, while the moment of inertia was varied from 0.18 to 0.50 kg·m². The lower limit corresponds to the maximum permissible load inertia specified for the J4 axis, whereas the higher values represent increased equivalent mechanical loading considered for the purpose of the parametric analysis. This simulation set was used to evaluate the influence of mechanical inertia on the transient response of the proposed drive.

For both simulation sets, the settling time was defined as the time after which the system response remained within ±2% of its final value. Overshoot was also monitored to provide a more complete assessment of the transient behaviour.

3. RESULTS AND DISCUSSION

The simulated unit-step responses were first analysed for different values of the servo-valve time constant t_v, while the moment of inertia was maintained at its reference value of J=0.18 kg·m^2. The servo-valve time constant was varied from 5 to 50 ms to evaluate the influence of valve dynamics on the transient response of the proposed hydrostatic drive.

Figure 3 presents the unit-step responses obtained for the four considered values of t_v. An increase in the servo-valve time constant produced a progressively slower response. For t_v =5 ms, the system entered and remained within the specified ±2% tolerance band after approximately 0.145 s. When the time constant was increased to 50 ms, the settling time increased to 0.316 s.

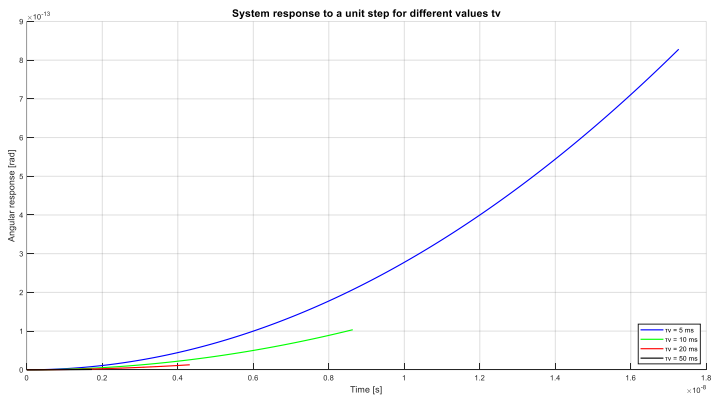

Figure 3 Unit-step responses of the system for different servo-valve time constants at J=0.18 kg·m^2

The calculated settling times are summarised in Table 4. The relative increase was determined with respect to the response obtained for t_v =5 ms.

Table 4 Settling time as a function of the servo-valve time constant

t_v, ms	Settling time t_s, s	Relative increase, %
5	0.145	–
10	0.178	22.8
20	0.235	62.1
50	0.316	117.9

Increasing t_v from 5 to 50 ms increased the settling time by approximately 118%. This result demonstrates that the servo-valve dynamics have a pronounced influence on the speed of the system response. A larger time constant

corresponds to a slower valve response and introduces a slower dynamic component into the overall system. The observed relationship is monotonic but not uniformly linear over the entire investigated range, as the incremental change in settling time decreases at higher values of t_v.

The influence of the mechanical-load inertia was subsequently examined by fixing the servo-valve time constant at t_v =10 ms and varying the moment of inertia from 0.18 to 0.50 kg·m² (Figure 4).

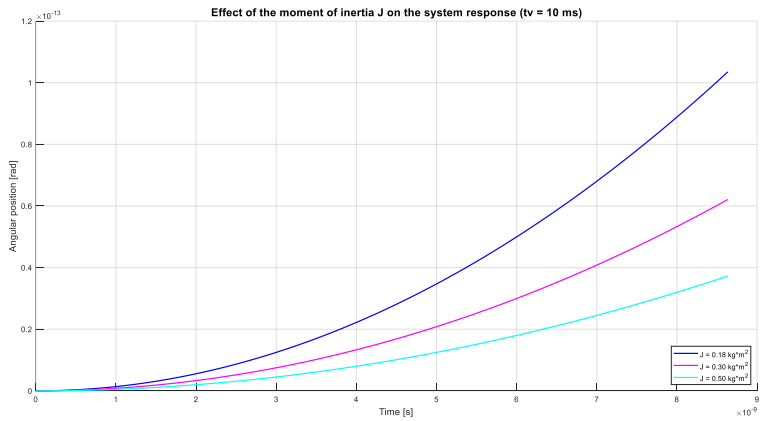

Figure 4. Unit-step responses of the system for different moments of inertia at J=0.18 kg·m²

The calculated settling times are presented in Table 5. The relative changes were determined with respect to the reference value J=0.18 N·kg·m².

Table 5 Settling time as a function of the moment of inertia

J, kg·m²	Settling time t_s, s	Relative increase, %
0,18	0,178	-
0,30	0,218	22,5
0,50	0,281	57,9

An increase in the moment of inertia from 0.18 to 0.50 kg·m² increased the settling time by approximately 58%. This behaviour is consistent with the mechanical interpretation of the system, because a larger equivalent inertia requires a greater drive torque to achieve the same angular acceleration. In the considered robotic application, an increase in the payload or a change in its position relative to the joint axis increases the equivalent load inertia and consequently reduces the speed of the transient response.

The results obtained from the two parametric simulation sets demonstrate that both the servo-valve time constant and the equivalent mechanical-load inertia influence the settling time of the system. Within the considered parameter ranges, increasing the servo-valve time constant produced a larger relative change in settling time than increasing the moment of inertia. However, this comparison applies only to the selected ranges and nominal values and should not be interpreted as a general ranking of parameter sensitivity (Saltelli et al., 2008).

The accuracy of the reduced-order model was evaluated by comparing its response with that of the complete third-order model for the nominal parameter values J=0.18 kg·m² and t_v=10 ms (Figure 5).

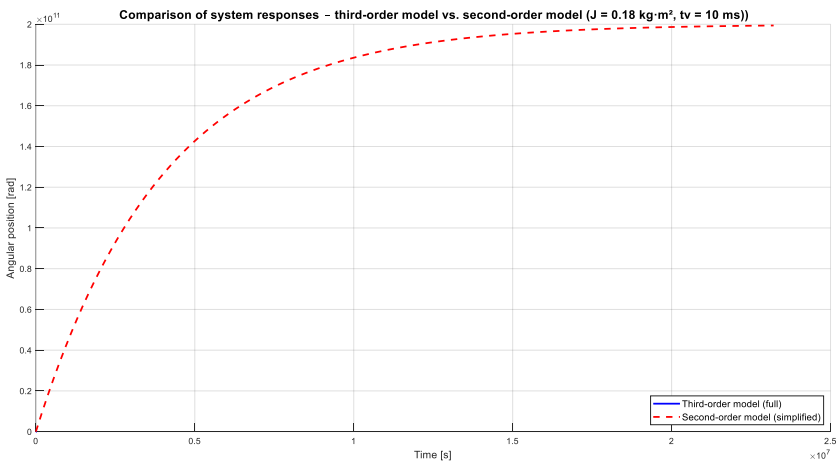

Figure 5 Comparison of the unit-step responses obtained using the complete third-order model and the reduced second-order model for J=0.18 kg·m² and t_v=10 ms

The responses of the two models were in close agreement under the nominal operating conditions. The maximum relative difference was 1.85%, while the mean error was 0.42%. Figure 6 presents the absolute and relative differences between the responses over the analysed simulation interval.

The obtained agreement indicates that the reduced second-order model provides an acceptable approximation of the dominant dynamics under the considered nominal conditions. For the adopted parameter values, the effects represented by the additional dynamics of the complete model have only a limited influence on the simulated unit-step response. The reduced model can therefore be used for a preliminary assessment of settling time and dominant transient behaviour (Watton, 1989; Chapple, 2010).

Nevertheless, this conclusion is limited to the investigated parameter set. Further simulations over wider ranges of the effective bulk modulus, fluid volume, and leakage coefficient would be required before concluding that fluid compressibility and leakage are negligible under all operating conditions. The complete model remains more appropriate when these effects are expected to become significant (Jelali & Kroll, 2003).

The results obtained from the two parametric simulation sets demonstrate that both the servo-valve time constant and the equivalent mechanical-load inertia influence the settling time of the system. Within the considered parameter ranges, increasing the servo-valve time constant produced a larger absolute relative change in settling time than increasing the moment of inertia. However, the parameters were varied over considerably different relative ranges. Therefore, the relative increases in settling time alone cannot be used to compare their proportional influence (Saltelli et al., 2008).

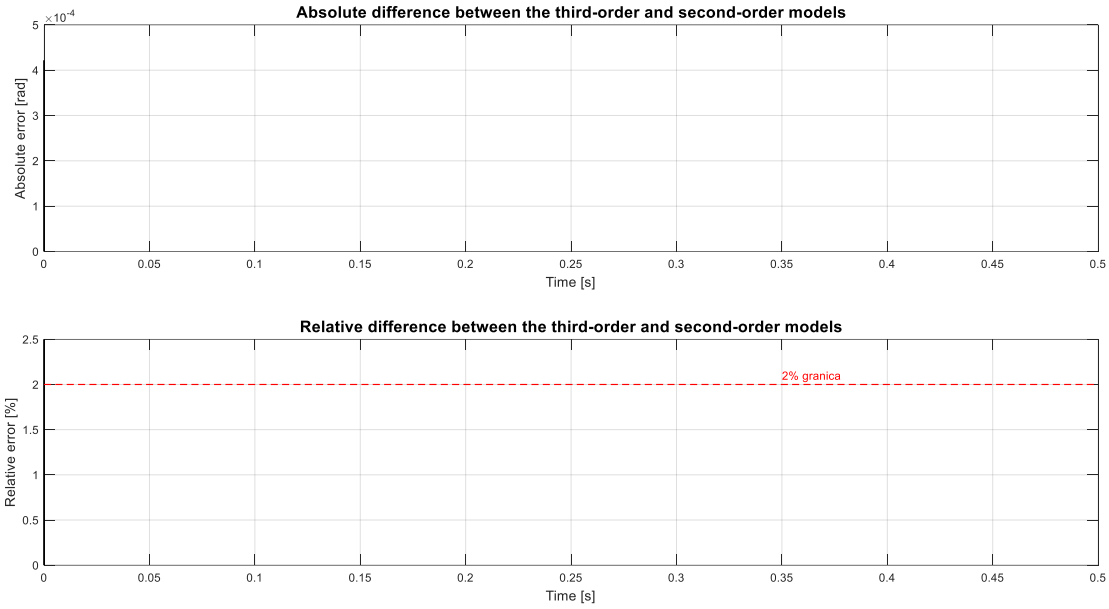

Figure 6 Absolute and relative differences between the responses of the complete and reduced-order models

To provide a normalised comparison, a sensitivity analysis was performed for the two investigated parameters. The normalised sensitivity of the settling time t_s to a parameter x was defined as (Saltelli et al., 2008):

$$S_x^{t_s} = \frac{\partial t_s}{\partial x} \cdot \frac{x}{t_s}, \tag{27}$$

The coefficient is dimensionless and expresses the relative change in settling time resulting from a relative change in the considered parameter. Since the relationship between the settling time and the investigated parameters was obtained numerically, the derivative in Equation (27) was approximated using the changes between the initial and final simulated values. The initial parameter value and its corresponding settling time were used as reference values. The calculated sensitivity coefficients are presented in Table 6.

Table 6 Relative sensitivity of the settling time to the investigated parameters

Parameter	Investigated range	Settling-time range	Sensitivity coefficient
t_v, ms	5 - 50	0.145–0.316 s	0.13
J, kg·m^2	0.18 – 0.50	0.178–0.281 s	0.33

These findings have practical implications for the design of hydrostatic servo drives for robotic applications. A faster transient response can be achieved by limiting the equivalent moment of inertia and selecting a servo valve with a small time constant. The equivalent inertia can be reduced by limiting the payload, positioning it closer to the joint

axis, and reducing the mass of the moving components. Conversely, an increase in payload, particularly when it is positioned farther from the joint axis, increases the equivalent moment of inertia and adversely affects the dynamic response of the system (Човић & Лазаревић, 2008).

The calculated coefficients represent average relative sensitivities over the investigated parameter intervals and should not be interpreted as local sensitivity coefficients at the nominal operating point. Nevertheless, they provide a concise quantitative comparison of the two parameters considered in this study (Saltelli et al. 2008).

4. CONCLUSION

In this study, a mathematical model of a hydrostatic servo system was developed to analyze the dynamic behavior of a rotary joint drive, using the J4 axis of the Mitsubishi RV-2FRL industrial robot as a reference application. A linearized third-order transfer function relating the servo-valve control signal to the angular position of the output shaft was derived by combining the mechanical-load dynamics, hydraulic motor behavior, servo-valve dynamics, and fluid-flow continuity. A reduced second-order model was also considered to enable a simplified assessment of the dominant system dynamics.

The effects of the servo-valve time constant t_v, and the equivalent moment of inertia J on the transient response were evaluated in MATLAB using unit-step simulations. Increasing t_v from 5 to 50 ms increased the settling time from 0.145 to 0.316 s, corresponding to an increase of approximately 118%. Increasing J from 0.18 to 0.50 kg·m², at t_v =10 ms, increased the settling time from 0.178 to 0.281 s, corresponding to an increase of approximately 58%. These results confirm that both servo-valve dynamics and equivalent mechanical loading have a pronounced influence on the response speed of the proposed drive.

The normalized sensitivity coefficients calculated over the investigated parameter intervals were 0.33 for the moment of inertia and 0.13 for the servo-valve time constant. Therefore, relative to the magnitude of the applied parameter variation, the settling time was more sensitive to changes in the equivalent moment of inertia. This finding indicates that payload magnitude, payload position relative to the joint axis, and the mass of the moving components must be considered together with the dynamic characteristics of the selected servo valve.

The comparison between the complete third-order model and the reduced second-order model showed a maximum relative difference of 1.85% and a mean error of 0.42% under the considered nominal conditions. The reduced model therefore provides an acceptable approximation of the dominant transient behavior for preliminary analysis and component selection. However, this conclusion is limited to the adopted parameter values and does not imply that fluid compressibility and leakage can be neglected under all operating conditions.

The obtained results indicate that hydrostatic actuation has theoretical potential as an alternative drive solution for the considered robotic joint, provided that a sufficiently fast servo valve is employed and the equivalent mechanical-load inertia is appropriately limited. Within the investigated range, servo valves with smaller time constants produced considerably faster responses. Nevertheless, the unit-step response and settling time alone are not sufficient to confirm that the original positioning repeatability of the Mitsubishi RV-2FRL can be maintained. Experimental validation and an evaluation of positioning error, disturbance rejection, and closed-loop performance are required before the practical feasibility of the proposed drive can be confirmed.

Future research will focus on experimental validation of the developed model, the identification of hydraulic parameters using a physical test system, and the development of an appropriate closed-loop control strategy. The model may also be extended to include nonlinear valve characteristics, pressure-dependent fluid properties, friction, variable payloads, and joint-dependent loading conditions.

ACKNOWLEDGMENTS

The research results presented in this paper were obtained within projects financially supported by the Ministry of Science, Technological Development and Innovation of the Republic of Serbia, under Contract No. 451-03-34/2026-03/200107, dated 5 February 2026.

REFERENCES

Blackburn, J. F., Reethof, G., & Shearer, J. L. (1960). *Fluid Power Control*. Cambridge, USA: The M.I.T. Press.

Chapple, J. P. (2010). Hydraulic servo system modelling and simulation. In *Proceedings of the 5th International Conference on Fluid Power* (pp. 45–52). Florence, Italy, 15–17 April 2010.

Човић, В., & Лазаревић, М. П. (2008). Механика робота. Београд, Србија: Машински факултет.

Jelali, M., & Kroll, A. (2003). *Hydraulic Servo-systems: Modelling, Identification and Control*. London, UK: Springer.

MathWorks. (2024). *Control System Toolbox Documentation*. Natick, USA: The MathWorks Inc.

Merritt, H. E. (1967). *Hydraulic Control Systems*. New York, USA: John Wiley & Sons.

Merritt, H. (1971). *Hydraulic servo systems*. Machine Design, 43(15), 92–99.

Mitsubishi Electric. (2020). MELFA RV-2FRL Series Standard Specifications Manual. Mitsubishi Electric Corporation.

Nichols, B. L., & Reistad, H. M. (1999). *Hydraulic servo systems*. In M. R. Adams (Ed.), Fluid Power Design Handbook (3rd ed., pp. 245–289). New York, USA: Marcel Dekker.

Saltelli, A., Ratto, M., Andres, T., Campolongo, F., Cariboni, J., Gatelli, D., Saisana, M., & Tarantola, S. (2008). *Global Sensitivity Analysis: The Primer*. Chichester, UK: John Wiley & Sons.

Watton, J. (1989). *Fluid Power Systems: Modeling, Simulation, Analog and Microcomputer Control*. Hemel Hempstead, UK: Prentice Hall.

The 11th International Congress
Motor Vehicles & Motors 2026
Kragujevac, Serbia
October 8th - 9th, 2026

Motor Vehicles & Motors

MVM2026-022
https://doi.org/10.24874/CMVM2026.022
Original scientific paper

Marko Delić[1]
Vesna Mandić[2]
Nada Ratković[3]
Nikola Komatina[4]
Dušan Arsić[5]
Nikola Kastratović[6]

ANALYSIS OF THE INFLUENCE OF IMPORTANT FORMING PARAMETERS IN SHEET METAL STAMPING IN AUTOMOTIVE INDUSTRY USING FEA

ABSTRACT: Manufacturing of parts using stamping technology is very common in the auto industry. In this paper, for a hood inner panel, the effects of manufacturing parameters were analysed using the finite element method. The influence of blank holding force, holding surface and tribological conditions is considered. The success of the process was analysed using the forming limit diagram, which in combination with FEA provides significant opportunities for process improvement. Results shows that friction have great impact on fracture occurring and quality of parts.

KEYWORDS: stamping, FEA, FLD

[1] *Marko Delić, Faculty of Engineering, University of Kragujevac, Sestre Janjić 6, marko.delic@kg.ac.rs,* https://orcid.org/0000-0001-5493-7569
[2] *Vesna Mandić, Faculty of Engineering, University of Kragujevac, Sestre Janjić 6, mandic@kg.ac.rs,* https://orcid.org/0000-0003-1624-3536
[3] *Nada Ratković, Faculty of Engineering, University of Kragujevac, Sestre Janjić 6, nratkovic@kg.ac.rs,* https://orcid.org/0000-0003-1446-8678
[4] *Nikola Komatina, Faculty of Engineering, University of Kragujevac, Sestre Janjić 6, nkomatina@kg.ac.rs,* https://orcid.org/0000-0001-6964-5673
[5] *Dušan Arsić, Faculty of Engineering, University of Kragujevac, Sestre Janjić 6, dusan.arsic@kg.ac.rs,* https://orcid.org/0000-0003-0326-0898
[6] *Nikola Kastratović, Faculty of Engineering, University of Kragujevac, Sestre Janjić 6, nikolakastratovic@gmail.com*

ANALIZA UTICAJA BITNIH PARAMETARA PRI DUBOKOM IZVLAČENJU DELOVA U AUTO INDUSTRIJI KORIŠĆENJEM MKE

REZIME: Izrada delova tehnologijom dubokog izvlačenja je veoma zastupljena u auto industriji. U ovom radu su za unutrašnji panel poklopca motora korišćenjem metode konačnih elemenata analizirani uticaji proizvodnih parametara. Razmatran je uticaj sile držanja, površine držanja i triboloških uslova. Uspešnost procesa je analizirana korišćenjem dijagrama granične deformabilnosti (DGD) koji u kombinaciji sa MKE pruža značajne mogućnosti unapređenja procesa. Rezultati pokazuju da trenje ima veliki uticaj na pojavu loma i kvalitet delova.

KLJUČNE REČI: duboko izvlačenje, MKE, DGD

INTRODUCTION

Stamping technology produces very important parts in the automotive industry that have complex geometry. Numerous parameters affect the success of the process. For faster tool development, software that uses the finite element method is often used. The result of numerical simulation is the stress and strain state, and recently, the forming limit diagram, which is integrated into numerical simulation software, has been used significantly for process analysis.

In the numerical experiment, the influence of lubrication and surface condition was considered using different values of the friction coefficient. Coulomb friction was used and the values of the friction coefficient were 0.05, 0.1 and 0.15. The case where the friction coefficient has a value of 0.05 represents an example of excellent lubrication when using special oils. The coefficient of 0.1 represents an average value with some deep drawing oils and finally the coefficient of 0.15 represents an unfavourable case.

According to Stefanović et al. (1997), lubricants have the role of minimizing friction losses, reducing tool wear, improving surface quality, and enabling control of metal flow.

It is a well-known fact that proper blank holding has a significant influence on the accuracy of the forming operation. Radonjić et al. (2015) experimentally and numerically demonstrated that, by optimizing the stiffness of the blank holder, it is possible to prevent fracture occurrence in the stamping process of an automotive fender.

The stamping process is influenced by numerous parameters; therefore, Liu et al. (2024) applied artificial neural networks to determine the optimal parameter values for the stamping of battery covers used in electric vehicles.

A similar study was conducted by Jia-Yin et al. (2025), who optimized the manufacturing parameters for stamping a highly complex cover geometry by combining the finite element method with a Genetic Algorithm–Optimized Back Propagation Neural Network.

Khatir et al. (2017) demonstrated that lubrication, i.e., friction conditions, plays a significant role in the manufacturing process of bipolar plates made of SS316L stainless steel with a thickness of 0.1 mm. The use of lubricants helped maintain a more uniform sheet thickness distribution and deformation throughout the forming process.

In this study, the influence of friction conditions will be numerically investigated using three different coefficients of friction, while three different blank holder pressure levels will also be applied. The first part of the study, aimed at evaluating the influence of tribological conditions alone, was carried out without an active blank holder. In this case, the blank holder was fixed in position and served solely as a calibration element. The combined effect of friction and blank holding force was evaluated in the second part of the study.

NUMERICAL EXPERIMENT

The component considered in this study is a hood inner panel with a complex geometry. The component is intended to be manufactured from sheet metal cut from a coil strip. The manufacturing process is planned to consist of three operations: stamping, hole piercing, and trimming. Although it would probably be more favourable

to cut the sheet with radius at the ends, this would require an additional operation, which would further increase the production cost.

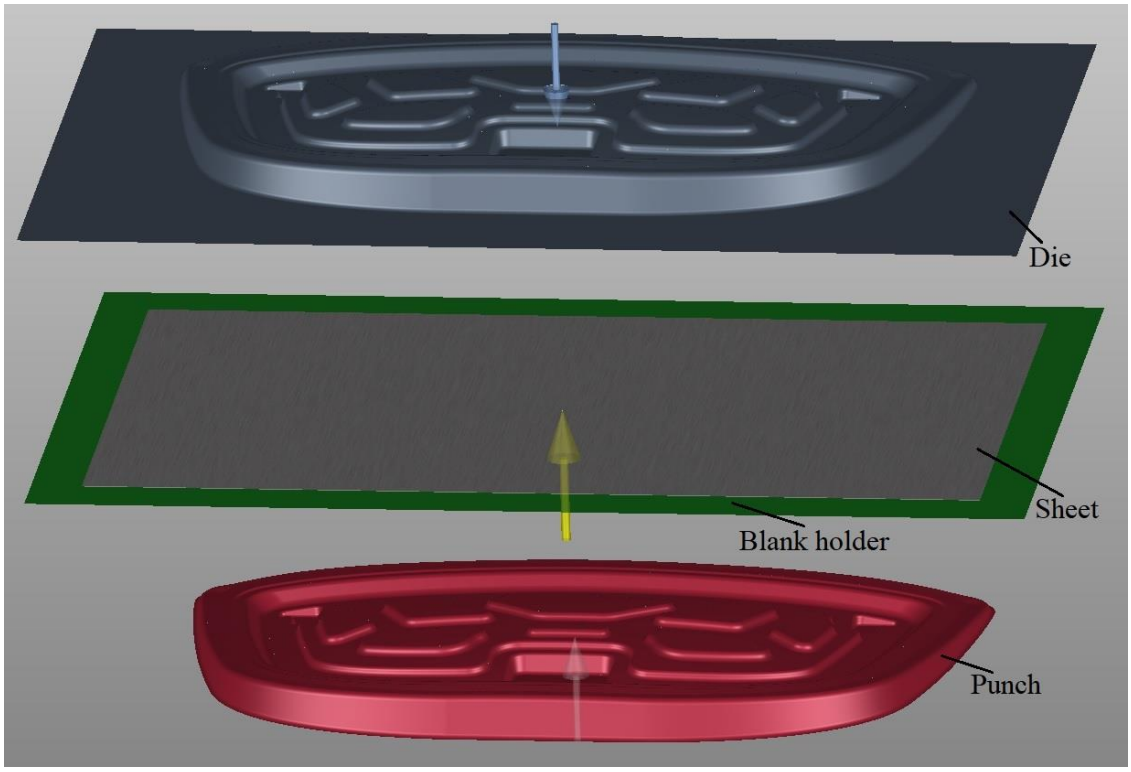

Figure 1 Tools for first operation

In this numerical study, the case of forming from a flat sheet blank will be analysed. The most important aspect is the design of all stamping tool components, particularly the blank holder, which plays a crucial role in preventing wrinkling. The prepared tools are shown in Figure 1. The punch is stationary and is positioned on the machine table. The sheet is clamped between the die and the blank holder. Low-carbon steels, high-strength steels, and aluminium alloys are commonly used for manufacturing such components in the modern automotive industry. In this study, DC04 carbon steel with a thickness of 0.8 mm was used.

The manufacturing process of the component is shown in Figure 2. Figure 2 presents the following stages:

a) the initial sheet blank,
b) the component after the stamping operation,
c) the component after the punching operation, and
d) the final hood inner panel.

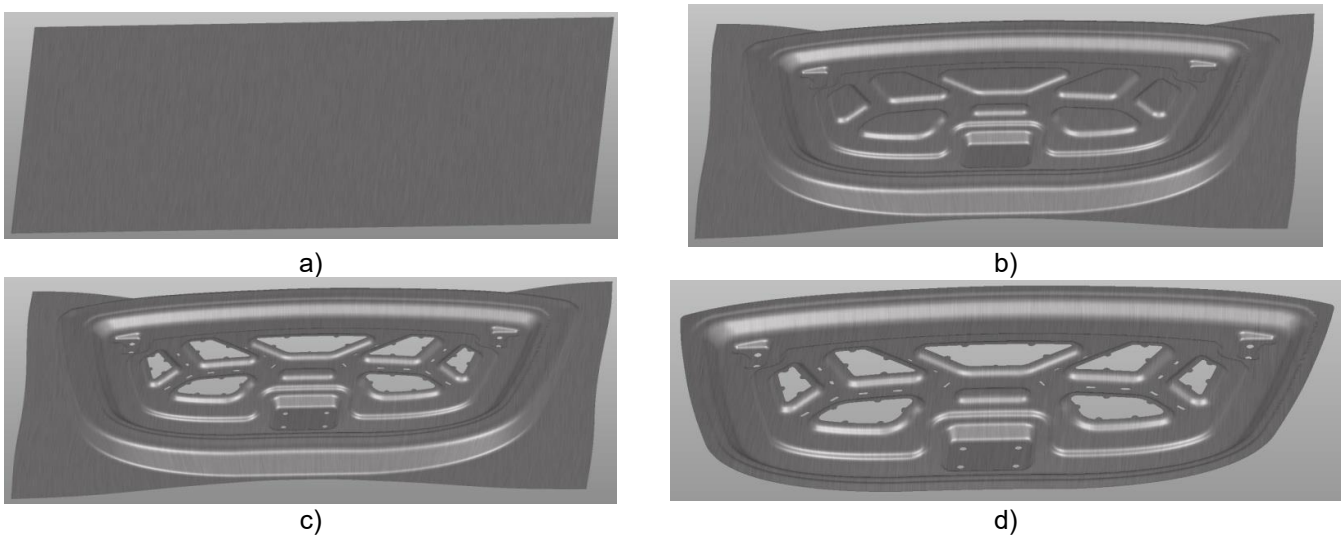

Figure 2 *a) Blank b) stamping operation c) punching operation d) trimming operation*

In this case, the simulation was performed using the Coulomb friction model, with identical tribological conditions defined for all tool surfaces. The following material properties were defined: a yield strength of 165.4 MPa, an ultimate tensile strength of 309.5 MPa, and a strain-hardening exponent of n = 0.219.

An important advantage of this steel is its good formability combined with a relatively low cost, which makes it suitable for the production of components with complex geometries.

Results of the first part of the experiment

The results of the first part of the experiment are presented in Figures 3, 4, and 5. Figure 3 shows the results obtained for a coefficient of friction of 0.15. An initial analysis of the geometry clearly indicates that the most critical region is the depression in the front section of the component. In this case, fracture occurred precisely in this region. The FLD diagram for this case is shown in Figure 3b, clearly demonstrating that, at a high coefficient of friction, the forming operation cannot be successfully completed and fracture will occur.

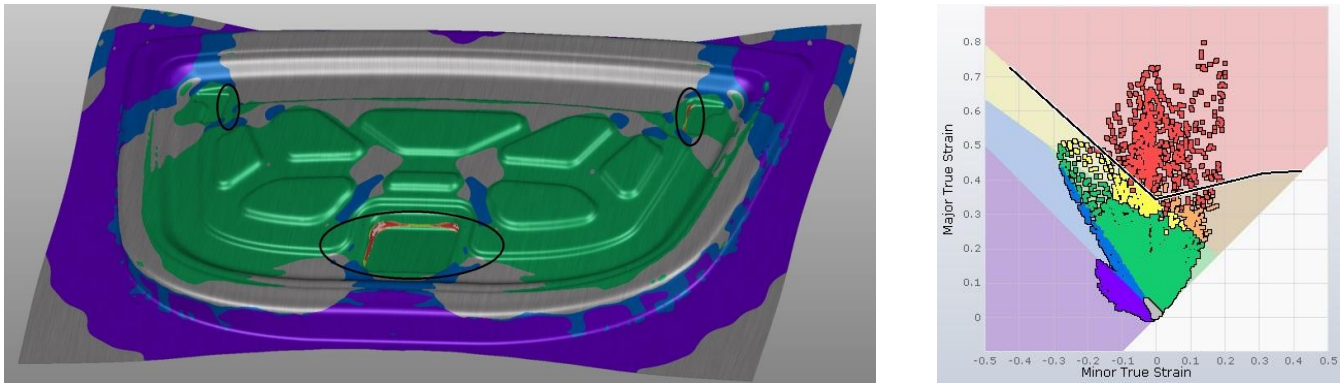

a) b)

Figure 3 Results for friction coefficient 0.15: a) sheet after first operation b) FLD diagram

Figure 4 presents the results obtained for a coefficient of friction of 0.1. As in the previous case, fracture occurs in the same region. Analysis of the FLD diagram shows that the forming operation is close to being successfully completed, with only a small portion of the strain state extending beyond the forming limit curve.

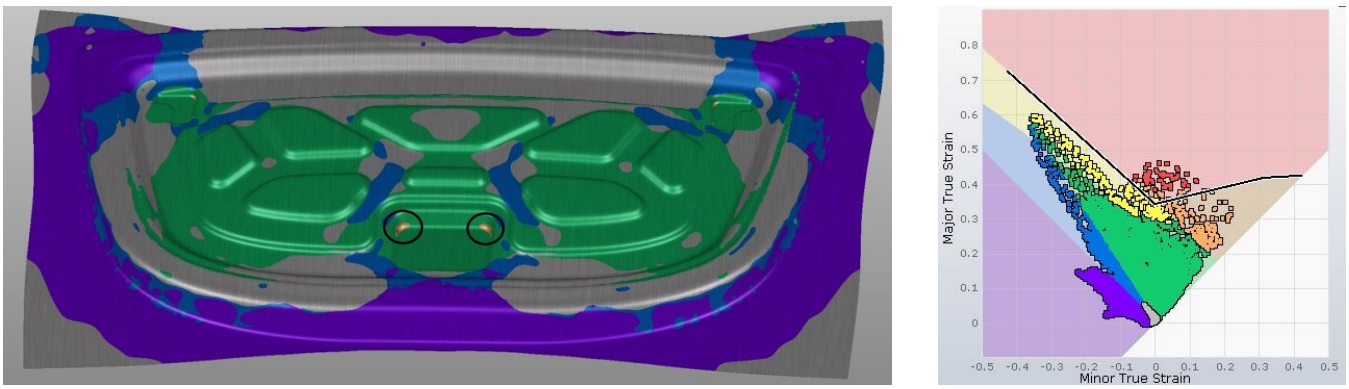

a) b)

Figure 4 Results for friction coefficient 0.1: a) sheet after first operation b) FLD diagram

In the final case considered, the forming operation was successfully completed without fracture. The results are presented in Figure 5. It can be clearly seen from the figure that the process was successful and that reducing the influence of friction conditions achieved the desired outcome.

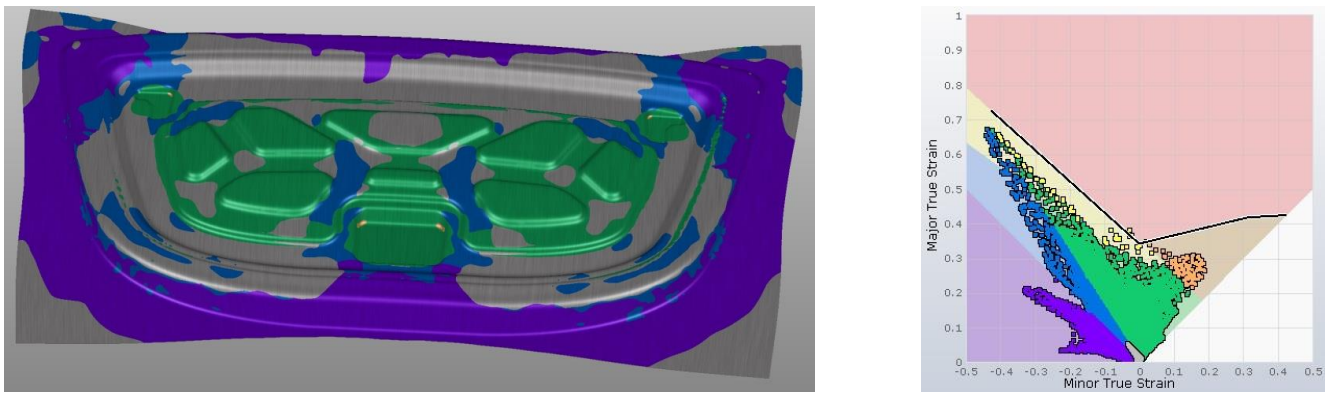

a) b)

Figure 5 Results for friction coefficient 0.05: a) sheet after first operation b) FLD diagram

The three cases considered clearly demonstrate the importance of achieving appropriate tool surface conditions and lubrication conditions when stamping complex components. In addition to evaluating the success of the forming operation, the forming forces can also be analysed. The force values are presented in Table 1. Based on the results presented in Table 1, it can be observed that friction has a significant influence on the forming force. The forming force decreases as the coefficient of friction decreases.

Table 1 Forces obtained by numerical simulation

	0.15	0.1	0.05
Die	2698.6 kN	2688.8 kN	2565.4 kN
Punch	2468.4 kN	2353 kN	2242.8 kN
Binder (blank holder)	367 kN	399.9 kN	475.1 kN

Results of the Second Part of the Experiment

In the second part of the experiment, the influence of the blank holding force was analysed. Theoretically, the blank holding force is calculated based on the blank holder area and the specific blank holder pressure. According to the domestic literature, the recommended blank holder pressure is between 2 and 3 MPa. Therefore, three cases were considered in the second part of the experiment: 1.5 MPa in the first case, 2.5 MPa in the second case, and 3.5 MPa in the third case. The experiment was performed for all three values of the coefficient of friction.

The results of the second part of the experiment were as expected. The use of a blank holder produced significantly better results. The results of the numerical experiment are presented in Table 2. For a coefficient of friction of 0.05, the forming operation was successfully completed for all three blank holder pressure values. When the coefficient of friction was 0.1, the results were identical, with no fracture occurring in any of the three cases. This result demonstrates the importance of using a blank holder for the successful execution of the forming operation, since the operation was not successfully completed when forming was performed without a blank holder. When the coefficient of friction was 0.15, the forming operation was unsuccessful for all three blank holder pressure values.

Analysis of the FLD shows that, in the first case (μ = 0.05), the forming process is completely safe and no fracture is expected to occur. Increasing the blank holder pressure reduces the possibility of wrinkling. In the second case (μ = 0.1), the tendency for wrinkling increases compared with the previous case. At a blank holder pressure of 3.5 MPa, which is slightly higher than the recommended value, the sheet is very close to fracture. The case with a coefficient of friction of 0.1 is the most realistic scenario. Therefore, this example demonstrates that the influence of blank holder pressure should be carefully considered. In the case of the highest coefficient of friction (μ = 0.15), it can be seen that successful forming is not possible.

Table 2 FLD diagrams for all cases

	1.5 MPa	2.5 MPa	3.5 MPa
0.05	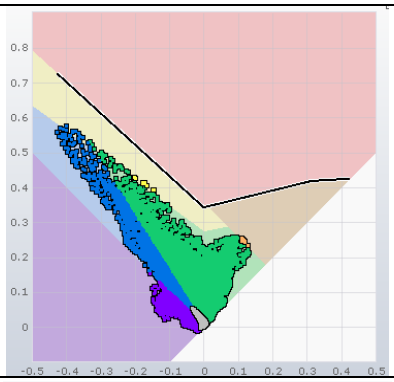	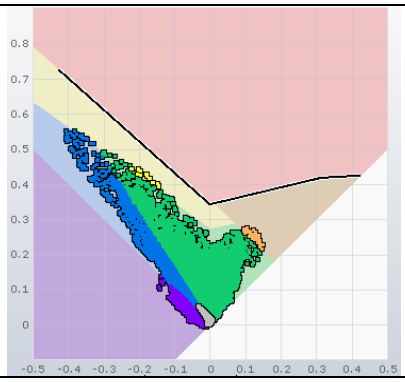	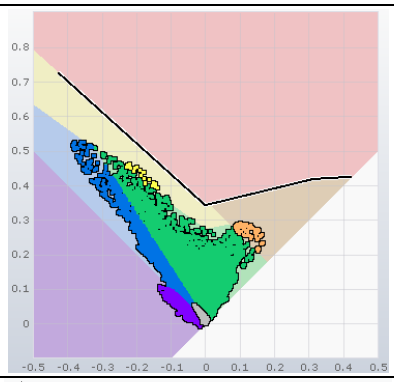
0.1	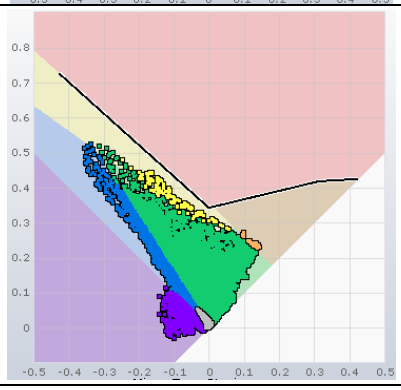	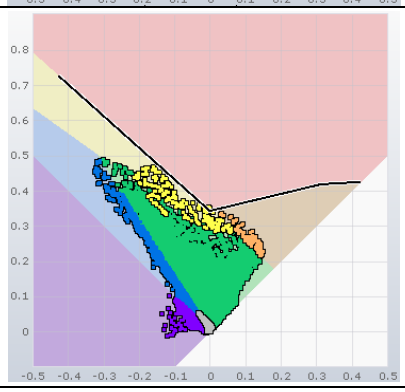	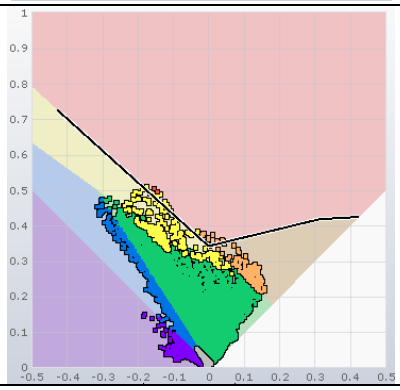

Table 2 (continuation)

0.15	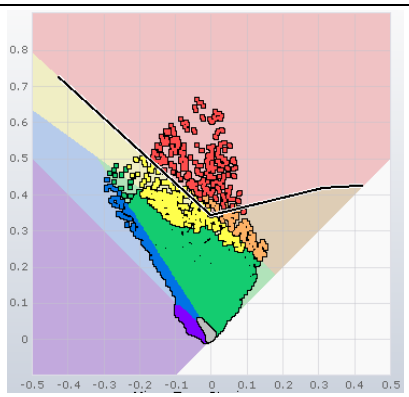	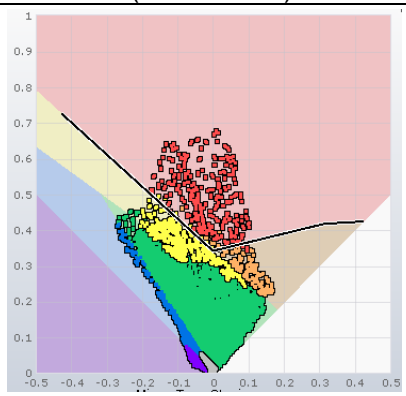	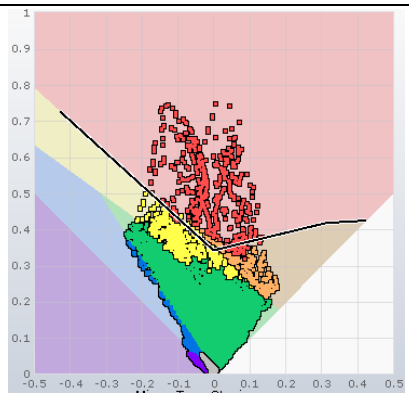

Different tribological conditions during the forming process result in different levels of sheet thinning, eventually leading to fracture. The sheet thickness distributions for two cases, with coefficients of friction of 0.1 and 0.15 and the same blank holder pressure of 2.5 MPa, are presented in Figure 6. In the less favourable case, the sheet thinning is approximately 30–40% greater than in the case with a coefficient of friction of 0.1.

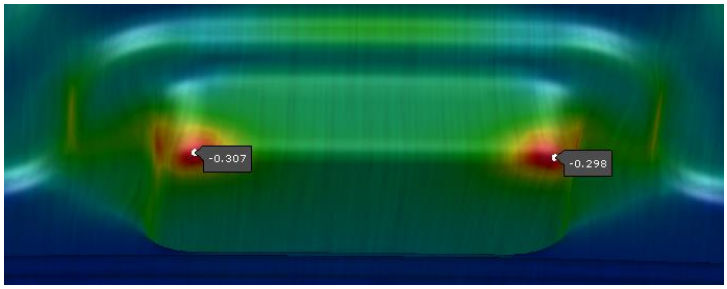

a)

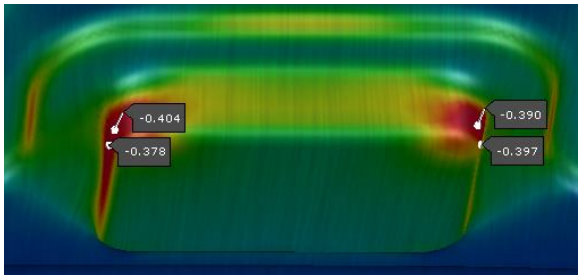

b)

Figure 6 Sheet thickness for two cases a) 0.1 and b) 0.15

CONCLUSIONS

Based on the results of the numerical simulations for the manufacturing of the selected automotive component, conclusions were drawn regarding the influence of the main process parameters on the success of the forming operation. It was concluded that the use of a blank holder is necessary. In the case of stamping without a blank holder, the operation was successfully completed only when the coefficient of friction was 0.05, which represents an almost ideal situation. In the absence of a blank holder, the tendency for wrinkling increases significantly.

In the second part of the experiment, in which the influence of friction and blank holder pressure was investigated, the significant effect of friction was confirmed once again. When the friction conditions were ideal (μ = 0.05) and realistic (μ = 0.1), the forming operation was successfully completed for all three blank holder pressure values (1.5 MPa, 2.5 MPa, and 3.5 MPa). However, at a blank holder pressure of 3.5 MPa, the component was close to fracture.

A reduction in the blank holder pressure increases the risk of wrinkling, therefore, it was concluded that particular attention should be paid to the blank holder pressure and that it should be maintained within the recommended range. Excessive blank holder pressure results in excessive sheet thinning and increases the risk of fracture. The results showed that the best overall results were achieved at the recommended blank holder pressure of 2.5 MPa. Future research will focus on investigating the control of the stamping process under friction conditions that vary across different tool surfaces, as well as on the influence of variable blank holder pressure.

ACKNOWLEDGMENTS

The present work was funded by the Ministry of Science, Technological Development and Innovation, Republic of Serbia, Agreement No. 451-03-34/2026-03/200107.

REFERENCES

Stefanovic, M., Aleksandrovic, S. (1997). Lubrication and the choice of lubricants for deep-drawing. *Journal for Technology of Plasticity*, 22 (1-2), 13-22.

Radonjic, R., Liewald, M., Han, F. (2015, June 15-17). Optimisation of the blank holder stiffness in deep drawing processes by using FEA. The 10th European LS-DYNA Conference, Würzburg, Germany.

Liu, N., Gao, Y., & Liu, P. (2024). Design of battery shell stamping parameters for vehicles based on fusion of various artificial neural network models. *Heliyon*, 10(5), e26406. https://doi.org/10.1016/j.heliyon.2024.e26406

Jia-yin, S., Zhen, Y., Yang-qing, W., Cui, W., Shui-gen, N., Bing-xin, C., & Hai-dong, Z. (2025). Optimization and experimental verification of stamping process parameters for battery pack top cover based on GA-BP algorithm. *International Journal of Lightweight Materials and Manufacture*. https://doi.org/10.1016/j.ijlmm.2025.11.008

Khatir, F. A., Elyasi, M., Ghadikolaee, H. T., & Hosseinzadeh, M. (2017). Evaluation of effective parameters on stamping of metallic bipolar plates. *Procedia Engineering*, 183, 322-329. https://doi.org/10.1016/j.proeng.2017.04.047

The 11th International Congress
Motor Vehicles & Motors 2026
Kragujevac, Serbia
October 8th - 9th, 2026

Motor Vehicles & Motors

MVM2026-024
https://doi.org/10.24874/CMVM2026.024
Technical paper

Milan Simonović[1]
Dragan Adamović[2]
Đorđe Ivković[3]
Marko Simonović[4]

ANALYSIS OF THE POSSIBILITY OF PREDICTING THE TENSILE STRENGTH OF ADVANCED STRUCTURAL STEELS USED IN THE AUTOMOTIVE INDUSTRY USING ARTIFICIAL NEURAL NETWORKS WITH DIFFERENT NUMBERS OF NEURONS IN THE HIDDEN LAYER

ABSTRACT: This paper presents the possibility of predicting the tensile strength of advanced structural steels used in the automotive industry by means of an artificial neural network. The prediction was performed in the MATLAB R2020a software package using five neural network models with different numbers of neurons in the hidden layer in order to determine the optimal neuron configuration that provides the most accurate results. The tensile strength (Rm) was predicted based on the chemical composition of the steel and the heat-treatment temperature, which served as the input variables. The dataset was divided into subsets as follows: 70% for training, 15% for validation, and the remaining 15% for testing. The criteria used for selecting the best neural network were the maximum value of the correlation coefficient obtained on the testing dataset and the consistency of correlation coefficients across the training, validation and testing datasets, thereby ensuring the stability and reliability of the model. Particular emphasis was placed on the results obtained for the testing dataset, as they represent the most relevant assessment of the model's ability to predict output values for data that were not used during the network training process.

KEYWORDS: Artificial intelligence, neural networks, structural steels, tensile strength, automotive industry.

[1] *Milan Simonović, Military Technical Institute, Ratka Resanovića 1, Beograd, milan.simonovic@mod.gov.rs,*
https://orcid.org/0009-0001-5502-7708
[2] *Dragan Adamović, Faculty of Engineering, University of Kragujevac, Sestre Janjić 6, adam@kg.ac.rs,*
https://orcid.org/0000-0003-3459-3011
[3] *Đorđe Ivković, Faculty of Engineering, University of Kragujevac, Sestre Janjić 6, djordje.ivkovic@fink.rs,*
https://orcid.org/0000-0002-5747-7876
[4] *Marko Simonović, Military Technical Institute, Ratka Resanovića 1, Beograd, marko.simonovic@mod.gov.rs,*
https://orcid.org/0009-0007-5531-6175

ANALIZA MOGUĆNOSTI PREDVIĐANJA ZATEZNE ČVRSTOĆE SAVREMENIH KONSTRUKCIONIH ČELIKA U AUTOMOBILSKOJ INDUSTRIJI, UPOTREBOM VEŠTAČKE NEURONSKE MREŽE, VARIRANJEM BROJA NEURONA U SKRIVENOM SLOJU

REZIME: U ovom radu prikazana je mogućnost predviđanja zatezne čvrstoće savremenih konstrukcionih čelika, koji se koriste u automobilskoj industriji, pomoću veštačke neuronske mreže. Predviđanje je izvršeno u programskom paketu MatLab R2020a, upotrebom pet modela neuronskih mreža, sa različitim brojem neurona u skrivenom sloju mreže, kako bi se odredila najoptimalnija kombinacija broja neurona, koja će omogućiti dobijanje što preciznijih rezultata. Zatezna čvrstoća Rm je predviđana na osnovu hemijskog sastava čelika i temperature termičke obrade, koji predstavljaju ulazne podatke. Čelici su podeljeni u skupove i to: 70% pripada skupu za učenje, 15% skupu za validaciju, a preostalih 15% skupu za testiranje. Kao kriterijumi za odabir najbolje mreže korišćeni su maksimalna vrednost koeficijenta korelacije u skupu za testiranje, kao i ujednačenost koeficijenata korelacije u skupovima za učenje, validaciju i testiranje, čime su obezbeđeni stabilnost i pouzdanost modela. Poseban značaj dat je rezultatima u skupu za testiranje, jer oni predstavljaju najrealniju procenu sposobnosti modela da predviđa izlazne vrednosti za podatke, koji nisu korišćeni tokom procesa učenja mreže.

KLJUČNE REČI: Veštačka inteligencija, neuronske mreže, konstrukcioni čelici, zatezna čvrstoća, automobilska industrija.

INTRODUCTION

Increasing safety and reducing fuel consumption represent challenges that vehicle manufacturers continuously face, and they therefore constantly seek new materials in order to meet increasingly demanding standards. In addition, several other factors drive research and material selection for automotive applications, including environmental protection, manufacturability, durability and quality. In the highly competitive automotive industry, cost is an extremely important factor in material selection. As the motivation to reduce vehicle mass continues to grow, vehicle manufacturers strive to maximize the efficiency of their material-selection decisions. Materials in the automotive industry are selected so as to reduce weight while simultaneously meeting key criteria, including crash performance, stiffness and formability requirements (Hu & Feng, 2021). Among the most important mechanical properties of these materials is tensile strength (Rm), which represents one of the fundamental indicators of the load-bearing capacity and resistance of a material to external loads.

Initially, vehicles were made of steel of a certain thickness. With advances in steel development, material thickness has been reduced, and today very thin sheets (sometimes as thin as 0.5 mm) are used in body production. In addition, many steel components are being replaced by parts made of lighter materials, thereby reducing the unladen vehicle mass and increasing its payload capacity. Moreover, reduced vehicle mass leads to lower fuel consumption, which directly contributes to environmental protection. It is essential that material substitution and thickness reduction do not compromise passenger safety. The group of materials that stands out most prominently in meeting these requirements is advanced high-strength steel (AHSS). High-strength steels were developed at the end of the 19th century and are now widely used in all branches of mechanical engineering. They are characterized by favorable mechanical properties (strength and ductility) while maintaining good processability (forming, welding, etc.). Today, the manufacturing processes for these steels have advanced to such an extent that their price is often comparable to that of conventional low-carbon steels, while their mechanical properties are significantly better. The high strength of these steels results from the application of complex thermal, thermomechanical and mechanical processing procedures. Consequently, high strength enables smaller component cross-sections, reducing both the amount of material used and the weight of structures. In the vehicle manufacturing industry, the amount of advanced high-strength steel (AHSS) used in vehicle body production increases every year. Today, high-strength steels are used in vehicles not only for body components but also for more critical automotive components (Arsić et al. 2025).

The application of artificial intelligence methods in material testing and selection offers a very broad range of possibilities, facilitating the solution of many design problems that arise during product development. The development of methods based on artificial intelligence has enabled a transition from an exclusively experimental approach to one that combines test results with advanced models for predicting material properties, thereby increasing efficiency and accelerating the development of modern structural steels for the automotive industry. These methods can be used to model various material-property testing processes and thus predict material behavior in

service. The properties themselves can also be modeled by increasing or decreasing the percentage of a particular material element, thereby examining its characteristics under different conditions. In addition, these methods can be applied to the selection of an appropriate material, which is one of the most important stages of product development (Filetin, 2000).

Neural networks are a powerful tool for modeling the behavior of modern structural steels, as well as other widely used materials, because they are capable of predicting mechanical properties with a high degree of accuracy on the basis of existing experimental data. By integrating experimental testing methods and artificial intelligence algorithms, it is possible to accelerate the development of new generations of steels intended for the automotive industry and reduce the costs of their characterization. The increasing availability of experimental data on the chemical composition and mechanical properties of steels has created favorable conditions for the successful application of artificial neural networks in materials engineering.

This paper considers the possibility of predicting the tensile strength (Rm) of modern structural steels used in the automotive industry by applying artificial neural networks based on their chemical composition and heat-treatment temperature, with the aim of developing a reliable model for estimating the mechanical properties of materials. Artificial neural network algorithms make it possible to establish relationships between chemical composition, heat treatment and nominal material-property values, thereby significantly reducing the need for a large number of costly and time-consuming experimental tests. In this way, artificial intelligence becomes an important tool for optimizing the development of new steels and improving material-design processes in the automotive industry.

ARTIFICIAL INTELLIGENCE

Artificial intelligence is a scientific and engineering field that combines theory and practice and is concerned with the development of systems with characteristics similar to those of the human brain. An artificial-intelligence-based system should possess perception, problem-solving, planning, learning and adaptation capabilities. As a scientific objective, artificial intelligence should fully support several engineering-relevant activities, such as the development of intelligent agents, the formalization of knowledge and the mechanization of reasoning in all areas in which substantial effort is required to solve a problem (Tecuci, 2012).

According to one definition, artificial intelligence may be described as a way of reasoning and acting on derived conclusions with complete reliance on logic, where such reasoning and action are performed not by a human or any other living organism, but by machines in the broadest sense of the word. The term “machine” does not refer only to a device composed of various machine elements and assemblies, but rather to something capable of independently performing certain complex functions instead of a living being. One of the basic aims of artificial intelligence is to substitute for the human brain in functions that can be performed by machines, with such functions being carried out incomparably faster and more accurately than by humans. Typical examples of this use of artificial intelligence include various calculations, ranging from calculators to modern software applications that almost instantaneously perform complex statistical and other operations involving a large number of variables: calculation of correlations and application of higher-order forms and models for measuring relationships among numerous variables, particularly those that, because of their complexity, cannot be observed directly but are described by a larger number of simpler variables (Branković, 2017).

Artificial neural networks

The concept of artificial neural networks dates back to the mid-1950s. Artificial neural networks are based on deep-learning algorithms. Deep learning is a set of techniques within machine learning that enables machines to adopt a human-like approach to problem solving, i.e. to learn through examples. Examples of deep-learning applications include image recognition, natural-language processing and speech recognition. Unlike the human brain, a computer operates according to predefined algorithms created by the human brain and therefore does not possess its own creativity during the decision-making process; in other words, a computer operates according to deterministic principles. It follows that artificial neural networks represent a set of programs, i.e. a simulation that, in certain respects, imitates the operation of the human brain (Stanković, 2019). Artificial neural networks were developed according to the model of biological neural networks, although they differ considerably from them. The human brain consists of a large number of interconnected neurons. The relationships among neurons and the strength of their interconnections determine the behavior of a biological neural network. The behavior of a biological neural network changes over time as the strength of connections between neurons in the so-called synapses increases or decreases. By changing the strength of connections between biological neurons, living organisms learn. Artificial neural networks are far less complex than the brain, although important similarities exist between natural and artificial neural networks: the elements from which both types of networks are constructed are interconnected, while the connections between the elements determine the behavior of the network (Žmak, 2009).

The layers of a network in which neurons are arranged may be input, hidden and output layers. The input layer receives data and forwards them to the hidden layers. In the hidden layers, information is processed and subsequently sent to the neurons of the output layer. The information then propagates backward through the network, while the values of the weights between neurons are adjusted toward the desired output. This process is repeated in the network as many times as necessary to obtain an output as close as possible to the desired (actual) output, which is subsequently presented. The strength of the connection between two neurons is represented by the connection weight, while the process of determining the values of the connection weights between neurons is referred to as learning (Dumančić, 2014).

The operating phases of artificial neural networks can be divided into:

- the learning (training) phase,
- the selection phase,
- the testing phase, and
- the operational phase.

The learning and testing phases are most commonly identified as the two basic operating phases of artificial neural networks. During the selection phase, the network seeks to optimize the training duration and the number of hidden neurons, after which the resulting network is stored and tested. The operational phase refers to the application of the neural network to new cases with unknown results and fixed weights. Learning is the process of changing the weights in the network. The data represented in the output layer are the desired values of the output variables. Before learning begins, it is necessary to define the model (input and output variables) and prepare the data to which the network will be applied. The data are most often divided into two samples: a training sample and a testing sample. There is no precisely defined rule for dividing data into samples, although it is recommended that the largest portion of the data be reserved for network training. After defining the model and preparing the input/output data and learning rules, the network must be trained to recognize relationships among the data and predict output values on the basis of the inputs (Dumančić, 2014).

The learning phase is essentially the process of adjusting the weights in the network and takes place through multiple repetitions (passes through the network). A network is commonly trained through several thousand iterations, and the most important issue is to determine how long the network should be trained in order to obtain the best possible result, i.e. the smallest possible error. There is no exact rule for the duration of learning. The second phase of a neural network is testing, which may be regarded as the decisive phase for evaluating the network itself. During testing, the network no longer learns; the weight values are fixed at those obtained during the learning phase. New input values (which did not participate in the learning process) are then presented to the network, which is expected to produce the corresponding output value for each new input (Dumančić, 2014).

The network is evaluated by calculating an error or another measure of accuracy, by comparing the network output with the actual output values. The success or failure of the network, as well as its usability, is interpreted using the error obtained on the validation sample. The most common error calculated for neural networks can be expressed by the following equation:

$$\sigma = \sqrt{\frac{\sum_{i=1}^{n-1}(t_i - o_i)^2}{n}} \tag{1}$$

where:

ti – calculated output produced by the network,
oi – desired (actual) output for case (i), and
n – number of cases in the sample.

Mean squared error, mean absolute error and correlation coefficients can also be used as performance measures (Dumančić, 2014).

Examples of artificial neural network applications in mechanical engineering

The application of artificial neural networks in the field of materials is very broad. They can be used to predict material service life, behavior under given environmental conditions, behavior under specific stresses, corrosion initiation and many other material characteristics. The possibility of predicting fatigue-crack propagation in aluminum alloys under loading has been demonstrated experimentally. Artificial neural networks show considerable potential for predicting fatigue fracture behavior, particularly by interpolation within the tested range. However, their usefulness decreases when the model is required to extrapolate beyond the available experimental data (Mohanty et al., 2009). Modern software tools, particularly artificial intelligence methods, enable the development of methods for designing the chemical composition of alloyed structural steels, which constitute one of the fundamental groups of metallic

engineering materials. A case study has presented a method for designing chemical composition based on the known and required shape of a hardenability curve using neural networks (Dobrzański & Sitek, 2003).

Artificial neural networks can also be applied to assess the quality of a machined surface. By entering input data, a trained network can provide output values of surface roughness within a short period of time. Such a network is particularly suitable for less experienced engineers because it reduces technological preparation and production time (Šimunović et al. 2009). In addition to mechanical and physical properties, chemical composition and other data, knowledge of the microstructure is required in order to assess the quality and applicability of each individual material. Along with the development of technologies for digitizing and storing large numbers of images, sequential systems were developed and applied to image analysis and statistical image processing. Only with the development of artificial-intelligence systems did image recognition become a computer-solvable task. A developed system for recognizing material microstructures demonstrated the applicability of neural networks to this highly complex classification task (Galinec & Filetin, n.d.).

An intelligent system for predicting the mechanical properties of materials based on metallographic images has been developed. The system consists of two modules. The first module is an algorithm for extracting features from metallographic images. The second module is a system for predicting the mechanical properties of the material (Paulič et al., 2015). Modeling and prediction of the service life of composite materials can be performed using artificial intelligence. Mechanical properties such as tensile strength, compressive strength and fracture resistance can be used as input parameters. With regard to loading parameters, maximum and minimum stress, as well as relative stress, can be used (Mathur et al., 2007). Artificial neural networks are successfully used to classify steels on the basis of ultrasonic non-destructive testing data or to identify standardized grades on the basis of chemical composition. Backpropagation systems are used to predict steel microstructure and strength. Austenite grain size and cooling rate in different temperature intervals of phase transformations can be used as independent variables for microstructure prediction (Žmak, 2003). Material-processing operations in which artificial neural networks are applied for various purposes include cold rolling, welding (for example, qualification of an appropriate welding procedure for particular welded joints or verification of a friction-welding procedure), steel hardening, etc. (Atuwo, 2018).

In addition to the examples listed above, there are many other cases in which artificial neural networks or other artificial intelligence methods have been used to solve complex problems arising during the design or manufacture of a product.

ADVANCED STRUCTURAL STEELS IN THE AUTOMOTIVE INDUSTRY

Approximately 30 types of steel are currently used in the automotive industry and can be classified according to three designations: metallurgical designation, strength and formability. The metallurgical designation provides information on steel composition, manufacturing process and microstructure. Steels for the automotive industry can be classified as traditional low-carbon steels, conventional high-strength steels (HSS) and advanced high-strength steels (AHSS). Another important method of classifying steels in the automotive industry is based on their strength.

The terms “HSS” and “AHSS” are generally used to designate all high-strength steels. AHSS steels are sometimes also referred to as “Extra-HSS” or “Ultra-HSS” for tensile strengths greater than 780 MPa and 1000 MPa, respectively. However, the terminology used to classify HSS steels varies considerably worldwide because of the continuous development of new generations of AHSS steels. Steel formability is defined as its ability to be formed into simple and complex shapes by different manufacturing processes. Important parameters characterizing formability are a high strain-hardening exponent and total elongation. While a high strain-hardening exponent contributes to the ability of sheet metal to stretch and distribute deformation uniformly under loading, total elongation determines the extent to which the steel can be stretched before fracture (Hu & Feng, 2021).

Figure 1 presents tensile-strength and total-elongation diagrams that are frequently used as a guideline when selecting steels with respect to strength and formability. However, recent studies have shown that materials belonging to similar AHSS grades but produced by different steel manufacturers can exhibit very different hole-expansion formability, which is a very common operation in the automotive industry. It has been established that differences in the properties of the phases constituting the steel microstructure are among the most important factors affecting material deformability and fracture resistance under localized deformation, such as hole expansion, where cross-sectional necking does not occur (Hu & Feng, 2021).

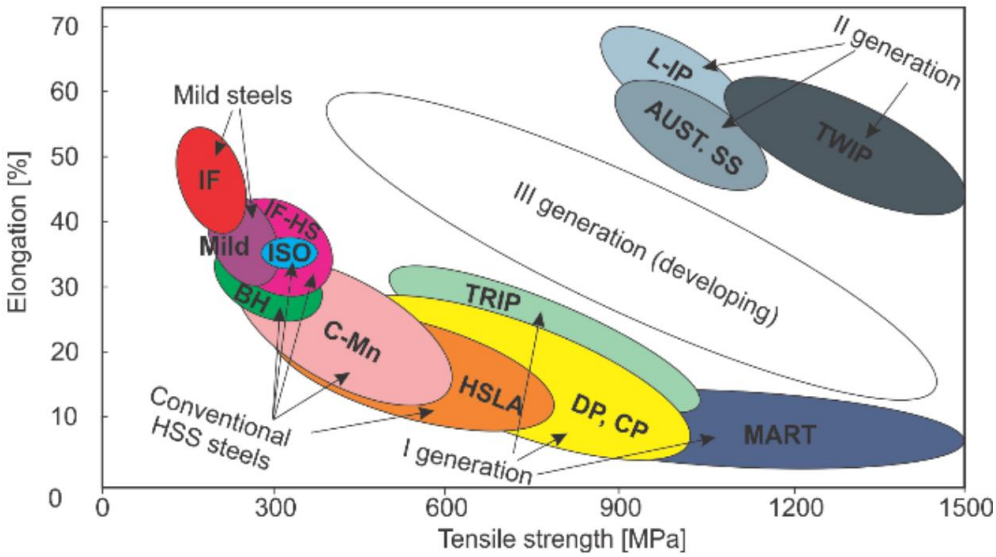

Figure 1 Tensile strength and total elongation diagrams (Arsić et al. 2025)

The steel designations shown in the figure are:

- IF – interstitial-free steel,
- IF-HS – high-strength interstitial-free steel,
- BH – bake-hardening steel,
- HSLA – high-strength low-alloy steel,
- TRIP – transformation-induced plasticity steel,
- DP – dual-phase steel,
- CP – complex-phase steel,
- MART – martensitic steel,
- L-IP – lightweight steel with aluminum addition and induced plasticity,
- TWIP – twinning-induced plasticity steel, and
- AUST. SS – austenitic stainless steel.

AHSS steels are produced through a complex thermomechanical production cycle characterized by intensive hot rolling followed by rapid cooling in order to obtain a specific microstructure. Depending on the type of steel, rolling temperatures, cooling rates and subsequent heat treatments vary. For example, the production of cold-rolled dual-phase (DP) steels primarily involves heating previously cold-rolled steel strips of an appropriate chemical composition to a temperature between Ac1 and Ac3. In this temperature range, the steel microstructure consists of ferrite and austenite. As the heating temperature increases (approaching the critical Ac3 temperature), the fraction of austenite increases, as does the amount of carbon that can dissolve in the austenite. On the other hand, the production of transformation-induced plasticity (TRIP) steel begins with rolling in the austenitic region, followed by cooling to 800 °C. At this temperature, the steel is held for 60 seconds, after which it is rapidly cooled to 450 °C, where it is held isothermally for 90 seconds. This isothermal holding results in the formation of a certain amount of bainite in the ferritic matrix. After holding at 450 °C, the steel is coiled and cooled to ambient temperature. The microstructure of these steels is also multiphase and consists of a ferritic matrix with retained austenite and bainite (Arsić et al. 2025).

EXPERIMENTAL INVESTIGATION

Prediction of the tensile strength of advanced structural steels based on chemical composition and heat treatment was performed using neural networks in the MATLAB R2020a software package. Five two-layer neural-network architectures were used for prediction; the numbers of hidden neurons are shown in Table 1. The table presents different neural-network architectures that were tested in order to identify the configuration that best predicts the mechanical properties of steel. Based on the results, an architecture was selected that provides accurate predictions and stable behavior in both the testing and validation datasets. Learning was performed using the error-backpropagation algorithm. A bipolar sigmoid function with a slope of $\sigma=2$ was used in the hidden layer, while a linear activation function was used in the output layer. The Levenberg-Marquardt algorithm was employed. The initial value of the Marquardt parameter was set to $\mu=0.001$. The decrease factor for this parameter was 0.1 and the increase factor was 10. The parameter is multiplied by the decrease factor at each step in which the objective function decreases. It is multiplied by the increase factor if the objective function increases at a given learning step. If the value of the Marquardt parameter rises above the limiting value of 1010, learning is stopped. The maximum number of learning steps was set to 1000.

Table 1 Number of neurons in the hidden and output layers

Model	1	2	3	4	5
Number of neurons	5	10	15	20	25
	1	1	1	1	1

For the prediction of mechanical properties, 124 structural steels from different groups shown in Figure 1 were selected. The input data were divided into three datasets: training (70%), validation (15%) and testing (15%). The first 86 steels belonged to the training dataset, the next 19 to the validation dataset and the remaining 19 to the testing dataset. Chemical compositions, heat-treatment temperatures and tensile-strength values were obtained from manufacturers' websites and scientific papers.

The optimal neural-network architecture was selected on the basis of the maximum value of the correlation coefficient in the testing dataset, as well as the consistency of the correlation coefficients across the training, validation and testing datasets, thereby ensuring model stability and reliability. Particular emphasis was placed on the results obtained for the testing dataset, because they represent the most realistic assessment of the model's ability to predict output values for data that were not used during the network learning process.

In addition to the correlation coefficients, model accuracy and reliability were examined by calculating the relative prediction error and analyzing the percentage of samples belonging to defined deviation intervals. This presentation enables a more detailed assessment of prediction quality because it shows not only the average model deviation but also the distribution of errors across the entire dataset.

Input data

As previously stated, the input data consist of chemical composition and heat-treatment temperatures, whose values were obtained from the websites of renowned global steel manufacturers such as SSAB, Nippon, Metal Zenith, POSCO, ArcelorMittal, BENTELER, ESB and U.S. Steel Košice (ArcelorMittal, n.d.; BENTELER, n.d.; ESB Group, n.d.; Metal Zenith, n.d.; Nippon Steel Corporation, n.d.; POSCO, n.d.; SSAB, n.d.; U. S. Steel Košice, n.d.). Table 2 presents the steel groups and their corresponding subgroups, as well as the ranges of the chemical elements that constitute their chemical composition.

Table 2 Chemical composition of the investigated steels

Chemical composition / **Steel groups**	C	Si	Mn	P	S	Al	Cu	B	Nb+Ti	Cr+Mo
AHSS – DP, CP, QB, FB, MS, TRIP	0.05-0.40	0-2.0	1.0-3.5	≤0.10	≤0.02	0.02-1.50	0-0.50	≤0.005	≤0.20	≤2.0
HSLA – S...MC, HC...LA, HCT...LA, HX...LAD	0.03-0.15	0-0.50	0.50-1.80	≤0.05	≤0.02	0.02-0.10	0-0.50	≤0.003	≤0.30	≤2.0
PHS – Usibor, Ductibor, BTR, Docol PHS, MBW	0.20-0.38	0.10-0.40	1.0-1.50	≤0.03	≤0.01	0.02-0.08	0-0.20	0.001-0.008	0-0.10	0-0.80
Conventional structural steels – S...GD, HX...YD, HX...BD	0.001-0.12	0-0.10	0.05-0.80	≤0.10	≤0.03	0.02-0.10	0-0.20	0	0.11	0-0.25

Table 3 presents the ranges of characteristic processing temperatures for the previously listed steel groups.

Table 3 Range of characteristic processing temperatures

Steel group	**Range of characteristic processing temperatures [°C]**	**Heat treatment**
Conventional structural steels (S…GD, HX…YD, HY…BD)	650 – 900	Recrystallization annealing, continuous annealing or normalizing
HSLA (S…MC, HX…LAD, HC…LA, HCT…LA)	850 – 950	Normalizing or austenitization temperatures during thermomechanical processing
AHSS (DP)	760 – 900	Intercritical annealing between Ac1 and Ac3

Table 3 (continuation)

AHSS (FB, CP)	800 – 950	Austenitization or intercritical annealing with controlled cooling (FB) or accelerated cooling (CP)
AHSS (QB)	800 – 950	Austenitization before quenching and carbon partitioning
AHSS (MS)	850 – 950	Austenitization before quenching
AHSS (TRIP)	780 – 900	Intercritical annealing before bainitic transformation
PHS (Usibor, Ductibor, BTR, MBW)	880 – 950	Austenitization before hot stamping and die quenching

Tensile-strength prediction

For the purpose of predicting tensile strength Rm using artificial neural networks, several network architectures with different numbers of neurons in the hidden layer were analyzed. Model performance was evaluated on the basis of the correlation coefficient R for the training, validation and testing datasets. In order to select the optimal network architecture, models with 5, 10, 15, 20 and 25 neurons in the hidden layer were compared. The obtained correlation coefficients are presented in Table 4, while the diagrams compare the nominal and predicted tensile-strength Rm values for the analyzed models.

Table 4 Values of the correlation coefficient, R

Models / **Coefficient R**	5	10	15	20	25
Training	0.885	0.99766	0.91065	0.88796	0.98803
Validation	0.70907	0.88058	0.95909	0.84466	0.89438
Testing	0.81478	0.85998	0.79438	0.87189	0.88539

Based on the analysis of the correlation coefficient R in the training, validation and testing datasets, the neural network with 20 neurons in the hidden layer was selected as the optimal model. This model exhibited the most stable performance and the best generalization ability, since the correlation-coefficient values were the most mutually consistent (similar). The small differences among these values indicate an absence of model overfitting, confirming that the network successfully approximates the relationship between input and output parameters even for data that were not used during the learning process. The criterion for selecting the optimal network architecture was therefore not only the maximum correlation coefficient but also the stability of model performance in the validation and testing datasets.

In addition to the numerical analysis of correlation coefficients, a visual analysis of the predicted and nominal Rm diagrams and regression diagrams was performed in order to assess the accuracy and stability of the individual models in greater detail. In the diagrams shown in Figures 2, 3, 4, 5 and 6, the black line represents the nominal Rm values, while the orange line represents the values predicted by the neural network. Analysis of the diagrams shows that all models successfully follow the general trend of tensile-strength variation; however, differences exist in prediction stability and accuracy. The model with the smallest number of neurons (5 neurons) shows larger deviations and a weaker ability to approximate more complex changes in the values, particularly at higher tensile strengths. As the number of neurons increases, the ability of the network to follow nonlinear changes in the nominal values improves. However, the models with 10 and 25 neurons exhibit more pronounced local oscillations in the predicted values, which may indicate model overfitting, i.e. excessive adaptation to the training data. The model with 15 neurons shows good agreement in certain intervals but larger deviations at some extreme values.

In contrast, the model with 20 neurons provides the most stable tracking of the experimental curve, with the smallest overall deviations and without pronounced oscillations in the predicted values. Based on the visual analysis of the diagrams and the correlation-coefficient values, it can be concluded that the neural network with 20 neurons in the hidden layer represents the optimal model architecture for tensile-strength prediction, because it provides the best balance between prediction accuracy and model generalization ability.

For a more detailed assessment of the quality of the optimal model, regression diagrams of the neural network with 20 neurons in the hidden layer were analyzed (Figure 7). The diagrams show the relationship between the nominal (target) values and the values predicted by the neural network in the training, validation and testing datasets. The regression line is shown together with the ideal line Y=T, which represents perfect agreement between nominal and predicted values. The distribution of experimental points shows that most data lie close to the ideal regression line, confirming the ability of the neural network to successfully approximate the relationship between the input parameters and tensile strength Rm. Certain deviations are present for individual samples with higher tensile-strength values, which may be associated with the complex nonlinear relationship between chemical composition, heat-treatment parameters and the mechanical properties of advanced structural steels.

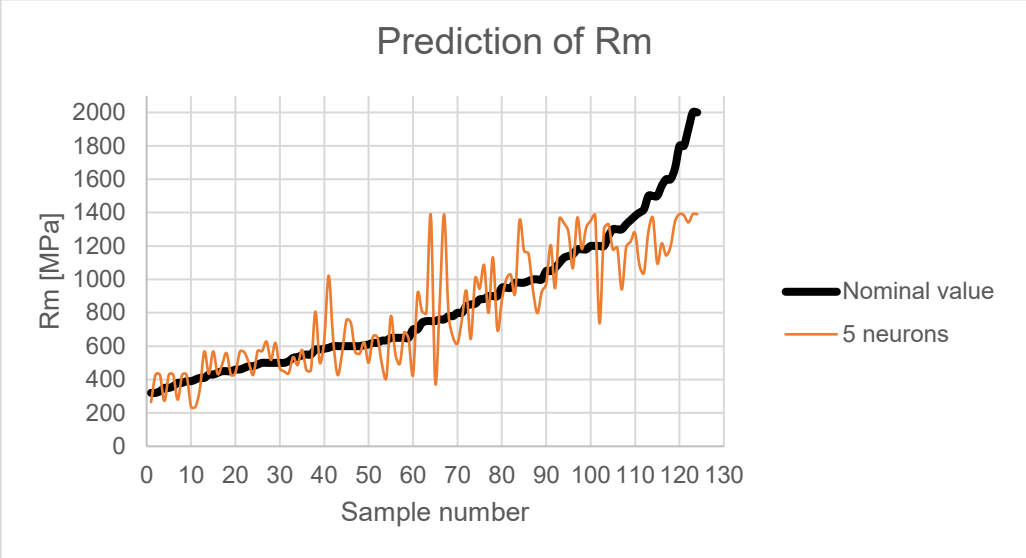

Figure 2 Prediction of Rm using a network with 5 neurons in the hidden layer

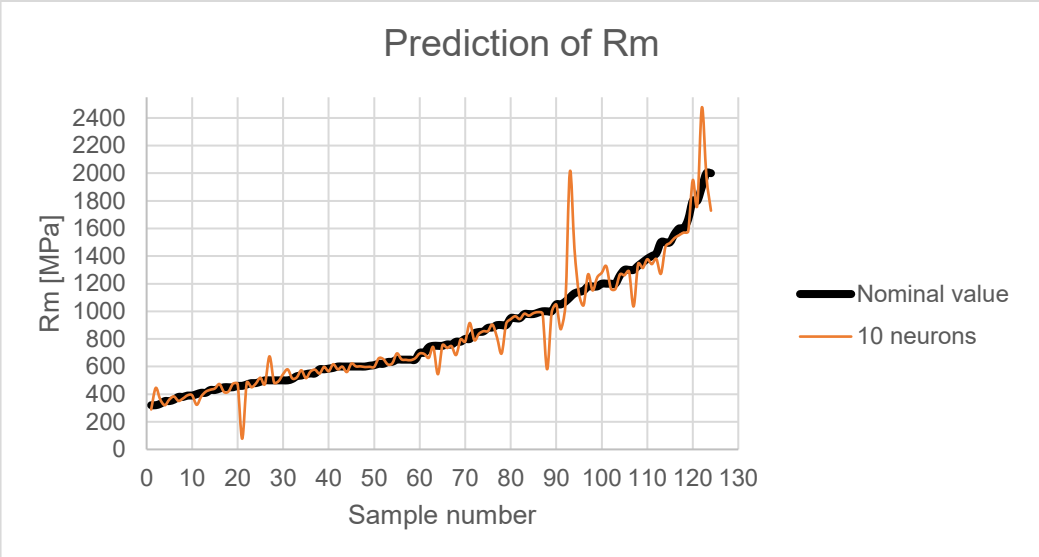

Figure 3 Prediction of Rm using a network with 10 neurons in the hidden layer

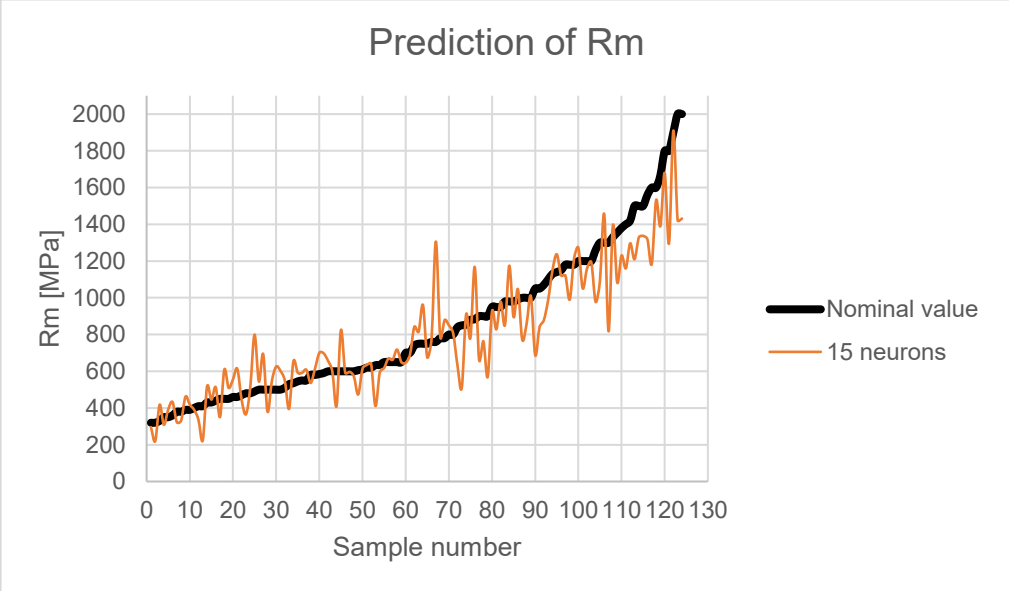

Figure 4 Prediction of Rm using a network with 15 neurons in the hidden layer

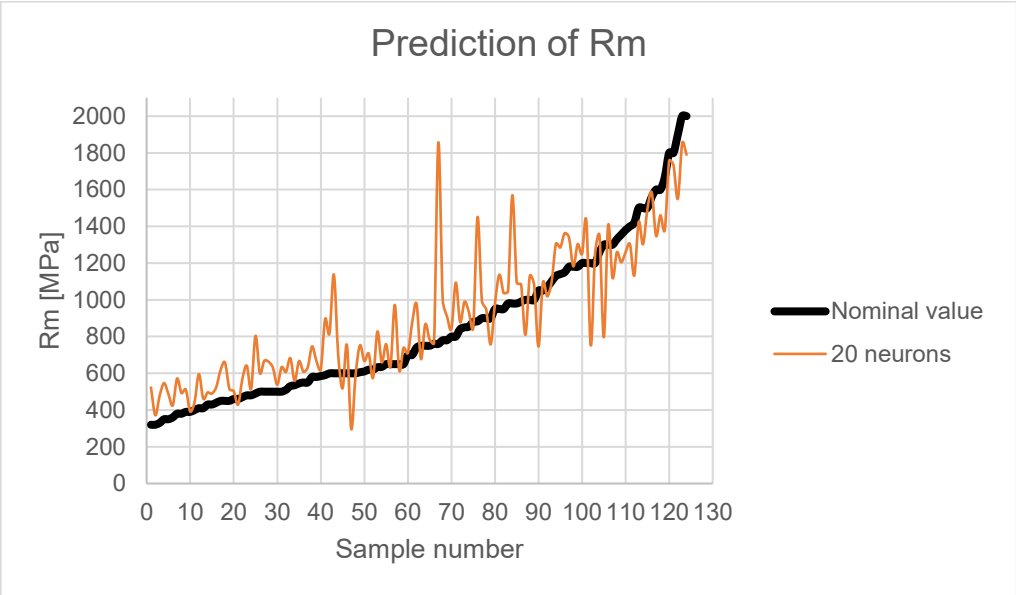

Figure 5 Prediction of Rm using a network with 20 neurons in the hidden layer

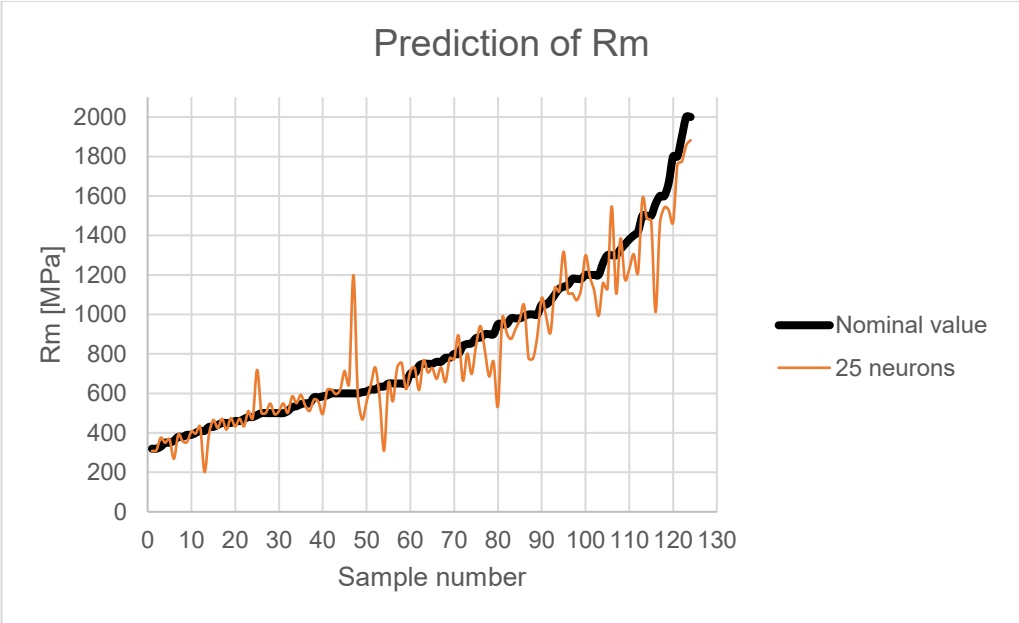

Figure 6 Prediction of Rm using a network with 25 neurons in the hidden layer

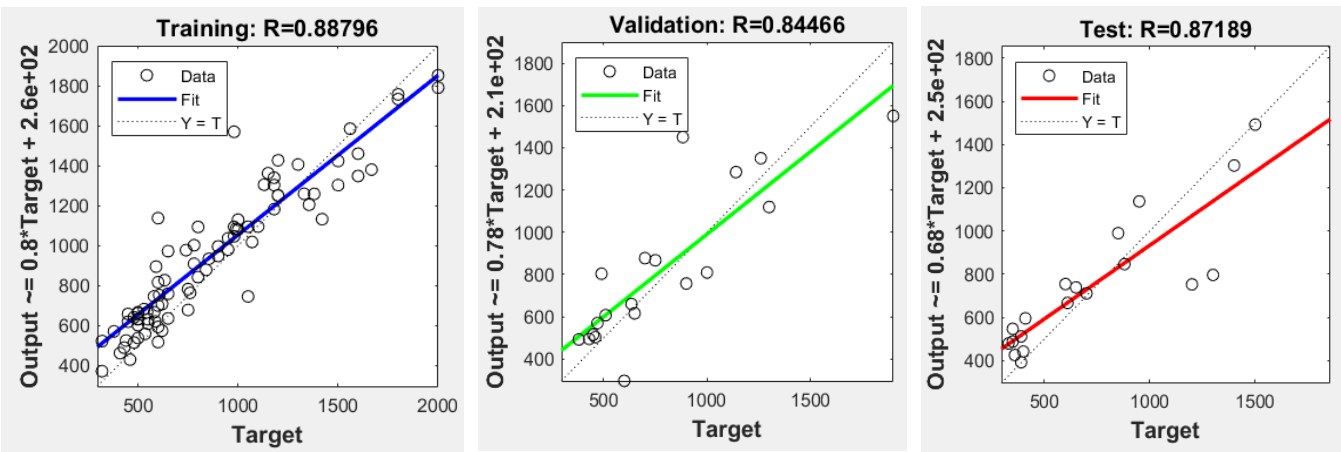

Figure 7 Regression diagrams of the neural network with 20 neurons in the hidden layer

Figure 8 presents the distribution of deviations between nominal and predicted values in the form of a histogram. The presented results show that the largest percentage of samples for all models has a relative error below 10%, confirming the good accuracy of the developed neural-network models. The model with 20 neurons shows the most balanced error distribution, with the largest number of samples concentrated in regions of smaller relative deviations.

At the same time, this model does not exhibit a significant increase in the number of samples with large relative-error values, further confirming its good generalization ability.

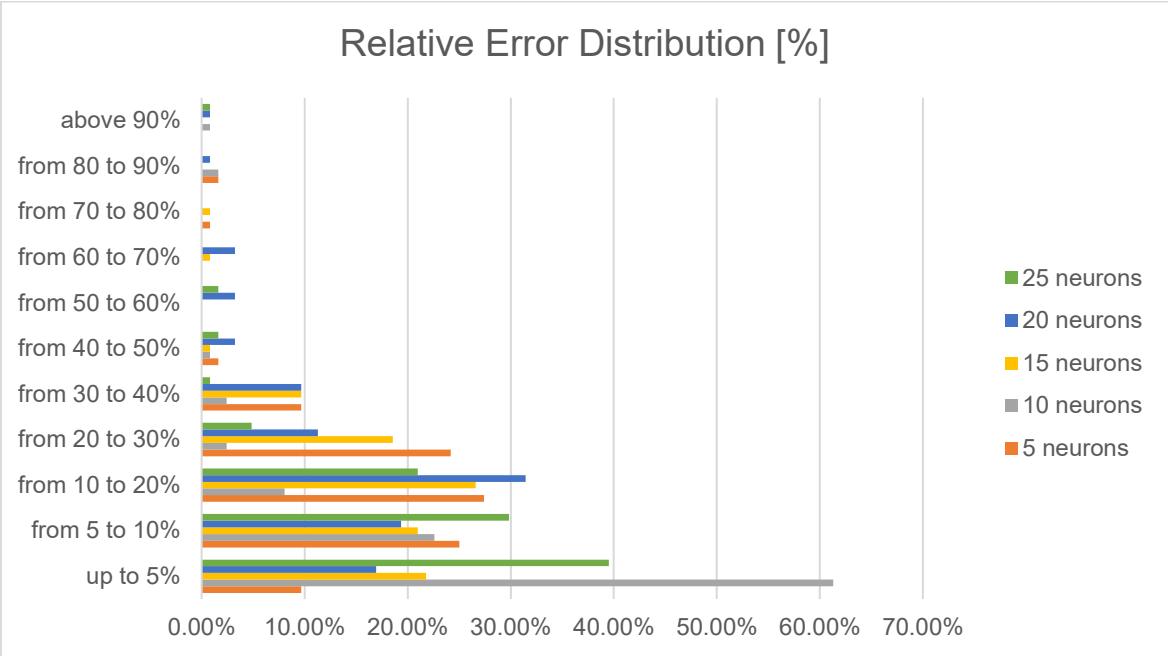

Figure 8 Histogram of the relative-error distribution

CONCLUSION

Based on the conducted research, it can be concluded that artificial intelligence, and artificial neural networks in particular, represent a highly significant tool in the field of testing and predicting the mechanical properties of advanced structural materials. The ability of neural networks to recognize complex nonlinear relationships among a large number of input parameters enables the successful application of these methods to the analysis of materials for which classical analytical models are often insufficient to describe material behavior accurately.

In this study, the input data used to predict tensile strength Rm included the chemical composition and heat-treatment temperatures of advanced structural steels for the automotive industry. Several neural-network architectures with different numbers of neurons in the hidden layer were analyzed, and model performance was compared on the basis of correlation coefficients, regression diagrams and the distribution of relative error. The obtained results showed that neural networks can predict tensile-strength values with satisfactory accuracy, with the model containing 20 neurons in the hidden layer being identified as optimal. This model achieved the best balance between prediction accuracy and generalization ability, with stable correlation-coefficient values and relatively small deviations between nominal and predicted values.

The research results confirm the considerable potential of artificial-intelligence methods in materials engineering, particularly in the development of new materials, optimization of technological processes and reduction of the need for extensive experimental testing. The application of neural networks can contribute significantly to faster, more efficient and more economical development of advanced structural steels for the automotive industry.

ACKNOWLEDGEMENTS

This work was supported by the Ministry of Science, Technological Development and Innovation of the Republic of Serbia (Contract No. 451-03-34/2026-03/200325).

REFERENCES

ArcelorMittal. (n.d.). *ArcelorMittal*. Retrieved June 4, 2026, from https://corporate.arcelormittal.com/

Arsić, D., Ivković, Dj., Adamović, D., Mandić, V., Delić, M., Mitrović, A., & Ratković, N. (2025). Application of high strength steels in automotive industry. *Mobility & Vehicle Mechanics*, *51*(1), 65–74. https://doi.org/10.24874/mvm.2025.51.01.05

Atuwo, T. (2018). Application of artificial neural networks in cold rolling process. *International Journal of Control Science and Engineering*, *8*(1), 22–30. https://doi.org/10.5923/j.control.20180801.03

BENTELER. (n.d.). *BENTELER*. Retrieved June 4, 2026, from https://www.benteler.com/en/

Branković, S. (2017). Veštačka inteligencija i društvo. *Srpska politička misao*, *56*(2), 13–32. https://doi.org/10.22182/spm.5622017.1

Dobrzański, L. A., & Sitek, W. (2003). Application of neural networks in steels' chemical composition design. *Journal of the Brazilian Society of Mechanical Sciences and Engineering*, *25*(2), 185–188. https://doi.org/10.1590/S1678-58782003000200012

Dumančić, S. (2014). *Neuronske mreže* [Undergraduate thesis]. Sveučilište Josipa Jurja Strossmayera u Osijeku.

ESB Group. (n.d.). *ESB Group*. Retrieved June 4, 2026, from https://www.esb-group.com/en/

Filetin, T. (2000). Odlučivanje o materijalima pri konstruiranju. In J. Božičević & A. Caharija (Eds.), *Zbornik radova „Kreativno rješavanje zadataka“, sa savjetovanja „Modeliranje u znanosti, tehnici i društvu“,* 97–105.

Galinec, J., & Filetin, T. (n.d.). *Mogućnosti primjene neuronskih mreža u ispitivanju materijala*, Zavod za materijale, Fakultet strojarstva i brodogradnje, Sveučilište u Zagrebu.

Hu, X., & Feng, Z. (2021). *Advanced high-strength steel–Basics and applications in the automotive industry* (ORNL/TM-2021/2047). Oak Ridge National Laboratory. https://doi.org/10.2172/1813170

Mathur, S., Gope, P. C., & Sharma, J. K. (2007). Prediction of fatigue lives of composites material by artificial neural network. In *Proceedings of the SEM 2007 Annual Conference and Exposition* (Paper 260). Society for Experimental Mechanics.

Metal Zenith. (n.d.). *Metal Zenith*. Retrieved June 4, 2026, from https://metalzenith.com/

Mohanty, J. R., Verma, B. B., Parhi, D. R. K., & Ray, P. K. (2009). Application of artificial neural network for predicting fatigue crack propagation life of aluminum alloys. *Archives of Computational Materials Science and Surface Engineering*, *1*(3), 133–138.

Nippon Steel Corporation. (n.d.). *Nippon Steel Corporation*. Retrieved June 4, 2026, from https://www.nipponsteel.com/en/

Paulič, M., Močnik, D., Ficko, M., Balič, J., Irgolič, T., Klančnik, S. (2015). Intelligent system for prediction of mechanical properties of material based on metallographic images. *Tehnički vjesnik*, *22*(6), 1419–1424. https://doi.org/10.17559/TV-20130718090927

POSCO. (n.d.). *POSCO*. Retrieved June 4, 2026, from https://www.posco.co.kr/

Stanković, I. (2019). *Primena modela inteligentnih agenata u procesu donošenja strategijskih odluka* [Doctoral dissertation]. Univerzitet Union-Nikola Tesla.

Šimunović, G., Šarić, T., & Lujić, R. (2009). Primjena neuronskih mreža u procjenjivanju kvalitete obrađene površine. *Tehnički vjesnik*, *16*(2), 43–47.

SSAB. (n.d.). *SSAB*. Retrieved June 4, 2026, from https://www.ssab.com/en

Tecuci, G. (2012). Artificial Intelligence. *WIREs Computational Statistics*, *4*(2), 168–180. https://doi.org/10.1002/wics.200

U. S. Steel Košice. (n.d.). *U. S. Steel Košice.* Retrieved June 4, 2026, from https://www.usske.sk/en/

Žmak, I. (2003). *Predviđanje svojstava materijala neuronskim mrežama* [Master’s thesis]. Sveučilište u Zagrebu, Fakultet strojarstva i brodogradnje, Zagreb.

Žmak, I. (2009). *Modeliranje strukture i svojstva nodularnog lijeva neuronskim mrežama* [Doctoral dissertation]. Sveučilište u Zagrebu, Fakultet strojarstva i brodogradnje, Zagreb.

The 11th International Congress
Motor Vehicles & Motors 2026
Kragujevac, Serbia
October 8th - 9th, 2026

Motor Vehicles & Motors

MVM2026-026
https://doi.org/10.24874/CMVM2026.026
Technical paper

Nenad Petrović[1]
Živana Jovanović Pešić[2,*]
Dragan Džunić[3]
Vladimir Kočović[4]
Strahinja Milenković[5]

CREATING CURVED MESHES BY HEAT-FORMING 3D-PRINTED PARTS

ABSTRACT: This research investigates the creation of curved mesh structures through heat-forming of 3D-printed parts, producing dome-like shapes using only a 3D printer and manual pressing. Compared to conventional 3D modeling methods, this approach is faster, reduces material waste by eliminating support structures, and can achieve a smoother surface finish through deformation of planar meshes. The study used PLA mesh wafers with hexagonal infill patterns at 20% and 40% densities, printed in thicknesses of 1 mm and 2 mm. All other printing parameters remained unchanged. Before forming, the samples were heated on the heated bed of an enclosed 3D printer. The wafers were shaped using a one-piece PET-G mould with a hemispherical profile raised 10 mm above the base. Vertical guides were incorporated to improve alignment during the forming process. The formed parts closely matched the intended geometry, with only minor imperfections caused by twisting during manual pressing. While further improvements in guidance and pressing stability are needed, the results demonstrate that heat forming is a viable method for producing curved mesh structures. As a proof of concept, the research confirms that complex dome-like forms can be successfully created using simple equipment and a low-cost manufacturing process.

KEYWORDS: 3D-printing, heat-forming, infill, PLA, meshing

[1] *Nenad Petrović, University of Kragujevac, Faculty of Engineering, Sestre Janjić 6, 34000 Kragujevac, npetrovic@kg.ac.rs, https://orcid.org/0000-0002-7563-9883*
[2] *Živana Jovanović Pešić, University of Kragujevac, Faculty of Engineering, Sestre Janjić 6, 34000 Kragujevac, zixi90@gmail.com, https://orcid.org/0000-0002-1373-0040 (*Corresponding author)*
[3] *Dragan Džunić, University of Kragujevac, Faculty of Engineering, Sestre Janjić 6, 34000 Kragujevac, dzuna@kg.ac.rs, https://orcid.org/0000-0002-1914-1298*
[4] *Vladimir Kočović, University of Kragujevac, Faculty of Engineering, Sestre Janjić 6, 34000 Kragujevac, vladimir.kocovic@kg.ac.rs, https://orcid.org/0000-0003-1231-0041*
[5] *Strahinja Milenković, 1University of Kragujevac, Institute for Information Technologies - National Institute of the Republic of Serbia, Liceja Kneževine Srbije 1A 34000 Kragujevac, strahinja.milenkovic@kg.ac.rs, https://orcid.org/0000-0002-5822-4846*

IZRADA ZAKRIVLJENIH MREŽASTIH STRUKTURA TERMIČKIM OBLIKOVANJEM 3D ŠTAMPANIH DELOVA

REZIME: Ovo istraživanje ispituje mogućnost izrade zakrivljenih mrežastih struktura termičkim oblikovanjem 3D štampanih delova, pri čemu se kupolasti oblici dobijaju korišćenjem samo 3D štampača i ručnog presovanja. U poređenju sa konvencionalnim metodama 3D modelovanja, ovaj pristup je brži, smanjuje količinu otpadnog materijala eliminisanjem potpornih struktura i omogućava postizanje glađe završne obrade površine deformacijom ravnih mrežastih struktura. U istraživanju su korišćeni PLA mrežasti uzorci sa heksagonalnom mrežom ispune gustine 20% i 40%, štampani u debljinama od 1 mm i 2 mm. Svi ostali parametri štampe ostali su nepromenjeni. Pre oblikovanja, uzorci su zagrevani na grejnoj podlozi zatvorenog 3D štampača. Oblikovanje je vršeno pomoću jednodelnog kalupa napravljenog od PET-G materijala, sa hemisferičnim profilom izdignutim 10 mm iznad osnove. U kalup su ugrađene vertikalne vođice radi boljeg poravnanja tokom procesa oblikovanja. Dobijeni delovi su u velikoj meri odgovarali predviđenoj geometriji, uz manje nepravilnosti izazvane uvijanjem tokom ručnog presovanja. Iako su potrebna dodatna unapređenja u vođenju i stabilnosti presovanja, rezultati pokazuju da je termičko oblikovanje efikasna metoda za izradu zakrivljenih mrežastih struktura. Kao dokaz koncepta, istraživanje potvrđuje da se složeni kupolasti oblici mogu uspešno proizvesti jednostavnom opremom i ekonomičnim proizvodnim postupkom.

KLJUČNE REČI: 3D štampa, termičko oblikovanje, ispuna, PLA, mrežasta struktura

INTRODUCTION

Fused deposition modelling (FDM) has seen rapid advancements in the availability, reliability, printing speed and precision of printers, different slicing techniques, as well as a widening of the range of applications of printed goods. The proliferation of so-called print farms has positioned 3D-printed parts in use cases outside of just one-off designs or prototype refinement and made it an integral part of a lot of small- to medium-sized production runs. The ability to create geometrical shapes which were unimaginable due to technological limitations allows engineers to create more use-appropriate parts with optimized geometries and allows midcycle optimization of the design without having to stop production to retool and remould.

The limitations of FDM 3D printing with polymers are well known and documented. Some practical limitations in assembled mechanisms can be overcome with the combined use of off-the-shelf industrial parts and their implementation using various fitment means, as was done by Palić et al. (2025), Vasić et al. (2025) and Jovanović Pešić et al. (2025). Over the years, some limitations have been mitigated to a certain extent through clever use of slicer settings; however, some feature shapes still lend themselves better to parts produced by conventional injection moulding.

One such feature is a protruding or dome-shaped mesh. Conventionally, this process would require support material, which would be difficult to remove from thin meshes, and it would also make the outer and inner surfaces of the domed mesh rigid because layered deposition is planar. This would create not only aesthetic issues but also structural ones, since the ridges would be stress concentration points, especially for shallower domes. Vapour polishing, as presented by Mathew et al. (2023), could be a solution for the aesthetic problem for specific materials, but due to the thin mesh structure having little material, it would create new problems with potential geometrical distortion. Maity et al. (2023) further advanced non-planar printing techniques, enabling improved surface quality on curved layers with geometries extending along the X-, Y-, and Z-axes. This approach is particularly advantageous for components such as aerofoils, where surface quality can have a direct impact on functional performance. Beyond improving surface finish, non-planar printing has also demonstrated the potential to increase the printable overhang angle without requiring additional support structures. This capability was demonstrated by Vele and Achten (2023) using unconventional printing materials, specifically through experiments involving clay, while Wüthrich et al. (2021) investigated the use of PLA filaments. Another potential solution for the ridging issue was presented by Lalegani Dezaki et al. (2020), Alinaghipour et al. (2026) and Antonelli et al. (2025); however, this can only be applied to solid models and would not work well with thin mesh structures. This means that the best solution for this type of problem would be to avoid producing the dome using conventional means.

Printing out of plane has been done before and has its limitations, as has been shown by Hrib et al. (2023), where the authors propose a new approach to the 3D printing process by using a robotic arm to ensure more than 3 degrees of freedom and deposition paths with spatial orientation. They proposed two types of working: nonplanar with the tip normal to the working plane and nonplanar with the tip normal to the trajectory. This approach, however, is costly and requires additional equipment most do not have. Other research in the field of non-planar slicing, such as Li et al. (2025), Yao et al. (2024) and Li et al. (2026), shows the possibility of using the slicer to instruct the printhead to use a path which follows the shape; however, for meshed domes, this could be problematic as the bottom side of the

structure needs to be hollow and bridging in this manner would lead to incorrect geometry. The use of a support structure has its limitations in this regard as well, since there needs to be clearance for the nozzle geometry, resulting in geometries with smooth curves but shallow depth.

This research focuses on the creation of an easy-to-create and accessible way to make meshed domes using just an FDM 3D printer. The idea is to show the benefits and limitations of the chosen process and, through experimental results, provide guidelines for implementing this method in practice. This process can be useful in the auto industry in the prototyping phase for producing meshes for air intakes, speaker covers, etc., as well as in the customization and repair sectors for creating replacement parts which are unavailable due to being discontinued.

PROBLEM FORMULATION

For the purposes of this research, two options were considered for mesh generation. One was to have four different models with the desired meshes designed into features of a part file, which would be converted into .STL files for slicing, in which case the mesh would be considered by the slicer as walls. This approach was ultimately not accepted due to the difficulty in giving a precise percentage of mesh coverage and a messy toolpath in the slicer. Another option was to use the slicer's ability to create infill meshes and remove the top and bottom layers, making the inner circle an exact percentage infill with clean paths and precise thicknesses. This approach meant that in order to make the outer rim of the design sturdy, the wall line count would need to go up in order to not have the rim be hollow and lose rigidity. Ultimately, this was the method which was chosen, as the preparation was easier and faster to do, as well as easy to control.

The geometry of all wafers followed the same formula with identical inner and outer diameters and used a formula for determining the lip height so the total part height would be $a_1 = 2{,}5b$. Two mesh densities of 20% and 40% were selected, as well as two thicknesses of *b*=1 mm and *b*=2 mm. The four samples were created from two-part files, which were both full cross-section circular discs with a lip, as shown in the dimension sketch in Figure 1a. The part files created in Autodesk Inventor were then saved as .STL files and opened in Bambu Studio V2.5.0.66, where slicer options for meshing were set to 20% and 40%, respectively, and a wall-count number of 10 with top and bottom layers set to 0mm. This is illustrated in Figure 1b, where the sliced preview is given for the 20% infill *b*=2 mm model. Finally, all four parts were printed using a Bambu Lab H2S AMS Combo using AzureFilm white PLA filament, with all other slicer settings set to their default values. Figure 1c shows an example of the resulting mesh.

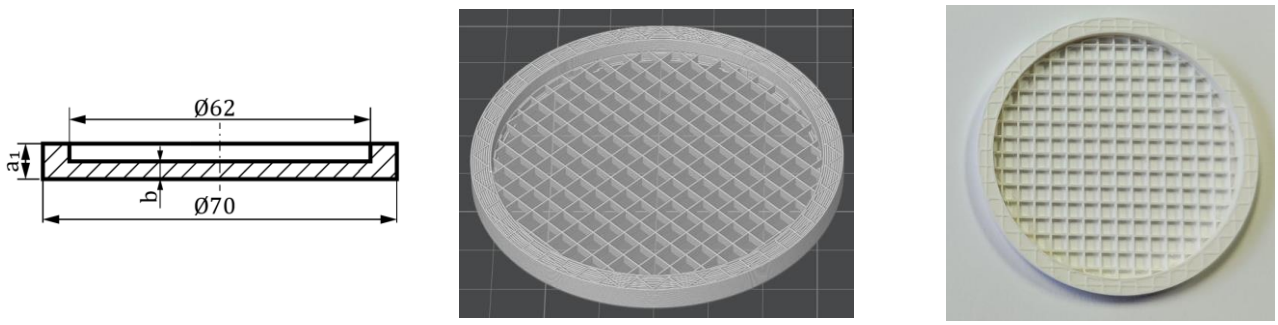

a) b) c)

Figure 1 Mesh example: a) dimensions of 3D models, b) sliced part and c) final printed part before moulding

This process was repeated for all four models, with printing taking roughly 12 to 20 minutes for each mesh. All models were printed using 0.16 mm resolution.

MOULD DESIGN

To create a dome-like shape with the printed mesh wafers, a mould was designed to guide and shape the 2D meshes into the desired form. The mould was chosen with a dome height of 10mm, which, accounting for some spring-back, was expected to increase the part height by roughly 9mm. Since little literature is available for specific spring-back rates of meshed 3D-printed parts, the authors relied on previous experience with thermoforming PLA. The mould was designed in Autodesk Inventor using the dimensions shown in Figure 2a, and the model (Figure 2b) was sliced and printed in purple DevilDesign PET-G with a 0.2 mm (Figure 2c) resolution since the surface finish of the dome was expected not to have an impact on the moulding process, as the ridging would not be able to imprint onto the meshes given the low temperature of forming, small forces being applied and lack of pressure on the meshed surface itself. The tension of the material stretching over the dome ensured a smooth inner surface of the moulded parts.

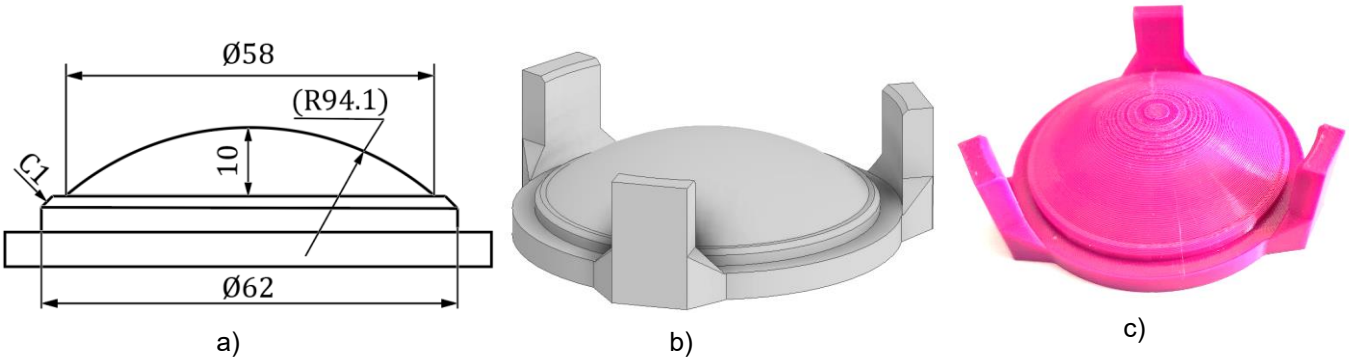

Figure 2 Mould design a) dimensions, b) 3D model and c) final printed part

The mould's inner diameter is Ø58 to allow room for a gradual bend on the bottom side, avoiding stress concentration and making pressing easier. This creates a smoother geometric transition, as illustrated in Figure 4, which shows half the cross-section. The mould also has a chamfer of 1mm around the Ø62 diameter in order to more easily centre the rim onto the mould once it reaches that level.

RESULTUS

The moulding process was found through trial and error. It was found that using the print bed preheated to 100 °C was sufficient to make the parts mouldable after only 15 seconds. The enclosed bed of the Bambu Lab H2S AMS Combo, used to print all the parts, was also used to heat the parts for moulding. Parts were moulded one at a time by preheating the print bed. Once the bed reached 100 °C a mesh was placed, flat side down, on the print bed along with the mould. After 15 seconds, the wafer was flipped and pressed onto the mould by hand down to the limiting surface and held there until the parts were cooled, which was roughly 30 seconds. After that, the parts were removed from the mould and left to cool to room temperature. The process was repeated for all four examples. Figure 3 shows the resulting meshes.

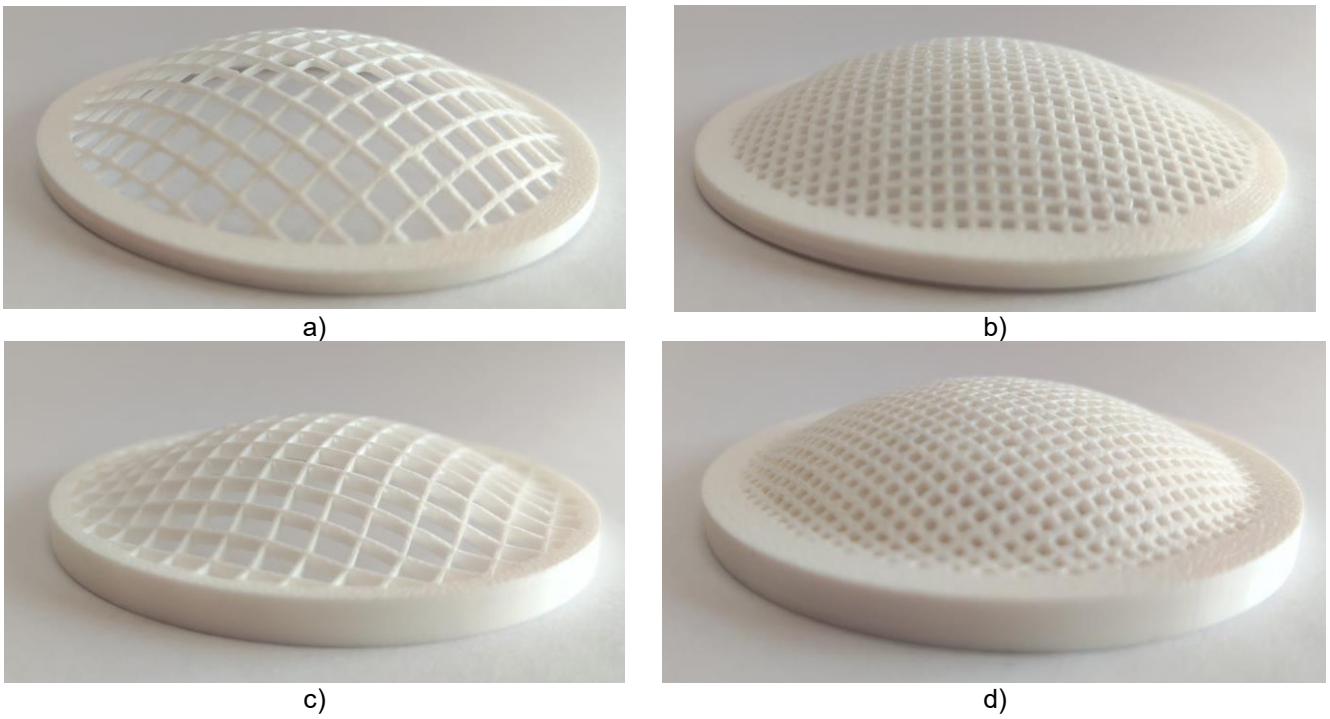

Figure 3 Moulded parts a) 20%, b=1mm, b) 40%, b=1mm, c) 20%, b=2mm and d) 40%, b=2mm

The created meshes showed some spring-back, as expected, and slight shrinkage in the inner diameter. Figure 4 illustrates the dimensions which were examined after the moulded parts had cooled.

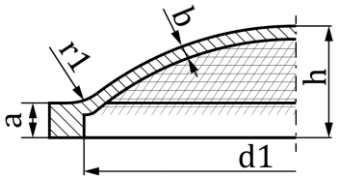

Figure 4 Type the title of the Figure here

Table 1 provides the dimensions of the moulded meshes according to Figure 4. Measurements were done using Vernier callipers and a radius gauge.

Table 1 Resulting geometry dimensions

Dimension	20%, b=1 mm	40%, b=1 mm	20%, b=2 mm	40%, b=2 mm
d1	61	60.2	61.1	61.2
r1	8	15	14.5	7.5
a	2.6	2.8	4.8	4.9
h	13	13	13.8	14.2

CONCLUSIONS

This paper focused on the practical application of hot-forming by hand-pressing grid-type meshes into a specific dome shape using only the available means provided by the 3D printer and geometry slicer. The proposed method successfully formed round grid meshes with 20% and 40% infill into a dome 10 mm tall using grids of 1 and 2 mm thickness. All models started as round Ø70 mm plates with 1- and 2-mm-thick Ø62 mm inbored circles and a 1.5x-taller lip around the part. Parts were sliced in Bambu Studio V2.5.0.66 with the specified infills, and the top and bottom layers were removed to create a see-through mesh in the middle and thick walls using a high wall line count. Parts were printed in PLA and later moulded inside the Bambu Lab H2S AMS Combo. The forming tool was printed on the same printer using PET-G to ensure there is no deformation of the mould during the short heating time. The wafers were hand-pressed after 15 seconds at 100 °C on the print bed and held in place for 30 seconds before being removed from the mould. The achieved results demonstrate little noticeable difference in part geometry compared to the ideal shape they were intended to be moulded into. There was a decrease of ~1 mm in the 20% mesh and 40% mesh diameter of the 1 mm thick model, as well as the 2 mm 20% mesh model, while the 40% mesh with 2 mm thickness decreased by less than 0.5 mm.

It should be noted that since this technique is intended for hand pressing, there will inevitably be some twist in the resulting shape unless the design incorporates some form of guide, either through the addition of a notch, or some other shape, or just by forming shapes which are not completely round. In this research, minor warping due to a small twist during the forming process had resulted in the geometry being skewed by less than 0.5 mm, which did not significantly impact the structure, nor is it easily visible to the naked eye. The models have also slightly warped out of the circle plane after cooling, with a height variation of less than 0.5 mm, which is insignificant but noteworthy.

This experiment proves that simple shapes can be easily hot-formed with just an enclosed 3D printer and a controlled process. The application of these types of formed meshes is possible in a wide range of use cases. Future research will focus on more experimentation using different thicknesses, mesh infills and mould radii, as well as mould depth, in order to map out the results and show the limits of feasibility using this method of mesh forming. Another thing which will be interesting to test is the strength under load of formed meshes compared to flat meshes, since the shape should have better stress distribution, but it is still unclear how much of an impact the internal stresses of the forming process and the deformation itself have on the strength of the part.

ACKNOWLEDGMENTS

This paper is the result of research conducted under the authors' scientific research work agreements contracts no. 451-03-34/2026-03/200107, and 451-03-33/2026-03/200378.

REFERENCES

Palić, S., Petrović, N., Palić, N., Milenković, S., & Pešić, Z. J. (2025). Using experimental results to determine calculation parameters for press fitting ball bearings into 3D printed parts. In M. Rackov, A. Miltenović, & M.

Banić (Eds.), *Machine and industrial design in mechanical engineering* (Vol. 174, pp. 92–101). Springer Nature Switzerland. https://doi.org/10.1007/978-3-031-80512-7_9

Vasić, M. R., Vučetić, S., Miljić, V., Vorkapić, M., Terzić, A., Ćosić, M., & Bajić, D. M. (2025). *Does material deterioration caused by aging affect the joint between metal brass insert and plastic? Drone arm case study* [Preprint]. Preprints.org. https://doi.org/10.20944/preprints202504.1937.v1

Jovanović Pešić, Ž., Petrović, N., Milenković, S., Kostić, N., & Džunić, D. (2025). Functional surfaces roughness analysis of 3D printed PET-G housings used for press-fitting steel ball bearings. *Tribology in Industry*. https://doi.org/10.24874/ti.1947.04.25.06

Mathew, A., Kishore, S. R., Tomy, A. T., & Rajan, J. A. (2023). Vapour polishing of fused deposition modelling (FDM) parts: A critical review of different techniques, and subsequent surface finish and mechanical properties of the post-processed 3D-printed parts. *Progress in Additive Manufacturing, 8*(6), 1–18. https://doi.org/10.1007/s40964-022-00391-7

Maity, M., Das, S., Kumar, R., & Mondal, J. K. (2023). Experimental investigation for enhancing surface quality in 3D printing process using non-planar layer method. In A. Kumar, M. Zunaid, K. A. Subramanian, & H. Lim (Eds.), *Recent advances in manufacturing and thermal engineering* (pp. 191–200). Springer Nature Singapore. https://doi.org/10.1007/978-981-19-8517-1_14

Vele, J., & Achten, H. H. (2023). Clay non-planar printing of overhangs. In *Digital Architectural Research – DARe* (pp. 46–61). Bialystok University of Technology Publishing Office.

Wüthrich, M., Gubser, M., Elspass, W. J., & Jaeger, C. (2021). A novel slicing strategy to print overhangs without support material. *Applied Sciences, 11*(18), 8760. https://doi.org/10.3390/app11188760

Lalegani Dezaki, M., Mohd Ariffin, M. K. A., & Ismail, M. I. S. (2020). Effects of CNC machining on surface roughness in fused deposition modelling (FDM) products. *Materials, 13*(11), 2608. https://doi.org/10.3390/ma13112608

Alinaghipour, M., Adibi, H., & Rezaei, S. M. (2026). Advancements in five-axis 3D printing for process and surface enhancement: Optimizing Cartesian FDM through DOE. *Progress in Additive Manufacturing, 11*(6), 5217–5231. https://doi.org/10.1007/s40964-026-01581-3

Antonelli, M. G., Brunetti, J., D'Ambrogio, W., Mattei, E., & Stampone, N. (2025). Surface quality improvement of 3D-printed components by a cobot-based contouring machining. *Robotica, 43*(11), 3942–3958. https://doi.org/10.1017/S0263574725102567

Hrib, V.-F., Chifan, F., Ciorap, M., & Dumitraș, C. G. (2023). An study regarding a new concept of 3D printing using a 6 axis industrial robotic arm. *Bulletin of the Polytechnic Institute of Iași. Machine Constructions Section, 69*(3), 85–98. https://doi.org/10.2478/bipcm-2023-0026

Li, Y., Shi, C., & Yan, X. (2025). Curved-layer slicing and continuous path planning for multi-axis printing of fiber-reinforced composite structures. *Processes, 13*(2), 473. https://doi.org/10.3390/pr13020473

Yao, Y., Cheng, L., & Li, Z. (2024). A comparative review of multi-axis 3D printing. *Journal of Manufacturing Processes, 120*, 1002–1022. https://doi.org/10.1016/j.jmapro.2024.04.084

Li, Y., Wang, T., & Li, N. (2026). Mapping-based path planning on large-curvature surface for multi-axis 3D printing. *Procedia CIRP, 142*, 180–184. https://doi.org/10.1016/j.procir.2026.05.244

The 11th International Congress
Motor Vehicles & Motors 2026
Kragujevac, Serbia
October 8th - 9th, 2026

Motor Vehicles & Motors

MVM2026-050
https://doi.org/10.24874/CMVM2026.050
Review paper

Danijela Tadić[1]
Jasna Glišović[2]
Nikola Komatina[3]

COMPARATIVE ANALYSIS OF OBJECTIVE CRITERIA WEIGHTING METHODS FOR ELECTRIC VEHICLE EVALUATION

ABSTRACT: Electric vehicles (EVs) play an important role in sustainable development. Nowadays, many automotive companies manufacture different types of EVs. The selection of the most suitable EV depends on the number and type of criteria used for evaluation, as well as on the weights assigned to these criteria. Determining criteria weights is often based on the subjective judgments of decision-makers, which may affect the accuracy of the final selection. Therefore, this paper presents several objective multi- criteria decision-making methods for determining criteria weights. This constitutes the main contribution of the study. The proposed methods are applied to determine the weights of six criteria for EV evaluation identified from the relevant literature.

KEYWORDS: Electric vehicles, criteria weights, FANMA, Entropy method, CRITIC method

KOMPARATIVNA ANALIZA OBJEKTIVNIH METODA ZA ODREĐIVANJE TEŽINA KRITERIJUMA PRI OCENJIVANJU ELEKTRIČNIH VOZILA

REZIME: Električna vozila (EV) imaju značajnu ulogu u održivom razvoju. Danas mnoge automobilske kompanije proizvode različite tipove električnih vozila. Izbor najpogodnijeg električnog vozila zavisi od broja i vrste kriterijuma koji se koriste za njihovu ocenu, kao i od težina koje su tim kriterijumima dodeljene. Određivanje težina kriterijuma često se zasniva na subjektivnim procenama donosilaca odluka, što može uticati na tačnost konačnog izbora. Stoga ovaj rad predstavlja nekoliko objektivnih višekriterijumskih metoda za određivanje težina kriterijuma. To predstavlja glavni doprinos rada. Predložene metode primenjene su za određivanje težina šest kriterijuma za ocenu električnih vozila identifikovanih na osnovu relevantne literature.

[1] Danijela Tadić, University of Kragujevac, Faculty of Engineering, Sestre Janjić 6, 34000 Kragujevac, Serbia, galovic@kg.ac.rs , https://orcid.org/0000-0003-2236-967X
[2] Jasna Glišović, University of Kragujevac, Faculty of Engineering, Sestre Janjić 6, 34000 Kragujevac, Serbia, jaca@kg.ac.rs, https://orcid.org/0000-0002-8251-1722
[3] Nikola Komatina, University of Kragujevac, Faculty of Engineering, Sestre Janjić 6, 34000 Kragujevac, Serbia, nkomatina@kg.ac.rs, https://orcid.org/0000-0001-6964-5673

KLJUČNE REČI: električna vozila; težine kriterijuma; FANMA; metoda entropije; CRITIC metoda

INTRODUCTION

Strategy development in almost all countries is based on the concept of sustainable development, which, among other things, implies environmental protection and the use of renewable energy sources. This approach is particularly important for the automotive industry. Many automotive companies, such as Ford, Hyundai, Fiat, General Motors, BMW, Tata Motors, Mitsubishi, and others, have already started the commercial production of electric vehicles (EVs) with distinct features. These vehicles use alternative energy sources, including natural gas, ethanol, methanol, propane, electricity, biodiesel, and hydrogen, which are considered substitutes for gasoline and other fossil fuels. Therefore, the use of EVs can contribute to sustainable development (Deuten et al., 2020; Egnér & Trosvik, 2018). Compared with conventional vehicles with internal combustion engines, EVs can contribute to reducing greenhouse gas emissions by minimizing dependence on fossil fuels (Liu et al., 2020). Nowadays, EVs are gaining popularity due to several advantages, including efficient battery capacity, reduced emissions of hazardous gases, government subsidies and other purchase incentives, improved vehicle performance, and other environmental benefits (Biswas & Das, 2019; Langbroek et al., 2017). Nowadays, many government organizations are promoting the adoption of EVs by introducing various policies, incentives, and other support measures.

At the operational management level, one of the most crucial tasks for logistics managers in industrial organizations is to develop a well-defined sustainable transport system. This is aimed at minimizing environmental problems and resource depletion while, in a broader sense, also maximizing social and economic welfare (Zhao et al., 2020). Some authors (Biswas & Das, 2019; Langbroek et al., 2017) argue that EVs possess several advantages, including efficient battery capacity, reduced emissions of hazardous gases, government subsidies and other purchase incentives, enhanced vehicle performance, and various other environmental benefits. Based on the findings of the study by (Gustafsson et al., 2021)**,** the negative environmental impact can be reduced by using EVs instead of diesel vehicles. However, customer demand for EVs primarily depends on support measures, such as financial incentives.

Defining the distinct features of EVs and evaluating different EV models with respect to the considered features is a very complex task. Almost all authors dealing with this problem consider that defining the list of criteria according to which EVs are evaluated represents one of the most important issues, as its solution directly affects the selection of EVs. In the literature, numerous studies can be found in which authors have defined lists of criteria with respect to different aspects (Biswas & Das, 2019; Das et al., 2019; Sonar & Kulkarni, 2021; Tadić et al., 2024, 2025; Yagcitekin et al., 2015; Zarazua De Rubens et al., 2020).

Determining criteria weights is a critical issue that can significantly influence the final outcome. Over the last few decades, researchers worldwide have focused their attention on addressing this problem. Most authors suggest dividing the approaches to determining criteria weights into subjective and objective approaches (Zhu et al., 2015). In the literature, many studies can be found in which determining criteria weights is adequately based on the assessments of decision-makers (DMs) (Arsić et al., 2025; Komatina et al., 2023; Milanovic et al., 2020). They base their assessments on their knowledge, experience, and the results of best practices. In this case, criteria weights are significantly influenced by the subjective attitudes of DMs. In order to increase the accuracy of criteria weights, many authors promote the use of subjective multi- criteria decision-making methods, which are briefly described below. The Analytic Hierarchy Process (AHP) (Saaty, 2013) is the most commonly used subjective Multi-Criteria Decision-Making (MCDM) method for determining criteria weights. The criteria weights of EVs have been determined using the AHP (Biswas & Das, 2019; Sonar & Kulkarni, 2021). Other subjective MCDM methods that have been widely applied to determining criteria weights include the Best–Worst Method (BWM) (Rezaei, 2015), the Decision-Making Trial and Evaluation Laboratory (DEMATEL) method (Falatoonitoosi et al., 2013), and Data Envelopment Analysis (DEA) (Charnes et al., 1978).

The main advantage of these methods is that they enable DMs to assess the relative importance of the considered criteria based on their knowledge and experience. The estimated or measured values of alternatives do not affect the assessments of DMs. The main disadvantage of subjective MCDM methods is that the assessment of the relative importance of the considered criteria is, to a significant extent, related to the value system, experience, and personal preferences of DMs, as well as the influence of the social groups to which they belong and other related factors.

On the other hand, objective MCDM methods used for determining criteria weights include the FANMA (Mandal et al., 2025; Milićević & Župac, 2012), Entropy (Eskov et al., 2017; Saraiva, 2023), and Criteria Importance Through Intercriteria Correlation (CRITIC) methods (Diakoulaki et al., 1995). In the literature, many papers can be found in which authors use objective MCDM methods for determining criteria weights (Chen, 2021; Komatina & Marinković, 2025; Krishnan, 2025).

The values of criteria weights depend on the amount and accuracy of the values contained in the elements of the decision matrix. On the other hand, if the set of alternatives in the considered problem changes, for example, if the set of considered EVs is expanded or different types of EVs are considered, this leads to changes in the values of criteria weights. This dependence of the obtained weights on the considered set of alternatives can be regarded as one of the main limitations of objective MCDM methods.

Based on the above brief discussion of MCDM methods used for determining criteria weights, it can be concluded that both approaches have their advantages as well as disadvantages. DMs must possess sufficient knowledge and experience when selecting an appropriate method, since criteria weights can significantly influence the selection of the most suitable EV.

The increasing number of available EV models and the diversity of their characteristics make the selection of the most suitable EV a complex decision-making problem. Since the final selection can be significantly influenced by the criteria weights, it is important to investigate different approaches for their determination and to analyse the differences in the obtained results.

The aim of this paper is to apply and compare three objective methods, namely FANMA, Entropy, and CRITIC, for determining the weights of criteria used for EV evaluation. The obtained criteria weights are also compared with the AHP weights reported by (Sonar & Kulkarni, 2021), which were determined based on DMs' assessments.

The paper is organized as follows. The methodology used in this study is presented in Section 2. Section 3 presents the determination of criteria weights using data obtained from the literature and compares the obtained results. Concluding remarks and directions for future research are discussed in Section 4.

METHODOLOGY

In this section, the considered objective MCDM methods used in this research are briefly presented.

Defining EV Criteria

Nowadays, automotive companies produce and offer customers EVs with numerous characteristics, such as style, color, quality, size, battery capacity, seating capacity, driving range, price, torque, acceleration, charging time, charging infrastructure, and others. In this paper, the set of criteria is adopted from (Sonar & Kulkarni, 2021), where the criteria were identified based on purchasers' preferences when selecting an EV. The procedure used for defining the list of criteria is briefly described below.

In (Sonar & Kulkarni, 2021) authors defined a list of criteria based on the preferences of customers who had already purchased passenger EVs or were willing to purchase EVs in the near future. By using Pareto analysis (Flores & Whybark, 1987), they defined a list of the most significant criteria. It should be noted that, in the MCDM approach, the number of criteria should be optimal in order to enable DMs to assess the relative importance of the criteria in a sufficiently simple and accurate manner. This statement is particularly important when subjective methods for determining criteria weights are used.

These criteria are formally represented by a set of indices $\{1, \dots, k, \dots, K\}$, where $K = 6$. The considered criteria are: price (measured in Lakh Rs.) ($k = 1$), driving range (measured in kilometres) ($k = 2$), charging time (measured in hours) ($k = 3$), battery capacity (measured in kWh) ($k = 4$), seating capacity (number of passengers) ($k = 5$), and torque (measured in Nm) ($k = 6$).

FANMA method

The FANMA method is based on determining the distances from the ideal point. The algorithm for implementing the FANMA method is carried out through the following steps:

Step 1. The decision matrix is defined as:

$$[x_{ik}]_{IxK} \tag{1}$$

Step 2. The normalized decision matrix is constructed by applying the linear normalization procedure:

$$[r_{ik}]_{IxK} \tag{2}$$

where:

$$r_{ik} = \frac{x_{ik}}{\sum_{i=1,..,I} x_{ik}} \tag{3}$$

Step 3. The reference point, r_k^*, is determined as:

$$r_k^* = \max_{i=1,..,I} r_{ik} \tag{4}$$

Step 4. The weight of criterion $k, k = 1, \dots, K$, is determined as:

$$\omega_k = \frac{1}{\sum_{i=1,..,I}(r_k^* - r_{ik})^2 \cdot \sum_{k=1,..,K} \frac{1}{\sum_{i=1,..,I}(r_k^* - r_{ik})^2}} \tag{5}$$

Entropy method

In the Entropy method, the determination of criteria weights is based on Shannon's concept of the entropy measure of information contained in the decision matrix (Shannon, 1948). Based on the determined measures of uncertainty associated with the criteria, a set of criteria weights can be obtained. The algorithm for implementing the Entropy method is carried out through the following steps:

Step 1. The decision matrix is defined as:

$$[x_{ik}]_{IxK} \tag{6}$$

Step 2. The normalized decision matrix is constructed by applying the linear normalization procedure:

$$[r_{ik}]_{IxK} \tag{7}$$

Step 3. The entropy degree for each criterion $k, k = 1, \dots, K$, is determined as:

$$E_k = -\frac{1}{\ln I} \cdot \sum_{i=1,..,I} r_{ik} \cdot \ln r_{ik} \tag{8}$$

Step 4. The entropy deviation degree is obtained according to the following expression:

$$\vartheta_k = 1 - E_k \tag{9}$$

Step 5. The normalized vector of criteria weights is determined by applying the linear normalization procedure:

$$\omega_\kappa = \frac{\vartheta_k}{\sum_{\kappa k=1,..,K} \vartheta_k} \tag{10}$$

CRITIC method

The proposed algorithm can be implemented through the following steps:

Step 1. The decision matrix is defined as:

$$[x_{ik}]_{IxK} \tag{11}$$

Step 2. The normalized decision matrix is constructed using the linear normalization procedure, as proposed in the conventional CRITIC method.

$$[r_{ik}]_{IxK} \tag{12}$$

Step 3. The weights of the EV criteria, $W_k, k = 1, \dots, K$, are determined according to the following formula:

$$W_k = \sigma_k \cdot \sum_{k=1,..,K} (1 - \rho_{kk'}) \tag{13}$$

Where σ_k is the standard deviation of the values for criterion k, and $\rho_{kk'}$ is the correlation coefficient between each pair of EV criteria.

Step 4. The normalized vector of EV criteria weights is denoted as:

$$[\omega_k]_{Kx1} \tag{14}$$

where:

$$\omega_k = \frac{W_k}{\sum_{k=1,..,K} W_k} \tag{15}$$

Application of the Proposed Methods and Results Analysis

The objective of the study is to determine the weights of the criteria used for EV evaluation. Initially, six criteria have been identified based on purchasers' preferences when selecting an electric vehicle.

Application of the FANMA Method

The decision matrix was adopted from (Sonar & Kulkarni, 2021) and is presented in Table 1 (Step 1).

Table 1 The decision matrix

	$k=1$	$k=2$	$k=3$	$k=4$	$k=5$	$k=6$
$i=1$	23.86	452	6.10	39.20	5	395
$i=2$	13.95	140	11.30	18.55	5	91
$i=3$	8.23	110	6	10.08	4	70
$i=4$	20.88	340	16	44.50	5	353
$i=5$	10.61	213	11.5	21.50	5	105
$i=6$	14.99	312	8.50	30.20	5	245

By applying the linear normalization procedure, the normalized decision matrix and the reference point are obtained (Steps 2 and 3) and presented in Table 2.

Table 2 The normalized decision matrix

	$k=1$	$k=2$	$k=3$	$k=4$	$k=5$	$k=6$
$i=1$	0.2579	0.2884	0.1027	0.2389	0.1724	0.3137
$i=2$	0.1508	0.0893	0.1902	0.1131	0.1724	0.0723
$i=3$	0.0889	0.0702	0.1010	0.0615	0.1379	0.0556
$i=4$	0.2257	0.2169	0.2694	0.2713	0.1724	0.2804
$i=5$	0.1147	0.1359	0.1936	0.1311	0.1724	0.0834
$i=6$	0.1620	0.1991	0.1431	0.1841	0.1724	0.1946
r_k^*	0.2579	0.2884	0.2694	0.2713	0.1724	0.3137

The criteria weights are determined using the proposed FANMA algorithm (Step 4). The input data are presented in Table 3.

Table 3 The input data

	$k=1$	$k=2$	$k=3$	$k=4$	$k=5$	$k=6$
$i=1$	0	0	0.0278	0.0010	0	0
$i=2$	0.011	0.0396	0.0063	0.0250	0	0.0583
$i=3$	0.0286	0.0476	0.0284	0.0440	0.0012	0.0667
$i=4$	0.0010	0.0051	0	0	0	0.0011
$i=5$	0.0205	0.0233	0.0057	0.0197	0	0.0530
$i=6$	0.0092	0.0080	0.0159	0.0076	0	0.0142
Step 4 results	14.1300	8.0930	11.8833	10.2771	833.3333	5.1737

$$\omega_1 = \frac{1}{0.0708 \cdot (14.1300 + 8.093 + 11.8833 + 10.2771 + 833.3333 + 5.1737)}$$

$$\omega_1 = \frac{1}{0.0708 \cdot 882.8904} = 0.016$$

The weights of the remaining criteria are determined in a similar manner. Thus, the criteria weights vector is:

$$[0.016 \quad 0.010 \quad 0.090 \quad 0.012 \quad 0.944 \quad 0.006]$$

Application of the Entropy Method

The decision matrix (Step 1) and the normalized decision matrix (Step 2) are obtained and presented in Tables 1 and 2, respectively. The entropy degree and entropy deviation degree are determined using the proposed procedure (Steps 3 and 4) and presented in Table 4.

Table 4 The entropy degree of the considered criteria

	$k=1$	$k=2$	$k=3$	$k=4$	$k=5$	$k=6$
$i=1$	-0.3495	-0.3586	-0.2337	-0.3421	-0.3031	-0.3637
$i=2$	-0.2853	-0.2158	-0.3157	-0.2465	-0.3031	-0.1899
$i=3$	-0.2152	-0.1865	-0.2316	-0.1714	-0.2732	-0.1607
$i=4$	-0.3359	-0.3315	-0.3533	-0.3539	-0.3031	-0.3565
$i=5$	-0.2483	-0.2713	-0.3179	-0.2663	-0.3031	-0.2072
$i=6$	-0.2949	-0.3213	-0.2782	-0.3116	-0.3031	-0.3185
E_k	0.9651	0.9404	0.9658	0.9442	0.9983	0.8910
ϑ_k	0.0349	0.0596	0.0342	0.0558	0.0017	0.1089

The weight of the first criterion (Step 5) is determined as follows:

$$\omega_1 = \frac{0.03492}{0.03492 + 0.0596 + 0.03424 + 0.05579 + 0.0017 + 0.1089} = 0.118$$

The weights of the remaining criteria are determined in a similar manner. Thus, the criteria weights vector is:

$$[0.118 \quad 0.202 \quad 0.116 \quad 0.189 \quad 0.006 \quad 0.369]$$

Application of the CRITIC Method

The decision matrix (Step 1) and the normalized decision matrix (Step 2) are obtained and presented in Tables 1 and 2, respectively.

The standard deviation values for each criterion are:

$\sigma_1 = 0.0645$ $\quad$ $\sigma_2 = 0.0832$ $\quad$ $\sigma_3 = 0.0645$

$\sigma_4 = 0.0796$ $\quad$ $\sigma_5 = 0.0141$ $\quad$ $\sigma_6 = 0.1127$

The correlation coefficients are calculated and presented in Table 5.

Table 5 Correlation coefficients

	$k=1$	$k=2$	$k=3$	$k=4$	$k=5$	$k=6$
$k=1$	1					
$k=2$	0.9029	1				
$k=3$	0.1760	0.0100	1			
$k=4$	0.9176	0.9061	0.4049	1		
$k=5$	0.5899	0.5678	0.4989	0.6475	1	
$k=6$	0.9475	0.9616	0.1221	0.9524	0.4827	1

By applying the described procedure, the criteria weights are determined (Step 3). The calculation procedure for the first criterion is illustrated as follows:

$$W_1 = 0.0645 \cdot \begin{pmatrix} (1-1) + (1-0.9029) + (1-0.1760) + (1-0.9176) + \\ (1-0.5899) + (1-0.9475) \end{pmatrix} = 0.0946$$

The weights of the remaining criteria are determined in a similar manner, resulting in:

$W_2 = 0.1374$ $\quad$ $W_3 = 0.2346$ $\quad$ $W_4 = 0.0933$ $\quad$ $W_5 = 0.0312$ $\quad$ $W_6 = 0.1729$

The normalized criteria weights are then calculated (Step 4) as:

$$[0.124 \quad 0.180 \quad 0.307 \quad 0.122 \quad 0.041 \quad 0.226]$$

Discussion of the Obtained Results

In (Sonar & Kulkarni, 2021), the criteria weights were determined using the AHP method. The authors defined a representative group of DMs. These DMs were considered technology enthusiasts and possessed good knowledge of the technological criteria relevant to EV selection. They belonged to various economic sectors, and semi-structured interviews were conducted with the selected DMs. The assessed relative importance of the considered criteria was expressed using a pairwise comparison matrix:

$$\begin{bmatrix} 1 & 3 & 3 & 3 & 5 & 9 \\ & 1 & 3 & 1 & 7 & 7 \\ & & 1 & 1 & 5 & 3 \\ & & & 1 & 5 & 3 \\ & & & & 1 & 3 \\ & & & & & 1 \end{bmatrix}, \quad CR = 0{,}0892$$

Since the consistency ratio (CR) was lower than 0.1, the judgments provided by the DMs can be considered sufficiently consistent, and therefore, the inconsistency of the pairwise comparisons does not significantly affect the reliability of the obtained results.

The criteria weights vector obtained using the AHP method is:

$$[0.036 \quad 0.054 \quad 0.154 \quad 0.134 \quad 0.233 \quad 0.390]$$

The criteria weights obtained by applying the AHP, FANMA, Entropy, and CRITIC methods are presented in Figure 1 and Table 6.

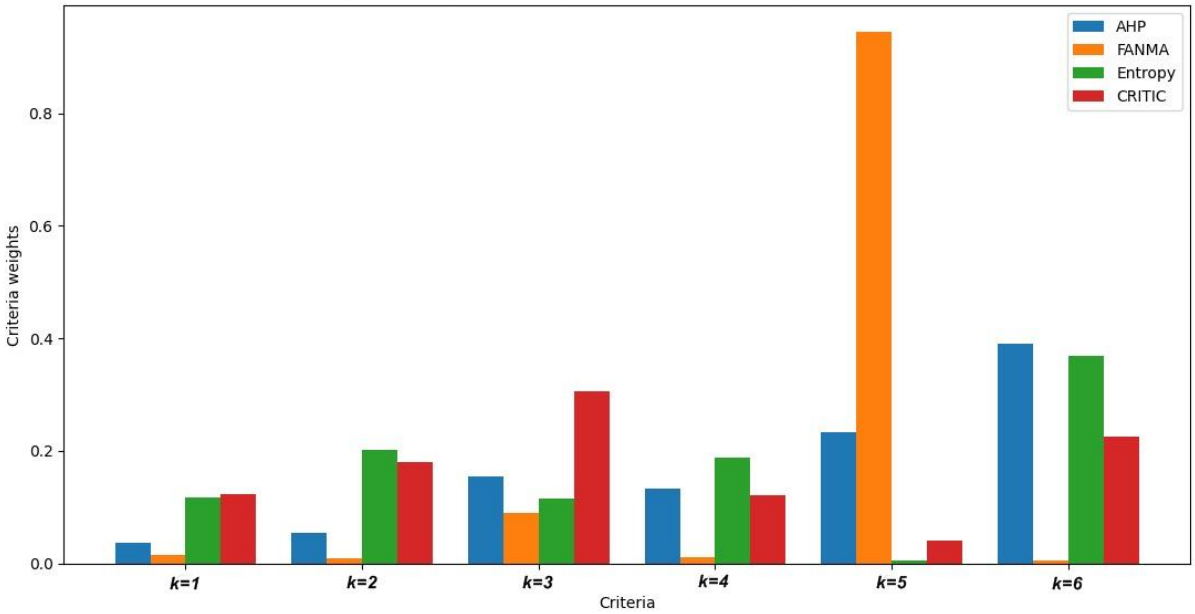

Figure 1 Comparison of criteria weights obtained using different methods

Table 6 Comparative analysis of the obtained criteria weights

Method	Criterion with the highest weight	Criterion with the lowest weight
AHP	$k = 7$	$k = 1$
FANMA	$k = 6$	$k = 1$
Entropy	$k = 7$	$k = 6$
CRITIC	$k = 3$	$k = 6$

Based on the obtained results, it can be clearly observed that the criteria weights used for EV evaluation differ significantly depending on the applied method. This raises the question of which method is the most appropriate. A definitive answer cannot be provided based solely on the obtained results.

If DMs possess sufficient knowledge and experience, and if the data collection procedure is properly conducted while considering the problem from different perspectives, the AHP method can be considered an appropriate approach for determining criteria weights. However, one of the main limitations of the AHP method is related to the increasing number of criteria, since a larger number of criteria requires a substantially larger number of pairwise comparisons.

On the other hand, if a larger number of criteria is considered and sufficiently accurate data are available, objective MCDM methods may be preferred. Based on the obtained results (see Table 6), it can be observed that the obtained criteria weights are not stable with respect to the applied weighting method.

Based on the results obtained for the considered sample, it is not possible to draw a clear and precise conclusion regarding which method is the most appropriate for determining criteria weights in the considered domain. However, it is well known that changes in criteria weights can lead to changes in the ranking results of the considered EVs. Therefore, the problem of determining criteria weights represents an important task for DMs.

CONCLUSIONS

The demands of an increasingly competitive automotive market require automotive strategic management teams to define, implement, and monitor strategies based on changes in customer preferences. It is believed that stricter environmental regulations will lead to the increased adoption of EVs. In this paper, the problem of evaluating a set of electric vehicles selected from the literature is addressed.

The first novelty of the paper lies in the application of objective MCDM methods for determining the criteria weights used for EV evaluation. The characteristics of these methods are particularly important when decision-making problems involve a large number of criteria and alternatives. The application of objective MCDM methods enables the objective determination of criteria weights, thereby reducing the influence of subjective assessments provided by DMs and providing an alternative approach to subjective weighting procedures.

The second novelty is the comparison of the criteria weights obtained using different objective MCDM methods, as well as their comparison with the weights obtained using the AHP method. In this research, the authors used an linear normalization procedure that does not distinguish between benefit and cost criteria. However, the authors believe that the applied normalization procedure is suitable for the problem under consideration.

The proposed approach is flexible with respect to changes in the number of criteria and the number of considered EV models.

However, the proposed approach has certain constraints. The main constraints include the selection of an appropriate number and type of EV models, as well as the identification of EV characteristics that adequately reflect customer preferences and other requirements of the decision-making environment.

Future research should investigate the robustness and sensitivity of the obtained results under different normalization procedures, particularly when a larger number of different types of EVs is considered. Additionally, the proposed approach can be extended to analyse other management decision-making problems in various research areas.

REFERENCES

Arsić, D., Ivković, D., Sudžum, R., Marinković, D., & Komatina, N. (2025). Selection of Base Materials for Repair Welding Using BWM-TOPSIS and BWM-RADAR Approaches. *Materials*, *18*(24), 5696. https://doi.org/10.3390/ma18245696

Biswas, T. K., & Das, M. C. (2019). Selection of Commercially Available Electric Vehicle using Fuzzy AHP-MABAC. *Journal of The Institution of Engineers (India): Series C*, *100*(3), 531–537. https://doi.org/10.1007/s40032-018-0481-3

Charnes, A., Cooper, W. W., & Rhodes, E. (1978). Measuring the efficiency of decision making units. *European Journal of Operational Research*, *2*(6), 429–444. https://doi.org/10.1016/0377-2217(78)90138-8

Chen, P. (2021). Effects of the entropy weight on TOPSIS. *Expert Systems with Applications*, *168*, 114186. https://doi.org/10.1016/j.eswa.2020.114186

Das, M. C., Pandey, A., Mahato, A. K., & Singh, R. K. (2019). Comparative performance of electric vehicles using evaluation of mixed data. *OPSEARCH*, *56*(3), 1067–1090. https://doi.org/10.1007/s12597-019-00398-9

Deuten, S., Gómez Vilchez, J. J., & Thiel, C. (2020). Analysis and testing of electric car incentive scenarios in the Netherlands and Norway. *Technological Forecasting and Social Change*, *151*, 119847. https://doi.org/10.1016/j.techfore.2019.119847

Diakoulaki, D., Mavrotas, G., & Papayannakis, L. (1995). Determining objective weights in multiple criteria problems: The critic method. *Computers & Operations Research*, *22*(7), 763–770. https://doi.org/10.1016/0305-0548(94)00059-H

Egnér, F., & Trosvik, L. (2018). Electric vehicle adoption in Sweden and the impact of local policy instruments. *Energy Policy*, *121*, 584–596. https://doi.org/10.1016/j.enpol.2018.06.040

Eskov, V. M., Eskov, V. V., Vochmina, Yu. V., Gorbunov, D. V., & Ilyashenko, L. K. (2017). Shannon entropy in the research on stationary regimes and the evolution of complexity. *Moscow University Physics Bulletin*, *72*(3), 309–317. https://doi.org/10.3103/S0027134917030067

Falatoonitoosi, E., Leman, Z., Sorooshian, S., & Salimi, M. (2013). Decision-Making Trial and Evaluation Laboratory. *Research Journal of Applied Sciences, Engineering and Technology*, *5*(13), 3476–3480. https://doi.org/10.19026/rjaset.5.4475

Flores, B. E., & Whybark, D. C. (1987). Implementing multiple criteria ABC analysis. *Journal of Operations Management*, *7*(1–2), 79–85. https://doi.org/10.1016/0272-6963(87)90008-8

Gustafsson, M., Svensson, N., Eklund, M., & Fredriksson Möller, B. (2021). Well-to-wheel climate performance of gas and electric vehicles in Europe. *Transportation Research Part D: Transport and Environment*, *97*, 102911. https://doi.org/10.1016/j.trd.2021.102911

Komatina, N., & Marinković, D. (2025). An Objective Multi-Attribute Decision-Making Framework for Identifying Critical Phases in Automotive Component Manufacturing. *Journal of Engineering Management and Systems Engineering*, *5*(1), 1–9. https://doi.org/10.56578/jemse050101

Komatina, N., Tadić, D., Aleksić, A., & Jovanović, A. D. (2023). The assessment and selection of suppliers using AHP and MABAC with type-2 fuzzy numbers in automotive industry. *Proceedings of the Institution of Mechanical Engineers, Part O: Journal of Risk and Reliability*, *237*(4), 836–852. https://doi.org/10.1177/1748006X221095359

Krishnan, A. R. (2025). Research trends in criteria importance through intercriteria correlation (CRITIC) method: A visual analysis of bibliographic data using the Tableau software. *Information Discovery and Delivery*, *53*(2), 233–247. https://doi.org/10.1108/IDD-02-2024-0030

Langbroek, J. H. M., Franklin, J. P., & Susilo, Y. O. (2017). Electric vehicle users and their travel patterns in Greater Stockholm. *Transportation Research Part D: Transport and Environment*, *52*, 98–111. https://doi.org/10.1016/j.trd.2017.02.015

Liu, J., Wang, J., Ding, X., Shao, W., Mei, C., Li, Z., & Wang, K. (2020). Assessing the mitigation of greenhouse gas emissions from a green infrastructure-based urban drainage system. *Applied Energy*, *278*, 115686. https://doi.org/10.1016/j.apenergy.2020.115686

Mandal, N., Sarkar, P., & Petrović, N. (2025). Multi-Criteria Decision-Making for Ranking Renewable Energy Sources: A Case Study from the Republic of Serbia. *Journal of Engineering Management and Systems Engineering*, *4*(2), 109–121. https://doi.org/10.56578/jemse040203

Milanovic, M., Misita, M., & Komatina, N. (2020). Determination of the optimal production plan by using fuzzy AHP and fuzzy linear programming. *Journal of Intelligent & Fuzzy Systems*, *38*(4), 4315–4325. https://doi.org/10.3233/JIFS-190913

Milićević, M. R., & Župac, G. Ž. (2012). An objective approach to determining criteria weights. *Vojnotehnicki Glasnik*, *60*(1), 39–56. https://doi.org/10.5937/vojtehg1201039M

Rezaei, J. (2015). Best-worst multi-criteria decision-making method. *Omega*, *53*, 49–57. https://doi.org/10.1016/j.omega.2014.11.009

Saaty, T. L. (2013). The Modern Science of Multicriteria Decision Making and Its Practical Applications: The AHP/ANP Approach. *Operations Research*, *61*(5), 1101–1118. https://doi.org/10.1287/opre.2013.1197

Saraiva, P. (2023). On Shannon entropy and its applications. *Kuwait Journal of Science*, *50*(3), 194–199. https://doi.org/10.1016/j.kjs.2023.05.004

Shannon, C. E. (1948). A Mathematical Theory of Communication. *Bell System Technical Journal*, *27*(3), 379–423. https://doi.org/10.1002/j.1538-7305.1948.tb01338.x

Sonar, H. C., & Kulkarni, S. D. (2021). An Integrated AHP-MABAC Approach for Electric Vehicle Selection. *Research in Transportation Business & Management*, *41*, 100665. https://doi.org/10.1016/j.rtbm.2021.100665

Tadić, D., Lukić, J., & Komatina, N. (2024). A two-stage model for electric vehicle evaluation: CRITIC-ELECTRE approach. *Mobility and Vehicle Mechanics*, *50*(1), 39–55. https://doi.org/10.24874/mvm.2024.50.01.04

Tadić, D., Lukić, J., Komatina, N., Marinković, D., & Pamučar, D. (2025). A Fuzzy Decision-Making Approach to Electric Vehicle Evaluation and Ranking. *Tehnicki Vjesnik/Technical Gazette*, *32*(3), 1066–1075. https://doi.org/10.17559/TV-20250223002410

Yagcitekin, B., Uzunoglu, M., Karakas, A., & Erdinc, O. (2015). Assessment of electrically-driven vehicles in terms of emission impacts and energy requirements: A case study for Istanbul, Turkey. *Journal of Cleaner Production*, *96*, 486–492. https://doi.org/10.1016/j.jclepro.2013.12.063

Zarazua De Rubens, G., Noel, L., Kester, J., & Sovacool, B. K. (2020). The market case for electric mobility: Investigating electric vehicle business models for mass adoption. *Energy*, *194*, 116841. https://doi.org/10.1016/j.energy.2019.116841

Zhao, X., Ke, Y., Zuo, J., Xiong, W., & Wu, P. (2020). Evaluation of sustainable transport research in 2000–2019. *Journal of Cleaner Production*, *256*, 120404. https://doi.org/10.1016/j.jclepro.2020.120404

Zhu, G.-N., Hu, J., Qi, J., Gu, C.-C., & Peng, Y.-H. (2015). An integrated AHP and VIKOR for design concept evaluation based on rough number. *Advanced Engineering Informatics*, *29*(3), 408–418. https://doi.org/10.1016/j.aei.2015.01.010

The 11th International Congress
Motor Vehicles & Motors 2026
Kragujevac, Serbia
October 8th - 9th, 2026

Motor Vehicles & Motors

MVM2026-052
https://doi.org/10.24874/CMVM2026.052
Original scientific paper

Dragan Čukanović[1]
Gordana Bogdanović[2]
Aleksandar Radaković[3]
Petar Knežević[4]

APPLICATION, MODELLING AND BENDING ANALYSIS OF COMPOSITE LAMINATES IN MODERN VEHICLES

ABSTRACT: The paper highlights the importance of the continuous development of composite materials as one of the key trends in the modern automotive industry. Particular attention is devoted to the advantages offered by composite materials in terms of vehicle weight reduction, improved energy efficiency, and enhanced mechanical performance of structural components. In addition, various mathematical models developed for describing the behaviour of laminated composite plates are considered. Based on the adopted mathematical formulations, a static bending analysis of these structural elements subjected to transverse loading was carried out. The obtained results are presented and analysed with the aim of providing a comprehensive insight into the potential applications of composite materials and their more efficient integration into the structures of modern electric vehicles.

KEYWORDS: modern automotive vehicles, composite materials, mathematical models of composite plates, elastic foundations, static analysis

PRIMENA, MODELIRANJE I ANALIZA SAVIJANJA KOMPOZITNIH LAMINATA U SAVREMENIM VOZILIMA

REZIME: U radu je istaknut značaj kontinuiranog razvoja kompozitnih materijala kao jednog od ključnih trendova u savremenoj automobilskoj industriji. Posebna pažnja posvećena je prednostima koje kompozitni materijali pružaju u pogledu smanjenja mase vozila, povećanja energetske efikasnosti i unapređenja mehaničkih performansi konstrukcionih elemenata. Takođe, razmatrani su različiti matematički modeli namenjeni opisu ponašanja laminatnih kompozitnih ploča. Na osnovu usvojenih matematičkih formulacija sprovedena je statička analiza savijanja

[1] *Dragan Čukanović, University of Priština, Faculty of Technical Sciences, Knjaza Miloša 7, 38220 Kosovska Mitrovica, dragan.cukanovic@pr.ac.rs, https://orcid.org/0000-0001-8370-748X*
[2] *Gordana Bogdanović, University of Kragujevac, Faculty of Engineering, Sestre Janjić 6, 34000 Kragujevac, gocab@kg.ac.rs, https://orcid.org/0000-0001-7231-7400*
[3] *Aleksandar Radaković, Institute for Information Technologies Kragujevac, Jovana Cvijića bb, 34000 Kragujevac, Serbia, aradakovic@uni.kg.ac.rs, https://orcid.org/0000-0002-7355-7403*
[4] *Petar Knežević, University of Priština, Faculty of Technical Sciences, Knjaza Miloša 7, 38220 Kosovska Mitrovica, petar.knezevic@pr.ac.rs, https://orcid.org/0000-0003-4187-2879*

navedenih konstrukcionih elemenata pod dejstvom poprečnog opterećenja. Dobijeni rezultati su prikazani i analizirani u cilju sagledavanja mogućnosti primene kompozitnih materijala i njihove efikasnije integracije u konstrukcije savremenih električnih vozila.

KLJUČNE REČI: savremena motorna vozila, kompozitni materijali, matematički modeli kompozitnih ploča, elastična podloga, statička analiza

INTRODUCTION

The development of electric vehicles represents one of the most significant directions in the ongoing transformation of the automotive sector, primarily driven by the need to reduce greenhouse gas emissions, improve energy efficiency and enhance the sustainability and performance of electric vehicle technologies. Modern vehicles require structures capable of simultaneously providing low weight, high stiffness and strength, impact and fatigue resistance as well as adequate thermal and electrical protection. A particular challenge arises from the fact that the battery system represents a significant proportion of the total mass of an electric vehicle. Therefore, reducing the mass of other structural components represents one of the key directions in the development of electric vehicles. According to available research, a reduction in vehicle mass of approximately 10% can result in a reduction in energy consumption of about 6–8%, although the actual effect depends on the vehicle type, driving conditions, and characteristics of the propulsion system. Wazeer, A. et al. (2023), Kumar, S. and Bharj, R. S. (2018), and Khan, F. et al. (2025) highlight the significant potential of composite materials for reducing vehicle mass while maintaining the required mechanical performance and structural integrity.

In this context, composite laminates represent a particularly important class of materials. Unlike conventional metallic materials, whose mechanical properties are generally isotropic, the properties of composite laminates can be tailored by selecting the type of fibres and matrix, reinforcement content, thickness of individual plies, and, in particular, the orientation and stacking sequence of the plies. This design flexibility represents one of the major advantages of laminated composites over conventional materials and enables the development of structures tailored to the specific requirements of modern automotive vehicles.

Accordingly, carbon fibre reinforced polymer (CFRP) and glass fibre reinforced polymer (GFRP) laminates are among the most commonly considered composite materials for vehicle structural components. CFRP laminates exhibit a particularly favourable stiffness- and strength-to-weight ratio, making them an attractive solution for components where weight reduction is a primary requirement. GFRP laminates are characterized by lower cost and good mechanical properties and can therefore represent a more economical alternative to CFRP. In addition, hybrid laminates combining different types of fibres, as well as thermoplastic composite laminates and sandwich structures, are being increasingly investigated as reported by Bazan, P. et al. (2026).

Under operating conditions vehicle and their structural components are subjected to various static and dynamic loading conditions, including vibration, impact, and cyclic loading associated with material fatigue. These loading conditions require adequate strength, stiffness, and durability of structural components, particularly when they are manufactured from composite materials. Consequently, mathematical modelling of composite laminates, together with their static and dynamic analysis, is becoming increasingly important in the modern design of vehicle structures. Lin, Y. et al. (2025) emphasize the importance of structural integrity and mechanical performance of composite materials under various loading conditions, while Atallah, K. E. et al. (2025) demonstrate the application of advanced numerical models for the static, free vibration, and buckling analysis of laminated composite plates. Numerous studies have therefore focused on the development and application of numerical models for predicting the mechanical response of composite structures under different loading conditions.

APPLICATIONS OF COMPOSITE LAMINATES

In the development and design of modern electric vehicles, composite materials are increasingly being used not only for body components but also for chassis and load-bearing structures, protective elements, battery pack enclosures, and other functional components.

One of the most significant application areas of composite laminates is battery pack enclosures. These structures perform multiple functions: they support the battery modules, protect the cells from external mechanical loads, transfer loads to the vehicle structure, and provide adequate protection in the event of a crash. At the same time, the enclosure must withstand vibrations, temperature variations, moisture, and corrosive environments. Consequently, CFRP and GFRP laminates are increasingly being investigated as alternatives to steel and aluminium battery enclosures.

The application of composite laminates in battery enclosures is particularly important from the perspective of impact protection and crashworthiness. Unlike ductile metals, in which energy is absorbed primarily through plastic deformation, composite laminates absorb energy through a combination of different damage mechanisms, including fibre fracture, matrix cracking, delamination, and local crushing. Through appropriate laminate stacking-sequence design, progressive damage and controlled energy absorption can be achieved. This is particularly important in electric vehicles because mechanical damage to the battery enclosure can result in deformation or damage to the battery cells themselves. Research by Isaac, C. W. and Ezekwem, C. (2021) and Capretti, M. et al. (2024) on the crashworthiness of composite structures indicates that material selection, geometry, and stacking sequence must be considered simultaneously, as even a small change in laminate configuration can significantly alter the failure mechanism and the total amount of absorbed energy. Therefore, composite laminates have significant potential for application in electric vehicles, particularly in battery enclosures and battery pack covers, where they can provide low weight combined with the required stiffness, mechanical protection, impact resistance and the possibility of tailoring material properties through changes in ply orientation, as discussed by Liu, Y. et al. (2026).

In load-bearing vehicle structures, including the vehicle floor structure, chassis components, and structural supports, composite laminates enable weight reduction while maintaining adequate load-carrying capacity and stiffness. In addition, the fibre direction can be oriented according to the predominant loading directions. In body components, such as roof, floor, and door panels, composite laminates enable vehicle weight reduction while providing sufficient stiffness and flexibility for manufacturing components with complex geometries. Composite laminates are also applied in bumpers, supports, and other components designed for controlled energy absorption, where their progressive damage behaviour can be exploited to improve the crashworthiness characteristics of the vehicle.

MODELLING COMPOSITE LAMINATES ON ELASTIC FOUNDATION

The static analysis of composite laminates is based on different plate theories. For thin laminated plates, the classical plate theory (CPT) is applied, whereas the first-order shear deformation theory (FSDT) is most commonly used for moderately thick plates, accounting for the effect of transverse shear deformation. For thicker laminated plates, higher-order shear deformation theories (HSDT) are employed, providing a more accurate description of the deformation and stress states through the plate thickness. An additional level of model complexity can be achieved by incorporating an elastic foundation, such as the Winkler, Pasternak, or Kerr models, which enables the analysis of the interaction between the composite laminate and the supporting foundation, as demonstrated by Akavci, S. S. (2005).

In this paper, the mechanical behaviour of composite laminates resting on elastic foundations is investigated using the higher-order shear deformation theory (HSDT), which accounts for transverse shear deformation without requiring an additional shear correction factor and provides an appropriate framework for the analysis of moderately thick laminated plates. The interaction between the composite laminate and the supporting medium is modelled using three commonly adopted elastic foundation models, namely the Winkler, Pasternak, and Kerr models. The Winkler model represents the foundation as a set of independent vertical springs and therefore considers only the local transverse response of the foundation (Figure 1a). In contrast, the Pasternak model introduces an additional shear layer that establishes interaction between neighbouring foundation points and consequently accounts for the transverse shear interaction within the supporting medium (Figure 1b). The Kerr foundation model further extends this concept by incorporating two independent layers of elastic springs connected through a shear layer, enabling a more flexible representation of the foundation response (Figure 1c).

Within the framework of the higher-order shear deformation theory the kinematic relationships between the displacement and strain fields are established by introducing appropriate assumptions for the displacement components:

$$u = u_0(x,y) - zw_{0,x} + f(z)\theta_x, \quad v = v_0(x,y) - zw_{0,y} + f(z)\theta_y, \quad w = w_0(x,y), \tag{1}$$

where are:

- $u_0(x,y), v_0(x,y), w_0(x,y)$ - displacements of the mid-surface in the *x*, *y* and *z* directions, respectively;
- $w_{0,x}, w_{0,y}$ - rotations of transverse cross-sections about the *y* and *x* axes, respectively;
- θ_x, θ_y - higher-order terms which, in combination with the shape function *f*(*z*), enable the interpolation of shear deformation across the plate thickness;
- *f*(*z*) - shape function proposed by authors in the follow form:

$$f(z) = -\left(\frac{z^2 \sinh\left(\frac{z}{h}\right)}{h} - 0{,}8z \right) \tag{2}$$

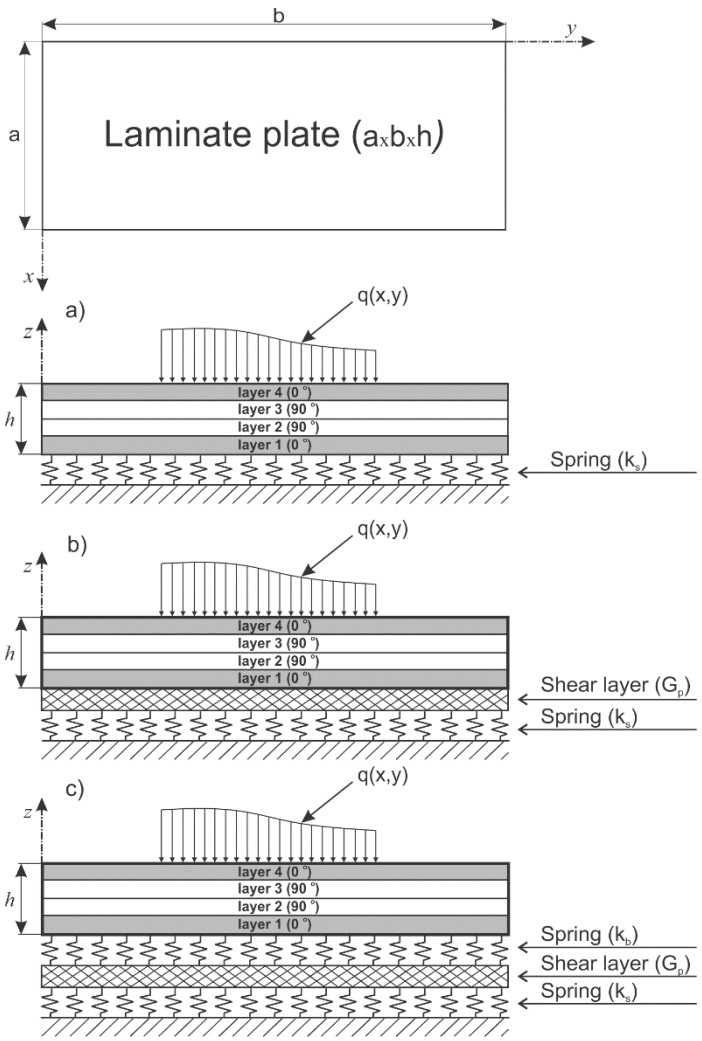

$q_e(x,y)$ - foundation reaction

U_e - strain energy of the elastic foundation

$$q_e^{Winkler} = k_s w$$

$$U_e^{Winkler} = \int_A \frac{1}{2} k_s w^2 dA$$

$$q_e^{Pasternak} = k_s w - G_p \nabla^2 w\,, \qquad \nabla^2 = \frac{\partial^2}{\partial x^2} + \frac{\partial^2}{\partial y^2}$$

$$U_e^{Pasternak} = \frac{1}{2}\int_A \left\{ k_s w^2 + G_p \left[\left(\frac{\partial w}{\partial x}\right)^2 + \left(\frac{\partial w}{\partial y}\right)^2 \right] \right\} dA$$

$$q_e^{Kerr} = \frac{k_s k_b}{k_s + k_b} w - \frac{G_p k_b}{k_s + k_b} \nabla^2 w$$

$$U_e^{Kerr} = \frac{1}{2}\int_A \left\{ \frac{k_s k_b}{k_s + k_b} w^2 + \frac{G_p k_b}{k_s + k_b} \left[\left(\frac{\partial w}{\partial x}\right)^2 + \left(\frac{\partial w}{\partial x}\right)^2 \right] \right\} dA$$

Figure 1 The geometry of composite laminate plate on elastic foundation: a) Winkler foundation, b) Pasternak foundation, c) Kerr foundation

The determination of the unit-load components requires the application of the displacement–strain relationships within the framework of linear elasticity. Accordingly, the constitutive equations describing the elastic behaviour of anisotropic materials can be expressed as follows:

$$\sigma_{ij} = C_{ijkl} \varepsilon_{kl} \tag{3}$$

where:

- σ_{ij} are the stress components in different directions;
- C_{ijkl} is the material elasticity tensor;
- ε_{kl} are the strain components.

In order to apply the principle of minimum potential energy:

$$\delta U + \delta V + \delta U_e = \delta\left(U + V + U_e\right) \equiv \delta \Pi = 0 \tag{4}$$

it is necessary to define work under external load V for the plate bending problem subjected to a sinusoidal transverse load q(x,y):

$$V = -\frac{1}{2}\int_A q w dA, \quad \text{where is} \quad q(x,y) = q_0 \sin\left(\frac{\pi x}{a}\right) \sin\left(\frac{\pi y}{b}\right) \tag{5}$$

as well as plate strain energy deformation U in the follow form:

$$U = \int_A (N_{xx}\varepsilon_{xx}^{(0)} + N_{yy}\varepsilon_{yy}^{(0)} + N_{xy}\gamma_{xy}^{(0)} + M_{xx}k_{xx}^{(0)} + M_{yy}k_{yy}^{(0)} + M_{xy}k_{xy}^{(0)} + P_{xx}k_{xx}^{(1)} + P_{yy}k_{yy}^{(1)} + P_{xy}k_{xy}^{(1)} + R_x k_{xz}^{(2)} + R_y k_{yz}^{(2)})dA \tag{6}$$

while strain energy of the elastic foundation Ue is already defined according figure 2, depending on the particular foundation model considered.

Upon substitution of the strain components into the governing formulation and application of the variational principle, the corresponding equilibrium equations are obtained as follows:

$$\begin{aligned}
&\delta u_0: \quad N_{xx,x} + N_{xy,y} = 0 \\
&\delta v_0: \quad N_{yy,y} + N_{xy,x} = 0 \\
&\delta w_0: \quad M_{xx,xx} + 2M_{xy,xy} + M_{yy,yy} + N_{xx}w_{0,xx} + 2N_{xy}w_{0,xy} + N_{yy}w_{0,yy} + q - \frac{k_s k_b}{k_s + k_b}w_0 + \frac{G_p k_b}{k_s + k_b}\left(w_{0,xx} + w_{0,yy}\right) = 0 \\
&\delta\theta_x: \quad P_{xx,x} + P_{xy,y} - R_x = 0 \\
&\delta\theta_y: \quad P_{xy,x} + P_{yy,y} - R_y = 0
\end{aligned} \tag{7}$$

where:

$$\mathbf{N}=\left\{N_{xx} \quad N_{yy} \quad N_{xy}\right\}^T, \mathbf{M}=\left\{M_{xx} \quad M_{yy} \quad M_{xy}\right\}^T, \mathbf{P}=\left\{P_{xx} \quad P_{yy} \quad P_{xy}\right\}^T, \mathbf{R}=\left\{R_x \quad R_y\right\}^T \tag{8}$$

represents the force, moments and higher order moment resultants.

Equilibrium equations (7) correspond to the model of a composite laminate plate resting on Kerr's type of elastic foundation.

In the case of the Pasternak type of elastic foundation, the third equation has the form:

$$\delta w_0: \quad M_{xx,xx} + 2M_{xy,xy} + M_{yy,yy} + N_{xx}w_{0,xx} + 2N_{xy}w_{0,xy} + N_{yy}w_{0,yy} + q - k_s w_0 + G_p\left(w_{0,xx} + w_{0,yy}\right) = 0 \tag{9}$$

and finally, for the simplest Winkler-type elastic foundation:

$$\delta w_0: \quad M_{xx,xx} + 2M_{xy,xy} + M_{yy,yy} + N_{xx}w_{0,xx} + 2N_{xy}w_{0,xy} + N_{yy}w_{0,yy} + q - k_s w_0 = 0 \tag{10}$$

For the analytical solution of the system of equations (7), appropriate displacement fields and boundary conditions are assumed in accordance with Navier's solution, as described by Čukanović, D. et al. (2018).

NUMERICAL EXAMPLES

The numerical examples presented in this section are conducted to verify the theoretical formulation developed in the previous sections and to demonstrate its applicability to the analysis of composite laminated plates. A symmetric cross-ply square laminate [0°/90°/90°/0°] resting on different type of elastic foundation is considered as the reference model. The plate is subjected to a sinusoidally distributed transverse load, while the material properties of the individual orthotropic layers are defined by their prescribed engineering constants:

$$E_1 / E_2 = 25, \quad G_{12} / E_2 = 0.6, \quad G_{13} / E_2 = 0.6, \quad G_{23} / E_2 = 0.5, \quad \nu_{12} = \nu_{13} = \nu_{23} = 0.25 \tag{11}$$

The numerical procedure is implemented to determine the mechanical response of the laminated plate under the considered loading and boundary conditions. The obtained results provide a basis for verifying the theoretical predictions and for further examining the influence of the considered elastic foundation models on the response of the composite plate. The numerical examples was performed by using MATLAB program package. The obtained numerical values were subsequently processed and normalized to facilitate their presentation and comparison:

$$\bar{w} = \frac{100E_2h^3}{q_0a^4}w\left(\frac{a}{2},\frac{b}{2},0\right); \quad \bar{\sigma}_{xx} = \frac{h^2}{qb^2}\sigma_{xx}\left(\frac{a}{2},\frac{b}{2},\frac{h}{2}\right)$$
$$\bar{\sigma}_{yy} = \frac{h^2}{q_0b^2}\sigma_{yy}\left(\frac{a}{2},\frac{b}{2},\frac{h}{4}\right); \quad \bar{\tau}_{xy} = \frac{h^2}{q_0b^2}\sigma_{xy}\left(0,0,\frac{h}{2}\right) \tag{12}$$
$$\bar{\tau}_{yz} = \frac{h}{q_0b}\sigma_{yz}\left(\frac{a}{2},0,0\right); \quad \bar{\tau}_{xz} = \frac{h}{q_0b}\sigma_{xz}\left(0,\frac{b}{2},0\right)$$

Based on the presented results in table 1, it can be observed that the selection of the elastic foundation model has a significant effect on the mechanical response of the laminated plate, particularly in terms of the normalized maximum displacement and the distribution of stress components. For the Winkler foundation, which represents the simplest model of the plate–foundation interaction, the normalized maximum displacement is 1.1189 for the geometric ratio a/h=4 and 0.4272 for a/h=20. This result indicates a pronounced influence of the geometric characteristics of the plate on its global deformation response. By introducing shear stiffness through the Pasternak model, the normalized displacement is reduced compared with the Winkler model, while the Kerr model, owing to the additional consideration of shear and local interaction characteristics, exhibits an even greater restriction of deformation. A similar dependence can be observed for the normalized normal stresses, with the Winkler foundation generally producing higher values of the stress response, whereas the additional stiffness parameters of the Pasternak and Kerr foundations contribute to its reduction. The change in the elastic foundation model also affects the values of the shear stresses, indicating that the characteristics of the foundation influence not only the global deformation of the plate but also the local distribution of stresses through the laminate thickness. Overall, the results demonstrate that the application of the Pasternak and Kerr foundation models enables a more detailed description of the interaction between the laminated plate and the elastic foundation compared with the Winkler model, while an increase in the effective stiffness of the system results in a reduction in both the deformation and, to a certain extent, the stress response of the plate.

Table 1 Normalized values of displacement and stresses of symmetric cross-ply square laminate [0°/90°/90°/0°] resting on different type of elastic foundation

Theory	k_s	G_p	k_b	a/h	$\bar{w}$	$\bar{\sigma}_{xx}$	$\bar{\sigma}_{yy}$	$\bar{\tau}_{xy}$	$\bar{\tau}_{yz}$	$\bar{\tau}_{xz}$
Winkler	100			4	1.1189	0.3997	0.3682	0.0266	0.1492	0.1292
				20	0.4272	0.4561	0.2623	0.0195	0.1082	0.2552
Pasternak	100	30		4	0.3313	0.1203	0.1103	0.0079	0.0456	0.0389
				20	0.2292	0.2463	0.1396	0.0109	0.0589	0.1354
Kerr	100	100	100	4	0.2376	0.0892	0.0784	0.0059	0.0345	0.0276
				20	0.1788	0.1965	0.1106	0.0081	0.0463	0.1060

By analysing the normalized displacement values shown in Figure 2, with the change of the ratio a/h=4 to 20, the following can be concluded:

- Winkler foundation - the normalized displacement changes by about 2.6 times,
- Pasternak foundation - the normalized displacement changes approximately 1.45 times,
- Kerr foundation - the normalized displacement changes approximately 1.3 times.

Thus, the normalized displacement is most sensitive to changes in the a/h ratio for the Winkler foundation and least sensitive for the Kerr foundation.

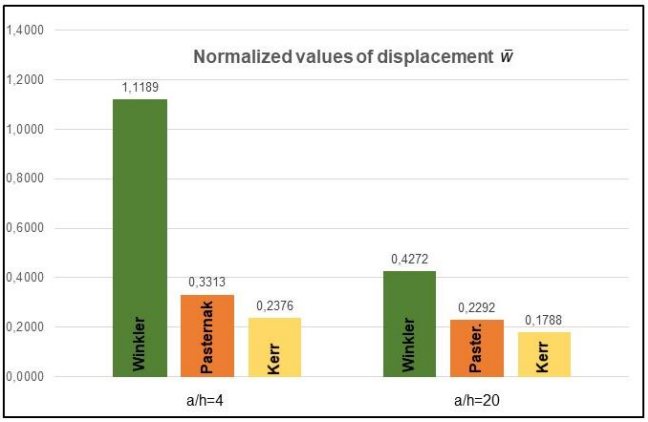

Figure 2 Comparative results of normalized displacement values for plates with length to thickness ratio of a/h=4 and a/h=20

CONCLUSIONS

The presented paper confirms the significant potential of composite materials for application in modern automotive and electric vehicle structures, particularly due to their favourable mechanical performance and potential for weight reduction. The developed theoretical formulation for the static analysis of laminated composite plates provides an effective framework for investigating their response under transverse loading and was verified through the presented numerical examples. The results demonstrate that the elastic foundation model has a pronounced influence on the deformation and stress response of the laminated plate, with the Pasternak and Kerr models providing a more comprehensive representation of plate–foundation interaction than the Winkler model. An increase in the length-to-thickness ratio generally leads to changes in normalized displacement and stresses components, highlighting the importance of plate geometry in the structural analysis. Overall, the obtained results demonstrate that an appropriate combination of laminate configuration, material properties, geometric parameters, and elastic foundation characteristics can significantly influence the mechanical behaviour of composite plates.

As a direction for future research, the developed model could be extended to asymmetric laminated plates in order to assess its applicability and accuracy for more complex laminated plate configurations. Particular attention could be devoted to investigating the influence of different layer arrangements and orientations on the deformation and stress response. Further research could also focus on the optimization of the laminate structure and elastic foundation parameters with respect to predefined criteria, such as minimum displacement, maximum allowable stress, or the simultaneous minimization of mass and deformation.

REFERENCES

Wazeer, A., Das, A., Abeykoon, C., Sinha, A., & Karmakar, A. (2023). Composites for electric vehicles and automotive sector: A review. *Green Energy and Intelligent Transportation*, 2(1), 100043. https://doi.org/10.1016/j.geits.2022.100043

Kumar, S., & Bharj, R. S. (2018). Emerging composite material use in current electric vehicle: A review. *Materials Today: Proceedings*, 5(14), 27946-27954. https://doi.org/10.1016/j.matpr.2018.10.034

Khan, F., Hossain, N., Mim, J. J., Rahman, SM M., Iqbal, Md. J., Billah, M., & Chowdhury, M. A. (2025). Advances of composite materials in automobile applications – A review. J*ournal of Engineering Research*, 13(2) 1001-1023. https://doi.org/10.1016/j.jer.2024.02.017

Bazan, P., Przybek, A., Lach, M., Badura, K., Duda, P., & Bielaczyc, P. (2026). Materials used in electric vehicle battery housings: Recycling pathways and circular design - A Review. *Materials*, 19(13), 2808. https://doi.org/10.3390/ma19132808

Lin, Y., Qian W., Lei, L., Liu, Y., Zhang, J., Li, J., Kong, W., Hu, Y., Shi, Y., Wu, Z., Liu, H., & Wu, S. (2025). Structural integrity issues of composite materials and structures in future transportation equipment. *Composite Structures*, 358, 118943. https://doi.org/10.1016/j.compstruct.2025.118943

Atallah, K. E., Ouinas, D., Zaoui, F. Z., Khoussa, H., Achour, B., Hassan, M. F., & Siregar, J. P. (2025). A refined quasi-3D higher-order shear deformation theory for static, free vibration, and buckling of laminated composite plates on kerr-type foundation. *Next Materials*, 9, 101352. https://doi.org/10.1016/j.nxmate.2025.101352

Isaac, C. W., & Ezekwem, C. (2021). A review of the crashworthiness performance of energy absorbing composite structure within the context of materials, manufacturing and maintenance for sustainability. *Composite Structures*, 257, 113081. https://doi.org/10.1016/j.compstruct.2020.113081

Capretti, M., Bianco, G. D., Giammaria, V., & Boria, S. (2024). Natural fibre and hybrid composite thin-walled structures for automotive crashworthiness: A Review. *Materials*, 17(10), 2246. https://doi.org/10.3390/ma17102246

Liu, Y., Li, X., Huang, X., Wang, Y., & Tan, J. (2026). A review of composite mold design for battery enclosures and upper covers in new energy vehicles. *Frontiers in Mechanical Engineering*, 12. https://doi.org/10.3389/fmech.2026.1884600

Akavci, S. S. (2005). Analysis of thick laminated composite plates on an elastic foundation with the use of various plate theories. *Mechanics of Composite Materials*, 41, 445-460. https://doi.org/10.1007/s11029-005-0070-4

Čukanović, D., Radaković, A., Bogdanović, G., Milanović, M., Redžović, H., & Dragović, D. (2018). New shape function for the bending analysis of functionally graded plate. *Materials*, 1(12), 2381. https://doi.org/10.3390/ma11122381

The 11th International Congress
Motor Vehicles & Motors 2026
Kragujevac, Serbia
October 8th - 9th, 2026

Motor Vehicles & Motors

MVM2026-053
https://doi.org/10.24874/CMVM2026.053
Technical paper

Mihajlo Jevtić[1]
Aleksandra Obradović[2]
Bogdan Todorović[3]
Nebojša Hristov[4]
Damir Jerković[5]

FINITE ELEMENT ANALYSIS OF STRUCTURAL SUPPORT REACTIONS IN WHEELED MOBILE PLATFORM UNDER HIGH-INTENSITY IMPULSIVE LOADING

ABSTRACT: The structural behaviour of support systems for mobile platforms subjected to high-intensity impulsive forces represents an important aspect in the assessment of their load-carrying capacity, stability, and operational reliability. This paper presents preliminary numerical analysis of the dynamic response of a three-dimensional support structure mounted on a military cargo vehicle for weapon system integration. The analysis was performed using the Finite Element Method (FEM) under short-duration impulsive force. A three-dimensional finite element model was developed, incorporating the relevant geometric characteristics, material properties, and boundary conditions of the structure. The impulsive force was applied in different spatial directions, and the resulting stress distribution, structural displacements, and support reactions were evaluated. Particular attention was given to the influence of load direction on the magnitude and distribution of support reactions in order to examine the load transfer mechanism within the structure. The study represents a preliminary assessment of the proposed structural solution based on a representative military cargo vehicle and weapon system configuration. The analysis enabled the identification of critical loading cases and highly stressed regions, providing a basis for further structural optimization and more detailed investigations of structural performance under impulsive loading.

KEYWORDS: FEM, mobile platform, impulsive loading, support reactions, dynamic response

[1] *Mihajlo Jevtić, University of Kragujevac, Faculty of Engineering, Sestre Janić 6, Kragujevac, Serbia, mixxerskate@gmail.com, https://orcid.org/0009-0004-4176-4936*
[2] *Aleksandra Obradović, Military Technical Institute, Ratka Resanovića 1, Belgrade, Serbia, aleksandraobradovic.va@gmail.com, https://orcid.org/0000-0001-7973-8590*
[3] *Bogdan Todorović, Matikon GmbH & Co. KG, Milana Mijalkovića 21, Jagodina, Serbia, bogdanto2000@gmail.com, https://orcid.org/0009-0008-4572-1318*
[4] *Nebojša Hristov, University of Defence in Belgrade, Military Academy, Veljka Lukića Kurjaka 33, Belgrade, Serbia, nebojsahristov@gmail.com, https://orcid.org/0000-0002-8163-2223*
[5] *Damir Jerković, University of Defence in Belgrade, Military Academy, Veljka Lukića Kurjaka 33, Belgrade, Serbia, damir.jerkovic@va.mod.gov.rs, https://orcid.org/0000-0001-5182-7057*

ANALIZA REAKCIJA OSLONACA MOBILNE PLATFORME NA TOČKOVIMA PRIMENOM METODE KONAČNIH ELEMENATA PRI IMPULSNOM OPTEREĆENJU VISOKOG INTENZITETA

REZIME: Strukturno ponašanje sistema oslonaca mobilnih platformi izloženih impulsnim opterećenjima visokog intenziteta predstavlja važan aspekt pri oceni njihove nosivosti, stabilnosti i operativne pouzdanosti. U ovom radu prikazana je preliminarna numerička analiza dinamičkog ponašanja noseće konstrukcije vojnog teretnog vozila, koja je namenjena integraciji sistema naoružanja. Analiza je sprovedena primenom metode konačnih elemenata (MKE) za slučaj kratkotrajnog impulsnog opterećenja. Razvijen je trodimenzionalni model konačnih elemenata koji obuhvata relevantne geometrijske karakteristike, mehaničke osobine materijala i granične uslove konstrukcije. Impulsno opterećenje primenjeno je u različitim prostornim pravcima, a analizirani su raspodela napona, pomeranja konstrukcije i reakcije u osloncima. Posebna pažnja posvećena je uticaju pravca opterećenja na reakcije u osloncima, u cilju sagledavanja mehanizma prenosa opterećenja kroz konstrukciju. Istraživanje predstavlja inicijalnu procenu predloženog konstruktivnog rešenja zasnovanog na reprezentativnom primeru vojnog teretnog vozila i sistema naoružanja. Analiza je omogućila identifikaciju kritičnih slučajeva opterećenja i oblasti sa povišenim naprezanjima, što predstavlja osnovu za dalju optimizaciju konstrukcije i detaljnija ispitivanja njenog ponašanja u uslovima impulsnog opterećenja.

KLJUČNE REČI: MKE, mobilna platforma, impulsno opterećenje, reakcija u osloncima, dinamičko ponašanje

INTRODUCTION

Vehicle stability is a fundamental consideration in the design and operation of heavy-duty vehicles and mobile platforms. The stability of such systems is determined not only by their geometric configuration and loading conditions but also by the mechanical characteristics of the supporting structure and the distribution of external loads. Therefore, the development of mathematical and mechanical models for the determination of support reactions and assessment of structural stability is essential for predicting the mechanical response of the vehicle and ensuring its safe and reliable operation. The objective of this study is to develop a preliminary mathematical and mechanical model for evaluating the stability of a mobile wheel-supported vehicle platform as part of a conceptual engineering study on the integration of a weapon system onto an existing vehicle platform. The study is intended to assess the technical feasibility of the proposed integration and to identify the critical structural and stability conditions resulting from the additional loads imposed by the integrated weapon system. The structural response of the vehicle chassis to an impulsive external load is investigated using the Finite Element Method (FEM), (Ghazaly 2014) emphasizes the importance of finite element analysis in evaluating the stress distribution within vehicle chassis structures. Numerical analysis enables the determination of stress and deformation fields within structural components, thereby providing a basis for evaluating their load-bearing capacity, structural integrity, and the overall structural performance of the proposed vehicle configuration. In this regard, the FEM represents a robust numerical framework for assessing the response of structural systems subjected to various loading conditions, while also enabling the consideration of both linear and nonlinear material and structural behaviour (Kojić et al. 2010; Dunica & Kolundžija, 1985).The analysis of vehicle chassis structures should account for their response to both static and dynamic loading conditions, as each loading regime may have a significant influence on the structural integrity of the chassis (Han Fui & Abd. Rahman, 2007).

From the standpoint of internal ballistics, the firing process generates a transient impulse that is transmitted from the weapon system to its supporting structure. The resulting recoil force represents the mechanical response to the rapid momentum change associated with the acceleration of the projectile and the movement of the recoiling masses. The magnitude and time history of this impulse depend on the ballistic characteristics of the weapon system and the associated firing conditions. Previous studies have demonstrated that the determination of recoil impulse and its transmission to the supporting structure is an important factor in assessing structural loads, support reactions, and overall firing stability. The design of weapon systems requires consideration of internal ballistic phenomena and the interaction between the gunpowder gases, projectile, and weapon barrel, as these processes directly influence the overall performance of the system (Tančić, 2014).

The mechanical model of the analysed vehicle, together with the acting external forces and support reactions, is presented in Figure 1. The vehicle is supported by four contact points, designated as A, B, C, and D. The four supports form the complete support configuration through which the external loads are transferred from the vehicle structure to the supporting surface.

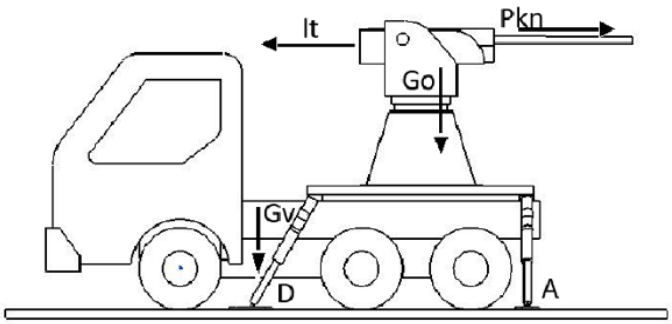

Figure 1 Vehicle with acting forces and support resistance

The external forces considered in the mechanical model are defined as follows:

- Pkn denotes the tractive force;
- It represents the inertial force associated with the moving or recoiling mass;
- Go denotes the gravitational force corresponding to the mass of the tractive-force source;
- Gv represents the gravitational force due to the vehicle mass.

The tractive force Pkn acts in the longitudinal direction of the vehicle and represents the load transmitted during acceleration. The inertial recoil force It results from the acceleration of the moving mass and acts in the opposite direction to the corresponding acceleration. The forces Go and Gv act vertically downward through the respective centres of gravity. The reactions at supports A, B, C, and D represent the resultant forces transmitted between the vehicle structure and the supporting surface. Their distribution is determined by the magnitude and direction of the applied forces, the positions of their points of application, the locations of the centres of gravity, and the geometric configuration of the support points. Determination of these reactions is therefore necessary for establishing the equilibrium conditions and evaluating the stability of the vehicle under the considered loading scenario.

DEVELOPMENT OF THE FINITE ELEMENT MODEL AND ANALYSIS

The finite element model of the supporting platform was developed from the three-dimensional CAD geometry. The geometry was simplified by removing non-load-bearing details and features that do not significantly affect the global stiffness and load distribution of the structure. The simplified geometry retained the principal load-bearing members, connection regions, and hydraulic outriggers, which are critical for the transfer of loads from the weapon system to the ground. The model was formulated as a shell finite element model. Four-node shell elements without midside nodes were used for the discretization of the structural surfaces. The FEM model is shown in Figure 2.

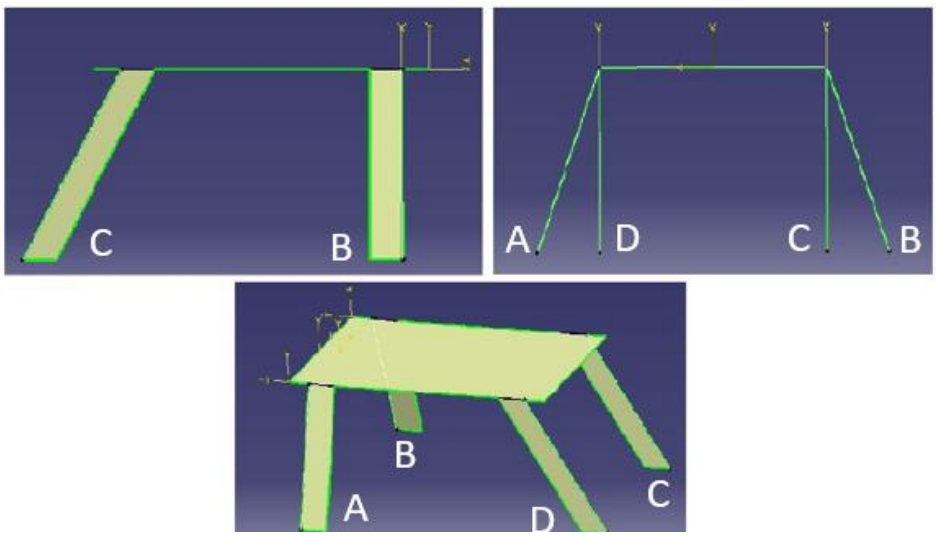

Figure 2 The FEM model

The finite element mesh was generated using four-node shell elements without midside nodes, with an appropriate mesh density to adequately represent the structural behaviour, particularly in regions where higher stresses and support reactions were expected. The resulting finite element mesh and boundary conditions are presented in Figure 3.

The applied loads consist of the inertial recoil force It, the gravitational force of the mounted system Go, and the gravitational force of the vehicle Gv. The forces were applied at the corresponding nodes defined in Table 1. The gravitational forces Go and Gv act vertically downward along the negative (Z)-axis, while the inertial recoil force It acts in the spatial direction defined by the elevation angle θ and direction angle ψ. Therefore, the direction and magnitude of the inertial recoil force It vary according to the considered loading configuration.

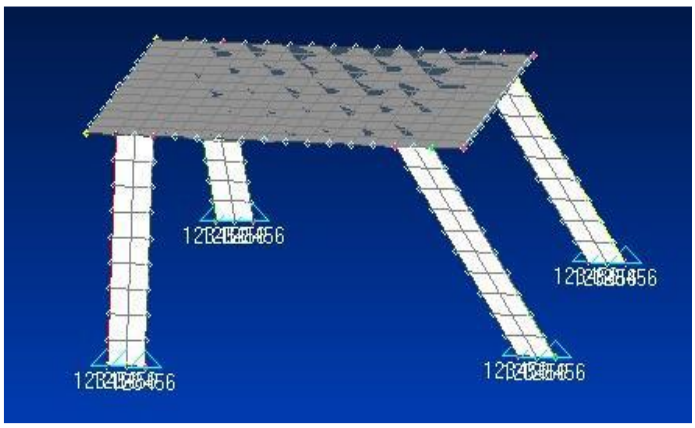

Figure 3 The finite element mesh

Table 1 Locations of force application node

Force	**Position (description / mm)**
Weight of the mounted system (Go)	Center node of the supporting plate
Vehicle weight (Gv)	(0, 1900, 0)
Inertial recoil force (It)	Center node of the supporting plate (0, 1280, 1200)

The stress analysis was performed for different combinations of elevation and direction angles. For each loading case, the resulting stress state, deformation, and support reactions were determined. The locations of the supports at which the reactions were evaluated, and 3D model are shown in Figure 4. For each support, the node with the maximum resultant reaction was selected as the representative value for further analysis. Numerical analysis based on the finite element method can be used to assess the structural behaviour of a vehicle chassis, including the distribution of stresses and deformations, as well as the identification of critical areas within the structure. In addition to static loading conditions, the dynamic behaviour of a vehicle can significantly affect the loads transmitted through the structure; therefore, the effects of dynamic loading should also be considered when evaluating the structural response of vehicle chassis (Kengkongan Ary et al. 2020; Kwasniewski et al. 2006).

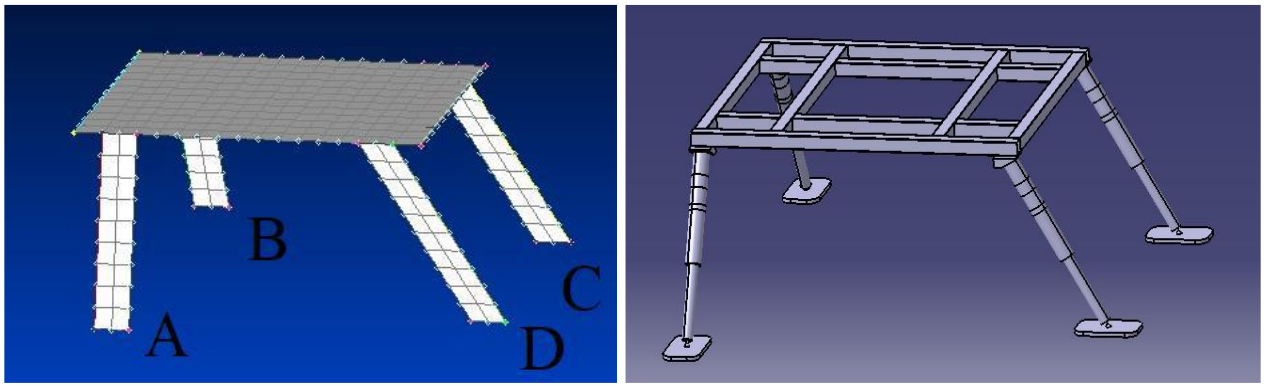

Figure 4 The locations of the supports and 3D model of platform

Boundary conditions and loading applied in the FEM model:

- the lower surfaces of the hydraulic supports were defined as fixed supports;
- all six degrees of freedom were constrained at the corresponding support nodes;
- translational displacements in the (Ox), (Oy), and (Oz) directions were constrained;
- rotations about the (Ox), (Oy), and (Oz) axes were constrained;
- forces Go and Gv were applied vertically downward along the negative (Oz) axis;
- inertial recoil force It was applied at the defined load application nodes according to the considered angles values of θ and ψ;
- the magnitude and spatial orientation of inertial recoil force It were varied according to the analysed loading cases;
- the hydraulic supports were assumed to remain stationary relative to the ground throughout the analysis.

Determining the unit vector of Inertial recoil force

The inertial recoil force It has a spatial orientation defined by the elevation angle θ and the direction angle ψ. Its line of action and spatial orientation are presented in Figure 5. These angular parameters define the orientation of inertial recoil force It with respect to the vehicle coordinate system and are used in determining its corresponding force components and moments. The resulting force components and moments are subsequently considered in the formulation of the equilibrium equations and in the evaluation of the support reactions.

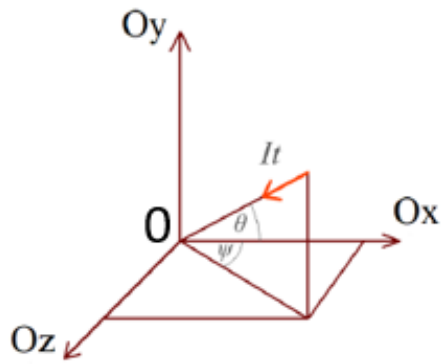

Figure 5 The spatial orientation of force It

Accurate determination of the magnitude and direction of the acting forces is essential for evaluating the stability and load-bearing capacity of the vehicle support structure. Under impulsive loading conditions, the external and inertial forces affect the distribution of support reactions and the resulting stresses in the vehicle structure. FEM analysis enables the structural response to these loads to be evaluated and provides a basis for assessing the stability and structural integrity of the vehicle. The allowable azimuth and elevation ranges are defined by the operational requirements and mechanical constraints of the weapon system intended to be integrated onto the vehicle. The azimuth angle is limited to the range ±60°, while the elevation angle is limited to -5° to 20°. These angular limits define the operational envelope of the weapon system considered for integration and are used to establish the loading conditions for the structural analysis of the supporting platform.

From the standpoint of overall vehicle stability, the theoretically most critical elevation condition corresponds to an elevation angle of 0°. At this configuration, the resulting moment generated by the inertial recoil force It reaches its maximum value for a direction angle of 0°, which represents the most critical condition with respect to potential failure of the supporting structure. For azimuth angles of ±60° the corresponding loading configuration becomes critical with respect to the overturning stability of the vehicle. In contrast, from the structural load-bearing standpoint, the most critical condition for the supporting structure corresponds to the maximum permissible elevation angle. At this configuration, the force transmitted to the supporting structure reaches its highest vertical component, resulting in the greatest structural loading. Therefore, both the minimum-elevation condition and the maximum-elevation condition must be considered when assessing the stability and structural integrity of the vehicle.

The components of the inertial recoil force It are defined by the following equations:

$$xIt = I_t \cdot cos\theta \cdot sin\psi \tag{1}$$

$$yIt = I_t \cdot cos\theta \cdot cos\psi \tag{2}$$

$$zIt = I_t \cdot sin\theta \tag{3}$$

Since the considered problem exhibits axial symmetry, the analysis of the azimuth angle can be limited to one direction without loss of generality. This approach reduces the number of required load cases and consequently improves the computational efficiency of the numerical analysis. The corresponding components of the recoil inertial force It are presented in the following Table 2.

Table 2 The corresponding components of the recoil inertial force It

Angles		Components of the recoil inertial force It		
θ [°]	ψ [°]	It_X [KN]	It_Y [KN]	It_Z [KN]
-5	60	137.6	79.4	-13.9
-5	30	79.4	137.6	-13.9
-5	0	0	158.9	-13.9
0	60	138.1	79.7	0
0	30	79.7	138.1	0
0	0	0	159.5	0

Table 2 (continuation)

Angles		Components of the recoil inertial force It		
θ [°]	ψ [°]	It_X [KN]	It_Y [KN]	It_Z [KN]
5	60	137.6	79.4	13.9
5	30	79.4	137.6	13.9
5	0	0	158.9	13.9
10	60	136	78.5	27.7
10	30	78.5	136	27.7
10	0	0	157	27.7
15	60	133.4	77	41.2
15	30	77	133.4	41.2
15	0	0	154	41.2
20	60	129.8	74.9	54.5
20	30	74.9	129.8	54.5
20	0	0	149.9	54.5

FEM ANALYSIS

The analysis was conducted as a preliminary structural assessment aimed at evaluating the feasibility of integrating the considered weapon system onto a mobile vehicle platform. Accordingly, generalized mechanical properties representative of conventional structural steel were adopted for the numerical model, including the corresponding Young's modulus, Poisson's ratio, and density. Material-specific properties associated with a particular steel grade or final production material were not considered at this stage. This approach was adopted because the objective of the analysis is to assess the general structural feasibility and load-transfer characteristics of the proposed integration concept rather than to provide a final design verification of the structure.

The FEM model of the vehicle supporting platform was developed from the three-dimensional geometric model of the supporting structure and hydraulic outriggers. The supporting structure consists of welded rectangular hollow sections with dimensions of 100 x 100 mm and a wall thickness of 4 mm. The hydraulic outriggers were modelled as integral load-bearing components of the platform. To reduce computational complexity while preserving the relevant structural characteristics, the geometry was simplified and discretized using four-node shell elements without midside nodes.

The FEM analysis was conducted for different combinations of elevation and azimuth angles, representing the considered loading conditions of the vehicle. For each configuration, the stress and deformation state of the supporting structure and the resultant reactions at supports A, B, C, and D were determined. The obtained numerical results were used to identify the critical loading conditions and to assess the structural integrity, load-bearing capacity, and stability of the supporting platform under impulsive loading. The magnitudes and positions of the forces acting on the supporting platform are defined according to the previously established mechanical model. The corresponding force values applied to the platform are presented in Table 3.

Table 3 Force values

Force	Value
Weight of the mounted system (Go)	12.552 N
Vehicle weight (Gv)	117.680 N
Inertial recoil force (It)	Table 2

The following section presents the FEM analysis of the supporting platform for three representative loading configurations defined by elevation and direction angles. These loading cases were selected to evaluate the structural response of the supporting platform for different orientations of the inertial recoil force It. The analysis considers the resulting stress distribution and support reactions, with the objective of determining the most critical loading condition and verifying the structural integrity of the platform. Static and modal analyses based on the finite element method provide useful information about the structural behaviour and dynamic characteristics of vehicle chassis structures (Rajappan & Vivekanandhan, 2013).

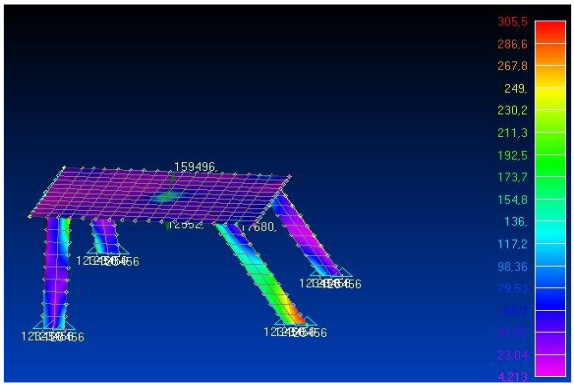

a)

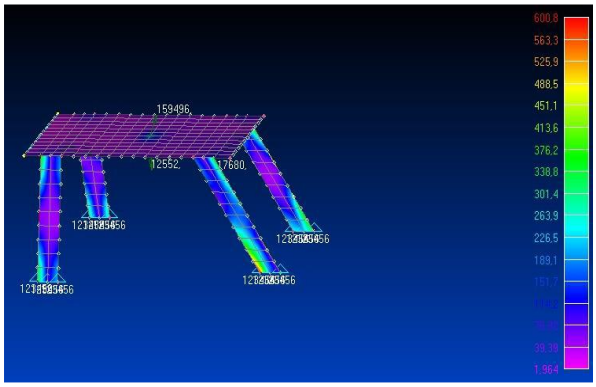

b)

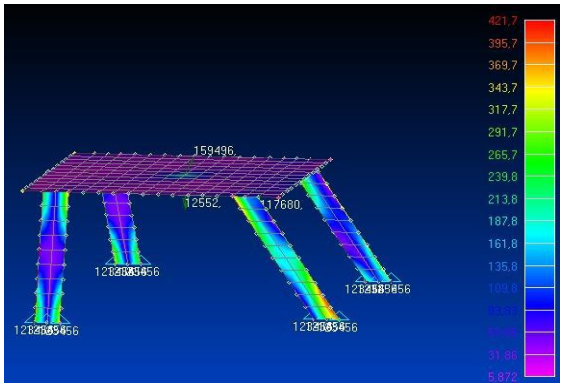

c)

Figure 6 Support reactions and stress distribution for the investigated loading conditions
a) θ=20°and ψ=30° with a maximum reaction of 34 kN at support A, b) θ=-5°and ψ=0° with a maximum reaction of 49 kN at support B, c) θ=-5°and ψ=60° with a maximum reaction of 86 kN at supports C and D

THE RESULTS

The FEM analysis was performed as a preliminary assessment of the proposed concept for integrating the weapon system onto a mobile vehicle platform. The analysis was conducted to evaluate the load-transfer characteristics of the supporting structure and to determine the support reactions resulting from the applied recoil force It for different combinations of elevation angle θ and azimuth angle ψ. The results were used to identify the critical loading configurations and the regions of the structure subjected to the highest loads. The results presented below correspond to the conceptual integration of the weapon system onto the mobile platform. For each analysed combination of θ and ψ, the reactions at supports A, B, C, and D were determined.

For θ=20° and ψ=30° the maximum reaction occurs at support A and is approximately 34 kN, as shown in Figure 6 a). For θ=-5° and ψ=0° the maximum reaction is obtained at support B, with a value of approximately 49 kN. The maximum overall reactions occur for θ=-5° and ψ=60° with approximately 87 kN at support C, and 86 kN at support D. As shown in Figure 6, the maximum stress concentrations occur at the lower sections of the hydraulic outriggers and in the central region of the supporting plate. The latter is primarily a consequence of the gravitational load of the weapon system. Based on the obtained results, the most critical loading condition is θ=-5° and ψ=60°, with the maximum support reaction. The support reactions resulting from the applied loading are summarized in Table 4. The table presents the maximum reaction obtained at each support, together with the corresponding values of θ and ψ at which the maximum reaction occurs.

Table 4 Results of support reactions A, B, C and D

Angles [°]		**Support A [N]**		
θ	**ψ**	**Oz**	**Ox**	**Oy**
20	60	7116	-11867	-13464
20	30	2986	-17580	-13746
20	0	-2860	-18491	-10134
Angles [°]		**Support B [N]**		
θ	**ψ**	**Oz**	**Ox**	**Oy**
-5	60	5640	-9718	6160
-5	30	826	-18276	14335
-5	0	-5530	-22660	21267

Table 4 (continuation)

Angles [°]		Support C [N]		
θ	**ψ**	**Oz**	**Ox**	**Oy**
-5	60	-27178	-9052	50833
-5	30	-18296	-14882	31997
-5	0	-6197	-16809	6395
Angles [°]		**Support D [N]**		
θ	**ψ**	**Oz**	**Oz**	**Oz**
-5	60	-27272	-7443	51189
-5	30	-18459	-13688	32612
-5	0	-6385	-16181	7107

The adopted horizontal angular range is consistent with the operating envelopes commonly encountered in existing concepts of self-propelled artillery systems and weapon system mounted on a two-support carriage. The considered azimuthal range therefore represents a realistic design assumption for the proposed integration concept. In contrast, the vertical field of operation is primarily determined by the elevation capabilities and mechanical characteristics of the weapon system intended for integration. The adopted elevation range is therefore defined in accordance with the operational requirements and intended application of the system. These angular limits provide an appropriate basis for evaluating the load transfer and structural response of the mobile platform within the intended operating envelope.

CONCLUSIONS

The present study investigated the structural response of a supporting platform mounted on a chassis using the FEM, with the primary objective of assessing the feasibility of integrating the considered weapon system onto an existing mobile platform. The analysis represents a conceptual assessment of the proposed integration and was performed to evaluate the general load-transfer behaviour of the supporting structure under the action of recoil forces. The FEM analysis was conducted for selected characteristic combinations of elevation angle θ and azimuth angle ψ, corresponding to loading configurations considered potentially critical for the supporting structure and vehicle stability. For each configuration, the resulting support reactions and structural response were determined. The numerical results show that the recoil load is predominantly transferred to the ground through the hydraulic outriggers. For θ=20° and ψ=30° the maximum reaction at support A is approximately 34 kN, while for θ=-5° and ψ=0°, the maximum reaction at support B is approximately 49 kN. The maximum support reactions are obtained for θ=-5° and ψ=60°, with approximately 87 kN at support C and 86 kN at support D. This configuration represents the governing load case among those considered. The calculated stress distribution indicates that the most critical regions are located in the vicinity of the hydraulic outriggers and in the central portion of the supporting plate. The results demonstrate that the elevation and azimuth angles have a significant influence on the load-transfer mechanism and the resulting support reactions. Due to the longitudinal symmetry of the structural model, the azimuth angle was analysed in only one direction, while the opposite direction would produce an equivalent response with the reactions exchanged between the corresponding symmetric supports.

It should be emphasized that the presented FEM analysis represents a preliminary engineering assessment intended to investigate the feasibility of the proposed integration concept. Standardized and generalized material parameters were adopted for the numerical model, without using material-specific properties corresponding to a particular production material or final structural design.

The adopted angular operating envelope provides a realistic basis for the proposed integration concept. The horizontal operating range is consistent with the characteristics of existing self-propelled artillery systems and weapon system mounted on a two-support carriage. The vertical operating range is primarily determined by the operational requirements and performance and mechanical characteristics of the weapon system intended for integration, while also being consistent with its intended purpose. The defined operating envelope therefore provides an appropriate basis for evaluating the structural response and load-bearing capability of the proposed mobile platform.

Consequently, the obtained results should be considered indicative of the structural response and load-transfer characteristics rather than as a final verification of the structural strength or serviceability of the platform. The results indicate that the proposed concept provides a basis for further investigation of the integration of the weapon system onto the selected mobile platform. For complete structural verification, subsequent analyses should incorporate the actual material properties and detailed structural geometry, together with more comprehensive static, dynamic, stability, and fatigue analyses. Experimental validation would additionally be required to confirm the numerical results and assess the structural behaviour of the final configuration under realistic loading conditions.

ACKNOWLEDGMENTS

The paper is a part of the research done within the project of the University of Defence in Belgrade, No. VA-TT/1/24-26.

REFERENCES

Dunica, Š., & Kolundžija, B. (1985). *Nonlinear analysis of structures*. University of Belgrade, Faculty of Civil Engineering. (In Serbian).

Ghazaly, N. M. (2014). Applications of finite element stress analysis of heavy truck chassis: Survey and recent development. *Journal of Mechanical Design and Vibration*, 2(3), 69–73. https://doi.org/10.12691/jmdv-2-3-3

Han Fui, T., & Abd. Rahman, R. (2007). Statics and dynamics structural analysis of a 4.5 ton truck chassis. *Jurnal Mekanikal*, 24, 56–67.

Kengkongan Ary, A., Rio Prabowo, A., & Imaduddin, F. (2020). Structural assessment of an energy-efficient urban vehicle chassis using finite element analysis: A case study. *Procedia Structural Integrity*, 27, 69–76. https://doi.org/10.1016/j.prostr.2020.07.010

Kojić, M., Slavković, R., Živković, M., & Grujović, N. (2010). *Finite element method I—Linear analysis*. University of Kragujevac, Faculty of Mechanical Engineering. (In Serbian).

Kwasniewski, L., Li, H., Wekezer, J., & Malachowski, J. (2006). Finite element analysis of vehicle–bridge interaction. *Finite Elements in Analysis and Design*, 42(11), 950–959. https://doi.org/10.1016/j.finel.2006.01.014

Rajappan, R., & Vivekanandhan, M. (2013). Static and modal analysis of chassis by using FEA. *The International Journal of Engineering and Science*, 2(2), 63–73.

Tančić, Lj. (2014). *Internal ballistics design*. University of Defence, Military Academy, Media Center Defence. (In Serbian).

The 11th International Congress
Motor Vehicles & Motors 2026
Kragujevac, Serbia
October 8th - 9th, 2026

Motor Vehicles & Motors

MVM2026-059
https://doi.org/10.24874/CMVM2026.059
Technical paper

Dušan Milojević[1]
Nikola Kotorčević[2]
Đorđe Damljanović[3]
Nikola Živčević[4]
Dušan Arsić[5]
Fatima Živić[6]

EFFECTS OF UNIT CELL GEOMETRY AND STRUT THICKNESS ON THE COMPRESSIVE BEHAVIOR OF 3D-PRINTED MECHANICAL METAMATERIALS

ABSTRACT: This study analyzes the compressive behavior of 3D-printed mechanical metamaterials with three unit-cell geometries and three nominal strut thicknesses. Nine specimens made of polylactic acid (PLA) were fabricated using fused deposition modeling (FDM). The specimens had approximate dimensions of 21 × 21 × 21 mm and consisted of regularly arranged 3 × 3 × 3 unit cells. Honeycomb, elliptic, and triangular geometries were investigated, with nominal strut thicknesses of 0.7, 1.0, and 1.4 mm for each geometry. The maximum recorded forces and fracture behavior were analyzed. Complete failure occurred in three specimens, whereas the remaining six did not fail completely within the testing machine's load limit of 500 N. The observed fracture was predominantly brittle, with cracks initiating at strut junctions, corresponding to the expected stress-concentration zones.

KEYWORDS: mechanical metamaterials, FDM 3D printing, lattice structures, honeycomb unit cell, elliptic unit cell, triangular unit cell

[1] *Dušan Milojević, University of Kragujevac, Faculty of Engineering, Sestre Janjic 6, 34000 Kragujevac, Serbia, dusanmilojevic@uni.kg.ac.rs , https://orcid.org/0009-0005-0113-3918*
[2] *Nikola Kotorčević, University of Kragujevac, Faculty of Engineering, Sestre Janjic 6, 34000 Kragujevac, Serbia, kotorcevic@kg.ac.rs, https://orcid.org/0000-0002-5664-9832*
[3] *Đorđe Damljanović, University of Kragujevac, Faculty of Engineering, Sestre Janjic 6, 34000 Kragujevac, Serbia, djordjedamljanovic12@gmail.com*
[4] *Nikola Živčević, University of Kragujevac, Faculty of Engineering, Sestre Janjic 6, 34000 Kragujevac, Serbia, nikolazivcevic1994@gmail.com*
[5] *Dušan Arsić, University of Kragujevac, Faculty of Engineering, Sestre Janjic 6, 34000 Kragujevac, Serbia, dusan.arsic@fink.rs, https://orcid.org/0000-0003-0326-0898*
[6] *Fatima Živić, University of Kragujevac, Faculty of Engineering, Sestre Janjic 6, 34000 Kragujevac, Serbia, zivic@kg.ac.rs, https://orcid.org/0000-0003-2509-187X*

UTICAJ GEOMETRIJE JEDINIČNE ĆELIJE I DEBLJINE NOSEĆIH GREDICA NA PONAŠANJE PRI PRITISKU 3D-ŠTAMPANIH MEHANIČKIH METAMATERIJALA

REZIME: Cilj rada je analiza ponašanja pri pritisku 3D štampanih mehaničkih metamaterijala sa tri geometrije jedinične ćelije i tri nominalne debljine nosećih gredica. FDM postupkom izrađeno je devet PLA uzoraka približnih dimenzija 21 × 21 × 21 mm, sa pravilno raspoređenim jediničnim ćelijama u konfiguraciji 3 × 3 × 3. Ispitane su heksagonalna, eliptična i trouglasta geometrija, sa debljinama nosećih gredica od 0,7, 1,0 i 1,4 mm za svaku geometriju. Analizirane su maksimalne zabeležene sile i ponašanje uzoraka pri lomu. Potpuni lom nastao je kod tri uzorka, dok kod preostalih šest nije zabeležen u raspoloživom opsegu opterećenja do 500 N. Uočeni lom bio je pretežno krt, sa nastankom prslina na spojevima nosećih gredica, odnosno u očekivanim zonama koncentracije napona.

KLJUČNE REČI: mehanički metamaterijali, FDM 3D štampa, rešetkaste strukture, heksagonalna jedinična ćelija, eliptična jedinična ćelija, trouglasta jedinična ćelija

INTRODUCTION

Mechanical metamaterials are engineered materials whose effective mechanical properties are determined not only by the constituent material but also by their internal architecture, particularly the unit-cell geometry (Jiao, P. et al. 2023). The geometry and arrangement of unit cells significantly affect the mechanical performance of lattice structures, including their compressive response, load-bearing capacity, and energy absorption (Qin, D. et al. 2022). FDM-printed lattice structures have been investigated for automotive crash absorbers, where cell size and strut diameter can be tailored to improve energy absorption and achieve a smoother force–displacement response (Boursier Niutta, C. et al. 2022). Owing to their low weight, high energy-absorption capacity, and favorable stiffness-to-weight ratio, lattice structures are promising for lightweight energy-absorbing applications, particularly in the automotive sector (Wu, B. et al. 2023; Saleh, M. et al. 2022). Studies of FDM-printed structures have also demonstrated that the selected infill pattern affects compressive force, deformation, and dimensional accuracy (Zisopol, D. G. et al. 2023). Therefore, this study aims to compare the compressive behavior of three unit-cell geometries—honeycomb, elliptic, and triangular—fabricated from polylactic acid (PLA) using FDM, with nominal strut thicknesses of 0.7, 1.0, and 1.4 mm.

MATERIALS AND METHODS

The specimens were fabricated from PLA filament using a Bambu Lab X1E 3D printer, with 100% infill of the struts and a layer height of 0.16 mm. A total of nine specimens, with approximate dimensions of 21 × 21 × 21 mm and a 3 × 3 × 3 unit-cell arrangement, were produced. Three unit-cell geometries—honeycomb, elliptic, and triangular—were investigated, with nominal strut thicknesses of 0.7, 1.0, and 1.4 mm for each geometry, as shown in Figure 1.

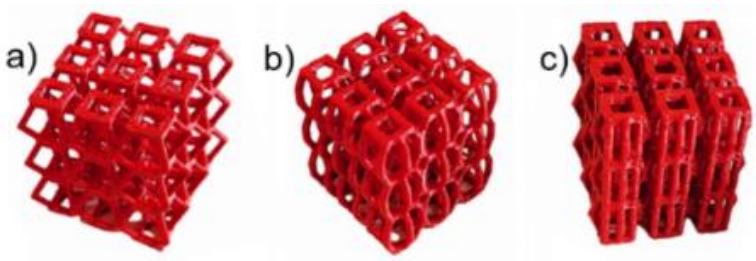

Figure 1 Actual 3D-printed unit-cell geometries: (a) honeycomb, (b) elliptic, and (c) triangular.

Compression tests were performed using an Ametek Brookfield CT3 texture analyzer (Middleboro, MA, USA), following the general procedure of ASTM D695 (D20 Committee, 2026). The specimens were loaded in the negative Z-direction at a constant displacement rate of 0.02 mm/s. Testing was terminated when complete failure occurred or when the machine load limit of 500 N was reached. Force–displacement data were recorded, and the fracture zones were examined by optical microscopy at 40× magnification.

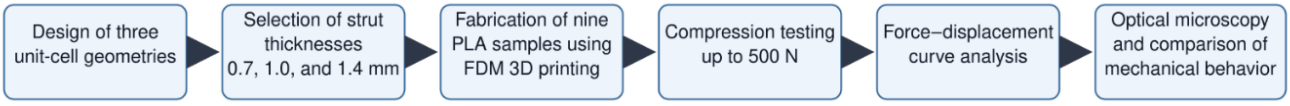

Figure 2 Flowchart of the main steps of the experimental procedure, from specimen design and 3D printing to compression testing and analysis of the results.

RESULTS AND DISCUSSION

Three specimens failed completely; the other six reached the 500 N machine limit without complete failure. Figure 3 shows the maximum recorded forces. At 0.7 mm, honeycomb, elliptic, and triangular specimens reached 131, 369, and ≥500 N, respectively. Honeycomb reached 294 N at 1.0 mm and 500 N at 1.4 mm; elliptic specimens at 1.0 and 1.4 mm and all triangular specimens reached 500 N. Thus, their actual maximum forces and the precise effect of strut thickness could not be determined.

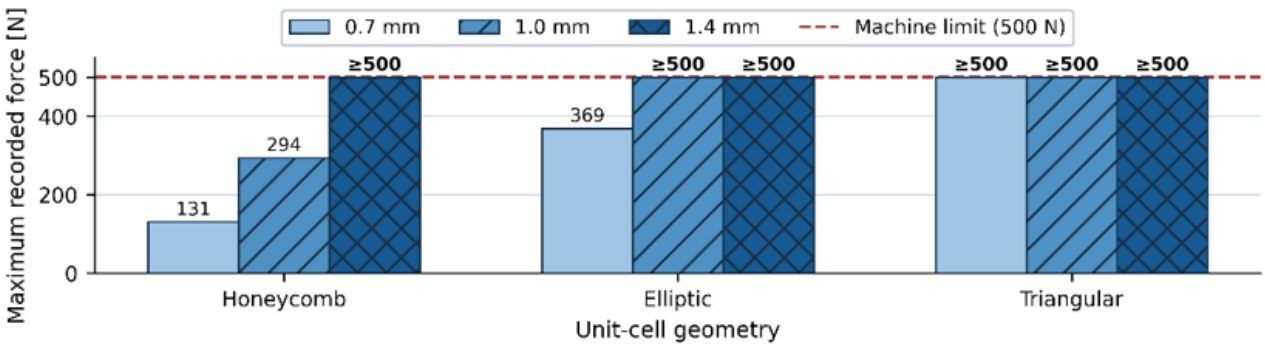

Figure 3 Maximum recorded forces for the investigated 3D-printed mechanical metamaterials. Values marked as ≥500 N indicate that the specimens reached the load limit of the testing machine

In the present tests, the honeycomb geometry showed the greatest susceptibility to fracture. Previous studies have shown that unit-cell geometry affects the compressive response and energy-absorption behavior of 3D-printed metamaterials (Jayswal, A. et al. 2025). In the present tests, brittle fracture was observed, with cracks initiating at strut junctions, which represent local stress-concentration zones. The observed brittle fracture and crack initiation at highly stressed regions are consistent with published research (Xiong, S. Et al. 2026). Layer delamination was also observed. Manufacturing defects in honeycomb cell walls may additionally influence the mechanical response (Rahaman, K. M. et al. 2018).

CONCLUSIONS

- Unit-cell geometry and nominal strut thickness influenced the recorded compressive behavior of the investigated 3D-printed mechanical metamaterials.
- At 0.7 mm, the maximum recorded forces were 131 N for the honeycomb, 369 N for the elliptic, and at least 500 N for the triangular geometry.
- For the honeycomb geometry, the maximum recorded force increased from 131 N to 294 N and then to at least 500 N as the strut thickness increased from 0.7 to 1.4 mm.
- The honeycomb specimen at 1.4 mm, the elliptic specimens at 1.0 and 1.4 mm, and all triangular specimens reached the 500 N machine limit. Therefore, their actual maximum compressive forces and the precise effect of strut thickness could not be determined.
- Complete failure occurred in three of the nine specimens. Fracture was predominantly brittle, with cracks initiating at strut junctions, while layer delamination was also observed.
- Replicate testing of stronger specimens on a higher-capacity machine is needed to assess repeatability, actual load capacity, and the effects of manufacturing imperfections.

ACKNOWLEDGMENTS

This research was supported by the A-SIDE project within the EIT Higher Education Initiative, coordinated by EIT RawMaterials and funded by the European Union. Additional support was provided by the Ministry of Science, Technological Development and Innovation of the Republic of Serbia under project No. 451-03-34/2026-03/200107.

REFERENCES

Boursier Niutta, C., Ciardiello, R., & Tridello, A. (2022). Experimental and numerical investigation of a lattice structure for energy absorption: application to the design of an automotive crash absorber. *Polymers*, 14(6), 116. https://doi.org/10.3390/polym14061116

D20 Committee. (2026). Standard test method for compressive properties of rigid plastics. https://doi.org/10.1520/D0695-23

Jayswal, A., Angelopoulou, P. P., Rohewal, S. S., Kearney, L. T., Gupta, S., Bowland, C. C., Toomey, M. D., & Amit, K. (2025). High compressive energy absorption and shape recovery behavior of additively manufactured textile-inspired cylindrical braided metamaterials. *Additive Manufacturing*, 110, 104925. https://doi.org/10.1016/j.addma.2025.104925

Jiao, P., Mueller, J., Raney, J. R., Zheng, X., & Alavi, A. H. (2023). Mechanical metamaterials and beyond. *Nature Communications*, 14(1), 6004. https://doi.org/10.1038/s41467-023-41679-8

Qin, D., Sang, L., Zhang, Z., Lai, S., & Zhao, Y. (2022). Compression Performance and Deformation Behavior of 3D-Printed PLA-Based Lattice Structures. *Polymers*, 14(5), 1062. https://doi.org/10.3390/polym14051062

Rahman, K. M., Hu, Z., & Letcher, T. (2018). In-plane stiffness of additively manufactured hierarchical honeycomb metamaterials with defects. *Journal of Manufacturing Science and Engineering*, 140(1), 011007. https://doi.org/10.1115/1.4038205

Saleh, M., Anwar, S., Al-Ahmari, A. M., & Alfaify, A. (2022). Compression performance and failure analysis of 3d-printed carbon fiber/PLA composite TPMS lattice structures. *Polymers*, 14(21), 4595. https://doi.org/10.3390/polym14214595

Wu, B., Chen, Q., Liu, F., Chen, M., Lu, Y., Jiang, D., & Yi, Y. (2023). Study on dynamic mechanics of node-enhanced graded lattice structure and application optimization in automobile energy absorbing box. *Materials*, 16(21), 6893. https://doi.org/10.3390/ma16216893

Xiong, S., Liu, X., He, L., Huang, J., Yang, L., Liu, X. W., Yan, C., & Shi, Y. (2026). State-of-the-art advances in crack propagation control of lattice metamaterials: A review," *Review of Materials Research*, 2(1), 100153. https://doi.org/10.1016/j.revmat.2026.100153

Zisopol, D. G., Minescu, M., Iacob, D. V. (2023). A Study on the evaluation of the compression behavior of PLA lattice structures manufactured by FDM. *Engineering, Technology & Applied Science Research*, 13(5), 11801–11806. https://doi.org/10.48084/etasr.6262

The 11th International Congress
Motor Vehicles & Motors 2026
Kragujevac, Serbia
October 8th - 9th, 2026

Motor Vehicles & Motors

MVM2026-060
https://doi.org/10.24874/CMVM2026.060
Original scientific paper

Nebojša Arsić[1]
Nenad Kostić[2],*
Nenad Petrović[3]
Nenad Marjanović[4]

APPLICATION OF 3D SCANNING AND CAD DEVIATION ANALYSIS AS A BASIS FOR PRESS TOOL OPTIMISATION IN THE AUTOMOTIVE INDUSTRY

ABSTRACT: The aim of this paper is to analyse the geometrical deviations of a stamped part in relation to the nominal CAD model and to identify critical zones after the first trial of a press tool. The analysed sample is the left-hand stamped part obtained using a press tool intended for manufacturing left- and right-hand parts. After the first tool trial, the part was scanned using an EinScan-SE 3D scanner, resulting in an STL model of the manufactured part. The resulting model was processed by removing local noise and mesh irregularities generated during scanning, while preserving the basic geometry of the part. After alignment with the nominal CAD model, a comparative deviation analysis was performed. The results are presented as a deviation map, which enables the identification of zones with the most pronounced deviations. Special attention is given to the use of 3D scanning as a preliminary procedure in the early stage of tool adjustment, providing a faster overview of part geometry before final verification by more precise contact measurement methods. The identified critical zones indicate that the press tool elements involved in bending and final calibration should be inspected first, providing a basis for targeted corrections in subsequent trials.

KEYWORDS: 3D scanning, CAD model, press tool, stamped part, quality control

[1] *Nebojša Arsić, Faculty of Engineering, University of Kragujevac, Serbia, nebojsa.arsic@kg.ac.rs,*
https://orcid.org/0009-0009-2605-8108
[2] *Nenad Kostić, Faculty of Engineering, University of Kragujevac, Serbia, Corresponding author: nkostic@kg.ac.rs,*
*https://orcid.org/0000-0002-0157-7501 (*Corresponding author)*
[3] *Nenad Petrović, Faculty of Engineering, University of Kragujevac, Serbia, npetrovic@kg.ac.rs,*
https://orcid.org/0000-0002-7563-9883
[4] *Nenad Marjanović, Faculty of Engineering, University of Kragujevac, Serbia, nesam@kg.ac.rs,*
https://orcid.org/0000-0002-8441-4328

PRIMENA 3D SKENIRANJA I CAD ANALIZE ODSTUPANJA KAO OSNOVA ZA OPTIMIZACIJU PRESERSKOG ALATA U AUTOINDUSTRIJI

REZIME: Cilj rada je analiza geometrijskih odstupanja otpreska u odnosu na nominalni CAD model i identifikacija kritičnih zona nakon prve probe preserskog alata. Analizirani uzorak predstavlja levi otpresak dobijen na preserskom alatu namenjenom za izradu levog i desnog dela. Nakon prve probe alata, otpresak je skeniran pomoću 3D skenera EinScan-SE, čime je dobijen STL model izrađenog dela. Dobijeni model je obrađen uklanjanjem lokalnog šuma i nepravilnosti mreže nastalih tokom skeniranja, uz očuvanje osnovne geometrije dela. Nakon poravnanja sa nominalnim CAD modelom sprovedena je uporedna analiza odstupanja. Rezultati su prikazani pomoću mape odstupanja, koja omogućava identifikaciju zona sa najizraženijim odstupanjima. Posebna pažnja posvećena je primeni 3D skeniranja kao preliminarnog postupka u ranoj fazi podešavanja alata, čime se omogućava brži uvid u geometriju dela pre završne provere preciznijim kontaktnim mernim metodama. Identifikovane kritične zone ukazuju na to da najpre treba proveriti elemente preserskog alata koji učestvuju u savijanju i završnoj kalibraciji, što predstavlja osnovu za ciljane korekcije u narednim probama.

KLJUČNE REČI: 3D skeniranje, CAD model, preserski alat, otpresak, kontrola kvaliteta

INTRODUCTION

In the automotive industry, stamped sheet-metal parts must be manufactured within prescribed dimensional and geometrical tolerances because their geometry directly affects assembly, functionality and the quality of the final product. During the first trial of a press tool, deviations from the nominal CAD geometry may arise from tool geometry, forming conditions, material flow and springback (Wagoner, R. H. et al. 2013; Hartmann, C. et al. 2021). Early identification of such deviations is important because it enables critical regions of the part to be detected before subsequent tool trials and provides guidance for further inspection and correction of the press tool.

Dimensional inspection of stamped parts can be performed using conventional measuring instruments and coordinate measuring machines (CMMs), while optical 3D scanning offers the possibility of rapidly acquiring a large amount of geometrical information over the accessible surface of a part. Rękas, A. et al. 2021 applied a 3D optical measurement system to the inspection of large stamped automotive components by comparing measured geometry with nominal CAD models. Varda, K. et al. 2022 compared the application of coordinate measuring machines and 3D scanners for the control of dimensions, shape and position. Paunoiu, V. et al. 2022 demonstrated the use of 3D scanning in the inspection of automotive body parts, while Morovič, L. et al. 2019 showed that deviation maps can be used to visualise differences between scanned and nominal geometries. Kuş, A. 2009 also reported the application of optical 3D scanning in automotive inspection, including the comparison of manufactured sheet-metal parts with CAD models.

An important advantage of optical 3D scanning is the high density of acquired geometrical data, which enables the spatial distribution of deviations to be observed rather than evaluating only a limited number of discrete measuring points. Brajlih, T. et al. 2011 highlighted this advantage in the inspection of geometrically complex components, while also noting that optical scanning does not replace high-precision coordinate measurement when strict dimensional verification is required. The reliability of optical scanning also depends on factors such as surface visibility, optical properties and measurement coverage. Koutecký, T. et al. 2016 demonstrated the importance of these factors when planning the scanning of sheet-metal parts. Therefore, 3D scanning is particularly suitable as a rapid preliminary inspection method during the early stage of press tool adjustment, while critical dimensions and geometrical characteristics close to tolerance limits can subsequently be verified using more precise measurement methods.

The usefulness of deviation analysis is not limited to identifying whether a manufactured part differs from the nominal geometry. When the spatial distribution of deviations is considered together with the sequence of forming operations, the observed critical zones can also indicate which regions of the press tool should be inspected first. Springback is one of the important phenomena influencing the final geometry of formed sheet-metal parts, as discussed by Wagoner, R. H. et al. 2013 and Hartmann, C. et al. 2021. Tool-geometry correction and compensation procedures have therefore been investigated as a means of reducing deviations after forming. Mole, N. et al. 2014 presented a method for optimisation of forming-tool geometry considering springback and sheet thinning, while Siswanto, W. A. et al. 2014 proposed an alternative approach to springback compensation through modification of tool geometry. In this context, the combination of 3D scanning and CAD-based deviation analysis can support an iterative procedure consisting of part inspection, identification of critical zones, targeted tool correction and a subsequent tool trial.

The aim of this paper is to examine the application of 3D scanning and CAD deviation analysis for the rapid identification of critical zones on a stamped part after the first trial of a press tool. The method is not intended to replace final high-precision inspection using a coordinate measuring machine, but to provide a fast and accessible preliminary assessment of the manufactured geometry. The contribution of the paper lies in using the spatial distribution of deviations between the scanned STL model and the nominal CAD model to identify critical regions of the stamped part and to relate these regions to the corresponding bending and final calibration operations, thereby providing guidance for targeted inspection and correction of the press tool.

MATERIALS AND METHODS

The analysed sample was a left-hand stamped part produced during the first trial of a press tool intended for manufacturing both left- and right-hand components. The part was manufactured from EN 10130–DC01 cold-rolled steel sheet with a nominal thickness of 1.5 mm. The nominal geometry of the component was defined by the corresponding CAD model, while the manufactured part was digitised by 3D scanning and represented by an STL model.

Figure 1 shows the position of the analysed component within the press tool strip layout and the sequence of manufacturing operations. Particular attention was paid to the bending and final calibration operations because these stages determine the final geometry of the side walls, bend regions and transition surfaces that are subsequently considered in the deviation analysis.

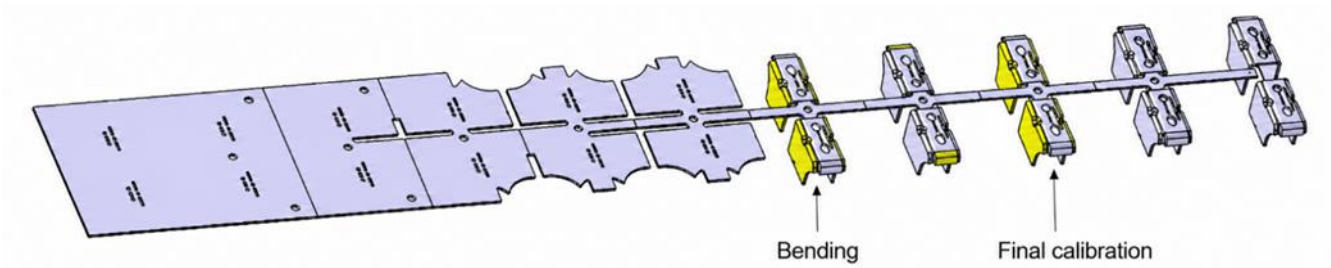

Figure 1 Press tool strip layout with the bending and final calibration operations highlighted

The geometrical requirements relevant to the analysed component were taken from the technical drawing. Figure 2 presents a simplified extract showing the A–B–C reference arrangement, datum targets A1–A3, selected areas E–I and the related profile-tolerance indication. The original title block and all company, customer, product and document identifiers were omitted. The remaining dimensions are shown only to clarify the positions of the selected features and were not evaluated separately in this study.

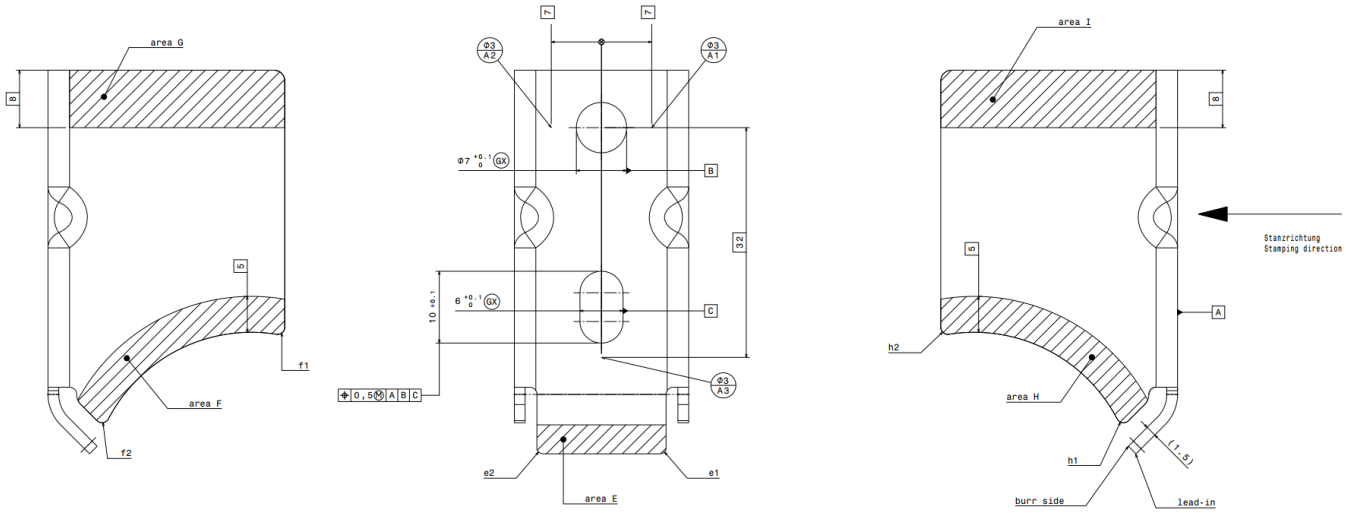

Figure 2 Simplified technical drawing of the analysed stamped part

The technical drawing specifies a surface profile tolerance zone with a total width of 2 mm relative to datum system A–B–C for the general formed surfaces and 0.5 mm for the designated areas E–I. These values were used as reference criteria for interpreting the global deviation map. Since the individual tolerance regions were not evaluated separately, the analysis was used to identify areas requiring further inspection rather than to establish formal conformity of the complete part.

3D Scanning and STL Model Preparation

The stamped part was digitised using a SHINING 3D EinScan-SE desktop structured-light 3D scanner together with a rotary table. Data acquisition and initial processing were performed using EXScan S v3.1.2.0. Before data acquisition, the scanner was calibrated using the procedure provided by the manufacturer, followed by white-balance adjustment.

Scanning was performed in Fixed Scan mode using the rotary table. No matte coating or reference markers were used. The numerical exposure settings and other fine acquisition parameters were not retained in the working record and are therefore reported as a limitation of reproducibility.

The EinScan-SE has a declared single-scan accuracy of ≤ 0.1 mm and a point distance of 0.17–0.20 mm (SHINING 3D n.d.). These values represent the specifications of an individual scan and should not be interpreted as the measurement uncertainty of the complete procedure, which also includes acquisition from different part orientations, scan alignment, mesh generation and subsequent CAD comparison.

The final dataset was acquired from four different orientations of the stamped part. Eight angular views were acquired in each orientation using the rotary table, resulting in a total of 32 accepted scans. The use of different orientations enabled surfaces that could not be completely captured from a single position to be scanned.

Figure 3 Experimental setup for 3D scanning of the stamped part using the EinScan-SE scanner and rotary table

The acquired scans were organised into scan groups and subsequently aligned in EXScan S. Corresponding points were selected on overlapping scanned regions, after which the aligned groups were merged to obtain a more complete digital representation of the stamped part. Figure 4 illustrates the alignment of the scan groups and the resulting merged scan data.

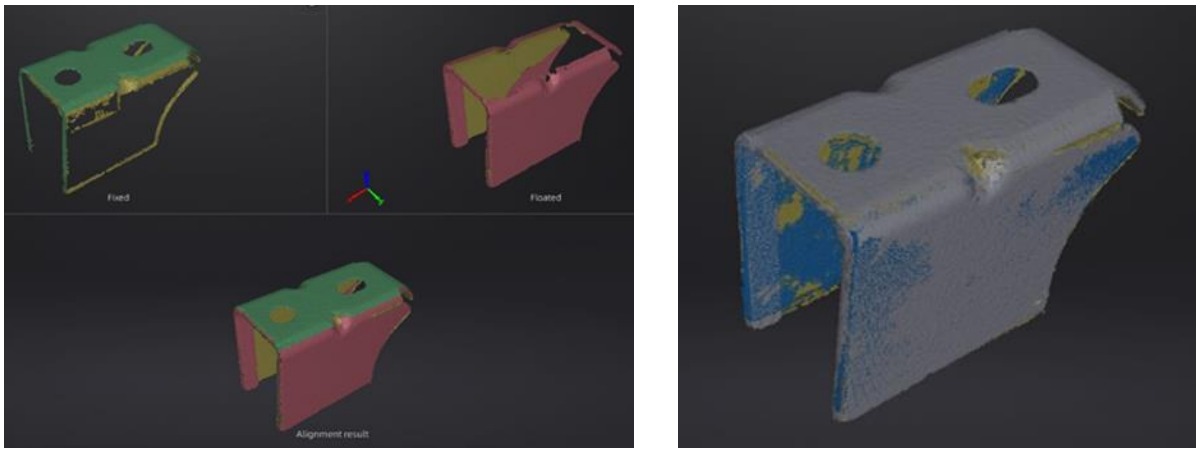

a) b)

Figure 4 Data processing in EXScan S: a) initial alignment of two scan groups using three manually selected pairs of corresponding points; b) merged dataset of 32 accepted scans

After the scan groups had been merged, a polygonal mesh was generated. Limited optical access resulted in incomplete data in some internal regions of the part. Gaps and local mesh irregularities in these regions were repaired during post-processing, while the measured external geometry was preserved. The repaired regions remained in the final STL model and therefore represent reconstructed rather than directly measured geometry. This limitation was taken into account when interpreting the deviation map. The processed model was exported in STL format for subsequent CAD-based deviation analysis.

CAD Deviation Analysis

Figure 5 shows the analysed stamped part and the corresponding nominal CAD and processed STL models.

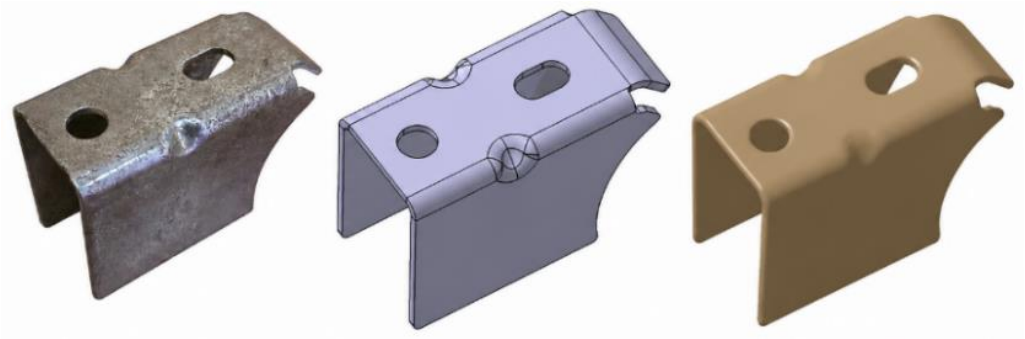

a) b) c)

Figure 5 Analysed stamped part and corresponding digital models: a) manufactured stamped part; b) nominal CAD model; c) processed STL model

Before the deviation analysis, the processed STL model was manually aligned with the nominal CAD model in CATIA V5 using the component features corresponding to the A–B–C reference arrangement shown in Figure 2. The Deviation Analysis function was then applied to determine the magnitude and spatial distribution of the surface deviations. The alignment supported a comparative CAD–STL assessment and was not used for formal verification of datum-related positional tolerances. The final analysis included 27,856 evaluated surface points.

Particular attention was paid to the side walls, bend regions and transition surfaces. The locations of pronounced deviations were subsequently considered together with the sequence of bending and final calibration operations in order to identify regions of the press tool that should receive priority during further inspection and adjustment. In this way, the deviation analysis was used as a preliminary engineering procedure for locating critical regions and providing guidance for subsequent tool corrections.

RESULTS AND DISCUSSION

The results are presented by means of the deviation map shown in Figure 6. The map provides an overview of the magnitude and spatial distribution of deviations over the analysed surface of the stamped part.

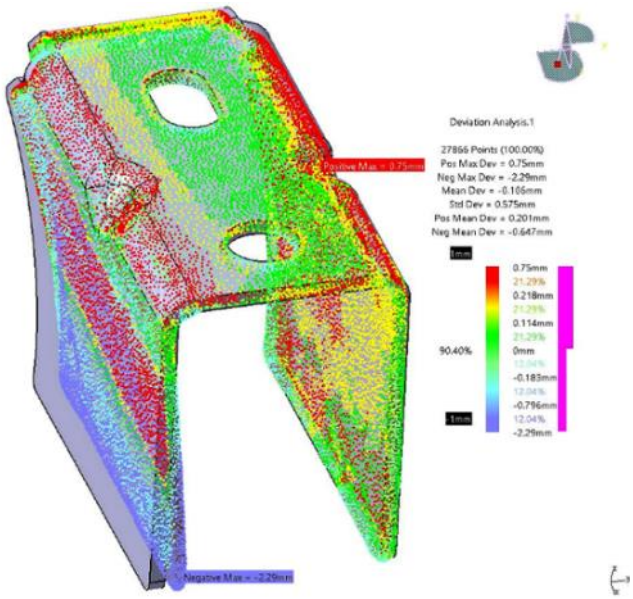

Figure 6 Deviation map between the nominal CAD model and the processed STL model of the stamped part

The maximum positive deviation was +0.75 mm, while the minimum deviation was −2.29 mm. The minimum value occurred near the lower mesh boundary and was therefore interpreted with caution because boundary and reconstruction effects may have contributed to it. The deviations were not uniformly distributed over the part, and the most pronounced zones occurred mainly on the side walls, in bend regions and on transition surfaces. The value of 90.40% shown in the CATIA legend denotes the proportion of evaluated mesh points within the displayed interval of ±1 mm and not the conformity percentage of the complete part.

The deviation pattern suggests additional closing of one side of the part relative to the nominal geometry. Since this region is influenced by the final calibration operation, priority should be given to inspection of the corresponding calibration element and its driving mechanism. The observed deviations may also be influenced by springback and local contact conditions during forming, as discussed by Hartmann, C. et al. 2021. Therefore, the deviation map is used to identify the most critical regions and to guide subsequent tool inspection and correction, rather than to establish the exact physical cause of the deviation.

The deviation map provides a rapid preliminary assessment of the manufactured geometry, but it does not represent a formal verification of all geometrical tolerances specified in the technical drawing. Characteristics close to their tolerance limits should therefore be verified using a calibrated measurement method with suitable measurement uncertainty.

CONCLUSIONS

This paper presents the application of 3D scanning and CAD deviation analysis for the preliminary geometrical assessment of a stamped part after the first trial of a press tool. Comparison of the processed STL model with the nominal CAD geometry enabled the identification of critical regions, with the most pronounced deviations occurring mainly on the side walls, bend regions and transition surfaces.

The observed deviation pattern suggests that the press tool elements involved in bending and final calibration should be inspected first. The proposed procedure can therefore support targeted tool corrections during subsequent trials. However, the deviation map does not replace characteristic-specific geometrical inspection of the complete part. Features with narrow tolerance requirements and results close to tolerance limits should be verified using a calibrated measurement method with suitable measurement uncertainty.

Future work should include repeated measurements after tool correction in order to evaluate whether the implemented modifications reduce the observed deviations.

ACKNOWLEDGMENTS

This research was supported by the Ministry of Science, Technological Development and Innovation of the Republic of Serbia, Agreement No. 451-03-34/2026-03/200107.

REFERENCES

Brajlih, T., Tasič, T., Drstvenšek, I., Valentan, B., Hadžistević, M., Pogačar, V., Balič, J., & Ačko, B. (2011). Possibilities of using three-dimensional optical scanning in complex geometrical inspection. *Strojniški vestnik – Journal of Mechanical Engineering*, 57(11), 826–833. https://doi.org/10.5545/sv-jme.2010.152

Hartmann, C., Maier, L., & Volk, W. (2021). Springback and compensation in sheet metal forming reconsidered as an ill-posed problem. *IOP Conference Series: Materials Science and Engineering*, 1157(1), 012044. https://doi.org/10.1088/1757-899X/1157/1/012044

Koutecký, T., Paloušek, D., & Brandejs, J. (2016). Sensor planning system for fringe projection scanning of sheet metal parts. Measurement, 94, 60–70. https://doi.org/10.1016/j.measurement.2016.07.067

Kuş, A. (2009). Implementation of 3D optical scanning technology for automotive applications. Sensors, 9(3), 1967–1979. https://doi.org/10.3390/s90301967

Mole, N., Cafuta, G., & Štok, B. (2014). A 3D forming tool optimisation method considering springback and thinning compensation. *Journal of Materials Processing Technology*, 214(8), 1673–1685. https://doi.org/10.1016/j.jmatprotec.2014.03.017

Morovič, L., Urminský, J., & Ridzoň, M. (2019). Shape distortion analysis of drawing die by optical 3D scanning. *MATEC Web of Conferences*, 299, 05007. https://doi.org/10.1051/matecconf/201929905007

Paunoiu, V., Teodor, V. G., Afteni, C., Costin, G., & Baroiu, N. (2022). Application of 3D scanning in inspection of the automotive body parts. Ingineria Automobilului, 62(1), 9–13.

Rękas, A., Kaczmarek, T., Wieczorowski, M., Gapiński, B., Jakubowicz, M., Grochalski, K., Kucharski, D., & Marciniak-Podsadna, L. (2021). Analysis of tool geometry for the stamping process of large-size car body components using a 3D optical measurement system. *Materials*, 14(24), 7608. https://doi.org/10.3390/ma14247608

SHINING 3D. (n.d.). EinScan-SE specs – Desktop 3D scanner. EinScan. Retrieved June 29, 2026, from https://www.einscan.com/einscan-se/einscan-se-specs/

Siswanto, W. A., Anggono, A. D., Omar, B., & Jusoff, K. (2014). An alternate method to springback compensation for sheet metal forming. *The Scientific World Journal*, 2014, 301271. https://doi.org/10.1155/2014/301271

Varda, K., Softić, A., Zaimović-Uzunović, N., & Bešlagić, E. (2022). Comparison of dimensions, shapes and positions control using CMM and 3D scanner. In Measurement for a Better Life: Joint IMEKO TC11 & TC24 Hybrid Conference. IMEKO. https://doi.org/10.21014/tc11-2022.01

Wagoner, R. H., Lim, H., & Lee, M. G. (2013). Advanced issues in springback. *International Journal of Plasticity*, 45, 3–20. https://doi.org/10.1016/j.ijplas.2012.08.006

The 11th International Congress
Motor Vehicles & Motors 2026
Kragujevac, Serbia
October 8th - 9th, 2026

Motor Vehicles & Motors

MVM2026-061
https://doi.org/10.24874/CMVM2026.061
Review paper

Sandra Gajević[1]
Slavica Miladinović[2]
Nikola Mitrović[3]
Zorica Djordjević[4]
Saša Milojević[5]
Blaža Stojanović[6]

APPLICATION OF LAMINATED COMPOSITES IN THE AUTOMOTIVE, AVIATION AND MARINE INDUSTRY

ABSTRACT: The paper presents the application of laminated composites in the automotive, aerospace and marine industries. Laminated composites are characterised by a high strength–to–weight ratio, durability, corrosion resistance and the ability to tailor properties by designing the laminate structure. In the automotive industry, they are used to produce body elements, chassis structures and suspension components, contributing to weight reduction while maintaining the required mechanical properties and safety. In the aerospace industry, they are used in wings, fuselage structures, unmanned aerial vehicles, hybrid laminated composites and multifunctional composite systems. In the marine industry, laminated composites are used in hull and sandwich structures due to their low weight, corrosion resistance and favourable behaviour under fatigue loading. Despite these advantages, wider application remains limited by high production costs, repair complexity, degradation during long–term operation and recycling challenges. Future development will be directed towards optimising the laminate structure, improving production technologies, developing hybrid and multifunctional structures, and increasing recycling capabilities.

KEYWORDS: laminated composites, CFRP, automotive industry, aviation industry, marine industry

[1] *Dr Sandra Gajević, assist. prof. Faculty of Engineering University of Kragujevac, Kragujevac 34000, Sestre Janjić 6, Serbia, sandrav@kg.ac.rs, https://orcid.org/0000-0002-7169-8907*
[2] *Dr Slavica Miladinović, research associate. FacultyofEngineeringUniversityof Kragujevac, Kragujevac 34000, Sestre Janjić 6, Serbia, slavicam@kg.ac.rs, https://orcid.org/0000-0002-4408-0634*
[3] *Nikola Mitrović, M.Sc. Faculty of Engineering University of Kragujevac, Kragujevac 34000, Sestre Janjić 6, Serbia, mitrovicnikola70@gmail.com*
[4] *Dr Zorica Djordjević, full prof. Faculty of Engineering University of Kragujevac, Kragujevac 34000, Sestre Janjić 6, Serbia, zoricadj@kg.ac.rs, https://orcid.org/0000-0003-0194-4698*
[5] *Dr Saša Milojević, prof. assist. Faculty of Engineering University of Kragujevac, Kragujevac 34000, Sestre Janjić 6, Serbia, sasa.milojevic@kg.ac.rs, https://orcid.org/0000-0003-0569-047X*
[6] *Dr Blaža Stojanović, full prof. FacultyofEngineeringUniversityof Kragujevac, Kragujevac 34000, Sestre Janjić 6, Serbia, blaza@kg.ac.rs, https://orcid.org/0000-0003-4790-2856*

PRIMENA LAMINATNIH KOMPOZITA U AUTOMOBILSKOJ VAZDUHOPLOVNOJ I POMORSKOJ INDUSTRIJI

REZIME: U radu je prikazana primena laminatnih kompozita u automobilskoj, vazduhoplovnoj i pomorskoj industriji. Laminatne kompozite karakterišu visok odnos čvrstoće i mase, trajnost, otpornost na koroziju i mogućnost prilagođavanja svojstava projektovanjem strukture laminata. U automobilskoj industriji se primenjuju za izradu elemenata karoserije, struktura šasije i delova sistema oslanjanja, doprinoseći smanjenju mase uz zadržavanje zahtevanih mehaničkih svojstava i bezbednosti. U vazduhoplovnoj industriji se primenjuju za izradu krila, konstrukcije trupa bespilotnih letelica, hibridnih laminatnih kompozita i multifunkcionalnih kompozitnih sistema. U pomorskoj industriji laminatni kompoziti se primenjuju za izradu konstrukcije trupa i sendvič panela zbog male mase, otpornosti na koroziju i dobre otpornosti na zamorno opterećenje. I pored navedenih prednosti, njihova šira primena i dalje je ograničena visokim troškovima proizvodnje, složenošću popravke, degradacijom tokom dugotrajne eksploatacije i izazovima reciklaže. Budući razvoj biće usmeren ka optimizaciji strukture laminata, unapređenju proizvodnih tehnologija, razvoju hibridnih i multifunkcionalnih struktura i povećanju mogućnosti reciklaže.

KLJUČNE REČI: laminatni kompoziti, CFRP, automobilska industrija, avio industrija, pomorska industrija

INTRODUCTION

The development of modern transportation systems is conditioned by increasingly stringent requirements in terms of weight reduction, increased safety, energy efficiency and reduced environmental impact. In this context, advanced materials, and in particular laminated composites, occupy an important place in the construction of vehicles, primarily in the automotive industry.

Laminated composites enable the design of lightweight and mechanically efficient structures, where the desired properties are achieved by controlling the orientation of the fibres, the choice of the matrix and the application of appropriate production technologies. Thanks to their high specific strength, corrosion resistance and energy absorption capacity, these materials are increasingly used in structural and semi–structural components of vehicles (Fatima et al. 2025; Jovanović et al. 2025; Mohammadi et al. 2022).

In the modern automotive industry, the application of composite materials such as carbon fibre reinforced plastic-CFRP and glass fibre reinforced polymer–GFRP is becoming increasingly important due to the need to reduce weight and improve mechanical properties. Spasenović and Blagojević indicate that CFRP and GFRP contribute to reducing weight and increasing energy efficiency of vehicles, while maintaining adequate stiffness and resistance to loads (Spasenović & Blagojević, 2021).

Research by Mititelu et al. focuses on multi–criteria evaluation of the behaviour of CFRP laminated composites in car frames, emphasising the importance of mechanical testing and analysis in the design of structural elements (Mititelu et al. 2022).

In the aerospace industry, CFRP composites are widely used in aircraft load–bearing structures due to their high specific modulus and specific strength, which is confirmed through systematic literature reviews on the global application of CFRP in aero–structures (Zhang et al. 2023). Contemporary reviews also emphasise the importance of integrated design and manufacturing technologies of CFRP structural parts in aerospace, with a focus on process optimisation and structural development of high–performance materials (Bai et al. 2025).

The application of laminated composites in the automotive industry has gained increasing attention in recent decades, primarily due to the need for vehicle weight reduction, increased energy efficiency and reduced emissions of harmful gases. Materials such as carbon and glass fibre reinforced composites exhibit an extremely favourable strength–to–weight ratio, as well as good resistance to corrosion and fatigue, which makes them suitable for use in load–bearing and safety–critical vehicle components. Research shows that the use of CFRP materials can lead to a 30–40% reduction in the mass of vehicle structural parts, while simultaneously improving mechanical performance (Faizal Herum Ibrahim et al. 2025).

This review aims to analyse the application of laminated composites in modern transportation systems, with a special focus on the automotive, aerospace and marine industries. The paper covers the basic types of laminated composites, relevant materials and production technologies, as well as key challenges and future trends in their application in modern transportation technologies.

LAMINATED COMPOSITES

Laminated composites are layered composite materials composed of multiple individual layers (laminae), whose properties largely depend on the stacking order, fibre orientation, layer thickness, and type of materials used. Figure 1 shows a laminate composite. Due to their low density, high specific strength and stiffness, as well as good resistance to corrosion and fatigue, laminated composites have significant applications in transportation systems (Kreculj, 2013).

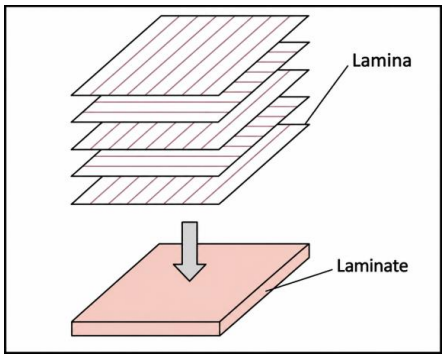

Figure 1 Laminated composite (Mitrović, 2024)

The lamina is the basic structural layer of a composite, in which the fibres can be unidirectional oriented or arranged in multiple directions. By combining multiple laminae of different orientations, a laminate is formed. The total thickness and mechanical properties of laminate depend on the number, orientation and order of the layers. The orientation of the fibres plays a key role in load transfer, as layers with unidirectional oriented fibres exhibit high strength and stiffness in the fibre direction, but significantly lower properties in the transverse direction. By appropriately arranging the layers oriented at angles of 0°, ±45° and 90°, a quasi–isotropic laminate can be formed, which exhibits approximately uniform mechanical properties in the plane of the laminate, which makes it suitable for use in structural components (Campbell, 2010; Kreculj, 2013; Mitrović, 2024).

Reinforcement of Laminated Composites – Fibres

Fibre material

In transportation applications, glass, carbon and aramid fibres are most commonly used (Figure 2). Glass fibres are characterised by a favourable price–to–mechanical properties ratio, good corrosion resistance and relatively simple processing, which is why they are widely used in the automotive and marine industries.

Aramid fibres are characterised by low density, high tensile strength and pronounced impact resistance, which makes them suitable for passive safety system components, although their application is limited by their higher cost and more complex production (Dharmavarapu & M.B.S, 2022; Đorđević, n.d.).

Carbon fibres have extremely high specific strength and stiffness, as well as good fatigue resistance, which is why they are increasingly used in the automotive industry, especially in body parts, chassis, suspension systems and drivetrain elements (Huang, 2009).

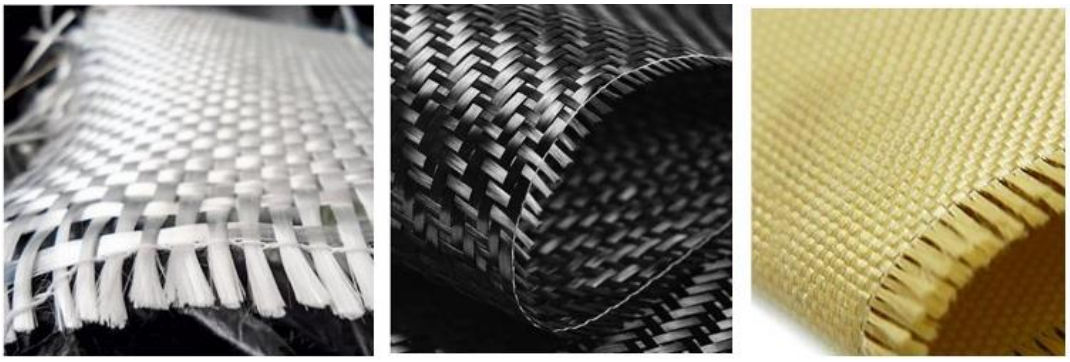

a) b) c)

Figure 2 Comparative presentation of fibres made from different materials: a) glass fibres, b) carbon fibres, c) aramid fibres (Carbon Fiber Reinforced Plastic Tank Repair in OH – RAK, 2024; What's Fiberglass, and How Does the Delicate Material Reinforce Thousands of Products?, 2024)

Fibre shape

Fibres are used in the production of laminated composites in the form of unidirectional oriented bundles, as well as in the form of various types of weaving. The choice of fibre shape depends on the requirements in terms of mechanical properties, the complexity of the geometry and the applied production technology.

Unidirectional weaves allow for maximum strength and stiffness in a particular direction, while weaves with multidirectional fibre orientation provide more balanced properties and better adaptability to complex shapes. Knitted and randomly oriented fabrics are mainly used for less loaded or non–structural elements (Campbell, 2010; Đorđević, n.d.; Hall & Javanbakht, 2021).

Types of Matrices

The matrix in laminated composites has the role of fibre connection, load transfer, and protection of the reinforcement from external influences. Thermosetting matrices, primarily epoxy, phenolic and polyester resins, are widely used in transportation applications. Epoxy resins are characterised by good mechanical resistance, low shrinkage and good fatigue resistance, which makes them suitable for highly loaded structural components in the automotive industry (Jin et al., 2015; Saba et al., 2016). Phenolic resins have good resistance to high temperatures and flame, while polyester resins are mainly used in less demanding and more economically accessible solutions (Asim et al., 2018; El-Din Saleh, 2012).

Fabrication Methods of Laminated Composites

The production of laminated composites can include various open and closed mould techniques. The choice depends on the type of material, the component geometry, the required quality and the production volume. In the transportation industry, closed mould processes, such as Resin Transfer Moulding (RTM), High–Pressure RTM and pressing processes, are of particular importance, as they enable controlled quality, high repeatability and integration into mass production (Biswas & Anurag, 2019; Campbell, 2010; Hall & Javanbakht, 2021; Mitrović, 2024).The choice of process depends on the requirements in terms of mechanical properties, repeatability, production cycle and cost–effectiveness.

APPLICATION OF LAMINATED COMPOSITES

Due to increasingly stringent requirements for weight reduction, increased energy efficiency and reduced emissions, laminated composites are becoming important materials in transportation systems. Their application is particularly pronounced in the automotive, aerospace and marine industries, where they contribute to the reduction of structural weight, safety improvement and reduced maintenance costs.

In modern vehicles, laminated composites, especially CFRP and GFRP, are used in various structural components such as body panels, supporting beams, floor structures and parts of the suspension system. These materials are often used due to their high strength–to–weight ratio, which allows a significant reduction in vehicle weight while maintaining mechanical strength and resistance (Spasenović & Blagojević, 2021). Composite structures show favourable behaviour in terms of energy absorption during impact, which makes them suitable for use in elements that contribute to the passive safety of vehicles (Lukaszewicz, 2013). Furthermore, advanced reviews indicate that properly designed composites allow for optimisation of fibre orientation, thickness, and layer sequence to achieve the required mechanical properties and performance in specific automotive parts (Khan et al., 2025a).

Application of Laminated composites in the Automotive Industry

In the modern automotive industry, laminated composites play a significant role in reducing vehicle weight while simultaneously meeting requirements for strength, stiffness, and safety. They are most commonly used in the manufacture of body parts such as hoods, bumpers, doors, roofs, and spoilers, as well as certain chassis elements, suspension systems, and drive components.

A typical example of the application of laminated composites is the hood of a vehicle. By using CFRP laminated composites, it is possible to achieve a weight reduction of up to about 30% compared to metal alternatives, while maintaining the required strength and stiffness (Khan et al., 2025b). In a light electric vehicle, Bere et al. showed that the use of CFRP can lead to an even more significant weight reduction: the tested composite hood was approximately 2.5 times lighter than a corresponding steel structure, with an increase in lateral and torsional stiffness (Bere et al., 2021).

Laminated composites are increasingly used in the manufacture of vehicle chassis, where they contribute to improved handling, reduced overall weight and fuel consumption, increased resistance to corrosion and fatigue. A particular advantage of these materials is their ability to dampen vibrations and maintain long–term structural stability.

Laminated composites also have significant applications in passive safety systems, primarily in bumpers. Materials such as CFRP and GFRP have shown good energy absorption capabilities during low–speed collisions, thereby reducing vehicle damage and increasing passenger safety. In a recent study, an optimised CFRP bumper beam achieved a 57.18% weight reduction compared to the initial aluminium version, while meeting the crashworthiness requirements (Dai et al., 2024).

In addition, laminated composites are used to produce leaf springs, which, compared to steel ones, have lower weight, longer service life, better corrosion resistance, and improved shock and vibration damping (Khan et al., 2025b). In one experimental study, an optimised GFRP leaf spring had a weight of approximately 9.75 kg, compared to 31.24 kg for the corresponding steel structure, which represents a weight reduction of approximately 69% while meeting the requirements for bending stiffness and strength. In addition to the significant weight reduction, the design of the GFRP leaf spring can be adapted to the requirements of the suspension system by appropriately adjusting the geometry and structure of the laminate. The position of the composite leaf spring in a vehicle and its typical construction is shown in Figure 3.

Figure 3 Location and typical construction of a GFRP composite leaf spring (Ma et al., 2021)

Typical examples of the application of laminated composites in the automotive industry are shown in Figure 4.

a) b) c)

Figure 4 Application of laminated composites in the automotive industry: a) Air filter housing, b) Hood, c) Spoiler (*Corvette Stingray C8 2020-2023 Tuning Kit*, n.d.; Gao et al., 2018; Sedlacek & Lasova, 2017)

Sedlacek et al. (Sedlacek & Lasova, 2017) used numerical analysis and the finite element method to design and optimise an air filter housing for a racing motorcycle. The goal was to reduce mass by 70% while maintaining stiffness and strength. The models included fibre orientation and overlap, cut and splice locations, and a prototype was fabricated from impregnated carbon fibres.

Gao et al. (Gao et al., 2018) investigated a CFRP hood, optimising the orientation and thickness of the layers for maximum stiffness and minimum mass. ABAQUS and FEM software were used, and the DMTO method was used for optimisation. The prototype was fabricated using the VARTM method, and experimental test results confirmed the numerical analysis.

The examples show that the application of laminated composites in the automotive industry is based on the simultaneous optimisation of fibre orientation, layer thickness, and production process to achieve minimal mass while meeting strength and stiffness requirements.

Application of Laminated Composites in the Aerospace Industry

Due to their high strength–to–weight ratio, laminated composites are widely used in the aerospace industry, for wings, fuselage sections, stabilizers, floor structures, and other load–bearing and semi–load–bearing components. As these are highly responsible structures, these materials are subjected to numerous static, dynamic, fatigue, and impact tests (Linganiso & Anandjiwala, 2016).

A typical example of the application of hybrid laminate structures is GLARE (glass–reinforced aluminium laminate), which consists of alternating thin aluminium layers and layers of glass fibres in an epoxy matrix. In the Airbus A380 aircraft, GLARE is used in the upper fuselage panels, with the total area of these structures being approx. 469 m² and comprising of 27 panels. According to Park and Choi, the use of GLARE in the A380 fuselage structure can achieve a weight reduction of approximately 794 kg, or about 10% compared to a corresponding aluminium structure. In addition to weight reduction, the importance of this material is also reflected in its favourable fatigue resistance and damage tolerance (Yoon Park & Jong Choi, 2019).

Laminated composites are also of particular interest in the development of unmanned aerial vehicles, where weight reduction is of key importance for increasing flight time and energy efficiency. In these applications, CFRP is most often used for the manufacture of wings, propellers, housings and supporting structures, where various laminate manufacturing techniques are applied.

In the aerospace industry, laminated composites are used for the manufacture of structural parts of satellites, as well as in the development of multifunctional composite batteries. Figure 5 shows examples of the application of laminated composites in the aerospace industry.

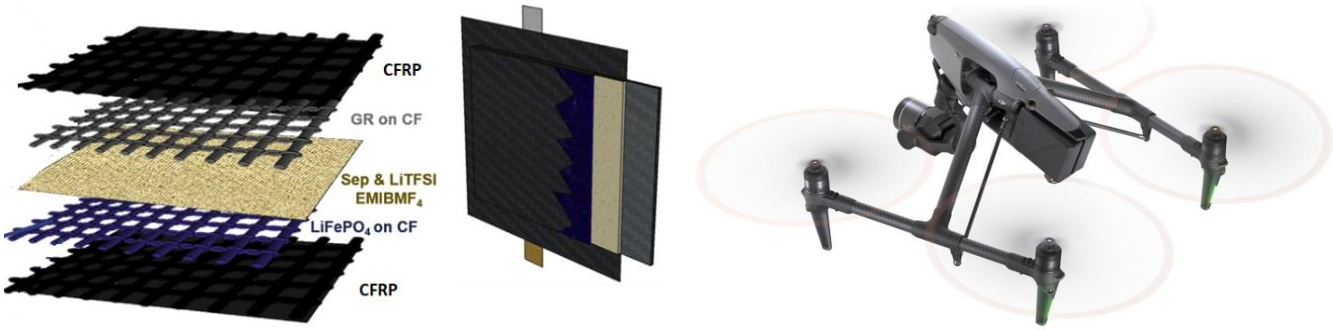

a) b)

Figure 5 Applications of laminated composites in the aerospace industry: a) CFRP–reinforced lithium battery, b) Drone (*DJI Inspire 3 – Master the Unseen*, 2024; Moyer et al., 2020)

Moyer et al. (Moyer et al., 2020) have demonstrated the production of a composite lithium battery with an epoxy matrix and woven carbon fibres as a reinforcement and collector. The lamination was performed using the “Wet lay–up” process, and the active elements of the battery were embedded in the fibre layers. The resulting plate serves both as a structural element and as a power source in cubic satellites, allowing for more rational use of space and integration of other components.

A special group of laminate materials are fibre–reinforced metal laminated composites (Fibre–Metal Laminated composites – FML), which consist of alternating thin metal layers and layers of fibre–reinforced polymer composites. The most well–known types are GLARE, ARALL and CARALL. By combining the properties of metal and composite layers, low mass, high fatigue and impact resistance, as well as good tolerance to damage are achieved. FML materials were primarily developed for aerospace structures, while their application is gradually expanding to the automotive and marine sectors (Etri et al., 2022).

Application of Laminated Composites in the Marine Industry

The application of laminated composites in the marine industry is widespread, primarily due to their corrosion resistance, low mass and good fatigue resistance. These materials are used for the manufacture of hulls, superstructures, decks, steering systems and protective domes for sonar.

Laminated composites are particularly used in high–speed vessels, patrol and military vessels, where they contribute to weight reduction and improved performance. For smaller and medium–sized vessels, such as fishing boats, yachts and rescue boats, GFRP is most often used (Chandra Chakraborty, 2022; Rubino et al., 2020). An additional advantage of laminated composites in military applications is reflected in the ability to dampen vibrations and reduce radar visibility.

As an example of the application of GFRP laminated composites, the construction of the hull of a composite yacht can be highlighted. In the analysed vessel, individual parts of the hull are made with different numbers of laminate layers, depending on the position and expected load. The hull construction and appearance of the GFRP laminated plate are shown in Figure 6.

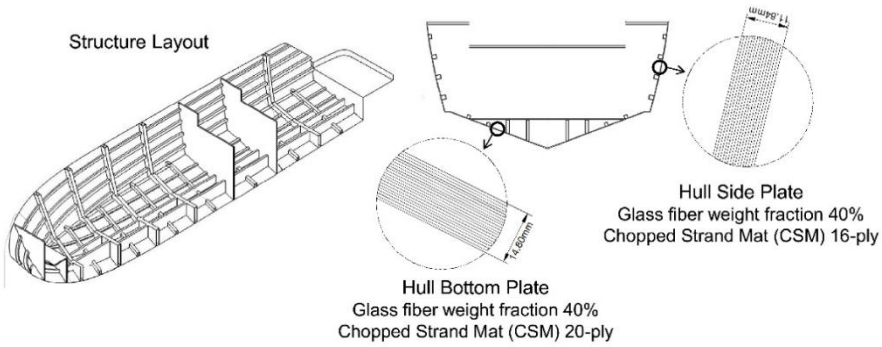

Figure 6 Hull construction and GFRP laminated panel of a composite yacht

This example shows that the laminate structure in marine structures can be adapted to local loading conditions by selecting the number and arrangement of layers. In this case, the control of the actual proportion of glass fibres and internal defects plays an important role in ensuring the required mechanical properties of the manufactured structure. One of particular importance in marine structures are sandwich laminate structures, which consist of outer load–bearing layers made of GFRP, CFRP or aramid composites and a lightweight core, most often made of polymer foam or honeycomb structure. This type of structure allows for high bending stiffness with low mass, which is why it is used in hulls, decks and superstructures of vessels. Mass reduction can contribute to increasing load capacity, reduction of fuel consumption and improvement of vessel stability (Yoon Park & Jong Choi, 2019).

A typical example of the use of sandwich–laminate structures is the Swedish Visby–class corvette, whose hull is made of sandwich panels with carbon and glass reinforcements and a polymer matrix. The use of carbon fibres has enabled a reduction in the hull mass by approximately 30%, while maintaining the necessary structural resistance and favourable characteristics for military applications (Yoon Park & Jong Choi, 2019). However, long–term exposure to seawater and moisture is a significant factor in the design of these structures, since moisture penetration into the polymer matrix and the fibre–matrix interface can lead to degradation of the mechanical properties of the laminate. Therefore, when choosing materials for marine applications, in addition to the initial mechanical properties, it is necessary to consider their long-term resistance in the marine environment (Osa–Uwagboe et al., 2024a).

Compared to aviation applications, where minimal mass and high specific stiffness are the dominant requirements, corrosion resistance, durability, and cost–effectiveness are of particular importance in marine structures.

DISCUSSION

Analysis of the presented applications shows that the main reasons for the introduction of laminated composites are similar in different transport sectors and primarily include weight reduction, high specific strength and stiffness, as well as the possibility of adapting the laminate structure to specific load conditions. The importance of individual requirements varies depending on the field of application. In the automotive industry, in addition to mechanical properties, price and short production cycle time are crucial, while in aviation, minimal weight, high specific stiffness and reliability are dominant. In marine structures, in addition to low weight, corrosion resistance, durability and stability of properties during exposure to an aggressive marine environment are of particular importance.

Although laminated composites show significant advantages in terms of weight reduction, mechanical properties and performance improvement, their wider application, especially in automotive mass production, is still limited by a number of factors. First of all, the high cost of materials and manufacturing processes, as well as the complexity of forming technologies, pose a significant challenge to their economic viability. Recent reviews indicate that the lack of fast and energy–efficient manufacturing processes, the high cost of CFRP and other composite materials, and the limitations of existing tools and procedures for design and repair significantly limit their application in the automotive industry compared to conventional metals such as steel and aluminium (Sarfraz et al. 2021).

Additional limitation is the behaviour of composite structures during long–term operation. This is particularly pronounced in marine conditions, where moisture and seawater ingress can lead to matrix plasticisation, weakening of the fibre–matrix bond, and a reduction in tensile, flexural, and inter–laminar shear properties. Review of research shows that the degree of degradation depends on the type of fibre and matrix, the order of layers, the manufacturing method, the temperature and the exposure time, indicating that not only the initial mechanical properties but also their long–term stability must be considered when designing laminated composites (Osa–Uwagboe et al., 2024b).

The challenges related to recycling and end–of–life waste management represent a significant obstacle to the widespread application of laminated composites in transportation systems. Due to the use of thermosetting matrices and the combination of different materials, the separation of components during recycling remains technologically complex, and existing methods often damage the mechanical properties of the material or require energy–intensive, economically disadvantageous processes. Despite the development of several mechanical, chemical and thermal methods, the limited possibility of obtaining recycled CFRP material with properties comparable to virgin material still represents a significant challenge for integration into the circular economy and reuse in transportation applications (Aldosari et al. 2024; Butenegro et al. 2021; Spasenović & Blagojević, 2021; Zhang et al. 2020).

Sustainability issue is particularly acute for large marine structures, which often have a design life of 20–30 years. Modern approaches increasingly include the selection of alternative fibres and matrices, recycling and reuse of materials, life cycle analysis, and the development of more sustainable sandwich structures (Baley et al., 2024).

Market data indicate a continued growth in industrial interest in composite materials produced by lay-up processes. According to a report by Markets and Markets, the global lay–up composites market is estimated at USD 43.18 billion in 2024 and USD 47.23 billion in 2025. Further market growth is expected in the coming period, with its value forecast to reach approximately USD 72.87 billion by 2030, at a compound annual growth rate (CAGR) of 9.3%. In 2024, the automotive industry represented the largest end–use sector, while significant applications of these materials were also recorded in the aerospace, marine and energy industries. The main drivers of further growth are the requirements for weight reduction and the use of lightweight materials with high mechanical properties, with additional development potential in the field of electric vehicles and marine structures (Lay–up Composites Market by Fiber Type, Resin Type, End–Use Industry and Region – Global Forecast to 2030, 2026).

A special example of the modern development of laminate structures is represented by fibre-reinforced metal laminated composites (FML – Fibre–Metal Laminated composites), which combine thin metal layers and fibre–reinforced composite layers to combine the advantages of both groups of materials. The importance of FML structures is particularly pronounced in aerospace, but their application is also developing in the automotive and marine industries. The distribution of the FML materials market by application in 2024 is shown in Figure 7 (Pulidindi & Yadav, 2025).

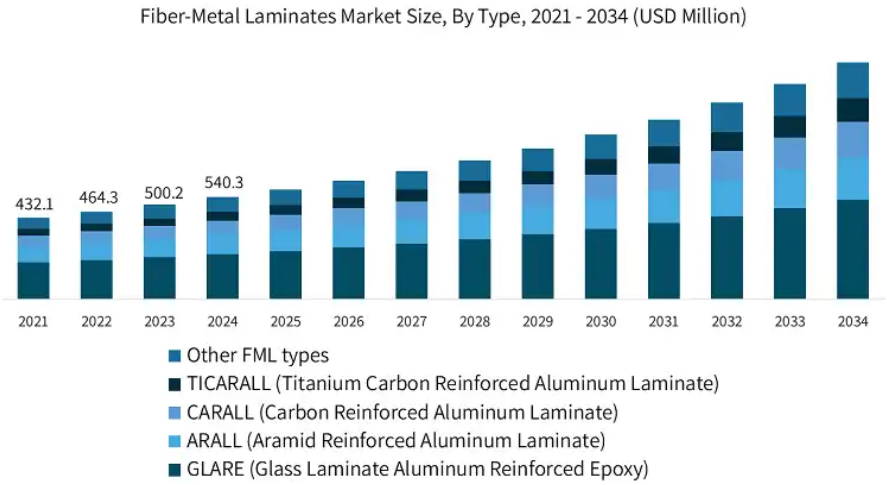

Figure 7 Market share of FML materials by application area (Pulidindi & Yadav, 2025)

The data presented in Figure 7 show a clear dominance of the aerospace and defence industry in the application of FML materials. In 2024, this sector had a market share of 61.5%, which corresponds to a value of approximately 332.5 million USD. This share can be associated with the requirements of aerospace structures for weight reduction, high fatigue resistance and reliability under long–term cyclic loads. At the same time, market analysis indicates the expansion of the application of FML structures in the automotive sector, especially in electric and hybrid vehicles, as well as in marine structures, where their application is associated with the requirements for weight reduction, increased corrosion resistance and durability of the structure (Pulidindi & Yadav, 2025).

The potential for further development is also confirmed by the estimate that the global FML market was worth approximately USD 540.3 million in 2024, while it is expected to reach approximately USD 1.25 billion by 2034, with a forecasted CAGR of 8.9% (Pulidindi & Yadav, 2025).

Although the above market indicators indicate significant potential for further growth and wider application of laminated composites, their future development will largely depend on overcoming the previously discussed technological, economic and environmental limitations. In this regard, research is directed towards the simultaneous improvement of materials, construction and production technologies. The development of hybrid and multifunctional structures allows for the combination of the advantages of different materials, while processes such as RTM, HP–RTM and AFP contribute to higher repeatability, automation and shortening of production cycles. At the same time,

the development of materials with lower environmental impact, improved recycling and reuse capabilities, and more reliable prediction of the long-term behaviour of laminate structures under different operating conditions are of increasing importance (Automotive Composites Market, n.d.; Osa–Uwagboe et al., 2024b; Sarfraz et al., 2021).

CONCLUSIONS

Laminated composites represent a significant group of materials in modern transportation systems, especially in the automotive, aerospace, and marine industries. Their application allows for a significant reduction in the mass of structures while maintaining or improving mechanical properties, which can improve energy efficiency, performance, and safety of transportation systems.

The analysis of the presented applications shows that their main advantage is not only in high specific strength and stiffness, but also in the ability to design the laminate structure in accordance with specific load conditions. By choosing the material, orientation, number, and sequence of layers, it is possible to adapt the mechanical behaviour of the component to the requirements of its application. This possibility of structural adaptation is one of the main reasons for the increasingly widespread use of laminated composites in the transportation industry.

However, the criteria for their application are not the same in all transport sectors. In the automotive industry, in addition to reducing weight and meeting strength and safety requirements, cost–effectiveness and the possibility of serial production play a significant role. In aerospace and space applications, the requirements for minimum weight, high specific stiffness and structural reliability dominate, while in the marine industry, corrosion and fatigue resistance, durability and stability of properties in the marine environment are particularly important. Sandwich-laminate and hybrid structures, including FML materials, show special potential, in which the combination of different materials seeks to achieve more favourable ratios of weight, mechanical properties and durability.

Although the presented applications and market trends indicate a further growth in the importance of laminated composites, their wider application is still conditioned by solving the problems of high material and production costs, the complexity of repair, recycling and preservation of mechanical properties during long-term exploitation. Future development will therefore be directed towards automation and improvement of production processes, optimization of material selection, orientation, number and sequence of layers in accordance with specific loading conditions, development of hybrid and multifunctional structures, increasing the possibilities of recycling and reuse, as well as more reliable prediction of long-term behaviour of laminated composites in different exploitation conditions. These directions of development, along with compliance with increasingly stringent industrial and environmental requirements, represent the basis for a wider and more sustainable application of laminated composites in future transport systems.

ACKNOWLEDGMENTS

This work has been performed as a part of activities within the projects 451–03–33/2026–03/200107 and 451–03–34/2026–03/200107, supported by the Republic of Serbia, Ministry of Science, Technological Development and Innovation.

REFERENCES

Aldosari, S. M., AlOtaibi, B. M., Alblalaihid, K. S., Aldoihi, S. A., AlOgab, K. A., Alsaleh, S. S., Alshamary, D. O., Alanazi, T. H., Aldrees, S. D., & Alshammari, B. A. (2024). Mechanical Recycling of Carbon Fiber-Reinforced Polymer in a Circular Economy. *Polymers*, *16*(10), 1363. https://doi.org/10.3390/polym16101363

Asim, M., Saba, N., Jawaid, M., Nasir, M., Pervaiz, M., & Alothman, O. Y. (2018). A Review on Phenolic Resin and its Composites. *Current Analytical Chemistry*, *14*(3), 185–197. https://doi.org/10.2174/1573411013666171003154410

Automotive Composites Market. (n.d.). Retrieved June 23, 2026, from https://www.marketsandmarkets.com/Market-Reports/automotive-composite-market-10869121.html

Bai, Q., Hao, Q., Dai, H., Chen, Y., & Dai, N. (2025). A review on integrated design and manufacturing technologies for continuous fiber-reinforced polymer composite lightweight structures in aerospace. *Thin-Walled Structures*, *217*, 113750. https://doi.org/10.1016/j.tws.2025.113750

Baley, C., Davies, P., Troalen, W., Chamley, A., Dinham-Price, I., Marchandise, A., & Keryvin, V. (2024). Sustainable polymer composite marine structures: Developments and challenges. *Progress in Materials Science*, *145*, 101307. https://doi.org/10.1016/j.pmatsci.2024.101307

Bere, P., Dudescu, M., Neamțu, C., & Cocian, C. (2021). Design, Manufacturing and Test of CFRP Front Hood Concepts for a Light-Weight Vehicle. *Polymers*, *13*(9), 1374. https://doi.org/10.3390/polym13091374

Biswas, S., & Anurag, J. (2019). Fabrication of Composite Laminated composites. In P. K. Bajpai & I. Singh (Eds.), *Reinforced Polymer Composites* (1st ed., pp. 39–53). Wiley. https://doi.org/10.1002/9783527820979.ch3

Butenegro, J. A., Bahrami, M., Abenojar, J., & Martínez, M. Á. (2021). Recent Progress in Carbon Fiber Reinforced Polymers Recycling: A Review of Recycling Methods and Reuse of Carbon Fibers. *Materials*, *14*(21), 6401. https://doi.org/10.3390/ma14216401

Campbell, F. C. (2010). *Structural Composite Materials*. ASM International. https://books.google.rs/books?id=D3Wta8e07t0C

Carbon Fiber Reinforced Plastic Tank Repair in OH - RAK. (2024, August 15). Rakcorp.Com.

Chandra Chakraborty, B. (2022). FRP for Marine Application. In M. Alberto Masuelli (Ed.), *Fiber-Reinforced Plastics*. IntechOpen. https://doi.org/10.5772/intechopen.101332

Corvette Stingray C8 2020-2023 Tuning Kit. (n.d.). LARTE Design. Retrieved October 8, 2026, from https://larte-design.com/tuning-kits/corvette/stingray/c8-2020-2023/

Dai, C., Yu, P., Yin, M., & Long, J. (2024). Optimization of the crashworthiness design of carbon fiber-reinforced polymer bumper beam. *International Journal of Crashworthiness*, *29*(1), 163–177. https://doi.org/10.1080/13588265.2023.2230628

Dharmavarapu, P., & M.B.S, S. R. (2022). Aramid fibre as potential reinforcement for polymer matrix composites: A review. *Emergent Materials*, *5*(5), 1561–1578. https://doi.org/10.1007/s42247-021-00246-x

DJI Inspire 3—Master the Unseen. (2024, December 9). Dji.Com.

Đorđević, Z. (n.d.). *Composite structures (Kompozitne konstrukcije)*. Faculty of Engineering Universitz of Kragujevac. (Original work published 2018)

El-Din Saleh, H. M. (Ed.). (2012). *Polyester*. IntechOpen.

Etri, H. E., Korkmaz, M. E., Gupta, M. K., Gunay, M., & Xu, J. (2022). A state-of-the-art review on mechanical characteristics of different fiber metal laminated composites for aerospace and structural applications. *The International Journal of Advanced Manufacturing Technology*, *123*(9–10), 2965–2991. https://doi.org/10.1007/s00170-022-10277-1

Faizal Herum Ibrahim, Agus Priyanto, Sigit Saifudin, Andi Eko Saputro, & Ikhwanul Qiram. (2025). Composite Material Innovation in Automotive Structure Applications. *Journal of Educational Engineering and Environment*, *4*(1), 5–9. https://doi.org/10.36526/jeee.v4i1.5505

Fatima, N., Alam, S., Islam, M. N., Hasan, M. M., & Sany, M. Z. I. (2025). *Lightweighting the Future: A Comprehensive Review of Materials in Automotive Design*. Engineering. https://doi.org/10.20944/preprints202510.1192.v1

Gao, Y., Gao, Y., Qian, R., Xu, Y., & Wu, C. (2018). *Concurrent Optimization of Ply Orientation and Thickness for Carbon Fiber Reinforced Plastic (CFRP) Laminated Engine Hood*. 2018-01–1121. https://doi.org/10.4271/2018-01-1121

Hall, W., & Javanbakht, Z. (2021). *Design and Manufacture of Fibre-Reinforced Composites* (1st ed. 2021). Springer International Publishing. https://doi.org/10.1007/978-3-030-78807-0

Huang, X. (2009). Fabrication and Properties of Carbon Fibers. *Materials*, *2*(4), 2369–2403. https://doi.org/10.3390/ma2042369

Jin, F.-L., Li, X., & Park, S.-J. (2015). Synthesis and application of epoxy resins: A review. *Journal of Industrial and Engineering Chemistry*, *29*, 1–11. https://doi.org/10.1016/j.jiec.2015.03.026

Jovanović, J., Mitrović, N., Gajević, S., Miladinović, S., Blagojević, J., Skulić, A., & Stojanović, B. (2025). Study of abrasive action on surface roughness and worn mass of laminated composites: Production and evaluation. *Advanced Technologies & Materials*, *50*(1), 9–16. https://doi.org/10.24867/ATM-2025-1-002

Khan, F., Hossain, N., Mim, J. J., Rahman, S. M., Iqbal, Md. J., Billah, M., & Chowdhury, M. A. (2025a). Advances of composite materials in automobile applications – A review. *Journal of Engineering Research*, *13*(2), 1001–1023. https://doi.org/10.1016/j.jer.2024.02.017

Khan, F., Hossain, N., Mim, J. J., Rahman, S. M., Iqbal, Md. J., Billah, M., & Chowdhury, M. A. (2025b). Advances of composite materials in automobile applications – A review. *Journal of Engineering Research*, *13*(2), 1001–1023. https://doi.org/10.1016/j.jer.2024.02.017

Kreculj, D. (2013). *Modeling of impact damage in laminate composite structures (Modeliranje udarnog oštećenja u laminarnim kompozitnim strukturama)* [PhD thesis]. University of Belgrade.

Lay-up Composites Market by Fiber Type, Resin Type, End-use Industry and Region – Global Forecast to 2030 (CH 9649). (2026). Markets and Markets.

Linganiso, L. Z., & Anandjiwala, R. D. (2016). Fibre-reinforced laminated composites in aerospace engineering. In *Advanced Composite Materials for Aerospace Engineering* (pp. 101–127). Elsevier. https://doi.org/10.1016/B978-0-08-100037-3.00004-3

Lukaszewicz, D. H. -J. A. (2013). Automotive Composite Structures for Crashworthiness. In A. Elmarakbi (Ed.), *Advanced Composite Materials for Automotive Applications* (1st ed., pp. 99–127). Wiley. https://doi.org/10.1002/9781118535288.ch5

Ma, L., He, J., Gu, Y., Zhang, Z., Yu, Z., Zhou, A., Tam, L., & Wu, C. (2021). Structure Design of GFRP Composite Leaf Spring: An Experimental and Finite Element Analysis. *Polymers*, *13*(8), 1193. https://doi.org/10.3390/polym13081193

Mititelu, I., Petrișor, S. M., Savin, A., Šturm, R., Bergant, Z., Steigmann, R., Stanciu, M. D., & Bârsănescu, P. D. (2022). Multi-Criteria Evaluation of the Failure of CFRP Laminated composites for Frames in the Automotive Industry. *Polymers*, *14*(21), 4507. https://doi.org/10.3390/polym14214507

Mitrović, N. (2024). *The influence of finishing on the surface roughness of laminated composites (Uticaj završne obrade na površinsku hrapavost laminatnih kompozita)* [Master thesis]. Faculty of Engineering, University of Kragujevac.

Mohammadi, H., Ahmad, Z., Mazlan, S. A., Faizal Johari, M. A., Siebert, G., Petrů, M., & Rahimian Koloor, S. S. (2022). Lightweight Glass Fiber-Reinforced Polymer Composite for Automotive Bumper Applications: A Review. *Polymers*, *15*(1), 193. https://doi.org/10.3390/polym15010193

Moyer, K., Meng, C., Marshall, B., Assal, O., Eaves, J., Perez, D., Karkkainen, R., Roberson, L., & Pint, C. L. (2020). Carbon fiber reinforced structural lithium-ion battery composite: Multifunctional power integration for CubeSats. *Energy Storage Materials*, *24*, 676–681. https://doi.org/10.1016/j.ensm.2019.08.003

Osa-uwagboe, N., Silberschmidt, V. V., & Demirci, E. (2024a). Review on Mechanical Performance of Fibre-Reinforced Plastics in Marine Environments. *Applied Composite Materials*, *31*(6), 1991–2018. https://doi.org/10.1007/s10443-024-10247-8

Osa-Uwagboe, N., Silberschmidt, V. V., & Demirci, E. (2024b). Review on Mechanical Performance of Fibre-Reinforced Plastics in Marine Environments. *Applied Composite Materials*, *31*(6), 1991–2018. https://doi.org/10.1007/s10443-024-10247-8

Pulidindi, K., & Yadav, K. (2025). *Fiber-Metal Laminated composites Market Size & Share 2025–2034. Global Market Insights, June 2025* (GMI14258). Global market insights. https://www.gminsights.com/industry-analysis/fiber-metal-laminated%20composites-market

Rubino, F., Nisticò, A., Tucci, F., & Carlone, P. (2020). Marine Application of Fiber Reinforced Composites: A Review. *Journal of Marine Science and Engineering*, *8*(1), 26. https://doi.org/10.3390/jmse8010026

Saba, N., Jawaid, M., Alothman, O. Y., Paridah, M., & Hassan, A. (2016). Recent advances in epoxy resin, natural fiber-reinforced epoxy composites and their applications. *Journal of Reinforced Plastics and Composites*, *35*(6), 447–470. https://doi.org/10.1177/0731684415618459

Sarfraz, M. S., Hong, H., & Kim, S. S. (2021). Recent developments in the manufacturing technologies of composite components and their cost-effectiveness in the automotive industry: A review study. *Composite Structures*, *266*, 113864. https://doi.org/10.1016/j.compstruct.2021.113864

Sedlacek, F., & Lasova, V. (2017). Design and optimization of composite parts using numerical simulations. *2017 International Conference on Mechanical, System and Control Engineering (ICMSC)*, 16–21. https://doi.org/10.1109/ICMSC.2017.7959434

Spasenović, J., & Blagojević, I. (2021). Composite materials in automotive industry: A review. *Industrija*, *49*(2), 57–68. https://doi.org/10.5937/industrija49-34540

What's fiberglass, and how does the delicate material reinforce thousands of products? (2024, August 15). Acs.Org.

Yoon Park, S., & Jong Choi, W. (2019). The Guidelines of Material Design and Process Control on Hybrid Fiber Metal Laminate for Aircraft Structures. In K. Y. Maalawi (Ed.), *Optimum Composite Structures*. IntechOpen. https://doi.org/10.5772/intechopen.78217

Zhang, J., Chevali, V. S., Wang, H., & Wang, C.-H. (2020). Current status of carbon fibre and carbon fibre composites recycling. *Composites Part B: Engineering*, *193*, 108053. https://doi.org/10.1016/j.compositesb.2020.108053

Zhang, J., Lin, G., Vaidya, U., & Wang, H. (2023). Past, present and future prospective of global carbon fibre composite developments and applications. *Composites Part B: Engineering*, *250*, 110463. https://doi.org/10.1016/j.compositesb.2022.110463

The 11th International Congress
Motor Vehicles & Motors 2026
Kragujevac, Serbia
October 8th - 9th, 2026

Motor Vehicles & Motors

MVM2026-067
https://doi.org/10.24874/CMVM2026.067
Original scientific paper

Luka Milić[1]
Ilija Vidović[2]
Matija Simanić[3]
Momir Drakulić[4]
Aleksandar Đurić[5]

ADDITIVE MANUFACTURING AS A FABRICATION METHOD FOR A LIGHTWEIGHT TRACKED ROBOT PLATFORM

ABSTRACT: Additive manufacturing has evolved from a rapid-prototyping niche into a production-grade fabrication method spanning distinct polymer and metal process families, each defined by a different trade-off between accessibility, precision, and mechanical performance. This paper traces that development, from the earliest stereolithography and selective laser sintering patents through material extrusion and metal powder-bed fusion, and examines how these trade-offs translate into a concrete fabrication decision. Fused Deposition Modelling (FDM) using Polylactic Acid (PLA) and Thermoplastic Polyurethane (TPU) was selected for the design and fabrication of a lightweight tracked robot platform, chosen for its low cost, minimal training requirement, and iterative design flexibility despite known limitations in surface resolution and interlayer strength. The resulting platform combines a multipart, dovetail-jointed PLA chassis with a fully 3D-printed drivetrain, a 68-tooth TPU track loop engaging a PLA drive sprocket at a fixed circular pitch, demonstrating that a functional tracked mobility system can be produced entirely by fused deposition modelling, without tooling, from a small number of printed parts. The platform serves as an applied case validating the process and material trade-offs discussed throughout the paper.

KEYWORDS: additive manufacturing; fused deposition modelling; material extrusion; PLA; TPU; tracked robot platform

[1] *Luka Milić, University of Defence in Belgrade, Military Academy, Veljka Lukića Kurjaka 33, Belgrade, Serbia, luka.milic777@gmail.com*
[2] *Ilija Vidović, University of Defence in Belgrade, Military Academy, Veljka Lukića Kurjaka 33, Belgrade, Serbia, ilijavidovic50@gmail.com*
[3] *Matija Simanić, University of Defence in Belgrade, Military Academy, Veljka Lukića Kurjaka 33, Belgrade, Serbia, msimanic4@gmail.com*
[4] *Momir Drakulić, University of Defence in Belgrade, Military Academy, Veljka Lukića Kurjaka 33, Belgrade, Serbia, momir.drakulic@va.mod.gov.rs, https://orcid.org/0000-0002-8367-7281*
[5] *Aleksandar Đurić, University of Defence in Belgrade, Military Academy, Veljka Lukića Kurjaka 33, Belgrade, Serbia, aleksandar.djrc@gmail.com, https://orcid.org/0000-0002-2165-528X*

PRIMENA ADITIVNIH TEHNOLOGIJA U IZRADI LAKOG GUSENIČNOG ROBOTA

REZIME: Aditivne tehnologije su se razvile od tehnologije pretežno korišćene za brzu izradu prototipova do proizvodnog metoda izgradnje industrijskog nivoa, koji obuhvata različite porodice procesa zasnovanih na polimerima i metalima, pri čemu svaku karakteriše drugačiji odnos između pristupačnosti, preciznosti i mehaničkih performansi. Ovaj rad prati taj razvoj, počevši od najranijih patenata stereolitografije i selektivnog laserskog sinterovanja, preko ekstruzije materijala do topljenja metalnog praha u sloju, i razmatra kako se ovi kompromisi prevode u konkretnu odluku o načinu izrade. Modelovanje topljenim nanosom (FDM), uz upotrebu polilaktidne kiseline (PLA) i termoplastičnog poliuretana (TPU), izabrana je za projektovanje i izradu lake gusenične robot-platforme, zbog niske cene, minimalnih zahteva za obukom i fleksibilnosti za iterativno projektovanje, uprkos poznatim ograničenjima u pogledu kvaliteta površine i čvrstoće veze između slojeva. Dobijena platforma kombinuje višedelnu šasiju od PLA materijala, spojenu vezom tipa „lastin rep" (dovetail), sa pogonskim sklopom koji je u potpunosti izrađen 3D štampom, gusenicom od TPU materijala sa 68 zubaca koja se uklapa u pogonski lančanik od PLA materijala pri konstantnom koraku. Ovo pokazuje da je funkcionalan gusenični sistem kretanja moguće izraditi isključivo tehnologijom modelovanja topljenim nanosom (FDM), bez alata, od malog broja štampanih delova. Platforma služi kao primenjeni primer koji potvrđuje kompromise u izboru procesa i materijala razmatrane u radu.

KLJUČNE REČI: aditivne tehnologije; modelovanje topljenim nanosom (FDM); ekstruzija materijala; PLA; TPU; gusenična robot-platforma

INTRODUCTION

Modern mechanical engineering depends increasingly on production technologies that allow fast, precise and economical fabrication of technical systems. Conventional subtractive methods, like machining, casting and other related processes, remain the backbone of industrial production, but they struggle to fabricate complex geometries efficiently and offer limited room for rapid design iteration.

Additive manufacturing takes the opposite approach: material is added layer by layer, directly from a digital three-dimensional model, instead of being removed from a solid block. This shifts the constraints of production. Geometric complexity that would be expensive or impossible to machine becomes routine, material waste drops sharply, and, most importantly for early-stage development, a functional prototype can be produced directly from a CAD file within hours rather than weeks.

That last property, rapid prototyping, is the reason additive manufacturing was chosen as the fabrication method for a lightweight tracked robot platform developed as a demonstrator. The platform is not the subject of this paper on its own terms; it is the applied case through which the technology classification and historical development discussed below translate into an actual design decision: material extrusion was selected over the alternative processes precisely because of the trade-offs described in the historical and classification sections below. The chassis design, the resulting material selection, and the design, dimensioning and fabrication of the tracked drive system are addressed in the sections that follow.

Additive manufacturing today spans mechanical, automotive, aerospace, biomedical and robotic engineering, and its role has expanded well beyond producing quick prototypes to include the development of finished, functional parts and production-grade components. Understanding how it reached that position, and how its main process families differ from one another, is a necessary starting point before any discussion of a specific fabrication choice.

HISTORICAL DEVELOPMENT OF ADDITIVE MANUFACTURING

The origin of additive manufacturing goes back to the early 1980s, when researchers first explored building physical objects layer by layer from digital data. The earliest documented account of this idea comes from the Japanese engineer Hideo Kodama, who in 1981 described a method for building a three-dimensional model by progressively hardening a UV-sensitive photopolymer one layer at a time (Kodama, 1981). Kodama did not secure patent protection in time, and the concept did not reach commercial application at that stage.

The turning point came in the mid-1980s. In 1986, the American engineer Charles Hull patented stereolithography (SLA), a process in which thin layers of photopolymer are cured by a directed ultraviolet light source (Hull, 1986).

Hull co-founded *3D Systems* the same year, the first company in the world dedicated exclusively to the production of 3D printers, and stereolithography became the first commercially available additive manufacturing technology.

Two more foundational processes followed within a few years, each hardening material by a different physical mechanism. In 1989, Carl Deckard, then a student at the University of Texas at Austin, patented Selective Laser Sintering (SLS), in which a laser selectively fuses particles of a powdered material into a solid mass (Deckard, 1989). Around the same time, Scott Crump developed Fused Deposition Modelling (FDM), in which a thermoplastic material is heated to a molten state and deposited layer by layer through a nozzle, filing the founding patent in 1989 (Crump, 1992). Crump and his wife founded *Stratasys*, which brought FDM to market, and after the original patent expired, opened the door to the low-cost desktop 3D printers now common in hobbyist and educational settings.

Through the 1990s and into the early 2000s, additive manufacturing gradually shifted from a tool limited to rapid prototyping toward direct production of functional parts. Metal-focused processes emerged in this period, chiefly Direct Metal Laser Sintering (DMLS) and Selective Laser Melting (SLM), enabling parts to be built from metal powder rather than polymer and opening the way to serious industrial application (Wohlers & Gornet, 2015). This shift in capability was accompanied by a shift in terminology: the industry and research community gradually moved away from the narrower term "Rapid Prototyping" toward the broader "Additive Manufacturing," a usage since formalized by the international standard ISO/ASTM 52900 (ISO/ASTM, 2021).

CLASSIFICATION AND GENERAL WORKFLOW OF ADDITIVE MANUFACTURING PROCESSES

General process workflow

Regardless of the specific process, every additive manufacturing technology follows the same underlying workflow, building a part layer by layer from a digital model (Godec et al. 2022).

The starting point is a CAD model of the part. Virtually every modern CAD package can export geometry suitable for additive manufacturing, on one condition: the model must be watertight, with no gaps or self-intersecting surfaces in its mesh, or the export that follows will fail to generate a consistent build path.

The watertight model is exported as an STL file, a mesh representation of the surface as a set of triangulated facets, which has become the de facto standard interchange format between CAD software and slicers regardless of the underlying additive process.

The STL file is then processed by slicer software, which cuts it into a stack of horizontal cross-sections of a chosen layer height and generates the machine-readable build path (G-code for material extrusion machines, or an equivalent exposure/scan pattern for laser-based processes) for each layer.

Once the model is sliced and the build path generated, the machine begins physical fabrication. Independent of the underlying technology, the same cycle repeats: one layer is completed, the build platform (or, in some processes, the tool) shifts by the height of that layer, and the cycle repeats until the part is complete. Most additive processes may also call for some form of post-processing, like support removal, cleaning of residual material, sandblasting or heat treatment, once the build finishes. How extensive this post-processing is depends on the technology and material used (Godec et al. 2022).

This shared workflow, from digital model to physical part, is illustrated in Figure 1, and is what separates additive processes from conventional subtractive manufacturing, regardless of how different the individual hardening mechanisms are from one another.

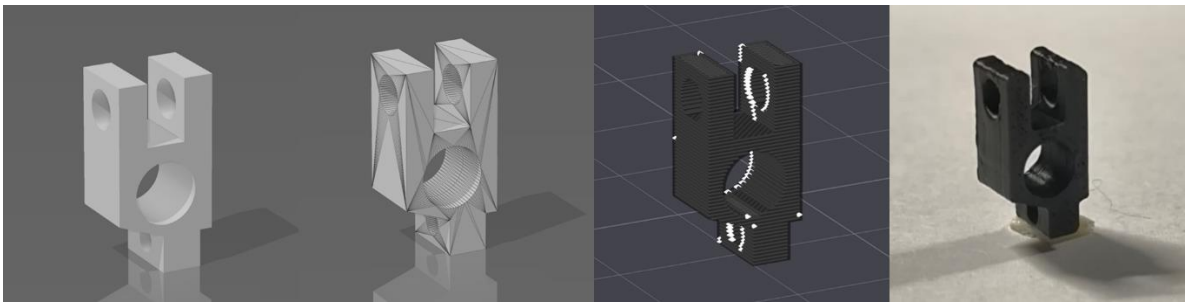

Figure 1 The additive manufacturing workflow applied to the track tensioner mount: solid CAD model; triangulated STL mesh export; sliced build path showing the generated toolpath; the finished part after fused deposition modelling

Classification of additive manufacturing processes

Despite a large number of commercial names and patented variants, additive processes can be grouped into a small number of categories based on the physical state of the feedstock and the mechanism used to consolidate it into a solid part. Four process families account for the large majority of current use: SLA, SLS, FDM and SLM/DMLS.

Photopolymer- and powder-based polymer processes (SLA and SLS)

Stereolithography (SLA) belongs to the category of processes in which a liquid photopolymer is selectively cured by directed light, most commonly a UV laser. The light source traces the cross-section of the current layer across the resin surface, causing local curing, after which the platform shifts by one layer height and a new liquid layer flows over the cured surface (Kodama, 1981; Hull, 1986). The cycle repeats until the part is complete.

Selective Laser Sintering (SLS) follows the same principle of layer-by-layer selective consolidation by a scanning laser, applied to a different feedstock state. A powdered material, spread in a thin layer across the build area, is struck by a laser that selectively heats and fuses (sinters) the particles exactly along the cross-section of the current layer (Deckard, 1989).

Material extrusion (FDM)

Fused Deposition Modelling (FDM) is based on extruding a thermoplastic filament, heated to its melting point and forced through a small nozzle that moves along the path defined by the cross-section of the current layer, depositing molten material onto the previously built layer, where it cools and solidifies (Crump, 1992).

FDM spans a wide material range for a single process. Common thermoplastics such as PLA, ABS and PETG cover general-purpose and educational use. Engineering-grade materials such as polyamide, polycarbonate and fiber-reinforced composites extend the process into higher strength and temperature applications. Flexible filaments such as TPU behave closer to rubber than to a rigid plastic, extending FDM into parts that need to bend or absorb impact rather than hold a fixed shape.

No other additive process has reached the accessibility of FDM. Where SLA and SLS require expensive, controlled build environments, FDM machines and materials are comparatively inexpensive, require no laser, no powder handling and no UV source, and the training needed for routine operation is minimal. Finished parts are, aside from any support removal, immediately usable, without the chemical post-curing SLA requires or the powder-recovery process SLS requires (Godec et al. 2022). Because switching between designs on an FDM machine is simply a matter of loading a new file, the process is particularly well suited to rapid prototyping and small production runs, where the geometry is expected to change across several design iterations before it is finalized.

That accessibility comes at a cost. FDM parts are mechanically anisotropic, meaning that the bond between printed layers is consistently weaker than the material itself, so a part is markedly weaker when loaded across layers than along them. Another limitation is surface resolution, limited on two independent axes: vertically, by the chosen layer height, which produces a visible stepped effect on curved surfaces regardless of print quality, and horizontally, by the nozzle diameter, which sets a hard lower bound on wall thickness and feature size that no amount of slicer tuning can overcome (Godec et al. 2022). For context, SLA achieves markedly finer surface detail, since its resolution is set by the width of the light source rather than a physical nozzle, and SLS achieves more isotropic mechanical properties without the pronounced interlayer weakness that characterizes FDM.

The trade-off is consistent across the comparison: FDM exchanges precision and mechanical isotropy for cost, simplicity and accessibility, which is exactly the exchange that favours it during the prototyping stage of product development, and exactly the exchange that stops favouring it once a part must carry a real structural or thermal load in service.

Metal powder-bed fusion (SLM/DMLS)

There is a point beyond which no thermoplastic, reinforced or not, can meet a part's requirements, whether because of temperature exceeding what a polymer can tolerate, a load that the anisotropy of a layered polymer structure would make risky to carry, or simply a functional need for the part to be metal.

At that point, additive manufacturing shifts from polymer to metal, and with that shift comes an entirely different set of technical requirements. Molten metal, unlike molten thermoplastic, has very low viscosity, which in turn means it behaves more like water than a thick paste, and cannot be extruded through a nozzle while holding a precise layer geometry.

For this reason, SLM and DMLS machines do not deposit molten metal at all. Instead, a thin layer of metal powder is selectively melted, point by point, by a laser, and solidifies as the laser moves on to the next location (Ponnusamy et al., 2020). Because metal particles at high temperature react readily with oxygen, the entire process takes place inside a chamber filled with inert gas, typically nitrogen or argon, preventing oxidation during the build.

SLM and DMLS are frequently used as synonyms, though a technical distinction exists between them: DMLS, a term originally introduced by EOS, denotes partial sintering, particles bond at the molecular level without complete melting, which is best suited to multi-component alloys, while SLM denotes complete melting into a homogeneous mass, suited to pure metals. In current practice, most machines achieve full melting regardless of the manufacturer's chosen name, making the distinction largely historical (Ponnusamy et al. 2020).

Commonly used metal powders include stainless steels, titanium alloys, aluminium alloys and nickel superalloys, selected according to the specific requirement of the application, like titanium for its strength-to-weight ratio or nickel superalloys for resistance to extreme temperature (Tuli et al. 2024).

Once the metal is fully melted, the resulting parts reach approximately 99% density, with mechanical properties comparable to a wrought part of the same composition (Ponnusamy et al., 2020), a fundamental departure from FDM, where interlayer anisotropy remains a permanent limitation regardless of process parameters. This combination of full geometric freedom, which allows for internal channels, lattice structures, topology-optimized forms, and forged-equivalent material quality is why SLM and DMLS are established in biomedical implants tailored to patient-specific anatomy, and in the aerospace and automotive industries (Ponnusamy et al. 2020).

Comparing FDM against metal powder-bed fusion is most useful not in terms of cost or mechanical properties directly, but in terms of the role each plays in product development. FDM is the technology of rapid materialization: hours, not days or weeks, separate a digital model from a physical prototype, which lets design decisions be tested physically before significant resources are committed, catches errors early, and keeps the cost of each design iteration low. In that phase, where the goal is to verify form, fit and concept, anisotropy and limited strength are an acceptable trade for the speed and accessibility FDM offers. Metal additive technologies enter the picture once a prototype needs to become a functional, service-reliable part, at which point the geometric freedom additive manufacturing offers becomes valuable precisely in combination with mechanical properties comparable to wrought metal (Ponnusamy et al., 2020). That is the point in development where the cost and complexity of the metal process become justified, because the alternative is conventional manufacturing with all of its own constraints on geometric freedom. The two technologies are, in that sense, not competitors but two steps along the same development path.

APPLICATION CONTEXT: FROM INDUSTRIAL PRODUCTION TO FIELD LOGISTICS

The capability to produce a finished, service-reliable metal part without tooling or a long production chain has found application across a wide range of industries. Two examples illustrate this shift: one from automotive manufacturing, the other from military field logistics.

In the automotive industry, metal additive manufacturing has moved beyond prototyping into structural, production-grade components. The clearest example is the *Czinger 21C hypercar*, built by *Czinger Vehicles* in partnership with *Divergent 3D*, whose chassis nodes and rear subframe are generatively designed by AI and then produced directly by metal powder-bed fusion in aluminium alloys, replacing the tooling, casting and stamping steps of conventional vehicle manufacturing entirely (Kerns, 2021). This combination of generative design and metal AM is the automotive-scale expression of the same geometric freedom discussed above in the context of biomedical and aerospace applications.

At the 2024 NATO exercise *Steadfast Defender*, the largest NATO exercise in Europe since the Cold War, the British Army used mobile 3D printers to fabricate spare parts directly in the field for the first time, under a program known as *Project Brokkr*, replacing the standard procedure of waiting for a replacement part to arrive from a depot (UK Ministry of Defence, 2024). This approach directly reduces dependence on long, costly supply chains, and gains particular significance for older vehicles whose parts are no longer available from the original manufacturer.

CHASSIS DESIGN AND FABRICATION

The robot chassis is the geometrically most complex single component in the platform (Figure 2), since it must simultaneously house the power and drive electronics, carry the loads transmitted by the torsion-spring suspension, the drive motor, and the track tensioning mechanism, and do so within two fixed physical constraints: the minimum

volume required by the components themselves, and the maximum build volume of the 3D printer, 180 mm along each axis.

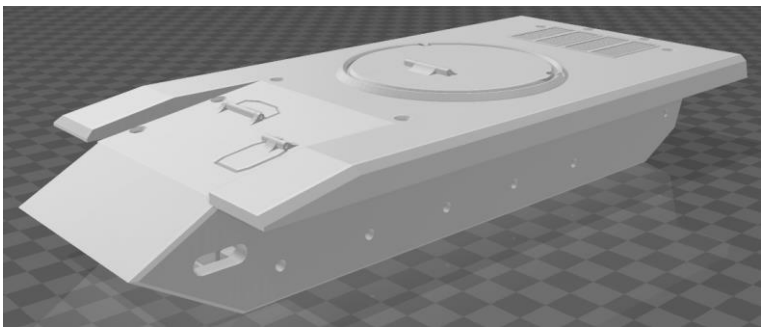

Figure 2 Model of platform's chassis

Material Choice

PLA was selected as the chassis material for two reasons directly tied to the constraints above. First, the component carries structural loads rather than needing to flex, so PLA's characteristic stiffness and brittleness, a limitation for the flexible track components discussed below, is an advantage here rather than a drawback. Second, PLA's low coefficient of thermal expansion limits shrinkage and warping during cooling, which is what makes the dovetail joint between the two printed halves viable at all: a material more prone to warping would introduce enough dimensional drift at the joint face to compromise the fit the slicer's automated dovetail profile depends on.

Spatial Constraints and Sectioning

The chassis body exceeds the printer's build volume on its own, with a total length of 230 mm. Rather than redesigning the geometry to fit within a single print, the body was split into two separate sections using the printer software's built-in model-cutting function, which generates a dovetail-profile joint at the cut automatically. The chassis lid was split the same way and for the same reason, giving the assembled chassis four printed sections in total. This gives each pair of halves a mechanically positioned connection without any additional fasteners, and the decision to leave the joints unengineered in the CAD model itself, relying on the slicer to resolve them, was made deliberately: defining fit tolerances at the design stage would have added time without a corresponding benefit, since the automated dovetail already provides adequate mechanical registration between each pair of halves.

Anisotrophy as a Design Parameter

FDM's characteristic anisotropy, discussed above as a general limitation of the process, was treated as a design parameter rather than an obstacle in three specific areas of the chassis. In the zones where the torsion springs introduce concentrated loads into the body, a local print-parameter override was used to increase wall count and infill density only within that region, without affecting the print settings of the rest of the part, raising local strength exactly where the layer-to-layer bond would otherwise be the weakest point in the structure, without adding unnecessary mass or print time elsewhere. The axle bushings and the track tensioner mount were oriented so that the working load acts along the plane of the printed layers, the strongest loading direction for an FDM part, while the precision bores for the axles were oriented perpendicular to the print plane, where FDM achieves its highest geometric accuracy.

DRIVETRAIN DESIGN AND FABRICATION

Following the fabrication of the robot chassis and the definition of the centre distance between the drive sprocket and the idler wheel, the design of the drivetrain proper begins.

Concept Selection

A continuous flexible track loop was selected over a conventional articulated segmented track. The primary motivation stems from the fact that the robot is fabricated by 3D printing: producing a functional articulated track at this scale would require printing a large number of miniature components, intricate assembly, and the insertion of metallic or plastic pins, increasing the risk of mechanical failure and complicating maintenance on a small-scale platform.

The continuous-loop approach instead allows the entire flexible element of the drive system to be manufactured in a single printing process using TPU, yielding a homogeneous structure. This eliminates mechanical joints, the points where friction and accelerated wear typically occur in a segmented track, extending the track's operational lifespan, and is significantly faster to manufacture, since the loop is produced as a single continuous body with integrated driving teeth for positive engagement with the drive sprocket. This also contributes to a reduction in the platform's overall mass.

Geometric Dimensioning of the Drive Sprocket

The chassis design imposed a strict spatial constraint, limiting the maximum outer diameter of the drive sprocket to 20 mm. All other transmission parameters, the sprocket's pitch diameter, tooth height, and track pitch, were derived from this primary constraint.

The drive sprocket was fabricated from PLA at 100% infill, chosen for its high strength, which improves durability under load despite the stress concentration inherent to gear teeth, and resists tooth wear over extended operation.

Standard theoretical gearing formulas served only as an initial baseline, since they assume a rigid mechanical element; the final geometry was established empirically through iterative printing, testing, and refinement. Engagement between the rigid sprocket and the printed track loop is governed by the circular pitch, the arc distance between adjacent tooth axes measured along the sprocket's pitch circle. The initial theoretical tooth root thickness of 3.556 mm produced excessive friction and mechanical binding when rounding curves, caused by the flexibility of the TPU track and microscopic filament bleed during printing, and was empirically reduced to 3 mm, which allowed smooth engagement at rotational speeds up to 200 rpm. The tooth itself was given a height of 2 mm and a top face width of 2 mm, with a slightly tapered trapezoidal profile at a 20° pressure angle, the standard engineering compromise between tangential and radial force, which here also lets the tooth enter and exit the track aperture at an angle without binding or deforming the track material.

Based on these derived and empirically adjusted parameters, the drive sprocket was modelled in CATIA (Figure 3), annotated with the dimensions used to generate the printing G-code.

A separate alignment problem emerged from the drive motor's output shaft, which proved too short to bring the sprocket into the same lateral plane as the idler and road wheels, causing the track to twist across its width during rotation instead of running flat. This was resolved by extending the rear face of the sprocket with an adjustable mounting boss, bringing the sprocket back into alignment with the rest of the drivetrain without requiring a longer motor shaft or a redesign of the wheel train itself (Figure 4).

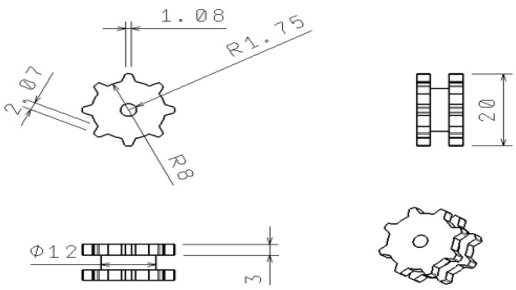

Figure 3 Model of the drive sprocket

Figure 4 Finished drive sprocket with added mount

Geometric Dimensioning of the Continuous Track

The track loop was fabricated from TPU as a continuous closed ring with internal gearing, chosen so the highly deformable, elastic loop could install directly onto the chassis and conform to the geometry of the wheels and guide elements without a separate assembly step.

Track pitch. Continuous power transmission at operating speeds up to 200 rpm without binding or destructive friction requires the pitch of the track's internal apertures to match the circular pitch calculated on the sprocket's pitch circle exactly.

Track cavity, thickness, and profile. Unlike the sprocket, where tooth thickness was empirically reduced to 3.0 mm, the track's apertures had to remain dimensioned to allow that same tooth to enter and exit freely along curved paths. As the TPU loop negotiates the drivetrain's 20 mm bend radius, it deforms and contracts slightly along its inner circumference; against the theoretical tooth root width of 3.556 mm, a functional backlash clearance of 0.556 mm was provided for smooth engagement. The internal drive teeth on the track are 2 mm high, the base track thickness

is 4 mm, sufficient to resist elongation and disengagement during motion, and a 4 mm guiding ridge works with the road wheels to further reduce the risk of track derailment.

Track length and segment count. The number of teeth must be an integer for the loop to close into a continuous ring without a pitch discontinuity; the calculation yielded 68 internal cavities, and prototype testing confirmed this segment count, combined with the elastic deformability of the TPU, produces optimal tensioning across the chassis frame. Total track length was determined from the perimeter of the triangle formed by the idler, support, and drive wheels, giving a maximum usable length of 478 mm and a minimum of 465 mm; the tensioning system's axial movement of the idler wheel accommodates this range.

CAD modelling in CATIA. The track loop was modelled to maintain a constant pitch of 6.89 mm around its full perimeter, with the pitch circle diameter derived from the target total loop length. A construction circle of 149.14 mm diameter was defined in the Sketcher workbench to represent the track's neutral kinematic axis, and the cross-sectional profile of a single tooth was defined within its corresponding 5.29° angular sector. A circular pattern replicated this segment 68 times around the central axis; because the pitch circle diameter was mathematically exact, the final segment closed seamlessly into the first, producing a continuous, internally geared ring without pitch error or geometric discontinuity (Figure 5). The finished track loop, printed in TPU, is shown in Figure 6.

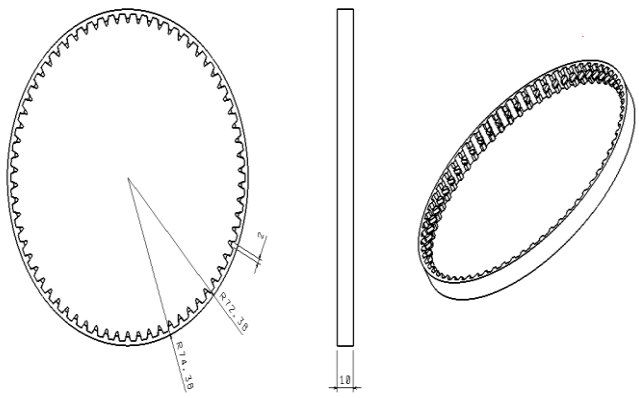

Figure 5 Model of the circular ring with internal gearing

Figure 6 The completed TPU track loop after printing

MATERIAL SELECTION FOR THE DRIVETRAIN

The development of modern unmanned ground platforms and lightweight military robots requires materials that balance structural strength, ductility, resistance to environmental factors, and minimal self-mass. A hybrid concept combining two thermoplastic polymers, Polylactic Acid (PLA) and Thermoplastic Polyurethane (TPU), was selected for the rigid structural elements and flexible components of the drive system respectively (Demirtas et al. 2023).

PLA: Structural Components

The dimensional stability behind the chassis' dovetail joint, discussed above, follows from PLA's specific thermal behaviour: a glass transition temperature between 55 °C and 65 °C, a melting point between 150 °C and 180 °C, and a low coefficient of thermal expansion that results in minimal shrinkage during cooling and limits warping at the corners of a printed part (Demirtas et al. 2023).

The mechanical properties of printed PLA components are anisotropic and depend directly on layer orientation, extrusion temperature, and infill density. An optimally printed PLA component is characterized by a tensile strength between 50 MPa and 70 MPa, comparable to certain cast aluminium alloys under static stress; a Young's modulus between 3 GPa and 3.5 GPa, which imparts significant stiffness and resists shaft deflection under track tension; and high compressive strength, though the material remains brittle, with elongation at break of only 2–6%.

TPU: Flexible Track Components

For continuous track loops and road wheel rings, which are constantly subjected to dynamic fatigue, repetitive bending, and terrain abrasion, high elasticity, shock-absorption capacity, and durability are essential, requirements PLA cannot meet but which TPU fulfils directly. TPU is a linear segmented block copolymer of alternating soft and hard segments, with hardness measured on the Shore scale; TPU 95A, or the slightly softer TPU 85A, is most commonly used for mobile robot tracks (Demirtas et al. 2023).

TPU 95A exhibits elongation at break exceeding 400%, with high elastic recovery, allowing track segments to articulate over small-diameter drive sprockets and tension idlers without cracking or strain-fatigue failure. As a polymer, it also shows exceptionally low abrasive wear against sand, damp soil, and gravel, making it considerably more durable than conventional natural rubber under similar operating conditions. Its high mechanical energy absorption further attenuates dynamic impacts from ground irregularities within the material itself, preventing shock transmission to the rigid PLA wheels and chassis frame (Jayswal et al. 2022).

CONCLUSIONS

Additive manufacturing has moved from a rapid-prototyping niche into a production-grade fabrication method spanning polymer and metal processes, each defined by a distinct trade-off between accessibility, precision, and mechanical performance. Among these, material extrusion offers the combination of low cost, minimal training requirement, and design flexibility that makes it the appropriate choice for early-stage development of small robotic platforms, despite its inherent limitations in surface resolution and interlayer strength.

This trade-off was validated in practice through the design and fabrication of a lightweight tracked robot platform. PLA was selected for the structural chassis and drive sprocket, where its stiffness and dimensional stability under cooling supported a two-part, dovetail-jointed chassis design and a wear-resistant drive wheel, while TPU was selected for the continuous track loop, where its high elongation at break and elastic recovery allowed a single-piece, internally geared ring to articulate over a small-diameter sprocket without cracking or fatigue failure. The resulting drivetrain, a 68-tooth TPU track loop engaging a 20 mm PLA sprocket at a fixed circular pitch, demonstrates that a fully 3D-printed tracked mobility system, requiring no tooling and assembled from a small number of printed parts, is a viable approach for rapid, low-cost development of small mobile platforms.

Taken together, the process and material trade-offs discussed in the historical and classification sections of this paper translate directly into the design decisions behind the chassis and drivetrain, and the resulting prototype serves as a concrete demonstration that FDM, despite sitting at the accessible end of the additive manufacturing spectrum, is capable of producing a complete, functional mobility platform (Figure 7).

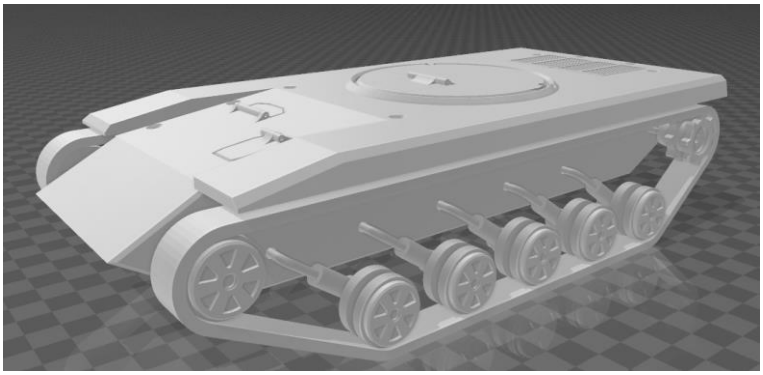

Figure 7 Model of completed platform

ACKNOWLEDGMENTS

This work was supported by the Ministry of Defence, Serbia, under the project „Modelling of Automotive Vehicle Assemblies for the Optimization of Dynamic Parameters", No. VA-TT/1/26-28.

REFERENCES

Crump, S. (1992). Apparatus and method for creating three-dimensional objects (U.S. Patent No. 5,121,329).

Deckard, C. R. (1989). Method and apparatus for producing parts by selective sintering (U.S. Patent No. 4,863,538).

Demirtas, B., Sevim, C. & Demirbas, M. D. (2026). Composition-dependent mechanical and thermal behavior of TPU-modified PLA and ABS filaments for FDM applications. *Polymers*, 18(8), 949. https://doi.org/10.3390/polym18080949

Godec, D., Pilipović, A., & Breški, T. (2022). General process workflow in additive manufacturing. In D. Godec et al. (Eds.), A guide to additive manufacturing (pp. 45–57). Springer International Publishing. https://doi.org/10.1007/978-3-031-05863-9_2

Hull, C. W. (1986). Apparatus for production of three-dimensional objects by stereolithography (U.S. Patent No. 4,575,330).

International Organization for Standardization/ASTM International. (2021). Additive manufacturing — General principles — Fundamentals and vocabulary (ISO/ASTM 52900:2021).

Jayswal, A., Liu, J., Harris, G., & Mailen, R. (2023). Creep behavior of 3D printed polymer composites. *Polymer Engineering & Science*, 63(11), 3519-3918. https://doi.org/10.1002/pen.26486

Kerns, J. (2021). Metal 3D printing in automotive: How the Czinger 21C is redefining next-generation car manufacturing. Metal AM Magazine, 7(4). https://www.metal-am.com/articles/metal-3d-printing-in-automotive-how-the-czinger-21c-is-redefining-next-generation-car-manufacturing/

Kodama, H. (1981). Automatic method for fabricating a three-dimensional plastic model with photo-hardening polymer. *Review of Scientific Instruments*, 52(11), 1770–1773. https://doi.org/10.1063/1.1136492

Ponnusamy, P., Rahman Rashid, R. A., Masood, S. H., Ruan, D., & Palanisamy, S. (2020). Mechanical properties of SLM-printed aluminium alloys: A review. *Materials*, 13(19), 4301. https://doi.org/10.3390/ma13194301

Tuli, N. T., Khatun, S., & Rashid, A. B. (2024). Unlocking the future of precision manufacturing: A comprehensive exploration of 3D printing with fiber-reinforced composites in aerospace, automotive, medical, and consumer industries. *Heliyon*, 10(5), e27328. https://doi.org/10.1016/j.heliyon.2024.e27328

UK Ministry of Defence. (2024). World-leading 3D printer used by British Army in the field for first time. GOV.UK. https://www.gov.uk/government/news/world-leading-3d-printer-used-by-british-army-in-the-field-for-first-time

Wohlers, T., & Gorne, T. (2015). *History of additive manufacturing*. https://wohlersassociates.com/wp-content/uploads/2022/08/history2015.pdf

The 11th International Congress
Motor Vehicles & Motors 2026
Kragujevac, Serbia
October 8th - 9th, 2026

Motor Vehicles & Motors

MVM2026-070
https://doi.org/10.24874/CMVM2026.070
Original scientific paper

Dobrivoje Ćatić[1]
Vladimir Ćatić[2]

A COMBINED FTA-FMEA PROCEDURE FOR PRODUCT DEVELOPMENT

ABSTRACT: Reliability and safety assessments of complex technical systems require a comprehensive understanding of component dependencies and potential failure mechanisms. While Fault Tree Analysis (FTA) and Failure Modes and Effects Analysis (FMEA) are widely implemented standalone methodologies, they exhibit inherent limitations regarding either detailed criticality assessment or systemic interdependency modelling. This paper presents a structured procedure for the combined application of FTA and FMEA methods in the product development phase. By leveraging a deductive fault tree construction and integrating it with an inductive FMEA worksheet, the proposed framework establishes a robust sequential approach where FTA qualitative and quantitative outputs – such as minimal cut sets and structural importance measures – directly enhance risk prioritization. Furthermore, to mitigate complexity and optimize time management, a recursive execution model across the system's structural hierarchy is introduced. The integrated approach ensures the swift isolation of critical areas in both design and manufacturing processes, thereby fostering targeted quality and reliability improvements.

KEY WORDS: failure analysis, combined FTA–FMEA, product development

KOMBINOVANI FTA-FMEA POSTUPAK U RAZVOJU PROIZVODA

REZIME: Procene pouzdanosti i bezbednosti složenih tehničkih sistema zahtevaju sveobuhvatno razumevanje međusobnih zavisnosti komponenti i potencijalnih mehanizama otkaza. Iako su Analiza stabla otkaza (FTA) i Analiza načina i posledica otkaza (FMEA) široko primenjivane samostalne metodologije, one pokazuju inherentna ograničenja u pogledu detaljne procene kritičnosti ili modeliranja sistemskih međuzavisnosti. Ovaj rad predstavlja strukturirani postupak za kombinovanu primenu FTA i FMEA metoda u fazi razvoja proizvoda. Povezivanjem deduktivnog pristupa konstrukcije stabla otkaza i njegovim integrisanjem sa induktivnim FMEA obrascem, predloženi okvir uspostavlja robustan sekvencijalni pristup u kome se kvalitativni i kvantitativni izlazi FTA analize - kao što su minimalni preseci događaja i mere strukturne važnosti – direktno koriste za poboljšanje prioritetizacije rizika. Pored toga, radi smanjenja kompleksnosti i optimizacije upravljanja vremenom, uveden je rekurzivni model izvršavanja kroz strukturnu hijerarhiju sistema. Integrisani pristup obezbeđuje brzo izdvajanje kritičnih mesta kako u konstrukciji, tako i u proizvodnim procesima, čime se omogućavaju ciljana poboljšanja kvaliteta i pouzdanosti.

[1] *Dobrivoje Ćatić, Full Profesor, Faculty of engineering, University of Kragujevac,34000 Kragujevac, 6 Sestre Janjić Street, Serbia, caticd@kg.ac.rs, https://orcid.org/0000-0003-3636-8301*
[2] *Vladimir Ćatić, Software engineer, HTEC Group, Bulevar Milutina Milankovica 7Đ, Belgrade 11070, Serbia, vladimir.catic@htecgroup.com*

KLJUČNE REČI: analiza otkaza, kombinovana FTA-FMEA), razvoj proizvoda

INTRODUCTION

Reliability analysis of technical systems is based on the failure analysis of their components. For failure analysis of technical systems and their components, a number of methods have been developed. Among these methods, Fault Tree Analysis (FTA) and Failure Modes and Effects Analysis (FMEA) are the most widely used (Modarres et al. 2021; Berg, 2023). FTA is a deductive analytical method in which, for a predefined top event representing the failure of the considered structural unit or system, the causal events leading to that failure are identified. The FTA method was developed in the early 1960s in the United States for the reliability and safety assessment of military systems. The method is particularly suitable for analysing systems whose failures could result in catastrophic effects for human life and the environment. FMEA is an inductive method for performing a qualitative analysis of the reliability and safety of a system, proceeding from the lowest to the highest system level (Carlson, 2020). It is based on the examination of all potential failure modes of the system components and their effects on the overall system, with the objective of identifying those failure modes that have the most severe impact on system performance.

The standalone application of FTA and FMEA methods for risk assessment is time-consuming and does not provide a comprehensive insight into the criticality of system components and their failure modes. Combining these methods leverages their respective strengths while simultaneously minimizing their limitations. A significant contribution to this field is presented in (Peaters et al. 2017), which proposes a method where FTA and FMEA are applied recursively across different system levels. In this approach, FTA is first utilized to identify potential causes of system failures, after which FMEA is applied to assess the criticality of the identified failures. This procedure is repeated at various levels of the system hierarchy, thereby enabling a detailed analysis of system behaviour and a more efficient identification of critical components. Further development of integrated methods is presented in (Shafiee et al., 2019), which proposes an integrated FTA-FMEA model for risk analysis in complex engineering systems. In this approach, the minimal cut sets identified by FTA are used to determine the importance of individual events within the system. The obtained values are then used to modify the Risk Priority Number (*RPN*) index within the FMEA, resulting in a more accurate risk assessment and better identification of critical system components.

Although the aforementioned studies demonstrate the benefits of integrating FTA and FMEA, they often lack a structured, step-by-step procedure suitable for the dynamic environment of the product development phase. To address this gap, this paper proposes a novel integrated framework that operationalizes the combined FTA-FMEA method through a structured, recursive algorithm executed across the system's structural hierarchy. The main contribution of this work lies in the methodological linking of Concept, Design, and Process FMEA within a single cause-and-effect chain derived directly from the fault tree, combined with the application of specific risk intervention thresholds based on Pareto analysis. This approach significantly reduces analytical complexity and execution time, providing engineering teams with a practical tool to isolate critical system units and root causes of failure simultaneously.

FAULT TREE ANALYSIS

Fault Tree Analysis (FTA) operates as a top-down, deductive analytical approach designed to identify the root causes of a specific system-level failure, known as the top event. The graphical representation utilizes Boolean logic gates (primarily AND and OR gates) to map the causal pathways from basic component failures to the undesirable system state. The primary objective of qualitative FTA is the determination of minimal cut sets, which represent the smallest combinations of basic events that can collectively cause the top event to occur (Birolini, 2024). Quantitative analysis subsequently utilizes these cut sets to calculate the overall system failure probability and determine the structural importance of individual events. While highly effective for complex dependency modeling, standalone FTA requires substantial specialized system knowledge and does not inherently prioritize risk based on operational severity or detectability (Ericson, 2021; Zafiropoulos, 2026).

FAILURE MODES AND EFFECTS ANALYSIS

Failure Modes and Effects Analysis (FMEA) and its extended variant for criticality analysis, Failure Modes, Effects, and Criticality Analysis (FMECA), represent methods for analyzing the reliability of technical systems. According to (Lazor, 1995), FMEA can be defined as a systematized group of procedures intended for:

- identifying and evaluating potential product failures and their effects;
- determining measures and activities to eliminate or reduce the probability of failure occurrence and
- documenting the previous two procedures.

As a basis for the evaluation procedure of solutions in the product development phase (product or production process designs), the following are considered:

- potential product failure modes and their probabilities of occurrence in operation;
- potential effects of failures manifested toward the user or the environment and
- the capability to detect the potential cause of failure (error) during the product and technology development phase, thereby preventing the manufacture of non-conforming products.

In accordance with the foregoing, all potential failure modes must be quantified based on their probability of occurrence, the significance of their effects, and the planned measures for design verification. Evaluation is conducted through the failure occurrence risk factor (O), the failure effect risk factor (S), and the detection risk factor of the failure cause (D), based on the expert assessment of the FMEA team members. Based on the estimated risk factor values, the Risk Priority Number (RPN) is determined as their product.

Depending on the specific focus within the product lifecycle, FMEA is deployed through three interrelated variants: Concept FMEA, Design FMEA, and Process FMEA, forming a methodological hierarchy from abstract system functions down to final manufacturing processes (Lazor, 1995; Carlson, 2020).

COMBINED APPLICATION OF FTA-FMEA METHODS

The standalone application of FTA and FMEA methods has certain limitations. Constructing a fault tree for complex technical systems is time-consuming, leading to delayed results during the product development phase. The focus of fault tree analysis is placed on analysing the root causes of failures that lead to system failure. The consequences of failures on the potential system breakdown, people, and the environment are not considered. In addition, the FTA method has limited capabilities regarding component criticality analysis. FMEA focuses on the analysis of individual components and often neglects complex interdependencies between various events within the system. FMEA is not suitable for application in complex technical systems. Consequently, numerous researchers have proposed integrated approaches that combine FTA and FMEA to leverage the advantages of both methods and mitigate their individual limitations.

The combined FTA-FMEA method utilizes deductive and inductive approaches as needed. The constructed fault tree for the adopted top event, the constituent components, and their functions are considered in parallel. The objective of the method is to perform a comprehensive analysis of the causes, modes, and consequences of component failures based on the constructed fault tree and the completed FMEA worksheet. The fault tree enables a complete analysis of cause-and-effect relationships between events. Procedures defined within the FMEA method are used to analyse the criticality of component failure modes. The results of the quantitative fault tree analysis, in the form of minimal cut sets of events, enable the correction of RPN values and an improved risk assessment. The columns of the FMEA worksheet regarding failure modes, causes, and consequences of component failures are filled out based on the constructed fault tree. This implies that the results of the FTA method are used as an input for the FMEA analysis, representing a sequential approach.

In order to reduce the time required to obtain results on element criticality in complex technical systems, as well as to minimize the complexity of the analysis, it is expedient to execute the combined FTA-FMEA recursively across the structural levels. The example of FMEA in the product development phase illustrates a sequential analysis execution that could be fully applied to the combined FTA-FMEA method.

From the perspective of the subject of analysis in the product development phase, there are three types of FMEA methods (Lazor, 1995; Carlson, 2020): Concept FMEA**,** Design FMEA**,** and Process FMEA. All three types of the FMEA method utilize the same operational methodology and the same form for documenting the procedure. The differences between them lie in the subject of analysis, the time of implementation, the company function driving the activity, etc.

There is a methodological correlation between the aforementioned FMEA procedures in the product development phase, as illustrated in Figure 1. As can be seen from the figure, Process FMEA is based on the results of Design FMEA, which in turn is based on the results of Concept FMEA. The cause-and-effect chain represents a hierarchical ladder of the operational system-spanning from the production process, through the component, to the system itself. In other words, it moves from the cause of failure to the failure mode, and from the failure mode to its effects, all of which are monitored and supported by the FMEA method.

Figure 1 also illustrates the sequence of FMEA application at different levels during the product development phase. By analysing the system's operating principles, potential failure modes can be identified, resulting in the total or partial failure to achieve the system's target function. A detailed, individual analysis of each system failure allows for the identification of the causes and effects of those failures. The causes of a system failure are, in fact, the failures of its components. Furthermore, analysing the causes of component failures reveals the errors in the

production process that induce them. Likewise, a system failure represents the effect of a component failure, just as a component failure represents the effect of an error in the production process.

Based on the foregoing, it can be concluded that in order to achieve efficient application of the FMEA method and rational time management, Concept FMEA should be conducted first. Upon identifying the critical components of the system, a Design FMEA is performed for those specific components. Finally, based on the results of the preceding analyses, a Process FMEA is carried out for the production processes that cause the critical failure modes of the components. In this manner, the analyst's attention is directed toward the true root causes of failure, allowing for the swift detection of critical areas in both design and the manufacturing process.

Types of FMEA	Product Process	Function	Effects of failure	Failure mode	Cause of failure
Concept FMEA	System name	Function of system	Influence on user and environment	Failure of the system	Failure of the component
Design FMEA	Component name	Function of component	Failure of the system	Failure of the component	Process fault
Process FMEA	Process name	Process function	Failure of the component	Process fault	Cause of process fault

Figure 1 Methodological connection between different types of FMEA methods in product development phase

Analogous to the described procedure, the combined FTA-FMEA method can also be implemented recursively. A proposed procedure for determining critical units across the system's structural levels using the combined FTA-FMEA method is presented in Figure 2. The procedure includes only the essential steps of FTA and FMEA that enable the identification of critical elements that exert a limiting effect on the reliable and safe operation of the system:

1. Forming the team for combined FTA-FMEA. Upon establishing the need to implement a combined FTA and FMEA method, the first step involves forming a team of experts. To organize the activities and appoint the responsible person (leader) for forming the team within the enterprise, appropriate guidelines for the FMEA method could be utilized. Most frequently, the project manager also serves as the team leader. The selection of the remaining team members is conducted through an agreement between the person responsible for forming the team and the managers of the professional departments from which the members are appointed.

2. Work plan and preparation for analysis are of the utmost importance for the successful implementation of the combined FTA-FMEA procedure. In the preparatory phase, the team leader uses relevant documentation (project brief, basic data on the product and product structure, technical specifications, design documentation, test reports, maintenance manuals, customer complaints, etc.) to familiarize the team members with the structure and operational principles of the system under consideration. To analyse potential system failures, it is necessary to record and code all structural units, which is most easily achieved by creating a structural block diagram. After gaining familiarity with the subject of analysis, each team member prepares relevant documentation and information regarding the subject from the specific field covered by their functional department within the company. The collected information is processed using statistical methods and made available to other team members through the team leader. Based on the gathered information, each team member draws their own conclusions.

3. Analysis of potential failures can be performed using the Fault Tree Analysis (FTA) method. At the beginning of this analysis, the definition is provided, and the boundaries and objectives of the mechanical system are established. For practical reasons, all assumptions relating to the system that will be used in subsequent work are stated.

The top event in the fault tree, depending on the analysed system, can be general (in the form of a system failure) or specific (if it includes only certain states of the system or its components). A careful choice of the top event is crucial for the success of the analysis. If the event is too general, the analysis becomes cumbersome and unmanageable. Conversely, if the event is too specific, the analysis does not provide sufficient insight into the system. The top event must be fully defined so that causal events can be clearly identified.

Analysts are required to thoroughly study the system from the standpoint of its structure, operating principles, and the interrelationships of its constituent elements before proceeding to construct the fault tree. Only a complete understanding of how the system and its elements' function, as well as knowledge of their interconnections, enables the execution of a logical analysis that determines the necessary and sufficient conditions for the realization of the top event.

The constructed fault tree forms the basis for qualitative and quantitative analysis (Lazor, 1995). Qualitative fault tree analysis refers to the process of constructing and logically analysing the fault tree, determining the set of

minimal cut sets, analysing common causes, etc. Determining the set of minimal cut sets provides the foundation for most quantitative-type fault tree analyses. A cut set is a basic event or a combination of basic events whose occurrence leads to the top event. A minimal cut set is a cut set of basic events that cannot be reduced any further while still causing the top event. Similarly, a set of minimal cut sets is a collection comprising all the minimal cut sets for a single tree that cannot be reduced. Among the quantitative fault tree analysis procedures, the most frequently used in practice are the ranking (comparison) of basic events according to their structural importance, the ranking of basic events according to their importance regarding the probability of occurrence, and determining the probability of the top event's occurrence as a function of the basic events' occurrence probabilities. The structural importance of a basic event in a fault tree is determined based on the frequency of its appearance in minimal cut sets and the number of members within those sets.

Based on the constructed fault tree, the causes of potential failure modes of constituent components can be identified. Although this activity is not an inherent part of the FTA analysis itself, for the purpose of risk factor assessment, it is necessary at this stage to record the planned control measures for detecting the causes of failure.

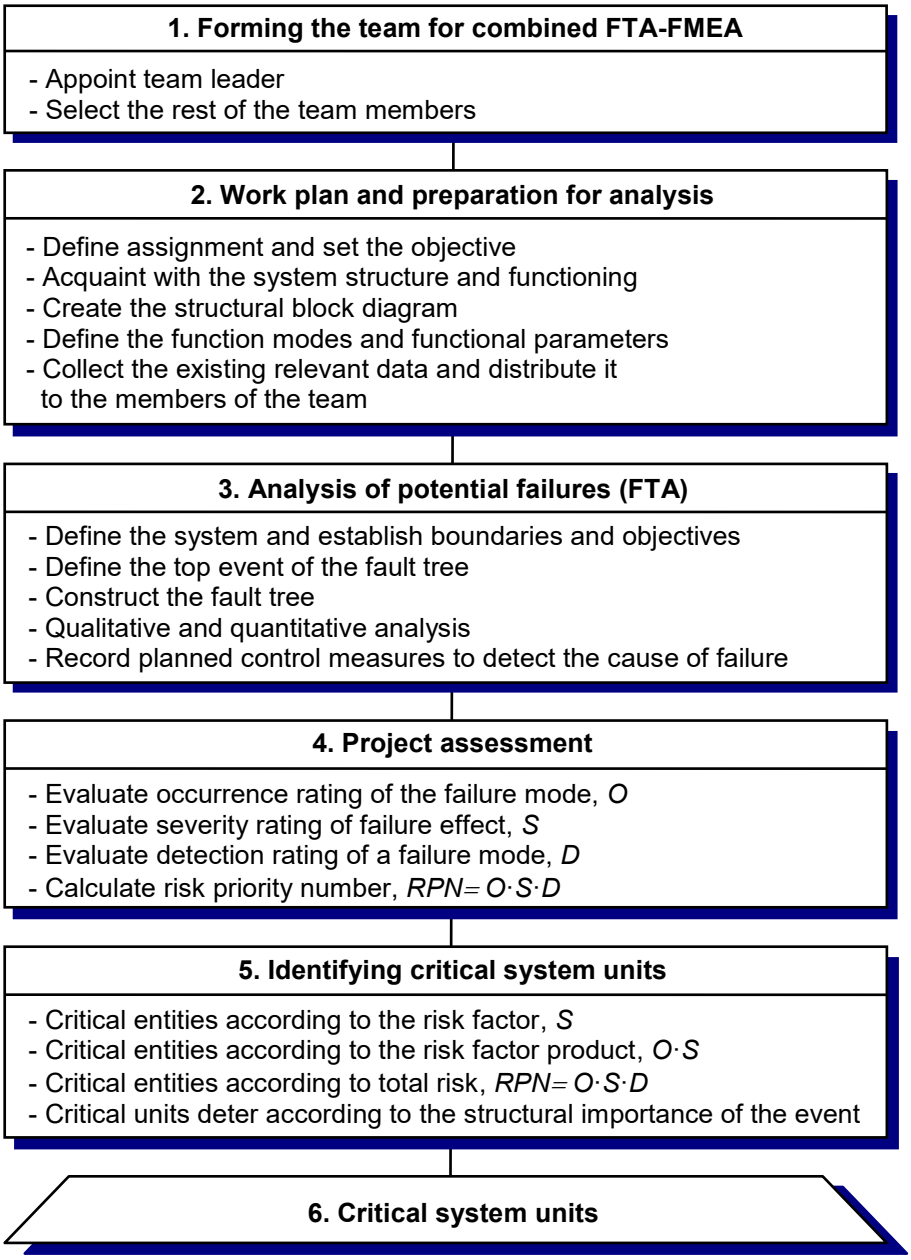

Figure 2 The algorithm of the methodology of the combined FTA-FMEA methods

4. Design evaluation. As previously stated, in the design evaluation phase, based on the collected data for each failure cause-failure pair, a team assessment is conducted for the failure occurrence risk factor (*O*), the severity of the failure effects (*S*), and the detection risk factor of the failure cause (*D*). The overall risk factor (Risk Priority Number – *RPN*) is calculated as their product. Furthermore, the estimated and calculated risk factor values provide the basis for identifying the critical units of the considered object from the perspective of reliability and operational safety.

5. Identifying critical system units. The assessment of failure mode criticality should be carried out in the following sequence (Lazor, 1995):

1. the failure mode has an effect (*S*) with a severity rank of 9 or 10;
2. the product of the failure occurrence risk factor (*O*) and the failure effect risk factor (*S*) exceeds a critical value determined by the agreement of the FMEA team members and
3. the Risk Priority Number (*RPN*) value exceeds a critical value adopted by the agreement of the FMEA team.

As supplementary information for identifying the most critical units of the considered mechanical system, the results of the quantitative fault tree analysis can be utilized – specifically, the analysis of the structural importance of basic events within the fault tree.

6. Critical system units. As a final result of the combined application of the FTA-FMEA methods, the critical units of the considered object of analysis are, among other things, obtained. Given that a complex dataset is generated, the combined FTA-FMEA team must adopt criteria regarding the significance of individual results. Through a comprehensive and objective analysis of the obtained results, those critical units that exert a limiting effect on the reliable and safe operation of the considered object of analysis can be isolated.

Ultimately, applying the Pareto principle within this integrated framework demonstrates that focusing mitigation efforts on the top 20% of critical product defects can yield a 70 – 80% overall improvement in quality and operational safety (Lazor, 1995). The established criteria and orientation thresholds for risk evaluation serve as a practical foundation for engineering teams to optimize time, manage complex datasets, and efficiently implement preventative and corrective measures in modern manufacturing and design environments.

CONCLUSIONS

The integration of Fault Tree Analysis (FTA) and Failure Modes and Effects Analysis (FMEA) provides a more effective and comprehensive solution for evaluating the reliability of complex technical systems compared to their standalone applications. By linking the deductive nature of FTA with the inductive structure of FMEA, this combined methodology successfully addresses the individual limitations of both techniques, bridging the gap between root cause isolation and systematic criticality analysis. A key contribution of the described procedure is its recursive application across the structural hierarchy of a system during the product development phase. Moving systematically from Concept FMEA, through Design FMEA, and finally to Process FMEA ensures that the analyst's focus remains directed toward the true root causes of failure. The inclusion of quantitative FTA results – specifically minimal cut sets and structural importance rankings – provides objective data that significantly refines the determination of Risk Priority Numbers (RPN).

ACKNOWLEDGMENTS

This research was supported by the Faculty of engineering, University of Kragujevac [grant number 451-03-34/2026-03/200107, dated February 05. 2026].

REFERENCES

Berg, H. A. (2023). *FMEA fundamentals: Mastering failure mode and effect analysis quickly*. Quality Engineering Series.

Birolini, A. (2024). *Reliability engineering: Theory and practice* (9th ed.). Springer.

Carlson, C. S. (2020). *Effective FMEAs: Achieving safe, reliable, and economical products and processes using failure mode and effects analysis*. John Wiley & Sons.

Ericson, C. A. (2021). *Fault tree analysis primer* (2nd ed.). Kindle.

Lazor, J. D. (1995). Failure mode and effects analysis (FMEA) and fault tree analysis (FTA) (success tree analysis - STA). In W. G. Ireson, C. F. Coombs, & R. Y. Moss (Eds.), *Handbook of reliability engineering and management* (2nd ed., pp. 6.1–6.46). McGraw-Hill.

Modarres, M., Kaminskiy, M. P., & Krivtsov, V. (2021). *Reliability engineering and risk analysis: A practical guide* (3rd ed.). CRC Press.

Peeters, J. F. W., Basten, R. J. I., & Tinga, T. (2018). Improving failure analysis efficiency by combining FTA and FMEA in a recursive manner. *Reliability Engineering & System Safety*, *172*, 36–44. https://doi.org/10.1016/j.ress.2017.11.024

Shafiee, M., Enjema, E., & Kolios, A. (2019). An integrated FTA-FMEA model for risk analysis of engineering systems. *Applied Sciences*, *9*(6), 1192. https://doi.org/10.3390/app9061192

Zafiropoulos, E. (2026). Reliability analysis using fault tree analysis: An updated review. *International Journal of Systems Reliability*, *14*(2), 115–128.

The 11th International Congress
Motor Vehicles & Motors 2026
Kragujevac, Serbia
October 8th - 9th, 2026

Motor Vehicles & Motors

MVM2026-073
https://doi.org/10.24874/CMVM2026.073
Original scientific paper

Milan Blagojević[1]
Milan Bojović[2]
Živče Šarkoćević[3]

REVERSE ENGINEERING OF A COMPLETE VEHICLE FOR THE DEVELOPMENT OF A MODULAR VEHICLE PLATFORM

ABSTRACT: This paper presents a case study of the complete reverse engineering of a road vehicle for which technical documentation does not exist. An existing production vehicle with no available technical documentation was used as the physical reference for creating a reusable digital platform. The vehicle was completely disassembled and digitized over five working days. A TRITOP photogrammetric system established the global reference network, while an ATOS Compact Scan 5M structured-light scanner with the MV600 measuring volume captured detailed surface geometry. Measurement data were processed in ATOS Professional, and the polygonal models were converted into engineering CAD geometry in Geomagic Design X. The global digitization accuracy was estimated at approximately 0.1 mm from the photogrammetric residuals. The resulting digital platform provides a geometric basis for multiple special-purpose variants, including a fire-fighting vehicle and other superstructure configurations.

KEYWORDS: reverse engineering, vehicle digitalization, structured-light scanning, photogrammetry, modular vehicle platform

REVERZNI INŽENJERING KOMPLETNOG VOZILA KAO OSNOVA ZA RAZVOJ MODULARNE PLATFORME

REZIME: U radu je prikazana studija slučaja kompletnog reverznog inženjeringa drumskog vozila za koje ne postoji tehnička dokumentacija. Postojeće serijski proizvedeno vozilo korišćeno je kao fizička osnova za kreiranje digitalne platforme namenjene višestrukoj upotrebi. Vozilo je potpuno rastavljeno i digitalizovano tokom pet radnih dana. Globalna referentna mreža uspostavljena je fotogrametrijskim sistemom TRITOP, dok je detaljna geometrija površina snimljena skenerom strukturirane svetlosti ATOS Compact Scan 5M, sa mernim volumenom MV600. Merni podaci obrađeni su u softveru ATOS Professional, a poligonalni modeli pretvoreni su u inženjersku CAD geometriju u softveru Geomagic Design X. Globalna tačnost digitalizacije procenjena je na približno 0,1 mm na osnovu

[1] *Milan Blagojević, Univesity of Pristina, Faculty of Technical Sciences, Knjaza Miloša 7, Kosovska Mitrovica, milan.blagojevic@pr.ac.rs, https://orcid.org/0000-0003-0710-5297*
[2] *Milan Bojović, University of Kragujevac, Faculty of Engineering, Sestre Janjić 6, Kragujevac, milan.bojovic@uni.kg.ac.rs, https://orcid.org/0000-0002-8655-1668*
[3] *Živče Šarkoćević, Univesity of Pristina, Faculty of Technical Sciences, Knjaza Miloša 7, Kosovska Mitrovica, zivce.sarkocevic@pr.ac.rs, https://orcid.org/0000-0001-5110-6620*

fotogrametrijskih reziduala. Dobijena digitalna platforma predstavlja geometrijsku osnovu za razvoj više varijanti vozila posebne namene, uključujući vatrogasno vozilo i druge konfiguracije nadgradnje.

KLJUČNE REČI: reverzni inženjering, digitalizacija vozila, optičko 3D skeniranje, fotogrametrija, modularna platforma

INTRODUCTION

Reverse engineering converts information obtained from a physical object into a digital engineering model. The established workflow comprises data acquisition, preprocessing, segmentation, surface fitting and CAD-model generation (Várady et al. 1997). The required level of geometric interpretation depends on the intended use of the reconstructed model (Buonamici et al. 2018). For a complete vehicle, the task therefore extends beyond surface acquisition: component positions, assembly relationships and functional interfaces must be retained in a form suitable for subsequent engineering work.

The investigated case concerned a production vehicle for which technical documentation does not exist. Although the customer has vehicle-manufacturing capabilities, the limited planned series did not justify development of a new base vehicle and dedicated tooling. The study objective was to establish a verified geometric basis that could be reused for a fire-fighting variant and other vehicle configurations. This follows the product-platform principle of sharing a common technical basis across a family of related products (Simpson, 2004).

CASE STUDY AND RECONSTRUCTION REQUIREMENTS

The reconstruction scope was defined at vehicle, assembly and component levels. The required output was not a visually complete digital replica, but an editable assembly containing the overall envelope, principal structural geometry and interfaces needed for positioning future superstructures. All measured elements therefore had to be expressed in a common coordinate system while preserving their relative positions.

Systematic disassembly was necessary to expose surfaces and components that could not be measured in the assembled condition. The acquisition sequence was planned before disassembly so that every stage remained connected to the vehicle reference system. This provided traceability between the original assembly state, the individual measured components and the subsequent CAD reconstruction.

MEASUREMENT STRATEGY AND DIGITALIZATION

Measurement architecture

A hierarchical measurement strategy combined a vehicle-scale photogrammetric reference network with dense local structured-light acquisition. This separation was required because nominal sensor performance within one measuring volume does not directly characterize the accuracy of a large dataset assembled from numerous sensor positions. The two systems were therefore treated as connected levels of the measurement chain, in accordance with the principles of multi-view optical measurement described in VDI/VDE 2634-3 (2008) and ISO 10360-13 (2021). Table 1 summarizes the equipment configuration and its role in the workflow.

Table 1 Measurement and data-processing systems used in the study

System	Configuration	Role in the workflow
TRITOP	Photogrammetric reference network	Global coordinates and registration framework; residual-based accuracy estimate of approximately 0.1 mm
ATOS Compact Scan 5M	MV600; nominal local accuracy approximately 0.04 mm	Detailed full-field surface acquisition of the disassembled vehicle and its components
ATOS Professional	Photogrammetry and structured-light data processing	Image evaluation, scan transformation, registration and polygonal-mesh generation
Geomagic Design X	Mesh-to-CAD reverse-engineering environment	Feature recognition, surface reconstruction, parametric modelling and assembly preparation

Global photogrammetric reference network

Coded and uncoded reference points were distributed over the vehicle structure and the surrounding measurement area. Scale bars as calibrated references were included in the TRITOP image set, while convergent images and redundant observations provided network stability in accordance with close-range photogrammetric practice (Luhmann et al. 2020). ATOS Professional was used to calculate the three-dimensional marker coordinates and evaluate the photogrammetric residuals. These residuals were subsequently used as an indicator of global network accuracy.

Structured-light surface acquisition

Detailed surface geometry was acquired with an ATOS Compact Scan 5M based on fringe projection and stereoscopic triangulation, principles widely used for dense non-contact measurement of industrial surfaces (Sansoni et al. 2009). The MV600 configuration provides a measuring volume of approximately 600 × 450 × 450 mm and a nominal local measurement accuracy of approximately 0.04 mm. Components were captured from multiple orientations to reduce occlusions, and the reference-point network transformed the individual scans into the common coordinate system without relying solely on best-fit surface registration.

After each acquisition stage, the data were checked for missing regions, transformation instability and local artefacts before further components were removed. Representative stages of target placement and structured-light measurement are shown in Figure 1.

Figure 1 Vehicle digitalization: (a) reference-target placement; (b) structured-light scanning

DATA PROCESSING AND CAD RECONSTRUCTION

Polygonal-data processing

ATOS Professional was used to verify transformations, remove acquisition artefacts and generate polygonal surface models. The resulting meshes were inspected for continuity and completeness before being transferred to Geomagic Design X. This processing stage produced a consistent measured representation while retaining the common coordinate system established during acquisition.

CAD reconstruction and platform definition

CAD reconstruction combined recognized analytical features with manually defined sections, curves and freeform surfaces. Such a hybrid procedure is characteristic of industrial reverse engineering, where automatic feature extraction is supplemented by engineering interpretation (Várady et al. 1997; Buonamici et al. 2018). Reconstructed components were organized as an assembly, and coordinate systems and principal connection interfaces were defined for later modification. The result was editable engineering geometry rather than a collection of unrelated meshes (Raja & Fernandes, 2008). Figure 2 compares the polygonal input with the reconstructed CAD model.

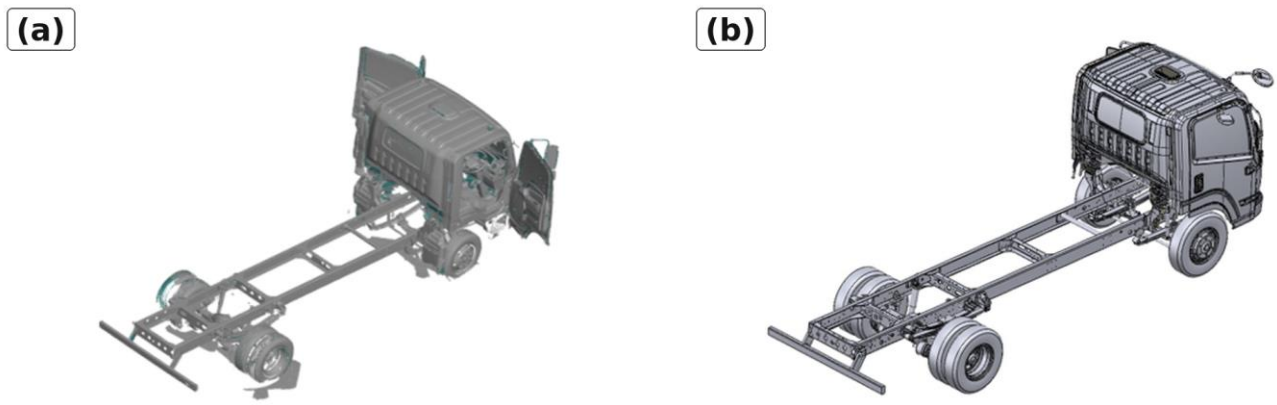

Figure 2 Vehicle geometry: (a) polygonal STL model; (b) reconstructed CAD model

RESULTS AND DISCUSSION

The complete digitalization campaign, including staged disassembly and measurement of exposed geometry, was completed in five working days. The photogrammetric residuals corresponded to an estimated global accuracy of approximately 0.1 mm. This value characterizes the consistency of the vehicle-scale reference network and integrated dataset; it is not a full measurement-uncertainty statement and should not be interpreted as the nominal local accuracy of the structured-light sensor.

The principal engineering result is an editable assembly in which the vehicle envelope, structural geometry and connection interfaces are represented in one coordinate system. This allows variant-specific superstructures to be developed without repeating complete vehicle digitalization and distributes the initial reconstruction effort across the intended product family (Simpson, 2004). The model provides geometric input for layout and interface development, but it does not independently define materials, design loads, manufacturing tolerances or regulatory compliance. These remain subjects of subsequent design and validation.

CONCLUSIONS

The presented case study demonstrates a systematic workflow for reconstructing a complete vehicle when technical documentation does not exist. Controlled disassembly, photogrammetric referencing and structured-light scanning enabled the geometry of the vehicle, its components and relevant interfaces to be integrated into a unified dataset. The estimated global accuracy of approximately 0.1 mm, derived from the photogrammetric residuals, was considered sufficient for the intended reconstruction.

The conversion of polygonal data into an editable CAD assembly provided a common digital platform for further engineering development. The reconstructed geometry can support packaging studies, design modifications, interference analysis and the development of different superstructure layouts. A fire-fighting variant represents one possible application of the platform.

Further work will include verification of selected functional and assembly interfaces; refinement of the CAD models and validation of the first vehicle configuration developed from the reconstructed platform.

ACKNOWLEDGMENTS

The part of this research is funded by Ministry of Science, Technological Development and Innovation of the Republic of Serbia, Contract No. 451-03-65/2024-03/200155.

REFERENCES

Buonamici, F., Carfagni, M., Furferi, R., Governi, L., Lapini, A., & Volpe, Y. (2018). Reverse engineering modeling methods and tools: A survey. *Computer-Aided Design and Applications*, 15(3), 443–464. https://doi.org/10.1080/16864360.2017.1397894

International Organization for Standardization. (2021). ISO 10360-13:2021 Geometrical product specifications (GPS)—Acceptance and reverification tests for coordinate measuring systems (CMS)—Part 13: Optical 3D CMS.

Luhmann, T., Robson, S., Kyle, S., & Boehm, J. (2020). *Close-range photogrammetry and 3D imaging* (3rd ed.). De Gruyter.

Raja, V., & Fernandes, K. J. (Eds.). (2008). *Reverse engineering: An industrial perspective*. Springer. https://doi.org/10.1007/978-1-84628-856-2

Sansoni, G., Trebeschi, M., & Docchio, F. (2009). State-of-the-art and applications of 3D imaging sensors in industry, cultural heritage, medicine, and criminal investigation. *Sensors*, 9(1), 568–601. https://doi.org/10.3390/s90100568

Simpson, T. W. (2004). Product platform design and customization: Status and promise. *Artificial Intelligence for Engineering Design, Analysis and Manufacturing*, 18(1), 3–20. https://doi.org/10.1017/S0890060404040028

University of Stuttgart, Institute for Metal Forming Technology. (2020). GOM ATOS Compact Scan 5M, https://www.ifu.uni-stuttgart.de/forschung/006_Anlagen/28_Atos.pdf

Várady, T., Martin, R. R., & Cox, J. (1997). Reverse engineering of geometric models—An introduction. *Computer-Aided Design*, 29(4), 255–268. https://doi.org/10.1016/S0010-4485(96)00054-1

VDI/VDE. (2008). VDI/VDE 2634 Part 3: Optical 3-D measuring systems—Multiple view systems based on area scanning.

The 11th International Congress
Motor Vehicles & Motors 2026
Kragujevac, Serbia
October 8th - 9th, 2026

Motor Vehicles & Motors

MVM2026-076
https://doi.org/10.24874/CMVM2026.076
Original scientific paper

Nenad Miloradović[1]
Rodoljub Vujanac[2]
Mirjana Piskulić[3]

WAREHOUSE SYSTEMS IN THE AUTOMOTIVE INDUSTRY: A COMPARATIVE STUDY OF STORAGE SYSTEMS, HANDLING EQUIPMENT AND SAFETY CLEARANCE

ABSTRACT: The paper presents a comparative analysis of the impact of storage methods, handling equipment, and safety clearance on the selection of warehouse systems in the automotive industry. Pallet racking systems are straightforward, efficient, and widely utilized for storing goods on pallets. They offer immediate and unhindered access to each pallet at any given moment. After defining the storage unit, the beams and upright frames were sized accordingly. Suitable handling and retrieval equipment was then selected. The layout of the racks within the warehouse was designed based on standard storage system principles. To ensure the proper design, manufacturing, assembly, and operation of warehouses, it is essential to accurately define the tolerances, deformations, and clearances of the system elements. Finally, proper structural components were chosen, the total warehouse capacity was determined, and a comparative analysis was done to evaluate both transverse and longitudinal pallet placement for selective racking.

KEYWORDS: warehouse, material handling equipment, storage and retrieval machines

SKLADIŠNI SISTEMI U AUTOMOBILSKOJ INDUSTRIJI: UPOREDNA ANALIZA SISTEMA SKLADIŠTENJA, OPREME ZA RUKOVANJE I SIGURNOSNIH ZAZORA

REZIME: U radu je prikazana uporedna analiza uticaja načina skladištenja, opreme za rukovanje robom i sigurnosnih zazora na izbor skladišnih sistema u automobilskoj industriji. Paletni regalni sistemi su jednostavni, efikasni i široko rasprostranjeni za skladištenje paletizovane robe. Oni omogućavaju trenutan i nesmetan pristup svakoj paleti u bilo kom trenutku. Nakon definisanja skladišne jedinice, izvršeno je odgovarajuće dimenzionisanje greda i stubova regala. Zatim je izabrana odgovarajuća oprema za rukovanje i preuzimanje robe. Raspored regala u

[1] *Nenad Miloradović, University of Kragujevac, Faculty of Engineering, 6 Sestre Janjić Str., 34000 Kragujevac, Serbia, mnenad@kg.ac.rs , https://orcid.org/0000-0001-6846-6091*
[2] *Rodoljub Vujanac, University of Kragujevac, Faculty of Engineering, 6 Sestre Janjić Str., 34000 Kragujevac, Serbia, vujanac@kg.ac.rs , https://orcid.org/000-0002-8215-5668*
[3] *Mirjana Piskulić, University of Kragujevac, Faculty of Engineering, 6 Sestre Janjić Str., 34000 Kragujevac, Serbia, mirjana.piskulic@kg.ac.rs , https://orcid.org/0009-0005-7199-1280*

skladištu je projektovan na osnovu standardnih principa skladišnih sistema. Da bi se obezbedilo pravilno projektovanje, izrada, montaža i rad skladišta, neophodno je precizno definisati tolerancije, deformacije i zazore elemenata sistema. Na kraju, izabrane su odgovarajuće strukturne komponente, određen je ukupan kapacitet skladišta i urađena je uporedna analiza kako bi se procenilo i poprečno i uzdužno postavljanje paleta kod selektivnih regala.

KLJUČNE REČI: skladište, oprema za manipulaciju materijalom, regalne dizalice

INTRODUCTION

The automotive industry operates on a massive scale. It requires high speed, accuracy, and efficiency. Every car is made of thousands of parts. Managing these parts is a complex job. Intralogistics, the movement of goods within a warehouse, is the backbone of this industry. Automotive supply chains rely heavily on Just-In-Time and Just-In-Sequence manufacturing. This means parts must arrive at the assembly line exactly when they are needed. Because of this, picking the right warehouse systems, handling equipment, and safety rules is important for the smooth operation of automotive factories.

The primary objective of modern storage systems is the efficient storage and rapid distribution of large quantities of goods within a designated space. A standard pallet racking system comprises three core components: the racks, the pallets, and the handling equipment or forklifts. Each component is selected based on the specific materials stored, operational demands, positioning systems, and the chosen management model (Vujanac & Miloradović, 2023). Generally, the spatial frame structure of a pallet rack consists of upright frames and horizontal beams. These are typically manufactured from thin-walled, cold-formed profiles to create the final rack configuration.

Selective pallet racking remains the most widely used solution, accommodating a diverse range of unit loads while providing direct access to every pallet (Miloradović & Vujanac, 2025). To upgrade standard layouts, double-deep pallet racking can be implemented, allowing each shelf to hold two rows of pallets instead of one. Alternatively, mobile pallet racking maximizes space utilization by eliminating multiple static aisles. Other highly efficient solutions include drive-in and drive-through racking systems. Additionally, pallet flow systems utilize gravity, wheels, or rollers to dynamically transfer and store pallets. The basic components of any pallet racking system include vertical frames, horizontal beams, baseplates with anchors, and row spacers. Applying European standards and regulations to the determined structural properties allows for a comprehensive analysis of the rack configuration and its individual components (EN 1993, 2005; FEM 10.2.02, 2000; EN 15512:2020+A1:2022, 2022).

Depending on the requirements placed on rack warehouses, a large number of different types of rack configurations have been developed. These requirements relate to storage capacity, storage methods, retrieval methods, the characteristics of the stored material, and the handling equipment used. Some of the characteristic pallet rack configurations are shown in Figure 1.

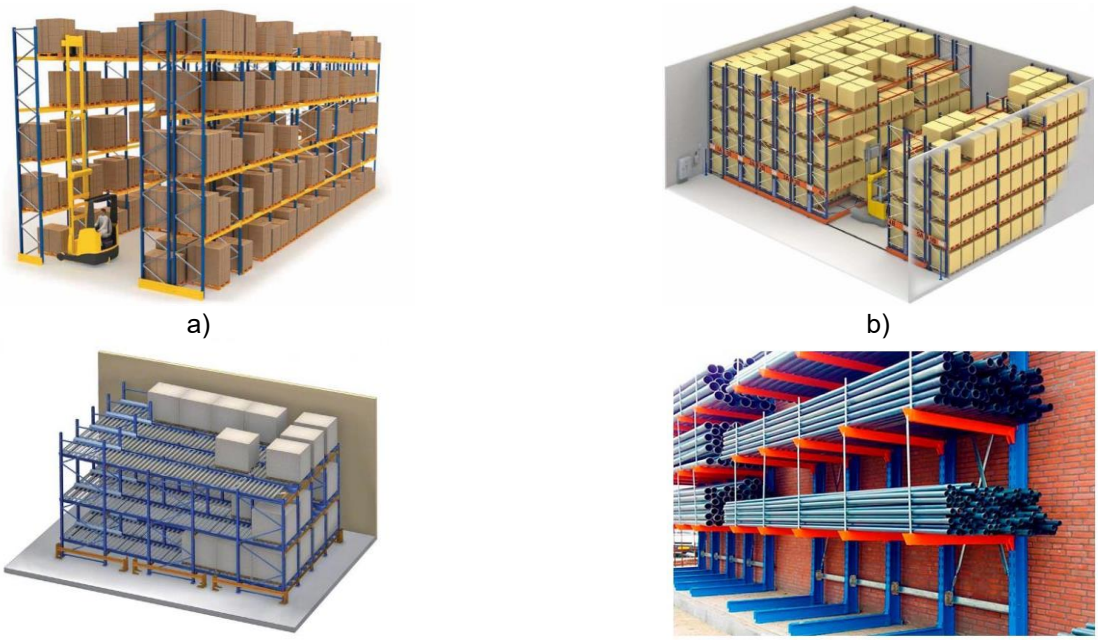

a) b) c) d)

Figure 1 Different types of pallet racks: a) self-supporting racks, b) mobile racks, c) pallet flow racks, d) cantilever racks

WAREHOUSE SYSTEM

The selection of racking structural components primarily depends on the available storage space and the characteristics of the storage unit.

Configuration of Pallet Racking

The spatial frame of a pallet racking system consists of side frames and horizontal beams, which are typically made from thin-walled, cold-formed steel profiles. Stability across the aisles is provided by a system of horizontal and vertical bracing. To ensure down-aisle stability, specialized beam-to-column connectors with features like tabs, studs, or hooks are either welded to the beams or integrated directly into them. These connectors lock into the column perforations, creating a rigid connection that keeps the entire structure stable along the corridor (Vujanac et al., 2020).

A typical selective pallet rack configuration is shown in Figure 2.

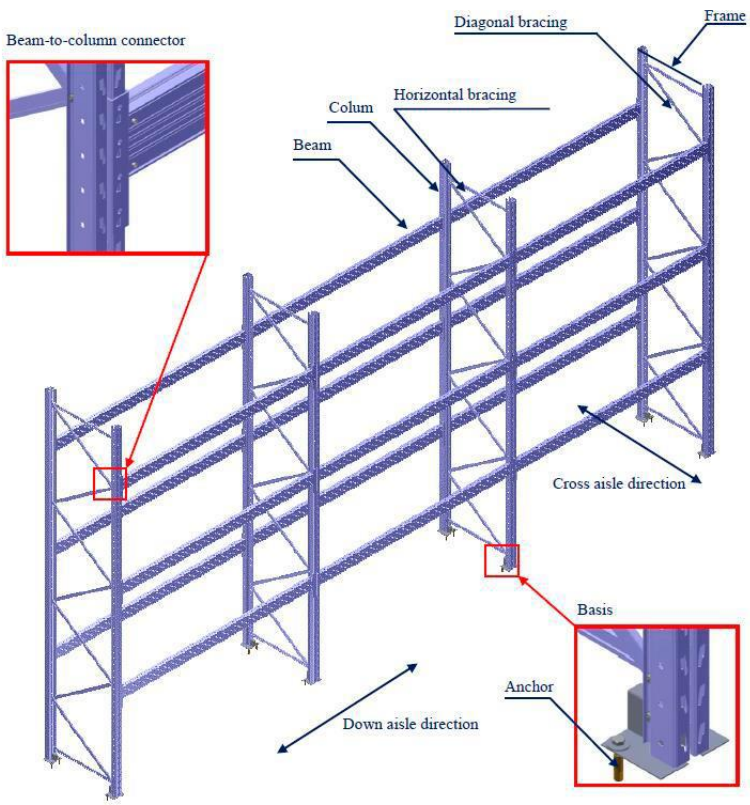

Figure 2 Typical configuration of a pallet rack structure

Storage and retrieval equipment

Forklifts commonly operate within rack warehouses, serving as a highly advanced type of material handling equipment that can actively retrieve, position, and vertically stack loads

To fulfil the investor's primary objective of maximizing storage capacity and volume within the available space, designers must thoroughly understand the capabilities of storage and retrieval equipment, the selection of which depends on:

- storage unit,
- frequency of the storage units entering into and exiting from the warehouse,
- orientation of the entrance - exit zones,
- the number of the storage units within the high-bay warehouse (storage capacity),
- warehouse connections with external transport.

In this manner, the primary advantage of such warehouses - maximizing space utilization and enhancing operational efficiency - will be fully realized.

Safety clearance

Adjustable pallet rack system can be installed in two configurations: wide aisle or narrow aisle pallet racking. In both solutions some protective components of pallet racking (rack protectors) are necessary even they are not mandatory equipment. Protective components for pallet racking have been designed, manufactured and applied in accordance with current EN standards and FEM regulations:

- Structural design in accordance with EN 15512. Steel static storage systems - Adjustable pallet racking systems - Principles for structural design, (EN 15512, 2009).
- Parameters for application in accordance EN 15620. Steel static storage systems - Adjustable pallet racking - Tolerances, deformation and clearances, (EN 15620, 2008).
- In terms of basic applications and installation locations of column and frame protectors EN 15629. Steel static storage systems - Specification of storage equipment, (EN 15629, 2008).
- In terms of dimensions, construction and required resistance to damage FEM 10.2.16. The Design and Use of Rack Protection for Adjustable Pallet Racking - Upright and Frame Protection, (FEM 10.2.16, 2017).

Correct protection of pallet rack systems against material handling equipment impacts is essential for preventing structural damage to the racking system. Upright protectors are designed as corner or internal protectors within the aisles. The frame guard shown in Figure 3 protects the corner and rear uprights with frame bracing. The allowable clearance within the rack bay is determined by the EN 15620 standard. The clearance between the edge of the upright protector and the side of the upright is also defined (≤40 mm), as shown in Figure 4 a). If the specified distance is greater, then the total clearance is additionally increased in accordance with the recommendations in Figure 4 b). Also, protectors must be designed to withstand and absorb the appropriate impact energy in accordance with standards.

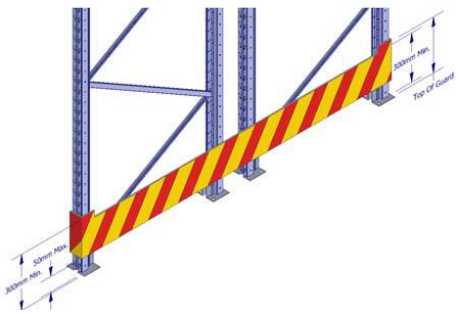

Figure 3 Frame protector

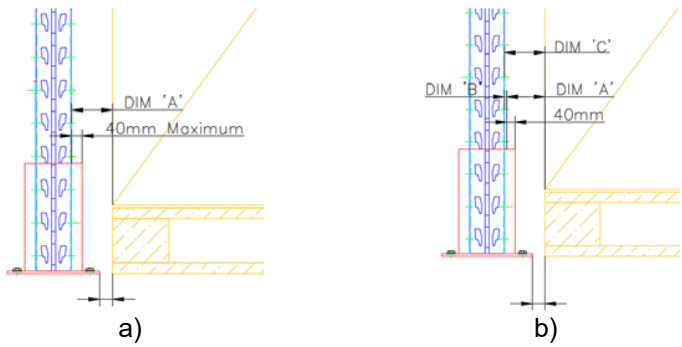

Figure 4 The minimum distance from the upright to the protector

A special place in storage technology belongs to the so-called narrow aisle racks, which are characterized by the corridor width that is sufficient only for the straight-line passage of the storage and retrieval machines (S/R) carrying the unit load, with very small operational clearances, (FEM 10.3.01., 1997; FEM 9.101., 1997).

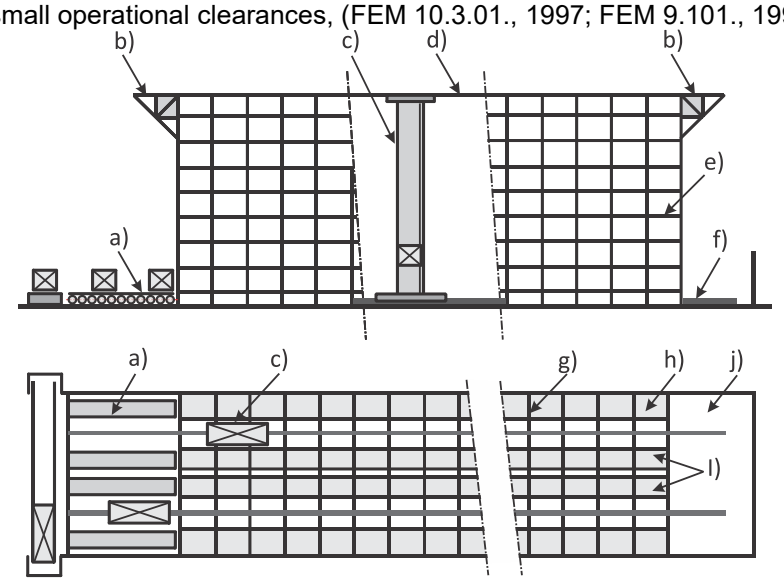

Figure 5 Narrow aisle racks: a) conveyors, b) S/R machines run-out, c) S/R machines, d) upper guide rail, e) beam, f) bottom rail, g) portal tie beam, h) single entry run, i) double entry run, j) maintenance area

Clearances exist to prevent collisions within the storage systems. Actually, they are required nominal distances between fixed and moving parts, taking into account all individual tolerances and deformations. The entry clearances are the clearances between the load make-up accessory and the load handling device. The rack compartment clearances exist between the unit load and the rack structure, while the aisle clearances are the clearances between

the outer most edge of the S/R machine and the outermost edge of the rack structure or the load, as well as the clearances at the rear of the stored load.

The calculation of clearances takes into account the following influencing factors: floor slab, floor rail, upper guide rail, unit load, S/R machines and rack structure.

The fork entry clearances that exist between the load handling device and the load make-up accessory are shown in Figure 6:

- X_1 - on the side of the load handling device which is the furthest from the mast,
- X_2 - on the side of the load handling device which is the closest to the mast,
- Y_1 - between the load handling device and the load supporting beam and
- Y_2 - between the load handling device and the load make-up accessory.

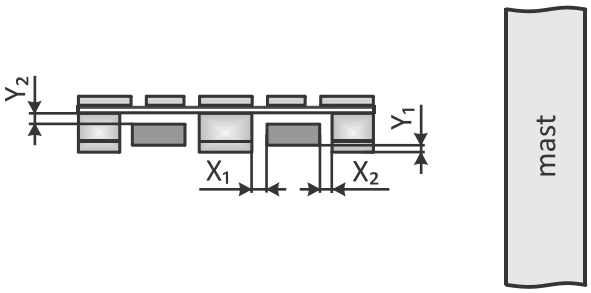

Figure 6 Fork entry clearances

The rack compartment clearances are the minimum distances shown in Figure 7:

- $X_{3.1}$ - between the unit loads and the uprights on the side which is the furthest from the mast.
- $X_{3.2}$ - between the unit loads and the uprights on the side which is the closest to the mast,
- X_4 - between the individual unit loads,
- Y_3 - between the top of the unit load and the rack structure and/or other obstructions,
- Y_4 - between the underside of the raised unit load and the top of the lower support beam,
- Y_5 - between the underside of the higher support beam and the top of the raised unit load.

While overly small clearances pose a risk to operational safety and can disrupt warehouse handling operations, excessively large clearances result in wasted storage space.

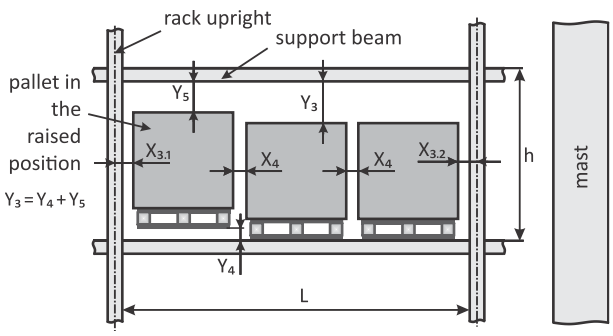

Figure 7 Rack compartment clearances

The aisle clearances are the minimum distances shown in Figure 8:

- $Z_{1.1}$ - between the unit load and any obstruction on the building side (e.g. building structure, rainfall pipe).
- $Z_{1.2}$ - between the unit load and the rack structure inner racks,
- $Z_{2.1}$ - between the outermost point of the lifting carriage or the unit load on the lifting carriage and the nominal position of the stored load or the rack structure with a protruding load in the stored position on the outer rack side,
- $Z_{2.2}$ - the same, on the inner rack side,
- $Z_{3.1}$ – between fixed obstructions on the S/R machine (e. g. lifting mechanism or platform) and the stored load or the rack structure. Outer rack side.
- $Z_{3.2}$ – the same, on the inner rack side.

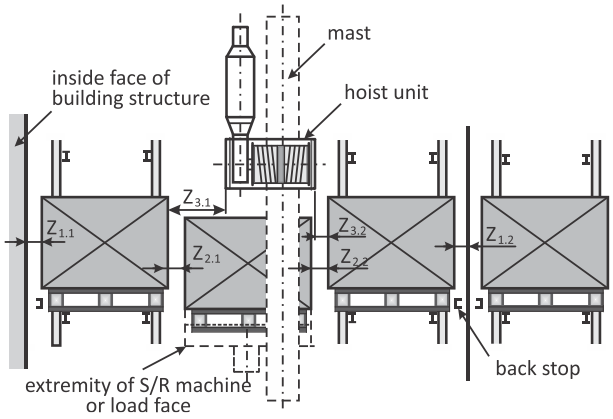

Figure 8 Aisle clearances

COMPARATIVE ANALYSIS

The proposed warehouse layout features a length of 34,500 mm, a width of 28,500 mm, and a height of 7,500 mm. Standard EURO pallets (800 mm x 1,200 mm) serve as the storage medium, with each unit measuring 1,200 mm in height and weighing up to 1,000 daN.

The facility is configured with separate entry and exit points located on opposite sides at the same elevation. For the storage framework, a modular, boltless racking system is utilized, where beam end connectors join the horizontal beams directly to the upright columns.

The comparative analysis focuses on how storage units are deposited into the selective racks. Consequently, the warehouse design evaluates both transverse and longitudinal pallet placement (Figures 9 and 10). For both stacking scenarios, specific parameters were established: standard beam length, upright frame height, and floor height clearance.

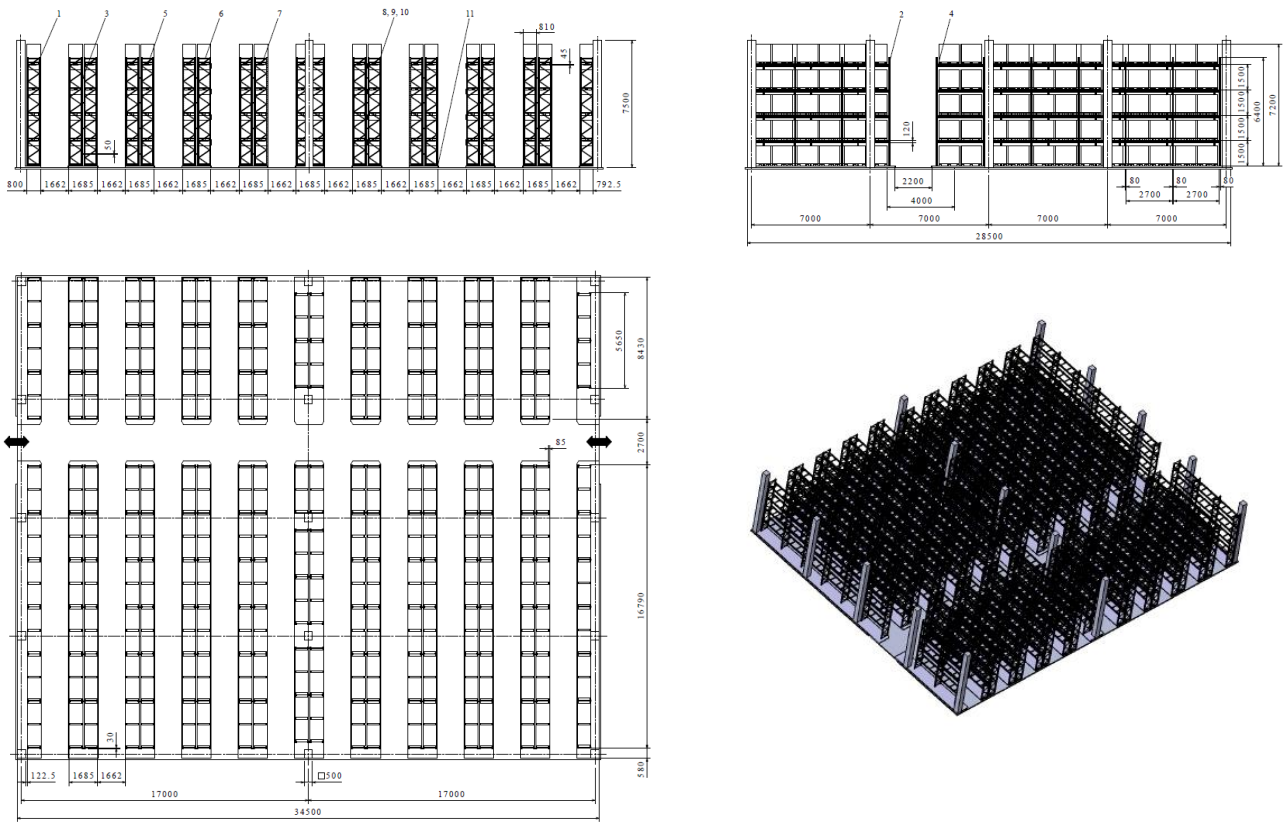

Figure 9 Warehouse layout with transverse pallet stacking

The material handling operations rely on a STILL NXV 16 very narrow aisle truck equipped with a swivel traverse fork. This vehicle offers highly flexible application across diverse loads and warehouse layouts, featuring a 1,500 kg lifting capacity, a 6,350 mm maximum lift height, and requiring a working aisle width of 1,662 mm.

The comparative analysis will be conducted based on the method of stacking storage units into the selective racks. Consequently, warehouse designs featuring both transverse and longitudinal pallet stacking were evaluated.

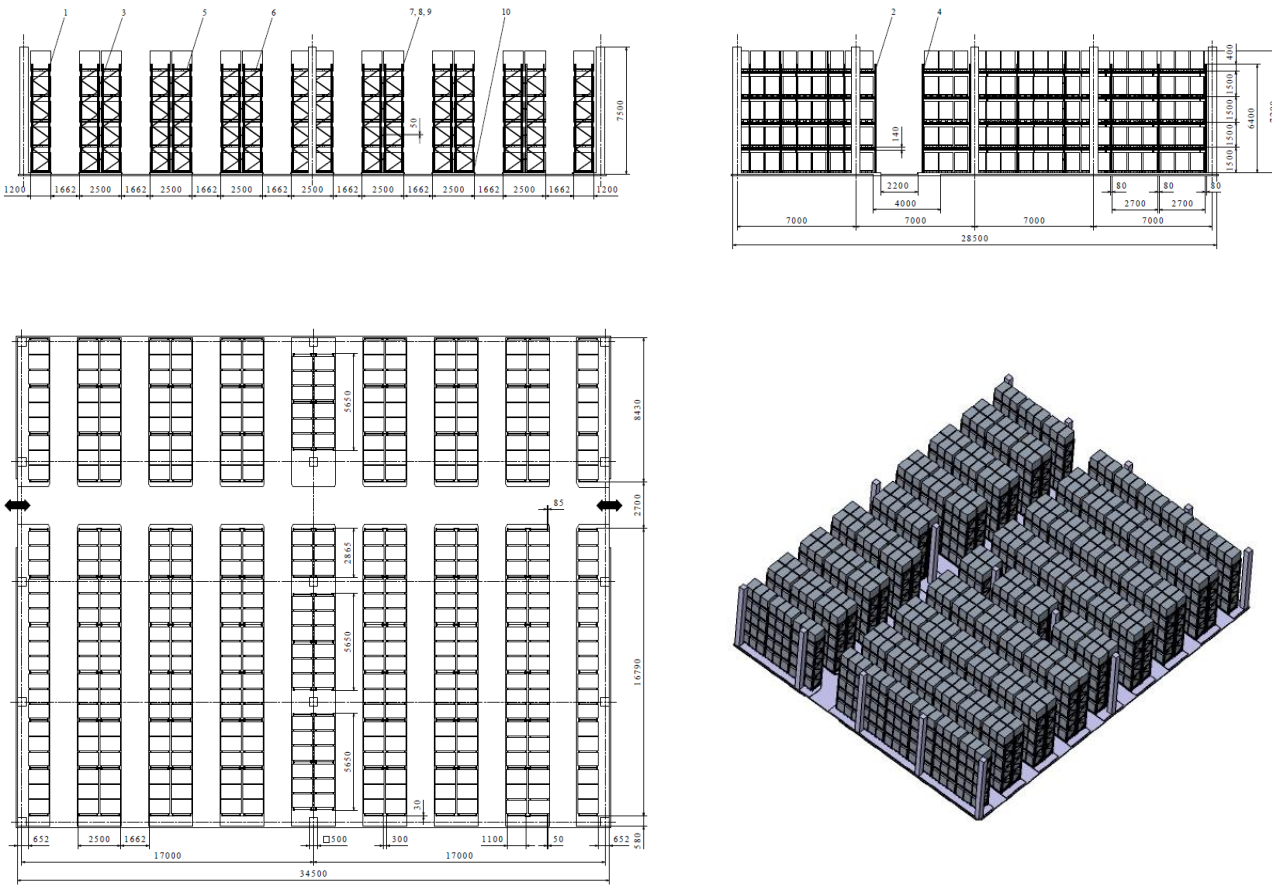

Figure 10 Warehouse layout with longitudinal pallet stacking

Based on the defined loads acting on the racking structure, it can be concluded that the structural load is greater in longitudinal stacking than in transverse stacking, specifically by the weight of one storage unit per bay. This assertion is further confirmed by the selected profiles for the upright frames and beams; the longitudinal configuration requires profiles with larger dimensions and higher load capacities than the transverse arrangement.

The comparative analysis of the rack layout refers to both the achieved capacity and the weight of the rack structure. The total weight of all elements of the rack support structure with transverse stacking is 37,088 kg, while with longitudinal stacking it is 28,683 kg.

Based on the data provided, it can be concluded that the optimal solution regarding the weight of the analysed racking configurations is the one with longitudinal stacking.

Considering the dimensions of the racks, the frame width is greater for longitudinal stacking. Although the racks for transverse stacking are more structurally compact, the longitudinal configuration achieves a 20% higher storage capacity while utilizing fewer racks.

Regarding the number of components, the longitudinal stacking configuration utilizes significantly fewer elements due to the lower number of racking rows.

CONCLUSIONS

Pallet rack damage can be extremely costly and dangerous. To prevent the collapse of the rack structure and the load itself, minimizing the risk of damage to pallet racking is one of the major challenges facing today's automotive warehousing industry.

In order to achieve maximum utilization of the storage space and work efficiency, in addition to the previously covered conditions, it is necessary to take into account certain design rules. These rules are reflected in the following: A single-row rack should be placed against the wall of the storage space. Placing racks in the same space in two different directions should be avoided, as this wastes a lot of space for manipulation and intersects transport routes.

Racks should always be placed along the longer side of the intended storage space, which results in fewer long corridors, reduces transport aisles, and increases the economic feasibility of the racks. Corridors should not be placed along the perimeter of the walls of the space.

Based on the achieved capacity, structural weight, and component count, the longitudinal stacking configuration proves to be more economical. Furthermore, the disadvantage of transverse stacking lies in the requirement for additional cross-beams, which increases both structural complexity and manufacturing costs.

ACKNOWLEDGMENTS

This research was supported by the Ministry of science, technological development and innovation of the Republic of Serbia, contract number 451-03-34/2026-03/200107.

REFERENCES

Vujanac, R., Miloradović, N. (2023). *Basics of storage and transport systems* (in Serbian). The Faculty of engineering of the University of Kragujevac, Kragujevac

Miloradović, N., Vujanac, R. (2025). Comparative analysis of applications of different storage systems. In *Proceedings of the 17th International Conference on Accomplishments in Mechanical and Industrial Engineering 'DEMI 2025*, 389–397

EN 1993 (2005). *Eurocode 3 - Design of Steel Structures*. Brussels, Belgium

FEM 10.2.02 (2000). *Design of Static Steel Pallet Racking*. Brussels, Belgium

EN 15512:2020+A1:2022 (2022). *Steel static storage systems - Adjustable pallet racking systems - Principles for structural design*. Brussels, Belgium

Vujanac, R., Miloradović, N., Vulović, S., Pavlović, A. (2020). A comprehensive study into the boltless connections of racking systems. *Metals*, 10(2), 276. https://doi.org/10.3390/met10020276

EN 15512 (2009). Steel static storage systems -Adjustable pallet racking systems - Principles for structural design. European Committee for Standardization. Brussels

EN 15620 (2008). Steel static storage systems - Adjustable Pallet Racking – Tolerances, deformations and clearances. European Committee for Standardization. Brussels

EN 15629 (2008). Steel static storage systems – Specification of storage equipment. European Committee for Standardization. Brussels

FEM 10.2.16 (2017). The Design and Use of Rack Protection for Adjustable Pallet Racking Upright and Frame Protection. European Racking Federation. Hitchin

FEM 10.3.01. (1997). Adjustable Beam Pallet Racking (APR) Tolerances Deformation and Clearances. Section X of FEM, Brussels, Belgium

FEM 9.101. (1997). Terminology Storage and Retrieval Machines Definitions. *Section IX of FEM*, Brussels, Belgium

SECTION

C

Vehicle Dynamics and Intelligent Control Systems

- Aerodynamics
- Vehicle Ride and Handling
- Intelligent Safety Systems
- Tires/Braking Systems/Steering/Suspension
- AI in Automotive Technology
- Autonomous Vehicles

The 11th International Congress
Motor Vehicles & Motors 2026
Kragujevac, Serbia
October 8th - 9th, 2026

Motor Vehicles & Motors

MVM2026-001
https://doi.org/10.24874/CMVM2026.001
Original scientific paper

Miroslav Demić[1]
Mikhail P. Malinovsky[2]
Andrija Vujičić[3]

THEORETICAL-EXPERIMENTAL APPROACH TO THE DEVELOPMENT OF A METHOD FOR IDENTIFYING THE HEAT DISSIPATION RATE OF MOTOR VEHICLE SHOCK ABSORBERS

ABSTRACT: This paper develops and presents a methodological framework for analysing thermal loading of passenger vehicle shock absorbers under conditions of stochastic road excitation. In contrast to conventional approaches based on simplified quarter- or half-vehicle models, the study employs a spatial 7-DOF model, enabling precise simulation of coupled heave, pitch, and roll dynamics. The key scientific contribution of the paper is the introduction of a nonlinear shock absorber model, in which the force is defined as a function of relative velocity and relative displacement of the piston with respect to the body, thereby achieving a higher level of energy consistency compared to linear viscous models. By formulating the governing equations in the state-space domain, a direct link is established between numerical simulation and automatic control methods (system identification, spectral analysis, and Singular Value Decomposition - SVD), enabling identification of the frequency distribution of dissipated thermal power directly from experimental data. The analysis of the coupling between excitation signals and the thermal power generated in the shock absorbers indicates a strong influence of nonlinearity, as the partial coherence function is below approximately 0.25. Since these results were obtained through dynamic simulation, apart from the negligible influence of numerical methods, no additional noise sources were present; thus, the low values can be attributed to the nonlinear parameters of the vehicle oscillatory systems. On the other hand, the analysis of partial transfer functions shows that the highest thermal power of the shock absorbers is generated up to approximately 30 Hz. Considering the characteristics of nonlinear oscillatory systems, this is evidently a consequence of the resonant frequencies of sprung and unsprung masses. The developed method can also be applied in experimental investigations, where it is necessary to simultaneously measure forces and relative velocities of the piston with respect to the shock absorber body. The application of the SVD method enables a more detailed analysis of heat generation within the shock absorbers.

KEYWORDS: passenger vehicle, 7-DOF model, shock absorber, thermal power, stochastic excitation, system identification, SVD method

[1] *Miroslav Demić, Ph.D., retired professor, University of Kragujevac, Faculty of Engineering Kragujevac, Sestre Janjić 6, Kragujevac, Serbia, demic@kg.ac.rs , https://orcid.org/0000-0003-2168-1370*
[2] *Mikhail P. Malinovsky, Ph.D., Moscow Automobile and Road Construction State Technical University (MADI), Federal State Unitary Enterprise "Central Scientific Research Automobile and Automotive Engines Institute" (FSUE "NAMI"), Moscow, Russia, ntbmadi@gmail.com , https://orcid.org/0000-0001-7812-5653*
[3] *Andrija Vujičić, Ph.D., Centre for Research and Development Activities in the Automotive Industry (CIRD), Belgrade, Serbia, andrija.vujicic@cird.rs , https://orcid.org/0009-0008-9526-9972*

TEORIJSKO-EKSPERIMENTALNI PRISTUP RAZVOJU METODE ZA IDENTIFIKACIJU GENERISANE TOPLOTNE SNAGE AMORTIZERA MOTORNIH VOZILA

REZIME U radu je razvijen i predstavljen metodološki okvir za analizu toplotnog opterećenja amortizera putničkog vozila u uslovima stohastičke pobude puta. Nasuprot konvencionalnim pristupima koji koriste uprošćene modele četvrtine ili polovine vozila, u istraživanju je primenjen prostorni model sa sedam stepeni slobode (7-DOF), koji omogućava preciznu simulaciju spregnutih vertikalnih i ugaonih kretanja (galopiranje i valjanje). Ključni naučni doprinos rada predstavlja uvođenje nelinearnog modela amortizera, gde je sila definisana kao funkcija relativne brzine i relativnog pomeranja klipa u odnosu na telo, čime je postignuta viša energetska objektivnost u poređenju sa linearnim viskoznim modelima. Formulisanjem jednačina u prostoru stanja, uspostavljena je direktna veza između numeričke simulacije i metoda automatskog upravljanja (identifikacija sistema, spektralna analiza i SVD metoda), što omogućava identifikaciju frekventne raspodele disipirane toplotne snage neposredno iz eksperimentalnih podataka. Analiza podataka o sprezi signala pobude i toplotne snage koja se razvija u amortizerima pokazuje veliki uticaj nelinearnosti, jer je parcijalna funkcija koherence manja od oko 0,25. Kako su ovi rezultati dobijeni dinamičkom simulacijom, osim veoma malog uticaja numeričkih metoda, drugih šumova nije bilo, pa se njihove niske vrednosti mogu objasniti uticajem korišćenih nelinearnih parametara oscilatornih sistema vozila. Sa druge strane, analiza parcijalnih prenosnih funkcija je pokazala da se najveća toplotna snaga amortizera razvija do oko 30 Hz, a imajući u vidu karakteristike nelinearnih oscilatornih sistema, očigledno je da je to posledica rezonantnih učestanosti oslonjene i neoslonjenih masa. Razvijena metoda se može koristiti i tokom eksperimentalnih istraživanja, kada je neophodno istovremeno registrovati sile i relativne brzine kretanja klipa u odnosu na telo amortizera. Primenom metode SVD je moguća detaljnija analiza stvaranja toplote u njima.

KLJUČNE REČI: putničko vozilo, model sa sedam stepeni slobode, amortizer, toplotna snaga, stohastička pobuda, identifikacija sistema, SVD metoda.

INTRODUCTION

The dynamic behaviour of passenger vehicles under real road excitation conditions represents one of the most challenging problems in modern vehicle dynamics, as it directly affects ride comfort, stability, and structural durability (Gillespie, T. D. 1992; Savaresi, S. M. et al. 2010; Poussot-Vassal, C. et al. 2012; Genta, G. 2003; Milliken, W. F. & Milliken, D.L. 1995; Mitschke, M. & Wallentowitz, H. 2004; Crolla, D. A. 1988; Rajamani, R. 2005; Demić, M. 1997).

In the scientific literature, research often focuses on control strategies and the thermal stability of suspension systems (Rajamani, R. 2005; Demić, M. 1997; Demić, M. & Diligenski, B. 2018). In (Savaresi, S. M. et al., 2010), the design of semi-active suspension control systems is analysed in detail, emphasising the importance of adaptive algorithms for improving vehicle performance. Similarly, (Poussot-Vassal, C. et al., 2012) provides a comprehensive review of control strategies, highlighting the advantages of semi-active systems over passive ones in terms of energy efficiency and response.

The issue of heat generation within shock absorbers under random excitation is crucial for component durability. In (Demić, M. & Diligenski, Đ. 2018), the thermal behaviour of shock absorbers subjected to real operating conditions is investigated. For the identification of parameters of such systems, (Demić, M. & Belingardi, G. 2011; Ljung, L. 1999) provide a theoretical basis that enables precise definition of the behaviour of complex dynamic systems through mathematical models.

A particular contribution to the modelling of shock absorbers and their influence on vehicle performance is given in (Demić, M. & Diligenski, Đ. 2016), where numerical simulations of the thermal loading of shock absorbers in semi-active systems are specifically developed, directly correlating with the need for cooling optimisation.

Although simplified models (quarter-vehicle or half-vehicle) are often used in the literature for easier numerical treatment, they cannot adequately represent the spatial coupling of motions nor enable a precise assessment of the energy balance and thermal loading of shock absorbers under real conditions. The primary objective of this paper is the development and verification of a methodological framework which, based on an advanced spatial vehicle model, enables objective identification of the thermal power of shock absorbers (Demić, M. & Diligenski, Đ. 2016; Lang, G. H. et al., 2007). In contrast to conventional approaches, the proposed method is based on:

- a spatial model with seven degrees of freedom (7-DOF), encompassing vertical and angular motions (pitch and roll), thereby achieving high fidelity in simulating the real vehicle response (Demić, M. 1997),

- a nonlinear constitutive model of the shock absorber, in which the force is not solely a function of velocity but also of the relative displacement of the piston, ensuring the energy objectivity required for accurate quantification of dissipated heat (Demić, M. & Belingardi, G. 2011), and
- integration with automatic control methods, establishing a direct link between numerical simulations and real service life testing measurements (Doyle, J. C. et al., 1992; Tomović, R. et al., 1974).

By formulating the model in the state-space domain, the application of spectral analysis and the Singular Value Decomposition (hereinafter SVD) method is enabled for identifying the frequency distribution of thermal power directly from the vehicle model or from experimentally measured kinematic quantities and forces (Rotenberg, V. 1972; Demić, M. 2026). In this way, the paper goes beyond the scope of theoretical vibration analysis and offers a practical method applicable in real testing, thereby providing a systematic basis for optimising shock absorber design and their cooling systems under real operating conditions.

METHOD

Since the objective of this study was to define a method for assessing the thermal loading of shock absorbers under real conditions, it was considered appropriate to develop it using a spatial nonlinear vehicle model subjected to random vibrations due to motion over an uneven road surface. The developed method can also be applied during experimental investigations.

It is well known that, in practice, models of varying levels of complexity exist; however, the aim should always be to adopt a model of minimal structure that includes the parameters of interest for the analysis, as will be discussed further.

Vehicle vibratory model

The analysis is based on a spatial model of a passenger vehicle with seven degrees of freedom (7-DOF), which includes:

- vertical motion of the sprung mass,
- angular motions about the transverse and longitudinal axes (pitch and roll),
- vertical motions of the four unsprung masses (Demić, M. 1997).

In this way, simultaneous consideration of the coupled vertical–angular response and the individual dynamics of each wheel under spatially distributed stochastic road excitation is enabled. The geometric parameters (wheelbase, track width, positions of the centres of mass), masses, and moments of inertia are defined on the basis of a real vehicle.

The equations of motion are formulated using the Newton–Euler equations and expressed as a system of second-order differential equations, which, for numerical solution, are transformed into a system of first-order differential equations.

In contrast to the classical linear viscous model, in which the force is proportional to relative velocity, this study adopts an extended constitutive model of the shock absorber, ensuring the energy objectivity required for accurate quantification of heat dissipation, in which the force depends on (Demić, M. & Belingardi, G. 2011):

- the relative velocity between the piston and the housing,
- the relative displacement between the piston and the housing.

The mathematical relations will be presented later in the text. This formulation enables a more objective representation of the real behaviour of the shock absorber, particularly in regimes where nonlinear and hysteretic effects are present. From an energy perspective, it provides a direct link between the mechanical work of the force and energy dissipation in the form of heat.

It is emphasised that the aim of this paper is not to analyse the mechanisms of heat transfer and dissipation, but exclusively to quantify heat generation as a consequence of mechanical energy dissipation.

As is well known, a vehicle represents a spatial oscillatory system subjected to random vibrations due to macro- and micro-irregularities of the road surface, engine operation, wind effects, and similar disturbances (Gillespie, T. D. 1992; Savaresi, S. M. et al. 2010; Poussot-Vassal, C. et al. 2012; Genta, G. 2003; Milliken, W. F. & Milliken, D.L. 1995; Mitschke, M. & Wallentowitz, H. 2004; Crolla, D. A. 1988; Rajamani, R. 2005; Rotenberg, V. 1972).

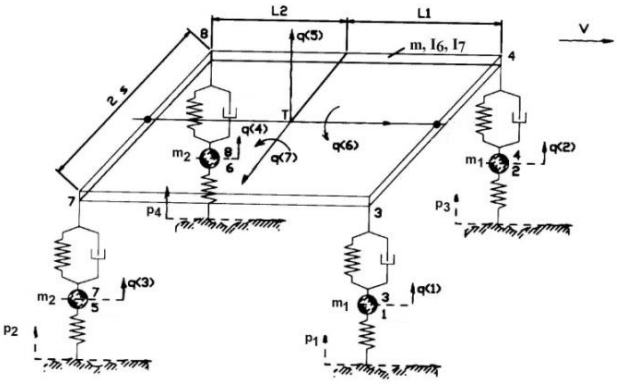

Figure 1 Vibratory model of the vehicle

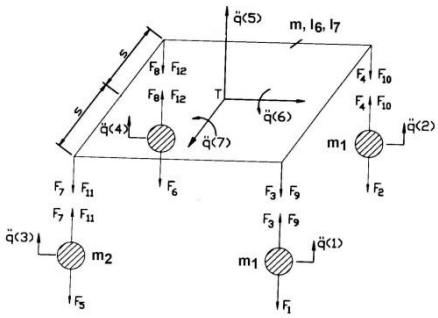

Figure 2 Forces acting on the adopted vehicle model

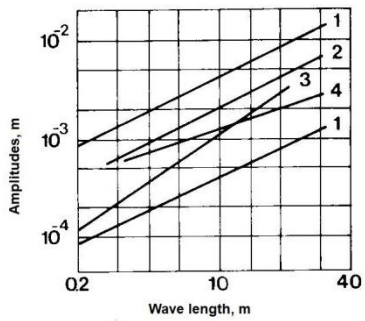

Figure 3 Amplitudes of road surface irregularities for modern roads:1 - limit values, 2 - road with poor concrete pavement, 3 - road with poor asphalt pavement, 4 - road with good asphalt pavement

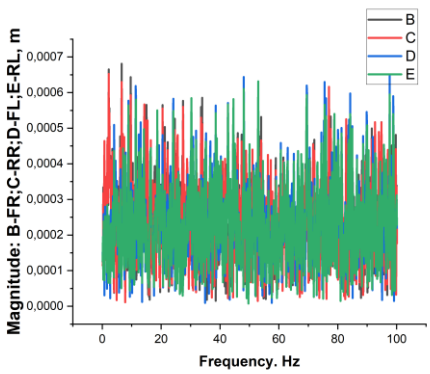

Figure 4 Excitation spectra at the wheels (B-front right; C-front left; D-rear right; E-rear left)

As is well known (Gillespie, T. D. 1992; Savaresi, S. M. et al. 2010; Poussot-Vassal, C. et al. 2012; Genta, G. 2003; Milliken, W. F. & Milliken, D.L. 1995; Mitschke, M. & Wallentowitz, H. 2004; Crolla, D. A. 1988; Rajamani, R. 2005; Rotenberg, V. 1972), a vehicle represents a spatial oscillatory system subjected to random vibrations under the influence of macro- and micro-irregularities of the road surface, engine operation, wind action, and similar disturbances. In the general case, since a vehicle consists of elastic elements, it possesses an infinite number of degrees of freedom of motion. As the analysis of such systems is extremely complex, a common simplification

assumes that the system consists of lumped masses interconnected by elastic–damping elements. In this case, each considered mass has six degrees of freedom of motion (Demić, M. 2026), and the motion of such systems can be described by the so-called Newton–Euler equations, Lagrange's differential equations of the second kind, and related formulations (Demić, M. 2026).

In the present case, a passenger motor vehicle with independent suspension at all four wheels and seven degrees of freedom (Figure 1) is considered (Demić, M. 2026). The vehicle moves in uniform rectilinear motion with velocity v, while the secondary oscillatory motions include vertical oscillations of the lumped wheel masses (four degrees of freedom), as well as vertical oscillations of the centre of mass of the sprung mass together with its angular motions of pitch and roll. Given that even such a system is difficult to analyse, it is considered appropriate to study small linear oscillations of the aforementioned masses about the vehicle's equilibrium position (Demić, M. 1997; Goldstein, H. et al. 2001). For clarity, the oscillatory model used in this study is briefly described below.

Based on the above considerations, Figure 1, and the simplification that the attachment points of the elastic–damping elements move along a chord rather than an arc (due to small angular displacements), the equations describing the deformations can be written as follows:

a) Springs

$$\begin{aligned} D_{1,2} &= q(5) + l_1 q(7) \mp s q(6) - q(1,2) \\ D_{3,4} &= q(5) + l_2 q(7) \mp s q(6) - q(3,4) \end{aligned} \tag{1}$$

b) Tyres

$$D_{4,5,6,7} = q(1,2,3,4) - p(1,2,3,4) \tag{2}$$

c) Relative velocities of the piston with respect to the shock absorber body

$$\begin{aligned} D_{9,10} &= \dot{q}(5) + l_1 \dot{q}(7) \, m \, s \, \dot{q}(6) - \dot{q}(1,2) \\ D_{11,12} &= \dot{q}(5) + l_2 \dot{q}(7) \, m \, s \, \dot{q}(6) - \dot{q}(3,4) \end{aligned} \tag{3}$$

Expressions (1–3) represent a standard linearised approximation of kinematic relations for small oscillations, which has been shown in the literature to be sufficient for analysing frequency characteristics of vehicle oscillatory systems.

Since the forces in the elastic–damping elements depend on the deformation of the elastic components and the relative velocity of the piston with respect to the shock absorber body, taking into account Figure 1 and expressions (1–3), and adopting the force characteristics given in (Demić, M. & Belingardi, G. 2011), the following relations can be formulated:

a) Tyres

$$\begin{aligned} F_{1,2} &= x(1) D_{5,6} + x(2) D^2{}_{5,6} - x(3) D^3{}_{5,6} \\ F_{5,6} &= x(4) D_{7,8} + x(5) D^2{}_{7,8} - x(6) D^3{}_{7,8} \end{aligned} \tag{4}$$

b) Springs

$$\begin{aligned} F_{3,4} &= x(7) D_{1,2} + x(8) D^3{}_{1,2} \\ F_{7,8} &= x(9) D_{3,4} + x(10) D^3{}_{3,4} \end{aligned} \tag{5}$$

c) Shock absorbers

$$\begin{aligned} F_{9,10} &= x(11) + x(12) D_{9,10} + x(13,14) sqr(D_{9,10}) Sign(D_{9,10}) + \\ &\quad + x(15) + x(16) D_{1,2} + x(17) sqr(D_{1,2}) Sign(D_{1,2}) \\ F_{11,22} &= x(18) + x(19) D_{9,10} + x(20,21) sqr(D_{11,12}) Sign(D_{11,12}) + \\ &\quad + x(22) + x(23) D_{3,4} + x(24) sqr(D_{3,4}) Sign(D_{3,4}) \end{aligned} \tag{6}$$

where:

- $x(1)$ to $x(24)$ – stiffness and damping parameters of the oscillatory system,

- $x(1)$ to $x(6)$– tyre stiffness parameters,
- $x(7)$, $x(8)$, $x(9)$, $x(10)$ – spring stiffness parameters,
- $x(11)$ to $x(24)$ – shock absorber damping parameters (where $x(13)$ and $x(20)$ refer to compression, and $x(14)$ and $x(21)$ to rebound of the shock absorber) (Demić, M. & Belingardi, G. 2011).

Based on Figure 2 and the Newton–Euler equations, after simplification, the differential equations describing the motion of the lumped masses of the vehicle can be written as follows:

a) Front right wheel

$$\ddot{q}(1) = (F_3 + F_9 - F_1) / m_1 \tag{7}$$

b) Front left wheel

$$\ddot{q}(2) = (F_4 + F_{10} - F_2) / m_1 \tag{8}$$

c) Rear right wheel

$$\ddot{q}(3) = (F_7 + F_{11} - F_5) / m_2 \tag{9}$$

d) Rear left wheel

$$\ddot{q}(4) = (F_8 + F_{12} - F_6) / m_2 \tag{10}$$

e) Vertical vibrations of the sprung mass

$$\ddot{q}(5) = -(F_3 + F_9 + F_4 + F_{10} + F_7 + F_{11} + F_8 + F_{12}) / m \tag{11}$$

f) Roll motion of the sprung mass

$$\ddot{q}(6) = (F_3 + F_9 + F_7 + F_{11} - F_4 - F_{10} - F_8 - F_{12}) s / I_6 \tag{12}$$

g) Pitch motion of the sprung mass

$$\ddot{q}(7) = [(F_7 + F_{11} + F_8 + F_{12}) l_2 - (F_3 + F_9 + F_4 + F_{10}) l_1] / I_7 \tag{13}$$

where:

- m_1, m_2, m_3, m_4 – masses of the wheels and associated assemblies,
- m – sprung mass of the vehicle (body),
- I_6– moment of inertia about the longitudinal axis of symmetry of the sprung mass,
- I_7– moment of inertia about the transverse axis of symmetry of the sprung mass,
- q_1, q_2, q_3, q_4 – vertical displacements (vibrations) of the wheels,
- q_5, q_6, q_7 – vertical displacement of the sprung mass and its roll and pitch motions,
- $\ddot{q}_1, \ddot{q}_2, \ddot{q}_3, \ddot{q}_4$ – accelerations of the vertical vibrations of the wheels,
- $\dot{q}_5, \dot{q}_6, \dot{q}_7$ – velocities of the vertical vibration of the sprung mass and its roll and pitch motions,
- $\ddot{q}_5, \ddot{q}_6, \ddot{q}_7$ – accelerations of the vertical vibration of the sprung mass and its roll and pitch motions,
- s – half-track of the wheels and tyres (for simplicity, it is assumed to be the same for both axles), and
- l_1, l_2 – coordinates of the centre of gravity of the sprung mass measured from the front and rear axles, respectively.

Table 1 Vehicle inertial parameters

m_1= 27.5, kg	I_7=53, kgm^2
m_2=25, kg	l_1=1.4, m
m=1090, kg	l_2=1.1, m
I_6=1680, kgm^2	s=0.7, m

The excitation function can be defined based on standard curves (ISO 8608, 2016). However, analyses have shown that these curves do not allow direct definition of the road excitation function in the time domain; therefore, it was considered appropriate to use the curves shown in Figure 3 (Rotenberg, V. 1972). With this in mind, it is

assumed that the excitation at the wheels is polyharmonic with real-valued amplitudes. The expression defining the excitation at the front right wheel is given in (Demić, M. 1997):

$$p_1(t) = \sum_1^{NH} A(f)\sin[(2\pi ft + \theta(f)] \tag{14}$$

where:

- A(f) – amplitude spectrum of road micro-irregularities (Figure 3),
- f – frequency,
- NH – number of harmonics, and
- θ – phase angle.

In the absence of experimental data, the following relation is adopted:

$$\theta(f) = 2\pi(RND - 0.5) \tag{15}$$

where RND denotes a random variable uniformly distributed in the interval {0,1}.

Table 2 Vehicles vibratory parameters

Parameter	Value
$x(1)$, N/m	60000
$x(2)$, N/m^2	47000
$x(3)$, N/m^3	19000
$x(4)$, N/m	60000
$x(5)$, N/m^2	39000
$x(6)$, N/m^3	22000
$x(7)$, N/m	23000
$x(8)$,N/m^3	6500
$x(9)$, N/m	35000
$x(10)$, N/m	67000
$x(11)$, N	67.51
$x(12)$, Ns/m	-3.17
$x(13)$, Ns^2/m^2	0.0028
$x(14)$, Ns^2/m^2	-2.10
$x(15)$, N	-0.0077
$x(16)$, N/m	-2.10
$x(17)$, N/m^2	0.057
$x(18)$, N	87.75
$x(19)$, Ns/m	-4.12
$x(20)$, Ns^2/m^2	0.0036
$x(21)$, Ns^2/m^2	-2.73
$x(22)$,N	0.0101
$x(23)$, N/m	-2.73
$x(24)$, N/m^2	0.074

The dependence of the excitation amplitude on vehicle speed is given by the expression (Demić, M. 1997):

$$A(f_p) = (A_0 + B_0 / f_p) / V \tag{16}$$

where:

- A_0, B_0 – ordinates taken from Figure 3,
- f_p – reciprocal value of the wavelength of road irregularities (Figure 3),
- v – vehicle speed.

The excitation acting on the rear right wheel is defined as:

$$p_3(t) = p_1(t - L / V) \tag{17}$$

To define the excitations on the left-hand side of the vehicle, it is assumed that they possess a different frequency content and include a time delay relative to the right-hand side.

Taking into account that in (Demić, M. 2026) the excitation function at all wheels is described in detail (neglecting the influence of tyre elasticity and wheel diameter), it was considered appropriate here to perform a frequency analysis of the wheel excitations. The magnitudes of the spectra are shown in Figure 4, it can be observed that the spectra are random functions of frequency.

Thermal loading of shock absorbers

The mechanical work realised in shock absorbers through the action of relative velocities and damping forces is entirely dissipated in the form of heat. The instantaneous power of dissipation in a damping element is equal to the product of the damping force and the relative velocity between the connected masses (Bojić, M. 2011; Atkins, P. 2010). Since the damping force is a function of relative velocity, the dissipated power has a distinctly non-linear character and directly depends on the oscillatory regime of the vehicle system.

This approach enables a direct link between the dynamic behaviour of the vehicle and the thermal loading of the shock absorbers.

In the present case, the thermal power is calculated using the expression:

$$P_{tp} = F_d \, v_{rel} \tag{18}$$

where:

- F_d – damping force in the corresponding damping element, and
- v_{rel} – corresponding relative velocity calculated from (1).

Considering the nature of the solutions of the differential equations (3), it is evident that the thermal power will also be of a random character, which will be discussed later.

Connection with automatic control methods

Given that the objective was to develop a method applicable in experimental investigations, the formulation of the model in the state-space domain enables the direct application of methods from automatic control and system identification. Based on measured quantities (shock absorber forces and relative velocities), it is possible to:

- estimate transfer functions between road excitation and dissipated power,
- determine the spectral distribution of generated heat,
- identify the parameters of the shock absorber constitutive model.

In this way, the developed methodology goes beyond purely numerical simulation and becomes applicable in operational and experimental studies.

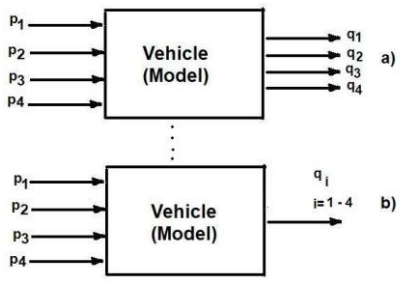

Figure 5 Procedure for solving a MIMO system by decomposition into multiple MISO subsystems

Since it is both desirable and useful to apply automatic control procedures during experimental investigations (Doyle, J. C. et al., 1992; Tomović, R. et al. 1974), one possible approach will be briefly outlined. The influence of wheel excitations and the generated thermal power can be represented as a multiple-input, multiple-output (MIMO) system (Figure 5a). The solution of such systems is based on reducing the MIMO system to multiple inputs and a single output (Figure 5b), where the input variables should be mutually independent. As the excitations in this case are not independent, decoupling methods must be applied (Demić, M. 2026). Since their application to this vehicle model has been described in detail in (Demić, M. 2026), and the same excitations are used here, it will not be discussed further. It is emphasised that the SVD method has been employed.

The proposed method integrates:

- a spatial dynamic vehicle model,
- a realistic constitutive model of the shock absorber,
- an energy-based formulation of dissipation, and

- spectral analysis and system identification.

This establishes a unified framework for quantifying the generation of thermal power in shock absorbers as a function of excitation frequency under real operating conditions of a vehicle travelling over an uneven road surface.

It should be noted that the system of first-order differential equations was solved numerically using the Runge–Kutta method, with an integration step of 0.001, s, over 16,384 points. This enabled reliable analysis in the frequency range from 0.06 Hz to 500 Hz (Bendat, J. & Piersol, A. 2000; Bendat, J. & Piersol, A. 2011). Considering that the resonant frequencies of the lumped masses of motor vehicles are approximately within the range 1 Hz – 25 Hz (Mitschke, M. & Wallentowitz, H. 2004), it was deemed appropriate to analyse only the frequency range 0.06 Hz – 100 Hz.

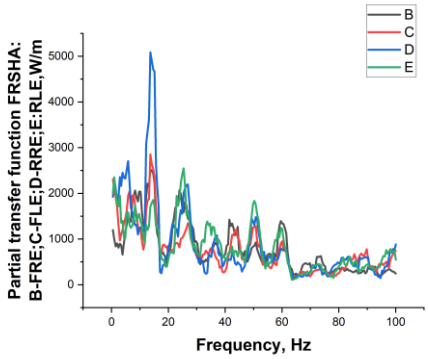

Figure 6 Partial transfer function: front right shock absorber – road excitations (FRE – front right wheel, RRE – rear right wheel, FLE – front left wheel, RLE – rear left wheel)

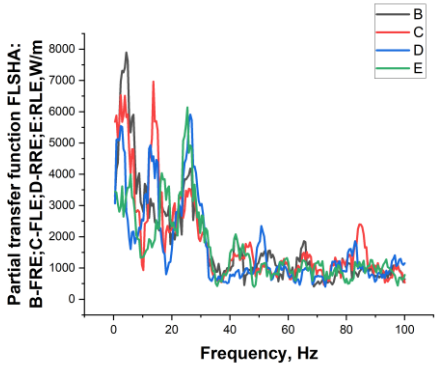

Figure 7 Partial transfer function: front left shock absorber – road excitations (FRE – front right wheel, RRE – rear right wheel, FLE – front left wheel, RLE – rear left wheel)

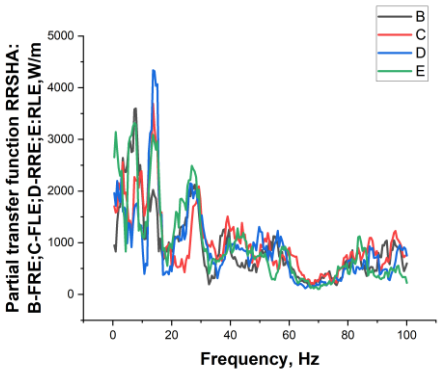

Figure 8. Partial transfer function: rear right shock absorber – road excitations (FRE – front right wheel, RRE – rear right wheel, FLE – front left wheel, RLE – rear left wheel)

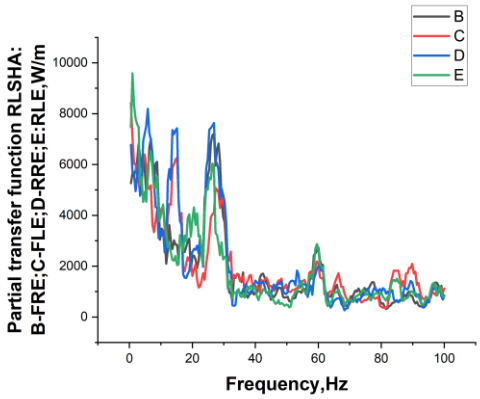

Figure 9 Partial transfer function: rear left shock absorber – road excitations (FRE – front right wheel, RRE – rear right wheel, FLE – front left wheel, RLE – rear left wheel)

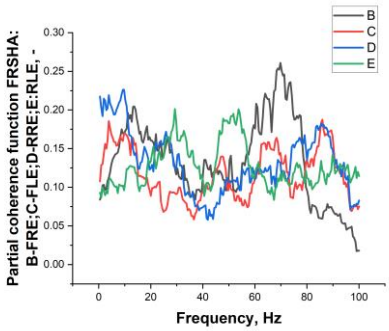

Figure 10 Partial coherence function: front right shock absorber – road excitations (FRE – front right wheel, RRE – rear right wheel, FLE – front left wheel, RLE – rear left wheel)

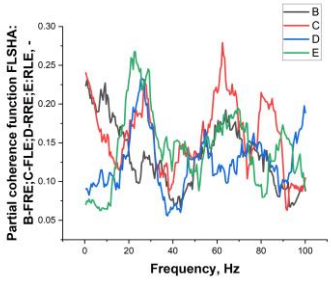

Figure 11 Partial coherence function: front left shock absorber – road excitations (FRE – front right wheel, RRE – rear right wheel, FLE – front left wheel, RLE – rear left wheel)

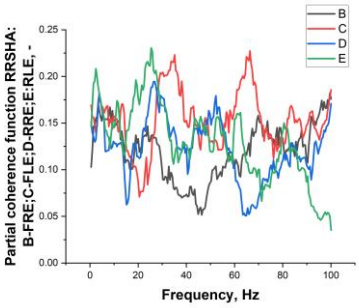

Figure 12 Partial coherence function: rear right shock absorber – road excitations (FRE – front right wheel, RRE – rear right wheel, FLE – front left wheel, RLE – rear left wheel)

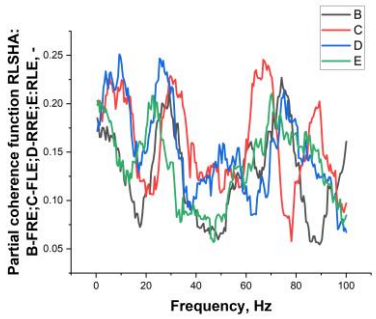

Figure 13 Partial coherence function: rear left shock absorber – road excitations (FRE – front right wheel, RRE – rear right wheel, FLE – front left wheel, RLE – rear left wheel)

DATA ANALYSIS

Analysis of the data presented in Figures 6–9 indicates that the generated thermal power depends on the position of the shock absorber. The rear wheels, particularly on the left-hand side, exhibit significantly higher peak values, reaching nearly 10,000 W/m, whereas the maxima at the front wheels are generally below 8000 W/m. This suggests that the rear part of the system is subjected to greater thermal loading in the low-frequency range, which is often a consequence of mass distribution or suspension stiffness.

An asymmetry between the left and right sides is also observed. For example, the left-hand side (FLSHA and RLSHA) shows higher values at the very beginning (close to 0 Hz) compared to the right-hand side. This difference in the initial part of the curves may indicate an uneven distribution of loads or different damping characteristics between the left and right sides of the model.

It is also of interest to analyse the positions of the resonant frequencies.

From Figure 6, resonant frequencies can be observed up to approximately 1.95 Hz, followed by a second resonance in the range 5.85 Hz – 6.34 Hz, and a third in the range 23.92 Hz – 25.39 Hz. At higher frequencies, the amplitudes of the transfer functions decrease (due to system nonlinearity).

Figure 7 shows resonant frequencies in the range 2.44 Hz –4.39 Hz, followed by a second resonance between 10.74 and 13.67 Hz, and a third in the range 22.46 Hz – 25.39 Hz. At higher frequencies, the amplitudes again decrease (as a result of system nonlinearity).

From Figure 8, resonant frequencies are identified in the range 2.92 Hz –3.41 Hz, followed by a second resonance between 9.27 Hz and 9.76 Hz, and a third in the range 25.87 Hz – 28.32 Hz. At higher frequencies, the amplitudes decrease due to nonlinear effects.

Figure 9 shows resonant frequencies up to 2.92 Hz, followed by a second resonance between 4.39 Hz and 6.83 Hz, and a third in the range 22.46 Hz – 24.41 Hz. At higher frequencies, the amplitudes of the transfer functions decrease (again due to system nonlinearity).

A common feature of all the analysed figures is that the transfer functions depend on frequency. Since a nonlinear vehicle model is considered, multiple peaks appear in the transfer functions. The lowest frequencies can be associated with the resonance of the sprung mass, while the higher ones correspond to the resonances of the wheels.

As is well known (Bendat, J. & Piersol, A. 2000; Bendat, J. & Piersol, A. 2011), partial coherence functions indicate the degree of linear correlation between two signals, i.e. whether nonlinearities or noise significantly influence the system.

When analysing partial coherence functions, it should be borne in mind that nonlinear oscillatory parameters of the vehicle were used and that noise arises only from minimal numerical errors.

The coherence values in Figures 10–13 are relatively low (below 0.30), which in signal analysis theory often indicates that the system is nonlinear, or that there is a significant influence of noise, or that the analysed partial inputs do not fully capture all causes of variation in the output signal.

It is observed that the partial coherence functions depend on both frequency and the position of excitation (front–rear and left–right sides of the vehicle), which indicates the complexity of the transformation of mechanical work into generated thermal power in the shock absorbers.

Considering that the partial coherence functions are low, this confirms that the system is nonlinear, and that only negligible noise is present, originating from the applied numerical methods.

From Figure 10, it can be determined that the minimum value of the partial coherence function occurs for the rear right wheel (41.99 Hz - 0.057), while the maximum value occurs for the front right wheel (68.84 Hz - 0.253).

From Figure 11 (front left wheel), the minimum value occurs at approximately (37.59 Hz - 0.055), while the maximum occurs for excitation at the front left wheel (62.50 Hz - 0.279).

In Figure 12, the maximum value occurs for the rear left wheel (27.34 Hz - 0.206), while the minimum occurs for excitation at the rear right wheel (66.40 Hz - 0.054).

From Figure 13, it can be seen that the maximum value occurs for the rear right wheel (9.27 Hz - 0.251), while the minimum occurs for excitation at the front right wheel (89.35 Hz - 0.054).

It should be noted that under real operating conditions, coherence rarely reaches ideal values due to tyre hysteresis and the progressive characteristics of springs.

It can therefore be concluded that the partial coherence functions of all shock absorbers depend on both frequency and excitation position, which must be taken into account when planning and interpreting experimental investigations.

Finally, it is emphasised that the developed method has been illustrated using a nonlinear vehicle model, but it is of general significance, as it can be applied in experimental testing of vehicles. In such cases, thermal power can be calculated based on measured shock absorber forces and the relative velocities of the piston with respect to the body.

CONCLUSIONS

The conducted research on the development of a method for identifying the thermal power of shock absorbers enables the following conclusions to be drawn:

- necessity of spatial modelling: the use of a 7-DOF model is justified, as only such an approach can capture the complex longitudinal and diagonal dynamic coupling between the wheels, which directly affects the distribution of thermal loading within the suspension elements.
- refinement of the shock absorber model: abandoning the linear viscous representation and introducing force dependence on both relative velocity and piston displacement is essential for a physically consistent estimation of instantaneous and mean thermal power.
- identification of dominant frequencies: a critical frequency range has been identified, corresponding to the resonant frequencies of the considered lumped masses of the system, within which maximum dynamic amplification and intensive energy dissipation occur, regardless of the primary location of excitation.
- specificity of energy transfer: the analysis has shown that maximum thermal loads may occur in shock absorbers that are not directly subjected to the primary excitation (e.g. diagonally opposite wheels), which is of crucial importance for fatigue analysis and the thermal stability of the shock absorber oil.
- experimental applicability: the proposed method, based on automatic control procedures (MIMO and MISO systems), successfully bridges the gap between theoretical simulations and measurements under real operating conditions, enabling identification of the energy balance based on standard measurable kinematic quantities.

This methodology provides a foundation for further research in the field of thermal loading of vehicle suspension systems, particularly in high-performance vehicles and heavy-duty trucks, where the shock absorber “fading” effect represents a critical safety factor.

REFERENCES

Atkins, P. (2010). *The laws of thermodynamics: a very short introduction*. Oxford University Press, Oxford. https://doi.org/10.1093/actrade/9780199572199.001.0001

Bendat, J., & Piersol, A. (2000). *Random Data: Analysis and Measurement Procedures (3rd ed.)*. John Wiley & Sons, New York/LondonISBN: 978-0471317302.

Bendat, J. S., & Piersol, A. G. (2011). Random Data: Analysis and Measurement Procedures (4th ed.). John Wiley & Sons, Hoboken, NJ. https://doi.org/10.1002/9781118032428

Bojić, M. (2011). *Thermodynamics (Termodinamika)*. Faculty of Engineering Sciences, Kragujevac. ISBN: 978-86-81037-34-8.

Crolla, D. A. (1988). Vehicle dynamics — theory into practice. *Proceedings of the Institution of Mechanical Engineers, Part D: Transport Engineering*, 202(2), 83–94. https://doi.org/10.1243/PIME_PROC_1996_210_250_02

Demić, M. (1997). *Optimization of motor vehicle oscillatory systems (Optimizacija oscilatornih sistema motornih vozila)*. Faculty of Mechanical Engineering, Kragujevac. ISBN: 86-80581-22-2

Demić, M. (2026). Contribution to the research of the influence of coherent random road excitations on the frequency characteristics of passenger motor vehicle vibrations. *Science Journal of Transportation*, 25(1), 19-37.

Demić, M., & Belingardi, G. (2011). A Contribution to shock absorber modelling and analysis of their influence on vehicle ride characteristics. *Journal of Middle European Construction and Design of Cars (MECCA)*, 9(1), 6-17. https://doi.org/10.2478/v10138-011-0002-4

Demić, M., & Diligenski, Đ. (2016). Numerical simulation of shock absorbers heat load for semi-active vehicle suspension system. Thermal Science, 20(5), 1725–1739. https://doi.org/10.2298/TSCI150624005D

Demić, M., & Diligenski, Đ. (2018). A contribution to the study of thermal loads of hydraulic and active mounts of powertrain of a freight motor vehicle. *Journal of Applied Engineering Science*, 16(2), 217–224. https://doi.org/10.5937/jaes16-15905

Doyle, J. C., Francis, B. A., & Tannenbaum, A. R. (1992). *Feedback control theory*. Macmillan Publishing Company, NY. ISBN: 978-0023305511.

Genta, G. (2003). *Motor vehicle dynamics: modeling and simulation*. World Scientific Publishing. https://doi.org/10.1142/3329

Gillespie, T. D. (1992). *Fundamentals of vehicle dynamics*. SAE International, Warrendale, PA. https://doi.org/10.4271/R-114

Goldstein, H., Poole, C. P., & Safko, J. L. (2001). *Classical Mechanics (3rd Edition)*. Addison-Wesley. ISBN: 978-0201657029.

ISO 8608 (2016). Mechanical vibration — Road surface profiles — Reporting of measured data. International Organization for Standardization, Geneva. 30 pages.

Lang, G. H., et al. (2007). Development of Suspension Design Technology Applying Principal Elastic Axes. *SAE Technical Paper*, 2007-01-0857. https://doi.org/10.4271/2007-01-0857

Ljung, L. (1999). System Identification: Theory for the User (2nd ed.). Prentice Hall, Upper Saddle River, NJ. ISBN: 978-0136566953

Milliken, W. F., & Milliken, D. L. (1995). *Race car vehicle dynamics*. SAE International, Warrendale. ISBN: 978-1560915263

Mitschke, M., & Wallentowitz, H. (2004). *Dynamik der kraftfahrzeuge (motor vehicle dynamics)*. Springer-Verlag, Berlin. https://doi.org/10.1007/978-3-662-06802-1

Poussot-Vassal, C., Sename, O., Dugard, L., & Gáspár, P. (2012). A survey on semi-active suspension control strategies. *Vehicle System Dynamics*, 50(2), 221–247. https://doi.org/10.3182/20110828-6-IT-1002.00446

Rajamani, R. (2006). *Vehicle dynamics and control*. Springer Science+Business Media, NY. https://doi.org/10.1007/0-387-28823-6

Rotenberg, V. (1972). Vehicle suspension (Podveska avtomobilya). Mashinostrojenie, Moscow. (In Russian).

Savaresi, S. M., Poussot-Vassal, C., Spelta, C., Sename, O., & Dugard, L. (2010). *Semi-active suspension control design for vehicles*. Elsevier (Butterworth-Heinemann), Oxford. https://doi.org/10.1016/C2009-0-63839-3

Tomović, R., Vukobratović, M., & Rakić, R. (1974). Introduction to Nonlinear Automatic Control Systems (Uvod u nelinearne sisteme automatskog upravljanja). Naučna knjiga, Belgrade.

The 11th International Congress
Motor Vehicles & Motors 2026
Kragujevac, Serbia
October 8th - 9th, 2026

Motor Vehicles & Motors

MVM2026-002
https://doi.org/10.24874/CMVM2026.002
Original scientific paper

Aleksandar Jovanović[1]

Katarina Kukić[2]

Ana Uzelac[3]

Dušan Teodorović[4]

DEEP Q-LEARNING ALGORITHM FOR TRAFFIC CONTROL AT A DISPLACED LEFT-TURN INTERSECTION

ABSTRACT: In recent years, alternative intersection designs have become popular in traffic engineering practice. A growing number of implemented solutions, especially in the United States, have proven the applicability of these innovative concepts. Among them, the Displaced Left-Turn intersection stands out due to its ability to accommodate congested traffic demands under near-saturated conditions from both the main and side roads. Left-turning vehicles from the main road are redirected to separated left-turn pockets on the opposite side of the road. This arrangement allows through movements at the main intersection to be served without conflict with left-turning vehicles, thereby increasing the capacity of the intersection. This configuration leads to the creation of two additional intersections downstream of the main one, which are typically controlled by traffic signals. Such a layout requires more sophisticated traffic signal control compared to traditional fixed-time control, which is still common in practice. We developed a Deep Q-Learning algorithm to control a Displaced Left-Turn intersection. This algorithm extends the classical Q-learning approach, which cannot effectively handle many possible states. A simulation environment was created using PTV Vissim, coupled with Python code via the COM interface. The results indicate promising potential of the proposed algorithm for controlling Displaced Left-Turn intersections.

KEYWORDS: Displaced left-turn intersection, deep Q-learning, alternative intersections, microsimulation, traffic signal control

[1]*Aleksandar Jovanović, Faculty of Engineering, University of Kragujevac, Sestre Janjic 6, 34000 Kragujevac, Serbia, a.jovanovic@kg.ac.rs, https://orcid.org/0000-0003-4208-5703*
[2]*Katarina Kukić, Faculty of Transport and Traffic Engineering, University of Belgrade, Vojvode Stepe 305, 11010 Belgrade, Serbia, k.kukic@sf.bg.ac.rs, https://orcid.org/0000-0001-7369-2456*
[3]*Ana Uzelac, Faculty of Transport and Traffic Engineering, University of Belgrade, Vojvode Stepe 305, 11010 Belgrade, Serbia, ana.uzelac@sf.bg.ac.rs, https://orcid.org/0000-0002-7203-9567*
[4]*Dušan Teodorović, Serbian Academy of Sciences and Arts, Knez Mihailova 35, 11000 Belgrade, Serbia, duteodor@gmail.com, https://orcid.org/0000-0002-7535-2727*

DEEP Q-LEARNING ALGORITAM ZA UPRAVLJANJE SAOBRAĆAJEM NA DISPLACED LEFT-TURN RASKRSNICI

REZIME: Poslednjih godina alternativne raskrsnice se sve češće primenjuju u saobraćajnom inženjerstvu. Veliki broj realizovanih rešenja, posebno u Sjedinjenim Američkim Državama, pokazao je da ovi koncepti mogu imati značajnu praktičnu primenu. Među njima se izdvaja Displaced Left-Turn (DLT) raskrsnica, koja može efikasno i bezbedno da opsluži velika saobraćajna opterećenja, čak i u uslovima bliskim zasićenju. Vozila koja sa glavnog pravca skreću levo preusmeravaju se u posebne trake za levo skretanje, koje se nalaze sa suprotne strane kolovoza. Na taj način se na glavnoj raskrsnici uklanja konflikt između pravolinijskih i levih skretanja, čime se povećava njen kapacitet. Ovakva organizacija saobraćaja zahteva formiranje još dve dodatne raskrsnice ispred glavne raskrsnice, koje se najčešće takođe regulišu svetlosnim signalima. Zbog složenije organizacije saobraćajnih tokova, upravljanje svetlosnim signalima na DLT raskrsnici zahteva drugačiji pristup u odnosu na klasično upravljanje u fiksnom režimu rada svetlosnih signala. U ovom radu razvijen je Deep Q-Learning algoritam za upravljanje DLT raskrsnicom. Ovaj algoritam predstavlja proširenje klasičnog Q-learning pristupa, koji postaje nepraktičan kada postoji veliki broj mogućih stanja sistema. Simulaciono okruženje formirano je u programu PTV Vissim, koji je povezan sa programskim kodom u Python-u preko COM interfejsa. Dobijeni rezultati ukazuju na potencijal predloženog algoritma za upravljanje saobraćajem na DLT raskrsnicama.

KLJUČNE REČI: Displaced left-turn raskrsnica, deep Q-learning, alternativne raskrsnice, mikrosimulacija, upravljanje saobraćajem

INTRODUCTION

Urban traffic control is increasingly shaped by the need to achieve several objectives that do not always point in the same direction. Transport authorities are expected to maintain safe and reliable operation, limit delays and queues, and reduce the environmental burden of road traffic, often without substantial changes to the available infrastructure. At the same time, economic activity and urban development continue to generate additional travel demand.

Conventional signalized intersections may become inefficient when heavy left-turn demand requires separate phases. Alternative intersection designs address this problem by relocating or reorganizing movements of the classical intersections. One such design is the Displaced Left Turn (DLT) intersection, in which left-turning vehicles cross the opposing traffic stream at an auxiliary signalized intersection located upstream of the main intersection. After entering the displaced traffic lanes, these vehicles approach the main intersection on the left side of the opposing through lanes. They can consequently complete the left turn at the same time as the opposing through movement. This arrangement removes the left-turn conflict from the main intersection and commonly enables a simpler phase structure. Although it also introduces additional signalized points that must operate in coordination with the main signal.

This study considers a partial DLT intersection, where the major-road left turns are displaced while the side-street approaches retain their conventional geometry. Such a configuration is particularly suitable for locations at the transition between urban and suburban areas, where traffic demand on the major road is high, but the side street must still accommodate several competing movements. The operational benefit of the DLT geometry, however, does not eliminate the signal control problem. The main and the upstream intersection together form a coupled system, and an unsuitable signal decision at one location can produce queues or unused green time at another. This becomes especially important when the distribution of traffic demand changes during the analysis period.

Fixed-time control can provide satisfactory operation when traffic volumes remain close to the conditions for which the signal plan was developed. Its performance decreases when actual arrivals differ substantially from the assumed demand. Actuated control partly addresses this limitation by using detector information to terminate, extend, or call individual phases. However, its decisions are under predefined parameters and rules, which may restrict its ability to respond to stochastic traffic behaviour. A DLT intersection with variable demand therefore provides a relevant setting for examining whether learning-based control can offer an additional operational benefit.

In this paper, as the main technique, we applied Deep Q-learning (DQL). It retains the basic decision mechanism of Q-learning but replaces the Q-table with a neural network that approximates the action-value function. The resulting Deep Q-Network can process a more detailed description of traffic conditions without requiring a separate table entry for every possible combination of state variables. DQL has produced encouraging results under time-varying traffic conditions (Gao et al. 2017; Wei et al. 2018). Whether the additional model complexity provides a clear operational advantage over tabular Q-learning at a DLT intersection remains insufficiently examined.

The objective of this paper is to compare four traffic signal control strategies at a partial DLT intersection: fixed-time control, actuated control, classical Q-learning, and Deep Q-learning. All techniques are implemented and tested in the Vissim microscopic simulation environment using the geometry of an existing DLT intersection in Salt Lake City, Utah. Their performance is evaluated across typical traffic-demand scenarios for a DLT intersection using average vehicle delay, queue length, and the number of stops. Attention is given to the comparison between Q-learning and DQL, since this allows the effect of replacing a discrete Q-table with a neural-network approximation to be assessed independently of the intersection geometry and simulation conditions.

Researchers have shown considerable interest in applying DQL to traffic signal control (TSC). Zhong et al. (2023) investigated conflicts associated with multiphase bus priority at intersections using DQL. Their SUMO-based simulations showed a reduction in vehicle delay of nearly 40%. Ren et al. (2024) proposed a multi-agent DQL algorithm for optimizing TSC across multiple intersections. In this approach, individual agents act independently while contributing to a global optimization objective. Magnana et al. (2024) combined DQL with an actuated TSC algorithm designed for cyclists. Their results showed that the proposed approach reduced delays more effectively than traditional methods, with improvements observed across individual hourly intervals. The wider development and application of DQL in traffic engineering were examined by Zhao et al. (2024), who reviewed its use in controlling traffic systems under dynamic conditions. Beyond DQL-based methods, Chiou (2024) proposed a co-evolutionary RL framework for traffic signal control in road networks subject to stochastic capacity variations. The framework combines multi-agent learning with a co-evolutionary decomposition strategy to adjust signal timings dynamically, reduce congestion, and outperform conventional RL methods.

The contributions of the paper are threefold. First, four control strategies are evaluated within a common simulation framework. Second, a DQL is developed for coordinated real-time operation of the main intersection and auxiliary signalized intersections of a partial DLT. Third, the study provides a direct comparison between tabular and deep Q-learning under the same traffic scenario, state information, control constraints, and performance measures. This comparison makes it possible to determine whether the use of a deep neural network produces a meaningful improvement over classical Q-learning or merely introduces additional computational requirements.

The remainder of the paper is organized as follows. Section 2 describes the applied methodology for the problem defined. Section 3 reports and discusses the results obtained under the analysed traffic scenario. Finally, Section 4 summarizes the main findings and identifies directions for further research.

PROBLEM DEFINITION AND METHODOLOGY

Zhao et al. (2015) identified as many as ten geometric configurations of the DLT. Among these, the partial DLT is the configuration most implemented in practice. The layout presented in **Figure 1** is based on the geometry and lane arrangement of an existing DLT in Salt Lake City, Utah, USA (40°41′47.8″N, 111°58′51.1″W).

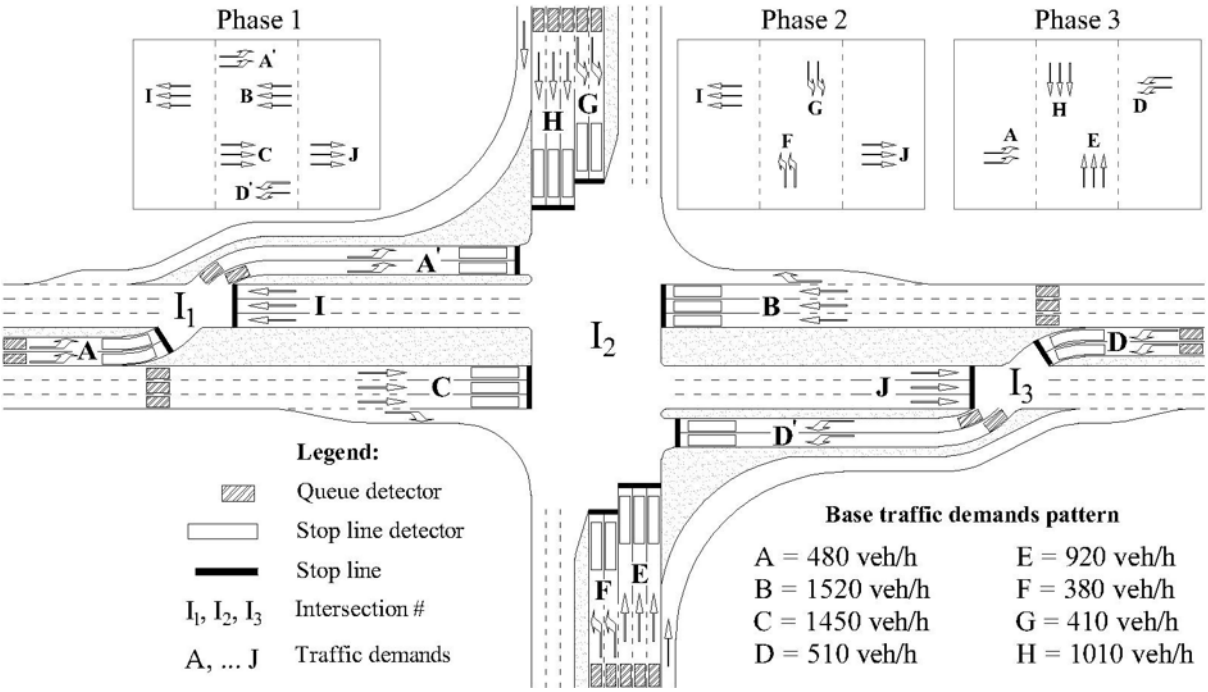

Figure 1 Salt Lake City DLT layout

A DLT is particularly suitable for corridors where traffic volumes are close to the capacity of a conventional intersection and left-turning vehicles account for a substantial portion of the total demand. Such intersections are most often constructed in suburban settings, where sufficient right-of-way is available and heavy vehicles represent a notable share of the traffic stream. Figure 1 presents a representative demand distribution for the lane arrangement used at the Salt Lake City DLT (Steyn et al. 2014).

The adopted phase sequence is also shown in Figure 1. It is designed to preserve progression along the main street, including the approaches with displaced left-turn lanes. Under this sequence, movements I and J operate with near-optimal progression, preventing the development of persistent queues. These two movements are therefore excluded from the detector-based control inputs. The order of the phases is kept fixed throughout the analysis. The proposed control strategy relies on a single controller for the main and downstream intersections.

Fixed-time traffic control parameters are calculated for selected traffic volumes and remain unchanged during operation. If the demand for a particular movement increase, the assigned green time may become insufficient, causing longer queues, delays, and more stops. When the demand decreases, part of the green time may remain unused. For this reason, several control strategies that adjust signal timings according to current traffic conditions were also tested. A conventional fully actuated system was first applied. Its detector layout, presented in Figure 1, and control settings follow the recommendations provided by Steyn et al. (2014). More advanced strategies are then formulated using reinforcement learning.

The purpose of the analysis is to determine which of these strategies provides the most reliable operation for the typical demand condition. All control methods are compared in terms of average vehicle delay, average queue length, and average number of stops.

Reinforcement Learning algorithms

Reinforcement Learning (RL) determines control decisions through repeated interaction between an agent and its environment. In traffic signal applications, the agent observes the current traffic state, selects a signal action, and receives a reward that reflects the consequences of that action. Classical Q-learning stores the estimated value of each state–action pair in a Q-table. This makes the decision process relatively transparent and computationally manageable when the state space is small. However, the traffic variables must be divided into a finite number of intervals, and the number of table entries increases rapidly as additional detectors, traffic variables, or discretization levels are introduced.

Q-learning

For each phase p, where $p \in \{1, 2, 3\}$, the largest measured traffic lane occupancy $Occ'_p(t)$ is determined according to outputs from detectors. The three values obtained at time t form the basis of the traffic state used by the agent (controller). Before entering the Q-learning procedure, each value is assigned to one of five occupancy ranges:

$$discr(Occ'_p) = \begin{cases} 1 & if\ Occ'_p < 0{,}1 \\ 2 & if\ 0{,}1 \le Occ'_p < 0{,}2 \\ 3 & if\ 0{,}2 \le Occ'_p < 0{,}4 \\ 4 & if\ 0{,}4 \le Occ'_p < 0{,}6 \\ 5 & if\ Occ'_p \ge 0{,}6 \end{cases} \tag{1}$$

The state at time t is recorded as an ordered combination of the three discrete occupancy levels: $s_t = [\mathrm{discr}(\mathrm{Occ}'_1), \mathrm{discr}(\mathrm{Occ}'_2), \mathrm{discr}(\mathrm{Occ}'_3)]$. Since each component can take five values, the complete state space contains $|S| = 5^3 = 125$.

An action determines which of the three phases receives the green time. Let $A = \{a_1, a_2, a_3\}$ denote the set of all possible actions. If $a_t = p$, phase p is active, while the remaining two phases are stopped. Phase changes are restricted to the sequence $1 \rightarrow 2 \rightarrow 3 \rightarrow 1$.

A phase therefore cannot be skipped or introduced outside the prescribed order. With 125 states and three phase-related actions, the Q-matrix contains 125 × 3 elements.

The controller makes a decision once per simulation second. It can retain the current phase or request the next phase in the sequence. A requested change is applied only after the corresponding yellow and all-red intervals have expired. The green indication must last for at least 5 s. Its upper limit is taken from the fixed-time optimization.

The controller is evaluated using the total occupancy measured at the current time step. The immediate reward is calculated as:

$$r_t = -\sum_{l=1}^{L} Occ_l(t) \tag{2}$$

where L is the total number of traffic lanes, l = 1,2,... $|L|$. Since the reward is non-positive, actions that reduce the total occupancy produce values closer to zero and are therefore preferred during learning.

Actions are selected by the ε-greedy rule. The action with the largest Q-value is chosen with probability $1 - \varepsilon_t$; with probability ε_t, an action is selected randomly. The value of ε is updated after each time step according to:

$$\varepsilon_{t+1} = max(\varepsilon_t \cdot \varepsilon_{decay}, \varepsilon_{min}) \tag{3}$$

The decay factor is set to 0,99, while the minimum value of ε is 0,01. At the beginning of learning, ε is set to 0,9. Random actions are consequently frequent during the initial simulation steps, allowing different state-action combinations to be tested. As ε decreases, the controller increasingly relies on the actions associated with the highest Q-values.

During learning, the controller stores one Q-value for every admissible state-action pair. A table entry estimates the cumulative return that can be obtained by applying a particular action in a given state and continuing control from that point. These estimates are not known in advance. They are formed gradually from the transitions recorded during simulation.

At time step t, the agent observes state s_t and applies action a_t. The system then moves to s_{t+1} and returns reward r_{t+1}. This transition is used to correct the Q-value of the executed state-action pair:

$$Q_{t+1}(s_t, a_t) = Q_t(s_t, a_t) + \alpha_t \left[r_{t+1} + \gamma \max_{a' \in A} Q_t(s_{t+1}, a') - Q_t(s_t, a_t)\right] \tag{4}$$

where $a`$ is a possible action in the next state s_{t+1}.

The expression in brackets is the difference between the new one-step target and the previous estimate. The complete return from later time steps is not available when the update is made. For that reason, it is replaced by the largest Q-value currently assigned to the next state. The discount factor γ determines how strongly this estimate of future operation affects the update, while α_t determines how much the new transition changes the stored value.

The same calculation is repeated after every observed transition. Learning can be stopped when successive changes in the Q-table become negligible or when another prescribed limit is reached, such as the maximum number of iterations, the available simulation time, or a selected performance criterion.

The learning rate is reduced as training proceeds. Large corrections are allowed at the beginning, when the Q-table contains little useful information, whereas later updates are made more gradually. The following schedule was used:

$$\alpha_t = max\{\frac{\alpha_{init}}{1 + \frac{t}{c}}, \alpha_{min}\} \tag{5}$$

where c controls the rate of decay, while the maximum operator prevents the learning rate from falling below its prescribed minimum. Based on preliminary tests, the initial learning rate was set to 0,1, its lower bound to 0,001, and c to 10 000. The discount factor was kept at γ = 0,8.

Deep Q-learning

In the Deep Q-learning (DQL) approach, Q-values are estimated by a deep neural network rather than stored in a Q-table. Figure 2. shows the structure of the DQL agent used for signal control at the three-phase DLT intersection. It includes the state and action representations, the Q-network, the Target network, and the experience replay buffer.

The agent learns from the transitions observed while controlling the DLT intersection. At time t, it receives the current traffic state $s(t)$ and applies action $a(t)$. The environment then returns reward $r(t+1)$ and the state observed at the next time step, $s(t+1)$. One transition is therefore written as:

$$e(t) = [s(t), a(t), r(t+1), s(t+1)] \tag{6}$$

Each transition is stored in the experience replay buffer. The buffer is gradually filled as the agent controls the signals, while the Q-network parameters remain unchanged until at least N_{min} transitions have been collected. During this initial period, actions are selected according to the initial ε-greedy policy. Since the starting value of ε is usually high, random actions are selected frequently and the buffer receives transitions from different traffic conditions.

Training starts when the number of stored transitions reaches N_{min}. A mini-batch of B transitions, in this case 64, is selected randomly and used for one update of the Q-network parameters. Random sampling breaks the temporal

order of consecutive observations and allows the same transition to be used in more than one training step. Once the buffer reaches its specified capacity, newly recorded transitions replace the oldest ones. Unlike a Q-table, the replay buffer does not contain Q-values for all possible state-action pairs. It stores only the transitions that occurred during control.

Three hidden layers were used in the Q-network, with 256, 128 and 128 neurons. *ReLU* was used in these layers. The last layer is linear and gives the Q-values for the three available actions. *Adam* was used for training, with a learning rate of 0.001, while the discount factor γ was set to 0.8.

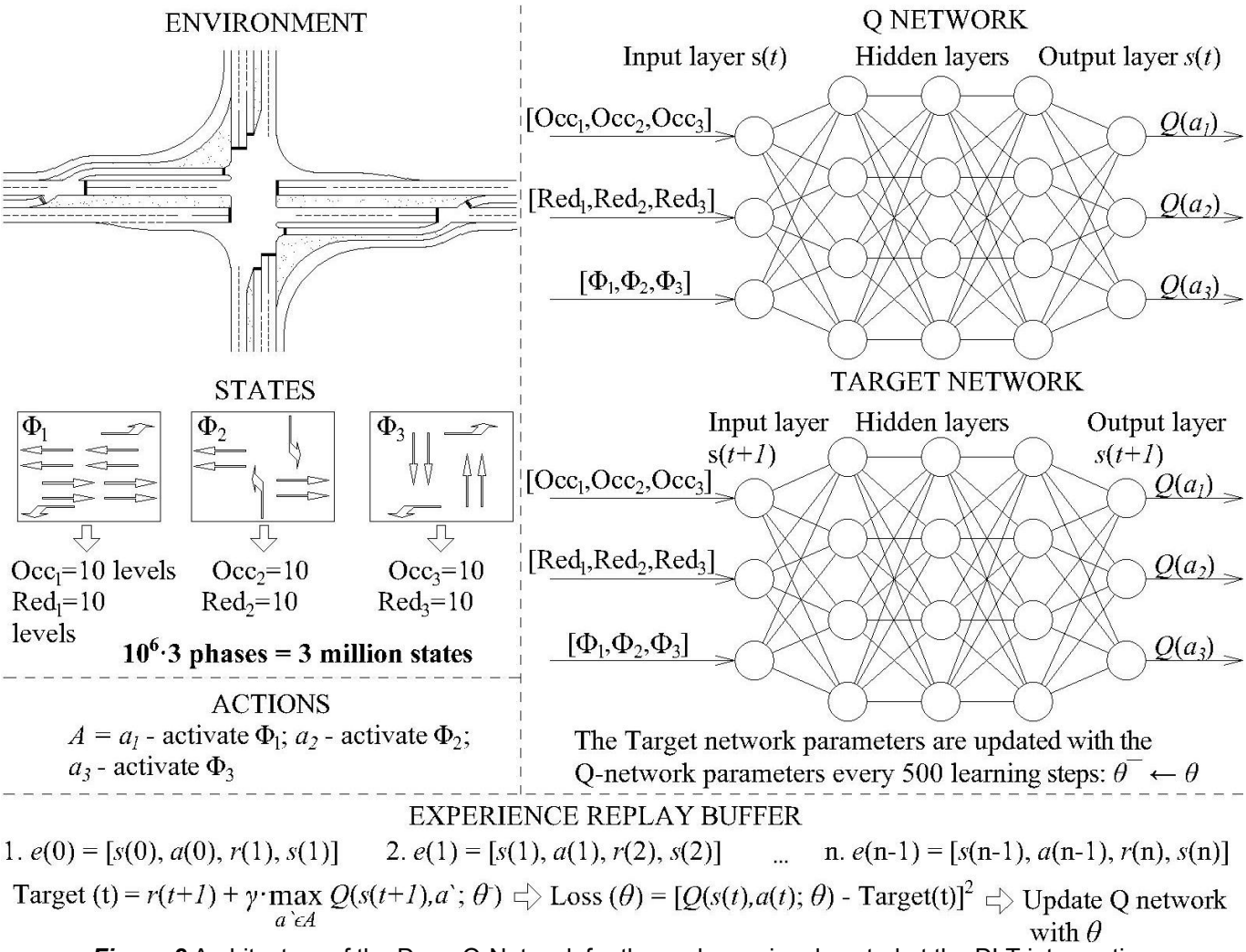

Figure 2 Architecture of the Deep Q-Network for three-phase signal control at the DLT intersection

The traffic state used by the DQN is defined by three phase-related traffic lane occupancy measures, three corresponding detector-based red time measures, and the currently active signal phase. Each occupancy and red time measure is discretised into ten uniform levels. This results in 10^6 possible combinations of traffic conditions, which, together with the three possible active phases, corresponds to approximately three million possible states. The DQN uses this compact state representation to estimate the Q-values associated with the three available signal-control actions.

The Deep Q-Network (DQN) agent shown in Figure 2 contains two neural networks with the same architecture. The Q-network has parameters θ, while the Target network has parameters θ^-. Their parameter values are equal at the beginning of training. The Q-network receives the current state $s(t)$ and produces one Q-value for each action:

$$Q(s(t), a_1;\ \theta), Q(s(t), a_2;\ \theta), Q(s(t), a_3;\ \theta) \tag{7}$$

These values are used when selecting the signal phase, and the parameters θ are adjusted during training. The Target network receives the next state $s(t+1)$. Its outputs are used only to calculate the target value and its parameters are not changed by backpropagation. For each transition selected from the replay buffer, the target value is calculated as:

$$Target(t) \ = \ r(t+1) \ + \ \gamma \max_{a' \in A} Q(s(t+1), a';\ \bar{\theta}) \tag{8}$$

where A denotes the set of admissible actions in state $s(t+1)$. Actions that would violate the prescribed phase sequence are excluded before the maximum is determined. The first term in Equation (8) is the reward received after action $a(t)$, while the second term estimates the best discounted return available from the next state. The discount factor γ determines the contribution of this estimate.

The state $s(t+1)$ is not available when the action is selected. The target can be calculated only after the action has been applied and the resulting state and reward have been observed. For the same transition, the Q-network provides the estimate assigned to the action that was actually taken: $Q(s(t), a(t);\ \theta)$. The difference between this estimate and the target value represents the learning error. For one transition, the squared error is:

$$L_t(\theta) \ = \ [Q(s(t), a(t);\ \theta) \ - \ \mathrm{Target}(t)]^2 \tag{9}$$

Only the output corresponding to action $a(t)$ enters the loss for that transition. The parameters θ are then adjusted by backpropagation so that the Q-value assigned to the selected action moves closer to the target. The parameters θ^- of the Target network remain unchanged during this update. When the mini-batch contains B transitions, the loss is calculated as the mean squared error over all sampled transitions:

$$L(\theta) \ = \ \frac{1}{B} \sum_{\mathrm{i}=1}^{B} [Q(s_i, a_i;\ \theta) \ - \ Target_i]^2 \tag{10}$$

where s_i, a_i, and $Target_i$ refer to the i-th transition in the mini-batch.

The use of two networks prevents the target from changing after every adjustment of the Q-network. If the same network were used both to calculate the current estimate and to form its target, each parameter update would change both sides of Equation (9). This may produce oscillations and unstable learning. The Target network provides a fixed reference during a prescribed number of training updates.

In the example presented in *Figure 2*, the parameters of the Q-network are copied to the Target network after every 500 training steps: $\bar{\theta} \ \leftarrow \ \theta$. The value of 500 is an algorithm parameter rather than a general DQN requirement. Between two copying steps, the Target network parameters remain fixed. Once training has been completed, the Q-network is used to select actions and control the traffic signals. The Target network and the experience replay buffer are required primarily during training.

The execution of RL algorithms

Figure 3 shows the procedure used to run the reinforcement learning algorithm. The DLT intersection was first modelled in PTV Vissim, a microscopic traffic simulation program. Within the developed framework, Vissim represents the traffic environment in which the DQN agent operates. Detectors were placed on the relevant lanes to measure lane occupancy (*Occ*) at one-second intervals. At each time step (t), the collected occupancy values are combined into the traffic state (s_t) and transferred through the Vissim COM interface to the Python code. The described DQL algorithm was developed in Python using the Gym library.

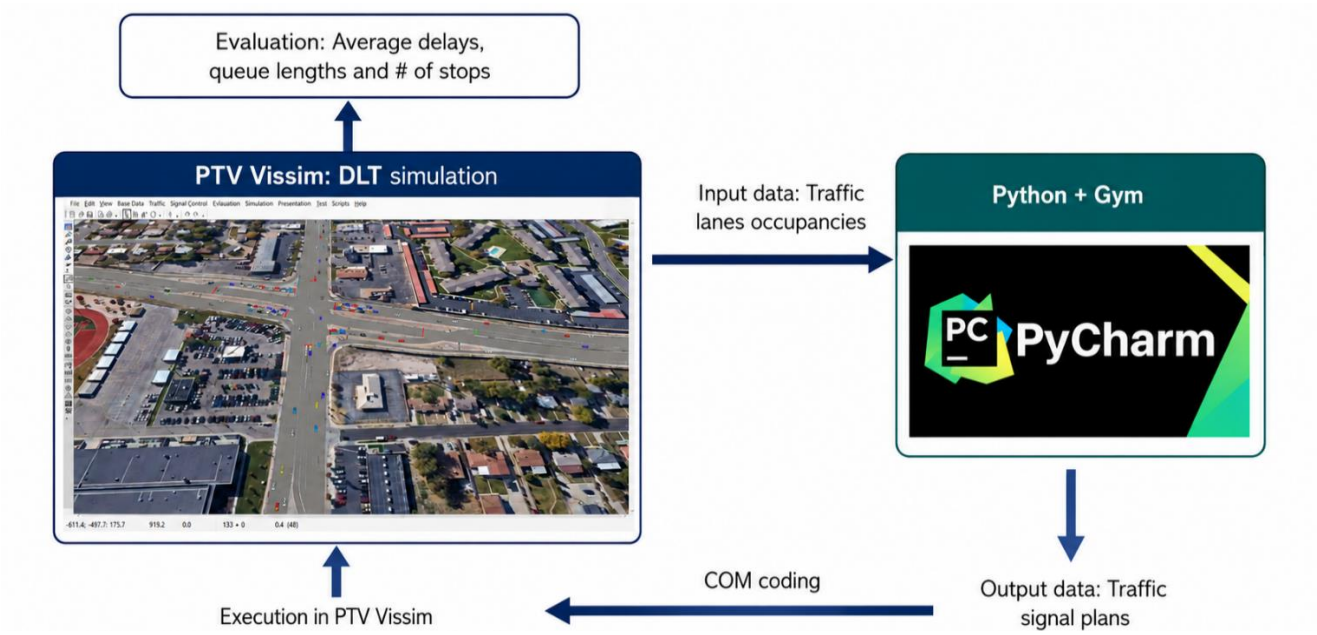

Figure 3 Simulation framework for the execution of the RL-based traffic signal control

After receiving (s_t), the DQN agent estimates the Q-value of each available action and selects the signal plan for the current decision step. Through the COM interface, the Python code assigns the selected signal plan to the DLT controller in Vissim. Vissim then continues the simulation under the selected signal plan. Detector measurements collected in the following second form the new state ($s(t+1)$), while the reward (r_t) is calculated from the resulting traffic conditions according to the adopted reward function. The transition from (s_t) to ($s(t+1)$), together with the selected action and the obtained reward, is used to update the DQL model. This sequence is repeated at every decision step until the end of the simulation.

Vissim also records the measures used for the final evaluation of each control strategy. These include average vehicle delay, average queue length, and the number of stops. After completing the simulation runs, the results obtained with the DQL controller are compared with those produced by fixed-time control, actuated control, and classical Q-learning.

Fixed time and actuated time traffic control for DLT intersection

Fixed-time control was defined for the base traffic demand shown in **Figure 1**. Signal timings were obtained from traffic volumes representative of the analyzed period and were then kept unchanged during the simulation. The optimization was carried out in Python using *NetworkX*, following the procedure presented by Jovanovic et al. (2024). For the considered demand, the resulting cycle length was 102 s, with green times of 37 s, 25 s and 25 s for the three phases. Yellow and all-red intervals were set to 3 s and 2 s, respectively. Saturation flow rates used in the optimization were estimated according to the HCM procedure (Ryus et al., 2010), with a basic saturation flow of 1900 veh/h per lane. The resulting fixed-time plan was implemented in Vissim using VISSIG.

The actuated controller used the stop-line detectors presented in Figure 1. Detector calls were used to determine whether the current phase should be extended or terminated and followed by the next phase in the predefined sequence. The minimum green time was 5 s, while the maximum green times were taken from the fixed-time solution. A 3 s extension was used for the main-road movements and 2 s for the side-street movements, following the FHWA guidance for alternative intersections (Huges et al., 2009). Actuated control was run in Vissim with the Ring Barrier Controller (RBC).

NUMERICAL EXAMPLE AND RESULTS

The Salt Lake City DLT shown in **Figure 1** was modelled in Vissim. The displaced left-turn crossovers are located 120 m (approximately 395 ft) from the main intersection. A uniform lane width of 3.5 m (approximately 12 ft) is used throughout the network, while the left-turn lanes on the minor approaches provide 110 m (approximately 360 ft) of storage. The traffic demands used in the simulation are shown in Figure 1 and were kept unchanged for all four control strategies.

Desired speeds were selected to match the posted speed limits at the actual site. Vehicles travel at 70 km/h (approximately 45 mph) along the main arterial and at 50 km/h (approximately 30 mph) on the minor street. The available space within the displaced left-turn lanes limits the length of their queue detection areas. On the remaining approaches, queue detectors extend 160 m (approximately 525 ft) upstream of the main-street stop lines and 100 m (approximately 328 ft) upstream of the minor-street stop lines.

The results for all control strategies are given in Table 1. Average delay, average queue length, and the average number of stops were recorded. The percentage difference from the best-performing strategy is also reported for each measure. The best values are shown in bold. Each control strategy was tested using five random seeds: 12, 22, 32, 42 and 52. The values reported in Table 1 are the averages obtained from these five simulation runs. The 3,600 s evaluation period was also divided into ten 360 s intervals to show the change in performance during the simulation, with 150 s of the warm-up time.

Table 1 Results

Average from 5 different seeds	Average delay (s/veh)	Average # of stops (stops/veh)	Average queue (m)	The percentage difference between the best logic (b.l.) and others logic		
				Delay	# of stops	Queue
Fixed time TC (FTTC)	27.63	0.81	9.08	40,35 %	17,28 %	55,4 %
Actuated TC (ATTC)	24.2	0.71	6.89	31,9 %	5,63 %	41,22 %
Q learning TC (QLTC)	19.36	0.75	4.54	14,88 %	10,67 %	10,79 %
Deep Q learning TC (Deep QLTC)	**16.48***	**0.67***	**4.05***	b.l.	b.l.	b.l.

A paired *t*-test was used to compare the best and the second-best control strategies for each performance measure, using the results obtained with the five random seeds. An asterisk (*) indicates that the best-performing strategy is significantly better than the second-best strategy at the 95% confidence level.

Deep QLTC gave the lowest values for all three measures: an average delay of 16,48, an average of 0,67 stops, and an average queue of 4,05. Compared with FTTC, these values were lower by 40,35%, 17,28%, and 55,40%, respectively. The reductions in relation to ATTC were 31,90% for delay, 5,63% for stops, and 41,22% for queue length. The differences between QLTC and Deep QLTC were 14,88% for delay, 10,67% for stops, and 10,79% for queue length, in favor of Deep QLTC. QLTC gave lower delay and queue values than FTTC and ATTC. For the number of stops, ATTC was better than QLTC (0.71 compared with 0.75). Deep QLTC had the lowest value for all three measures.

Figure 4 shows the results for the tested control logics under the base traffic demand. The one-hour simulation was divided into ten intervals of 360 s.

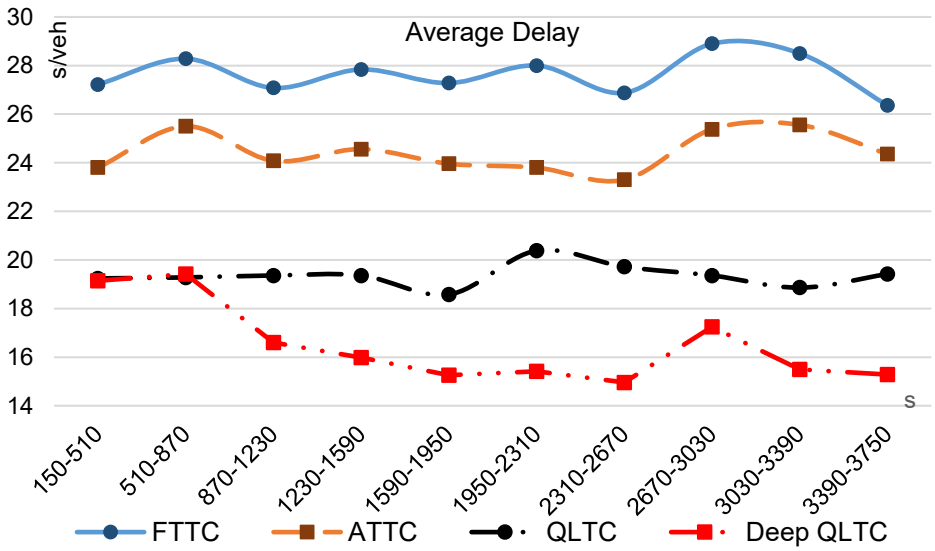

Figure 4 A graphical presentation of the average delay during the simulation

Overall, for the analyzed traffic demand scenario, Deep Q-Learning traffic control gave the best results among the tested control logics.

CONCLUSIONS

This paper examined the use of deep Q-learning for traffic control at a displaced left-turn intersection. Deep QLTC was compared with classical Q-learning, fixed-time control, and actuated control. The four control logics were tested on the same DLT model in Vissim. Deep Q-learning and Q-learning were programmed in Python and connected to Vissim through the COM interface.

Deep Q-learning gave lower delay and queue values than fixed-time control and actuated control, although actuated control produced fewer stops than Q-learning traffic control. Deep Q-learning was the only control logic that gave the best result for all three measures.

The analysis was carried out for one DLT layout and the base traffic demand pattern. More tests are needed under other traffic conditions. The next step is to improve the robustness of Deep QLTC when traffic volumes and turning movements change during operation, especially when actual demand differs from the conditions used for training. Near-saturated and oversaturated flows, uneven approach demands, and sudden changes in vehicle arrivals should also be tested. The method can later be extended to coordinated control along corridors and to networks with several conventional or alternative intersections.

REFERENCES

Chiou, S.-W. (2024). Co-evolutionary traffic signal control using reinforcement learning for road networks under stochastic capacity. *Applied Soft Computing, 161*, Article 111701. https://doi.org/10.1016/j.asoc.2024.111701

Gao, J., Shen, Y., Liu, J., Ito, M., & Shiratori, N. (2017). *Adaptive traffic signal control: Deep reinforcement learning algorithm with experience replay and target network*. arXiv. https://doi.org/10.48550/arXiv.1705.02755

Hughes, W., Jagannathan, R., Sengupta, D., & Hummer, J. (2009). Alternative intersections/interchanges: Informational report (AIIR) (No. FHWA-HRT-09-060). United States Federal Highway Administration, Office of Research, Development, and Technology. 2010. https://rosap.ntl.bts.gov/view/dot/37466

Jovanović, A., Uzelac, A., Kukić, K., & Teodorović, D. (2024). The shortest-path and bee colony optimization algorithms for traffic control at a single intersection with NetworkX application. *Demonstratio Mathematica*, 57, 20230160. https://doi.org/10.1515/dema-2023-0160

Magnana, L., Rivano, H., & Chiabaut, N. (2024). A deep reinforcement learning solution to help reduce the cost in waiting time of securing a traffic light for cyclists. *Journal of Cycling and Micromobility Research, 2*, 100046. https://doi.org/10.1016/j.jcmr.2024.100046

Ren, F., Dong, W., Zhao, X., Zhang, F., Kong, Y., & Yang, Q. (2024). Two-layer coordinated reinforcement learning for traffic signal control in traffic network. *Expert Systems with Applications, 235*, 121111. https://doi.org/10.1016/j.eswa.2023.121111

Ryus, P., Vandehey, M., Elefteriadou, L., Dowling, R. G., & Ostrom, B. K. (2011). New TRB publication: Highway Capacity Manual 2010. *TR News*, 273, 45–48. https://trid.trb.org/View/1102481

Steyn, H., Bugg, Z., Ray, B., Daleiden, A., Jenior, P., & Knudsen, J. (2014). *Displaced left turn intersection: Informational guide* (Report No. FHWA-SA-14-068). U.S. Department of Transportation, Federal Highway Administration, Office of Safety. https://rosap.ntl.bts.gov/view/dot/29475

Wei, H., Zheng, G., Yao, H., & Li, Z. (2018). IntelliLight: A reinforcement learning approach for intelligent traffic light control. In Y. Guo & F. Farooq (Eds.), *Proceedings of the 24th ACM SIGKDD International Conference on Knowledge Discovery & Data Mining* (pp. 2496-2505). Association for Computing Machinery. https://doi.org/10.1145/3219819.3220096

Zhao, J., Ma, W., Head, K. L., & Yang, X. (2015). Optimal operation of displaced left-turn intersections: A lane-based approach. *Transportation Research Part C: Emerging Technologies, 61*, 29–48. https://doi.org/10.1016/j.trc.2015.10.012

Zhao, H., Dong, C., Cao, J., & Chen, Q. (2024). A survey on deep reinforcement learning approaches for traffic signal control. *Engineering Applications of Artificial Intelligence, 133*, 108100. https://doi.org/10.1016/j.engappai.2024.108100

Zhong, N., Liu, K., & Li, Y. (2023). Deep Q-learning network model for optimizing transit bus priority at multiphase traffic signal controlled intersection. *Mathematical Problems in Engineering, 2023*, 9137889. https://doi.org/10.1155/2023/9137889

The 11th International Congress
Motor Vehicles & Motors 2026
Kragujevac, Serbia
October 8th - 9th, 2026

Motor Vehicles & Motors

MVM2026-014
https://doi.org/10.24874/CMVM2026.014
Original scientific paper

Boris Stojić[1]
Nebojša Nikolić[2]
Luka Sekicki[3]

A FLEXIBLE COMPUTATIONAL MODEL FOR FUEL CONSUMPTION ESTIMATION IN ARBITRARY VEHICLE DRIVING CYCLES

ABSTRACT: Vehicle fuel consumption and related topics have long attracted considerable research interest because of their economic, environmental and social implications. In this paper, the FuelSim_v1.0 computer program for vehicle fuel-consumption estimation was developed in GNU Octave programming environment. Consumption estimation model is based on the vehicle longitudinal dynamics and uses quasi-static method of the fuel consumption estimation. This approach divides the driving cycle into a large number of short time intervals, applies a steady-state calculation to each interval, and subsequently sums the corresponding partial fuel-consumption quantities. Input data for vehicle and driving cycle are provided through externally configurable files so that different kinds of vehicles can be examined in wide spectrum of driving conditions. Program, that is primarily conceived as educational and research tool, can be used for analysis of various types of motor vehicles in various usage patterns. It enables examination of influence of multiple kinds of design and/or operation parameters on the result, parameter sensitivity analyses etc. Preliminary examination of the simulation outputs indicated correct program functionality and consistency of the results obtained with the expected qualitative behaviour of the simulated vehicle. Formal validation, however, is left for the future work.

KEYWORDS: motor vehicle, fuel consumption, energy consumption, driving cycle, simulation

FLEKSIBILNI RAČUNARSKI MODEL ZA PROCENU POTROŠNJE GORIVA U PROIZVOLJNIM VOZNIM CIKLUSIMA VOZILA

REZIME: Potrošnja goriva vozila i srodne teme već dugo privlače značajnu pažnju istraživača zbog svojih ekonomskih, ekoloških i društvenih implikacija. U ovom radu razvijen je računarski program FuelSim_v1.0 za procenu potrošnje goriva motornih vozila, u programskom okruženju GNU Octave. Model za procenu potrošnje zasnovan je

[1] *Boris Stojić, University of Novi Sad, Faculty of Technical Sciences, Trg Dositeja Obradovića 6, 21000 Novi Sad, Serbia, bstojic@uns.ac.rs, https://orcid.org/0000-0001-8344-1466*
[2] *Nebojša Nikolić, University of Novi Sad, Faculty of Technical Sciences, Trg Dositeja Obradovića 6, 21000 Novi Sad, Serbia, nebnik@uns.ac.rs, https://orcid.org/0000-0003-4657-3640*
[3] *Luka Sekicki, University of Novi Sad, Faculty of Technical Sciences, Trg Dositeja Obradovića 6, 21000 Novi Sad, Serbia, luka.sekicki@uns.ac.rs, https://orcid.org/0009-0007-9170-8352*

na uzdužnoj dinamici vozila i koristi kvazistatičku metodu procene potrošnje goriva. Ovaj pristup podrazumeva podelu voznog ciklusa na veliki broj kratkih vremenskih intervala, primenu proračuna za slučaj ustaljenog kretanja u svakom od njih, a zatim sabiranje odgovarajućih parcijalnih količina potrošenog goriva. Ulazni podaci za vozilo i vozni ciklus zadati su putem eksterno konfigurabilnih datoteka, tako da se mogu analizirati različite vrste vozila u širokom spektru uslova vožnje. Program, koji je prvenstveno zamišljen kao obrazovni i istraživački alat, može se koristiti za analizu različitih vrsta motornih vozila pri različitim načinima upotrebe. Omogućava ispitivanje uticaja različitih konstrukcionih i/ili eksploatacionih parametara na rezultat, analize osetljivosti na promenu parametara i slično. Preliminarno ispitivanje rezultata simulacije ukazalo je na ispravno funkcionisanje programa i usklađenost dobijenih rezultata sa očekivanim kvalitativnim ponašanjem simuliranog vozila. Formalna validacija, međutim, ostavljena je za buduća istraživanja.

KLJUČNE REČI: motorno vozilo, potrošnja goriva, potrošnja energije, vozni ciklus, simulacija

INTRODUCTION

Vehicle energy consumption, and the associated consumption of fuel or other energy resources, has long been an important economic, environmental and social concern. The importance of this topic stems largely from its direct consequences, including resource depletion and pollutant emissions. The study of energy and fuel consumption in motor vehicles along with connected topics has therefore long attracted considerable research attention and has been addressed in numerous publications. Besides directly addressing fuel saving potentials and pollutant minimization, other topics that are frequently dealt with by researchers comprise e.g. control optimisation, route planning, smart resource exploitation, alternative and renewable energy sources research etc. Examples include e.g. the works of researchers such as Ben-Chaim, M. et al. (2013), Dekraker, P. et al (2018)., Genikomsakis, K. N. & Mitrentsis, G. (2017), Pfriem, M. & Gauterin, F. (2016), Yuan, X. et al. (2017), and many others.

Therefrom, motivation for this paper arises in order to provide further contributions to this research field. Goal of the paper is to develop simulation tool, i.e., computer program for implementation of the model aimed to estimate the fuel consumption of arbitrary motor vehicle in arbitrary driving cycle. Program should exhibit flexibility with regard to characteristics of the applied driving cycle, vehicle parameters and powertrain operating conditions, since these parameters substantially impact consumption. Flexibility is provided in a way that both driving cycles and vehicle-related parameters are provided as externally configurable datasets, allowing analysis of the broad spectrum of motor vehicles and driving situations without modification of the computational structure itself.

The presented approach is primarily intended as a flexible research and educational tool suitable for comparative analysis of vehicle design and operating conditions, driving cycle and transmission strategies influence on estimated fuel consumption. In addition to calculation of consumption itself, such tool should be capable of being implemented for more general studies, such as:

- Comparison of various standardized and non-standardized driving cycles.
- Influence study of the vehicle design and operational parameters.
- Sensitivity analysis.
- Assessing the effectiveness of technologies regarding fuel consumption.
- Assessing driving style impact and saving potentials through its improvement.
- Different areas of optimisation (design parameters, control strategies, gear shifting schedule, route planning...).

Method should be computationally efficient, relying on simple but accurate physical model of vehicle longitudinal dynamics, not requiring highly-detailed vehicle and its subsystems description and complex datasets. Model and software structure are supposed to be convenient for further upgrades, enhancements and extensions with new features.

Generally, procedures for consumption estimation share many common elements and approaches regardless of the powertrain type in regard. Additionally, in some cases powertrain-specific aspects still have to be accounted for. This paper and work carried out herein focuses on powertrain that can still be considered as conventional one, i.e., one consisting of the internal combustion (IC) engine as a prime mover, main clutch and a gearbox with the finite number of gear ratios. This approach should be viewed as an introductory development phase, as future developments of the program and its capabilities are intended.

THEORETICAL BASICS OF VEHICLE ENERGY AND FUEL CONSUMPTION

Motion resistances and driving cycle energy requirements

During arbitrary driving conditions, vehicle encounters a range of sources of energy consumption. Impact of these individual sources, i.e., their contribution to overall energy consumption in relation to each other, depends on vehicle type and design parameters, as well as current driving pattern and conditions.

External driving resistances

External motion resistances are summarized in Figure 1 and briefly described subsequently.

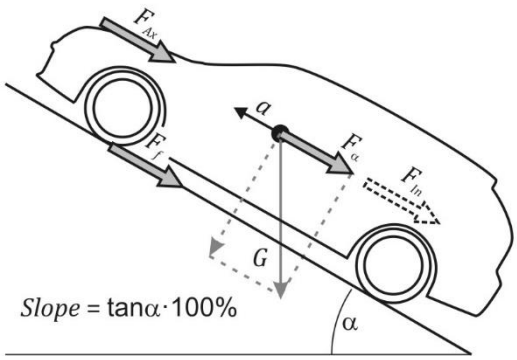

Figure 1 Motion resisting forces: $\boldsymbol{F_f}$ – rolling resistance (summary for all wheels); $\boldsymbol{F_{Ax}}$ – aerodynamic resistance; $\boldsymbol{F_\propto}$ – road gradient resistance; $\boldsymbol{F_{In}}$ – D'Alembert inertial force ($\boldsymbol{a}$ – acceleration); $\boldsymbol{G}$ – vehicle weight; $\boldsymbol{\alpha}$ – road gradient angle

First dissipative force, which always accompanies vehicle motion, is rolling resistance F_f originating from internal friction or hysteresis in rolling tyre. It is usually described by expression (1):

$$F_f = m \cdot g \cdot f \cdot \cos\alpha \tag{1}$$

Here, m is vehicle mass, g is gravitational acceleration, α is road gradient or slope angle, and f is rolling resistance coefficient, for which dependency on multiple factors such as vehicle speed, ground force and/or tire pressure can be introduced by modelling if required, which is omitted herein. For values of road gradients typically encountered by road vehicles, cosine from expression (1) remains very close to unity and can therefore usually be approximated as 1. Should, however, vehicle encounter higher road gradients, such as in off road driving or other extreme conditions, it's more exact value should be used.

Next dissipative force is aerodynamic resistance F_{Ax} (expression (2)), originating from complex interactions of the moving vehicle with the surrounding air.

$$F_{Ax} = C_{Ax} \cdot A \cdot \frac{\rho \cdot v^2}{2} \tag{2}$$

Here, C_{Ax} is aerodynamic drag coefficient, A is vehicle frontal area, ρ is air density, and v is vehicle speed, providing no wind is present (otherwise, relative speed between vehicle and wind has to be used, possibly including dependency on the yaw angle of the wind direction with regard to the vehicle). If vehicle moves at very low speed, contribution of the aerodynamic resistance to vehicle energy consumption can be practically neglected compared to other effects. On the other hand, at highway speeds it typically becomes one of the dominant contributors to the vehicle's motion resistance.

Road gradient resistance $F_\propto$ (expression (3)) is present when vehicle negotiates upward road slope. It represents component of gravitational force acting along the direction of travel. Contrary to rolling and air resistances, this force, originating from gravitational potential energy due to altitude changes, is conservative. For downward slope, numerical value of this force is negative, meaning that it aids vehicle motion instead of opposing it.

$$F_\propto = m \cdot g \cdot \sin\alpha \approx m \cdot g \cdot \frac{Slope\ [\%]}{100} \tag{3}$$

As shown in expression (3), for determination of the road gradient resistance F_α, road $Slope$ in percent can also be used instead of the angle α, taking into account that $\tan\alpha = Slope/100$ (see also Figure 1), and that approximation $\sin\alpha \approx \tan\alpha$ for small angles is fairly useful for road vehicles (e.g. Mitschke, M. & Wallentowitz, H. 2014).

Next conservative effect is storing of kinetic energy in the vehicle, which requires vehicle to accelerate until certain amount of it is reached. Effect of the kinetic energy accumulation through the acceleration is described by expression (4) through fictitious inertial force F_{In} according to the D'Alembert principle:

$$F_{In} = \left(m + \frac{J_{Equ}}{r_W^2}\right) \cdot a \approx \delta \cdot m \cdot a \tag{4}$$

Here, a is vehicle longitudinal acceleration, and J_{Equ} represents equivalent moment of inertia of all rotational masses as felt at the wheels. For calculation simplification, this quantity can be replaced by the coefficient δ, describing the same effect in the empirical way. Finally, r_W is effective wheel radius.

In this paper, empirical relationship according to Gillespie, T. (2021) will be used in order to evaluate coefficient δ, as given by the expression (5). This value depends on overall transmission ratio, since it is influenced by the share of rotational masses in overall kinetic energy of the vehicle. Therefore, it has to be calculated for every transmission gear individually.

$$\delta = 1.04 + 0.0025 \cdot i_{Tr}^2 \tag{5}$$

Here, i_{Tr} represents the current value of the overall transmission gear ratio, i.e., in the gear currently selected.

Internal driving resistances and summary of internal dissipative effects

Transmission losses (also dissipative by nature) and drive of auxiliary units can be regarded as internal driving resistance. Most frequently, they are taken into account in the simplified way through the overall transmission efficiency η_{Tr} that is assumed to have constant value, as given e.g. by Gillespie, T. (2011), Mitschke, M. & Wallentowitz, H. (2014), Guzzella, L. & Sciarretta, A. (2022). As shown subsequently, dissipative effects of the friction braking (and possibly energy losses of the recuperative braking if applied) also have to be taken into account if entire driving cycle energy balance is considered.

Wheel force and driving cycle energy balance

Driving wheel force F_W required to overcome all driving resistances can be calculated according to the expression (6):

$$F_W = F_f + F_{Ax} \pm F_\alpha + F_{In} \tag{6}$$

On the other hand, value of this force that is available from the powertrain is given by the expression (7):

$$F_W = \frac{T_W}{r_W} = \frac{T_e \cdot i_{Tr} \cdot \eta_{Tr}}{r_W} \tag{7}$$

Here, T_W is the summary driving torque applied to the driving wheels, T_e is the engine torque, i_{Tr} is current value of overall transmission gear ratio, and η_{Tr} is overall transmission efficiency.

If negative value of required wheel force is obtained in certain phases of driving cycle by using expression (6), that means that the vehicle is under braking instead of driving (braking torque is being applied to the wheels). In that case, the power flow changes direction, going from the vehicle to the wheels, and therefrom to the transmission, and eventually to the engine (which then provides braking torque) if the main clutch is not disengaged. This backward flowing power / energy can then, partially or entirely, be used for overcoming transmission losses, auxiliary units drive and engine friction and pumping losses, at a cost of vehicle kinetic or gravity energy. If all these losses and energy requirements are completely covered by available kinetic energy of the decelerating vehicle, and/or gravitational energy of the downwards driving one, the engine fuel supply can be cut off for consumption savings and pollutant emission reduction. Should available backward power be larger than this limit value for a finite amount of time, remaining energy can be partially recuperated if appropriate system is installed in the vehicle. Without such system, all braking energy is lost by dissipation through the action of friction braking system or engine braking. At this place it should be highlighted that, even when using recuperating device, its own efficiency has to be taken into account

because some energy losses will inevitably occur during energy conversion steps. These losses also add to dissipative effects.

As long as the vehicle is in motion, i.e., as long as any amount of kinetic energy remains available, it will be dissipated through rolling and air resistances, even during braking. This prevents full amount of kinetic energy stored in the vehicle to be supplied to recuperation system during recuperative braking.

If zero-wheel force is obtained by expression (6), that means that wheels are in the state of the free rolling, which occurs when external motion resistances are in balance with mechanical energy stored in the vehicle. Some amount of fuel will, even in such situation, be consumed for covering internal losses mentioned above.

Considering energy balance of the vehicle motion, vehicle itself can be seen as a storage system for conservative energy forms (kinetic and altitude gravity potential), supplied to the vehicle by the powertrain, for which itself certain amount of energy supply through the fuel consumption is required. On the other hand, different aforementioned dissipative mechanisms and auxiliary units drive can be seen as effects that drain this energy storage (Guzzella, L. & Sciarretta, A. 2022). Dissipative effects require constant energy supply through powertrain for the vehicle to keep moving, as opposed to conservative effects, which require a corresponding amount of energy to be supplied only once. On the other hand, as shown, compensation of energy dissipation partially occurs also through conservative mechanical energy that has already been stored in the vehicle.

Finally, to establish connection between vehicle and engine operating point (defined by pairs (F_W, v) and (T_e, n_e), respectively), required for fuel consumption calculation, relationship between vehicle speed and engine speed is required. This is given by expression (8):

$$v = \frac{\pi \cdot r_W \cdot n_e}{30 \cdot i_{Tr}} \tag{8}$$

Here, v is vehicle speed in [m/s] and n_e is engine speed in revolutions per minute. If unit of [km/h] is used for calculations, appropriate unit conversion has to be carried out.

Prime mover – from energy to fuel consumption

Prime movers convert fuel energy to mechanical energy required for vehicle to negotiate certain driving cycle. This way, vehicle energy consumption turns to fuel consumption (which is also directly related to CO_2 and other pollutants emission, although this important topic is not covered by this paper). IC engines are generally characterized by relatively low efficiency. Peak efficiency values are typically not much higher than around 30% for spark-ignition engines and 40% for compression-ignition engines (Heywood, 2018). At partial loads, which occur frequently under typical road-vehicle driving conditions, efficiency is substantially lower. These relatively low efficiencies represent a major limitation in the overall conversion of fuel energy into mechanical energy.

Energy efficiency and/or fuel consumption data for IC engines can be provided by several mutually dependent indicators: thermal efficiency ratio (η_e, [-] or [%]), brake-specific fuel consumption (BSFC - g_e, [g/kWh] or equivalent unit) or fuel rate (g_h, [g/h] or equivalent unit).

Efficiency indicator values vary significantly with engine load and speed, usually exhibiting optimum at relatively high engine loads and moderate speeds. Two kinds of the diagrams for engine efficiency and fuel consumption are shown in Figure 2, indicating their general shape.

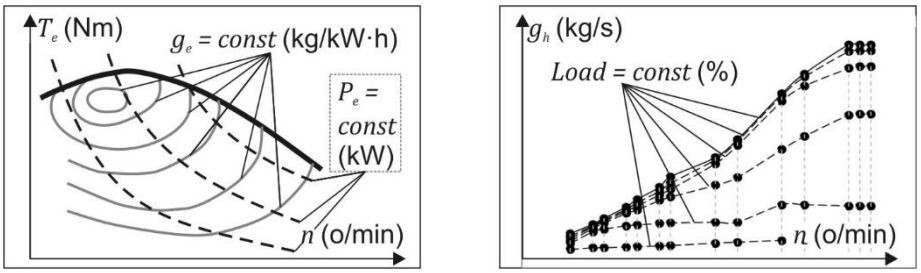

a) b)

Figure 2 a) Engine efficiency or BSFC map (shell diagram): thick line – engine torque at full load; thin lines: constant values of engine efficiency or BSFC; dashed lines: constant-power curves.
b) Fuel rate vs. engine rpm, for different values of engine load

Figure 2 a) shows efficiency/consumption map also known as shell diagram. This type of chart uses contour lines connecting points with equal efficiency values, indicated through thermal efficiency ratio or BSFC. While this type of

map is better suited for theoretical considerations, the second one, shown in Figure 2b), is more appropriate for practical calculations. This chart shows curves of fuel rate as a function of engine rotational speed (usually given by revolutions per minute – rpm), for constant values of engine load[1]. This is graphical representation of the tabular dataset, which is convenient to use when carrying out calculations. Alternatively, dataset can also provide fuel rate as a function of engine rpm and torque, which is also convenient for practical applications.

Transmission influence on fuel consumption

Besides transmission impact on vehicle energy and fuel consumption through unwanted energy losses, second and more important influence of the transmission is the possibility of changing engine operating point by controlling gear selection for the same vehicle operating conditions, thereby potentially improving engine efficiency. For given vehicle operating point, engine operating point can be located theoretically anywhere on the appropriate constant-power curve in the scope of available engine torque and rpm limits (Figure 2a). Particular engine operating point is determined by current transmission gear ratio. An upshift results in an increase in the required engine torque accompanied by a decrease in engine speed for the same vehicle operating point. This may move the engine operating point towards a region of higher efficiency. Shifting strategy that is optimized for a certain vehicle driving pattern can therefore contribute to fuel savings (Guzzella, L. & Sciarretta, A. 2022).

IMPLEMENTATION OF FuelSim_v1.0 COMPUTER PROGRAM IN GNU OCTAVE PROGRAMMING ENVIRONMENT

Basic principles

Calculating of the fuel consumption for the steady-state vehicle motion (constant speed, constant wheel force and constant gear selected) is straightforward and generally does not require any aid of sophisticated computational tools. Knowing vehicle operating point and the transmission gear applied, engine operating point is determined by using relationships discussed in previous part of the paper. Therefrom, fuel rate value is determined using engine map data. This is then easily converted into some other appropriate unit, e.g., typically litres per 100 km.

Regarding driving cycles with operating points changing in time, approach becomes more demanding. As described by Guzzella, L., & Sciarretta, A. (2022), one possible solution is to use method described for steady-state drive, assuming averaged out value of engine efficiency. This is easy to implement, but gives very rough and unreliable consumption assessment. Next solution is forward physical modelling of longitudinal vehicle dynamics, integrating differential equations of motion starting from engine torque-rpm curves and using integrated driver closed loop control model in order to obey given speed profile in time. In other words, starting from the engine torque map and given load input, vehicle motion is determined. Then energy and fuel consumption can be obtained along with other results of such simulation. This is most correct approach from physical point of view, but most demanding to implement.

A compromise between these approaches is to use quasi-static method, that uses backward modelling approach. That means that, starting from the current vehicle operating point prescribed, current required engine operating point is determined. Method is applied by dividing driving cycle into many discrete short time intervals, so that partial quantities of the fuel consumed are determined for every of them by using steady-state approach described above. Total consumption is then obtained by summing these partial results. Implementation of this approach, if appropriate tailor-made software tool is not available, requires at least basic level of computer programming skills due to loops and branches required in general case to simulate vehicle negotiating given driving profile. Despite some characteristic limits and constraints that will be addressed in a subsequent section, this approach has been proven to provide very accurate and reliable computational results as stated by Dekraker, P. et al. (2018).

In the scope of this work, software tool named FuelSim_v1.0 was developed in GNU Octave version 9.4.0 programming environment, Eaton, J. W. et al. (2024).

GNU Octave programming environment

GNU Octave uses a programming language with syntax that is very similar to and highly compatible with MATLAB. It is free software distributed under the terms of the GNU General Public License (GPL), as published by the Free Software Foundation (Free Software Foundation, 2007). GNU Octave provides extensive support for numerical computations, matrix operations, interpolation, and data processing, making it well suited for the implementation of

[1] In order not to confuse "engine load" and "engine torque", what is meant by "load" here is the current position of the engine load control device, which can roughly be seen as an accelerator pedal position.

the proposed model. Its high compatibility with MATLAB also facilitates potential future migration of the developed code to the MATLAB environment.

Description of the model and algorithm

FuelSim is a computational model developed for estimating the fuel consumption of a road vehicle over an arbitrary driving cycle, defined by a vehicle speed–time profile and, optionally, a road-gradient profile. Although the general principles of the model are largely independent of the propulsion concept, the present version, FuelSim_v1.0, is specifically configured for a vehicle powered by an IC engine and equipped with a gearbox with finite number of gear ratios and a friction clutch. The model also incorporates a predefined gear-shifting strategy based on vehicle speed and engine load.

The required input data include vehicle parameters, transmission ratios and efficiency, engine torque characteristics, fuel-flow maps, upshift and downshift schedules, and the prescribed driving cycle. Engine torque and fuel-flow data are provided as functions of engine speed and load. The driving cycle is represented by discrete time–speed points, with road gradient optionally assigned to each point.

The calculation is performed sequentially over the driving cycle using a quasi-static approach. For each time step, vehicle acceleration and the corresponding inertia, rolling, aerodynamic and road gradient-resistance forces are determined. Their combination gives the required wheel force. Based on the currently engaged gear, the corresponding engine speed and required engine torque are then calculated, while interpolation of the engine map provides the associated engine load.

The calculated operating point is checked against the engine operating limits. If the required torque exceeds the maximum available engine torque, a forced downshift is performed where possible. Conversely, if the prescribed engine-speed threshold is exceeded, a forced upshift is applied. After each such gear change, the engine operating point and the gear-dependent inertia effects are recalculated.

For the final engine operating point, the instantaneous fuel mass flow is obtained by two-dimensional interpolation of the fuel-consumption map as a function of engine speed and load. Fuel consumed during each time step is calculated from the corresponding fuel mass flow and time-step duration and accumulated over the complete driving cycle. The resulting total fuel mass can subsequently be converted into conventional fuel-consumption measures, such as l/100 km.

Finally, the regular gear-shifting strategy is applied using predefined upshift and downshift curves. For the current engine load and gear, the corresponding shift speed is obtained by interpolation and compared with the current vehicle speed. If the respective criterion is satisfied, the selected gear is changed for the following calculation step.

The program was tested using several purpose-built driving cycles designed to verify various aspects of its functionality.

Model limitations

The present version of FuelSim is intended as a relatively simple and flexible tool for fuel-consumption assessment and therefore incorporates several simplifying assumptions. The model follows a quasi-static (quasi-steady-state) approach, which is based on determining required engine operating point based on the currently given operation point of the vehicle. Unlike a forward dynamic simulation, in which vehicle motion is obtained by integrating the equations of motion from the powertrain output and applied control inputs, the quasi-static approach determines the engine operating point required to satisfy a prescribed instantaneous vehicle state. In quasi-static model, the vehicle and engine operating conditions are evaluated at discrete time steps without modelling the transient behaviour of the powertrain. Consequently, effects such as engine torque response dynamics, turbocharger dynamics, and the duration and transient behaviour of gear shifts are not considered.

The transmission model is also simplified. Transmission efficiency is assumed to be constant, while clutch slipping losses during vehicle launch and gear shifts, as well as interruptions in power flow during shifting, are neglected. Hydrodynamic torque converters and continuously variable transmissions are not included in the present model.

The implemented regular shifting strategy assumes that upshifts occur during acceleration and downshifts during deceleration only. Furthermore, once the corresponding shift criterion is satisfied, the newly selected gear is applied from the following calculation step. These simplifications may not fully reproduce actual transmission or driver behaviour under all operating conditions. The discretisation of the driving cycle may therefore also affect the calculated engine operating points, gear-shift timing and, ultimately, the estimated fuel consumption.

Results example

Vehicle data

Some of the program capabilities are briefly demonstrated by example shown herein. The input data used in this example do not represent any specific vehicle; instead, they constitute an illustrative dataset representative of a generic passenger car. Data are shown in the Table 1, as well as additionally in Figure 3.

Table 1 Vehicle data

Quantity	Label	Unit	Value
Vehicle mass	m	kg	1350
Frontal area	A	m^2	2.65
Drag coefficient	C_{Ax}	-	0.35
Wheel radius	r_W	m	0.33
Number of gears	-	-	7
Gearbox ratios	$i_{G,j}, j = 1 \div 7$	-	4.38, 2.86, 1.92, 1.37, 1, 0.82, 0.7
Final drive ratio	i_{FD}	-	3.98
Transmission efficiency	η_{Tr}	-	0.9
Gear shifting schedule	-	-	Figure 3 c
Engine torque map	$T_e(n, Load)$	Nm	Figure 3 a
Engine fuel consumption map	$g_h(n, Load)$	kg/s	Figure 3 b

Engine torque map (Figure 3 a) and fuel consumption map (Figure 3 b) are given as a function of engine rpm for a number of engine load values, as numerical tabular dataset. Since this data form is inconvenient to be represented, they are illustrated herein as charts based on these data. The same principle applies for gear-shift schedule (Figure 3 c), which is given as a series of curves of shifting speed vs. engine load, for all gears and for both shifting directions.

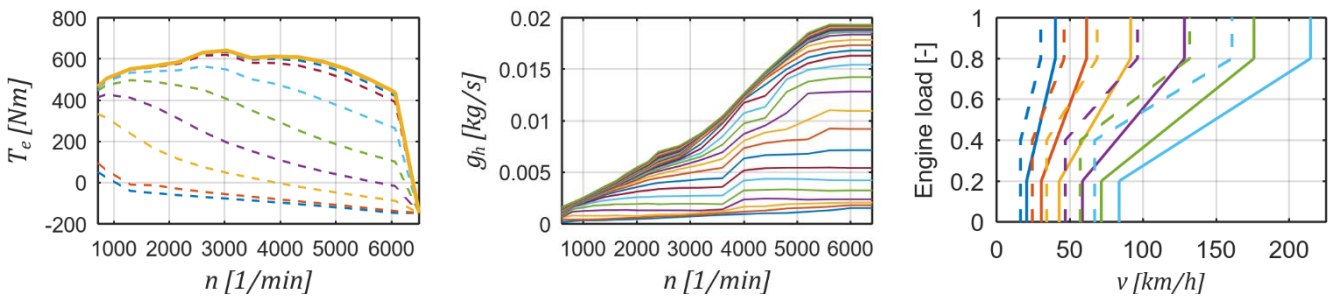

a) b) c)

Figure 3 Graphical representation of tabular datasets used for calculations: a) Engine torque map; b) Engine consumption map; c) Gear-shifting schedule (solid lines upshifts, dashed lines downshifts)

Driving cycle and simulation output examples

For the results demonstration, Worldwide harmonized Light-duty vehicles Test Cycle (WLTC) Class 3 (United Nations Economic Commission for Europe [UNECE], 2025) has been chosen. It is implemented in the scope of Worldwide Harmonised Light vehicles Test Procedure (WLTP), which represents widely adopted standard for determination of fuel consumption and the levels of pollutants emission for vehicles with various types of the powertrain (UNECE, 2025).

Firstly, distance travelled is calculated by the program. Result obtained is:

S = 23.266 km – total distance travelled

This corresponds to the distance declared by (UNECE, 2025).

Main fuel consumption results are:

m_F = 1.65 kg – total mass of fuel consumed

$V_{l/100km}$ = 8.86 l/100 km – average fuel consumption

Figure 4a shows speed profile of the WLTC Class 3 which is used as simulation input for the vehicle driving profile. Other parts of the Figure 4 show changes of several selected parameters during cycle duration:

- Figure 4b: total mass of fuel consumed.
- Figure 4c: gear selected.
- Figure 4d: engine load (roughly corresponding to accelerator pedal position).
- Figure 4e: engine rpm

Detailed discussion and interpretation of results represented herein will be omitted. Their purpose is just to provide preliminary insight in overall simulation features. Based on numerical values and visual appearance of time curves, it can be empirically assessed that simulation results exhibit physical plausibility and consistency with the expected qualitative behaviour of the simulated vehicle. Detailed verification and validation are, however, left to the next phase of the research.

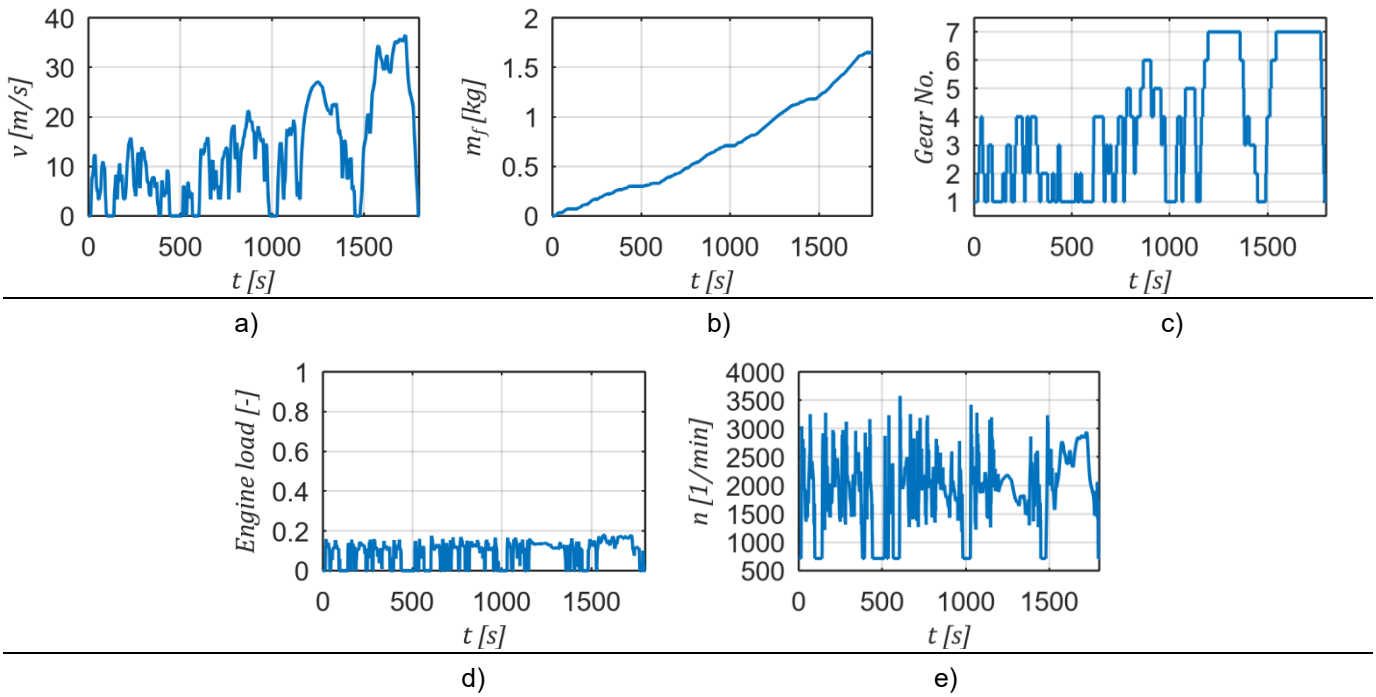

Figure 4 Simulation results: a) WLTC speed profile, b) mass of fuel consumed, c) gear selected, d) engine load (roughly corresponding to accelerator pedal position), e) engine rpm.

CONCLUSIONS

FuelSim_v1.0 provides a functional and flexible educational and research framework for quasi-static estimation of vehicle fuel consumption over arbitrary prescribed driving cycles. Its externally configurable vehicle, engine, transmission and driving-cycle data allow the same computational framework to be applied to a broad range of comparative studies.

The implemented approach exhibits certain limitations that should be taken into account by users, and that result from both intrinsic features of the applied modelling technique itself and some simplifications adopted for easier model implementation. Main limitations of the quasi-static modelling technique are among others inability to capture transient phenomena and possible susceptibility to the temporal resolution of the driving cycle. Further model limitations are mostly connected with some simplification in transmission behaviour representation, e.g., omitting of the clutch slip impact and somewhat simplified implementation of the gear shifting schedule.

In this work WLTC driving cycle was used to demonstrate some of the simulation outputs. Results obtained generally show proper function of the program. The numerical values and time histories obtained appear physically plausible and consistent with the expected qualitative behaviour of the simulated vehicle. However, formal verification and validation of the model is most important next step in forthcoming research. Other future development prospects can include e.g.:

- Formal verification/validation and benchmarking.
- Improved transmission, braking/fuel-cut-off and energy-loss modelling.
- Extension to additional powertrain architectures.
- Possible transition towards higher-fidelity forward dynamic simulation.

ACKNOWLEDGMENTS

This research has been supported by the Ministry of Science, Technological Development and Innovation (Contract No. 451-03-34/2026-03/200156) and the Faculty of Technical Sciences, University of Novi Sad through project "Scientific and Artistic Research Work of Researchers in Teaching and Associate Positions at the Faculty of Technical Sciences, University of Novi Sad 2026" (No. 01-3609/1).

REFERENCES

Ben-Chaim, M., Shmerling, E., & Kuperman, A. (2013). *Analytic modeling of vehicle fuel consumption. Energies*, 6 (1), 117–127. https://doi.org/10.3390/en6010117

Dekraker, P., Barba, D., Moskalik, A., & Butters, K. (2018, April). Constructing engine maps for full vehicle simulation modeling. In *WCX World Congress Experience 237382*. https://doi.org/10.4271/2018-01-1412

Eaton, J. W., Bateman, D., Hauberg, S., & Wehbring, R. (2024). *GNU Octave version 9.4.0 manual: A high-level interactive language for numerical computations*. GNU Octave. GNU Octave 9.4.0 Manual, https://www.gnu.org/software/octave/doc/v9.4.0/, accessed 2024.

Free Software Foundation. (2007). *GNU General Public License* (Version 3). GNU General Public License v3.0. https://www.gnu.org/licenses/gpl-3.0.html

Genikomsakis, K. N., & Mitrentsis, G. (2017). A computationally efficient simulation model for estimating energy consumption of electric vehicles in the context of route planning applications. *Transportation Research Part D: Transport and Environment*, 50, 98-118. https://doi.org/10.1016/j.trd.2016.10.014

Gillespie, T. (2021). *Fundamentals of vehicle dynamics*. SAE international.

Guzzella, L., & Sciarretta, A. (2022). *Vehicle propulsion systems: Introduction to modeling and optimization* (4th ed.). Springer. https://doi.org/10.1007/978-3-030-91891-3

Heywood, J. B. (2018). *Internal combustion engine fundamentals* (2nd ed.). McGraw-Hill Education.

Mitschke, M., & Wallentowitz, H. (2014). *Dynamik der Kraftfahrzeuge* (5th ed.). Springer Vieweg. https://doi.org/10.1007/978-3-658-05068-9

Pfriem, M., & Gauterin, F. (2016). Development of real-world driving cycles for battery electric vehicles. *World Electric Vehicle Journal*, 8(1), 14-24. https://doi.org/10.3390/wevj8010014

United Nations Economic Commission for Europe. (2025). *UN Global Technical Regulation No. 15: Worldwide harmonized Light vehicles test procedure (WLTP).* United Nations.

Yuan, X., Zhang, C., Hong, G., Huang, X., & Li, L. (2017). Method for evaluating the real-world driving energy consumptions of electric vehicles. *Energy*, 141, 1955-1968. https://doi.org/10.1016/j.energy.2017.11.134

The 11th International Congress
Motor Vehicles & Motors 2026
Kragujevac, Serbia
October 8th - 9th, 2026

Motor Vehicles & Motors

MVM2026-018
https://doi.org/10.24874/CMVM2026.018
Technical paper

Dušan Opsenica[1]
Ivan Blagojević[2]
Saša Mitić[3]

THE INFLUENCE OF ELECTRIC VEHICLE CONFIGURATION ON VEHICLE DYNAMIC CHARACTERISTICS

ABSTRACT: The influence of electric vehicle configuration on vehicle dynamic characteristics was analyzed through a comparative study of two electric propulsion configurations. The first configuration includes a vehicle with one electric motor per axle, while the second configuration consists of four electric motors integrated into the wheels (in-wheel). The research was conducted using co-simulation between MSC Adams/Car and MATLAB Simulink software packages. The vehicle models were developed in MSC Adams/Car software, in which the analysis and post-processing of the obtained results were performed. MATLAB Simulink software was used for propulsion system control, as well as for the analysis of vehicle energy efficiency. The research results were presented for the ISO Double Lane-Change maneuver, while the analysis was performed based on vehicle speed values, tire slip angles, achievable traction performance, and energy consumption values, with the aim of determining the influence of electric propulsion architecture on vehicle dynamic behavior and energy efficiency. The final results demonstrate that the optimized independent 4EM architecture provides a more stable dynamic response requiring a reduced steering wheel angle, while simultaneously achieving slightly better overall energy efficiency despite a 105 kg vehicle mass penalty compared to the centralized 2EM system.

KEYWORDS: electric vehicles, electric propulsion configuration, double lane-change maneuver, vehicle dynamics, energy efficiency

UTICAJ KONFIGURACIJE ELEKTRIČNOG POGONA NA DINAMIČKE KARAKTERISTIKE VOZILA

REZIME: Uticaj konfiguracije električnog pogona na vučno-dinamičke karakteristike vozila je sagledan uporednom analizom dve konfiguracije električnog pogona. Prva konfiguracija obuhvata vozilo sa po jednim elektromotorom na svakoj osovini, a druga četiri elektromotora koja su smeštena u svakom točku vozila (*in-wheel*). Istraživanje je sprovedeno primenom kosimulacije između *MSC Adams/Car* i *MATLAB Simulink* softverskih paketa. Modeli vozila

[1] *Dušan Opsenica, MSc, Faculty of Mechanical Engineering, University of Belgrade, Belgrade, Serbia,* dopsenica@mas.bg.ac.rs, https://orcid.org/0009-0009-4920-5940
[2] *Ivan Blagojević, PhD, Faculty of Mechanical Engineering, University of Belgrade, Belgrade, Serbia,* iblagojevic@mas.bg.ac.rs, https://orcid.org/0000-0002-5776-5990
[3] *Saša Mitić, PhD, Faculty of Mechanical Engineering, University of Belgrade, Belgrade, Serbia,* smitic@mas.bg.ac.rs, https://orcid.org/0000-0001-6999-5921

su razvijeni u *MSC Adams/Car* softveru, u kom je izvršena i analiza i obrada dobijenih rezultata. *MATLAB Simulink* softver je korišćen za upravljanje pogonskim sistemom, kao i za analizu energetske efikasnosti modela vozila. Rezultati istraživanja su prikazani za *ISO Double Lane-Change* manevar, pri čemu je analiza izvršena na osnovu vrednosti brzina vozila, proklizavanja pogonskih točkova, ostvarivih vučnih performansi, kao i vrednosti potrošnje energije, sa ciljem određivanja uticaja arhitekture električnog pogona na dinamičko ponašanje i energetsku efikasnost vozila. Konačni rezultati pokazuju da optimizovana nezavisna 4EM arhitektura pruža stabilniji dinamički odziv zahtevajući smanjen ugao zakretanja volana, dok istovremeno postiže blago bolju ukupnu energetsku efikasnost uprkos povećanoj masi vozila od 105 kg, u poređenju sa centralizovanim 2EM sistemom.

KLJUČNE REČI: električna vozila, konfiguracija električnog pogona, *manevar dvostruke promene trake*, dinamika vozila, energetska efikasnost

INTRODUCTION

The development of electric vehicles (EVs) has brought changes to the approach of the vehicle dynamics control. Unlike conventional internal combustion engine vehicles (ICE vehicles), electric motors enable fast, precise and asymmetric torque response. This opens up new possibilities for improving active safety, vehicle stability and energy efficiency under different driving conditions.

Previous research on electric vehicle dynamics has extensively demonstrated the benefits of independent torque control. Early foundational studies by Sawase et al. 2006 and Sawase & Ushiroda, 2008 highlighted significant improvements in vehicle cornering stability and lateral dynamics response through left-right torque vectoring. Building upon this foundation, Cong Geng et al. 2009 and Jalali et al. 2012 successfully implemented advanced control strategies, including fuzzy logic observers and slip-based control systems, to optimize the dynamic behavior of in-wheel motored vehicles. Furthermore, in their comprehensive dynamic modeling of various EV powertrains, De Novellis et al. 2014 and Park et al. 2014 emphasized the critical importance of selecting optimal torque distribution criteria to maximize both active safety and energy efficiency. Despite these advancements, quantifying the exact performance and energy trade-offs between centralized architectures and independent in-wheel configuration remains a critical area of investigation.

Among modern electric vehicles architectures, concepts featuring two electric motors (one on each axle – 2EM) and concepts with four independent in-wheel electric motors (in-wheel motors – 4EM) stand out in particular. While 2EM systems offer advanced longitudinal traction through intelligent power distribution between the front and rear axles, 4EM systems enable completely independent traction and braking control on each individual wheel. Instead of using the conventional braking system for stabilization, the 4EM architecture can continuously generate a corrective yaw moment through dynamic allocation of driving forces.

The main objective of this paper is the comparative analysis and performance evaluation between 2EM and 4EM electric vehicle architectures. To conduct simulation, multy-body vehicle models were developed in the MSC Adams software. The research is based on the application of co-simulation, where the physical vehicle model from Adams is coupled with the MATLAB/Simulink environment. Torque control was executed directly through Simulink based on vertical wheel loads, yaw rate, and steering wheel angle, enabling flexible power allocation during simulation maneuvers.

Through simulation analysis of a ISO standardized Double Lane-Change maneuver, the paper evaluates the behavior of both drive concepts with primary focus on vehicle stability and energy consumption, clearly quantifying the advantages and limitations of independent torque vectoring compared to central drive solutions.

DYNAMIC MODELS USED FOR SIMULATIONS

To conduct the comparative analysis two models were used, which are developed using MSC Adams software package. First model consists of 4EM, one in each wheel (in-wheel vehicle design). Other one is 2EM vehicle model (one electric motor per axle). Model architectures and mass distribution are presented below. It is important to mention that all systems, except powertrain systems, which are used are same for both models.

4EM – In-wheel motors vehicle architecture

The model which consists of four independent in-wheel electric motors is shown on Figure 1. This architecture enables complete independence in traction and braking control for each individual wheel. Through co-simulation with the MATLAB/Simulink environment, the system performs Yaw-Moment control by allocating driving forces to inner

and outer wheels, actively assisting vehicle cornering stability while reducing the required steering angle. Vehicle mass and its distribution is shown in Table 1.

Table 1 In-wheels motors vehicle model characteristics

Characteristic	Unit	Value
Total weight	N	15592
Front ground reaction	N	8183
Rear ground reaction	N	7409

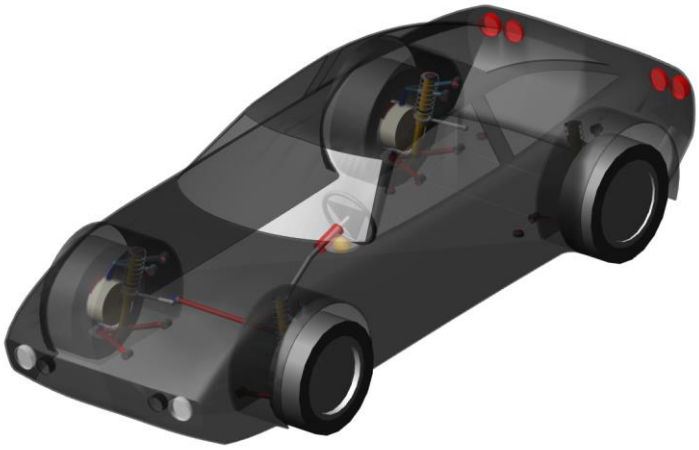

Figure 1 In-wheel motors vehicle model

2EM – Electric vehicle with central motors architecture

The model with two central electric motors (one on each axle) presents a more conventional approach for electric vehicles architecture. Model is shown on Figure 2. In this model, torque is delivered centrally to the axle (with a maximum limit of 80 Nm per axle for a fair comparison with the 4EM system), from where it is distributed to the wheels via mechanical differentials. The control algorithm is based on longitudinal power distribution depending on axle vertical loads, without the capability of asymmetric left-right torque distribution. Vehicle mass and its distribution is shown in Table 2.

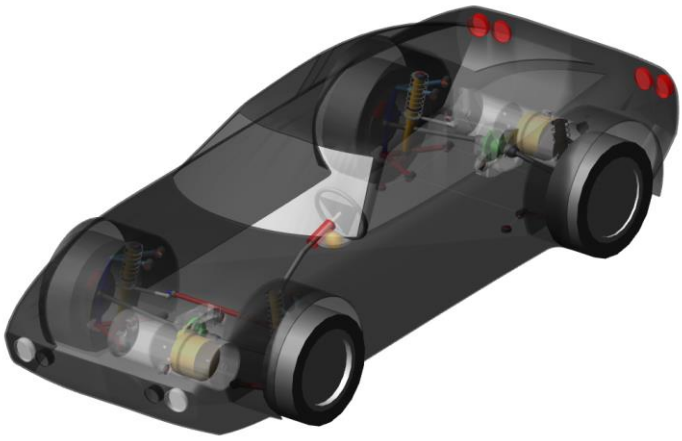

Figure 2 Two central electric motors vehicle model

Table 2 Two central electric motors model characteristics

Characteristic	Unit	Value
Total weight	N	14565
Front ground reaction	N	7654
Rear ground reaction	N	6911

SIMULATION MANEUVER – DOUBLE LANE-CHANGE (DLC)

For the evaluation and comparative analysis of the behavior of 2EM and 4EM electric vehicle architectures, the DLC maneuver was selected. This maneuver is standardized according to the ISO 3888-1:2018 standard (International Organization for Standardization, 2018), and MSC Adams/Car uses this standardized maneuver for simulation. As highlighted by De Novellis et al., 2012, this maneuver represents a realistic situation of suddenly evading an unexpected obstacle on the road. Double lane change track and designation of section are shown on Figure 3, while dimensions of the double lane-change track are shown in Table 3. Mentioned dimensions are in meters.

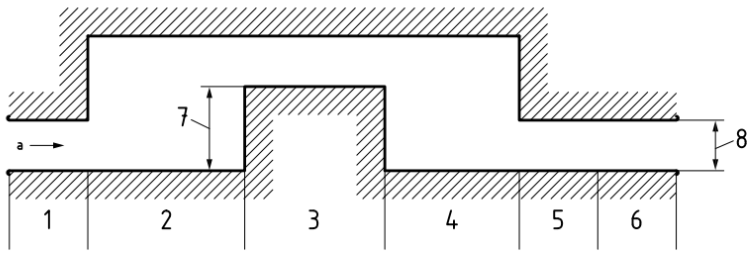

Key

1 section 1
2 section 2
3 section 3
4 section 4
5 section 5
6 section 6
7 lane offset
8 width
a Driving direction.

Figure 3 Double lane-change track and designation of sections

Table 3 Dimensions of the double lane-change track

Section	Length	Lane offset	Width
1	15	-	1,1 x vehicle width +0,25
2	30	-	-
3	25	3,5	1,2 x vehicle width +0,25
4	25	-	-
5	15	-	1,3 x vehicle width +0,25
6	15	-	1,3 x vehicle width +0,25

The maneuver consists of series of consecutive and opposing turns: a sudden transition of the vehicle into the opposite lane, and return to original lane. During co-simulation within MSC Adams software environment, the test was performed at an initial reference speed of 75 km/h on a road surface with a friction coefficient of $\mu = 1.0$, which respresents the default value in the MSC Adams environment. Through the ISO DLC maneuver test, the differences in lateral stability, required steering angle, tire loading, and total energy consumption between the 2EM and 4EM drive solutions are demonstrated.

CONTROL STRATEGIES AND VEHICLE REFERENCE MODEL

To achieve co-simulation between the MSC Adams software environment and MATLAB-Simulink, a torque control system utilizing vehicle dynamics feedback was implemented in Simulink, adapting the methodologies described by Eriksson, 2014; Fan, 2007; Pinheiro et al., 2019 and Saha & Amrr, 2020. The control structure is based on defining an ideal reference response and comparing it with the actual model behavior in real-time.

Vehicle Reference Model (2-DOF Linear Bicycle model)

To generate the desired (reference) yaw rate, a linear two-degrees-of-freedom (2-DOF) bicycle model was utilized, following the dynamic principles outlined by Rajamani, 2012. This model serves as a mirror of ideal vehicle behavior while neglecting vertical and longitudinal body dynamics.

The ideal steady-state yaw is defined as:

$$\dot{\psi}_{ref} = \frac{v_x}{L + K_{understeer} \cdot v_x^2} \cdot \delta \tag{1}$$

where v_x is the longitudinal vehicle speed, L is the total vehicle wheelbase, and δ is the calculated front wheel steering angle. The parameter $K_{understeer}$ respresents the understeer gradient, calculated based on vehicle mass, load distribution, and equivalent tire cornering stiffness, which is obtained from MSC Adams software based on the models defined by Pacejka, 2012:

$$K_{understeer} = \frac{m}{L \cdot C_f \cdot C_r}(L_r \cdot C_r - L_f \cdot C_f) \tag{2}$$

By comparing the calculated reference yaw rate ($\dot{\boldsymbol{\psi}}_{\boldsymbol{ref}}$) with the actual yaw rate from the Adams model ($\dot{\boldsymbol{\psi}}_{\boldsymbol{actual}}$), the regulation error is obtained. This value is multiplied by the gain to obtain the corrective moment.

Torque Control for the 4EM Architecture (Torque Vectoring)

In the 4EM architecture, torque allocation is performed independently across all four wheels. The control algorithm combines a PID controller, used to maintain target vehicle speed, and a corrective torque obtained from controller that calculates the yaw rate error.

On figure 4 is shown torque distribution on left and right wheels of vehicle, during the test. The values shown in the plot correspond to the individual wheel torque, featuring an equal front-to-rear torque split. As can be seen in the 4EM torque distribution diagram, during ISO DLC maneuver, the torque curves on the left and right sides of the vehicle diverge dynamically:

- Outer wheels receive significantly higher torque to push the vehicle into the desired direction.
- Inner wheels drop into negative values (regenerative braking mode), creating an asymmetric yaw moment that physically pulls the vehicle into the corner and reduces the required steering angle.

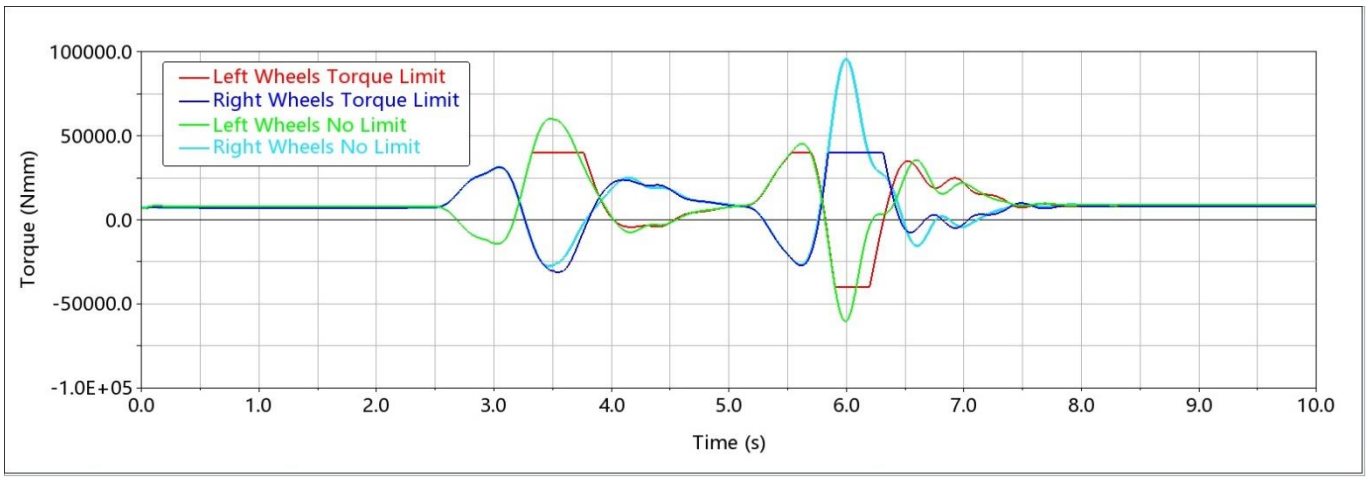

Figure 4 4EM torque distribution

As shown in the diagram, two different torque control algorithms were evaluated. In the first algorithm, the corrective torque limit is set to 40Nm (40000 Nmm), while the second one operates without this restriction. For both algorithms, the same proportional gain of the TV controller was applied. The value for this coefficient is determined to be optimal, based on the analysis of values for the yaw rate error.

Torque Control for the 2EM Architecture

In the 2EM architecture, control relies on central drive units (one electric motor on each axle) with a maximum limit of 80 Nm per axle, ensuring a fair energy balance compared to the 4EM system.

Unlike the 4EM architecture, the 2EM control algorithm relies solely on a single PID controller designed to maintain the target vehicle speed, without incorporating an additional corrective controller for the yaw rate error. Because the 2EM setup utilizes one motor per axle, it lacks the capability for left-right asymmetric torque distribution required for active Torque Vectoring. The 2EM torque distribution graph is shown on Figure 5. The graph indicates that both the front and rear axles synchronously distribute torque to the wheels. However, a slight difference between the axles is observable, as the front motor generates a slightly higher torque output due to the dynamic distribution of the vertical load, where the increased front vertical reaction dictates a proportionally larger torque allocation. Furthermore, during sharp maneuvers, the algorithm commands a transient increase in torque, consistent with the behavior observed in the 4EM vehicle.

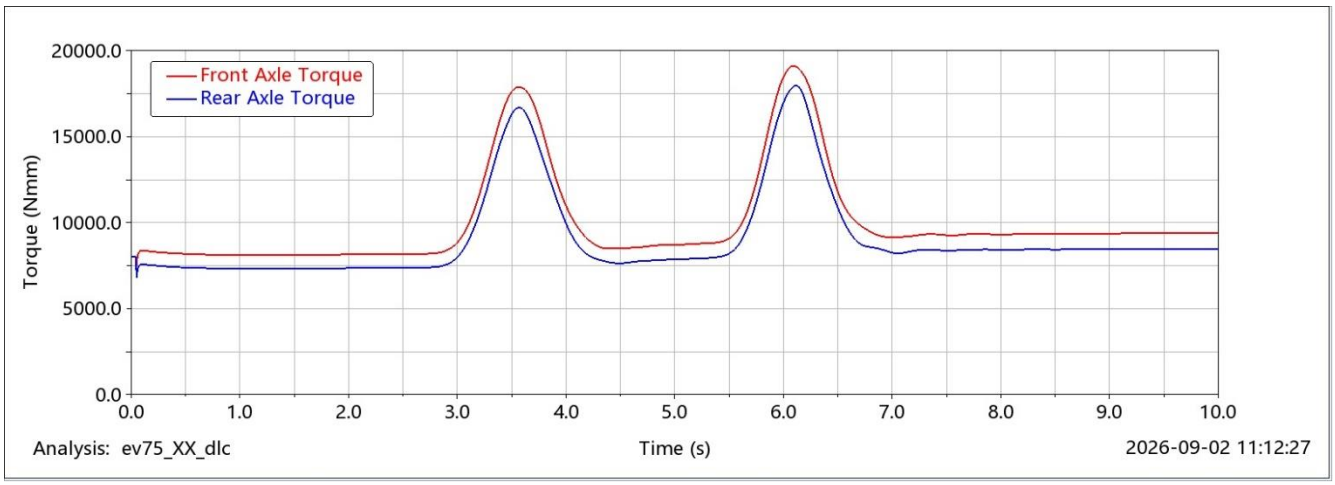

Figure 5 2EM torque distribution algorithm

As it is mentioned maximum limit was set on 80 Nm, but this vehicle also didn't reach that value during maneuver.

Vehicle Speed During the Maneuver

During the standardized DLC maneuver, the longitudinal vehicle speed was regulated to a reference value of $75\ km/h$ using a closed-loop PID controller. The analysis of the velocity graph (Figure 6) shows that both architectures (including both the limited and unrestricted 4EM torque algorithms) successfully maintain the target speed throughout the maneuver, establishing a strict and identical baseline for the energy consumption comparison. Minor transient velocity fluctuations occur during the sharp lane changes are caused by a sudden increase in cornering resistance and torque demand. Specifically, as the vehicle maneuvers, it requires additional torque to maintain its longitudinal speed, simultaneously, the generation of vehicle yaw rate introduces a yaw rate error that the control system must actively compensate for. When reacting to these sudden and coupled torque demands, only the 4EM model with the torque limit (red line) exhibits a slight, observable dip in speed due to its constrained corrective authority. In contrast, both the 2EM model and the unrestricted 4EM model show a small, barely perceptible increase in speed. Ultimately, all tested control systems effectively dampen this transient effect, keeping the vehicle speed closely aligned with the $75\ \mathrm{km/h}$ target without significant deviations.

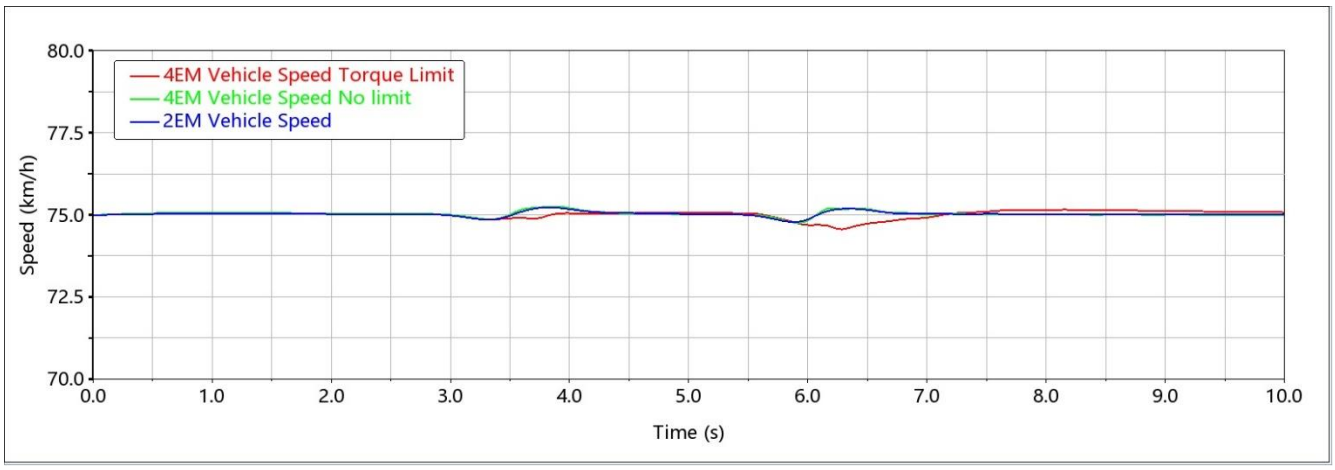

Figure 6 Vehicles Speed During the Maneuver

SIMULATION RESULTS

Following the co-simulation of the ISO double lane-change maneuver at a reference speed of $75\ km/h$, a comparative analysis of the dynamic response and energy efficiency between the 4EM (both torque control algorithms) and 2EM architectures was performed. The results clearly indicate the effectiveness of the independent torque vectoring system (featuring the 40 Nm torque limit) in terms of stability, steering system unburdening, and energy consumption.

Vehicle Lateral Dynamics and Steering inputs

The lateral chassis displacement analysis, shown in Figure 7, confirms that all tested models successfully negotiate the defined trajectory, shifting approximately 3600 mm into the adjacent lane before returning to the zero axis. However, the dynamics of achieving this trajectory differ between the observed architectures. Specifically, the 4EM model tracks the target trajectory more precisely and returns to the straight-line path slightly earlier than the 2EM model, confirming its improved dynamic response, especialy the one without torque restriction.

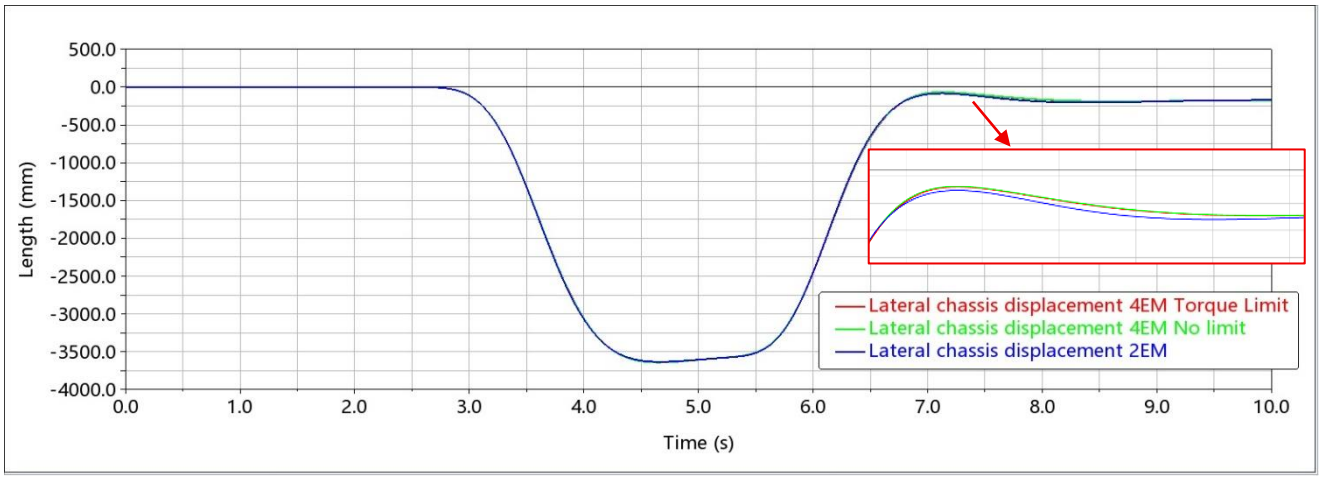

Figure 7 Lateral chassis displacement

The steering wheel angle graph (Figure 8) illustrates the effect of the torque control system in the 4EM architecture. While the 2EM model reaches steering amplitudes of approximately 111° on the second turn, the 4EM models execute the same maneuver with a lower steering wheel angle (around 95°). This represents a reduction of around 16%.

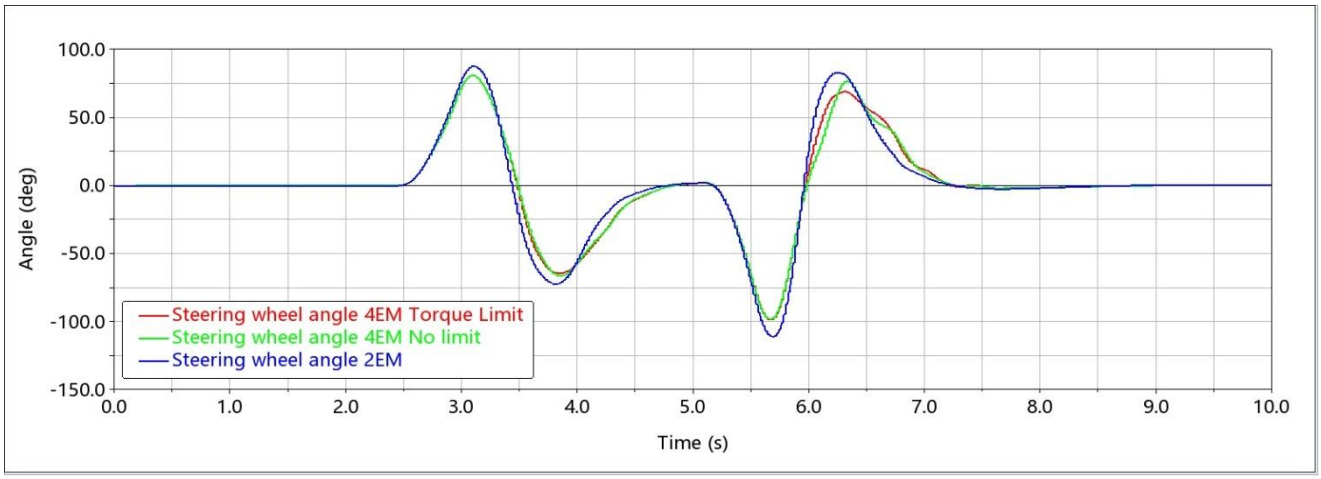

Figure 8 Steering wheel angle during the maneuver

Instead of relying on extreme driver inputs to negotiate the trajectory, the 4EM models achieve the required vehicle rotation by utilizing the asymmetric torque distribution to actively “pull” the vehicle into the corner. As observed in the yaw rate diagram (Figure 9), the dynamic responses of all models closely align during the initial phase of the maneuver. However, during the second curve, distinct behaviors emerge: the 2EM model initially exhibits a slightly lower yaw rate compared to the 4EM models, followed immediately by a slightly higher peak in the opposite direction. In contrast, the 4EM configurations maintain a more consistent and tightly controlled yaw response through this transition.

Importantly, the graphs demonstrate that imposing the 40 Nm torque limit (red line) does not have a significant impact on these macro-dynamic parameters. The vehicle responses – in terms of steering input and yaw rate, are almost identical to those of the unrestricted 4EM algorithm (green line), indicating that the torque restriction does not alter or compromise the core handling characteristics of the vehicle during this maneuver.

Lateral accelerations for both models (Figure 10) are within similar ranges (around 0.8g), due to the similar values for vehicle masses and similar driving speeds during the maneuver, indicating a similar utilization of the available road friction in both systems.

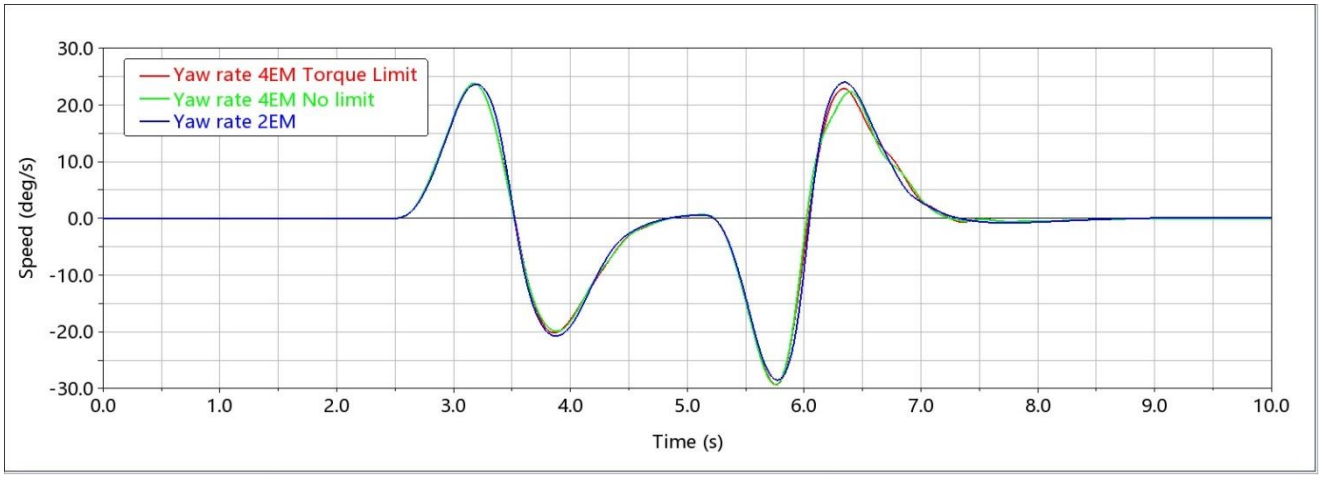

Figure 9 Yaw rate during the maneuver

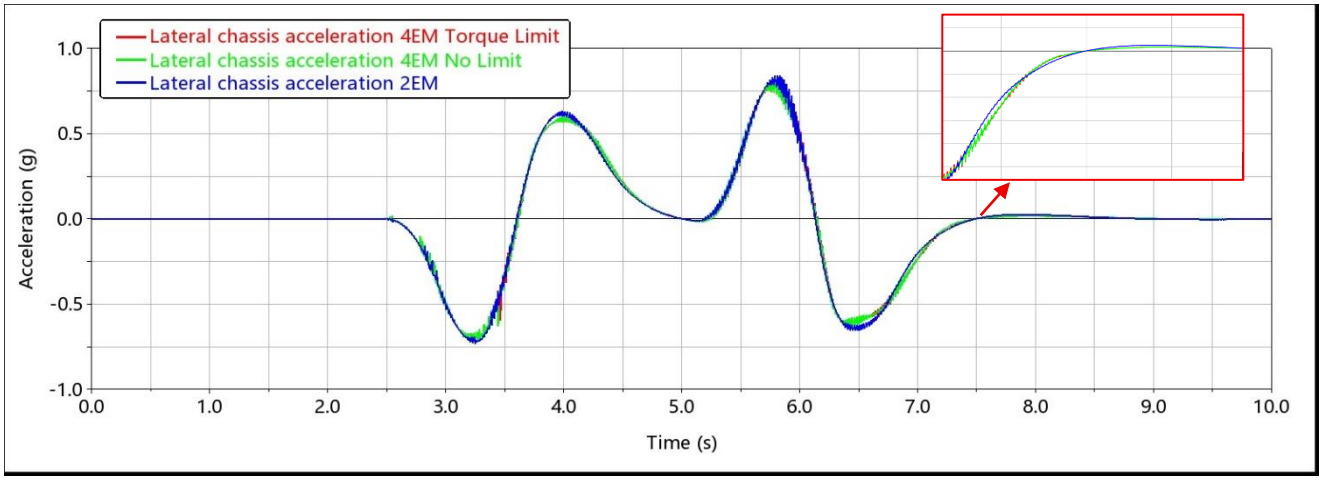

Figure 10 Lateral chassis acceleration during the maneuver

Slip angles

The differences in drive concepts can also be tracked through the responses of the front and rear axles.

- **Front Axle:** The front axle slip angle graph (Figure 11) shows a higher slip angle values for the 2EM model, which relies primarily on the change in the front wheel angle to generate lateral force. In contrast, both 4EM configurations record lower slip angle values on the front axle, further demonstrating that the torque vectoring system reduces the cornering burden on the front tires.

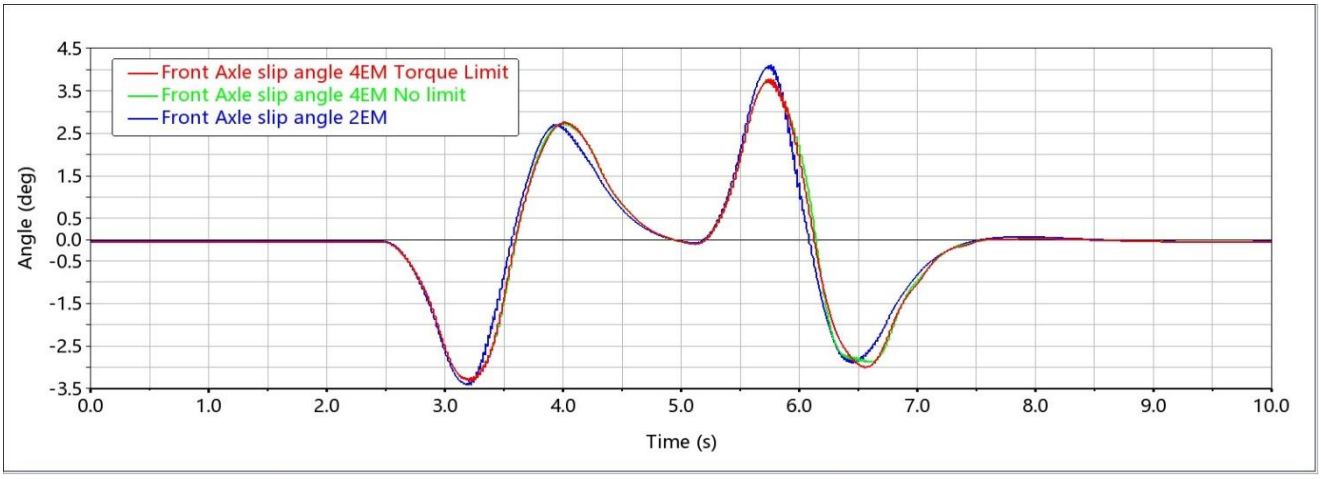

Figure 11 Front Axle slip angles during the maneuver

- **Rear Axle and Vehicle Side Slip:** Due to the application of asymmetric torque to the wheels, the 4EM system induces higher slip angles on the rear axle (Figure 12), as well as a higher overall vehicle side slip angle, shown on Figure 13 (reaching approximately 3.0° compared to 2.5° for the 2EM model). This increase in the rear axle slip angle represents the mechanism by which the algorithm rotates the vehicle around

vertical axis during cornering. Consistent with the steering and yaw rate data, the 4EM model with the 40 Nm limit exhibits nearly identical slip angle trajectories to the unrestricted model, confirming once again that the torque restriction does not hinder the vehicles dynamic performance.

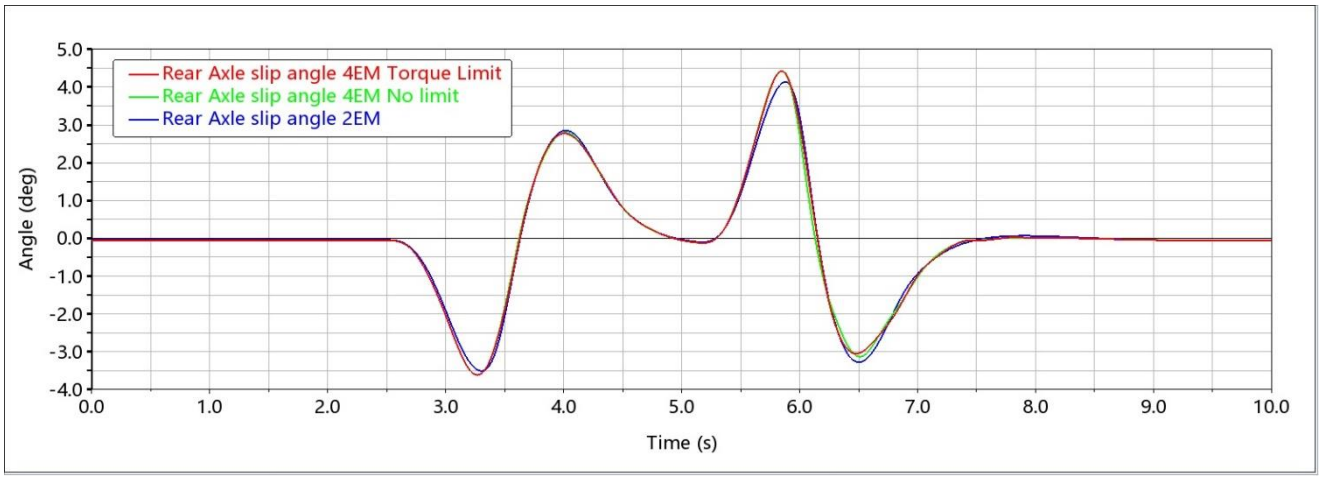

Figure 12 Rear Axle slip angles during the maneuver

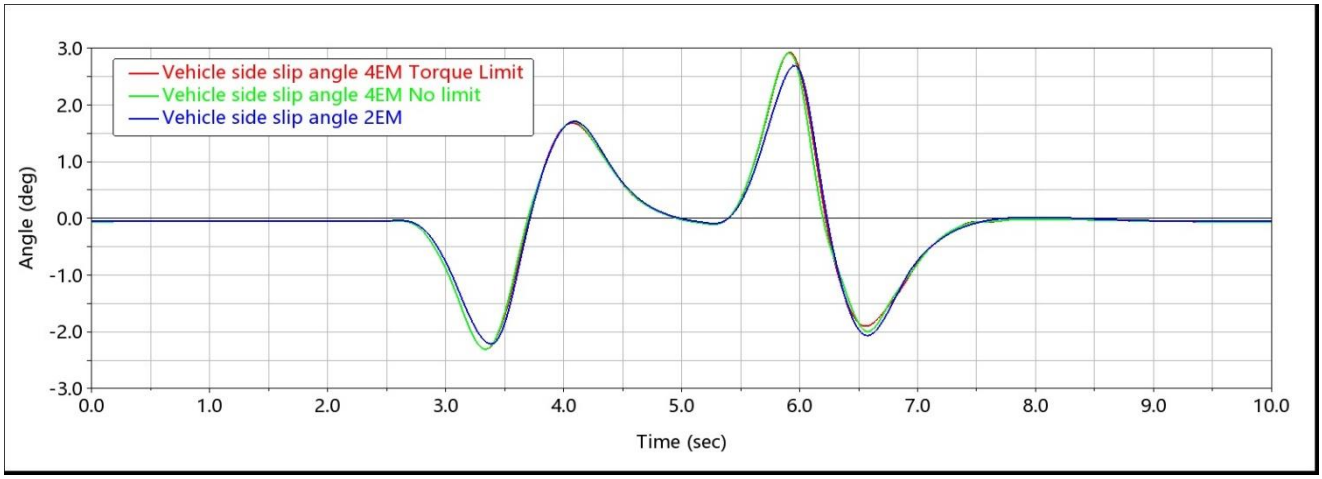

Figure 13 Vehicle side slip angles during the maneuver

Energy Consumption

The analysis of total energy consumption during the DLC maneuver, presented in Figure 14, provides crucial insight into the efficiency of the implemented control strategies.

- Unrestricted 4EM Energy Penalty: The unrestricted 4EM model (green line) exhibits the highest overall energy consumption, finalizing the maneuver at approximately $34.1\,Wh$. Because the unconstrained controller commands torque values that push the tires into saturation, a significant portion of this electrical energy is wasted on tire slip rather than being converted into useful lateral or longitudinal vehicle motion.
- 2EM Baseline: The 2EM architecture (blue line) establishes the baseline energy requirement for the maneuver, accumulating a steady increase in energy and concluding at approximately $30.94\,Wh$.
- Torque Limited 4EM Efficiency: The application of the 40 Nm torque limit (red line) improves the efficiency of the 4EM architecture. By capping the corrective torque, the algorithm prevents excessive energy waste. Notably, between 5.5 and 6.5 seconds, the energy curve exhibits a distinct plateau, indicating that the controller successfully truncates excessive torque request. Ultimately, the optimized 4EM model with the torque limit concludes the manoeuvre with a slight overall energy saving compared to the baseline (approximately $30.72\,\mathrm{Wh}$). This efficiency gain is particularly significant considering the 4EM vehicle architecture carries an inherent weight penalty of approximately 105 kg compared to the 2EM model. Achieving lower total energy consumption while moving a heavier mass confirms that the 40 Nm restriction successfully delivers all the handling benefits of independent torque vectoring without any energetic compromise.

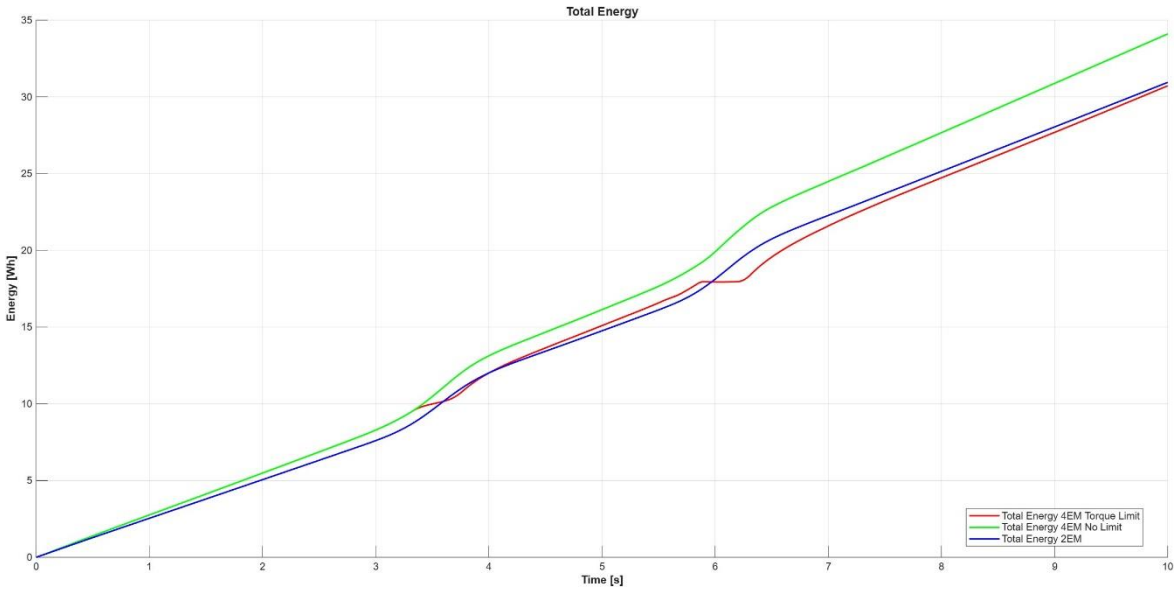

Figure 14 Total Energy 4EM

CONCLUSIONS

In this paper, a comparative analysis of the dynamic behavior and energy efficiency of electric vehicles with two central motors (2EM) and four independent in-wheel motors (4EM) was conducted. The evaluation of the concepts was performed through co-simulation in the MSC Adans and MATLAB/Simulink software environments, utilizing the standardized double lane change maneuver according to the ISO 3888-1:2018 norm. Crucially, the study evaluated both an unrestricted 4EM torque vectoring algorithm and an optimized algorithm featuring a 40 Nm torque limit.
Based on the presented results, the following conclusions are drawn:

Lateral Dynamics and Steering Effort

The application of the torque vectoring control system in the 4EM architecture results in significantly lower steering wheel angle values required to successfully execute the maneuver. Torque vectoring facilitates more precise tracking of the desired trajectory and unburdens the front axle in terms of lateral force generation requirements. Implementing the 40 Nm torque limit ensures these benefits are achieved smoothly.

Cornering

Relying on the asymmetric distribution of torque, the 4EM system induces a slight increase in the slip angle of the rear axle. This indicates that the torque control algorithm actively uses the rear wheels to rotate the vehicle around its vertical axis, contributing to a highly controlled dynamic response without requiring extreme peak yaw rates, while preserving trajectory stability. The data confirms that capping the torque at 40 Nm does not alter those core characteristics, proving the limitation is both sufficient and effective.

Energy efficiency

In addition to the difference in dynamic behavior, measurable differences in energy consumption were recorded. The analysis revealed that an unrestricted torque vectoring system incurs a severe energy penalty. However, the optimized 4EM model with the 40 Nm limit successfully prevented this energy waste. Compared to the 2EM system, the limited 4EM concept recorded a slight overall reduction in energy consumption during the tested maneuver. This efficiency gain is particularly notable given that the 4EM vehicle architecture carries an inherent weight penalty of approximately 105 kg. This is a direct consequence of the fact that the 4EM system generates the necessary corrective moment by applying regenerative braking, simultaneously correcting the trajectory and recuperating kinetic energy back into the system.

Finally, it can be concluded that the independent wheel torque control (4EM), specifically when optimized with a well-defined torque limit, provides a more favorable balance between the required steering effort, dynamic stability, and energy consumption during dynamically demanding obstacle avoidance maneuvers, compared to the more conventional architecture based on a central drive system (2EM).

Future research will be directed towards the further optimization of the torque vectoring algorithm in the 4EM architecture. Specifically, studies will focus on analyzing the influence of the proportional gain (*Kp*) factor and varying torque limitation thresholds to achieve even better dynamic vehicle behavior and overall system efficiency. Furthermore, subsequent investigations will explore the adaptive, unequal distribution of torque across individual wheels in response to dynamic changes in available tire grip and varying road surface conditions.

ACKNOWLEDGMENTS

The research presented in this paper is funded by Ministry of Science, Technological Development and Innovation of the Republic of Serbia under agreement No. 451-03-34/2026-03/200105 dated 5.2.2026.

REFERENCES

Bayar, K. (2020). Performance comparison of electric-vehicle drivetrain architectures from a vehicle dynamics perspective. *Proceedings of the Institution of Mechanical Engineers, Part D: Journal of Automobile Engineering*, *234*(4), 915–935. https://doi.org/10.1177/0954407019867491

Cong Geng, Mostefai, L., Denai, M., & Hori, Y. (2009). Direct yaw-moment control of an in-wheel-motored electric vehicle based on body slip angle fuzzy observer. *IEEE Transactions on Industrial Electronics*, *56*(5), 1411–1419. https://doi.org/10.1109/TIE.2009.2013737

De Novellis, L., Sorniotti, A., & Gruber, P. (2014). Wheel torque distribution criteria for electric vehicles with torque-vectoring differentials. *IEEE Transactions on Vehicular Technology*, *63*(4), 1593–1602. https://doi.org/10.1109/TVT.2013.2289371

De Novellis, L., Sorniotti, A., Gruber, P., Shead, L., Ivanov, V., & Hoepping, K. (2012). Torque Vectoring for Electric Vehicles with Individually Controlled Motors: State-of-the-Art and Future Developments. *World Electric Vehicle Journal*, *5*(2), 617–628. https://doi.org/10.3390/wevj5020617

Eriksson, T. (2014). *Co-Simulation of Full Vehicle Model in Adams and Anti-Lock Brake System Model in Simulink*.

Fan, B. S.-M. (2007). *Modeling and Simulation of A Hybrid Electric Vehicle Using MATLAB/Simulink and ADAMS*.

International Organization for Standardization. (2018). *Passenger cars - Test track for a severe lane-change manoeuvre - Part 1: Double lane-change* (ISO Standard No. 3888-1:2018).

Jalali, K., Uchida, T., McPhee, J., & Lambert, S. (2012). Development of a fuzzy slip control system for electric vehicles with in-wheel motors. *SAE International Journal of Alternative Powertrains*, *01*(1), 46–64. https://doi.org/10.4271/2012-01-0248

Pacejka, H. B. (2012). *Tire and vehicle dynamics* (3rd ed.). Butterworth-Heinemann.

Park, G., Lee, S., Jin, S., & Kwak, S. (2014). Integrated modeling and analysis of dynamics for electric vehicle powertrains. *Expert Systems with Applications*, *41*(5), 2595–2607. https://doi.org/10.1016/j.eswa.2013.10.007

Pinheiro, H. d. C., Messana, A., Sisca, L., Ferraris, A., Airale, A. G., & Carello, M. (2019). *Torque Vectoring in Electric Vehicles with In-wheel Motors.* In: Uhl, T. (eds) Advances in Mechanism and Machine Science. IFToMM WC 2019. Mechanisms and Machine Science, vol 73. Springer, Cham. https://doi.org/10.1007/978-3-030-20131-9_308

Rajamani, R. (2012). *Vehicle dynamics and control* (2nd ed.). Springer Science & Business Media.

Saha, S., & Amrr, S. M. (2020). Design of slip-based traction control system for EV and validation using co-simulation between Adams and Matlab/Simulink. *SIMULATION*, *96*(6), 537–549. https://doi.org/10.1177/0037549719897834

Sawase, K., & Ushiroda, Y. (2008). Improvement of vehicle dynamics by right-and-left torque vectoring system in various drivetrains. *Mitsubishi Motors Technical Review*, 20, 14-20.

Sawase, K., Ushiroda, Y., & Miura, T. (2006). Left-Right Torque Vectoring Technology as the Core of Super All Wheel Control (S-AWC). *Mitsubishi Motors Technical Review,* 18, 18-24.

Wu, J., Liang, J., Ruan, J., Zhang, N., & Walker, P. D. (2018). Efficiency comparison of electric vehicles powertrains with dual motor and single motor input. *Mechanism and Machine Theory*, *128*, 569–585. https://doi.org/10.1016/j.mechmachtheory.2018.07.003

The 11th International Congress
Motor Vehicles & Motors 2026
Kragujevac, Serbia
October 8th-9th, 2026

Motor Vehicles & Motors

MVM2026-023
https://doi.org/10.24874/CMVM2026.023
Original scientific paper

Snežana Petković[1]
Valentina Golubović Bugarski[2]
Jelena Adžić[3]
Milan Eremija[4]

ANALYSIS OF PARAMETERS INFLUENCING ROAD TANKER ROLLOVER

ABSTRACT: Road tanker rollovers in road transportation represent a serious safety concern due to the potential for significant material damage, risks to human life, and environmental pollution, particularly during the transportation of hazardous materials. The subject of this paper is the analysis of the most important parameters affecting the stability and rollover propensity of road tankers during exploitation. The study examines factors such as vehicle speed, the liquid sloshing effect within the tank, the position of the center of mass, tank structural characteristics, road surface conditions, vehicle technical condition, and the influence of the human factor. Special attention is given to the dynamic behavior of the vehicle when negotiating curves and during sudden changes in direction. The aim of the research is to determine the mutual influence of the aforementioned parameters on the occurrence of vehicle instability and to define measures for reducing the risk of rollover. The results of the analysis indicate that proper tank design, the application of modern active safety systems, regular vehicle maintenance, and adequate driver training significantly contribute to improving transportation safety. The obtained results may serve as a basis for the improvement of technical standards and preventive measures in the field of hazardous materials transportation.

KEYWORDS: road tanker rollover; hazardous materials; vehicle stability; influencing parameters

ANALIZA UTICAJNIH PARAMETARA NA PREVRTANJE CISTERNI

REZIME: Prevratanje cisterni u drumskom saobraćaju predstavlja ozbiljan bezbjednosni problem zbog mogućnosti nastanka velikih materijalnih šteta, ugrožavanja ljudskih života i zagađenja životne sredine, posebno prilikom transporta opasnih materija. Predmet rada odnosi se na analizu najvažnijih parametara koji utiču na stabilnost i

[1] *Snežana Petković, University of Banja Luka, Faculty of mechanical engineering,* Banja Luka
snezana.petkovic@mf.unibl.org, *https://orcid.org/0009-0009-2878-0436*
[2] *Valentina Golubović Bugarski, University of Banja Luka, Faculty of mechanical engineering, Banja Luka,*
valentina.golubovic-bugarski@mf.unibl.org, https://orcid.org/0009-0007-1516-5114
[3] *Jelena Adžić, University of Banja Luka, Faculty of mechanical engineering, Banja Luka,*
jelena.adzic@mf.unibl.org, *https://orcid.org/0009-0008-7892-7208*
[4] *Milan Eremija, University of East Sarajevo, Faculty of Traffic Engineering, Doboj, eremijamilan5@gmail.com*,
https://orcid.org/0009-0000-1551-1231

mogućnost prevrtanja cisterni tokom eksploatacije. U radu su analizirani faktori kao što su brzina kretanja vozila, efekat talasanja tečnosti unutar rezervoara, položaj centra mase, konstrukcione karakteristike cisterne, stanje kolovoza, tehnička ispravnost vozila i uticaj ljudskog faktora. Posebna pažnja posvećena je dinamičkom ponašanju vozila u krivinama i pri naglim promjenama pravca kretanja. Cilj istraživanja je utvrđivanje međusobnog uticaja navedenih parametara na pojavu nestabilnosti vozila i definisanje mjera za smanjenje rizika od prevrtanja. Rezultati analize ukazuju da pravilna konstrukcija cisterni, primjena savremenih sistema aktivne bezbjednosti, redovno održavanje vozila i adekvatna obuka vozača značajno doprinose povećanju bezbjednosti transporta. Dobijeni rezultati mogu poslužiti kao osnova za unapređenje tehničkih standarda i preventivnih mjera u oblasti transporta opasnih materija.

KLJUČNE REČI: prevrtanje cisterne, opasne materije, stabilnost, uticajni parametri.

INTRODUCTION

Road tanker rollover is a major concern in terms of the stability and safety of vehicles used to transport liquid cargo. Accidents of this type may result in injuries or fatalities, as well as substantial damage to the vehicle and road infrastructure. An additional risk is tank damage and leakage of the liquid cargo, which may also cause environmental pollution when hazardous materials are transported. Unlike other heavy vehicles, road tankers allow relative motion of the liquid inside the tank. Vehicle motion causes the liquid cargo to shift and changes the position of its center of mass, thereby affecting vehicle dynamics and stability. Therefore, in addition to vehicle and tank characteristics, an analysis of road tanker stability must also account for the behavior of the liquid during vehicle motion.

Road tanker rollover is influenced by numerous interrelated factors, including vehicle and tank characteristics, the quantity and behavior of the liquid cargo, road characteristics, and operating conditions. Their individual and combined effects determine the lateral stability of the vehicle and whether the rollover threshold is reached. Owing to the complexity of this problem, road tanker stability has been investigated through numerous theoretical, numerical, simulation-based, and experimental studies.

Zheng et al. (2017) analyzed the stability of partially filled road tankers while accounting for liquid sloshing. They considered tanks with elliptical cross-sections, varying the ellipse axis ratio from 1 to 2 and the filling level from 0% to 100%. Three approaches were used to describe the effect of the liquid on vehicle stability: a quasi-static model, an improved quasi-static model, and an equivalent mechanical model. The quasi-static approach enables a simpler estimate of the center-of-mass position and rollover threshold, whereas the equivalent mechanical model provides a more detailed representation of liquid dynamics and their interaction with vehicle motion. Yu and Chu (2019) developed a model for analyzing the lateral stability of a partially filled road tanker in which liquid motion was represented by an equivalent mechanical model. The equation of motion was derived using the Lagrangian approach, and the liquid model was coupled with the vehicle dynamic model. The tank geometry was optimized on the basis of the liquid center-of-mass position and rollover moment to improve lateral stability. Other studies extended the analysis by including additional parameters and operating conditions. Tran et al. (2022) analyzed the effects of road profiles and filling levels using a road tanker dynamic model and a vehicle roll model. Zheng et al. (2025) examined rollover risk on road sections combining horizontal curvature and longitudinal grade, including the effects of vehicle speed and curve radius. This paper analyzes the main factors affecting road tanker stability and rollover propensity. Particular attention is devoted to the mathematical analysis of the effects of tank filling level and horizontal-curve conditions on the liquid-cargo center of mass and the lateral-stability threshold. In addition to the mathematical-model results, the effects of vehicle design and technical condition, road characteristics, and the human factor are considered. The objective is to relate these effects to provide a more complete understanding of the rollover mechanism and the possibilities for reducing rollover risk under operating conditions.

PARAMETERS AFFECTING ROAD TANKER STABILITY AND ROLLOVER

The lateral stability of a road tanker is determined by its ability to maintain wheel contact with the road under lateral loading and to avoid the limiting condition in which the rollover moment exceeds the stabilizing moment. Road tanker stability is affected by several interrelated factors. Vehicle design determines the basic geometric conditions of stability, among which the overall center-of-mass position and vehicle track width are particularly important. A higher center of mass increases rollover propensity, while the technical condition of the suspension, tires, and braking system affects load transfer between the left and right sides of the vehicle and its ability to maintain a stable path during lateral motion. Modern active-safety systems, including ABS, electronic stability control, and rollover-control support systems, play an important role in maintaining vehicle controllability and stability in critical situations. However, they cannot fully compensate for unfavorable operating conditions or driver misjudgment.

Liquid cargo is a distinctive feature of road tankers because its position changes relative to the tank during motion. The filling level determines the liquid mass, the initial position of its center of mass, and the space available for

relative motion. Changes in the driving regime cause liquid displacement and oscillation of the free surface, i.e., sloshing, thereby changing the center-of-mass position and the forces exerted by the liquid on the tank. The intensity of this motion also depends on tank shape and dimensions. Internal baffles can restrict liquid motion and reduce sloshing intensity, but cannot eliminate it completely (Ibrahim, 2005; Kolaei et al., 2014).

The importance of the filling level is also recognized in the ADR provisions (Agreement concerning the International Carriage of Dangerous Goods by Road). For certain tanks intended for liquids, liquefied gases, or refrigerated liquefied gases that are not divided by partitions or surge plates into compartments with a maximum capacity of $7{,}500\ l$, ADR requires the filling level to be no more than $20\ \%$ or no less than $80\ \%$ of tank capacity. This avoids the intermediate filling range of $20\ \%$ to $80\ \%$, in which a substantial liquid mass and sufficient free space for more intense sloshing are simultaneously present. At high filling levels, the space available for relative liquid motion decreases. At very low filling levels, the liquid mass participating in the motion is considerably smaller, although more space is available for its displacement. This requirement is not a general rule for all road tankers; its application also depends on tank design and capacity, the presence of individual compartments, and the substance transported (UNECE, 2025).

Stability is also affected by road characteristics and operating conditions. Curve geometry, longitudinal and transverse grade, pavement condition, and changes in direction affect the magnitude and direction of the lateral loads acting on the vehicle. The human factor is also important because driving behavior directly determines whether the vehicle approaches its stability limit. Timely speed adjustment, proper assessment of road conditions, and avoidance of sudden maneuvers can reduce the risk of loss of stability. Conversely, inappropriate actions may further increase lateral loading and rollover risk. The human factor must therefore be considered together with the characteristics of the vehicle, liquid cargo, and road as part of an interconnected system that determines overall road tanker stability.

MATHEMATICAL MODEL FOR ROAD TANKER ROLLOVER ANALYSIS

A simplified mathematical model was adopted for the road tanker rollover analysis. The objective was to examine the effects of tank filling level and road-curve conditions. Appropriate model simplifications were introduced. The vehicle travels at constant speed through a horizontal curve without road superelevation. The model includes lateral displacement of the liquid cargo, while longitudinal liquid motion during acceleration and braking is not considered. Roll and oscillation of the vehicle and tank structure, tire deformation, suspension dynamics, and the influence of internal tank baffles are also excluded. The liquid cargo is represented by a simplified equivalent mechanical model; consequently, the results provide an estimate of lateral stability under the adopted assumptions rather than a complete hydrodynamic simulation. The analysis considers a tank with a circular cross-section of radius R. The variable parameters are the tank filling level λ and the horizontal curve radius R_k.
For the parametric analysis, a constant vehicle speed was adopted:

$$v = 60\frac{km}{h} = 16{,}67\frac{m}{s} \tag{1}$$

In this case, lateral acceleration is calculated from the vehicle speed and the horizontal curve radius (Jankovic & Todorović, 1990):

$$a_y = \frac{v^2}{R_k} \tag{2}$$

The mathematical model uses the geometric parameters of a heavy-fuel-oil tank manufactured by ZOVKO (ZOVKO OIL d.o.o. Žepče, n.d.). The actual tank contains four internal baffles, whose influence is not considered separately in this model. The filling level was varied over the adopted range in increments of 0.1. For each filling level, the vehicle was analyzed while traveling at a constant speed of $60\frac{km}{h}$ through horizontal curves of different radii. The curve radius R_k was varied from $50\ m$ to $150\ m$ in increments of $10\ m$. For every value of R_k, the corresponding lateral acceleration was calculated using Eq. (2), followed by calculation of the liquid dynamic response and vehicle lateral stability. For each filling level, the initial liquid center-of-mass position at rest was first determined. In the adopted equivalent mechanical model, the liquid cargo is represented by a concentrated mass whose motion is described by a pendulum model. For a tank with a circular cross-section of radius R, the circle equation is:

$$x^2 + y^2 = R^2 \tag{3}$$

The cross-sectional area occupied by the liquid is determined by the filling level λ:

$$A = \lambda A_{cisterne} = \lambda R^2 \pi \tag{4}$$

The initial position of the liquid center of mass is determined using an area integral, where the differential area can be written as:

$$dA = w(y)dy \tag{5}$$

where $w(y)$ denotes the width of an elementary horizontal strip of the circular segment at the considered height.

Introducing the substitution:

$$h_o = uR \tag{6}$$

and applying the geometric relations for a circular segment yields the vertical coordinate of the initial liquid center of mass relative to the coordinate-system origin:

$$y_0 = -\frac{2R}{3\pi\lambda}\left(1 - \frac{h_0^2}{R^2}\right)^{\frac{3}{2}} \tag{7}$$

The negative value in Eq. (7) indicates that the center of mass is below the center of the circular cross-section. The initial vertical coordinate of the center of mass, measured from the bottom of the tank, is determined as:

$$y_{CG,0} = R - |y_0| \tag{8}$$

After determining the initial center-of-mass position, its displacement under lateral acceleration was considered. The relative motion of the liquid was represented by a simplified equivalent mechanical model, in which the liquid center-of-mass displacement is described by the angle φ and the corresponding radius of the center-of-mass path r (Ibrahim, 2005; Yu & Chu, 2019; Zheng et al., 2017). The adopted model does not consider roll of the vehicle and tank structure.

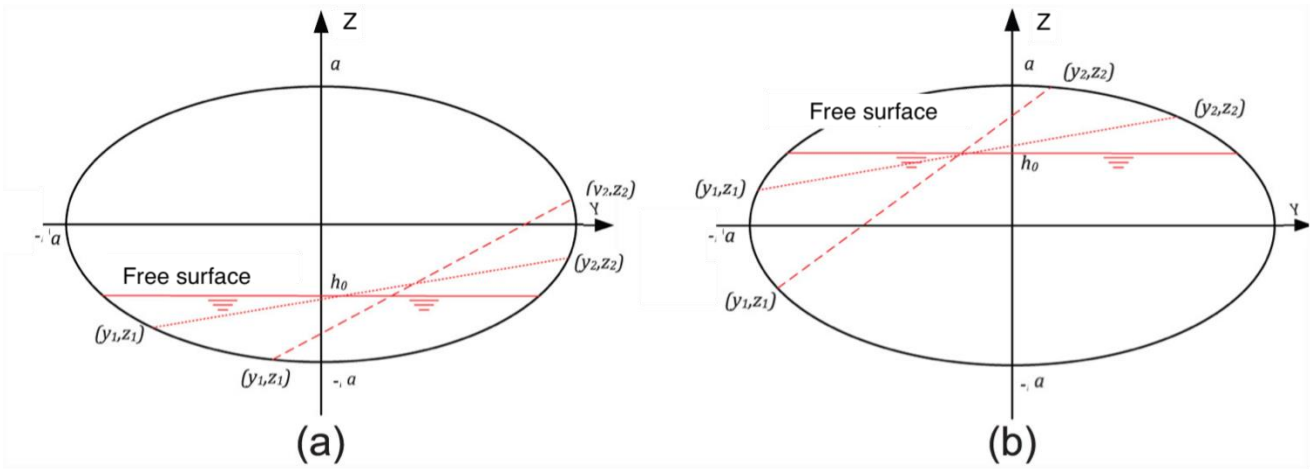

Figure 1 Liquid free-surface position during vehicle cornering for different filling levels

The equation of motion was derived using the Lagrangian approach (Yu & Chu, 2019; Zheng et al., 2017). The equivalent-pendulum center-of-mass position is defined by the generalized coordinate φ, while vehicle lateral acceleration represents the external excitation of the system.

The kinetic energy of the system is determined from the velocity of the liquid center of mass:

$$E_k = \frac{1}{2}m_t v_{CG}^2 = \frac{1}{2}m_t[\dot{x}^2 + 2\dot{x}\dot{\varphi}rcos\varphi + r^2\dot{\varphi}^2cos^2\varphi + \dot{\varphi}^2r^2sin^2\varphi] \tag{10}$$

where m_t is the liquid mass and v_{CG} is the velocity of the equivalent center of mass.

The potential energy is determined from the vertical position of the center of mass:

$$E_p = m_t g y_{CG} = m_t g(R - rcos\varphi) \tag{11}$$

The Lagrangian is defined as the difference between the kinetic and potential energies:

$$L = E_k - E_p \tag{12}$$

The equation of motion of the system is derived using Lagrange's equation of the second kind:

$$\frac{d}{dt}\left(\frac{\partial L}{\partial \dot{\varphi}}\right) - \frac{\delta L}{\delta \varphi} = 0 \tag{13}$$

After evaluating the required partial derivatives and rearranging the terms, the differential equation of motion of the equivalent pendulum is obtained:

$$mr^2\ddot{\varphi} + mra_y \cos\varphi + mgrsin\varphi = 0 \tag{14}$$

After dividing Eq. (14) by mr^2, the angular acceleration can be written as:

$$\ddot{\varphi} = -\frac{a_y cos\varphi + gsin\varphi}{r} \tag{15}$$

Differential equation (15) was solved numerically in MATLAB/Simulink. Double integration of the angular acceleration yields the time history of the angle $\varphi(t)$, and subsequently the coordinates of the displaced liquid center of mass. In this manner, the liquid-cargo center-of-mass position was determined for every analyzed filling level and horizontal curve radius at the corresponding lateral acceleration.

Moment calculation and determination of the critical radius for lateral stability

The calculated center-of-mass coordinates are used to determine the force lever arms relative to the potential rollover axis. In the lateral-stability analysis, moments are calculated about the potential rollover axis, defined in this model by the line of contact between the outer wheels and the road surface. The liquid mass depends on the tank filling level and is determined as:

$$m_t = \rho\lambda V \tag{16}$$

where ρ is the density of the liquid transported in the tank, λ is the filling level, and V is the total tank volume.

For the purposes of the calculation, the density of heavy fuel oil was assumed to be $\rho = 950\frac{kg}{m^3}$ at the reference temperature of $15\ °C$. Under actual transport conditions, due to its high viscosity, heavy fuel oil may be transported at an elevated temperature, with its density decreasing as the temperature. For each curve radius, the lateral inertial force of the liquid cargo is determined as:

$$F_{y,t} = m_t a_y \tag{17}$$

For the empty vehicle:

$$F_{y,v} = m_v a_y \tag{18}$$

where m_v is the vehicle mass.

The horizontal curve radius R_k directly affects lateral acceleration and thus the lateral inertial forces. At constant speed, reducing the curve radius increases lateral acceleration and the corresponding inertial forces, thereby increasing the rollover moment. The total destabilizing moment is:

$$M_{prev} = m_t a_y h_t + m_v a_y h_v \tag{19}$$

where h_t and h_v are the vertical distances of the liquid and empty-vehicle centers of mass from the rollover axis.

The stabilizing moment results from gravitational forces and is calculated as:

$$M_{stab} = m_t g d_t + m_v g d_v \tag{20}$$

where d_t and d_v are the horizontal distances of the liquid and empty-vehicle centers of mass from the rollover axis.

The liquid center-of-mass position and the corresponding distances are obtained from the previously calculated liquid dynamic response. The lateral-stability threshold is defined by:

$$M_{prev} = M_{stab} \tag{21}$$

For $M_{prev} < M_{stab}$, the road tanker is in the stable region according to the adopted criterion. Equality of the moments represents the lateral-stability threshold, whereas $M_{prev} > M_{stab}$ indicates that the limiting condition has been exceeded and rollover may occur.

The critical curve radius R_{krit}, is particularly important in this analysis. It is the radius at which the stabilizing and rollover moments become equal for the adopted constant speed and a specified filling level. For $R_k > R_{krit}$ the vehicle is in the stable region according to the adopted model, whereas for $R_k < R_{krit}$, the lateral-stability limit is exceeded.

SIMULATION MODEL IN MATLAB/SIMULINK

A simulation model was developed in MATLAB/Simulink on the basis of the previously defined mathematical model. MATLAB was used to define input parameters, determine geometric quantities for different filling levels, automate the simulation cases, and process the results, while the differential equation governing the equivalent mechanical model was implemented in Simulink.

For each simulation case, the first maximum deflection φ_{max} was extracted from the time response. It corresponds to the first extreme position of the equivalent liquid center of mass. At that instant, angular velocity reaches zero and the direction of motion subsequently changes. From φ_{max}, the displaced liquid center-of-mass coordinates x_{CG} and y_{CG} were determined.

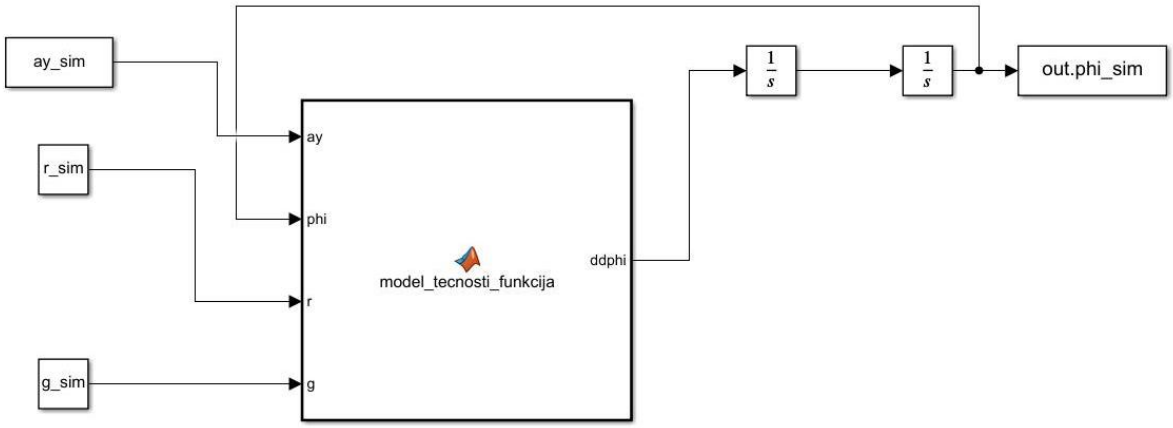

Figure 2 Simulation model of the equivalent liquid-cargo motion in MATLAB/Simulink

The calculated center-of-mass coordinates were used to determine the force level arms and calculate the stabilizing moment M_{stab} and rollover moment M_{prev}. The procedure was automated in MATLAB and repeated for all combinations of the analyzed filling levels and horizontal curve radii.

RESULTS AND DISCUSSION

The results show a clear dependence of lateral stability on the horizontal curve radius. At constant vehicle speed, reducing the curve radius increases lateral acceleration and consequently the lateral inertial forces acting on the empty vehicle and liquid cargo. The rollover moment therefore increases. As the curve radius increases, lateral acceleration decreases, the rollover moment declines, and the lateral-stability margin increases. The filling level affects the liquid-cargo mass and the position of its center of mass, thereby changing its displacement under lateral acceleration. Consequently, the same curve radius and vehicle speed do not produce the same ratio of stabilizing to destabilizing moment at different filling levels. This behavior is consistent with previous studies, which also emphasize the importance of the position and displacement of the liquid-cargo center of mass when assessing the stability of partially filled road tankers (Yu & Chu, 2019; Zheng et al. 2017).

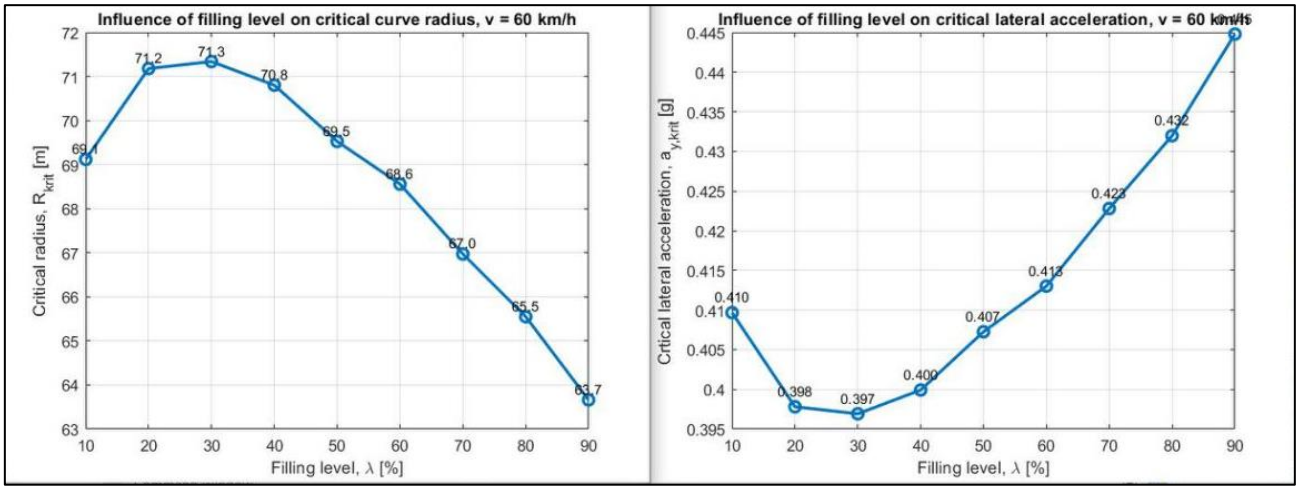

Figure 3 Effect of filling level on (a) critical curve radius and (b) critical lateral acceleration at a constant vehicle speed of $60\frac{km}{h}$

The results shown in Figure 3 demonstrate that the dependence of lateral stability on filling level is nonlinear. Within the analyzed range, the least favorable region occurs at partial filling levels of approximately $20 - 30\%$. At a filling level of 30%, the largest critical curve radius of approximately $71.3\,m$ and the lowest critical lateral acceleration of approximately $0.397g$ were obtained. As the filling level increases further, the critical curve radius decreases while the critical lateral acceleration increases.

For a detailed presentation of the limiting condition, filling levels of 30% and 80% were selected. Figure 4 shows the stabilizing and rollover moments as functions of curve radius at a constant speed of $60\frac{km}{h}$.

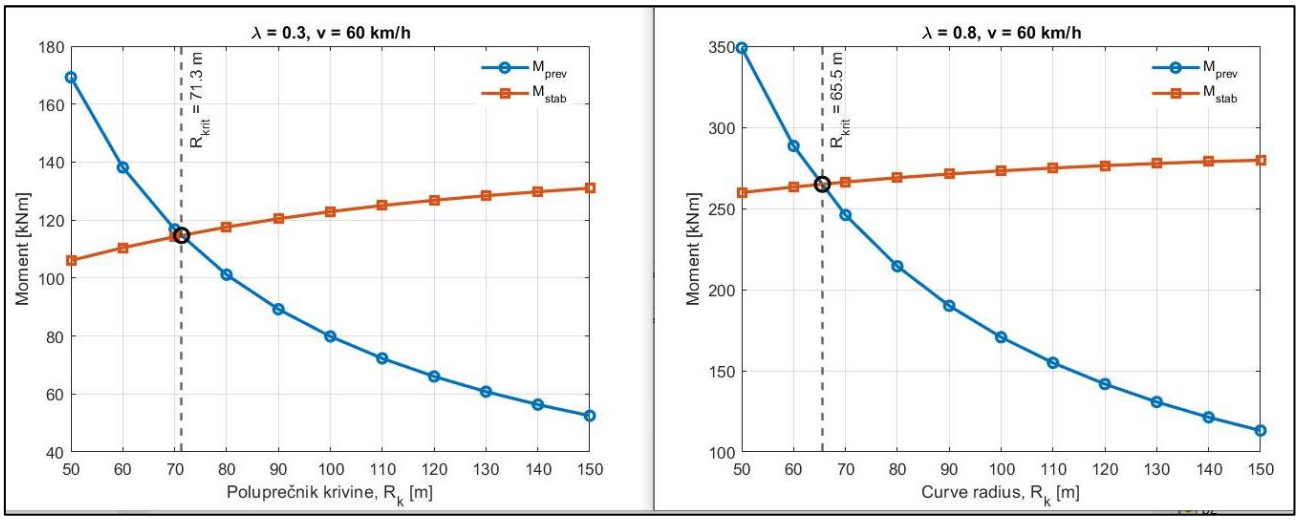

Figure 4 Stabilizing and rollover moments as functions of curve radius for $\lambda = 0.3$ and $\lambda = 0.8$ at $v = 60\frac{km}{h}$

The intersection of the M_{prev} and M_{stab} curves represents the lateral-stability threshold. At a filling level of $30\ \%$, the critical curve radius is approximately $R_k = 71.3\ m$, whereas at a filling level of $80\ \%$ it is $R_k = 65.5\ m$.

For $R_k < R_{krit}$, the rollover moment exceeds the stabilizing moment and the lateral-stability limit is exceeded according to the adopted criterion. For $R_k > R_{krit}$, the stabilizing moment becomes greater than the rollover moment and the road tanker is in the stable region according to the adopted model.

The results show that at a filling level of 30% the limiting condition is reached at a larger curve radius than at a filling level of $80\ \%$. Thus, within the adopted model, a partial filling level of $30\ \%$ represents the less favorable case because the limiting condition is reached on a gentler curve. This result demonstrates that a higher filling level does not necessarily imply lower lateral stability, because stability is simultaneously affected by liquid-cargo mass, the position and displacement of its center of mass, and the relationship between the stabilizing and rollover moments.

The combined three-dimensional representation in Figure 5 confirms the previously observed behavior over the entire analyzed range of filling levels and curve radii. The intersection of the M_{stab} and M_{prev} surfaces represents the lateral-stability boundary.

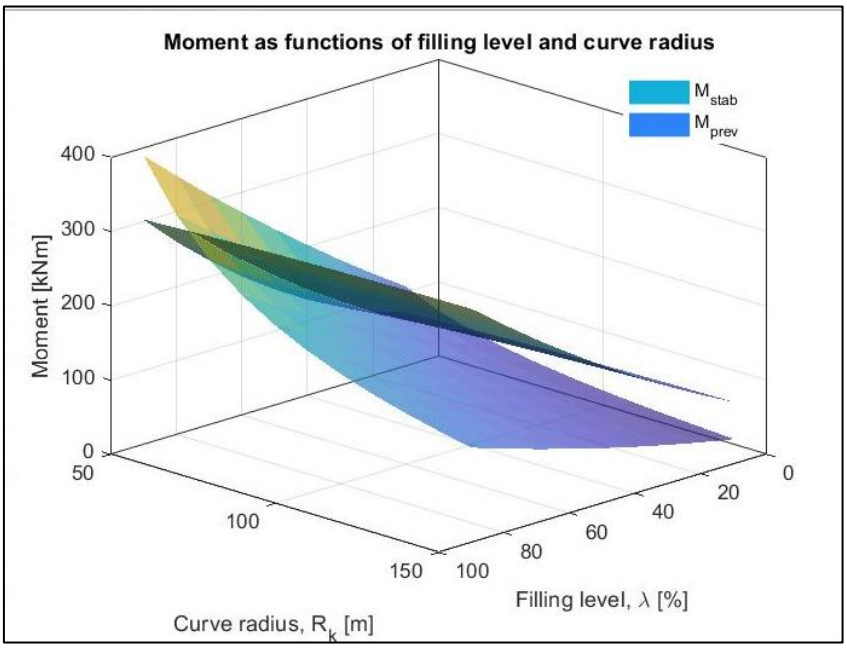

Figure 5 3D representation of the stabilizing and rollover moments as functions of filling level and curve radius at $v = 60\frac{km}{h}$

Stability was additionally evaluated using the coefficient $K = \frac{M_{stab}}{M_{prev}}$, where $K > 1$ corresponds to the stable region, $K = 1$ to the limiting condition, and $K < 1$ to exceedance of the stability criterion. Because the limiting condition ($K = 1$) generally lies between two adjacent analyzed curve radii, the critical values presented in Table 1 were estimated by linear interpolation between the last unstable and first stable calculated cases.

Table 1 Approximate critical values of road tanker stability at a speed of $v = 60\frac{km}{h}$

Filling level, λ [%]	Critical curve radius, $R_{k,krit}$ $[m]$	Critical lateral acceleration, $\frac{a_{y,krit}}{g}$
10	69.0	0.411
20	71.0	0.399
30	71.2	0.398
40	70.7	0.401
50	69.5	0.408
60	68.3	0.416
70	66.6	0.427
80	65.2	0.437
90	63.3	0.450

Note: The values $R_{k,krit}$ and $\frac{a_{y,krit}}{g}$ are approximate values for the condition $K = 1$, obtained by linear interpolation between adjacent calculated cases. They therefore do not represent additional directly simulated cases.

The results in Table 1 show that the approximate critical lateral accelerations in the analyzed range lie between $0.398g$ and $0.450g$. The lowest critical value was obtained at a filling level of 30 % and is approximately $0.398g$, at a critical curve radius of approximately $71.2\ m$. A very similar value was obtained at a filling level of 20%. According to the adopted model, the least favorable range is therefore associated with partial filling levels of approximately 20% to 40%.

Above a filling level of 40 %, the critical lateral acceleration gradually increases. At a filling level of 90 %, the limiting condition was estimated at a lateral acceleration of approximately $0.450g$. At the same time, the critical curve radius decreases from approximately $71.2\ m$ at a filling level of 30 % to approximately $63.3\ m$ at a filling level of 90%.

When interpreting the results, it should be noted that the adopted model does not represent the complete hydrodynamic behavior of the liquid, including intense sloshing, free-surface deformation, and liquid impacts against the tank walls and baffles. Including these effects could further modify the dynamic loads and the lateral-stability boundary, particularly for a partially filled tank. The calculated values therefore represent stability limits according to the adopted simplified model rather than an absolute rollover limit for an actual vehicle.

CONCLUSION

The analysis demonstrates that coupling the dynamic displacement of the liquid-cargo center of mass with vehicle cornering conditions can be used to assess the approach to the lateral-stability limit of a road tanker. The applied method makes it possible to identify unfavorable combinations of operating conditions and filling levels that may increase rollover risk. The results also emphasize the importance of vehicle operation, particularly appropriate speed adjustment when entering a curve. Because increasing speed at a constant curve radius increases lateral acceleration and the rollover moment, timely speed adjustment is an important factor in maintaining road tanker lateral stability.

The developed model provides a basis for further research on road tanker stability. Future work may include a more detailed representation of liquid hydrodynamics, internal baffles, and suspension-system characteristics. Tire–road adhesion should also be included so that the possibility of lateral skidding before rollover can be analyzed in addition to the rollover threshold. Combining these effects would enable the development of a more comprehensive vehicle–liquid cargo–road model and a more realistic assessment of rollover risk under operating conditions.

REFERENCES

Ibrahim, R. A. (2005) *Liquid sloshing dynamics: Theory and applications*. Cambridge University Press

Janković, D. & Todorović. J. (1990) *Theory of Motor Vehicle Motion*. Faculty of Mechanical Engineering, Belgrade

JP Putevi Srbije. (n.d.) *Priručnik za projektovanje puteva u Republici Srbiji – Projektni elementi puta*, JP Putevi Srbije.

Kolaei, A., Rakheja, S., & Richard, M. J. (2014). Effects of tank cross-section on dynamic fluid slosh loads and roll stability of a partly filled tank truck. *European Journal of Mechanics - B/Fluids*, 46, 46-58. https://doi.org/10.1016/j.euromechflu.2014.01.008

Tran, V. N., Nguyen, X. N., Vu, V. T., Dang, T. P. (2022). Rollover stability analysis of liquid tank truck taking into account the road profiles. Journal of Applied Engineering Science, 20(4), 1133-1142. https://doi.org/10.5937/jaes0-36578

United Nations Economic Commission for Europe. (2025) - *Agreement concerning the International Carriage of Dangerous Goods by Road (ADR 2025)*.

Yu, D., & Chu, J. (2019) Study on roll-stability model optimization for partially filled tanker trucks. *Advances in Mechanical Engineering*, 11(4), 1-8. https://doi.org/10.1177/1687814019837805

Zheng, X., Zhang, H., Ren, Y., Wei, Z., Song, X. (2017) Rollover stability analysis of tank vehicles based on the solution of liquid sloshing in partially filled tanks. *Advances in Mechanical Engineering*, 9(6), 1-26. https://doi.org/10.1177/1687814017703894

Zheng, X., et al. (2025) Modeling of tank vehicle rollover risk assessment on curved–slope combination sections for sustainable transportation safety. *Sustainability*, 17(3), 906. https://doi.org/10.3390/su17030906

ZOVKO OIL d.o.o. Žepče. (n.d.) *Technical documentation for a heavy-fuel-oil road tanker* [Internal technical documentation].

The 11th International Congress
Motor Vehicles & Motors 2026
Kragujevac, Serbia
October 8th - 9th, 2026

Motor Vehicles & Motors

MVM2026-028
https://doi.org/10.24874/CMVM2026.028
Technical paper

Momir Drakulić[1]
Aleksandar Đurić[2]
Sreten Perić[3]

SENSITIVITY ANALYSIS OF A TERRAMECHANICS MODEL OF TRACK-TERRAIN INTERACTION WITH RESPECT TO VEHICLE DESIGN PARAMETERS

ABSTRACT: This paper presents a sensitivity analysis of a terramechanics model of track-terrain interaction based on shear stress theory. The aim of the study is to identify the design parameters of a tracked vehicle that have the greatest influence on the generation of contact forces, traction performance, and vehicle stability. The effects of variations in vehicle mass, center of gravity height, moment of inertia and distance between the centerlines of the tracks on the distribution of contact forces within the contact zone are investigated. The model was implemented in the MATLAB/Simulink environment and applied to the BVP M80A tracked vehicle. Numerical simulations were performed for the turning manoeuvre, while the influence of individual parameters on the model outputs was quantified. The obtained results indicate that certain design parameters have a dominant effect on traction performance, contact force distribution, and vehicle stability. The presented sensitivity analysis enables the identification of key parameters for the optimization of tracked vehicle design and provides a basis for the further development of efficient terramechanics models intended for simulation and mobility enhancement of vehicles operating on deformable terrain.

KEYWORDS: terramechanics, tracked vehicle, sensitivity analysis, contact forces

ANALIZA OSETLJIVOSTI TERAMEHANIČKOG MODELA INTERAKCIJE GUSENICE I PODLOGE NA PROMENU KONSTRUKCIONIH PARAMETARA VOZILA

REZIME: U radu je predstavljena analiza osetljivosti teramehaničkog modela interakcije gusenice i deformabilne podloge zasnovanog na teoriji smicajnih napona. Cilj istraživanja je identifikacija konstrukcionih parametara guseničnog vozila koji imaju najveći uticaj na generisanje kontaktnih sila, vučne karakteristike i stabilnost kretanja.

[1] *University of Defence in Belgrade, Military Academy, Veljka Lukica Kurjaka 33, Belgrade,*
momir.drakulic@va.mod.gov.rs, https://orcid.org/0000-0002-8367-7281
[2] *University of Defence in Belgrade, Military Academy, Veljka Lukica Kurjaka 33, Belgrade,*
aleksandar.djuric@va.mod.gov.rs, https://orcid.org/0000-0002-2165-528X
[3] *University of Defence in Belgrade, Military Academy, Veljka Lukica Kurjaka 33, Belgrade,*
sreten.peric@va.mod.gov.rs, https://orcid.org/0000-0002-7270-5187

Analizirani su efekti promena mase, visine težišta, momenta inercije, širine traga, dužine kontakta gusenice i podloge i širine gusenice vozila na raspodelu kontaktnih sila u kontaktnoj zoni. Model je implementiran u MATLAB/Simulink okruženju i primenjen na gusenično vozilo BVP M80A. Numeričke simulacije sprovedene su za različite režime kretanja, uključujući pravolinijsko kretanje i skretanje, pri čemu je izvršena kvantifikacija uticaja pojedinačnih parametara na izlazne veličine modela. Dobijeni rezultati pokazuju da određeni konstrukcioni parametri imaju dominantan uticaj na vučne performanse, raspodelu kontaktnih sila i stabilnost kretanja vozila, dok promene ostalih parametara izazivaju znatno manje promene odziva modela. Predstavljena analiza omogućava identifikaciju ključnih parametara za optimizaciju konstrukcije guseničnih vozila i predstavlja osnovu za dalji razvoj efikasnijih teramehaničkih modela namenjenih simulaciji i unapređenju mobilnosti vozila na deformabilnim podlogama.

KLJUČNE REČI: teramehanika, gusenično vozilo, analiza osetljivosti, kontaktne sile

INTRODUCTION

Tracked vehicle steering is governed by the complex interaction between the vehicle and the terrain, with the resulting response depending on both the vehicle characteristics and the parameters used to describe the track-terrain interaction. Variations in parameters such as vehicle mass, yaw moment of inertia, centre-of-gravity height and track spacing can affect the distribution of contact forces and consequently the vehicle trajectory, turning radius, and dynamic response (Chakravarthy & Sharma, 2024; Drakulic et al., 2025; Garber & Wong, 1981a, 1981c). Therefore, understanding the influence of individual model parameters is essential for assessing the reliability and robustness of numerical predictions.

In (Drakulic et al., 2025), a numerical model of track-terrain interaction during steering of a high-speed tracked vehicle was developed and experimentally validated using measurements obtained from a BVP M80A vehicle. The model demonstrated good agreement with the experimental results and provided a reliable basis for further numerical investigations. However, experimental validation performed for a nominal set of parameters does not indicate how sensitive the predicted outputs are to variations in individual model parameters.

The mathematical description of track-terrain interaction requires the coupling of the vehicle equations of motion with a formulation describing the generation and distribution of stresses within the contact region. In terramechanics-based approaches, the normal and shear stresses developed between the track and deformable terrain are related to the mechanical properties of the terrain, track geometry, normal loading, and shear displacement. Integration of these stresses over the track-terrain contact area provides the longitudinal and lateral forces acting on the vehicle, which subsequently determine its translational and rotational motion (Chen et al., 2025; Du et al., 2018; Garber & Wong, 1981b).

The resulting mathematical model represents a coupled system in which changes in vehicle and geometric parameters can influence both the contact force distribution and the overall vehicle response. Parameters such as vehicle mass and yaw moment of inertia directly affect the equations of motion, while track spacing and centre-of-gravity height influence the geometric and force relationships within the model (Dimauro et al., 2024; Lv et al., 2023). Consequently, variations in these parameters may produce different levels of change in the calculated forces and kinematic characteristics, even when the same steering manoeuvre and terrain conditions are maintained.

For numerical analysis, the mathematical formulation is implemented in MATLAB/Simulink, where the individual relationships describing vehicle motion, track kinematics, and track-terrain interaction are represented by interconnected computational blocks. This implementation enables the model parameters to be systematically varied while maintaining the same initial conditions and operating scenario. The resulting model outputs can therefore be directly compared for different parameter values, providing a consistent framework for evaluating the influence of individual parameters on the simulated vehicle response.

The aim of this study is to investigate the influence of selected model parameters on the output results of the experimentally validated numerical model. The effects of variations in vehicle mass, yaw moment of inertia, centre-of-gravity height and track spacing are analyzed with respect to the main dynamic outputs of the vehicle. The obtained results are used to identify the parameters with the greatest influence on the model response and to assess their relative importance for accurate simulation of tracked vehicle steering.

SIMULATION MODEL

Considering the wide range of methods available for modelling track-terrain interaction, different terramechanical approaches have been developed to describe the behaviour of deformable terrain (Chakravarthy & Sharma, 2024; Garber & Wong, 1981b; Jia et al., 2023). In the present study, the Janosi-Hanamoto semi-empirical formulation is used to characterize the shear response of the terrain. This approach provides a suitable compromise between the

representation of the essential physical mechanisms, numerical robustness, and computational requirements, making it appropriate for integration into a vehicle-level simulation model. The selected formulation has also been employed within the modelling framework considered in this study and experimentally evaluated for the BVP M80 infantry fighting vehicle (Drakulic et al. 2025).

Within the Janosi-Hanamoto formulation, the key coupling variable between vehicle kinematics and soil response is the shear displacement, which arises due to the relative motion between the track and the deformable soil (Meywerk et al., 2016). This quantity governs the development of shear stress within the contact patch and provides a direct link between slip conditions and traction generation. The shear stress is described by the exponential relationship:

$$\tau = (c + \sigma tan\phi)\left(1 - e^{-\frac{j}{K}}\right) \tag{1}$$

where c is the soil cohesion, σ is the normal stress, φ is the internal friction angle, j is the shear displacement, and K is the shear deformation modulus.

The mathematical formulation of the model is based on the terramechanics approach, in which the interaction between the vehicle tracks and deformable terrain is described through the distribution of normal and shear stresses within the track-terrain contact region. The shear stress distribution is determined according to the vehicle kinematics, loading conditions, and mechanical properties of the terrain. The resulting longitudinal and lateral contact forces acting on the left and right tracks are obtained by integrating the corresponding stress components over the contact area (Dimauro et al. 2024; Tota et al. 2021). The detailed procedure for the development and formulation of the mathematical model is presented in (Drakulic et al. 2025). In the present study, the established mathematical formulation is implemented in MATLAB/Simulink and subsequently used to investigate the influence of selected model parameters on the calculated vehicle response (Figure 1).

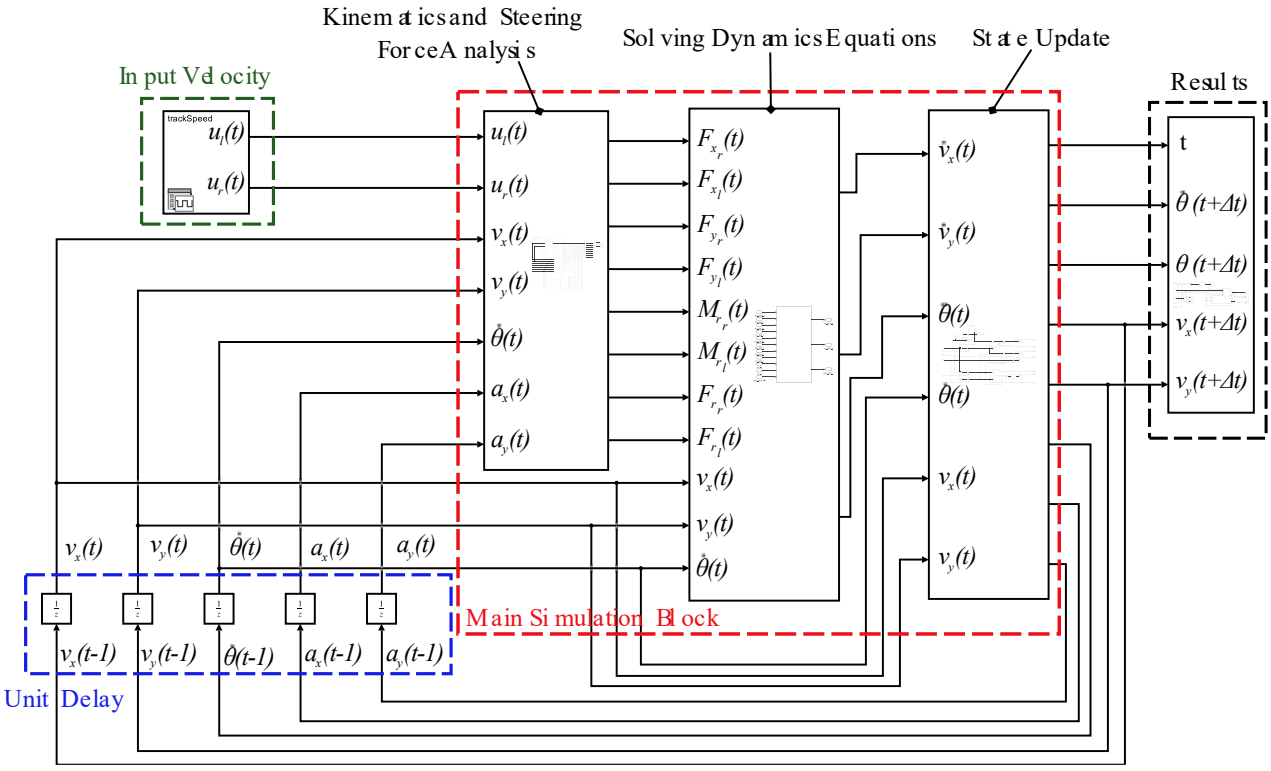

Figure 1 Simulation model (Drakulic et al. 2025)

The implemented simulation model consists of several interconnected functional blocks that describe the vehicle motion, track kinematics, and track-terrain interaction. The vehicle motion module provides the kinematic quantities required for the calculation of the local slip and shear displacement within the track-terrain contact region. These quantities are combined with the terrain and vehicle parameters to determine the stress distribution and the resulting longitudinal and lateral contact forces for the left and right tracks. The calculated forces are then introduced into the vehicle dynamics equations, forming a coupled computational structure in which the track-terrain interaction directly affects the simulated vehicle motion.

For the purposes of the present analysis, the model is evaluated under a predefined steering manoeuvre and fixed terrain conditions, while selected vehicle and model parameters are varied individually. The investigated parameters include vehicle mass, yaw moment of inertia, centre-of-gravity position and track spacing. For each parameter, a range of values around the nominal configuration is considered, while the remaining parameters and simulation

conditions are kept unchanged. The resulting changes in the model outputs are subsequently analysed in terms of longitudinal and lateral track forces and steering resistance torques. This approach enables the relative influence of each parameter on the simulated vehicle behaviour to be evaluated systematically.

SENSITIVITY ANALYSIS OF THE MODEL

Sensitivity analysis is performed to evaluate how variations in selected vehicle parameters affect the response of the developed simulation model. The analysis is focused on the response of the model outputs to changes in individual input parameters, rather than on the absolute influence of the vehicle parameters themselves. The terrain parameters are kept constant throughout the analysis, using the values defined for the selected terrain condition (Table 1). This ensures that the observed changes in the simulation results can be attributed exclusively to variations in the investigated vehicle parameters.

Table 1 Terrain Parameters for Wet grassy

Parameter	Value	Unit
c	15	kPa
φ	25	^{0}
K	0.05	m

Four vehicle parameters are selected for the simulation model sensitivity analysis: vehicle mass m, yaw moment of inertia of the tracked vehicle about the z - axis - Iz, distance between the centerlines of the tracks on both sides - B, and centre-of-gravity height - h (Table 2). These parameters are selected because changes in their values affect different parts of the mathematical model. Vehicle mass modifies the loading conditions and consequently the forces developed at the track-terrain interface. The yaw moment of inertia affects the rotational response of the vehicle, while track spacing directly influences the moment generated by the forces acting on the two tracks. The centre-of-gravity height affects the distribution of normal loads and the dynamic response of the vehicle during steering.

Table 2 Vehicle Parameters

Parameter	Value	Unit
m	*13 850*	kg
Iz	*42 086*	kgm²
B	*2.526*	m
h	*1.139*	m

For each investigated parameter, its nominal value is systematically varied within a predefined range, while all other model parameters and simulation conditions are maintained at their nominal values (Drakulic et al., 2025). The response of the model is calculated for each parameter value and compared with the response obtained for the nominal configuration. In this way, the sensitivity of the model to each individual parameter can be evaluated independently. The same steering manoeuvre, initial conditions, terrain characteristics, and track velocity conditions are used in all simulations to ensure consistency between the investigated cases.

The sensitivity of the model is evaluated by analysing changes in the principal output variables, including the longitudinal and lateral track-terrain contact forces and steering resistance torques. The magnitude and nature of the changes in these outputs are examined as a function of the corresponding variation in each input parameter. This allows the response of the model to parameter perturbations to be identified and provides an indication of whether a particular output is weakly or strongly sensitive to the investigated parameter.

The results of the sensitivity analysis are used to compare the relative response of the model to variations in the four selected parameters. Attention is given to the parameters that produce the largest changes in the calculated output quantities, as these parameters have the greatest effect on the numerical prediction of vehicle behaviour. The analysis therefore provides a quantitative basis for assessing the robustness of the model and for identifying the vehicle parameters that require particular attention during model parameterisation and further experimental characterisation. In the considered steering manoeuvre, the left track represents the outer track, whereas the right track represents the inner track, therefore, the subscripts l and r denote the left and right tracks, respectively.

Sensitivity of the model to vehicle mass

To assess the sensitivity of the developed simulation model to variations in vehicle mass, a series of simulations was performed in which the nominal vehicle mass was varied within a predefined range (±25% and ±50% relative to the nominal value), while all other vehicle, steering, and terramechanical parameters were kept constant. This approach allows the effect of vehicle mass to be evaluated independently and provides a direct assessment of the response of the model to changes in this parameter. The results of the performed simulations are presented in Figure 2.

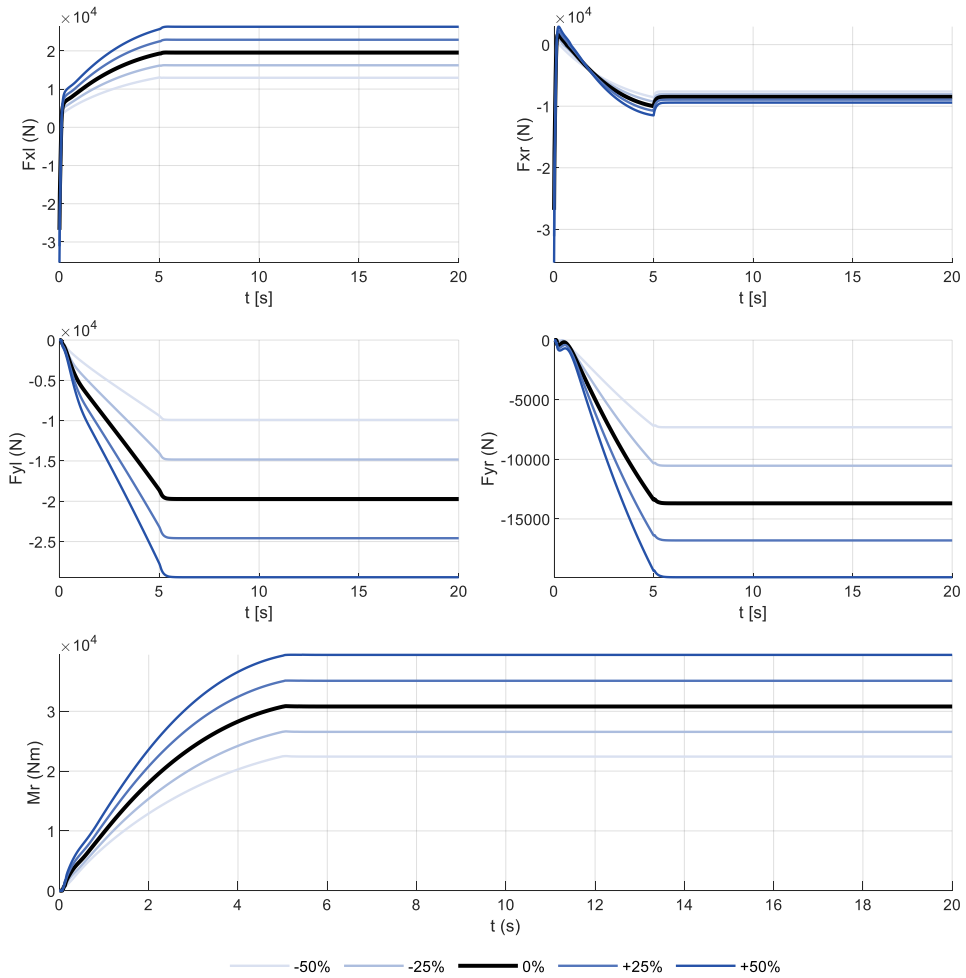

Figure 2 Influence of vehicle mass on model response during steering manoeuvre

The variation in vehicle mass has a pronounced effect on the track-terrain contact forces in both the longitudinal and lateral directions (Fx and Fy force). As the vehicle mass increases, the normal load acting on the tracks increases, which directly affects the distribution of contact stresses and the resulting interaction forces. Consequently, an increase in mass leads to higher longitudinal forces on both tracks. This behaviour is associated with the increased loading of the track-terrain interface and the higher forces required to maintain the prescribed vehicle motion during the steering manoeuvre. Within the investigated range, the steady-state longitudinal force on the outer track (Fxl) decreases to approximately 13 kN at -50% mass to approximately 26 kN at +50% mass, relative to a nominal value of approximately 19.5 kN — a change of roughly -35%/+25%.

An increase in vehicle mass also results in a noticeable change in the lateral contact forces. The absolute values of the lateral forces increase with increasing mass, which can be attributed to the greater dynamic loading of the vehicle during the steering manoeuvre. At the same time, a clear difference between the lateral forces generated by the inner and outer tracks can be observed. This asymmetry results from the different kinematic and loading conditions of the two tracks during steering and reflects their different contributions to the lateral and rotational response of the vehicle. The inner-track lateral force (Fyr) ranges from approximately -10 kN to -30 kN relative to a nominal value of approximately -19.5 kN, while the outer-track lateral force (Fyl) ranges from approximately -7 kN to -19.5 kN relative to a nominal value of approximately -14 kN — indicating a proportionally larger relative sensitivity for the outer track.

A particularly pronounced dependence on vehicle mass is observed for the steering resistance moment. As the vehicle mass increases, the normal loading of the tracks and the corresponding interaction forces with the terrain also increase. Consequently, greater resistance to the change in vehicle heading is generated, resulting in an increase in the steering resistance moment. This indicates that vehicle mass affects not only the magnitude of the individual track-terrain forces but also the overall resistance associated with the steering manoeuvre. The steering resistance moment (Mr) increases from approximately 22 kNm at -50% mass to approximately 39 kNm at +50% mass relative to a nominal value of approximately 31 kNm, corresponding to the largest relative variation (approximately ±25%) among the analyzed output quantities.

The obtained results demonstrate that the simulation model exhibits a pronounced sensitivity to vehicle mass, with the most significant effects observed in the track-terrain contact forces and steering resistance moment. The systematic increase in these quantities with increasing vehicle mass is consistent with the physical behaviour

expected from the increased normal loading of the tracks. The results therefore confirm the importance of accurately defining vehicle mass in the model, particularly when the model is used for predicting track-terrain interaction forces and steering behaviour under different vehicle configurations.

Sensitivity of the model to yaw moment of inertia

The influence of the yaw moment of inertia on the simulated vehicle response was examined by varying this parameter within a range of ±25% and ±50% relative to its nominal value, while the remaining vehicle, steering, and terramechanical parameters were held fixed at their nominal settings. Isolating the yaw moment of inertia in this manner makes it possible to distinguish its effect on the model response from that of the other investigated parameters. The corresponding results are shown in Figure 3.

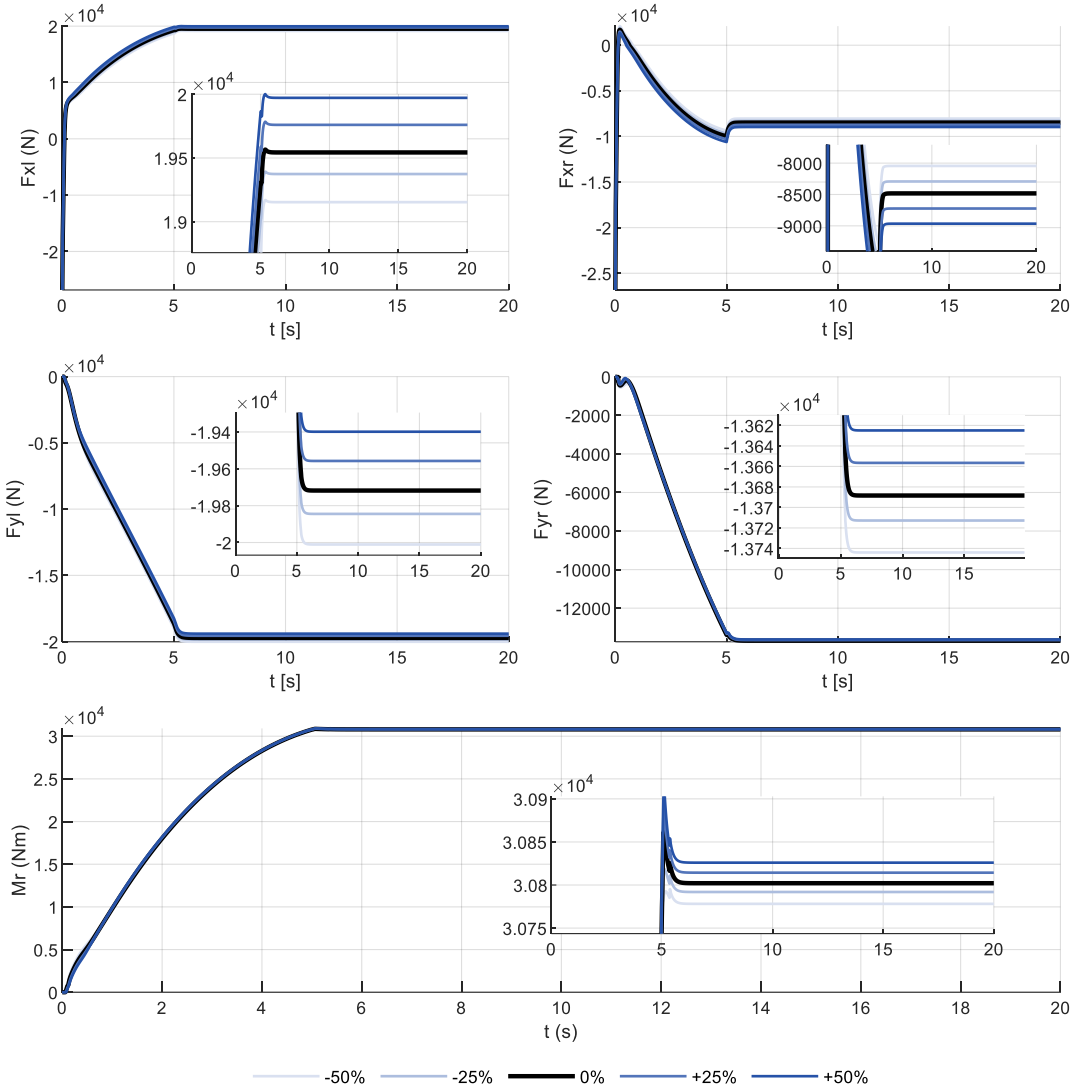

Figure 3 Influence of yaw moment of inertia on model response during steering manoeuvre

The analysis of the track-terrain contact forces shows that variations in the yaw moment of inertia have a negligible influence on the longitudinal and lateral forces in the steady-state steering regime. The force responses corresponding to different values of the parameter practically coincide once the transient phase has ended. The steady-state spread across the full ±50% range remains within a few percent of the nominal value for all four force components — approximately 1.9 to 2.0 kN for Fxl, -8.0 to -9.0 kN for Fxr, and -19.4 to -19.8 kN for Fyl, while Fyr shows the tightest band of all, varying only between approximately -13.64 kN and -13.74 kN. This behaviour is expected because the yaw moment of inertia does not directly affect the normal loading of the tracks or the quasi-static distribution of contact stresses. Its influence is primarily related to the dynamic response of the vehicle during changes in angular motion.

The effect of the yaw moment of inertia is therefore mainly observed during the initial phase of the manoeuvre. Higher values of the yaw moment of inertia result in a slower development of the vehicle rotational response, which is reflected in a slightly slower increase in the lateral contact forces and steering resistance moment. As the vehicle approaches the steady-state condition, these differences gradually disappear and the corresponding output values

converge. This is particularly visible in the steering resistance moment, where the response briefly overshoots to approximately 30.85 kNm for lower values of Iz before settling to a steady-state value within roughly 0.3% of the nominal 30.8 kNm - confirming that the parameter's effect is confined almost entirely to the transient phase of the manoeuvre. The results indicate that the model has low sensitivity to the yaw moment of inertia with respect to steady-state contact forces, while its influence becomes more relevant when analysing the transient steering response.

Sensitivity of the model to distance between the centerlines of the tracks on both sides

Unlike the previously discussed parameters, track spacing was examined over a narrower interval of ±10% and ±20% relative to its nominal value, since larger deviations would no longer correspond to realistic design variations of the vehicle undercarriage. All other vehicle, steering, and terramechanical parameters were kept fixed at their nominal settings throughout this analysis, and the corresponding results are shown in Figure 4.

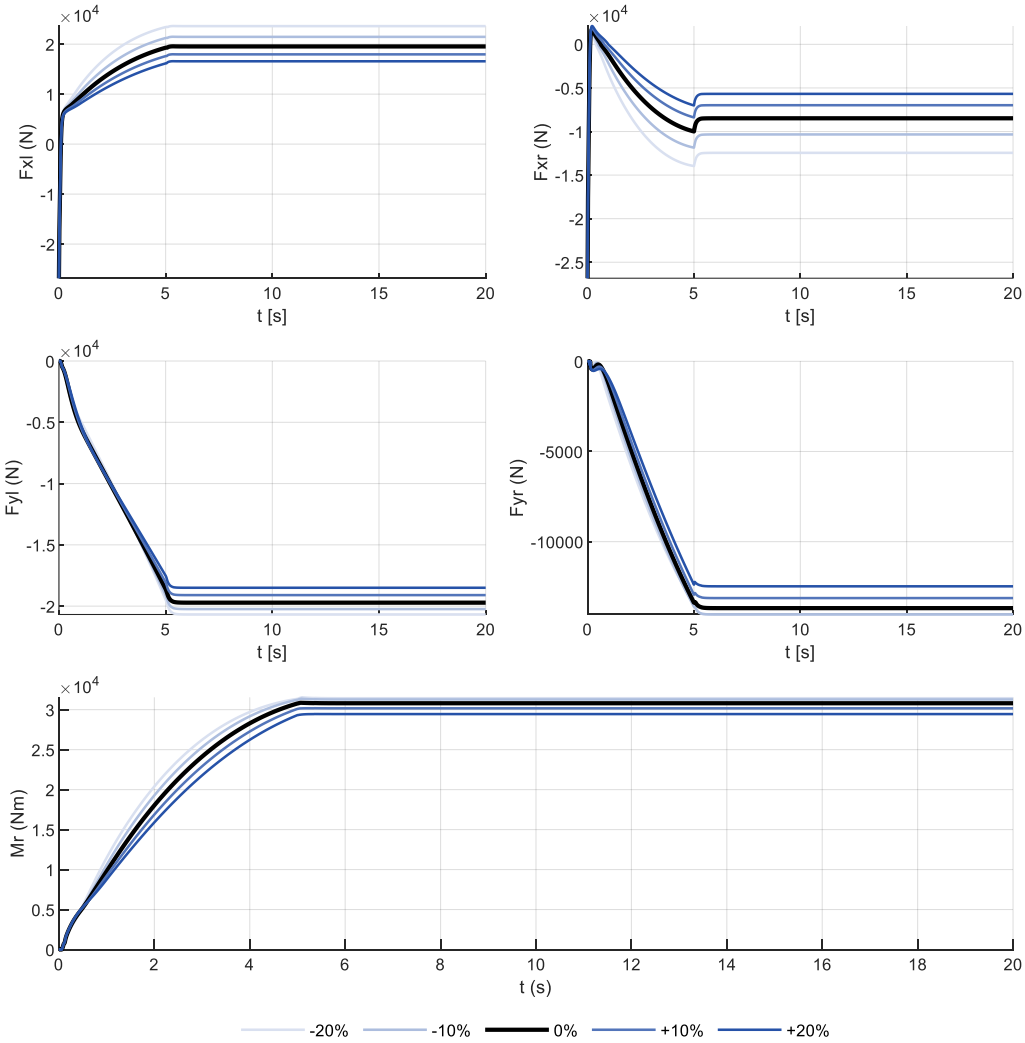

Figure 4 Influence of track spacing on model response during steering manoeuvre

Even within this comparatively narrow interval, track spacing clearly redistributes the contact forces between the two tracks. The steady-state longitudinal force on one track shifts from roughly 17.5 kN at -20% to roughly 23 kN at +20% relative to a nominal value of approximately 19.5 kN (Fxl), while the opposite track shows the largest relative shift among all five monitored outputs, moving from approximately -6 kN to -12 kN around a nominal value of -8 kN (Fxr). The lateral forces move in the opposite sense: Fyl stays confined to a narrow band of roughly -18 to -20 kN, whereas Fyr spans a wider interval of approximately -12 kN to -14kN around a nominal value near -13 kN. This redistribution reflects the altered steering geometry - a wider track spacing changes the effective radius at which the driving forces act, reducing the lateral slip needed to complete the prescribed turning manoeuvre.

The steering resistance moment is comparatively insensitive to this parameter by comparison, staying within roughly 29 - 31 kNm of the nominal 30.5 kNm across the full ±20% interval - a narrower relative band than either of the lateral forces. Beyond the contact forces shown in Figure 4, track spacing also affects the turning radius and the lateral velocity/acceleration components: a larger spacing widens the turning radius and lowers the lateral velocity, whereas

the longitudinal and total vehicle speed remain governed almost entirely by the prescribed track velocities and are only marginally affected by this parameter.

Taken together, these results place track spacing among the parameters worth prioritizing during vehicle parameterisation - not because of its effect on the steering moment, which is modest, but because of how strongly it redistributes load and lateral force between the two tracks, with direct consequences for turning geometry.

Sensitivity of the model to centre-of-gravity height

Of the four parameters considered in this study, centre-of-gravity height proved to have the most limited influence on the model outputs. Simulations were performed for values of this parameter varied by ±25% and ±50% relative to its nominal setting, with all other vehicle, steering, and terramechanical parameters held constant; the corresponding results are shown in Figure 5.

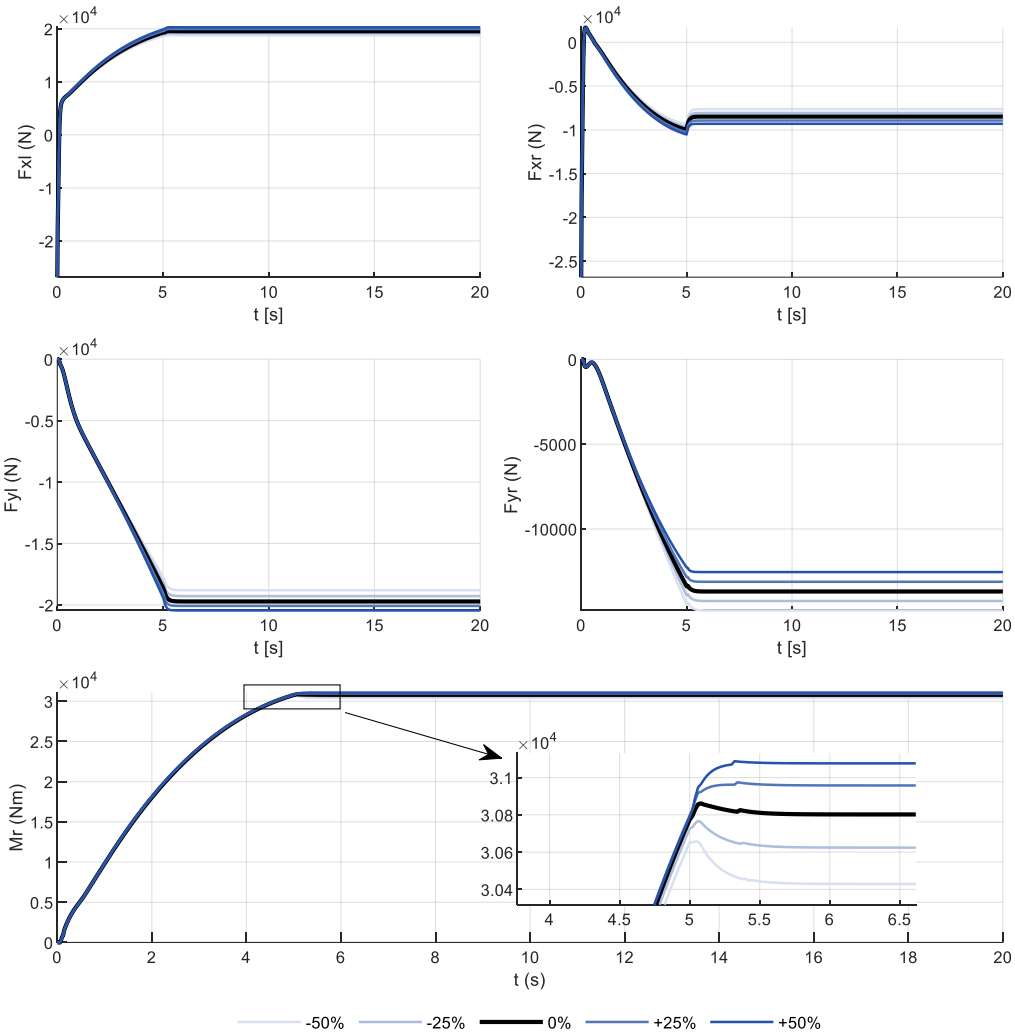

Figure 5 Influence of centre-of-gravity height on model response during steering manoeuvre

The longitudinal forces are scarcely affected by this parameter, with Fxl remaining within roughly 0.1 kN of its nominal 19 kN value and Fxr similarly staying close to its nominal value of approximately -8 kN across the entire investigated range. This behaviour is consistent with the fact that the total normal reaction at the track-terrain interface is governed primarily by vehicle weight, whereas variations in centre-of-gravity height do not directly alter its overall magnitude. The influence of this parameter is instead associated with the dynamic load transfer occurring during the steering manoeuvre, which may modify the distribution of normal loads and consequently affect the resulting contact forces. The lateral forces respond somewhat more visibly to this parameter, particularly on the outer track: Fyl stays confined to a tight band around -19 kN, while Fyr ranges from approximately -12 kN to -14.5 kN around a nominal value near -13.5 kN, representing the largest relative variation among the monitored outputs for this parameter, although the change remains modest in absolute terms.

The steering resistance moment follows the same pattern of limited responsiveness: the steady-state value shifts by no more than approximately 0.5 - 1 kNm around its nominal 30.8 kNm across the full ±50% interval, with the visible

differences in Figure 5 concentrated in a brief overshoot just after the transient phase rather than in the settled response. Taking the four investigated parameters together, centre-of-gravity height contributes the smallest overall variation to the model outputs, suggesting that within the range considered here, it can be assigned lower priority than vehicle mass or track spacing when calibrating the model for a new vehicle configuration.

CONCLUSIONS

This study investigated the sensitivity of a terramechanics-based numerical model of a tracked vehicle to variations in vehicle mass, yaw moment of inertia, track spacing, and centre-of-gravity height. The model was implemented in MATLAB/Simulink, while the terrain, steering conditions, and all non-investigated parameters were kept constant, allowing the individual influence of each selected parameter on the track-terrain interaction and vehicle response to be evaluated in isolation.

The analysis demonstrates that the sensitivity of the investigated terramechanics model is strongly dependent on the physical mechanism through which individual vehicle parameters affect the coupled vehicle-terrain system. Parameters influencing the normal loading conditions and steering geometry, particularly vehicle mass and track spacing, produce the most pronounced changes in the calculated interaction forces. Conversely, parameters primarily associated with the transient vehicle dynamics, such as the yaw moment of inertia, have only a limited influence on the steady-state force predictions.

Vehicle mass and track spacing emerged as the two parameters governing the largest share of the model's response, though through different mechanisms. Across the ±50% mass range, the steering resistance moment varied from approximately 22 to 39 kNm around a nominal value of 31 kNm, while the lateral force on the inner track ranged from approximately -10 to -30 kN - the largest relative spread of any monitored output. Track spacing, investigated over a narrower ±20% interval, produced a comparable redistribution of forces between the two tracks: the outer-track longitudinal force shifted from approximately -6 to -12 kN around a nominal -8 kN, while the steering resistance moment remained comparatively stable, within roughly 29-31 kNm of its nominal 30.5 kNm. Vehicle mass therefore primarily scales the overall force and moment levels, whereas track spacing reshapes how those forces are distributed between the inner and outer tracks.

By contrast, the yaw moment of inertia had almost no bearing on the steady-state outputs: Fxl remained within approximately 19 - 20 kN, Fxr within -8.0 to -9.0 kN, and Fyl within -19.4 to -19.8 kN across the full ±50% range, while Fyr showed the tightest band of all, varying only between approximately -13.64 kN and -13.74 kN. Its effect was instead confined to the transient phase of the manoeuvre, where the steering resistance moment briefly overshot to approximately 30.85 kNm before settling within roughly 0.3% of the nominal 30.8 kNm, and higher values of the parameter delayed the development of the rotational response. Centre-of-gravity height behaved similarly to a lesser degree: the longitudinal forces were essentially unaffected (Fxl within 0.1 kN of its nominal 19 kN, Fxr close to its nominal -8 kN), while the outer-track lateral force showed the most visible response of the four monitored quantities for this parameter, spreading from approximately -12 to -14.5 kN around a nominal -13.5 kN, and the steering resistance moment shifted by no more than approximately 0.5 - 1 kNm around its nominal 30.8 kNm.

These findings should be interpreted within the scope of the adopted one-at-a-time approach, a single terrain condition, and a single steering manoeuvre, potential interaction effects between parameters, as well as the influence of alternative terrain and manoeuvre conditions, were not addressed and remain open for further investigation. Within these limits, the results suggest that vehicle mass and track spacing warrant the greatest care during model parameterisation and experimental characterisation, whereas the yaw moment of inertia and centre-of-gravity height can be defined with comparatively less precision without substantially compromising the accuracy of the predicted steady-state track-terrain interaction.

ACKNOWLEDGMENTS

This work was supported by the Ministry of Defence, Serbia, under the project „Modelling of Automotive Vehicle Assemblies for the Optimization of Dynamic Parameters”, No. VA-TT/1/26-28.

NOMENCLATURE

τ - shear stress

σ - normal stress

φ - internal friction angle

c - soil cohesion
j - shear displacement
K - shear deformation modulus
m - vehicle mass
Iz - yaw moment of inertia of the tracked vehicle about the z-axis
B - distance between the centerlines of the tracks (track spacing)
h - centre-of-gravity height
Fx - total longitudinal force (both tracks)
Fy - total lateral force (both tracks)
Fxl - longitudinal force on the outer (left) track
Fxr - longitudinal force on the inner (right) track
Fyl - lateral force on the outer (left) track
Fyr - lateral force on the inner (right) track
Fr_l - resultant contact force – left track
Fr_r - resultant contact force – right track
Mr - total steering resistance moment
t - time
Δt - time step
u_l - left track (input) velocity
u_r - right track (input) velocity
v_x - longitudinal velocity of the vehicle
v_y - lateral velocity of the vehicle
$\dot{v}_x$ - rate of change of longitudinal velocity
$\dot{v}_y$ - rate of change of lateral velocity
a_x - longitudinal acceleration
a_y - lateral acceleration
$\dot{\theta}$ - yaw rate
$\ddot{\theta}$ - yaw angular acceleration

REFERENCES

Chakravarthy, P. N., & Sharma, P. K. (2024). Terramechanics Models for Tracked Vehicle Terrain Interaction Analysis A Review. *Defence Science Journal*, 74(4), 469–481. https://doi.org/10.14429/dsj.74.19029

Chen, Y., Xu, X., Wang, W., Gao, X., & Yang, C. (2025). Optimization of Grouser–Track Structural Parameters for Enhanced Tractive Performance in Unmanned Amphibious Tracked Vehicles. *Actuators*, 14(8), 390. https://doi.org/10.3390/act14080390

Dimauro, L., Venturini, S., Tota, A., Galvagno, E., & Velardocchia, M. (2024). High-speed tracked vehicle model order reduction for static and dynamic simulations. *Defence Technology*, 38, 89–110. https://doi.org/10.1016/j.dt.2024.01.006

Drakulic, M., Peric, S., Djuric, A., & Rakic, S. (2025). Track–terrain interaction during steering of high-speed tracked vehicles: Numerical modeling and experimental validation. *Measurement*, 256, 118225. https://doi.org/10.1016/j.measurement.2025.118225

Du, Y., Gao, J., Jiang, L., & Zhang, Y. (2018). Development and numerical validation of an improved prediction model for wheel-soil interaction under multiple operating conditions. *Journal of Terramechanics*, 79, 1–21. https://doi.org/10.1016/j.jterra.2018.04.005

Garber, M., & Wong, J. Y. (1981a). Prediction of ground pressure distribution under tracked vehicles—I. An analytical method for predicting ground pressure distribution. *Journal of Terramechanics*, 18(1), 1–23. https://doi.org/10.1016/0022-4898(81)90015-X

Garber, M., & Wong, J. Y. (1981b). Prediction of ground pressure distribution under tracked vehicles—I. An analytical method for predicting ground pressure distribution. *Journal of Terramechanics*, 18(1), 1–23. https://doi.org/10.1016/0022-4898(81)90015-x

Garber, M., & Wong, J. Y. (1981c). Prediction of ground pressure distribution under tracked vehicles—II. Effects of design parameters of the track-suspension system on ground pressure distribution. *Journal of Terramechanics*, 18(2), 71–79. https://doi.org/10.1016/0022-4898(81)90001-X

Jia, W., Liu, X., Zhang, C., Qiu, M., Tan, Y., & Yu, Z. (2023). Design of Zero-Differential steering Controller for tracked vehicles with Hydraulic-Mechanical transmission based on particle swarm optimization Algorithm. *IEEE Access*, 11, 32187–32200. https://doi.org/10.1109/access.2023.3262515

Lv, G., Lv, H., Chen, Z., Chu, W., & Mao, J. (2023). Research on inertia transfer in load simulation of tracked vehicle under complex working conditions. *Frontiers in Materials*, 10, 1188411. https://doi.org/10.3389/fmats.2023.1188411

Meywerk, M., Fortmüller, T., Fuhr, B., & Baß, S. (2016). Real-time model for simulating a tracked vehicle on deformable soils. *Advances in Mechanical Engineering*, 8(5), 1687814016647889. https://doi.org/10.1177/1687814016647889

Tota, A., Galvagno, E., & Velardocchia, M. (2021). Analytical study on the cornering behavior of an articulated tracked vehicle. *Machines*, 9(2), 38. https://doi.org/10.3390/machines9020038

The 11th International Congress
Motor Vehicles & Motors 2026
Kragujevac, Serbia
October 8th - 9th, 2026

Motor Vehicles & Motors

MVM2026-031
https://doi.org/10.24874/CMVM2026.031
Technical paper

Marko Simonović[1]
Dragan Adamović[2]
Đorđe Ivković[3]
Milan Simonović[4]

SELECTION OF MATERIALS FOR FRICTION COMPONENTS OF THE BRAKE MECHANISM

ABSTRACT: The aim of this paper is the multi-criteria selection of a friction material for brake mechanism components using the Digital Logic Method. Fourteen alternative friction materials were analysed on the basis of ten mechanical, physical, tribological, thermal, and environmental criteria. In the first stage, the defined limit values of the criteria were applied, after which alternatives M6, M8, and M12 were identified as acceptable. The relative importance of the criteria was determined by pairwise comparison using the Digital Logic Method, followed by the final evaluation of the remaining alternatives. The obtained evaluation index values were 0.001 for M6, 0.026 for M12, and 0.074 for M8, where a lower value represents a more favourable alternative. Based on the results, M6 was identified as the most favourable material within the considered set of alternatives and adopted criteria.

KEYWORDS: friction materials, braking systems, material selection, coefficient of friction

IZBOR MATERIJALA ZA FRIKCIONE KOMPONENTE KOČIONOG MEHANIZMA

REZIME: Cilj rada je višekriterijumski izbor frikcionog materijala za komponente kočionog mehanizma primenom digitalno-logičke metode. Analizirano je 14 alternativnih frikcionih materijala na osnovu deset mehaničkih, fizičkih, triboloških, termičkih i ekoloških kriterijuma. U prvoj fazi primenjene su definisane granične vrednosti kriterijuma, nakon čega su kao prihvatljive izdvojene alternative M6, M8 i M12. Relativni značaj kriterijuma određen je njihovim parnim poređenjem primenom digitalno-logičke metode, a zatim je izvršeno konačno vrednovanje preostalih alternativa. Dobijene vrednosti pokazatelja vrednovanja iznosile su 0,001 za M6, 0,026 za M12 i 0,074 za M8, pri

[1] *Marko Simonović, Military Technical Institute, Ratka Resanovića 1, Beograd, marko.simonovic@mod.gov.rs,*
https://orcid.org/0009-0007-5531-6175
[2] *Dragan Adamović, Faculty of Engineering, University of Kragujevac, Sestre Janjić 6, adam@kg.ac.rs*
https://orcid.org/0000-0003-3459-3011
[3] *Đorđe Ivković, Faculty of Engineering, University of Kragujevac, Sestre Janjić 6, djordje.ivkovic@fink.rs*
https://orcid.org/0000-0002-5747-7876
[4] *Milan Simonović, Military Technical Institute, Ratka Resanovića 1, Beograd, milan.simonovic@mod.gov.rs,*
https://orcid.org/0009-0001-5502-7708

čemu niža vrednost predstavlja povoljniju alternativu. Na osnovu rezultata, M6 je izdvojen kao najpovoljniji materijal u okviru razmatranog skupa alternativa i usvojenih kriterijuma.

KLJUČNE REČI: frikcioni materijali, kočioni sistemi, izbor materijala, koeficijent trenja

INTRODUCTION

Friction materials are essential for the operation, safety, and environmental acceptability of modern automotive braking systems. They are complex, multiphase composites that usually consist of four functional groups: binders, reinforcements, fillers, and friction modifiers (Gehlen, G.S. et al. 2026). The materials of the elements forming friction pairs have an exceptionally strong influence on brake quality and, consequently, on the ability of the vehicle braking system to perform its tasks (Todorović, J. 1988).

Brakes and clutches on vehicles differ completely in terms of appearance, purpose, and operating principle, but both systems rely to a large extent on friction. Brakes use friction to reduce speed or bring the vehicle to a complete stop, whereas in clutches friction is used to control power transmission. In these systems, friction is generated by components made of friction materials (Tokai Carbon n.d.).

Friction materials used in brakes play a vital role in braking performance with respect to vehicle speed control and thus ensure the safety of the vehicle and road users. A good brake friction material should have a high and stable coefficient of friction over a wide range of operating temperatures, contact pressures, sliding speeds, and humidity levels. It should also have high wear resistance in order to provide a long service life of the braking element. However, the friction material should have a hardness that does not cause excessive wear of the drum or disc. It should possess high thermal and oxidation resistance because a large amount of kinetic energy is converted into heat during braking. In addition to all the required characteristics, it should also be economical (Talegaonkar, R. P., & Gopinath, K. 2005). Figure 1 summarizes the requirements for friction materials (Todorović, J. 1988).

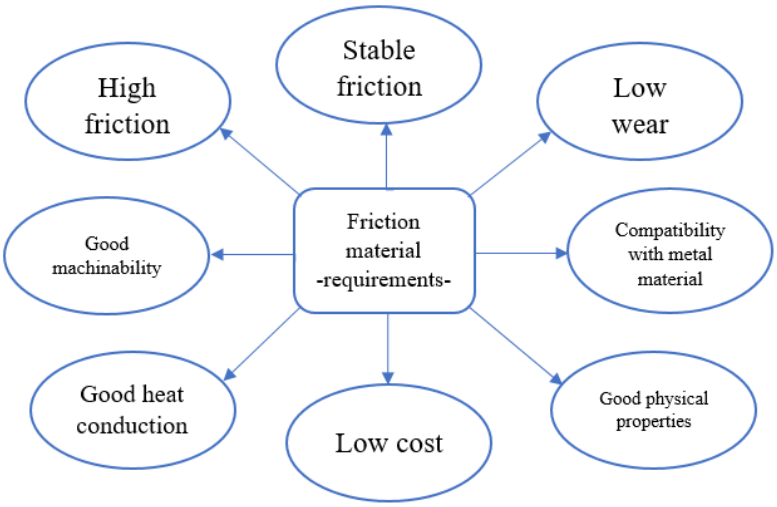

Figure 1 Requirements for friction materials (Todorović, J. 1988)

The above requirements can be satisfied by using several types of materials with different compositions and manufacturing processes. In percentage terms, the contents of the four basic groups in a friction material are as follows:

- binders: 5-25%;
- reinforcements: 20-50%;
- fillers: 0.5-1%;
- friction modifiers: 30-60% (Petar, P. 2025).

Binders play an important role in determining the performance of friction materials. Although they are not the main component by volume or cost, binders represent the “heart” of friction materials. They are used to bind the other components in friction materials and to maintain the structural integrity of the composite under mechanical and thermal stresses (Peng, C. et al. 2025).

The primary task of reinforcements is to provide the friction material with the required mechanical properties, namely strength and toughness. In addition, reinforcements provide the necessary integrity of the friction material

during the manufacturing stage by connecting all ingredients into a mixture that enables subsequent chemical and physical shaping (Todorović, J. 1988).

Fillers are intended to “fill” the friction material mixture, i.e., to provide the required volume in accordance with the design documentation requirements. Since fillers do not significantly contribute to the properties of friction materials, inexpensive minerals, and sometimes metals, are used for this purpose. It is important that the hardness of the filler is not too high, because higher hardness may affect material properties and, in particular, may cause an unfavourable effect of the friction material on the mating metallic element (Todorović, J. 1988).

Friction modifiers are intended to provide the required relationships between the important operating characteristics of friction materials, particularly with respect to friction and wear. Materials of very different origin can be used, including minerals, metals, and organic resins, in various forms and proportions in the mixture (Todorović, J. 1988).

The most widely used friction materials include:

- asbestos friction materials;
- organic friction materials (NAO – Non-Asbestos Organic);
- sintered metallic friction materials;
- semi-metallic friction materials;
- low-metallic NAO friction materials;
- ceramic friction materials;
- carbon-carbon composite (C/C) friction materials;
- carbon-ceramic (C/C-SiC) composite friction materials.

The aim of this study is to perform a multi-criteria selection of the optimal friction material using the digital-logic method for the production of friction components of a braking mechanism. The selection criteria will be based on the mechanical, physical, tribological, thermal and environmental properties of the alternative materials, which have been adopted from scientific studies. The experimental procedure will be presented in greater detail in Section 3.

BRAKING SYSTEMS

The braking system is designed for controlled changes in vehicle speed, stopping the vehicle, and keeping it stationary after stopping. Brakes are one of the most important safety features of any vehicle. (Atlantic Tire Service n.d.) The process of slowing down or stopping a vehicle is generally achieved by friction. (Medium. n.d.) Unlike most machine elements, in which friction is a highly undesirable phenomenon, in motor vehicle brakes friction is one of the fundamental principles of operation and an essential prerequisite for performing the function of the braking system. Friction enables the transformation of kinetic energy into thermal energy, thereby slowing down and stopping the vehicle (Todorović, J. 1988).

The braking system consists of three mechanisms:

- control mechanism – pressure applied by the driver to the brake pedal;
- transmission mechanism – according to the method of transmitting force from the control to the actuator, this mechanism may be mechanical, hydrostatic, pneumatic, or hydropneumatic (combined);
- actuating mechanism – vehicle braking.

The braking system comprises four subsystems (Figure 2).

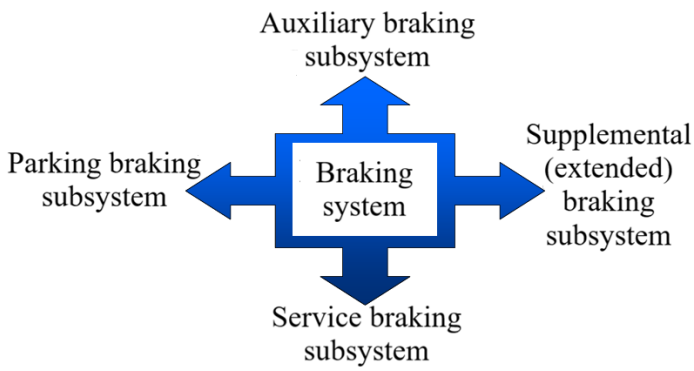

Figure 2 Subsystems of the braking system (Aleksendrić, D. n.d.)

Disc brakes

Disc brakes are standard on most cars today, although, for certain reasons, drum brakes are still used even on more expensive and powerful vehicles. The operating principle of disc brakes is most easily understood by observing a bicycle brake. On a bicycle, the calipers press rubber pads against the rim and thus slow down wheel rotation.

Disc brakes on a car operate in the same way, except that the brake calipers press against a disc located on the wheel hub (Polovni automobili n.d.).

The basic components of a disc brake (Figure 3) are:

- brake pads,
- caliper with piston,
- disc (rotor), mounted on the vehicle wheel hub (howstuffworks n.d.).

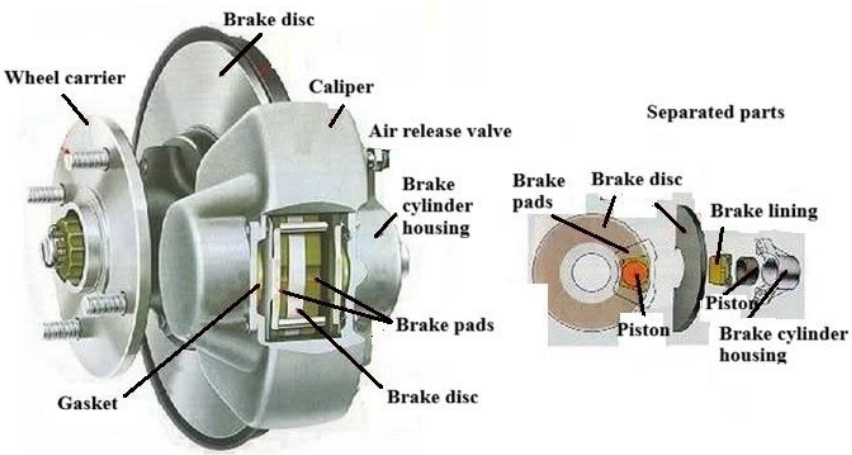

Figure 3 Disc brake (Popravka automobila n.d.)

Drum brakes

Drum brakes are a type of brake commonly used on two-wheeled and four-wheeled vehicles. Their operating principle is almost the same in both types of vehicles. Drum brakes operate on the same principle as disc brakes: the linings press against a rotating surface. In this system, that surface is called the drum (Wuling motors n.d.).

Many cars have drum brakes on the rear wheels and disc brakes on the front wheels. Drum brakes comprise more components than disc brakes and are more difficult to maintain, but they are less expensive to manufacture (howstuffworks n.d.).

The basic components of a drum brake are:

- drum,
- brake linings (brake shoes),
- hydraulic wheel cylinder with piston,
- spring system. (Kwikfit. (n.d.), Akebono. (n.d.))

Figure 4 Drum brake (Akebono. (n.d.))

MATERIAL SELECTION METHODS

In addition to designing the geometry of the components that make up a product, product development also involves selecting the appropriate materials from which those components will be made. Material selection represents an almost constant challenge for designers, regardless of their level of experience in this field (Petković, D. 2016).

The selection of material for a particular product largely determines its functionality. Therefore, the material selection process is very complex and requires expert knowledge. In addition, material cost, product shape, environmental impact, market availability, and other factors further complicate the material selection problem, making it a time-consuming task. The material selection problem often also involves conflicting criteria, such as hardness–toughness or aesthetic appearance–cost, which requires the decision-maker to clearly define the objectives to be achieved.

An inadequate selection of material for a product may lead to premature product failure, resulting in reduced profit, productivity, and company reputation (Petković, D. 2016).

Initial material screening

At the outset, designers consider various initial ideas related to material selection. Ideas that are immediately identified as unsuitable are rejected, while those that appear practical are considered further. Quantitative methods can be used for initial material screening in order to narrow the choices to a manageable number for further processing and evaluation. Initial material screening can be achieved by first classifying performance requirements as:

- rigid requirements – requirements that must be satisfied;
- soft requirements – relative requirements (Farag, M. 2016).

Rigid requirements are those that a material must satisfy in order to be considered at all. For example, metallic materials are eliminated when selecting a material for an electrical insulator. If the insulator also needs to be flexible, the field is narrowed further because all ceramic materials are eliminated.

Soft requirements are those that are subject to trade-offs and deviations. Examples of soft requirements include mechanical properties, specific weight, and cost. Soft requirements can be compared in terms of their relative importance, which depends on the application being studied (Farag, M. 2016).

Comparison and ranking of materials

Selecting an appropriate material is a difficult process that requires handling a large amount of information about material properties. After narrowing the field of possible materials by one or more quantitative methods for initial screening, quantitative methods can be used to further reduce the set of possible materials and match manufacturing processes to several promising candidates that provide good combinations of soft requirements. It is important to emphasize that, at this stage of selection, no quantitative method can replace engineering judgment and experience. These methods are intended only to help engineers make reasonable choices and trade-offs with confidence for a given situation and to ensure that no realistic solution is overlooked (Farag, M. 2016).

Material selection methods can be divided into two groups:

- multi-criteria decision-making (MCDM) methods and
- optimization methods. (Jahan A. et al. 2009)

Multi-Criteria Decision-Making (MCDM) methods comprise a set of techniques and approaches used to support decision-making in situations where multiple criteria or objectives must be taken into account. In many practical situations, decisions cannot be made on the basis of a single criterion because they often involve trade-offs and conflicting objectives (Frank, E. 2024).

MCDM methods have attracted considerable attention and gained popularity in various fields and industries. They are particularly applicable in situations where decisions have significant consequences, where resources are limited, and where stakeholders have different and often conflicting objectives. By incorporating multiple criteria, MCDM methods help decision-makers consider a broader range of factors and make more informed and balanced decisions (Frank, E. 2024).

Multi-criteria decision-making is one of the most accurate approaches to decision-making and may be regarded as a major advancement in this field. It considers various qualitative and quantitative criteria that must be established in order to identify the best solution. For example, cost or price and the quality of products and processes are

among the most common criteria in many decision-making problems. In addition, expert groups assign different weights to the criteria in such problems, based on the importance of each criterion in a particular case (Taherdoost H. et al. 2023).

MCDM methods are divided into three main groups:

- Multiple Attribute Decision-Making (MADM) approaches,
- fuzzy multi-criteria decision-making methods, and
- Multiple Objective Decision-Making (MODM) approaches (Jahan A. et al. 2009).

Multiple Attribute Decision-Making approaches

In contemporary research, material performance is evaluated on the basis of multiple criteria. Selecting the optimal material for an engineering design or manufacturing process from two or more alternative materials on the basis of two or more criteria is a Multiple Attribute Decision-Making (MADM) problem. Decision variables may be quantitative or qualitative. Some criteria can be expressed numerically, such as density or thermal conductivity; some can be expressed as Boolean values (for example, recyclability). In addition, some criteria can only be expressed as a rank (for example, corrosion resistance – poor, good), while others can only be represented by text and images (Jahan A. et al. 2009).

Some of the best-known MADM methods are:

- DLM – Digital Logic Method;
- SAW – Simple Additive Weighting Method;
- AHP – Analytic Hierarchy Process;
- ANP – Analytic Network Process;
- TOPSIS – Technique for Order Preference by Similarity to Ideal Solution;
- ELECTRE – Elimination and Choice Expressing the Reality;
- PROMETHEE – Preference Ranking Organization Method for Enrichment Evaluations;
- VIKOR – Multi-Criteria Optimization and Compromise Solution. (Farag, M. 2016; Jahan, A. et al. 2009; Štirbanović, Z. et al. 2023).

DLM – Digital Logic Method

Before explaining the Digital Logic Method, it is necessary to briefly describe the Weighted Property Method (WPM). The Weighted Property Method is very useful when there are many important requirements (properties) to compare and evaluate. Each material requirement or property is assigned a certain weight depending on its importance to product performance. Numerical values of property β are multiplied by the weighting factor or index α. The sum of the products of the numerical property values and weighting factors represents the performance index γ. The combination of the base material and the corresponding manufacturing process with the highest performance index represents the optimal solution (Farag, M. 2016; Talur, S. 2015).

$$\gamma = \sum(\beta * \alpha) \tag{1}$$

γ – performance index
β – numerical value of the property
α – weighting factor

The weighting factor α represents the relative priorities assigned to material properties. The value of each weighting factor should be assigned according to its importance in the product. (Talur, S. 2015.)

When numerous material properties are specified and the relative importance of a property is not clear, determining the weighting factor may be largely intuitive, which reduces the reliability of the selection. Digital logic can be used as a systematic tool for determining weighting factors. To determine the relative importance of each property or objective, a table is constructed. The properties or objectives are listed in the left-hand column, while comparisons are made in the columns to the right, as shown in Table 1. The table presents the simultaneous evaluation of only two properties at a time (Farag, M. 2016).

When comparing two properties, the more important property is assigned the numerical value one (1), and the less important property is assigned zero (0). The total number of possible decisions is determined by the expression:

$$N = n(n-1)/2 \tag{2}$$

n – number of properties or objectives under consideration

The weighting factor is obtained by dividing the number of positive decisions for each property (m) by the total number of possible decisions (N). In this case (Table 1), Σα = 1.

Table 1 Determination of the relative importance of properties (objectives) using the Digital Logic Method (Farag, M. 2016)

Property (objective)	**Number of possible decisions $N = n(n-1)/2$**										**Positive decisions**	**Weighting factor α**
	1	2	3	4	5	6	7	8	9	10		
1	1	1	0	1							3	0,3
2	0				1	0	1				2	0,2
3		0			0			1	0		1	0,1
4			1			1		0		0	2	0,2
5				0			0		1	1	2	0,2
Total number of positive decisions											10	Σα=1

To increase the accuracy of decisions based on the Digital Logic Method, the evaluation can be modified by assigning grading scores ranging from 1 (no difference in importance) to 3 (large difference in importance). In this case, the total grading scores for each selection criterion are obtained by summing the individual grading scores. The weighting factors are then determined by dividing these totals by their overall sum (Farag, M. 2016).

EXPERIMENTAL INVESTIGATION

Friction materials are marketed under various commercial names, with only some characteristics stated, which can serve as a basic orientation for selection or preliminary decision-making by vehicle manufacturers. Therefore, the final selection of a friction material for a particular brake, vehicle, and expected braking-system operating regimes is based on subsequent detailed analyses and, above all, on experiments covering all relevant requirements.

It should be taken into account that, for each friction material, its composition and manufacturing technology are proprietary information of the manufacturer, so assessments or selection decisions cannot be based on composition alone. However, in many cases, confidentiality regarding friction-material composition is not of key importance because materials with the same basic composition but produced using different technologies can exhibit quite different characteristics, especially under certain operating conditions (Todorović, J. 1988).

This section presents an experiment for selecting materials for friction components of a brake mechanism using the Digital Logic Method.

The friction materials used in the experiment were taken from scientific papers in which researchers experimentally investigated mechanical, physical, and tribological properties using a large number of formulations created by adding different constituents and varying their amounts. The aim was to meet the required braking performance while complying with environmental regulations, i.e., replacing materials that adversely affect human health and the environment. Fourteen materials were adopted for the experiment, and their mechanical, physical, and tribological characteristics are presented in Table 2.

All the presented characteristics of the materials listed in Table 1 represent criteria that will be used for selection.

Therefore, the criteria are as follows:

K1 – hardness
K2 – thermal conductivity
K3 – density
K4 – coefficient of friction
K5 – coefficient of friction stability
K6 – wear rate
K7 – environmental acceptability
K8 – stability under different environmental conditions
K9 – thermal shock resistance
K10 – flame resistance

Table 3 presents all alternatives with the defined criteria.

The Digital Logic Method (Limit Value Method) will be applied to evaluate and select materials on the basis of the defined criteria and their limit values. Starting from the requirements imposed on friction materials for braking systems, a limit or target value was defined for each criterion. Depending on the nature of the criterion, the desirable property may be expressed by a lower limit value, an upper limit value, or a target value toward which the selection should be directed. The alternatives are evaluated on the basis of the limits defined in this way.

Ten previously defined criteria will be considered in the material selection process. Table 4 presents the classification of the criteria according to the type of limit value.

Table 2 Selected materials and their characteristics

Materials / Characteristics/ criteria	M1 (Patil, R.S. et al. 2020)	M2 (Ige, O. E. et al. 2019)	M3 (Ige, O. E. et al. 2019)	M4 (Nwankwo, E. I. et. al. 2025)	M5 (Jadhav Sachin, S. P. et. al. 2023)	M6 (Kumar, M. et. al. 2010)	M7 (Kumar, M. et. al. 2010)]	M8 (Kumar, M. et. al. 2010)	M9 (Kumar, M. et. al. 2010)	M10 (Adeyemi I. O. et. al. 2016)	M11 (Adekunle A. et. al. 2023)	M12 (Kolluri D. et. al. 2009)	M13 (Kumar M. et. al. 2013)	M14 (Kumar M. et. al. 2011)
Hardness [HV]	162	10.3	13.03	241	180	20	28	22	21	12.27	70	30	25	23
Thermal conductivity [W/mK]	0.429	0.539	0.312	0.126	0.65	2.17	2.51	3.75	1.98	0.239	5.261	2.1	2.3	2.41
Density [g/cm^3]	1.71	1.89	0.85	1.5	1.74	2.2	2.26	2.27	2.09	1.01	0.962	1.153	2.28	2.31
Coefficient of friction	0.28	0.35	0.39	0.40	0.38	0.4	0.43	0.44	0.57	0.32	0.35	0.35	0.41	0.41
Coefficient of friction stability [%]	94.8	71.43	92.21	77.8	33.8	86.1	78	92.3	77	96.3	87.5	92.3	93.5	92.5
Wear rate [mg/m]	7.77	3.8	2.146	4.4	0.0012	0.098	0.222	0.178	0.085	3.934	1.424	0.334	0.183	0.154
Environmental acceptability [scale 1-5]	4	1	5	5	5	3	3	3	4	5	4	3	2	2
Stability under different environmental conditions [scale 1-5]	4	4	3	3	4	4	4	4	3	4	4	4	4	4
Thermal shock resistance [scale 1-5]	4	4	4	3	4	4	4	5	3	3	4	4	4	4
Flame resistance [%]	21.4	100	46	44	75	75	60	80	70	35	70	85	80	80

Table 3 Alternatives and defined criteria

Alternatives / Criteria	M1	M2	M3	M4	M5	M6	M7	M8	M9	M10	M11	M12	M13	M14
K1	162	10.3	13.03	241	180	20	28	22	21	12.27	70	30	25	23
K2	0.429	0.539	0.312	0.126	0.65	2.17	2.51	3.75	1.98	0.239	5.261	2.1	2.3	2.41
K3	1.71	1.89	0.85	1.5	1.74	2.2	2.26	2.27	2.09	1.01	0.962	1.153	2.28	2.31
K4	0.28	0.35	0.39	0.40	0.38	0.4	0.43	0.44	0.57	0.32	0.35	0.35	0.41	0.41
K5	94.8	71.43	92.21	77.8	33.8	86.1	78	92.3	77	96.3	87.5	92.3	93.5	92.5
K6	7.77	3.8	2.146	4.4	0.0012	0.098	0.222	0.178	0.085	3.934	1.424	0.334	0.183	0.154
K7	4	1	5	5	5	3	3	3	4	5	4	3	2	2
K8	4	4	3	3	4	4	4	4	3	4	4	4	4	4
K9	4	4	4	3	4	4	4	5	3	3	4	4	4	4
K10	21.4	100	46	44	75	75	60	80	70	35	70	85	80	80

Table 4 Classification of criteria according to the type of limit value

Designation	Criterion	Type of limit value
K1	Hardness	Target value
K2	Thermal conductivity	Lower limit value
K3	Density	Upper limit value
K4	Coefficient of friction	Target value
K5	Coefficient of friction stability	Lower limit value
K6	Wear rate	Upper limit value
K7	Environmental acceptability	Lower limit value
K8	Stability under different environmental conditions	Lower limit value
K9	Thermal shock resistance	Lower limit value
K10	Flame resistance	Lower limit value

The rationale for each type of limit value used to define the criteria is given below.

K1 – hardness – target value – excessive hardness may increase wear of the brake-disc surface, whereas insufficient hardness may lead to increased wear of the friction material itself. Therefore, an appropriate, i.e., target, value is sought.
K2 – thermal conductivity – lower limit value – higher thermal conductivity enables more efficient dissipation of the heat generated during braking and contributes to reducing local heating of the friction material.
K3 – density – upper limit value – lower density contributes to reducing the mass of the friction components. Therefore, an upper density limit is set, assuming that the other functional properties remain satisfactory.
K4 – coefficient of friction – target value – efficient and stable braking requires an appropriate coefficient of friction. An unlimited increase in its value is not necessarily favourable; therefore, a target value is defined.

K5 – coefficient of friction stability – lower limit value – a stable coefficient of friction provides more uniform and predictable braking behaviour. Therefore, higher stability values are more favourable.
K6 – wear rate – upper limit value – a lower wear rate indicates greater resistance of the material to mass loss and a longer service life of the friction component.
K7 – environmental acceptability – lower limit value – greater environmental acceptability is a more favourable property because it reduces the negative environmental impact of the material during production, use, and disposal.
K8 – stability under different environmental conditions – lower limit value – the friction material should retain satisfactory properties under changes in temperature, humidity, and other environmental conditions. Accordingly, higher stability is more favourable.
K9 – thermal shock resistance – lower limit value – greater resistance reduces the possibility of material degradation and damage caused by sudden temperature changes, which is important during intensive braking.
K10 – flame resistance – lower limit value – greater flame resistance reduces the material's tendency to ignite and sustain combustion at elevated temperatures, thereby contributing to the safety and thermal stability of the friction component.

The specific limit values for each criterion must now be determined. These criterion limit values will be used to eliminate unfavourable alternatives. Table 5 presents the criterion limit values.

Table 5 Criterion limit values

Criterion	Limit value
K1	≥ 20 HV
K2	≥ 0.25 W/mK
K3	≤ 2.30 g/cm^3
K4	≥ 0.30
K5	≥ 70%
K6	≤ 1.00 mg/m
K7	≥ 3
K8	≥ 3
K9	≥ 4
K10	≥ 70 %

After the limit values have been defined, the next step is to check each alternative against each criterion. If an alternative fails to satisfy the limit value of even one criterion, it is eliminated from further consideration. Table 6 presents the status of the alternatives on the basis of the limit values.

Table 6 Status of alternatives based on the limit values

Criterion / Alternative	K1	K2	K3	K4	K5	K6	K7	K8	K9	K10	Alternative status
M1	✓	✓	✓	✕	✓	✕	✓	✓	✓	✕	Does not satisfy
M2	✕	✓	✓	✓	✓	✕	✕	✓	✓	✓	Does not satisfy
M3	✕	✓	✓	✓	✓	✕	✓	✓	✓	✕	Does not satisfy
M4	✓	✕	✓	✓	✓	✕	✓	✓	✕	✕	Does not satisfy
M5	✓	✓	✓	✓	✕	✓	✓	✓	✓	✓	Does not satisfy
M6	✓	✓	✓	✓	✓	✓	✓	✓	✓	✓	**Satisfies**
M7	✓	✓	✓	✓	✓	✓	✓	✓	✓	✕	Does not satisfy
M8	✓	✓	✓	✓	✓	✓	✓	✓	✓	✓	**Satisfies**
M9	✓	✓	✓	✓	✓	✓	✓	✓	✕	✓	Does not satisfy
M10	✕	✕	✓	✓	✓	✕	✓	✓	✕	✕	Does not satisfy
M11	✓	✓	✓	✓	✓	✕	✓	✓	✓	✓	Does not satisfy
M12	✓	✓	✓	✓	✓	✓	✓	✓	✓	✓	**Satisfies**
M13	✓	✓	✓	✓	✓	✓	✕	✓	✓	✓	Does not satisfy
M14	✓	✓	✕	✓	✓	✓	✕	✓	✓	✓	Does not satisfy

All considered alternatives were checked against the defined limit values. An alternative is considered acceptable if its values satisfy the specified limit conditions for all criteria. In this way, the initial set of 14 alternatives was reduced to three acceptable alternatives: M6, M8, and M12, as shown in Table 7.

The relative importance of the individual criteria must then be determined. For this purpose, the Digital Logic Method, i.e., a criterion-comparison method, is applied, in which each criterion is compared with every other criterion. For each pair of criteria, the criterion that is more important for material selection is assigned the value one, while the less important criterion is assigned zero. Based on these comparisons, a criterion comparison matrix is formed, as shown in Table 8.

Table 7 Alternatives that passed the elimination stage

Alternatives / Criteria	M6	M8	M12
K1	20	22	30
K2	2.17	3.75	2.1
K3	2.2	2.27	1.153
K4	0.4	0.44	0.35
K5	86.1	92.3	92.3
K6	0.098	0.178	0.334
K7	3	3	3
K8	4	4	4
K9	4	5	4
K10	75	80	85

Table 8 Criterion comparison matrix

	K1	K2	K3	K4	K5	K6	K7	K8	K9	K10	Number of positive decisions P_i	Weighting factor W_i
K1	-	1	1	0	0	0	1	0	0	1	4	0.0889
K2	0	-	1	0	0	0	1	0	0	1	3	0.0667
K3	0	0	-	0	0	0	0	0	0	0	0	0.0000
K4	1	1	1	-	0	1	1	0	1	1	7	0.1556
K5	1	1	1	1	-	1	1	1	1	1	9	0.2000
K6	1	1	1	0	0	-	1	0	1	1	6	0.1333
K7	0	0	1	0	0	0	-	0	0	1	2	0.0444
K8	1	1	1	1	0	1	1	-	1	1	8	0.1778
K9	1	1	1	0	0	0	1	0	-	1	5	0.1111
K10	0	0	1	0	0	0	0	0	0	-	1	0.0222
										Total:	$\sum P_i = 45$	**1.0000**

The weighting factor of each criterion must now be determined. The criterion weighting factor represents the ratio between the number of positive decisions for the i-th criterion and the total number of positive decisions for all criteria. The values of the weighting factors for each criterion are also given in Table 8. This factor is determined using the following equation:

$$W_i = \frac{P_i}{\sum P_i} \tag{3}$$

where:

W_i – weighting factor of the i-th criterion
P_i – number of positive decisions for the i-th criterion
$\sum P_i$ – total number of positive decisions (45 in this case)

After determining the weighting factor of each criterion, the evaluation index M must be calculated for each individual material. The evaluation index M is calculated according to the expression:

$$M = \left[\sum_{i=1}^{n_d} B_i \frac{Y_i}{X_i}\right]_d * \left[\sum_{j=1}^{n_g} B_j \frac{X_j}{Y_j}\right]_g * \left[\sum_{k=1}^{n_c} B_k \left|\left(\frac{Y_k}{X_k}\right) - 1\right|\right]_c \rightarrow min. \tag{4}$$

where:

d, g, and c refer to the lower, upper, and target values of the property under consideration;
n_d, n_g, n_c,... – denote the numbers of lower, upper, and target property values;
B_i, B_j, B_k,... – are the importance factors for the lower, upper, and target property values;
X_i, X_j, X_k,... – *are the lower, upper, and target values of the material properties under consideration;*
Y_i, Y_j, Y_k,... – *are the specific lower, upper, and target property values* (Filetin, T. 2006).

Table 9 summarizes all input data required to determine the evaluation index. The importance factor B is the same as the weighting factor Wi calculated by the Digital Logic Method.

Based on these input data, as well as the previously defined limit and target criterion values, the contribution of individual criteria is calculated for all three remaining alternatives. Depending on the criterion type, the

corresponding equation is applied to calculate the lower-limit, upper-limit, and target-value components. These are, in fact, the elements of the main equation for calculating the evaluation index (Equation 4). Tables 10, 11, and 12 present the obtained calculation results for all three alternatives.

Table 9 Input data for calculating the evaluation index M

Criterion	Criterion type	Limit value X	Importance factor B	M6	M8	M12
K1	Target	20	0.0889	20	22	30
K2	Lower limit	0.25	0.0667	2.17	3.75	2.1
K3	Upper limit	2.3	0	2.2	2.27	1.153
K4	Target	0.3	0.1556	0.4	0.44	0.35
K5	Lower limit	70	0.2	86.1	92.3	92.3
K6	Upper limit	1	0.1333	0.098	0.178	0.334
K7	Lower limit	3	0.0444	3	3	3
K8	Lower limit	3	0.1778	4	4	4
K9	Lower limit	4	0.1111	4	5	4
K10	Lower limit	70	0.0222	75	80	85

Table 9 Calculation results for the lower-limit, upper-limit, and target-value components of alternative M6

Criterion	Lower limit value	Upper limit value	Target value
K1	0	0	0
K2	0.579	0	0
K3	0	0	0
K4	0	0	0.039
K5	0.246	0	0
K6	0	0.013	0
K7	0.044	0	0
K8	0.237	0	0
K9	0.111	0	0
K10	0.024	0	0
Total:	**1.241**	**0.013**	**0.039**

Table 10 Calculation results for the lower-limit, upper-limit, and target-value components of alternative M8

Criterion	Lower limit value	Upper limit value	Target value
K1	0	0	0.008
K2	1.001	0	0
K3	0	0	0
K4	0	0	0.050
K5	0.264	0	0
K6	0	0.749	0
K7	0.044	0	0
K8	0.237	0	0
K9	0.139	0	0
K10	0.025	0	0
Total:	**1.710**	**0.749**	**0.058**

Table 11 Calculation results for the lower-limit, upper-limit, and target-value components of alternative M12

Criterion	Lower limit value	Upper limit value	Target value
K1	0	0	0.030
K2	0.560	0	0
K3	0	0	0
K4	0	0	0.022
K5	0.264	0	0
K6	0	0.399	0
K7	0.044	0	0
K8	0.237	0	0
K9	0.111	0	0
K10	0.027	0	0
Total:	**1.244**	**0.399**	**0.052**

Finally, the final values of the evaluation index for the alternatives are calculated as:

MM6 = 1.241*0.013*0.039 = 0.001
MM8 = 1.710*0.749*0.058 = 0.074
MM12 = 1.244*0.399*0.052 = 0.026

Since the objective for the evaluation index is minimization, as can be seen from Equation 4, the alternative with the lowest value is the most favourable. Table 12 presents the final ranking of the three alternatives.

Table 12 *Final ranking of alternatives using the Limit Value Method*

Alternative	Evaluation index M	Rank
M6	0.001	1
M12	0.026	2
M8	0.074	3

CONCLUSION

Proper material selection is one of the most important steps in the design and development process of any product because it directly determines its functional characteristics: reliability, service life, safety, cost-effectiveness, and manufacturability. No material has ideal properties for all operating conditions; therefore, material selection is always the result of a compromise between different and often conflicting requirements. With the development of new materials and the increasing number of available alternatives, the selection process becomes considerably more complex and requires the application of systematic and objective decision-making methods that enable the simultaneous consideration of multiple criteria.

This paper addressed friction materials. Proper selection of friction materials is of great importance in braking systems because their characteristics affect braking efficiency and the safety of road users. Friction materials must provide a stable coefficient of friction over a wide range of operating temperatures and loads, high wear resistance, adequate heat-dissipation capability, etc. Changes in formulation composition can significantly influence the tribological behaviour of the material; therefore, it is necessary to identify an optimal combination that satisfies the requirements of real operating conditions.

Using the Digital Logic Method, 14 friction materials were evaluated according to ten defined criteria. First, alternatives that did not satisfy the minimum requirements were eliminated using the limit values, reducing the initial set of 14 materials to three acceptable alternatives: M6, M8, and M12. In this way, an initial screening was performed for materials that simultaneously satisfy the specified requirements in terms of mechanical, physical, thermal, tribological, and environmental characteristics. The relative importance of the criteria was then determined using the Digital Logic Method. Final evaluation of the remaining alternatives produced a ranking in which M6 was placed first, M12 second, and M8 third. According to the Digital Logic Method, M6 is the most favorable alternative, indicating that this material provides the best compromise among all the criteria considered.

The obtained result should be interpreted within the framework of the adopted criteria, their limit values, and weighting factors. Future research should focus on sensitivity analysis of the obtained ranking with respect to changes in weighting factors and limit values, as well as on experimental verification of the highest-ranked alternatives under identical test conditions.

ACKNOWLEDGMENTS

This work was supported by the Ministry of Science, Technological Development and Innovation of the Republic of Serbia (Contract No. 451-03-34/2026-03/200325).

REFERENCES

Adekunle A., Okunlola M., Omoniyi P., Adeleke A., Ikubanni P., Popoola T., & Ibrahim H. (2023). Development and analysis of friction material for eco-friendly brake pad using seasheel composite. *Scientia Iranica*, 30, 1562-1571. https://doi.org/10.24200/sci.2022.59835.6454

Adeyemi I. O., Ademoh N. A., & Okwu M. O. (2016). Development and Assessmwnt of Composite Brake Pad Using Pulverized Cocoa Beans Shells Filler. *International Journal of Materials Science and Applications*, 5, 66-78. https://doi.org/10.11648/j.ijmsa.20160502.16

Akebono. (n.d.) Akebono. Retrieved February 27, 2026. from https://www.akebono-brake.com/

Aleksendrić, D. (n.d.). Kočni sistemi, Mašinski fakultet, Univerziteta u Beogradu.

Atlantic Tire Service. (n.d.) Atlantic Tire Service. Retrieved February 19, 2026. from https://www.atlantictireonline.com/

Cai P., Wang Y., Wang T., & Wang Q. (2025). Effect of resins on thermal, mechanical and tribological properties of friction materials. *Tribology International*, 87, 1-10. https://doi.org/10.1016/j.triboint.2015.02.007

Farag M. M. (2016) *Materials and process selection for engineering design – third edition*, International Standard Book Number-13: 978-1-4665-6410-7.

Filetin T. (2006). *Izbor materijala pri razvoju proizvoda*, Fakultet strojarstva i brodogradnje, Zagreb. ISBN 978-953-6313-84-6.

Frank E. (2024). Overview of Multi-Criteria Decision-Making (MCDM) Methods. *EasyChair Preprint*, 13272. https://easychair.org/publications/preprint/hhpb

Gehlen S.G., Valentini F., Nogueira P.A., Masciocchi R., Barbieri A., & Straffelini G. (2026). Addition of Al anodizing waste in a commercial friction material in an industrial symbiosis perspective. *Wear*, 589, 206553. https://doi.org/10.1016/j.wear.2026.206553

howstuffworks. (n.d.) howstuffworks. Retrieved February 25, 2026. from https://auto.howstuffworks.com/auto-parts/brakes/

Ige O. E., Inambao F. L., & Adewumi G. A. (2019). Biomass-based composites for brake pads: A review. *International Journal of Mechanical Engineering and Technology*, 10, 920-943.

Jadhav S. S. P., Sawant S. S. H., & Bhosale D. D. G. (2023). Characterization of newly developed asbestos and copper-free low metallic friction material for automotive brake pad application. Research Square, https://doi.org/10.21203/rs.3.rs-2657149/v1

Jahan A., Ismail Y.M., Sapuan M.S., & Mustapha F. (2010). Material screening and choosing methods – A review. *Materials & Design*, 31, 696-705. https://doi.org/10.1016/j.matdes.2009.08.013

Kolluri D., Ghosh A. K., & Bijwe J. (2009) Analysis of load-speed sensitivity of friction composites based on various synthetic graphites. *Wear*, 266, 266-274. https://doi.org/10.1016/j.wear.2008.06.023

Kumar M., & Bijwe J. (2010). Role of different metallic fillers in non-asbestos organic (NAO) friction composites for controlling sensitivity of coefficient of friction to load and speed. *Tribology International*, 43(5-6), 965-974. https://doi.org/10.1016/j.triboint.2009.12.062

Kumar M., & Bijwe J. (2011). Non-asbestos organic (NAO) friction composites: Role of copper; its shape and amount. *Wear*, 270, 269-280. https://doi.org/10.1016/j.wear.2010.10.068

Kumar M., & Bijwe J. (2013). Optimized selection of metallic for best combination performance properties of friction materials: A comprehensive study. *Wear*, 303(1-2), 569-583. https://doi.org/10.1016/j.wear.2013.03.053

Kwikfit. (n.d.) Kwikfit. Retrieved February 27, 2026. from https://www.kwik-fit.com/brakes/

Medium. (n.d.) Medium. Retreived February 19, 2026 from https://medium.com/@margamgirish/

Nwankwo E. I., Onyenanu I. U., Nwobi-Okoye C. C., & Ezechukwu V. C. (2025). Agro-waste reinforced brake pads: a systematic review of environmental and economic benefits. *American Journal of Advanced Materials Research*, 1, 27-36. https://doi.org/10.54536/ajamr.v1i1.4903

Patil R.S., Miraje A.A., & Waghmode S.B. (2020). Development, production and testing of brake pads from pistachio shell composite. *International Journal of Engineering Sciences & Research Technology*, 9(1), 13-25. https://doi.org/10.5281/zenodo.3609538

Petar P. (2025) Petar Petar. Retrieved March 30, 2026. from https://www.scribd.com/document/815402513/

Petković Lj. D. (2016). *Izbor biomaterijala – Višekriterijumska analiza i razvoj sistema za podršku odlučivanju*, [Doctoral dissertation]. Univerzitet u Nišu, Mašinski fakultet, Niš.

Polovni automobili. (n.d.) Polovni automobili. Retreived February 25, 2026. from https://www.polovniautomobili.com/

Popravka automobila. (n.d.) Popravka automobila. Retrieved February 19, 2026. from https://www.deloviautomobila.rs/auto-delovi/uredaji-za-zaustavljanje-kocenje/

Štirbanović Z., Stanujkić D., Sokolović J., & Ilić I. (2023). Application of multi-criteria decision-making methods in mineral processing – a review. *Materials Proceedings*, 15(1), 32. https://doi.org/10.3390/materproc2023015032

Taherdoost H., & Madanchian M. (2023). Multi-Criteria Decision Making (MCDM) Methods and Concepts. *Encyclopedia*, 3(1), 77-87. https://doi.org/10.3390/encyclopedia3010006

Talegaonkar P.R., Gopinath K. (2005). Asbestos based brake friction material: Pros and Cons. Department of Mechanical Engineering, Indian Institute of Technology Madras, Chennai, India.

Talur S., Kumar P.K., & Madhusudhan T. (2015). Selection of material by weighted property method for savonius vertical axis wind turbine rotor blade. *International Research Journal of Engineering and Technology*, 2(1), 439-443.

Todorović J. (1988). *Kočenje motornih vozila*. Zavod za udžbenike i nastavna sredstva – Beograd.

TOKAI CARBON. (n.d.) TOKAI CARBON. Retrieved June 17, 2026. from https://www.tokaicarbon.co/
Wuling motors. (n.d.) Wuling motors. Retrieved February 27, 2026. from https://wuling.id/en/blog/autotips/

The 11th International Congress
Motor Vehicles & Motors 2026
Kragujevac, Serbia
October 8th-9th, 2026

Motor Vehicles & Motors

MVM2026-032
https://doi.org/10.24874/CMVM2026.032
Original scientific paper

Zoran Papić[1]
Nenad Saulić[2]
Milja Simeunović[3]

PREDICTION OF EES VALUES IN VEHICLE IMPACTS USING AI

ABSTRACT: The energy equivalent speed (EES) is an important parameter for determining vehicle impact speed. It represents the portion of a vehicle's speed dissipated through deformation work during a collision. While this value can be calculated, determining it requires data on the depth of vehicle deformation across the entire width of the damaged area. This information is most often documented through photographs. Consequently, in traffic accident analysis, the EES value is usually estimated subjectively by experts through a comparison of photographs taken during or after the accident with reference images from electronic EES catalogues. The application of information technology (IT) in traffic accident analysis has enabled the use of artificial intelligence (AI) to predict EES values based on the correspondence between the observed damage to the vehicle under analysis and the damage documented for similar vehicles in EES catalogues. This paper presents an analysis of the capabilities and reliability of AI-based tools for estimating EES values for vehicles using tools integrated into the PC-Crash software environment based on convolutional neural networks (CNNs).

KEYWORDS: Energy Equivalent Speed, (EES), artificial intelligence (AI), convolutional neural networks (CNN), PC-Crash, estimation

PREDIKCIJA EES VREDNOSTI U SUDARIMA VOZILA PRIMENOM VEŠTAČKE INTELIGENCIJE

REZIME: Energija ekvivalentne brzine (EES), koja se tokom sudara utroši na rad deformacije, predstavlja važan parametar za određivanje udarne brzine vozila. Ova vrednost se može izračunati, ali njeno određivanje zahteva podatke o dubini deformacije vozila duž cele širine oštećenog područja, koji su najčešće dokumentovani samo fotografijama. Zbog toga se u analizi saobraćajnih nezgoda vrednost EES-a obično procenjuje subjektivno od strane veštaka, na osnovu poređenja fotografija snimljenih tokom ili nakon saobraćajne nezgode sa referentnim slikama iz elektronskih EES kataloga. Primena informacionih tehnologija (IT) u analizi saobraćajnih nezgoda omogućila je primenu veštačke inteligencije (AI) za predviđanje vrednosti EES-a na osnovu podudarnosti između

[1] *Zoran Papić, University of Novi Sad, Faculty of technical sciences, Department for traffic, Dositej Obradović Sq. 6, 21000 Novi Sad, z.papic@uns.ac.rs, https://orcid.org/0000-0003-1264-0913*
[2] *Nenad Saulić, University of Novi Sad, Faculty of technical sciences, Department for traffic, Dositej Obradović Sq. 6, 21000 Novi Sad, nenadsaulic@gmail.com, https://orcid.org/0000-0002-1151-6737*
[3] *Milja Simeunović, University of Novi Sad, Faculty of technical sciences, Department for traffic, Dositej Obradović Sq. 6, 21000 Novi Sad, mlekovic@uns.ac.rs, https://orcid.org/0000-0001-9650-2635*

oštećenja uočenih na vozilu koje je predmet analize i oštećenja dokumentovanih na sličnim vozilima u EES katalozima. U ovom radu predstavljena je analiza mogućnosti i pouzdanosti alata zasnovanih na veštačkoj inteligenciji za procenu vrednosti EES-a na vozilima, korišćenjem alata integrisanih u softversko okruženje PC-Crash, koji se zasnivaju na konvolucionim neuronskim mrežama (CNN).

KLJUČNE REČI: Ekvivalent brzine izgubljene na deformacioni rad (EES), veštačka inteligencija (AI), konvolucione neuronske mreže (CNN), PC Crash, procena

INTRODUCTION

Vehicle collisions are the most common type of road traffic accident. One of the most complex problems in the investigation of traffic accidents is determining the directions of vehicle movement and their speeds at the moment of the collision. Methods for determining collision speeds are based on fundamental physical laws, primarily the laws of conservation of linear momentum and energy.

The energy method assumes that the total kinetic energy of the vehicles at the moment of collision is equal to the sum of the energy dissipated during and after the collision. This includes the energy absorbed through vehicle deformation, the remaining kinetic energy and the energy dissipated in the form of vibrations, sound and heat. An approach to establish a relationship between crash speed and the extent of vehicle deformation resulting from an impact with a stationary, non-deformable obstacle was developed based on the results of crash tests that began to be conducted extensively in the USA during the second half of the 1960s. Increasing attention to vehicle passive safety, particularly following criticism of the safety of vehicles of that period by the American lawyer and journalist Nader (1968), contributed to the development of this approach. Mackay (1968) formalised this concept by introducing the term 'Equivalent Barrier Speed' (EBS), which enables the comparison of vehicle damage observed in real-world traffic accidents with damage produced under controlled crash-test conditions. Based on the analysis of crash tests, it was determined that most of the vehicle's kinetic energy at the moment of impact is dissipated through plastic deformation, that is, through deformation work, while the remaining portion of the energy is associated with the motion of the vehicle during the post-collision phase. The kinetic energy of the vehicle immediately after the collision, at the beginning of the restitution phase, depends on its structural characteristics and, consequently, on the elasticity of the collision, which is characterized by the coefficient of restitution, k. The coefficient of restitution is defined as the ratio of the relative velocity of the vehicles after the collision, at the end of the restitution phase, to their relative velocity at the moment of impact.

$$k = \frac{V_2' - V_1'}{V_1 - V_2} \tag{1}$$

where:

V_1, V_2 – vehicle impact speeds;
$V_{1'}$, $V_{2'}$ - vehicle speeds at the and of the restitution phase.

Research has shown that, in real-world traffic accidents, the coefficient of restitution typically ranges from 0.05 to 0.3, with higher values corresponding to more elastic collisions.

In order to establish a relationship between the equivalent speed corresponding to the energy dissipated through vehicle deformation during an impact with a non-deformable obstacle (EBS) and real-world collisions involving two vehicles, Burg & Zeidler (1980) introduced the concept of EES (Energy Equivalent Speed). According to the ISO/DIS 12353-1:1996 standard, EES is defined as the speed at which a vehicle would have to collide with a stationary, non-deformable obstacle to absorb an amount of deformation energy equivalent to that associated with the damage observed on the vehicle.

$$EES = EBS \cdot \sqrt{1 - k^2} \tag{2}$$

The EES value of a vehicle involved in a collision can be calculated with varying degrees of simplification; however, such a calculation requires data on the depth and shape of the vehicle deformations, the vehicle stiffness coefficient, vehicle mass, and other relevant parameters. In practice, however, vehicle deformations resulting from traffic accidents are often not adequately documented, and measurements of the deformed areas that could be used to calculate the EES value are therefore unavailable. Consequently, the calculation of vehicle impact speeds using the energy method relies to a large extent on the expert's visual assessment of the EES value based on the observed vehicle damage.

To investigate the reliability of EES estimates based on damage visible in photographs, Papić et al. (2022) asked 23 experts in traffic accident analysis to estimate the EES values for eight damaged vehicles. The results showed

that the accuracy of the estimates depended largely on the magnitude of the vehicle impact speed. For the lower EES values (10 and 20 km/h), the estimates did not differ statistically significantly from the actual EES values. This result was expected, given the relatively low severity of the vehicle damage. In contrast, a statistically significant difference between the actual and estimated EES values was found for EES values in the range of 40–80 km/h. Within this range, the respondents predominantly tended to underestimate the EES values, which is consistent with the findings reported by Spek (2017).

The PC-Crash software package includes the DSD Recon Data database, an electronic catalog that provides EES values based on expert assessments by specialists in the field of vehicle collisions. The catalog classifies vehicles according to make, type, model, year of manufacture, mass, and location of damage, and provides expert estimates of the vehicle speed lost through deformation during a collision.

The reliability of the estimated EES values in this database is indicated by circular symbols displayed in green, yellow, or red. A green symbol indicates that the estimated EES value can be considered reliable evidence when determining the vehicle's collision speed. A yellow symbol indicates that the estimated value may be considered sufficiently reliable, but should be verified using additional parameters, such as the depth of vehicle deformation, the vehicle stiffness coefficient, and other relevant data. According to Goertz (2018), a red symbol indicates a wide range of estimated EES values and, consequently, that the value should not be considered fully reliable when determining the collision speed in a traffic accident reconstruction.

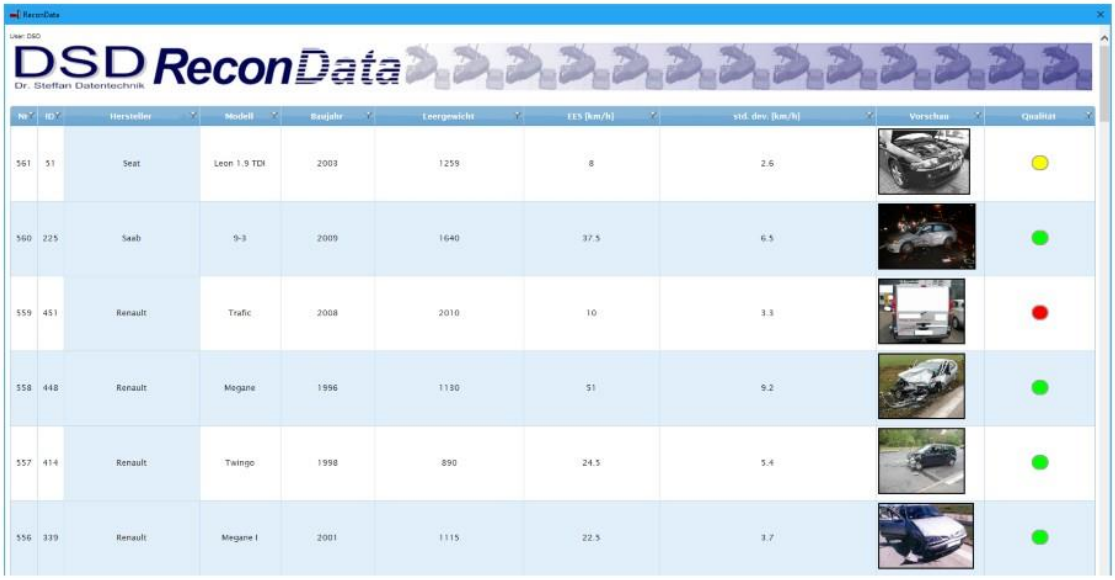

Nr	ID	Hersteller	Modell	Baujahr	Leergewicht	EES [km/h]	std. dev. [km/h]	Vorschau	Qualität
561	51	Seat	Leon 1.9 TDI	2003	1259	8	2.6		
560	225	Saab	9-3	2009	1640	37.5	6.5		
559	451	Renault	Trafic	2008	2010	10	3.3		
558	448	Renault	Megane	1996	1130	51	9.2		
557	414	Renault	Twingo	1998	890	24.5	5.4		
556	339	Renault	Megane I	2001	1115	22.5	3.7		

Figure 1 EES value database in the PC-Crash software package

	Fahrzeug 1	Fahrzeug 2	Fahrzeug 3
Hersteller:	Audi	Hyundai	
Modell:	A6 Avant TDI	Getz 1.4	
Baujahr:	2008-01-01	2008-01-01	
Leergewicht [kg]:	1825	1100	
ID:	721097	721098	0

Fragestellung:
EES

Name	EES 1	EES 2		Energieverteilung	
1	45-55	70-80	km/h	42%	58%
2	55-57	63-67	km/h	55%	45%
3	57-64	62-68	km/h	59%	41%
4	35-40	50-55	km/h	46%	54%
5	40-50	40-50	km/h	62%	38%
6	45-50	55-65	km/h	51%	49%
7	40-50	45-55	km/h	57%	43%
8	35-40	38-43	km/h	59%	41%
9	45-55	60-65	km/h	51%	49%
10	45-55	50-60	km/h	58%	42%
11	30-40	35-45	km/h	56%	44%
12	48-53	65-70	km/h	48%	52%
13	45-55	60-70	km/h	50%	50%
14	37-43	47-53	km/h	51%	49%
15	52-60	60-70	km/h	55%	45%
16	30-35	55-65	km/h	33%	67%
17	45-55	75-85	km/h	39%	61%

Min/Max	30-64	35-85	km/h
Mittelwert	46.6	58.7	km/h
Median	50	60	km/h
Standardabweichung	7.9	11.3	km/h
Def-Energie Median	176	152.8	kJ
Sigma/Median Energieverhältnis	34	41	%
Qualitätsindikator			

Figure 2 Expert assessment of the EES value for a case in the PC-Crash database

Artificial intelligence (AI) is increasingly being applied in the field of traffic accident reconstruction. One of the aspects of AI application in the analysis of traffic accidents, particularly vehicle collisions, involves estimating the equivalent speed of a vehicle dissipated through deformation work, i.e., the EES value. In the analysis of vehicle collisions, AI can be used to obtain, based on photographs taken during the accident scene investigation or after the traffic accident, as well as under controlled conditions, information on the make and type of the vehicle involved in the traffic accident, the classification and type of collision, as well as the EES value corresponding to the vehicle's deformations and damage.

FUNDAMENTALS OF *AI* AND TERMINOLOGY

The term artificial intelligence (AI) was introduced in the 1950s and can be broadly defined as the development of intelligent machines, particularly computer programs designed to solve problems that have traditionally required human intelligence and decision-making. In this context, artificial intelligence involves the use of computer-based systems to process information and perform tasks by learning from data and applying knowledge acquired through previous experience.

Machine learning (ML) is a subset of artificial intelligence that encompasses techniques enabling computers to learn from available data and derive conclusions based on:

- a database containing numerical, textual, or image-based data;
- mathematical models, expressed as functions, used to generate predictions;
- model adjustment through parameter optimization based on the detection and magnitude of prediction errors;
- model evaluation based on tests using data that were not used to develop the model.

Artificial neural networks (ANNs) are interconnected systems of nodes based on simplified models of biological neurons in the human brain. The main components of an ANN are:

- **Input parameters (inputs)** – each input represents a specific piece of information expressed as a numerical value, which may be any real number;
- **Connections (weights)** – each connection between two neurons is assigned a numerical weight that represents the strength or importance of that connection. Each neuron in a given layer receives information from the neurons in the preceding layer and passes the processed information to the next layer. As the information propagates through the network, previously hidden features of the input data are extracted and combined to generate new representations;
- **Summation function** – combines the input values and the corresponding connection weights to calculate a weighted sum, which is then used as the input to the activation function;
- **Activation function** – determines the output of a neuron based on the weighted sum of its inputs. Similar to a biological neuron, which generates a signal when a certain activation threshold is reached, an artificial neuron produces an output when the activation function is applied to the weighted sum of its inputs.

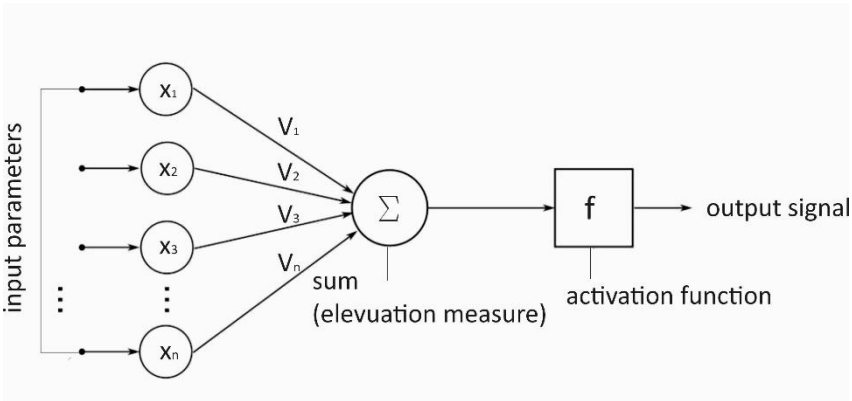

Figure 3 Architecture of an artificial neural network (ANN)

Deep learning (DL) is a subset of machine learning that uses multilayer artificial neural networks to solve complex problems by learning increasingly abstract representations from data. As the number of hidden layers increases, deep neural networks can achieve high levels of accuracy in tasks such as object detection, speech recognition, and the translation of written or spoken language. Deep learning techniques enable the automatic learning, extraction, and transformation of features from datasets, such as images, videos, and text, without the need to explicitly define rules or manually program the features used for these tasks.

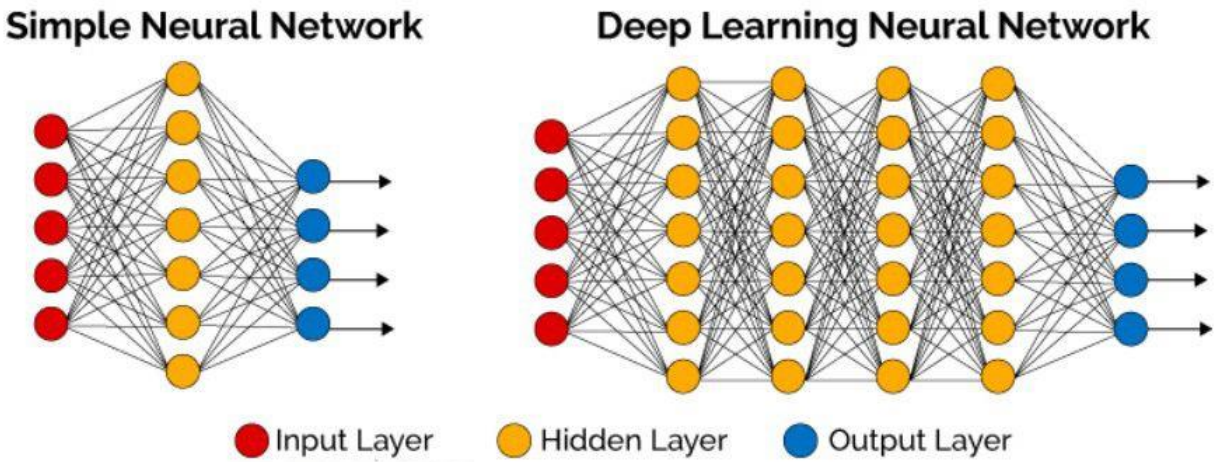

Figure 4 Difference between a simple artificial neural network (ANN) and a deep neural network (DL)

Unlike simple neural networks, which are less complex and often require greater knowledge of the relevant data features for feature selection and engineering, deep neural networks can automatically learn relevant features from raw data, eliminating the need for predefined feature selection. They can also automatically optimize model parameters during the training process.

Convolutional Neural Networks (CNNs) are deep artificial neural networks primarily used for image processing and classification. They can classify images based on their visual content, group visually similar images, and detect and recognize objects within an image. The application of CNNs has enabled their practical use in various traffic-related tasks, including vehicle recognition, traffic sign and signal recognition, and identification of the surrounding environment relevant to the analysis of a particular traffic event. More recently, CNNs have also been applied to the recognition of vehicle drivers.
In machine learning, different learning approaches are generally classified into three main categories: **supervised learning, unsupervised learning, and reinforcement learning**.

Supervised learning involves a dataset in which each example is associated with a known output label, which may be either discrete or continuous. In this approach, the learning algorithm is trained using labeled data, where the desired output is known for each input example. The model learns the relationship between the input data and the corresponding output labels and uses this relationship to make predictions for previously unseen data. Supervised learning includes techniques such as linear regression, logistic regression, and classification using decision trees.

APPLICATION OF DEEP NEURAL NETWORKS FOR VEHICLE RECOGNITION AND EES ESTIMATION

Artificial intelligence based on deep convolutional neural networks (CNNs) has enabled the application of these methods to increasingly specialized problems across various fields. In order to achieve better performance, there has been a need to develop deeper neural networks. However, in practice, it has been observed that increasing network depth beyond a certain number of layers (approximately 20–30) does not necessarily improve performance and may, in some cases, lead to performance degradation.

In order to overcome this problem, an approach based on learning residual functions was developed, in which the network does not learn the complete transformation of the input data but only the deviations (residuals) from the identity function. This concept enabled the efficient training of very deep neural networks, with more than 100 layers, resulting in more stable learning and improved accuracy of the output.

ResNet-152 is a deep neural network designed for image processing and consists of 152 layers. It was developed by Microsoft Research in 2015 and represents one of the key architectures in the development of modern artificial intelligence for computer vision. The network can be used for object recognition in images, medical diagnostics based on X-ray and MRI images, the development of autonomous vehicles, video analysis, and AI-based systems for assessing vehicle damage, among other applications. Thus, based on the previously trained ResNet-152 network using the Stanford Cars Dataset, a vehicle recognition system was first developed. According to Krause et al. (2013), the dataset contains 16,185 images covering 196 different vehicle models. Using this network, an accuracy of 88.7% was achieved in recognizing the vehicle manufacturer and model.

PC Crash EES CNN

Since the results achieved in vehicle manufacturer and model recognition met expectations, the same approach was applied to the classification of EES values in newer versions of the PC-Crash software (version 15.0 and later), as part of the integration of machine learning methods with vehicle damage databases. In this context, an AI-based tool was developed to estimate the EES value of a vehicle based on photographs of its damage. For training purposes, photographs of damaged vehicles from the DSD ReconData EES catalog developed by Moser and Steffan (2019) were used. The catalog contains approximately 4,000 photographs, with EES values ranging from 5 to 85 km/h. The best results are obtained from photographs in which the depth of the vehicle deformation is clearly visible.

As an example of the user interface used for EES-CNN analysis, photographs and data collected during the DSD workshop were used. These data were obtained as part of crash tests conducted in 2018, at a time when the results of these tests had not yet been included in the databases used for deep learning. The test involved an “OPEL ZAFIRA” passenger car, with a mass of 1395 kg, colliding with the rear of a stationary “MAN” truck, with a mass of 10754 kg, in a full-overlap collision at a speed of 70.8 km/h. Figure 5 shows the speed profile of the “OPEL ZAFIRA” during the test.

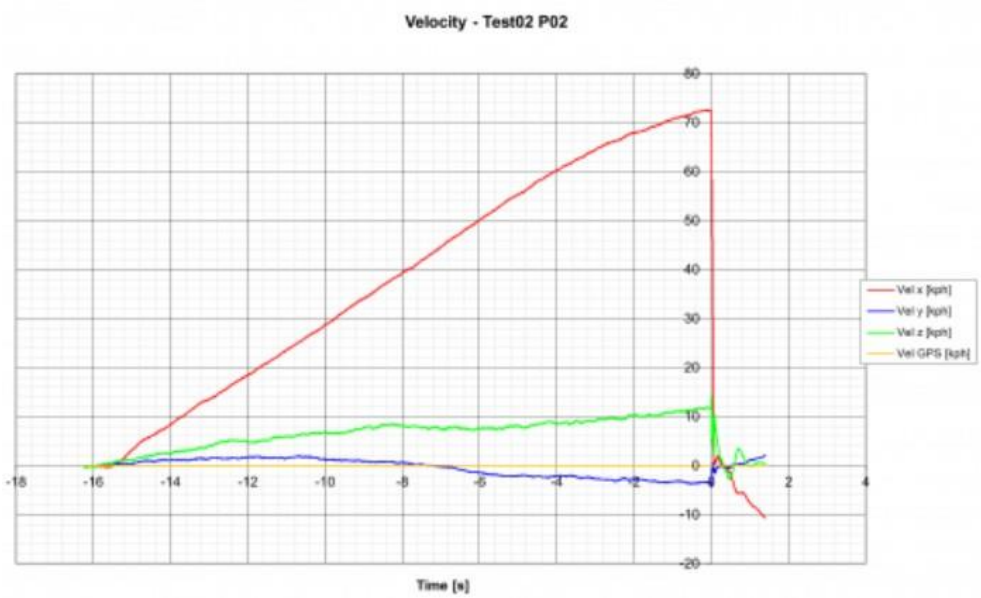

Figure 5 Speed profile of the “OPEL” passenger car during the collision with the “MAN” truck

The position of the vehicle at the moment of collision and immediately thereafter is shown in Figures 5 and 6.

Figures 6, 7 Positions of the “OPEL” passenger car and the “MAN” truck at the moment of collision and after coming to a stop

Given that the truck was displaced forward by approximately 1–1.5 m as a result of the collision, and that part of the kinetic energy of the “OPEL” passenger car at the moment of impact was also dissipated through deformation of the rear part of the truck, the EES value of the “OPEL” was lower than its impact speed and was realistically estimated to be in the range of 60–65 km/h. After the collision, the "OPEL" car was photographed in detail from several angles. The selected photographs used for the analysis of the EES-CNN values, showing the damage to the front of the vehicle, are presented in Figures 7 and 8.

Figures 8, 9 Front-end damage to the "OPEL" car following the collision with the "MAN" truck

After opening the EES-CNN user window, if the vehicle is selected for analysis in the PC-Crash program, its make and model are displayed in the upper-left corner. Below this, there is an option to import photographs showing the damage to the vehicle. For the purpose of EES analysis, multiple photographs of the vehicle damage, taken from different angles, can be uploaded. Once a photograph has been uploaded, a histogram showing the estimated EES values for that particular photograph, together with the corresponding estimation reliability, is displayed in the window on the right.

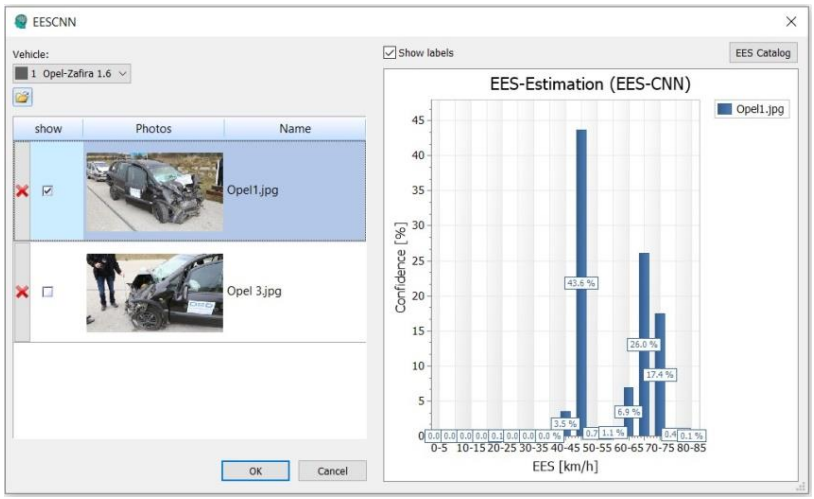

Figure 10 EES-CNN assessment of the damage to the "OPEL" car shown in Figure 7

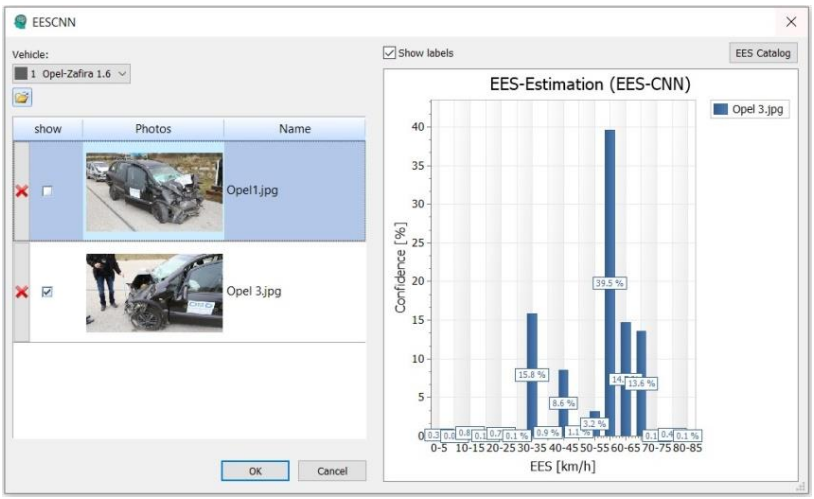

Figure 11 EES-CNN assessment of the damage to the "OPEL" car shown in Figure 8

As can be seen in Figure 9, where the damage to the "OPEL" car was recorded at a slight angle relative to the front-right corner of the vehicle, the EES interval of 45–50 km/h was identified as the most reliable estimate, with a reliability of 43.6%. If the estimated EES interval of 60–75 km/h, which encompasses the actual EES value, were considered as a whole, the reliability of the estimate would be approximately 51%.

In Figure 10, where the damage to the vehicle was recorded from the left side and the deformation depth can be observed more clearly, the EES interval of 55–60 km/h was identified as the most reliable estimate, with a reliability

of 39.5%. However, if the EES interval of 55–75 km/h, which encompasses the actual EES value, were considered as a whole, the reliability of the assessment would be approximately 68%.

RELIABILITY OF EES VALUE ESTIMATION: AI VERSUS EXPERT ASSESSMENT

According to Papić et al. (2022), a total of 23 respondents participated in the assessment of the reliability of expert EES value estimation based on photographs of vehicle damage, 22 of whom are actively engaged in traffic accident reconstruction and expert examination. The respondents were provided with questionnaires in which, among other tasks, they were asked to subjectively estimate the EES value for eight vehicles. For each vehicle, two photographs showing the damage caused in collisions under controlled conditions were provided. The photographs were selected from the Crash Test Database included in the PC-Crash software package. Photographs showing vehicle damage resulting from collisions with a stationary, non-deformable obstacle were selected for the analysis. Under such collision conditions, practically all of the vehicle's kinetic energy at the moment of impact is dissipated through deformation work, i.e.:

$$V_s \approx EBS \approx EES \tag{3}$$

Of all EES values estimated by the respondents who participated in the study, 32.6% were correctly estimated, while 67.4% were incorrectly estimated. Most of the incorrect estimates (53.8%) were lower than the actual EES values, whereas the remaining 13.6% represented an overestimation. It is important to note that an estimate was considered correct if it deviated by no more than ±5 km/h from the actual EES value.

The same photographs used in the aforementioned study were also used to analyze the reliability of EES value estimation using artificial intelligence, specifically the EES-CNN tool integrated into the PC-Crash software package. Since the reliability of the EES estimates provided by this tool is expressed as a percentage in the form of a histogram, with a certain degree of dispersion, only the 5 km/h-wide speed intervals with the highest reliability percentage were considered in the analysis.

Based on the conducted analysis, it was determined that the reliability of the EES estimates ranged from 48.5% to 99%. However, a high reliability percentage assigned by the AI system does not necessarily mean that the estimated EES value is accurate. If the same criterion used in the study of expert EES assessment is applied, namely, a deviation of ±5 km/h from the actual EES value, the following conclusions can be drawn:

- in five cases, the EES values estimated by EES-CNN were within ±5 km/h of the actual EES values;
- in one case, the estimated EES value deviated from the actual value by more than 15 km/h;
- in two cases, the estimated EES values deviated from the actual values by more than 20 km/h.

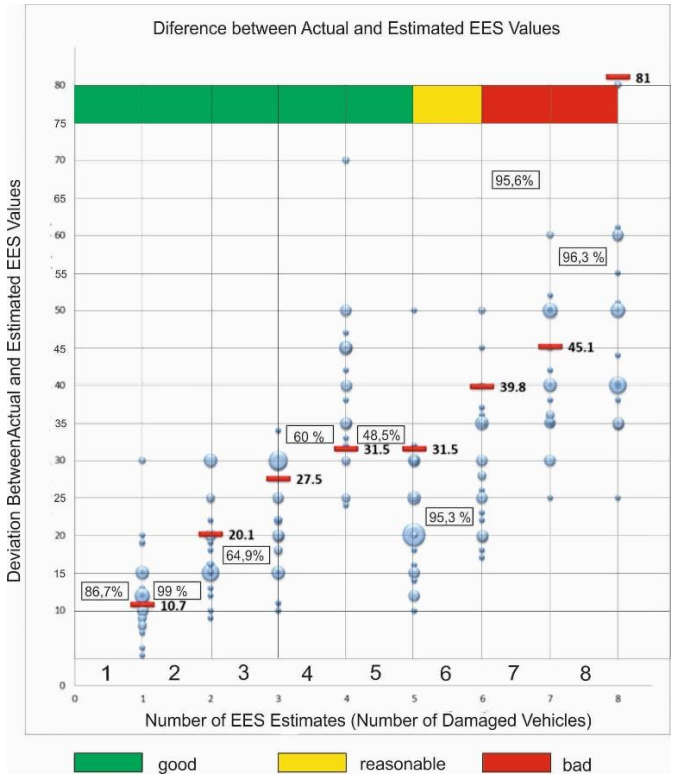

Figure 12 Comparative analysis of actual EES values, expert assessments, and EES-CNN estimates

Based on the conducted analysis, it can be concluded that AI provides greater consistency in assessments, while the expert approach enables a deeper understanding of the specific circumstances of the accident. Therefore, the optimal approach lies in combining these two methods, with AI tools serving as a rapid and objective support, while the final assessment should be based on a comprehensive expert analysis.

CONCLUSION

Based on the theoretical considerations presented and the analyses conducted, it can be concluded that EES (Energy Equivalent Speed) represents one of the key parameters in the reconstruction of traffic accidents, particularly within the framework of energy-based methods for estimating vehicle crash speeds. Although the EES value can be calculated based on physical laws and measurements of vehicle deformation, in practice, this procedure is often limited by the lack of precise data. Consequently, a significant proportion of EES assessments relies on visual evaluation by experts.

The research results show that the accuracy of expert assessments depends on the extent of vehicle damage, with assessments being more reliable for lower EES values, while higher EES values tend to be underestimated. On the other hand, the application of modern AI methods, particularly convolutional neural networks (CNNs), enables the automated analysis of vehicle damage photographs and provides more stable and consistent results with a certain degree of reliability. However, the analyzed AI-based approach also has certain limitations, primarily related to image quality, the camera angle, and the inability to directly assess internal structural damage to the vehicle. Therefore, its results should not be regarded as definitive, but rather as supplementary information within the overall accident analysis process.

The comparative analysis indicates that AI systems provide greater consistency in EES assessments, while the expert approach, despite its inherent subjectivity, enables a deeper understanding of the specific circumstances of an accident.

In this context, the optimal approach to EES estimation involves integrating artificial intelligence with expert knowledge. AI tools can be used as rapid and objective support during the initial assessment, while the final evaluation should be based on a comprehensive expert analysis, thereby improving the reliability and objectivity of the traffic accident reconstruction process. From a practical perspective in traffic accident reconstruction and forensic analysis, this combination of methods represents a realistic and applicable approach to everyday expert practice.

Considering its practical application, it can be expected that further research in the field of AI-based vehicle damage recognition and assessment will focus on expanding and diversifying training datasets, incorporating information on the geometry and depth of vehicle deformations, and integrating multimodal data sources, such as photographs, 3D images, and vehicle technical specifications. These developments could contribute to improving the accuracy and robustness of EES estimation under real-world traffic accident conditions.

ACKNOWLEDGMENTS

The results presented in this paper are part of the research conducted within the project “Researching trends in the development of sustainable transport and logistics systems”, established by the Department of Traffic Engineering, Faculty of Technical Sciences, University of Novi Sad, Republic of Serbia.

REFERENCES

Burg, H., & Zeidler, F. (1980). EES - ein Hilfsmittel zur Unfallrekonstruktion und dessen Auswirkung auf die Unfallforschung. *Der Verkehrsunfall*, 4, 75-78.

Goertz, M. (2018). *Modell zur Bestimmung von Deformationsenergien an Fahrzeugen nach Verkehrsunfaellen*, Dissertation. University of Žilina.

Krause, J., Stark, M., Deng, J., & Fei-Fei, L. (2013, 2-8 December), 3D Object Representations for Fine-Grained Categorizatio. *4th International IEEE Workshop on 3D Representation and Recognition (3dRR-13*). Sydney, Australia. https://doi.org/10.1109/ICCVW.2013.77

Mackay, M. (1968). Injury and collision severity, *SAE Technical Paper*, 680779, 3108-3113. https://doi.org/10.4271/680779

Moser, A., & Stefan, H. (2019). Artifical Inteligence (AI) in Accident Reconstruction. EVU Congress, Proceedings, Barcelona.

Nader, R. (1965). *Unsafe at any speed*. New York, Grossman.

Papić, Z., Bogdanović, V., Simeunović, M., Saulić, N., & Jović, A. (2022, 19-21 Maj). Pouzdanost procene EES vrednosti u analizi sudara vozila. *Savetovanje-Saobraćajne nezgode, Zbornik radova*, Zlatibor.

PC-Crash 15.1. (2019). A Simulation program for Vehicle Accidents 15.1 - Operating Manual.

Spek, A. (2017). Collaborative study on the estimation of EES-values, EVU Congress, Proceedings, Haarlem, The Netherlands.

The 11th International Congress
Motor Vehicles & Motors 2026
Kragujevac, Serbia
October 8th-9th, 2026

Motor Vehicles & Motors

MVM2026-035
https://doi.org/10.24874/CMVM2026.035
Original scientific paper

Marijana Jeremić[1]
Lazar Krstić[2]
Miloš Ivanović[3]
Mihailo Lazarević[4]
Milan Matijević[5]

DIGITAL TWIN DESIGN FOR TORSIONAL STIFFNESS ESTIMATION IN MOTOR-LOAD OSCILLATORY SYSTEMS USING PHYSICS-INFORMED NEURAL NETWORKS

ABSTRACT: The modern development of electric vehicles (EVs) faces significant challenges driven by the high power density and rapid torque response of electric motors. These characteristics frequently excite undesirable torsional oscillations in the drivetrain (motor-load coupling), adversely affecting ride comfort, efficiency, and the structural longevity of mechanical components. Real-time monitoring of dynamic stiffness within these systems is crucial for predictive maintenance and adaptive control. However, direct stiffness measurement requires expensive and fragile physical sensors. This paper proposes a Digital Twin framework for monitoring the stiffness of a torsional oscillatory system using Physics-Informed Neural Networks (PINNs). Unlike purely data-driven black-box AI models, the proposed PINN approach embeds the governing physics of the mechanical system directly into the neural network's loss function. This allows the time-varying stiffness parameter to be accurately estimated even with sparse training data, relying only on standard vehicle sensor inputs like speed encoders. Simulation results demonstrate that the developed Digital Twin successfully identifies stiffness degradation in real-time, providing a robust baseline or advanced vibration damping and control strategies in modern electric vehicles.

KEYWORDS: digital twin, electric vehicles, torsional oscillations, physics-informed neural networks, stiffness estimation

[1] *Marijana Jeremić, Faculty of Engineering at University of Kragujevac, Sestre Janjić 6, 34000 Kragujevac, Serbia, marijanajeremic002@gmail.com, https://orcid.org/0009-0002-5620-1445*
[2] *Lazar Krstić, University of Kragujevac, Faculty of Science, Radoja Domanovica 12, Kragujevac, 34000, Serbia, lazar.krstic@pmf.kg.ac.rs, https://orcid.org/0000-0002-4703-2291*
[3] *Miloš Ivanović, Faculty of Information Studies, Ljubljanska cesta 31a, 8000 Novo Mesto, Slovenia, milos.ivanovic@fis.unm.si, https://orcid.org/0000-0002-8974-2267*
[4] *Mihailo Lazarević, Faculty of Mechanical Engineering at University of Belgrade, Kraljice Marije 16, 11000 Beograd, Serbia, mlazarevic@mas.bg.ac.rs, https://orcid.org/0000-0002-3326-6636*
[5] *Milan Matijević, Faculty of Engineering at University of Kragujevac, Sestre Janjić 6, 34000 Kragujevac, Serbia, matijevic@kg.ac.rs, https://orcid.org/0000-0001-5307-0027*

PROJEKTOVANJE DIGITALNOG BLIZANCA ZA PROCENU TORZIONE KRUTOSTI U OSCILATORNIM SISTEMIMA MOTOR-OPTEREĆENJE KORIŠĆENJEM NEURONSKIH MREŽA PODRŽANIH FIZIČKIM ZAKONIMA

REZIME: Savremeni razvoj električnih vozila (EV) suočava se sa značajnim izazovima koji proizilaze iz velike gustine snage i brzog odziva obrtnog momenta električnih motora. Ove karakteristike često izazivaju neželjene torzione oscilacije u pogonskom sistemu (sprega motor–opterećenje), što negativno utiče na udobnost vožnje, energetsku efikasnost i dugotrajnost mehaničkih komponenti. Praćenje dinamičke krutosti ovih sistema u realnom vremenu od ključnog je značaja za prediktivno održavanje i adaptivno upravljanje. Međutim, direktno merenje krutosti zahteva primenu skupih i osetljivih fizičkih senzora. U ovom radu predlaže se okvir digitalnog blizanca za praćenje krutosti torzionog oscilatornog sistema korišćenjem neuronskih mreža vođenih fizičkim zakonima (Physics-Informed Neural Networks – PINNs). Za razliku od klasičnih pristupa zasnovanih isključivo na podacima i modelima veštačke inteligencije tipa „crne kutije“, predloženi PINN pristup ugrađuje fizičke zakonitosti mehaničkog sistema direktno u funkciju greške neuronske mreže. Na taj način omogućena je precizna procena vremenski promenljive krutosti čak i u uslovima ograničene količine podataka za obuku, oslanjajući se samo na standardne senzorske informacije dostupne u vozilu, kao što su enkoderi brzine. Rezultati simulacija pokazuju da razvijeni digitalni blizanac uspešno identifikuje degradaciju krutosti u realnom vremenu, čime predstavlja pouzdanu osnovu za razvoj naprednih strategija prigušenja vibracija, upravljanja i prediktivnog održavanja u savremenim električnim vozilima.

KLJUČNE REČI: digitalni blizanac, električna vozila, torzione oscilacije, neuronske mreže informisane fizikom (pinns), procena krutosti

INTRODUCTION

Electrified drivetrains combine high power density with rapid torque transients, making flexible shafts, couplings, gears, and connected inertias susceptible to torsional oscillation. These oscillations affect vibration, acoustic behavior, transmitted loads, and component durability (Hua, X. & Gandee, E. 2021). Torsional stiffness is therefore both a structural parameter and a potential condition indicator: a progressive decrease may reflect coupling degradation, loosening, fatigue, or another loss of mechanical integrity (Li, W. et al. 2016; Park, Y.-H. et al. 2023). Because direct time-resolved stiffness measurements are rarely available in standard drive systems, its evolution must be inferred from accessible excitation and encoder information (Li, W. et al. 2016).

Digital twins integrate a physical representation of an asset with operating information and an updating computational mode. For predictive maintenance, the useful output is not merely a fitted signal but a physically interpretable parameter that can be tracked as degradation develops. In a motor–load system, electromagnetic torque and motor/load encoder speeds provide practical inputs, while the torsional stiffness remains latent. The resulting inverse problem is challenging because errors in reconstructed relative motion can be absorbed by the stiffness estimate, particularly when high-order derivatives are obtained from a flexible neural approximation. Physics-informed neural networks incorporate governing equations into learning objectives and have been established for forward and inverse identification problems (Ivanović, M. 2023; Ivanović, M. et al. 2026). The broader physics-informed machine-learning framework offers a route to combine partial observations, prior physical knowledge, and constrained parameter estimation (Ivanović, M. 2023). In the present problem, however, a pointwise second-order residual can produce an apparently accurate state fit while retaining a biased stiffness estimate. The proposed formulation mitigates the identifiability difficulty by predicting relative angle and relative speed as separate states and enforcing the motor–load dynamics through overlapping weak integral residuals that avoid second derivatives.

The resulting digital twin couples a first-order RelativeStateNet with a physically bounded, monotonically decreasing sigmoid stiffness model. It is evaluated through constant-stiffness controls, clean and noisy time-varying degradation, reduced sensor supervision with 751 sensor-labelled instants and dense unlabeled physics collocation, and causal warm-started online updates. The study uses the time vector and electromagnetic-torque profile provided in the jera1.mat dataset; the motor and load encoder-speed responses are synthetic signals generated by the reference ODE model. Accordingly, the contribution is presented as a simulation validation of time-varying stiffness identification and causal near-real-time monitoring on the tested CPU, while experimental drivetrain validation remains future work. However, the combination of time-varying torsional-stiffness identification,

weak first-order physics enforcement, reduced sensor supervision, and causal degradation monitoring has received considerably less attention in flexible motor–load digital twins.

Related Work

Reduced-order torsional models remain useful because they preserve dominant drivetrain modes while keeping parameter identification tractable (Ivanović, M. et al. 2026). Detailed electric-drive studies show that torque ripple, gear excitation, stiffness, and inertial coupling materially affect drivetrain vibration (Hua, X. & Gandee, E. 2021). Online parameter estimators with limited sensors have traditionally used recursive or adaptive schemes, whereas predictive-maintenance studies emphasize traceable health indicators and uncertainty-aware validation (Li, W. et al. 2016; Park, Y.-H. et al. 2023).

Physics-Informed Neural Networks (PINNs) combine data fitting with governing differential-equation constraints through a composite loss function. In inverse problems, unknown physical parameters can be estimated jointly with latent system states by minimizing both data-mismatch and physics-residual terms (Ivanović, 2023). The present work extends this physics-informed principle by replacing the conventional pointwise second-order formulation with weak integral constraints over temporal windows. The flexible motor–load reference implementation that motivated the physical structure is available as a software repository. Here the weak form is applied to a two-inertia ODE and is used specifically to identify a bounded time-varying torsional stiffness from encoder-derived relative quantities. In contrast to approaches focused primarily on forward state prediction or control-input reconstruction, the present work formulates torsional stiffness itself as the latent health-related parameter and investigates its evolution under clean, noisy, reduced-supervision, and causal monitoring conditions. A closely related study applied PINNs to inverse modelling of a flexible motor–load system by embedding the coupled torsional dynamics directly into the neural-network loss function (Ivanović, M. et al. 2026).

MOTOR–LOAD TORSIONAL MODEL

The considered drivetrain is represented by an equivalent two-inertia motor–load system connected through a flexible coupling (Ivanović, M. et al. 2026). The model consists of the motor inertia ($\mathrm{J_m}$), load inertia ($\mathrm{J_l}$), viscous torsional damping ($\mathrm{b_v}$), and time-varying torsional stiffness ($\mathrm{k(t)}$). The motor is excited by the electromagnetic torque ($\mathrm{M_{em}(t)}$), while no independent external load torque is considered in the present simulation study. This reduced-order representation captures the dominant torsional dynamics of the flexible drivetrain while retaining a sufficiently simple structure for inverse parameter identification.

The motor- and load-side angular positions and angular velocities are denoted by ($\mathrm{\theta_m(t)}$), ($\mathrm{\theta_l(t)}$), ($\mathrm{\omega_m(t)}$), and ($\mathrm{\omega_l(t)}$), respectively. The equations of motion are

$$\dot{\theta}_m(t) = \omega_m(t),]M_{em}(t) b_v[\omega_m(t) - \omega_l(t)]k(t)[\theta_m(t) - \theta_l(t)], \tag{1}$$

$$\dot{\theta}_l(t) = \omega_l(t),]b_v[\omega_m(t) - \omega_l(t)] + k(t)[\theta_m(t) - \theta_l(t)]. \tag{2}$$

The equal and opposite coupling torque transmitted between the two inertias is therefore

$$b_v[\omega_m(t) - \omega_l(t)] + k(t)[\theta_m(t) - \theta_l(t)]. \tag{3}$$

To formulate the inverse problem in variables that directly describe the deformation of the flexible coupling, the relative angular displacement and relative angular velocity are introduced as

$$\delta(t) = \theta_m(t) - \theta_l(t), v_\delta(t) = \omega_m(t) - \omega_l(t). \tag{4}$$

Consequently,

$$\dot{\delta}(t) = v_\delta(t). \tag{5}$$

Subtracting the motor- and load-side acceleration equations yields the first-order relative dynamics

$$\dot{v}_\delta(t) + b_v \Gamma v_\delta(t) + k(t)\Gamma\delta(t) - \frac{M_{em}(t)}{J_m} = 0. \tag{6}$$

Where

$$\Gamma = \frac{1}{J_m} + \frac{1}{J_l}. \tag{7}$$

This relative-state formulation is particularly suitable for torsional-stiffness identification because the unknown stiffness enters the dynamics directly through the coupling term $(\mathrm{k(t)\delta(t)})$. The quantities $(\delta(\mathrm{t}))$ and $(\mathrm{v}_\delta(\mathrm{t}))$ therefore contain the information most directly associated with deformation and relative motion of the flexible transmission.

The nominal physical parameters used in the simulations are summarized in Table 1. The healthy and degraded stiffness values define the reference degradation range used for performance evaluation. Importantly, the reference time-varying stiffness trajectory is not supplied to the PINN as a training target and is used only after optimization for quantitative assessment of the estimated stiffness.

Table 1 Physical parameters of the two-inertia motor–load model

Parameter	Symbol	Value	Unit	Role
Motor inertia	(J_m)	6.2×10^{-4}	kg·m²	Known model parameter
Load inertia	(J_l)	2.2×10^{-4}	kg·m²	Known model parameter
Viscous torsional damping	(b_v)	0.004	N·m·s/rad	Known model parameter
Healthy stiffness	(k_0)	350	N·m/rad	Evaluation reference
Degraded stiffness	(k_f)	245	N·m/rad	Evaluation reference

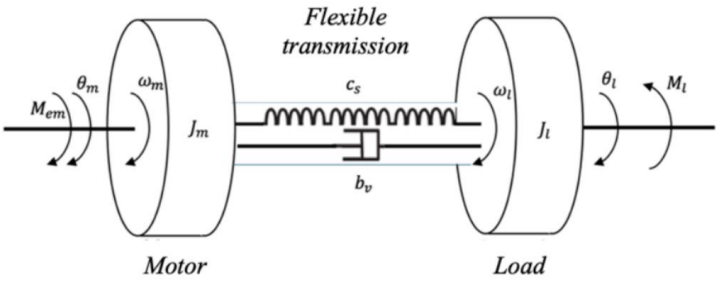

Figure 1 Equivalent two-inertia motor–load system with flexible coupling. In the present formulation, the coupling stiffness $\boldsymbol{c_s}$ shown in the conventional schematic is generalized to the time-varying stiffness $\boldsymbol{k(t)}$, while the independent load torque $\boldsymbol{M_l}$ is set to zero. The motor is excited by the electromagnetic torque $\boldsymbol{Mem(t)}$, and the motor- and load-side angular velocities $\boldsymbol{\omega_m(t)}$ and $\boldsymbol{\omega_l(t)}$ represent the encoder-accessible quantities used in the proposed digital twin.

PROPOSED WEAK FIRST-ORDER PHYSICS-INFORMED MODEL

The proposed digital twin combines a first-order neural representation of the relative torsional states with a bounded model of the time-varying stiffness. The architecture is designed to avoid the numerical sensitivity associated with second-order neural derivatives while retaining direct physical dependence between the estimated stiffness and the deformation of the flexible coupling.

Relative-state neural representation

The RelativeStateNet predicts two separately normalized outputs, $\hat{\delta}(\mathrm{t}), \hat{\mathrm{v}}_\delta(\mathrm{t})$ representing the relative angular displacement and relative angular velocity, respectively.

The relative angular velocity available from the encoder signals is defined as

$$v_{\delta,\mathrm{meas}}(t) = \omega_m(t) - \omega_l(t). \tag{8}$$

Since direct relative-angle measurements are not available, an encoder-derived angular quantity is obtained by cumulative numerical integration,

$$\delta_{\mathrm{int}}(t) = \int_0^t v_{\delta,\mathrm{meas}}(\tau)\, d\tau. \tag{9}$$

with $\delta(0) = 0$.

Importantly, δ_{int} does not represent an additional physical sensor measurement. It is derived entirely from the available motor- and load-side encoder-speed information.

The state network uses a Fourier representation of time to improve its ability to reproduce the oscillatory torsional dynamics. During state pretraining, the network is constrained using the available relative-state supervision together with the first-order kinematic consistency condition

$$\frac{d\hat{\delta}}{dt} - \hat{v}_\delta = 0. \tag{10}$$

Time-varying stiffness representation

After state pretraining, the unknown torsional stiffness is represented by a bounded monotone sigmoid function,

$$\hat{k}(t) = k_{\text{low}} + \frac{k_{\text{high}} - k_{\text{low}}}{1 + exp(wt - t_c)}. \tag{11}$$

where k_{high} and k_{low} denote the upper and lower stiffness levels, t_c determines the centre of the degradation transition, and w controls its temporal width.

The parameterization constrains the stiffness estimate to a physically meaningful range while describing the progressive degradation scenario considered in this study. The initialization of the stiffness parameters is independent of the reference degradation trajectory, and the true stiffness is not used as a training target.

Weak physics-informed residuals

Instead of enforcing the relative dynamics through pointwise second-order derivatives, the proposed formulation uses weak integral residuals over overlapping time windows $[t_a, t_b]$.

The weak kinematic residual is

$$r_{\text{kin}} = \hat{\delta}(t_b) - \hat{\delta}(t_a) - \int_{t_a}^{t_b} \hat{v}_\delta\,(t)\,dt. \tag{12}$$

Defining

$$\Gamma = \frac{1}{J_m} + \frac{1}{J_l}. \tag{7}$$

the weak dynamic residual becomes

$$= \hat{v}_\delta(t_b) - \hat{v}_\delta(t_a) + b_v \Gamma \int_{t_a}^{t_b} \hat{v}_\delta\,(t)\,dt + \Gamma \int_{t_a}^{t_b} \hat{k}\,(t)\hat{\delta}(t)\,dt - \frac{1}{J_m}\int_{t_a}^{t_b} M_{\text{em}}\,(t)\,dt. \tag{13}$$

All integrals are evaluated using trapezoidal quadrature on the actual temporal coordinates.

The main advantage of this formulation is that the dynamic constraint does not require direct evaluation of $\frac{d^2\hat{\delta}}{dt^2}$.

or equivalently high-order derivatives of the neural approximation. This reduces the sensitivity of the inverse stiffness-identification problem to local differentiation errors.

Training objective

The complete objective function combines four components,

$$L_{\text{total}} = \lambda_{\text{data}} L_{\text{data}} + \lambda_{\text{kin}} L_{\text{kin}} + \lambda_{\text{dyn}} L_{\text{dyn}} + \lambda_{\text{IC}} L_{\text{IC}}. \tag{14}$$

Here,

- L_{data} provides supervision from encoder-derived relative quantities;
- L_{kin} enforces first-order kinematic consistency;
- L_{dyn} imposes the weak integral form of the motor–load dynamics;
- L_{IC} constrains the initial condition.

For the constant-stiffness verification experiments, the pretrained state representation is fixed while a single stiffness parameter is identified. For the main time-varying experiment, the bounded stiffness parameters are

optimized using the weak physics-informed objective. In the reduced-supervision configuration, sensor-labelled observations are reduced while the dense unlabeled physics-collocation grid is retained.

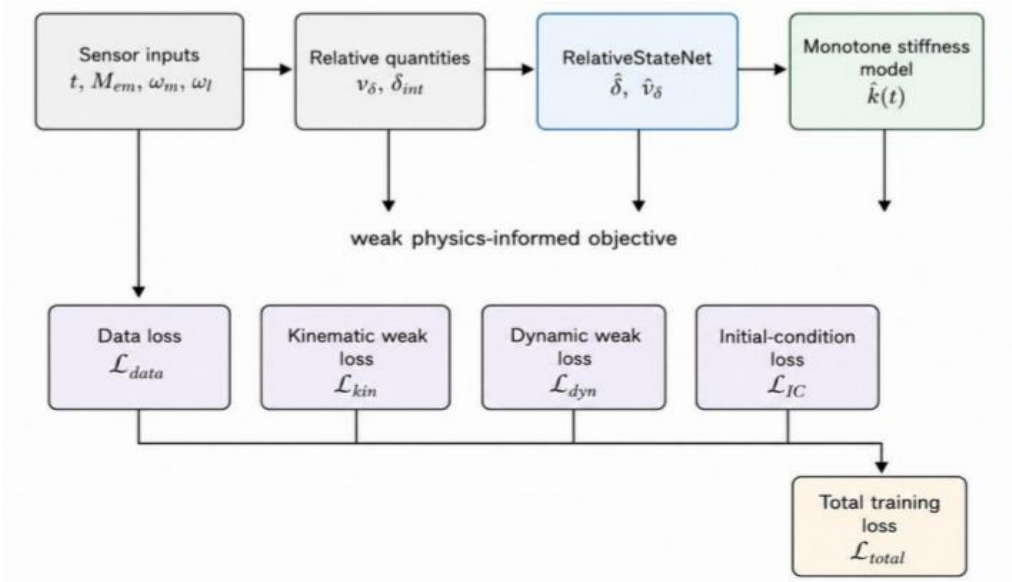

Figure 2 Proposed weak first-order PINN architecture for torsional-stiffness estimation. Motor- and load-side encoder information is transformed into relative quantities and processed by the RelativeStateNet to estimate $\hat{\boldsymbol{\delta}}(\boldsymbol{t})$ and $\hat{\boldsymbol{v}}_{\boldsymbol{\delta}}(\boldsymbol{t})$. The time-varying stiffness $\hat{\boldsymbol{k}}(\boldsymbol{t})$ is represented by a bounded monotone model, while sensor supervision, weak kinematic and dynamic residuals, and the initial-condition constraint are combined in the total training objective.

SIMULATION AND EVALUATION SETUP

The proposed weak first-order physics-informed digital twin is evaluated through a sequence of simulation experiments designed to assess inverse stiffness-identification accuracy, robustness to measurement noise, performance under reduced sensor supervision, and computational feasibility for causal online monitoring. The evaluation begins with controlled constant-stiffness cases and is then extended to a time-varying degradation scenario, noisy encoder-derived observations, and progressively reduced temporal sampling. A second-order physics-informed formulation is retained as a baseline for comparison. All experiments use the same two-inertia motor–load model and physical parameters introduced in MOTOR–LOAD TORSIONAL MODEL, while the reference stiffness trajectory is used exclusively for post-training performance assessment and is never supplied to the neural network as a training target. The following subsections describe the data and sampling configuration, validation scenarios, evaluation metrics, and constant-stiffness verification procedure.

Data and sampling configuration

The analysed time interval extends from (0) to (0.75) s and contains 1501 uniformly spaced samples, corresponding to a sampling frequency of (2) kHz and a sampling interval of (0.5) ms. The electromagnetic-torque profile $(\mathrm{M_{em}(t)})$ and the time vector are provided by the available jera1.mat dataset. Since experimental motor- and load-side encoder trajectories are not available, the corresponding angular-speed responses are generated using a high-accuracy reference ODE model driven by the supplied torque profile.

The weak physics-informed formulation is evaluated over overlapping temporal windows containing 101 samples. Each window therefore spans approximately (50) ms. Consecutive windows are shifted by 25 samples, corresponding to a stride of (12.5) ms. This configuration retains several oscillatory cycles within each weak integration interval while providing substantial overlap between neighbouring windows.

Validation scenarios

The proposed inverse formulation is evaluated through a sequence of increasingly demanding validation scenarios. First, three constant-stiffness control cases are considered, $[\mathrm{k} = 350, 300, 245\ \mathrm{N, m/rad,}]$ representing healthy, intermediate, and degraded mechanical conditions. For each case, a RelativeStateNet is pretrained using the corresponding simulated state response and subsequently fixed while the scalar stiffness parameter is optimized. All stiffness-identification runs start from the same initial estimate, $[\mathrm{k_{init}} = 288.75\ \mathrm{N, m/rad,}]$ thereby providing a consistent comparison between the three operating conditions. The main experiment considers a continuously

varying monotone stiffness degradation. The same formulation is subsequently evaluated with (0.3%) noise introduced into the encoder-derived velocity supervision.

A reduced-supervision experiment is also performed using 751 uniformly distributed sensor-labelled samples over the complete (0)–(0.75) s interval. In this case, the physics-informed constraints are still evaluated at all 1501 time points. The additional physics-collocation points do not contain true stiffness, relative-angle, or relative-speed labels; they provide only the time coordinates, known torque excitation, and governing physical equations. The term reduced sensor supervision refers specifically to the reduction of labelled encoder-derived observations; it does not imply a reduction of the physics-collocation grid.

Finally, strongly reduced sampling configurations containing 121 and 401 sensor-labelled points are considered to investigate the limits imposed by insufficient temporal resolution.

Evaluation criteria

Stiffness-estimation performance is quantified using the root-mean-square error (RMSE), relative RMSE, coefficient of determination (R2), mean absolute error (MAE), maximum absolute error, and the initial and final stiffness errors.

For the constant-stiffness verification cases, relative identification error is used as the primary metric. For the time-varying experiments, both trajectory-level error and (R2) are reported in order to evaluate not only the overall magnitude of the error but also the ability of the estimator to reproduce the temporal evolution of degradation.

State-reconstruction quality is evaluated separately from stiffness-identification quality. This distinction prevents an accurate stiffness estimate from obscuring inadequate reconstruction of the auxiliary relative states.

Model selection is performed exclusively using training-objective information. The reference stiffness trajectory is not used for checkpoint selection, early stopping, or optimization and is introduced only after training for quantitative evaluation.

Constant-stiffness verification

Before addressing time-varying degradation, the inverse formulation is verified using the three constant-stiffness cases summarized in Table 2.

Table 2 Constant-stiffness inverse-identification results

Reference stiffness, (k) [N·m/rad]	Initial estimate [N·m/rad]	Estimated stiffness [N·m/rad]	Absolute error [N·m/rad]	Relative error [%]
350	288.75	351.21	1.208	0.345
300	288.75	300.24	0.240	0.080
245	288.75	245.23	0.234	0.096

Despite the common initialization, the estimated stiffness converges close to the corresponding reference value in all three cases. The largest relative error is approximately (0.35%), observed for the healthy $(350\ \mathrm{N,m/rad})$ condition, while the intermediate and degraded cases remain below (0.10%). These results provide a controlled verification of the inverse objective before the stiffness model is extended to the time-varying degradation scenario.

Table 3 Data provenance in the simulation study

Quantity	Source	Used as
(t)	jera1.mat	Time coordinate
$(M_{em}(t))$	jera1.mat	Known excitation / physics input
$THref$	jera1.mat	Available, not used in stiffness loss
$(\omega_m(t))$	Reference ODE	Synthetic encoder response
$(\omega_l(t))$	Reference ODE	Synthetic encoder response
$(v_\delta(t))$	Derived from encoders	State supervision
$(\delta_{\mathrm{int}}(t))$	Integrated encoder difference	Derived supervision
$(k_{\mathrm{ref}}(t))$	Simulation reference	Evaluation only

RESULTS AND DISCUSSION

The proposed weak first-order physics-informed formulation was evaluated with respect to three central objectives: accurate reconstruction of the time-varying torsional stiffness, robustness to measurement noise and reduced sensor supervision, and improvement over the conventional second-order inverse formulation. The results show that the proposed approach consistently follows the imposed stiffness degradation while retaining physically meaningful estimates under all successful validation scenarios.

Time-Varying Torsional-Stiffness Identification

Figure 3 compares the reference time-varying torsional stiffness with the estimates obtained using the proposed weak first-order formulation under three different sensor conditions and with the conventional second-order baseline. The reference trajectory represents a monotone degradation from the healthy stiffness region toward the degraded operating condition and is used exclusively for post-training evaluation.

The full-rate clean estimate closely follows the reference stiffness trajectory over the complete analysed interval. The proposed estimator achieves a relative stiffness RMSE of (2.8717%) and a coefficient of determination of $(\mathrm{R}_{\mathrm{k}}^2 = 0.95245)$. Although a small initial overestimation is present, the estimated trajectory accurately reproduces the principal degradation transition and converges to approximately $(244.3\ \mathrm{N,m/rad})$, which is very close to the degraded reference value of $(245\ \mathrm{N,m/rad})$.

The 0.3% noise case exhibits behaviour very similar to the clean experiment. The corresponding relative stiffness RMSE is (2.9032%), while $(\mathrm{R}_{\mathrm{k}}^2 = 0.9514)$. The close overlap between the clean and noisy curves indicates that the proposed weak integral formulation retains its stiffness-identification capability under the investigated level of encoder-speed perturbation. This behaviour is consistent with the use of temporally integrated physical constraints, which reduce the sensitivity of the inverse estimation process to small local disturbances in the sensor-derived signals.

The reduced-supervision estimate, shown for the configuration with 751 sensor-labelled instants and 1501 unlabeled physics-collocation points, also reproduces the main degradation trend. In this case, the relative stiffness RMSE increases to (3.7483) and the coefficient of determination decreases to $(\mathrm{R}_{\mathrm{k}}^2 = 0.91898)$. The largest deviation is visible primarily around the onset and timing of the stiffness transition. Nevertheless, the overall shape and final degraded stiffness remain well represented. Since the number of sensor-labelled observations is reduced by approximately (49.97%), this result demonstrates that the physical constraints can partially compensate for reduced measurement supervision when they are enforced on a sufficiently dense collocation grid.

The distinction between sensor-labelled observations and physics-collocation points is important. The additional collocation points do not contain reference values of stiffness or hidden relative states and therefore do not represent additional sensor measurements. They provide only the known time coordinates, electromagnetic-torque excitation, and locations at which the governing equations are enforced.

The second-order baseline, in contrast, follows a substantially different trajectory. Its relative stiffness RMSE is approximately (10.87), with $(\mathrm{R}_{\mathrm{k}}^2 \approx 0.319)$. Although the baseline retains a smooth decreasing trend, it fails to reproduce both the timing and magnitude of the reference degradation and remains significantly above the degraded stiffness level at the end of the interval.

This comparison provides an important motivation for the proposed formulation. In the second-order inverse approach, small errors in the neural approximation can be amplified by higher-order differentiation and subsequently compensated through an incorrect stiffness estimate. The first-order weak formulation avoids direct evaluation of second derivatives and instead imposes the governing dynamics through integral constraints over temporal windows. The resulting inverse problem therefore exhibits substantially improved stiffness-identification performance in the investigated system.

Overall, Figure 3 demonstrates three central properties of the proposed digital twin: accurate reconstruction of the time-varying stiffness trajectory under clean conditions, robustness to moderate encoder-speed noise, and preservation of useful identification accuracy under substantially reduced sensor supervision. The simultaneous comparison with the second-order baseline further indicates that the improvement is associated with the proposed first-order weak physics-informed formulation rather than merely with the flexibility of the neural-network approximation.

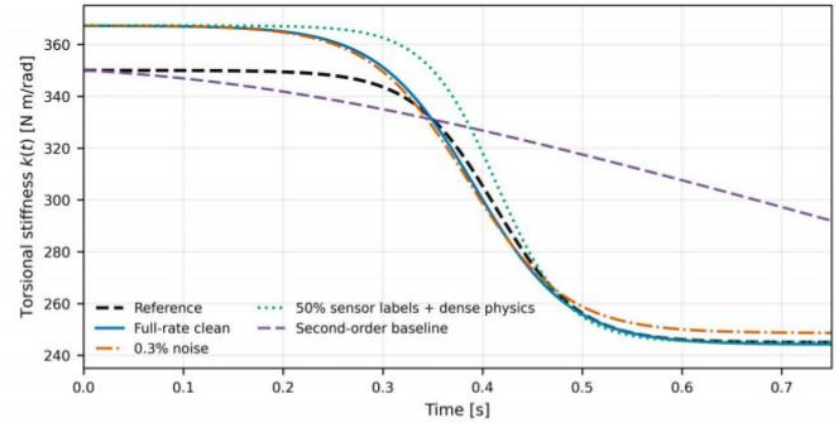

Figure 3 Time-varying torsional-stiffness identification under different validation conditions. The reference degradation trajectory is compared with the proposed weak first-order estimates obtained using full-rate clean data, 0.3% encoder-speed noise, and 751 sensor-labelled samples with dense unlabeled physics collocation, together with the conventional second-order baseline.

Relative-state reconstruction was additionally evaluated as a physical-consistency check for the proposed inverse model. In the full-rate clean experiment, the RelativeStateNet achieved $(R^2 = 0.9702)$ for the relative angular displacement $(\delta(t))$ and $(R^2 = 0.9982)$ for the relative angular velocity $(v_\delta(t))$. These results indicate that the accurate stiffness estimate is accompanied by a physically consistent reconstruction of the underlying torsional dynamics, rather than being obtained solely through compensation within the stiffness parameter. Under reduced sensor supervision, the relative-angle reconstruction remained acceptable, whereas the relative-speed reconstruction degraded more noticeably, showing that accurate identification of the lower-dimensional stiffness trajectory does not necessarily imply equally accurate reconstruction of all auxiliary states.

Reduced Sensor Supervision and Sampling Limitations

An important objective of the proposed physics-informed digital twin is to reduce the amount of sensor-labelled information required for stiffness identification while preserving the physical resolution needed to describe the dominant torsional dynamics. For this purpose, three reduced-sampling configurations containing 121, 401, and 751 sensor-labelled time instants were investigated. Figure 4 compares their influence on the estimation of the time-varying torsional stiffness.

In the most strongly reduced configuration, only 121 uniformly distributed samples are retained over the complete (0)–(0.75) s interval. This corresponds to an effective sampling frequency of approximately $f_s = 160\ \mathrm{Hz}$.

Since the dominant torsional frequency of the considered system is approximately $f_{tor} = 230.5\ \mathrm{Hz}$, this sampling rate is insufficient to satisfy the classical Nyquist condition. The configuration provides only approximately 0.69 samples per dominant torsional period. Consequently, the oscillatory dynamics cannot be represented without aliasing, and the resulting stiffness estimate fails to reproduce the reference degradation trajectory.

Increasing the number of uniformly distributed samples to 401 raises the effective sampling frequency to approximately $f_s = 533.3\ \mathrm{Hz}$, with a corresponding Nyquist frequency of approximately. $f_N = 266.7\ \mathrm{Hz}$. The dominant torsional component is therefore formally below the Nyquist limit. Nevertheless, only approximately 2.31 samples are available per dominant oscillation period. Although this temporal resolution is sufficient for basic spectral separation, it remains inadequate for accurate reconstruction of the oscillatory waveform and for reliable numerical evaluation of the weak integral constraints. The corresponding stiffness trajectory consequently remains substantially biased.

A different behaviour is obtained when 751 sensor-labelled samples are retained. This configuration corresponds to approximately 4.34 samples per dominant torsional period. More importantly, only the amount of sensor supervision is reduced: the weak physical constraints continue to be evaluated on the complete grid of 1501 unlabeled physics-collocation points. Thus, the number of sensor-labelled observations is reduced from 1501 to 751, corresponding to a reduction of approximately 49.97%.Despite this reduction, the estimated stiffness retains good agreement with the reference degradation trajectory. The relative stiffness RMSE is $R_k^2 = 0.91898$. his result demonstrates that the number of sensor-labelled observations can be substantially reduced without a proportional loss of stiffness-identification accuracy, provided that the governing dynamics continue to be enforced on a sufficiently dense temporal grid.

A key distinction must therefore be made between sensor-labelled samples and physics-collocation points. The additional collocation points do not contain reference values of the stiffness (k(t)), relative angular displacement ($\delta(t)$), or relative angular velocity ($v_\delta(t)$). They do not represent additional physical measurements. Instead, they provide only the time coordinates, the known electromagnetic-torque excitation, and locations at which the governing equations are enforced. Their role is to constrain the inverse solution through the physical model rather than through additional labelled data.

The results in Figure 4 also show that satisfying the classical Nyquist criterion alone is not sufficient for reliable physics-informed inverse identification. The 401-sample configuration formally satisfies the Nyquist condition but still fails to provide sufficient temporal resolution for accurate reconstruction and weak-form integration. Reliable identification therefore depends not only on spectral admissibility but also on the number of samples available within each dominant torsional period and on the accuracy with which the integral physics constraints can be evaluated.

Overall, the comparison indicates that reducing both the measurement and physics grids simultaneously leads to a substantial deterioration of the inverse solution, whereas reducing only the sensor-labelled supervision while retaining dense unlabeled physics collocation provides a considerably more effective strategy. This finding is particularly relevant for practical condition-monitoring applications, where labelled sensor information may be limited while the governing physical model remains available.

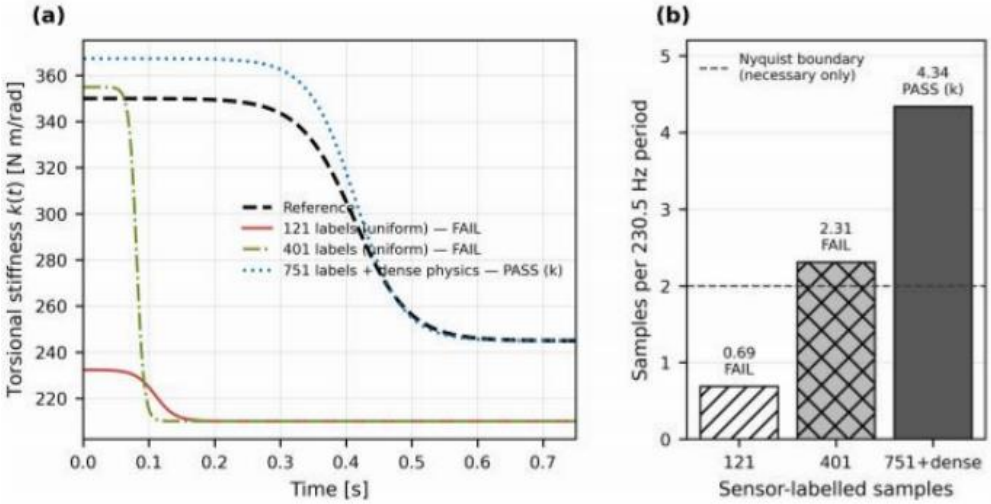

Figure 4 Influence of sensor-sampling density on time-varying torsional-stiffness identification. (a) Reference stiffness trajectory and estimates obtained using 121, 401, and 751 sensor-labelled samples, with the complete 1501-point unlabeled physics-collocation grid retained for the 751-label configuration. (b) Number of samples per dominant torsional period for the investigated sampling configurations. The comparison demonstrates that satisfaction of the classical Nyquist condition alone does not guarantee reliable inverse reconstruction.

Causal Online Degradation Monitoring

An addition to offline stiffness identification, the proposed digital twin was evaluated in a causal online configuration to investigate its suitability for condition-monitoring applications. At each update instant, the estimator uses only information available at the current and previous time instants; no future samples are included in the estimation window. The RelativeStateNet remains fixed after offline pretraining, while the parameters of the bounded stiffness model are updated within each causal window. The resulting procedure should therefore be interpreted as a warm-started causal estimator, rather than as a cold-start online learning algorithm.

Figure 5(a) compares the reference stiffness trajectory with the corresponding causal online estimate. A degradation threshold of $k_{th} = 315\ \mathrm{N, m/rad}$ is introduced as an illustrative condition-monitoring limit. The estimated stiffness crosses this threshold at approximately $t_{det} = 0.300\ s$, whereas the reference trajectory crosses the same threshold at approximately $t_{ref} = 0.3839\ s$. The corresponding threshold-crossing offset is therefore approximately $t_{det} - t_{ref} - 83.9\ \mathrm{ms}$.The negative value indicates an early threshold crossing rather than a detection delay. This result demonstrates that the estimator responds to the developing degradation before the reference trajectory reaches the selected threshold. However, the early crossing should not be interpreted as an exact estimate of fault-onset time, since the online stiffness trajectory remains less accurate than the corresponding offline estimate. For the selected five-step online configuration, the relative stiffness RMSE is 6.7267%, with $R_k^2 = 0.7394$. The accuracy is lower than in the offline full-rate experiment, which is expected because each causal update has access only to past and present information and is restricted to a small number of optimization steps. Nevertheless, the estimated trajectory preserves the overall degradation trend and provides a usable condition-monitoring signal.

Computational performance was evaluated independently for three online configurations using 3, 4, and 5 Adam optimization steps per update. Each configuration was repeated ten times, resulting in 290 measured update latencies per configuration. The five-step configuration was selected because it provided the lowest stiffness-estimation error while still remaining well below the (25) ms computational target in the final repeated benchmark.

For the selected configuration, the measured mean update latency was $2.5410\ \mathrm{ms}$, with a 95th percentile of $4.0309\ \mathrm{ms}$, a 99th percentile of $6.4649\ \mathrm{ms}$, and a maximum measured latency of $6.8162\ \mathrm{ms}$. No deadline misses were observed among the 290 measured updates in the final repeated test. Figure 5(b) shows the individual measured latencies together with the (25) ms computational target.

These results demonstrate that the proposed estimator can perform causal stiffness updates at near-real-time rates on the tested CPU while maintaining useful degradation-tracking capability. The benchmark does not constitute hard-real-time certification or a formal worst-case execution-time guarantee, since operating-system scheduling and hardware conditions may influence individual update times. The result is therefore interpreted as evidence of causal near-real-time computational feasibility rather than deterministic real-time performance.

Overall, the online experiment complements the offline identification results by showing that the proposed physics-informed digital twin can provide sequential estimates of torsional stiffness without access to future measurements. This capability represents an important step toward future integration with condition-monitoring, predictive-maintenance, and adaptive-control systems.

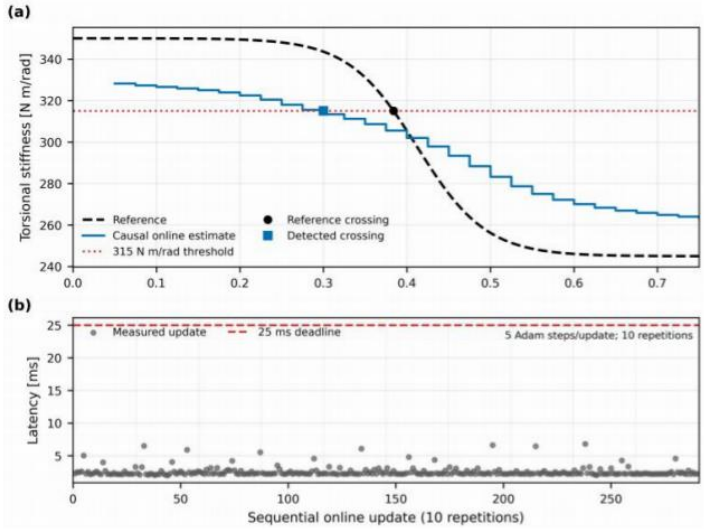

Figure 5 Causal online torsional-stiffness monitoring and computational performance. (a) Reference and warm-started causal stiffness estimates together with the illustrative 315 Nm/rad degradation threshold and corresponding threshold crossings. (b) Measured update latencies for the selected five-Adam-step configuration over ten repeated runs (290 updates), compared with the 25 ms computational target.

Table 4. Repeated causal online benchmark for different numbers of optimization steps per update

Adam steps/update	Mean [ms]	P95 [ms]	P99 [ms]	Max [ms]	Deadline misses	Relative (k)-RMSE [%]
3	1.9662	3.7804	4.8888	5.8089	0/290	6.8711
4	2.5400	4.6835	6.1140	9.0540	0/290	6.8105
5	**2.5410**	**4.0309**	**6.4649**	**6.8162**	**0/290**	**6.7267**

LIMITATIONS AND FUTURE WORK

The present study provides a simulation-based validation of the proposed physics-informed digital twin. The time vector and electromagnetic-torque profile are obtained from the available jera1.mat dataset, whereas the motor- and load-side encoder-speed responses are generated using the reference ODE model. Consequently, the current results do not yet account for effects that may arise in a physical drivetrain, including encoder quantization, sensor bias, temperature variation, backlash, friction nonlinearities, structural uncertainties, and unmodelled disturbances. The present formulation also neglects an independently varying external load torque. Future studies should investigate joint or robust identification under unknown load disturbances in order to distinguish stiffness degradation from variations in external mechanical loading.

The physical parameters (J_m), (J_l), and (b_v) are assumed to be known, while the stiffness evolution is represented by a bounded monotone sigmoid function. This parameterization is suitable for the progressive degradation scenario considered in this work, but it cannot describe stiffness recovery, intermittent behaviour, multiple abrupt faults, or more complex non-monotone degradation trajectories. Future work should therefore investigate more flexible stiffness representations and quantify the sensitivity of the inverse estimate to uncertainty in the assumed mechanical parameters.

Although the reduced-supervision experiment demonstrates that the number of sensor-labelled observations can be decreased by approximately (49.97%), the dense physics-collocation grid is retained. The result should therefore be interpreted as a reduction in measurement supervision rather than a reduction in the number of physics evaluations. Further research could investigate adaptive collocation strategies in which physics points are concentrated in dynamically informative regions, potentially reducing the computational burden without sacrificing identification accuracy.

The online estimator is causal within each temporal window, but it uses a RelativeStateNet pretrained offline. A fully adaptive cold-start implementation using only an incoming sensor stream has not yet been evaluated. Future developments should therefore investigate continual or online state adaptation, embedded implementation, and hardware-in-the-loop validation. Particular attention should be given to deterministic scheduling and worst-case execution-time analysis before the method is considered for hard-real-time deployment.

Another important extension concerns the transition from condition monitoring to active control and prognostics. The estimated stiffness ($k(t)$) could be used as an online scheduling or adaptation variable for vibration-suppression, feedforward, model-predictive, or adaptive-control strategies. Similarly, the estimated degradation trajectory could provide an input to higher-level prognostic models for fault-probability assessment and remaining-useful-life estimation.

Finally, experimental validation using measured motor- and load-side encoder signals represents the most important next step. A laboratory motor–load test bench with controlled stiffness variation would enable direct evaluation of the method under realistic noise, modelling uncertainty, disturbances, and repeatability conditions. Multi-seed training studies and uncertainty-aware confidence intervals should also be included in future validation in order to quantify the statistical robustness of the identified stiffness trajectory. As a longer-term research direction, hybrid quantum–classical learning architectures may also be investigated for physics-constrained inverse parameter identification, provided that their computational or representational advantages over the present classical PINN formulation can be demonstrated quantitatively.

CONCLUSION

This paper presented a weak first-order physics-informed digital twin for inverse estimation of time-varying torsional stiffness in a flexible motor–load system. By reconstructing relative torsional states and enforcing the governing dynamics through weak integral residuals, the proposed formulation avoids direct dependence on second-order neural derivatives and improves the robustness of the inverse stiffness-identification problem.

The proposed method was first verified using constant-stiffness control cases and subsequently evaluated under time-varying clean, noisy, and reduced-supervision conditions. In the clean full-rate experiment, the relative stiffness RMSE was (2.8717) with ($R_k^2 = 0.95245$), while the (0.3%) noise experiment retained a similar accuracy with a relative RMSE of (2.9032%). When the number of sensor-labelled observations was reduced from 1501 to 751 while preserving the dense 1501-point physics-collocation grid, the relative stiffness RMSE remained (3.7483%) with ($R_k^2 = 0.91898$). The strongly reduced 121- and 401-sample configurations further demonstrated that satisfaction of the classical Nyquist criterion alone is not sufficient for reliable physics-informed inverse reconstruction.

A causal warm-started online implementation additionally demonstrated the feasibility of sequential stiffness monitoring on the tested CPU. The selected five-step configuration achieved a relative online stiffness RMSE of (6.7267%), while all 290 measured updates in the final repeated benchmark remained below the (25) ms computational target.

Overall, the results demonstrate that the proposed weak first-order physics-informed formulation can accurately identify a hidden time-varying torsional stiffness while remaining robust to moderate measurement noise and substantially reduced sensor supervision. The developed framework therefore provides a promising methodological basis for future experimental digital twins aimed at drivetrain condition monitoring, predictive maintenance, and adaptive vibration-control applications.

ACKNOWLEDGMENTS

This research was supported by the Science Fund of the Republic of Serbia, Grant No. 214, within the project "Parametric and Nonparametric Methods for Data-Driven Optimal Control of Mechatronic Systems with Flexible Coupling - DDOC".

REFERENCES

Hua, X., & Gandee, E. (2021). Vibration and dynamics analysis of electric vehicle drivetrains. *Journal of Low Frequency Noise,* Vibration and Active Control, 40(3), 1241–1251. https://doi.org/10.1177/1461348420979204

Ivanović, M. (2023). *Neuronske mreže podržane fizičkim zakonima – Praktikum.* Prirodno-matematički fakultet, Univerzitet u Kragujevcu. https://scidar.kg.ac.rs/bitstream/123456789/18602/5/pinn-skripta-lat.pdf

Ivanović, M., Matijević, M., Krstić, L., & Jeremić, A. (2026). I*nverse modeling of flexible rotational systems via hybrid physics-informed and data-driven learning*

Jeremić, M., Krstić, L., Ivanović, M., Lazarević, M., & Matijević, M. (2026). *Physics-informed digital twin for torsional stiffness estimation* [Computer software]. GitHub. https://github.com/poni0107/pinn-torsional-stiffness-digital-twin

Li, W., Chai, Z., Wang, M., Hu, X., & Guo, Y. (2016). *Online identification and verification of the elastic coupling torsional stiffness. Shock and Vibration, 2016,* Article 2016432. https://doi.org/10.1155/2016/2016432

Park, Y.-H., Lee, H.-B., & Kim, G.-W. (2023). Crack monitoring in rotating shaft using rotational speed sensor-based torsional stiffness estimation with adaptive extended Kalman filters. *Sensors, 23(5)*, 2437. https://doi.org/10.3390/s23052437

The 11th International Congress
Motor Vehicles & Motors 2026
Kragujevac, Serbia
October 8th - 9th, 2026

Motor Vehicles & Motors

MVM2026-040
https://doi.org/10.24874/CMVM2026.040
Original scientific paper

Nebojša Jovičić[1]
Angelina Cvetanović[2,*]
Goran Bošković[3]

EVALUATING THE EFFICIENCY OF OPTIMIZED WASTE COLLECTION ROUTES USING DATA ENVELOPMENT ANALYSIS

ABSTRACT: Efficient waste collection has an important role in sustainable urban transport systems, since it directly affects operational costs, fuel consumption, and environmental performance. This paper explores how VRP-based route planning combined with data envelopment analysis can help evaluate and improve waste collection routes in the city of Kragujevac. Alternative route configurations were generated using the Vehicle Routing Problem (VRP) solver implemented in ArcGIS Network Analyst, with the aim of reducing travel distance while maintaining the required level of collection service. To assess their performance, an input-oriented DEA model assuming variable returns to scale was applied to evaluate the pure technical efficiency of the optimized routes. Operational factors, specifically route length and travel time, were selected as input variables to be minimized, while indicators related to waste collection services were used as outputs.
By using this approach, it is possible to distinguish the efficient routes from the inefficient ones and identify specific ways to reduce resource consumption without compromising service quality. This paper provides a decision-support framework for fleet management in public utilities by combining VRP-based route planning with multidimensional efficiency evaluation.

KEYWORDS: municipal waste management, data envelopment analysis (DEA), geographic information systems (GIS), route optimization, waste collection

[1] *Nebojša Jovičić, Faculty of Engineering, Department of Energy and Process Engineering, University of Kragujevac, Republic of Serbia, njovicic@kg.ac.rs, https://orcid.org/0000-0002-6505-6457*
[2] *Angelina Cvetanović, Faculty of Engineering, Department of Energy and Process Engineering, University of Kragujevac, Republic of Serbia, angelina.pavlovic@uni.kg.ac.rs, https://orcid.org/0000-0001-5249-1102 (*Corresponding author)*
[3] *Goran Bošković, Faculty of Engineering, Department of Energy and Process Engineering, University of Kragujevac, Republic of Serbia, goran.boskovic@kg.ac.rs, https://orcid.org/0000-0003-3200-0120*

PROCENA EFIKASNOSTI OPTIMIZOVANIH RUTA ZA SAKUPLJANJE OTPADA KORIŠĆENJEM ANALIZE OBAVIJANJA PODATAKA

REZIME: Efikasno sakupljanje otpada ima važnu ulogu u održivim sistemima urbanog transporta, budući da direktno utiče na operativne troškove, potrošnju goriva i ekološke performanse. Ovaj rad istražuje kako kombinovanje planiranja ruta zasnovanog na problemu rutiranja vozila (VRP) sa analizom obavijanja podataka (DEA) može doprineti proceni i unapređenju ruta za sakupljanje otpada u gradu Kragujevcu. Alternativne konfiguracije ruta generisane su korišćenjem VRP solvera implementiranog u ArcGIS Network Analyst, sa ciljem smanjenja dužine putovanja uz zadržavanje zahtevanog nivoa usluge sakupljanja otpada. Za procenu njihovih performansi primenjen je DEA model orijentisan na ulaze, uz pretpostavku varijabilnih prinosa na obim, kako bi se ocenila čista efikasnost optimizovanih ruta. Kao ulazne varijable koje je potrebno minimizovati odabrani su operativni faktori, odnosno dužina rute i vreme putovanja, dok su kao izlazi korišćeni pokazatelji povezani sa uslugom sakupljanja otpada.

Primenom ovog pristupa moguće je razlikovati efikasne od neefikasnih ruta i identifikovati konkretne mogućnosti za smanjenje potrošnje resursa bez ugrožavanja kvaliteta pružene usluge. Ovaj rad predstavlja okvir za podršku odlučivanju u upravljanju voznim parkom javnih komunalnih preduzeća, zasnovan na kombinovanju planiranja ruta primenom VRP-a i višedimenzionalne procene efikasnosti.

KLJUČNE REČI: upravljanje komunalnim otpadom, analiza obavijanja podataka (DEA), geografski informacioni sistemi (GIS), optimizacija ruta, sakupljanje otpada.

INTRODUCTION

Municipal solid waste (MSW) is an unavoidable consequence of most human activities and has become an increasingly important environmental concern (Choiron et al. 2023). It is also recognized as a significant contributor to climate change and global warming, highlighting the need for more sustainable approaches to waste management (Son, 2014; Amal et al., 2020). Effective MSW management is therefore an essential public service, while appropriate regulations can encourage greater innovation, sustainability, and operational efficiency within the sector. Over recent decades, considerable attention has been given to improving MSW management systems worldwide, particularly by enhancing the efficiency of their individual components. In general, an MSW management system consists of five main stages: waste generation, collection and transportation, transfer, treatment, and final disposal (Bošković et al. 2024). Among these stages, waste collection constitutes a substantial share of municipal expenditure (Daraio et al. 2024). Namely, the waste collection and transportation represent a major logistical activity in urban areas and typically account for approximately 60-80% of the total costs associated with waste management. Improving this part of the system is therefore particularly important for increasing energy efficiency and reducing the financial burden on municipalities. Furthermore, efficient MSW collection plays a central role in supporting the transition toward a circular economy and the development of more sustainable modern communities (Sousa et al. 2024). This phase of MSW management system represents a significant cost to municipal budgets due to fuel consumption, labour requirements, vehicle maintenance, and travel time. Consequently, improving the efficiency of waste collection routes has become an important goal for municipalities seeking to reduce operating costs while improving environmental sustainability.

In recent years, geographic information systems (GIS) have become one of the most widely used decision-support tools for planning and optimizing waste collection routes. GIS is a powerful tool that enables precise mapping, spatial analysis, and route optimisation, ultimately leading to cost savings and improved service quality (Robin et al. 2019; Das et al. 2024). GIS enables the implementation of spatial analysis, using well-established routing algorithms like the Dijkstra algorithm to determine the shortest or most cost-effective routes between various points (Dijkstra, 1959; Amal et al. 2020). Route optimization contributes to reducing travel distance, travel time, fuel consumption, and greenhouse gas emissions, thereby supporting the development of sustainable urban transport systems.

Although the optimization process can improve route planning, it does not provide a comprehensive assessment of operational efficiency. Route optimization is generally based on minimizing a predefined objective function, whereas the overall performance of a route depends simultaneously on multiple operational and environmental indicators. Therefore, additional evaluation methods are required to determine whether optimized routes actually utilize available resources efficiently. In this context, an efficiency assessment approach capable of considering several variables or performance indicators simultaneously can provide a more comprehensive evaluation of the resulting routes. Data Envelopment Analysis (DEA) is one of the most widely used methods for evaluating the efficiency of systems that involve multiple inputs and outputs. DEA is a non-parametric mathematical programming technique widely applied

for measuring the relative efficiency of comparable decision-making units (DMUs) (Li & Xu, 2008). Unlike conventional performance indicators, DEA simultaneously evaluates several input and output variables without requiring assumptions regarding their functional relationship. In transportation and logistics systems, DEA has been successfully applied for evaluating vehicle fleets, public transport systems, ports, airports, and municipal services. However, studies integrating VRP-based route planning with DEA for municipal solid waste collection remain relatively limited.

The city of Kragujevac in the Republic of Serbia provides an appropriate case study for investigating the integration of spatial optimization and efficiency evaluation. Waste collection routes in Kragujevac have already been optimized using the ArcGIS Network Analyst extension, resulting in reductions in travel distance for several routes (Bošković & Jovičić, 2015; Bošković et al. 2024). However, the efficiency of these optimized routes has not yet been assessed by considering multiple operational performance indicators simultaneously.

Therefore, this study aims to combine VRP-based route planning in ArcGIS Network Analyst with DEA to evaluate municipal waste collection routes. The analysis compares the existing routes with the optimized ones using an input-oriented DEA model with variable returns to scale. In this way, the routes are evaluated not only according to the improvements achieved through optimization, but also according to how efficiently the available resources are used. Combining VRP-based route planning and DEA makes it possible to examine route performance from both spatial and operational perspectives. The findings can help municipalities better understand the effects of route optimization, improve the use of their vehicle fleets and other resources, and make waste collection operations more efficient as well as sustainable.

METHODOLOGY OF RESEARCH

With increasing MSW generation and growing operational demands, efficient waste collection and transportation are becoming increasingly important for sustainable waste management. Since waste collection accounts for a substantial share of overall waste management costs, careful route planning and efficient use of available resources are essential for improving system performance (Bošković et al. 2024). The methodological framework used in this study is presented in Figure 1. The analysis begins with the collection and preparation of operational and spatial data describing the existing waste collection system. These data are then used to reconstruct the current collection routes and develop the street network required for the subsequent VRP-based route planning in ArcGIS Network Analyst. In the next step, alternative route configurations are generated using the VRP solver in ArcGIS Network Analyst based on the developed street network and defined operational constraints, followed by a comparison with the existing routes. The final stage uses an input-oriented DEA model under the variable returns to scale assumption to assess the relative efficiency of the analysed routes.

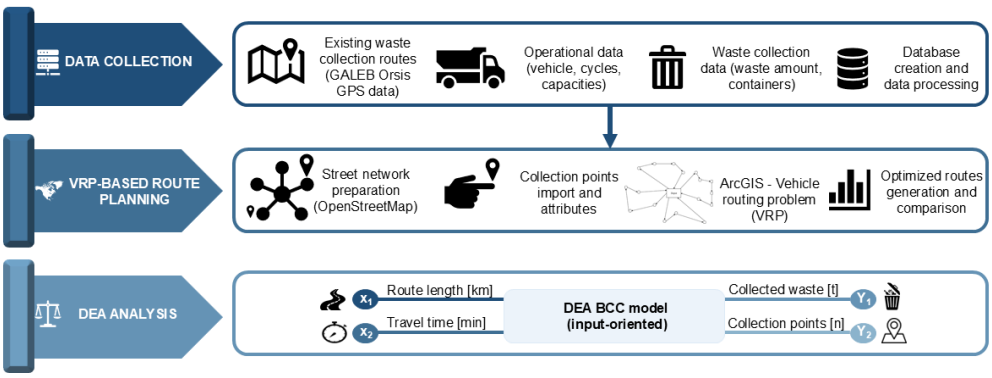

Figure 1 Methodological framework of research

This methodological framework enables not only a comparison between the existing and alternative route configurations but also an examination of whether shorter and better-planned routes lead to more efficient use of available resources.

Study area and data collection

The study was conducted using MSW collection routes operated by the Public Utility Company (PUC) Šumadija in the city of Kragujevac, Serbia. The company is responsible for the collection and transportation of mixed municipal solid waste and recyclable waste generated in residential, commercial, and public areas of the city. Waste collection is organized according to the characteristics of different parts of the city. Collection frequency varies between streets and neighbourhoods depending on the amount and type of waste generated, housing characteristics, the number of commercial facilities and waste containers, as well as local traffic conditions. Based on these characteristics, the city is divided into six waste collection zones: Extra, First, Second, Third, Fourth, and Fifth Zone (PUC Šumadija, 2026).

Different types of vehicles are used depending on the waste collection system and the type of container being serviced. The municipal fleet includes 18 waste collection vehicles that collect waste from 1.1 m³ containers and 140 litres household bins, while larger containers are serviced by hook-lift vehicles. Additional vehicles are used for specific operations, including the collection of bulky waste. The collection system covers approximately 2,300 containers located throughout the city, together with around 4,000 140 litres bins distributed to households in residential areas. A separate system is in place for recyclable packaging waste. It includes 120 plastic containers of 1.1 m³ placed at 60 locations across the city. In rural areas, households use waste collection bags, which are distributed twice a month (PUC Šumadija, 2026).

Although the municipal collection system covers different waste streams, container types, and collection arrangements, this study focuses on Monday routes for mixed municipal solid waste. A total of 14 Monday routes were included in the DEA efficiency assessment. Of these, nine routes primarily serving 1.1 m³ containers were selected for VRP-based route planning, while routes MON14 - MON18, which predominantly serve individual household bins, were retained only in the DEA analysis.

Spatial data preparation and GIS database development

Route optimization requires a spatial database that accurately represents both the street network and the existing waste collection system. The data used in this study were obtained from the operational records of PUC Šumadija Kragujevac and complemented by spatial data prepared in a GIS environment. The database included three main spatial components: the street network, georeferenced waste collection points, and the existing routes used by waste collection vehicles (Bošković et al. 2024). Data describing the existing routes, including vehicle movements and route-related operational parameters, were obtained from the GALEB Orsis11 (Galeb System, 2023) fleet monitoring software used by the company.

Street network preparation

The quality of route optimization depends strongly on how accurately the street network reflects the actual conditions in which waste collection vehicles operate. In this study, the street network for the City of Kragujevac was developed using OpenStreetMap data (OpenStreetMap, 2023). The street segments extending beyond the administrative boundary of the city were retained when they formed part of the existing waste collection routes. The network was represented by polyline features, with each street segment linked to relevant attributes such as street name and length. To reflect actual vehicle movement more realistically, one-way streets and turning restrictions were also incorporated into the network. These constraints ensured that the routes generated during the optimization process followed the traffic rules represented in the developed street network.

Waste collection points

Waste collection points were mapped using the available spatial data and existing digital maps, allowing their locations to be accurately represented within the study area. Each point was linked to a set of operational attributes, including the type and number of waste containers, collection day, service time, street location, and other relevant field information. The analysis was limited to collection points equipped with 1.1 m³ containers for mixed municipal solid waste and included in the Monday collection schedule. The selected points were linked to the prepared street network and defined as required stops in the subsequent route optimization. Their spatial distribution across the study area is shown in Figure 2.

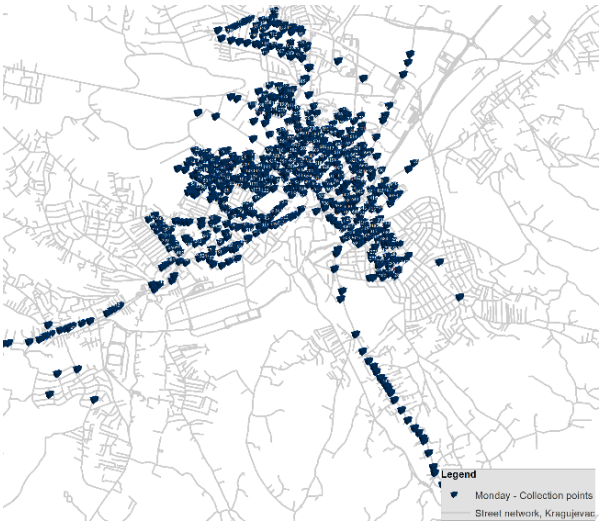

Figure 2 Spatial distribution of 1.1 m³ municipal solid waste containers served on Mondays

This spatial representation provides a clear picture of the collection system and establishes the basis for the route analysis presented in the following section.

Existing route characteristics and VRP-based route planning in ArcGIS

Before optimization, the operational characteristics of the 14 selected Monday routes were compiled to establish the baseline scenario. The dataset covered the main characteristics of each route, including the service area, number of collection points, number of 1.1 m³ containers and waste bins, amount of collected waste, route length, travel time, number of collection cycles, and estimated fuel consumption (Table 1). These data were used to describe the baseline operating conditions and later served as a reference for evaluating the changes achieved through route optimization. Since fuel consumption was not measured directly for individual routes, it was estimated using a representative waste collection vehicle with an average fuel consumption of 55.6 liters/100 km. The same consumption rate was applied to the distance travelled on each route to obtain the corresponding estimated fuel consumption.

Table 1 Operational characteristics of existing waste collection routes

*	Route	Service area	Collection points [n]	1.1 m³ containers [n]	Waste bins [n]	Collected waste [t]	Route length [km]	Travel time [min]	Collection cycles [n]	Estimated fuel consumption per route [l]
1.	MON11	Centrala radionica i Pivara	71	160	0	7.64	39.89	177.97	2	22.18
2.	MON12	Erdoglija	75	206	0	10.54	36.20	114.00	2	20.13
3.	MON13	BKM + Kneza Mihaila + Kraljevačkog bataljona	81	187	0	9.44	31.53	102.47	1	17.53
4.	MON14	Korićani	32	0	666	3.22	28.88	153.75	1	16.06
5.	MON15	Stanovo	33	0	771	7.52	28.16	146.27	1	15.66
6.	MON16	Ibarski rudara + Drenovac + Đuriselo	17	29	519	4.12	54.53	163.82	1	30.32
7.	MON17	Ćava	21	4	627	9.16	49.25	171.08	2	27.38
8.	MON18	Grošnica + Ćava	25	2	649	6.20	46.64	144.17	1	25.93
9.	MON21	Centar + Beloševac	88	207	0	10.52	39.62	121.83	2	22.03
10.	MON22	Aerodrom	63	205	0	12.40	29.88	105.20	2	16.61
11.	MON23	Mala Vaga + Erdoglija	79	201	0	8.74	37.74	164.38	2	20.98
12.	MON31	Centar	67	202	0	7.74	29.55	105.87	2	16.43
13.	MON32	Centar 2	86	220	0	9.80	37.03	136.38	2	20.59
14.	MON33	Bubanj + Vašarište	82	224	0	8.77	35.91	131.60	2	19.97

Route planning was carried out in ArcGIS Network Analyst 10.8 using its Vehicle Routing Problem (VRP) solver (ESRI, 2026). VRP is commonly used to organize vehicle routes when a set of locations has to be served under operational constraints, which makes it suitable for municipal waste collection (Xin et al., 2021). In this study, each predefined Monday route was considered separately rather than solving a single fleet-allocation problem for the entire city. Collection points remained assigned to their existing routes, while their visiting order and distribution between collection cycles could be changed. Although the VRP can be solved using either distance or travel time as the impedance (Bošković et al. 2024; ESRI, 2026), distance was used as the routing criterion in this study.

Each collection point was represented as a required node, with demand based on the number of 1.1 m³ containers at that location. The same vehicle capacity was used for all analysed routes. Vehicles departed from the municipal garage of PUC Šumadija and returned there after completing the route, while the Jovanovac landfill was used as the unloading location. Depending on the number of containers to be serviced, collection was completed in one or two collection cycles. Most routes were completed in two collection cycles, with unloading at the landfill after each cycle. The total route length covered the complete vehicle movement, including travel from the municipal garage, visits to all assigned collection points, unloading at the landfill, and the final return to the garage. Service times for individual collection points were obtained from the operational database and were kept unchanged during route planning.

The street network was prepared to reflect actual vehicle movement as closely as possible. In addition to correct network connectivity and elevation levels at grade-separated crossings, one-way streets and turning restrictions were included. Shortest paths between network locations were calculated over this network, while the order in which collection points were visited was determined by the heuristic procedure used by the Network Analyst VRP solver. Consequently, the resulting route configurations are considered feasible improvements over the recorded routes, without implying that they represent mathematically proven global optima. Since the collection service was represented by point locations and not by street segments, the problem was formulated as a node-routing VRP rather than an arc-routing problem.

Data envelopment analysis

The final stage of the methodological framework focused on determining whether the improvements achieved through VRP-based route planning were also reflected in the operational efficiency of the collection system. For this purpose, DEA was applied to evaluate and compare the efficiency of the existing and optimized waste collection routes. The DEA is a linear programming approach widely used to assess the relative efficiency of comparable decision-making units (DMUs). It evaluates how efficiently each unit transforms multiple inputs into outputs by comparing its performance with an empirical efficiency frontier formed by the best-performing units. Depending on the assumptions of the model, DEA can account for different returns to scale, allowing efficiency to be assessed under different operating conditions (García-Sánchez, 2008). DEA efficiency can be assessed under either constant returns to scale (CRS) or variable returns to scale (VRS), depending on the assumptions regarding the relationship between inputs and outputs. Charnes et al. (1978) introduced a linear programming approach for evaluating the relative efficiency of decision-making units under the assumption of CRS. The CRS model assumes that all DMUs operate at an optimal scale and that changes in inputs result in proportional changes in outputs. For *n* entities using *m* inputs *x* to generate *s* outputs *y*, the input-oriented model seeks to minimize the required level of inputs while maintaining the observed output levels. The model can be expressed as (Mirmozaffari & Kamal, 2024):

$$\theta^* = min\theta \tag{1}$$

Subject to:

$$\sum_{j=1}^{n} \lambda_j \, x_{ij} \ \leq \theta x_{i0}, i = 1,2, \dots, m \tag{2}$$

$$\sum_{j=1}^{n} \lambda_j \, y_{rj} \ \geq y_{r0}, r = 1,2, \dots, s \tag{3}$$

$$\lambda_j \geq 0, j = 1,2, \dots, n \tag{4}$$

where λ represents non-negative intensity variables used to construct the reference frontier, while θ represents the technical efficiency score of the evaluated entity. A value of θ closer to 1 indicates a higher level of relative efficiency. Banker et al. (1984) subsequently extended the CRS model by introducing the VRS framework. The VRS model incorporates an additional convexity constraint: $\sum_{j=1}^{n} \lambda_j = 1$, which allows efficiency to be assessed independently of differences in operating scale. While the CRS model provides an overall technical efficiency (TE) score that incorporates both technical and scale effects, the VRS model measures pure technical efficiency (PTE) by accounting for variations in scale. Consequently, comparing the efficiency scores obtained under the two models makes it possible to identify whether inefficiency arises from managerial or operational performance or from operating at a non-optimal scale.

Since the objective of this study was to determine the potential reduction of operational resources while maintaining the current service level, an input-oriented BCC model assuming VRS was adopted. Each waste collection route operated on Mondays was considered a DMU. The number of DMUs should be carefully considered when applying DEA, particularly in relation to the number of input and output variables included in the model. Using too many variables with a limited number of DMUs can make it difficult for the model to distinguish between efficient and inefficient units. As a general rule of thumb, the number of DMUs should therefore be at least twice the combined number of inputs and outputs (Golany & Roll, 1989). The selection of input and output variables was based on operational characteristics commonly used in municipal waste collection studies. As shown in Figure 1, two inputs and two outputs were included in the DEA model. Route length, expressed in kilometres, and travel time, expressed in minutes, were selected as input variables, while the amount of collected waste, expressed in tonnes, and the number of collection points served along each route were used as outputs. The selected inputs represent the main operational resources associated with route performance and are therefore intended to be minimized, whereas the outputs reflect the level of waste collection service that should be maintained. The amount of collected waste is frequently used as an output variable in DEA-based assessments of waste collection systems, as it directly reflects the service provided by each route (Lombardi et al., 2021). Fuel consumption could also be considered a relevant operational and environmental indicator. However, in this study, fuel consumption was estimated as a direct function of the distance travelled rather than measured independently for each route. Including both route length and estimated fuel consumption as separate DEA inputs would therefore introduce redundant information into the model. For this reason, fuel consumption was excluded from the DEA specification.

To distinguish between efficiency within each scenario and changes resulting from route optimization, the DEA was carried out in two stages. In the first stage, a scenario-specific analysis was performed, in which the existing and optimized route scenarios were evaluated separately using the same input-oriented BCC/VRS model. This analysis provided an overview of the relative efficiency structure within each scenario. However, since each scenario generates its own efficiency frontier, the resulting efficiency scores cannot be directly compared to determine whether optimization improved the efficiency of individual routes. For this reason, a second-stage common-frontier analysis

was performed (Ruiz & Sirvant, 2016; Nasrabadi, 2018). The 14 existing routes and their 14 corresponding optimized configurations were combined into a single dataset of 28 observations and evaluated simultaneously against the same BCC/VRS efficiency frontier. The input-output specification was kept unchanged: route length and travel time were used as inputs, while collected waste and the number of collection points served were treated as outputs. The main difference compared to the first stage of analysis was that both the existing and optimized configurations were evaluated against the same reference set. Under the common-frontier approach, the efficiency change for route i was calculated as:

$$\Delta\theta_i = \theta_{i,O} - \theta_{i,\ E} \tag{5}$$

where $\theta_{i,\ E}$ represents the efficiency score of the existing route configuration and $\theta_{i,O}$ represents the score of its optimized configuration, with both scores obtained from the common-frontier model. A positive value of $\Delta\theta_i$ indicates an improvement in relative efficiency following optimization, zero indicates no change, and a negative value indicates a decrease. Since both configurations are evaluated against the same frontier, a route that remains unchanged in terms of its inputs and outputs will necessarily receive the same efficiency score in both configurations.

All DEA models were solved using the Simplex linear programming algorithm implemented in Microsoft Excel Solver.

RESULTS AND DISCUSSION

Route optimization is an important part of the operational planning of PUC Šumadija Kragujevac, as the organization of collection routes directly affects the distance travelled by waste collection vehicles and the resources required to provide the service. Detailed characteristics of the existing and optimized routes are provided in Table 2, based on operational data obtained from the GALEB Orsis11 fleet monitoring software. The existing routes were compared with alternative configurations generated using the VRP solver in ArcGIS Network Analyst, with the aim of identifying shorter travel paths without changing the required level of waste collection service. The analysis showed that the potential for improvement was not the same across all routes. Routes MON14-MON18, where waste is predominantly collected from individual household bins, were excluded from further optimization. Their collection pattern is closely linked to the spatial distribution of individual households and the layout of the local street network, leaving relatively little flexibility to reorganize the sequence of collection. The optimization therefore focused on routes serving 1.1 m³ containers for mixed municipal solid waste, where changes in the order and configuration of collection points offered greater opportunities to reduce the distance travelled.

Table 2 Summary of VRP-based route planning results

Route	Collection cycles [n]	Existing route [km]	Optimized route [km]	Distance saving [km]	Distance saving [%]	Collection points [n]	1.1 m³ containers [n]	Max. containers per cycle I [n]	Max. containers per cycle II [n]	Max collection points - cycle I [n]	Max collection points - cycle II [n]
MON11	2.00	39.89	39.89	0.00	0.00%	71	160	90	70	40	31
MON12	2.00	36.20	32.59	3.61	9.97%	75	206	110	96	40	35
MON13	1.00	31.53	31.53	0.00	0.00%	81	187	187	/	81	/
MON21	2.00	39.26	39.26	0.00	0.00%	88	207	107	100	45	43
MON22	2.00	29.88	29.08	0.80	2.69%	63	205	105	100	35	28
MON23	2.00	37.74	36.97	0.77	2.05%	79	201	105	96	43	36
MON31	2.00	29.55	28.20	1.35	4.55%	67	202	105	97	35	32
MON32	2.00	37.03	29.70	7.33	19.81%	86	220	115	105	46	40
MON33	2.00	35.91	33.30	2.61	7.28%	82	224	125	99	46	36

Among the routes included in the optimization, MON11, MON13, and MON21 remained unchanged. Under the defined network conditions and optimization criteria, no shorter alternative was identified, and the optimized solution therefore followed the same route as the existing one. This indicates that these routes were already well organized from the perspective of travel distance and that further spatial rearrangement alone would provide little or no additional benefit.

The situation was different for the remaining routes, where VRP-based route planning identified opportunities to shorten the existing travel paths. Taken together, these changes reduced the daily distance travelled by approximately 16.4 km, corresponding to an overall saving of about 5.2%. The magnitude of the reduction differed from one route to another, showing that the benefits of optimization depend strongly on the spatial and operational

characteristics of each collection route. Nevertheless, the results indicate that relatively small changes in route configuration can reduce unnecessary vehicle movement without reducing the level of collection service. Since the greatest distance saving was achieved for MON32, this route was selected as a representative example for comparing the existing and optimized configurations in Figure 3.

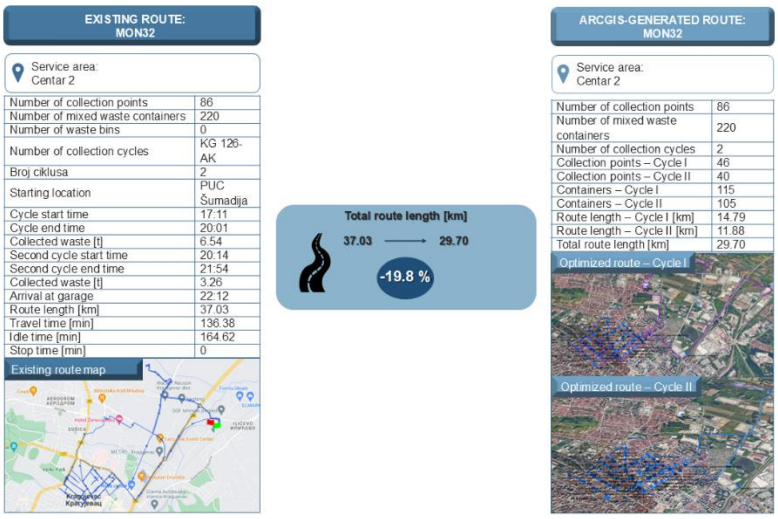

Figure 3 Comparison of the existing and ArcGIS-generated waste collection route (MON32)

Figure 3 illustrates the existing and optimized waste collection MON 32 route. The existing route serves 86 collection points with 220 mixed-waste containers and consists of two collection cycles. The recorded route length was 37.03 km. Following VRP-based route planning, the collection points and containers were distributed between two cycles, with 46 collection points and 115 containers assigned to the first cycle and 40 collection points and 105 containers to the second. The resulting route lengths were 14.79 km and 11.88 km, respectively. The optimized solution reduced the total route length to 29.70 km, corresponding to a distance saving of 7.33 km, or 19.81%, while maintaining the same number of collection points and containers.

These findings show that VRP-based route planning can reduce the distance travelled by waste collection vehicles while maintaining the required level of collection service. However, distance alone does not provide a complete picture of route performance. Routes differ not only in their length, but also in the amount of waste collected, the number of collection points served, travel time, and other operational characteristics. A route that is shorter is therefore not necessarily more efficient when the resources used and the service provided are considered together. To capture these differences, the analysis was extended by applying an input-oriented BCC DEA model under the assumption of VRS. Both the existing and optimized routes were evaluated to determine how efficiently operational inputs were used relative to the level of waste collection service provided. The resulting efficiency scores range from 0 to 1, with a score of 1 indicating a route located on the efficiency frontier, while values below 1 indicate different degrees of relative inefficiency. Figure 4 presents the efficiency scores obtained for the existing waste collection routes.

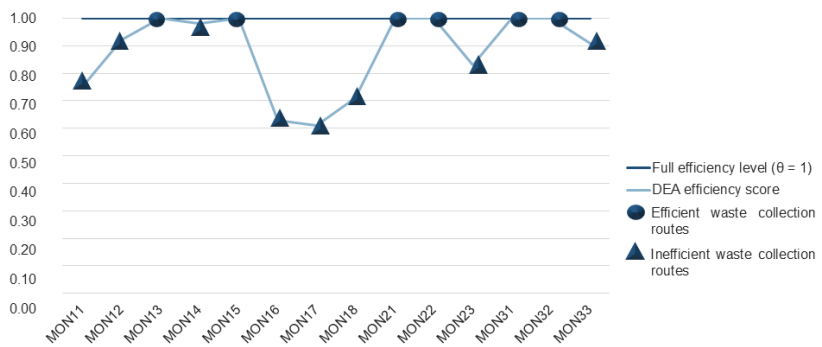

Figure 4 DEA efficiency scores of existing routes

The results show how much the inputs could be reduced while maintaining the same level of outputs, revealing clear differences in operational efficiency among routes within the same municipal collection system. It should be noted that routes MON14-MON18 were retained in the DEA analysis even though they were excluded from the subsequent optimization process. This distinction reflects the different purposes of the two methods. The VRP procedure implemented in Network Analyst was used to identify opportunities for spatial reorganization and distance reduction, which were limited for routes predominantly serving individual household bins. DEA, on the other hand, evaluates how efficiently each route uses its operational inputs relative to the collection service it provides. For this reason,

MON14-MON18 remained relevant decision-making units and were included when assessing the relative efficiency of the existing collection system. Their inclusion also provides a broader benchmark for comparing routes with different operational and service characteristics. The DEA results further support the importance of this distinction. Although routes MON14-MON18 offered limited scope for spatial route optimization, their efficiency was not necessarily high. In particular, MON16 and MON17 recorded some of the lowest efficiency scores in the analysed sample, while MON18 also remained below the efficiency frontier. This suggests that the absence of opportunities for further distance-based optimization should not be interpreted as evidence of overall operational efficiency. Inefficiency may instead arise from the relationship between travel time and distance on the input side and the amount of waste collected and number of collection points served on the output side. Table 3 compares the efficiency scores obtained for the existing and VRP-based route planning scenarios. The efficiency pattern changed only slightly after route optimization. Six routes (MON13, MON15, MON21, MON22, MON31, and MON32) recorded an efficiency score of 1.00 in both scenarios, meaning that they remained on the efficiency frontier. For most of the remaining routes, the differences between the two scenarios were relatively small.

Table 3 Scenario-specific DEA efficiency scores for existing and VRP-based route planning scenarios

Route	Existing - route frontier	Optimized - route frontier	Difference ($\Delta\theta_i$)	Trend
MON11	0.75	0.76	+0.010	↑
MON12	0.92	0.91	-0.010	↓
MON13	1.00	1.00	0.0000	→
MON14	0.98	0.98	0.00	→
MON15	1.00	1.00	0.000	→
MON16	0.63	0.63	0.000	→
MON17	0.61	0.63	+0.020	↑
MON18	0.71	0.71	0.000	→
MON21	1.00	1.00	0.000	→
MON22	1.00	1.00	0.000	→
MON23	0.83	0.81	-0.020	↓
MON31	1.00	1.00	0.000	→
MON32	1.00	1.00	0.000	→
MON33	0.91	0.89	-0.020	↓

Note: ↑ indicates an increase, → no change, and ↓ a decrease in relative DEA efficiency

Among the inefficient routes, MON11 showed a slight improvement, increasing from 0.75 to 0.76, while small decreases were observed for MON12 (0.92 to 0.91), MON23 (0.83 to 0.81), and MON33 (0.91 to 0.89). A lower DEA score after the optimization process does not necessarily mean that these routes became operationally worse. The VRP-based route planning primarily targets travel distance, whereas DEA considers the relationship between both inputs and the outputs. Moreover, since each scenario was evaluated against its own efficiency frontier, improvements achieved by other routes can influence the relative position of an individual DMU. The DEA results should be interpreted as changes in relative efficiency within each scenario rather than as a direct measure of the physical improvement achieved through optimization. An interesting result can be observed for MON17. This route was not modified during the optimization because it belongs to the group of routes predominantly serving individual household bins. Nevertheless, its DEA efficiency score increased from 0.61 to 0.63. This change does not reflect an improvement in the route itself, since its input and output values remained unchanged. Rather, it illustrates the relative nature of DEA. Because the existing and optimized scenarios were evaluated separately, differences in the performance of other routes affected the efficiency frontier and, consequently, the relative position of MON17 within the analysed set. In other words, a DEA score can change even when the characteristics of an individual route remain unchanged, if the reference environment against which it is evaluated changes. MON32 shows a different pattern, achieving the largest improvement through VRP-based route planning, with the route length reduced from 37.03 km to 29.70 km, resulting in a distance saving of 19.81%. Despite this substantial reduction, its DEA score remained at 1.00. MON32 was already located on the efficiency frontier before optimization and remained there afterward, since the improvement in route length could not produce a further increase in its DEA score beyond the maximum value of 1.00.

While this scenario-specific comparison is useful for understanding the relative efficiency of routes within each operational scenario, it does not allow the effect of route optimization to be measured directly. This is because the efficiency scores for the existing and optimized configurations are calculated against different efficiency frontiers. As a result, differences in θ may arise not only from changes in the individual routes, but also from changes in the frontier used as the benchmark. To overcome this limitation and provide a more direct and consistent comparison between the existing and optimized configurations, an additional DEA analysis using a common frontier was performed. Using a common frontier makes the efficiency scores directly comparable across the two scenarios. The results of the common-frontier DEA analysis are presented in Table 4, which reports the efficiency scores and corresponding input

reduction potentials for both the existing and optimized route configurations, together with the change in efficiency for each route.

Table 4 Common-frontier DEA efficiency scores for existing and alternative route configurations

Route	Existing efficiency - $\theta_{i,\ E}$	Existing input reduction potential	Optimized efficiency - $\theta_{i,O}$	Optimized input reduction potential	Difference - $\Delta\theta_i$	Trend
MON11	0.746	25.40%	0.746	25.40%	0.000	➡
MON12	0.916	8.40%	0.903	9.70%	-0.013	⬇
MON13	1.000	0.00%	1.000	0.00%	0.000	➡
MON14	0.975	2.50%	0.975	2.50%	0.000	➡
MON15	1.000	0.00%	1.000	0.00%	0.000	➡
MON16	0.626	37.40%	0.626	37.40%	0.000	➡
MON17	0.612	38.80%	0.612	38.80%	0.000	➡
MON18	0.711	28.90%	0.711	28.90%	0.000	➡
MON21	1.000	0.00%	1.000	0.00%	0.000	➡
MON22	1.000	0.00%	1.000	0.00%	0.000	➡
MON23	0.817	18.30%	0.801	19.90%	-0.016	⬇
MON31	1.000	0.00%	1.000	0.00%	0.000	➡
MON32	0.986	1.40%	1.000	0.00%	0.014	⬆
MON33	0.895	10.50%	0.887	11.30%	-0.008	⬇

Note: ↑ indicates an increase, → no change, and ↓ a decrease in relative DEA efficiency

The common-frontier analysis provides a clearer and more consistent basis for comparing the existing and optimized route configurations. As shown in Table 4, routes for which the input and output values remained unchanged also retained the same efficiency scores. An adequate example is MON17, with an efficiency score of 0.612 in both configurations. In the scenario-specific analysis (Table 3), however, its efficiency score increased from 0.61 to 0.63 despite no change in the route itself. This difference can therefore be attributed to the change in the reference frontier rather than to route optimization. By evaluating both configurations against the same frontier, the common-frontier analysis eliminates this benchmarking effect and allows changes in efficiency to be interpreted more directly.

The same pattern can be seen for the other routes that remained unchanged. MON11 retained an efficiency score of 0.746, while MON13 remained fully efficient at 1.000. No change was also observed for MON14, MON15, MON16, MON18, MON21, MON22 and MON31. This confirms that, when route characteristics remain unchanged, the common-frontier approach produces the same efficiency assessment for both configurations. Among the routes affected by optimization, the clearest improvement was observed for MON32. Its efficiency score increased from 0.986 to 1.000 ($\Delta\theta_i$ = +0.014), meaning that the optimized configuration reached the common efficiency frontier. This improvement coincided with a substantial reduction in route length, from 37.03 km to 29.70 km. Interestingly, this change was not visible in the scenario-specific analysis, where MON32 was classified as fully efficient under both separately estimated frontiers. However, a reduction in route distance did not necessarily lead to a higher DEA efficiency score. The efficiency score of MON12 decreased slightly from 0.916 to 0.903, while MON23 decreased from 0.817 to 0.801 and MON33 from 0.895 to 0.887. This can be explained by the multidimensional nature of the DEA model. Although route optimization primarily targeted travel distance, DEA evaluates route length and travel time simultaneously in relation to the outputs produced. A shorter route therefore does not automatically result in a higher efficiency score, as the final DEA assessment depends on the combined relationship between inputs and outputs.

Overall, the two DEA analyses provide complementary perspectives on route performance. While the scenario-specific analysis characterizes relative efficiency within each operational scenario, the common-frontier analysis provides a consistent benchmark for directly assessing efficiency changes associated with route optimization and is therefore used as the primary basis for evaluating its effects.

CONCLUSION

This study showed that combining VRP-based route planning with DEA provides a useful way to evaluate municipal waste collection from different perspectives. VRP-based route planning identified opportunities to reduce unnecessary travel, although the potential for improvement varied between routes. Among the analysed routes, MON32 showed the greatest reduction in distance, decreasing by 7.33 km (19.81%), while several existing routes

remained unchanged. The DEA results provided an additional perspective by showing that shorter routes are not necessarily more efficient when route length, travel time, collected waste, and the number of collection points are considered simultaneously. The scenario-specific analysis showed how the routes performed relative to one another within each operational scenario. The common-frontier analysis then allowed the existing and optimized routes to be assessed using the same benchmark. Under this comparison, MON32 improved from 0.986 to 1.000 and reached the efficiency frontier, while some routes became slightly less efficient despite reductions in travel distance. These findings highlight the value of combining VRP-based route planning with DEA rather than evaluating route performance based on travel distance alone.

The ArcGIS-generated route configurations should be interpreted as heuristic improvements over the recorded routes, as global optimality was not assessed in this study. The purpose of the routing stage was to generate a feasible alternative operational scenario for subsequent efficiency evaluation rather than to compare the performance of different optimization algorithms. A comparative evaluation of heuristic, metaheuristic, and exact solution approaches could therefore be considered in future research. Overall, the proposed approach can support more efficient route planning and resource use in municipal waste collection, while reductions in travel distance may also contribute to lower fuel consumption and associated operating costs. Future research could also broaden the assessment by incorporating environmental variables, particularly fuel consumption and related emissions. Their inclusion would require direct measurements for individual routes and would allow efficiency to be evaluated from both operational and environmental perspectives.

REFERENCES

Amal, L., Son, L. H., Chabchoub, H., & Lahiani, H. (2020). Analysis of municipal solid waste collection using GIS and multi-criteria decision aid. *Applied Geomatics*, 12(2), 193-208. https://doi.org/10.1007/s12518-019-00291-6

Banker, R.D., Charnes, A., & Cooper, W.W. (1984). Some models for estimating technical and scale inefficiencies in Data Envelopment Analysis. *Management Science*, 30(9), 1078-1092.

Bošković, G., Cvetanović, A. M., Jovičić, N., Jovanović, A., Jovičić, M., & Milojević, S. (2024). Digital technologies for advancing future municipal solid waste collection services. In F. Theofanidis, O. Abidi, A. Erturk, S. Colbran, & E. Coşkun (Eds.), Digital transformation and sustainable development in cities and organizations (pp. 167-192). IGI Global Scientific Publishing. https://doi.org/10.4018/979-8-3693-3567-3.ch008

Bošković, G., Jovičič, N. (2015). Fast methodology to design the optimal collection point locations and number of waste bins: a case study. *Waste management & Research*, 33(12), 1094-1102. https://doi.org/10.1177/0734242X15607426

Charnes, A., Cooper, W.W., & Rhodes, E. (1978). Measuring the efficiency of decision-making units. *European Journal of Operational Research*, 2(6), 429-444.

Choiron, M., Rusdianto, A. S., & Amilia, W. (2023). Recent Trend of Renewable Energy From Agricultural Wasted Biomass. In A. Al-Baarri & D. Afifah (Eds.), Food Sustainability, Environmental Awareness, and Adaptation and Mitigation Strategies for Developing Countries, pp. 151-166. IGI Global Scientific Publishing. https://doi.org/10.4018/978-1-6684-5629-3.ch009

Daraio, C., Di Leo, S., & Simar, L. (2024). Viable eco-efficiency targets for waste collection communities. *Scientific Reports,* 14, Article 15038. https://doi.org/10.1038/s41598-024-66077-y

Das, S., Baral, A., Rafizul, I. M., & Berner, S. (2024). Efficiency enhancement in waste management through GIS-based route optimization. *Cleaner Engineering and Technology*, 21, 100775. https://doi.org/10.1016/j.clet.2024.100775

Dijkstra, E. W. (1959). A note on two problems in connexion with graphs. *Numerische Mathematik*, 1(1), 269-271. https://doi.org/10.1007/BF01386390

ESRI. (2026, August 1st). ArcGIS Network Analyst: https://www.esri.com/en-us/arcgis/products/arcgis-network-analyst/overview

Galeb System. (2023, October 11th). Galeb Orsis fleet monitoring system: http://gps.galeb.com/oris11/

García-Sánchez, I. M. (2008). The performance of Spanish solid waste collection. *Waste Management & Research*, 26(4), 327-336. https://doi.org/10.1177/0734242X07081486

Golany, B., & Roll, Y. (1989). An application procedure for DEA. *Omega*. 17 (3), 237-250. https://doi.org/10.1016/0305-0483(89)90029-7

Li, B., & Xu, J. (2008). An evaluation model based on data envelopment analysis and its application to county circular economy. *World Journal of Modelling and Simulation*, 4(1), 35-43.

Lombardi, G. V., Gastaldi, M., Rapposelli, A., & Romano, G. (2021). Assessing efficiency of urban waste services and the role of tariff in a circular economy perspective: An empirical application for Italian municipalities. *Journal of Cleaner Production*, 323, 129097. https://doi.org/10.1016/j.jclepro.2021.129097

Mirmozaffari, M., & Kamal, N. (2024). A data envelopment analysis model for optimizing transfer time of ischemic stroke patients under endovascular thrombectomy. *Healthcare Analytics*, 6, 100364. https://doi.org/10.1016/j.health.2024.100364

Nasrabadi, N. (2018). A sequence of targets toward a common best practice frontier in DEA. *Journal of Industrial Engineering International.* 15, 695-707. https://doi.org/10.1007/s40092-018-0300-8

OpenStreet. (2023, October 25th). OpenStreetMap: www.openstreetmap.org

PUC Šumadija. (2026, August 20th). PUC Šumadija: https://www.jkpsumadija.rs/

Robin, T. A., Khan, M. A., Kabir, N., Rahaman, S. T., Karim, A., Mannan, I. I., George, J., & RashidI. (2019). Using spatial analysis and GIS to improve planning and resource allocation in a rural district of Bangladesh. *BMJ Global Health,* 4(Suppl 5), e000832. https://doi.org/10.1136/bmjgh-2018-000832

Ruiz, J.L., Sirvant, I. (2016). Common benchmarking and ranking of units with DEA. *Omega* 65, 1-9. https://doi.org/10.1016/j.omega.2015.11.007

Son, L. H. (2014). Optimizing Municipal Solid Waste collection using Chaotic Particle Swarm Optimization in GIS based environments: A case study at Danang city, Vietnam. *Expert Systems with Applications*, 41(18), 8062-8074. https://doi.org/10.1016/j.eswa.2014.07.02 0

Sousa, V., Drumond, A., & Meireles, I. (2024). Fuel consumption rate and emissions variability in waste collection services routes: Case study of Cascais Ambiente. *Environmental Science and Pollution Research International*. 31, 17732-17747. https://doi.org/10.1007/s11356-023-29045-z

Xin, C., Wang, L., Liu, B., Yuan, Y. H., & Tsai, S. B. (2021). An Empirical Study for Green Transportation Scheme of Municipal Solid Waste Based on Complex Data Model Analysis. *Mathematical Problems in Engineering*, 6614312, 1-17. https://doi.org/10.1155/2021/6614312

The 11th International Congress
Motor Vehicles & Motors 2026
Kragujevac, Serbia
October 8th - 9th, 2026

Motor Vehicles & Motors

MVM2026-046
https://doi.org/10.24874/CMVM2026.046
Original scientific paper

Aikaterini Zafeiri[1]
Clio Vossou[2]
Dimitrios Koulocheris[3]

FLUID-STRUCTURE INTERACTION IN A TANK VEHICLE TRANSPORTING LIQUID FUEL

ABSTRACT: Sloshing in tank vehicles transporting liquid fuels is influencing the vehicle stability during braking and cornering manoeuvres, increasing the rollover risk. The requirements for the design and the construction of metallic tanks intended for the carriage of liquid fuels are described in EN13094. According to this standard, finite element analysis of the tank simulating dynamic driving conditions, operating conditions and test pressure conditions is required for the assessment of the structural integrity of the tank as well as its mounting on the heavy vehicle. In this paper, a two-way fluid-structure interaction finite element model of a box-shaped tank during the braking conditions described in EN13094 is built in Ansys Workbench. A computational fluid dynamics simulation with the volume of fluid (VOF) method is coupled to a transient structural simulation in order to model the movement of the fluid in the tank and monitor its effect on the structural dynamic response of the tank construction. Two different filling ratios have been simulated (80% and 20% of its maximum carrying capacity) and the stress distribution on the tank shell as well as the forces developed on mounting of the tank on the vehicle are investigated providing a useful insight for the construction of the tank vehicle.

KEYWORDS: tank vehicle, sloshing, fluid-structure interaction, EN13094, structural integrity

INTERAKCIJA FLUIDA I KONSTRUKCIJE CISTERNE ZA TRANSPORT TEČNOG GORIVA

REZIME: “Pljuskanje“ u cisternama koje prevoze tečna goriva utiče na stabilnost vozila tokom kočenja i manevara u krivinama, povećavajući rizik od prevrtanja. Zahtevi prema projektovanju i konstrukciji metalnih rezervoara namenjenih za prevoz tečnih goriva opisani su u standardu EN13094. Prema ovom standardu, analiza rezervoara metodom konačnih elemenata koja simulira dinamičke uslove vožnje, uslove rada i uslove pritiska pri ispitivanju potrebna je za procenu strukturnog integriteta rezervoara, kao i njegovog postavljanja na teško vozilo. U ovom radu,

[1] *Aikaterini Zafiri, Mechanical Engineer, Vehicles Laboratory, School of Mechanical Engineering, National Technical University of Athens, Zografou Campus, 9, Iroon Polytechniou str, 15772 Zografou*
[2] *Clio Vossou, Assistant professor, Vehicles Laboratory, School of Mechanical Engineering, National Technical University of Athens, Zografou Campus, 9, Iroon Polytechniou str, 15772 Zografou, klvossou@mail.ntua.gr, https://orcid.org/0000-0002-4665-7759*
[3] *Dimitrios Koulocheris, Professor, Vehicles Laboratory, School of Mechanical Engineering, National Technical University of Athens, Zografou Campus, 9, Iroon Polytechniou str, 15772 Zografou, dbkoulva@mail.ntua.gr, https://orcid.org/0000-0002-1379-5805*

izgrađen je u Ansys Workbench-u dvosmerni model konačnih elemenata interakcije fluida i strukture rezervoara u obliku kutije tokom uslova kočenja opisanih u EN13094. Računarska simulacija dinamike fluida metodom zapremine fluida (VOF) povezana je sa prolaznom strukturnom simulacijom kako bi se modeliralo kretanje fluida u rezervoaru i pratio njegov uticaj na strukturni dinamički odziv konstrukcije rezervoara. Simulirana su dva različita odnosa punjenja (80% i 20% njegove maksimalne nosivosti) i ispitana je raspodela napona na omotaču rezervoara, kao i sile koje se razvijaju pri montaži rezervoara na vozilo, što pruža koristan uvid za konstrukciju cisterne.

KLJUČNE REČI: cisterna, „pljuskanje“ tečnosti, interakcija fluida i konstrukcije, EN13094, strukturni integritet

INTRODUCTION

Liquid fuels are critical energy carriers used in the industrial and commercial activities as well as in transport. Their supply chain includes long-distance transportation by marine tankers, pipelines, and rail tank wagons, followed by shorter-distance distribution using road tank vehicles. Maritime transport mainly supports international and intercontinental flows of crude oil and refined products, whereas pipelines provide continuous transfer between production, storage, and refining facilities. Tank vehicles constitute a primary means of supplying fuel stations, industrial plants and local distribution networks. Liquid fuels, in the Agreement concerning the International Carriage of Dangerous Goods by Road (ADR 2025) are classified as Class 3 – flammable liquids. Consequently, their transportation is subjected to strict technical and operational safety requirements. One of the operational safety requirements in ADR (2025) regarding tanks that are not subdivided in compartments by partitions or surge plates with a capacity not exceeding 7500 l, specifies a filling ratio of either no more than 20% or no less than 80% of the tank capacity.

Furthermore, the design and construction requirements for metallic gravity-discharge tanks intended for the carriage of dangerous goods by road and rail is described in detail in EN 13094:2020+A1:2022. This Standard includes design and construction requirements related to the tank shell, openings, closures, pipework, mountings and structural equipment and describes the functional and test loads applied on the tank by the transported material. For the structural verification of the tank shell, its attachments and the structural equipment, the Standard specifies that the tank shall withstand, separately, an acceleration of 2 g in the direction of travel, simulating braking conditions, an acceleration of 1 g acting at right angles to the direction of travel simulating cornering manoeuvre, an acceleration of 1 g acting downwards and 2 g acting upwards, all of them applied to the maximum design mass.

The dynamic behaviour of liquid cargo in partially filled tanks is an important factor affecting road transport safety. This phenomenon, commonly referred to as sloshing, describes the oscillatory motion of the liquid free surface when the tank is subjected to external excitation, such as acceleration, braking, cornering, lane-change manoeuvres. Abramson (1966) provided one of the fundamental contributions to the study of liquid dynamics in moving containers and established a theoretical and experimental basis for subsequent sloshing research. Liquid motion causes time-dependent changes in the pressure distribution acting on the tank walls, generating dynamic forces and moments and, in some cases, local impact loads at wave-impingement regions. In road tank vehicles, these effects may influence the structural loading of the tank shell, internal baffles and support connections, while also affecting vehicle dynamic stability, braking performance and rollover risk. Li et al. (2013) investigated the driving stability of tank vehicles using an equivalent pendulum-based representation of liquid sloshing, while Talebitooti et al. (2015) examined the influence of sloshing on the rollover-threshold acceleration of tank vehicles. The severity of sloshing is primarily governed by the filling ratio of the tank, the tank geometry, the presence and arrangement of baffles or surge-control devices, the properties of the transported liquid and the characteristics of the imposed motion. Particularly adverse conditions may occur when the excitation frequency approaches the natural frequencies of the liquid, resulting in amplified free-surface motion and hydrodynamic loads.

In the literature, sloshing has been investigated through experimental, theoretical and numerical approaches. Experimental studies are commonly conducted using scaled or full-scale tanks subjected to representative acceleration, braking, cornering or lane-change manoeuvres, while the liquid and structural responses are monitored through pressure sensors, free-surface measurements, accelerometers and force and moment measuring systems. Such experiments are essential because sloshing is highly nonlinear and transient and they also provide the data required for numerical model validation. Xie et al. (2024) combined experimental, theoretical and numerical approaches to investigate sloshing behaviour, while Firoozkoohi et al. (2010) examined experimentally and numerically the effect of swash bulkheads on sloshing mitigation. Early theoretical approaches were primarily based on potential-flow theory, usually assuming inviscid and incompressible flow. These methods are mainly employed to estimate free-surface natural frequencies and to describe small-amplitude oscillations in relatively simple tank geometries. Within this framework, Nakayama and Washizu (1981) applied the Boundary Element Method to two-dimensional nonlinear sloshing problems. Although potential-flow and Boundary Element approaches involve relatively low computational cost, they are limited in their ability to represent viscous effects, turbulence, wave breaking, and local impact pressures.

Equivalent mechanical models have also been developed for vehicle-dynamics applications, in which liquid motion is represented by lumped masses, springs, dampers, or equivalent pendula. Such models are suitable for multi-degree-of-freedom vehicle models and stability-control analyses because they substantially reduce computational cost. Shrimali and Jangid (2011) employed simplified mechanical representations to investigate the response of liquid-containing structures under dynamic excitation, whereas Li et al. (2013) proposed an equivalent pendulum formulation for the study of tank-truck stability. More recently, Qi et al. (2023) combined a multi-degree-of-freedom pendulum model with a free-surface fluctuation sensor to support real-time observation of liquid sloshing. However, equivalent mechanical models cannot accurately reproduce local wall-pressure distributions, impact loads, or the three-dimensional flow field developing around baffles and internal structural members.

The development of Computational Fluid Dynamics (CFD) has enabled a more detailed investigation of sloshing through the solution of the Navier–Stokes equations and the tracking of the air–liquid interface using multiphase-flow models. In particular, the Volume of Fluid (VOF) method is widely applied because it can capture the free surface, large wave deformation, liquid impact on tank walls, and interaction with internal baffles. Gómez-Goñi et al. (2013) performed a two-phase VOF analysis of sloshing in a rectangular container, while Ambade and Kale (2013) employed a CFD–VOF approach to investigate sloshing in a tank under acceleration and deceleration conditions. Ranganathan et al. (2008) also developed and validated a CFD–VOF model to assess different transverse-baffle configurations in a road tanker under braking, showing that baffle geometry, orifice location, and filling level strongly affect sloshing forces and pitch moments. Beyond the hydrodynamic response, Fluid–Structure Interaction (FSI) becomes important when thin-walled tanks, baffles, and support regions are considered. Arora and Vasudevan (2017) investigated sloshing-induced loads on a fuel tank structure and demonstrated the importance of coupled fluid and structural modelling. Arora et al. (2018) subsequently presented a partitioned FSI methodology for analysing sloshing-induced loads on a fuel tank structure.

In the present study, the sloshing in a road tank vehicle transporting liquid fuels is numerically investigated and the results are compared to the results of a static structural analysis. In more detail abrupt braking of a tank designed following the requirements of EN13094 (2022) is simulated. The followed approach combines a three-dimensional transient CFD simulation based on the Volume of Fluid (VOF) method, used to capture the air–liquid interface and calculate time-dependent hydrodynamic loads with a nonlinear transient finite-element structural analysis. A two-way Fluid–Structure Interaction (FSI) approach is implemented to account for the mutual interaction between liquid-induced pressure and the deformation of the tank structure. The structural response of the tank parts and the stress developed on the bolted connections of the tank to the vehicle is evaluated in terms of stress, displacement and reaction forces. The results are presented along with those obtained from a static structural analysis conducted using the EN 13094:2020+A1:2022 design loads. Moreover, two filling ratios, 20% and 80% of the maximum design mass, are examined using the FSI approach, corresponding to the limiting filling conditions specified in ADR (2025) for tank vehicles.

The remainder of this paper is organised as follows. Section 2 presents the description of the computational model including the CFD, structural and FSI-coupling methodology. Section 3 presents the numerical results, including the free-surface motion, hydrodynamic pressure, stress, displacement and response of the connection between the tank and the vehicle. Section 4 discusses the results obtained for each approach. Finally, Section 5 summarises the main conclusions.

ROAD TANK VEHICLE COMPUTATIONAL MODELLING

In this section the geometrical and the numerical modelling of the road tank vehicle is presented with emphasis to the CFD and the structural computational modelling.

Geometrical models

Two geometrical models have been implemented, one for the CFD and one for the Structural simulation. The tank geometry was developed in SolidWorks CAD software based on a design compliant with the requirements of EN 13094 (2022). As illustrated in ***Figure 1***, the tank has a box-shaped cross-section with rounded corners and is divided into six compartments by internal baffles. The tank shell cross-section has a width of 2348 mm, a height of 1608 mm, and a corner radius of 584 mm. The tank has an overall length of 6910 mm and a total volume of 22124 l. The structural model includes the shell, the covers, baffles, the six manholes, the four supports and the eight support plates. The support plates connect the tank to the vehicle chassis through bolted connection. Through the bolted connection forces and moments arising from the tank weight and the sloshing-induced hydrodynamic loads are transferred to the vehicle chassis.

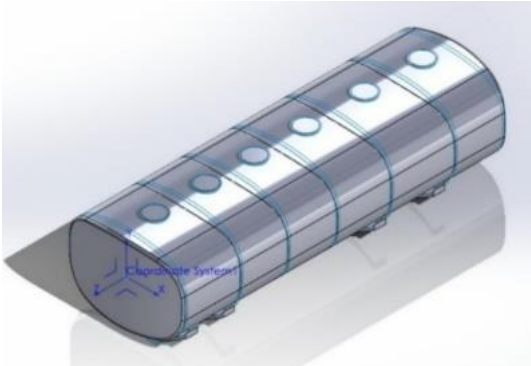

Figure 1 Three-dimensional geometrical model of the tank

The fluid domain was derived from the internal volume of the tank and it was designed in SolidWorks, as well, as the inverse volume of the solid tank model. This approach ensured geometrical consistency between the CFD and structural model of the tank. ***Figure 2*** illustrates the computational fluid domain corresponding to one compartment of the tank.

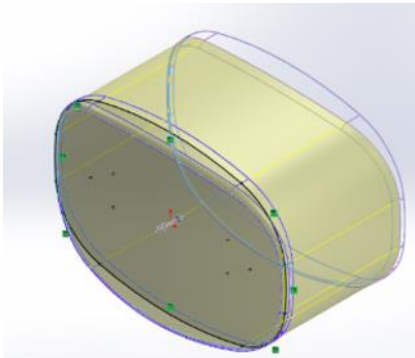

Figure 2 CAD model of the fluid domain of one tank compartment

Computational modelling

The movement of the liquid and the structural response of the tank structure are both modelled with CFD and Mechanical systems in ANSYS Workbench and they are coupled using the FSI tool.

Structural model

Within this framework, the tank geometry was imported into ANSYS Workbench as a thickness-free surface model. The thickness of each individual component was assigned using shell sections. Particularly, a thickness of 6 mm was assigned to the shell, covers, baffles and manholes, 8 mm were assigned to the supports and 20 mm were assigned to the support plates. The tank was manufactured with aluminium alloy EN AW-5186 (O/H111) with the mechanical properties provided in Table 1.

Table 1 Mechanical properties of EN AW-5186 (EN 14286, 2008)

Mechanical property	Unit	Value
Density	kg/m^3	2660
Elastic modulus	MPa	70300
Poisson's ratio		0.30
Tensile strength	MPa	125

All connections between the individual structural components of the tank were defined as bonded representing the welded joints of the structure. Consequently, no relative sliding or separation was allowed between the connected surfaces, ensuring load transfer between the shell, covers, baffles, supports and support plates.

The boundary conditions applied to the structural model are shown in ***Figure 3***. The eight support plates were assigned fixed support boundary conditions to represent the connection between the tank and the vehicle chassis. The self-weight of the structure was taken into account by applying standard earth gravity. In addition, the internal tank surfaces in contact with the liquid were defined as a System Coupling Region to enable data exchange with the fluid model.

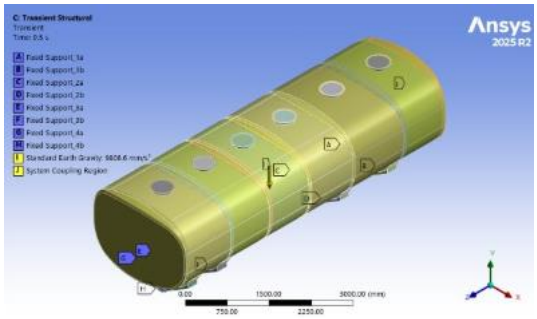

Figure 3 Boundary conditions of the structural model in ANSYS Transient Structural

The surface geometry of the tank was discretized using SHELL181 finite elements, which are suitable for the modelling of thin-walled metallic structures. Meshing was performed in the ANSYS Meshing environment using a characteristic element size of approximately 73 mm. The final structural mesh comprised 37742 FE and 39371 nodes. The mean aspect ratio was 1.11, while the mean element quality was 0.99, indicating a high-quality mesh.

The transient structural analysis was performed using a constant time step of 0.0001 s. This time step was selected to match that of the Fluent simulation and ensure temporal consistency during the two-way FSI coupling.

CFD model

The liquid fuel, in the CFD model was considered to have the properties of water and its flow was considered transient, incompressible and two-phase, consisting of water and air. The free-surface motion was simulated using the Volume of Fluid (VOF) multiphase model, which enables tracking of the water-air interface and representation of the large liquid motions. An inviscid flow assumption was adopted to provide a computationally efficient representation of the global sloshing response and the resulting transient wall-pressure distribution. The fluid domain was meshed in ANSYS Meshing using the CFD/Fluent meshing option and a characteristic element size of 150 mm. The final mesh comprised 605896 cells and 136985 nodes. The resulting computational mesh is presented in Figure 4.

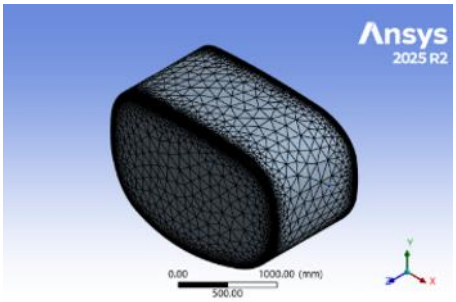

Figure 4 Computational mesh of the fluid model

The simulations were performed using the pressure-based solver in ANSYS Fluent. Pressure-velocity coupling was achieved using the PISO algorithm. The Body Force Weighted scheme was employed for pressure discretization, the Second Order Upwind scheme for the momentum equations and the Compressive scheme for volume-fraction discretization. Time integration was performed using the First Order Implicit scheme. To account for changes in the computational domain during the solution, the dynamic mesh model was activated in ANSYS Fluent. Mesh motion was handled using smoothing with implicit update, without remeshing. In the two-way fluid-structure interaction analyses, the tank wall surfaces participated in the coupling with the structural model through ANSYS System Coupling.

The flow field was initialized at rest, with zero initial velocity throughout the domain. The initial distribution of the liquid phase was imposed using cell registers and patching to represent tank filling levels of 80% and 20%. The simulations were performed with a constant time step of 0.0001 s and a maximum of 20 inner iterations per time step. For the braking simulation, standard gravitational acceleration was applied in the vertical direction, while a longitudinal acceleration of 2g was imposed for the first 0.05 s of the analysis to be in accordance with the braking dynamic load specified in EN 13094 (2022). The duration of the imposed acceleration was defined in the present numerical model to initiate the liquid motion and reproduce the subsequent transient sloshing response. After 0.05 s, the longitudinal acceleration was set to zero, allowing the subsequent sloshing response of the liquid inside the tank to develop. The total simulation time was 0.50 s.

RESULTS

The presented results focus on the displacement along the longitudinal axis, the equivalent Von Mises stress, the time evolution of the water-probe level at the tank centre and the corresponding evolution of the fluid field. For each filling ratio, representative result snapshots and time histories of the corresponding quantities are presented. In the plots, the original time-history signal is shown together with its FFT-filtered counterpart, while the maximum value of the filtered signal is also indicated. Furthermore, the results of the static structural analysis provisioned in EN13094 (2022) simulating braking are presented.

Filling ratio of 80%

The time history of the Von Mises stress for the 80% filling ratio is presented in Figure 6. The plot shows the original signal, the filtered signal and the maximum value of the filtered response. The maximum filtered von Mises stress is equal to 60.70 MPa and occurs at t=0.105s.

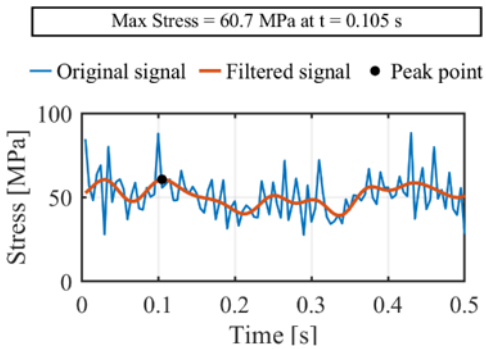

Figure 6 Time history of Von Mises stress during longitudinal braking, 80% filling level

The distribution of the equivalent Von Mises stress at the time of its maximum value (t=0.105 s) is shown in Figure 5 for the (a) tank and the (b) component with the maximum value.

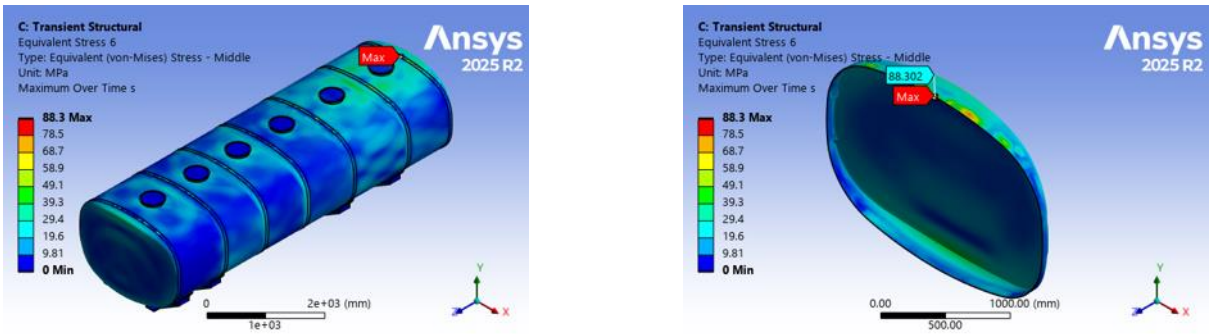

(a) (b)

Figure 5 Equivalent Von Mises stress distribution in the tank at the time of maximum stress during longitudinal braking (80% filling ratio)

The time history of the directional deformation is presented in Figure 6 (a) and the distribution of the longitudinal deformation in the braking direction, on the tank baffles at the instant of its maximum value is presented in Figure 6 (b). The maximum filtered longitudinal displacement is 6.07 mm, occurring at t= 0.025s.

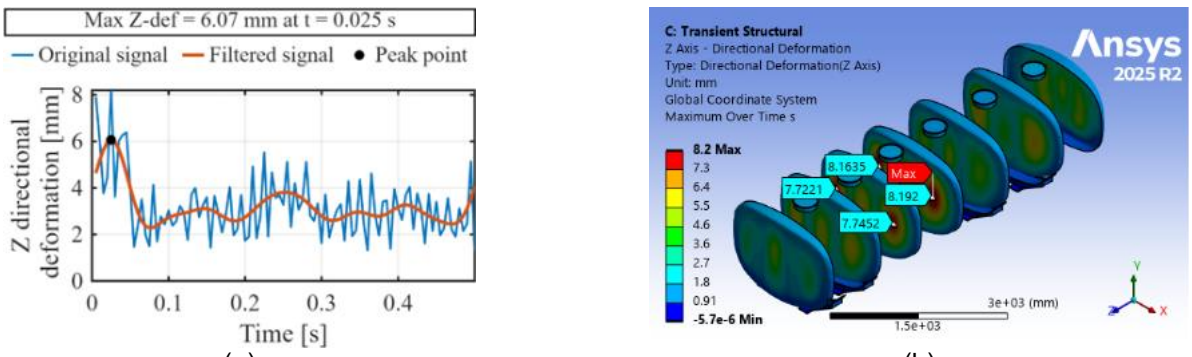

(a) (b)

Figure 6 Longitudinal directional deformation along the z-axis during longitudinal braking, 80% filling level: (a) ANSYS contour result; (b) time history of the z-directional deformation

The time history of the water-probe variable at the centre of the tank is presented in Figure 7(a). A snapshot of the fluid volume-fraction field at the time corresponding to the selected free-surface configuration is shown in Figure 7(b).

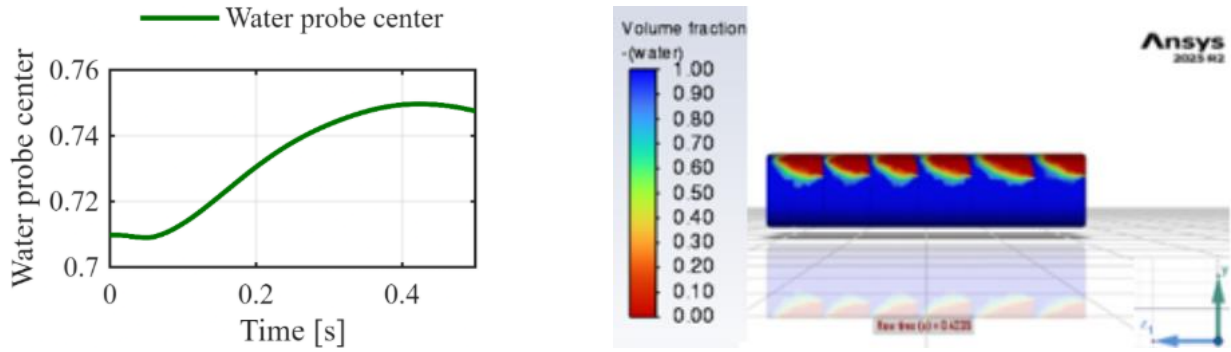

(a) (b)

Figure 7 Fluid response during longitudinal braking, 80% filling level: (a) central water-probe time history; (b) volume-fraction distribution at the selected time instant

Filling ratio of 20%

In the case of a filling ratio equal to 20% the time-history of the Von Mises stress during braking is presented in Figure 8(a). The maximum value of the filtered Von Mises stress is 8.25 MPa and it occurs at t=0.045 s. The distribution of the equivalent von Mises stress in the tank baffles is presented in Figure 8(b) at the same instant.

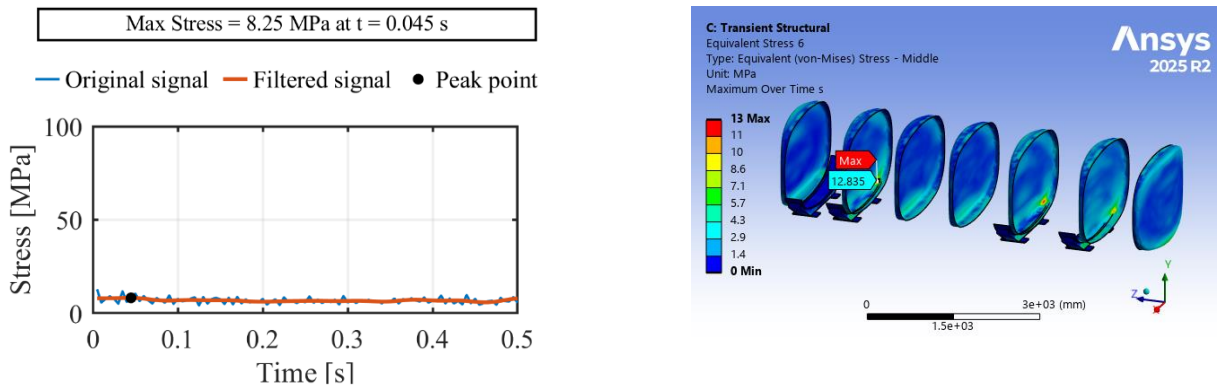

(a) (b)

Figure 8 Equivalent von Mises stress results for longitudinal braking at a 20% filling level (a) time history of the maximum equivalent von Mises stress, including the original and FFT-filtered signals, (b) equivalent von Mises stress distribution in the tank baffles at the instant of maximum stress

The distribution of the longitudinal displacement (Z-axis) on the tank baffles, on the braking direction along with the time history of the maximum value of longitudinal displacement is presented in Figure 9. In more detail, Figure 9 (a) includes the original signal, the filtered signal, and the point corresponding to the maximum value of the filtered signal. The maximum filtered longitudinal displacement is 0.39 mm, occurring at t=0.025 s.

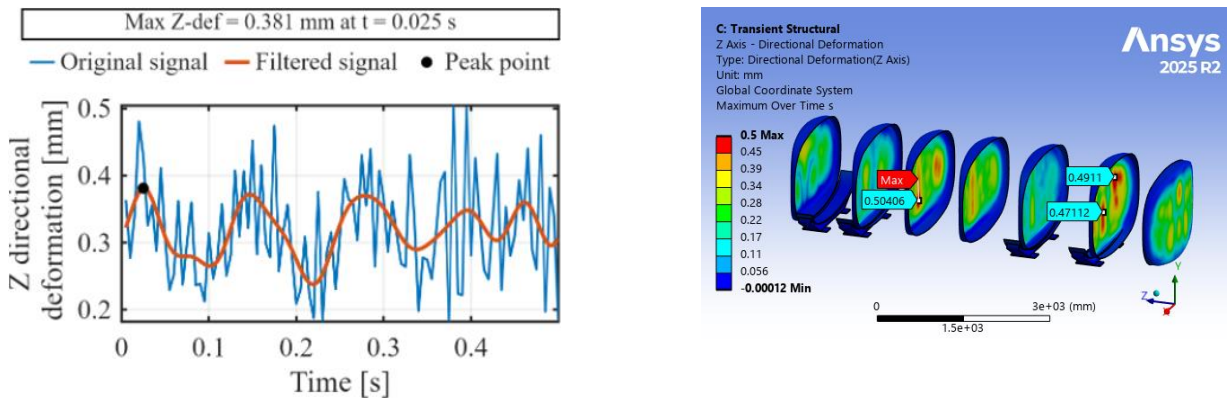

(a) (b)

Figure 9 Longitudinal displacement during braking, 20% filling: (a) baffle displacement distribution; (b) maximum displacement time history

For the 20% filling ratio, the time history of the water-probe variable at the tank center is presented in Figure 10 (a). The corresponding snapshot of the liquid volume-fraction field is shown in Figure 10 (b), at the time instant corresponding to the maximum water-probe value.

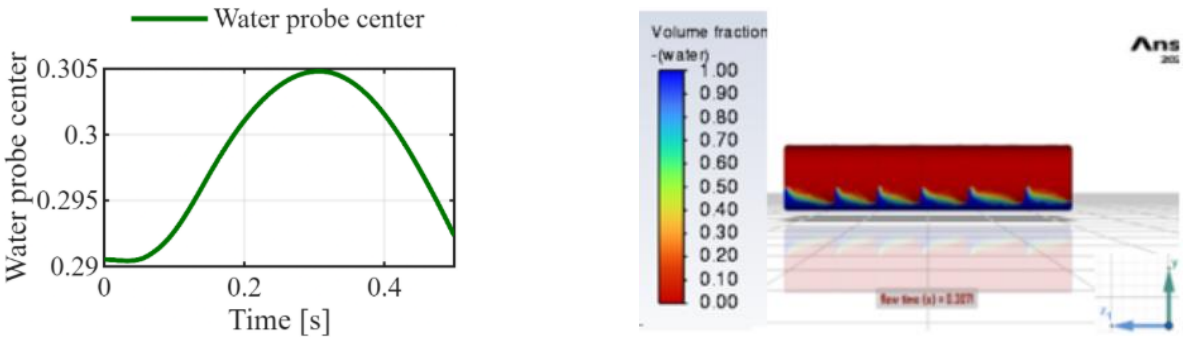

(a) (b)

Figure 10 Fluid response during longitudinal braking at a 20% filling level: (a) time evolution of the water-probe variable at the tank centre (b) liquid volume-fraction field at the instant of maximum water-probe value

Static structural analysis

In the case of the static structural analysis, a reference simulation was performed for a fully filled tank subjected to the longitudinal braking design load. In addition to gravity and a longitudinal acceleration of 2 g, a breather-valve pressure of 0.012 MPa and compartment-dependent pressures acting on the internal bulkheads were considered. The latter pressures represent the longitudinal inertial effect of the fully filled liquid cargo.

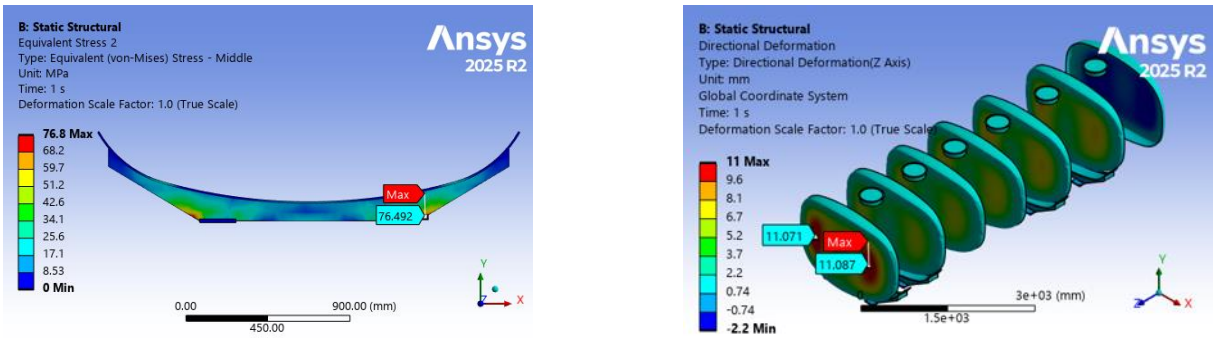

(a) (b)

Figure 11 Static structural response under longitudinal braking for the fully filled tank: (a) equivalent von Mises stress; (b) longitudinal displacement

The equivalent von Mises stress distribution obtained from the static analysis is shown in Figure 11 (a), while the longitudinal displacement along the z-axis, i.e., in the braking direction, is presented in Figure 11(b). The maximum equivalent von Mises stress was 76.8 MPa and occurred in the region of the first tank support. The maximum longitudinal displacement was approximately 11 mm and was observed at the first baffle.

Support plates

The locations of the support plates considered in the analysis are shown in Figure 12. For the 80% filling ratio, the maximum equivalent von Mises stress is equal to 374.1 MPa and it appears on the plate F3b. In contrast, for the 20% filling ratio, the plate with the maximum Von Mises stress shifts to F2a and the maximum value is limited to 58.8 MPa.

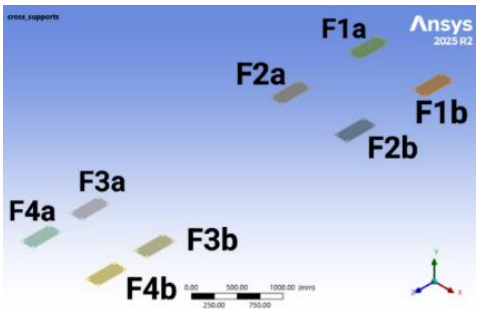

Figure 12 Tank support plates

DISCUSSION

Reviewing the structural response of the tank in the two filling ratios is obvious that both the peak value and the time of the peak value changes. The maximum filtered von Mises stress is 60.7 MPa for the 80% filling ratio, compared with 8.25 MPa for the 20% filling ratio. Therefore, the stress obtained at 80% filling is approximately 7.4 times higher than that at 20% filling ratio. This ratio is greater than the ratio of the filling ratios, which is equal to 4. Consequently, the structural response under braking does not exhibit a linear dependence on the filling ratio. This difference can be attributed to the combined effects of the varying liquid mass, inertial loading, free-surface evolution, and fluid–structure interaction. The time at which the maximum filtered Von Mises stress occurs also differs between the two cases. For the 80% filling ratio, the maximum occurs 0.08 s later compared to the 20% filling level. The shift in peak time indicates that the dynamic evolution of the sloshing phenomenon and the transfer of loads to the tank structure are affected by the filling ratio.

In all approaches maximum value of equivalent Von Mises stress remains below both the material yield strength of 125 MPa and the design stress value of 93.75 MPa, corresponding to $0.75Re$ (EN13094, 2022). Therefore, the static braking load case does not exceed the adopted design criterion for the tank structure in any approach.

A similar variation is observed in the longitudinal deformation. The maximum filtered directional deformation is 6.07 mm for the 80% filling ratio, whereas it is 0.39 mm for the 20% filling ratio. This comparison reveals that the structural displacement in the braking direction is substantially greater at the higher filling ratio.

In Table 2 the value of the stress developed on the support plates, hence the bolted connection between the tank and the vehicle, is presented for the static structural analysis as well as the two FSI simulations.

Table 2 Maximum bolt stresses at the critical support plate under longitudinal braking

		Stress (MPa)		
Simulation	Critical plate	Axial	Shear	Equivalent
Static structural analysis	F4b	100	190	343
FSI, 80% filling	F3b	238	167	375
FSI, 20% filling	F2a	49	19	59

Table 2 shows that the 80% two-way FSI case produces the highest equivalent von Mises stress in the bolts, equal to 375 MPa at plate F3b. The static fully filled case produces a slightly lower equivalent stress of 343 MPa at plate F4b, but the highest shear stress, equal to 190 MPa. In contrast, the 20% two-way FSI case produces substantially lower axial, shear, and equivalent stresses, with a maximum equivalent stress of 59 MPa at plate F2a.

The comparison of the braking cases at 80% and 20% filling levels confirms that the 80% filling condition is clearly more critical for the bolted support connections while the static structural analysis provide stress values lower than that of the FSI for filling ration of 80%. Furthermore, the most critical support plate is not the same in all three cases. This indicates that both the approach and the filling ratio affect the mechanical response of the structure. The maximum equivalent stress, in the case of the static analysis, on the support plates is 343 MPa, which is slightly lower than the maximum value obtained by the FSI approach with 80% filling ratio.

CONCLUSIONS

In this paper, a tank for road transport of liquid fuels, designed according to EN13094 (2022), is computationally simulated in braking conditions, using two different approaches (two-way FSI and Static structural). Using the two-way FSI approach two filling ratios have been simulated, 80% and 20%. The results of the analyses demonstrated that the filling ratio has a substantial effect on the structural response of the road tank during longitudinal braking.

In more detail, it was shown that the static structural approach revealed the maximum value of Von Mises stress (76.80 MPa) followed by two-way FSI with 80% filling ratio which led to significantly more severe response compared to 20% filling ratio. Therefore, the maximum value of Von Mises stress obtained with FSI was 21% lower in the case of 80% filling ratio and 90% lower in the case of 20% filling ratio. The same observation was made for the axial deformation. Still, no approach led to stress values above design stress.

As far as the equivalent Von Mises stress developed on the support plates the FSI approach considering the filling ratio of 80% led to 10% higher value compared to the static structural approach. Comparing the different filling ratio is observed that a decrease of 4 times in the volume of the carried liquid lead to a reduction of the equivalent Von Mises stress by 83%.

Overall, the two-way FSI approach provided a detailed representation of the coupled liquid and structural response during the investigated braking manoeuvre. The static analysis, based on EN13094 (2022) is the reference approach

for structural verification, while the transient simulations complement it by capturing the evolution of sloshing-induced loads and their effect on the tank structure and its connection to the vehicle.

REFERENCES

Abramson, H. N. (1966). *The dynamic behavior of liquids in moving containers*. NASA SP 106. https://ntrs.nasa.gov/api/citations/19670006555/downloads/19670006555.pdf

ADR (2025), European Agreement Concerning the International Carriage of Dangerous Goods by Road (ADR); Economic Commission for Europe: Geneva, Switzerland; Committee on Inland Transport: Geneva, Switzerland; United Nations: New York, NY, USA, 2025.

Ambade, R., & Kale, R. (2013). CFD analysis of sloshing within tank. *International Journal Innovative Research of Technology and Science*, 15-120, 2.

Arora, S., & Vasudevan, S. (2017). Analysis of Sloshing-Induced Loads on the Fuel Tank Structure. Gothenburg: Chalmers University of Technology. https://odr.chalmers.se/bitstreams/899b3ee0-51ad-4dac-b264-a7960301fbba/download

Arora, S., Vasudevan, S., Etemad, S., & Sasic, S. (2018). A Partitioned FSI Methodology for Analysis of Sloshing-Induced Loads on a Fuel Tank Structure. *Proceedings of the 6th European Conference on Computational Mechanics and the 7th European Conference on Computational Fluid Dynamics*. Glasgow.

EN13094 (2022). Tanks for the Transport of DANGEROUS Goods-Metallic Tanks with a Working Pressure not Exceeding 0.5 Bar Design and Construction; British Standards Institution (BSI): London, UK, 2022.

Firoozkoohi, R., & Firoozkoohi, M. (2010). Experimental and Numerical Investigation of the Effect of Swash Bulkhead on Sloshing. *Proceedings of the 20th International Offshore and Polar Engineering Conference*. Beijing, International Society of Offshore and Polar Engineers (ISOPE).

Hasheminejad, S. M., & Amini, M. (2015). Effect of baffles on the sloshing in road tankers carrying lpg: a comparative numerical study. *Mathematical Problems in Engineering*, 359470. https://doi.org/10.1155/2015/359470

Khalid, M., Akhtar, M., Kumar, S. V. N., & Usman, U. A. (2014). Investigation and Development of Fuel Slosh CAE Methodologies. *SAE International*, Warrendale, PA. https://doi.org/10.4271/2014-01-1632

Kolaei, A. (2013). Liquid slosh and its influence on braking and roll responses of partly filled tank vehicles. Montreal, Concordia University.

Nakayama, T., & Washizu, K. (1981). The boundary element method applied to the analysis of two-dimensional nonlinear sloshing problems. *International Journal for Numerical Methods in Engineering*, 1631-1646, 17(11). https://doi.org/10.1002/nme.1620171105

Qi, Xiaojin, Zhang, Yingchao, Gao, Bolin. (2023). Observing liquid sloshing based on a multi-degree-of-freedom pendulum model and free surface fluctuation sensor. Sensors, 23(21), 8831. https://doi.org/10.3390/s23218831

Ranganathan, S. A., Ismail, K. A. R., & Al-Kaabi, A. A. (2008). Baffle design analysis for a road tanker: transient fluid slosh approach. *SAE* International, 2008-01-2670. https://doi.org/10.4271/2008-01-2670

Shrimali, M. K., Jangid, R. S. (2011). Earthquake response of liquid storage tanks with sliding systems. *Journal of Seismology and Earthquake Engineering*, 4(2&3), 51-61.

The 11th International Congress
Motor Vehicles & Motors 2026
Kragujevac, Serbia
October 8th - 9th, 2026

Motor Vehicles & Motors

MVM2026-048
https://doi.org/10.24874/CMVM2026.048
Original scientific paper

Ognjen Jovanović[1]
Milan Matijević[2]

APPLICATION OF THE TIA PORTAL ENVIRONMENT FOR SOFTWARE-IN-THE-LOOP SIMULATION OF PLC CONTROL OF A FIRST-ORDER DYNAMIC SYSTEM

ABSTRACT: In the modern production systems, PLC technology represents one of the fundamental elements of industrial automation, while its successful implementation requires verification of the control logic before connection to a real controlled process. This paper presents a simple and educationally applicable Software-in-the-Loop simulation approach in the Siemens TIA Portal environment. As an illustrative example, PLC control of a DC motor is considered, where the motor dynamics are represented by a discrete first-order system model. The PLC program implements basic START/STOP logic, calculation of the dynamic response using a difference equation, acquisition of relevant signals, and their visualization. Special attention is given to displaying the control and output signals on a virtual HMI device, enabling real-time observation of transient processes without using a real motor or expensive laboratory equipment. The presented approach is particularly useful in engineering education, as it helps students understand the relationship between PLC programming, system dynamics, data acquisition, and process visualization. The paper demonstrates that TIA Portal can serve as an effective environment for safe, accessible, and reproducible verification of basic control concepts.

KEYWORDS: PLC, TIA Portal, Software-in-the-Loop, HMI, real-time simulation, DC motor, data acquisition

PRIMENA TIA PORTAL OKRUŽENJA ZA SOFTWARE-IN-THE-LOOP SIMULACIJU PLC UPRAVLJANJA DINAMIČKIH SISTEMA PRVOG REDA

REZIME: U savremenim proizvodnim sistemima PLC tehnologija predstavlja jedan od osnovnih elemenata industrijske automatizacije, dok njena uspešna primena zahteva proveru upravljačke logike pre povezivanja sa realnim objektom upravljanja. U radu je predložen nov i obrazovno primenljiv pristup Software-in-the-Loop simulaciji u Siemens TIA Portal okruženju. Kao ilustrativni primer korišćeno je upravljanje DC motorom, čija se dinamika opisuje diskretnim modelom sistema prvog reda. PLC program realizuje osnovnu START/STOP logiku, izračunavanje

[1] *Ognjen Jovanović, Faculty of Engineering at University of Kragujevac, Sestre Janjić 6, 34000 Kragujevac, Serbia, ognjen.jovanovic@fink.rs, https://orcid.org/0009-0001-1659-8399*
[2] *Milan Matijević, Faculty of Engineering at Univeristy of Kragujevac, Sestre Janjić 6, 34000 Kragujevac, Serbia, matijevic@kg.ac.rs, https://orcid.org/0000-0001-5307-0027*

dinamičkog odziva primenom diferencne jednačine, akviziciju relevantnih signala i njihovu vizuelizaciju. Posebna pažnja posvećena je prikazu upravljačkog i izlaznog signala na virtuelnom HMI uređaju, čime se omogućava praćenje prelaznih procesa u realnom vremenu bez korišćenja realnog motora ili skupih laboratorijskih modela. Prikazani pristup ima značajnu primenu u inženjerskom obrazovanju, jer studentima omogućava razumevanje veze između PLC programiranja, dinamike sistema, akvizicije podataka i vizuelizacije procesa. Rad pokazuje da TIA Portal može biti efikasno okruženje za bezbednu, pristupačnu i reproduktivnu proveru osnovnih upravljačkih koncepata.

KLJUČNE REČI: PLC, TIA Portal, Software-in-the-Loop, HMI, simulacija u realnom vremenu, DC motor, akvizicija podataka

INTRODUCTION

One of the most significant directions in the modern production systems (John, K. H. & Tiegelkamp, M. 2010a) is industrial automation, where Programmable Logic Controllers (PLCs) (Stojić, M. R. 1994; Bolton, W. 2015; Dorf, R. C. & Bishop, R. H. 2017), have proven to be an effective solution for implementing control algorithms in a wide range of technological processes. In terms of flexibility and integration within industrial communication networks, PLCs have become the modern and standard solution (Matijević, M. et al. 2008) for industrial control applications. Software-in-the-Loop (SIL) verification enables the testing of control algorithms in a simulation environment before their implementation on physical hardware (Striffler, N., & Voigt, T. 2023; Simens AG 2024b). Its primary purpose is to reduce development costs, improve system safety, and accelerate the design process of automatic control systems.

TIA Portal (Siemens AG. 2024b; Siemens AG. 2025a; Siemens AG. 2025b; Siemens AG. 2026) is an integrated engineering environment used for PLC programming, communication configuration, HMI development, and system diagnostics. In addition, TIA Portal provides programming languages that enable the implementation of advanced control tasks (Salzmann, C., & Jones, C. 2017), including the modeling and execution of dynamic systems. As an introductory step in this research, a first-order dynamic system is considered. The dynamic model is implemented using a discrete difference equation, allowing its execution within the PLC environment. Data acquisition is performed through a virtual HMI, which monitors the system response in real time and provides graphical visualization of the process variables (Siemens AG. 2026).

The main contribution of this work is educational in nature, demonstrating the practical feasibility of Software-in-the-Loop simulation and presenting a systematic methodology for PLC-based implementation and verification of dynamic system models. Such an approach provides students, researchers, and engineers with a practical framework for connecting systems theory, programming fundamentals, mathematical modeling, and process visualization. Consequently, it serves as a foundation for the development and adoption of more advanced methodologies for the design and implementation of automatic control systems.

METHODOLOGY: Mathematical Model of a First-Order System

A first-order approximation is sufficiently accurate for a wide range of engineering problems, particularly in cases where the time constant predominantly determines the system behavior and transient response. Such models are commonly used to describe low-power electrical drives, heating, ventilation and process (HVP) systems, as well as various industrial processes in which transient behavior must first be analyzed before an appropriate control algorithm is implemented (Dorf, R. C., & Bishop, R. H. 2017; Salzmann, C., & Jones, C. 2017).

The paper will also use an illustrative scenario involving the ON/OFF excitation of a first-order plant (a DC motor shown in Figure 1) and the analysis of the resulting transient responses.

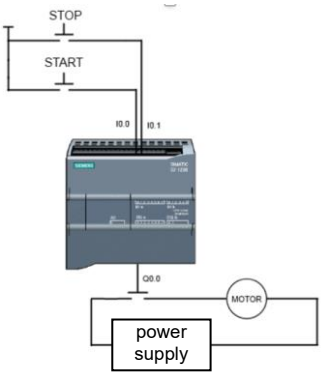

Figure 1 *On/Off Control for DC motor*

The DC motor excitation example was also studied through a MOOC course.

In this study, the controlled object is represented by a first-order system with the transfer function (Stojić, M. R. 1994):

$$G(s) = \frac{1}{\tau s + 1} \tag{1}$$

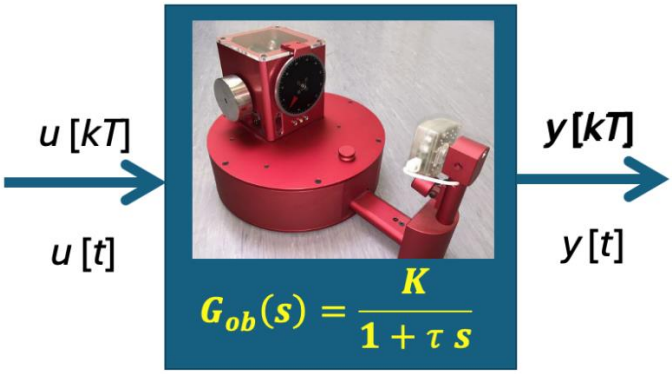

Figure 2 *Illustration of a controlled plant*
(DC motor with an associated mechanism that can be described by a first-order linear dynamical mode)

The model represents a stable linear system with a unit static gain and a time constant of one second, where *u(t)* denotes the control input and *y(t)* represents the system output (Åström, K. J., & Murray, R. M. 2021; Franklin, G. F. et al. 2019).

One of the key advantages of PLC-based implementation is deterministic real-time execution. However, since PLCs operate in discrete time, a continuous-time mathematical model cannot be directly implemented in the control program (Franklin, G. F. et al. 2019). Therefore, the continuous model must be discretized firstly (Stojić, M. R. 1994; John, K. H., & Tiegelkamp, M. 2010b). In this work, the Zero-Order Hold (ZOH) discretization method is used to convert the continuous-time model into its discrete-time equivalent suitable for PLC execution (Bolton, W. 2015; Stojić, M. R. 1985).

The resulting discrete-time model can be expressed in the following equation form (Stojić, M. R. 1994):

$$y_{k+1} = ay_k + bu_k \tag{2}$$

y(t) represents output at the current sampling instant, y_{k+1} is an output at next sampling instant, u_k denotes the control input. For *ZOH* discretization of the first order, coefficients (*a)* and (*b)* are defined as:

$$a = e^{\frac{-Ts}{\tau}} \tag{3}$$

$$b = 1 - e^{\frac{-Ts}{\tau}} \tag{4}$$

where *T* is system constant, T_s is the sampling period (Stojić, M. R. 1985).

The coefficients *(a)* and *(b)* depend on the selected sampling period. This discrete difference equation forms the mathematical basis for implementing the first-order dynamic model within the TIA Portal environment.

An additional advantage of this approach is that no external simulation or numerical libraries are required. The dynamic system is implemented entirely using standard PLC instructions, making the proposed methodology fully compatible with industrial PLC programming practices (Lewis, R. W. 2016). Consequently, the necessary foundation for Software-in-the-Loop (SIL) simulation in a virtual environment is established (International Electrotechnical Commission. 2013).

Since we are working within the simulation domain, the output signal *u[kT]* is obtained by discretizing the first-order model (Stojić, M. R. 1994).

$$\tau\dot{y}(t) + y(t) = Ku(t) \tag{5}$$

The linear first-order system model can also be expressed in the form of a continuous transfer function.

$$G_{ob}(s) = \frac{Y(s)}{U(s)} = \frac{K}{\tau s + 1} \tag{6}$$

where K is the static gain, and τ is the time constant of the controlled plant (Salzmann, C., & Jones, C. 2017).

By applying a sampling period T and assuming that the control signal remains constant during the sampling interval (the “ZOH” discretization method, in which the D/A converter holds the control signal *u[kT]* constant), the following discrete transfer function is obtained (Åström, K. J., & Wittenmark, B. 1984):

$$G_{ob}(z) = \frac{Y(z)}{U(z)} = Z\left[G_{oh}(s)\frac{K}{\tau s+1}\right] = Z\left[\frac{1-e^{-Ts}}{s}\frac{K}{\tau s+1}\right] = \frac{K(1-e^{-\frac{T}{\tau}})}{z-e^{-\frac{T}{\tau}}} \tag{7}$$

Differential equation corresponding to the models:

$$y(kT) = e^{-\frac{T}{\tau}}y(kT-T) + K\left(1-e^{-\frac{T}{\tau}}\right)u(kT-T) \tag{8}$$

or, equivalently:

$$y(kT) = Ay(k-1) + Bu(k-1) \tag{9}$$

$$A = e^{-\frac{T}{\tau}}, B = K(1-e^{-\frac{T}{\tau}}) \tag{10}$$

where the coefficients A and B depend on the selected sampling period *T* and the parameters of the first-order controlled plant model, namely the static gain *K* and the time constant τ .

MODEL IMPLEMENTATION IN THE TIA PORTAL ENVIRONMENT

The control algorithm is implemented using Structured Control Language (SCL), the high-level programming language supported by Siemens TIA Portal. SCL is particularly suitable for implementing discrete-time mathematical models, numerical algorithms, and difference equations within PLC applications (Siemens AG. 2025a; Siemens AG. 2025b; Siemens AG. 2026; Siemens AG. 2024a, b & c).

The implementation is based on cyclic PLC execution. During each execution cycle, the control input signal is acquired, the current output value is calculated using the discrete difference equation, the previous output is updated, and the computed result is transferred to the Human–Machine Interface (HMI) for real-time visualization.

The implementation of the first-order dynamic system is presented in Listing 1, see Appendix A (MathWorks. 2025a &b; MathWorks Support Team. 2019).

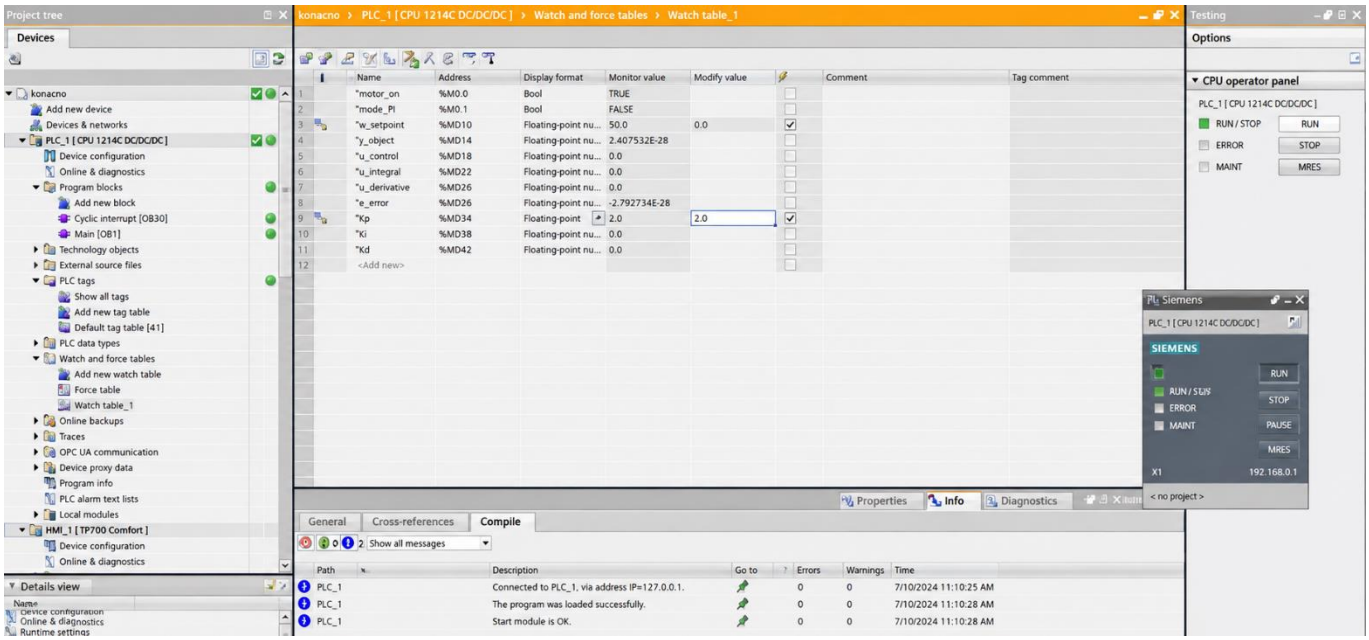

Figure 3 SCL implementation of the first-order dynamic model in TIA Portal

The mathematical model of the first-order system, previously developed in the MATLAB/Simulink environment, was implemented in the TIA Portal environment. The implementation was carried out using **Siemens TIA Portal V20/16** in combination with **PLCSIM Advanced**, enabling Software-in-the-Loop (SIL) verification of the control algorithm.

The validation was performed by comparing the characteristic response parameters of both models, including the **rise time**, **settling time**, **steady-state value**, and **maximum overshoot**. The SIL implementation successfully reproduced the dynamic behavior of the original mathematical model, demonstrating a high level of agreement between the simulation and the PLC-based implementation. The obtained results indicate that the steady-state error is practically negligible, while the observed deviations in the dynamic characteristics are small and consistent with those expected from a discrete-time PLC implementation. Therefore, the proposed methodology confirms the correctness and reliability of the implemented first-order dynamic model within the TIA Portal environment.

INTEGRATION

For this project, a function block named **FB_FirstOrder** was developed to implement the discrete mathematical model of the first-order system. The function block is called from the main organizational block (**OB1**), where the control input signal **U_in** is applied to the model input, while the output variable **Y_out** represents the process response.

The implementation is executed cyclically with the PLC scan cycle, ensuring deterministic execution and periodic updating of the mathematical model. During each cycle, the current input value is processed, the output is calculated using the discrete difference equation, and the updated output is stored for the next execution cycle. This approach accurately reproduces the behavior of a first-order dynamic system while maintaining compatibility with standard PLC programming practices.

The system response is monitored in real time using the **Trend View** tool available in the TIA Portal environment. As can be observed, after applying a unit-step input signal, the first-order system exhibits the expected exponential response. The output gradually increases and asymptotically reaches its steady-state value, thereby confirming the correctness of the implemented discrete mathematical model.

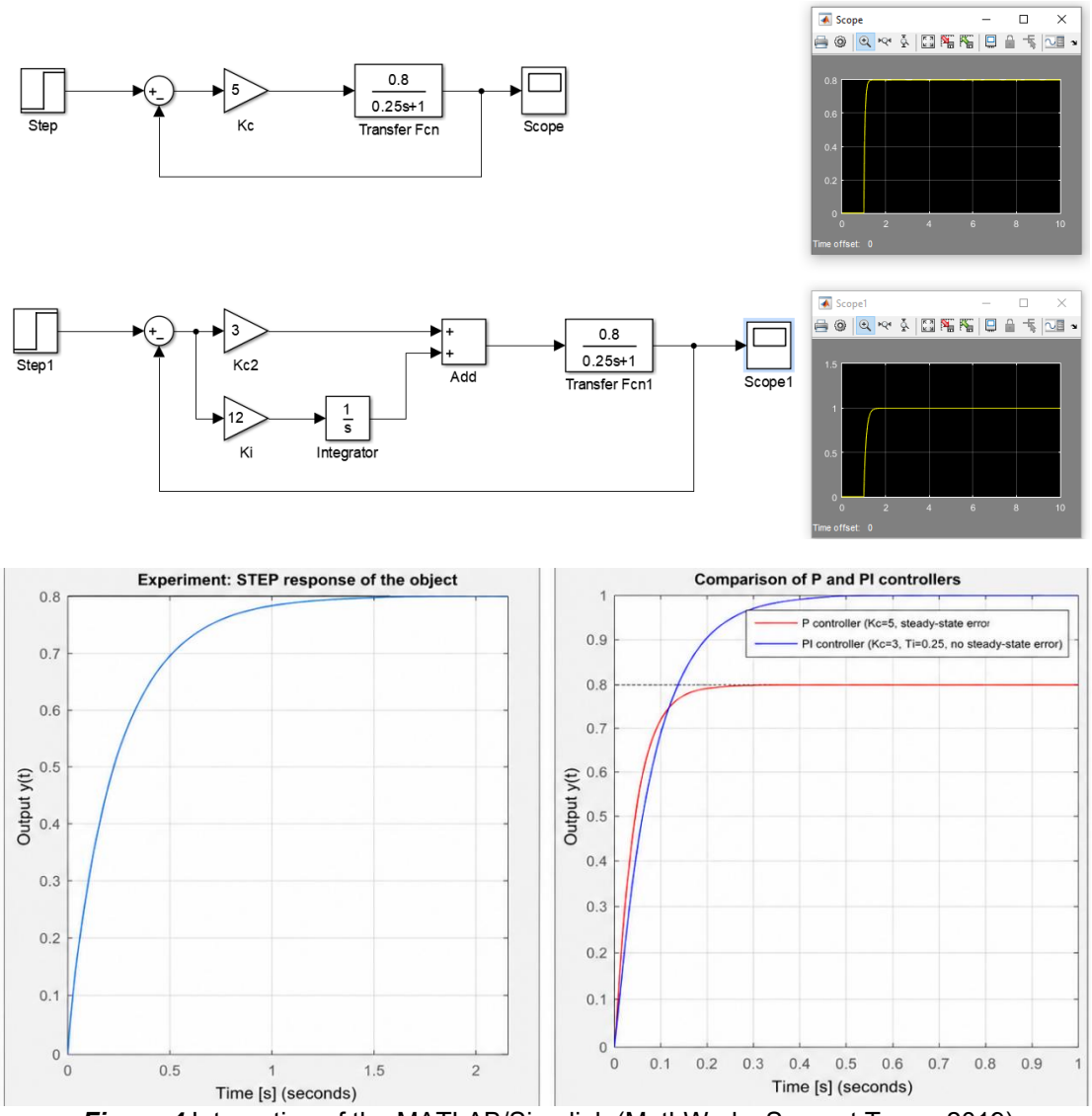

Figure 4 Integration of the MATLAB/Simulink (MathWorks Support Team. 2019)

The obtained response closely matches the theoretical behavior predicted by the continuous-time model, demonstrating that the discretization procedure and PLC implementation preserve the essential dynamic characteristics of the system. This confirms the suitability of the proposed approach for Software-in-the-Loop (SIL) verification and provides a reliable foundation for the implementation of more advanced control algorithms in future work.

Table 1 Main Components of the Integration Process

Component	**Function**	**Purpose in the Integration Process**
OB1	Main organizational block	Executes the control program cyclically and calls the **FB_FirstOrder** function block.
FB_FirstOrder	Function block	Implements the discrete mathematical model of the first-order system using the difference equation.
U_in	Input signal	Represents the control input applied to the mathematical model.
Y_out	Output signal	Represents the calculated process response generated by the discrete model.
Trend View	Monitoring tool	Displays the real-time evolution of the process response and enables validation of the system behavior.
PLCSIM Advanced	PLC simulator	Executes the PLC program in a virtual environment for Software-in-the-Loop (SIL) verification.

Table 1 summarizes the main components involved in the integration of the mathematical model within the TIA Portal environment. The implementation is based on the interaction between the **OB1** organizational block, which cyclically executes the control program, and the **FB_FirstOrder** function block, where the discrete mathematical model is implemented. The input signal (**U_in**) is processed during each PLC scan cycle, while the corresponding output (**Y_out**) is calculated and visualized in real time using the **Trend View** tool. The complete execution is performed in a virtual PLC environment using **PLCSIM Advanced**, enabling reliable Software-in-the-Loop (SIL) verification before deployment to industrial hardware.

The data acquisition methodology is based on the configuration of PLC variables together with auxiliary variables used to control the simulation process (Start_mem and Stop_mem). All defined variables are collected using the Cyclic Acquisition mode, allowing their values to be continuously recorded throughout the execution of the PLC program.

Additionally, the HMI interface can also be designed as follows. The older interface is presented below. When solving such problems, engineers may sometimes encounter older notation and terminology, and therefore, the interface may also appear in the following form:

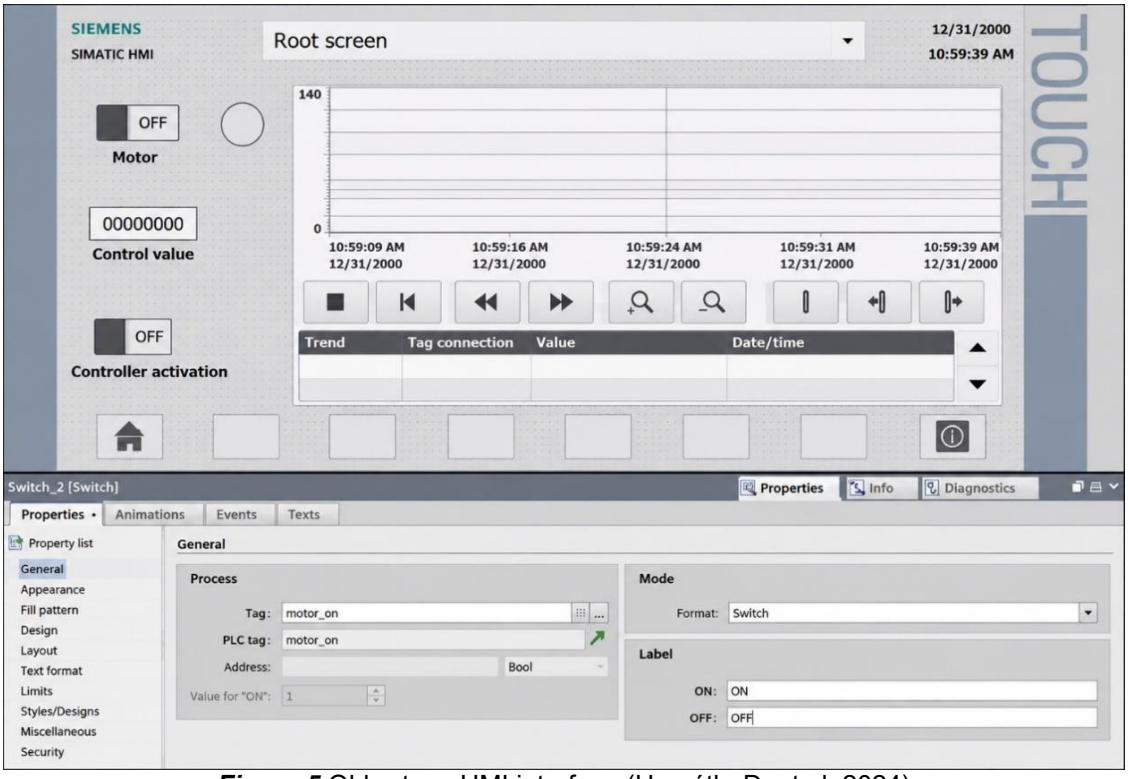

Figure 5 Older-type HMI interface (Horváth, D. et al. 2024)

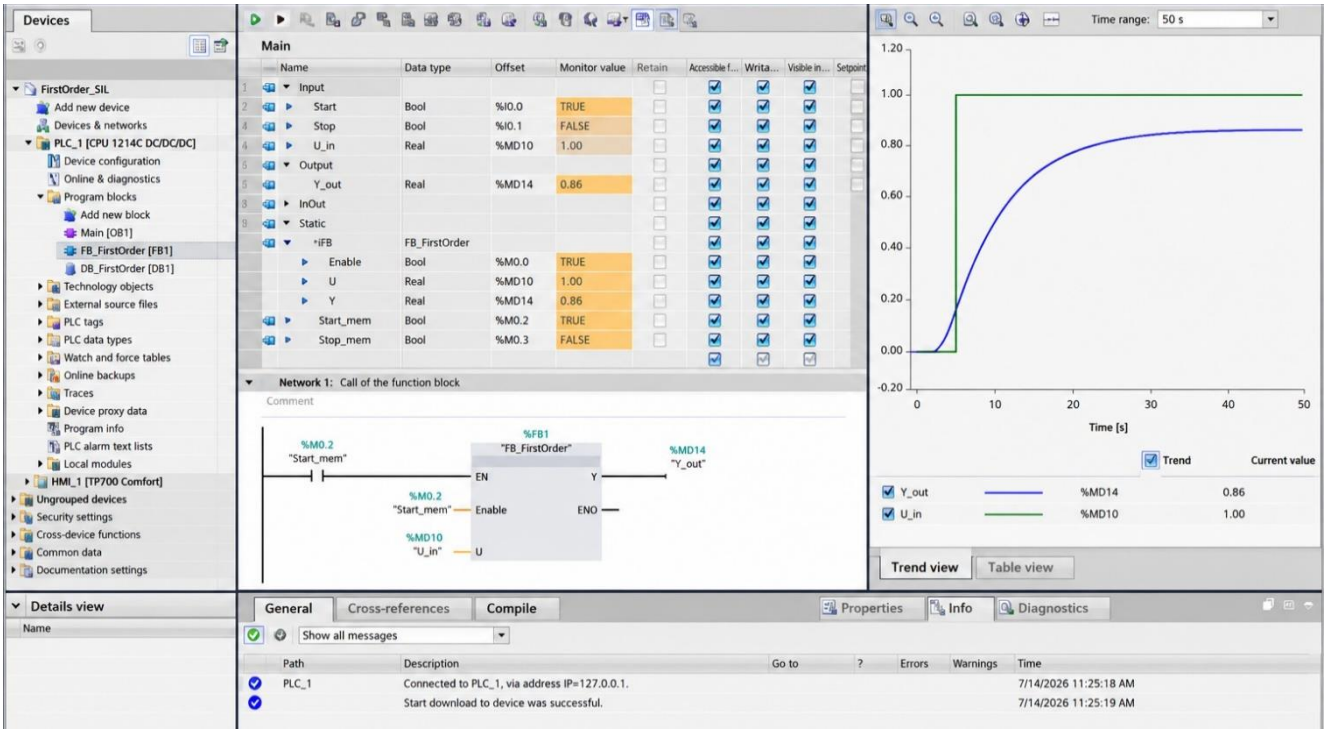

Figure 6 Software-in-the-Loop (SIL) Verification in TIA Portal

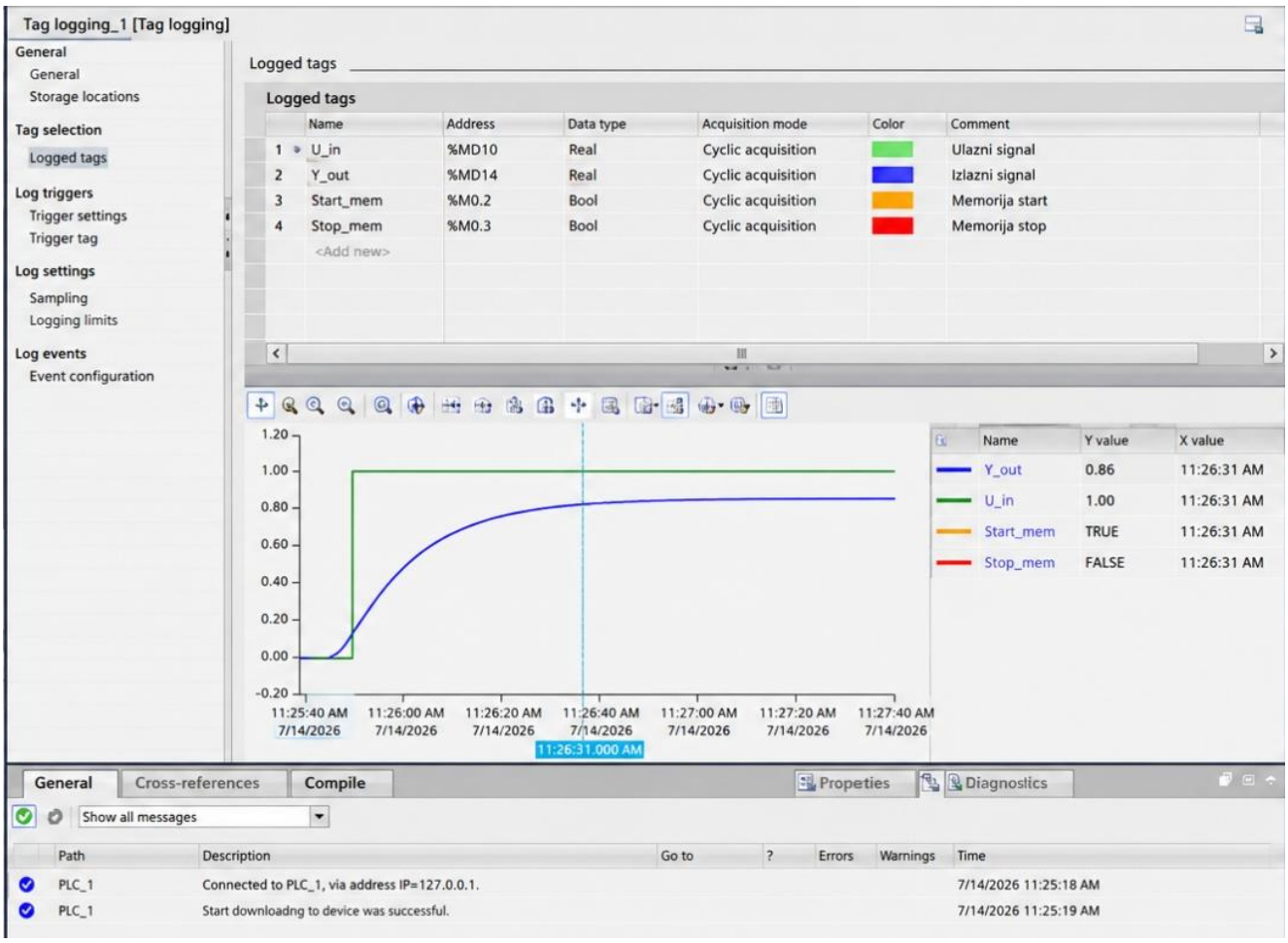

Figure 7 Data Acquisition Methodology

The Tag Logging tool provides reliable data acquisition during the Software-in-the-Loop (SIL) simulation and enables subsequent analysis of the recorded process variables. The acquired data are visualized through a virtual Human–Machine Interface (HMI) and trend diagrams, providing real-time monitoring of both input and output signals. This approach facilitates the evaluation of the dynamic system behavior and confirms the correct operation of the implemented mathematical model throughout the simulation. Once the SIL verification and data acquisition have been completed, the proposed methodology can be applied to a theoretical quarter-car vehicle model. The rationale

for extending the work in this direction is based on several considerations. A basic methodology for solving a first-order dynamic system has been established, providing a fundamental theoretical and methodological framework for addressing engineering problems involving dynamic systems. Building upon this foundation, the reduced-order model will be introduced as the next step in the development of the proposed approach. As the methodology is further developed and refined, increasingly complex engineering problems can be considered (Ogata, K. 2010; Nise, N. S. 2020).

The quarter-car model (Simić, D. 1980) represents one of the fundamental examples in this progression, as it introduces a more comprehensive engineering problem in which the engineer must establish the system model, perform system identification and analysis, and formulate the corresponding state-space equations. In this way, the transition from a simple first-order dynamic system toward more complex vehicle dynamic models becomes systematic and clearly defined.

APPLICATION OF A FIRST-ORDER LINEAR DYNAMIC SYSTEM BASED ON A REDUCED-ORDER QUARTER-CAR MODEL

Reduced-order model represents a simplified representation of the dynamics of a quarter-car active suspension system. In order to reduce the model complexity and adapt its structure to PLC-based implementation, the complete system dynamics are approximated by a first-order dynamic system. In this way, the dominant dynamic behavior of the suspension system is retained, while secondary dynamic effects that are not essential for the considered analysis are neglected.

where the discrete-time coefficients are defined as (Stojić, M. R. 1994; Åström, K. J., & Wittenmark, B. 1984):

$$b = K(1 - 1 - e^{-\frac{T}{\tau}}) \tag{11}$$

where final state-space model is:

$$\dot{x}(t) = -\frac{1}{\tau}x(t) + \frac{K}{\tau}u(t) \tag{12}$$

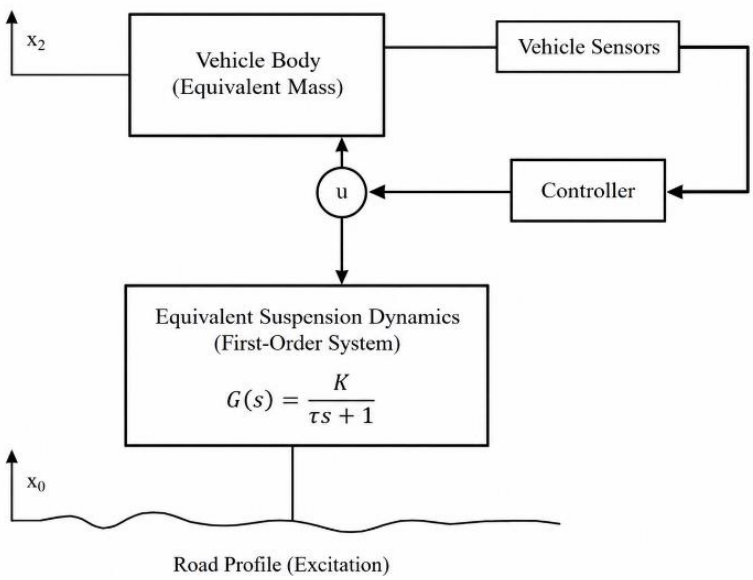

Figure 8 Reduced-Order Model of the Quarter-Car Vehicle Suspension System (Simić, D. 1980)

For the dynamics itself, from your figure:

$$G(s) = \frac{K}{\tau s + 1} \tag{13}$$

For an ideal sensor:

$$H(s) = 1 \tag{14}$$

For P controller:

$$Cp(s)=Kc \tag{15}$$

For PI controller:

$$Cpi(s) = Kc(1 + \frac{1}{Tis}) \tag{16}$$

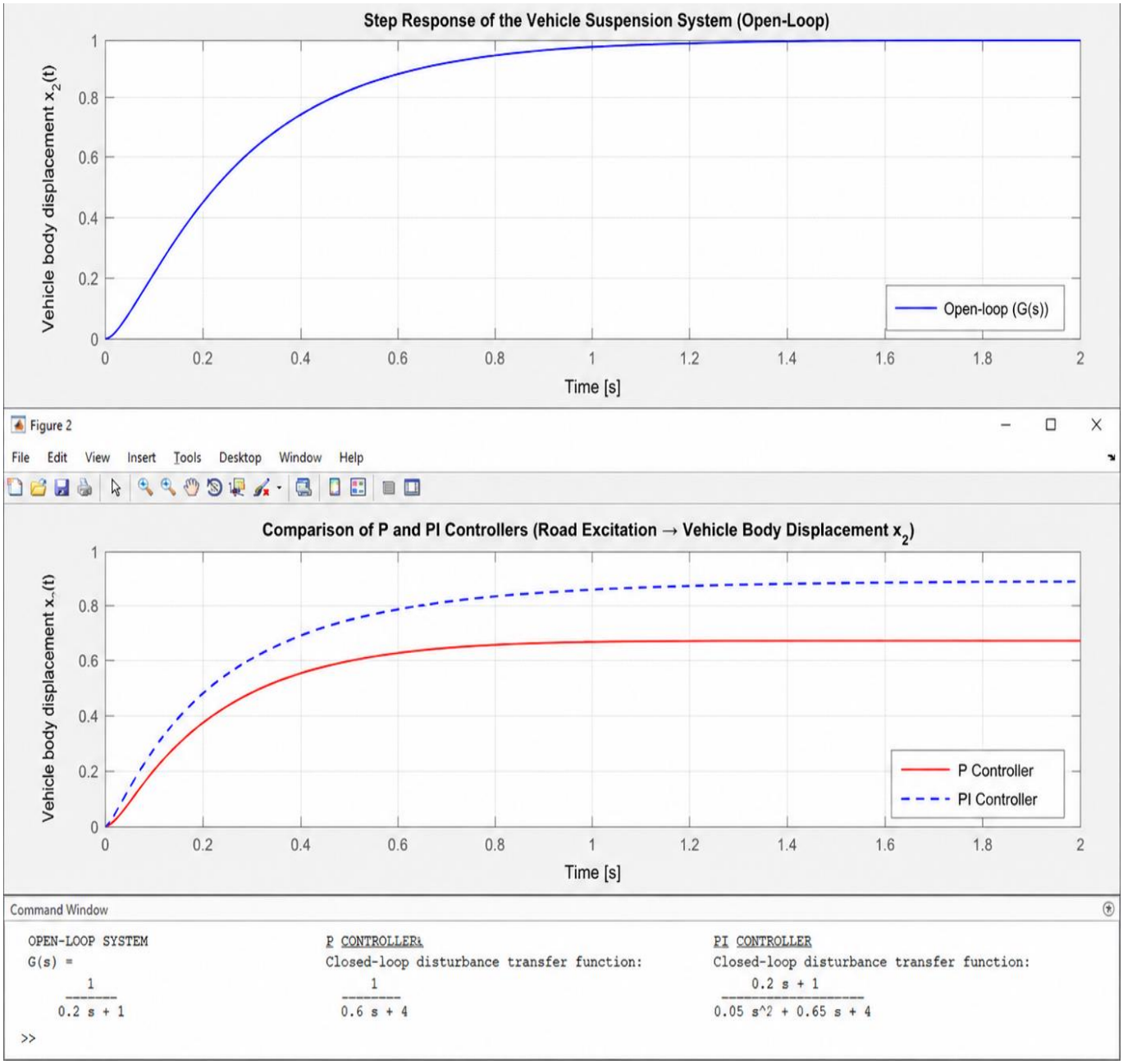

Figure 9 MATLAB Results of Reduced-Order Model of the Quarter-Car Vehicle P & PI controllers (MathWorks. 2025a; MathWorks Support Team. 2019)

CONCLUSIONS

This paper presented the implementation and Software-in-the-Loop (SIL) verification of a first-order dynamic system model in the Siemens TIA Portal environment. The proposed methodology was based on the implementation of a discrete mathematical model using a function block programmed in Structured Control Language (SCL). The obtained results confirmed the correctness and effectiveness of the implementation by accurately reproducing the expected system response to a unit-step input signal.

The implemented model successfully reproduced the dynamic behavior of the first-order system, exhibiting the characteristic exponential transient response without oscillations and reaching the expected steady-state value.

These results demonstrate that the proposed PLC-based implementation accurately represents the theoretical mathematical model.

Data acquisition was achieved through direct communication with PLC variables during program execution, while real-time visualization of the process variables was provided using the Human–Machine Interface (HMI) and the Trend View tool. This enabled continuous monitoring of both input and output signals throughout the simulation process.

The proposed methodology demonstrates that Software-in-the-Loop verification within the TIA Portal environment represents an effective and reliable approach for validating dynamic system models before deployment on industrial hardware. Furthermore, the presented approach provides a practical foundation for the implementation and verification of more advanced control algorithms in future research and industrial applications.

REFERENCES

Bolton, W. (2015). *Programmable logic controllers* (6th ed.), Newnes.

Dorf, R. C., & Bishop, R. H. (2017). *Modern control systems* (13th ed.), Pearson.

Franklin, G. F., Powell, J. D., & Emami-Naeini, A. (2019). *Feedback control of dynamic systems* (8th ed.), Pearson.

Horváth, D., Klaučo, M., & Strémy, M. (2024). Virtual commissioning with TIA Step7 and Simulink without S-functions. *Journal of Engineering, 2024*, Article 2822711. https://doi.org/10.1155/2024/2822711

International Electrotechnical Commission. (2013). *Programmable controllers—Part 3: Programming languages* (IEC Standard No. 61131-3:2013, 3rd ed.). https://webstore.iec.ch/en/publication/4552

John, K. H. & Tiegelkamp, M. (2010a). *IEC 61131-3: Programming industrial automation systems* (2nd ed.), Springer.

John, K. H., & Tiegelkamp, M. (2010b). *IEC 61131-3: Programming industrial automation systems: Concepts and programming languages, requirements for programming systems, decision-making aids* (2nd ed.). Springer. https://doi.org/10.1007/978-3-642-12015-2

Lewis, R. W. (2016). *Programming industrial control systems using IEC 61131-3* (3rd ed.), Institution of Engineering and Technology.

MathWorks. (2025a) *MATLAB and Simulink for PLC simulation and model-based design*, MathWorks.

MathWorks. (2025b) *Simulink PLC Coder user's guide*, MathWorks.

MathWorks Support Team. (2019, January 2). *What are MIL, SIL, PIL, and HIL, and how do they integrate with the Model-Based Design approach?* MATLAB Answers. https://www.mathworks.com/matlabcentral/answers/440277-what-are-mil-sil-pil-and-hil-and-how-do-they-integrate-with-the-model-based-design-approach

Matijević, M., Jakupović, G., & Car, J. (2008). *Računarski podržano merenje i upravljanje*. Mašinski fakultet u Kragujevcu.

Nise, N. S. (2020). *Control systems engineering* (8th ed.), John Wiley & Sons.

Ogata, K. (2010). *Modern control engineering* (5th ed.), Prentice Hall.

Salzmann, C., & Jones, C. (2017). *Control Systems* [MOOC]. École polytechnique fédérale de Lausanne (EPFL). https://courseware.epfl.ch/courses/course-v1:EPFL+controlsys+2017_T1/about

Siemens AG. (2024a). *SIMATIC S7-1200 programmable controller system manual*, Siemens AG.

Siemens AG. (2024b, December 5). *SIMATIC STEP 7 incl. Safety, S7-PLCSIM and WinCC V20 trial download* (Document ID 109963850) [Software download]. https://support.industry.siemens.com/cs/document/109963850/

Siemens AG. (2024c). *SIMATIC STEP 7 (TIA Portal) programming guideline for S7-1200/S7-1500*, Siemens AG.

Siemens AG. (2025a, February 27). *Installation TIA Portal V20—STEP 7, WinCC & other SW* (Document ID 109982542) [FAQ]. https://support.industry.siemens.com/cs/document/109982542/

Siemens AG. (2025b, May 30). *S7-PLCSIM Advanced function manual* (Document ID 109989787, V7 Update 1) [Function manual]. https://support.industry.siemens.com/cs/document/109989787/

Siemens AG. (2026, February 18). *TIA Portal Cloud—Test free for 21 days (trial)* (Document ID 109772248) [Product note]. https://support.industry.siemens.com/cs/document/109772248/

Simić, D. (1980). *Dynamics of Motor Vehicles*, Naučna knjiga.

Stojić, M. R. (1985). *Continuous Systems of Automatic Control*, Naučna knjiga, Beograd.

Stojić, M. R. (1994). *Digitalni sistemi upravljanja*, III izmenjeno i dopunjeno izdanje, Nauka, Beograd

Striffler, N., & Voigt, T. (2023). Concepts and trends of virtual commissioning—A comprehensive review. *Journal of Manufacturing Systems, 71*, 664–680. https://doi.org/10.1016/j.jmsy.2023.10.013

Åström, K. J., & Wittenmark, B. (1984). *Computer controlled systems: Theory and design*, Prentice-Hall.

Åström, K. J., & Murray, R. M. (2021) *Feedback systems: An introduction for scientists and engineers*, Princeton University Press.

APPENDIX A

Listing 1 „Structured Control Language“ & MATLAB code

SCL implementation of the first-order dynamic system

```
*******************************************
FUNCTION_BLOCK FB_FirstOrder

VAR_INPUT
   Enable : BOOL;     // Enable signal for system execution
   U      : REAL;     // Control input signal
END_VAR

VAR_OUTPUT
   Y      : REAL;     // System output signal
END_VAR

VAR
   // Continuous-time system parameters
   K      : REAL := 1.0;      // Static gain
   T      : REAL := 1.0;      // Time constant [s]
   Ts     : REAL := 0.04;     // Sampling period [s]

   // Discrete-time model coefficients
   A      : REAL := 0.960789; // A = exp(-Ts/T)
   B      : REAL := 0.039211; // B = K*(1-exp(-Ts/T))

   // Previous output value (system state)
   Y_prev : REAL := 0.0;

END_VAR
BEGIN
   // ---------------------------------------------------------
   // Discrete-time first-order system
   //
   // Continuous-time transfer function:
   //
   //              K
   // G(s) = -------------
   //            T*s + 1
   //
   // Parameters:
   // K  = 1.0
   // T  = 1.0 s
   // Ts = 0.04 s
   //
   // Zero-Order Hold discretization:
   //
   // A = exp(-Ts/T)
   //   = exp(-0.04/1.0)
   //   = 0.960789
   //
```

```
    // B = K*(1-exp(-Ts/T))
    //   = 1.0*(1-exp(-0.04))
    //   = 0.039211
    //
    // Difference equation:
    //
    // y[k+1] = A*y[k] + B*u[k]
    //
    // y[k+1] = 0.960789*y[k] + 0.039211*u[k]
    // -------------------------------------------------------

    IF Enable THEN

        // Calculate the next system output
        Y := A * Y_prev + B * U;

        // Store the current output as the state
        // for the next PLC execution cycle
        Y_prev := Y;

    ELSE

        // Reset the system when simulation is disabled
        Y := 0.0;
        Y_prev := 0.0;

    END_IF;

END_FUNCTION_BLOCK
*****************************************
```

This can also be written as the following SCL code:

```
IF "motor_on" THEN

    // Calculation of the control error
    "e_greska" := "w_setpoint" - "y_objekat";

    // Controller algorithm
    IF "mode_PI" THEN

        "u_integral" := "u_integral" + ("Ki_step" * "e_greska");

        // ARW - Limiting the integrator to the range (0 - 125)
        IF "u_integral" > 125.0 THEN
            "u_integral" := 125.0;
        ELSIF "u_integral" < 0.0 THEN
            "u_integral" := 0.0;
        END_IF;

        "u_upravljanje" := ("Kc_PI" * "e_greska") + "u_integral";

    ELSE

        // P Controller with variable Kc_P
        "u_integral" := 0.0;
        "u_upravljanje" := "Kc_P" * "e_greska";

    END_IF;

    // First-order plant simulation
    "y_objekat" := (0.86207 * "y_objekat") + (0.11034 * "u_upravljanje");

    // Physical limitation of the motor output (0 - 100)%
    IF "y_objekat" > 100.0 THEN
        "y_objekat" := 100.0;
```

```
   ELSIF "y_objekat" < 0.0 THEN
      "y_objekat" := 0.0;
   END_IF;

ELSE

   // Controller reset when the motor is turned off
   "u_integral" := 0.0;
   "u_upravljanje" := 0.0;
   "y_objekat" := 0.0;
   "e_greska" := 0.0;

END_IF;
*********************************************
```

Furthermore, the reduced-order system can also be represented, as shown in the MATLAB listing:

```
*********************************************
%% VEHICLE SYSTEM MODEL - ACTIVE SUSPENSION
% Equivalent first-order suspension dynamics:
%
%             K
% G(s) = --------------
%           tau*s + 1
%
% x0 - road profile excitation
% x2 - vehicle body displacement
% u  - control input
%
% Negative feedback through vehicle sensors

clear all;
close all;
clc;

%% SYSTEM PARAMETERS

K = 1;              % System gain
tau = 0.2;          % Time constant [s]

%% LAPLACE OPERATOR

s = tf('s');

%% EQUIVALENT SUSPENSION DYNAMICS

G = K/(tau*s + 1);

disp('Transfer function of the system G(s):');
G

%% VEHICLE SENSOR

% Ideal vehicle sensor with unit gain

H = 1;

%% CONTROLLER

% P controller
Kc = 3;
C_P = Kc;

% PI controller
Ti = 0.25;
```

```
C_PI = Kc*(1 + 1/(Ti*s));

%% CLOSED-LOOP SYSTEM WITH P CONTROLLER

% Closed-loop transfer function from reference to output
T_P = feedback(C_P*G,H);

% Transfer function from road excitation x0 to
% vehicle body displacement x2
D_P = G/(1 + C_P*G);

%% CLOSED-LOOP SYSTEM WITH PI CONTROLLER

% Closed-loop transfer function from reference to output
T_PI = feedback(C_PI*G,H);

% Transfer function from road excitation x0 to
% vehicle body displacement x2
D_PI = G/(1 + C_PI*G);

%% SIMULATION TIME

t = 0:0.001:2;

%% ROAD PROFILE EXCITATION

% Unit step road excitation

x0 = ones(size(t));

%% OPEN-LOOP SYSTEM RESPONSE

x2_open = lsim(G,x0,t);

%% RESPONSE WITH P CONTROLLER

x2_P = lsim(D_P,x0,t);

%% RESPONSE WITH PI CONTROLLER

x2_PI = lsim(D_PI,x0,t);

%% GRAPHICAL REPRESENTATION

figure;

plot(t,x2_open,'b','LineWidth',2);
grid on;

xlabel('Time [s]');
ylabel('Vehicle body displacement x_2(t)');
title('Step Response of the Vehicle Suspension System');

%% COMPARISON OF P AND PI CONTROLLERS

figure;

plot(t,x2_P,'r','LineWidth',2);
hold on;

plot(t,x2_PI,'b','LineWidth',2);

grid on;

xlabel('Time [s]');
```

```
ylabel('Vehicle body displacement x_2(t)');

title('Comparison of P and PI Controllers');

legend( ...
    'P Controller', ...
    'PI Controller');

%% DISPLAY TRANSFER FUNCTIONS

disp('-----------------------------------------');
disp('OPEN-LOOP SYSTEM');
disp('G(s) = ');
G

disp('-----------------------------------------');
disp('P CONTROLLER');
disp('Closed-loop disturbance transfer function:');
D_P

disp('-----------------------------------------');
disp('PI CONTROLLER');
disp('Closed-loop disturbance transfer function:');
D_PI

disp('-----------------------------------------');
*********************************************
```

The 11th International Congress
Motor Vehicles & Motors 2026
Kragujevac, Serbia
October 8th - 9th, 2026

Motor Vehicles & Motors

MVM2026-058
https://doi.org/10.24874/CMVM2026.058
Original scientific paper

Nikola Gunić[1]
Hana Stefanović[2]
Milan Matijević[3]

A NEW GENERATION OF WHEEL POSITION AND SPEED INTELLIGENT SENSORS FOR MOTOR VEHICLES

ABSTRACT: Advanced Driver Assistance Systems (ADAS) and autonomous driving systems rely on accurate real-time information about wheel position and speed. This paper presents the operating principles as well as experimental results from laboratory measurements of current variations in an active wheel position and speed Hall sensor that utilizes an AK communication protocol. Measurements were performed under real operating conditions, where the sensor output signal was observed in the time domain in order to analyse its behaviour at different wheel speeds or in a stationary state. The analysis highlights the importance of a high-quality and robust communication layer, which is essential for application in advanced vehicle systems with a high hierarchical level of safety, not only for assessing the current state of the vehicle, but also for supporting decision-making processes in automation and autonomous control.

KEYWORDS: ADAS – Advanced Driver Assistance System, AK communication protocol, active Hall sensor, measurement of wheel position and speed.

NOVE GENERACIJE INTELIGENTNIH SENZORA POLOŽAJA I BRZINE TOČKOVA MOTORNIH VOZILA

REZIME: Napredni sistemi pomoći vozaču (ADAS – Advanced Driver Assistance System) i autonomne vožnje oslanjaju se na tačne informacije o položaju i brzini točkova u realnom vremenu. U ovom radu prikazani su principi rada, kao i eksperimentalni rezultati laboratorijskog merenja promene struje aktivnog Holovog senzora položaja i brzine točkova koji koristi AK komunikacioni protokol. Merenja su vršena u realnim uslovima rada, gde se izlazni signal senzora posmatra u vremenskom domenu kako bi se analiziralo njegovo ponašanje pri različitim brzinama točka ili u stanju mirovanja. Analiza ističe važnost kvalitetnog i robusnog komunikacionog sloja, što je neophodno za upotrebu u naprednim sistemima vozila sa hijerarhijski visokim nivoom sigurnosti, ne samo prilikom procene trenutnog stanja vozila, nego i prilikom donošenja određenih odluka u automatizaciji i autonomiji upravljanja.

[1] *Nikola Gunić, dipl.ing, Self-employed researcher, ngelectronic@yahoo.com, https://orcid.org/0009-0005-2647-4196*
[2] *Hana Stefanović, PhD, Professor of Applied Studies, School of Electrical and Computer Engineering - VIŠER, Vojvode Stepe 283, 11010 Beograd, hanas@viser.edu.rs, https://orcid.org/0000-0003-0890-4410*
[3] *Milan Matijević, PhD, Full Professor, Faculty of Engineering, University of Kragujevac, Sestre Janjić 6, 34000 Kragujevac, matijevic@kg.ac.rs, https://orcid.org/0000-0001-5307-0027*

KLJUČNE REČI: ADAS – Advanced Driver Assistance System, AK komunikacioni protokol, aktivni senzor Holovog tipa, merenje položaja i brzine točkova.

INTRODUCTION

Advanced Driver Assistance Systems (ADAS) and vehicle-dynamics control systems rely on accurate and reliable information from vehicle sensors. Wheel-speed information is particularly important for functions such as Anti-lock Braking System (ABS), electronic stability control, traction control, and other vehicle-motion-related applications (Martí et al. 2019; Pandharipande et al. 2023).

Active wheel-speed sensors (AWSS) provide several advantages over conventional passive inductive sensors, including reliable operation at very low rotational speeds and the possibility of transmitting additional information such as wheel-rotation direction (Gussmann et al. 2000; Infineon Technologies AG, 2018).

The objective of this paper is to experimentally investigate the behaviour of an active wheel-speed sensor with an AK communication interface under stationary and rotating conditions. Particular attention is given to the time-domain waveform, wheel-speed pulses, and additional information transmitted through the AK interface.

AK PROTOCOL FOR WHEEL SPEED SENSORS

The AK communication protocol uses a two-wire current interface for both sensor supply and communication. Wheel-speed information is represented by speed pulses, while additional sensor information is transmitted through a Manchester-coded data sequence following the speed pulse (Daimler AG, 2008).

Depending on the sensor implementation, the transmitted data may include rotation direction, validity information, air-gap-related information, signal status, and parity information. During wheel standstill, a dedicated standstill sequence may be transmitted.

In a documented AK implementation, the typical current levels are 7 mA, 14 mA, and 28 mA for the low, mid, and high states, respectively (Infineon Technologies AG, 2018). These values are presented only as reference values for that implementation.

For experimental analysis, voltage variations associated with changes in the sensor output current are observed using an oscilloscope. The recorded waveform therefore allows the speed pulses and the subsequent data sequence of an active wheel-speed sensor with an AK interface to be examined in the time domain.

Table 1 presents the data-bit assignments of an AK protocol implementation (Infineon Technologies AG, 2018).

Table 1 Reference example of AK data-bit assignments

Bit	Name	Abbreviation	Meaning
0	Air-gap reserve / Error	LR / ERR	Indicates insufficient magnetic field (air-gap reserve) or an error condition, depending on sensor variant 1: magnetic-signal amplitude below the reserve threshold dB_LR 0: no LR warning. Standstill handling applies.
1	Signal-level measurement validity	SLM	Indicates whether the air-gap/magnetic-field measurement in bits 5–7 is valid 0: LM data valid 1: invalid.
2	Not assigned	---	Reserved/not assigned in the standard implementation. Transmitted as 0.
3	Direction validity	GDR	Indicates whether the direction information in bit 4 is valid 1: DR valid 0: invalid.
4	Direction of rotation	DR	Indicates the detected direction of wheel rotation: 0: positive 1: negative, relative to the sensor coordinate system.
5	Air-gap measurement, LSB	LM0	Least significant bit of the 3-bit air-gap/magnetic-field indication

Table 1 *(continuation)*

Bit	Name	Abbreviation	Meaning
5	Air-gap measurement, LSB	LM0	Least significant bit of the 3-bit air-gap/magnetic-field indication
6	Air-gap measurement	LM1	Middle bit of the air-gap/magnetic-field indication
7	Air-gap measurement, MSB	LM2	Most significant bit of the air-gap/magnetic-field indication
8	Parity	P	Parity bit for error detection in the preceding data bits. The total number of ones in bits 0–8, including the parity bit, is even.

The LM bits provide eight possible code values representing magnetic-signal amplitude associated with the available air-gap reserve, rather than a direct measurement of mechanical air gap. The corresponding amplitude thresholds depend on the sensor implementation. SLM indicates the validity of the LM value and should not be interpreted as a general confirmation that all calibration procedures have been completed. Similarly, DR should be interpreted only when GDR indicates valid direction information. Device-specific handling of these fields during startup and standstill must also be considered (Infineon Technologies AG, 2018).

AK communication continues while the wheel is stationary and the sensor remains powered. If no speed pulse is generated for a predefined standstill interval, typically around 150 ms, the sensor transmits a standstill message indicating that it remains active although no wheel motion is detected. The tolerance of this interval is specified by the sensor manufacturer. In the documented Infineon implementation, it is specified as ±20%. The leading pulse of the standstill message is transmitted at the mid-current level instead of the high-current level used for a regular speed pulse. Standstill messages are transmitted periodically while the stationary condition persists. A newly detected encoder increment takes precedence over standstill communication. Consequently, at very low rotational speeds, standstill messages may also occur between consecutive speed pulses (Infineon Technologies AG, 2018).

EXPERIMENTAL RESULTS

The tested device was a vehicle-installed active wheel-speed sensor with a two-wire AK communication interface. The sensor model, manufacturer, and internal magnetic sensing principle could not be verified because the sensor was examined as an encapsulated vehicle component. Therefore, the experimental investigation was limited to the externally observable electrical behaviour of its AK interface.

The sensor contains a magnetic sensing element and signal-processing electronics. The sensing element is exposed to the changing magnetic field produced by the rotating encoder.

As the encoder rotates, the magnetic field at the sensing element changes periodically. The sensor electronics detect the magnetic transitions associated with wheel rotation and generate output events whose frequency is related to rotational speed. The AK interface also supports communication while the wheel is stationary.

The experimental method consists of observing the sensor-interface voltage waveform in the time domain. An oscilloscope is connected to the available measurement points of the sensor circuit. The voltage scale, time base, trigger level, and coupling mode were adjusted to obtain a clear display of the individual signal sequences. The recorded voltage variations correspond to changes in the sensor output current.

Experimental measurements are performed under two basic operating conditions, with the wheel stationary and with the wheel rotating, as shown in Figure 1.

The recorded waveforms are evaluated qualitatively according to their relative voltage levels and temporal structure. The manufacturer-specified current values presented below are reference values for a documented AK implementation and were not calculated from the oscilloscope traces.

The AK current interface uses three characteristic current levels. In the reference implementation, the nominal low, mid, and high current levels are approximately 7 mA, 14 mA, and 28 mA, respectively. The high-current level represents the normal speed pulse, while the low- and mid-current levels are used for data transmission. The measured signals were recorded in the time domain using an oscilloscope.

Figure 2 shows the sensor-interface signal while the wheel is stationary. Although no wheel rotation occurs, a distinct structured sequence of signal-level transitions is observed. Because the wheel was stationary and the pronounced high-current speed pulse observed during rotation is absent, the recorded waveform is identified as an individual AK

standstill message. The presented time window shows the structure of the message but does not determine its repetition interval.

Figure 1 Experimental measurement setup. Source: Authors

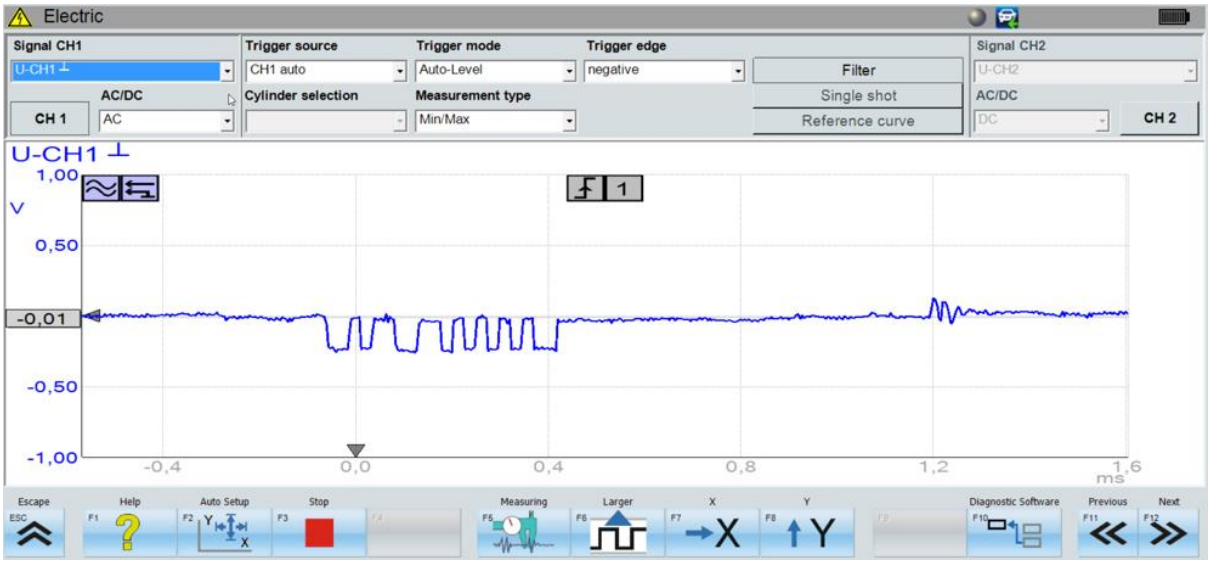

Figure 2 Measured signal for the stationary-wheel condition

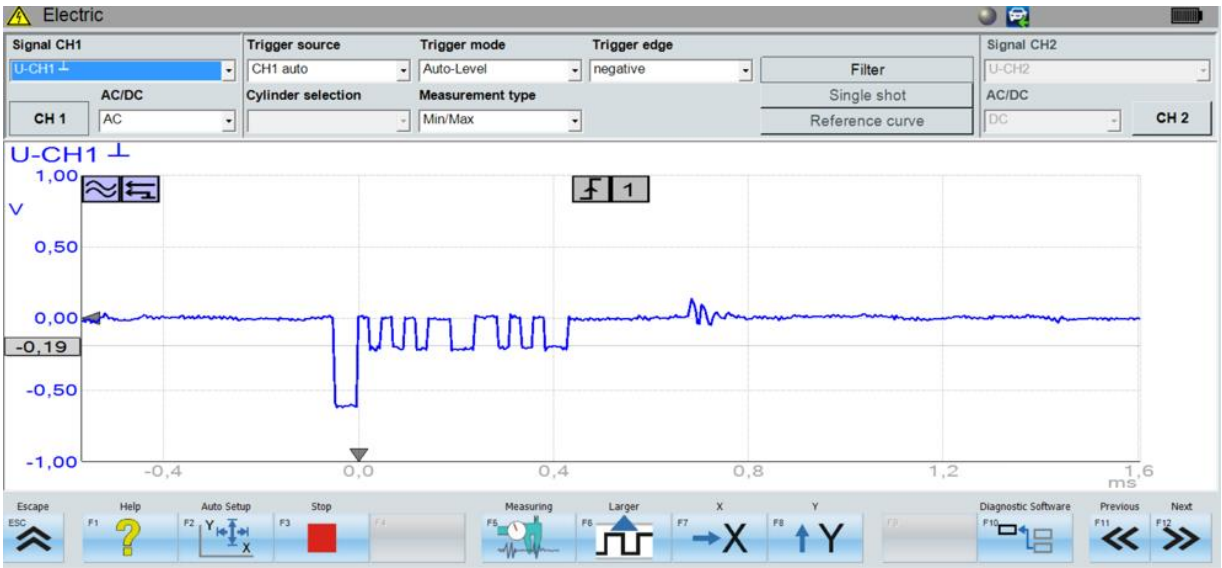

Figure 3 Measured signal for the rotating-wheel condition

Figure 3 shows the corresponding sensor-interface signal while the wheel is rotating. A similar sequence of data-level transitions is preceded by a substantially larger initial voltage excursion. This excursion is consistent with the high-current speed pulse generated by an encoder increment. The speed pulse is followed by the AK data sequence before the signal returns to its initial level.

CONCLUSIONS

This paper presents an experimental investigation of the externally observable signal of an active wheel-speed sensor using a two-wire current-based AK communication interface. Because the sensor model, manufacturer, and internal magnetic sensing principle could not be verified, the conclusions are limited to the measured behaviour of the AK interface. The sensor-interface signal was investigated under stationary and rotating wheel conditions to identify the differences between standstill and motion-related communication.

Voltage variations associated with changes in the sensor output current were recorded in the time domain using an oscilloscope. The measured waveforms exhibited distinct relative signal levels and structured sequences corresponding to the current-modulated communication used by the AK interface.

Under stationary-wheel conditions, a structured signal sequence was observed despite the absence of wheel rotation. The waveform was identified as an individual AK standstill message. When the wheel was rotated, the waveform contained a substantially larger initial excursion consistent with the speed pulse generated by an encoder increment, followed by the data sequence transmitted through the same two-wire interface.

The measurements demonstrate that direct waveform analysis can distinguish standstill communication from motion-related speed pulses. This provides a basis for oscilloscope-based characterization and diagnostic analysis of AK wheel-speed sensor interfaces without relying exclusively on processed ECU data.

Further work will include quantitative determination of current levels and timing parameters, identification and decoding of the transmitted data bits, parity verification, and analysis of direction and magnetic-amplitude information. A longer observation interval will also be used to determine the repetition period of the standstill messages and to compare the measured parameters with publicly available specifications of wheel-speed sensors compliant with AK Protocol Version 4.0.

REFERENCES

Daimler AG. (2008, February 13). *Requirement specifications for standardized interface for wheel speed sensors with additional information* – AK-Protocol Version 4.0.

Gussmann, V., Draxelmayr, D., Reiter, J., Schneider, T., & Rettig, R. (2000). Intelligent Hall effect-based magnetosensors in modern vehicle stability systems. In *Convergence 2000 International Congress on Transportation Electronics* (SAE Technical Paper 2000-01-C058). SAE International.

Infineon Technologies AG. (2018, July). TLE4943C: Hall based differential wheel speed sensor with AK protocol [Data sheet]. https://www.infineon.com/assets/row/public/documents/24/49/infineon-tle4943c-datasheet-en.pdf

Martí, E., de Miguel, M. Á., García, F., & Pérez, J. (2019). A review of sensor technologies for perception in automated driving. *IEEE Intelligent Transportation Systems Magazine*, 11(4), 94–108. https://doi.org/10.1109/MITS.2019.2907630

Pandharipande, A., Cheng, C. H., Dauwels, J., Gurbuz, S. Z., Ibanez-Guzman, J., Li, G., Piazzoni, A., Wang, P., & Santra, A. (2023). Sensing and machine learning for automotive perception: A review. *IEEE Sensors Journal*, 23(11), 11097–11115. https://doi.org/10.1109/JSEN.2023.3262134

The 11th International Congress
Motor Vehicles & Motors 2026
Kragujevac, Serbia
October 8th - 9th, 2026

Motor Vehicles & Motors

MVM2026-065
https://doi.org/10.24874/CMVM2026.065
Original scientific paper

Danijela Miloradović[1]
Jasna Glišović[2]
Jovanka Lukić[3]
Nadica Stojanović[4]

CONDITIONAL SPECTRAL ANALYSIS OF VEHICLE VIBRATION DATA

ABSTRACT: Conditional spectral analysis is an advanced statistical and engineering method that has application in many areas of science and engineering. Its ability to e.g. isolate specific influences, remove background noise, and identifies hidden patterns makes it very useful in vehicle dynamics analysis. In this research, an example of application of conditional spectral analysis to determine the contributions of vertical wheels' vibrations to vibrations at the specific point on the car body was presented. For this purpose, an experiment was designed in order to measure vertical accelerations at the centres of all four wheels of a passenger car and at front-left shock absorbers connecting point with the car body. A multiple input – single output (MISO) model with four inputs and one output was created and appropriate conditional spectral analysis was done. The obtained results in the form of optimal frequency response functions and partial coherence function confirm the importance of decoupling the inter-connections between inputs in order to determine the exact contribution of each of them to the output. In this way, clear guidelines for vehicle dynamics optimization may be obtained.

KEYWORDS: conditional spectral analysis, vehicle, vibration, MISO model

USLOVNA SPEKTRALNA ANALIZA PODATAKA O OSCILOVANJU VOZILA

REZIME: Uslovna spektralna analiza je napredna statistička i inženjerska metoda koja se primenjuje u mnogim oblastima nauke i tehnike. Njena sposobnost da, na primer, izoluje određene uticaje, ukloni pozadinski šum i identifikuje skrivene obrasce čini je veoma korisnom u analizi dinamike vozila. U ovom istraživanju prikazan je primer

[1] *Danijela Miloradović, Ph.D., professor, Faculty of engineering, University of Kragujevac, Sestre Janjić 6, 34000 Kragujevac, Serbia, neja@kg.ac.rs, https://orcid.org/0000-0003-1427-9789*
[2] *Jasna Glišović, Ph.D., professor, Faculty of engineering, University of Kragujevac, Sestre Janjić 6, 34000 Kragujevac, Serbia, jaca@kg.ac.rs, https://orcid.org/0000-0002-8251-1722*
[3] *Jovanka Lukić, Ph.D., professor, Faculty of engineering, University of Kragujevac, Sestre Janjić 6, 34000 Kragujevac, Serbia, lukicj@kg.ac.rs, https://orcid.org/0000-0002-5893-3976*
[4] *Nadica Stojanović, Ph.D., assist. prof., Faculty of engineering, University of Kragujevac, Sestre Janjić 6, 34000 Kragujevac, Serbia, nadica.stojanovic@kg.ac.rs, https://orcid.org/0000-0002-4199-0587*

primene uslovne spektralne analize za određivanje doprinosa vertikalnih vibracija točkova vibracijama na određenoj tački karoserije automobila. U tu svrhu osmišljen je eksperiment radi merenja vertikalnih ubrzanja u centrima sva četiri točka putničkog automobila, kao i na mestu spoja prednjeg levog amortizera sa karoserijom. Formiran je model sa više ulaza i jednim izlazom (MISO) i sprovedena je odgovarajuća uslovna spektralna analiza. Dobijeni rezultati, u vidu optimalnih funkcija frekventnog odziva i funkcije parcijalne koherencije, potvrđuju značaj razdvajanja međusobnih veza između ulaza kako bi se utvrdio tačan doprinos svakog od njih izlazu. Na taj način se mogu dobiti jasne smernice za optimizaciju dinamike vozila.

KLJUČNE REČI: uslovna spektralna analiza, vozilo, vibracije, model “više ulaza-jedan izlaz“

INTRODUCTION

Methodology of conditioned spectral analysis (CSA), although originating from seismology, have found its application in many other branches of science. It is the advanced statistical and engineering method that enables the analysis of frequency characteristics of signals and time series. Unlike classical spectral analysis, which views the system as a whole, conditional spectral analysis isolates specific influences, removes background noise, and identifies hidden patterns (hidden frequencies) depending on the data context.

In vehicle dynamics, CSA represents a powerful mathematical and experimental method used for system identification and vibration analysis under the influence of multiple interconnected inputs. It enables separation (decoupling) of excitation sources. This is crucial, because modern vehicles are extremely complex mechanical systems in which the mix of vibrations occurs that originates from: engine, gearbox, tires, steering forces, aerodynamic drag and road micro-roughness. Thus, some of the key applications of CSA in automotive industry and vehicle testing include: separation of noise and vibration sources (Noise, Vibration, and Harshness - NVH analysis), assessment of comfort and impact on the driver (ride comfort) and dynamic tracking of rotating components (order tracking).

In NVH analysis, CSA may determine which amount of car body vibrations originate directly from the engine operation and which amount comes from the tire-road contact at different speeds. It can analyse multiple vibration sources as in Chen et al. (2018), locate the specific noise source contribution as in Leclere et al. (2005) or identify vibro-acoustical sources of noise emitted inside of vehicle compartment as in Hosseini Fouladi et al. (2009). CSA is used in vehicle ergonomics to determine how human body reacts to specific vibrations in Demić et al. (2002) and Demić & Lukić (2009), which aids the development of better suspension systems and seats as explained in Qui & Griffin (2004).

Analysis of influence of road roughness on stochastic loads of steering system tie-rod during straight line drive on different roads was conducted using CSA in Miloradović & Glišović (2004). It was concluded that the type of the road has influence on the intensity of power spectrum of tie-road’s normal load – worse roads induce higher normal loads during drive with the same constant speed. Also, they reduce the intensity of optimal function of frequency response of the channel “vertical acceleration at the centre of the wheel – tie rod’s normal load”. Another example of the application of CSA in identification of vehicle system dynamics from the aspect of interaction between the steering and suspension systems of a passenger car can be found in Miloradović et al. (2022). As a result of the spectral analysis, the nonparametric model was identified in the form of discrete values of frequency characteristics.

In this research, CSA was used to determine the influence of the vertical vibrations of all four wheels of the passenger car on vertical vibration at the chosen point of car body – the shock absorbers connection point to the car body. Source data originate from vibration measurements on vehicle driving along different straight roads with different constant speeds. Since the vibrations were measured during straight-line driving at constant speeds, vibration data are ideal for CSA as they fall into the class of stationary stochastic processes. This means that the statistical properties of the signal are stable over time, which drastically simplifies the task of identifying the structural resonances of the vehicle body and the transfer paths from the excitation source.

EXPERIMENTAL SETUP

For measurement purposes, four vertical acceleration sensors HBM B12/200 were placed at the centres of all four wheels (inputs) and one identical sensor at the front left shock absorbers connecting point to the car body (output), Figure 1. The inputs generate the combination of deterministic excitation frequencies (imbalance of tires, bearings,…) and stochastic “noise” (road micro-structure). The “output” (shock absorber connection point) filters those excitations through suspension dynamics. This approach is crucial because the shock absorber mounting point is subjected to the direct transmission of high-frequency forces from the wheel to the chassis, which directly affects material fatigue, acoustic comfort and the longevity of the vehicle structure.

a) b) c)

Figure 1 Placement of vertical acceleration sensors: a) front wheels, b) rear wheels, c) shock absorbers connection point to car body (Miloradović et al., 2022)

The coupling of experimental and theoretical vehicle dynamics, or the interface between vehicle dynamics, road and environment, manifests itself at the stage of recording vertical accelerations at the wheel centres, Figure 2. From reference point B, Figure 2 a), located at the centre of the front-left wheel, connections extend to the centres of the other wheels (points C, D, and E), to the road roughness at the tire-ground contact patch (point O), and to a selected point on the vehicle car body, specifically point A, where the left front shock absorber connects to the vehicle car body. Figure 2 b) presents the corresponding model for nonparametric identification of the influence of wheel vibrations on the vibration of the car body with four coupled inputs (vertical accelerations at the centres of the four wheels) and one output (vertical acceleration at the shock absorbers connecting point to car body.

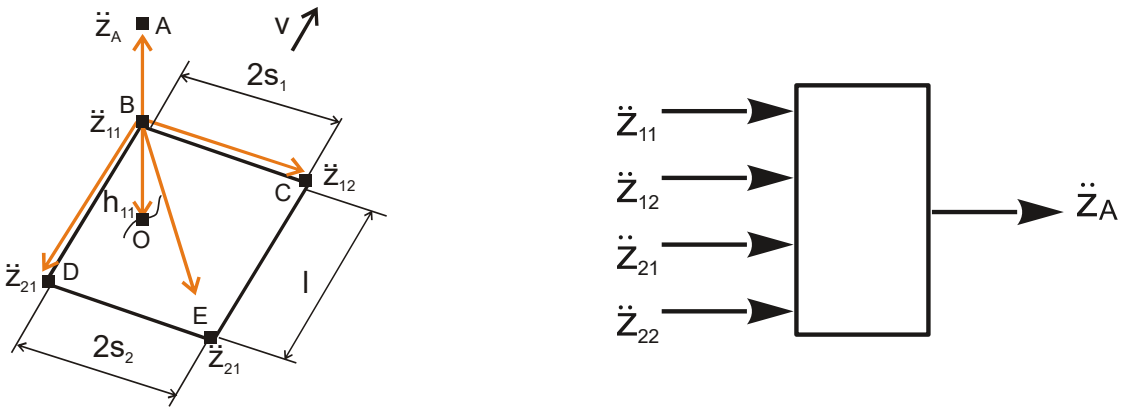

a) b)

Figure 2 Interface between vehicle dynamics and road excitations in time domain: a) at the level of acquired vertical accelerations at the centres of the wheels (B, S, D, E) and at the shock absorbers connecting point to car body (A), b) model used for nonparametric identification

Vertical acceleration at the centre of the front-left wheel, $\ddot{z}_{11}$, is coupled with the other state variables (vertical accelerations at the front-right wheel, $\ddot{z}_{12}$, the rear-left wheel, $\ddot{z}_{21}$, rear right wheel, $\ddot{z}_{22}$, or at the shock absorber connecting point, $\ddot{z}_A$) and with input from the road (road roughness height h_{11}), serving as a starting point for tracking mechanical and functional couplings from a performance perspective. Vehicle speed, *v*, as a motion regime parameter, along with the vehicle's geometric characteristics (wheelbase, *l*, front axle track, $2s_1$, and rear axle track, $2s_2$) determine the road's influence on vehicle vibration and define the vehicle's excitation characteristics.

If the vehicle is designed with identical track widths across both axles ($2s_1 = 2s_2$), then the front and rear wheels on the same side of the vehicle experience the same excitation from road roughness, phase-shifted by a time interval Δt that corresponds to the time it takes the vehicle, moving at speed *v*, to cover a distance *l* equal to the wheelbase: $\Delta t = \frac{l}{v}$. If the vehicle has different track widths on its axles ($2s_1 \neq 2s_2$), then each wheel goes over different road roughness profile. Stronger coupling between the vibrations of wheel centres on the same axle may occur if a dependent suspension system is used on that axle.

The data acquired during the straight-line highway drive of the vehicle with constant speed of *v* = 70 km/h were analysed in this paper. The chosen sample rate was 100 Hz. It makes the Nyquist frequency to be 50 Hz, as the maximum frequency that can be sensed by the sensors without aliasing. In automotive industry, the frequency range from 0 to 50 Hz is extremely critical because it covers the primary ride comfort and vehicle macro-dynamics. At this frequency range, the following key phenomena are happening:

- 1 Hz – 3 Hz: natural frequencies of the car body (bounce, pitch),
- 10 Hz – 20 Hz: natural frequencies of unsuspended masses (wheels and suspension – wheel hop) and

- 20 Hz – 50 Hz: the first structural modes of car body bending and torsion vibrations, as well as low frequency engine vibrations.

MISO MODEL FORMULATION

The model for nonparametric system identification presented in Figure 2 b) is the classical multiple input / single output (MISO) system in time domain. By using the Fourier transforms to obtain the spectra of its inputs and output:

- spectrum of vertical acceleration at the centre of the front left wheel, $\ddot{Z}_{11}(f) = X_1$,
- spectrum of vertical acceleration at the centre of the front right wheel, $\ddot{Z}_{12}(f) = X_2$,
- spectrum of vertical acceleration at the centre of the rear left wheel, $\ddot{Z}_{21}(f) = X_3$,
- spectrum of vertical acceleration at the centre of the rear right wheel, $\ddot{Z}_{22}(f) = X_4$,
- spectrum of vertical acceleration at the top of the front left shock absorber, $\ddot{Z}_A(f) = X_5$,

and introducing the output noise spectra, *N*, the model transforms to MISO coupled model in frequency domain as shown in Figure 3. Noise spectrum represents all possible deviations from the linear model due to time delays, nonlinearities, statistical errors, non-stationarity, instrument noise, etc. Each input, X_i, $i = \overline{1,4}$, affects the output X_5 through corresponding transfer channels characterized by optimum constant parameter ordinary linear frequency response functions, H_{i5}, $i = \overline{1,4}$.

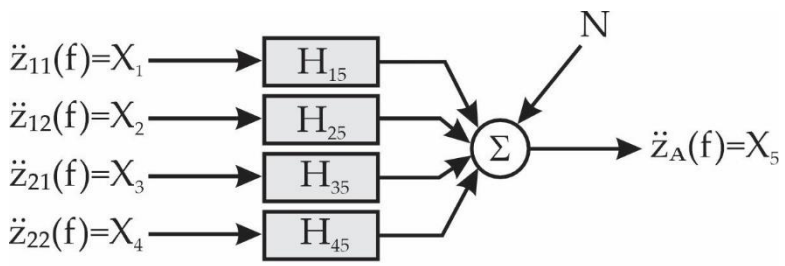

Figure 3 MISO model for coupled inputs

To begin the analysis, the spectra of the inputs and the output, X_i, $i = \overline{1,5}$, are calculated via Fourier transforms. Then, the auto-spectra, S_{ii}, $i = \overline{1,5}$, and the cross-spectra, S_{ij}, $i = \overline{1,5}$, $j = \overline{1,5}$, $i \neq j$, of the inputs and the output and S_{nn} of the output noise are calculated using the following expression, for a definite data record length of *T*:

$$S_{ij} = \frac{1}{T} \cdot E\left[X_i^* \cdot X_j\right],\ i = \overline{1,5},\ j = \overline{1,5}\ ,$$
$$S_{nn} = \frac{1}{T} \cdot E\left[N_i^* \cdot N_j\right]\ , \tag{1}$$

where: *E* is the mathematical expectation function, while X_i^*, $i = \overline{1,5}$ and N^* are complex conjugate values of spectra X_i, $i = \overline{1,5}$ and *N*, respectively.

In this coupled system, the movement of the front left wheel is directly influenced by forces coming not only from the road beneath it, but also from the remaining three wheels and the inertia of the body (due to pitch and roll coupling). Ordinary spectral analysis cannot separate how much each axle or side of the road individually contributes to the front left shock absorber cup vibrations. Therefore, *conditional spectral analysis* is introduced, which uses partial coherence functions to "eliminate" the influence of other wheels and isolate the pure contribution of only one specific input. in this case, it allows to identify the contribution of each individual wheel (input) to the body vibrations (output), thereby eliminating the mutual correlation that exists between the inputs due to the movement of the same vehicle on the same road.

Figure 4 shows conditioned MISO model with eliminated correlation between inputs by optimal transfer function. The original inputs were decoupled using the conditioned spectral analysis and replaced by a set of ordered conditioned inputs, $X_{i\cdot(i-1)!}$, $i = \overline{1,4}$. The ordinary frequency response functions were replaced with optimal frequency response functions, L_{i5}, $i = \overline{1,4}$, of the system with conditioned inputs. They are different from the frequency response

functions of the system with arbitrary selected inputs. Spectrum of the output noise N, and spectrum of the output, X_5, remain the same.

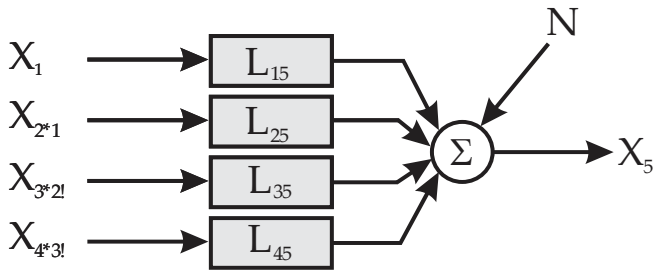

Figure 4 MISO model for conditional (decoupled) inputs

ALGORITHM FOR CONDUCTING CONDITIONAL SPECTRAL ANALYSIS

The theoretical foundations of conditional spectral analysis presented by Bendat and Piersol (2010), served as the basis for developing an algorithm for this special implementation.

First, using an iterative process, the optimal frequency response functions of the system with four conditional (decoupled) inputs, $L_{i,j}$, $i,j=\overline{1,4}$, and the conditional power cross-spectra, $S_{i,j\bullet r!}$, $r=\overline{1,3}$, are calculated alternately, in the following order:

$$
\begin{aligned}
&L_{1j}=\frac{S_{1j}}{S_{11}}, && j=\overline{2,5}\\
&S_{ij\cdot 1!}=S_{ij}-L_{1j}S_{i1}, && i=\overline{2,5},\quad j=\overline{i,5}\\
&L_{2j}=\frac{S_{2j\cdot 1!}}{S_{22\cdot 1!}}, && j=\overline{3,5}\\
&S_{ij\cdot 2!}=S_{ij\cdot 1!}-L_{2j}S_{i2\cdot 1!}, && i=\overline{3,5},\quad j=\overline{i,5}\\
&L_{3j}=\frac{S_{3j\cdot 2!}}{S_{33\cdot 2!}}, && j=\overline{4,5}\\
&S_{ij\cdot 3!}=S_{ij\cdot 2!}-L_{3j}S_{i3\cdot 2!}, && i=\overline{4,5},\quad j=\overline{i,5}\\
&L_{45}=\frac{S_{45\cdot 3!}}{S_{44\cdot 3!}}, &&\\
&S_{nn}=S_{55\cdot 3!}-L_{45}S_{54\cdot 3!} &&
\end{aligned}
\tag{2}
$$

The conditionally uncoupled system inputs are obtained based on the following iterative procedure:

$$
\begin{aligned}
X_{2\cdot 1!}&=X_2-\frac{S_{12}}{S_{11}}X_1\\
X_{3\cdot 2!}&=X_3-\frac{S_{13}}{S_{11}}X_1-\frac{S_{23\cdot 1!}}{S_{22\cdot 1!}}X_{2\cdot 1!}\\
X_{4\cdot 3!}&=X_4-\frac{S_{14}}{S_{11}}X_1-\frac{S_{24\cdot 1!}}{S_{22\cdot 1!}}X_{2\cdot 1!}-\frac{S_{34\cdot 2!}}{S_{33\cdot 2!}}X_{3\cdot 2!}\\
N=X_{5\cdot 4!}&=X_5-\frac{S_{15}}{S_{11}}X_1-\frac{S_{25\cdot 1!}}{S_{22\cdot 1!}}X_{2\cdot 1!}-\frac{S_{35\cdot 2!}}{S_{33\cdot 2!}}X_{3\cdot 2!}-\frac{S_{45\cdot 3!}}{S_{44\cdot 3!}}X_{4\cdot 3!}\ .
\end{aligned}
\tag{3}
$$

The frequency response functions of the original system with coupled inputs, H_{i5}, $i=4,3,2,1$, can be determined (in reverse order) from the previously calculated optimal frequency response functions of the system with conditional inputs, L_{ij}, $i=\overline{1,4},\ j=\overline{i,5}$, according to the following iterative procedure:

$$
\begin{aligned}
H_{45} &= L_{45} \\
H_{35} &= L_{35} - L_{34}H_{45} \\
H_{25} &= L_{25} - L_{23}H_{35} - L_{24}H_{45} \\
H_{15} &= L_{15} - L_{12}H_{25} - L_{13}H_{35} - L_{14}H_{45}.
\end{aligned}
\tag{4}
$$

Partial coherence functions between conditional inputs and output are calculated based on the expressions:

$$
\begin{aligned}
\gamma_{15}^2 &= \frac{|S_{15}|^2}{S_{11}S_{55}} \\
\gamma_{25\cdot 1!}^2 &= \frac{|S_{25\cdot 1!}|^2}{S_{22\cdot 1!}S_{55\cdot 1!}} \\
\gamma_{35\cdot 2!}^2 &= \frac{|S_{35\cdot 2!}|^2}{S_{33\cdot 2!}S_{55\cdot 2!}} \\
\gamma_{45\cdot 3!}^2 &= \frac{|S_{45\cdot 3!}|^2}{S_{44\cdot 3!}S_{55\cdot 3!}}
\end{aligned}
\tag{5}
$$

The multiple coherence function of the four-input, single-output system is calculated using:

$$
\gamma_{5:4!}^2 = \frac{S_{55} - S_{nn}}{S_{55}} = \frac{S_{55} - S_{55\cdot 4!}}{S_{55}} \tag{6}
$$

When the inputs are uncorrelated (as is the case with models with conditional inputs), the following expression also holds for the multiple coherence function:

$$
\gamma_{5:4!}^2 = \sum_{i=1}^{4} \gamma_{i5}^2 \tag{7}
$$

Based on the presented algorithm, corresponding programs were written in the MATLAB environment and appropriate diagrams needed for the vibration analysis were generated.

RESULTS AND DISCUSSION

Figure 5 shows the amplitude spectra of vertical accelerations at the centres of all four wheels and at the shock absorber-to-body connection point measured during straight line drive of the vehicle with constant speed of 70 km/h. The red curves represent vertical accelerations in the coupled state (prior to decoupling), while the blue curves show the conditioned (or decoupled) spectra following the elimination of cross-coupling effects from the excitations. The amplitude spectra are displayed on a dB scale.

From diagrams in Figure 5 b), c) and d) it can be seen that the decoupling effect is most pronounced in the frequency range 0 – 10 Hz. At some points, the blue curves are 10 dB to 15 dB lower than the red ones. This demonstrates that vibrations originating from body motion (pitch and roll coupling) or from the other wheels have been successfully eliminated from the signal.

The main resonant wheel-hop domain (10 Hz – 20 Hz) is the most energy-intensive zone on the diagrams, where peaks reach absolute maximums of approximately 52 dB to 60 dB at frequencies between 11 Hz and 15 Hz. This corresponds to the natural frequency of the unsprung mass (the wheel). Following decoupling (blue curve), a general drop in energy level of several dB is observed, and the spectrum is "cleared" of extreme parasitic spikes.

In frequency range above 20 Hz, acceleration intensity gradually decreases toward values of 20 dB – 30 dB. In this domain, the curves converge significantly and intertwine. This indicates that high-frequency behaviour is dominated by the local dynamics of the wheel itself and road roughness, over which the global decoupling of the suspension systems no longer exerts a dominant influence.

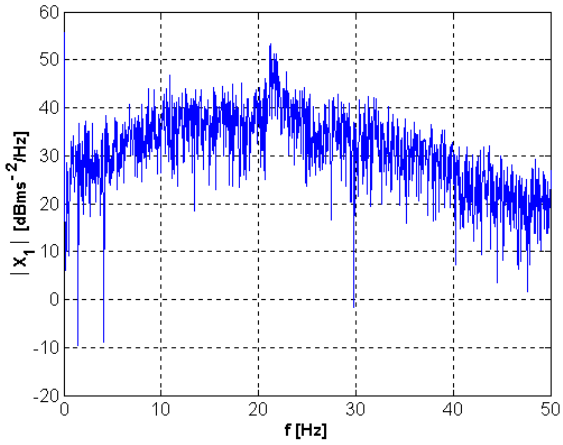

a) Amplitude spectrum of vertical acceleration at the centre of front left wheel

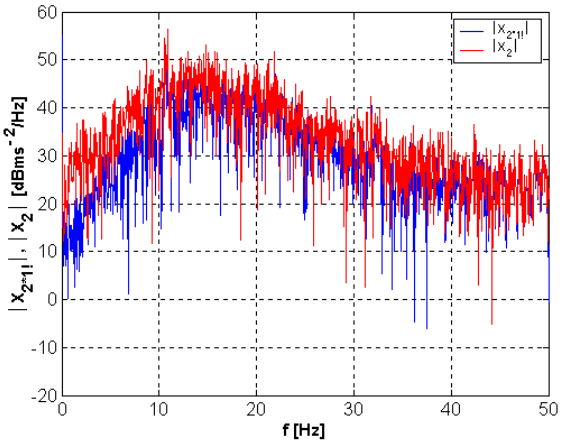

b) Amplitude spectrum of vertical acceleration at the centre of front right wheel after and before decoupling

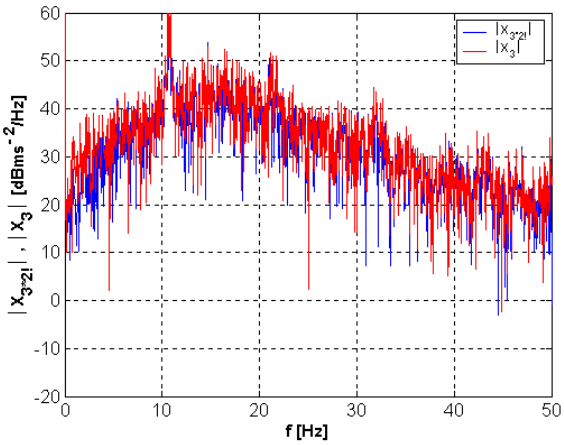

c/ Amplitude spectrum of vertical acceleration at the centre of rear left wheel after and before decoupling

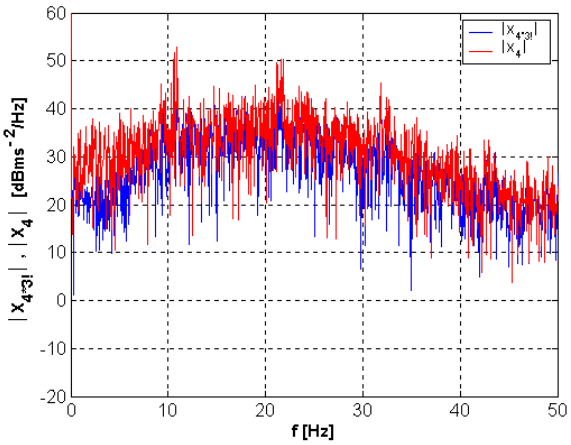

d/ Amplitude spectrum of vertical acceleration at the centre of rear right wheel after and before decoupling

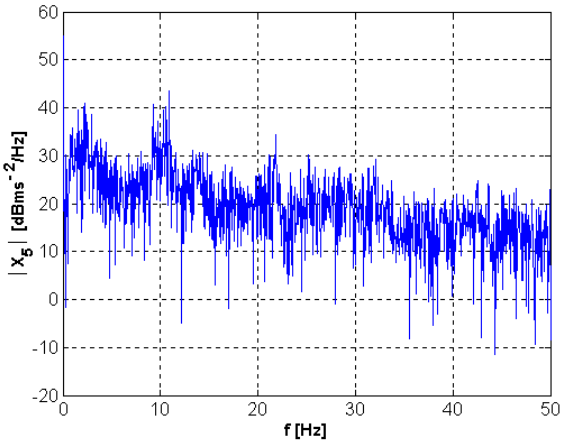

e/ Amplitude spectrum of vertical acceleration at the shock absorber-to-body connection point

Figure 5 Amplitude spectra of vertical accelerations at the centres of four wheels and the shock absorber-to-body connection point for straight line drive with constant speed of v = 70 km/h

Figure 6 shows the amplitude-frequency characteristics (AFC) of the frequency response functions for vertical acceleration transfer channels from all four wheels to the shock absorber-to-body connection point, for straight-line drive at a constant speed of v = 70 km/h and for the original (coupled) inputs. Given that the study involves experimental measurements on an actual vehicle, the displayed diagrams reflect all the imperfections and complexities of the real-world system - aspects often overlooked by classical theoretical studies. The pronounced oscillations, "noise," and sharp drops in the diagram are direct consequences of the actual measurement conditions.

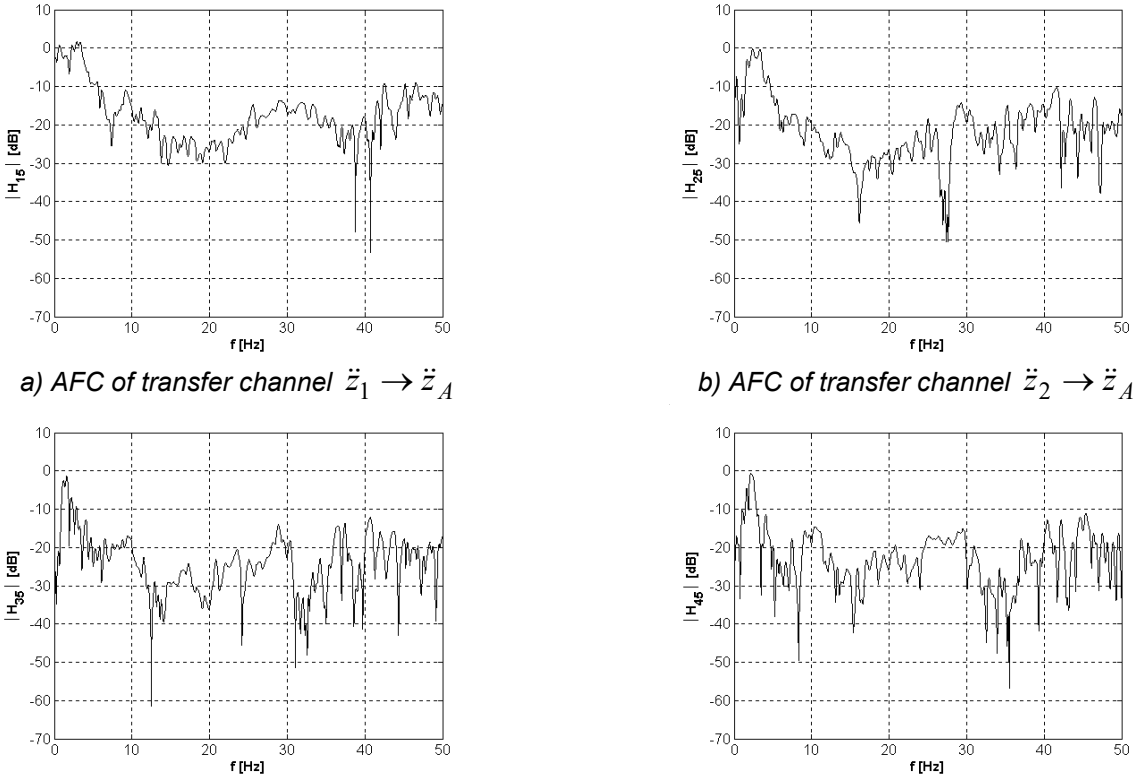

a) AFC of transfer channel $\ddot{z}_1 \rightarrow \ddot{z}_A$

b) AFC of transfer channel $\ddot{z}_2 \rightarrow \ddot{z}_A$

c) AFC of transfer channel $\ddot{z}_3 \rightarrow \ddot{z}_A$

d) AFC of transfer channel $\ddot{z}_4 \rightarrow \ddot{z}_A$

Figure 6 Amplitude-frequency characteristics (AFC) of ordinary frequency response functions for straight-line drive at constant speed v = 70 km/h for the original inputs

Analysis of characteristic frequency zones on the diagrams in Figure 6 shows the following:

- The amplitude reaches a maximum in the range of vehicle body resonance. Road excitation in this range is transmitted to the vehicle body at a 1:1 ratio. Distinct peaks are observed around 2 Hz, representing the resonance of the sprung mass (car body).
- In the range of wheel resonance (10 Hz to 20 Hz), the curves show a drop in the overall level to between -20 dB and -30 dB. A local maximum is visible around 10 Hz, resulting from the resonance of the unsprung mass (the wheel hop).
- In the range of structural vibrations (above 20 Hz) the diagrams display complex waveforms with pronounced fluctuations. Dynamics at these frequencies are determined not only by spring stiffness but also by the elasticity of the vehicle body structure itself. Some extremely sharp drops in amplitude (anti-resonances) are observed that indicate that complete cancellation of dynamic forces occurs at the shock absorber mounting point (structural zeros). At these frequencies, vibrational energy is transferred in another direction (e.g., transverse or longitudinal motion), or phase cancellation of the waves occurs between the point of excitation (tire contact patch) and the point of measurement (accelerometer on the shock absorber mount). In the higher ranges, the amplitude rises again. This indicates the presence of high-frequency structural modes of the chassis or suspension components.

Figure 7 shows amplitude frequency characteristics (AFC) and phase frequency characteristics (FFC) of optimal frequency response functions of the model of straight-line drive at constant speed v = 70 km/h with decoupled inputs.

The example analysis of AFC in Figure 7 a) of frequency response functions of the transfer path between the vertical acceleration at the front left wheel centre and the shock absorber-to-body connection point shows a clear peak slightly above 0 dB that represents the resonance of the vehicle body (sprung mass), where the system amplifies vertical vibrations originating from the road. Second resonance around 10 Hz to 12 Hz represents a secondary local peak that corresponds to the resonance of the wheel and tire (wheel hop), characterized by pronounced vibrations of the unsprung mass. In frequency domain above 20 Hz, the amplitude drops, indicating that the suspension successfully dampens high frequencies. Pronounced fluctuations at higher frequences indicate the presence of additional vibration sub-modes, such as vibrations of the seat, engine, or elastic chassis mounts.

Analysis of FFC in Figure 7 a) shows that the phase starts at 0° and decreases toward -100° and -150° as frequency rises, indicating a natural time lag (delay) in the vehicle mass response relative to road excitation. Phase jumps are seen as abrupt vertical transitions from -180° to +180° that represent so-called „phase wrapping“. This is a computational/graphical effect occurring in software (such as MATLAB) when the phase crosses the ±180° boundary. It also indicates the system's high sensitivity and complexity at these frequencies.

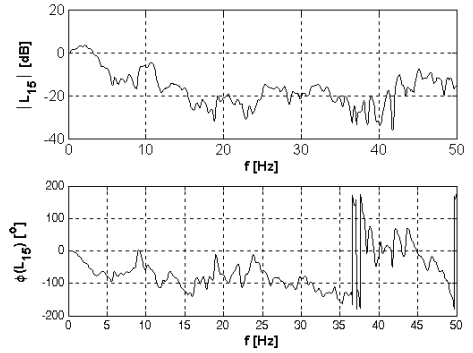

a) AFC and FFC of channel $X_1 \rightarrow X_5$

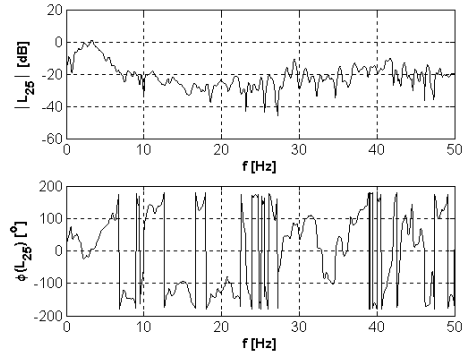

b) AFC and FFC of channel $X_{2*1!} \rightarrow X_5$

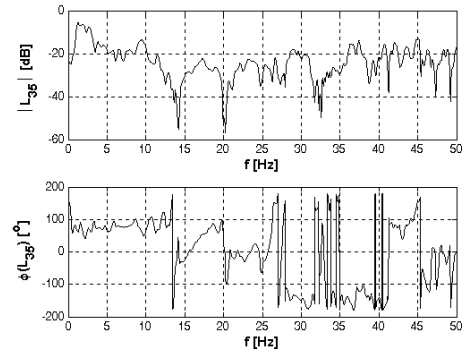

c) AFC and FFC of channel $X_{3*2!} \rightarrow X_5$

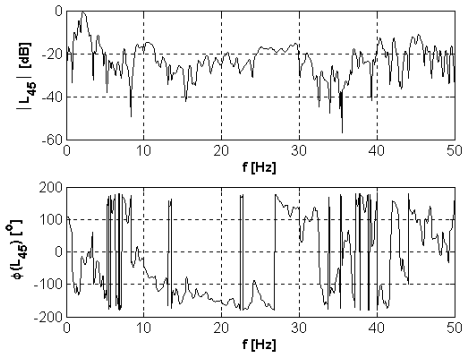

d) AFC and FFC of channel $X_{4*3!} \rightarrow X_5$

Figure 7 AFC and FFC of frequency response functions for the model of straight-line drive at constant speed v = 70 km/h with decoupled inputs

Analysis of partial coherence functions is an advanced method in signal processing and vibration analysis that is used to determine the linear dependence between two signals after mathematically removing the influence of other measured sources from input and output signals. In this case, „other sources“ are: the influence of the remaining three wheels, the engine, aerodynamic noise, etc.

Figure 8 shows partial coherence functions for a model of straight-line drive at constant speed of v = 70 km/h. Based on the provided diagrams, a detailed analysis of the wheel–shock absorber transmission system's behaviour can be performed across several characteristic frequency zones in the 0 to 20 Hz range. The example presented in diagram in Figure 8 a) shows the following:

- Extremely high linearity is observed in low frequency zone (0 – 3 Hz), with coherence values between 0.85 and 1.0 and maximum at 0.5 Hz – 1 Hz. This range is dominated by basic car body resonances (bounce and pitch). The car body directly follows macro-movements of the wheel, with minimal influence of nonlinearities.
- In frequency zone between 3 Hz and 5 Hz, a drop in coherence values to 0.55 is evident. This means that the system begins to lose its strictly linear coupling. Frequently, it is the zone in which the first effects of shock absorber damping and suspension elasto-kinematics occur.
- Pronounced vibrations and nonlinearity occur in the frequency range between 5 Hz and 15 Hz. The partial coherence values fluctuate between 0.25 to 0.70 with the occurrence of local peaks and sharp falls. This range encompasses the frequency of the unsprung mass (so-called "wheel hop"), typically between 10 Hz and 15 Hz). The fluctuations indicate the pronounced nonlinear effects (asymmetry of shock absorber damping - difference between the compression and expansion strokes, dry friction in gaskets and nonlinear behaviour of rubber silent blocks).
- The loss of linear coupling and isolation induces the dramatic drop of coherence values in the frequency range between 15 Hz and 19.5 Hz. At these frequencies, vertical wheel acceleration at shock absorber connecting point is no longer linearly coupled with the acceleration at the wheel centre. Also, low coherence indicates that local structural resonances begin to dominate at the shock absorber connecting point.
- Above 19.5 Hz, there is a renewed growth in coherence values towards 0.5, which hints at the entrance to the new zone of structural couplings, or resonance above 20 Hz.

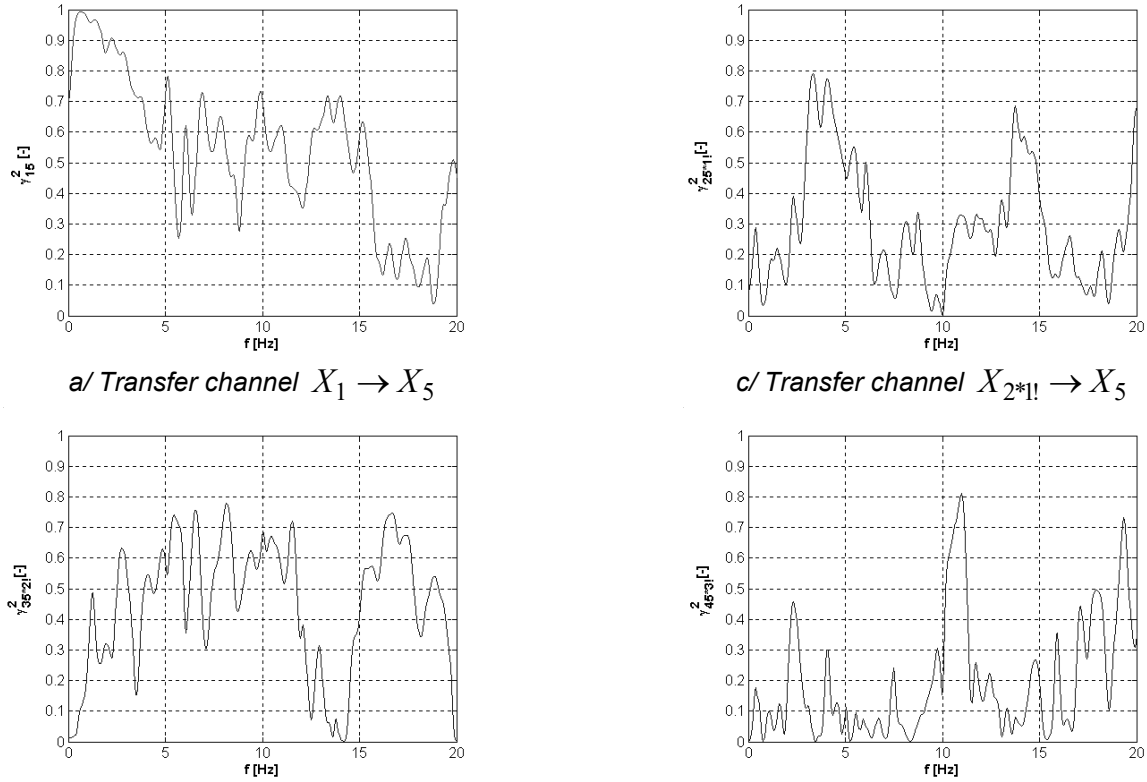

a/ Transfer channel $X_1 \rightarrow X_5$

c/ Transfer channel $X_{2*1!} \rightarrow X_5$

e/ Transfer channel $X_{3*2!} \rightarrow X_5$

g/ Transfer channel $X_{4*3!} \rightarrow X_5$

Figure 8 Partial coherence functions for a model of straight-line drive at constant speed of v = 70 km/h

A comparison between partial coherence plots in diagrams shown in Figure 8 a) (path between front left wheel vertical acceleration and front left shock absorber vertical acceleration) and d) (path between rear right wheel vertical acceleration and front left shock absorber vertical acceleration), clearly reveals that the front-left wheel housing is subjected to two completely different types of excitation: at low frequencies, it is driven by the local (left) wheel, whereas at frequencies of 11 Hz and 19.3 Hz, it is dominated by energy transmitted from the diagonally opposite (rear-right) wheel through the vehicle body structure.

The frequency of 11 Hz corresponds to the resonance of the unsprung mass. With a rear solid axle of the experimental vehicle, this resonance does not occur solely in the vertical plane; instead, it triggers a "trampoline effect" (bouncing combined with rotation), causing the axle to oscillate laterally and vertically around its centre of mass. When the rear right wheel enters resonance at 11 Hz, the solid beam acts as a lever, transferring force to the left side of the axle. In the absence of a rear stabilizer bar to dampen this tilting motion, the combined force (vertical force plus torsional moment) is transmitted to the chassis via the trailing arms and axle mounting points. This energy wave travels through the floor and strikes the front-left suspension, which is coupled to the front axle via the front stabilizer bar. The result is a cross-coherence peak exceeding 0.8, indicating that the front-left suspension is subjected to mechanical stress caused by the resonance of the rear solid axle.

Figure 9 presents the multiple coherence function during straight-line drive at constant speed of v = 70 km/h.

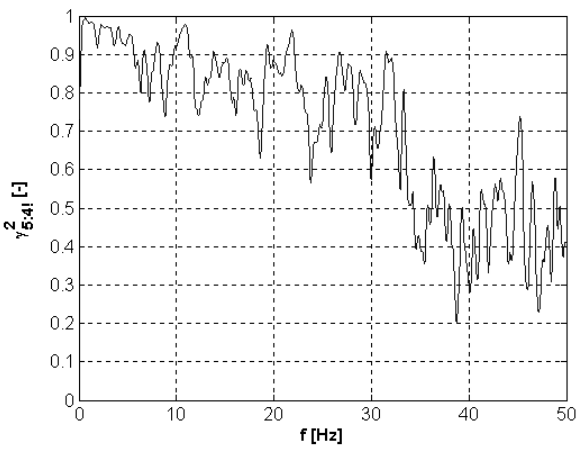

Figure 9 Multiple coherence function for the output during straight-line drive at constant speed of v = 70 km/h

The multiple coherence function values confirm a strong linear dependence between the four inputs (vertical accelerations at wheels) and the point on the vehicle body (output – vertical acceleration at the front left shock absorber connecting point) in the range up to 33 Hz, followed by a sharp drop and coherence dispersion at higher frequencies. Multiple coherence is extremely high (between 0.85 and 0.98) in the frequency range between 0 and 10 Hz. Almost all of the vibration at the shock absorber mount is a direct, linear consequence of excitation from the wheels. The system is nearly perfectly linear here. Coherence remains at a high level (mostly between 0.65 and 0.95) in the range between 10 Hz and 33 Hz, but with noticeable drops. The unsprung mass resonance occurs around 10 Hz to 15 Hz. The system continues to predominantly transmit energy from the wheels to the body. The drops at 19 Hz and 24 Hz may indicate local nonlinearities or the brief interference of another vibration source. In the range above 33 Hz, multiple coherence drops sharply and fluctuates between 0.2 and 0.7. Vibrations at the shock absorber mount at frequencies above 33 Hz can no longer be explained solely by the vertical movement of the wheels.

CONCLUSIONS

The application of the conditional spectral analysis (CSA) to calculate frequency response functions is the most methodologically correct approach when dealing with experimental measurements on roads with multiple coupled inputs. If a simple (classical) frequency response function between the front-left shock absorber vertical acceleration and the front-left wheel vertical acceleration is calculated, the cross-coupling from e.g. front right wheel would introduce a systematic error (bias). CSA successfully solves this problem.

Decoupling done by application of CSA gave excellent results in reducing the transmitted energy at low and medium frequencies (0 – 25 Hz). This confirmed that the pure contribution of the primary excitation of the front left wheel was successfully isolated, which in practice provides a more accurate identification of suspension parameters and a better analysis of tire-road contact. The experiment confirmed that the connection between the wheels at the selected vehicle speed is highly linearly dependent at low frequencies (up to 10 Hz), partially dependent in the wheel resonance zone (10 Hz – 25 Hz), and completely independent at high frequencies (above 25 Hz). The CSA successfully isolated the own dynamics of the front left wheel, cleaning the signal from the influence of the opposite side of the vehicle.

Based on the CSA and the conditional spectra, clear guidelines for vehicle optimization may be obtained. For example, the manner in which the stiffness of the shock absorber cup should be adjusted can be obtained. If the CSA shows high coherence at frequencies above 30 Hz, the rubber element at the shock absorber - body connection point must be softer to absorb the structure-borne noise. In view of damping optimisation, CSA allows the isolation of "false" peaks in the spectrum that originate from the subsequent sway of the rear of the vehicle, guiding engineers to the exact frequencies at which the damper itself effectively cancels the ground energy.

Key advantages of this analysis in NVH (Noise, Vibration, and Harshness) area may be seen in performing structural stiffness isolation. CSA allows engineers to see whether the transmission of vibrations from the left side or from the rear axle is due to the road being similar (excitation correlation) or because the body is too flexible (mechanical transmission).

ACKNOWLEDGMENTS

Research presented in this paper was supported by Ministry of science, technological development and innovation of the Republic of Serbia, contract registration number 451-03-34/2026-03/200107.

REFERENCES

Bendat, J. S., & Piersol, A. G. (2010). *Random Data: Analysis and Measurement Procedures* (4th edn). John Wiley & Sons, Inc.

Chen Ke, Li Mengyu, & Li Chunping. (2018). Application of coherence analysis study on identification of vehicle noise sources. *JVE Journal of Vibroengineering*, *20*(7), 2745–2757.

Demić, M., & Lukić, J. (2009). Investigation of the transmission of fore and aft vibration through the human body. *Applied Ergonomics*, *40*, 622–629. https://doi.org/doi:10.1016/j.apergo.2008.05.002

Demić, M., Lukić, J., & Milić, Ž. (2002). SOME ASPECTS OF THE INVESTIGATION OF RANDOM VIBRATION INFLUENCE ON RIDE COMFORT. *Journal of Sound and Vibration*, *253*(1), 109–129. https://doi.org/doi:10.1006/jsvi.2001.4252

Hosseini Fouladi, M., Mohd. Nor, Mohd. J., & Kamal Ariffin, A. (2009). Spectral analysis methods for vehicle interior vibro-acoustics identification. *Mechanical Systems and Signal Processing*, *23*, 489–500. https://doi.org/doi:10.1016/j.ymssp.2008.04.001

Leclere, Q., Pezerat, C., Laulagnet, B., & Polac, L. (2005). Application of multi-channel spectral analysis to identify the source of a noise amplitude modulation in a diesel engine operating at idle. *Applied Acoustics*, *66*, 779–798. https://doi.org/doi:10.1016/j.apacoust.2004.11.001

Miloradović, D., & Glišović, J. (2004). Spectral analysis of passenger vehicle's tie-rod loads due to road roughness. *Proceedings of XIII International Scientific Meeting 'Motor Vehicle & Engines*, 203–212.

Miloradović, D., Lukić, J., Glišović, J., & Miloradović, N. (2022). Identification of Vehicle System Dynamics from the Aspect of Interaction between the Steering and the Suspension Systems. *Machines*, *10*, 1–28. https://doi.org/10.3390/machines10010046

Qui, Y., & Griffin, M. J. (2004). Transmission of vibration to the backrest of a car seat evaluated with multi-input models. *Journal of Sound and Vibration*, *274*, 297–321.

The 11th International Congress
Motor Vehicles & Motors 2026
Kragujevac, Serbia
October 8th - 9th, 2026

Motor Vehicles & Motors

MVM2026-066
https://doi.org/10.24874/CMVM2026.066
Original scientific paper

Matija Simanić[1]
Ilija Vidović[2]
Luka Milić[3]
Momir Drakulić[4]
Aleksandar Đurić[5]

SIMULATION-BASED MOTION ANALYSIS OF A LIGHTWEIGHT TRACKED ROBOT USING WEBOTS

ABSTRACT: This paper presents the modelling of a lightweight tracked robot and the simulation of its motion using the Webots software package. The robot model was developed in Webots based on an existing model of the Jaguar robot, while the simulation was performed on a scaled 3D representation of the Military Academy grounds in Belgrade. The motion analysis includes the analysis of various kinematic and dynamic parameters, such as the robot's trajectory, travelled distance, speed and acceleration, orientation angle, and longitudinal motion force. Using the Python programming language, a controller was developed directly in Webots to enable the robot's motion and data collection for motion analysis. A single simulation run was performed using one complex trajectory. The robot travelled approximately 143 m during 97 s of simulation, with an average speed of 1.47 m/s compared with the set speed of 1.5 m/s, corresponding to a relative deviation of approximately 2.0%. The consistency of the developed model was assessed based on the obtained kinematic and dynamic parameters.

KEYWORDS: Tracked robot, Webots, Kinematic parameters, Dynamic parameters, Python.

ANALIZA KRETANJA LAKOG GUSENIČNOG ROBOTA ZASNOVANA NA SIMULACIJI KORIŠĆENJEM WEBOTS PLATFORME

REZIME: Ovaj rad predstavlja modeliranje lakog guseničnog robota i simulaciju njegovog kretanja korišćenjem softverskog paketa Webots. Model robota je razvijen u Webots-u na osnovu postojećeg modela robota Jaguar, dok je simulacija izvršena na skaliranoj 3D reprezentaciji kompleksa Vojne akademije u Beogradu. Analiza kretanja

[1] *Matija Simanić, University of Defence in Belgrade, Military Academy, msimanic4@gmail.com*
[2] *Ilija Vidović, University of Defence in Belgrade, Military Academy, ilijavidovic50@gmail.com*
[3] *Luka Milić, University of Defence in Belgrade, Military Academy, luka.milic777@gmail.com*
[4] *Momir Drakulić, University of Defence in Belgrade, Military Academy, momir.drakulic@va.mod.gov.rs,*
https://orcid.org/0000-0002-8367-7281
[5] *Aleksandar Đurić, University of Defence in Belgrade, Military Academy, aleksandar.djrc@gmail.com,*
https://orcid.org/0000-0002-2165-528X

obuhvata analizu različitih kinematskih i dinamičkih parametara, kao što su: putanja robota, pređeni put, brzina i ubrzanje, ugaoni položaj i sila uzdužnog kretanja. Koristeći programski jezik Python, u Webots-u je razvijen kontroler koji omogućava kretanje robota i prikupljanje podataka za analizu kretanja. Jedna simulacija je izvršena korišćenjem jedne složene putanje. Robot je prešao približno 143 m tokom 97 s simulacije, sa prosečnom brzinom od 1,47 m/s u poređenju sa podešenom brzinom od 1,5 m/s, što odgovara relativnom odstupanju od približno 2,0%. Konzistentnost razvijenog modela je procenjena na osnovu dobijenih kinematskih i dinamičkih parametara.

KLJUČNE REČI: gusenični robot, Webots, kinematski parametri, dinamički parametri, Python

INTRODUCTION

Bruzzone et al. (2022) state that tracked robots are widely used for operation on uneven and soft terrain, since their specific ground pressure is significantly lower than that of wheeled robots, while they are more mobile than legged robots. In addition, they provide greater stability and better obstacle-crossing capability. Due to these characteristics, they are widely used in military, rescue, and other tasks performed in complex environments.

Simulators are widely used for conducting tests due to their significant advantages over testing with physical prototypes. Some of the main advantages include:

- Lower financial costs,
- Reduced testing time,
- The possibility of repeating tests,
- Rapid modification of simulation parameters,
- Determination of the required characteristics of a real system.

Gunjal (2021) demonstrated that motion simulations can be performed using the Webots software package, which was also used in this work. Other software tools that can be used include Simulink within the MATLAB software package, as described by Haidar (2024), as well as Gazebo, which Rivera et al. (2019) describe as an important software tool in mobile robotics due to its high flexibility and realistic simulation of physical processes.

Webots enables the simulation of both passive and active objects, as well as the use of different types of sensors and control mechanisms. Control algorithms can be implemented using different programming languages, while Python was selected for the purposes of this study. The physics engine enables physical characteristics such as moments, forces, contact between bodies, and rigid-body motion dynamics to be taken into account. Webots also enables the simulation of contact between the ground and the tracked locomotion system.

The aim of this work is to develop a tracked robot model based on the real Jaguar robot and to create a simulation environment representing the Military Academy grounds, in which complex robot motion can be simulated. Finally, the kinematic and dynamic parameters obtained from the simulation are analyzed and the consistency of the developed robot model is assesed. The main contribution of this work is the development and application of a Webots-based model that combines a modified tracked robot representation with a scaled 3D terrain for the analysis of complex robot motion. The study investigates whether the developed model can adequately reproduce the expected kinematic and dynamic behavior of the tracked robot under the considered simulation conditions.

Kinematic model

Hellström (2011) states that the motion of tracked robots is based on the principle of differential steering. Separate drive mechanisms are present on the left and right tracks, and therefore the direction of motion is controlled by changing the relative speeds of the left and right tracks. Thus, if both tracks have the same speed and direction of motion, the robot moves in a straight line, while if the tracks have different speeds, the robot follows a circular trajectory. Bruzzone et al. (2022) also describe a steering condition in which the tracks have the same speed but opposite directions of motion, causing the robot to rotate about its own vertical axis. This type of steering was also used to control the robot during the simulation.

Kozłowski and Pazderski (2004) describe skid-steer steering as a more realistic approach to modeling tracked robot motion. It is based on the principle of differential steering, with lateral slipping occurring due to the interaction between the robot and the ground, as described by Bruzzone et al., (2022)

In the present simulation, differential steering is used as the control principle, while lateral track slip is not explicitly defined through a separate skid-steering model. Instead, the interaction between the tracked locomotion system and the terrain is handled implicitly by the Webots physics engine through the Track and Physics nodes. Therefore, the

kinematic equations presented in this section represent the idealized differential-steering model, while the simulated dynamic response additionally reflects the physical interaction implemented in Webots.

The position of a mobile robot is defined using a coordinate system. Thus, the robot can be represented by the coordinates of its center and its orientation angle with respect to the coordinate system. The state vector is commonly defined in the following form:

$$q = [x, y, \theta] \tag{1}$$

Figure 1 presents the kinematic model of a tracked robot with differential steering. The linear velocities of the left and right tracks, denoted as v_{left} and v_{right}, respectively, are shown, as well as the angular velocity of the robot about its vertical axis, denoted by ω. The position and orientation of the robot are defined with respect to the coordinate system (x_w,y_w), while the angle ϑ represents the robot orientation with respect to the coordinate system, i.e., its direction of motion. The track width, denoted by w, can also be observed.

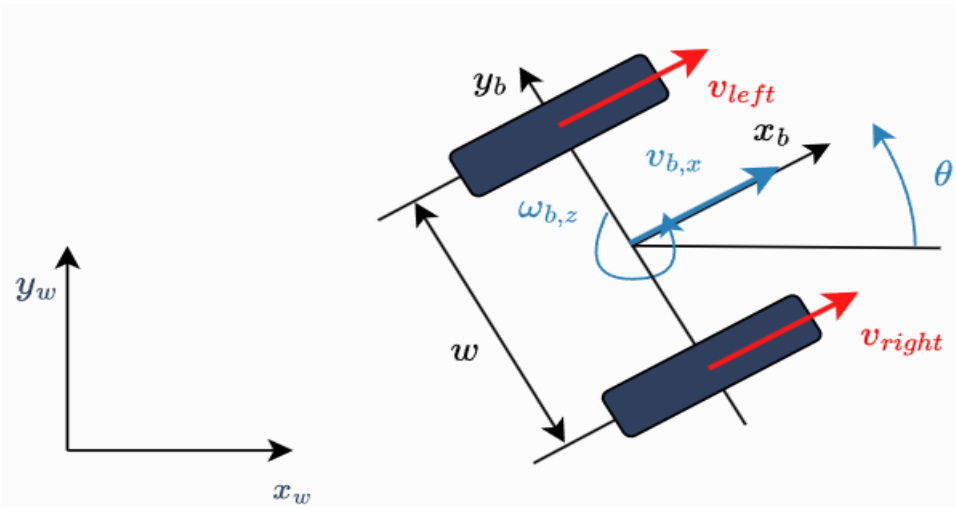

Figure 1 Kinematics of a differentially controlled tracked robot *(ROS 2 Control maintainers, n.d.)*

According to Muždeka and Rakić (2008), the linear velocity of the robot center is calculated as the average of the left and right track velocities, while the difference between the left and right track velocities divided by the track width represents the angular velocity of the robot. This can be expressed by the following equations.

$$v = \frac{v_{left} + v_{right}}{2} \tag{2}$$

$$\omega = \frac{v_{left} - v_{right}}{w} \tag{3}$$

Based on these equations, the equation for the robot's turning radius can be derived as follows:

$$R = \frac{w}{2}\frac{v_{left} + v_{right}}{v_{left} - v_{right}} \tag{4}$$

This equation confirms that when the track velocities are approximately equal, the robot tends to move in a straight line, while an increasing difference between the track velocities results in a circular trajectory with a smaller turning radius.

Modelling of the tracked robot and simulation environment in Webots

As previously mentioned, the aim of this work was to develop a tracked robot model in the Webots software package based on the real Jaguar robot, perform a simulation of complex robot motion, and subsequently analyse the obtained results. The modelling and simulation were performed using Webots R2025a with the Open Dynamics Engine (ODE) physics engine. The robot modelling process began with the selection of the existing SurveyorSrv1 tracked robot model, shown in Figure 2.

The existing upper structure with sensors and cameras was first removed from this robot. This modification, as well as all subsequent changes, was performed within the PROTO node, which is used to modify and define the characteristics of the robot. In order to obtain the final appearance of the robot, its physical, geometric, and structural

characteristics were modified, including the track width, wheel diameter, chassis dimensions, robot colour and mass, as well as the addition of a camera mount with a camera positioned at the same height as on the real robot. Table 1 represents robot parameters that are modified in PROTO node.

Table 1 *Robot parameters*

Robot mass [kg]	14
Distance between tracks [m]	0.370
Track wheel radius [m]	0.075
Track width [m]	0.059
Distance between front/rear track wheels [m]	0.495

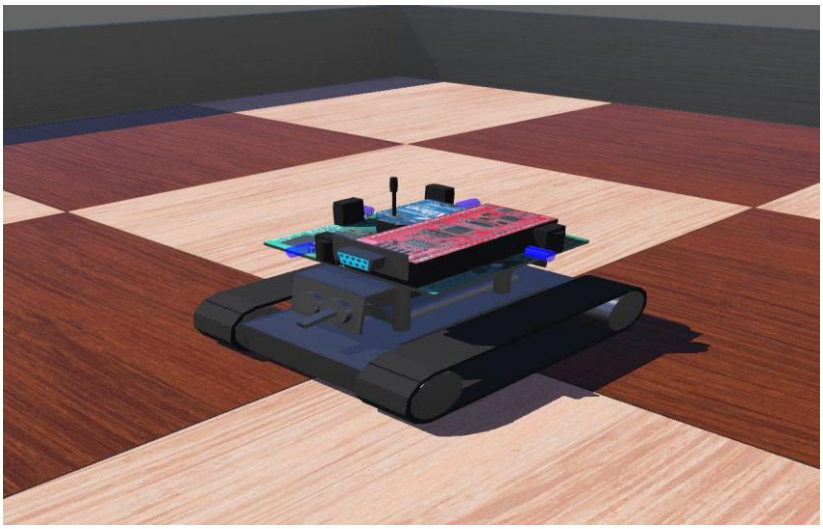

Figure 2 Tracked robot SurveyorSrv1

This approach resulted in a model that closely corresponds to the real Jaguar robot. The final appearance of the tracked robot modelled in Webots is shown in **Error! Reference source not found.**, while **Error! Reference source not found.** presents the real Jaguar robot.

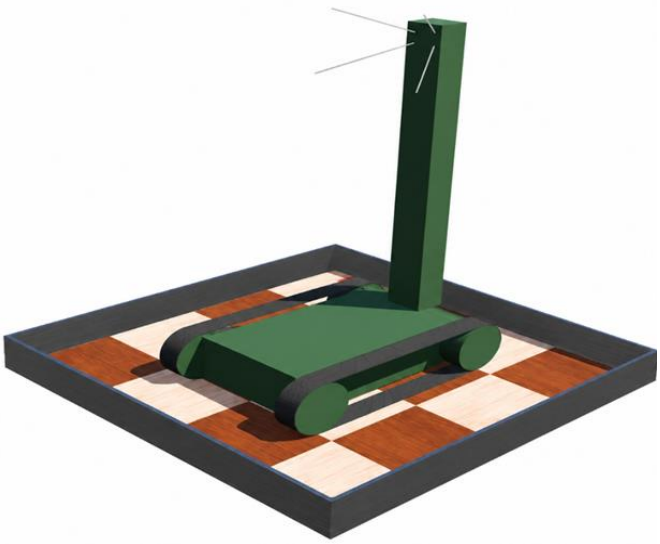

Figure 3 Model of the tracked robot in Webots

Figure 4 Model of the real tracked robot Jaguar

To achieve realistic contact between the ground and the tracked locomotion system, the Track node was used. It enables the definition of the track shape and trajectory, the addition of drive elements, animation of the tracked mechanism, and simulation of its interaction with the ground. LinearMotor elements were used to control the motion, while TrackWheel elements were used to define the drive and idler wheels. According to Cyberbotics Ltd., n.d. (2026, May 26), the animatedGeometry parameter defines the appearance and geometry of the animated objects, while geometriesCount defines the number of animated objects that move along the track trajectory. In this work, these parameters were used for the visual representation of the tracks.

The boundingObject element was used to define the collision geometry of the chassis and, more importantly, the tracked locomotion system. An important feature of boundingObject is that it does not have to exactly follow the geometry of the object whose collision it represents, but can instead approximate its physical behaviour. In this work,

this feature was used to define the collision object of the tracked locomotion system, which was represented by two cylinders and one box element. The cylinders follow the geometry of the wheels, while the box provides contact with the ground along the entire length of the tracked system.

In order to enable contact and motion of the robot, as well as to take other physical laws into account, the Physics node was included.

Table 2 represents specified values in Webots nedeed for simulation.

Table 2 *Specified values in Webots*

Robot speed [m/s]	1.5
Friction coefficient	0.8
Rolling resistance coefficient	0.05

No experimental measurements from the real Jaguar robot were used for calibration or quantitative validation of the simulation model. The model parameters were defined based on the available physical and geometric characteristics of the real robot, while the consistency of the developed model was assessed through the internal consistency of the simulated kinematic and dynamic parameters.

The scaled representation of the Military Academy grounds was created using the Blosm add-on within the Blender software package. It was used to obtain a 3D model of the terrain and its real configuration. Additional modifications of the terrain were then performed in Blender to facilitate its use in the simulation. The prepared terrain was exported in the .obj format and imported into Webots, where the Solid and Mesh nodes were used to display and utilize the complex terrain within the simulation. Here, the boundingObject element was also required to provide the reaction of the ground to the tracked locomotion system and thus enable its motion. **Error! Reference source not found.** shows the terrain imported into Webots.

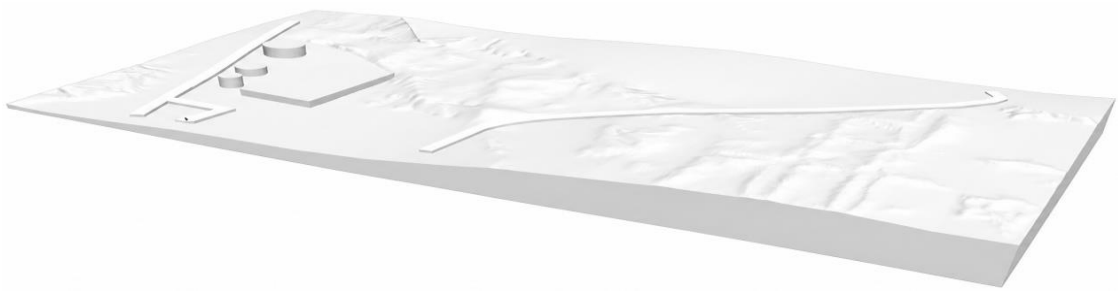

Figure 5 Display of scaled-down terrain of the Military academy

Simulation setup and data collection

Robot motion control was implemented using the Python programming language and the Webots Python API. The API provides access to nodes, sensors, actuators, and other simulation elements through the controller module, enabling robot motion and control within the simulation. Motion control was achieved by changing the speeds of the left and right tracks using the LinearMotor element. The robot was controlled manually using keyboard commands:

- W – forward motion,
- S – backward motion
- D – turning right,
- A – turning left.

Since the robot was controlled manually using keyboard commands, the exact trajectory cannot be reproduced with the same precision in repeated simulations. Therefore, the presented results are representative of the considered simulation scenario rather than a statistically repeatable experimental dataset. Automated trajectory generation and predefined control inputs would enable more objective comparison and improved repeatability in future studies.

In addition, the control code was used to collect the data required for motion analysis. Knowing this it is clear that a single simulation was run on a complex trajectory.

The following parameters were recorded:

- time,
- lateral displacement,
- longitudinal displacement,
- horizontal displacement,

- travelled distance,
- speed,
- acceleration,
- orientation angle,
- terrain inclination angle,
- acceleration-induced force,
- slope-induced force,
- rolling resistance force,
- total longitudinal force acting on the robot.

The simulation was performed using a single complex motion on the imported terrain. The complex motion consisted of straight-line motion, turns, downhill motion, and uphill motion. To facilitate the interpretation and verification of the validity of the obtained simulation results, Figure 6 presents the robot's trajectory during the simulation. This trajectory enables the obtained diagrams to be related to specific sections of the robot's motion, including straight-line motion, turning, uphill, and downhill sections.

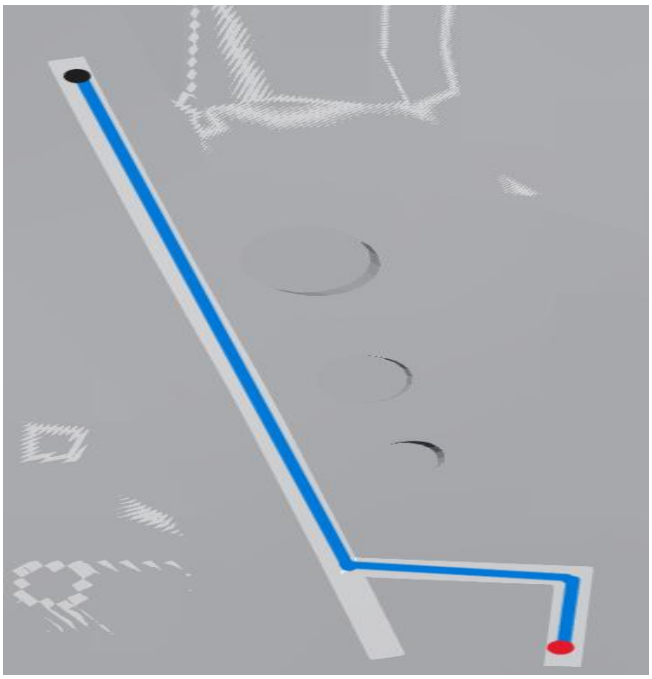

Figure 6 Robot trajectory during the simulation

Results and Discussion

At the beginning of the simulation, the robot control code began recording the data described in the previous section. The simulation results were obtained directly from the control code and used to generate graphs describing the robot's motion. The recorded data include the robot's trajectory, travelled distance, speed, acceleration, orientation angle, and longitudinal force. These parameters are analysed to evaluate the robot's motion during the simulation and the consistency of the developed model. Particular attention is given to the relationship between the robot's motion, changes in terrain configuration, and the analysed kinematic and dynamic parameters.

Robot trajectory

Error! Reference source not found. and **Error! Reference source not found.** present the 3D trajectory of the robot and its trajectory in the XY plane, respectively. Based on **Error! Reference source not found.**, changes in height with respect to the coordinate system can be observed, corresponding to the uphill and downhill sections that the robot traversed during the simulation. **Error! Reference source not found.** enables a more straightforward analysis of changes in the direction of motion. The diagrams clearly show the straight-line sections of the trajectory, as well as the points at which changes in the direction of motion occurred.

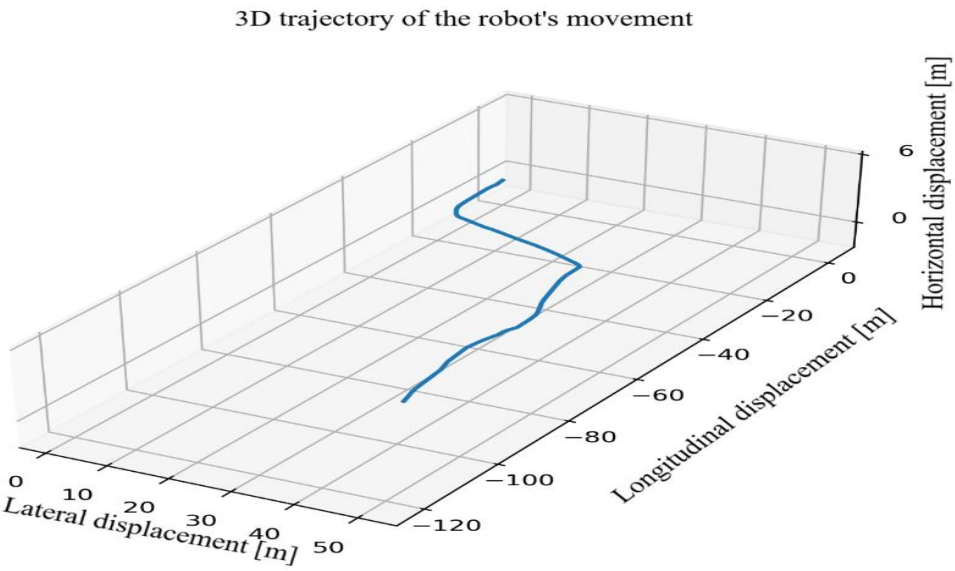

Figure 7 3D trajectory of the robot's movement

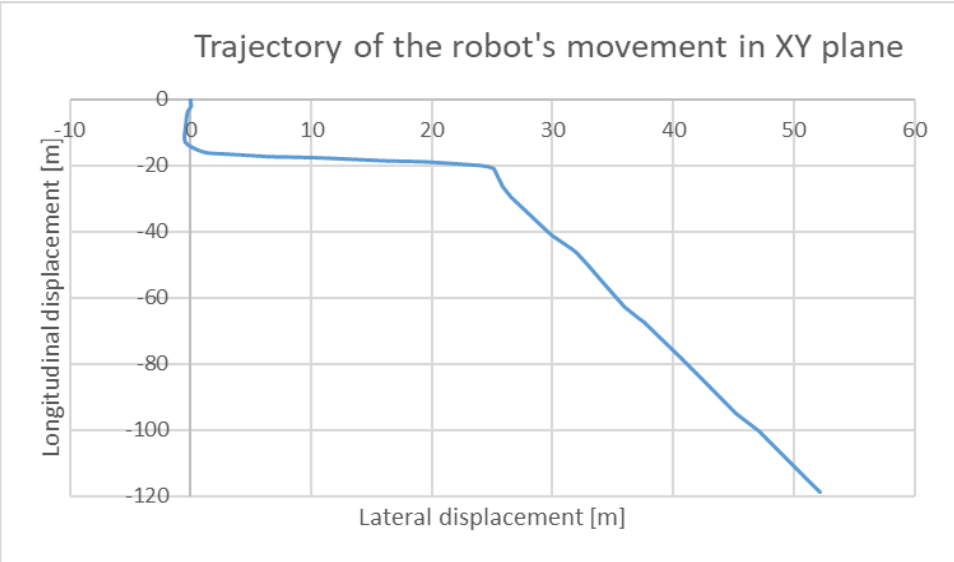

Figure 8 Trajectory of the robot's movement in XY plane

Travelled distance

Figure 9 shows the total travelled distance as a function of time. The diagram shows that the robot travelled approximately 143 m during 97 s of simulation. The average speed of the robot can be determined by dividing the total travelled distance by the simulation time. The obtained average speed was 1.47 m/s compared with the set speed of 1.50 m/s, corresponding to a relative deviation of approximately 2.0%. The diagram also shows that the robot moved continuously throughout the simulation, without stopping.

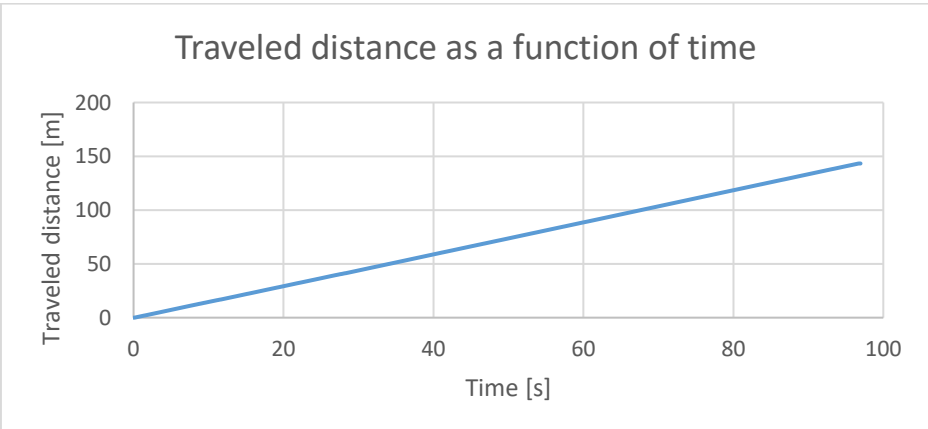

Figure 9 Travelled distance as a function of time

Robot speed and acceleration

The analysis of the robot's speed and acceleration is one of the most important aspects of the motion analysis, as these parameters enable the evaluation of motion dynamics, control stability, and the robot's response to changes in terrain configuration.

Error! Reference source not found. shows that the robot maintained an almost constant speed throughout the simulation, with small oscillations. These oscillations may occur during changes in the direction of motion, when encountering slopes or terrain irregularities, but they can also be significantly attributed to the numerical method used to calculate the speed. The speed was calculated based on the distance travelled during each simulation step. The simulation time step was 64 ms, which is a very small-time interval. Since the robot does not travel exactly the same distance during every simulation step, variations in the calculated speed occur, including occasional decreases to values below 1 m/s. These variations do not represent an error, but rather reflect the numerical method used for calculating the speed.

On the other hand, **Error! Reference source not found.** shows the robot's acceleration during the simulation. It can be observed that the acceleration is almost constantly equal to zero, which is consistent with the nearly constant speed of the robot. Oscillations also occur for the same reason as in the speed diagram. Positive acceleration values indicate an increase in speed, while negative values indicate a decrease in speed. From Table 3 it can be seen that maximum acceleration and deceleration have almost exact values, which indicates a nearly symmetrical response of the robot during acceleration and deceleration.

Table 3 *Acceleration and deceleration maximum values*

Maximum acceleration [m/s²]	8.133
Maximum deceleration [m/s²]	8.066

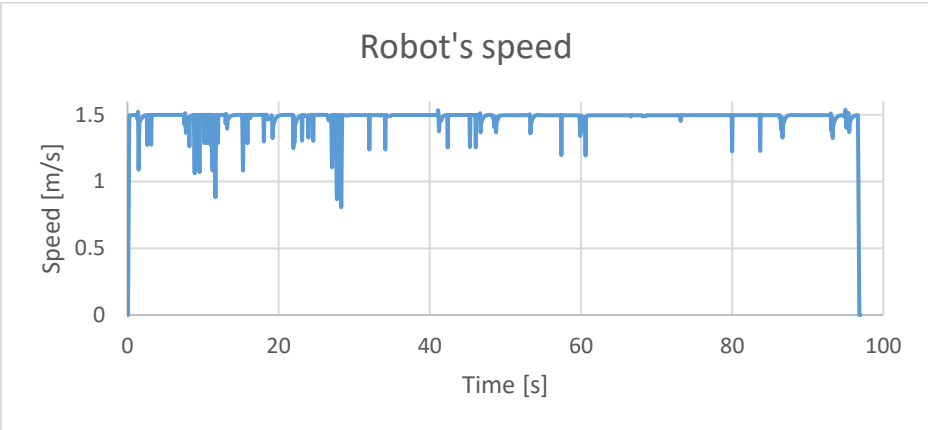

Figure 10 Robot speed during the simulation

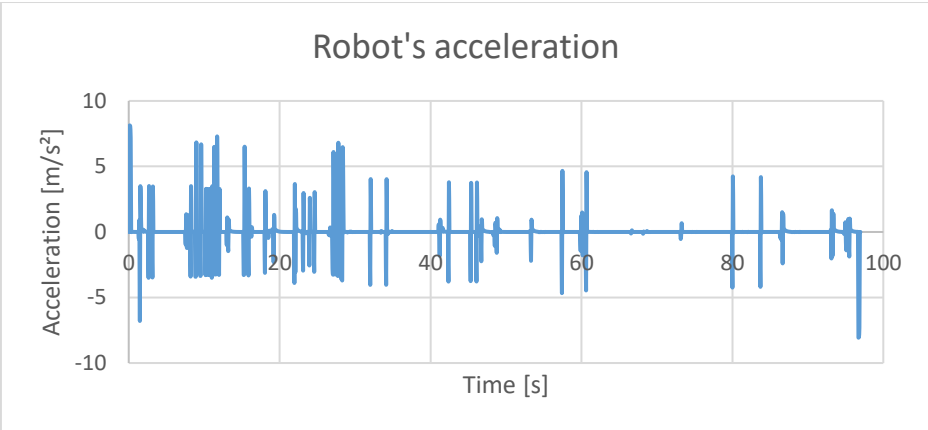

Figure 11 Robot acceleration during the simulation

Orientation angle

Figure 12 shows the variation of the robot's orientation angle during the simulation. It enables the analysis of changes in the robot's direction of motion, identification of straight-line motion and turns, as well as verification of the robot's motion trajectory.

Analysis of the diagram confirms that the robot did not maintain a constant direction of motion, but performed multiple changes in direction. Rapid changes in the orientation angle indicate changes in the robot's direction of motion, while approximately constant angle values correspond to periods of straight-line motion.

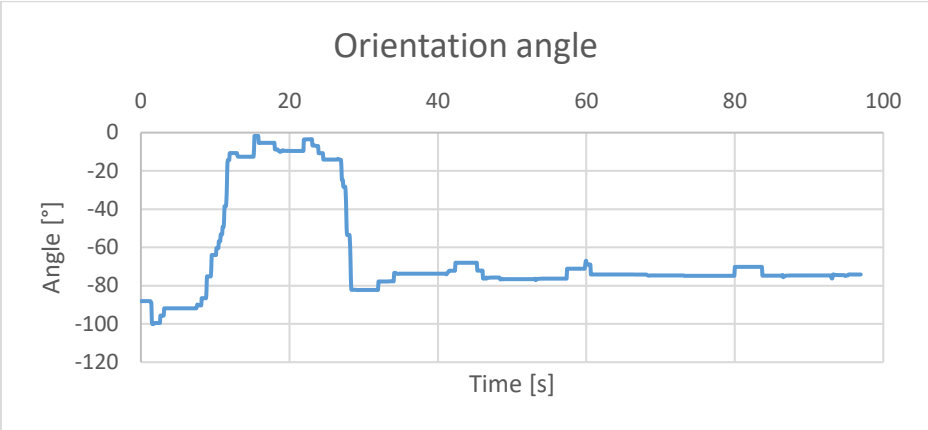

Figure 12 Orientation angle of the robot during the simulation

Longitudinal driving force of the robot

Longitudinal force represents one of the most important dynamic parameters of robot motion, as it directly describes the force required to overcome rolling resistance, terrain inclination, and changes in speed.

The total longitudinal force acting on the robot was calculated as follows:

$$F = F_a + F_g + F_k \tag{5}$$

where:
F_a: Acceleration force;

$$F_a = ma \tag{6}$$

m: Robot mass;
a: Acceleration;
F_g: Slope force;

$$F_g = mg \sin \alpha \tag{7}$$

g: Acceleration due to gravity;
$\sin\alpha$: Sine of the angle of inclination;
F_k: Rolling resistance force;

$$F_k = \mu mg \tag{8}$$

μ: Rolling resistance coefficient.

Accordingly, Figure 13 does not represent the directly measured traction force of the motor or the force acting on the tracks, but rather the resultant longitudinal force that the robot needs to overcome in order to maintain its motion.

As can be observed from Figure 13 the longitudinal force remains almost constant throughout most of the simulation. This corresponds to the nearly constant speed of the robot, for which the acceleration force is approximately equal to zero. In this case, the main components contributing to the longitudinal force are the slope force and rolling resistance force. The rolling resistance force remains constant because the parameters determining it, which can be seen in equation *(8)*, remain unchanged throughout the simulation. Therefore, its variation with changes in the normal force due to terrain inclination was not explicitly considered. This represents a simplifying assumption of the adopted longitudinal force model.

At certain points, the total longitudinal force takes negative values. This can be explained by the robot decelerating or moving downhill, in which case the component of slope force acts in the direction of motion and reduces the force required to overcome rolling resistance. The oscillations in the total longitudinal force are caused by variations in the

acceleration force, which result from the numerical method used to calculate the speed and, consequently, the acceleration.

The analysis of the longitudinal force diagram shows that the robot operated in a stable motion regime during most of the simulation, with the required longitudinal force remaining approximately constant.

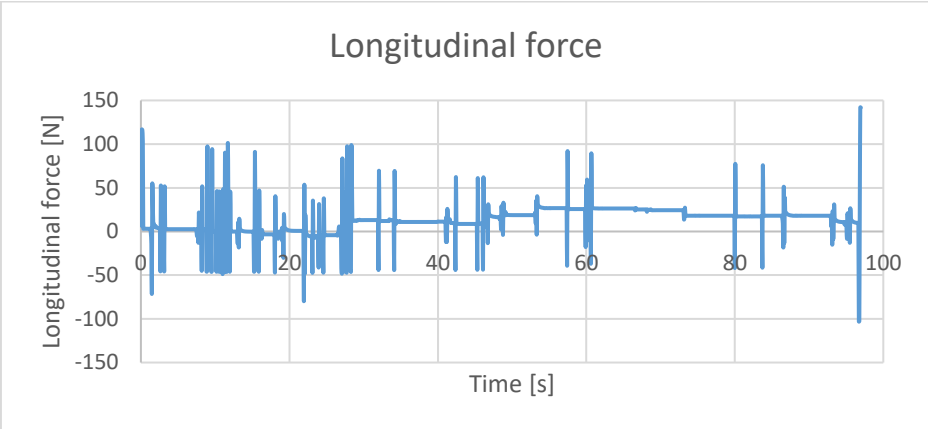

Figure 13 Longitudinal driving force of the robot

CONCLUSIONS

Within this work, the modelling of a lightweight tracked robot, the development of the simulation environment, and the collection and analysis of simulation data were successfully performed. The developed model enabled the analysis of the robot's trajectory, speed, acceleration, orientation angle, and longitudinal force, providing an overall insight into its motion under the considered simulation conditions.

The robot travelled approximately 143 m during 97 s of simulation, with an average speed of 1.47 m/s compared with the set speed of 1.50 m/s. The relative deviation of approximately 2.0% indicates good agreement between the prescribed and achieved motion. In addition, the analysed changes in trajectory, orientation angle, acceleration, and longitudinal force were mutually consistent and logically interconnected, supporting the consistency of the developed simulation model. The similar magnitudes of the maximum acceleration and deceleration values also indicate a nearly symmetrical dynamic response of the robot during changes in speed.

Based on the obtained results, it can be concluded that the developed model successfully reproduces the considered robot motion regime and provides a suitable basis for analysing the dynamic behaviour of a tracked robot in a simulated environment. The simulation approach also enables investigation of robot motion on more complex terrains, rapid modification of simulation parameters, and testing of different motion scenarios and robot configurations.

The main limitations of the presented approach are the use of manual robot control, the analysis of a single simulation run, and the absence of experimental measurements from the real Jaguar robot for quantitative validation. Therefore, future work should focus on implementing automated trajectory generation and autonomous control, performing repeated simulations under different conditions, and comparing the simulation results with experimental measurements obtained from the real robot. Such an approach would enable a more comprehensive assessment of the accuracy and applicability of the developed simulation model.

ACKNOWLEDGMENTS

This work was supported by the Ministry of Defense, Serbia, under the project „Modelling of Automotive Vehicle Assemblies for the Optimization of Dynamic Parameters”, No. VA-TT/1/26-28.

REFERENCES

Bruzzone, L., Nodehi, S. E., & Fanghella, P. (2022). Tracked Locomotion Systems for Ground Mobile Robots: A Review. *Machines*, 10(8), 648. https://doi.org/10.3390/machines10080648

Cyberbotics Ltd. (n.d.). (2026, May 26) Webots documentation. Cyberbotics. https://cyberbotics.com/doc/guide/index

Gunjal, S. R. (2021). *Development of virtual simulation for evaluation of robotic assistive environment* [Master's thesis]. The University of Texas at Arlington.

Haidar, F. (2024). Integrated vehicle dynamics modeling, path tracking, and simulation: A MATLAB implementation approach. *Engineering Perspective*, 1(1), 7–16. https://doi.org/10.29228/eng.pers.75106

Hellström, T. (2011). Kinematics Equations for Differential Drive and Articulated Steering. Umea University. https://www8.cs.umu.se/kurser/5DV122/HT13/material/Hellstrom-ForwardKinematics.pdf

Kozłowski, K., & Pazderski, D. (2004). Modeling and control of a 4-wheel skid-steering mobile robot. *International Journal of Applied Mathematics and Computer Science*, 14(4), 477–496.

Muždeka, S., & Rakić, S. (2008). Konstrukcija borbenih vozila. Centar za vojnonaučnu dokumentaciju, informacije i bibliotekarstvo.

Rivera, Z. B., De Simone, M. C., & Guida, D. (2019). Unmanned ground vehicle modelling in gazebo/ros-based environments. *Machines*, 7(2), 42. https://doi.org/10.3390/machines7020042

ROS 2 Control maintainers. (n.d.). Wheeled Mobile Robot Kinematics. ROS 2 Control Documentation. Retrieved May 25, 2026, from https://control.ros.org/rolling/doc/ros2_controllers/doc/mobile_robot_kinematics.html

The 11th International Congress
Motor Vehicles & Motors 2026
Kragujevac, Serbia
October 8th - 9th, 2026

Motor Vehicles & Motors

MVM2026-075
https://doi.org/10.24874/CMVM2026.075
Original scientific paper

Branko Miličić[1]
Nikola Frlić Sekulić[2]
Miloš Mitrović[3]
Ivan Blagojević[4]

IDENTIFICATION OF EFFECTIVE THERMO-PNEUMATIC TIRE PARAMETERS FROM REAL-WORLD ROAD TEST DATA

ABSTRACT: This study investigates the identification of effective thermo-pneumatic tyre parameters using real-world road test data collected under representative operating conditions. Pneumatic tyres exhibit complex coupled behaviour influenced by internal air pressure dynamics, temperature evolution, viscoelastic energy dissipation, rolling conditions, and environmental factors. Characterising these interactions is essential for vehicle safety, tyre condition monitoring, and operational efficiency. The research is based on an extensive experimental dataset obtained from long-distance road testing, incorporating continuous measurements of tyre pressure, temperature, vehicle speed, travelled distance, and other relevant operating parameters. The analysis focuses on extracting effective tyre characteristics from measured transient responses. Attention is given to pressure–temperature relationships, thermal stabilisation behaviour, heat generation trends, and condition-dependent deviations that may indicate changes in tyre operating state. The results demonstrate that tyre pressure and temperature exhibit strongly coupled, transient behaviour under real-world driving conditions, with the distance required to reach a quasi-steady thermal state being highly dependent on the driving environment.

KEYWORDS: tyres, thermo-pneumatic behaviour, transient response analysis, tyre condition monitoring

[1] *Branko Miličić, MSc, University of Belgrade – Faculty of Mechanical Engineering, Kraljice Marije 16, bmilicic@mas.bg.ac.rs, https://orcid.org/0000-0003-2297-524X*
[2] *Nikola Frlić Sekulić, MSc, University of Belgrade – Faculty of Mechanical Engineering, Kraljice Marije 16, nfrlic@mas.bg.ac.rs, https://orcid.org/0009-0000-5722-5268*
[3] *Miloš Mitrović, MSC, University of Belgrade – Faculty of Mechanical Engineering, Kraljice Marije 16, nmitrovic@mas.bg.ac.rs, https://orcid.org/0009-0004-7955-0554*
[4] *Ivan Blagojević, PhD, University of Belgrade – Faculty of Mechanical Engineering, Kraljice Marije 16, iblagojevic@mas.bg.ac.rs, https://orcid.org/0000-0002-5776-5990*

IDENTIFIKACIJA EFEKTIVNIH TEMPERATURNO-PNEUMATSKIH PARAMETARA PNEUMATIKA NA OSNOVU ISPITIVANJA U REALNIM USLOVIMA EKSPLOATACIJE

REZIME: Ova rad istražuje identifikaciju efektivnih termo-pneumatskih parametara pneumatika korišćenjem podataka prikupljenih tokom ispitivanja u realnim uslovima eksploatacije. Pneumatici ispoljavaju složeno ponašanje koje je uslovljeno dinamikom unutrašnjeg pritiska vazduha, promenom temperature, viskoelastičnom disipacijom energije, uslovima kotrljanja i uticajem okoline. Karakterizacija ovih interakcija od značaja je za bezbednost vozila, praćenje stanja pneumatika i operativnu energetsku efikasnost. Istraživanje se zasniva na eksperimentalnom skupu podataka dobijenom tokom ispitivanja u realnim uslovima vožnje, uključujući kontinualno merenje pritiska i temperature pneumatika, brzine vozila, pređenog puta i relevantnih radnih uslova. Analiza je usmerena na izdvajanje efektivnih karakteristika pneumatika iz merenih prelaznih odziva. Posebna pažnja biće posvećena odnosu pritiska i temperature, ponašanju pri dostizanju termičke stabilnosti, trendovima generisanja toplote i odstupanjima zavisnim od radnog stanja, koja mogu ukazivati na promene u eksploatacionom stanju pneumatika.
Rezultati pokazuju da pritisak i temperatura pneumatika ispoljavaju snažno spregnuto, prelazno ponašanje u realnim uslovima vožnje, pri čemu dužina puta potrebnog za dostizanje kvazistatičkog temperaturnog stanja u velikoj meri zavisi od okruženja u kojem se vozilo kreće.

KLJUČNE REČI: pneumatici, termo-pneumatsko ponašanje, analiza tranzijentnog odziva, praćenje stanja pneumatika

INTRODUCTION

The safety implications associated with abnormal tire behaviour can range from relatively moderate operational problems to severe failures that may directly compromise vehicle safety. At the lower end of the risk spectrum, tire standing waves may occur during high-speed operation of an underinflated tire. This phenomenon is characterized by periodic oscillations of the tread and can lead to excessive deformation and rapid structural deterioration. Uneven tire pressure, particularly pressure asymmetry between tires, represents a further safety concern, as differences in inflation pressure can adversely affect vehicle stability, handling characteristics, and tire wear. More severe consequences may arise when abnormal operating conditions result in a tire blowout, defined as a sudden and complete loss of inflation pressure caused by structural failure of the tire. At the highest danger level, abnormal tire pressure or catastrophic tire failure may lead to a vehicle accident, particularly when the resulting loss of tire performance causes a significant reduction in vehicle stability and controllability. Overall, these phenomena demonstrate that tire pressure and the associated thermo-mechanical operating state are directly connected to both tire durability and vehicle safety, ranging from progressive degradation of tire performance to sudden failures with potentially severe consequences.

Numerical modelling has been extensively applied to investigate the mechanical behaviour of pneumatic tires under rolling conditions. Korunović et al. (2011) developed and experimentally validated a three-dimensional Finite Element model for steady-state tire rolling on a drum, demonstrating that tire deformation, contact forces, and rolling interaction can be successfully reproduced using an appropriately calibrated FE approach. The study by Korunović et al. further demonstrated the importance of experimental validation and parameter calibration in tire modelling, as the agreement between numerical and experimental results was substantially improved after calibration of the tire–surface friction characteristics.

The increasing integration of sensors and monitoring systems into modern vehicles has created new opportunities for the continuous assessment of tire operating conditions. While conventional Tire Pressure Monitoring Systems (TPMS) are primarily intended to detect deviations in inflation pressure, the development of intelligent tire sensing technologies enables the acquisition of additional parameters during vehicle operation. Among these parameters, tire temperature is of particular interest because it represents the combined response of the tire to mechanical loading, deformation, rolling speed, inflation pressure, and environmental conditions. The continuous monitoring and interpretation of tire temperature therefore represents a potential basis for advanced tire condition assessment and future intelligent tire monitoring systems.

As Zhang et al. (2025) have investigated, TPMS can broadly be classified into Direct Tire Pressure Monitoring Systems (DTPMS) and Indirect Tire Pressure Monitoring Systems (ITPMS). DTPMS employs sensors installed on or within the tire to directly measure inflation pressure and, in many implementations, tire temperature, whereas ITPMS estimates the tire inflation state by methods described in Table 1. DTPMS can be further classified according to the sensor power supply as active or passive systems and according to sensor location as internal or

external configurations. In contrast to ITPMS, which relies on indirect relationships between tire pressure and measurable vehicle responses, DTPMS provides direct measurements of the tire's thermo-pneumatic state and therefore offers a suitable basis for experimental investigation of the evolution of tire pressure and temperature during vehicle operation.

Table 1 Pressure state relation with the different phenomena measurement in the ITPMS

ITPMS approach	Measurable phenomenon
Rolling radius comparison	Effective rolling radius / wheel speed
Tire stiffness analysis	Longitudinal/torsional stiffness
Frequency analysis	Tire natural/resonance frequency
Vehicle dynamics model	Yaw rate, lateral acceleration, longitudinal dynamics
Tire friction model	Tire–road friction
Deep learning	Combined tire/vehicle signals

Based on the ITPMS comparison table that Zhang et al. (2025) gave on the classification of the TPMS, we can conclude that for some of the methods, especially Tire stiffness method, are sensitive to temperature change, model and wear of the tire.

Bachman et. al. (2018) reported that air-cavity temperature increases rapidly during the warm-up phase, whereas measurable cooling occurs during the fuel-measurement intervals between successive test runs. Correspondingly, inflation pressure increased by approximately 50–70 kPa during the warm-up run, while, after the tire had reached a warmed condition, pressure variations during individual test runs were considerably smaller, typically in the range of 15–20 kPa. Furthermore, the relationship between inflation pressure and rolling resistance obtained from SAE J1269 measurements was found to be approximately linear over the investigated pressure range, with increasing inflation pressure corresponding to a reduction in rolling resistance. This relationship was subsequently used to estimate the effect of changes in inflation pressure, normalized with respect to the cold inflation pressure, on vehicle fuel consumption. Data underlining this from our test is shown in the Figure 1.

Hyttinen et al. (2024) showed that a tire does not exhibit a uniform temperature distribution, and that the measured temperature depends strongly on the measurement location. Differences in material thickness, heat conduction and cooling conditions across the tire result in different thermal responses at the shoulder, tread and inner liner.

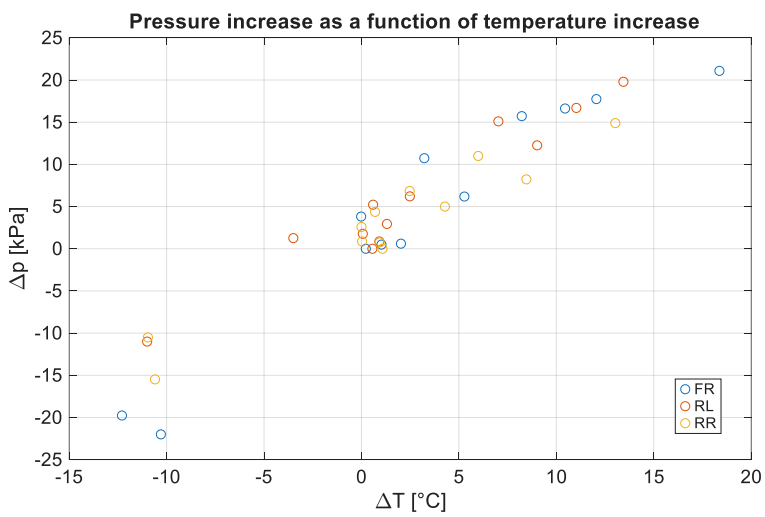

Figure 1 Pressure change vs. Temperature, obtained in the road tests. Legend is colour coded and shows FR – Front Right, RL – Rear Left and RR – Rear Right Tire data. FL – Front Left Tire data is omitted because of the corresponding sensor malfunction

He et al. (2022) stated that heat build-up in rolling tires is primarily caused by the viscoelastic hysteresis of rubber materials subjected to cyclic deformation. During each rolling cycle, a portion of the mechanical energy associated with tire deformation is dissipated as heat, with the magnitude of this dissipation depending on temperature, strain amplitude, and strain rate. The resulting thermal behaviour is therefore governed by a coupled interaction between internal heat generation and heat transfer to the surrounding environment. Experimental observations have shown that increased loading generally produces higher tire temperatures due to increased deformation and hysteretic energy losses, while the influence of rotational speed depends on the balance between increased cyclic loading frequency and enhanced convective heat dissipation. Consequently, tire temperature represents a dynamic response to both the mechanical operating conditions and the thermal boundary conditions of the tire.

The thermal response of a tire is governed not only by the rate of internal heat generation but also by the thermal properties and multilayer structure of the tire. Allouis et al. (2016) identified thermal diffusivity (α – m^2/s) as a key parameter for the thermodynamic characterization of tire structures, defined as the ratio of thermal conductivity (k – W/mK) to the product of density (ρ – kg/m^3) and specific heat capacity (c_v – J/kgK).

$$\alpha = \frac{k}{\rho \cdot c_v} \tag{1}$$

Their experimental investigation demonstrated that different tire layers exhibit substantially different thermal dynamics, with the tread responding considerably faster than the bulk and innerliner regions due to their different thermal inertia. Consequently, the temperature measured at a given tire location represents a time-dependent response to both internal heat generation and heat propagation through the tire structure, rather than an instantaneous measure of the current operating condition. Therefore, the analysis of tire temperature should account for its transient nature and the thermal history of the tire rather than treating the measured temperature as a direct response to the instantaneous operating conditions.

The relationship between longitudinal slip and tire energy dissipation was recently investigated experimentally by Biffi et. al. (2025), who introduced the Tyre Rolling Dissipation Index (TRDI) as a measure of tire rolling loss. The proposed formulation relates the power dissipated by the tire to the wheel angular velocity and expresses the resulting dissipation in terms of an equivalent moment. Their experimental results demonstrated that tire rolling loss increases progressively with increasing longitudinal slip during braking. Furthermore, the tire power dissipation ratio was found to increase approximately linearly with the magnitude of longitudinal slip, indicating that an increasing proportion of the total braking power is dissipated within the tire as longitudinal slip increases. For a braking manoeuvre reaching 20% longitudinal slip, the average contribution of tire-dissipated power to the total braking power was reported to be approximately 17. In real-world driving, such events are embedded within a continuously varying operating history, meaning that the measured thermo-pneumatic response may reflect the cumulative effect of preceding longitudinal slip and other driving conditions rather than only the instantaneous vehicle speed.

Yang et al. (2022) showed that measurements obtained from sensors integrated into tires can provide valuable information about tire state and tire–road interaction, while also emphasizing the complexity of interpreting tire signals under real-world operating conditions. In particular, tire responses are influenced by vehicle dynamics, road excitation, tire characteristics, and environmental conditions, and therefore represent inherently variable time-series data that are evaluated and discussed in our tests.

Test description

During the test programme, continuous measurements of tyre inflation pressure, tyre temperature, vehicle speed, travelled distance, geographical position, and vehicle accelerations were recorded using an integrated data acquisition system. Tyre pressure and temperature data were collected individually for each wheel, while vehicle dynamics data included longitudinal and lateral acceleration measurements. The recorded signals enabled simultaneous monitoring of tyre thermodynamic behaviour and vehicle operating conditions throughout the test.

Tyre behaviour during vehicle operation is influenced by a complex interaction of thermal, mechanical, and environmental factors. Parameters such as inflation pressure, tyre temperature, vehicle speed, travelled distance, and vehicle accelerations continuously change during driving and together determine the operating condition of the tyre. The reliability of conclusions derived from experimental tyre testing depends not only on the quality of the measurements but also on the methodology used for data processing, filtering, synchronisation, and statistical evaluation. Raw measurement signals often contain noise, transient events, sensor delays, and operating condition variations that may obscure the underlying physical phenomena. Consequently, appropriate data processing procedures are required to ensure that the analysed parameters accurately represent the behaviour of the tyre under real operating conditions. To investigate the applicability of such procedures, a comprehensive road test was conducted using an instrumented passenger vehicle equipped with a tyre pressure monitoring system, temperature sensors, GPS-based vehicle tracking, and inertial measurements. The test included approximately 1,000 km of operation under varying road, traffic, and environmental conditions.

The objective of this paper is not to evaluate the performance of a specific tyre technology, but rather to present a methodology for processing and analysing experimental tyre data obtained during real-world vehicle operation. Particular attention is given to signal conditioning, data filtering, identification of representative operating conditions, and the extraction of engineering-relevant parameters that can be used for subsequent investigations of tyre pressure evolution, thermal behaviour, and operational stability.

EXPERIMENTAL SETUP

The experimental measurements were performed using an integrated data acquisition system consisting of tyre pressure and temperature sensors, vehicle positioning equipment, CAN bus data loggers, and reference pressure measurement instrumentation. Data were sampled at a frequency of 50 Hz. The TPMS sensors provided continuous measurements of tyre inflation pressure and the corresponding internal air temperature throughout the test programme. Reference tyre inflation pressure measurements were periodically verified using a calibrated WIKA mechanical pressure gauge with a measurement range of 0–6 bar. For more details about equipment used, see the Table 2.

Table 2 List of equipment used during the Road Tests

Equipment	Measurement / acquisition role	Data used in analysis
HBM QuantumX MX840A (2 units)	CAN data acquisition and signal synchronization	CAN channels, synchronized signals
AIM TPMS (4 units)	Tyre pressure and temperature monitoring	Tyre pressure, tyre temperature
Racelogic GPS Speed Sensor (5 Hz)	Vehicle positioning and speed measurement	Vehicle speed, travelled distance, GPS position
WIKA Pressure Gauge	Reference tyre-pressure measurement	Initial tyre inflation pressure
Laptop computer	Data logging and storage	Recorded measurement datasets

The tyre pressure and temperature were measured using an AIM TPMS system. The system provided continuous measurements of tyre inflation pressure and internal tyre temperature, which were acquired together with the vehicle CAN data and synchronized with the vehicle operating parameters. Specifications of TPMS are shown in Table 3.

Table 3 AIM Technologies TPMS system specifications

Parameter	Specification
Measurement	Tyre pressure and temperature
Pressure range	0 bar – 8 bar
Pressure resolution	15,7 mbar
Pressure accuracy	20 mbar
Temperature range	0 °C – 125 °C
Temperature resolution	1 °C
Sampling rate	50 Hz
Sensor position	Inside each tyre / valve-mounted, etc.
Data interface	CAN

The road test was divided into twelve sections (RS1–RS12), covering a total distance of 979.8 km as shown in Table 2. The test route included different road types as indicated and this division enabled the recorded data to be analysed separately for individual road sections and driving conditions.

Table 4 Road sections of the test. Time column represents start time of the Road section, $T_{enviroment,avg}$ – represents average environment temperature from the start of the test

Road section	Route	Road type	Date	Time	$T_{enviroment, avg}$ [°C]	Distance [km]
RS1	Belgrade urban area	Urban	20.2.2026	08:51	7	3,43
RS2	Belgrade – Paraćin	Motorway	20.2.2026	10:48	11	152,15
RS3	Paraćin – Zaječar	Regional	20.2.2026	14:17	4	85,67
RS4	Zaječar – Negotin	Regional	20.2.2026	15:26	6	56,15
RS5	Negotin – Stubik	Regional	20.2.2026	17:58	4	19,35
RS6	Stubik – Golubac	Regional	20.2.2026	20:08	6	89,98
RS7	Golubac – Vrbovac	Regional	20.2.2026	21:22	5	69,24
RS8	Vrbovac – Belgrade	Motorway	20.2.2026	22:16	6	66,56
RS9	Belgrade – Krnješevci	Mixed	24.2.2026	14:14	10	60,01
RS10	Belgrade urban area	Urban	26.2.2026	7:35	2	5,23
RS11	Belgrade – Subotica	Motorway	26.2.2026	9:35	5	183,68
RS12	Subotica – Belgrade	Motorway	26.2.2026	14:31	10	188,3
						979,8

EFFECTIVE TYRE PARAMETERS

Under approximately sealed conditions, the inflation pressure of a tyre is expected to increase with internal air temperature according to the ideal-gas relationship. Assuming constant gas mass and approximately constant cavity volume, the absolute pressure-to-temperature ratio remains approximately constant. This relationship provides a theoretical reference for evaluating the measured pressure–temperature behaviour during the road tests. Deviations from the ideal-gas prediction may arise from changes in tyre cavity volume, heat transfer, pressure losses, sensor uncertainty, and transient operating conditions.

The objective of the present analysis is not to identify fundamental material or structural properties of the tyre, but to determine a set of **effective thermo-pneumatic parameters** that describe the tyre response under real-world operating conditions. These parameters are derived directly from measured tyre pressure, tyre temperature, vehicle speed, travelled distance, and environmental conditions. They therefore represent the combined effect of tyre construction, inflation state, vertical loading, rolling conditions, heat generation, and heat dissipation during vehicle operation. The following quantities are considered particularly relevant for the interpretation of the measured data:

Effective thermal time constant

As Hyttinen et al. (2023) state, the **effective thermal time constant**, τ_T, characterises the rate at which the tyre approaches its thermal equilibrium following a change in operating conditions. It can be obtained by approximating the transient temperature response using a first-order model:

$$T(t) = T_{\text{eq}} + \left(T_0 - T_{\text{eq}}\right)e^{-t/\tau_T}. \tag{2}$$

Where T_0 is the initial tyre temperature and T_{eq} is the asymptotic or effective equilibrium temperature. The parameter τ_T has units of **seconds (s)**. A smaller value indicates a faster thermal response, whereas a larger value indicates slower heating or cooling of the tyre.

Effective equilibrium temperature

The **effective equilibrium temperature**, T_{eq}, represents the temperature towards which the tyre tends under approximately constant operating conditions. It corresponds to a state in which the average heat generation within the tyre is approximately balanced by heat dissipation to the surrounding environment.

The quantity is expressed in **degrees Celsius (C)** when reporting measured tyre temperatures. For thermodynamic calculations, the corresponding absolute temperature should be expressed in **kelvin (K)**:

$$T_{abs} = T + 273{,}15. \tag{3}$$

Unlike a material property, Teq is an operating-condition-dependent parameter. It can therefore vary with vehicle speed, vertical load, inflation pressure, ambient temperature, road conditions, and other factors affecting tyre heat generation and heat transfer.

Effective temperature rate

The instantaneous temperature rate,

$$\dot{T} = \frac{dT}{dt}. \tag{4}$$

describes the rate of tyre temperature change during transient operation. It is particularly useful for distinguishing the initial warm-up phase from the subsequent thermal stabilisation phase. Its unit is **kelvin per second (K/s)**, numerically equivalent to **°C/s**. A positive value indicates heating, while values approaching zero indicate thermal stabilization. For long-distance road testing, the corresponding distance-based quantity can also be introduced:

$$\dot{T} = \frac{dT}{ds}. \tag{5}$$

with units of **K/km** or **°C/km**. This parameter expresses the thermal development per unit of travelled distance and can be useful when comparing road sections with different durations or average speeds.

DATA PROCESSING

Valid measurement begins when the sensor signal enters a physically plausible range and remains statistically stable for a defined period. Methodology for data processing consists of Data quality control, Signal processing and Physical interpretation of obtained signal.

Prior to the analysis, the recorded data were subjected to a multi-stage quality-control procedure as depicted in Figure 2. The vehicle-motion signals obtained from the GPS sensor were additionally evaluated against the known performance limits of the tested vehicle and the physical limits of tyre–road interaction. In particular, longitudinal acceleration was constrained to a maximum physically meaningful range, with positive acceleration limited to vehicle specific performance limits. This criterion was selected conservatively, since longitudinal acceleration exceeding the values obtained during the vehicle acceleration tests can occur during downhill driving or other transient operating conditions. The resulting quality-control procedure was used to identify and flag suspicious measurements without unnecessarily removing potentially meaningful transient behaviour.

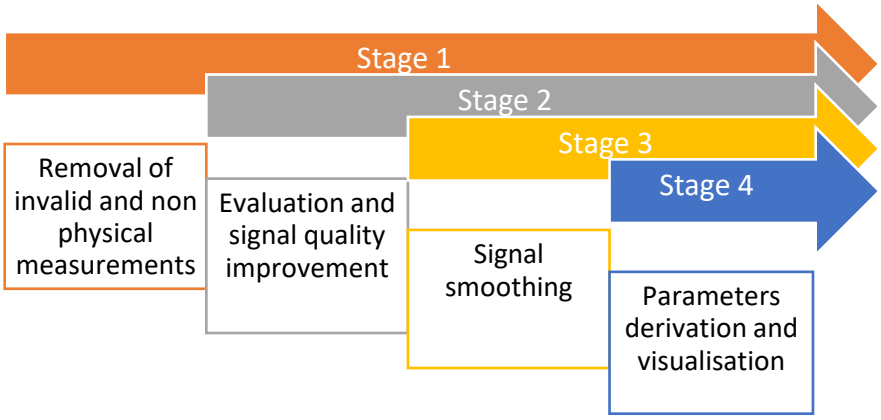

Figure 2 Flow chart of the data processing and visualisation

For the tyre-related signals, the original measurements and their associated quality flags were retained in the dataset. In addition, smoothed pressure and temperature signals were generated using a moving-average procedure. A 120 s window was selected after comparison with shorter and longer windows, as it provided an appropriate compromise between suppression of the TPMS temperature resolution effects and preservation of the actual thermal evolution of the tyre. The smoothed signals were subsequently used for the calculation of derived thermo-pneumatic quantities, while the original measurements were preserved for traceability and independent assessment of the raw data, see Figure 3.

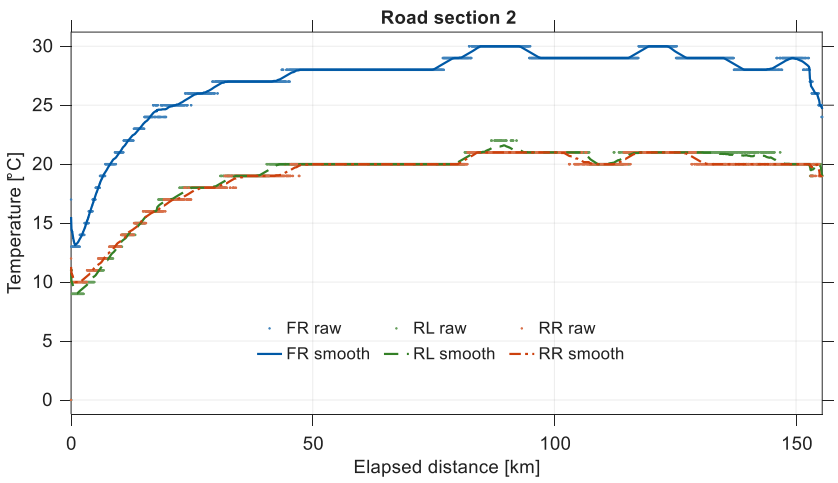

Figure 3 Example of the smoothed signal with the raw data of the tire temperature

Due to a malfunction of the TPMS sensor installed on the front-left (FL) wheel, reliable pressure and temperature measurements were not available for this tire. Consequently, the FL tire data were excluded from the analysis. All subsequent analyses were therefore performed using the remaining functional TPMS sensors.

The data analysis was conducted across all 12 road sections using measurements from the three valid tyre positions (FR, RL, and RR), together with the corresponding vehicle motion and road-profile data, as shown in the Figure 4. For each tyre and test section, characteristic heating parameters were identified, including the initial and

maximum tyre temperatures, temperature increase, time and distance required to reach the maximum temperature, and the mean positive temperature gradient (dT/ds). To investigate the relationship between tyre heating and operating conditions, positive (dT/ds) values were classified into predefined intervals of lateral acceleration magnitude, longitudinal acceleration, and road inclination, and the resulting distributions were statistically evaluated for every road section. Figure 5 shows mean positive temperature gradient classified in bins of longitudinal acceleration. It is important to point out that we have measured heating during particular driving conditions, not isolated each factor's contribution to heating.

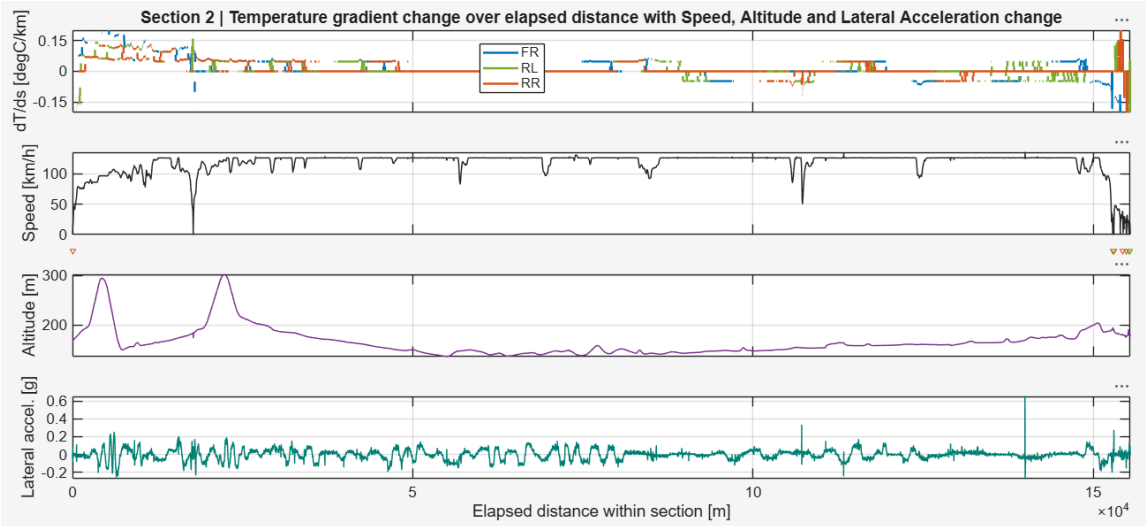

Figure 4 Road Section 2 Tire Temperature gradients over elapsed distance, shown with the change of vehicle speed, altitude and the lateral acceleration

An important transient effect reported by Hyttinen et al. (2024), which is important to point out here, is that a reduction in vehicle speed does not necessarily result in an immediate reduction in tire temperature or pressure. Following a speed reduction, the tire temperature may initially increase because convective and road-related cooling are reduced while previously stored thermal energy continues to propagate through the tire structure.
The same statistical analysis procedure, shown in Figure 5, was applied to each road section using three vehicle-dynamic criteria: lateral acceleration, longitudinal acceleration, and road inclination. For each criterion, the measured data were grouped into predefined bins, and the mean positive tyre temperature gradient dT/ds was calculated together with the corresponding number of positive-heating samples. This approach enabled a consistent comparison of tyre heating behaviour under different dynamic and road-loading conditions across all investigated road sections.

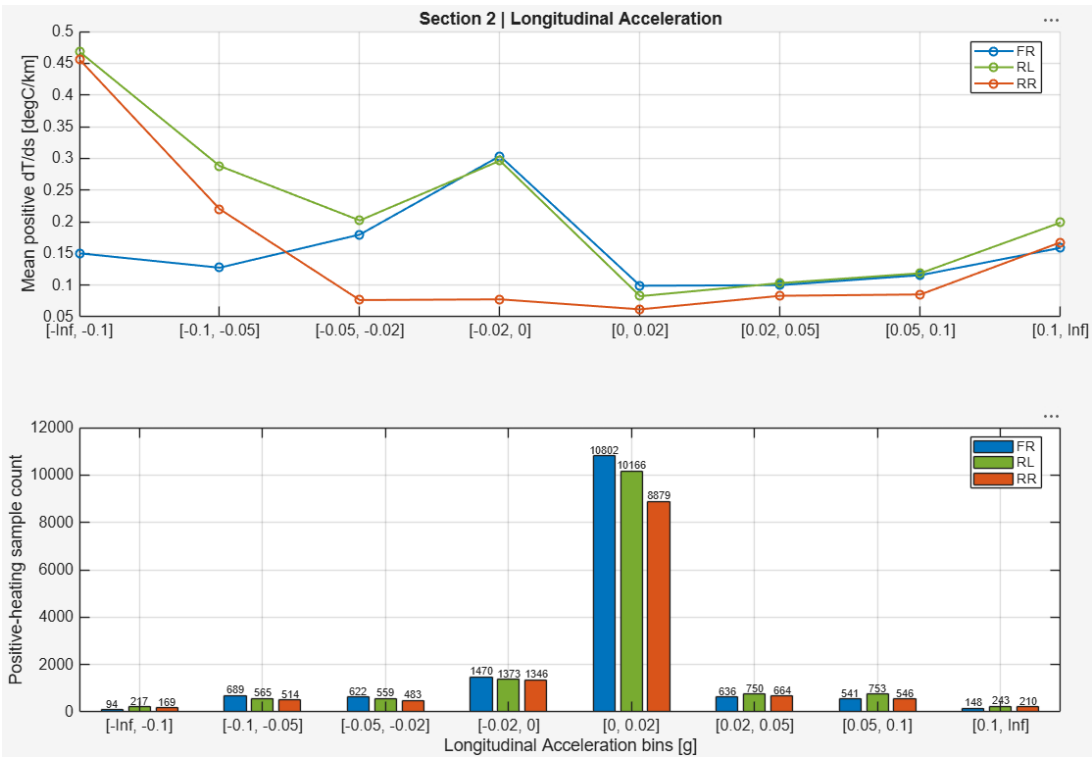

Figure 5 Mean positive tyre temperature gradient dT/ds and corresponding positive-heating sample count for FR, RL, and RR tyres across longitudinal acceleration bins in Road Section 2

Across the analysed motorway sections, higher mean positive temperature gradients were generally observed under negative longitudinal acceleration, as shown in the Figure 5, indicating an increased tyre heating rate during braking conditions. This tendency was particularly pronounced in the higher-deceleration ranges. However, the number of observations in the extreme braking bins was considerably lower than under near-steady longitudinal acceleration; therefore, these results should be interpreted with consideration of the corresponding sample distribution.

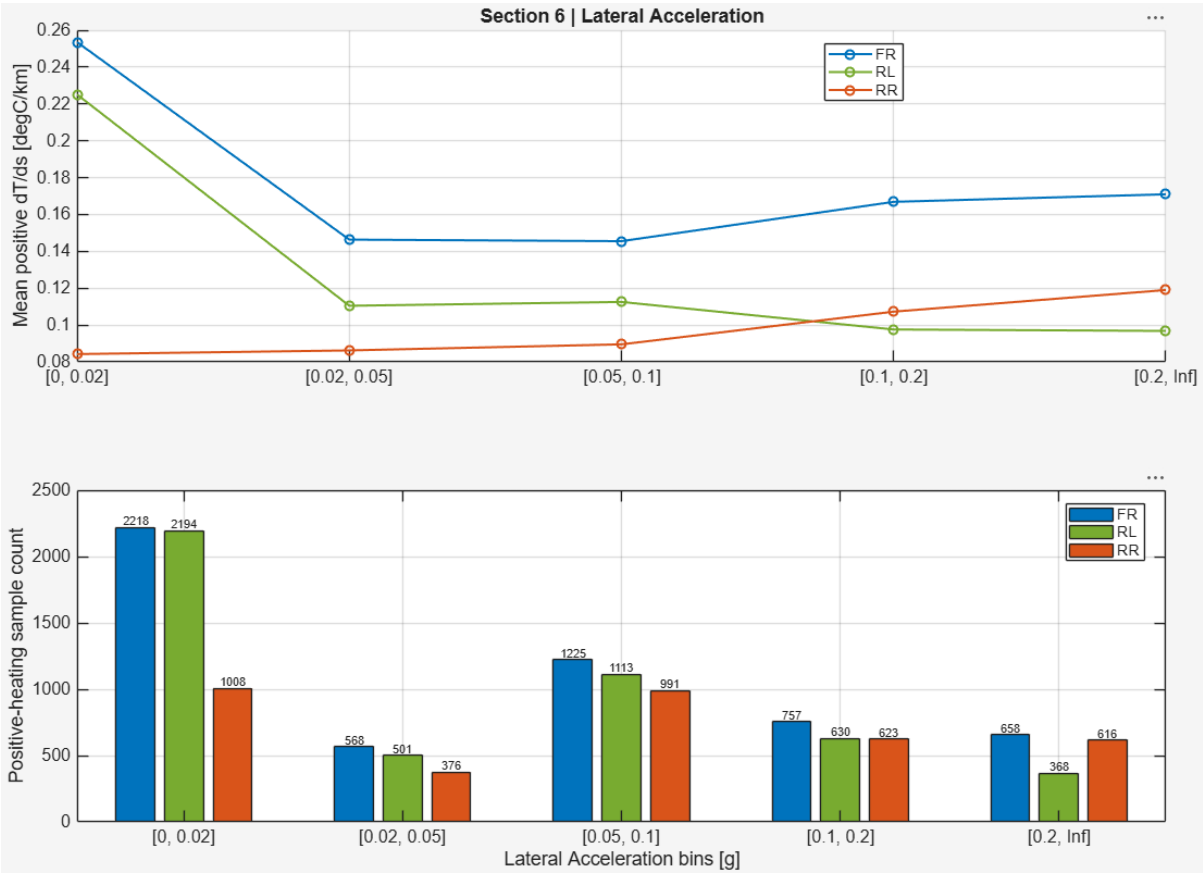

Figure 6 Mean positive tyre temperature gradient dT/ds and corresponding positive-heating sample count across lateral acceleration bins for Road Section 6

For the analysed regional-road section, the highest positive temperature gradients for the FR and RL tyres were observed in the lowest lateral-acceleration range, as shown in Figure 6. This operating range also contained the largest number of samples, indicating that low lateral acceleration represented the predominant driving condition on the section. However, the higher mean dT/ds values cannot be attributed solely to the greater number or duration of these events, since tyre temperature response is affected by thermal inertia and by the preceding operating history.

The observed relationship should not be interpreted as a direct correlation between lateral acceleration and tyre heating, but rather as an indication that acceleration values within this range contribute most to the observed temperature increase. Higher lateral accelerations typically occur only for short periods; although they generate heat at the tyre–road interface, the duration may be insufficient for this heat to propagate through the tyre structure and significantly affect the measured internal temperature.

DATA ANALYSIS AND DISCUSSION

As summarized in Table 5, analysis of the measured data showed that the tyre heating behaviour differed considerably between road types and between the driven and non-driven tyres. In Table 5, $\mathbf{T_{max}}$ denotes the maximum measured tyre temperature, while $\mathbf{\Delta T = T_{max} - T_0}$ represents the temperature increase relative to the initial tyre temperature. The parameter **dT/ds** represents the mean temperature gradient with respect to travelled distance. The value reported as **dT/ds** to $\mathbf{T_{max}}$ characterizes the heating phase preceding the maximum temperature, whereas the section mean represents the positive temperature gradient evaluated over the considered road section.

Table 5 Average thermal response parameters of the front-right (FR) and rear-right (RR) tyres for different road operating conditions

Road type	Tyre	Mean time to T_{max} [min]	Mean distance to T_{max} [km]	Mean temperature increase ΔT [°C]	Mean dT/ds to T_{max} [°C/km]	Mean section dT/ds [°C/km]
Urban	FR	2,47	1,72	1,73	0,633	0,472
Urban	RR	0,50	6,35	0,02	0,077	0,077
Regional	FR	32,97	37,05	4,40	0,147	0,146
Regional	RR	32,60	36,59	2,38	0,107	0,107
Motorway	FR	50,13	90,23	12,26	0,127	0,119
Motorway	RR	65,01	112,11	8,41	0,221	0,219

Although the highest mean temperature gradient for the front-right (FR) driven tyre was obtained under urban driving conditions 0,633 °C/km, the urban-road results were excluded from further comparative analysis because the number of valid samples was insufficient to provide a representative assessment. For the remaining road types, the mean temperature gradient up to the maximum recorded temperature was 0,147 °C/km on regional/interurban roads and 0,127 °C/km on motorways. For the rear-right (RR) non-driven tyre, the corresponding values were 0,107 °C/km and 0,221 °C/km, respectively, with the highest heating gradient therefore observed during motorway driving.

The temperature increase, ΔT, showed a more pronounced dependence on road type. For the FR driven tyre, the mean temperature increase was approximately 4,4 °C on regional/interurban roads and 12,26 °C on motorways. For the RR non-driven tyre, the corresponding increases were 2,38 °C and 8,41 °C, respectively. These results indicate that motorway operation produced the largest overall tyre temperature increase for both tyre positions, although the rate of temperature increase per unit distance differed between the driven and non-driven tyres.

CONCLUSIONS

The increasing development of intelligent tire systems demonstrates the growing importance of obtaining tire-related information directly during vehicle operation. The present study follows this general concept from a thermo-pneumatic perspective by investigating the evolution of tire inflation pressure and temperature during real-world driving. Rather than using tire measurements primarily for instantaneous state estimation, the objective was to characterize their temporal and spatial evolution and to identify measurable indicators that describe the tire's operating state under realistic, non-stationary conditions.

In road measurements presented here, the inner-liner temperature and tire pressure exhibited very similar time histories, with both quantities increasing toward higher operating temperature and decreasing during cooling periods. The inner-liner temperature provides the most representative temperature measurement for estimating tire inflation pressure. The nearly constant temperature-to-pressure ratio further indicated that pressure changes during driving were close to isochoric.

The distance required to reach a quasi-steady tyre temperature was found to depend strongly on the driving environment. Under regional-road conditions, quasi-steady tyre temperature thermal stabilization was reached after approximately 37 km, whereas motorway driving required approximately 112 km for the rear, nondriven tires. Driven tire needed also 37 km in regional road and 90 km on motorway. This behaviour is consistent with the transient thermal nature of pneumatic tyres reported in the literature, where tyre temperature evolves as a balance between internally generated heat and heat dissipation to the surroundings and exhibits a speed-dependent thermal inertia. For comparison, ISO 28580 specifies a 30 min warm-up period for passenger-car tyres prior to steady-state rolling-resistance measurements, indicating that a substantial operating period is required before a thermally stabilized condition can be assumed.

The temperature variations observed are relevant from a vehicle-dynamics perspective. Angrick et al. (2014) reported that even relatively small differences in tyre temperature can lead to considerable changes in tyre characteristics, particularly cornering stiffness. Consequently, the temperature variations observed in the present measurements should not be regarded only as a thermodynamic effect, but also as a potentially relevant factor influencing tyre dynamic behaviour.

ACKNOWLEDGMENTS

The results presented here stem from research supported by the Ministry of Science, Technological Development and Innovation of the Republic of Serbia, under Contract No. 451-03-34/2026-03/200105 dated February 5, 2026.

REFERENCES

Allouis, C, Farroni, F., Sakhnevych, A., & Timpone, F. (2016, 29 June–1 July). Tire Thermal Characterization: Test Procedure and Model Parameters Evaluation. In *Proceeding of the world congress on engineering*, London, pp.1199–1204.

Angrick, C., van Putten, S., & Prokop, G. (2014). Influence of Tire Core and Surface Temperature on Lateral Tire Characteristics. *SAE International Journal of Passenger Cars - Mechanical Systems*, 7(2), 468-481. https://doi.org/10.4271/2014-01-0074

Bachman L. J. (2018). Do changes in temperature and inflation pressure affect rolling resistance during road and track testing for fuel economy of class 8 tractor-trailers? *Tire science & technology*, 46(2), 93–104. https://doi.org/10.2346/tire.18.460203

Biffi, A., Massimiliano G., & Gianpiero, M. (2025). Tyre rolling resistance and tyre rolling loss: a theoretical and experimental study based on a new trailer. *Meccanica*, 60(8), 2561–85. https://doi.org/10.1007/s11012-025-01983-7

He, Hong, Jinming Liu, Yaru Zhang, Xue Han, William V. Mars, Liqun Zhang, and Fanzhu Li. (2022). Heat build-up and rolling resistance analysis of a solid tire: experimental observation and numerical simulation with thermo-mechanical coupling method. *Polymers*, 14(11), 2210. https://doi.org/10.3390/polym14112210

Hyttinen, J., Ussner, M., Österlöf, R., Jerrelind, J., & Drugge, L. (2023). Truck tyre transient rolling resistance and temperature at varying vehicle velocities - measurements and simulations. *Polymer Testing*, 122, 108004. https://doi.org/10.1016/j.polymertesting.2023.108004

Jukka, H., Ussner, M., Österlöf, R., Jerrelind, J., & Drugge, L. (2024a). Estimating Tire Pressure Based on Different Tire Temperature Measurement Points. *SAE International*. https://doi.org/10.4271/2024-01-5002

Jukka, H., Ussner, M., Österlöf, R., Jerrelind, J., & Drugge, L. (2024b). Investigating the influence of heat-insulated wheelhouses on truck tyre temperature and rolling resistance. *Energies*, 17(23), 6030. https://doi.org/10.3390/en17236030

"ISO 28580:2018." ISO. https://www.iso.org/standard/67531.html

Korunović, N., Trajanović, M., Stojković, M., Mišić, D., & Milovanović, J., (2011). Finite Element Analysis of a Tire Steady Rolling on the Drum and Comparison with Experiment. *Strojniški vestnik – Journal of Mechanical Engineering*, 57(12), 888–97. https://doi.org/10.5545/sv-jme.2011.124

Yang, S., Chen, Y., Shi, R., Wang, R., Cao, Y., Lu, J. (2022). A Survey of Intelligent Tires for Tire-Road Interaction Recognition Toward Autonomous Vehicles. *IEEE Transactions on Intelligent Vehicles*, 7(3), 520-532. https://doi.org/10.1109/TIV.2022.3163588

SECTION

D

Driver/Vehicle Interface, Information and Assistance Systems

- Communication & Informatics
- Noise & Vibration
- Human Comfort & Thermal Management
- Vehicle Security & Occupant Protection
- Driver Assistance & Information Systems

The 11th International Congress
Motor Vehicles & Motors 2026
Kragujevac, Serbia
October 8th - 9th, 2026

Motor Vehicles & Motors

MVM2026-005
https://doi.org/10.24874/CMVM2026.005
Technical paper

Slobodan Mišanović[1]

THE INFLUENCE OF ENERGY DEMAND FOR PASSENGER COMPARTMENT CLIMATE CONTROL OF THE ENERGY EFFICIENCY OF ELECTRIC BUS

ABSTRACT: Thermal comfort in the passenger and driver compartments of the bus is very important is a very important aspect of the quality of public transport. In the case of electric buses (E-bus), in addition to the consumption of electricity for traction, the operation of the heating, ventilation and cooling (HVAC) system is a significant factor in the consumption of electricity, which has a great impact on the energy efficiency of the vehicle, the required battery capacity, and the autonomy of the vehicle. The HVAC system is the most important technical component that regulates thermal comfort in the bus passenger compartment and air quality. The HVAC system configuration must be carefully designed to ensure that climate parameters remain within acceptable ranges for thermal comfort in the bus passenger compartment while optimizing energy efficiency. Proper use of the HVAC system in accordance with recommended thermal comfort in the bus passenger compartment standards should mitigate excessive energy consumption, and enable planned daily autonomy, while ensuring thermal comfort in the bus passenger compartment for occupants. The paper will present the specifics of thermal comfort in the bus passenger compartment in buses, the standards and recommendations that are applied for thermal comfort in the bus passenger compartment in buses, and the results of measuring the electricity consumption of the HVAC system in the Higer KLQ6125GEV3 electric bus on the EKO2 line in Belgrade in different periods of the year, and the impact on the energy efficiency of E-buses.

KEYWORDS: thermal comfort in the bus passenger compartment, energy efficiency, HVAC system, E-bus

UTICAJ POTRAŽNJE ENERGIJE ZA KLIMATIZACIJU PUTNIČKOG PROSTORA NA ENERGETSKU EFIKASNOST AUTOBUSA NA ELEKTRIČNI POGON

REZIME: Termička udobnost u putničkom i vozačkom prostoru autobusa je veoma važan aspekt kvaliteta javnog prevoza. U slučaju električnih autobusa (E-bus), pored potrošnje električne energije za vuču, rad sistema grejanja, ventilacije i hlađenja (HVAC) je značajan faktor u potrošnji električne energije, što ima veliki uticaj na energetsku efikasnost vozila, potreban kapacitet baterije i autonomiju vozila. HVAC sistem je najvažnija tehnička komponenta koja reguliše termičku udobnost u putničkom prostoru autobusa i kvalitet vazduha. Konfiguracija HVAC sistema mora biti pažljivo projektovana kako bi se osiguralo da klimatski parametri ostanu u prihvatljivim opsezima za termičku udobnost u putničkom prostoru autobusa, uz optimizaciju energetske efikasnosti. Pravilna upotreba HVAC sistema u skladu sa preporučenim standardima termičke udobnosti u putničkom prostoru autobusa trebalo bi da ublaži prekomernu potrošnju energije i omogući planiranu dnevnu autonomiju, uz obezbeđivanje termičke udobnosti u

[1] *Slobodan Mišanović, PhD, Manager for energy efficiency of vehicles, City Public Transport Company "Belgrade", Kneginje Ljubice 29, 11000 Belgrade, slobodan.misanovic@gsp.co.rs, https://orcid.org/0009-0000-3754-5977*

putničkom prostoru za putnike. U radu će biti predstavljene specifičnosti termalnog komfora u putničkom prostoru autobusa, standardi i preporuke koji se primenjuju za termalni komfor u putničkom prostoru autobusa, kao i rezultati merenja potrošnje električne energije HVAC sistema u električnom autobusu Higer KLQ6125GEV3 na liniji EKO2 u Beogradu u različitim periodima godine, i uticaj na energetsku efikasnost električnih autobusa.

KLJUČNE REČI: termički komfor u putničkom prostoru autobusa, energetska efikasnost, HVAC sistem, E-bus

INTRODUCTION

One of the main challenges in the zero-emission bus sector (especially for battery electric vehicles) is travel range, which is significantly affected by the heating, ventilation, and air conditioning (HVAC) system. Unlike conventionally fueled buses (diesel, CNG), which use waste heat from the internal combustion engine to heat the passenger compartment, electric buses rely solely on their batteries. During extreme weather conditions, the need for heating and cooling increases, which significantly affects the travel range of electric buses. On extremely cold winter days, it is possible for the HVAC system and auxiliary systems to consume up to 70% of battery capacity (Chiriac, G. et al. 2021). The result of the reduced travel range is the need for larger batteries and a longer required period of the vehicle charging process, as well as an increase in exploitation costs. These options affect the increase in traction energy consumption due to the greater weight of the batteries, and the economic profitability of operating electric buses. An alternative approach is to reduce the need for heating and cooling through optimized HVAC systems. This is especially important at a time when passenger satisfaction and growing passenger numbers are key requirements for creating a competitive and viable public transport bus system in cities. Therefore, it is crucial to investigate and adapt the current recommended temperature settings in the E-bus in order to mitigate the energy consumption, allowing the planned travel autonomy while ensuring passenger comfort. In some E-bus models used in extremely cold operating conditions, heating systems with external combustion (Webasto) are used, which does not make the vehicle in such operating mode a zero-emission vehicle, which represents a significant disadvantage from an environmental point of view.

HVAC SYSTEM

Regulation of thermal comfort in the bus passenger compartment and air quality is carried out using the HVAC system. The system configuration must be designed to ensure that the climate parameters remain within acceptable ranges for thermal comfort in the bus passenger compartment while simultaneously optimizing energy efficiency. Figure 1 shows the HVAC system on an electric bus with a standard length of 12m (Valeo, 2021).

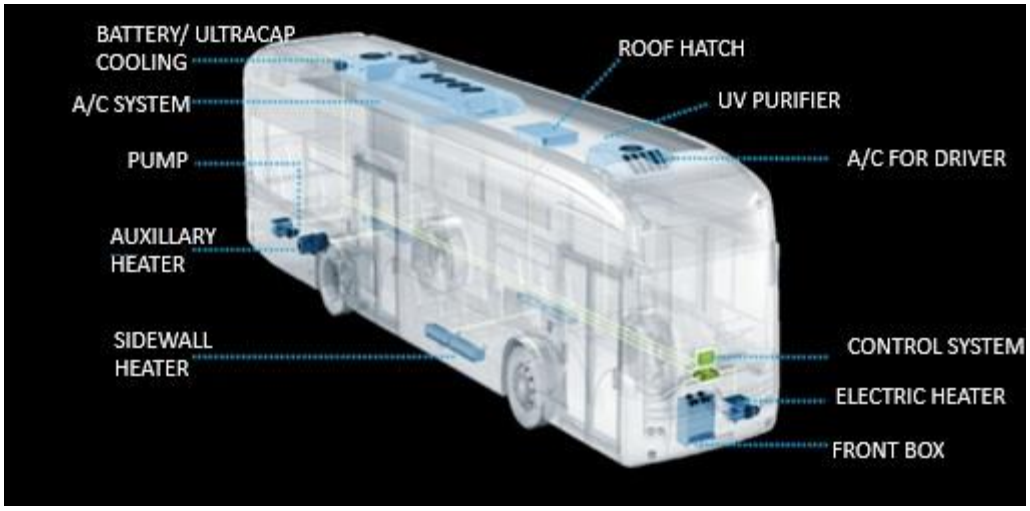

Figure 1 Elements of the HVAC system in buses

A complex system with interactive elements: Electric heater, Air conditioner, UV purifier, Driver's air conditioner, Side wall heater, Pump, Auxiliary heater, Battery/Ultracapacitor cooling system, and control system that ensures the required level of comfort and allows the system to always function optimally.

The electricity consumption of the HVAC system depends on several influencing factors:

- Outside temperature
- Internal temperature
- Number of passengers in the vehicle
- Number of doors for passenger entry/exit

- Duration of passenger entry/exit
- Vehicle insulation

The operation of heating and air conditioning systems and the impact on electricity consumption can be related to the outside temperature. In Figure 2, the area of external temperature in the range of -15 °C to +12 °C implies the use of a heating system. At outside temperatures of +13 °C to +21 °C, air ventilation ensures the set micro conditions of the passenger compartment. Ventilation can be achieved by "natural" flow through side windows or roof vents or by using a fan driven by an electric motor. In cases of using fans, there is an additional requirement for electricity consumption from the electricity storage system. At outside temperatures that are higher than +21 °C, air conditioning is used.

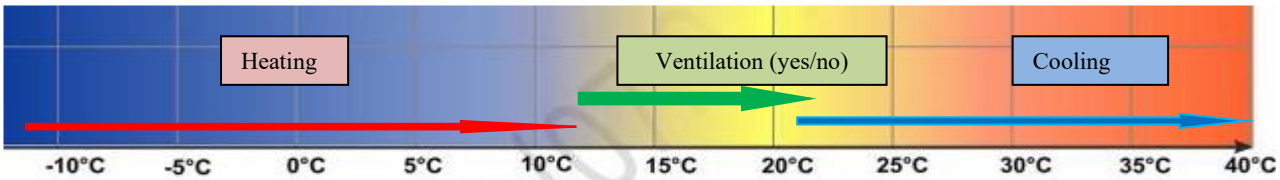

Outside Temperature [°C]

Figure 2 Using the HVAC system as a function of the outside temperature

In real operating conditions, the total electricity consumption of an electric bus, in the case of using an HVAC system, can be expressed as:

$$E_{e.bus} = E_{em_M} + E_{lem} + E_{ad} + E_{li} + E_{HVAC} \tag{1}$$

Where:

$E_{e.bus}$ - total energy consumed by the E-bus, kWh,

E_{em_M} - consumed energy of the drive system (electric motor-inverter), kWh,

E_{lem} - electrical losses in the drive system, kWh,

E_{ad} - consumed energy of auxiliary devices (air-compressor, steering pump, lighting, signaling), kWh,

E_{li} - electrical losses in cables and battery/supercapacitor, kWh,

E_{HVAC} - energy consumed by the HVAC system, kWh.

THERMAL COMFORT IN THE BUS PASSENGER COMPARTMENT

According to ASHRAE (American Society of Heating, Refrigerating and Air-Conditioning Engineers), thermal comfort in the bus passenger compartment is defined as "A state of mind that expresses satisfaction with the thermal environment and is assessed by subjective evaluation" (ASHRAE, 2013). The main influencing factors on the thermal comfort in the bus passenger compartment of passengers are: metabolism of the human body, ambient temperature, radiation temperatures, relative air humidity, air flow speed, and insulation of the passenger's clothing. The time spent in the bus is also important because the longer the human body is exposed to a hot or cold environment, the greater the demand for thermal comfort in the bus passenger compartment.

The human body releases a certain amount of heat as a result of chemical processes in the human body (metabolism) and physical activity. The unit of measure of metabolism is denoted by Met (1 Met = 58.15 W·m^{-2}) and refers to the unit of body surface (Ružić, D. 2016). Body surface area can be calculated according to the following formula (Fanger, P. O. 1970; Parsons, K. 2003):

$$A_{sp} = 0.202 \cdot m_b^{0.425} \cdot h_b^{0.725} \tag{2}$$

A_{sp} - surface area of the human body, m^2,
m_b – body weight, kg,
h_b – body height, m.

For an average passenger body weight of 68 kg and a height of 1.75 m, when the passenger is seated in the vehicle, during a ride corresponding to a value of about 1 Met, the passenger will emit heat of approximately 105 W.

Thermal comfort in the bus passenger compartment, according to the theory of Professor Fanger P.O, takes in to account the metabolic rate of the human body, age of the passenger, clothing insulation, and environmental factors (ambient temperature, relative air humidity, air flow) in order to predict and quantify thermal comfort in the bus passenger compartment (Fanger, P. O. 1970). This theory, supported by climate chamber experiments, remains

widely accepted. Derived models such as PMV-PPD aim to quantify thermal sensation (TS) and thermal comfort in the bus passenger compartment (TC), where TS measures how “cold” or “warm” one feels, and TC assesses overall comfort on a scale from comfort to unbearable.

TC can be affected by general and local discomfort. Local discomfort occurs due to certain parts of the body experiencing temperature variations. For example, cold feet or hot hands may cause local discomfort, despite overall comfort. Factors contributing to local discomfort include drafts and significant vertical temperature differences (ASHRAE, 2017). Addressing local discomfort is key, as it significantly affects overall comfort. The time spent in the vehicle is also of vital importance because prolonged exposure to certain climatic conditions can reduce the thermal comfort in the bus passenger compartment of an individual, which makes passengers more prone to discomfort during longer bus journeys (ASHRAE, 2017). Figure 3 shows the influencing factors on the thermal comfort in the bus passenger compartment of passengers in buses for public transport.

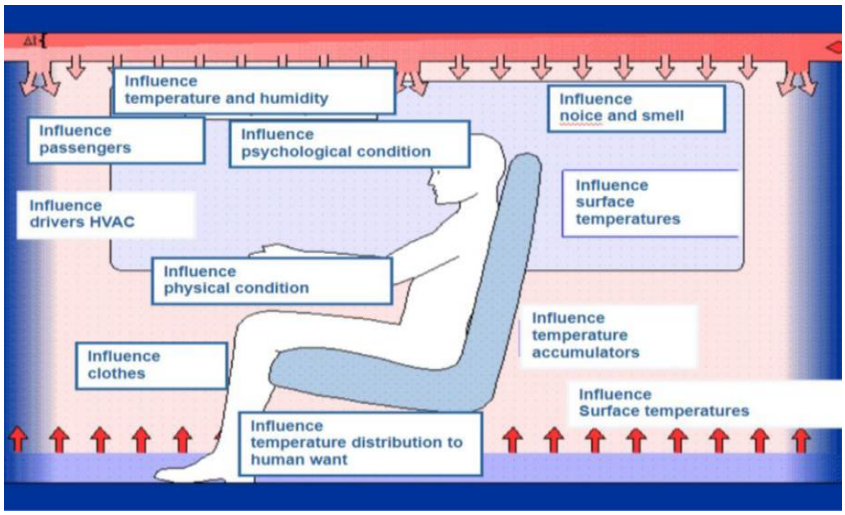

Figure 3 Factors affecting the human body from the aspect of thermal comfort in the bus passenger compartment

Using the PMV-PPD model, two indices are calculated: the predicted average number of satisfied (PMV) and the predicted percentage of dissatisfied (PPD). The first index represents the average thermal feeling of a group of people and is evaluated on the seven-point ASHRAE scale shown in Figure 4. The second index predicts the percentage of people who are likely to be dissatisfied with the climate conditions, and its correlation with the PMV value is shown in Table 1. According to ASHRAE Standard 55 (ASHRAE, 2021) and ISO 7730 (ISO, 1998), thermal comfort in the bus passenger compartment of passengers is maintained for PMV values between ±0.5.

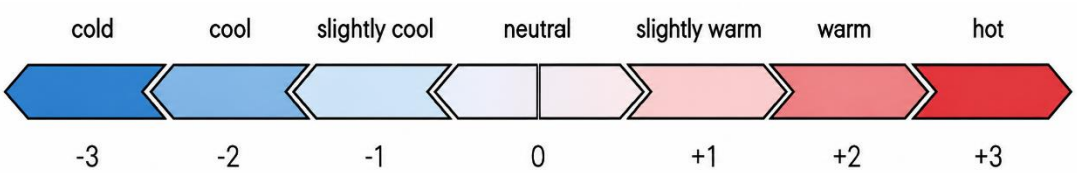

Figure 4 Predicted mean vote (PMV) evaluated along the 7-point ASHRAE scale

Table 1 Correlation between predicted mean vote (PMV) and percentage dissatisfied (PPD)

PMV		PPD
Thermal sensation	Value	Value
Cold	-3	100%
Cool	-2	99.80%
Slightly cool	-1	45.40%
Neutral	0	5%
Slightly warm	1	45.40%
Warm	2	99.80%
Hot	3	100%

STANDARDS AND RECOMMENDATIONS FOR THERMAL COMFORT IN THE BUS PASSENGER COMPARTMENT IN BUSES

The most important international standards related to thermal comfort in the bus passenger compartment in public transport vehicles are: VDV-236, ASHRAE Standard 55, ISO 7730, ISO 14505, and EN 14750. VDV is a German

standard that applies to buses with internal combustion engines and to electric buses and specifies the acceptable minimum performance of the HVAC system. ASHRAE includes standards for HVAC&R (heating, ventilation, air conditioning, and refrigeration systems). The International Organization for Standardization (ISO) provides a wide collection of standards in the field of technology and manufacturing. Which of the standards will be applied regarding thermal comfort in the bus passenger compartment in vehicles usually depends on the National Regulations of the states and the climatic areas of the cities where public transport buses are used. In general, climate zones are defined as: Very cold, cold, temperate, warm, and very warm. Table 2 shows characteristic climate zones (UITP, 2024).

Table 2 Climate zone classification

Climate zone	Average min. Temperature, °C	Average max. Temperature, °C
Very cold	<-8	>+10
Cold	<-1	>+10
Moderate	<+7	>+15
Hot	<+15	>+25
Very hot	<+25	>+34

The VDV-236 standard is intended for buses operating in the public transport system and is primarily designed for the conditions of Central Europe. The standard includes three parts, namely air conditioning requirements, HVAC system design requirements, and control systems required for city buses (Truong, M. T. 2019).

According to the standard, the internal temperature should be regulated according to the operating modes. The three operating modes are labeled as ventilation, cooling, and heating. In addition, the design should follow two characteristic comfort curves: an economic curve and a comfort curve that dictates how heating and cooling should be regulated in different operating modes. The characteristic comfort curve should include three intermediate points at external temperatures of -10 °C, 15 °C, and 35 °C, and a clear difference between the operating modes must be visible on the curve as shown in Figure 5 (Truong, M. T. 2019). The ventilation mode is between the cooling and heating modes and is in operation whenever there is no need for heating or cooling.

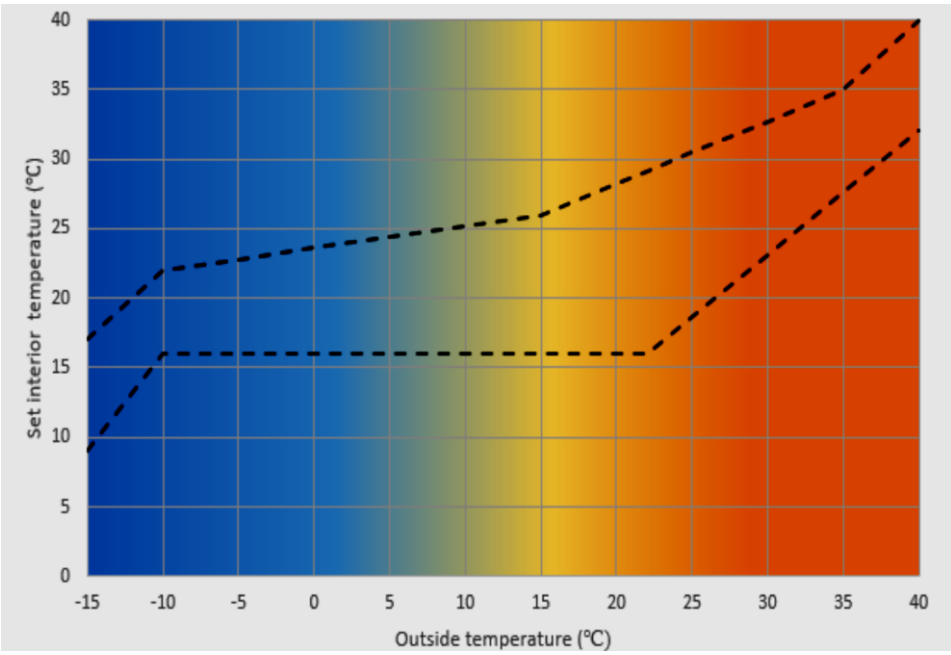

Figure 5 VDV characteristics comfort curve

Comfort curves must be implemented in two basic parameter settings. The comfort curve is particularly suitable for longer trips and is characterized by Heating at the upper limit of the characteristic curve and cooling at the lower limit of the characteristic curve. The economic curve is suitable for shorter journeys/shorter passenger dwell time and electric mobility, and is characterized by: Heating at the lower limit of the characteristic curve; and cooling at the upper limit of the characteristic curve. The curves must also be slightly adaptable to local conditions, allowing a shift of the target internal temperature by ± 2 °C in the heating mode and the initial temperature for the cooling mode by ± 2 °C (Truong, M. T. 2019).

The acceptable speed of air flow in the bus should comply with the EN 14750 standard, shown in Figure 6. It represents the maximum air speed for heating and ventilation for buses in city traffic, where the average travel time of passengers is up to 20 minutes.

The air should be discharged at low speed over a wide area, and it is important to prevent direct air flow on the passengers. In accordance with the current VDV-236 recommendations, Figure 7 shows the maximum permitted levels of relative humidity in buses. This means that in fully air-conditioned buses, the relative humidity must not exceed 70%, regardless of the internal temperature. In addition, for bus temperatures exceeding 30 degrees, relative humidity should be maintained below 50% to ensure satisfactory passenger comfort (Truong, M. T. 2019).

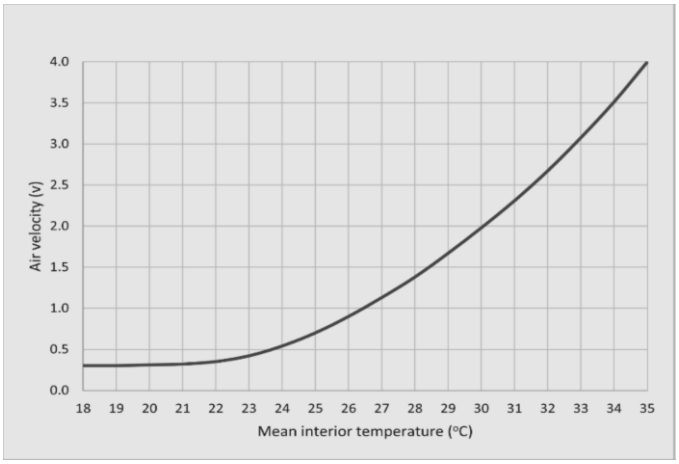

Figure 6 Recommended maximum air velocity according to EN 14750

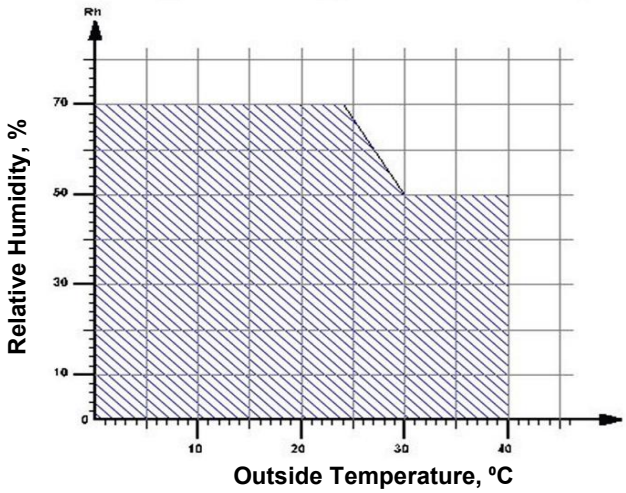

Figure 7 Recommended maximum relative humidity according to VDV-236

The standard for fresh air and air exchange in the vehicle must be in accordance with VDV-236. The HVAC system must be designed to allow the entry of at least 15 m^3 of fresh air per hour per person into the passenger compartment. The standard for air cleanliness must be set in accordance with VDV-236. All fresh air and recirculated air must pass through efficient filters. These filters should achieve a settling rate of at least 75% for particles larger than 0.3 micrometers. Although energy efficiency and thermal comfort in the bus passenger compartment are important, care must be taken not to prevent fresh air circulation. A CO_2 level of 1000 ppm or less is recommended to ensure healthy air with a reduced risk of virus transmission. This is relevant for both the driver's and the passengers (Truong, M. T. 2019).

As electric buses (E-buses) have a constant tendency to develop, it is necessary to investigate and improve HVAC control systems to ensure optimal comfort, efficiency, and safety for both drivers and passengers. The following key areas are recommended for further development (UITP, 2024):

- Develop systems that enable separate but integrated control of the passenger compartment and the driver's compartment. This feature will enable personalized climate settings, improving comfort without compromising the overall efficiency of the electric vehicle.
- Application of artificial intelligence: Development of "smart" HVAC systems capable of self-regulation and adaptive response to changing environmental conditions.
- Remote monitoring and management: This would allow manufacturers or operators to make operational adjustments
- HVAC system from the operation center, depending on the meteorological conditions (Current outdoor temperature, humidity).

The insulation of the vehicle's outer paneling, ceiling, and floor plays a key role in electric buses, which is reflected in the improvement of energy efficiency and thermal comfort in the bus passenger compartment of passengers. By carefully selecting lightweight, highly efficient insulation materials, electric bus manufacturers can optimize energy consumption and maximize passenger comfort. It is recommended that the insulation of the roof, floor, and walls of the bus be designed depending on the climatic conditions in which the bus is used. For countries with a cold climate, it is recommended that the average U-value be around 1.2 W/m2. It is especially important to insulate the windows using insulating glass, UV foils for protection against heat and UV radiation, taking in account the optimal entry of natural light.

Ensuring optimal thermal comfort in the bus passenger compartment and energy efficiency requires well-trained staff. From bus drivers to maintenance staff, adequate training plays a key role. Key areas where staff training is essential:

- Knowledge of temperature control systems in electric buses.
- Training on how adjusting the temperature in the vehicle affects passenger comfort and energy consumption.
- Training for proper use of automatic and manual HVAC operation modes.
- Understanding the different measurement locations in the bus and their importance in assessing thermal comfort in the bus passenger compartment.
- Training on safety protocols to prevent accidents involving measuring equipment.

- Training for efficient collection of passenger thermal comfort in the bus passenger compartment surveys.
- Compliance with standards and guidelines
- Understanding of relevant standards and guidelines related to thermal comfort in the bus passenger compartment and energy efficiency.
- Knowledge of the latest developments in technology and practices related to HVAC systems.

RESULTS OF MEASURING THE CONSUMPTION OF THE HVAC SYSTEM AND IMPACT ON ENERGY EFFICIENCY OF THE E-BUS ON THE EKO 2 LINE IN BELGRADE

Research on the impact of the HVAC system on the energy efficiency of the Higer KLQ 6125 GEV3 E-bus (Figure 8) in Belgrade was conducted in 2023 on the EKO 2 line (Dorcol/Sport centar-Belgarde Waterfront) (Misanovic, S. 2003). Technical data about the vehicle is shown in Table 3. Electric buses use a system of storing electricity using ultracapacitor with a capacity of 40 kWh. The HVAC system is fully electric. In the heating mode, there is a max. power of 30 kW and in cooling mode, 22 kW. Electric buses are charged at the terminals using 400 kW fast chargers after each full turn.

Figure 8 E-bus Higer KLQ6125GEV3

Table 3 Technical characteristics E-bus Higer KLQ6125 GEV3

Dimensions: length, width, height: 12.000x2.550x3.680 mm
Mass of empty vehicle: 12.120 kg
Number of places for sitting/standing: 28/62
- Number of doors: 3
Maximum speed: 70 km/h
Drive electric motor: Siemens 1DB2016 permanent magnet, central position
Max. power of the driving electric motor: 160/230 kW
Maximum torque: 2500 Nm
Drive controller: Siemens ELFA 3
Ultracapacitor: AOWEI
Capacity of Ultracapacitor: 40 kWh
Charging time: 2-5 min

Line EKO 2 is a typical city line (Figure 9). The average length of the line is 7.1 km, and the average transport speed is 13.8 $km \cdot h^{-1}$. The line connects the most attractive areas of the city: Belgrade on the water, Trg Slavija, Trg Republike, Kalemegdan, and Dorcol. 8 vehicles are operating on the line with an average arrival interval of 10 minutes (Misanovic, S. 2023). The research was conducted during different seasons to capture the full variation of outdoor temperatures and their impact on energy consumption. The acquisition of data on the electricity consumption of the HVAC system, drive system, auxiliary devices, ambient, and external temperature was taken from the vehicle's S-CAN and V-CAN network using a laptop device and the "Carmon-Abrites" application in real time.

Figure 9 Route of the EKO2 line

Two different settings, mainly “automatic” and “manual” modes, for the HVAC system were tested. Automatic mode is the recommended operating mode for the HVAC system by manufacturer and is presented during driver training upon vehicle delivery. During automatic mode, the HVAC system is set to maintain a temperature inside the bus of 23 °C. However, some drivers manually adjust the temperature in the bus passenger compartment during winter (26-27 °C) and summer (18-20 °C) due to subjective feelings of heat during extremely low temperatures in winter or extremely high temperatures in summer. An example of one measurement during an extremely high external temperature aperture on the EKO2 line is shown in Tables 4 and 5.

Table 4 Measurement data on the EKO2 line

E-bus Higer KLQ6125GEV3
Garage number: 2110
July 18, 2023
Outside temperature, 37 °C
After noon peak, period 15:57:31-16:29:43
Direction ”A” Sports Center-BW
Lenght: 6.94 km
Occupancy with passengers, max 50%
Traffic conditions-favorable (no traffic jams)
Included HVAC-"Auto" mod for the passenger and driver compartment

Table 5 Energy balance of E-bus electricity consumption

Ultracapacitor-delivered energy, kWh	14.997
Ultracapacitor-recovery energy, kWh	-4.319
Ultracapacitor-recovery efficiency coefficient, %	28.8
Ultracapacitor, ΔE, kWh	10.678
Motor-Consumed Energy, kWh	9.452
HVAC system, Consumed Energy, kWh	4.970
Auxiliary devices-Consumed Energy, kWh	0.972
Energy losses, kWh	0.890
E-bus, consumed energy, kWh	10.678
E-bus, consumed energy, kWh·km^{-1}	1.528

Figures 10 and 11 present the current electricity consumption of the HVAC system during the measurement period and the ambient temperature of the passenger/driver's compartment.

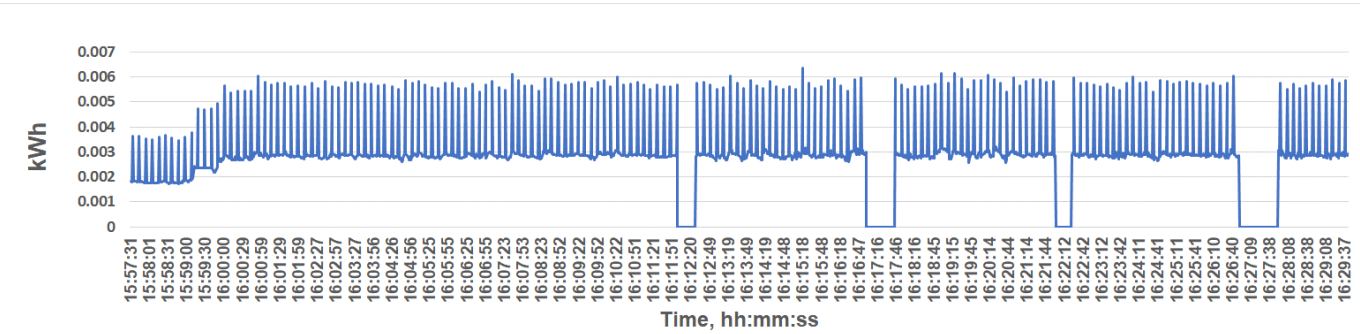

Figure 10 HVAC system, current electricity consumption, July 18, 2023, time: 15:57-16:29

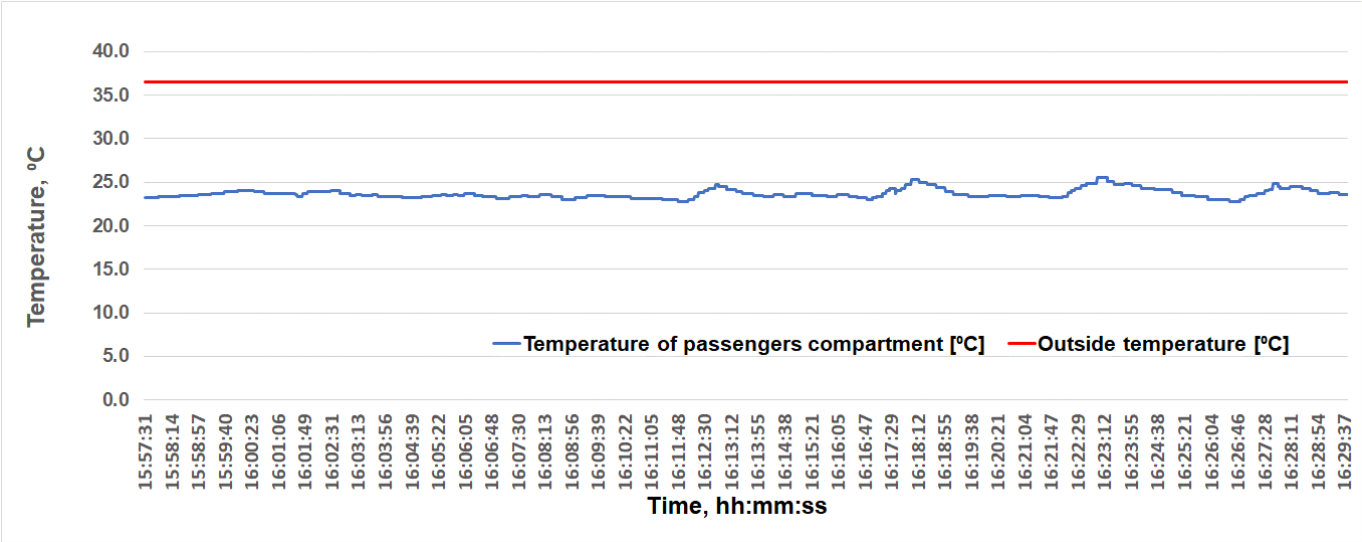

Figure 11 Current temperature of passengers compartment and outside temperature, July 18,2023, time: 15:57-16:29

Since the testing was carried out during the day, the interior lighting in the bus was turned off. The measurement results showed that of the total electrical energy consumed, the engine-inverter drive system consumed 9.452 kWh (63.0%), while the HVAC system consumed 4,970 kWh (33.1%). Auxiliary devices consumed 0.972 kWh (6.48%), while electricity losses amounted to 0.890 kWh (5.93%). The energy consumed by the signage and external displays of the e-buses was not taken in account it can be considered negligible, given that they use LED technology and are extremely low consumers. It is clearly shown that at extremely high outdoor temperatures of 37 °C, to achieve an acceptable level of thermal comfort in the bus passenger compartment in the passenger compartment of the vehicle (23-25.3 °C). The operation of the HVAC system significantly increases the electricity consumption of the E-bus, which amounted to 1.528 kWh·km^{-1}.

The achieved temperature values in the passenger compartment of the vehicle (23-25.2 °C) during the test are lower compared to the recommendations of the VDV-236 standard. For a typical intermediate outside temperature of 35 °C, the recommended internal temperature values in the passenger compartment is 27 °C (Figure 5). It should be noted that the maximum occupancy of passengers in the vehicle during the test was about 50%. At the initial and final stations, the occupancy was significantly lower by about 20%, which allowed the HVAC system to strive to achieve the set temperature in the passenger compartment of 23 °C. The smaller number of passengers in the vehicle also influenced the shorter dwell time at the passenger entry/exit stations, which was reflected in the fact that the vehicle doors were opened for a shorter time and therefore a lower flow of warm air into the vehicle interior, which affected the efficient operation of the HVAC system. Otherwise, with a vehicle occupancy higher than 80%, assuming that the human body emits heat energy of about 105 W (Fanger, P. O. 1970; Parsons, K. 2003) and longer periods of standing at stations due to passenger entry/exit, the achieved temperature level in the passenger compartment would be higher, but within the limits of the VDV-236 recommendation, with higher HVAC system consumption.

Based on a sample of 40 measurements of HVAC system energy consumption in different seasonal periods of exploitation (winter, spring/autumn, summer) (UITP, 2024; Misanovic, S. 2023), they proved that the electricity consumption of the HVAC system is highly correlated with the outdoor temperature (Figure 12). With the use of the HVAC system, the total electricity consumption of the E-bus also increases (Figure 13) (UITP, 2024; Misanovic, S. 2023).

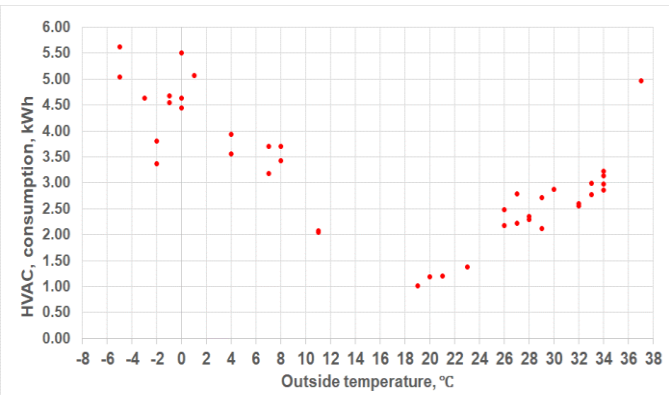

Figure 12 Energy consumption correlated to outside temperature for the HVAC system

The results obtained from the research show that the HVAC system is the largest energy consumer in the heating mode of the passenger and driver's compartment, followed by the cooling mode (air conditioning system). During the spring and autumn periods when the HVAC system are not used, for outdoor temperatures of 12-19 °C, the average consumption of the E-bus was 0.75 kWh·km^{-1}. This temperature range of outside temperatures is the most favorable from the aspect of energy efficiency of the E-bus. The average consumption during winter and summer when using the HVAC system was 1.46 kWh·km^{-1} and 1.13 kWh·km^{-1}, respectively. Expressed as a percentage, the total E-bus consumption when the HVAC system is used in the winter period is 29% higher than in the summer period.

Manual control of the HVAC system, as a result of non-recommended mode or subjective driver feeling, resulted in a significant increase in HVAC system energy consumption. A typical example can be seen in Figure 12, where at an outdoor temperature of 0°C in automatic mode, the HVAC system consumed 4.48 kWh, while in manual mode the consumption was 5.47 kWh, which is an increase of 22%. It is similar in the summer period, where at an outdoor temperature of 26°C in automatic mode the HVAC system consumed 2.17 kWh, and in manual mode 2.5 kWh, which is an increase of 15.2%.

The daily autonomy for the Higer KLQ3125GEV3 electric bus is not in question, as charging is carried out at the terminal using a 400 kW ultra-fast charger. The capacity of the ultra-capacitor is 40 kWh, gives the vehicle a large energy reserve even in the most unfavorable conditions of electricity consumption. Theoretically, with a consumption of 1.8 kWh·km^{-1}, the electric bus would consume 25.5 kWh for a full turn on a line with 14.2 km, and would therefore have 36 % of the remaining energy. This would only have an impact on the slightly longer charging time at the terminal and would not have an impact on schedule disruptions. The average charging time at the terminal after each turn on the line EKO 2 is about 3.5 minutes (Mišanović, S. 2024). Charging in the aforementioned extreme case would be about 5.5 minutes.

Unlike an electric bus that uses ultra-fast charging at the terminal, the HVAC system's impact on daily autonomy is more pronounced in a battery E-bus charged at the depot. The specificity of a battery E-bus is that, as a rule, it is charged once a day, usually at night, and has a battery with a capacity of 420-550 kWh, so uncontrolled use of the HVAC system could significantly reduce the planned daily autonomy. For example, if the HVAC system were used for 12 hours a day with an average power of 8 kW, it would consume 96 kWh of energy from the battery. In a battery E-bus, the lower limit of battery discharge must not reach 15%, so for a maximum battery capacity of 450 kWh, the effective capacity is 382 kWh. If the HVAC system in the above example consumes 96 kWh, the available battery capacity for operating the propulsion system and auxiliary devices is only 286 kWh, which can significantly reduce the daily autonomy of an electric bus (Mišanović, S. 2025).

CONCLUSIONS

Thermal comfort in the passenger compartment of a bus for passengers in public transport buses is an important factor that, in addition to punctuality, reliability and accessibility, should contribute to the quality of public transport service. The configuration of the HVAC system in the vehicle must be designed to ensure that the ambient temperature, relative humidity and air flow are within acceptable ranges for thermal comfort in the passenger compartment of the bus, while optimizing the energy efficiency of the vehicle. The choice of HVAC system to be installed in the vehicle largely depends on the geographical area of operation, using standards and recommendations related to thermal comfort in the passenger compartment of the bus, the way the HVAC system is used, improving the thermal insulation of the vehicle, and the application of advanced control systems and new technologies. The results of measuring the electricity consumption of the HVAC system of the Higer KLQ6125GEV3 E-bus on the EKO2 line in Belgrade in different periods of operation (winter, summer, transitional period) have shown that to maintain the set temperature in the passenger compartment of the bus in the recommended “automatic mode” of 23 °C, consumption increases with the intensity of use of the HVAC system depending on the outdoor temperature. The HVAC system of the Higer KLQ6125GEV3 E-bus at an extremely high outdoor temperature of 37 °C provided satisfactory thermal comfort in the passenger compartment of the bus in accordance with the recommendations of the VDV-236 standard. From the point of view of the energy efficiency of the E-bus, the transitional period (spring-autumn), when the HVAC system is not used or is used minimally, most often in the mode of air ventilation in the interior of the vehicle, achieves the lowest consumption of the E-bus. The winter operating period with low outdoor temperatures below 0 °C and the summer with extremely high outdoor temperatures above 34 °C affect the increased overall consumption of the E-bus.

The influence of electrical energy consumption of the HVAC system on the daily autonomy of the E-bus movement is not significant in the case of E-buses that use ultra-fast chargers at the terminus. The bigger impact is for battery buses that are charged at the depot. In order to reduce this impact, modern battery buses tend to increase the battery capacity, which increases the cost of the E-bus.

REFERENCES

ASHRAE. (2013). Standard 55 – Thermal Environmental Conditions for Human Occupancy.

ASHRAE. (2017). Thermal Environmental Conditions for Human Occupancy. https://www.ashrae.org/file%20library/technical%20resources/standards%20and%20guidelines/standards%20addenda/55_2017_d_20200731.pdf

ASHRAE. (2021). ASHRAE 55-2020. https://www.techstreet.com/ashrae/standards/ashrae-55-2020?product_id=2207271#document

Chiriac, G., Lucache, D. D., Nitucă, C., Dragomir, A., & Ramakrishna, S. (2021). Electric bus indoor heat balance in cold weather. *Applied Sciences*, 11(24), 11761. https://doi.org/10.3390/APP112411761

Fanger, P. O. (1970). *Thermal confort: analysis and applications in enviromental engineering*. McGraw-Hill, New York.

ISO. (1998). ISO 7726:1998 Ergonomics of the thermal environment - Instruments for measuring physical quantities.

Misanovic, S. (2023, October 27). The energy efficiency of new e-buses in belgrade- impact of hvac-system, uitp north america workshop on zero emission fleets, San Francisco, USA.

Mišanović, S (2024, 10-11 October). Performances of fast chargers for electric buses in Belgrade on the EKO 2 line, 10th International Congress Motor Vehicles and Motors (MVM 2024), pp. 485-491, Kragujevac, Serbia.

Mišanović, S. (2025, 18-20 November). The impact of the HVAC system on E-bus electricity consumption-Case Study, UITP E-bus Diploma programme, Module 3-Operation and Maintenance, Madrid.

Parsons, K. (2003). *Human thermal environments: The effect of hot, moderate and cold environments on human health, comfort and performance*. 2nd ed. Taylor&Francis, London.

Ružić, D. (2016). *Mikroklima u motornim vozilima*. Fakultet tehničkih nauka, Novi Sad.

Truong, M. T. (2019). Klimatisierung von Linienbussen der Zulassungsklassen I (Stadtbus) und II (Überlandbus), für konventionell angetriebene Diesel- und Gasbusse als auch für Hybrid-, Brennstoffzellen- und Elektrobusse.

UITP. (2024). Thermal comfort in the bus passenger compartment & Energy Efficiency on buses.

Valeo. 2021.Thermal commercial vehicles-Thermal Confort in E-buses.

The 11th International Congress
Motor Vehicles & Motors 2026
Kragujevac, Serbia
October 8th - 9th, 2026

Motor Vehicles & Motors

MVM2026-019
https://doi.org/10.24874/CMVM2026.019
Original scientific paper

Dragan Ružić[1]
Miloš Vujković[2]

DETERMINING THE FUEL CONSUMPTION REQUIRED FOR AIR-CONDITIONING OF A PASSENGER CAR UNDER REAL-WORLD CONDITIONS

ABSTRACT: This paper presents an investigation of the impact of air-conditioning system operation on fuel consumption in real operating modes of a used passenger car. The motivation for the work is to determine additional amount of fuel needed for cabin air-conditioning in real driving conditions without the use of complex laboratory equipment. Official data on standardized fuel consumption are determined with the air-conditioner switched off and under strictly controlled conditions. Data available from the car's diagnostic data connector were acquired, processed and analysed. The results showed that an air-conditioner with a variable compressor increases fuel consumption by about 0.5-0.6 l/100km at speed 70 km/h. At the same car velocity, the fuel consumption depends on selected gear, i.e. on the engine speed and compressor speed. In this experiment, the better results were achieved in higher gear, i.e. at lower engine and compressor speed. Depending on the architecture of the OBD system in the car, the presented method could be used for more complex research into individual factors on the energy management of the car's HVAC system as well as other systems.

KEYWORDS: passenger car, air-conditioning system, fuel consumption, microclimate, diagnostic scanner

ODREĐIVANJE POTROŠNJE GORIVA POTREBNE ZA RAD KLIMA-UREĐAJA AUTOMOBILA U REALNIM USLOVIMA

REZIME: Rad predstavlja istraživanje uticaja rada klima-uređaja na potrošnju goriva automobila u stvarnim uslovima. Cilj rada je određivanje vrednosti dodatne količine goriva potrebne za klimatizaciju kabine u realnim uslovima vožnje, bez primene kompleksne laboratorijske opreme. Zvanični podaci o potrošnji goriva nekog automobila se određuju na standardizovani način, sa isključenim klima-uređajem i u strogo kontrolisanim uslovima. Raspoloživi podaci sa dijagnostičkog priključka automobila su sakupljeni, obrađeni i analizirani. Rezultati su pokazali da klima-uređaj sa varijabilnim kompresorom u datim uslovima povećava potrošnju goriva za oko 0,5 do 0.6 l/100 km pri brzini 70 km/h. Pri istoj brzini kretanja potrošnja zavisi od stepena prenosa menjača, odnosno od broja obrtaja motora, tj. broja obrtaja kompresora. U zavisnosti od arhitekture OBD sistema u automobilu, prikazani metod bi se mogao koristiti i za kompleksnija istraživanja pojedinih faktora na upravljanje energijom HVAC sistema ali i drugih sistema.

[1] *Dragan Ružić, prof., University of Novi Sad, Faculty of Technical Sciences, Dositeja Obradovića square 6, Novi Sad, ruzic@uns.ac.rs, https://orcid.org/0000-0002-3320-4750*
[2] *Miloš Vujković, MSc, BIBUS Industry doo, Ćirila i Metodija 15, Šabac, vuj@bibus.rs*

KLJUČNE REČI: automobil, klima-uređaj, potrošnja goriva, mikroklima, dijagnostički uređaj

INTRODUCTION

Energy/fuel consumption is an area that has been continuously improved since the advent of vehicles, whether they are powered by internal combustion engines, hybrids, or electric drivetrains. A heating, ventilation and air-conditioning system (HVAC), as a standard equipment of nowadays cars, is the largest power consumer, excluding the propulsion system (Leighton and Ruth (2016), Grossmann (2010)). The thermal comfort requirements must be achieved in every vehicle as fast as possible, with fresh air supply of breathing zone, low air velocities, moderate surfaces' temperature and low noise of ventilation system. In contrast to vehicles powered by internal combustion engine (ICE), HVAC system in battery electric (BEV) or hybrid electric vehicle (HEV) significantly influences the available driving range, sometimes to factor of 2 (Cigarini et al. (2021), Mišanović et al. (2018)).

Official data about energy consumption and emission are provided under the conditions where only the equipment necessary for the operation of the vehicle during the test is in use (for example, UN ECE regulation No 101 says: The passenger compartment heating system shall be switched off, as shall any air conditioning system...). Standards for requirements of thermal comfort in vehicles (standards ISO 14505-2, DIN 1946-3 and ASABE 14269-2) does not consider the energy consumption of HVAC system.

The most advanced and repetitive method for investigation of vehicle's and its systems' performances are experiments performed in laboratory conditions. However, in area of microclimate and thermal conditions those facilities have very high costs and complexity as well as energy consumption (Ružić and Poznanović (2021)). Field experiments with more or less simple mobile equipment can provide useful results for further investigation or simulation. Modern vehicles offer easy approach to data from onboard sensors and actuators thank to on board diagnostics system (OBD) and standardized protocols and connector. In the case study of Šarkan et al. (2025), various methods of measuring fuel consumption in laboratory conditions were analysed, including the use of a fuel flowmeter, OBD scanner and calculation based on emission tests. A relative difference between the fuel consumption measured by the OBD device and the volumetric flowmeters was around 5%. Abukhalil et al. (2020) used data from OBD to form a relationship between the monitored parameters and the fuel consumption. Their model showed good correlation with the data obtained by the conventional methods. Data from OBD port for energy consumption calculation were used in the study of Li, C. et al. (2018). The authors examined the effects of different cabin air ventilation settings on air-conditioner (AC) power consumption in plug-in HEV. They found out that AC compressor used about 12% and 30% of total power consumption, in air recirculation and fresh air mode, respectively. Thermal conditions inside the passenger compartment were not in the focus of this research.

Taking into account that AC system in passenger cars is standard equipment for almost 20 years, total energy required for air-conditioning of cars in operation can not be negligible. Furthermore, cars with conventional propulsion system (internal combustion engine), manual gearboxes and mechanically driven AC compressors are still produced and sold. The objective of this study is to experimentally investigate difference in fuel consumption of a used mid-sized passenger car with and without AC system turned on, in hot outside conditions. The car was driven at constant speed, in fourth and fifth gear, in order to have measurement with two compressor speeds. Additionally, the thermal conditions inside the passenger compartment were measured. The results should give an insight in factors that influence percentage of the power required for air-conditioning of the used common car's cabin in typical summer conditions in Central Europe region.

THEORETICAL BACKGROUND

A moving vehicle consumes energy on outer resistances (rolling resistance, air drag, road slope, acceleration) and inner consumers (electric and electronic systems, comfort systems, auxiliary systems...). The sum of the power requirements reflects in total energy consumption, and sometimes is not easy separate individual power consumers. Instead of direct measurement of the power used by AC system, comparison of instantaneous fuel consumption between drive with AC system switched off and with AC system switched on under the same other conditions was used in this study.

This measurement can be done by installation of suitable measuring equipment on the vehicle's engine. However, available data from the vehicle electronic control units (ECU) can be used to obtain comparable results. Data from the ECU are readable by commercial diagnostic tool (scanners) that is connected to the vehicle over existing and standardized data link connector (DLC). Diagnostic tool is connected to laptop with diagnostic software, enabling monitoring and recording of the data from the vehicle. The method for data acquisition is use of real-time values from ECU and sensors, and recording them over a chosen period of time. Once recorded on the computer, the data can be analysed using a commercial mathematic software (MS Excel, for example).

Fuel consumption calculation

The basic data available from the engine ECU needed to calculate fuel consumption are

- injection fuel quantity, m_f, mm^3
- engine speed, n, RPM
- vehicle speed, v, km/h

If the ECU sends data on fuel consumption in milligrams, conversion of mass values to volume values by specific gravity of fuel is necessary.

The range of data and units depend on type of vehicle and on type of diagnostic tool and software used.

Hourly fuel volume consumption of 4-stroke 4-cylinder engine:

$$g_h = \frac{n \cdot m_f \cdot 3600}{30 \cdot 10^6}, \left[\frac{\mathrm{l}}{\mathrm{h}}\right] \tag{1}$$

Instantaneous fuel consumption in litres per 100 km:

$$g_{100} = 100 \cdot \frac{g_h}{v}, \left[\frac{\mathrm{l}}{100\ \mathrm{km}}\right] \tag{2}$$

Additional real-time value for monitoring of the AC system wokring conditions is the AC system high-side pressure, as well as other related to AC system that are available in particular OBD system.

Thermal conditions inside a cabin

Thermal conditions inside the car's cabin are also important indicator of AC efficiency. The basic parameter to describe thermal conditions is an air temperature. However, the other influences on heat exchange between the human body and the vehicle cabin must be considered (Grossmann H. (2010), Parsons K. (2003), Ružić and Časnji, (2012), standards ISO 14505-2 and DIN 1943-2). In this research, air temperature, air velocity and radiant temperature were measured in the co-driver's head zone.

MATERIAL AND METHOD

The experiment was performed on used passenger car, driving in different regimes on a selected public road. The same route was travelled with the AC system turned on and with the AC system turned off. Real driving conditions are consisted of nonstationary regimes of driving, but since acceleration, deceleration and braking can not be neither defined nor repeated precisely within the given conditions, the results from driving at steady speed controlled by cruise control were analysed in this paper. Since the test route was not without disturbances hence the driving resistances, the experiment conditions could be treated as quasi-steady driving conditions.

The vehicle specification

Experiments in this study were performed on the used passenger car Peugeot 307 (Figure 1). The vehicle specifications are given in the Table 1.

Figure 1 Passenger car used in the experiment: Peugeot 307, 2007

Table 1 The car specifications (https://www.ultimatespecs.com/car-specs/Peugeot/949/Peugeot-307-16-HDi-110.html, visited 06.03.2026.)

Make and model	Peugeot 307 1.6 HDI, 5-door hatchback
Model year/Year of manufacture	2005/2007
Test vehicle mass /Gross vehicle mass	1370 kg / 1810 kg
Tyres	195/65R15 M+S
Engine	PSA 9HZ DV6TED4: 4-cylinder turbodiesel, 80 kW at 4000 min^{-1}, 240 Nm at 1750 min^{-1}
Gearbox	manual, 5-speed, i_4 = 0.82, i_5 = 0.66, i_{fd} = 3.79
AC	variable compressor Sanden SD6C12, 120 cm^3, refrigerant r134a, pulley diameter 120 mm (1:0.76), automatic control
Body colour	black, metallic
Fuel Consumption (NEDC): City/Open road/Combined	6.1/4.3/4.9 l/100 km
CO_2 emission	129 g/km

Measuring equipment

Diagnostic scanner Bosch KTS 590 was connected with the car via standard DLC. The data were transferred to laptop with ESI[tronic] 2.0 software.

Recording the data from air temperature, air velocity and radiant temperature Brüel & Kjær sensors was carried out with Indoor climate analyser Brüel & Kjær 1213.

The pyranometer was used to record solar irradiation at the beginning and the end of the measurement.

The specification of the measuring equipment used in the experiment is presented in the Table 2.

Table 2 The specifications of the measuring equipment

Name	**Specifications**
Diagnostic scanner Bosch KTS 590 with Esi[tronic] 2.0 software	-
Brüel & Kjær 0034 air temperature sensor	Pt100, accuracy ±0.2°C from 5 to 40°C
Brüel & Kjær 0036 radiant temperature sensor	Pt100, range 50 K, accuracy 0.5 to 2.0 K
Brüel & Kjær 0038 air velocity sensor	constant temperature anemometer, range 0.05 to 1 m/s, accuracy ±0.05 m/s
Benning Sun 2 pyranometer, insolation measuring device	insolation range 100-1250 W/m^2

THE EXPERIMENTAL SETUP

The driving conditions:

- driving in both direction of chosen route on public road,
- steady speed of 70 km/h in cruise control mode,
- driving in 4th and in 5th gear.

Settings of HVAC system:

- AC in the lowest temperature settings,
- fan speed set to half,
- fresh air mode,
- the air vents on the instrument panel were set in horizontal middle position,
- all windows closed.

The vehicle condition:

- two persons inside the cabin,
- the engine on operating temperature (79-85°C),
- fuel tank half full,
- dipped beam switched on (daylight running lights),
- the AC was turned on before the measurements and the first set of measurements was performed with the air conditioner turned on, in order to stabilize the system operation.

Ambient conditions:

- date: 03.07.2025., start of the experiment at 10:40, end at 11:05,
- outside temperature 32 °C, (https://www.wunderground.com/weather/rs/novi-sad, visited 03.07.2025),
- relative humidity (RH) 20% (https://www.wunderground.com/weather/rs/novi-sad, visited 03.07.2025),
- insolation 916 W/m^2, clear sky,
- no wind.

Test road:

- Irmovo road, near Novi Sad, South Bačka District, Serbia,
- flat and paved,
- section of the road to which the displayed results refer: length 1.9 km, (Figure 2)

Figure 2 Road view and satellite view of measurement road section (https://www.google.com/maps/, visited 24.07.2026.)

The sensors for measuring thermal conditions inside the cabin, described in the Table 2, were placed in the co-driver's head zone on plastic dummy (Figure 3) and in one central air vent on the dashboard.

Figure 3 Layout of the sensors for measuring microclimate parameters

The results and discussion

Fuel consumption

The results of fuel consumption in litres per 100 km with AC turned on and off are graphically presented in figures 4 and 5, for constant speed drive in 4th and 5th gear, on the part of the road section. As can be seen from the results, the instantaneous fuel consumption is very variable, although the vehicle speed was maintained constant, because of small but significant changes in driving resistances. Therefore, the results from acceleration phases and other transient regimes were not presented in this study.

The car speed recorded by diagnostic scanner was in range from 66 to 67 km/h, while engine speed data was 1767 min^{-1} and 1413 min^{-1} in 4th and 5th gear, respectively.

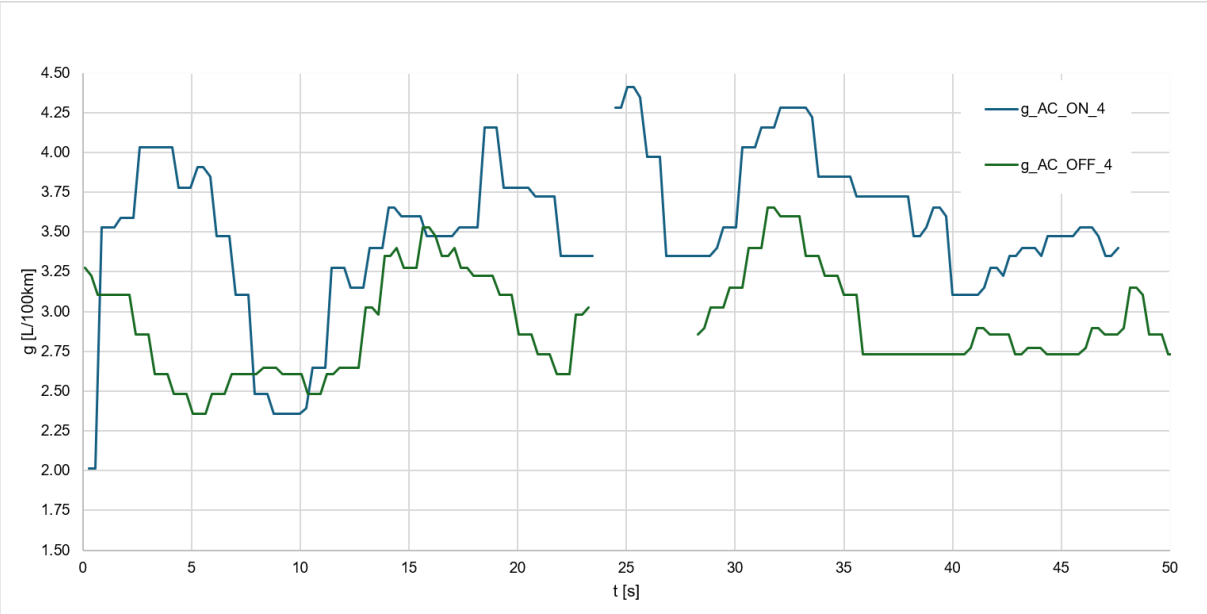

Figure 4 The results of instantaneous fuel consumption (*g*) for constant speed drive in 4th gear, in both direction

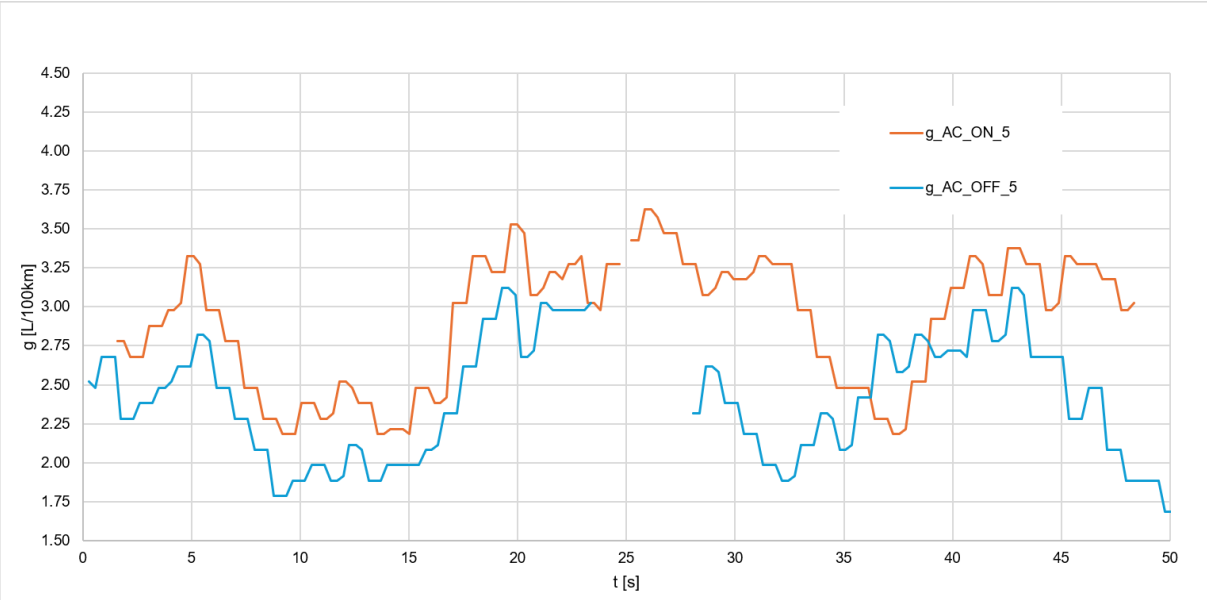

Figure 5 The results of instantaneous fuel consumption (*g*) for constant speed drive in 5th gear, in both direction

Table 3 gives insight in average values of fuel consumption, absolute and relative differences between the combination of driving regimes, during the steady car speed. The relative between consumption between 4th and 5th gear is showing percentage of the fuel consumption decrease.

Table 3. Average values of fuel consumption, absolute and relative differences between fuel consumption with and without air-conditioning, and between fuel consumption in 4th and 5th gear

	4th gear	5th gear	difference	reduction compared to 4th gear
AC on	3.52 l/100 km	2.91 l/100 km	0.61 l/100 km	17%
AC off	2.92 l/100 km	2.39 l/100 km	0.53 l/100 km	18%
difference	0.61 l/100 km	0.52 l/100 km	0.09 l/100 km	15%
relative increase compared to the AC off	21%	22%		
% of total energy	17%	18%		

A power required to move the car at 70 km/h is the same in the 4th and 5th gear. The absolute values in Table 3 shows that the efficiency of the IC engine is higher in the working point when the transmission is in 5th gear.

Almost the same values of the relative fuel consumption increase, and in turn the percentage of total energy required to drive the AC system, indicates that the AC system energy was approximately the same in both gears. Moreover, the percentage of total energy required to drive the AC system corresponds to the values given by Li, C. et al. (2018) for HEV.

The recirculation of the cabin air could reduce required power, but this is short-time solution (up to 15 minutes) because of influence on cabin air quality.

Air-conditioning system

The working points of AC system were

- 4th gear: high pressure 13,5 bar, compressor speed 2320 min^{-1}
- 5th gear: high pressure 12,3 bar, compressor speed 1860 min^{-1}

According to the compressor manufacturer's data, coefficient of performance (COP) decreases for around 5% with compressor speed, but available cooling power increases, depending on swept volume setting (Sanden, Figure 6). However, refrigerant flow rate as well as swept volume setting of the variable compressor could not be measured.

Comparing the thermal conditions in the cabin for the two modes, there was no significant difference in any of the monitored parameters.

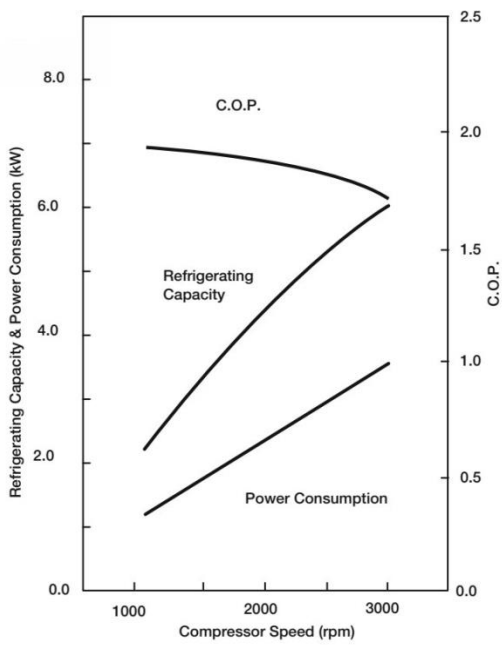

Figure 6. Performance curves of AC compressor Sanden SD6C12 (Sanden)

Cooling power was higher than initial cabin heat gain, since the air temperature and radiant temperature were decreasing when the AC was turned on. When the AC was turned on the air temperature in the air vents dropped from 30 °C to 8 °C in two minutes. The air temperature in the co-driver head zone has been changed from around 35 °C to 30 °C in 10 minutes.

Thermal conditions inside the cabin

An overview of the thermal conditions during the experiment is given in the Table 4.

Table 4. Thermal conditions in co-driver head zone

Parameter	Minimum	Maximum	Average	Comment
Air temperature	30.3 °C	36.5 °C	33.3 °C	corresponds to changes of the temperature in air vent
Air velocity	0.2 m/s	0.5 m/s	0.3 m/s	within comfort zone
Turbulence intensity	23%	59%	39%	within comfort zone
Radiant temperature	34.4 °C	41.6 °C	38.2 °C	the maximum value was from the direction of the windshield

Despite of activated AC system, the air and radiation temperatures in the cabin were very uncomfortable. The causes were high intensity of solar irradiation and relatively short time of the monitoring. The lowest values of air temperature and radiant temperature were recorded after the AC was turned on for a while. The temperatures will continue to drop until equalization of cooling power and cabin heat gain, if the same conditions were maintained longer.

The radiant temperature decreased more slowly than the air temperature, because it is related to the temperature of the cabin interior surfaces, which represents a thermal mass that must be cooled by convection. A higher level of thermal radiation was recorded from the direction of the windshield. Irradiation at horizontal surface under the windshield measured by the pyranometer was 404 W/m^2.

The air velocity and turbulence intensity were independent from air velocity and activation of AC system and they were within the comfort limits.

CONCLUSIONS

This paper presents the experimental investigation of fuel consumption required for air- conditioning in a used mid-sized passenger car under real-world conditions, in hot outside conditions. The fuel consumption was determined by difference in fuel consumption of a passenger car with and without air-conditioner turned on.

The data were collected under quasi-steady driving conditions, at a constant car speed using cruise control, in fourth and fifth gear. Thermal conditions inside the passenger compartment were measured as well.

This relatively simple experiment resulted in following concluding remarks:

- The instantaneous fuel consumption is very variable, even when the vehicle speed was maintained constant.
- The AC system required a power equivalent to increase of ICE fuel consumption from 0.5 to 0.6 l/100 km, depending on its working point.
- The percentage of total power required to drive the AC system was less than 20% when the car was driven at speed 70 km/h.
- In a car with manual transmission and ICE driven AC compressor, fuel consumption of both car and AC system relies on driver's decision about gear selection.
- Both AC system and ICE achieved a better efficiency in 5th gear, which means operation at lower engine and AC compressor speed.
- The air temperature and especially radiation temperature in the cabin were uncomfortable during the experiment and more time is needed to establish better thermal conditions, probably longer than 30 minutes under current conditions.

The boundary conditions in this experimental study were very unfavourable but also very common in a passenger car exploitation in typical summer conditions in Central Europe region. The power demand of the AC system is the highest at the beginning of cool-down regime, in order to as fast as possible obtain acceptable thermal conditions inside the cabin. The recirculation of the cabin air could reduce required power, but this is short-time solution (up to 15 minutes) because of influence on cabin air quality.

New BEVs and HEVs are already equipped with electricaly driven AC compressors and automatic control of thermal and energy management. However, conventionaly driven cars still have a large market share. Along with large number of conventional cars in operation equipped with AC, the use of AC in cars is longer and more frequent as a consequence of increasing global temperatures. One way to mitigate the problem with increased fuel consumption and in the same time emission due to air-conditioning of existing cars, would be an education of the car drivers about proper setting and control of the HVAC system as well as the car. The interface of the air conditioning system also plays an important role in the proper use of the system.

A direction of further investigations could be collecting a more data from real-word driving cases, depending on the architecture of the OBD system in different cars. Stable thermal conditions inside the cabin achieved after a sufficiently long drive should also be the subject of research, as the relationship between maximum cooling power during cabin cool-down regime and lower energy consumption during steady-state driving is important in terms of system dimensioning and selection of operating points with the highest efficiency. This would enable an expansion of the research into considering of more factors on the energy management of the car's HVAC system as well as other systems.

ACKNOWLEDGMENTS

This research has been supported by the Ministry of Science, Technological Development and Innovation (Contract No. 451-03-34/2026-03/200156) and the Faculty of Technical Sciences, University of Novi Sad through project "Scientific and Artistic Research Work of Researchers in Teaching and Associate Positions at the Faculty of Technical Sciences, University of Novi Sad 2026" (No. 01-3609/1).

REFERENCES

Abukhalil, T., AlMahafzah, H., Alksasbeh, M., & Alqaralleh, B. A. Y. (2020), Fuel consumption using OBD-II and support vector machine model. *Journal of Robotics*, 9450178, 9. https://doi.org/10.1155/2020/9450178

Anon. (2013). ECE Regulation No. 101. Rev. 3. Uniform provisions concerning the approval of passenger cars powered by an internal combustion engine only, or powered by a hybrid electric power train with regard to the measurement of the emission of carbon dioxide and fuel consumption and/or the measurement of electric energy consumption and electric range, and of categories M1 and N1 vehicles powered by an electric power train only with regard to the measurement of electric energy consumption and electric range, United Nations, Geneva

Anon. (2006). ISO 14505-2. Ergonomics of the thermal environment - Evaluation of the thermal environment in vehicles. Part 2: Determination of equivalent temperature, International Organization for Standardization, Geneva

Anon. (2003). DIN 1946-3, Raumlufttechnik, Teil 3: Ventilation von Personenkraftwagen und Lastkraftwagen, Deutsche Insitut fur Normung

Anon. (1997). ASABE/ISO 14269-2, Tractors and self-propelled machines for agriculture and forestry - Operator enclosure environment - Part 2: Heating, ventilation and air-conditioning test method and performance. International Organization for Standardization, Geneva

Anon. (2005). ISO 7730: Moderate Thermal Environments - Determination of the PMV and PPD Indices and Specification of the Conditions for Thermal Comfort, International Organization for Standardization, Geneva

Anon. (2021). A/C Compressor Guide and Practical Tips, Sanden International (Europe) GmbH

Cigarini, F., Fay, T.-A., & Göhlich, D. (2021). Modeling and experimental investigation of thermal comfort and energy consumption in a battery electric bus. *World Electric Vehicles Journal*, 12(1), 7. https://doi.org/10.3390/wevj12010007

Grossmann, H. (2010). *Pkw-Klimatisierung - Physikalische Grundlagen und technische Umsetzung*. Springer: Heidelberg. https://doi.org/10.1007/978-3-642-05495-2

Leighton, D., & Ruth J. (2016). Increasing EDV Range through Intelligent Cabin Air Handling Strategies. https://docs.nlr.gov/docs/fy16osti/65054.pdf

Li, C., Brewer, E., Pham, L., & Jung, H. (2018). Reducing Mobile Air Conditioner (MAC) Power Consumption Using Active Cabin-Air-Recirculation in A Plug-In Hybrid Electric Vehicle (PHEV). World Electric Vehicle Journal, 9(4), 51. https://doi.org/10.3390/wevj9040051

Mišanović, S., Taranović, D., Lukić, J., Pešić, R., & Glišović, J. (2018, October 4–5). *The impact of the System for Heating and Airconditioning on the Energy Efficiency of the Electric Drive Bus (e-bus)*. Proceedings of 7th International Congress Motor Vehicles & Motors 2018: Ecology - Vehicle and Road Safety - Efficiency, Kragujevac, Serbia, pp. 115-137.

Parsons, K. (2003). Human Thermal Environments: The Effects of Hot, Moderate and Cold Environments on Human Health, Comfort and Performance, 2nd ed. Taylor & Francis: London. https://doi.org/10.1201/9781420025248

Ružić, D., Časnji, F. (2012). Thermal interaction between a human body and a vehicle cabin. In Kazi, S. (Ed.), Heat *Transfer phenomena and applications* (pp. 295-318) InTech, Rijeka. https://doi.org/10.5772/51860

Ružić, D., & Poznanović N. (2021). *Experimental assessment of thermal environment in mobile machinery cab*. Transport and Logistics – TIL 2021, Niš, Serbia. https://til.masfak.ni.ac.rs/images/til-pedja/til2021_Proceedings_19.pdf

Šarkan, B., Loman, M., Caban, J., Malek, A., Richtár, M., & Stopková, M. (2025). Changing fuel consumption data in official vehicle documents—case study in the Slovak Republic. *Vehicles*, 7(7), 27. https://doi.org/10.3390/vehicles7010027

The 11th International Congress
Motor Vehicles & Motors 2026
Kragujevac, Serbia
October 8th - 9th, 2026

Motor Vehicles & Motors

MVM2026-020
https://doi.org/10.24874/CMVM2026.020
Original scientific paper

Dragan Stojadinović[1]
Aleksandar Đurić[2]
Snežana Jovanović[3]
Miroslav Jovanović[4]

THE INFLUENCE OF SEAT DESIGN AND SURFACE TYPE ON THE LEVEL OF VIBRATIONS EXPERIENCED BY A TRUCK DRIVER

ABSTRACT: This paper presents an experimental analysis of the vibrations to which a heavy-duty vehicle driver is exposed when using different seat types and operating the vehicle on different road surfaces. The study was conducted to evaluate the influence of seat design and road surface characteristics on the driver's vibration exposure. Measurements were performed using accelerometers mounted at appropriate measurement locations, while both a mechanical seat and a pneumatic seat were evaluated during driving on asphalt and gravel roads. Based on the recorded signals, the root mean square (RMS) acceleration values and the peak acceleration values were determined. The obtained results were compared with each other and evaluated against the recommendations of ISO 2631 for whole-body vibration exposure. The results indicate that the type of road surface has a significant effect on the vibration levels experienced by the driver, with the highest values recorded during driving on gravel roads. Furthermore, the pneumatic seat demonstrated superior vibration isolation performance compared with the mechanical seat, resulting in reduced vibration exposure and improved driver comfort during vehicle operation.

KEYWORDS: whole-body vibration, heavy-duty vehicle, seat, root mean square (RMS) acceleration, driver comfort.

[1]*Dragan Stojadinović, Technical Test Center, Vojvode Stepe Str. No. 445, 11000 Belgrade, Republic of Serbia, dragan.stojadinovic90@gmail.com, https://orcid.org/0009-0004-6534-8443*
[2]*Aleksandar Djurić, Military Academy, Veljka Lukića Kurjaka Str. No. 33, 11000 Belgrade, Republic of Serbia, aleksandar_djrc@yahoo.com, https://orcid.org/0000-0002-2165-528X*
[3]*Snežana Jovanović, Technical Test Center, Vojvode Stepe Str. No. 445, 11000 Belgrade, Republic of Serbia, sneza.jovanovic.toc@gmail.com, https://orcid.org/0009-0004-6468-7726*
[4]*Miroslav Jovanović, ZF Serbia, 7. Nova Str. No. 7, 26101 Pancevo, Republic of Serbia, jovanovic.miroslav.77@gmail.com, https://orcid.org/0000-0003-3448-3330*

UTICAJ KONSTRUKCIJE SEDIŠTA I VRSTE PODLOGE NA NIVO VIBRACIJA KOJIMA JE IZLOŽEN VOZAČ TERETNOG VOZILA

REZIME: Ovaj rad predstavlja eksperimentalnu analizu vibracija kojima je izložen vozač teretnog vozila pri korišćenju različitih tipova sedišta i upravljanju vozilom na različitim vrstama kolovoznih podloga. Istraživanje je sprovedeno sa ciljem procene uticaja konstrukcije sedišta i karakteristika kolovozne podloge na izloženost vozača vibracijama. Merenja su izvršena pomoću akcelerometara postavljenih na odgovarajućim mernim mestima, pri čemu su tokom vožnje na asfaltiranim i makadamskim putevima ispitivani mehaničko i pneumatsko sedište. Na osnovu registrovanih signala određene su efektivne (RMS) vrednosti ubrzanja, kao i maksimalne vrednosti ubrzanja. Dobijeni rezultati su međusobno upoređeni i procenjeni u skladu sa preporukama standarda ISO 2631 koje se odnose na izloženost vibracijama celog tela. Rezultati pokazuju da vrsta kolovozne podloge ima značajan uticaj na nivo vibracija kojima je vozač izložen, pri čemu su najviše vrednosti zabeležene tokom vožnje po makadamskim putevima. Pored toga, pneumatsko sedište pokazalo je bolje karakteristike izolacije vibracija u poređenju sa mehaničkim sedištem, što je rezultiralo smanjenom izloženošću vozača vibracijama i poboljšanim komforom tokom upravljanja vozilom.

KLJUČNE REČI: vibracije celog tela, teretno vozilo, sedište, efektivna (RMS) vrednost ubrzanja, komfor vozača.

INTRODUCTION

Vibrations experienced by heavy-duty vehicle drivers represent a significant factor affecting driving safety, work performance, and the long-term health of vehicle operators. During vehicle operation, vibrations are generated by the interaction between the tires and the road surface, the operation of the powertrain, and dynamic loads transmitted through the vehicle suspension system and the driver's seat to the human body. As emphasized by Dennerlein, J. T. et al. (2022), Kat, C.-J. et al. (2021), & Zhou, Z. and Griffin, M. J. (2014), prolonged exposure to whole-body vibration (WBV) may lead to fatigue, reduced concentration, driving discomfort, and various musculoskeletal disorders, particularly affecting the lumbar spine.

The intensity of the vibrations transmitted to the driver depends on several factors, including road surface characteristics, vehicle speed, suspension system design, tire condition, and seat design. Since the driver's seat represents the final element in the vibration transmission path between the vehicle and the driver, its characteristics play a crucial role in reducing vibration exposure and improving driving comfort. Consequently, modern heavy-duty vehicles increasingly employ pneumatic seat suspension systems to achieve more effective vibration isolation.

Whole-body vibration has been the subject of extensive research in the fields of ergonomics, transportation, and automotive engineering. Previous studies have focused on evaluating the effects of vibration on driver health and comfort, developing methods for vibration exposure assessment in accordance with the ISO 2631 standard (ISO, 1997), and investigating the effectiveness of different seat suspension systems in reducing vibration transmission. In their respective studies, Jovanović, B. S. & Djurić, S. A. (2009), Kia, K. et al. (2021), as well as Sekulić, D. et al. (2013, 2016) have devoted particular attention to the determination of root mean square (RMS) acceleration and vibration dose value (VDV), time-domain and frequency-domain vibration analyses, as well as the influence of road surface conditions, vehicle speed, and seat design on driver vibration exposure.

Although numerous studies have confirmed the importance of seat suspension systems in mitigating whole-body vibration, reported results vary depending on the vehicle type, operating conditions, and seat design characteristics. Therefore, there remains a need for experimental investigations comparing different seat types under realistic operating conditions in order to quantify their effectiveness in reducing driver vibration exposure.

In this study, an experimental investigation of whole-body vibration experienced by a heavy-duty vehicle driver was conducted using different seat types during operation on asphalt and gravel road surfaces. Vibration measurements were performed using a triaxial accelerometer mounted on the driver's seat, and the recorded signals were processed to determine the principal vibration parameters and to compare the vibration isolation performance of the investigated seats.

The objective of this study is to evaluate the influence of different seat suspension systems and operating conditions on the whole-body vibration exposure of a heavy-duty vehicle driver, and to identify the seat configuration that provides the most favorable vibration isolation performance under the investigated operating conditions.

MEASUREMENT METHODOLOGY

Theoretical background

Whole-body vibration (WBV) refers to mechanical oscillations transmitted to the driver's body through the seat, floor, or other contact surfaces during vehicle operation or machine use. In heavy-duty and off-road vehicles, these vibrations are primarily generated by road surface irregularities, powertrain operation, and dynamic loads occurring during vehicle operation. The level of vibration transmitted to the driver depends on several factors, including vehicle characteristics, operating conditions, suspension system performance, and seat design.

The assessment of whole-body vibration exposure is commonly performed in accordance with the requirements of the ISO 2631 standard (ISO, 1997), which specifies procedures for measuring, analyzing, and evaluating vibrations affecting the human body. The standard incorporates frequency weighting of vibration signals to account for the varying sensitivity of the human body to vibrations at different frequencies.

Within this regulatory framework, the primary parameter used for evaluating vibration exposure is the frequency-weighted root mean square (RMS) acceleration. This metric is defined as the square root of the mean value of the squared frequency-weighted acceleration over the observation period and is used to quantify the overall vibration exposure experienced by the driver. For translational vibrations, this parameter is expressed in m/s². The frequency-weighted RMS acceleration is calculated as follows:

$$a_w = \sqrt{\frac{1}{T}\int_0^T a_w^2(t)dt} \tag{1}$$

where:

- a_w – frequency-weighted root mean square (RMS) acceleration (m/s²);
- a_w (t) – instantaneous value of the frequency-weighted acceleration;
- T – measurement duration (s).

The ISO 2631 standard (ISO, 1997) defines the root mean square (RMS) acceleration as the average energy level of vibration during the measurement period and one of the most important parameters for evaluating whole-body vibration exposure. Consequently, lower RMS values indicate more effective vibration isolation and more favorable operating conditions in terms of driver comfort and occupational health protection.

In addition to this frequency-weighted RMS acceleration, peak acceleration and the vibration dose value (VDV) are also commonly used in whole-body vibration analysis. While the former parameter describes the average energy content of vibration over the observation period, the VDV parameter is more suitable for assessing exposure under conditions where the vibration signal contains pronounced shocks or transient excitations.

To address these specific conditions, the standard outlines that the VDV method is more sensitive to short-duration, high-intensity vibration events because it is based on the fourth power of the frequency-weighted acceleration signal, whereas the RMS method relies on the second power of the same signal. Consequently, individual shock events have a substantially greater influence on the resulting VDV value, enabling a more accurate assessment of vibration exposure under operating conditions characterized by intermittent high-intensity vibrations.

For translational vibrations, the vibration dose value (VDV) is calculated as follows:

$$VDV = \left\{\int_0^T [a_w(t)]^4 dt\right\}^{\frac{1}{4}} \tag{2}$$

Compared with the RMS parameter, the vibration dose value (VDV) provides a more comprehensive assessment of vibration exposure in situations where the vibration signal contains short-duration, high-intensity events. Since the VDV places greater emphasis on high-amplitude components of the measured vibration signal, it is commonly used as a complementary parameter to the RMS analysis. As outlined in the ISO 2631 standard (ISO, 1997), this parameter is essential for evaluating operating conditions and the effects of vibration exposure on the driver.

Vibration signals can be analyzed in either the time domain or the frequency domain. Time-domain analysis provides the fundamental characteristics of the vibration signal, including the RMS acceleration, peak acceleration, and VDV, whereas frequency-domain analysis provides insight into the distribution of vibration energy across the frequency spectrum. This dual approach enables the identification of the dominant dynamic components of the vehicle–seat–driver system in accordance with the standard's analytical framework.

Under these guidelines, the RMS value serves as the primary parameter for assessing whole-body vibration exposure when the vibration signal does not contain significant shock components, i.e., when the crest factor is less than 9. When the signal contains pronounced peaks and the crest factor exceeds this threshold, the use of additional evaluation metrics, such as the VDV, is recommended to provide a more comprehensive assessment of vibration exposure.

Measurement conditions and data acquisition

The characteristics of the driver's seat have a significant influence on the level of vibrations transmitted from the vehicle to the driver. The effectiveness of the seat suspension system depends on its design, damping characteristics, and vehicle operating conditions. Therefore, experimental vibration analysis under different operating conditions represents an important basis for evaluating the influence of seat design on the driver's whole-body vibration exposure.

Vibration measurements were performed in accordance with the ISO 2631 standard (ISO, 1997), using the coordinate system defined at the point of vibration transmission to the human body. Vibration signals were recorded in three mutually orthogonal directions: the x-axis (longitudinal direction), the y-axis (lateral direction), and the z-axis (vertical direction). The measurement system orientation was adjusted according to these requirements to ensure reliable vibration acquisition and mutual comparison of the obtained results. When complete alignment of the measurement axes is not possible, the standard allows sensor orientation deviations of up to ±15°, while transducers positioned at the same measurement location must remain mutually orthogonal.

For the purposes of this study, vibration acceleration, expressed in m/s², was selected as the measured quantity. Measurements were conducted using the Maestro measurement system manufactured by 01 dB, equipped with a triaxial accelerometer integrated into a seat pad adapter designed to measure vibrations transmitted to the driver's body (Figure 1). The accelerometer was positioned on the driver's seat in the area of body contact, enabling simultaneous recording of vibrations in all three measurement directions.

After data acquisition, the acceleration time signals were processed using vibration analysis software. Based on the processed signals, the root mean square (RMS) acceleration values were determined and used for comparing vibration levels for different seat types and operating conditions.

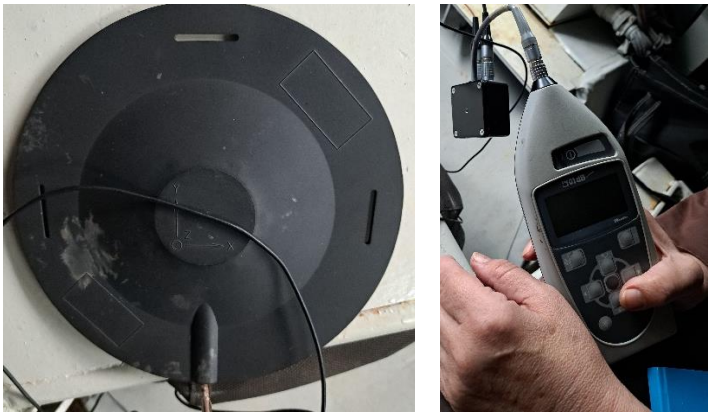

Figure 1 Elements of the measuring chain: Accelerometer (left) and Maestro vibration measurement device (right)

The experimental investigations were conducted on an unloaded heavy-duty vehicle, the main technical characteristics of which are presented in Table 1. The aim of the study was to evaluate the level of vibrations to which the driver is exposed under the previously described operating conditions.

Table 1 Technical characteristics of the test vehicle

Parameter	Specification
Drive configuration	6x6
Unladen vehicle mass	≈ 12 t
Engine power	205 kW
Suspension system type	Front axle: mechanical-hydraulic; second and third axles: mechanical
Tire dimensions	425/85 R21
Tire inflation pressure	4 bar

Within the experimental study, one mechanical seat and two pneumatic seats from different manufacturers were investigated. The mechanical seat is based on a conventional suspension system consisting of spring and damping elements, while the pneumatic seats utilize an air suspension system that provides more effective vibration attenuation and improved driver comfort.

The tests were performed on two types of surfaces: asphalt and gravel. The asphalt surface represented a relatively flat and uniform contact surface, whereas the gravel surface was selected to simulate more severe operating conditions with increased vibration excitation.

During the measurements, the vehicle was driven at an approximately constant speed. On the asphalt surface, the tests were conducted at a speed of 80 km/h, while on the gravel surface the vehicle speed was 20 km/h. Each measurement was repeated several times in order to reduce the influence of random deviations and improve the reliability of the obtained results.

Throughout all experiments, approximately constant test conditions were maintained, including vehicle loading conditions and tire inflation pressure. This minimized their influence on the measurement results and ensured the comparability of the experimental data.

EXPERIMENTAL RESULTS AND ANALYSIS

The measurement results (Table 2) were evaluated based on the comfort criteria defined in the ISO 2631 standard (ISO, 1997) and the health risk assessment criteria specified by Directive 2002/44/EC (European Parliament & Council, 2002) regarding occupational exposure to vibrations.

Table 2 Whole-Body Vibration results under different operating conditions

Road surface	Seat type	Speed (km/h)	Acceleration (m/s^2)			
			x	y	z	a_w
-	Mechanical	0	0.05	0.05	0.02	0.07
	Pneumatic – Manufacturer 1	0	0.05	0.05	0.05	0.09
	Pneumatic – Manufacturer 2	0	0.05	0.05	0.03	0.07
Gravel	Mechanical	20	0.47	0.6	1.18	1.41
	Pneumatic – Manufacturer 1	20	0.32	0.5	0.92	1.10
	Pneumatic – Manufacturer 2	20	0.44	0.6	0.83	1.11
Asphalt	Mechanical	80	0.27	0.15	0.59	0.67
	Pneumatic – Manufacturer 1	80	0.22	0.24	0.54	0.63
	Pneumatic – Manufacturer 2	80	0.23	0.14	0.63	0.68

The experimental results are presented in Figures 2–5, separately for each seat position, for an unloaded vehicle configuration, with a nominal tire inflation pressure of 4 bar, under different road surface conditions and vehicle speeds.

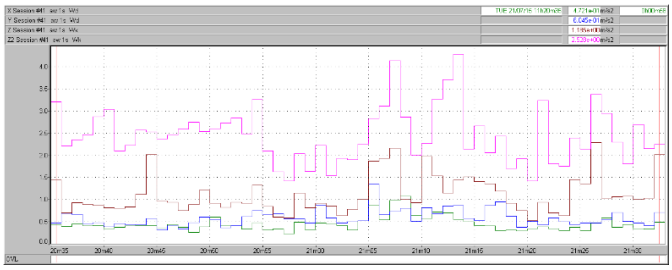

Figure 2 Mechanical seat on gravel surface

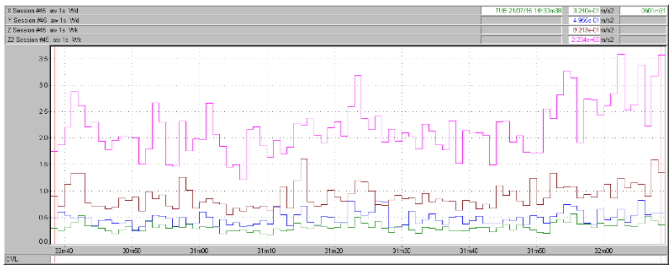

Figure 3 Pneumatic seat – M1 on gravel surface

Figures 2 and 3 show the time histories of acceleration signals recorded on the mechanical seat and the pneumatic seat from Manufacturer 1 (M1) during vehicle operation on a gravel surface at a speed of 20 km/h. The signals are presented using different colors and correspond to the acceleration components in the x, y, and z directions, as well as the calculated RMS acceleration value.

It can be observed that the pneumatic seat exhibits lower vibration amplitudes in all three measurement directions compared with the mechanical seat, indicating more effective vibration attenuation and lower RMS acceleration values.

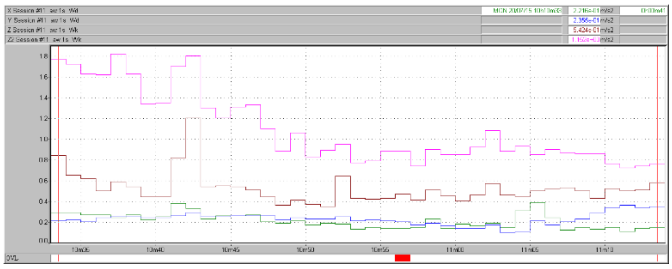

Figure 4 Pneumatic seat – M1 on asphalt surface

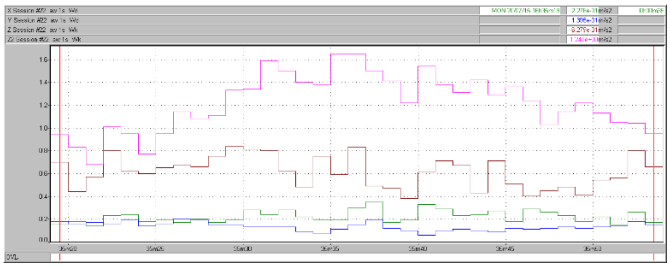

Figure 5 Pneumatic seat – M2 on asphalt surface

Figures 4 and 5 show the time histories of acceleration signals recorded on the pneumatic seat from Manufacturer 1 and the pneumatic seat from Manufacturer 2 (M2) during vehicle operation on an asphalt surface at a speed of 80 km/h. The signals are presented using different colors and correspond to the acceleration components in the x, y, and z directions, as well as the calculated RMS acceleration value.

A comparison of the presented signals reveals differences in the vibration levels between the investigated seats, indicating different vibration attenuation efficiencies of their suspension systems under driving conditions on an asphalt surface.

Comparison of RMS acceleration values for different seats

Figures 6 and 7 show the variation of RMS acceleration with respect to seat type under different road surface conditions (gravel and asphalt) and vehicle speeds.

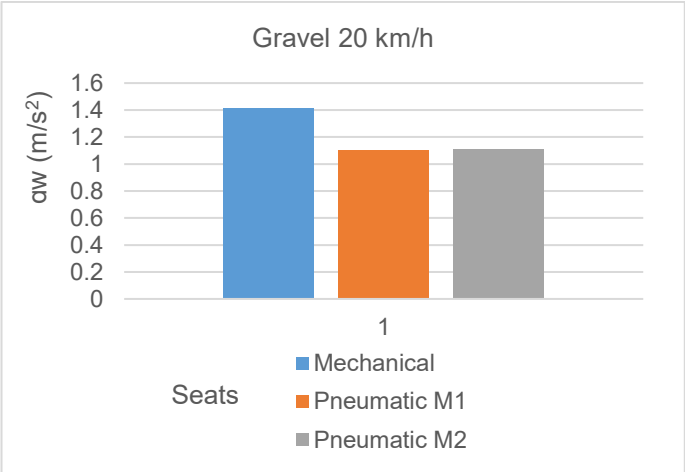

Figure 6 RMS acceleration for different seat types on a gravel surface

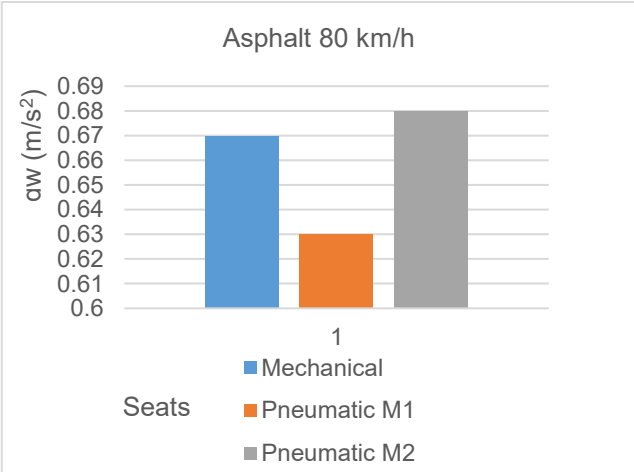

Figure 7 RMS acceleration for different seat types on an asphalt surface

It can be observed that, compared with the mechanical seat, the pneumatic seats generally achieved lower RMS acceleration values, indicating more effective attenuation of vibrations transmitted to the driver. The lowest RMS values were recorded for the pneumatic seat from Manufacturer 1 during vehicle operation on the gravel surface, indicating its highest effectiveness under conditions with pronounced surface irregularities. On the other hand, a deviation from this trend was observed for the seat from Manufacturer 2 on the asphalt surface. Namely, the pneumatic seat from Manufacturer 2 exhibited a higher RMS acceleration value compared with the mechanical seat, indicating that its advantages are not equally pronounced during driving on surfaces with lower vibration excitation levels.

These results indicate that the effectiveness of the seat suspension system depends not only on its design characteristics but also on the properties of the surface over which the vehicle is operated.

Effect of road surface conditions

Figure 8 presents the variation of RMS acceleration values for different road surface conditions and seat types.

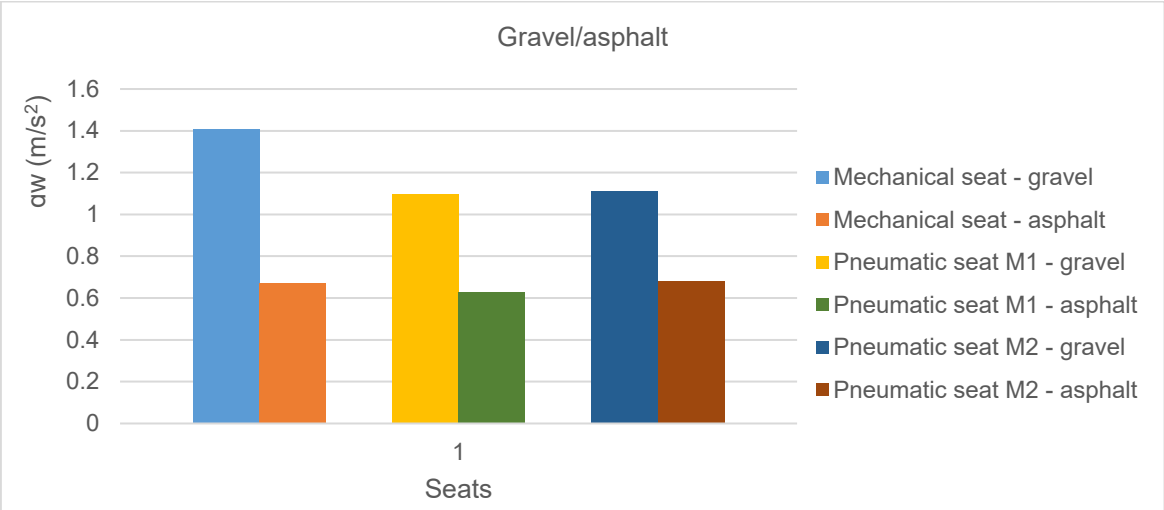

Figure 8 RMS acceleration for different seat types and road surface conditions

For each seat type, the RMS acceleration values obtained during driving on gravel and asphalt surfaces were compared. It can be observed that road surface characteristics have a significant influence on the level of vibrations transmitted to the seat. For all investigated seat types, the RMS values on the gravel surface were higher than those on the asphalt surface, which is an expected consequence of more pronounced surface irregularities and higher excitation generated by such a surface.

The mechanical seat exhibited the most pronounced difference between RMS values measured on gravel and asphalt surfaces, indicating a limited ability of this system to isolate vibrations caused by uneven road conditions. Both pneumatic seats achieved lower RMS values compared with the mechanical seat, particularly during driving on the gravel surface, where the vibration attenuation effect was most evident.

The pneumatic seat from Manufacturer 1 is particularly distinguished by achieving the lowest RMS value during driving on the gravel surface, indicating the highest vibration isolation capability under conditions of increased excitation. However, during driving on the asphalt surface, the differences between the seats were less pronounced, and the pneumatic seat from Manufacturer 2 exhibited a higher RMS value compared with the mechanical seat. This indicates that the characteristics of seat suspension systems affect vibration behavior differently under various operating conditions and that optimal performance depends on the combination of seat design and road surface type.

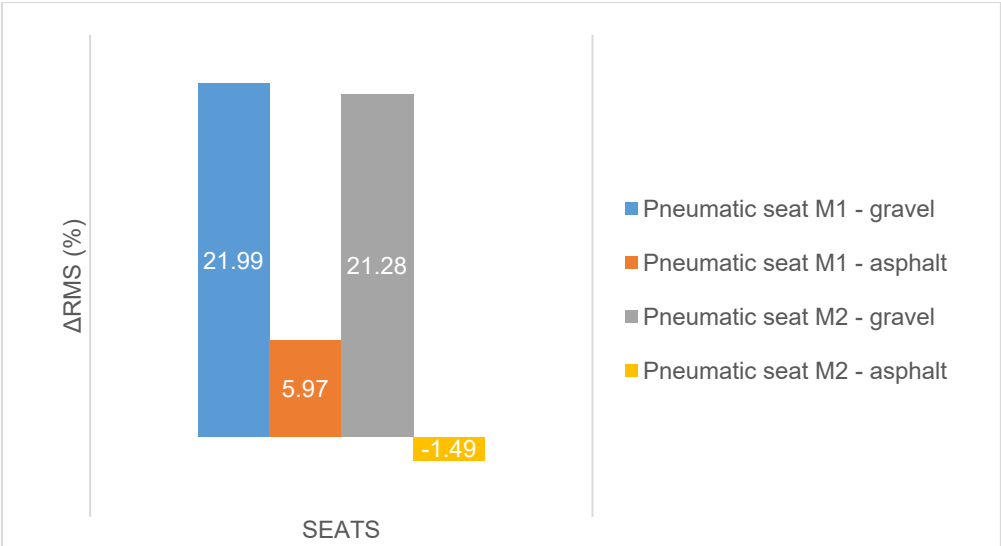

Figure 9 Percentage reduction of RMS acceleration for pneumatic seats compared with the mechanical seat on different road surfaces

Figure 9 presents the percentage differences in RMS acceleration values of the pneumatic seats compared with the mechanical seat. The negative value clearly indicates the case of the pneumatic seat from Manufacturer 2 on the asphalt surface, which exhibited a higher RMS acceleration value than the mechanical seat.

Evaluation of vibration exposure based on the ISO 2631 standard

The driver's vibration exposure level was assessed by comparing the obtained RMS values with the criteria specified in the ISO 2631 standard (Table 3).

Table 3 Comparison of RMS acceleration values with ISO 2631 comfort criteria

Condition	RMS (m/s^2)	ISO 2631 criteria	Reduction (%)
Gravel – Mechanical seat	1.41	Very uncomfortable	/
Gravel – Pneumatic seat M1	1.10	Uncomfortable	21,99
Gravel – Pneumatic seat M2	1.11	Uncomfortable	21.28
Asphalt – Mechanical seat	0.67	Fairly uncomfortable	/
Asphalt – Pneumatic seat M1	0.63	A little uncomfortable	5.97
Asphalt – Pneumatic seat M2	0.68	Fairly uncomfortable	-1.49

Under the guidelines of the ISO 2631 standard, an increase in RMS acceleration values indicates reduced comfort and heightened vibration exposure for the driver. The obtained results show that lower RMS values were recorded during driving on the asphalt surface compared with the gravel surface; however, all analyzed cases corresponded to the “fairly uncomfortable” level based on these criteria.

Significantly higher RMS values were recorded on the gravel surface, indicating a higher vibration load on the driver. The highest value was measured for the mechanical seat, while both pneumatic seats achieved lower RMS values, confirming their higher effectiveness in vibration attenuation under more demanding operating conditions.

During driving on the asphalt surface, the differences between the investigated seats were considerably less pronounced. The pneumatic seat from Manufacturer 1 achieved the lowest RMS value, while the RMS value recorded for the seat from Manufacturer 2 was approximately equal to, or slightly higher than, that of the mechanical seat. These results indicate that the effect of applying a pneumatic seat suspension system depends not only on the operating principle of the seat but also on its design characteristics and operating conditions.

CONCLUSIONS

This paper presents an experimental analysis of whole-body vibrations to which a truck driver is exposed when using different seat design solutions and under various operating conditions. The study included a comparison of a mechanical seat and pneumatic seats during vehicle operation on asphalt and gravel surfaces. Based on the measured acceleration signals, the main vibration parameters were determined and analyzed, with particular emphasis on RMS acceleration values.

The obtained results confirm that road surface characteristics represent one of the dominant factors influencing the level of vibrations transmitted to the driver. Driving on a gravel surface resulted in significantly higher vibration acceleration levels compared with asphalt, as a consequence of more pronounced surface irregularities, higher dynamic excitation, and less favorable vibration transmission conditions through the vehicle–seat–driver system.

The analysis of the influence of seat design showed that pneumatic seats generally demonstrated improved vibration attenuation performance compared with the conventional mechanical seat under the tested conditions. The lower RMS acceleration values recorded for pneumatic seats indicate a higher vibration isolation capability and a reduction in the vibration exposure transmitted to the driver. Compared with the mechanical seat, the pneumatic seat from Manufacturer 1 achieved an RMS acceleration reduction of approximately 22%, while the pneumatic seat from Manufacturer 2 achieved a reduction of approximately 21%. These differences were observed on the gravel surface, where the effect of the seat suspension system was most pronounced.

The comparison of different seat types indicates that the design characteristics of the suspension system have a significant influence on vibration transmission at the driver–vehicle contact interface. The application of pneumatic seat suspension systems can contribute to reducing whole-body vibration exposure and improving driver comfort, particularly in vehicles operating under variable and demanding conditions.

Based on the conducted research, it can be concluded that the selection of an appropriate seat suspension system represents an important factor in improving the driver's working environment in heavy-duty vehicles. The obtained results provide a basis for further investigations focused on detailed frequency-domain analysis of vibration signals, determination of transfer characteristics of the vehicle–seat–driver system, and development of advanced approaches for vibration exposure assessment under real operating conditions.

REFERENCES

Dennerlein, J. T., Cavallari, J. M., Kim, J. H., & Green, N. H. (2022). The effects of a new seat suspension system on whole body vibration exposure and driver low back pain and disability: Results from a randomized controlled trial in truck drivers. *Applied Ergonomics*, 98, Article 103588. https://doi.org/10.1016/j.apergo.2021.103588

European Parliament & Council. (2002). Directive 2002/44/EC of the European Parliament and of the Council of 25 June 2002 on the minimum health and safety requirements regarding the exposure of workers to the risks arising from physical agents (vibrations). Official Journal of the European Communities, OJ L 177, 13–19.

International Organization for Standardization. (1997). Mechanical vibration and shock – Evaluation of human exposure to whole-body vibration – Part 1: General requirements (ISO Standard No. 2631-1:1997). iso.org

Jovanović, B. S., & Djurić, S. A. (2009). Analysis of the adverse effects of vibration on crew in Serbian Armed Forces transport vehicles. Military Technical Courier, 9(4), 93–107. DOI:10.5937/vojtehg0904093J.

Kat, C.-J., Jooste, J. S., Grant, C. C., Becker, P. J., & Els, P. S. (2021). Cardiovascular response to whole-body vibration on an automobile seat. *Ergonomics*, 64(11), 1405–1415. https://doi.org/10.5937/vojtehg0904093J

Kia, K., Johnson, P. W., & Kim, J. H. (2021). The effects of different seat suspension types on occupants' physiologic responses and task performance: Implications for autonomous and conventional vehicles. Applied Ergonomics, 93, Article 103380. DOI:10.1016/j.apergo.2021.103380.

Sekulić, D., Dedović, V., Rusov, S., & Obradović, A. (2016). Definition and determination of the bus oscillatory comfort zones. *International Journal of Industrial Ergonomics*, 53, 328–339. https://doi.org/10.1016/j.ergon.2016.04.003

Sekulić, D., Dedović, V., Rusov, S., Šelmić, M., & Obradović, A. (2013). Analysis of vibration effects on the comfort of intercity bus users by oscillatory model with ten degrees of freedom. *Applied Mathematical Modelling*, 37(18), 8629–8644. https://doi.org/10.1016/j.apm.2013.03.060

Zhou, Z., & Griffin, M. J. (2014). Response of the seated human body to whole-body vertical vibration: Biodynamic responses to sinusoidal and random vibration. *Ergonomics*, 57(5), 693–713. https://doi.org/10.1080/00140139.2014.898798

The 11th International Congress
Motor Vehicles & Motors 2026
Kragujevac, Serbia
October 8th - 9th, 2026

Motor Vehicles & Motors

MVM2026-063
https://doi.org/10.24874/CMVM2026.063
Original scientific paper

Slavica Mačužić Saveljić[1]
Ognjen Matić[2]
Igor Saveljić[3]

MACHINE LEARNING-BASED PREDICTION AND EXPLAINABILITY OF DRIVER DISCOMFORT AND FATIGUE: A DATA-DRIVEN EXTENSION OF A RAMSIS-BASED DIGITAL HUMAN MODEL STUDY

ABSTRACT: Driver comfort and fatigue depend on a complex interaction between seat geometry, backrest angle and driver anthropometry, traditionally assessed with digital human models such as RAMSIS. An earlier study evaluated discomfort and fatigue of eleven anthropometrically diverse populations (1% female and 99% male percentiles) in a lower-medium-class vehicle for backrest angles between 80° and 105°. This paper extends that dataset with a machine-learning layer: four regression algorithms (linear regression, Random Forest, Gradient Boosting, Gaussian Process) predict overall discomfort and fatigue, plus eight body-part scores, from backrest angle, driving/resting condition and four anthropometric variables. Using population-grouped cross-validation, tree-based models explain 66-73% of variance, outperforming a linear baseline (57-61%), indicating a non-linear relationship. SHAP analysis quantifies variable contributions: backrest angle (43-50%) and shoulder breadth (22-29%) dominate, while condition contributes comparatively little to tree-based importance despite a consistent offset in raw data. A classifier separating comfortable from uncomfortable postures reaches AUC=0.90. An inverse optimisation procedure recommends backrest angles minimising predicted discomfort. Results show ML surrogates can reproduce and explain RAMSIS-based trends, but given the limited training data, models are best viewed as proof-of-concept, requiring further validation before design deployment.

KEYWORDS: driver discomfort, fatigue, digital human modelling, RAMSIS, machine learning

[1] *Slavica Mačužić Saveljić, University of Kragujevac, Faculty of Engineering, 6 Sestre Janjić Str., 34000 Kragujevac, Serbia, s.macuzic@kg.ac.rs, https://orcid.org/0000-0003-2635-2496*
[2] *Ognjen Matić, University of Kragujevac, Faculty of Engineering, 6 Sestre Janjić Str., 34000 Kragujevac, Serbia, ognjenmatic95@gmail.com, https://orcid.org/0009-0009-6697-029X*
[3] *Igor Saveljić, Institute for Information Technologies, University of Kragujevac, bb Jovana Cvijića Str., 34000 Kragujevac, Serbia, isaveljic@kg.ac.rs, https://orcid.org/0000-0002-0707-5174*

PREDVIĐANJE I OBJAŠNJIVOST NELAGODNOSTI I ZAMORA VOZAČA PRIMENOM MAŠINSKOG UČENJA: PROŠIRENJE STUDIJE DIGITALNOG MODELA ČOVEKA ZASNOVANE NA SISTEMU RAMSIS

REZIME: Udobnost i zamor vozača zavise od složene interakcije između geometrije sedišta, ugla naslona i antropometrijskih karakteristika vozača, koje se tradicionalno procenjuju primenom digitalnih modela čoveka, kao što je RAMSIS. U prethodnoj studiji analizirani su nelagodnost i zamor jedanaest antropometrijski različitih populacija (1. percentil žena i 99. percentil muškaraca) u putničkom vozilu niže srednje klase pri uglovima naslona sedišta od 80° do 105°. U ovom radu taj skup podataka je proširen primenom metoda mašinskog učenja. Četiri regresiona algoritma (linearna regresija, Random Forest, Gradient Boosting i Gaussian Process) korišćena su za predviđanje ukupne nelagodnosti i zamora, kao i ocena za osam delova tela, na osnovu ugla naslona, režima vožnje (vožnja/odmor) i četiri antropometrijske promenljive. Primenom unakrsne validacije grupisane po populacijama, modeli zasnovani na stablima odluke objasnili su 66–73% varijanse, nadmašivši linearnu regresiju (57–61%), što ukazuje na nelinearnu povezanost između ulaznih i izlaznih promenljivih. SHAP analiza pokazala je da najveći uticaj na predikciju imaju ugao naslona (43–50%) i širina ramena (22–29%), dok režim vožnje, uprkos doslednoj razlici u izvornim podacima, relativno malo doprinosi značaju promenljivih u modelima zasnovanim na stablima. Klasifikator za razlikovanje udobnih i neudobnih položaja tela ostvario je vrednost AUC = 0,90. Takođe je razvijen postupak inverzne optimizacije kojim se određuje ugao naslona koji minimizuje predviđenu nelagodnost. Dobijeni rezultati pokazuju da modeli mašinskog učenja mogu uspešno reprodukovati i objasniti trendove dobijene primenom sistema RAMSIS. Međutim, zbog ograničenog skupa podataka za obučavanje, razvijene modele treba posmatrati kao dokaz koncepta, čija je dalja validacija neophodna pre primene u procesu projektovanja.

KLJUČNE REČI: nelagodnost vozača, zamor vozača, digitalno modelovanje čoveka, RAMSIS, mašinsko učenje

INTRODUCTION

Driver comfort is one of the central design objectives of the automotive industry, since posture, seat geometry and long-term exposure to an unsuitable driving position are known to affect both wellbeing and performance behind the wheel, as Looze et al. (2003) and Helander and Zhang (1997) have shown. Ergonomic evaluation of a vehicle interior has traditionally relied on physical mock-ups and human subject trials; however, digital human models (DHM), such as RAMSIS (Rechnergestütztes Anthropometrisches Mathematisches System zur Insassen-Simulation), integrated with CAD packages such as CATIA V5, now allow discomfort and fatigue to be estimated computationally for a wide range of body sizes and postures without building physical prototypes, as described by Duffy (2008).

In a previous study, Mačužić and Lukić (2018) used RAMSIS to evaluate the discomfort and fatigue of eleven anthropometrically distinct populations (1% female and 99% male percentiles), seated in a lower-medium-class passenger vehicle, for five seat-backrest angles (80°, 85°, 90°, 100° and 105°) in both driving and resting postures. That study reported that discomfort increases with backrest angle beyond 90°, that the 1% female population consistently experiences higher discomfort than the 99% male population, and that the neck is the body part most affected by fatigue and discomfort. The analysis reported by Mačužić and Lukić (2018), however, was purely descriptive (means, standard errors and correlation coefficients) and did not attempt to build a predictive model capable of estimating discomfort for anthropometric profiles that were not explicitly simulated in RAMSIS.

This paper extends the study of Mačužić and Lukić (2018) along two directions. First, the RAMSIS output tables recorded for four of the five original backrest angles (85°, 90°, 100° and 105°) are consolidated, together with the corresponding anthropometric input parameters (stature, sitting height, foot length and shoulder breadth), into a single structured dataset suitable for supervised learning. Second, several regression and classification algorithms are trained on this dataset to (i) predict overall discomfort and fatigue as a function of seat angle, driving condition and anthropometry, (ii) explain which of these variables drives the model's predictions using SHAP values, (iii) predict discomfort separately for each body part, (iv) classify a posture as comfortable or uncomfortable, and (v) recommend, for a given anthropometric profile, the backrest angle that minimises predicted discomfort. The intention is not to replace RAMSIS - which remains the physically grounded reference tool - but to build a fast, explainable surrogate model that can be used for rapid screening of new target populations, complementing the original descriptive-statistics approach. It should be emphasized that the present work is intended as a feasibility study, demonstrating the potential of ML-based surrogates on a limited DHM dataset, rather than a fully validated design tool.

RELATED WORK

Sitting comfort and discomfort in vehicles have been studied extensively from an ergonomic and biomechanical perspective. Comfort is generally treated as a distinct construct from discomfort, related to wellbeing and relaxation, whereas discomfort is associated with pain, fatigue and biomechanical loading, as Helander and Zhang (1997) and Looze et al. (2003) note. Posture, muscular activity, pressure distribution, and seat/backrest angle are among the most frequently studied factors, as documented by Helander and Zhang (1997), Vink (2005) and Bridger (2009). Porter and Gyi (1998) linked interface pressure distributions to subjective seat discomfort ratings, while Schmidt et al. (2014) reviewed the literature on optimum and preferred joint angles in automotive sitting posture and reported that a backrest inclination between roughly 100° and 110° to the horizontal is generally preferred, broadly consistent with the RAMSIS-based results obtained by Mačužić and Lukić (2018).

Digital human modelling tools such as RAMSIS allow this body of ergonomic knowledge, gathered from physical experiments on more than a hundred subjects, to be applied virtually to arbitrary vehicle geometries and body-size populations, as discussed by Duffy (2008). While DHM tools such as RAMSIS provide physically interpretable discomfort and fatigue indices, they require a dedicated simulation run for every new combination of vehicle interior, posture and anthropometric population, which can be time-consuming when many design variants or target markets must be screened.

Machine learning offers a complementary approach: once a sufficiently informative set of DHM simulations has been produced, a statistical model can be trained to approximate the DHM output as a function of a small number of geometric and anthropometric variables, and then be queried instantly for new combinations. Tree-based ensemble methods, in particular Random Forest, introduced by Breiman (2001), and Gradient Boosting, introduced by Friedman (2001), are well suited to this task because they can capture non-linear interactions between variables without requiring an assumed functional form, and remain tractable with the relatively small sample sizes typical of DHM-based ergonomic studies. Gaussian Process regression, as formulated by Rasmussen and Williams (2006), provides an alternative, probabilistic formulation that additionally yields a predictive uncertainty estimate. To interpret the resulting non-linear models - which, unlike a linear regression, do not offer directly readable coefficients - SHAP (SHapley Additive exPlanations) values, introduced by Lundberg and Lee (2017), provide a game-theoretically grounded way of attributing each prediction to the contribution of individual input variables, both globally (which variables matter overall) and locally (why a specific case was predicted the way it was). All models in this study were implemented using the scikit-learn library described by Pedregosa et al. (2011).

METHODOLOGY

Dataset construction

The RAMSIS output tables recorded in the original study by Mačužić and Lukić (2018) for backrest angles of 85°, 90°, 100° and 105° were digitised and merged into a single long-format dataset (the 80° angle reported by Mačužić and Lukić (2018) was not available in a re-usable tabulated form and is therefore not included in the present analysis). Two anthropometric extremes were originally simulated: a 1% female percentile and a 99% male percentile population, for eleven regional populations (West Africa, North India, Eastern Europe, North Europe, Australia, South East Europe, Central Europe, South East Africa, Middle East, South India and North Asia). For the 85° and 90° backrest angles only the 99% male results were available in tabulated form, whereas both the 1% female and 99% male results were available for the 100° and 105° angles. This yields 132 individual records (88 at 100°/105° combining both percentile groups, and 44 at 85°/90° for the male percentile group only), each described by:

- Seat-backrest angle (85°, 90°, 100° or 105°);
- Posture/condition (driving or resting);
- Four anthropometric variables taken from the percentile input table of Mačužić and Lukić (2018): stature, sitting height, foot length and shoulder (biacromial) breadth;
- Overall RAMSIS Fatigue and Discomfort scores, and eight body-part discomfort scores (neck, shoulders, back, buttocks, left/right leg, left/right arm).

This asymmetric coverage (full male+female data at two angles, male-only at the other two) is an acknowledged limitation of the present dataset and is revisited in Section Discusion.

Predictive models

Four regression algorithms were trained to predict overall Fatigue and Discomfort from the six input variables described above (angle, condition, stature, sitting height, foot length, shoulder breadth): (i) ordinary linear regression, used as a baseline; (ii) Random Forest regression with 400 trees and a maximum depth of 5, following Breiman

(2001); (iii) Gradient Boosting regression with 300 estimators, a maximum depth of 2 and a learning rate of 0.05, following Friedman (2001); and (iv) Gaussian Process regression with a combined radial-basis-function and white-noise kernel on standardised inputs, following Rasmussen and Williams (2006).

Because several rows in the dataset originate from the same regional population (differing only in angle or condition), a conventional random k-fold cross-validation would allow the model to see other records from the same body-size profile during training, which would overestimate its ability to generalise to a genuinely new target population. To obtain an honest estimate of generalisation, models were instead evaluated with a Group K-Fold cross-validation scheme (11 folds, one per regional population), in which all records belonging to a given population are held out together during validation. This directly emulates the intended use case: predicting discomfort/fatigue for an anthropometric profile that has not been explicitly simulated in RAMSIS.

Model explainability (SHAP)

To interpret the non-linear Random Forest model, SHAP values, as proposed by Lundberg and Lee (2017), were computed using the tree-specific SHAP explainer. Global feature importance was summarised with SHAP summary plots, and the marginal effect of the two most influential variables (backrest angle and shoulder breadth) was visualised with SHAP dependence plots. Gini-based feature importances from the Random Forest were computed in parallel as a cross-check.

Body-part-specific models

In addition to the overall Discomfort and Fatigue indices, the RAMSIS output includes discomfort scores for eight individual body parts (neck, shoulders, back, buttocks, left/right leg, left/right arm). A separate Random Forest model (identical configuration to Section Predictive models) was trained and evaluated (Group K-Fold by population) for each body part, to determine which regions of the body are best explained by the available anthropometric and posture variables.

Comfort classification

Following the discomfort threshold reported in the RAMSIS assessment scale and used descriptively by Mačužić and Lukić (2018) (a discomfort value above 5.5 corresponds to a markedly uncomfortable posture), a binary classification target was defined ("uncomfortable" = Discomfort > 5.5). A Random Forest classifier (same configuration as the regressor, with balanced class weights) was trained on the six input variables and evaluated with the same Group K-Fold-by-population scheme, reporting the area under the ROC curve (AUC) and the confusion matrix.

Inverse seat-angle optimisation

Finally, the trained Random Forest regressor was used in an inverse mode: for a fixed anthropometric profile and posture condition, predicted Discomfort/Fatigue was evaluated over a fine grid of backrest angles (85° to 105°, 1° steps), and the angle minimising the predicted score was identified. This is illustrated for a representative intermediate anthropometric profile (stature 1650 mm, sitting height 880 mm, foot length 250 mm, shoulder breadth 400 mm), chosen to fall between the eleven extreme percentile populations used for training. In practical use, this profile should be replaced with the actual percentile data of the target population under investigation.

RESULTS

Model comparison

Table 1 summarises the Group K-Fold cross-validation performance of the four regression models for overall Fatigue and Discomfort. For both targets, the tree-based ensembles (Random Forest, Gradient Boosting) clearly outperform the linear baseline, improving R^2 from 0.57 to 0.66 for Fatigue, and from 0.61 to 0.72-0.73 for Discomfort. Gaussian Process regression performs between the linear and tree-based models. This confirms that the relationship between backrest angle, anthropometry and perceived discomfort/fatigue is meaningfully non-linear, and justifies the use of a non-linear surrogate model rather than a simple regression equation.

Table 1 Group K-Fold (by population) cross-validation performance of the four regression models

Model	Target	R^2	MAE	RMSE
Linear regression	Fatigue	0.567	0.615	0.837
Random Forest	Fatigue	0.663	0.489	0.738

Table 1 (continuation)

Model	Target	R^2	MAE	RMSE
Gradient Boosting	Fatigue	0.662	0.502	0.739
Gaussian Process	Fatigue	0.596	0.511	0.808
Linear regression	Discomfort	0.612	0.770	0.969
Random Forest	Discomfort	0.719	0.573	0.825
Gradient Boosting	Discomfort	0.726	0.596	0.814
Gaussian Process	Discomfort	0.704	0.575	0.847

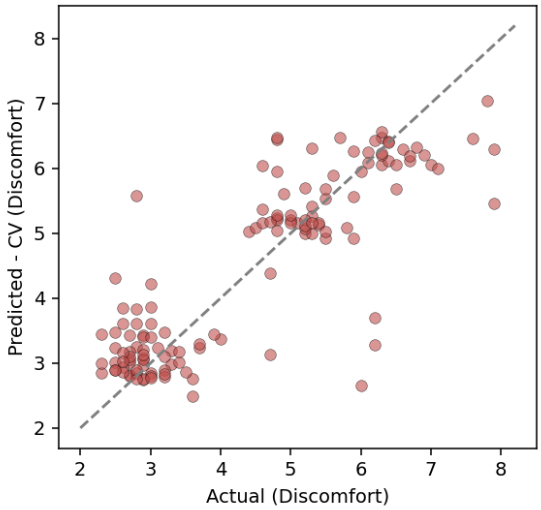

Figure 1 Predicted (Group K-Fold cross-validated) vs. actual Discomfort score, Random Forest model

Feature importance and explainability

Table 2 reports the Random Forest (Gini-based) feature importances for both targets, confirming that backrest angle and shoulder breadth are, by a substantial margin, the two most influential variables, together accounting for roughly 70-75% of total importance. Foot length and stature contribute secondary, comparable shares (8-11% each), while sitting height and the driving/resting condition contribute the least.

Table 2 Random Forest feature importance (Gini) for Fatigue and Discomfort

Feature	Importance - Fatigue	Importance - Discomfort
Backrest angle	0.426	0.496
Shoulder breadth	0.292	0.225
Foot length	0.107	0.086
Stature (height)	0.097	0.080
Condition (driving/resting)	0.044	0.075
Sitting height	0.034	0.038

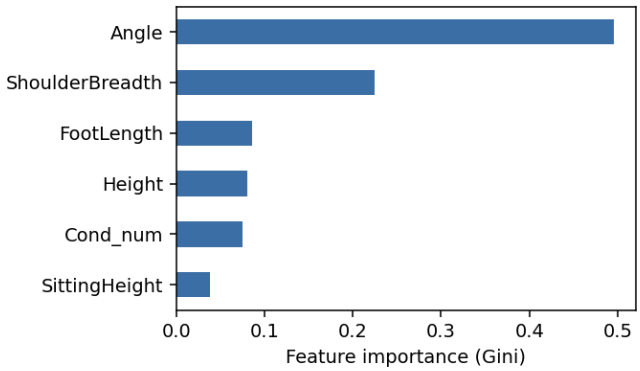

Figure 2 Feature importance for the Discomfort model

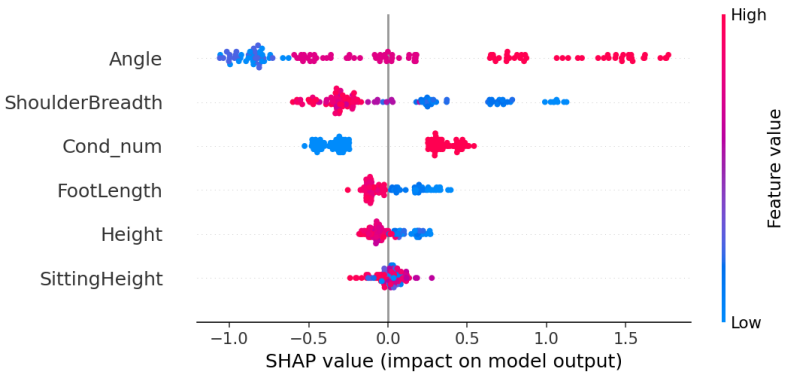

Figure 3 SHAP summary plot for the Discomfort model. Each point is one record; colour encodes the feature value (red = high, blue = low), and horizontal position shows the impact on the predicted discomfort score

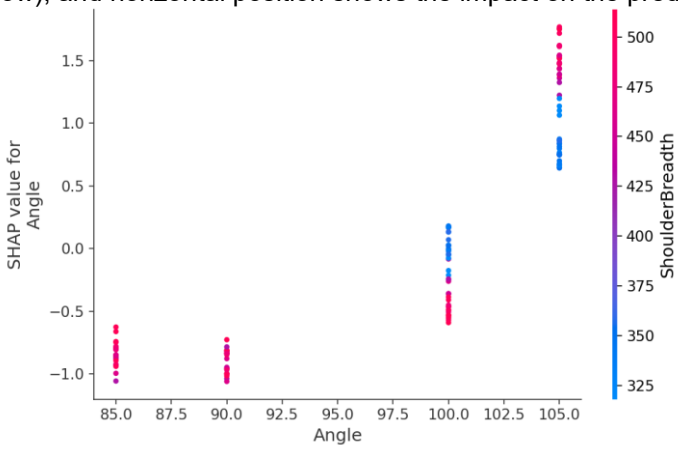

Figure 4 SHAP dependence plot: contribution of backrest angle to predicted Discomfort. The sharp increase beyond approximately 95-100° is consistent with the increase in discomfort reported descriptively by Mačužić and Lukić (2018) for the 105° condition

It is worth noting an apparent discrepancy between the low Gini/SHAP importance of the driving/resting condition and the fact that the original descriptive analysis by Mačužić and Lukić (2018) found driving posture to be consistently more uncomfortable than resting posture for every population and angle. This is not a contradiction: the condition variable produces a fairly constant additive offset (typically 1-2 discomfort points) across the whole range of angles and body sizes, whereas tree-based importance measures reward variables that produce large, non-linear changes in the split structure of the trees. A variable can therefore have a systematic, practically significant effect while still contributing a comparatively small share of a tree ensemble's internal importance metric - a useful methodological caveat for readers applying SHAP/Gini importance to ergonomic datasets.

Body-part-specific models

Table 3 and Figure 5 show the Group K-Fold R^2 obtained per body part. The back (R^2 = 0.805) and buttocks (R^2 = 0.725) are the best-predicted regions, which is consistent with their direct, relatively simple mechanical coupling to the backrest angle. The neck and arms occupy an intermediate position (R^2 = 0.66-0.68), while the shoulders are the least well predicted (R^2 = 0.560), suggesting that shoulder discomfort depends on additional factors not captured by the four anthropometric variables used here (e.g., arm/steering-wheel interaction, which was not separately parameterised in this dataset).

Table 3 Group K-Fold cross-validation R^2 and MAE per body part (Random Forest)

Body part	**R^2**	**MAE**
Back	0.805	0.318
Buttocks	0.725	0.448
Neck	0.680	0.569
Right arm	0.660	0.435
Left arm	0.660	0.435
Right leg	0.622	0.279
Left leg	0.605	0.286
Shoulders	0.560	0.459

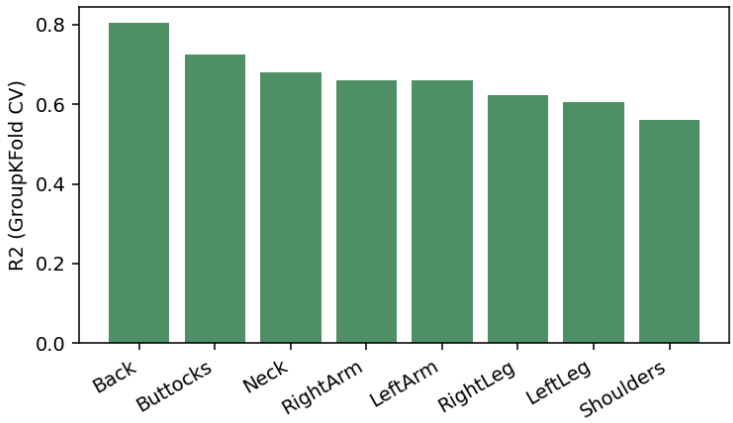

Figure 5 Prediction accuracy (R^2) per body part

Comfort classification

The Random Forest classifier separating comfortable from uncomfortable postures (Discomfort > 5.5) achieved an area under the ROC curve of 0.899 under Group K-Fold-by-population validation. The corresponding confusion matrix (Table 4) shows 83 true negatives, 15 false positives, 9 false negatives and 25 true positives, corresponding to a sensitivity (recall for the uncomfortable class) of 0.735 and a specificity of 0.847. Given that only 26% of the records in the dataset are labelled uncomfortable, an AUC of 0.90 indicates that the model discriminates well between the two classes even though it was never trained or validated on the target population itself.

Table 4 Confusion matrix for the comfort/discomfort classifier (Group K-Fold CV), AUC = 0.899

	Predicted: comfortable	**Predicted: uncomfortable**
Actual: comfortable	83	15
Actual: uncomfortable	9	25

Inverse seat-angle optimisation

Figure 6 shows the predicted Discomfort score as a function of backrest angle, for the representative intermediate anthropometric profile described in Section Inverse seat-angle optimisation, in the driving condition. For this particular profile, the model predicts a monotonic increase in discomfort with angle, from approximately 3.4 at 85-87° up to 5.7 at 103-105°, without reproducing the local optimum near 90° that was reported descriptively by Mačužić and Lukić (2018) for some of the extreme percentile populations. Two explanations are plausible: first, the chosen illustrative anthropometric profile lies between the eleven extreme populations used for training, i.e. in a region the model must interpolate rather than having observed directly; second, with only four discrete angles (85°, 90°, 100°, 105°) available for training, the Random Forest can only produce a piecewise-constant approximation of the angle-discomfort relationship, visible as flat plateaus in Figure 6, which limits its ability to resolve a narrow optimum. Both point to a concrete, actionable next step: training the model on a finer angle resolution (e.g. every 5°) and on real target-population anthropometric data, rather than an interpolated illustrative profile, before using this tool for design recommendations.

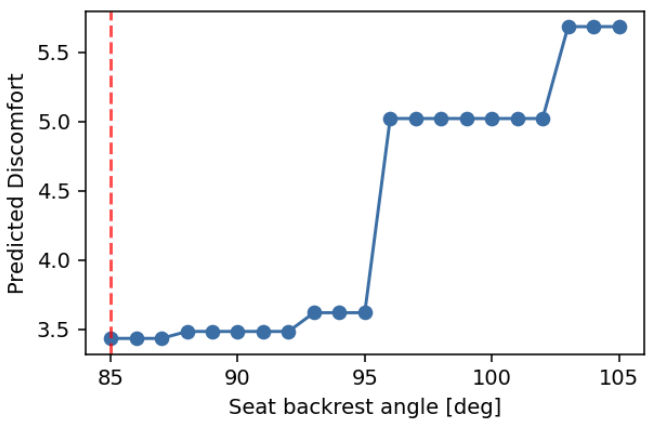

Figure 6 Predicted Discomfort vs. backrest angle for a representative intermediate anthropometric profile (driving condition); dashed line marks the predicted optimum

DISCUSSION

The results confirm, using an independent, cross-validated modelling approach, several qualitative findings of the original descriptive study by Mačužić and Lukić (2018): discomfort increases with backrest angle beyond roughly 90-100°, and body size (specifically, shoulder breadth) is a first-order determinant of discomfort alongside angle. Beyond confirmation, the ML layer adds three concrete capabilities that the original descriptive analysis did not provide: (i) a quantitative ranking of which variables matter and by how much (Section Feature importance and explainability), (ii) a classifier that flags a given angle/anthropometry combination as likely comfortable or uncomfortable without requiring a new RAMSIS run (Section Comfort classification), and (iii) a prototype inverse-optimisation tool that scans candidate backrest angles for a target population (Section Inverse seat-angle optimisation). Collectively, these capabilities establish the feasibility of using ML surrogates in this context; however, the current implementation should be viewed as a proof-of-concept, and its practical application would require further validation against a broader and more balanced anthropometric database.

The study has several limitations that should be addressed before the surrogate model is used for design decisions. First, the dataset comprises only 132 records derived from eleven regional populations and four backrest angles, with an asymmetric male/female coverage across angles (Section Dataset construction); this restricts both statistical power and the angular resolution of the model, as illustrated in Section Inverse seat-angle optimisation. Second, the anthropometric input is limited to four variables (stature, sitting height, foot length, shoulder breadth); other variables known to influence sitting posture (e.g. weight, limb segment lengths, age) were not available in the digitised RAMSIS tables and could not be included. Third, the RAMSIS discomfort/fatigue scores are themselves model-based estimates rather than measurements from real drivers, so the ML surrogate inherits any systematic bias of the underlying RAMSIS model. Finally, the illustrative inverse-optimisation example in Section Inverse seat-angle optimisation uses an interpolated anthropometric profile rather than a real target population and should be treated as a methodological demonstration rather than a design recommendation.

CONCLUSIONS

This paper extended a previous RAMSIS-based descriptive study of driver discomfort and fatigue by Mačužić and Lukić (2018) with a machine-learning layer trained on the same underlying simulation data. The main findings are:

- Tree-based ensemble models (Random Forest, Gradient Boosting) explain 66-73% of the variance in Discomfort and Fatigue scores under population-grouped cross-validation, clearly outperforming a linear baseline (57-61%), confirming a non-linear relationship between backrest angle, anthropometry and perceived discomfort.
- SHAP and Gini-based feature importance show that backrest angle and shoulder breadth jointly account for 70-75% of the predictive signal, while driving/resting condition, despite a real and consistent effect, contributes a comparatively small share of tree-based importance.
- Body-part-specific models predict back and buttocks discomfort most accurately ($R^2 > 0.72$) and shoulder discomfort least accurately ($R^2 = 0.56$), pointing to additional, unmeasured factors affecting shoulder loading.
- A Random Forest classifier separating comfortable from uncomfortable postures reaches an AUC of 0.90, demonstrating that a simple, fast classifier can flag problematic angle/anthropometry combinations without a new RAMSIS simulation.
- An inverse seat-angle optimisation prototype was demonstrated; its current angular resolution and reliance on an interpolated anthropometric profile are identified as concrete targets for improvement.

Future work should extend the digitised dataset to the full 80-105° angular range at finer resolution, incorporate additional anthropometric variables (e.g., weight, arm length) and real target-population data, and validate the surrogate model's predictions against real driver comfort surveys, alongside the RAMSIS digital human model that remains the physically grounded reference tool. Until such validation is performed, the present models are best used as an exploratory screening aid rather than a definitive design tool.

ACKNOWLEDGMENTS

This research was supported by the Ministry of Education, Science and Technological Development of the Republic of Serbia through Projects TR35041 (Faculty of engineering, University of Kragujevac) and 451-03-33/2026-03/200378 (Institute for Information Technologies, University of Kragujevac).

REFERENCES

Breiman, L. (2001). Random forests. *Machine Learning, 45*(1), 5–32. https://doi.org/10.1023/A:1010933404324

Bridger, R. S. (2009). *Introduction to ergonomics* (3rd ed.). Taylor & Francis. https://doi.org/10.1201/9781439894927

Duffy, V. G. (2008). *Handbook of digital human modeling: Research for applied ergonomics and human factors engineering*. CRC Press. https://doi.org/10.1201/9781420063523

Friedman, J. H. (2001). Greedy function approximation: A gradient boosting machine. *The Annals of Statistics, 29*(5), 1189–1232. https://doi.org/10.1214/aos/1013203451

Helander, M. G., & Zhang, L. (1997). Field studies of comfort and discomfort in sitting. *Ergonomics, 40*(9), 895–915. https://doi.org/10.1080/001401397187739

Looze, M. P. de, Kuijt-Evers, L. F. M., & van Dieën, J. (2003). Sitting comfort and discomfort and the relationships with objective measures. *Ergonomics, 46*(10), 985–997. https://doi.org/10.1080/0014013031000121977

Lundberg, S. M., & Lee, S.-I. (2017, December 4-9). A unified approach to interpreting model predictions. In *31st Conference on Neural Information Processing Systems (NIPS 2017)*, Long Beach, CA, USA. https://arxiv.org/pdf/1705.07874

Mačužić, S., & Lukić, J. (2018). Assessment of the human body discomfort in the vehicle. In *Proceedings of the International 9th Automotive Technologies Congress (OTEKON 2018),* Bursa, Türkiye. https://www.otekon.org/2018/index.asp?p=Bilimsel-Program

Pedregosa, F., Varoquaux, G., Gramfort, A., Michel, V., Thirion, B., Grisel, O., Blondel, M., Prettenhofer, P., Weiss, R., Dubourg, V., Vanderplas, J., Passos, A., Cournapeau, D., Brucher, M., Perrot, M., & Duchesnay, É. (2011). Scikit-learn: Machine learning in Python. *Journal of Machine Learning Research, 12*, 2825–2830.

Porter, J. M., & Gyi, D. E. (1998). Exploring the optimum posture for driver comfort. *International Journal of Vehicle Design, 19*(3), 255–266.

Rasmussen, C. E., & Williams, C. K. I. (2006). *Gaussian processes for machine learning*. MIT Press. https://doi.org/10.7551/mitpress/3206.001.0001

Schmidt, S., Amereller, M., Franz, M., Kaiser, R., & Schwirtz, A. (2014). A literature review on optimum and preferred joint angles in automotive sitting posture. *Applied Ergonomics, 45*(2, Pt. B), 247–260. https://doi.org/10.1016/j.apergo.2013.04.009

Vink, P. (Ed.). (2005). *Comfort and design: Principles and good practice*. CRC Press. https://doi.org/10.1201/9781420038132

The 11th International Congress
Motor Vehicles & Motors 2026
Kragujevac, Serbia
October 8th - 9th, 2026

Motor Vehicles & Motors

MVM2026-072
https://doi.org/10.24874/CMVM2026.072
Original scientific paper

Jovanka Lukić[1]
Jasna Glišović[2]
Danijela Miloradović[3]

COMPONENT COHERENCE-BASED ASSESSMENT OF MASKING EFFECTS IN TWO-DIRECTIONAL WHOLE-BODY VIBRATION

ABSTRACT: Masking of fore-and-aft whole-body vibration by simultaneous vertical excitation was investigated using component coherence analysis. The aim was to determine whether combined fore-and-aft and vertical excitation could be interpreted as a superposition of independent components or whether coupling between the excitation directions affected the head response. Experiments were conducted under six conditions combining three excitation levels (L_1–L_3) and two seat-backrest angles (A_1–A_2). Head acceleration was measured in the fore-and-aft (X_h) and vertical (Z_h) directions. Component coherence (C_{ptC}) together with total component coherence (C_{total}) and cancellation were used to characterize interactions between the two input directions. Because of the small sample size, non-parametric repeated-measures methods were applied. Overall differences among the six conditions were assessed using the Friedman test, followed by Wilcoxon signed-rank pairwise comparisons with Bonferroni correction. No significant overall differences were found for $X_{h\ Ctotal}$, $X_{h\ Cancellation}$, $Z_{h\ Ctotal}$, or $Z_{h\ Cancellation}$ (p = 0.6912, 0.2337, 0.5297, and 0.2761, respectively). None of the 15 pairwise comparisons remained significant after correction. The direct L_1–L_2 comparison showed a significant increase in $Z_{h\ Cancellation}$ (p = 0.03125). The coupling-related measures were relatively insensitive to the tested conditions.

KEYWORDS: whole-body vibration, masking, component coherence, cancellation, fore-and-aft vibration, vertical vibration.

[1] *Jovanka Lukić, Faculty of Engineering, University of Kragujevac, Sestre Janjić 6, Kragujevac, Serbia, lukicj@kg.ac.rs, https://orcid.org/0000-0002-5893-3976*
[2] *Jasna Glišović, Faculty of Engineering, University of Kragujevac, Sestre Janjić 6, Kragujevac, Serbia, jaca@kg.ac.rs , https://orcid.org/0000-0002-8251-1722*
[3] *Danijela Miloradović, Faculty of Engineering, University of Kragujevac, Sestre Janjić 6, Kragujevac, Serbia, neja@kg.ac.rs , https://orcid.org/0000-0003-1427-9789*

PROCENA EFEKATA MASKIRANJA PRI DVOOSNIM VIBRACIJAMA CELOG TELA NA OSNOVU KOMPONENTNE KOHERENCE

REZIME: Maskiranje vibracija celog tela pri istovremenoj pobudi u vertikalnom i napred-nazad pravcu ispitivano je analizom komponentne koherence. Cilj je bio da se utvrdi da li se dvoosna pobuda, istovremeno napred-nazad i vertikalna, može aproksimirati superpozicijom nezavisnih komponenti pobude, odnosno da li međusobna sprega između pobuda u različitim pravcima pobude utiče na odziv glave. Merenja su urađena u šest režima: tri nivoa pobude (L_1–L_3) i dva nivoa ugla naslona sedišta (A_1–A_2). Ubrzanje glave mereno je u napred-nazad (X_h) i vertikalnom (Z_h) pravcu. Komponentna koherenca (CptC), ukupna komponentna koherencija (Ctotal) i poništenje (Cancellation) korišćeni su za procenu interakcije između dva pravca pobuđivanja. Zbog malog broja ispitanika primenjene su neparametarske metode za ponovljena merenja. Razlike između šest uslova ispitane su Friedmanovim testom, nakon čega su sprovedena parna poređenja Wilcoxonovim testom uz Bonferroni korekciju. Nisu utvrđene statistički značajne ukupne razlike za $X_{hCtotal}$, $X_{hCancellation}$, $Z_{hCtotal}$ niti $Z_{hCancellation}$ (p = 0.6912, 0.2337, 0.5297 i 0.2761, redom). Nijedno od 15 poređenja parova nije ostalo statistički značajno nakon korekcije. Direktno poređenje L_1–L_2 pokazalo je statistički značajno povećanje $Z_{hCancellation}$ (p = 0.03125). Veličine koje opisuju spregu bile su relativno neosetljive na ispitivane eksperimentalne uslove. Promena $Z_{hCancellation}$ između L_1 i L_2 ukazuje da preraspodela vertikalnog odziva može zavisiti od nivoa pobude.

KLJUČNE REČI: vibracije celog tela, maskiranje, komponentna koherenca, poništenje, napred-nazad vibracije, vertikalne vibracije

INTRODUCTION

Whole-body vibration (WBV) is an important source of discomfort and fatigue in vehicle occupants. Vehicle vibration is rarely restricted to a single direction. Simultaneous excitation in the fore-and-aft, lateral, and vertical directions is frequently present. The human body responds to such multidirectional excitation through complex biomechanical mechanisms, and the response in one direction may be influenced by excitation in another direction.

The problem becomes particularly important when an excitation in one direction is used to mask or modify the perception of vibration in other direction. In the case of fore-and-aft vibration, simultaneous vertical excitation may alter both the mechanical transmission through the human body and the resulting head motion (Lukić et al., 2024). Consequently, the response measured in a given direction cannot necessarily be interpreted independently of the other excitation components.

A conventional approach to multidirectional vibration analysis is to treat the responses to individual excitation directions separately and subsequently combine them. Such an approach implicitly assumes that the contributions of the different input directions are independent or sufficiently weakly coupled. This assumption is not necessarily valid for the human body.

Coherence-based frequency-domain methods provide a means of investigating the relationship between excitation and response. Ordinary coherence describes the linear correlation between an input and an output, whereas partial coherence can be used to investigate the relationship between one input and the output, while statistically accounting for the effect of another input. In a two-input system, this distinction is important because the two excitation signals may themselves be correlated. (Howes et al., 2025)

In (Demić & Lukic, 2008) of the present experimental dataset, partial coherence demonstrated that the simultaneous fore-and-aft and vertical excitation is coupled and cannot in general be represented by simple addition of independently obtained responses. This observation motivated the use of component coherence (CptC) to quantify how individual excitation components contribute to the output response.

Coherence analysis is a useful method for evaluating the frequency-dependent relationship between an input vibration and a measured response. However, coherence should not be interpreted as a direct measure of vibration perception or masking. A low coherence value may result from measurement noise, nonlinearities, nonstationarity, signal leakage, or the presence of several correlated inputs (Allemang et al., 2022).

Brandt (2011) provides an important practical basis for vibration signal analysis. The author emphasizes the importance of appropriate sensor calibration, sampling frequency, windowing, spectral averaging, and frequency resolution. These factors are particularly relevant in whole-body vibration experiments because inadequate signal-

processing procedures can artificially reduce coherence and lead to incorrect conclusions regarding component interaction or masking (Brandt, 2011).

The limitations of ordinary coherence become more pronounced in multivariate systems. In two-directional whole-body vibration, for example, vertical and fore–aft inputs may be correlated because of mechanical coupling, cross-axis motion, or common excitation sources. Dodds and Robson (1975) showed that partial coherence can be used to evaluate the relationship between one input and an output after accounting for the influence of another input. This approach is therefore more suitable than ordinary coherence for estimating the independent contribution of each vibration direction (Dodds & Robson, 1975).

More recent work has extended this concept to systems with multiple correlated or uncorrelated inputs. Howes et al. (2025) proposed a generalized coherence framework for quantifying the contribution of individual inputs to a system response. This framework is particularly relevant to masking research because it may help determine whether the presence of a secondary vibration reduces the independent contribution of a target component. The reduction in estimated input contribution should not automatically be interpreted as perceptual masking. It may also reflect changes in mechanical transmission, posture, muscle activation, or measurement conditions.

The application of coherence analysis to whole-body vibration must also consider the biomechanical transmission of vibration through the seat and the human body. Qiu and Griffin (2003) demonstrated that fore–aft vibration transmission depends on excitation characteristics, seat properties, and participant-related factors. Their findings highlight the importance of realistic laboratory simulation and accurate measurement at the seat–body interface. However, their study primarily addressed vibration transmission rather than the interaction or masking between simultaneous directional components (Qiu & Griffin, 2003).

The reviewed literature reveals a clear research gap. Previous studies have established the theoretical basis of coherence and partial coherence (Dodds & Robson, 1975; Allemang et al., 2022), provided practical guidelines for reliable vibration measurements (Brandt, 2011), and examined vibration transmission in vehicle-seat systems (Qiu & Griffin, 2003). However, limited research has connected component-specific coherence with the perceptual masking of one vibration direction by another.

For the present study, masking should therefore be assessed by combining coherence-based measures with subjective or behavioural responses. A possible operational definition is that masking occurs when the addition of a secondary vibration produces a systematic reduction in the independent.

THEORETICAL BACKGROUND

The considered whole-body vibration system can initially be represented as a 2×2 multiple-input multiple-output (MIMO) system, with two input accelerations, (X_s) and (Z_s), and two output accelerations, (X_h) and (Z_h) (Demić & Lukić, 2009; Demić & Lukic, 2008). For the component coherence analysis, the MIMO system is reduced to a 2×1 multiple-input single-output (MISO) system by considering each output component separately. Thus, when (X_h) is selected as the output, the system is represented by the two inputs (X_s) and (Z_s) and the single output (X_h). When (Z_h) is selected, the system consists of the same two inputs, (X_s) and (Z_s), and the single output (Z_h). This reduction does not imply that one input or one output is removed from the physical system; rather, it represents an analytical decomposition of the original MIMO system into two 2×1 input–output configurations, enabling the contribution of each input component to a specific output component to be evaluated using component coherence measures.

Two-input, one-output vibration system

A two-input/one-output (2×1) system describes a dynamic system in which two simultaneously acting input signals contribute to a single output response. In the frequency domain, the relationship between the inputs and the output can be characterized using spectral densities, cross-spectral densities, and optimum frequency-response functions. When the two inputs are correlated, their individual contributions to the output cannot be fully described by conventional single-input coherence measures. Component coherence provides a suitable framework for multi-input systems by separating the output response into contributions associated with the individual inputs and terms describing their mutual interaction. For a two-input system, this interaction is represented by the off-diagonal component-coherence terms and may result in either amplification or cancellation of the combined response. This approach is therefore particularly useful for assessing the interaction between simultaneous fore-and-aft and vertical whole-body vibration components Figure 1.

Input signals in MIMO are:

- $X_1=X_s$ = seat acceleration in the X (fore-and-aft) direction,
- $X_2=Z_s$ = seat acceleration in the Z (vertical) direction

and the output is:

- Y = head acceleration, X_h or Z_h.

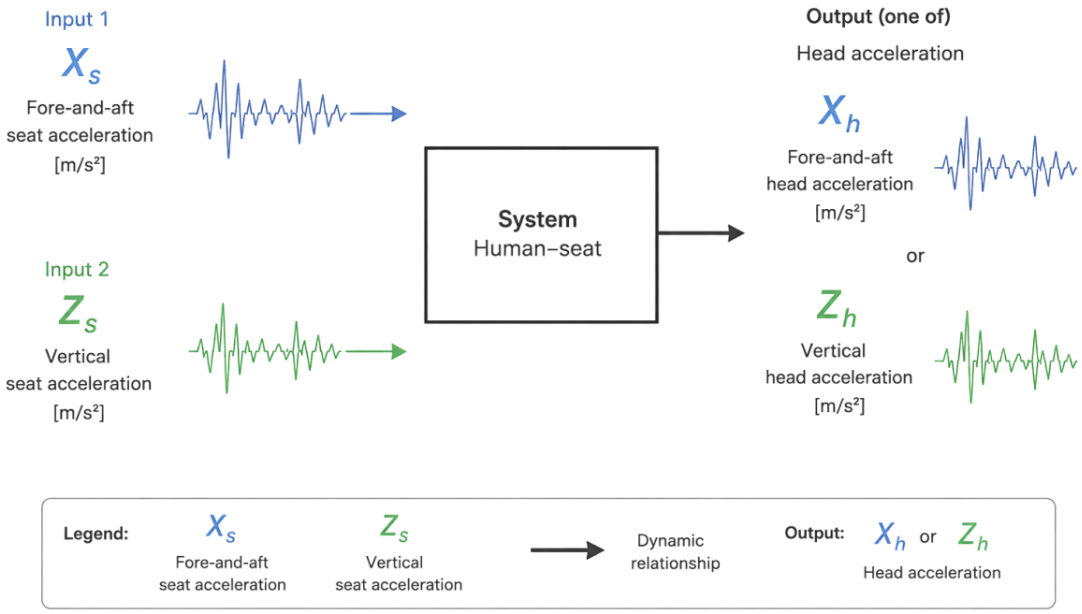

Figure 1 Two-input, one-output vibration system

Component coherence

For a two-input system, ordinary coherence between an individual input and output does not necessarily distinguish the contribution of that input from the contribution shared with the second input.

Component coherence was therefore used to decompose the relationship between the two input components and the output (Howes et al., 2025).

$$CptC = \begin{bmatrix} C_{11} & C_{12} \\ C_{21} & C_{22} \end{bmatrix} \tag{1}$$

where:

- C_{11} – contribution of the X_s input to the output.
- C_{22} – contribution of the Z_s input to the output.
- C_{12} – cross-component interaction term between the X_s and Z_s inputs.
- C_{21} – cross-component interaction term between the Z_s and X_s inputs.

Elements of the CptC matrix are calculated according to:

$$\begin{aligned} C_{11} &= \frac{H_1^* G_{11} H_1}{Gyy} \\ C_{22} &= \frac{H_2^* G_{22} H_2}{Gyy} \\ C_{12} &= \frac{H_1^* G_{12} H_2}{Gyy} \\ C_{21} &= \frac{H_2^* G_{21} H_1}{Gyy} \end{aligned} \tag{2}$$

where:

- * denotes the complex conjugate,
- G_{11}, G_{22}, G_{yy} -autospectrum of the first input, autospectrum of the second input, and autospectrum of the output, respectively,
- H_1 is the optimum frequency response function (FRF) associated with the X-direction seat input,
- H_2 is the optimum FRF associated with the Z-direction seat input (Bendat & Piersol, 2010)

Total component coherence

The quantity referred to as C_{total} in the present study represents the overall component coherence associated with the two simultaneously acting excitation components.

$$C_{total} = C_{11} + C_{22} + C_{12} + C_{21} \tag{3}$$

Direct component coherence

The direct component is:

$$C_{direct} = C_{11} + C_{22} \tag{4}$$

Therefore, C_{11} and C_{22} represent the direct contributions of the X_s and Z_s inputs, respectively, whereas C_{12} and C_{21} represent the cross-component interaction between the two excitation directions.

The combination of the input spectral matrix G_{ij} and the optimum FRFs Hi provides the component coherence terms C_{11}, C_{22}, C_{12}, and C_{21} used to characterize the interaction between the two excitation directions.

Cancellation

The second measure, referred to as *Cancellation*, describes the degree to which the component response associated with the combined multidirectional excitation differs from the response that would be obtained by treating the individual excitation components independently.

The *Cancellation* can be expressed as the relative reduction in the resultant component contribution:

$$Cancellation(f) = 100\left(1 - \frac{C_{total}(f)}{C_{direct}(f)}\right) \tag{5}$$

Therefore, C_{11} and C_{22} represent the direct contributions of the X and Z inputs, respectively, whereas C_{12} and C_{21} represent the cross-component interaction between the two excitation directions.

Both *CptC* components and C_{total} are dimensionless, while *Cancellation* is expressed as a percentage (%).

The combination of the input spectral matrix G_{ij} and the optimum FRFs provides the component coherence terms C_{11}, C_{22}, C_{12} and C_{21} used to characterize the interaction between the two excitation directions.

EXPERIMENTAL SETUP AND PROCEDURE

The experiment was designed to investigate the masking of fore-and-aft whole-body vibration by simultaneous vertical excitation and to characterize the interaction between the two excitation directions using component coherence analysis.

The experimental input consisted of two simultaneous broadband random vibration components applied to the seat: fore-and-aft acceleration (X_s) and vertical acceleration (Z_s). The resulting head acceleration was measured in the corresponding fore-and-aft (X_h) and vertical (Z_h) directions, Figure 2.

Six experimental conditions were investigated by combining three excitation levels (L_1=0.55 ms^{-2} r.m.s., L_2=1.75 ms^{-2} r.m.s. and L_3=2.25 m/s^2 r.m.s.) with two seat-backrest angles (A_1=115˚ and A_2=90˚respect to horizontal plane). Each experimental condition was repeated four times for each subject. During each trial, the seat and head accelerations were recorded simultaneously. Their combinations produced six experimental conditions.

The signals were acquired at a sampling frequency of 75 Hz. Frequency-domain analysis was performed using a 2048-point FFT, resulting in 1025 frequency points in the one-sided spectrum and a frequency resolution of approximately 0.0366 Hz. The analysed frequency range extended from approximately 0.037 to 37.5 Hz. Power and cross-power spectral densities were estimated using a Welch-based method with no overlap between adjacent segments.

For each measurement, the component coherence matrix was calculated over the 0.63–37.5 Hz frequency range. The frequency corresponding to the maximum absolute value of the cross-component term C_{12} was then identified, and C_{11}, C_{22}, C_{total}, C_{direct}, and Cancellation were evaluated at that frequency.
The subsequent analysis was restricted to frequencies above 0.63 Hz to ensure consistency with our previous whole-body vibration studies and to allow direct comparison with previously reported results. Frequencies below 0.63 Hz were excluded because this low-frequency region may be more susceptible to transient and non-stationary effects and reduced spectral reliability. Therefore, all subsequent analyses were performed over the frequency range of 0.63–37.5 Hz.

For each individual measurement, the component coherence matrix was calculated separately using the two seat acceleration inputs and the corresponding head acceleration output. Each repetition produced an independent component coherence estimate. The four repeated measurements obtained under the same experimental condition were subsequently averaged to obtain the representative component coherence measures for that subject and condition.

The component coherence analysis enabled the contributions associated with the individual excitation directions and their interaction to be evaluated separately. The analysis was performed for both head-response directions, (X_h) and (Z_h). The resulting component coherence measures were used to calculate the direct and total component contributions and the corresponding cancellation.

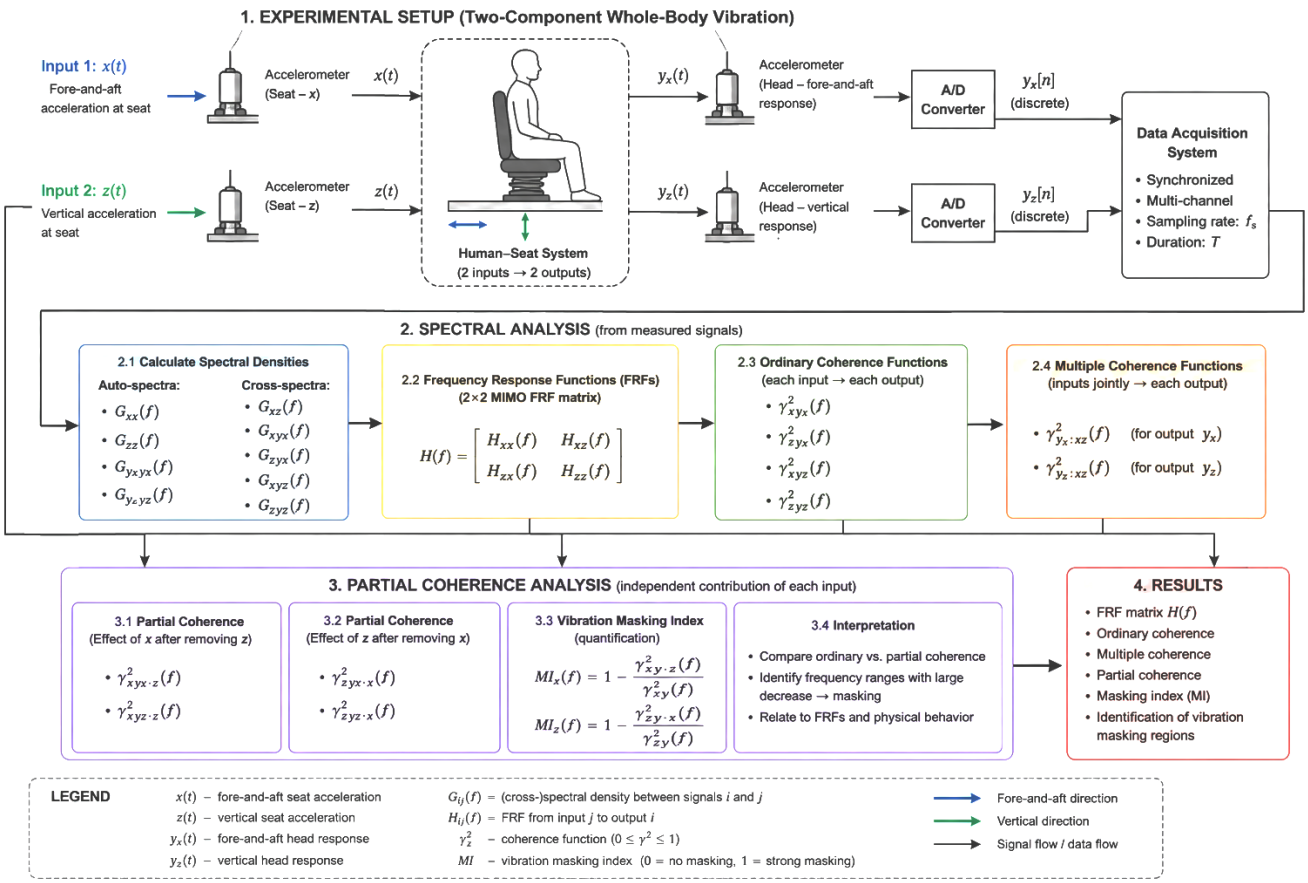

Figure 2 Experimental setup, (Demić & Lukic, 2008) modified with ChatGPT

SIGNAL PROCESSING AND COMPONENT COHERENCE ANALYSIS

Statistical analysis was performed using non-parametric methods because of the small sample size and the lack of evidence supporting the assumption of normally distributed data. For each subject and experimental condition, the four repeated measurements were first averaged after component coherence analysis, and the resulting subject-level values were used for statistical testing.

The effects of the six experimental conditions, defined by the combination of three excitation levels (L_1, L_2, and L_3) and two seat-backrest angles (A_1 and A_2), were evaluated using the Friedman test for repeated measures. Separate analyses were performed for the four investigated response measures: $X_{h\ Ctotal}$, $X_{h\ Cancellation}$, $Z_{h\ Ctotal}$, and $Z_{h\ Cancellation}$.

When pairwise comparisons among the six conditions were considered, the Wilcoxon signed-rank test was used as the non-parametric post-hoc test. Since six conditions result in 15 possible pairwise comparisons, the significance level was adjusted using the Bonferroni correction. Statistical significance was accepted at an adjusted ($p < 0.05$).

In addition to the six-condition analysis, a direct comparison between excitation levels L_1 and L_2 was performed using data from all six subjects. This comparison was conducted separately for each of the four response measures using the Wilcoxon signed-rank test. The L_1–L_2 comparison was considered separately from the six-condition post-hoc analysis because it represented a predefined comparison of excitation levels rather than an exploratory comparison among all experimental conditions.

For each statistical test, the corresponding *p*-value was reported. Where appropriate, effect size was also expressed using Kendall's coefficient of concordance (*W*) to quantify the magnitude of the overall differences detected by the Friedman test.

RESULTS AND DISCUSSION

The effects of excitation level (L), seat-backrest angle (A), and their interaction (L×A) were evaluated for $X_{hCtotal}$, $X_{h\ Cancellation}$, $Z_{h\ Ctotal}$, and $Z_{h\ Cancellation}$. The effect of excitation level across the three levels (L_1, L_2, and L_3) was assessed using the Friedman test. The magnitude of the effect was quantified using Kendall's coefficient of concordance (*W*).

The effect of seat-backrest angle was evaluated by comparing A_1 and A_2 using the Wilcoxon signed-rank test. The Rank-biserial correlation (r_{rb}) was used as the corresponding effect-size measure. The interaction between excitation level and seat-backrest angle was evaluated from the condition-specific differences between A_1 and A_2 across the three excitation levels.

The distribution of the four response measures was assessed prior to statistical analysis using a normality test. The results indicated different distribution characteristics among the investigated parameters. $X_{h\ Ctotal}$ (p=0.2243) and $Z_{h\ Cancellation}$ (p=0.4676) did not show statistically significant departures from normality. In contrast, $X_{h\ Cancellation}$ (p=0.0012) and $Z_{h\ Ctotal}$ (p=0.0118) showed statistically significant deviations from a normal distribution, Table 1.

Table 1 Normality assessment of the component-coherence parameters

Parameter	Normality test, (p)	Interpretation
$X_{h\ Ctotal}$	0.2243	No statistically significant departure from normality
$X_{h\ Cancellation}$	0.0012	Non-normal distribution
$Z_{h\ Ctotal}$	0.0118	Non-normal distribution
$Z_{h\ Cancellation}$	0.4676	No statistically significant departure from normality

Note: (p<0.05) indicates a statistically significant departure from normality.

In addition to the three-level analysis, a direct paired comparison between L_1 and L_2 was performed using the six subjects with complete data at both excitation levels. The Wilcoxon signed-rank test showed a statistically significant increase in $Z_{h\ Cancellation}$ from L_1 to L_2 (p=0.031). The mean increase was approximately 2.23 percentage points, and all six subjects showed the same direction of change. This result was interpreted as a consistent L_1–L_2 increase in the vertical cancellation component. It was considered separately from the six-condition analysis and should not be interpreted as evidence of a statistically significant general effect across all three excitation levels.

The statistical analysis indicates that the component-coherence measures were generally not strongly affected by the combined variation of excitation level and seat-backrest angle. The most pronounced effect was observed for $X_{h\ Cancellation}$, which showed a statistically significant and large effect of excitation level. $Z_{h\ Cancellation}$ exhibited a specific and consistent increase between L_1 and L_2, although the overall three-level effect did not reach statistical significance. No statistically significant L×A interaction was detected for any of the four component-coherence measures.

Because two of the four response measures deviated from normality, non-parametric methods were used, given the small sample size and repeated-measures design.

The results indicate that the masking behaviour was generally stable across the investigated excitation levels and seat-backrest angles. Among the analysed parameters, only $X_{h\ Cancellation}$ showed a statistically significant effect of excitation level (p = 0.041, W = 0.640), with cancellation decreasing from L_1 to L_3. This indicates that increasing excitation level slightly reduced the masking of the fore-and-aft head response, Table 2.

The $Z_{h\ Cancellation}$ showed an opposite descriptive trend, with cancellation increasing with excitation level; however, this effect was not statistically significant (p = 0.091). Similarly, neither $X_{h\ Ctotal}$ nor $Z_{h\ Ctotal}$ showed significant

dependence on excitation level. These results suggest that excitation magnitude primarily affected the degree of masking in the fore-and-aft direction, rather than producing a general change in component coherence.

Seat-backrest angle had no statistically significant effect on any parameter, and no significant *L* × *A* interaction was observed. Thus, within the investigated postural range, excitation level appears to be more relevant to the masking behaviour than seat-backrest angle.

The high cancellation values observed for both head-response directions demonstrate a strong interaction between the two excitation components. The significant dependence of $X_{h\ Cancellation}$ on excitation level further indicates that the masking effect is not completely invariant with excitation magnitude, supporting the use of component coherence analysis for characterising coupled two-directional whole-body vibration responses.

Table 2 Statistical analysis and effect sizes for excitation level, seat-backrest angle, and their interaction

Parametar	L: Kendall W	A: rank-biserial r	L×A: Kendall W
$X_{h\ Ctotal}$	0.040	+0.333	0.040
$X_{h\ Cancellation}$	0.640	−1.000	0.120
$Z_{h\ Ctotal}$	0.120	−0.333	0.120
$Z_{h\ Cancellation}$	0.480	−0.467	0.040

Table 2 summarizes the statistical analysis of the four response parameters: $X_{h\ Ctotal}$, $X_{h\ Cancellation}$, $Z_{h\ Ctotal}$, and $Z_{h\ Cancellation}$. The effect of excitation level (L) was assessed using the Friedman test, with Kendall's W reported as a measure of effect size. The effect of seat-backrest angle (A) was evaluated using the Wilcoxon signed-rank test, with the Rank-biserial correlation used as the corresponding effect-size measure. The L × A interaction was assessed by applying the Friedman test to the within-subject differences between A_2 and A_1 at each excitation level, with Kendall's W used to quantify the magnitude of this effect.

In addition to the six-condition analysis, a direct L_1 versus L_2 comparison was performed using all six subjects. This comparison was considered separately because it does not require measurements at L_3.

For $X_{h\ Ctotal}$, neither excitation level nor seat-backrest angle produced a statistically significant effect, with small effect sizes (W=0.04) and (r_{rb}=0.33), respectively. The L × A interaction was also not significant and showed a small effect (W=0.04).

In contrast, $X_{h\ Cancellation}$ showed a statistically significant effect of excitation level (p=0.041), accompanied by a large effect size (W=0.64). The seat-backrest angle did not reach statistical significance (p=0.063), although the rank-biserial correlation was maximal in magnitude (r_{rb}=-1.00), indicating a highly consistent direction of the A_2–A_1 differences across subjects. Importantly, the L × A interaction was not statistically significant (p=0.549) and had only a small effect (W=0.12).

For $Z_{h\ Ctotal}$, no statistically significant effects were detected for excitation level, seat-backrest angle, or their interaction. The corresponding effect sizes were small (W=0.12), (r_{rb}=-0.33), and (W=0.12).

For $Z_{h\ Cancellation}$, the effect of excitation level approached statistical significance (p=0.091) and was associated with a moderate effect size (W=0.48). Neither the seat-backrest angle (p=0.438), (r_{rb}=-0.47) nor the L × A interaction (p=0.819), (W=0.04) was statistically significant, Table 3.

Table 3 Effects of excitation level, seat-backrest angle, and their interaction

Parameter	Factor	Median values/effect	Statistical test	*p*	Effect size	Interpretation
$X_{h\ Ctotal}$	L	L_1=0.784 L_2=0.747 L_3=0.722	Friedman	0.819	(W=0.040)	Negligible effect
	A	A_1=0.733 A_2=0.770 Δ=+0.064	Wilcoxon	0.625	($r_{_rb}$=+0.333)	Small–moderate effect, n.s.
	L×A	Δ=−0.074 +0.055 +0.232	Friedman	0.819	(W=0.040)	No interaction
$X_{h\ Cancellation}$	L	L_1=99.075 L_2=97.480 L_3=96.585	Friedman	0.041	(W=0.640)	Large effect
	A	A_1=97.840 A_2=97.353 Δ=−0.240	Wilcoxon	0.063	(r_{rb}=-1.000)	Very large effect, n.s.

Table 3 (continuation)

Parameter	Factor	Median values/effect	Statistical test	*p*	Effect size	Interpretation
$X_{h\ Cancellation}$	L×A	Δ=+0.460 −1.360 −2.280	Friedman	0.549	(W=0.120)	No interaction
$Z_{h\ Ctotal}$	L	L_1=0.725 L_2=0.794 L_3=0.808	Friedman	0.549	(W=0.120)	Small effect, n.s.
	A	A_1=0.810 A_2=0.769 Δ=−0.072	Wilcoxon	0.625	(r_{rb}=-0.333)	Small–moderate effect, n.s.
	L×A	Δ=+0.042 0.000 +0.005	Friedman	0.549	(W=0.120)	No interaction
$Z_{h\ Cancellation}$	L	L_1=94.280 L_2=96.420 L_3=97.440	Friedman	0.091	(W=0.480)	Moderate–large effect, n.s.
	A	A_1=96.310 A_2=95.573 Δ=−0.810	Wilcoxon	0.438	(r_{rb}=-0.467)	Moderate effect, n.s.
	L×A	Δ=+0.700 −0.650 −1.450	Friedman	0.819	(W=0.040)	No interaction

Note: n.s. = not statistically significant

Table 4. Frequency of maximum cross-component interaction and component-coherence parameters for the six experimental conditions

Condition	X_h (f_{Cmax}) [Hz]	$X_{h\ Ctotal}$	$X_{h\ Cancellation}$ [%]	Z_h (f_{Cmax}) [Hz]	$Z_{h\ Ctotal}$	$Z_{h\ Cancellation}$ [%]
L_1-A_1	0.916	0.812	95.74	9.430	0.690	95.17
L_1-A_2	0.916	0.814	97.64	8.624	0.652	94.80
L_2-A_1	6.427	0.785	95.67	9.869	0.768	97.41
L_2-A_2	10.455	0.775	95.58	10.144	0.665	97.03
L_3-A_1	15.417	0.689	97.39	11.499	0.793	96.41
L_3-A_2	14.685	0.744	96.19	11.719	0.814	95.62

Note: f_{Cmax} denotes the frequency at which the absolute value of the cross-component coherence term (C_{12}) reached its maximum within the 0.63–37.5 Hz frequency range.

In the Table 4 the maximum-coherence frequency, total component coherence, and cancellation for the fore-and-aft (X_h) and vertical (Z_h) head-acceleration components under the six experimental conditions were summarized. For (X_h), the frequency of maximum component coherence shifted markedly toward higher frequencies with increasing excitation level, from 0.916 Hz at L_1 to approximately 14.7–15.4 Hz at L_3. In parallel, ($X_{h\ Ctotal}$) generally decreased with excitation level, particularly for A_1, whereas cancellation remained consistently high across all conditions (95.58–97.64%). For (Z_h), the maximum-coherence frequency increased more gradually, from approximately 8.6–9.4 Hz at L_1 to 11.5–11.7 Hz at L_3. In contrast to ($X_{h\ Ctotal}$), ($Z_{h\ Ctotal}$) tended to increase with excitation level, particularly at A_1. Cancellation in the vertical direction also remained high (94.80–97.41%), although its variation across excitation levels was non-monotonic. Differences between A_1 and A_2 varied with excitation level and response direction, with no consistent directional pattern. These descriptive results are consistent with the inferential analysis, which indicated a significant effect of excitation level only for (X_h) cancellation, while neither the seat-backrest angle nor the L × A interaction reached statistical significance for the four analysed parameters.

Based on the complete statistical analysis, it can be concluded that excitation level and backrest angle do not produce a general, statistically significant effect on the four observed component-coherence parameters across all six experimental conditions. The analysis revealed a specific pattern for the vertical head response.

The $Z_{h\ Cancellation}$ showed a tendency to increase with excitation level, from an average of 94.16% at L_1 to 96.75% at L_2, after which it slightly decreased to 96.01% at L_3. A direct paired comparison between L_1 and L_2, including all six participants with complete data for these two levels, showed an increase of 2.23 percentage points and a Wilcoxon p=0.03125, with all six participants showing the same direction of change. This result did not remain statistically significant after a strict Bonferroni correction for 15 pairwise comparisons. Therefore, the finding can be described as a consistent indication of an increase in the vertical cancellation component when moving from the lowest to the intermediate excitation level, rather than as conclusive evidence of a general effect of excitation level, Table 5.

At the same time, the absence of significant changes in C_{total} indicates that the effect cannot be explained simply by an increase in overall coherence. Combined with the previously established association between the *x* and *z* excitation components, these results support the conclusion that the masking effect is manifested primarily through changes in the relationship and mutual interaction of the response components, rather than through a uniform increase or decrease in overall component coherence. It is particularly significant that this change occurs between L_1 and L_2, whereas a further increase in excitation to L_3 does not produce an additional increase in the cancellation component. This suggests a possible nonlinear or saturation-like nature of the masking effect, which should be considered in relation to the frequency redistribution of the response and changes in the dominant frequencies within the frequency range of interest.

Table 5 Direct paired comparison between L_1 and L_2

Parameter	L_1	L_2	Change, percentage points	Wilcoxon (p)	Interpretation
$X_{h\ Ctotal}$	—	—	—	n.s.	No significant difference
$X_{h\ Cancellation}$	—	—	—	n.s.	No significant difference
$Z_{h\ Ctotal}$	—	—	—	n.s.	No significant difference
$Z_{h\ Cancellation}$	94.16%	96.75%	+2.23	0.03125	Significant L_1–L_2 increase

Note: The L_1–L_2 comparison included all six subjects with complete data at both excitation levels. The comparison was performed separately from the six-condition analysis.

Figure 3 illustrates the individual responses and median values across the three excitation levels. Considerable inter-subject variability is evident, particularly for $X_{h\ Ctotal}$ and $Z_{h\ Ctotal}$. Nevertheless, the median curves reveal clear response tendencies: $X_{h\ Ctotal}$ slightly decreases, $Z_{h\ Ctotal}$ slightly increases, $X_{h\ Cancellation}$ decreases, whereas $Z_{h\ Cancellation}$ increases with excitation level. The decreasing trend in $X_{h\ Cancellation}$ is consistent with the statistically significant effect of excitation level identified by the Friedman test.

The median was used because of the small sample size (N = 5), inter-subject variability, and non-normality of some variables. As a robust measure of central tendency, the median is less sensitive to extreme individual values than the mean and is therefore more appropriate for summarising these data. Its use is also consistent with the non-parametric statistical analysis applied in this study. Individual subject curves were retained to show the variability underlying the median trends, (Bendat, 2010).

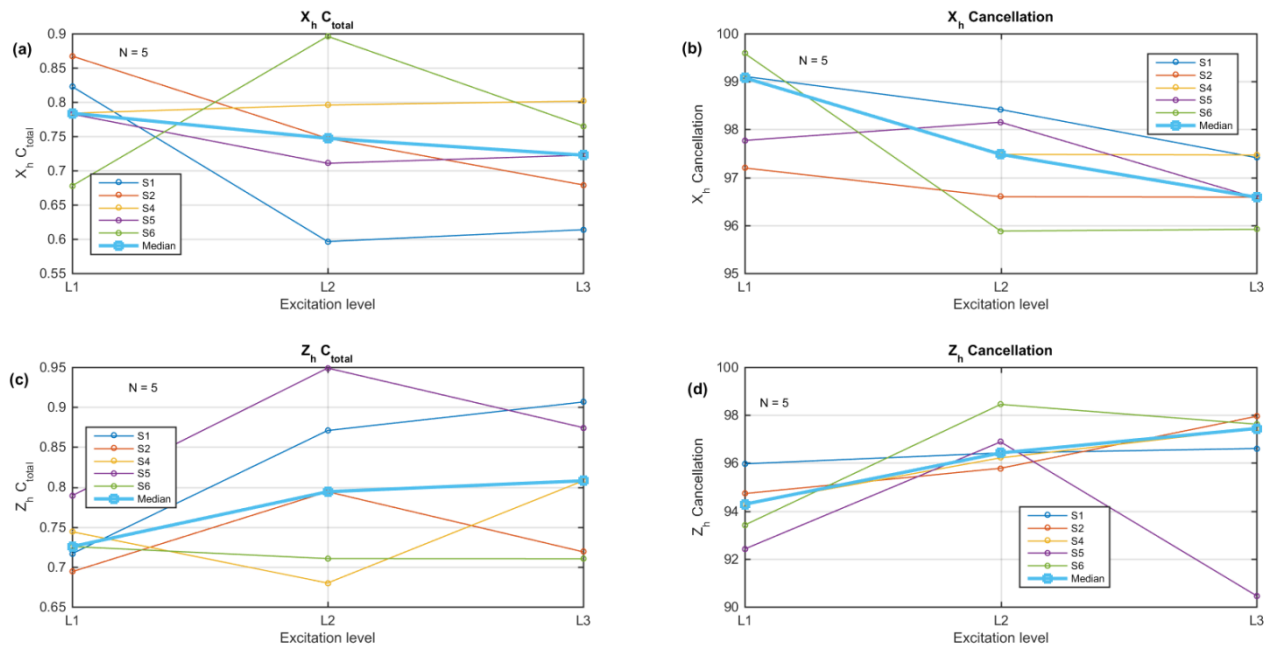

Figure 3 Effect of excitation level on component coherence and cancellation of head vibration in the fore-and-aft and vertical directions: (a) $X_{h\ Ctotal}$, (b) $X_{h\ Cancellation}$, (c) $Z_{h\ Ctotal}$, and (d) $Z_{h\ Cancellation}$. Individual lines represent the five subjects, while squares indicate the median response across subjects

Figure 4 shows that the effect of seat-backrest angle was generally small and variable across subjects. For $X_{h\ Ctotal}$, the median A_2−A_1 difference increased with excitation level, whereas $X_{h\ Cancellation}$ showed a tendency toward lower values at A_2, particularly at L_3. The effects on $Z_{h\ Ctotal}$ and $Z_{h\ Cancellation}$ were smaller and less consistent. Despite these descriptive differences, no significant effect of backrest angle or L × A interaction was found for any of the four parameters. The results therefore suggest that changes in excitation level have a stronger influence on the component coherence and cancellation characteristics than the change in seat-backrest angle.

Figure 5 shows considerable inter-subject variability in the changes associated with the backrest angle, with no consistent trend across excitation levels. Changes in (C_{total}) were generally smaller than changes in cancellation for

both (X_h) and (Z_h), suggesting that backrest angle primarily affected the interaction between the two input vibration components rather than their overall coherence. The variability in the direction and magnitude of the changes indicates that the effect of backrest angle was subject and condition-dependent. This is consistent with the statistical analysis, which showed no significant global differences among the six experimental conditions for any of the four parameters.

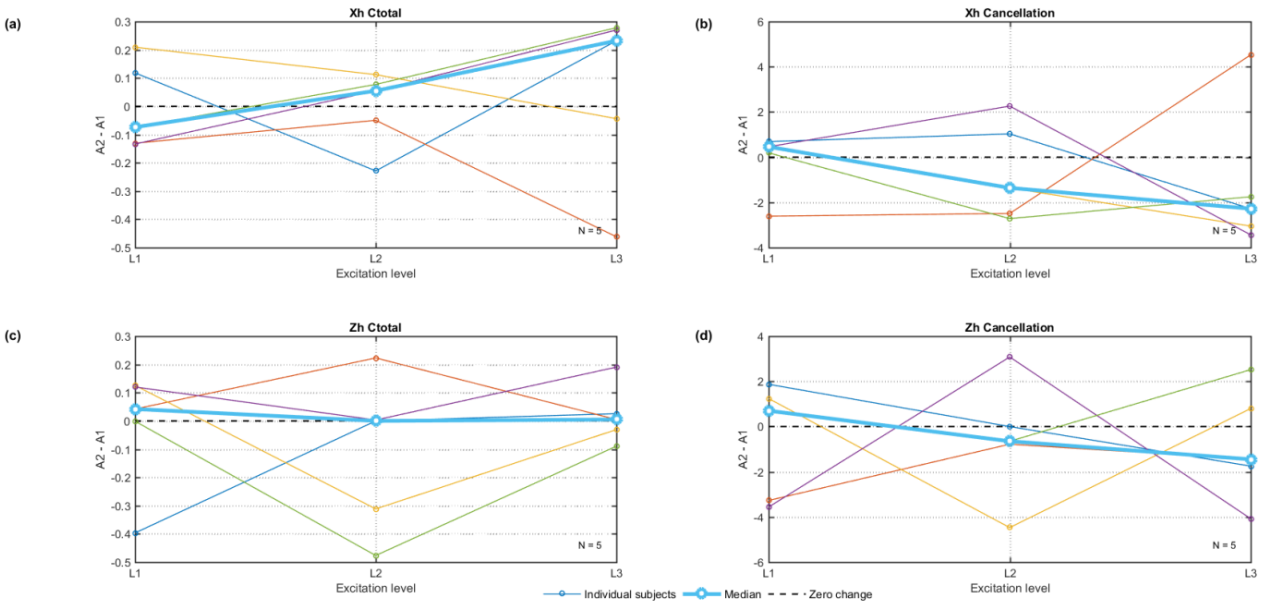

Figure 4 Effect of seat-backrest angle expressed as the difference between A_2 and A_1 ($A_2 - A_1$) across the three excitation levels for (a) fore-and-aft component coherence, $X_{h\ Ctotal}$), (b) fore-and-aft cancellation, $X_{h\ Cancellation}$, (c) vertical component coherence, $Z_{h\ Ctotal}$, and (d) vertical cancellation, $Z_{h\ Cancellation}$. Individual lines represent subjects, the solid line represents the median response, and the dashed horizontal line indicates zero difference

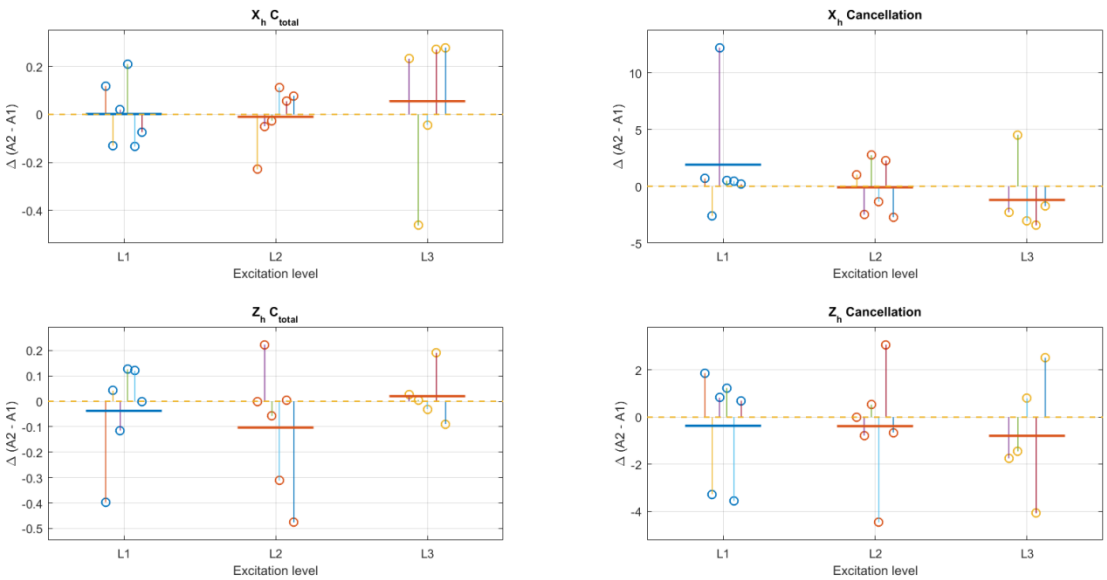

Figure 5 Effect of backrest angle on component coherence parameters Individual and mean changes (Δ=A2-A1=90˚-115˚) are shown for excitation levels L1–L3 for (a) (Xh Ctotal), (b) Xh cancellation, (c) (Zh Ctotal), and (d) Zh cancellation. The dashed line indicates zero change

The sensitivity analysis shows that the exclusion of the identified isolated subjects had a limited effect on the overall pattern of cancellation changes for both (X_h) and (Z_h). Although the magnitude of the changes was modified in some excitation conditions, the general trends remained comparable between the full dataset and the reduced dataset. This indicates that the observed cancellation behaviour was not determined solely by the isolated subjects and that the main findings were relatively robust to their exclusion, Figure 6.

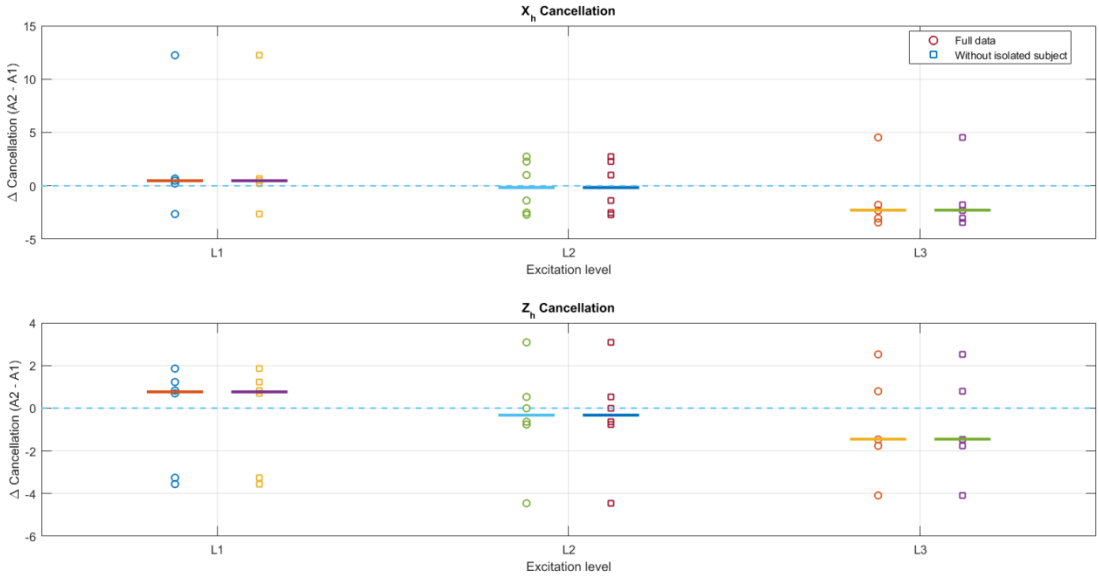

Figure 6 Sensitivity analysis of cancellation to isolated subjects

CONCLUSIONS

The principal conclusions are:

- No significant global differences were found among the six experimental conditions for any of the four evaluated parameters: $X_{h\ Ctotal}$, $X_{h\ Cancellation}$, $Z_{h\ Ctotal}$, and $Z_{h\ Cancellation}$. The Friedman test produced *p*-values of 0.6912, 0.2337, 0.5297, and 0.2761, respectively.
- None of the 15 pairwise comparisons were significant after Bonferroni correction. Therefore, no specific pair of the six experimental conditions can be identified as statistically different on the basis of the corrected analysis.
- Seat-backrest angle did not produce a statistically significant main effect on either component coherence or cancellation.
- No statistically significant interaction between excitation level and seat-backrest angle was identified.
- A separate direct comparison between L_1 and L_2, using all six subjects, revealed a significant increase in $Z_{h\ Cancellation}$ from 94.99% to 97.22% (p=0.03125). All six subjects showed the same direction of change.
- Difference L_1–L_2 does not survive the Bonferroni threshold of 0.003333 established for the complete 15-comparison family. It should therefore be regarded as an indication of a potentially meaningful excitation-level effect rather than as a confirmed corrected post-hoc effect.
- The results support the conclusion that the multidirectional human response is *coupled*, consistent with the previous partial coherence analysis, and that the combined (x+z) response cannot be interpreted reliably by simply adding independently measured single-direction responses.
- Component coherence therefore provides a useful framework for quantifying multidirectional vibration interaction and for studying masking phenomena in whole-body vibration.
- The coupling between fore-and-aft and vertical vibration is present but relatively robust to the tested changes in excitation level and seat-backrest angle, while vertical cancellation may show a more pronounced sensitivity to excitation level. Further studies with a larger number of subjects and frequency-specific statistical modelling are required to establish the robustness and physiological origin of this effect.

ACKNOWLEDGMENTS

This research was supported by the Ministry of Education, Science and Technological Development of the Republic of Serbia through Project 451-03-34/2026-03/200107.

REFERENCE

Allemang, R. J., Patwardhan, R. S., Kolluri, M. M., & Phillips, A. W. (2022). Frequency response function estimation techniques and the corresponding coherence functions: A review and update. Mechanical Systems and Signal Processing, 162, 108100. https://doi.org/10.1016/j.ymssp.2021.108100

Bendat, J. S., & Piersol, A. G. (2010). *Random Data*. Wiley. https://doi.org/10.1002/9781118032428

Brandt, A. (2011). Noise *and vibration analysis: Signal analysis and experimental procedures*. John Wiley & Sons. https://doi.org/10.1002/9780470978160

Demić, M., & Lukić, J. (2009). Investigation of the transmission of fore and aft vibration through the human body. *Applied Ergonomics*, 40(4), 622–629. https://doi.org/10.1016/j.apergo.2008.05.002

Demić, M. S., & Lukic, J. K. (2008). Human Body under Two-Directional Random Vibration. *Journal of Low Frequency Noise, Vibration and Active Control*, 27(3), 185–201. https://doi.org/10.1260/026309208785844103

Dodds, C. J., & Robson, J. D. (1975). Partial coherence in multivariate random processes. *Journal of Sound and Vibration*, 42(2), 243–249. https://doi.org/10.1016/0022-460X(75)90219-9

Howes, N. H., Allen, M. S., Farina, D., & Charles, S. K. (2025). A generalized coherence framework for quantifying input contributions in multi-input systems with correlated or uncorrelated inputs. *Biomedical Signal Processing and Control*, 104, 107522. https://doi.org/10.1016/J.BSPC.2025.107522

Lukić, J., Glišović, J., & Miloradović, D. (2024). *Masking fore and aft vibration under two axial whole body vibration*. In Burak Aydogldu, Emre Bulat, & Necmettin Kaya (Eds.), Proceedings of the International 11th Automotive Technologies Congress (pp. 1058–1063). Bursa Uludag University, Engineering Faculty.

Qiu, Y., & Griffin, M. J. (2003). Transmission of fore–aft vibration to a car seat using field tests and laboratory simulation. *Journal of Sound and Vibration*, 264(1), 135–155. https://doi.org/10.1016/S0022-460X(02)01171-9

OpenAI. (2026). ChatGPT (GPT-4o) [LLM]. https://chatgpt.com

The 11th International Congress
Motor Vehicles & Motors 2026
Kragujevac, Serbia
October 8th - 9th, 2026

Motor Vehicles & Motors

MVM2026-074
https://doi.org/10.24874/CMVM2026.074
Original scientific paper

Milan Blagojević[1]
Saša Milojević[2]
Živče Šarkoćević[3]
Ivica Čamagić[4]
Dragan Lazarević[5]

FIAT 500L REAR IMPACT PERFORMANCE IN EURO NCAP AND IIHS ASSESSMENTS

ABSTRACT: This paper examines Fiat 500L rear-impact performance by combining published Euro NCAP and IIHS assessments with video-based kinematic reanalysis of official Euro NCAP footage. Euro NCAP reported 2.3 points and marginal whiplash protection for the 2012 European variant, whereas IIHS rated the seat and head restraint of the United States model range as good. The ratings are not directly interchangeable because the programmes used different pulses, seat specifications, measured quantities and scoring rules. To supplement the published results, WhiplashApp was used as the motion-analysis tool. Two user-defined head-region points were tracked by Lucas-Kanade optical flow, and the smoothed trajectories were used to calculate angle of head, angular velocity and angular acceleration. The resulting curves identify motion reversal, extension-rebound and intervals of rapid head rotation. These observations complement the IIHS values for favourable restraint geometry and 56 ms head contact and help explain how a good IIHS rating can coexist with the marginal Euro NCAP result. The study demonstrates the value of traceable video kinematics for interpreting published automotive test results. WhiplashApp provides an effective tool for this workflow and a suitable basis for further whiplash and video-based biomechanical analyses with additional synchronised measurement channels.

KEYWORDS: whiplash, rear impact, motion analysis, seat, head restraint, Fiat 500L

[1] *Milan Blagojević, Univesity of Pristina, Faculty of Technical Sciences, Knjaza Miloša 7, Kosovska Mitrovica, milan.blagojevic@pr.ac.rs, https://orcid.org/0000-0003-0710-5297*
[2] *Saša Milojević, University of Kragujevac, Faculty of Engineering, Sestre Janjić 6, Kragujevac, sasa.milojevic@kg.ac.rs, https://orcid.org/0000-0003-0569-047X*
[3] *Živče Šarkoćević, Univesity of Pristina, Faculty of Technical Sciences, Knjaza Miloša 7, Kosovska Mitrovica, zivce.sarkocevic@pr.ac.rs, https://orcid.org/0000-0001-5110-6620*
[4] *Ivica Čamagić, Univesity of Pristina, Faculty of Technical Sciences, Knjaza Miloša 7, Kosovska Mitrovica, ivica.camagic@pr.ac.rs, https://orcid.org/0000-0003-4706-6333*
[5] *Dragan Lazarević, Univesity of Pristina, Faculty of Technical Sciences, Knjaza Miloša 7, Kosovska Mitrovica, dragan.lazarevic@pr.ac.rs, https://orcid.org/0000-0001-5106-554X*

FIAT 500L U EURO NCAP I IIHS PROCENAMA UDARA OTPOZADI

REZIME: U ovom radu analiziraju se performanse automobila Fiat 500L pri udaru otpozadi povezivanjem objavljenih rezultata Euro NCAP i IIHS ispitivanja sa naknadnom video-kinematičkom analizom zvaničnog snimka Euro NCAP testa. Euro NCAP je za evropsku varijantu vozila iz 2012. godine dodelio 2,3 poena i ocenio zaštitu od trzajne povrede vrata kao marginalnu, dok je IIHS sedište i naslon za glavu američke verzije modela ocenio kao dobre. Ove ocene nisu neposredno uporedive jer su u programima primenjeni različiti impulsi udara, specifikacije sedišta, merene veličine i pravila ocenjivanja. Kao dopuna objavljenim rezultatima, WhiplashApp je korišćen kao alat za analizu kretanja. Dve korisnički definisane tačke u oblasti glave praćene su primenom Lucas–Kanade metode optičkog toka, a izglađene putanje korišćene su za izračunavanje ugla glave, ugaone brzine i ugaonog ubrzanja. Dobijene krive omogućavaju identifikovanje promene smera kretanja, faze ekstenzije i povratnog kretanja, kao i vremenskih intervala brze rotacije glave. Ova zapažanja dopunjuju rezultate IIHS ispitivanja, koji ukazuju na povoljnu geometriju sistema za oslanjanje glave i ostvarivanje kontakta glave sa naslonom nakon 56 ms, i pomažu u objašnjenju kako dobra IIHS ocena može postojati istovremeno sa marginalnim rezultatom Euro NCAP ispitivanja. Istraživanje pokazuje značaj sledljive video-kinematičke analize za tumačenje objavljenih rezultata ispitivanja bezbednosti automobila. WhiplashApp predstavlja efikasan alat za ovakav postupak i odgovarajuću osnovu za dalji razvoj analiza trzajnih povreda vrata i drugih biomehaničkih ispitivanja zasnovanih na video-snimcima, uz mogućnost uključivanja dodatnih sinhronizovanih mernih kanala.

KLJUČNE REČI: trzajna povreda vrata, udar otpozadi, analiza kretanja, sedište, naslon za glavu, Fiat 500L

INTRODUCTION

Whiplash-associated disorders are commonly linked to low- and moderate-severity rear impacts. During the initial phase of such an event, the seat accelerates the torso while the head tends to remain behind because of inertia. The resulting relative motion depends on head-restraint geometry, seatback stiffness, energy absorption and the timing of head contact. Consumer assessment programmes therefore evaluate the seat and head restraint as a system rather than considering only the nominal presence of a restraint (IIHS, 2023).

The Fiat 500L provides an informative case because it was manufactured at the Kragujevac plant (Government of Serbia, 2012) and was assessed on both sides of the Atlantic. Euro NCAP awarded the vehicle five stars in 2012 and 94% for adult occupant protection but described its rear-impact whiplash protection as marginal. IIHS later assigned a good rating to the head restraints and seats of the United States model range. Reading these labels without the corresponding protocols could suggest a contradiction that is not supported by the available evidence.
The objective of this study is to establish which parts of the two assessments are comparable, quantify the published Fiat 500L results and identify the information required for a defensible experimental reanalysis. The study is a documentary case analysis; no unpublished manufacturer data or new sled tests are presented.

MATERIALS AND METHOD

The Euro NCAP record concerns a left-hand-drive Fiat 500L 1.4 petrol Easy 4x2, publication year 2012 and test mass 1245 kg. The published adult-occupant score was 34 points (94%), including 2.3 points for rear impact whiplash protection. Euro NCAP explicitly characterised the protection provided by the seat and head restraint as marginal (Euro NCAP, 2012a). The IIHS record identifies a manual cloth seat and states that the rating applies to 2014-2020 models. IIHS reports a good overall evaluation, good dynamic rating and good seat/head-restraint geometry (IIHS, n.d.-a).

The comparison was made at three levels: test object and occupant surrogate; excitation and positioning; and reported outputs. A value was treated as directly comparable only when its definition and unit were common to both sources. Programme-specific categories were compared qualitatively and were not converted to an artificial common numerical scale.

The Euro NCAP procedure current around the assessment period was based on three sled tests intended to represent the range of pulse shapes and velocity changes observed in rear crashes. The 2008 protocol specified low and medium pulses near 16 km/h and a high pulse near 24 km/h. Although the low and medium velocity changes were similar, their durations and acceleration-time histories differed. Thus, pulse severity cannot be described by

velocity change or peak acceleration alone. The seat was installed in a vehicle-representative geometry and loaded by a belted BioRID dummy (Euro NCAP, 2008).

Table 1 Crosswalk of the historical rear-impact assessment procedures

Characteristic	Euro NCAP procedure	IIHS procedure
Test object	Forward-facing front seat and head restraint mounted on a sled	Front seat and head restraint mounted on a sled
Occupant surrogate	BioRID rear-impact dummy, standardised seating and three-point belt	BioRID dummy with realistic articulated spine
Dynamic excitation	Three pulses: low, medium and high severity	One pulse with Δv about 16 km/h (10 mph)
Euro NCAP low	Δv 16.10 ± 0.80 km/h; 105.8 ± 3.0 ms; mean 42.35 ± 4.50 m/s²	Not applicable
Euro NCAP medium	Δv 15.65 ± 0.80 km/h; 91.0 ± 3.0 ms; mean 47.85 ± 4.00 m/s²	Closest in Δv, but not necessarily identical in shape
Euro NCAP high	Δv 24.45 ± 1.20 km/h; 107.7 ± 3.0 ms; mean 63.15 ± 4.85 m/s²	No corresponding pulse in the historical rating
Geometry	Included in protocol and assessment rules	Separate static height and backset assessment
Output	Points contributing to adult-occupant/star rating	Good, Acceptable, Marginal or Poor category

The historical IIHS evaluation used a two-stage logic. Static measurements first described the height and backset of the restraint relative to a 50th-percentile male reference. A dynamic sled test with BioRID then evaluated how the system managed occupant motion and crash energy. The dynamic pulse represented a velocity change of 10 mph, equivalent to a stationary vehicle being struck at 20 mph by a vehicle of equal mass (IIHS, 2023). This is close to the Euro NCAP medium pulse in velocity change, but equivalence of the complete acceleration histories and scoring thresholds should not be assumed.

BIOMECHANICAL AND KINEMATIC PARAMETERS

Euro NCAP assessment quantities

The Euro NCAP whiplash assessment combines complementary quantities because no single measurement fully describes the loading mechanism. The Neck Injury Criterion (NIC) represents the effect of relative horizontal acceleration and velocity between the head and the first thoracic vertebra. Nkm combines upper neck shear force and sagittal bending moment using normalising intercepts and therefore describes coupled force-moment loading. Head rebound velocity characterises forward head motion after seat and head-restraint interaction. These quantities are supplemented by upper-neck shear force, upper-neck tension, T1 acceleration and the time of head-restraint contact.

In the contemporaneous Euro NCAP adult-occupant assessment, each pulse could contribute up to three points. NIC, Nkm, rebound velocity, neck shear and neck tension each contributed up to 0.5 points, while a further 0.5 points was based on the better result from T1 acceleration or head-restraint contact time. Exceeding a capping limit in a principal criterion could reduce the complete pulse score to zero. The high-severity pulse also included a seatback-opening check, with a penalty for rotation of 32 degrees or more. Static geometry and worst-case geometry were then combined with the dynamic scores and scaled to the four-point whiplash contribution (Euro NCAP, 2013).

IIHS assessment quantities

The historical IIHS procedure divided the dynamic information into seat-design and dummy-response parameters. Time to head-restraint contact tested whether initially favourable geometry remained effective during deformation, while T1 acceleration reflected the ability of the seat to absorb crash energy and limit torso acceleration. Neck shear and neck tension were used to verify that early contact or energy absorption did not introduce unfavourable direct loading. A good dynamic rating required at least one seat design parameter to pass together with low neck forces (IIHS, 2020).

This difference in aggregation is important for the Fiat 500L. The IIHS values of 56 ms for head contact and 11.8 g for T1 acceleration describe two alternative seat-design paths in the IIHS rating logic. They cannot be inserted directly into the Euro NCAP score without confirming the pulse, reference time, filtering, dummy version and processing

window. Likewise, the reported IIHS shear and tension maxima do not reconstruct NIC, Nkm or rebound velocity, which require additional synchronised channels.

Whiplash software - Calculation of video-based kinematic quantities

For the video reanalysis, in-house WhiplashApp was used as a desktop motion-analysis application. The user manually selects points of interest in a video frame, after which the application tracks them through time by the Lucas-Kanade optical-flow method implemented through OpenCvSharp. The resulting trajectories are processed to calculate displacement, travelled distance, velocity, acceleration, distances between points, segment angles, angular velocity and angular acceleration, with smoothing applied to reduce tracking noise. Results are displayed as live plots on the WPF canvas and can be exported in CSV format.

In addition to video post-processing, the application integrates measurement hardware, including industrial cameras, the HBM Spider measurement system and Arduino triggers. This modular architecture supports synchronised experimental work and makes WhiplashApp applicable both to whiplash analysis and to related biomechanical and engineering test scenarios.

The official Euro NCAP recording of the 2012 Fiat 500L test was analysed in Whiplash software. Two points in the head region were tracked to obtain their image-coordinate histories and the orientation of the connecting segment, denoted as head angle A1. The same trajectories provided the input for the calculated translational and rotational quantities.

After spatial calibration, the tracked image coordinates x and y are expressed in physical units at equally spaced instants t_i, with the sampling interval Δt equal to the reciprocal of the verified frame rate. For an interior sample, translational velocity and acceleration can be estimated by central finite differences:

$$v_{x,i} = (x_{i+1} - x_{i-1})/(2\Delta t), \quad v_{y,i} = (y_{i+1} - y_{i-1})/(2\Delta t) \tag{1}$$

$$a_{x,i} = (x_{i+1} - 2x_i + x_{i-1})/\Delta t^2, \quad a_{y,i} = (y_{i+1} - 2y_i + y_{i-1})/\Delta t^2 \tag{2}$$

The corresponding velocity and acceleration magnitudes are obtained from their orthogonal components:

$$v_i = \sqrt{(v_{x,i}{}^2 + v_{y,i}{}^2)}, \quad a_i = \sqrt{(a_{x,i}{}^2 + a_{y,i}{}^2)} \tag{3}$$

The software calculates the unoriented angle between tracked vectors u and v from their scalar product. Angular velocity and angular acceleration then follow from the central-difference operator.

$$\theta_i = acos[(u_i \cdot v_i)/(|u_i||v_i|)] \tag{4}$$

$$\omega_i = (\theta_{i+1} - \theta_{i-1})/(2\Delta t) \tag{5}$$

$$\alpha_i = (\theta_{i+1} - 2\theta_i + \theta_{i-1})/\Delta t^2 \tag{6}$$

Before differentiation, the tracked x and y coordinates were smoothed by a centred moving-average filter with equal weights and a radius of six frames. The filtered position at sample i was calculated as.

$$\bar{p}_i = (1/N_i)\, \Sigma\, p_{i+k}, \quad k = -r, \dots, r \tag{7}$$

Translational speed was calculated from the filtered positions by a central difference over three frames.

$$v_i = ||\bar{p}_{i+3} - \bar{p}_{i-3}||/(6\Delta t) \tag{8}$$

Evaluation started at the fourth sample and ended three samples before the final sample; a value was recorded when both symmetric neighbours were valid. The speed series was then smoothed by a one-dimensional moving average with a radius of five samples.

Equation (4) yields an unoriented angle from 0 to 180 degrees, from which angular velocity and angular acceleration were calculated.

Table 2 Relationship between assessment parameters and video-derived quantities

Parameter	Euro NCAP	Historical IIHS	Video contribution
Head-restraint geometry	Static score	Static rating	Initial height and backset if scale and view permit
Head contact time	Alternative to T1 score	Seat-design parameter	Directly observable after time synchronisation
T1 acceleration	Alternative to contact-time score	Seat-design parameter	Can be estimated; instrumentation remains reference
Neck shear and tension	Separate criteria with caps	Dummy-response parameters	Not obtainable from video alone
NIC	Scored and capped	Not a rating parameter	Needs head and T1 kinematics with controlled differentiation
Nkm	Scored and capped	Not a rating parameter	Needs upper-neck force and moment channels
Head rebound velocity	Scored and capped	Not published for 500L	Derivable from calibrated head trajectory
Seatback opening	High-pulse modifier	Not part of published 500L values	Derivable from two or more seatback targets

RESULTS

The published vehicle-specific rear-impact results are summarised in Table 2, which places the Euro NCAP score beside the available IIHS rating and measured quantities. As Table 2 shows, the IIHS geometry is favourable: the restraint is relatively close to the back of the reference head and extends close to its top. The reported head-contact time of 56 ms indicates early engagement of the restraint within the dynamic event. IIHS also published a maximum T1 acceleration of 11.8 g, maximum neck shear of 52 N and maximum neck tension of 503 N. Equivalent channel maxima for the Euro NCAP Fiat 500L tests are not included in the public vehicle datasheet; therefore, a channel-by-channel numerical comparison is not possible from the identified sources.

Table 3 Published rear-impact results for the Fiat 500L

Quantity	Euro NCAP 2012	IIHS 2014-2020 applicability
Seat identification	500L 1.4 petrol Easy, LHD	Manual cloth seat
Overall rear-impact result	2.3 points; Marginal	Good
Dynamic rating	Included in programme score	Good
Geometry rating	No Fiat-specific values published in datasheet	Good
Backset	Not published	55 mm
Distance below top of head	Not published	26 mm
Maximum T1 acceleration	Not published	11.8 g
Head contact time	Not published	56 ms
Maximum neck shear force	Not published	52 N
Maximum neck tension	Not published	503 N

Figure 1 shows the two tracked head-region trajectories and the resulting head angle in Whiplash software. The analysed sequence is taken from the official Euro NCAP recording of the 2012 Fiat 500L test (Euro NCAP, 2012b).

Head angle A1 describes head-segment orientation. Its minimum, reached approximately 0.07 s after the start of the analysed interval, identifies motion reversal; the subsequent increase describes the extension-rebound phase. This event occurs in the same time range as the IIHS head-contact result of 56 ms, although the different time origins and test configurations prevent numerical equivalence. The comparison nevertheless demonstrates that Whiplash can locate candidate contact and rebound events directly from video and provide an independent check of timing parameters used in seat and head-restraint assessment.

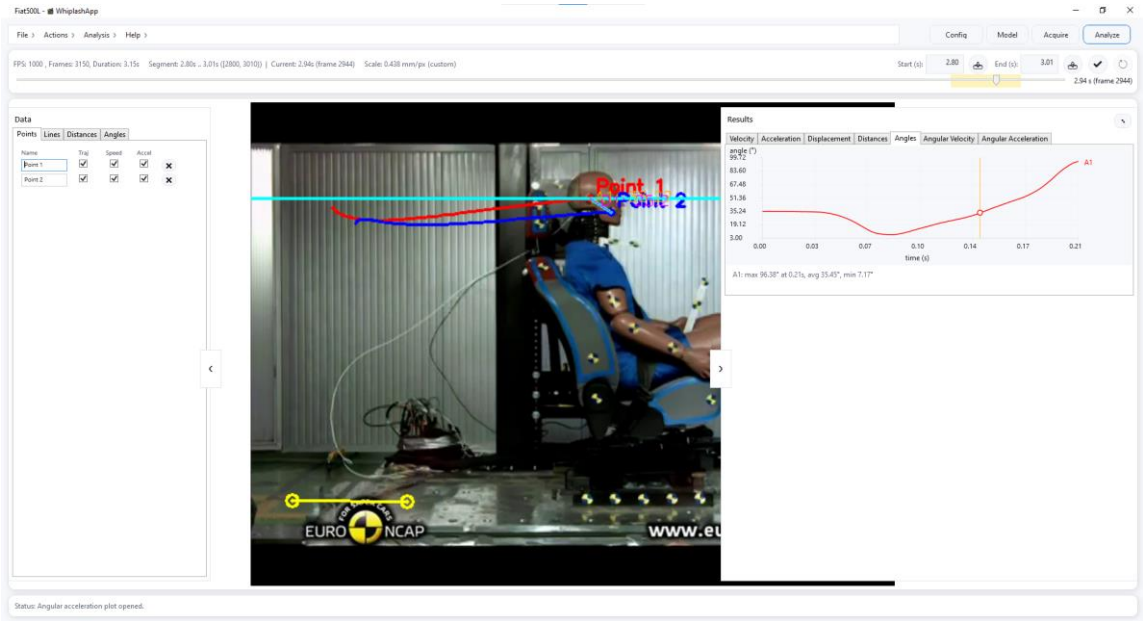

Figure 1 Fiat 500L head-point tracking and head angle in Whiplash software

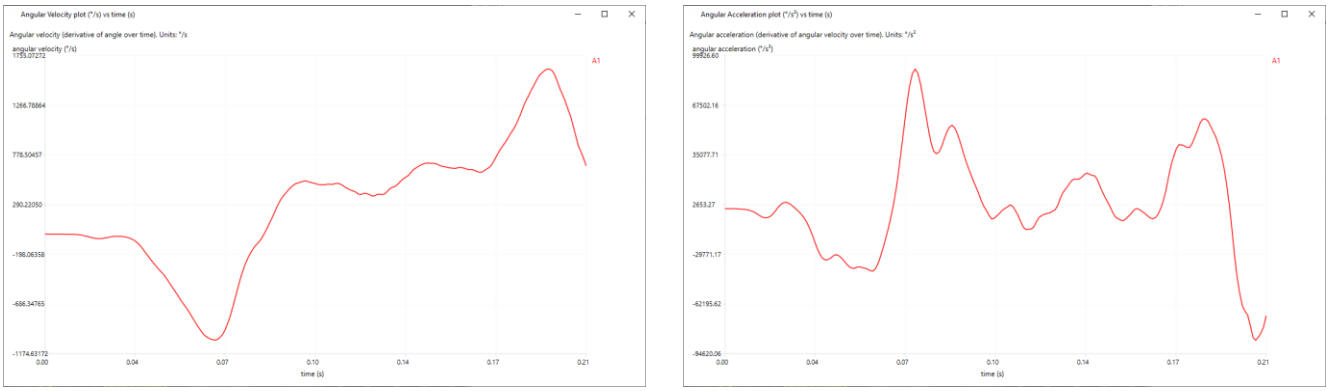

(a) (b)

Figure 2 Derived rotational kinematics of head angle: (a) angular velocity and (b) angular acceleration

As shown in Figure 2, the negative angular-velocity extremum near 0.07 s and the larger positive extremum near 0.19 s separate the initial reversal from the later rebound, while angular-acceleration peaks identify the most rapid changes in rotational response. These features complement the IIHS evidence of favourable geometry and early contact by showing how the head continues to move after engagement. They are also relevant to the Euro NCAP assessment, which additionally considers rebound and neck-loading criteria over three pulses. The pronounced rotational response cannot by itself explain the marginal Euro NCAP score, but it shows why the good IIHS result and the Euro NCAP result are not contradictory. Whiplash thus supplies a traceable kinematic layer between the test video and the protocol metrics; synchronised T1 and neck-load channels would extend the same analysis to NIC and Nkm.

DISCUSSION

The difference between the published ratings is consistent with four combined factors: pulse selection, aggregation of criteria, seat specification and prescribed adjustment. Euro NCAP used three pulses, including a 24.45 km/h high-severity test, whereas IIHS combined static geometry with one approximately 16 km/h pulse. A seat can therefore achieve early contact and low forces in the IIHS configuration while showing greater rebound, seatback rotation or relative head-torso motion under another pulse. In addition, the European Easy seat and the United States manual cloth seat may differ in foam, frame, head restraint or production revision. The Whiplash curves clarify the sequence and intensity of head rotation, but the published data do not isolate which of these factors produced the different final categories.

The analysis also defines a clear route for extending the Whiplash workflow. Direct protocol comparison requires tracking the head centre, T1, head restraint, pelvis, seatback and fixed sled references. Together with synchronised sled acceleration, upper-neck forces and bending moment, these channels would enable calculation of backset, contact time, rebound, seatback opening, NIC, Nkm and the IIHS dummy-response quantities.

Planned extensions include protocol-based time-zero alignment, signed angles, automatic contact and rebound detection, video-sensor synchronisation, uncertainty evaluation, threshold comparison and automated reporting, strengthening Whiplash as a complete and auditable environment for comparative sled-test analysis.
The interpretation is subject to the limitations of the available sources. Public Euro NCAP and IIHS records do not provide complete, equivalent time histories and refer to different markets and model years. The present curves therefore support event-level interpretation, not a numerical reconstruction of either rating or inference beyond this vehicle case.

CONCLUSIONS

The Euro NCAP and historical IIHS rear-impact assessments share the same fundamental test concept: a vehicle seat is mounted on a sled and loaded by a BioRID occupant surrogate to evaluate the combined action of the seat and head restraint. Their final ratings are nevertheless not directly interchangeable. Euro NCAP used three pulses and integrated the whiplash score into adult-occupant protection, while IIHS combined static geometry with one approximately 16 km/h dynamic pulse and reported a categorical seat rating.

For the Fiat 500L, Whiplash identifies motion reversal, extension-rebound and the intervals of greatest angular velocity and acceleration in the official Euro NCAP video. These results complement the IIHS values for geometry and early head contact and help explain why a good IIHS result can coexist with the marginal Euro NCAP score of 2.3 points. These capabilities demonstrate that Whiplash is developing in a technically sound direction and provide a strong basis for further improvement. Its traceable, extensible video-processing workflow is a promising platform not only for whiplash assessment but also for other biomechanical investigations based on automotive test recordings. Additional tracked landmarks and synchronised dummy channels would enable protocol-level calculations and direct comparison with Euro NCAP and IIHS limits.

ACKNOWLEDGMENTS

The part of this research is funded by Ministry of Science, Technological Development and Innovation of the Republic of Serbia, Contract No. 451-03-65/2024-03/200155.

REFERENCES

Euro NCAP. (2008). Euro NCAP whiplash test protocol, Version 2.8. European New Car Assessment Programme. https://www.vdrsyd.com/ancap_datasheets/xprotocol_archive/EuroNCAP/Euro-NCAP-Whiplash-test-protocol-V2.8.pdf

Euro NCAP. (2012a). Fiat 500L safety assessment datasheet. European New Car Assessment Programme. https://asset.moto.it/pricelist/auto/8a707164bd2a8632dace6f8c9f4762f5/it-euroncap-com_it_results_fiat_500l_487.pdf

Euro NCAP. (2012b). Fiat 500L - Crash Test 2012 [Video and still images]. © Euro NCAP. Reproduced with permission. Source: https://youtu.be/Jhs4QHBN2Ug?si=sjGhDOA5kj98spaK&t=112

Euro NCAP. (2013). Assessment protocol - Adult occupant protection, Version 5.5. European New Car Assessment Programme. https://cdn.euroncap.com/cars/assets/euro_ncap_assessment_protocol_aop_v55_08882358ea.pdf

Government of Serbia. (2012). Mass production of Fiat 500L in Kragujevac starts in April. https://www.srbija.gov.rs/vest/en/84138/mass-production-of-fiat-500-l-in-kragujevac-starts-in-april.php

Insurance Institute for Highway Safety. (n.d.-a). 2018 Fiat 500L: Head restraints and seats. Retrieved September 11, 2026, from https://www.iihs.org/ratings/vehicle/fiat/500l-4-door-hatchback/2018

Insurance Institute for Highway Safety. (n.d.-b). Head restraints: Discontinued test. Retrieved September 11, 2026, from https://www.iihs.org/ratings/about-our-tests/head-restraints

Insurance Institute for Highway Safety. (2023). Virtual testing will help us chart a new course in neck injury prevention. https://www.iihs.org/news/detail/virtual-testing-will-help-us-chart-a-new-course-in-neck-injury-prevention

Insurance Institute for Highway Safety. (2020). Vehicle seat/head restraint evaluation protocol, dynamic criteria, Version VI. https://www.iihs.org/media/30da9417-bb37-4247-807e-aeb5e78ba8b0/5rL9NQ/Ratings/Protocols/current/head_restraint_protocol_dynamic_vi.pdf

SECTION

E

Transport Challenges in Emerging Economies

- Safety
- Ecology & Energy
- Legislation
- Socio-economic Issues
- Personal/Public/Freight transportation
- Maintenance & Aftermarket

The 11th International Congress
Motor Vehicles & Motors 2026
Kragujevac, Serbia
October 8th - 9th, 2026

Motor Vehicles & Motors

MVM2026-033
https://doi.org/10.24874/CMVM2026.033
Original scientific paper

Janez Kopač[1]
Franci Pušavec[2]

HIGHWAY ROAD TRAPS AS HIDDEN SOURCES OF CRASH RISK

ABSTRACT: Roadworks and temporary traffic arrangements can create highway road traps: situations in which the geometry, markings, signs and expected driver behaviour no longer provide a coherent and recoverable path. This paper examines a set of observed road-trap mechanisms documented through photographs and field notes: very narrow lanes, interrupted or conflicting markings, staggered driving, overtaking pressure, short merge areas and interactions with construction vehicles. A simple geometric screening shows why a nominal 2.0 m lane can be inadequate even for a passenger vehicle. With an illustrative 1.75 m body width and 0.15 m mirror overhang on each side, the vehicle envelope is 2.05 m before any dynamic clearance is considered. The supplied case material also reports 48 crashes, collisions or contacts within two months at a 2.0/2.3 m-lane situation; this is treated as a case signal, not as an exposure-normalized crash rate. The analysis argues that such configurations are a systemic safety danger because they transfer design uncertainty to drivers at speed. Recommended measures are proactive road-safety audits, sufficient lateral and longitudinal reserve, consistent temporary traffic control, overtaking prevention, monitored merging, and data-driven intervention before serious injury occurs.

KEYWORDS: highway safety, roadworks, narrow lanes, temporary traffic control, overtaking, crash prevention

SAOBRAĆAJNE ZAMKE NA AUTOPUTEVIMA KAO SKRIVENI IZVORI RIZIKA OD UDESA

REZIME: Radovi na putu i privremene saobraćajne regulacije mogu stvoriti saobraćajne zamke na autoputu: situacije u kojima geometrija puta, oznake, znakovi i očekivano ponašanje vozača više ne pružaju koherentnu i „oprostivu" putanju. Ovaj rad razmatra skup uočenih mehanizama saobraćajnih zamki, dokumentovanih fotografijama i terenskim beleškama: veoma uske saobraćajne trake, prekinute ili međusobno suprotstavljene oznake, vožnju u zamaku, pritisak na preticanje, kratke zone za uključivanje i interakcije sa građevinskim vozilima. Jednostavna geometrijska provera pokazuje zašto nominalna traka širine 2,0 m može biti nedovoljna čak i za putnički automobil. Uz ilustrativnu širinu karoserije od 1,75 m i preklop retrovizora od 0,15 m sa svake strane, gabarit vozila iznosi 2,05 m i pre nego što se uzme u obzir bilo kakva dinamička bezbednosna rezerva. Dostavljeni materijal takođe navodi 48 sudara, kolizija ili kontakata u periodu od dva meseca na deonici sa trakom širine 2,0 m; ovaj podatak se tretira kao signal iz konkretnog slučaja, a ne kao stopa nezgoda normalizovana prema obimu saobraćaja. Analiza ukazuje da su ovakve konfiguracije sistemska bezbednosna opasnost jer prebacuju projektnu neizvesnost na vozače pri brzini kretanja. Preporučene mere obuhvataju proaktivne revizije bezbednosti puta, dovoljnu bočnu i podužnu rezervu prostora, doslednu privremenu saobraćajnu signalizaciju, sprečavanje

[1] *Janez Kopač, Faculty of Mechanical Engineering, UNM 8000 Novo Mesto, Slovenia, janez.kopac@fs.uni-lj.si*
[2] *Franci Pušavec, Faculty of Mech. Eng., UNI-LJ, Askerceva 6, 1000 Ljubljana, franci.pusavec@fs.uni-lj.si*

preticanja, nadzirano uključivanje u saobraćaj i intervenciju zasnovanu na podacima pre nego što dođe do teže povrede.

KLJUČNE REČI: bezbednost autoputeva, radovi na putu, uske saobraćajne trake, privremena saobraćajna signalizacija, preticanje, prevencija saobraćajnih nezgoda

INTRODUCTION

Highway roadworks are temporary, but the safety consequences of a temporary layout are immediate. Lane closures, shifts, crossovers and short access sections compress the space in which drivers must perceive a change, choose a manoeuvre and execute it. The problem becomes acute when passenger cars, vans, buses and heavy vehicles are expected to share a constrained path while maintaining speed and lateral separation.

This paper uses the term road trap for a roadway configuration that makes an otherwise normal manoeuvre unexpectedly unsafe. The term does not imply that a crash is caused by one careless driver. It identifies a system condition in which the available geometry, signs, markings and traffic behaviour do not provide enough time or space for ordinary human error. This interpretation is consistent with the Safe System approach, which treats road users as fallible and requires roads and operating conditions to prevent mistakes from becoming fatal or serious-injury events (World Health Organization [WHO], 2021).

The objective is to identify the main trap mechanisms visible in the supplied case material and to translate them into practical controls for road designers, road operators, contractors and enforcement agencies. The focus is on temporary and constrained highway sections, especially locations where a narrow lane is combined with a discontinuous centre line, a merge, or a strong incentive to overtake.

Recent highway-maintenance research supports treating a work zone as a planned system change rather than as an isolated lane closure. Abbasi et al. (2025a) combine maintenance condition data, traffic microsimulation and an optimization model to compare work-zone schedules using queue length and travel-time delay. Abbasi et al. (2025b) likewise show that different work-zone configurations produce different traffic impacts and should be evaluated with real traffic and geometry data before a maintenance plan is selected. These findings reinforce the central premise of this paper: a layout that is operationally possible is not automatically a safe layout.

MATERIALS AND METHODS

The analysis is a case-based safety screening. The input material consisted of ten photographs (shown further in the paper) and accompanying notes, including observations of stop control, temporary yellow markings, a 2.0 m lane, a 2.3 m alternative, staggered driving, short merging space and construction vehicles operating alongside traffic (table 1). The draft also reported 48 crashes, collisions or contacts over two months at a 2.0 m-lane situation. Because the supplied material does not provide traffic exposure, event definitions, injury outcomes or an independent crash database, the count is retained as a reported case observation and is not converted into a crash rate or generalized to all highways.

Table 1 Observed highway road-trap mechanisms and risk pathways

Observed condition	Primary risk pathway	Safety implication
2.0 m temporary lane	Vehicle envelope approaches or exceeds lane width; no recovery margin	Side contact, barrier strike or forced braking
Interrupted or conflicting marking	Driver expectation and actual path diverge	Late lane change, hesitation or encroachment
Staggered driving with overtaking pressure	Safety depends on all drivers preserving an offset	Close passing, sideswipe or head-on conflict
Short merge or entry section	High-speed entry occurs before a stable gap is available	Abrupt braking, weaving and rear-end risk
Construction vehicle beside live traffic	Large blind zones and changing lateral clearance	Loss of visibility, distraction and severe impact potential

The geometric screening compares the available lane width with a vehicle envelope that includes body width and exterior mirrors. For an illustrative passenger vehicle, the envelope is calculated as:

$$0.15\text{m}+1.75\text{m}+0.15\text{m} = 2.05\text{m} \quad (1)$$

The result is not a universal vehicle specification. It is a transparent example showing that a nominal lane width can be smaller than the width occupied by a vehicle before lateral movement, road curvature, barrier deflection, mirror clearance, wind effects and driver correction are considered. A qualitative risk chain was then applied: constraint -> perception or decision demand -> possible conflict -> control that restores time, space or predictability.

For a future validation study, the qualitative screen should be paired with two additional evidence layers. First, microsimulation can compare lane closure, carriageway deviation, merge and speed-control scenarios using local demand and geometry data (Abbasi et al., 2025a, 2025b). Second, trajectory-based surrogate safety measures can quantify lane changes, braking, lateral separation and vehicle interactions in the transition area. Wang et al. (2024) show that risk features can vary substantially between work zones, which is why the present observations are interpreted as site-specific signals rather than universal thresholds.

RESULTS OF REAL CASE INSPECTIONS

Insufficient lane width relative to the vehicle envelope

The most direct trap is a lane that is technically open but cannot provide a credible operating margin for the vehicle mix using it. In the 2.0 m example, a 2.05 m passenger-vehicle envelope already exceeds the nominal lane width. Even where the lane is increased to 2.3 m, only about 12 cm remains on each side for that illustrative vehicle if it is centred. That clearance is easily consumed by steering correction, road curvature, a barrier, a temporary delineator, a vehicle travelling off-centre, or the larger swept path of a commercial vehicle.

A narrow lane therefore changes the task from ordinary lane keeping to continuous clearance management. Drivers may slow down, move laterally, or avoid passing, but if the surrounding layout continues to signal normal highway flow, following drivers can interpret caution as unnecessary delay. The resulting pressure is a predictable operational risk, not merely a matter of driver attitude.

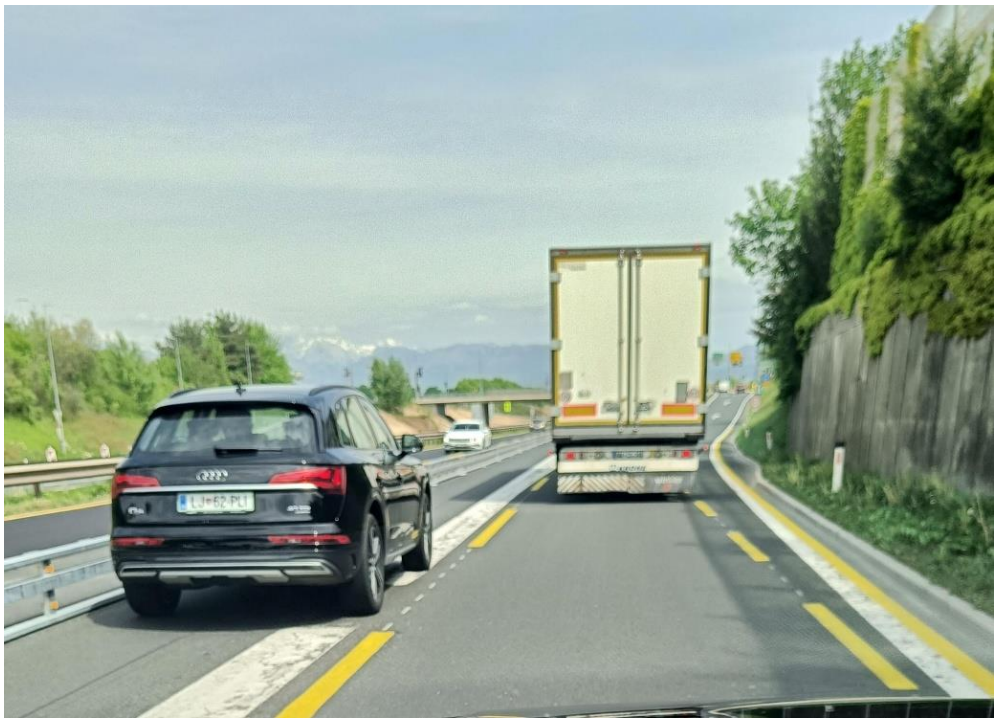

Figure 1 A 2.3m lane can be bigger that the wight of lane, but overtaking is still dangerous

Marking, signing and path-choice conflict

Temporary traffic control must tell the driver one coherent story: where the path goes, which lane is available, what speed is compatible with the path, and whether passing or crossing is permitted. The photographs show situations in which stop control, directional arrows, temporary yellow lines and lane shifts are visually close together. Each element may have a defined meaning, but the combined arrangement can still be difficult to interpret at approach speed if the path is not geometrically obvious.

A stop sign remains a stop sign, and a temporary marking remains a control device that must be followed (Figure 2). The safety issue is whether the approach gives enough advance visibility, deceleration distance and physical guidance for the driver to comply without an abrupt conflict with adjacent traffic. Work-zone guidance identifies advance warning, channelization, temporary markings and path guidance as interdependent controls rather than isolated signs (Federal Highway Administration [FHWA], 2024).

Figure 2 STOP means STOP: mandatory stop control at road works

Staggered driving and overtaking pressure

Driving in a staggered formation can create additional lateral separation when two traffic streams share a narrow section. It is, however, a behavioural operating rule rather than a substitute for geometric clearance. It works only when drivers understand the instruction, maintain a stable speed and offset, and do not attempt to recover “lost” time by overtaking. A truck or bus moving back toward the centre of the available path can remove the clearance that a following car assumed was guaranteed.

The supplied notes report 48 crashes, collisions or contacts in two months where a 2.0 m lane and an interrupted line were present (figure 3). The observation is important because it links a design condition with repeated operational conflict, but it should be validated with a formal event log before causal or statistical conclusions are made. A 2.3 m lane may be better than a 2.0 m lane, yet it does not by itself make overtaking safe when the vehicle envelopes, speeds and lateral movements remain incompatible.

Figure 3 Theoretical solution to drive in a staggered formation (RTV SLO)

Short merge areas and construction-vehicle interaction

A short acceleration or merge section creates a second type of road trap. An entering vehicle must find a gap, match speed and join a lane that may already be narrowed by barriers or work equipment. If the usable length is too short, the driver must either brake sharply, force a merge, or continue alongside traffic without a stable position. The same problem appears when an access point is placed immediately before a lane shift or a taper.

Construction vehicles introduce a moving obstruction whose width, turning path and blind zones change over time (figure 4). A road layout that is marginally tolerable for two passenger cars may be unsafe when a truck, bus or equipment carrier is present. The safe solution is to design and operate the work zone for the largest expected vehicle and the worst credible interaction, not for the average private car.

Figure 4 Reduced lane width caused by exceptional transport o heavy-duty equipment

Additional visual case evidence

Figure 5 presents the temporary yellow line used to guide traffic through the work zone. The marking is a key part of the driver's path guidance; when it is faded, interrupted, or inconsistent with the barrier line, drivers can interpret the usable lane differently. This creates a road trap because late correction occurs close to the conflict point, where braking or lateral movement can affect adjacent vehicles and workers

Figure 5 Temporary yellow lines are critical at road works

Figure 6 shows a lane with insufficient lateral clearance for the vehicle using the road. The available width leaves little recovery space when a heavy vehicle meets a passenger car or when drivers maintain a safe offset from barriers. The condition should therefore be treated as a geometric safety defect, not simply as a demand for greater driver attention.

Figure 6 To narrow lines in combination to wider vehicles

Figure 7 illustrates the particularly critical combination of a 2.0 m temporary lane and an interrupted separation line. The lane width approaches or falls below the envelope required by larger vehicles, while the marking interruption weakens the intended path. Together, these features can produce hesitation, encroachment, forced braking and side contact; the reported concentration of incidents makes this configuration a priority for inspection.

Figure 7 A 2.0 m lane and an interrupted line between two traffic streams

Figure 8 shows passenger cars and larger vehicles sharing a constrained section, with differences in vehicle width, speed and sight distance. These differences make a nominally available lane width less meaningful in practice. Overtaking or close following can consume the remaining lateral reserve and increase the likelihood of a sideswipe or barrier conflict.

Figure 8 **"**Squeezed" high width vehicle on two narrowed lines

Figure 9 documents the behavioural pressure to overtake in a constrained work-zone section. The instruction or expectation to go and overtake is unsafe when opposing or adjacent clearance cannot be guaranteed. Overtaking should be prohibited or physically prevented until a sufficiently long, visible and separated passing opportunity is provided.

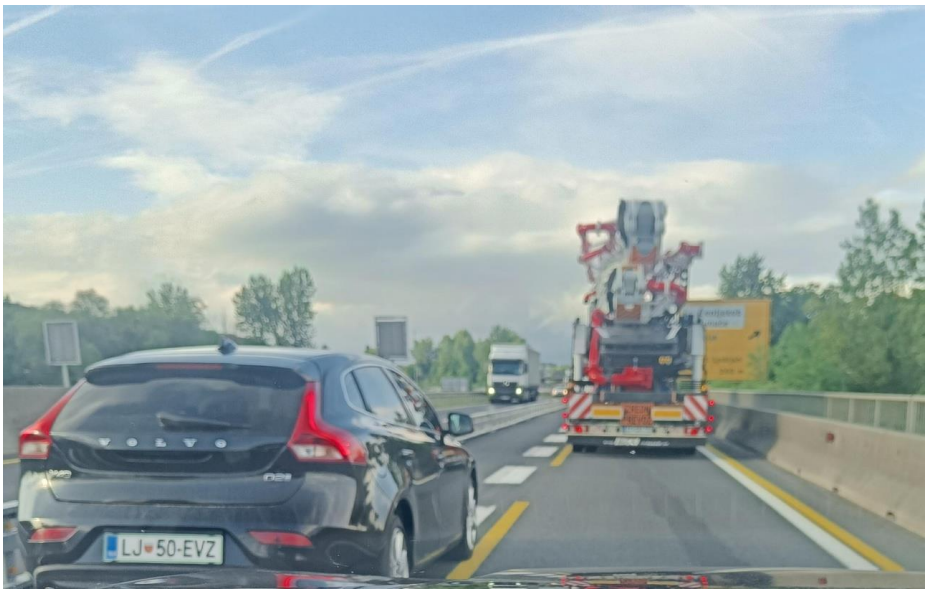

Figure 9 Normally expected situation for overtaking even though it is unsafe

Figure 10 shows a merge or entry section that is too short for a stable joining manoeuvre from a side connection. Drivers must select a gap, adjust speed and align with the temporary path over limited distance, often while

passing barriers or work vehicles. The resulting abrupt braking and weaving can create rear-end and side conflicts, so the access should be lengthened, relocated or closed during the work phase.

Figure 10 A merge lane that is too short for entry from a side connection

MODELING OF THE TRAFFIC IMPACT OF SAFETY IN MAINTENANCE WORK ZONES

Before the maintenance road regime is changed, the proposed layout should be represented and tested in a model that combines road and bridge geometry, vehicle envelopes, work-zone stages, traffic demand and control strategy. A partial lane closure, crossover, merge or speed restriction changes both the available path through the infrastructure and the interaction among vehicles. The decision should therefore be based on expected operating states and measurable risk indicators, not only on whether traffic can physically pass.

As example (Abbasi et al., 2025a, 2025b), reproduced here as Figure 11, provides the geometric basis for this modeling step. It shows the cross-section of a widened bridge, including the emergency lane, four traffic lanes, the relationship between the new and old bridge portions, and two span configurations. The figure demonstrates that a maintenance regime cannot be specified from nominal lane width alone: the location of the closure, the distribution of structural elements and the remaining emergency and traffic lanes must be represented together. Structural and traffic models should therefore be run before barriers are moved or traffic is transferred to a new path.

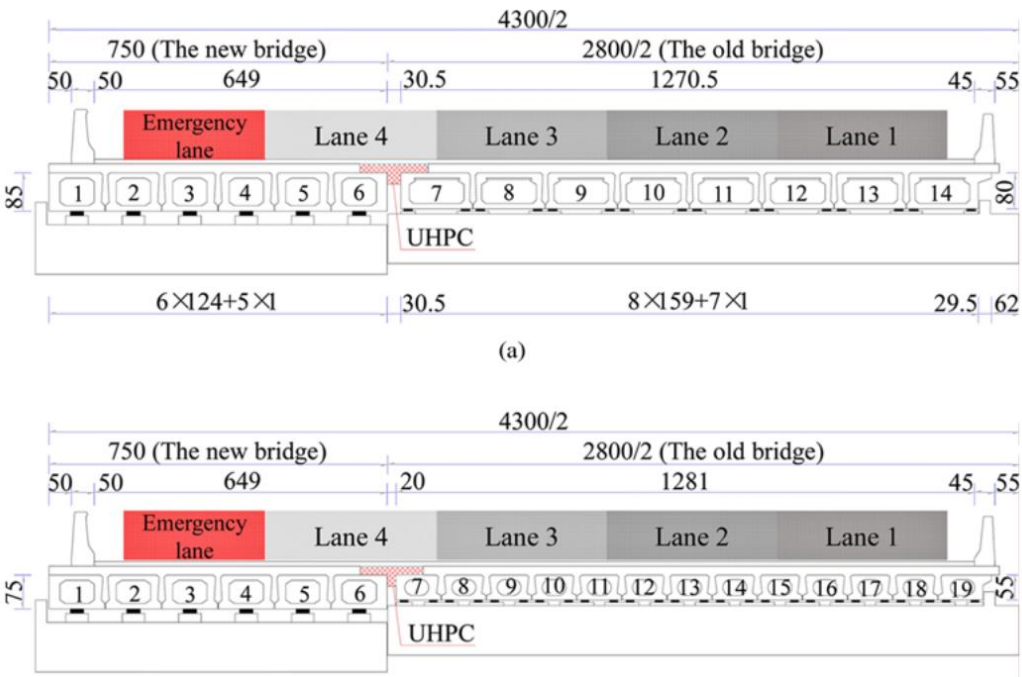

Figure 11 Mid-span cross-section of the widened bridge with different span lengths (source paper Fig. 1; Zhou et al., 2022)

Additionally, the functional stages should be included in the work-zone model, e.i. advance warning, transition, buffer, activity and termination areas (figure12). These stages create different driver tasks and different opportunities for conflict. A maintenance plan should test whether warning distance, taper length, buffer space and recovery distance remain adequate for the expected speeds and vehicle mix.

As a proof, why the model should represent interactions between the target vehicle, surrounding vehicles, traffic cones and barriers rather than treating the lane as an empty geometric strip, is shown in figure 13. The improved work-zone crash-risk field converts those interactions into a risk measure that can be compared across alternative layouts and operating regimes before field implementation. Corresponding output needed for a decision is shown in figure 14: a spatial heatmap of crash risk for alternative work-zone cases. Such a result can identify where risk concentrates, whether it shifts between lanes, and whether a proposed maintenance regime creates a new conflict at the transition area. Modeling should therefore precede the change, while field observation and trajectory data should be used afterward to verify that the selected regime behaves as predicted.

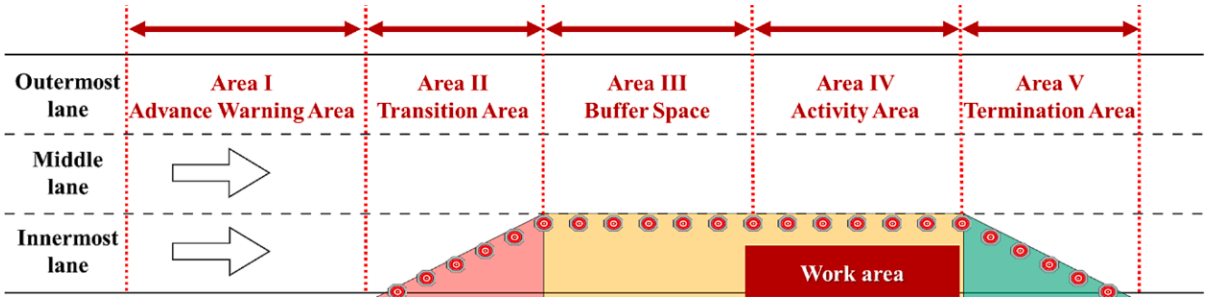

Figure 12 Components of a work zone on a one-way three-lane road (source paper Fig. 1; Wang et al., 2024).

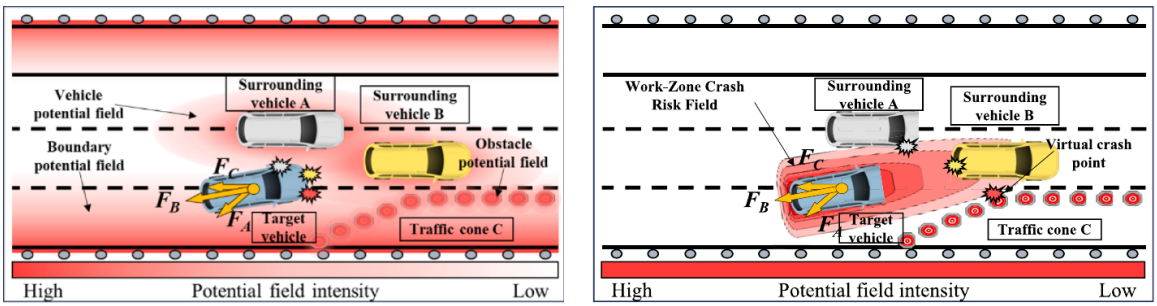

Figure 13 Conceptual diagram of improvements to the safety potential field (source paper Fig. 4; Wang et al., 2024)

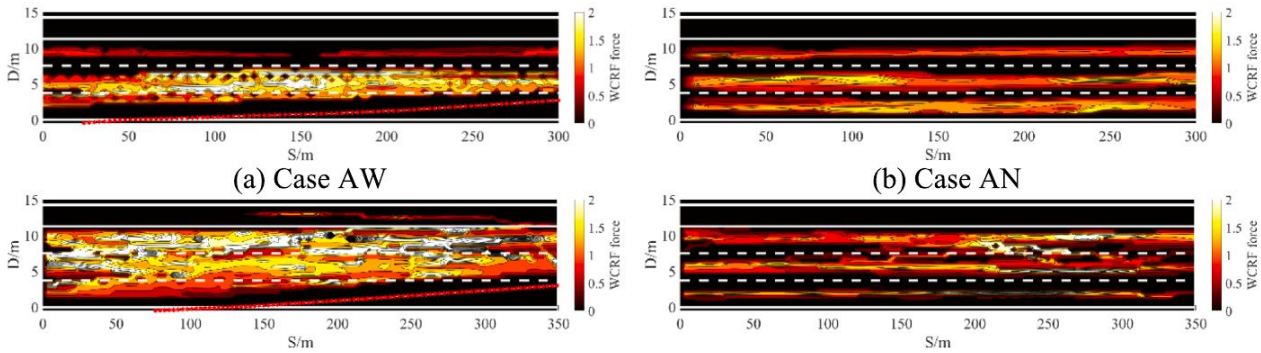

Figure 14 Spatial distribution heatmap of crash risk (source paper Fig. 10; Wang et al. 2024)

DISCUSSION

The attached studies broaden the meaning of a highway road trap. Abbasi et al. (2025a, 2025b) demonstrate that maintenance decisions influence both network performance and the immediate operating conditions around a work zone. Their results support evaluating queue formation, delay, transport demand, work duration and alternative configurations before work begins. This is particularly relevant to short merge sections and lane shifts, where a local geometric constraint can propagate upstream as braking, lane changing and unstable gaps.

Wang et al. (2024) provide an empirical crash-risk perspective for transition areas. Their trajectory-based analysis identifies elevated risk associated with lane-changing activity, traffic flow and speed, while also showing that the

important features differ across work zones. The implication for the present case is that a reported cluster of contacts should be followed by targeted observation of the transition area, not only by a generic warning to slow down. It also supports using precursor events, such as forced lane changes and insufficient lateral distance, as operational safety indicators.

The consequences can extend beyond vehicle conflict. Zhou et al. (2022) show that partial lane closures on widened bridges can redistribute traffic loads and reduce structural safety reserves; in their case, speed control alone did not guarantee safety. Tamasi (2026) therefore provides a useful network-level complement: planned renewal should consider alternative roads, traffic and weather time windows, high-fidelity simulation, user communication and a formal safety-management process. Road-trap prevention should consequently cover the road, the structure, the network and the information given to users.

The common feature of the observed traps is the loss of reserve. A driver needs reserve in time to detect and decide, reserve in space to maintain separation, and reserve in predictability so that other road users behave as expected. Narrow lanes consume spatial reserve; interrupted markings consume predictability; short merges consume time; overtaking consumes all three. When these constraints are combined, a small steering deviation can become a sideswipe, a barrier impact or a sudden braking conflict.

This is why the issue should be treated as a serious safety danger for drivers and road workers. The European Commission recommends proactive, feature-based network safety assessment that includes lane width, junction design, roadside layout and potential conflicts, in addition to reactive analysis based on recorded crashes (European Commission, 2023). The reported case count should therefore trigger an inspection and redesign process, not only a campaign asking drivers to be more careful.

The practical implication is a hierarchy of controls (Table 2). First, remove or reduce the geometric conflict. Second, make the intended path obvious and physically channelled. Third, reduce speed and prevent incompatible manoeuvres. Fourth, monitor actual behaviour and revise the arrangement when near misses or repeated contacts appear. Enforcement and driver education are useful, but they are weaker controls when the road itself creates an unavoidable conflict.

Table 2 Recommended control hierarchy for highway road traps

Control level	Action before or during operation	Verification indicator
Geometry	Check the complete vehicle envelope, swept path and lateral reserve for cars, vans, buses and HGVs.	No expected vehicle requires mirror, barrier or opposing-lane intrusion.
Path guidance	Align signs, temporary markings, barriers, tapers and arrows into one continuous path.	Drivers can identify the path and required lane well before the conflict point.
Manoeuvre control	Prohibit overtaking where clearance is not guaranteed; provide stable stagger or alternate one-way control where needed.	Observed passing and lane encroachment are rare and non-conflicting.
Speed and merge	Use advance speed management and provide sufficient taper, acceleration and merge length; close unsafe access points.	Approach speeds and merge speeds are compatible with available distance.
Monitoring	Record traffic volume, vehicle class and trajectories; monitor lane changes, speed, gaps and near misses using video or AI support.	Controls are changed when repeated conflicts, precursor events or threshold conditions occur (Wang et al., 2024).

CONCLUSIONS

Highway road traps are serious safety dangers because they can make safe driving physically difficult or behaviourally unstable. The supplied case material shows how a narrow temporary lane, an interrupted line, staggered driving, overtaking pressure, short merge space and construction traffic can interact. The geometric example is simple but decisive: a 2.0 m lane cannot provide a meaningful lateral margin to an illustrative 2.05 m passenger-vehicle envelope, while a 2.3 m lane remains sensitive to vehicle size and driver behaviour.

The reported 48 crashes, collisions or contacts in two months should be treated as an urgent case signal requiring validation, inspection and corrective action. The most effective prevention is to restore time, space and predictability through layout and operational changes before relying on enforcement or driver skill. A highway work zone is safe only when ordinary drivers, including cautious and imperfect drivers, can understand the path and recover from small errors without entering a conflict.

Additional visual case evidence

The following actions should be applied as a coordinated package rather than as isolated additions:

- Set a minimum operational envelope before opening each work-zone phase. Measure the usable width between barriers, not only the painted lane width, and include mirrors, vehicle sway and the swept path of heavy vehicles.
- Use continuous, high-contrast and mutually consistent temporary markings. Where a lane shift is required, repeat the advance warning, channelization and speed message early enough for a driver to decelerate and choose a path without an emergency manoeuvre.
- Do not rely on driver courtesy to create clearance. If passing cannot be performed with a positive lateral margin, physically or operationally prevent it through lane separation, one-way alternating control, a solid no-passing arrangement or a suitable diversion.
- Review every side-road and ramp connection as part of the work-zone design. If the acceleration or merge length is too short for the actual speed environment, move the merge upstream, extend the usable distance, reduce the approach speed or close the connection temporarily.
- Use road-safety audits and inspections before traffic is moved into a new phase and after any material change. A short observation period with video review can reveal close passes and lane encroachments before they appear in official crash statistics. Where data are available, record lane-change counts, speed distributions, longitudinal and lateral gaps, and surrogate measures such as time to collision or deceleration rate; trajectory-based risk models can then be calibrated to the specific work zone (Wang et al., 2024).
- Treat AI-based video detection as a monitoring aid, not as a replacement for geometry and traffic control. Useful indicators include repeated line crossing, close lateral passing, hard braking, wrong-way movement and queues reaching the previous decision point.
- Schedule the intervention using traffic demand, weather, work duration and available alternative routes. Compare the expected queue, delay and safety consequences of each feasible configuration and communicate major changes to road users and local authorities (Abbasi et al., 2025a, 2025b; Tamasi, 2026).

REFERENCES

Abbasi, M., Bilal, M. T., Consilvio, A., Giglio, D., Sacco, N., & Lopez Arevalo, P. (2025a). On minimizing the impact on traffic of maintenance work zones in a highway network. *Transportation Engineering*, 21, 100381. https://doi.org/10.1016/j.treng.2025.100381

Abbasi, M., Bilal, M. T., Consilvio, A., & Giglio, D. (2025b). On planning highway maintenance considering the impact on traffic flow due to different work zone configurations. *Transportation Research Procedia*, 86, 508-515. https://doi.org/10.1016/j.trpro.2025.04.064

AMZS. (2025, May). *Key road-safety studies*. AMZS revija.

European Commission. (2023, November 20). Road infrastructure guidelines: Network-wide road safety assessment and proactive road safety tools. https://road-safety.transport.ec.europa.eu/eu-road-safety-policy/priorities/infrastructure/road-infrastructure-guidelines_en

Federal Highway Administration. (2023, May 9). Work zones. U.S. Department of Transportation. https://highways.dot.gov/safety/other/work-zone

Federal Highway Administration. (2024, October 21). Implementing the proven safety countermeasures in work zones informational guide. U.S. Department of Transportation. https://highways.dot.gov/safety/proven-safety-countermeasures/implementing-proven-safety-countermeasures-work-zones

Pušavec, F., & Kopač, J. (2026). Large reserve in time and space as a key factor in preventing traffic accidents. *Conference contribution presented at Savetovanje Zlatibor 2026*.

RTV Slovenija. (2024, November). Television feature on traffic and road problems. TV1.

Tamasi, G. (2026). Beyond the work zone: What is next? Towards a new era of user-centered highway construction and renewal. *Procedia Structural Integrity*, 84, 725-732. https://doi.org/10.1016/j.prostr.2026.06.093

Wang, B., Chen, T., Zhang, C., Wong, Y. D., Zhang, H., & Zhou, Y. (2024). Toward safer highway work zones: An empirical analysis of crash risks using improved safety potential field and machine learning techniques. *Accident Analysis and Prevention*, 194, 107361. https://doi.org/10.1016/j.aap.2023.107361

World Health Organization. (2021, October 20). Global plan for the Decade of Action for Road Safety 2021-2030. https://www.who.int/publications/m/item/global-plan-for-the-decade-of-action-for-road-safety-2021-2030/

Zhou, J., Lu, Z., & Zhou, Z. (2022). Structural safety assessment and traffic control strategies of widened highway bridges under maintenance works requiring partial lane closure. *KSCE Journal of Civil Engineering*, 26(4), 1846-1857. https://doi.org/10.1007/s12205-022-0775-0

The 11th International Congress
Motor Vehicles & Motors 2026
Kragujevac, Serbia
October 8th - 9th, 2026

Motor Vehicles & Motors

MVM2026-044
https://doi.org/10.24874/CMVM2026.044
Original scientific paper

Nadica Stojanović[1]
Ali Belhocine[2]
Ivan Grujić[3]
Željko Đurić[4]
Suzana Petrović Savić[5]
Oday I. Abdullah[6,7,8]

THE IMPACT OF "DRUNK BUSTERS" ON THE ADEQUATE PERFORMANCE OF TASKS

ABSTRACT: Driving under the influence of alcohol has become a major issue in modern society, significantly contributing to the occurrence of traffic accidents. Traffic accidents caused by drivers under the influence of alcohol often result in more severe consequences. In the first part of the study, data obtained from the Traffic Safety Agency were analyzed, with alcohol impairment identified as a contributing factor to traffic accidents. Based on the conducted analysis, it was determined that 6.61% of all traffic accidents in 2025 occurred as a result of driving under the influence of alcohol. In addition, an experimental study was conducted involving twelve participants. Initially, the participants completed a short questionnaire, after which they performed a series of predefined tasks while wearing alcohol impairment simulation goggles. Of the participants involved in the experiment, 42% reported having driven under the influence of alcohol, while only one participant had previously been sanctioned by the police. During the experiment, participants completed four different tasks while wearing alcohol impairment simulation goggles. The goggles simulated three levels of intoxication: 0.06–0.08 BAC, 0.08–0.15 BAC, and 0.15–0.25 BAC. For the majority of participants, the most challenging tasks were performed while wearing goggles simulating a blood alcohol concentration of 0.08–0.15 BAC. Since the participants were required to evaluate the difficulty of each task, the results suggested that their self-assessments were not entirely objective. Therefore, it can be concluded that future studies should focus on observing participants' behavior and movement patterns during task performance, as well as measuring the time required to complete each assigned task.

[1] *Nadica Stojanovič, Faculty of Engineering, University of Kragujevac, 6 SestreJanjic STR., 34000 Kragujevac, Serbia, nadica.stojanovic@kg.ac.rs, https://orcid.org/0000-0002-4199-0587*
[2] *Ali Belhocine, Department of Mechanical Engineering, University Mustapha Stambouli of Mascara, 29000 Mascara, Algeria, al.belhocine@yahoo.fr, https://orcid.org/0000-0001-7957-7571*
[3] *Ivan Grujić, Faculty of Engineering, University of Kragujevac, 6 SestreJanjic STR., 34000 Kragujevac, Serbia, ivan.grujic@kg.ac.rs, https://orcid.org/0000-0003-0572-1205*
[4] *Željko Đurić, University of Banja Luka, Faculty of Mechanical Engineering, Bulevar vojvode Stepe Stepanovica 71, 78000 Banja Luka, Republic of Srpska, zeljko.djuric@mf.unibl.org, https://orcid.org/0009-0001-8573-6038*
[5] *Suzana Petrovic Savic, Faculty of Engineering University of Kragujevac, Sestre Janjic 6, 34000 Kragujevac, Serbia, petrovic.savic@kg.ac.rs, https://orcid.org/0000-0002-5629-6221*
[6] *Oday I. Abdullah, College of Engineering, Al-Naji University, Baghdad, Iraq, oday.abdullah@coeng.uobaghdad.edu.iq, https://orcid.org/0000-0001-5450-021X*
[7] *Department of Energy Engineering, College of Engineering, University of Baghdad, Iraq*
[8] *Department of Mechanics, Al-Farabi Kazakh National University, Almaty, Kazakhstan*

KEYWORDS: traffic safety, alcohol, traffic accident, Drunk Busters

UTICAJ PRIMENE "PIJANIH NAOČARA" NA ADEKVATNO IZVRŠAVANJE RADNJI

REZIME: Danas je vožnja pod dejstvom alkohola postala glavni problem savremenog društva, a što uzrokuje nastanak saobraćajnih nezgoda. Posledice saobraćajnih nezgoda koje je prouzrokovao vozač pod dejstvom alkohola imaju teže posledice. U prvom delu istraživanju, analizirani su podaci Agencije za bezbednost saobraćaja gde je kao uzročnik pojave saobraćajne nezgode uzet uticaj alkohola. Na osnovu izvršene analize dolazi se do zaključka da se 2025. godine 6,61% saobraćajnih nezgoda dogodilo upravo zbog vožnje pod dejstvom alkohola. Takođe, u radu je izvršeno ispitivanje dvanaest ispitanika koji su prvo popunjavali kratak upitnik, a zatim izvršili definisane radnje u kojima su nosili „pijane naočare". 42% ispitanika koji je učestvovao u eksperimentu je vozilo pod dejstvom alkohola, dok je samo jedan bio kažnjen od strane policije. Tokom eksperimenta ispitanici su izvršavali četiri različita zadatka i tokom svakog zadatka su nosili „pijane naočare". Prvo su nosili naočara koje se simulirale nivo pijanstva 0,06 to 0,08 BAC, zatim 0,08 to 0,15 BAC i na kraju 0,15 to 0,25 BAC. Gotovo svim ispitanicima je bilo najteže da izvrše zadatak dok su nosili naočare koje simuliraju nivo pijanstva 0,08 to 0,15 BAC. Kako su ispitanici trebali da ocene koliko im je zapravo bio težak da izvrše svaki zadatak, došlo se do zaključka da nisu bili iskreni. Dolazi se do zaključka da pri budućim istraživanjima treba gledati ponašanje/kretanje pri izvršenju zadatka, kao i da se meri vreme koliko je potrebno da izvrše zadati zadatak.

KLJUČNE REČI: bezbednost saobraćaja, alkohol, saobraćajna nezgoda, pijane naočare

INTRODUCTION

Driving under the influence of alcohol is one of the greatest concerns in road traffic safety. Operating a vehicle while intoxicated can result in severe injuries to road users and may even lead to fatal outcomes. Research indicates that the likelihood of severe injuries and fatalities is approximately 3.5 times higher in traffic accidents involving at least one participant under the influence of alcohol (Ogden, E. J. D. and Moskowitz, H. 2004). This issue is observed worldwide (Chan, Y. S. and Tsai, W. D. 2024). Behavioral changes caused by alcohol consumption significantly increase the risk of traffic accidents. Accidents involving an intoxicated participant are also frequently associated with speeding violations (Johnson, S. 2025; Soner, S. et al. 2022). According to data from the World Health Organization, between 16% and 21% of road traffic fatalities are attributed to driving under the influence of alcohol (World Health Organization, 2023).

The same amount of alcohol does not affect every individual in the same way, as its effects depend on a person's psychophysical condition (Sayette, M. A. 2017). To accurately assess these effects, participants would need to consume an identical amount of alcohol, after which their behavior and responses in characteristic situations could be evaluated. However, conducting such experiments in real traffic conditions is neither safe nor recommended. Therefore, investigations of this kind can only be performed using driving simulators. Yu, Y. et al. (2025) examined 30 young and middle-aged participants who were divided into two groups: a group that consumed alcohol (BAC (blood alcohol concentration): 50 mg/100 ml) and a control group that did not consume alcohol. The authors concluded that participants who had consumed alcohol exhibited more aggressive driving behavior and paid less attention to events occurring on their left and right sides, indicating a reduced level of situational awareness.

Alcohol intoxication impairs brain function (Ogden, E. J. D. and Moskowitz, H. 2004) and adversely affects safe driving performance (Jongen, S. et al. 2014). Consequently, drivers under the influence of alcohol may overestimate their driving abilities and thereby increase the likelihood of causing a traffic crash (Zhao, Y. et al. 2024). Furthermore, it has been established that driving performance deteriorates when the blood alcohol concentration reaches 0.07%, even though drivers are often unaware of this decline in their abilities (Garrisson, H. et al. 2022). Despite strict regulations and penalties imposed for driving under the influence of alcohol, alcohol-impaired drivers continue to be involved in a substantial proportion of traffic accidents worldwide (World Health Organization, 2023).

Driving under the influence of alcohol remains a highly relevant topic in the field of road traffic safety. Traffic accidents involving at least one intoxicated participant attract considerable attention from the World Health Organization, as well as from researchers whose work focuses on traffic safety. The key questions addressed in this study, and which require further investigation, are as follows:

- What is the severity of traffic accidents involving at least one participant under the influence of alcohol?
- What is the number of traffic accidents involving at least one participant under the influence of alcohol in the territory of the Republic of Serbia?

- How do participants behave when exposed to simulations of different levels of alcohol intoxication?
- What measures can be implemented to reduce the incidence and consequences of driving under the influence of alcohol?

The introductory section presents the severity of injuries sustained in traffic accidents involving at least one participant under the influence of alcohol, thereby addressing the first research question. The third chapter provides an overview of the situation in the Republic of Serbia with regard to the number of traffic accidents involving at least one alcohol-impaired participant. The effects of alcohol on human performance are examined in the fourth chapter, which describes an experiment conducted with a group of participants using Drunk Busters. Drunk Busters are goggles which simulate the visual and cognitive effects of drunkenness. This is followed by a discussion of measures aimed at reducing both the occurrence and consequences of driving under the influence of alcohol, thereby addressing the fourth research question. Finally, the paper concludes with the key findings and conclusions derived from the conducted research.

RESEARCH METHODOLOGY

The methods employed in this study can be classified into three categories: statistical, survey-based, and experimental methods. The statistical method was applied to analyze traffic accidents in the Republic of Serbia involving at least one participant under the influence of alcohol. In addition, statistical techniques were used to process and evaluate the results obtained from the experimental phase of the research. The survey-based research was conducted through the administration of a structured questionnaire consisting of pre-designed questions.

Statistical method

In this study, descriptive statistics were employed to analyze the state of road traffic safety in the Republic of Serbia during the period from 2021 to 2025. In addition, descriptive statistical methods were used to process and interpret the data obtained from both the survey and experimental investigations.

Survey method

The survey study was conducted to obtain a clearer understanding of the participants involved in the experimental research. Specifically, it was designed to collect information regarding their driving experience, including the number of years they had held a driver's license, as well as their previous experience with driving under the influence of alcohol. In addition, the survey examined whether participants had ever been sanctioned by the relevant authorities for alcohol-impaired driving.

Experimental method

The experimental investigation consisted of the performance of four tasks, and that:

1. Following a predefined path (Figure 1a);
2. Inserting a key into a lock (Figure 1b);
3. Colour-matching task (Figure 1c), and
4. Carrying a tray with glasses (Figure 1d).

(a) (b) (c) (d)

Figure 1 The tasks

The first task required participants to follow a predefined path, which, in the context of driving, corresponds to maintaining the vehicle within its designated lane without crossing into the opposing traffic lane. The second task can be associated with unlocking a vehicle door or inserting the key into the ignition to start the engine. The subsequent task involved matching colors, which, in practical driving situations, corresponds to recognizing and correctly interpreting traffic signal lights. The final task defined in this study required participants to carry a tray with glasses from one table to another, necessitating that they independently determine an appropriate path to the adjacent table

while ensuring that the glasses remained securely on the tray. In the context of driving, this task may be associated with the simultaneous execution of multiple actions that a driver must perform accurately and without error under real-world driving conditions.

The characteristics of Drunk Busters

During the performance of these tasks, the participants wore Drunk Busters, which simulate the effects of alcohol intoxication (Figure 2). The simulated levels of intoxication provided by the Drunk Busters were as follows:

- 0.06 to 0.08 BAC – blue Drunk Busters;
- 0.08 to 0.15 BAC – black Drunk Busters, and
- 0.15 to 0.25 BAC – red Drunk Busters.

The tasks were performed sequentially under different simulated levels of intoxication. Participants first completed all tasks while wearing Drunk Busters simulating the lowest level of intoxication, followed by the medium level, and finally the highest level of simulated intoxication.

Figure 2 Drunk Busters

The Drunk Busters (0.06 to 0.08 BAC) simulate the effects of a relatively low blood alcohol concentration. In addition, they reproduce the impact of this level of alcohol impairment under twilight conditions, thereby further increasing the difficulty of performing various tasks. The main characteristics of these goggles include:

- Tinted lenses that provide participants with a realistic simulation of nighttime driving conditions.
- Distortion of depth perception, causing distant objects to appear much closer than they actually are.
- A narrowed field of vision.

The Drunk Busters simulating a blood alcohol concentration of 0.08 to 0.15 BAC produce the following effects in participants:

- Double vision and impaired ability to accurately judge the distance of objects.
- Increased reaction time.
- Difficulty walking, particularly while maintaining a straight path.
- Reduced judgment and decision-making ability.

The Drunk Busters simulating a blood alcohol concentration of 0.15 to 0.25 BAC also replicate alcohol impairment under conditions of reduced visibility (twilight). They can be considered a combination of the characteristics exhibited by the previous two models. Their primary features include:

- Double vision accompanied by impaired spatial perception and inaccurate estimation of object location.
- Simulation of tunnel vision through a reduction in peripheral vision.
- Increased difficulty walking, particularly along a straight line.
- Disorientation and impaired decision-making ability.

ANALYSIS OF ROAD TRAFFIC SAFETY IN THE REPUBLIC OF SERBIA DURING THE PERIOD FROM 2021 TO 2025

This chapter presents an analysis of road traffic safety in the Republic of Serbia during the period from 2021 to 2025, with a particular focus on drivers under the influence of alcohol. The analysis was conducted from two perspectives: the occurrence of traffic accidents and the resulting consequences. The input data used in this study were obtained from the Integrated Database of Road Traffic Safety Characteristics maintained by the Road Traffic Safety Agency of the Republic of Serbia.

Analysis of Road Traffic Safety from the aspect of the number of traffic accidents

The analysis of traffic accidents involving at least one driver under the influence of alcohol is presented in Figure 3 for the period from 2021 to 2025. With regard to alcohol-impaired driving as one of the contributing factors to traffic

accidents, it can be observed that the highest number of fatalities during the analyzed period was recorded in 2022, followed by a subsequent decline in the following years. Similarly, the number of traffic accidents involving injured persons also showed a decreasing trend over the observed period. In contrast, the number of traffic accidents resulting solely in property damage was highest in 2021 and then decreased continuously until 2024. However, in 2025, the number of property-damage-only accidents increased compared to 2024, although it remained slightly lower than the level recorded in 2023.

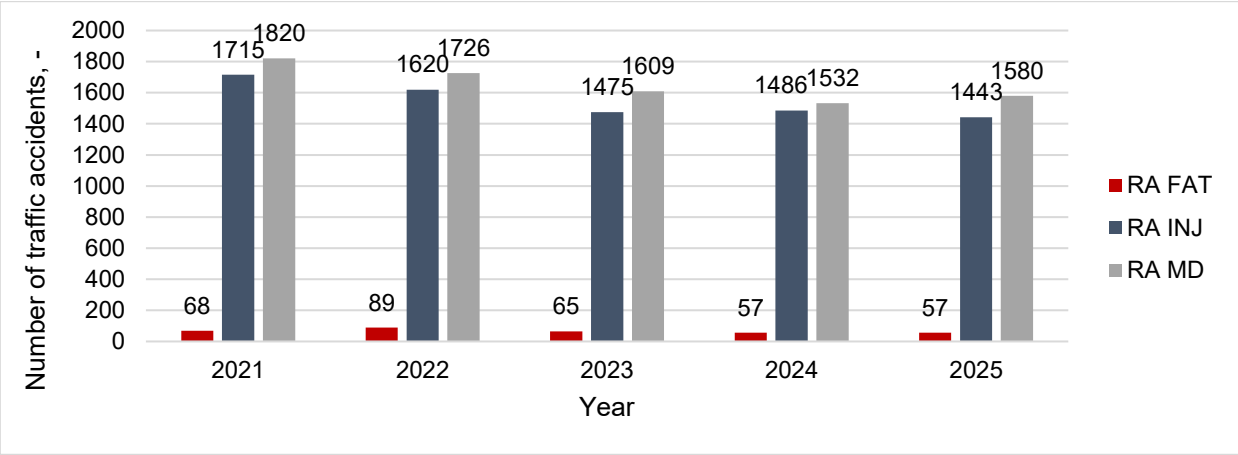

Figure 3 The number of traffic accidents with RA FAT, RA INJ and RA MD in period from 2021. to 2025.

Considering only the year 2025, the total number of fatal traffic accidents amounted to 862. The proportion of fatal traffic accidents involving at least one participant under the influence of alcohol accounted for 6.61% of the total number of fatal accidents. The total number of traffic accidents involving injured persons was 21,026, of which 6.86% involved at least one alcohol-impaired participant. Furthermore, the total number of property-damage-only traffic accidents was 25,372, with accidents involving at least one participant under the influence of alcohol representing 6.23% of this category. When considering the total number of traffic accidents regardless of severity, the proportion of accidents in which alcohol was identified as a contributing factor amounted to 6.52%.

Analysis of road traffic safety from the aspect of accident consequences

It is particularly important to determine the number of casualties involved in traffic accidents in order to gain a clearer understanding of the consequences suffered by road users. The number of fatalities during the analyzed period, classified according to the location at which death occurred, is presented in Figure 4. The highest number of fatalities occurred at the scene of the traffic crash. The second largest category consisted of individuals who succumbed to their injuries within 30 days following the crash. The smallest number of fatalities was recorded among individuals who died while being transported to the hospital as a result of injuries sustained in the traffic crash.

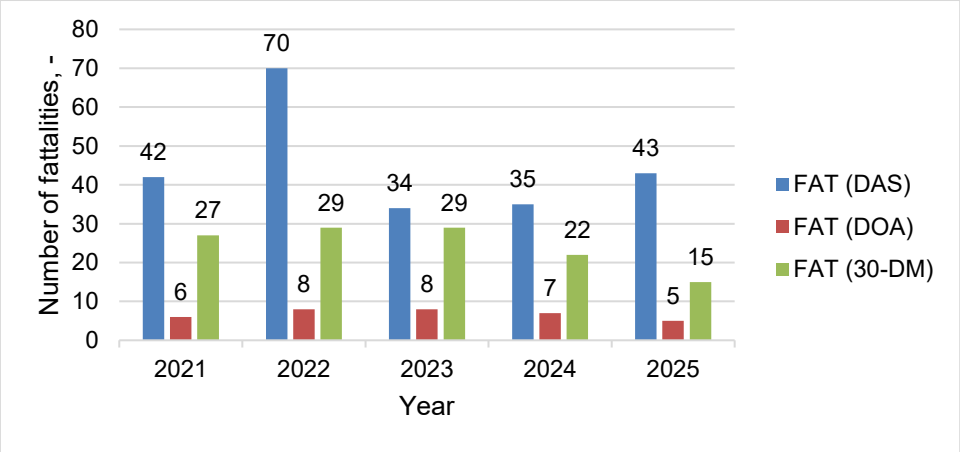

Figure 4 Number of fatalities in period from 2021. to 2025.

The total number of injured persons by injury severity category during the period from 2021 to 2025 is presented in Figure 5. The lowest number of injured persons was recorded in 2025. Furthermore, it can be observed that the overall number of injured persons generally decreased throughout the analyzed period, despite a slight increase in 2024 compared to 2023. A similar trend can be observed for the number of persons who sustained minor injuries, which also showed an overall decline during the study period. In contrast, the number of persons who sustained serious injuries exhibited greater variability. The highest number of seriously injured persons was recorded in 2024, while the lowest number was observed in 2023.

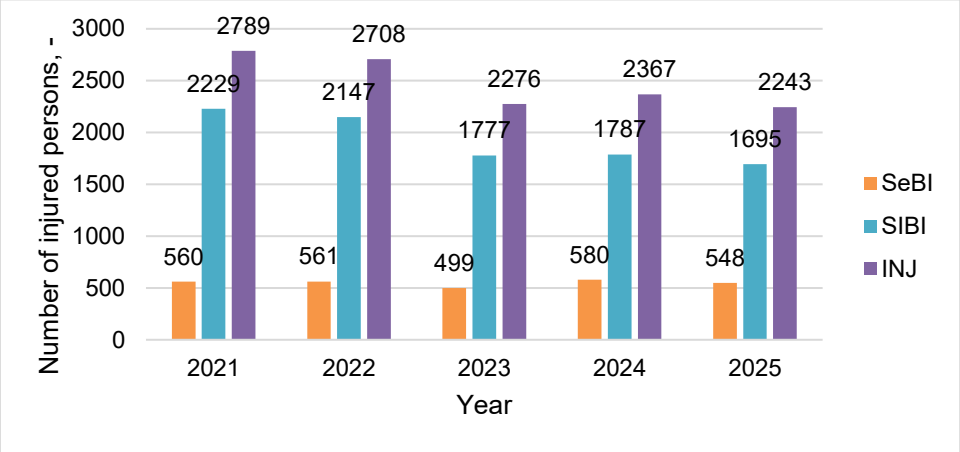

Figure 5 Number of injured persons in traffic accidents in period from 2021. to 2025.

RESULTS AND DISCUSSION OF THE SURVEY RESEARCH

The survey conducted as part of this study aimed to provide a better understanding of the characteristics of the participant group. The participants consisted of third- and fourth-year undergraduate students enrolled in academic study programs. The sample comprised twelve participants in total. One of the essential eligibility criteria for participation in the study was possession of a valid driver's license. The first survey question addressed the gender distribution of the participants. The study included seven female participants and five male participants. The following question concerned the length of time participants had held a driver's license. Given that the sample consisted of university students, it was expected that most participants would have less than five years of driving experience, as shown in Figure 6.

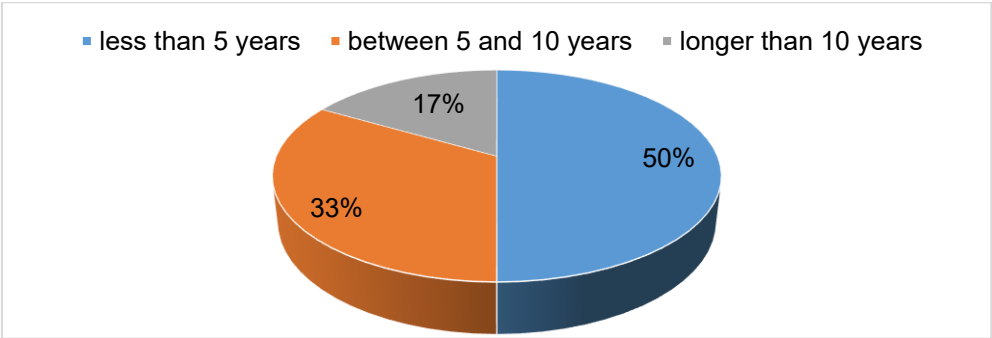

Figure 6 Duration of driving license possession

However, the length of time an individual has possessed a driver's license does not necessarily reflect the extent of their driving activity. For this reason, participants were asked the following question: “How many kilometers do you drive annually as a driver?” The largest proportion of participants (54%) reported driving between 1,000 km and 10,000 km per year, as shown in Figure 7. In contrast, 23% of participants reported driving more than 10,000 km annually, while the remaining 23% drove less than 1,000 km per year.

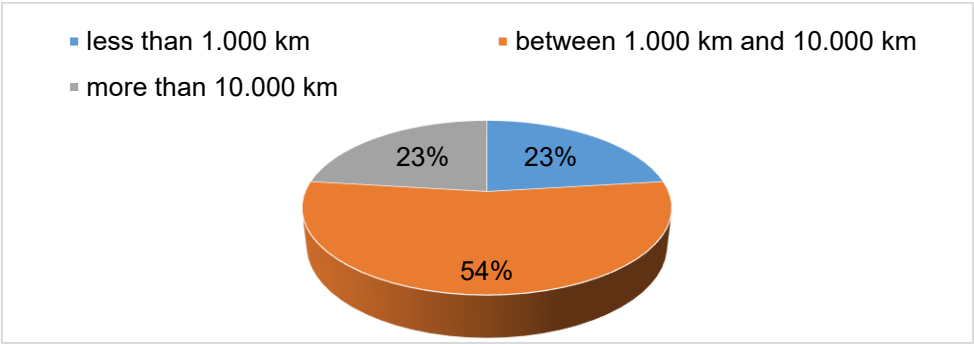

Figure 7 The average number of kilometres per year

As the core objective of this research is to examine the effects of alcohol on drivers, one of the essential survey questions was: “Have you ever driven under the influence of alcohol?” A total of 42% of participants responded affirmatively. This proportion of positive responses is particularly concerning, as it indicates that a substantial share

of the surveyed drivers had previously engaged in alcohol-impaired driving. The final survey question asked participants: “Have you ever been penalized by the police for driving under the influence of alcohol?” Only one participant provided an affirmative response to this question. This finding suggests that, although a considerable proportion of respondents admitted to driving under the influence of alcohol, only a small number had been sanctioned by law enforcement authorities for such behavior.

PRESENTATION AND ANALYSIS OF THE EXPERIMENTALLY OBTAINED RESULTS

The experiment consisted of four phases, which were described in the Research Methodology section. Participants were required to evaluate each task using a rating scale ranging from 1 (impossible to perform) to 5 (easy to perform). In studies of this nature, it is often expected that participants may not provide entirely objective self-assessments. Therefore, in addition to collecting subjective ratings, researchers recorded participants’ behavior during task performance, including observations of their movements, walking patterns, and overall task execution. To ensure participant anonymity while enabling data tracking, each participant was assigned a unique identification code. The code consisted of two components: a letter and a number. The letter indicated the participant’s gender, with F representing female participants and M representing male participants. The numerical component corresponded to the order in which the participant performed the experimental tasks.

Following a predefined path

The task consisted of picking up the glasses from a table, putting them on, turning around, walking to the starting point of the designated path, and then following the path itself. After completing the task, the participants evaluated its level of difficulty, as presented in Table 1. A number of participants did not provide entirely objective assessments of their performance. For example, participant F2 walked along the path very cautiously, taking small steps and maintaining a stooped posture. Participant F4 had to remove the Drunk Busters in order to reach the starting point of the path. Participant M1 walked with a wide stance to maintain balance and avoid falling. An interesting case was participant M3, who rated the task of following the path while wearing Drunk Busters simulating a BAC of 0.06–0.08 as easy to perform. However, he misjudged the distance to a door and collided with it. Several situations observed and recorded during the experiment are illustrated in Figure 8.

Table 1 Participants’ evaluation of following a predefined path according to the applied Drunk Busters intoxication level

	0.06 to 0.08 BAC	0.08 to 0.15 BAC	0.15 to 0.25 BAC
F1	2	1	1
F2	3	3	3
F3	3	2	3
F4	4	3	4
F5	4	4	4
F6	3	2	3
F7	3	2	2
M1	3	3	2
M2	3	3	1
M3	5	3	3
M4	3	2	3
M5	4	2	3

Figure 8 Participants’ behavior while following the predefined path

Inserting a key into a lock

The task of inserting a key into a lock consisted of four steps: putting on the glasses, picking up the key from the table, walking to the door, and inserting the key into the lock. Since the participants first put on the Drunk Busters, the next step was to locate the key on the table. Although they generally knew where the key had been placed, they were unable to determine its exact position visually and therefore searched for it by feeling around the table until they found it. Before attempting to insert the key into the lock, many participants examined the key by touch because they could not clearly perceive its orientation. Participants who initially failed to do so often experienced several unsuccessful attempts at inserting the key and subsequently resorted to feeling the key to determine its correct orientation. Most participants required a considerable amount of time to insert the key into the lock, and some even crouched down in an attempt to make the task easier. In addition to feeling the key, participants frequently felt around the lock itself in order to identify the correct insertion point. The participants' evaluations of the difficulty of this task are presented in Table 2, while Figure 9 illustrates selected situations observed during the experiment.

Table 2 Participants' evaluation of the key-insertion task according to the applied Drunk Busters intoxication level

	0.06 to 0.08 BAC	0.08 to 0.15 BAC	0.15 to 0.25 BAC
F1	1	1	1
F2	2	2	3
F3	3	3	2
F4	5	4	4
F5	4	4	4
F6	3	3	3
F7	3	2	2
M1	4	4	3
M2	2	2	1
M3	3	2	3
M4	1	3	1
M5	5	2	2

Figure 9 Inserting a key into a lock

Color-matching task

The colour-matching task required participants to place-coloured balls into bowls of the corresponding colour. At the beginning of the task, participants stood with their backs turned to the balls and bowls. While a participant was putting on the Drunk Busters, the experimenter rearranged the positions of both the balls and the bowls. Table 3 presents the participants' evaluations of the task difficulty according to the applied level of simulated intoxication. Several noteworthy observations were recorded during the experiment. Participant M1, while wearing Drunk Busters simulating a BAC of 0.08–0.15, placed the orange ball into the red bowl and the red ball into the orange bowl. A similar error was made by participant M4 while wearing Drunk Busters simulating a BAC of 0.15–0.25. Furthermore, participant M2, while wearing the BAC 0.15–0.25 glasses, missed the bowl entirely and placed the ball beside it. Missing the bowl at least once was a common occurrence among all participants. Because the Drunk Busters created a perception of double vision, participants frequently misjudged the location of the objects when attempting to grasp a ball. To compensate for this effect, many participants extended their hands in front of them and visually assessed their hand position in an attempt to estimate its actual location. Figure 10 illustrates participants performing the defined task during the experiment.

Table 3 Participants' evaluation of the color-matching task according to the applied intoxication level of the Drunk Busters

	0.06 to 0.08 BAC	0.08 to 0.15 BAC	0.15 to 0.25 BAC
F1	5	2	2
F2	5	4	3
F3	5	4	3
F4	5	4	4
F5	5	5	5
F6	4	3	3
F7	4	2	2
M1	5	3	3
M2	5	4	1
M3	5	5	5
M4	5	3	2
M5	5	4	3

Figure 10 Color-matching task

Tray-carrying

The tray-carrying task required participants to transport a tray with glasses from one table to another. The task consisted of the following steps: putting on the glasses, picking up the tray from the table, carrying the tray with one hand to a table located on the opposite side of the room, and placing the tray with the glasses on the table. Table 4 presents the participants' evaluations of task difficulty according to the applied level of intoxication simulated by the Drunk Busters. Participant M3, while wearing Drunk Busters simulating a BAC of 0.06–0.08, dropped the glasses while placing the tray on the table. In contrast, participant M2, while wearing Drunk Busters simulating a BAC of 0.15–0.25, dropped the glasses during the walking phase of the task. Participant F2, while wearing Drunk Busters simulating a BAC of 0.08–0.15, nearly missed the table and almost dropped the tray onto the floor. To avoid this, the participant moved a hand around until the table was located by touch and then successfully placed the tray on it. Participant M4, while wearing Drunk Busters simulating a BAC of 0.08–0.15, misjudged the distance to the table and collided with it. Furthermore, due to feelings of instability and reduced confidence, several participants carried the tray using both hands instead of the prescribed single-hand technique.

Table 4 Participants' evaluation of the tray-carrying task according to the applied intoxication level of the Drunk Busters

	0.06 to 0.08 BAC	0.08 to 0.15 BAC	0.15 to 0.25 BAC
F1	1	3	2
F2	4	4	3
F3	4	3	3
F4	4	3	4
F5	5	4	4
F6	4	3	4
F7	2	2	2
M1	5	4	3
M2	4	2	1
M3	3	4	5
M4	5	3	3
M5	5	4	3

Figure 11 Tray-carrying

CORRELATION ANALYSIS

To determine the relationship between two variables, a correlation coefficient is employed. Correlation analysis provides information regarding both the existence and the strength of the relationship between variables. In order to examine the relationship between driving experience and task performance under the different Drunk Busters conditions, as well as the relationship between participants' sex and task performance under the same conditions, both the Pearson correlation coefficient and the Spearman rank correlation coefficient were applied. Table 5 presents the interpretation thresholds for correlation coefficients according to the recommendations of Cohen, J. (1988).

Table 5 The analysis of the values of correlation coefficients (Cohen, J. 1988)

Pearson	Correlation	Spearman
<0.09	Very weak	<0.09
0.10÷0.29	Weak	0.10÷0.19
0.30÷0.49	Moderate	0.20÷0.29
≥0.50	Strong	≥0.30

Since the assessment of task difficulty was based on participants' subjective evaluations, these results should be interpreted with caution. As discussed previously, observations of participants' behavior during the experiment indicated that these evaluations were not entirely objective. Nevertheless, considering the interpretation of effect sizes in psychology and the social sciences, Funder D. C. and Ozer, D. J. (2019) proposed guidelines that may be regarded as relatively stringent. They argue that correlation coefficients ranging from 0.10 to 0.30 are often both empirically supported and theoretically meaningful, while emphasizing that statistical significance remains an essential criterion for interpretation.

The results of the Pearson and Spearman correlation (Table 6 and 7) analyses indicate that there is no statistically significant relationship between driving experience, or participants' sex, and successful task performance under the different levels of simulated alcohol impairment (0.06 to 0.08 BAC, 0.08 to 0.15 BAC, and 0.15 to 0.25 BAC). Specifically, in all analyzed cases, the significance values exceeded the threshold of 0.05 ($p > 0.05$), indicating that the observed correlations were not statistically significant and that no systematic relationship between the examined variables could be confirmed.

Table 6 Correlation analysis (Pearson)

		Driving experience		Gender	
		Correlation coefficient	Sig. (2-tailed)	Correlation coefficient	Sig. (2-tailed)
Following a predefined path	0.06 to 0.08 BAC	-0.400	0.198	0.302	0.339
	0.08 to 0.15 BAC	0.000	1.000	0.111	0.732
	0.15 to 0.25 BAC	-0.078	0.809	-0.340	0.280
Inserting a key into a lock	0.06 to 0.08 BAC	0.000	1.000	0.000	1.000
	0.08 to 0.15 BAC	0.198	0.538	-0.060	0.854
	0.15 to 0.25 BAC	0.287	0.365	-0.339	0.280
Colour-matching task	0.06 to 0.08 BAC	0.100	0.757	0.378	0.226
	0.08 to 0.15 BAC	-0.254	0.426	0.110	0.734
	0.15 to 0.25 BAC	0.119	0.713	-0.191	0.553
Carrying a tray with goggles	0.06 to 0.08 BAC	-0.154	0.634	0.395	0.204
	0.08 to 0.15 BAC	0.310	0.327	0.176	0.585
	0.15 to 0.25 BAC	0.036	0.912	-0.068	0.834

Examination of the Pearson correlation coefficients revealed that most of the obtained values fell within the categories of very weak or weak correlations, whereas a smaller number of cases exhibited moderate negative or positive associations. The most pronounced negative correlation was observed between driving experience and the lane-following task under the simulated blood alcohol concentration of 0.06 to 0.08 BAC ($r = -0.400$), whereas the most pronounced positive correlation was identified between participants' sex and the tray-carrying task under the same level of simulated alcohol impairment ($r = -0.395$), Table 6. However, neither correlation reached the threshold of statistical significance ($p = 0.198$ and $p = 0.204$), and therefore neither can be considered reliable evidence of a true association between the examined variables.

The Spearman correlation analysis yielded results that were largely consistent with those obtained from the Pearson correlation analysis, Tabeles 6 and 7. The correlation coefficients generally indicated very weak to moderate associations, with the highest values observed for the relationship between participants' sex and the tray-carrying task under the simulated blood alcohol concentration of 0.06 to 0.08 BAC ($\rho = 0.414$), as well as between driving experience and the key-insertion task under the simulated blood alcohol concentration of 0.15–0.25 BAC ($\rho = 0.395$). However, neither of these correlations reached statistical significance ($p > 0.05$), further confirming the absence of a reliable monotonic relationship between the analyzed variables.

Table 7 Correlation analysis (Spearman)

		Driving experience		Gender	
		Correlation coefficient	Sig. (2-tailed)	Correlation coefficient	Sig. (2-tailed)
Following a predefined path	0.06 to 0.08 BAC	-0.309	0.328	0.248	0.437
	0.08 to 0.15 BAC	0.132	0.683	0.132	0.683
	0.15 to 0.25 BAC	0.040	0.902	-0.359	0.251
Inserting a key into a lock	0.06 to 0.08 BAC	0.070	0.828	0.000	1.000
	0.08 to 0.15 BAC	0.257	0.420	-0.077	0.811
	0.15 to 0.25 BAC	0.395	0.204	-0.329	0.296
Colour-matching task	0.06 to 0.08 BAC	0.071	0.827	0.378	0.226
	0.08 to 0.15 BAC	-0.178	0.580	0.076	0.814
	0.15 to 0.25 BAC	0.209	0.515	-0.180	0.575
Carrying a tray with goggles	0.06 to 0.08 BAC	0.004	0.990	0.414	0.181
	0.08 to 0.15 BAC	0.297	0.349	0.212	0.509
	0.15 to 0.25 BAC	0.112	0.729	-0.077	0812

Although some of the correlation coefficients were classified as moderate according to the criteria proposed by Cohen, J. (1988), the absence of statistical significance warrants caution in their interpretation. Furthermore, given that the assessments of task difficulty were based on participants' subjective evaluations, the results should be regarded as indicative rather than as definitive evidence of an underlying relationship. In accordance with the recommendations of Funder D. C. and Ozer, D. J. (2019), correlations of relatively small magnitude may still be theoretically meaningful; however, only when they are supported by statistical significance, which was not the case in the present study.

Based on the obtained results, it can be concluded that neither driving experience nor participants' sex constituted factors that significantly influenced the successful performance of the analyzed psychomotor tasks under the different levels of simulated alcohol impairment. These findings suggest that the effect of simulated alcohol impairment on participants' performance was relatively independent of these two demographic characteristics, indicating that participants of different sexes and varying levels of driving experience exhibited similar patterns of task performance.

MEASURES FOR REDUCING THE NUMBER OF TRAFFIC ACCIDENTS

One of the simplest ways to prevent driving under the influence of alcohol is the installation of passive alcohol detection systems. These devices measure alcohol vapors within the vehicle cabin. Their purpose is to prevent alcohol-impaired driving; when the detected alcohol vapor concentration exceeds a predefined threshold, the vehicle is automatically disabled (Lukas, S. E. et al., 2017). Such systems are relatively inexpensive because they do not require costly components (Spaho, E. et al., 2024). Despite their low cost, laboratory testing has demonstrated that they provide a high level of measurement accuracy (Romero-González, J. S. et al., 2019). Another approach to preventing alcohol-impaired driving involves the installation of systems that measure the alcohol concentration in a driver's breath. If the measured concentration exceeds the permitted limit, the system prevents the driver from starting the vehicle (Gasparesc, G. 2018). However, these systems have a significant limitation: they are unable to distinguish whether the detected alcohol originates from the driver, the front-seat passenger, or another occupant of the vehicle (Kai, L. et al., 2024).

Another approach to preventing driving under the influence of alcohol involves the use of intelligent monitoring systems capable of detecting whether a driver has consumed alcohol. To ensure reliable detection, these systems collect and analyze multiple types of information simultaneously. The system consists of sensors and cameras, as illustrated in Figure 12. The sensor is installed on the steering wheel, while the cameras are positioned above the driver (Xu, Y. et al. 2026). In this configuration, the system continuously monitors the driver's breath alcohol concentration, facial expressions, and heart rate. The collected data are subsequently processed using advanced analytical and intelligent technologies, enabling the system to determine whether the driver is likely to be under the influence of alcohol and to initiate appropriate preventive measures when necessary.

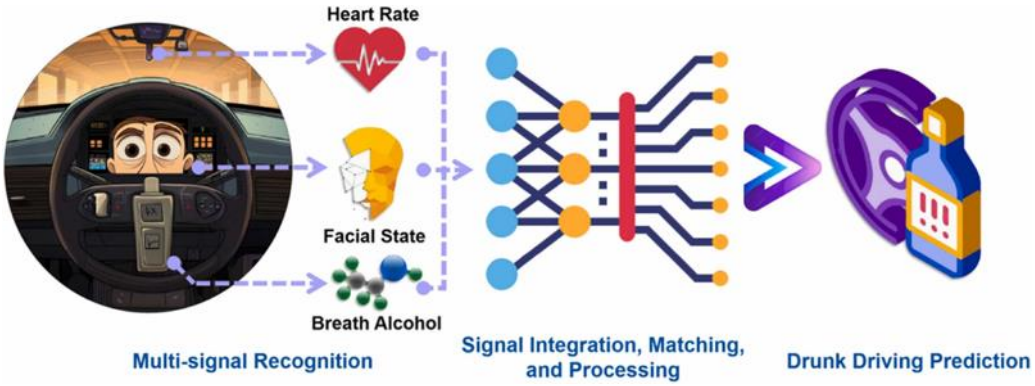

Figure 12 Intelligent system for detecting driving under the influence of alcohol (Xu et al., 2026)

CONCLUSIONS

The impact of alcohol on road traffic safety remains a highly relevant research topic. Drivers operating vehicles under the influence of alcohol tend to exhibit more aggressive behavior and are more likely to be involved in accidents that result in severe consequences. Based on the conducted research, the following conclusions can be drawn:

- Driving under the influence of alcohol is a widespread problem observed throughout the world.
- Previous studies have shown that the likelihood of severe injuries and fatalities is approximately 3.5 times higher in traffic accidents involving at least one participant under the influence of alcohol.
- The same amount of alcohol does not affect all individuals in the same manner.
- Drivers operating vehicles under the influence of alcohol tend to overestimate their driving abilities.
- From the perspective of crash occurrence, the number of traffic accidents involving injured persons decreased during the period from 2022 to 2025, with the lowest number recorded in 2025. The number of fatalities was also lowest in 2025.
- The number of property-damage-only traffic accidents in 2025 was higher than in 2024 but slightly lower than in 2023.
- In 2025, traffic accidents involving fatalities and at least one alcohol-impaired participant accounted for 6.61% of all fatal accidents.
- From the perspective of crash consequences, the highest number of fatalities occurred at the crash scene, followed by deaths occurring within 30 days after the crash, while the lowest number of fatalities occurred during transportation to a hospital.
- Among all injured persons, the largest proportion sustained minor injuries.
- The survey results indicated that 42% of participants had driven under the influence of alcohol at least once, which is a highly concerning finding. However, only one participant reported having been sanctioned by the police for this offense.
- Based on the experimental investigation and the participants' evaluations of task difficulty, it can be concluded that not all participants provided objective assessments when their ratings were compared with their actual performance during the defined tasks.
- Most participants reported that the most difficult tasks were those performed while wearing Drunk Busters simulating a BAC of 0.08–0.15.
- Correlation analysis demonstrated that there was no statistically significant relationship between driving experience or participants' sex and task performance.
- All newly manufactured vehicles should be equipped with systems capable of monitoring alcohol vapors in the driver's breath and preventing vehicle operation when alcohol is detected above the permitted threshold.
- Since not all drivers can afford new vehicles equipped with such technologies, greater emphasis should be placed on raising public awareness of the dangers of driving under the influence of alcohol and the severity of its consequences through educational programs, public campaigns, advertisements, surveys, and similar initiatives.

Future studies should not rely on participants' subjective evaluations of task difficulty. Instead, the experimenter should assess and document the manner in which each task is performed, providing a more objective evaluation of participant performance. Furthermore, if the key-insertion task is included in future experiments, the time required to successfully insert the key into the lock should also be measured. Incorporating task completion time as an additional performance indicator would provide a more comprehensive assessment of the effects of alcohol impairment on participants' motor and cognitive abilities.

ACKNOWLEDGMENTS

This research has been supported by the Ministry of Science, Technological Development and Innovation (Contract No. 451-03-34/2026-03/200107).

REFERENCES

Chan, Y. S., Tsai, W. D. (2024). The opportunistic behaviors under drunk driving policies in Taiwan: A study with population-based data. *Transportation Research Part F: Traffic Psychology and Behaviour*, 107, 848-860. https://doi.org/10.1016/j.trf.2024.09.018

Cohen, J. (1988). *Statistical power analysis for the behavioral sciences*. 2nd edition, Hillsdale, New York, ISBN 0-8058-0283-5.

Funder, D.C., Ozer, D.J. (2019). Evaluating effect size in psychological research: Sense and nonsense. *Advances in Methods and Practices in Psychological Science*, 2(2), 156–168. https://doi.org/10.1177/2515245919847202

Garrisson, H., Scholey, A., Verster, J. C., Shiferaw, B., Benson, S. (2022). Effects of alcohol intoxication on driving performance, confidence in driving ability, and psychomotor function: a randomized, double-blind, placebo-controlled study. *Psychopharmacology*, 239, 3893-3902. https://doi.org/10.1007/s00213-022-06260-z

Gasparesc, G. (2018). Driver alcohol detection system based on virtual instrumentation. *IFAC-PapersOnLine*, 51(6), 502-507. https://doi.org/10.1016/j.ifacol.2018.07.110

Johnson, M. B. (2025). Drunk driving has a speeding problem. *Traffic Injury Prevention*, 26(7), 755-759. https://doi.org/10.1080/15389588.2025.2456942

Jongen, S., Vuurman, E., Ramaekers, J., Vermeeren, A. (2014). Alcohol calibration of tests measuring skills related to car driving. *Psychopharmacology*, 231(12), 2435–2447. https://doi.org/10.1007/s00213-013-3408-y

Liu, K., Min, L., Zhihui, Z., Kewei, Z., Song, Y. (2024). Rational design and application of breath sensors for healthcare monitoring. ACS Sensors, 10(1), 15-32. https://doi.org/10.1021/acssensors.4c02313

Lukas, S. E., Zaouk, A., Ryan, E., McNeil, J., Shepherd, J., Willis, M., Dalal, N. Schwartz, K. (2017, June 5-8). Driver alcohol detection system for safety (dadss)-preliminary human testing results. 25th International Technical Conference on the Enhanced Safety of Vehicles (ESV). Detroit Michigan, United States. https://trid.trb.org/View/1485122

Ogden, E. J. D., Moskowitz, H. (2004). Effects of alcohol and other drugs on driver performance. *Traffic Injury Prevention* 5(3), 185-198. https://doi.org/10.1080/15389580490465201

Romero-González, J. S., Luna-García, H., Celaya-Padilla, J. M., Gamboa-Rosales, H., Galván-Tejada, J. I., Galván-Tejada, C. E., Arceo-Olague, J. G., Solís-Robles, R. (2019). Alcohol detection in a car's cab using MQ3 and first approaches to sensing: laboratory tests. In: P., Ruiz & V. Agredo-Delgado, (Eds.), *Human-computer interaction* (pp. 73-84). Springer, Cham. https://doi.org/10.1007/978-3-030-37386-3_6

Sayette, M. A. (2017). The effects of alcohol on emotion in social drinkers. *Behaviour Research and Therapy*, 88, 76-89. https://doi.org/10.1016/j.brat.2016.06.005

Soner, S., Litoriya, R., Pandey, P. (2022). Integrating blockchain technology with IOT and ml to avoid road crashes caused by drunk driving. *Wireless Personal Communications*, 125, 3001-3018. https://doi.org/10.1007/s11277-022-09695-x

Spaho, E., Jaupi, O., Cala, A. (2024). Implementation of a low-cost and intelligent driver monitoring system for engine locking in the presence of alcohol detection or drowsiness in drivers. In: L. Barolli, (Eds.) *Advances in Internet, Data & Web Technologies* (pp. 443-451). Springer, Cham. https://doi.org/10.1007/978-3-031-53555-0_42

World Health Organization. (2023). Global status report on road safety 2018. World Health Organ. https://iris.who.int/server/api/core/bitstreams/46275f9f-ef66-4892-8ddd-a496ef8c1b74/content

Xu, Y., Yhang, Y., Cao, L., Xiang, S., Jin, H. (2026). An intelligent in-vehicle drunk driving prediction system based on e-nose assisted multi-signal fusion technology. *Sensors and Actuators B: Chemical*, 447(2), 138852. https://doi.org/10.1016/j.snb.2025.138852

Yu, Z., Zhao, X., Jiang, K., Deng, Q., Yu, S., Huang, Z., Chen, J., Chen, Y., Zhai, L. (2025). Analyzing the effects of human error on automated driving takeovers. *Cognition, Technology & Work*, 27, 215-239. https://doi.org/10.1007/s10111-025-00794-w

Zhao, Y., Jiang, K., Yu, Z., Huang, Z. (2024). Emotion-matched in-vehicle assistants: an exploration in regulating drivers' incidental emotions and enhancing takeover performance and situational awareness. *Cognition, Technology & Work*, 26, 225-245. https://doi.org/10.1007/s10111-024-00756-8

The 11th International Congress
Motor Vehicles & Motors 2026
Kragujevac, Serbia
October 8th - 9th, 2026

Motor Vehicles & Motors

MVM2026-055
https://doi.org/10.24874/CMVM2026.055
Technical paper

Vladimir Vukašinović[1]
Dušan Gordić[2]
Vanja Šušteršič[3]
Mladen Josijević[4]

SUSTAINABLE BIOFUELS FOR THE DECARBONISATION OF THE TRANSPORT SECTOR IN CITIES

ABSTRACT: Decarbonising the transport sector is one of the major challenges in achieving climate neutrality in cities. In addition to high greenhouse gas emissions, this sector has a direct impact on the deterioration of air quality in urban areas. Integrating sustainable biofuels (biodiesel, biomethane, bioethanol, and renewable diesel) is one of the key ways to reduce pollution and achieve carbon neutrality. Modern technologies enable these biofuels to be produced from locally available feedstocks, such as used cooking oil and fats, the organic fraction of municipal waste, sewage sludge, etc. According to 2024 data, a total of 73,016 motor vehicles are registered in Kragujevac, accounting for approximately 30% of the city's final energy consumption. To evaluate the effects of substituting fossil fuels with locally produced alternatives, an analysis was conducted across three key mobility segments: the public transit system, the municipal vehicle fleet, and privately owned vehicles. The research results indicate that the use of sustainable biofuels in suitable blends can significantly reduce CO_2 emissions, as well as harmful pollutants. The use of sustainable biofuels represents an important and significant step in the energy transition, contributing to long-term improvements in air quality.

KEYWORDS: transport decarbonisation, sustainable biofuels, climate neutrality

UPOTREBA ODRŽIVIH BIOGORIVA ZA DEKARBONIZACIJU TRANSPORTNOG SEKTORA U GRADOVIMA

REZIME: Dekarbonizacija sektora transporta predstavlja jedan od najvećih izazova kada se radi o postizanju klimatske neutralnosti gradova. Pored visoke emisije gasova sa efektom staklene bašte, ovaj sektor ima direktan uticaj na pad kvaliteta vazduha u urbanim sredinama. Integracija održivih biogoriva (biodizel, biometan, bioetanol i

[1] *Vladimir Vukašinović, Faculty of Engineering, University of Kragujevac, Sestre Janjić No.6, Kragujevac, vladimir.vukasinovic@kg.ac.rs, https://orcid.org/0000-0001-6489-2632*
[2] *Dušan Gordić, Faculty of Engineering, University of Kragujevac, Sestre Janjić No.6, Kragujevac, gordic@kg.ac.rs, https://orcid.org/0000-0002-1058-5810*
[3] *Vanja Šušteršič, Faculty of Engineering, University of Kragujevac, Sestre Janjić No.6, Kragujevac, vanjas@kg.ac.rs, https://orcid.org/0000-0001-7773-4991*
[4] *Mladen Josijević, Faculty of Engineering, University of Kragujevac, Sestre Janjić No.6, Kragujevac, mladen.josijevic@fink.rs, https://orcid.org/0000-0001-9619-0897*

obnovljivi dizel) predstavlja jedan od ključnih koraka za smanjenje zagađenja i tranziciju ka karbonskoj neutralnosti. Savremene tehnologije omogućavaju proizvodnju biogoriva iz lokalno dostupnih sirovina, poput iskorišćenog jestivog ulja i masti, organske frakcije komunalnog otpada i kanalizacionog mulja. U Kragujevcu je, prema podacima iz 2024. godine, registrovano ukupno 73.016 motornih vozila, što čini oko 30% finalne potrošnje energije na nivou grada. Kako bi se procenili efekti supstitucije fosilnih goriva lokalno proizvedenim alternativama, sprovedena je analiza u tri ključna segmenta mobilnosti: sistemu javnog gradskog prevoza, voznom parku u nadležnosti grada i sektoru privatnih vozila. Rezultati istraživanja pokazuju da korišćenje održivih biogoriva u odgovarajućim mešavinama i udelima može značajno doprineti redukciji emisija CO_2. Upotreba održivih biogoriva predstavlja važan i značajan korak u energetskoj tranziciji dugoročno doprinoseći unapređenju kvalitet vazduha.

KLJUČNE REČI: dekarbonizacija transporta, održiva biogoriva, karbonska neutralnost

INTRODUCTION

Increasingly pronounced climate change represents one of the main issues of the modern era. Cities are recognised as key areas for mitigating these problems, as they are responsible for 70% of global carbon emissions and two-thirds of the world's energy consumption (Winkler et al. 2023; Lučić et al. 2025). One of the greatest potentials for decarbonisation is the transport sector, which predominantly relies on fossil fuels. At the global level, this sector has the fastest growth in emissions over the past decades. It accounts for around 29% of total energy consumption and 25% of total CO_2 emissions resulting from energy use (Yılbası, 2025; IPCC, 2023). In addition to high greenhouse gas emissions, road transport has a direct impact on the decline in air quality in urban areas. Transport contributed approximately 20% of total air pollution in Europe in 2020 by emitting pollutants such as particulate matter (PM) and volatile organic compounds (VOC). In this way, it directly endangers human health (Mbandi, et al. 2023; Coelho, et al. 2022).

The energy transition that is currently underway involves a shift from systems based on fossil fuels to systems based on renewable energy sources (RES), with the electrification of both heat and transport being one of its objectives. Although the electrification of transport is an inseparable part of the energy transition, it is a long-term process that requires strong integration of RES and the development of supporting infrastructure. The process of full electrification may take decades depending on the capacities of individual countries. Therefore, solutions that will enable a smooth and fair transition are necessary, primarily based on locally specific RES (Nikolić, et al. 2026). The legal framework for addressing this issue in the European Union was initially established by Directive 2009/28/EC and Directive 2018/2001 (RED II) (European Parliament and Council of the EU, 2018). The targets have been significantly strengthened by the latest Directive 2023/2413 (RED III) (European Parliament and the Council of the EU, 2023) which requires the share of renewable energy in transport to be at least 29% by 2030, while the share of advanced sustainable biofuels and renewable synthetic fuels must be at least 5.5%.

Sustainable biofuels are defined as fuels obtained from renewable, sustainable feedstocks, such as organic waste and non-food biomass. Due to their similar properties to conventional petroleum products, they can be used in existing internal combustion engines (ICEs) (Yılbası, 2025; Demuynck, et al. 2021). Their key advantage compared to fully electric systems and hydrogen systems is their volumetric energy density, as well as the possibility of using existing distribution infrastructure. Studies that have analysed life cycle assessment confirmed the importance of liquid biofuels in decarbonisation. The use of these fuels can reduce greenhouse gas emissions by 60% - 90% compared to conventional fossil fuels, depending on the choice of feedstock and processing technology (Correa, et al. 2019). For example, the consumption of one kilogram of biodiesel can result in an average reduction of 3 kg of CO_2, depending on the feedstock used for biodiesel production and the way it is used. In the case of urban buses, the use of blends, such as B20 (20% biodiesel), results in a 15.66% reduction in CO_2 emissions (Khan, et al. 2025). In addition to environmental benefits, the implementation of circular economy principles through the use of local resources (such as used cooking oil for biodiesel production) addresses the issue of organic waste management, reduces dependence on imported energy, and enables the decarbonisation of sectors that are the most technologically challenging to electrify.

Despite these potentials, transport is still predominantly dependent on fossil fuels (92.5%), while RES accounts for only 7.5%. Biofuels based on conventional crops account for 4%, while advanced biofuels and biogas account for only 0.8% of this share (ECA, 2023; Yılbası, 2025). At the European Union level, the share of biofuels in road transport amounted to 6.7% in 2023 (EUROSTAT, 2025). Currently, biodiesel, bioethanol, and biomethane are the most commonly used, while hydrotreated vegetable oil (HVO) has recently emerged as an exceptionally important solution. HVO was developed with the aim of overcoming certain technical disadvantages of traditional biodiesel. It is characterised by a higher energy content and higher cetane number, lower viscosity and a comparable or higher flash point, as well as significantly better storage stability (Knothe, 2010).

To encourage the use of biofuels, the Government of the Republic of Serbia passed the Regulation on the Share of Biofuels in the Market in 2019, which established a specific share of biofuels on the market, blended with oil-derived

fuels (Government of the Republic of Serbia, 2019). The market shares for the period 2022-2024 were determined by the Decision on Determining the Mandatory Share of Biofuels that System Obligated Parties Are Required to Place on the Market of the Republic of Serbia, which are 0.5% in 2022, 0.5% in 2023, and 1% in 2024 (Government of the Republic of Serbia, 2021). Given that the initial regulatory obligations were not adequately implemented in the market, the Government adopted the Decision on the Termination of Validity of the Decision on Determining the Mandatory Share of Biofuels that System Obligated Parties Are Required to Place on the Market of the Republic of Serbia (Government of the Republic of Serbia, 2023), resulting in the share of biofuels remaining negligible, i.e., 371 t in 2024 (Government of the Republic of Serbia,2024).

The implementation of sustainable biofuels at the local level represents a key step towards sustainable urban mobility, considering global targets and the need for rapid emission reductions in cities. This paper aims to present how sustainable biofuels can contribute to reducing CO_2 emissions from urban transport using a city (Kragujevac) in Serbia as an example.

METHODOLOGY

The calculation of CO_2 reduction was conducted based on the developed methodology presented in Figure 1. The methodology is based on the COPERT model (Ntziachristos & Samaras, 2025) and available statistical data and consists of several steps.

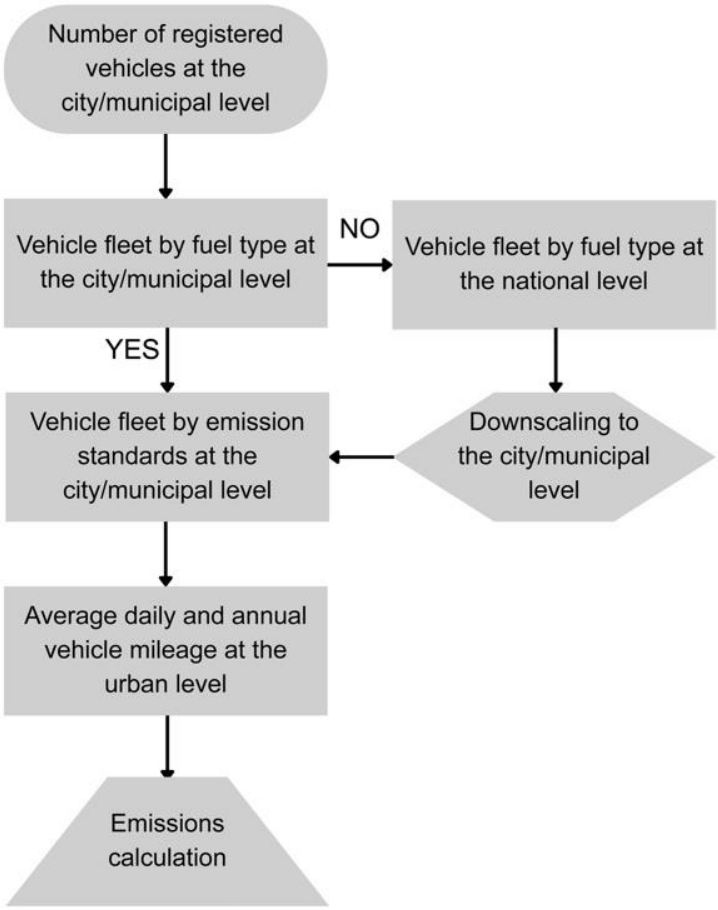

Figure 1 Proposed methodology

The number of registered vehicles in the transport sector in Serbia has been monitored annually. The data are published on a quarterly and annual basis. Some data are available at the municipality/city level and include the number of registered vehicles divided into categories (mopeds, motorcycles, passenger cars, buses, heavy trucks, work vehicles, and trailers) and by fuel type (petrol, diesel, and hybrids). Data on engine displacement and fuel used are available at the national or regional level. The methodology allows the number of vehicles by fuel type, as well as by engine size, to be determined based on available statistical data at the municipality/city level. In addition, local governments often adopt different strategic documents, such as the Energy Efficiency Programme, the Sustainable Energy and Climate Action Plan, and similar documents. These documents often contain more precise data on the number of vehicles.

Data on vehicles' emissions standards are defined based on statistical data on the import, sale, and registration of vehicles. In Serbia, it is possible to import vehicles with the EURO 3 emission standard and higher. These data are available at the national level, but they can be proportionally distributed to municipalities/cities. In addition, precise data are often available in the official strategic documents of municipalities/cities. The mileage by vehicles driven in urban areas on a daily and annual basis depends on several factors, such as citizen habits, the quality of the public transport system (the existence of metro-subway and urban railway lines), environmental restrictions, and the availability of public parking.

The calculation of emissions of pollutants from a certain vehicle fleet is carried out according to the official EMEP/EEA methodology for emission inventories (Ntziachristos & Samaras, 2025). The total mass of the emitted pollutant during the observed period *E* [g] can be expressed as (1):

$$E_{j,k} = N_{j,k} \cdot M_{j,k} \cdot ef_{j,k} \cdot mc \tag{1}$$

Where are:

$N_{j,k}$ [-] – number of registered vehicles within category *j* (passenger cars, light commercial vehicles, heavy-duty vehicles, buses, motorcycles) equipped with a *k* emission standard (Euro standard),
$M_{j,k}$ [km/god] – average annual mileage of a vehicle from category *j* with *k* emission standard,
$ef_{i,k}$ [g/km] – specific emission factor for category *j* with *k* emission standard,
mc [-] – correction factor due to degradation.

Calculating emissions and fuel (energy) consumption should include the cumulative mileage driven by the vehicle, as the same vehicle will not have the same emissions if it, for example, has driven 80,000 or 250,000 km. The total mileage for the vehicle is calculated using the years in which the specific EURO standard was implemented. To simplify calculation and obtain average values, the average of the years between two introduced standards is used. The total mileage is quantified by the correction factor due to degradation, *mc*.

The energy converted through the fuel consumption can be calculated using Equation (2):

$$EC_{j,k} = N_{j,k} \cdot M_{j,k} \cdot sf_{j,k} \cdot LHV \tag{2}$$

where are:

$sf_{j,k}$ [l/km] – specific fuel consumption of vehicle category j with k emission standard,
LHV [MJ/l] – lower heating value of fuel.

Based on the calculated emissions and energy, the average emission factor for petrol and diesel can be calculated for a certain territory. This value differs from the one defined by the EU directives due to the correction resulting from engine degradation as a result of the mileage driven. The average emission factor enables the calculation of reduction in emissions resulting from the use of biofuels. The average emission factor EF_{avg} [g/MJ] is calculated using Equation (3):

$$EF_{avg} = \frac{E}{EC} \tag{3}$$

The calculation of emission reductions resulting from the integration of biofuels is based on an energy consumption calculation. The volumetric shares of biofuel SH_{bio} [%] are converted into energy based on the lower heating value and conversion factors defined in the RED II Directive. The energy obtained by using a certain volumetric share of biofuels EC_{bio} [MJ] can be calculated as Equation (4):

$$EC_{bio} = EC \cdot SH_{bio} \cdot \frac{LHV_{bio}}{LHV_{fos}} \tag{4}$$

The CO_2 equivalent emissions resulting from the use of biofuels are calculated as Equation (5):

$$E_{bio} = EC_{bio} \cdot EF_{bio} \tag{5}$$

where:

EF_{bio} [g/MJ] – emission factors of biofuels defined in the RED II Directive.

Finally, the CO_2 equivalent emission reduction resulting from the use of a specific amount of biofuel as a substitute for fossil fuels is calculated according to Equation (6):

$$E_{new} = (EC - EC_{bio}) \cdot EF_{avg} + E_{bio} \tag{6}$$

SO_x emissions are only determined by the fuel's sulphur mass fraction. Vehicle technology is irrelevant in this context. Biofuels are sulphur-free, and using a particular proportion of biofuel reduces SO_x emissions linearly.

RESULTS AND DISCUSSION

According to data from the Statistical Office of the Republic of Serbia, a total of 73,016 motor vehicles (excluding work machinery) were registered in Kragujevac in 2024. This represents an increase of approximately 4% compared to the previous year. The total number of registered vehicles by year is shown in Figure 2.

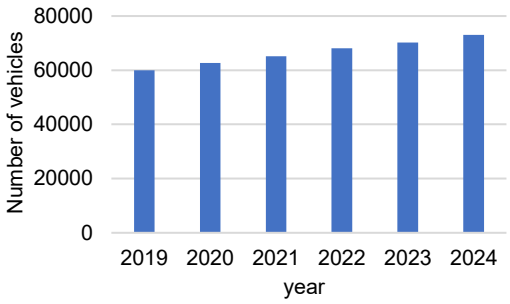

Figure 2 *Number of registered vehicles by years*

Passenger cars account for 89.21% of the total number of registered vehicles. The average age of vehicles in Kragujevac is 17.4 years, based on data from the Road Traffic Safety Agency (Road Traffic Safety Agency, 2022). Diesel vehicles account for 60%, petrol vehicles for 35%, while hybrid vehicles (most commonly with a petrol engine) and electric vehicles account for approximately 5%. According to engine displacement, among petrol vehicles, the dominant ones have an engine displacement of up to 1,399 cm^3, with a share of 67.5%. The vehicles with an engine displacement up to 1,999 cm^3 have a share of 30.9%, and vehicles with an engine displacement above 2,000 cm^3 have a share of 1.6%. Among vehicles powered by diesel engines, vehicles with an engine displacement of 1,400–1,999 cm^3 dominate, with a share of 85.3%, while vehicles with an engine displacement up to 1,399 cm^3 and above 2,000 cm^3 account for 8.6% and 6.1%, respectively.

An analysis conducted for the Sustainable Energy and Climate Action Plan (Centre for Development and Support, 2026) reveals that the majority of these vehicles belong to the EURO 3 and EURO 4 emission standards. This is largely because the regulation permitting the import of vehicles with EURO 3 engines and above is still in effect. Figure 3 shows the share of registered vehicles in Kragujevac by their emission standards.

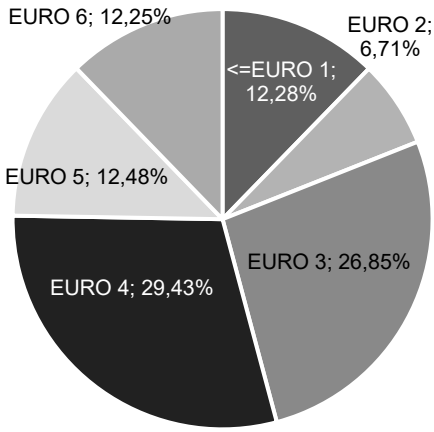

Figure 3 *Share of motor emission classes (EURO 1 includes vehicles before EURO standard)*

Some studies indicate that the average annual vehicle mileage in Serbia is approximately 10,000 km (Josijević, et al. 2022). (Živković, et al. 2016) states that average mileage in the city is about 3500 km annually. On the other hand, specialised unofficial platforms like CarVertical report a significantly higher average of around 16.000 – 18.000 km. However, data from these platforms is primarily obtained from authorised service centre databases. Since vehicles are typically maintained at authorised centres only while under the manufacturer's warranty, this higher figure likely overestimates the real national average. Furthermore, many of these vehicles belong to corporate fleets, making it difficult to isolate their mileage within specific municipalities. Due to the lack of exact local data, an approximation was performed. Aligning with broader European trends indicating that diesel vehicles generally cover greater distances (Marrero, et al. 2020), this study adopts an annual average of 13,000 km for diesel vehicles and 10,000 km for petrol vehicles.

The total mileage for each vehicle category was calculated based on the adopted average annual mileage and the number of years the respective emission standard was in effect Table 1.

Table 1 Total mileage of vehicle in Kragujevac

EURO standard	EURO 1	EURO 2	EURO 3	EURO 4	EURO 5	EURO 6
diesel [km]	416,000	364,000	305,500	247,000	188,500	78,000
petrol [km]	320,000	280,000	235,000	190,000	145,000	60,000
hybrid [km]						40,000

The public transport system in Kragujevac operates with 72 buses, covering an urban network of 336 km with an average route length of 14.6 km. When suburban transit is included, the total network expands to 638 km. The total number of buses registered within the city territory is 143. The buses operating in Kragujevac are powered by compressed natural gas (CNG) engines complying with the Euro 6 standard and diesel engines complying with the Euro 5 standard. The total annual mileage of the public transport bus fleet is approximately 3,000,000 km (RECEEKG, 2018).

The local government owns 49 passenger vehicles, 15 of which are powered by diesel engines and 34 by petrol engines. The public utility company Šumadija has 35 vehicles for waste collection and transportation.

The COPERT model considered three sectors: the urban public transport system, the vehicle fleet under the jurisdiction of the city, and the private vehicle sector. The carried out calculation showed that the annual converted energy amounts to 648.23 TJ for diesel vehicles, 312.29 TJ for petrol and hybrid vehicles, and 21.39 TJ for CNG buses.

Table 2 presents the energy consumption by fuel type and engine emission standards.

Table 2 Energy Consumption of the Vehicle Fleet by Fuel Type and EURO Emission Standard

EC	EURO 1	EURO 2	EURO 3	EURO 4	EURO 5	EURO 6	TOTAL
diesel [TJ]	79,88	46,12	173,1	173,45	103,48	72,2	648,23
petrol [TJ]	41,71	23,54	92,95	83,59	35,44	56,45	336,59
CNG [TJ]						21,39	21,39

Using the same methods, the CO_2 equivalent emissions have been computed as 48,197.65 t for diesel vehicles, 22,477.26 t for petrol vehicles and 1222,27 t for CNG buses. Results presented in Table 3 show that vehicles belonging to the EURO 3 and EURO 4 emission standards have the highest total emissions.

Table 3 Annual CO2e Emissions from the Vehicle Fleet by Fuel Type and EURO Emission Standard

E CO_2e	EURO 1	EURO 2	EURO 3	EURO 4	EURO 5	EURO 6	TOTAL
diesel [t]	5939,55	3428,92	12869,99	12896,52	7694,24	5368,43	48197.65
petrol [t]	3001,82	1694,63	6690,35	6013,57	2550,4	2526,49	24225.63
CNG [t]						1222,27	1222.27

Biofuels produced from biomass have often been considered as carbon-neutral fuels when they are produced in a sustainable manner. Given that they are predominantly of plant origin, it can be assumed that the amount of CO_2 emitted during their usage is equal to the amount of CO_2 absorbed by the plants from the atmosphere during their growth. However, crop cultivation, their transport, and processing require the use of certain technologies that are still largely based on fossil fuels. This means that biofuels are not completely carbon neutral. When considering biofuels that can be used at the local level, the feedstocks available in that region or country are of greatest importance.

Table 4 presents the lower heating values and emission factors for biofuels produced from crops cultivated in Serbia. In addition to crops, used cooking oils (UCO) are of particular importance as sustainable feedstocks for biodiesel and renewable diesel (HVO). Used cooking oils are generated in restaurants and hotels, and biofuels produced from them have significantly lower CO_2 emissions than those produced from crops.

Biodiesel and renewable diesel produced from UCO account for 24% of biofuel consumption in the EU, representing the largest share after biodiesel produced from rapeseed, which accounts for 34%. In Serbia, biodiesel and renewable diesel can also be produced from sunflower in addition to UCO and rapeseed, but sustainability aspects need to be taken into account.

In an attempt to support the integration of biofuels into the distribution system and contribute to the energy transition, the Government of the Republic of Serbia adopted the aforementioned Decision in 2021, but subsequently withdrew it in 2023. According to this Decision, the volumetric share of biofuels was to reach 1% by 2023. At the European Union level, the share of advanced sustainable biofuels and renewable synthetic fuels must account for at least 5.5% of the energy content by 2030.

Table 4 Lower heating values (LHV) and CO2e emissions of fossil fuels and biofuels

Fuel	LHV [MJ/l]	emission gCO_2e/MJ
petrol	32	69.3*
diesel	36	74.1*
CNG	50 [MJ/kg]	57.1*
bioethanol (sugar beet)	21	30.7 (38.2)
bioethanol (corn)	21	48.5 (56.8)
biodiesel (rapeseed)	33	45.5 (50.1)
biodiesel (UCO)	33	11.2 (14.9)
biodiesel (sunflower)	33	40.0 (47.0)
HVO (rapeseed)	34	45.8 (50.1)
HVO (UCO)	34	11.9 (16.0)
HVO (sunflower)	34	39.4 (43.6)
biomethane** (wet manure)	50 [MJ/kg]	-103.0 (35.0)
biomethane** (corn)	50 [MJ/kg]	26.0 (30.0)
biomethane** (biowaste)	50 [MJ/kg]	10.0 (14.0)

*calculated value

** close digestate with off-gas combustion

Biofuels such as biodiesel and bioethanol can be blended with conventional fossil fuels, although the maximum share that can be used without engine modification depends on the specific vehicle technology, age, and manufacturer approval. Standard, unmodified engines are generally compatible with lower biofuel blends, while the use of blends with higher biofuel shares requires compatibility with the specific vehicle and fuel standard. On the other hand, HVO and biomethane can, in suitable vehicles and applications, be used up to 100%, but there is an availability limit. Since the complete substitution of conventional fuels with biofuels is not practically feasible at the fleet level, the study considered three blending scenarios: a 1% volumetric share, a 5.5% energy share, and a 20% volumetric share. Emission reductions were calculated for each scenario.

If the volumetric share of biofuels were 1%, CO_2e emissions could be reduced by 229.80 to 507.05 t, depending on the type of biofuel used. The reduction directly depends on the feedstock used for biofuel production. Figure 4 shows the emission reductions depending on the feedstock from which the biofuels are produced. Biofuels produced from used cooking oil as a sustainable feedstock have the best effect in terms of emission reduction.

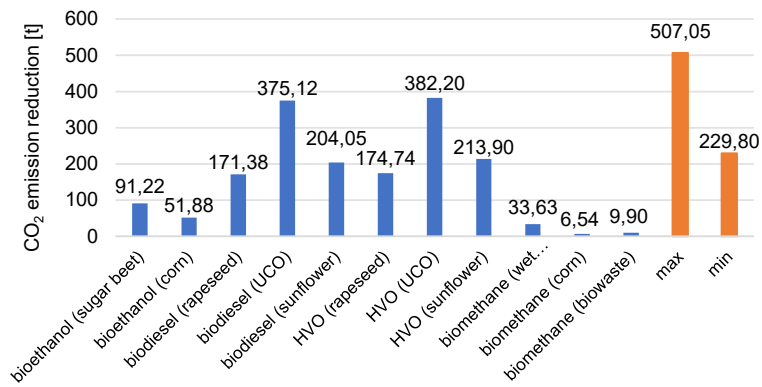

Figure 4 *CO_2e emission reduction at a 1% volumetric share by biofuel feedstock*

Achieving the European Union target of 5.5% of biofuels in the energy content could contribute to a reduction in emissions from 1,489.00 to 3,204.19 t CO_2e (Figure 5).

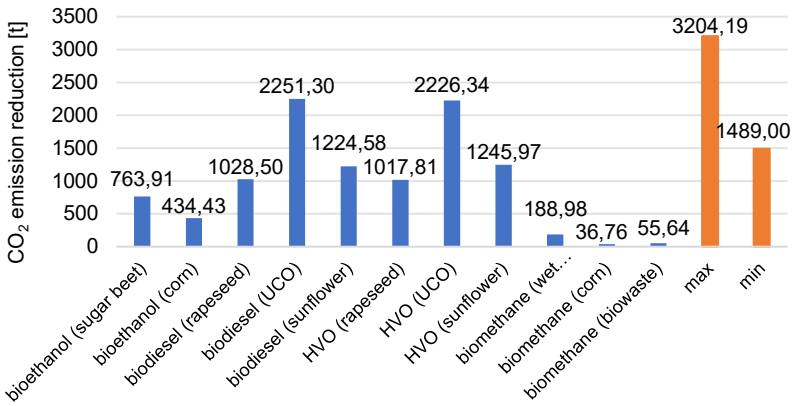

Figure 5 *CO_2e emission reduction at a 5.5% share in the energy by biofuel feedstock*

At a 20% volumetric share of biofuels, CO_2 equivalent emissions could be reduced by 4,598.77 to 10,155.76 t, depending on the type of biofuel used (Figure 6).

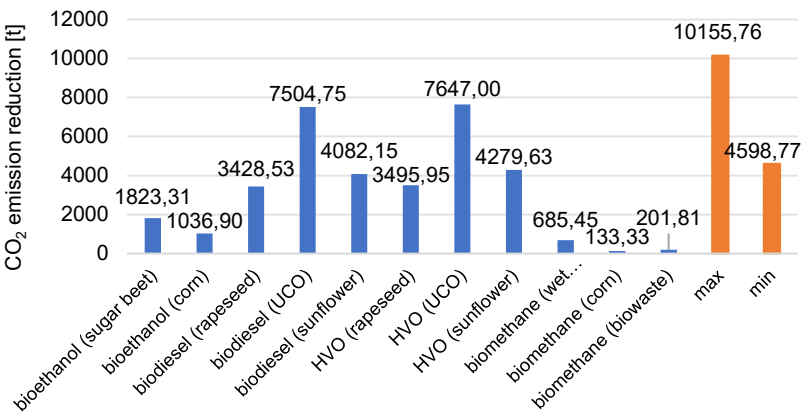

Figure 6 *CO_2e emission reduction at a 20% volumetric share by biofuel feedstock*

Three analysed cases show that biofuels produced from sustainable feedstocks, such as UCO, can have the greatest effects on CO_2e emission reduction. The maximum and minimum values shown in Figures 4-6 refer to the emissions that can be achieved through the simultaneous use of bioethanol in petrol vehicles, biodiesel or HVO in diesel vehicles, and biomethane in CNG buses.

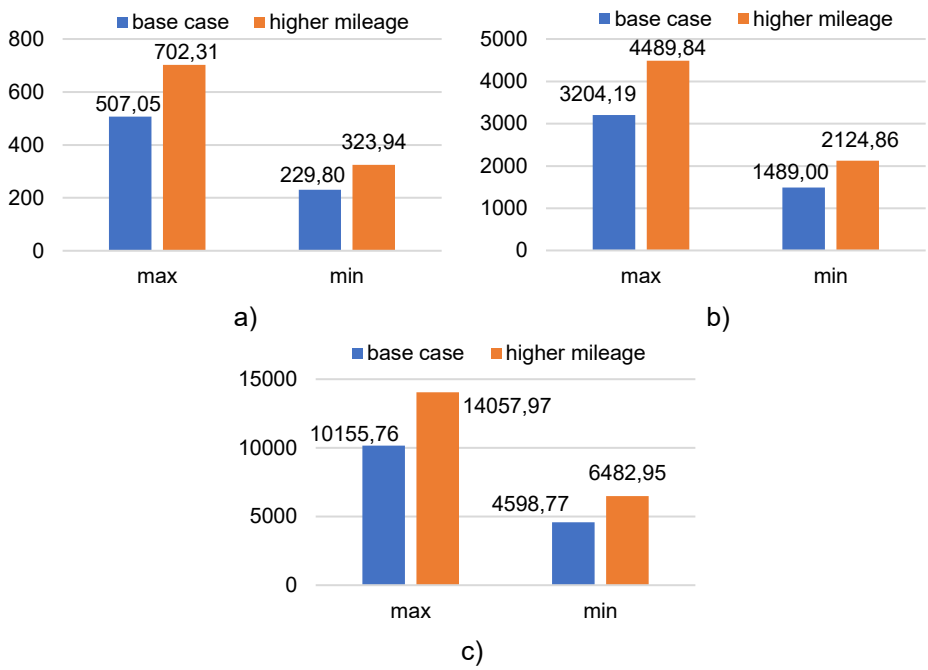

Figure 7 *Sensitivity analysis of CO_2e emission reductions under increased annual mileage scenarios: a) 1% volumetric share; b) 5.5% energy share; c) 20% volumetric share*

To evaluate how the model responds to changes in vehicle utilisation, a sensitivity analysis has been performed using an increased annual mileage of 18,000 km for diesel vehicles and 16,000 km for petrol and hybrid vehicles. The results show that an increase in annual mileage leads to a proportional increase in the total CO_2e emission reductions for all considered scenarios. For the 1% volumetric share, the maximum potential reduction increases from approximately 507 t to 702 t. For the 5.5% energy share, the corresponding reduction increases from around 3,200 t to almost 4,500 t, while for the 20% volumetric share it increases from 10,155 t to around 14,000 t. These results indicate that higher vehicle utilisation leads to greater absolute CO_2e emission savings from the use of sustainable biofuels.

CONCLUSIONS

The decarbonisation of urban transport requires a comprehensive approach that includes electrification, infrastructure improvement, and the indispensable integration of advanced biofuels. The research conducted on the example of a fleet of more than 73,000 vehicles in Kragujevac indicates that the direct substitution of conventional

fossil fuels with sustainable biofuels, such as bioethanol, hydrotreated vegetable oil (HVO), biodiesel, and biomethane produced from waste feedstocks, provides measurable and rapid benefits.

The application of a developed methodology which is based on the COPERT method showed that even conservative scenarios, with a biofuel share of 1%, result in a reduction in CO_2e emissions of up to 507 t annually. Alignment with the European Union Directive target of a 5.5% energy share would result in a several-fold greater reduction in emissions (more than 3,200 t), while an optimistic scenario involving a 20% volumetric share of biofuels could significantly decarbonise local transport, with emission reductions of more than 10,000 t. In addition to reducing the carbon footprint, replacing conventional diesel with sulphur-free biofuels leads to a linear decrease in SO_x emissions, which directly contributes to improving air quality in urban areas.

However, the calculated technical potential also indicates a significant gap with the current legislative framework. The suspension of the Decision on the mandatory biofuel share at the national level slows down the energy transition and makes it more difficult to achieve climate targets at the local level. The transition to sustainable biofuels, based on the principles of sustainability and the use of local waste feedstocks, does not require infrastructure or vehicle fleet modifications but only a supportive regulatory policy. Future research should focus on conducting a detailed techno-economic analysis of the possibilities for the production and supply chain of advanced biofuels at the local level.

ACKNOWLEDGMENTS

Authors acknowledge the Ministry of Education, Science and Technological Development of the Republic of Serbia for the support through Contracts No. 451-03-33/2026-03/200107 and 451-03-34/2026-03/200107.

REFERENCES

Center for Development and Support Tuzla. (2026). *Sustainable Energy and Climate Action Plan - Kragujevac.* Kragujevac: City of Kragujevac.

Coelho, S., Ferreira, J., Rodrigues, V., & Lopes, M. (2022). Source apportionment of air pollution in European urban areas: Lessons from the ClairCity project. *Journal of Environmental Management, 320*, 115899. https://doi.org/10.1016/j.jenvman.2022.115899

Correa, D., Beyer, H., Fargione, J., Hill, J., Possingham, H., Thomas-Hall, S., & Schenk, P. (2019). Towards the implementation of sustainable biofuel production systems. *Renewable and Sustainable Energy Reviews, 107*, 250-263. https://doi.org/10.1016/j.rser.2019.03.005

Demuynck, J., Dauphin, R., Yugo, M., Villafuerte, P., & Bosteels, D. (2021). Advanced emission controls and sustainable renewable fuels for low pollutant and CO_2 emissions on a diesel passenger car. *Sustainability, 13*, 12711. https://doi.org/10.3390/su132212711

ECA. (2023). *Special Report 29/2023: The EU's Support for Sustainable Biofuels in Transport—An Unclear Route Ahead.* London, UK: Royal Society Publishing.

European Parliament and Council of the EU. (2018). *DIRECTIVE (EU) 2018/2001 OF THE EUROPEAN PARLIAMENT AND OF THE COUNCIL of 11 December 2018 on the promotion of the use of energy from renewable sources.* Official Journal of the European Union.

European Parliament and the Council of the EU. (2023). *DIRECTIVE (EU) 2023/2413 OF THE EUROPEAN PARLIAMENT AND OF THE COUNCIL of 18 October 2023.* Official Journal of the European Union.

EUROSTAT. (2025, November). *Final energy consumption in transport - detailed statistics*. Retrieved 2026., from https://ec.europa.eu/eurostat/statistics-explained/index.php?title=Final_energy_consumption_in_transport_-_detailed_statistics

Government of the Republic of Serbia. (2019). *Regulation on the Share of Biofuels in the Market.* Belgrade: Official Gazette RS, br. 71/2019.

Government of the Republic of Serbia. (2021). *Decision on Determining the Mandatory Share of Biofuels that System Obligated Parties Are Required to Place on the Market of the Republic of Serbia.* Belgrade: Official Gazette RS, br. 104/2021.

Government of the Republic of Serbia. (2024.). *The Energy Balance of the Republic of Serbia for 2024.* Belgrade: Official Gazette RS, No. 8/2024.

IPCC. (2023). *Climate Change 2022: Mitigation of Climate Change. In Contribution of Working Group III to the Sixth Assessment Report of the Intergovernmental Panel on Climate Change IPCC.* Cambridge, UK: Cambridge University Press.

Josijević, M., Živković, D., Gordić, D., Končalović, D., & Vukašinović, V. (2022). The analysis of commercially available electric cars. *Mobility & Vehicle Mechanics (MVM), 48*(1), 19-36. https://doi.org/10.24874/mvm.2022.48.01.02

Khan, M., Sheikh, N., Jadoon, K., Ayub, A., Awotwe, T., & Tariq, R. (2025). Utilization of locally sourced waste fats for biodiesel production: Experimental characterization and environmental life cycle assessment. *194*, 107692. https://doi.org/10.1016/j.biombioe.2025.107692

Knothe, G. (2010). Biodiesel and renewable diesel: A comparison. *Progress in Energy and Combustion Science, 36*(3), 364-373. https://doi.org/10.1016/j.pecs.2009.11.004

Lučić, M., Vukašinović, V., Gordić, D., & Grujić, I. (2025). Ecological Effects of Using Biodiesel Obtained from Grape Seeds in the Fleet of Delivery Vehicles. *Energija, ekonomija, ekologija, XXVII*(4), 14-19.

Marrero, G., Rodríguez-López, J., & González, R. (2020). Car usage, CO_2 emissions and fuel taxes in Europe. *11*, 203-241.

Mbandi, A., Malley, C., Schwela, D., Vallack, H., Emberson, L., & Ashmore, M. (2023). Assessment of the impact of road transport policies on air pollution and greenhouse gas emissions in Kenya. *Energy Strategy Review, 49*, 101120. https://doi.org/10.1016/j.esr.2023.101120

Nikolić, J., Gordić, D., Živković, D., Vukašinović, V., & Batas-Bjelic, I. (2026). Cities in energy transition: Local responses to national challenges. *Thermal Science, 30*(2B), 1519-1533. https://doi.org/10.2298/TSCI250526175N

Ntziachristos, L., & Samaras, Z. (2025, June). (European Environment Agency) Retrieved 2026., from Methodology for the calculation of exhaust emissions – SNAPs 070100-070500, NFRs 1A3bi-iv: https://copert.emisia.com/copert/methodology/

RECEEKG. (2018). *Energy Efficiency Programme of the City of Kragujevac.* City of Kragujevac.

Road Traffic Safety Agency. (2022.). *Average Age of Vehicles in the Vehicle Fleet in the Republic of Serbia in 2022, by Police Department.*

Government of the Republic of Serbia. (2023). *Decision on the Termination of Validity of the Decision on Determining the Mandatory Share of Biofuels that System Obligated Parties Are Required to Place on the Market of the Republic of Serbia.* Belgrade: Official Gazette No. 54/2023.

Winkler, L., Pearce, D., & Babacan, O. (2023). The effect of sustainable mobility transition policies on cumulative urban transport emissions and energy demand. *Nature Communications, 14*(1), 2357. https://doi.org/10.1038/s41467-023-37728-x

Yılbası, Z. (2025). Biofuels, e-fuels, and waste-derived fuels: advances, challenges, and future directions. *Sustainability, 17*, 6145. https://doi.org/10.3390/su17136145

Živković, P., Tomić, M., Ayed, S., Milutinović, B., & Vukić, M. (2016). An assessment of the traffic-related emissions in the city on NIš. *Facta Universitatis - Working and Living Environmental Protection, 13*(2), 87-92.

The 11th International Congress
Motor Vehicles & Motors 2026
Kragujevac, Serbia
October 8th - 9th, 2026

Motor Vehicles & Motors

MVM2026-062
https://doi.org/10.24874/CMVM2026.062
Technical paper

Goran Bošković[1]
Nebojša Jovičić[2]
Angelina Cvetanović[3]
Saša Milojević[4]

ASSESSMENT OF THE NUMBER OF END-OF-LIFE VEHICLES IN THE REPUBLIC OF SERBIA

ABSTRACT: End-of-life vehicles (ELVs) represent a significant waste stream due to the large quantities of metals, plastics, glass, rubber, and hazardous materials they contain, requiring appropriate management. An efficient system for recording and tracking these vehicles provides the basis for circular economy planning and the improvement of waste management systems. This paper analyses available statistical data on the number of registered vehicles, imports of used vehicles, sales of new vehicles, and the quantities of officially recorded treated end-of-life vehicles in the Republic of Serbia. Based on the analysis, a vehicle fleet balance method was applied to estimate the number of vehicles that potentially reach the end of their service life. The results indicate a significant discrepancy between the estimated number of vehicles potentially reaching the end of their useful life and the officially reported quantities of treated ELVs, highlighting the need to improve monitoring and reporting systems.

KEYWORDS: Circular economy, End-of-life vehicles (ELV), Statistical analysis, Vehicle fleet balance, Waste management

ANALIZA I PROCENA BROJA VOZILA NA KRAJU ŽIVOTNOG VEKA U REPUBLICI SRBIJI

REZIME: Vozila na kraju životnog veka (eng. ELV - End-of-Life Vehicles) predstavljaju značajan tok otpada zbog prisustva velikih količina metala, plastike, stakla, gume i opasnih materija, što zahteva odgovarajuće upravljanje. Efikasan sistem evidencije i praćenja ovih vozila predstavlja osnovu za planiranje cirkularne ekonomije i unapređenje sistema upravljanja otpadom. U radu su analizirani raspoloživi statistički podaci o broju registrovanih vozila, uvozu upotrebljavanih vozila, prodaji novih vozila i broju zvanično tretiranih vozila u Republici Srbiji. Na osnovu sprovedene

[1] *Dr Goran Bošković, full prof. Faculty of Engineering University of Kragujevac, Kragujevac 34000, Sestre Janjić 6, Serbia, goran.boskovic@kg.ac.rs, https://orcid.org/0000-0003-3200-0120*
[2] *Dr Nebojša Jovičić, full prof. Faculty of Engineering University of Kragujevac, Kragujevac 34000, Sestre Janjić 6, Serbia, njovicic@kg.ac.rs, https://orcid.org/0000-0002-6505-6457*
[3] *Angelina Cvetanović, research associate, Faculty of Engineering University of Kragujevac, Kragujevac 34000, Sestre Janjić 6, Serbia, angelina.pavlovic@uni.kg.ac.rs, https://orcid.org/0000-0001-5249-1102*
[4] *Dr Saša Milojević, prof. assist. Faculty of Engineering University of Kragujevac, Kragujevac 34000, Sestre Janjić 6, Serbia, sasa.milojevic@kg.ac.rs, https://orcid.org/0000-0003-0569-047X*

analize primenjena je metoda bilansa voznog parka za procenu broja vozila koja potencijalno dostižu kraj svog životnog veka. Dobijeni rezultati ukazuju na značajno odstupanje između procenjenog broja vozila koja dostižu kraj životnog veka i zvanično evidentiranih količina tretiranih otpadnih vozila, što ukazuje na potrebu za unapređenjem sistema praćenja i izveštavanja.

KLJUČNE REČI: Cirkularna ekonomija, vozila na kraju životnog veka, statistička analiza, bilans voznog parka, upravljanje otpadom

INTRODUCTION

Over the past several decades, the number of motor vehicles in the Republic of Serbia has been continuously increasing, primarily due to the growing import of used vehicles and a gradual increase in the number of newly registered vehicles. At the same time, the expansion of the vehicle fleet has also resulted in an increasing number of vehicles reaching the end of their useful life and becoming a specific waste stream.

End-of-life vehicles represent a complex waste stream containing significant quantities of secondary raw materials, as well as hazardous components such as engine oils, coolants, batteries, and other materials that require controlled collection and treatment. Consequently, the European Union (EU) has established a system encompassing the registration, deregistration, collection, depollution, dismantling, recycling, and reporting of end-of-life vehicles.

In the Republic of Serbia, a legislative framework regulating the management of this waste category has been established. However, available statistical data indicate certain discrepancies between the number of vehicles that can be considered end-of-life vehicles and the quantities officially recorded as treated. These discrepancies may result from various factors, including incomplete coverage of all ELV waste streams, informal waste management practices, or an insufficiently developed recording and monitoring system.

The aim of this research is to estimate the number of vehicles potentially reaching the end of their useful life based on available statistical data on the number of registered vehicles, imports of used vehicles, sales of new vehicles, and data on treated end-of-life vehicles. Particular attention is given to analyzing the differences between the estimated and officially recorded quantities, as well as highlighting the need for further improvement of the monitoring and tracking system for this waste category.

Legislative Framework

In response to numerous problems and shortcomings in the existing legislation, the European Commission proposed a new Regulation, COM (2023) 451, on 13 July 2023, representing a fundamental reform of vehicle waste management. Following its adoption, Regulation (EU) 2026/1738 was published on 24 July 2026 and entered into force on 13 August 2026. It replaces Directives 2000/53/EC and 2005/64/EC with a single, directly applicable legal instrument. According to Regulation (EU) 2026/1738 (2026), the new legal framework covers the entire vehicle life cycle, from vehicle design to final treatment. It applies generally from 1 September 2028, with different dates specified for certain provisions.

One of the most significant changes is the introduction of mandatory requirements for the use of recycled materials in new vehicles. The Regulation requires a minimum of 15% of plastic by weight to be recycled from post-consumer plastic waste for new vehicle types approved from 1 September 2032, increasing to 25% from 1 September 2036. At least 20% of the applicable target must be achieved using plastic recycled from ELVs or from parts and components removed from vehicles during the use phase. This represents a key change compared with the previous Directive, which merely “encouraged” such practices. By creating mandatory demand for secondary raw materials, the EU not only reduces its strategic dependence on imports of primary materials but also establishes a strong and predictable market for high-quality recycled materials. This approach stimulates innovation in the recycling industry and strengthens the economic viability of the sector. The Regulation also empowers the Commission to establish targets for other materials, such as steel, aluminium, and critical raw materials, following the required assessments (Regulation (EU) 2026/1738, 2026).

To address the lack of traceability and transparency, the Regulation establishes a Digital Circularity Vehicle Passport (CVP) from 1 September 2032. The CVP will serve as a digital record containing information relevant to vehicle circularity. This tool will enable operators throughout the value chain from manufacturers to recyclers to access key information required for dismantling, reuse, and recycling. The CVP is a key digital enabler for implementing the new regulatory framework, ensuring more efficient information exchange and improved oversight (Regulation (EU) 2026/1738, 2026).

The Regulation introduces stricter requirements for the treatment of ELVs, including the mandatory removal of certain components prior to shredding, with the aim of maximizing reuse and recycling. From 1 September 2029, shredder

fractions containing non-inert waste may not be accepted in a landfill if they exceed the prescribed limit values. In terms of scope, the Regulation provides for a gradual extension to additional vehicle categories, including M2, M3, N2, N3, O and L categories from 1 September 2031, subject to the provisions specified in the Regulation (Regulation (EU) 2026/1738, 2026).

The new Regulation provides a detailed and harmonized framework for extended producer responsibility, thereby directly addressing the shortcomings of the previous Directive. The main principles are aligned with the Waste Framework Directive, meaning that producers bear full financial and organizational responsibility for managing their products at the end of their life.

Manufacturers' financial contributions will be modulated based on harmonized criteria, taking into account characteristics such as vehicle weight, type of propulsion, ease of dismantling, and the presence of hazardous substances. This mechanism creates economic incentives for manufacturers to design vehicles that are easier to recycle and contain fewer problematic materials. In addition, mechanisms for cross-border cooperation ("cross-border EPR") will be introduced to ensure that the treatment costs of a vehicle manufactured in one Member State but treated in another are appropriately covered.

The problem of missing vehicles, whereby a significant proportion of deregistered vehicles are not reported for official treatment, represents one of the major shortcomings affecting the effectiveness of the previous Directive. A key underlying cause of this problem is the economic incentive for individuals and companies to bypass official channels. The sale or illegal export of vehicles that are de facto end-of-life vehicles often generates higher returns than delivering them to an authorized treatment facility. Regulation (EU) 2026/1738 (2026) addresses this problem through vehicle-status checks, certificates of destruction, reporting and enforcement measures.

The Regulation introduces legally binding criteria for distinguishing a "used vehicle" from an ELV. This represents a key change compared with the previous non-binding guidelines, which were difficult for customs officials to apply in practice. The Regulation establishes stricter conditions for the export of used vehicles, requiring evidence that a vehicle is not an ELV and satisfies the applicable roadworthiness conditions before it may be exported from the EU. Electronic verification supports the application of these requirements at the point of export (Regulation (EU) 2026/1738, 2026).

Customs authorities will use interoperable registers and the EU Single Window Environment for Customs (which facilitates interoperability between customs and non-customs authorities through three main components: EU non-customs systems, national customs environments, and the EU customs system) to verify the validity and status of a vehicle before it leaves the EU customs territory. This measure not only helps prevent the illegal export of ELVs and the associated environmental damage in third countries but also strengthens the circular economy value chain within the EU. By reducing the number of old vehicles leaving the EU, a greater flow of raw materials and components for recycling and reuse is retained within the European market.

The Law on Waste Management (2025) regulates waste classification, waste management planning, waste management stakeholders, responsibilities and obligations in waste management, the organization of waste management, the management of special waste streams, conditions and procedures for issuing permits, transboundary movements of waste, waste reporting, financing of waste management, and supervision of waste management. Article 69 defines obligations relating to ELVs, while Article 113 provides for the continued application of by-laws adopted under the previous Act until new regulations are adopted. Under the current legislation, manufacturers/importers are required to provide information on the dismantling and appropriate treatment of vehicles that are no longer in use. The relationship between the current EU and Serbian frameworks is presented in Fig. 1.

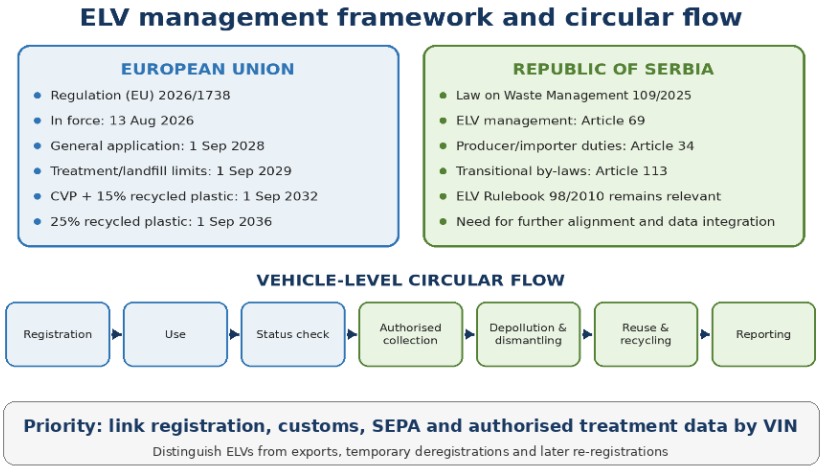

Figure 1 ELVs Management in the EU and the Republic of Serbia (From Legislation to Circular Economy)

Article 6 of the Law establishes the fundamental principles of waste management, including the principle of responsibility and the polluter pays principle. The principle of responsibility means that manufacturers, importers, distributors, and sellers of products that contribute to an increase in waste generation are responsible for the waste arising from their activities. The polluter pays principle means that the polluter bears the full costs of the consequences of its activities. Article 34 specifies responsibilities of producers and importers of products (Law on Waste Management, 2025).

Article 69 establishes provisions specifically related to the management of ELVs. Article 113 provides that, until regulations are adopted under the new Law, by-laws adopted under the previous Law on Waste Management continue to apply (Law on Waste Management, 2025).

Detailed provisions were adopted in 2010 through the Rulebook on the Method and Procedure for the Management of ELVs (Official Gazette of the Republic of Serbia, No. 98/2010). This Rulebook applies to vehicles and ELVs, including their components and materials, regardless of how the vehicle was serviced or repaired during its use and regardless of whether the vehicle is equipped with components supplied by the manufacturer or with other components installed as replacement parts (Rulebook on ELVs, 2010).

With regard to the management of hazardous substances, the Rulebook stipulates that, during the production of motor vehicles and spare parts or equipment for motor vehicles, measures shall be taken with the aim of:

- limiting the use of hazardous substances in vehicles and reducing their quantities as much as possible;
- designing and manufacturing new vehicles in a manner that facilitates dismantling, reuse, and treatment, particularly the recycling of ELVs, their components, and materials;
- increasing the use of recycled materials in vehicles and other products and promoting the development of markets for recycled materials.

Motor vehicles and their spare parts containing lead, mercury, cadmium, or hexavalent chromium may not be manufactured or imported, except for the materials and components listed in Annex 1 of the Rulebook.

Owner is obliged to deliver their ELV to an authorized entity engaged in the collection, transportation, storage, and/or treatment of ELVs. All such entities are required to complete the hazardous waste movement document. If the owner of an ELV is unknown, the collection and transfer of the vehicle shall be carried out by the local self-government unit. Vehicle must be accompanied by a copy of the owner's driving license, or by a report from the municipal inspection authority if the owner is unknown, or by a traffic accident report if the ELV resulted from a traffic accident.

Regarding the storage of ELVs, it is specified that dismantling may not be carried out at the storage site. Minimum technical requirements for storage facilities are prescribed. The transportation of ELVs must comply with the provisions governing the transport of hazardous waste and with the permit issued by the competent authority.

With regard to the treatment of ELVs, detailed provisions are established by the Rulebook. These include minimum requirements for treatment facilities, provisions concerning the removal of hazardous components, provisions on the separation of recyclable parts, and requirements for the removal of specific components. According to Annex 3 of the Rulebook on ELVs (2010), treatment operations must achieve the following reuse, recovery, and recycling targets:

- From 1 January 2015: reuse and recovery of at least 85% of the average mass of ELVs collected during the year, and reuse and recycling of at least 80% of their average mass.
- From 1 January 2019: reuse and recovery of at least 95% of the average mass of ELVs collected during the year, and reuse and recycling of at least 85% of their average mass.

It is also explicitly stipulated that ELVs must not be disposed of in landfills or incinerated. The obligation to pay a fee for vehicles placed on the market is prescribed by the Act on Fees for the Use of Public Goods (Official Gazette of the Republic of Serbia, No. 95/2018, as amended through No. 35/2026). Under this Act, the entity liable for the fee on products that become special waste streams after use including M1 and N1 category vehicles and three-wheeled motor vehicles, excluding motor tricycles (category L5 – heavy tricycles), in accordance with road traffic safety regulations is the manufacturer or importer that places such products on the market in the Republic of Serbia or uses them as the final consumer (Act on Fees for the Use of Public Goods, 2018).

The Act defines the basis for calculating the fee as the quantity of manufactured or imported vehicles, expressed in (kg), as specified in the vehicle type-approval documentation. It also defines the method for determining the fee, its amount, and the method of payment, as well as the obligation to maintain daily records on the quantity and type of manufactured and imported products and vehicles that become special waste streams after use, including ELVs. Based on these records, an annual report is prepared on the quantity and type of manufactured and imported vehicles placed on the market of the Republic of Serbia that will eventually become vehicles at the end of their useful life, and this report is submitted to the Serbian Environmental Protection Agency (SEPA).

Directive 2000/53/EC primarily applies to categories M1 and N1. Regulation (EU) 2026/1738 (2026) replaces that Directive from 1 September 2028 and progressively extends selected provisions to additional vehicle categories. The relevant type-approval categories are defined under Regulation (EU) 2018/858 (2018) and Regulation (EU) No. 168/2013.

MATERIALS AND METHODS

The research is based on an analysis of available statistical data on the vehicle fleet of the Republic of Serbia, data on the import of used vehicles and sales of new vehicles, as well as data on the quantities of ELVs recorded within the waste management system. The data sources included official statistical reports issued by the relevant institutions, available vehicle registration data, as well as data on the quantities of vehicles placed on the market and the quantities of end-of-life vehicles treated.

To estimate the potential number of vehicles reaching the end of their useful life, the vehicle fleet balance method was applied. The method is based on the assumption that the number of registered vehicles in a given year is determined by the number of vehicles registered in the previous year, increased by the number of newly registered vehicles (new and imported used vehicles), and reduced by the number of vehicles that have permanently or temporarily been withdrawn from service.

The estimated number of ELVs was calculated using the following equation:

$$N_{\mathrm{ELV}} = N_{\mathrm{reg,t-1}} + N_{\mathrm{import}} + N_{\mathrm{new}} - N_{\mathrm{reg,t}} \quad (1)$$

Where:

- N_{ELV} – estimated number of vehicles potentially reaching end-of-life, calculated as the residual of the vehicle fleet balance;
- $N_{\mathrm{reg,t-1}}$ – Number of Vehicles Registered in the Previous Year;
- N_{import} – Number of Imported Used Vehicles;
- N_{new} – Number of New Vehicles Placed on the Market;
- $N_{\mathrm{reg,t}}$ – Number of Vehicles Registered in the current Year.

The obtained values can be compared with the official data on the quantities of treated ELVs to assess potential discrepancies and identify possible shortcomings in the existing record-keeping system.

RESULTS AND DISCUSSION

Analysis of Vehicle Fleet Trends in the Republic of Serbia

End-of-life vehicles, or vehicles that are no longer in use, are generated in virtually all economic sectors. However, the majority of ELVs originate from private households. According to SEPA (2024), the mass of vehicles (categories M1 and N1) placed on the market in 2023 amounted to 102,973.85 t. Waste management operators reported to the SEPA that they treated 5,913 t of ELVs.

End-of-life vehicles, i.e., vehicles that are no longer roadworthy, are motor vehicles or their components that have become waste and that their owner intends to discard. According to the Waste Catalogue, ELVs are classified under group 16 01. There are no precise data on the quantities of ELVs generated annually. In the Republic of Serbia, there are approximately one million vehicles with an average age of more than 10 years. The collection and management of ELVs largely depend on supply and demand. Hazardous substances and components are not removed prior to the vehicle recycling process. Parts with positive economic value are recovered in smaller quantities, depending on their age and condition. A certain number of operators registered for metal waste recycling can meet the legal requirements for ELV recycling (Rulebook on Waste Classification, 2010; SEPA, 2024).

The first steps in the ELV treatment chain are declaring the vehicle as waste, deregistering it from the vehicle registry, and issuing a certificate of destruction. Deregistration of vehicles that have reached the end of their useful life is mandatory. General indicators for declaring a vehicle as waste include its age, emissions compliance, condition, and technical roadworthiness. According to the Law on Waste Management (2025), permits for hazardous waste management are issued only by the Ministry, the Autonomous Province of Vojvodina, or the City of Belgrade. A local self-government unit is required to arrange for the collection and delivery of an ELV, when its owner is unknown, to an entity authorized to treat such vehicles, and is entitled to recover the associated costs if the vehicle owner is subsequently identified. Local self-government units are authorized to issue permits for the collection, transport,

storage, treatment, and disposal of inert and non-hazardous waste within their territory. In addition, the City of Belgrade may issue permits for hazardous waste, including ELVs.

Data on the number of registered vehicles indicate a continuous growth of the vehicle fleet over the 2018–2024 period, Table 1. At the same time, a significant inflow of used vehicles is evident, which in most of the observed years was several times higher than the number of new vehicles entering the market. Such a market structure contributes to an increase in the average age of the vehicle fleet and, consequently, to an increase in the number of vehicles reaching the end of their useful life (Statistical Office of the Republic of Serbia, 2025).

Table 1 Trends in the Number of Registered Vehicles, Used Vehicle Imports, and New Vehicle Sales in the Republic of Serbia (2018–2024)

	2018	**2019**	**2020**	**2021**	**2022**	**2023**	**2024**
Imported Used Vehicles	81,796	141,918	115,000	152,803	115,347	131,905	135,000
New Vehicles Sold	30,731	34,202	26,400	30,416	22,785	25,422	27,862
Registered Vehicles	1,999,771	2,083,753	2,164,818	2,235,794	2,337,498	2,389,105	2,476,419
Estimated Potential ELVs	-	92,138	60,335	112,243	36,428	105,720	75,548

Based on the presented data, it can be observed that the number of registered vehicles increased from approximately 2 million in 2018 to nearly 2.5 million in 2024. At the same time, annual imports of used vehicles ranged from approximately 80,000 to 150,000 vehicles, while the number of new vehicles was significantly lower. These indicators confirm that the renewal of the vehicle fleet relies heavily on the import of used vehicles, contributing to an increase in the number of vehicles that reach the end of their useful life within a relatively short period.

To complement the vehicle fleet data presented in Table 1, Table 2 summarizes the officially reported quantities of vehicles placed on the market and treated ELVs in the Republic of Serbia during the period 2018–2023.

In 2023, a total of 2,389,105 vehicles were registered. During 2024, 135,000 used vehicles were imported and 27,862 new vehicles were placed on the market. If these values are added (2,389,105 + 135,000 + 27,862 = 2,551,967), the resulting figure should represent the total number of registered vehicles in 2024. However, a total of 2,476,419 vehicles were registered in 2024, indicating a difference of 75,548 vehicles (2,551,967 – 2,476,419). Vehicles that were not registered for a period of one year may be considered ELVs, as defined in some EU countries.

Table 2 Data on the Quantities of Vehicles Placed on the Market and Treated ELVs

	2018	**2019**	**2020**	**2021**	**2022**	**2023**
Quantity of Vehicles Placed on the Market, (t)	113,180	137,152	157,955	178,952	187,231	102,974
Quantity of Treated ELVs, (t)	2,548	2,109	2,391	3,280	2,212	5,913

According to SEPA (2024), a total of 102,974 t of N1 (for goods ≤ 3.5 t) and M1 (with no more than eight seats in addition to the driver's seat) category vehicles were placed on the domestic market. Assuming an average vehicle weight of 1 t (which is a relatively conservative estimate), this corresponds to approximately 100,000 vehicles. On the other hand, waste recovery operators reported to the SEPA that they treated only 5,913 t of this type of waste, corresponding to fewer than 6,000 ELVs.

For comparison, in Croatia, out of 1,840,767 registered vehicles in 2022, a total of 37,957 ELVs and their components were collected and officially treated.

By comparing these data, it can be concluded that the data on vehicles placed on the market and treated ELVs are not adequately monitored. The lack of incentives for delivering ELVs to collection points/authorized treatment facilities appears to be the main reason for these "statistical gaps" and may also contribute to illegal treatment.

For example, the Government of the Republic of Serbia introduced an incentive scheme to stimulate the recycling market for specific waste streams (i.e., waste batteries and waste oils) and to encourage the replacement of old vehicles with new vehicles equipped with advanced environmental protection systems. In addition, FIAT (STELLANTIS), a domestic vehicle manufacturer, provided incentives for the proper management of ELVs for several years, although these incentives were not provided continuously.

The ELV take-back system is explicitly established as free of charge for consumers. Dismantling and shredding facilities finance their operations through revenues generated from recovered scrap metal, spare parts, and materials recovered for recycling, such as batteries and catalytic converters.

Identified Reasons for Non-Compliance with Applicable Regulations:

- Trading of used vehicles within Republic of Serbia and subsequent re-registration in the destination city.
- Cases in which a used vehicle is delivered to Serbia (possibly with the intention of the exporter that it will be repaired, sold, and re-registered), but is ultimately not re-registered at the destination and eventually becomes an ELV. For such cases, there are no provisions ensuring the exchange of data on the appropriate treatment of the vehicle between the competent authorities of the countries involved.
- Temporary deregistration/suspension of registration: loss of traceability of the vehicle owner and the absence of incentives or penalty mechanisms that would encourage the owner to comply with legal requirements. Consequently, the owner is not required to submit export documentation or a Certificate of Destruction to the relevant authorities, as doing so does not provide any tangible benefit to the owner.
- Illegal dismantling at informal “car scrapyards.” Informal dismantlers seek to maximize their revenue from ELVs, while shredding facilities are absent in many unregulated waste-management systems. Informal dismantlers apply inadequate technological and professional practices during ELV dismantling and dispose of waste in an uncontrolled manner. This creates environmental and occupational problems and reduces the overall efficiency of ELV dismantling.
- Lack of incentives to make the delivery of ELVs to collection points/authorized treatment facilities more attractive.

From our perspective, the intensive application of digital technologies makes a significant contribution to improving and organizing waste collection and recycling systems (Bošković et al. 2024).

On the other hand, the process is becoming increasingly complex due to the growing number of vehicles, the diversity of propulsion systems, such as natural gas and electric vehicles, and other requirements associated with modern smart cities (Bošković et al. 2026; Milojević et al. 2025).

Estimation of the Number of ELVs

Using the vehicle fleet balance method, the number of vehicles that ceased to be part of the vehicle registration system during 2024 was estimated. The results indicate that the number of such vehicles was approximately 75,500, representing the potential number of vehicles that reached the end of their life, Table 1.

The obtained result does not represent exclusively the number of ELVs, but rather an estimate of the number of vehicles that have exited the registration system and may represent vehicles at the end of their life. Some of these vehicles may have been exported, temporarily deregistered, or returned to service; however, the obtained value provides a useful indicator of the magnitude of this waste stream.

Generally, a comparison of the estimated quantities with the number of vehicles officially recorded within the ELV management system reveals a significant discrepancy. Although the available data indicate a substantial gap between the estimated number of potential ELVs and the officially reported quantities of treated ELVs, a direct coverage rate cannot be calculated because the datasets differ in units and reporting periods. Such a discrepancy indicates that a proportion of vehicles is not covered by the official recording system, which may be attributable to informal dismantling, the sale of individual parts, unregulated handling, or other forms of vehicle disposal that are not captured by statistical reporting.

The vehicle fleet balance provides a first-order indication of the potential magnitude of the ELV stream, although the estimate remains subject to uncertainty. Although this method does not allow for the precise identification of each individual vehicle, it represents a useful tool for estimating the magnitude of the waste stream under conditions of limited data availability.

The differences between the estimated and officially recorded quantities indicate the need to improve the system for tracking the movement of vehicles from the time of deregistration to their final treatment. Establishing an integrated information system and enhancing cooperation among relevant institutions would enable the collection of more reliable data, which is particularly important for planning the capacity of treatment facilities and achieving circular economy objectives.

CONCLUSIONS

The analysis indicates that, although the Republic of Serbia has established a legislative framework for the management of end-of-life vehicles that is broadly aligned with European legislation, discrepancies remain between

the estimated number of vehicles potentially reaching the end of their useful life and the quantities officially recorded as treated. These discrepancies highlight the need to further improve the registration, traceability, reporting, and monitoring of ELVs throughout their entire life cycle. Strengthening these mechanisms, together with the gradual harmonization of Serbian legislation with the evolving EU regulatory framework, is essential for more effective ELV management and the development of a circular economy in Serbia.

The paper presents an estimation of the quantities of ELVs in the Republic of Serbia using a vehicle fleet balance method based on available statistical data. The analysis shows that the estimated number of vehicles leaving service significantly exceeds the number of vehicles covered by the official treatment system.

The obtained results indicate discrepancies between the estimated and recorded quantities, highlighting the need for further improvements in the systems for recording, tracking, and reporting on ELVs. The proposed approach can serve as a simple indicator for estimating the quantities of ELVs and as a basis for future research and the development of more reliable estimation methods.

ACKNOWLEDGMENTS

This work has been performed as a part of activities within the projects 451–03–33/2026–03/200107 and 451–03–34/2026–03/200107, supported by the Republic of Serbia, Ministry of Science, Technological Development and Innovation.

REFERENCES

Act on Fees for the Use of Public Goods, Official Gazette of the Republic of Serbia, No. 95/2018, as amended through No. 35/2026 (2018).

Bošković, G., Cvetanović, A. M., Jovičić, N., Jovanović, A., Jovičić, M., & Milojević, S. (2024). Digital technologies for advancing future municipal solid waste collection services. In F. Theofanidis, O. Abidi, A. Erturk, S. Colbran, & E. Coşkun (Eds.), *Digital transformation and sustainable development in cities and organizations* (pp. 167–192). IGI Global Scientific Publishing. https://doi.org/10.4018/979-8-3693-3567-3.ch008

Bošković, G., Jovičić, N., & Milojević, S. (2026). Opportunities for reducing emissions and congestion in cities through the use of eco-friendly minibuses in public transportation. *Facta Universitatis, Series: Working and Living Environmental Protection*, 111–122. https://doi.org/10.22190/FUWLEP251029011B

Law on Waste Management, Official Gazette of the Republic of Serbia, No. 109/2025 (2025).

Milojević, S., Stopka, O., Orynycz, O., Tucki, K., Šarkan, B., & Savić, S. (2025). Exploitation and maintenance of biomethane-powered truck and bus fleets to assure safety and mitigation of greenhouse gas emissions. *Energies, 18*(9), 2218. https://doi.org/10.3390/en18092218

Regulation (EU) 2018/858 of the European Parliament and of the Council of 30 May 2018 on the approval and market surveillance of motor vehicles and their trailers, and of systems, components and separate technical units intended for such vehicles, amending Regulations (EC) No. 715/2007 and (EC) No. 595/2009 and repealing Directive 2007/46/EC, Official Journal of the European Union L 151 (2018), pp. 1–218.

Regulation (EU) 2026/1738 of 8 July 2026 on circularity requirements for vehicle design and on management of end-of-life vehicles, amending Regulations (EU) No. 168/2013, (EU) 2018/858, (EU) 2019/1020 and (EU) 2023/1542 and repealing Directives 2000/53/EC and 2005/64/EC, Official Journal of the European Union L 2026/1738 (2026).

Rulebook on Categories, Testing and Classification of Waste, Official Gazette of the Republic of Serbia, Nos. 56/2010, 93/2019, 39/2021, and 65/2024 (2010).

Rulebook on the Manner and Procedure for the Management of End-of-Life Vehicles, Official Gazette of the Republic of Serbia, No. 98/2010 (2010).

Serbian Environmental Protection Agency. (2024). *Special waste streams in the Republic of Serbia in 2023*. Ministry of Environmental Protection of the Republic of Serbia.

Statistical Office of the Republic of Serbia. (2025). *Registered road motor vehicles and trailers and road traffic accidents, 2024*.

The 11th International Congress
Motor Vehicles & Motors 2026
Kragujevac, Serbia
October 8th - 9th, 2026

Motor Vehicles & Motors

MVM2026-064
https://doi.org/10.24874/CMVM2026.064
Original scientific paper

Bojana Bošković[1]
Nadica Stojanović[2]
Saša Babić[3]
Milena Petrović[4]
Anđela Egerić[5]

PREDICTION AND TIME-SERIES ANALYSIS OF ROAD DEATHS PER MILLION INHABITANTS IN THE REPUBLIC OF SERBIA AND THE EUROPEAN UNION FOR THE PERIOD 2012 TO 2030

ABSTRACT: The number of road traffic fatalities remains a significant road safety concern in the Republic of Serbia. This study aimed to identify an appropriate forecasting model for monitoring and predicting road traffic fatalities and to assess whether the target of the Decade of Action for Road Safety 2021–2030, which aims to reduce road traffic fatalities by 50% by 2030, is likely to be achieved. Three time-series forecasting models available in MINITAB software were applied: the linear trend model, quadratic trend model, and growth model. Forecasted values were compared with observed data, and the quadratic trend model demonstrated the highest forecasting accuracy, exhibiting the lowest percentage error for the period from 2012 to 2022. Therefore, this model was selected to predict road deaths per million inhabitants in Serbia for the period from 2022 to 2030. The results indicate a substantial projected increase in road fatalities during this period, representing an unfavorable trend for road safety. A comparative analysis with the European Union showed that road deaths per million inhabitants decreased by approximately 13% in Serbia between 2012 and 2022, compared with an average decrease of approximately 15% in the EU. Overall, the findings suggest that the 2030 target is unlikely to be achieved under current trends without additional interventions and systematic safety measures.

KEYWORDS: time-series analysis, road deaths per million inhabitants, traffic safety, MINITAB

[1] *Bojana Bošković, senior lecturer, Academy of Professional Studies Šumadija, College Trstenik, bboskovic@asss.edu.rs, https://orcid.org/0000-0001-8622-9874*
[2] *Nadica Stojanović, assistant professor, Faculty of Engineering, University of Kragujevac, Kragujevac, Serbia, nadica.stojanovic@kg.ac.rs, https://orcid.org/0000-0002-4199-0587*
[3] *Saša Babić, professor of applied studies, company, sbabic@asss.edu.rs, https://orcid.org/0000-0002-0005-723X*
[4] *Milena Petrović, teaching associate, Academy of Professional Studies Šumadija, College Trstenik, mpetrovic@asss.edu.rs, https://orcid.org/0009-0005-8443-7107*
[5] *Anđela Egerić, student assistant, Academy of Professional Studies Šumadija, College Trstenik, aegeric@asss.edu.rs, https://orcid.org/0009-0002-7550-5209*

PREDIKCIJA I ANALIZA VREMENSKIH SERIJA BROJA POGINULIH U SAOBRAĆAJNIM NEZGODAMA NA MILION STANOVNIKA U REPUBLICI SRBIJI I EVROPSKOJ UNIJI ZA PERIOD OD 2012. DO 2030. GODINE

REZIME: Broj poginulih u saobraćajnim nezgodama i dalje predstavlja značajan problem bezbednosti saobraćaja u Republici Srbiji. Cilj ovog istraživanja bio je da se identifikuje odgovarajući model za praćenje i predviđanje broja poginulih u saobraćajnim nezgodama, kao i da se proceni da li će cilj Dekade akcije za bezbednost saobraćaja 2021–2030, koji podrazumeva smanjenje broja poginulih u saobraćajnim nezgodama za 50% do 2030. godine, biti ostvaren. Primenjena su tri modela za predviđanje zasnovana na analizi vremenskih serija u softveru MINITAB: linearni trend model, kvadratni trend model i model rasta. Predviđene vrednosti upoređene su sa stvarnim podacima, pri čemu je kvadratni trend model pokazao najveću tačnost predviđanja, sa najmanjom procentualnom greškom za period od 2012. do 2022. godine. Zbog toga je ovaj model odabran za predviđanje broja poginulih na milion stanovnika u Srbiji za period od 2022. do 2030. godine. Rezultati ukazuju na značajan projektovani porast broja poginulih u posmatranom periodu, što predstavlja nepovoljan trend sa aspekta bezbednosti saobraćaja. Uporedna analiza sa Evropskom unijom pokazala je da je broj poginulih na milion stanovnika u Srbiji smanjen za približno 13%, dok je prosečno smanjenje u EU iznosilo oko 15%. Rezultati ukazuju da ostvarenje cilja do 2030. godine nije verovatno bez dodatnih intervencija i sistematskih mera za unapređenje bezbednosti saobraćaja.

KLJUČNE REČI: analiza vremenskih serija, broj poginulih u saobraćaju na milion stanovnika, bezbednost saobraćaja, MINITAB

INTRODUCTION

In the prediction of traffic accidents, in addition to traditional statistical methods, machine learning and deep learning techniques can also be applied. In recent years, increasing attention has been devoted to regression-based time-series models, as evidenced by the substantial number of publications addressing this topic in the scientific literature. Time-series analysis can be applied across a wide range of fields whenever a large number of events are observed over a specified period of time.

Examples include the number of defective products per unit of working time in industrial quality control, the number of stock market transactions per minute, the number of vehicles passing through a particular intersection or road section within a specified time interval, and the number of vehicles parked in a parking facility over a given period. Similarly, time-series methods can be applied to the analysis and prediction of traffic accidents occurring within different time intervals, such as 15 minutes, one hour, 24 hours, one week, one month, one year, three years, five years, or ten years.

Table 1 presents various statistical methods used for the prediction of road traffic accidents. The final three studies Gošić et al. (2022), Derentić et al. (2022), and Micić et al. (2022) present research conducted in the Republic of Serbia.

Table 1 Overview of different statistical methods for predicting road car accidents

Authors	Method
Khasnabis and Lyoo (1989)	Autoregressive Integrated Moving Average (ARIMA)
Bener et al. (2010)	Regression Analysis & Time-Series Data
Commandeur et al. (2013)	Traditional Regression Models (Linear, Generalized Linear & Non-Linear), ARMA-type & DRAG approaches
Mutangi (2015)	Autoregressive Integrated Moving Average (ARIMA)
Darma (2017)	Autoregressive Integrated Moving Average Model, Transfer Function-Noise Model & State-Space Model
Parvareh et al. (2018)	Autoregressive Integrated Moving Average (ARIMA) & Seasonal Autoregressive Integrated Moving Average (SARIMA)
Abdulhafedh (2018)	Poisson, Negative Binomial, Zero-Inflated, Logit and Probit, Neural Networks
Nanga (2019)	Seasonal Autoregressive Integrated Moving Average (SARIMA)

Table 1 (continuation)

Authors	Method
Jalalian (2019)	Autoregressive integrated moving average (ARIMA) & Prophet
Samson and Adewale (2020)	Time-Series Analysis (Quadratic, Growth & Linear)
Jomnonkwao et al. (2020)	Time-Series Analysis, Curve Estimation, Regression Analysis & Path Analysis
Getahun (2021)	Autoregressive Integrated Moving Average (ARIMA)
Vipin and Thekkedath (2021)	The Exploratory Data Analysis & Time-Series Regression
Sumit et al. (2021)	Time series analysis
Kaunitz (2022)	Logistic Regression & Time-Series Analysis
Khasawneh et al. (2022)	Time-Series Analysis
Cai and Di (2023)	Boosting, Autoregressive Integrated Moving Average (ARIMA) & Time-Series Count Data Model,
Gošić et al. (2022)	Chi-Squared Test, Student's t-Test, Linear Regression Analysis & Logarithmic Regression
Deretić et al. (2022)	Seasonal Autoregressive Integrated Moving Average (SARIMA)
Mićić et al. (2022)	Poisson, Negative Binomial, Random Effect Negative Binomial, Zero-Inflated Poisson & Zero-Inflated Negative Binomial Models

RESEARCH METHOD

Reporting on the state of traffic safety represents an integral component of the traffic safety monitoring process, contributing to the establishment and continuous improvement of the traffic safety system and supporting effective traffic safety management within a specific geographical area. In the Republic of Serbia, the development and state of traffic safety can be observed and analysed through five distinct stages, each characterized by specific trends, conditions, and developments.

The first stage covers the period from 1981 to 1990, followed by the second stage from 1991 to 2000 and the third stage from 2001 to 2010. The fourth stage encompasses the period from 2011 to 2020, while the fifth stage covers the period from 2021 to 2030. Each of these stages has its own specific characteristics, reflecting changes in traffic conditions, road safety policies, institutional frameworks, and measures implemented to improve traffic safety.

Improvements in road safety cannot be achieved through the efforts of an individual or a single institution alone. Continuous enhancement of cooperation and coordination among all relevant stakeholders is essential, particularly through the active involvement of academic and research institutions, the private sector, civil society organizations, the media, road traffic accident victims, and their families.

Although the Republic of Serbia, like most countries in the region, has adopted a national road safety strategy, the significance of this document has not been sufficiently promoted. Furthermore, key stakeholders do not always fully recognize or implement its objectives, while the implementation and achievement of the established goals are not systematically monitored. Consequently, the overall results remain unsatisfactory.

In order to improve the current situation, it is necessary for each local community to adopt its own strategic road safety documents, establish ambitious yet achievable objectives, and mobilize all available local resources. Through the continuous implementation of proven and effective measures, local communities can work systematically toward achieving their defined road safety goals, in accordance with the recommendations of Road Safety in Local Communities (2023).

Analysing the state of traffic safety within a specific area or along a particular road section represents an essential task in the field of traffic safety management. Measures and activities aimed at improving the level of traffic safety should be continuously assessed and further developed through systematic analyses, comparisons, and evaluations of the prevailing traffic safety conditions.

Comparative analyses involving appropriate reference areas can contribute significantly to the improvement and optimization of road safety measures and interventions. Average values within the same country for areas with similar characteristics, as well as data from comparable areas in OECD or European Union countries, may be used as reference benchmarks.

Figure 1 Stages of the state of traffic safety in the Republic of Serbia

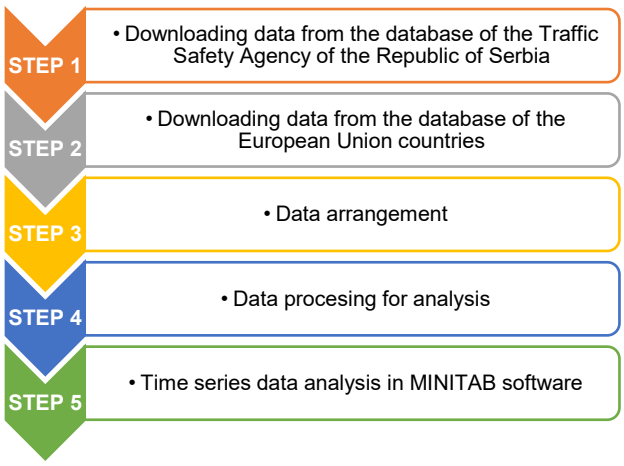

Figure 2 Study procedure

The level of traffic safety can be assessed using both direct and indirect indicators, as well as absolute and relative traffic safety indicators. However, for the purposes of comparative analysis, relative traffic safety indicators are generally considered more appropriate, as they enable meaningful comparisons between areas with different population sizes, traffic volumes, or other relevant characteristics.

$$\text{Road deaths per milion inhabitatnts} = \frac{\text{Road deaths}}{\text{Inhabitants}} \cdot 1\,000\,000 \tag{1}$$

In some countries, road traffic safety analyses take into account not only fatalities but also persons who have sustained slight or serious injuries. To account for differences in the severity of road traffic injuries, appropriate weighting factors are applied. This approach enables the conversion of absolute indicators into composite relative indicators that provide a more comprehensive assessment of the level of road traffic safety. In the Republic of Serbia, for example, Equation (2) is used:

$$\text{PWCR} = \frac{\text{SPI} \cdot \text{WF}_1 + \text{SI} \cdot \text{WF}_2 + \text{D} \cdot \text{WF}_3}{\text{Inhabitants}} \cdot 10\,000 \tag{2}$$

PWCR - public weighted casualty risk
SPI - slightly physically injured
SI - seriously injured

D - dead
WF_1 – weighting factor for slightly physically injured (WF_1=1)
WF_2 – weighting factor for seriously injured (WF_2=13)
WF_3 – weighting factor for dead (WF_3=99)

A direct comparison between the Republic of Serbia and the European Union would only be possible if all EU Member States collected and reported traffic safety data using the same definitions and weighting factors as those applied in the Republic of Serbia. However, this condition is not met, as national definitions of a seriously injured person in road traffic collisions differ among EU Member States. Consequently, a comparison based on injury-severity weighting factors is not methodologically appropriate. Therefore, Eq. (1) is used for the subsequent analysis.

The aim of this study is to analyse historical trends and forecast future trends in road fatalities per million inhabitants using time-series analysis implemented in the MATLAB software environment for the Republic of Serbia and the European Union. The analysis seeks to assess whether the target of reducing public road safety risk by 50%, as defined in the "Improving Global Road Safety" strategy, is likely to be achieved.

RESEARCH DATA

The data used in the first part of the analysis were obtained from the database of the Road Traffic Safety Agency of the Republic of Serbia. The dataset contains information on road fatalities per million inhabitants per year for the period from 2012 to 2022. These data were analysed using the MINITAB statistical software package.

MINITAB is a statistical data analysis software package that provides a range of tools for statistical analysis, including hypothesis testing, regression analysis, and analysis of variance (ANOVA). In this study, time-series models were developed to analyse historical trends and forecast the rate of road traffic fatalities in the Republic of Serbia over the period 2012–2022.

Trend analysis in MINITAB is a time-series forecasting approach used to identify and describe the underlying long-term movement of a variable over time and to generate forecasts for future periods. MINITAB provides several trend models, including the linear, quadratic, exponential growth, and S-curve models. Trend analysis is particularly appropriate when the observations exhibit a relatively consistent trend and do not contain a pronounced seasonal component.

The linear trend model assumes that the variable changes at a relatively constant rate over time. The model is expressed as:

$$Y_t=\beta_0+\beta_1 \cdot t+e_t \tag{3}$$

where Y_t represents the observed value at time t, β_0 is the constant, β_1 represents the average change from one period to the next, and e_t represents the random error. Consequently, a linear model is appropriate when the graphical representation of the time series indicates an approximately straight-line trend.

The quadratic trend model is applied when the time series exhibits curvature and the rate of change is not constant over time. Its general form is:

$$Y_t=\beta_0+\beta_1 \cdot t+\beta_2 \cdot t^2+e_t\,, \tag{4}$$

where the additional t^2 term enables the model to capture a curved trend. Therefore, compared with the linear model, the quadratic model can better represent situations in which the rate of increase or decrease changes throughout the observation period.

The growth curve model, referred to by MINITAB as the exponential growth trend model, is used when the time series demonstrates exponential growth or decline. The model is expressed as:

$$Y_t=\beta_0 \cdot \beta_1^t \cdot e_t \tag{5}$$

Changes in the observed variable are represented in terms of a multiplicative rather than a constant absolute change. This model is therefore suitable for time series in which the rate of change becomes progressively larger or smaller as time increases.

After estimating the selected trend model, MINITAB calculates fitted values and uses the estimated trend equation to obtain forecasts for future time periods. The suitability of different trend models can be assessed by comparing forecasting accuracy measures such as MAPE (Mean Absolute Percentage Error), MAD (Mean Absolute Deviation), and MSD (Mean Squared Deviation). In general, lower values indicate better model performance. However, MINITAB recommends that these numerical measures should not be considered independently, the fitted trend should also be examined graphically, particularly toward the end of the observed time series (Minitab, LLC).

The dataset used in the analysis is presented in Appendix A, Table A1. The data used in the second part of the analysis were obtained from the European Transport Safety Council (2023). The dataset contains information on road fatalities per million inhabitants for 2012 and 2022 for European countries, including the Republic of Serbia. Appendix B, Table B1, presents the ISO country codes and the corresponding values of road fatalities per million inhabitants for 2012 and 2022, which were used in the subsequent analyses.

ANALYSIS OF ROAD DEATHS PER MILLION INHABITANTS IN THE REPUBLIC OF SERBIA

The analysis of road deaths per million inhabitants provides an important basis for assessing the level of road safety and identifying changes in traffic mortality over time. In order to obtain a comprehensive overview of the road safety situation in the Republic of Serbia, the analysis is divided into several periods, allowing both historical trends and future projections to be considered. Particular attention is given to the period from 2012 to 2022, followed by an assessment of the projected trends from 2023 to 2030, while the overall period from 2012 to 2030 is considered in order to identify long-term developments and the expected direction of change in road mortality.

Analysis of road deaths per million inhabitants in Republic of Serbia in period from 2012 to 2022

MINITAB is a statistical data analysis software package that provides a range of tools for conducting statistical analyses, including hypothesis testing, regression analysis, and analysis of variance (ANOVA). The objective of this study is to develop time-series models for analysing historical trends and forecasting the rate of road traffic fatalities in the Republic of Serbia over the period from 2012 to 2022. The dataset used for the analysis is presented in Appendix C, Table C1.

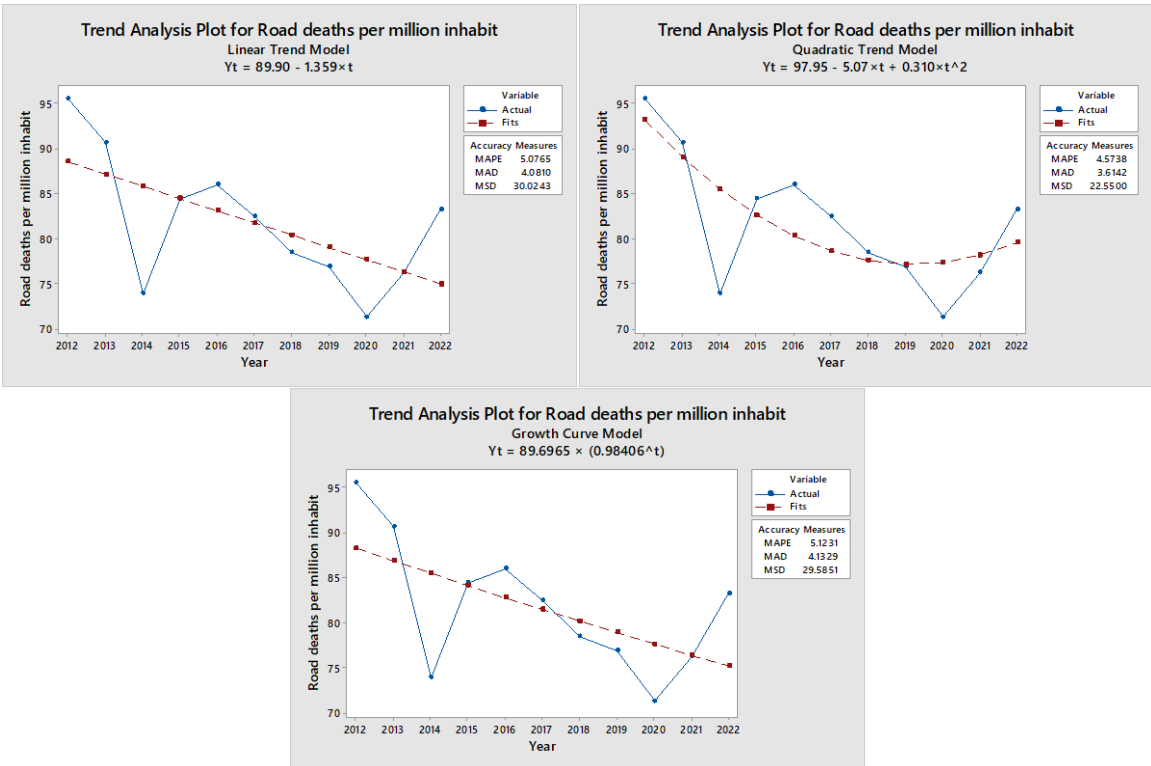

Figure 3 Graph of comparison of the Actual and Predicted Data in period from 2012 to 2022; Linear trend model, Quadratic trend model and Growth curve model, respectively

Following the completion of the time-series analysis, the forecast values generated by the respective models can be compared with the observed values over the ten-year period. As shown in Figure 3, the quadratic trend model

provides the closest fit to the observed data, exhibiting the lowest percentage error among the models considered. Therefore, the quadratic trend model, represented by Equation (6), was identified as the most appropriate model for forecasting road traffic fatalities in the Republic of Serbia for the analysed period from 2012 to 2022.

$$Y_t = 97.75 - 5.07 \cdot t + 0.310 \cdot t^2 \quad (6)$$

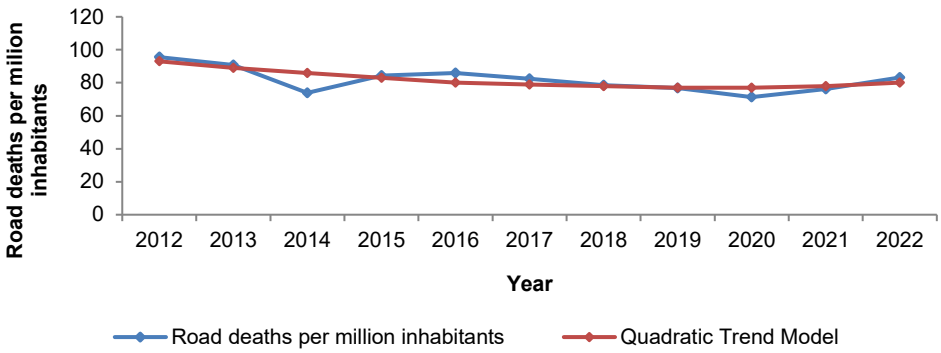

Figure 4 Comparison of road deaths per million inhabitants with the adopted model (quadratic model trend) in Republic of Serbia from 2012 to 2022

Figure 4 shows the comparison of road deaths per million inhabitants with the adopted model (quadratic model trend) in the Republic of Serbia from 2012 to 2022. This model deviates the least from the actual model as it is shown.

Analysis of road deaths per million inhabitants in Republic of Serbia in period from 2023 to 2030

The analysis of road deaths per million inhabitants in the Republic of Serbia in period from 2023 to 2030 was performed by using the Quadratic model Eq. (1) trend which proved to be a reference.

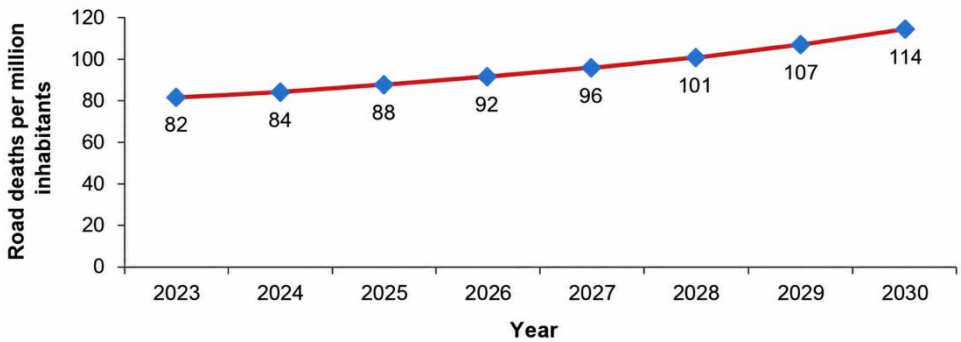

Figure 5 Prediction of road deaths per million inhabitants for the period from 2023 to 2030 using Quadratic model trend

Figure 5 indicates that, according to the quadratic trend model, the number of road fatalities per million inhabitants is projected to increase over the period from 2023 to 2030. This finding is particularly significant for the further analysis of road safety in the Republic of Serbia, which has set the objective of reducing the number of road fatalities per million inhabitants by 50% during the 2021–2030, defined by Decade of Action for Road Safety 2021–2030. The projected upward trend therefore indicates a potential divergence from the established road safety target and highlights the need for further analysis and the implementation of appropriate road safety measures.

Analysis of road deaths per million inhabitants in the Republic of Serbia from 2012 to 2030

This chapter presents an analysis of road fatalities per million inhabitants in the Republic of Serbia for the period from 2012 to 2030. The analysis was conducted using a quadratic trend model. Based on the observed data for the period from 2012 to 2022, forecasts were generated for the period from 2023 to 2030. The purpose of the analysis is to assess whether the target of reducing public road safety risk by 50%, as defined in the Improving Global Road Safety strategy, is likely to be achieved.

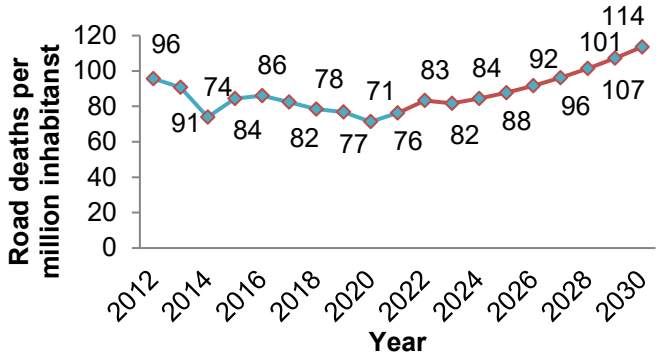

Figure 6 Prediction of road deaths per million inhabitants for the period from 2012 to 2030 using Quadratic model trend

As shown in Figure 6, the quadratic trend model forecasts the number of road fatalities per million inhabitants in the Republic of Serbia for the period from 2012 to 2030. The number of road fatalities per million inhabitants was 96 in 2012 and 83 in 2022, while the model projects a value of 144 fatalities per million inhabitants by 2030. Although a declining trend was observed between 2012 and 2022, the forecast indicates a substantial increase in road fatalities per million inhabitants over the period from 2023 to 2030. This projected trend is highly unfavourable from the perspective of road safety in the Republic of Serbia.

These findings indicate the need for a comprehensive assessment of the current road safety situation, including a detailed analysis of the underlying causes and contributing factors of road traffic accidents. Particular attention should be devoted to the identification of critical risk factors and to the development and implementation of targeted road safety measures and public awareness campaigns aimed at reversing the projected negative trend.

The results also indicate that the objectives established under the previous National Road Traffic Safety Strategy for the period 2015–2020 were not fully achieved. In particular, the planned increase in seat belt use was not attained, with particularly unfavourable results concerning seat belt use in rear seats. The intended reduction in speeding on Serbian roads was likewise not achieved, while the targeted level of child restraint system use remained unmet. Instead of increasing, helmet use among motorcycle riders declined. Furthermore, the planned reduction in driving under the influence of alcohol was not achieved, and the systematic application of road infrastructure safety assessment and improvement tools remained insufficient.

The situation concerning child road traffic injuries is particularly concerning, as the expected reduction in child injuries and the elimination of child fatalities were not achieved. On the contrary, an increase in the number of children killed and injured in road traffic was recorded. These shortcomings highlight the need for more effective implementation, coordination, and systematic monitoring of road safety measures and activities envisaged within the Decade of Action for Road Safety 2021–2030. Continuous monitoring of the implementation and effectiveness of these measures is essential to ensure progress toward the established road safety objectives and to prevent the continuation of the projected adverse trend.

ANALYSIS OF ROAD DEATHS PER MILLION INHABITANTS IN THE EUROPEAN UNION IN 2012 AND 2022

Road fatalities per million inhabitants in the European Union were analyzed for 2012 and 2022 in order to assess the changes achieved during this period, compare the road safety performance of the Republic of Serbia with that of EU Member States, and evaluate Serbia's position relative to the EU average. The data used in the analysis were obtained from the European Transport Safety Council (2023). The dataset, presented in Appendix D, Table D1, contains data on road fatalities per million inhabitants for European countries for the period from 2012 to 2022 and was analyzed using the MINITAB statistical software package.

A separate trend model was developed for each country. The most appropriate model was selected according to the minimum error criterion, with the corresponding results presented in Appendix D, Table D1. Using MINITAB, time-series trend analyses of road fatalities per million inhabitants were performed for the European countries based on the 2012 data, as illustrated in Figure 7.

For the Republic of Serbia, the Growth Curve model was identified as the most appropriate model according to the minimum error criterion. For the EU countries as a whole, the Quadratic Trend model, given by Equation (7), was identified as the most appropriate model based on the same criterion for the 2012 analysis.

$$Y_t = 23.4068 \cdot (1.03875^t) \quad (7)$$

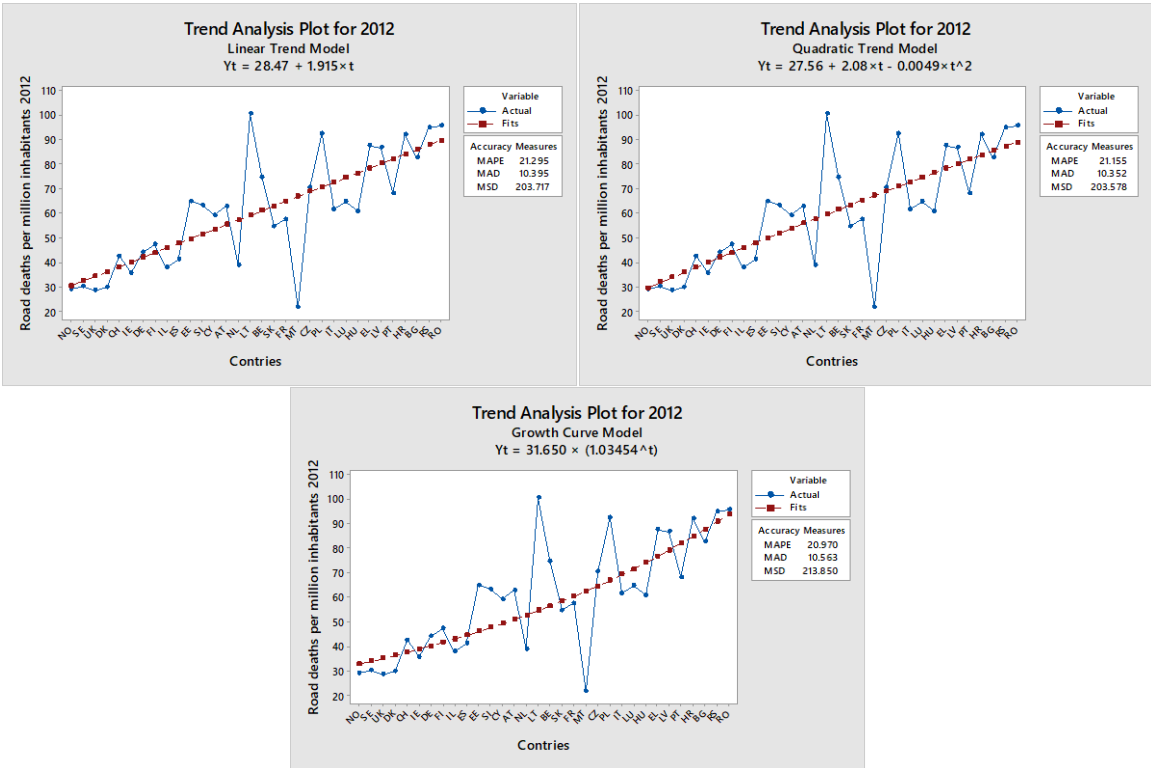

Figure 8 Time series analysis of road deaths per million inhabitants in 2022 in the EU

For 2022, a trend model was likewise selected for each country based on the minimum error criterion. The corresponding results are presented in Appendix E, Table E1. Using the MINITAB statistical software package, time-series trend analyses of road fatalities per million inhabitants for 2022 were performed for the European countries, as shown in Figure 8.

For the Republic of Serbia, no single trend model can be identified as the best model based solely on the minimum error criterion. As shown in Table E1, the Quadratic Trend and Growth Trend models produce the same percentage error. Therefore, neither model can be considered superior to the other according to this criterion alone.

For the comparative analysis of all European Union countries, the Growth Trend model, represented by Equation (8), was selected as the most appropriate model for 2022 based on the minimum percentage error criterion.

$$Y_t = 23.4068 \cdot (1.03875^t) \tag{8}$$

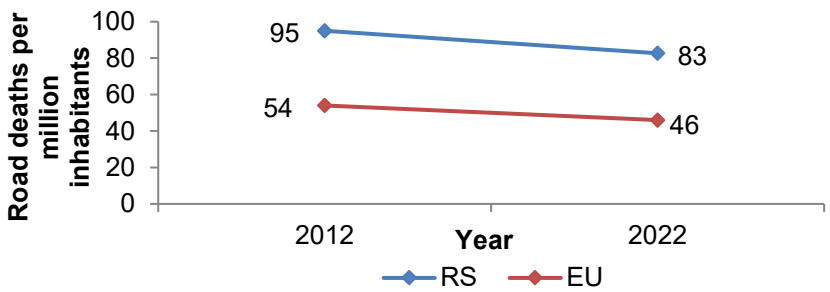

Figure 9 Comparative analysis of the road deaths per million inhabitants of the Republic of Serbia and the European Union for 2012 and 2022

Figure 9 presents a comparative analysis of road fatalities per million inhabitants in the Republic of Serbia and the European Union in 2012 and 2022. Over the ten-year period, the number of road fatalities per million inhabitants decreased by approximately 13% in the Republic of Serbia, while the European Union recorded an average reduction of approximately 15%. These results indicate that, although road safety improved in both the Republic of Serbia and the European Union during the observed period, the overall reduction in road fatalities per million inhabitants was slightly greater at the EU level.

CONCLUSIONS

This paper presents time-series models for analysing and forecasting road fatalities per million inhabitants in the Republic of Serbia and the European Union. The primary objective is to develop a statistical model capable of predicting future trends in road fatalities in the Republic of Serbia and assessing whether the target established under the Decade of Action for Road Safety 2021–2030 will be achieved.

The results indicate that the number of road fatalities per million inhabitants in the Republic of Serbia is projected to increase from 83 in 2022 to 144 by 2030. Consequently, based on the forecasts obtained, the objective of reducing road fatalities by 50% by 2030 is unlikely to be achieved.

The findings also emphasize the importance of addressing the shortcomings identified during the implementation of the previous road safety strategy. Measures and objectives that were not successfully achieved should be given particular attention within the current strategic framework. This requires the systematic organization, implementation, coordination, and continuous monitoring of the measures and activities envisaged under the Decade of action for road safety 2021–2030, with the aim of improving road safety performance and reversing the projected adverse trend.

ACKNOWLEDGMENTS

This work presents the results of research conducted within projects financially supported by the Ministry of Science, Technological Development and Innovation of the Republic of Serbia, under Contract No. 451-03-34/2026-03/200107, dated 5 February 2026.

REFERENCES

Abdulhafedh, A. (2018). Road Crash Prediction Models: Different Statistical Modeling Approaches. *Journal of Transportation Technologies*, 07(02), 190-205. https://doi.org/10.4236/jtts.2017.72014

Bener, A., Hussain, S. J., Al-Malki, M. A., Shotar, M. M., Al-Said, M. F., & Jadaan, K. S. (2010). Road traffic fatalities in Qatar, Jordan and the UAE: Estimates using regression analysis and the relationship with economic growth. *Eastern Mediterranean Health Journal,* 16(3), 318–323.

Road Safety in Local Communities. (2023). 18th International Conference: Road Safety in Local Communities [Conference program]. https://bslz.org/wp-content/uploads/2023/04/BSLZ-2023-program-1.pdf

Cai, B., & Di, Q. (2023). Different forecasting model comparison for near future crash prediction. *Applied Sciences*, 13(2), 759. https://doi.org/10.3390/app13020759

Commandeur, J. J. F., Bijleveld, F. D., Bergel-Hayat, R., Antoniou, C., Yannis, G., & Papadimitriou, E. (2013). On statistical inference in time series analysis of the evolution of road safety. *Accident Analysis & Prevention*, 60, 424–434. https://doi.org/10.1016/j.aap.2012.11.006

Darma, Y. (2017). A time series analysis of road traffic fatalities in Malaysia [Doctoral dissertation, University of Malaya]. University of Malaya Students' Repository. http://studentsrepo.um.edu.my/id/eprint/7961

Deretić, N., Stanimirović, D., Awadh, M. A., Vujanović, N., & Djukić, A. (2022). SARIMA modelling approach for forecasting of traffic accidents. *Sustainability*, 14(8), 4403. https://doi.org/10.3390/su14084403

European Transport Safety Council. (2023). Ranking EU progress on road safety: 17th Road Safety Performance Index report. https://etsc.eu/wp-content/uploads/ETSC-17th-PIN-Annual-Report-DIGITAL-1.pdf

Getahun, K. A. (2021). Time series modeling of road traffic accidents in Amhara Region. *Journal of Big Data*, 8, 102. https://doi.org/10.1186/s40537-021-00493-z

Gošić, A., Stefanović, S., & Mladenović, S. (2022). Statistical analysis of road safety in the Republic of Serbia. *KNOWLEDGE – International Journal*, 49(3), 543–549.

Jalalian, S. (2019). Time series forecasting for road accidents in UK. Towards Data Science. https://towardsdatascience.com/time-series-forecasting-for-road-accidents-in-uk-f940e5970988

Jomnonkwao, S., Uttra, S., & Ratanavaraha, V. (2020). Forecasting road traffic deaths in Thailand: Applications of time-series, curve estimation, multiple linear regression, and path analysis models. *Sustainability*, 12(1), 395. https://doi.org/10.3390/su12010395

Kaunitz, L. (2022). Severity prediction and time-series analysis of vehicle accidents using statistical models [Doctoral dissertation, University of California, Los Angeles]. UCLA eScholarship. https://escholarship.org/uc/item/94f5c7dw

Khasawneh, M. A., Al-Omari, A. A., & Ganam, B. (2022). Forecasting traffic accidents in developing countries using time series analysis. *Jordan Journal of Civil Engineering*, 16(1), 54–70.

Khasnabis, S., & Lyoo, S. H. (1989). Use of time series analysis to forecast truck accidents. *Transportation Research Record*, 1249, 30–36.

Minitab, LLC. (n.d.). Enter your data for Trend Analysis. Minitab Statistical Software. Minitab: Enter your data for Trend Analysis

Mićić, S., Vujadinović, R., Amidžić, G., Damjanović, M., & Matović, B. (2022). Accident frequency prediction model for flat rural roads in Serbia. *Sustainability*, 14(13), 7704. https://doi.org/10.3390/su14137704

Mutangi, K. (2015). Time series analysis of road traffic accidents in Zimbabwe. International Journal of Statistics and Applications, 5(4), 141–149. https://doi.org/10.5923/j.statistics.20150504.02

Nanga, S. (2019). Time series analysis of road accidents in Ghana. *Finance & Management Engineering Journal of Africa*, 1(4), 25–33. https://damaacademia.com/fmeja/

Parvareh, M., Karimi, A., Rezaei, S., Woldemichael, A., Nili, S., Nouri, B., & Esmail Nasab, N. (2018). Assessment and prediction of road accident injuries trend using time-series models in Kurdistan. *Burns & Trauma*, 6, 9. https://doi.org/10.1186/s41038-018-0111-6

Samson, A. O., & Adewale, L. A. (2020). Traffic crashes prediction of states in Nigeria using time series analysis. *Global Journal of Engineering and Technology Advances*, 3(1), 15–26. https://doi.org/10.30574/gjeta.2020.3.1.0024

Sumit, K., Ross, V., Ruiter, R. A. C., Polders, E., Wets, G., & Brijs, K. (2022). An exploration of characteristics and time series forecast of fatal road crashes in Manipal, India. *Sustainability*, 14(5), 2851. https://doi.org/10.3390/su14052851

Vipin, N., & Thekkedath, R. (2021). Road traffic accident mortality analysis based on time of occurrence: Evidence from Kerala, India. *Clinical Epidemiology and Global Health*, 11, 100745. https://doi.org/10.1016/j.cegh.2021.100745

APPENDICES

Appendix A

Table A1 Road deaths per million inhabitants in the Republic of Serbia in period from 2012 to 2022

Year	Road deaths per million inhabitants in the Republic of Serbia
2012	96
2013	91
2014	74
2015	84
2016	86
2017	82
2018	78
2019	77
2020	71
2021	76
2022	83

Appendix B

Table B1 ISO code for European countries and road deaths per million inhabitants in the EU for 2012 and 2022

Country	ISO Code	2012	2022
Austria	AT	63	41
Belgium	BE	75	45
Bulgaria	BG	83	78
Croatia	HR	92	71
Cyprus	CY	59	41
Czech	CZ	71	50
Denmark	DK	30	26
Estonia	EE	65	38
Finland	FI	47	34
France	FR	58	48
Germany	DE	44	33
Greece	EL	88	61
Hungary	HU	61	55
Ireland	IE	36	31
Italy	IT	62	54
Latvia	LV	87	60
Lithuania	LT	100	43
Luxembourg	LU	65	56
Malta	MT	22	50
The Netherlands	NL	39	42
Poland	PL	93	50
Portugal	PT	68	62
Romania	RO	96	86
Slovakia	SK	55	45
Slovenia	SI	63	40
Spain	ES	41	37
Sweden	SE	30	22
United Kingdom	UK	29	26
Israel	IL	38	37
Norway	NO	29	21
Serbia	RS	95	83
Switzerland	CH	43	28

Appendix C

Table C1 Road deaths per million inhabitants in the Republic of Serbia in period from 2012 to 2022

Year	Road deaths per million inhabitants	Linear Trend Model	Quadratic Trend Model	Growth Curve Model	% error (Linear)	% error (Quadratic)	% error (Growth)
2012	96	89	93	88	6.8	2.7	7.9
2013	91	87	89	87	4.1	1.9	4.1
2014	74	86	86	85	-16.4	-16.4	-15.0
2015	84	84	83	84	0.5	1.7	0.5
2016	86	83	80	83	3.5	7.0	3.5
2017	82	82	79	81	0.6	4.2	1.8
2018	78	80	78	80	-1.9	0.6	-1.9
2019	77	79	77	79	-2.7	-0.1	-2.7
2020	71	78	77	78	-9.4	-8.0	-9.4
2021	76	76	78	76	0.3	-2.3	0.3
2022	83	75	80	75	9.9	3.9	9.9

Appendix D

Table D1 Comparison of real data and the data obtained by time series analysis of road deaths per million inhabitants in 2012 in the EU

Country	Real data	Linear T rend Mo del	Quadratic Trend Model	Growth Curve Model	% error (Linear)	% error (Quadratic)	% error (Growth)
NO	29	30	30	33	-3.2	-3.2	-13.5
SE	30	32	32	34	-6.5	-6.5	-13.1
UK	29	34	34	35	-18.8	-18.8	-22.3
DK	30	36	36	36	-20.3	-20.3	-20.3
CH	43	38	38	38	10.8	10.8	10.8
IE	36	40	40	39	-12.5	-12.5	-9.6
DE	44	42	42	40	4.5	4.5	9.1
FI	47	44	44	42	6.8	6.8	11
IL	38	46	46	43	-21.6	-21.6	-13.7
ES	41	48	48	44	-16.5	-16.5	-6.8
EE	65	50	50	46	23	23	29.2
SI	63	51	52	48	19.4	17.8	24.1
CY	59	53	54	49	10.4	8.7	17.2
AT	63	55	56	51	12.5	11	18.9
NL	39	57	58	53	-46.7	-49.3	-36.4
LT	100	59	60	54	41.2	40.2	46.2
BE	75	61	62	56	18.2	16.8	24.9
SK	55	63	63	58	-15	-15	-5.9
FR	58	65	65	60	-12.8	-12.8	-4.1
MT	22	67	67	62	-210.8	-210.8	-187.6
CZ	71	69	69	65	2.3	2.3	8
PL	93	71	71	67	23.4	23.4	27.7
IT	62	73	73	69	-18.3	-18.3	-11.8
LU	65	74	75	72	-14.2	-15.8	-11.1
HU	61	76	76	74	-25.1	-25.1	-21.8
EL	88	78	78	77	10.9	10.9	12
LV	87	80	80	79	7.7	7.7	8.9
PT	68	82	82	82	-20.4	-20.4	-20.4
HR	92	84	84	85	8.6	8.6	7.5
BG	83	86	86	88	-4.1	-4.1	-6.5
RS	95	88	87	91	7.4	8.4	4.2
RO	96	90	89	94	5.9	6.9	1.7

Appendix E

Table E1 Comparison of real data and the data obtained by time series analysis of road deaths per million inhabitants in 2022 in the EU

Country	Real data	Linear Trend Model	Quadratic Trend Model	Growth Curve Model	% error (Linear)	% error (Quadratic)	% error (Growth)
NO	21	20	26	24	6.5	-21.6	-12.2
SE	22	22	26	25	-1.3	-19.7	-15.1
UK	26	23	27	26	11.2	-4.3	-0.4
DK	26	25	28	27	4.7	-6.8	-3
CH	28	27	29	28	2.1	-5.2	-1.5
IE	31	29	29	29	5.9	5.9	5.9
DE	33	30	30	31	10	10	7
FI	34	32	32	32	7	7	7
IL	37	34	33	33	7.1	9.9	9.9
ES	37	35	34	34	5.6	8.3	8.3
EE	38	37	35	36	1.4	6.8	4.1
SI	40	39	37	37	3.3	8.3	8.3

Table E1 (continuation)

Country	Real data	Linear Trend Model	Quadratic Trend Model	Growth Curve Model	% error (Linear)	% error (Quadratic)	% error (Growth)
CY	41	41	38	38	-0.3	7.1	7.1
AT	41	42	39	40	-1.9	5.4	2.9
NL	42	44	41	41	-5	2.1	2.1
LT	43	46	43	43	-7.6	-0.5	-0.5
BE	45	48	44	45	-7	1.9	-0.3
SK	45	49	46	46	-9.1	-2.5	-2.5
FR	48	51	48	48	-6.1	0.1	0.1
MT	50	53	50	50	-6.2	-0.2	-0.2
CZ	50	54	52	52	-7.8	-3.8	-3.8
PL	50	56	54	54	-11.2	-7.2	-7.2
IT	54	58	56	56	-8	-4.3	-4.3
LU	56	60	59	58	-7.6	-5.8	-4
HU	55	61	61	61	-10.5	-10.5	-10.5
EL	61	63	63	63	-3.8	-3.8	-3.8
LV	60	65	66	65	-7.9	-9.6	-7.9
PT	62	67	68	68	-7.5	-9.2	-9.2
HR	71	68	71	70	4.5	0.3	1.7
BG	78	70	74	73	9.8	4.7	6
RS	83	72	76	76	12.9	8	8
RO	86	73	79	79	14.9	7.9	7.9

The 11th International Congress
Motor Vehicles & Motors 2026
Kragujevac, Serbia
October 8th - 9th, 2026

Motor Vehicles & Motors

MVM2026-069
https://doi.org/10.24874/CMVM2026.069
Technical paper

Saša Jovanović[1]
Zorica Đorđević[2]
Danijela Nikolić[3]
Lozica Ivanović[4]
Saša Milojević[5]

A SAW–BASED DECISION SUPPORT MODEL FOR THE SELECTION OF NEW AND USED PASSENGER CARS

ABSTRACT: The selection of a passenger car is a complex decision–making problem involving technical, economic, operational, safety and practical characteristics, together with individual buyer preferences. The problem becomes particularly complex when new and used vehicles of different ages are considered simultaneously. This paper proposes a decision–support model based on the Simple Additive Weighting (SAW) method. Sixteen anonymized SUV/crossover alternatives are considered: four new vehicles and twelve used vehicles divided into approximately three–, six–, and ten–year–old groups. Ten criteria are used, including effective acquisition cost, age, mileage, fuel consumption, maintenance cost, reliability, safety, performance, practicality, and equipment/comfort. Three weighting scenarios represent balanced, economy–oriented, and family/safety-oriented buyers. The results show different preferred alternatives for the three profiles and demonstrate that a recent used vehicle can outperform new alternatives under suitable buyer priorities. Weight–sensitivity and input–data uncertainty analyses further distinguish robustness to preference changes from robustness to uncertain input values.

KEYWORDS: passenger car selection, multicriteria decision–making, SAW, new and used vehicles, vehicle age, buyer preferences

[1] *Dr Saša Jovanović, full prof. Faculty of Engineering University of Kragujevac, Kragujevac 34000, Sestre Janjić 6, Serbia, dviks@kg.ac.rs, https://orcid.org/0000-0001-5916-2483*
[2] *Dr Zorica Djordjević, full prof. Faculty of Engineering University of Kragujevac, Kragujevac 34000, Sestre Janjić 6, Serbia, zoricadj@kg.ac.rs, https://orcid.org/0000-0003-0194-4698*
[3] *Dr Danijela Nikolić, full prof. Faculty of Engineering University of Kragujevac, Kragujevac 34000, Sestre Janjić 6, Serbia, danijelan@kg.ac.rs, https://orcid.org/0000-0003-3267-3974*
[4] *Dr Lozica Ivanović, full prof. Faculty of Engineering University of Kragujevac, Kragujevac 34000, Sestre Janjić 6, Serbia, lozica@kg.ac.rs, https://orcid.org/0000-0002-9503-593X*
[5] *Dr Saša Milojević, prof. assist. Faculty of Engineering University of Kragujevac, Kragujevac 34000, Sestre Janjić 6, Serbia, sasa.milojevic@kg.ac.rs, https://orcid.org/0000-0003-0569-047X*

SAW MODEL PODRŠKE ODLUČIVANJU ZA IZBOR NOVIH I UPOTREBLJAVANIH PUTNIČKIH AUTOMOBILA

REZIME: Izbor putničkog automobila predstavlja složen problem odlučivanja koji obuhvata tehničke, ekonomske, eksploatacione, bezbednosne i praktične karakteristike, kao i individualne preferencije kupca. Problem je posebno složen kada se istovremeno razmatraju nova i polovna vozila različite starosti. U radu je predložen model podrške odlučivanju zasnovan na metodi Simple Additive Weighting (SAW). Razmatrano je 16 anonimizovanih SUV/crossover alternativa: četiri nova i dvanaest polovnih vozila podeljenih u grupe starosti približno tri, šest i deset godina. Ocena je izvršena prema deset kriterijuma, uz tri scenarija pondera koji predstavljaju uravnoteženog, ekonomično orijentisanog i porodično/bezbednosno orijentisanog kupca. Rezultati pokazuju da se optimalna alternativa menja sa prioritetima kupca, kao i da relativno novo polovno vozilo može nadmašiti nova vozila. Analize osetljivosti pondera i nesigurnosti ulaznih podataka dodatno ukazuju na razliku između stabilnosti prema preferencijama i stabilnosti prema kvalitetu ulaznih podataka.

KLJUČNE REČI: izbor putničkog automobila, višekriterijumsko odlučivanje, SAW, nova i upotrebljavana vozila, starost vozila, preferencije kupca

INTRODUCTION

The selection of a passenger car is a multicriteria decision problem in which purchase price must be considered together with vehicle age, mileage, fuel consumption, maintenance requirements, reliability, safety, performance, practicality, and equipment. The importance of these attributes differs among buyers: a cost–conscious buyer may prioritize acquisition and operating costs, while another buyer may emphasize safety, reliability, practicality, or comfort.

The decision becomes more complex when the choice is not restricted to new vehicles. Within a similar budget, a buyer may simultaneously consider a new vehicle with modest equipment, a more extensively equipped recent used vehicle, or an older vehicle at a substantially lower price. The lower price of an older vehicle can be accompanied by higher mileage, maintenance requirements, reduced reliability, or technological obsolescence, whereas a recent used vehicle may offer higher performance or equipment at a competitive price.

Multicriteria decision-making (MCDM) methods provide a systematic framework for such problems. Byun (2001) applied the Analytic Hierarchy Process to automobile purchase model selection, while Raut et al. (2011) and Sakthivel et al. (2013) introduced fuzzy, hybrid, and integrated approaches. Ulkhaq et al. (2018) also applied an AHP–TOPSIS combination to car selection. More recent research has increasingly focused on electric–vehicle selection, including combinations of subjective and objective weighting and ranking methods, as demonstrated by Grdinić-Rakonjac and Lučić (2025), Lučić and Grdinić–Rakonjac (2025), Tian et al. (2023), and Ziemba et al. (2024). Simple methods such as SAW remain attractive when transparency and direct interpretation are important.

Despite the substantial literature on vehicle selection, many published models consider relatively homogeneous sets of alternatives, particularly new cars or electric vehicles. Comparatively less attention has been devoted to a realistic purchasing situation in which new and used vehicles of substantially different ages compete directly in the same decision matrix. Introducing used vehicles adds decision dimensions such as age, accumulated mileage, maintenance requirements, and breakdown reliability.

Furthermore, the concept of the “best” passenger car cannot be separated from buyer preferences. A ranking obtained using one fixed set of criterion weights represents only one preference structure. Changes in the relative importance of economic, technical, safety, and practical characteristics may result in a different preferred alternative. Accordingly, this study develops a transparent SAW–based model for the simultaneous evaluation of new and used passenger cars belonging to different age groups. Sixteen anonymized alternatives are assessed according to ten criteria under three buyer profiles. The main contribution is not the identification of a universally best vehicle, but the explicit analysis of trade–offs between acquisition cost, age, mileage and other relevant characteristics, together with an assessment of ranking robustness.

METHODOLOGY

The proposed decision-support model includes selection of vehicle alternatives, definition and quantification of evaluation criteria, development of buyer–specific weighting scenarios, SAW ranking, and robustness assessment through weight sensitivity and input–data uncertainty analyses.

SAW Method

Let $A_i (i = 1, \dots, m)$ denote the vehicle alternatives and $C_j (j = 1, \dots, n)$ the evaluation criteria. The decision matrix is $X = [x_{ij}]$, where x_{ij} represents the performance of alternative A_i according to criterion C_j. Since the criteria have different units and optimization directions, min–max normalization was applied. For benefit (MAX) criteria, for which higher values are preferred, Eq. (1) was used, whereas cost (MIN) criteria, for which lower values are preferred, were normalized according to Eq. (2):

$$r_{ij} = (x_{ij} - x_{j,min})/(x_{j,max} - x_{j,min}), \text{ for benefit (MAX) criteria} \quad (1)$$

$$r_{ij} = (x_{j,max} - x_{ij})/(x_{j,max} - x_{j,min}), \text{ for benefit (MIN) criteria} \quad (2)$$

The overall SAW score for alternative A_i and buyer profile p was calculated as:

$$S_i(P) = \sum_{j=1}^{n} w_j(P) \cdot r_{ij}, \quad w_j(P) = 1 \quad (3)$$

Where are:

- S_i – The overall score of the *i–th* alternative.
- P – If it denotes a specific alternative (e.g., a passenger car–P).
- w_j – The weighting coefficient of the criterion.
- r_{ij} – The normalized value of the alternative with respect to the criterion.
- n – The number of criteria.

Alternatives were ranked in descending order of $S_i(P)$. The decision matrix remained unchanged for all buyer profiles; only criterion weights were varied.

Vehicle Alternatives

The case study comprises 16 SUV/crossover alternatives divided into four age groups: four new vehicles (2026), four approximately three–year–old vehicles (2023), four approximately six–year–old vehicles (2020), and four approximately ten–year–old vehicles (2016). Petrol, diesel, HEV and MHEV powertrains were included; battery–electric vehicles were excluded. The maximum acquisition–price threshold during selection was approximately EUR 35,000. Used vehicles with reported substantial existing damage capable of materially affecting the advertised price were excluded.

To avoid brand–related perceptions, the alternatives are anonymized as V1–V16. Exact vehicle identities, configurations and sources were retained in the internal research database for traceability.

Evaluation Criteria

The selection of new and used passenger cars requires the consideration of several technical, economic, operational, and environmental factors. Therefore, a set of evaluation criteria was defined to enable a comprehensive and systematic assessment of the available alternatives. The selected evaluation criteria are presented in Table 1.

Effective acquisition cost (C_1) includes the selling price and any immediate registration expenditure required after purchase. Vehicle age (C_2) and mileage (C_3) were retained separately because vehicles of the same age can have substantially different usage histories. Fuel consumption (C_4) was expressed in L/100 km, using harmonized values where different certification procedures required improved comparability, as reported by Tsokolis et al. (2016). Maintenance cost (C_5) represents standardized annual workshop/maintenance expenditure, primarily based on data provided by ADAC (2026a); technically matched proxy variants were used where an exact configuration was unavailable.

Table 1 Evaluation criteria considered in the decision–making process

Criterion	Description	Unit/scale	Type
C_1	Effective acquisition cost	EUR	MIN
C_2	Vehicle age	years	MIN
C_3	Mileage	km	MIN
C_4	Fuel consumption	L/100 km	MIN
C_5	Standardized maintenance cost	EUR/year	MIN
C_6	Breakdown reliability	0–100	MAX
C_7	Safety	0–100	MAX
C_8	Performance	0–100	MAX
C_9	Practicality	0–100	MAX
C_{10}	Equipment and comfort	0–100	MAX

Breakdown reliability (C_6) was primarily derived from the ADAC breakdown statistics, as reported by ADAC (2026b). The original breakdown frequency was transformed into a benefit-oriented 0–100 score, as shown in Equation (4).

$$C_{6i} = 100 \cdot (B_{max} - B_i)/(B_{max} - B_{min}) \tag{4}$$

Where are:

- C_{6i} – The normalized value of the 6th criterion for the i-th alternative.
- 6 – Denotes the ordinal number of the criterion.
- i – Denotes the alternative (vehicle).

Safety (C_7) was calculated as the arithmetic mean of the four Euro NCAP domains, as defined by the European New Car Assessment Programme (n.d.): Adult Occupant Protection (AOP), Child Occupant Protection (COP), Vulnerable Road Users (VRU), and Safety Assist (SA), Equation (5).

$$C_{7i} = (AOP_i + COP_i + VRU_i + SA_i)/4 \tag{5}$$

Performance (C_8) combines normalized 0–100 km/h acceleration and specific power with equal weighting, whereas practicality (C_9) combines normalized luggage volume and payload. Equipment and comfort (C_{10}) use a ten–feature binary checklist, with 10 points for each confirmed feature:

$$C_{8i} = 0.50 \cdot A_i^* + 0.50 \cdot SP_i^* \tag{6}$$

$$C_{9i} = 0.70 \cdot L_i^* + 0.30 \cdot PL_i^* \tag{7}$$

$$C_{10i} = 10 \cdot \sum_k e_{ik} \tag{8}$$

Where are:

- A_i^* – The normalized value of A_i.
- SP_i^* – The normalized value of $S_i(P)$.
- L_i^* – The normalized value of indicator L for the i–th alternative.
- PL_i^* – The normalized value of indicator PL for the i–th alternative.
- $(0.50, 0.70 \text{ and } 0.30)$ – The weighting coefficients.

For used vehicles, a conservative confirmed–equipment–only principle was applied. Where exact configuration–specific data for $C_5 - C_{10}$ were unavailable, technically matched proxy or, where necessary, imputed values were used and recorded as such.

Buyer Profiles and Criterion Weights

Three scenario–based profiles were considered: P1–balanced, P2–economy–oriented, and P3–family/safety–oriented. The weights are predefined preference scenarios rather than consumer–survey–derived values.

Table 2 Evaluation criteria considered in the decision–making process

Criterion	P1 Balanced	P2 Economy	P3 Family/Safety
C1	0.1	0.2	0.1
C2	0.1	0.07	0.07
C3	0.1	0.1	0.08
C4	0.1	0.18	0.06
C5	0.1	0.18	0.07

Table 2 (continuation)

C6	0.1	0.12	0.15
C7	0.1	0.07	0.22
C8	0.1	0.03	0.04
C9	0.1	0.03	0.13
C10	0.1	0.02	0.08
Σ	1	1	1

Sensitivity and Input–Data Uncertainty Analysis

Each criterion weight was independently varied by $\pm 20\%$, while the remaining nine weights were proportionally rescaled to maintain their sum equal to one. Including the baseline case, 21 scenarios were evaluated for each buyer profile (63 SAW calculations). Selected uncertain inputs were stress-tested separately, distinguishing preference uncertainty from uncertainty in individual decision–matrix values.

DECISION MATRIX AND CASE STUDY

Market and technical data were collected from official manufacturer specifications, standardized vehicle databases and testing organizations, and actual used–vehicle advertisements during 2026. The resulting matrix is divided into cost and benefit criteria for readability, Table 3 and 4.

Table 3 Decision matrix – cost criteria

Alt.	C_1, **EUR**	C_2, **y**	C_3, **km**	C_4, **L/100 km**	C_5, **EUR/y**
V1	27,322	0	0	6.80	1,020
V2	29,832	0	0	6.35	888
V3	34,233	0	0	4.90	912
V4	28,063	0	0	6.50	1,116
V5	26,500	3	73,266	6.70	1,464
V6	23,262	3	111,181	5.30	1,416
V7	20,304	3	148,485	5.40	1,740
V8	28,044	3	152,000	5.50	1,164
V9	26,500	6	180,000	7.10	1,716
V10	27,027	6	139,563	5.80	1,140
V11	30,262	6	102,261	6.10	1,872
V12	16,999	6	229,000	5.50	1,716
V13	12,800	10	214,000	7.38	1,800
V14	15,558	10	232,000	5.88	1,080
V15	12,800	10	146,300	7.50	1,464
V16	15,000	10	248,376	6.00	1,488
Type	MIN	MIN	MIN	MIN	MIN

Table 4 Decision matrix – benefit criteria

Alt.	C_6	C_7	C_8	C_9	C_{10}
V1	93.16	77.25	34.91	80.33	70
V2	98.05	75.75	56.40	41.87	50
V3	75.59*	84.25	39.10	29.48	60
V4	82.81	86.75	30.15	33.94	50
V5	93.16	77.25	74.02	73.74	100
V6	82.81	86.75	80.50	33.94	60
V7	100.00	74.00	0.00	36.97	80
V8	98.83	80.00	34.65	71.77	30
V9	83.01	73.50	68.71	100.00	100
V10	0.00	85.50	97.22	42.32	100
V11	93.16	89.00	61.09	32.05	60
V12	86.72	80.00	36.38	79.05	40
V13	69.92	78.25	55.91	43.56	70
V14	39.84	75.75	29.42	54.41	80
V15	58.59	77.50	4.87	38.92	70
V16	79.30	80.00	41.24	80.78	20
Type	MAX	MAX	MAX	MAX	MAX

** V3 reliability is based on an imputed baseline value and is separately examined in the uncertainty analysis.*

RESULTS AND DISCUSSION

Application of the SAW method produced three rankings of the same 16 alternatives. The preferred vehicle changes with the priorities assigned to the criteria; no alternative is universally optimal for all profiles.

Ranking Results for Different Buyer Profiles

The ranking results for the different buyer profiles are presented in Figure 1, which compares the SAW scores of the leading alternatives and highlights the differences in vehicle preferences among the considered buyer profiles.

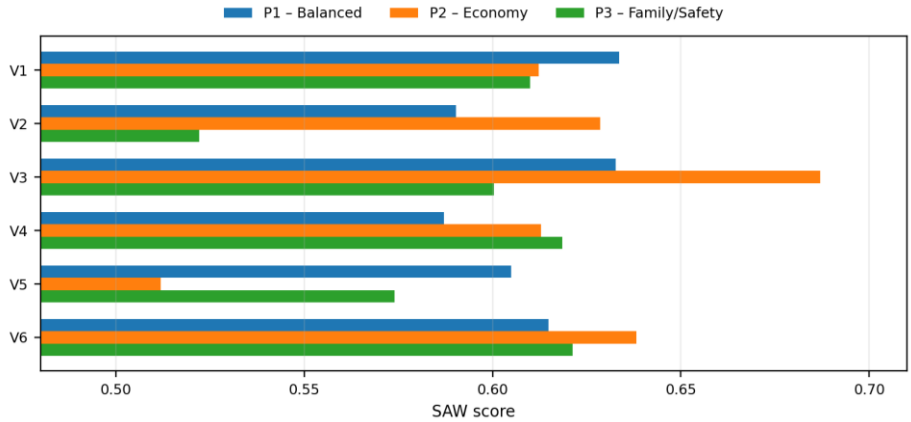

Figure 1 SAW scores of the leading alternatives for different buyer profiles

For P1, V1 achieved the highest score (0.6335), closely followed by V3 (0.6327) and V6 (0.6148). The difference between V1 and V3 is only 0.0008; therefore, these two alternatives should be regarded as highly competitive rather than interpreting first position as clear superiority.

For P2, V3 becomes the preferred alternative (0.6869), followed by V6 (0.6383) and V2 (0.6286). The relatively high acquisition cost of V3 is compensated by favorable fuel consumption, maintenance cost, age, and mileage, which receive considerable importance under this profile.

For P3, V6 achieves the highest score (0.6212), followed very closely by V4 (0.6185), while V1 ranks third (0.6100). Unlike the winners of P1 and P2, V6 is a three–year–old used vehicle. Thus, a recent used vehicle can outperform new alternatives when disadvantages related to age and mileage are compensated by favorable performance in criteria important to the buyer.

V1, V3, and V6 appear among the three highest–ranked alternatives under all profiles. The model therefore identifies a relatively stable group of competitive alternatives, while the final preference within this group depends on buyer priorities.

Influence of Vehicle Age and Buyer Preferences

Vehicle age alone does not determine attractiveness. New vehicles benefit from zero age and mileage and generally favorable maintenance characteristics, but require comparatively high acquisition expenditure. Recent used vehicles can compensate for age and mileage through lower purchase prices and favorable safety, reliability, performance, practicality, or equipment characteristics.

The result for V6 is illustrative: despite being approximately three years old, it ranks third for P1, second for P2, and first for P3. Conversely, the approximately ten–year–old alternatives generally occupy lower positions. Their price advantage is insufficient to compensate simultaneously for age, mileage and, depending on the vehicle, less favorable maintenance, reliability, consumption, performance, or equipment values.

Sensitivity Analysis

Ranking robustness was evaluated by independently varying each criterion weight by $\pm 20\%$ while proportionally rescaling the remaining weights. The main results are summarized in Table 5.

P2 exhibits the highest robustness: V3 remains first in all 21 scenarios. In P1, V1 retains first position in 13 scenarios (61.9%), while V3 becomes preferred in eight; however, V1 never falls below second place. This is consistent with

the very small baseline difference between V1 and V3 and indicates sensitivity of the order of two close competitors rather than a fundamental change in the preferred group.

Table 5 Summary of the weight sensitivity analysis

Profile	Baseline Winner	Winner Retained	Retention, %	Different Winners	Rank Range
P1–Balanced	V1	13/21	61.9	2	1-2
P2–Economy	V3	21/21	100.0	1	1-1
P3–Family/Safety	V6	13/21	61.9	3	1-2

A similar pattern occurs for P3. V6 remains first in 13 scenarios (61.9%), V4 becomes first in six, and V1 in two. V6 nevertheless remains first or second in all scenarios. These findings distinguish winner stability from leading–group stability: a change in first position does not necessarily imply an unstable decision model when the same small group remains dominant.

Input–Data Uncertainty and Limitations

Weight sensitivity does not account for uncertainty in decision–matrix values. This issue is relevant because exact model–year, engine, transmission, drivetrain and equipment data are not always available for every used vehicle. Technically matched proxy values were therefore used where necessary and explicitly identified.

The most important case concerns V3 reliability. A directly corresponding breakdown statistic was unavailable, so the baseline C6 value was imputed. In a separate stress test, the V3 reliability score was varied from 0–100. At the baseline score of 75.59, V3 ranks second for P1, first for P2 and fourth for P3. At substantially lower reliability scores, V3 loses first position under P2 and V6 becomes preferred; at very high assumed reliability, V3 can become preferred under all three profiles.

Thus, V3 is fully stable under the P2 weight–sensitivity scenarios but not unconditionally robust to uncertainty in its reliability input. Preference uncertainty and data uncertainty should therefore be interpreted separately.

A second stress test examined the V10 maintenance–cost proxy at EUR 1,140, 1,428 and 1,632 per year. These changes affected the individual score and rank of V10 but did not change the preferred alternative for any profile. This uncertainty is therefore less consequential for the main conclusions.

Discussion of the Main Findings

The comparison of the three profiles supports the central assumption of the proposed model: the “best vehicle” is conditional on the buyer’s preference structure. The same objective vehicle characteristics produce different preferred alternatives when criterion importance changes. This finding is consistent with the general rationale of MCDM-based vehicle-selection studies. Byun (2001), Raut et al. (2011), Sakthivel et al. (2013), Ulkhaq et al. (2018), Tian et al. (2023), Grdinić–Rakonjac and Lučić (2025), and Ziemba et al. (2024) have demonstrated the applicability of MCDM approaches to vehicle selection. However, the present case study extends the decision setting by allowing new and used vehicles of substantially different ages to compete directly.

The results also support retaining age and mileage as separate criteria. Alternatives within the same age group exhibit substantial differences in accumulated mileage. Similarly, maintenance cost and reliability provide different information: standardized maintenance expenditure does not necessarily correspond directly to breakdown frequency. Keeping these dimensions separate gives a more differentiated representation of used–vehicle ownership characteristics.

The model does not systematically favor new or used vehicles. Two new alternatives lead P1 and P2, while a three-year-old used alternative leads P3. At the same time, the oldest group generally remains outside the leading positions despite substantially lower acquisition prices. This suggests that price advantages alone are insufficient when age, mileage, ownership–related characteristics, safety, performance, practicality, and comfort are evaluated jointly.

Several limitations should be acknowledged. First, some C5–C10 values required technically matched proxies rather than exact configuration–specific observations. Second, C10 uses a conservative confirmed–equipment–only principle; an unreported feature was not assumed to be present, which may understate equipment scores for sparsely documented used vehicles. Third, Euro NCAP protocols evolve over time, so the C7 composite is transparent but not fully time–harmonized across vehicle generations. Finally, buyer–profile weights are scenario–based rather than survey–derived.

These limitations do not invalidate the model but define the appropriate interpretation of its results. SAW scores should be viewed as transparent decision–support indicators rather than exact measures of absolute vehicle

superiority. The practical value of the approach lies in structuring a complex purchasing problem, making trade–offs explicit, and showing how the preferred solution changes with buyer priorities and uncertain inputs.

For practical implementation, the internal database should therefore be maintained together with metadata describing the source and confidence level of each input. This is particularly important when the model is updated with new advertisements, model years, or reliability statistics, because the ranking may change not only due to market prices but also due to improved data quality.

CONCLUSIONS

This paper proposed a SAW–based multicriteria decision–support model for the simultaneous selection of new and used passenger cars belonging to different age groups. Sixteen anonymized alternatives were evaluated according to ten economic, age/use–related, operational, safety, performance, and practical criteria under three buyer profiles. Different alternatives achieved the highest rank for the three profiles: V1 for the balanced profile, V3 for the economy–oriented profile, and V6 for the family/safety–oriented profile. The fact that V6 is a three–year–old used vehicle demonstrates that a used vehicle may outperform new alternatives when its age and mileage disadvantages are compensated by favorable values of other criteria. Conversely, the generally lower positions of the oldest vehicles show that a low acquisition price alone is not sufficient to offset disadvantages associated with age, mileage, operating characteristics, maintenance, reliability, and other attributes.

Weight sensitivity showed that P2 is highly robust, whereas the exact first position in P1 and P3 changes under several $\pm 20\%$ perturbations. Nevertheless, the baseline winners remain within the top two in all tested scenarios. Input–data stress tests further showed that robustness to weight changes does not necessarily imply robustness to uncertain data, particularly when an uncertain value belongs to a highly ranked alternative.

The main advantage of the proposed approach is not identification of a universally optimal car, but transparent examination of how the preferred alternative changes with buyer priorities. Future research should include empirically elicited buyer weights, comparison with additional MCDM methods, and a more comprehensive treatment of input uncertainty and different powertrain and operating conditions.

ACKNOWLEDGMENTS

This research was performed as a part of activities within the projects 451–03–33/2026–03/200107 and 451–03–34/2026–03/200107, supported by the Republic of Serbia, Ministry of Science, Technological Development and Innovation.

REFERENCES

Allgemeiner Deutscher Automobil-Club e.V. (ADAC). (2026). ADAC Pannenstatistik 2026: Die Gewinner und Verlierer. https://www.adac.de/rund-ums-fahrzeug/unfall-schaden-panne/adac-pannenstatistik-2026/

Allgemeiner Deutscher Automobil-Club e.V. (ADAC). (2026). Übersicht: Autokosten aller Modelle von A bis Z. https://www.adac.de/rund-ums-fahrzeug/auto-kaufen-verkaufen/autokosten/uebersicht/

Byun, D. H. (2001). The AHP approach for selecting an automobile purchase model. *Information & Management*, 38(5), 289–297. https://doi.org/10.1016/S0378-7206(00)00071-9

European New Car Assessment Programme. (n.d.). Vehicle safety ratings and domain scores. https://www.euroncap.com/en/ratings-rewards/

Grdinić-Rakonjac, M., & Lučić, M. (2025). Electric vehicle selection with easy applicable MCDM methods. *Transportation Research Procedia*, 90, 782–789. https://doi.org/10.1016/j.trpro.2025.06.079

Lučić, M., & Grdinić-Rakonjac, M. (2025). Defining a new set of criteria for electric vehicle selection. *Transportation Research Procedia*, 83, 569–576. https://doi.org/10.1016/j.trpro.2025.03.027

Raut, R. D., Bhasin, H. V., & Kamble, S. S. (2011). Multi-criteria decision-making for automobile purchase using an integrated analytical quality fuzzy (AQF) technique. *International Journal of Services and Operations Management*, 10(2), 136–167. https://doi.org/10.1504/IJSOM.2011.042515

Sakthivel, G., Ilangkumaran, M., & Gaikwad, A. (2013). A hybrid MCDM approach for evaluating an automobile purchase model. *International Journal of Information and Decision Sciences*, 5(1), 50–85. https://doi.org/10.1504/IJIDS.2013.052017

Tian, Z. P., Liang, H. M., Nie, R. X., Wang, X. K., & Wang, J. Q. (2023). Data-driven multi-criteria decision support method for electric vehicle selection. *Computers & Industrial Engineering*, 177, 109061. https://doi.org/10.1016/j.cie.2023.109061

Tsokolis, D., Tsiakmakis, S., Dimaratos, A., Fontaras, G., Pistikopoulos, P., Ciuffo, B., & Samaras, Z. (2016). Fuel consumption and CO_2 emissions of passenger cars over the New Worldwide Harmonized Test Protocol. *Applied Energy*, 179, 1152–1165. https://doi.org/10.1016/j.apenergy.2016.07.091

Ulkhaq, M. M., Wijayanti, W. R., Zain, M. S., Baskara, E., & Leonita, W. (2018). Combining the AHP and TOPSIS to evaluate car selection. In *2018 2nd International Conference on High Performance Compilation, Computing and Communications (HP3C)* (pp. 112–117). https://doi.org/10.1145/3195612.3195628

Ziemba, P., Kannchen, M., & Borawski, M. (2024). Selection of the family electric car based on objective and subjective criteria–analysis of a case study of Polish consumers. *Energies, 17*(6), 1347. https://doi.org/10.3390/en17061347

9788663351325